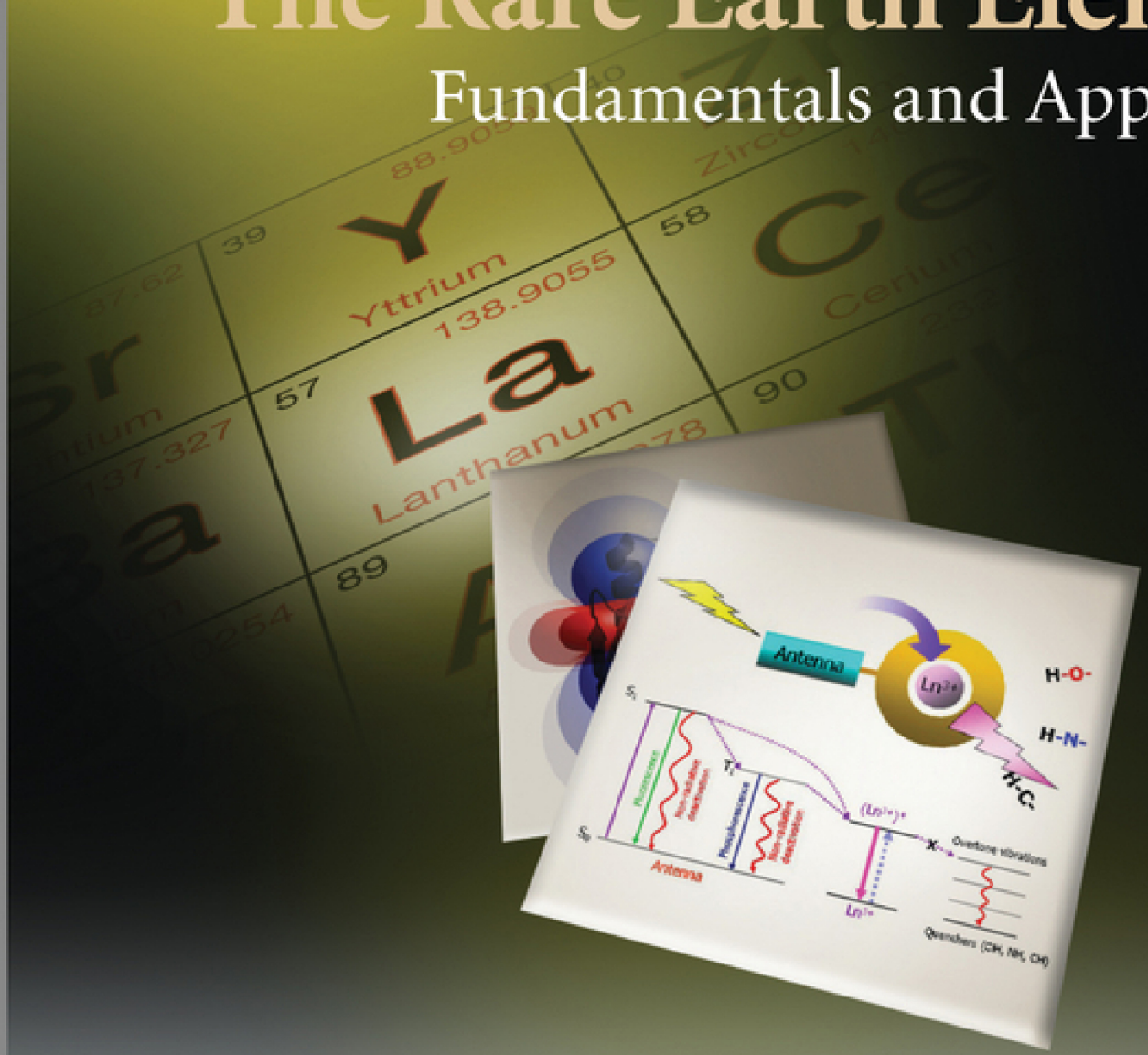
Editor
David A. Atwood

The Rare Earth Elements

Fundamentals and Applications



WILEY

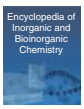
Encyclopedia of Inorganic and Bioinorganic Chemistry

Visit the online Encyclopedia of Inorganic and Bioinorganic Chemistry at
www.wileyonlinelibrary.com/ref/eibc

THE RARE EARTH ELEMENTS:

Fundamentals and Applications

EIBC Books



Application of Physical Methods to Inorganic and Bioinorganic Chemistry
Edited by Robert A. Scott and Charles M. Lukehart
ISBN 978-0-470-03217-6

Nanomaterials: Inorganic and Bioinorganic Perspectives
Edited by Charles M. Lukehart and Robert A. Scott
ISBN 978-0-470-51644-7

Computational Inorganic and Bioinorganic Chemistry
Edited by Edward I. Solomon, R. Bruce King and Robert A. Scott
ISBN 978-0-470-69997-3

Radionuclides in the Environment
Edited by David A. Atwood
ISBN 978-0-470-71434-8

Energy Production and Storage: Inorganic Chemical Strategies for a Warming World
Edited by Robert H. Crabtree
ISBN 978-0-470-74986-9

The Rare Earth Elements: Fundamentals and Applications
Edited by David A. Atwood
ISBN 978-1-119-95097-4

Forthcoming

Metals in Cells
Edited by Valeria Culotta and Robert A. Scott
ISBN 978-1-119-95323-4

Metal-Organic Frameworks Materials
Edited by Leonard R. MacGillivray and Charles M. Lukehart
ISBN 978-1-119-95289-3

Encyclopedia of Inorganic and Bioinorganic Chemistry

The Encyclopedia of Inorganic and Bioinorganic Chemistry (EIBC) was created as an online product in 2012 as a merger of the Encyclopedia of Inorganic Chemistry (which published online in 2006) and the Handbook of Metalloproteins (which published online in 2006). The resulting combination proves to be the defining reference work in the field of inorganic and bioinorganic chemistry. The online edition is regularly updated and expanded. For information see:

www.wileyonlinelibrary.com/ref/eibc

THE RARE EARTH ELEMENTS:

Fundamentals and Applications

Editor

David A. Atwood

University of Kentucky, Lexington, KY, USA



WILEY

This edition first published 2012
© 2012 John Wiley & Sons Ltd

Registered office

John Wiley & Sons Ltd, The Atrium, Southern Gate, Chichester, West Sussex, PO19 8SQ, United Kingdom

For details of our global editorial offices, for customer services and for information about how to apply for permission to reuse the copyright material in this book please see our website at www.wiley.com.

The right of the authors to be identified as the authors of this work has been asserted in accordance with the Copyright, Designs and Patents Act 1988.

All rights reserved. No part of this publication may be reproduced, stored in a retrieval system, or transmitted, in any form or by any means, electronic, mechanical, photocopying, recording or otherwise, except as permitted by the UK Copyright, Designs and Patents Act 1988, without the prior permission of the publisher.

Wiley also publishes its books in a variety of electronic formats. Some content that appears in print may not be available in electronic books.

Designations used by companies to distinguish their products are often claimed as trademarks. All brand names and product names used in this book are trade names, service marks, trademarks or registered trademarks of their respective owners. The publisher is not associated with any product or vendor mentioned in this book. This publication is designed to provide accurate and authoritative information in regard to the subject matter covered. It is sold on the understanding that the publisher is not engaged in rendering professional services. If professional advice or other expert assistance is required, the services of a competent professional should be sought.

Front Cover image credit:
This figure was published in: Uh H. and Petoud S. Novel antennae for the sensitization of near infrared luminescent lanthanide cations. C. R. Chimie 13 (2010) 668–680. Copyright © 2010 Académie des sciences. Published by Elsevier Masson SAS. All rights reserved.

A catalogue record for this book is available from the British Library.

ISBN-13: 978-1-119-95097-4

Set in 9½ / 11½ pt TimesNewRomanPS by Laserwords (Private) Limited, Chennai, India.
Printed and bound in Singapore by Markono Print Media Pte Ltd.

Encyclopedia of Inorganic and Bioinorganic Chemistry

Editorial Board

Editor-in-Chief

Robert A. Scott
University of Georgia, Athens, GA, USA

Section Editors

David A. Atwood
University of Kentucky, Lexington, KY, USA

Timothy P. Hanusa
Vanderbilt University, Nashville, TN, USA

Charles M. Lukehart
Vanderbilt University, Nashville, TN, USA

Albrecht Messerschmidt
Max-Planck-Institute für Biochemie, Martinsried, Germany

Robert A. Scott
University of Georgia, Athens, GA, USA

Editors-in-Chief Emeritus & Senior Advisors

Robert H. Crabtree
Yale University, New Haven, CT, USA

R. Bruce King
University of Georgia, Athens, GA, USA

International Advisory Board

Wolfram Bode
Martinsried, Germany

Michael Bruce
Adelaide, Australia

Tristram Chivers
Calgary, Canada

Mirek Cygler
Saskatchewan, Canada

Marcetta Darensbourg
TX, USA

Michel Ephritikhine
Gif-sur-Yvette, France

Robert Huber
Martinsried, Germany

Susumu Kitagawa
Kyoto, Japan

Thomas Poulos
CA, USA

David Schubert
Colorado, USA

T. Don Tilley
CA, USA

Karl E. Wieghardt
Mülheim an der Ruhr, Germany

Vivian Yam
Hong Kong

Contents

Contributors xi

Series Preface xv

Volume Preface xvii

Geology, Geochemistry, and Natural Abundances of the Rare Earth Elements **1**
Scott M. McLennan and Stuart Ross Taylor

Sustainability of Rare Earth Resources **21**
David A. Atwood

The Electronic Structure of the Lanthanides **27**
Ana de Bettencourt-Dias

Variable Valency **35**
Andrew W.G. Platt

Group Trends **43**
Andrew W.G. Platt

Solvento Complexes of the Lanthanide Ions **55**
Simon A. Cotton and Jack M. Harrowfield

Lanthanides in Living Systems **65**
Simon A. Cotton and Jack M. Harrowfield

Lanthanides: Coordination Chemistry **73**
Simon A. Cotton and Jack M. Harrowfield

Organometallic Chemistry Fundamental Properties **83**
Stephen T. Liddle

Lanthanides: ''Comparison to 3d Metals'' **105**
Simon A. Cotton

Luminescence **111**
Julien Andres and Anne-Sophie Chauvin

Lanthanides: Luminescence Applications **135**
Julien Andres and Anne-Sophie Chauvin

Magnetism 153
Bing-Wu Wang and Song Gao

The Divalent State in Solid Rare Earth Metal Halides 161
Gerd Meyer

Lanthanide Halides 175
Timothy J. Boyle and Leigh Anna M. Steele

Lanthanide Oxide/Hydroxide Complexes 183
Zhiping Zheng

Lanthanide Alkoxides 197
Timothy J. Boyle and Leigh Anna M. Steele

Rare Earth Siloxides 205
Clemens Krempner and Brian McNerney

Thiolates, Selenolates, and Tellurolates 215
John G. Brennan

Carboxylate 225
Jia-sheng Lu and Ruiyao Wang

Lanthanide Complexes with Amino Acids 237
Zhiping Zheng

β-Diketonate 249
Ke-Zhi Wang

Rare Earth Borides, Carbides and Nitrides 263
Takao Mori

Lanthanide Complexes with Multidentate Ligands 281
Xiaoping Yang, Richard A. Jones and Wai-Kwok Wong

Alkyl 299
Simon A. Cotton

Aryls 303
Simon A. Cotton

Trivalent Chemistry: Cyclopentadienyl 307
Roman A. Kresinski

Tetravalent Chemistry: Inorganic **313**
Farid M.A. Sroor and Frank T. Edelmann

Tetravalent Chemistry: Organometallic **321**
Farid M.A. Sroor and Frank T. Edelmann

Molecular Magnetic Materials **335**
Bing-Wu Wang and Song Gao

Near-Infrared Materials **347**
Lining Sun and Liyi Shi

Superconducting Materials **371**
Antonio J. Dos santos-García, Miguel Á. Alario-Franco and Regino Sáez-Puche

Metal–Organic Frameworks **385**
John Hamilton Walrod II and David A. Atwood

Upconversion Nanoparticles for Bioimaging Applications **389**
Jiefu Jin and Wing-Tak Wong

Oxide and Sulfide Nanomaterials **405**
Takuya Tsuzuki

Rare Earth Metal Cluster Complexes **415**
Gerd Meyer

Organic Synthesis **437**
Yuichiro Mori and Shũ Kobayashi

Homogeneous Catalysis **459**
Yingming Yao and Kun Nie

Heterogeneous Catalysis **475**
John Hamilton Walrod II and David A. Atwood

Supramolecular Chemistry: from Sensors and Imaging Agents to Functional Mononuclear and Polynuclear Self-Assembly Lanthanide Complexes **481**
Jonathan A. Kitchen and Thorfinnur Gunnlaugsson

Endohedral Fullerenes **495**
Daniel L. Burriss and David A. Atwood

Lanthanide Shift Reagents **501**
Carlos F.G.C. Geraldes

Lanthanides: Magnetic Resonance Imaging **521**
Sophie Laurent, Luce Vander Elst, Sebastien Boutry and Robert N. Muller

Luminescent Bioprobes **535**
Anne-Sophie Chauvin

Sensors for Lanthanides and Actinides **561**
Gabriela I. Vargas-Zúñiga and Jonathan L. Sessler

Index 575

Contributors

Miguel Á. Alario-Franco — *Universidad Complutense de Madrid, Madrid, Spain (EU)*
- Superconducting Materials

Julien Andres — *École Polytechnique Fédérale de Lausanne, Vaud, Switzerland*
- Lanthanides: Luminescence Applications
- Luminescence

David A. Atwood — *University of Kentucky, Lexington, KY, USA*
- Endohedral Fullerenes
- Heterogeneous Catalysis
- Metal–Organic Frameworks
- Sustainability of Rare Earth Resources

Ana de Bettencourt-Dias — *University of Nevada, Reno, NV, USA*
- The Electronic Structure of the Lanthanides

Sebastien Boutry — *University of Mons, Mons, Belgium*
- Lanthanides: Magnetic Resonance Imaging

Timothy J. Boyle — *Sandia National Laboratories, Albuquerque, NM, USA*
- Lanthanide Alkoxides
- Lanthanide Halides

John G. Brennan — *Rutgers, The State University of New Jersey, Piscataway, NJ, USA*
- Thiolates, Selenolates, and Tellurolates

Daniel L. Burriss — *University of Kentucky, Lexington, KY, USA*
- Endohedral Fullerenes

Anne-Sophie Chauvin — *École Polytechnique Fédérale de Lausanne, Vaud, Switzerland*
- Lanthanides: Luminescence Applications
- Luminescence
- Luminescent Bioprobes

Simon A. Cotton — *University of Birmingham, Birmingham, UK*
- Alkyl
- Aryls
- Lanthanides: ''Comparison to 3d Metals''
- Lanthanides: Coordination Chemistry
- Lanthanides in Living Systems
- Solvento Complexes of the Lanthanide Ions

Antonio J. Dos santos-García — *Universidad Complutense de Madrid, Madrid, Spain (EU)*
- Superconducting Materials

Frank T. Edelmann — *Chemisches Institut der Otto-von-Guericke-Universität Magdeburg, Magdeburg, Germany*
- Tetravalent Chemistry: Organometallic
- Tetravalent Chemistry: Inorganic

Song Gao *Peking University, Beijing, People's Republic of China*
- Magnetism
- Molecular Magnetic Materials

Carlos F.G.C. Geraldes *University of Coimbra, Coimbra, Portugal*
- Lanthanide Shift Reagents

Thorfinnur Gunnlaugsson *School of Chemistry, Trinity College, University of Dublin, Dublin 2, Ireland*
- Supramolecular Chemistry: from Sensors and Imaging Agents to Functional Mononuclear and Polynuclear Self-Assembly Lanthanide Complexes

Jack M. Harrowfield *Université de Strasbourg, Strasbourg, France*
- Lanthanides: Coordination Chemistry
- Lanthanides in Living Systems
- Solvento Complexes of the Lanthanide Ions

Jiefu Jin *The University of Hong Kong, Pokfulam, Hong Kong*
- Upconversion Nanoparticles for Bioimaging Applications

Richard A. Jones *University of Texas at Austin, Austin, TX, USA*
- Lanthanide Complexes with Multidentate Ligands

Jonathan A. Kitchen *School of Chemistry, Trinity College, University of Dublin, Dublin 2, Ireland*
- Supramolecular Chemistry: from Sensors and Imaging Agents to Functional Mononuclear and Polynuclear Self-Assembly Lanthanide Complexes

Shũ Kobayashi *The University of Tokyo, Tokyo, Japan*
- Organic Synthesis

Clemens Krempner *Texas Tech University, Lubbock, TX, USA*
- Rare Earth Siloxides

Roman A. Kresinski *Kingston University, Kingston-upon-Thames, UK*
- Trivalent Chemistry: Cyclopentadienyl

Sophie Laurent *University of Mons, Mons, Belgium*
- Lanthanides: Magnetic Resonance Imaging

Stephen T. Liddle *University of Nottingham, Nottingham, UK*
- Organometallic Chemistry Fundamental Properties

Jia-sheng Lu *Queen's University, Kingston, ON, Canada*
- Carboxylate

Scott M. McLennan *State University of New York at Stony Brook, Stony Brook, NY, USA*
- Geology, Geochemistry, and Natural Abundances of the Rare Earth Elements

Brian McNerney *Texas Tech University, Lubbock, TX, USA*
- Rare Earth Siloxides

Gerd Meyer *Universität zu Köln, Köln, Germany*
- Rare Earth Metal Cluster Complexes
- The Divalent State in Solid Rare Earth Metal Halides

Takao Mori *National Institute for Materials Science (NIMS), Namiki 1-1, Tsukuba, Japan*
- Rare Earth Borides, Carbides and Nitrides

Yuichiro Mori *The University of Tokyo, Tokyo, Japan*
- Organic Synthesis

Robert N. Muller *University of Mons, Mons, Belgium*
- Lanthanides: Magnetic Resonance Imaging

Kun Nie *Soochow University, Suzhou, People's Republic of China*
- Homogeneous Catalysis

Andrew W.G. Platt *Staffordshire University, Stoke-on-Trent, UK*
- Group Trends
- Variable Valency

Regino Sáez-Puche *Universidad Complutense de Madrid, Madrid, Spain (EU)*
- Superconducting Materials

Jonathan L. Sessler *University of Texas at Austin, Austin, TX, USA*
- Sensors for Lanthanides and Actinides

Liyi Shi *Shanghai University, Shanghai, People's Republic of China*
- Near-Infrared Materials

Farid M.A. Sroor *Chemisches Institut der Otto-von-Guericke-Universität Magdeburg, Magdeburg, Germany*
- Tetravalent Chemistry: Inorganic
- Tetravalent Chemistry: Organometallic

Leigh Anna M. Steele *Sandia National Laboratories, Albuquerque, NM, USA*
- Lanthanide Alkoxides
- Lanthanide Halides

Lining Sun *Shanghai University, Shanghai, People's Republic of China*
- Near-Infrared Materials

Stuart Ross Taylor *Australian National University, Canberra, Australia*
- Geology, Geochemistry, and Natural Abundances of the Rare Earth Elements

Takuya Tsuzuki *Deakin University, Geelong, VIC, Australia*
- Oxide and Sulfide Nanomaterials

Luce Vander Elst *University of Mons, Mons, Belgium*
- Lanthanides: Magnetic Resonance Imaging

Gabriela I. Vargas-Zúñiga *University of Texas at Austin, Austin, TX, USA*
- Sensors for Lanthanides and Actinides

John Hamilton Walrod II *University of Kentucky, Lexington, KY, USA*
- Heterogeneous Catalysis
- Metal–Organic Frameworks

Bing-Wu Wang *Peking University, Beijing, People's Republic of China*
- Magnetism
- Molecular Magnetic Materials

Ke-Zhi Wang *Beijing Normal University, Beijing, People's Republic of China*
- β-Diketonate

Ruiyao Wang *Queen's University, Kingston, ON, Canada*
- Carboxylate

Wai-Kwok Wong *Hong Kong Baptist University, Kowloon Tong, Hong Kong, People's Republic of China*
- Lanthanide Complexes with Multidentate Ligands

Wing-Tak Wong *The Hong Kong Polytechnic University, Hunghom, Kowloon, Hong Kong*
- Upconversion Nanoparticles for Bioimaging Applications

Xiaoping Yang *University of Texas at Austin, Austin, TX, USA*
- Lanthanide Complexes with Multidentate Ligands

Yingming Yao *Soochow University, Suzhou, People's Republic of China*
- Homogeneous Catalysis

Zhiping Zheng *Xi'an Jiaotong University, Xi'an, Shanxi, People's Republic of China and University of Arizona, Tucson, AZ, USA*
- Lanthanide Complexes with Amino Acids
- Lanthanide Oxide/Hydroxide Complexes

Series Preface

The success of the *Encyclopedia of Inorganic Chemistry* (EIC), pioneered by Bruce King, the founding Editor in Chief, led to the 2012 integration of articles from the *Handbook of Metalloproteins* to create the newly launched *Encyclopedia of Inorganic and Bioinorganic Chemistry* (EIBC). This has been accompanied by a significant expansion of our Editorial Advisory Board with international representation in all areas of inorganic chemistry. It was under Bruce's successor, Bob Crabtree, that it was recognized that not everyone would necessarily need access to the full extent of EIBC. All EIBC articles are online and are searchable, but we still recognized value in more concise thematic volumes targeted to a specific area of interest. This idea encouraged us to produce a series of EIC (now EIBC) Books, focusing on topics of current interest. These will continue to appear on an approximately annual basis and will feature the leading scholars in their fields, often being guest coedited by one of these leaders. Like the Encyclopedia, we hope that EIBC Books continue to provide both the starting research student and the confirmed research worker a critical distillation of the leading concepts and provide a structured entry into the fields covered.

The EIBC Books are referred to as ''spin-on'' books, recognizing that all the articles in these thematic volumes are destined to become part of the online content of EIBC, usually forming a new category of articles in the EIBC topical structure. We find that this provides multiple routes to finding the latest summaries of current research.

I fully recognize that this latest transformation of EIBC is built upon the efforts of my predecessors, Bruce King and Bob Crabtree, my fellow editors, as well as the Wiley personnel, and, most particularly, the numerous authors of EIBC articles. It is the dedication and commitment of all these people that is responsible for the creation and production of this series and the ''parent'' EIBC.

Robert A. Scott
University of Georgia
Department of Chemistry

November 2012

Volume Preface

The rare earth elements (REE) include lanthanum and the f-block elements, cerium through lutetium. Scandium and yttrium are included in this group as they have ionic radii similar to the lighter f-block elements and are found together in the same ores. The chemical similarities of the 17 REE make them unique in comparison to the other metals in the periodic table where two adjacent elements in a period typically have significantly different chemical properties. This makes the REE relatively difficult to separate from one another, although there are minerals where the lighter (La–Eu) and heavier (Y and Gd–Lu) REE are concentrated. REE research has benefited from this similarity, however, as compounds and materials formed with one REE can often be replicated with one or more of the other REE.

The sequential filling of the f orbitals beginning with cerium gives the REE very unique electronic, optical, luminescent, and magnetic properties. Over the past several decades these properties have been utilized in a wide range of synthetic, catalytic, electronic, medicinal, and military applications. The REE are now found in a multitude of consumer products such as computers, cell phones, and televisions. REE are used in automotive catalytic converters, petroleum refining, lasers, fuel cells, light-emitting diodes, magnetic resonance imaging (MRI), hybrid electric vehicles, solar energy, and windmills, to name but a few examples. REE are not only ubiquitous in modern society; they will be of critical importance in achieving a carbon-free, sustainable, global energy supply.

The Rare Earths: Fundamentals and Applications provides the knowledge of fundamental REE chemistry necessary to understand how the elements are currently being used and how they might be used in the future. The book is organized to provide a comprehensive description of the breadth of REE chemistry in four sequential sections: fundamental chemistry (Chapters 1–12), important representative compounds (Chapters 13–30), examples of solid-state materials (Chapters 31–36), and current and potential new applications (Chapters 37–45). It is designed to provide students, instructors, academic researchers, and industrial personnel with a fundamental understanding of the electronic, chemical, and physical properties of the rare earth elements. This knowledge may be used to understand the current use of the elements and, it is hoped, will inspire and encourage new developments. With the possibility that REE resources and supplies will become limited in the near future, some of the new REE developments should include reducing the environmental impacts related to mining and isolation, recovering and recycling the elements from existing products, finding elements and compounds that could be substituted for REE, and ultimately, designing products where the elements or product components can be readily and economically reused.

While this book describes many of the more important aspects of the REE, it would be impossible for a single volume to incorporate the vast number of compounds, materials, and applications that contain or utilize REE. New information will be addressed in future articles in the *Encyclopedia of Inorganic and Bioinorganic Chemistry (EIBC)*. For example, there will be new REE articles on mining and extraction, metals and alloys, similarities of the REE with elements in Groups 1, 2, and 13, computational studies, carbonate, silicate, and polyoxometallate solid state materials, single-molecule magnets, environmental speciation, recycling, and many others.

The Rare Earths: Fundamentals and Applications is an ideal starting point and foundation for educating students, instructors, academic researchers, and industrial personnel on the unique chemistry and applications associated with the rare earth elements. New EIBC articles will supplement the contents of the book and will provide information on a broader range of rare earth compounds, materials, applications, and new developments.

I am grateful to the many authors who made substantial contributions to the outline and content of this book while it was being organized. I am especially grateful to Simon Cotton for the excellent expert assistance, information, and ideas he provided throughout the process.

David A. Atwood
University of Kentucky, Lexington, KY, USA

May 2012

Geology, Geochemistry, and Natural Abundances of the Rare Earth Elements

Scott M. McLennan

State University of New York at Stony Brook, Stony Brook, NY, USA

and

Stuart Ross Taylor

Australian National University, Canberra, Australia

1	Summary	1
2	Introduction	2
3	General Geochemistry of the Rare Earth Elements	2
4	Mineralogy and Geology of Rare Earth Elements	6
5	Distribution of REE in Major Solar System Reservoirs	8
6	Distribution of REE in Terrestrial Reservoirs	10
7	Conclusions	17
8	Glossary	17
9	Related Articles	18
10	Abbreviations and Acronyms	18
11	References	18

1 SUMMARY

The rare earth elements (REE) are trace elements in most geological settings and are of great utility in understanding a wide variety of geological, geochemical, and cosmochemical processes that take place on the Earth, other planets, and other planetary bodies (e.g., Moon, asteroids). The properties that lead to this importance include the following: REE are an extremely coherent group of trace elements, by geochemical standards, in terms of ionic radius, charge, and mineral site coordination, which makes them especially valuable for monitoring magmatic processes; slight variations in their overall refractory nature provides insights into early solar system high-temperature processes; the distinctive redox chemistries of europium and cerium result in unique insights into magmatic and aqueous processes, respectively; their generally insoluble character in geological settings and resistance to remobilization beyond the mineralogical scale during weathering, diagenesis, and metamorphism makes them important tracers for characterizing various geochemical ‘‘reservoirs’’ (e.g., planetary crusts and mantles).

In addition to being of great value to general geochemistry investigations, the REE have proven of increasingly great commercial value. Modern applications involve many that are useful in high technology, including some of strategic/military use. Accordingly, understanding the geological conditions leading to REE concentrations that are sufficient for economically viable extraction is also seen as increasingly important.

This chapter addresses geological and geochemical factors that control REE distributions in rocks and minerals, both in the Earth and on other planetary bodies, and the processes that give rise to economic concentrations of REE in the Earth’s crust. We begin with a discussion of the fundamental geochemistry and cosmochemistry of REE. This is followed by describing processes that influence the distribution of REE in rocks and minerals and the geological

The Rare Earth Elements. Edited by David A. Atwood. © 2012 John Wiley & Sons, Ltd. ISBN 978-1-119-95097-4

conditions that give rise to ore-grade concentrations. Finally, we characterize abundances and distributions of REE in various reservoirs, such as bulk solar system, bulk Earth, crust, oceans, and so forth, that are relevant to understanding the origin and evolution of the Earth.

2 INTRODUCTION

Geochemists have long recognized the misnomer associated with the REE, aptly captured in the title of one early paper, ''Dispersed and not-so-rare earths.''[1] Although REE occur as trace elements in the vast majority of geological environments, their natural abundances in crustal rocks, mostly ranging from hundreds of parts per billion (terbium, holmium, thulium, lutetium) to tens of parts per million (lanthanum, cerium, neodymium), are not exceptionally low compared to many other elements. Thus, depending on the estimate, the most common REE, cerium, is approximately the 27th most abundant element in the continental crust of the Earth. Regardless of absolute amounts, the REE arguably are the single most important coherent suite of elements in nature for the purposes of interpreting a wide variety of geological processes for reasons discussed below. Accordingly, the absolute concentrations and embedded radiogenic isotopic systems (e.g., ^{147}Sm–^{143}Nd, ^{146}Sm–^{142}Nd, ^{176}Lu–^{176}Hf, ^{138}La–^{138}Ce) have been studied in exhaustive detail in a wide variety of rocks, minerals, and aqueous fluids on the Earth and other available solar system bodies.

Industrial uses of REE metals and compounds have expanded greatly over the past century, from the early application of mixing small amounts of cerium oxide with thorium oxide to produce incandescent gas light mantles, developed in the late nineteenth century, to being crucial components in a wide variety of cutting-edge technology applications.[2] Modern uses of the REE in high-technology applications include many of considerable strategic value.[3] Accordingly, geological processes giving rise to ore-grade concentrations of REE are also of increasing interest.

The history of meaningful geological and geochemical research using REE dates from the pioneering work of Victor Goldschmidt and Eiiti Minami in 1935, who used X-ray spectrography to first determine REE abundances in rock samples—European and Japanese shale composites.[4] At that time, most workers were of the opinion that relative REE distributions were not fractionated by geological processes and early differences in REE distributions noted between shales and meteorites were dismissed as analytical error. Modern REE geochemical research dates from the early 1960s with the development of rapid and precise instrumental techniques, notably radiochemical and instrumental neutron activation analyses pioneered by Larry Haskin, Roman Schmitt, and their colleagues.[5,6] (Various rapid high-precision mass spectrometry methods such as thermal ionization isotope dilution mass spectrometry and spark source mass spectrometry soon followed.) The seminal breakthrough of Haskin's work was that REE distributions in shales were indeed significantly fractionated from meteorites, having higher abundances and relative enrichment of the light rare earth elements (LREE), lanthanum through samarium, thus opening the door to the modern phase of REE geochemical research, summarized here.

In this chapter, we are concerned with four major issues: (i) general geochemistry and cosmochemistry of REE; (ii) geological conditions giving rise to normal concentrations of REE in rocks, minerals, and natural waters; (iii) geological conditions giving rise to ore-grade concentrations of REE; and (iv) the abundances and distributions of REE in various geochemical and cosmochemical ''reservoirs'' that are relevant to understanding the origin and evolution of the Earth.

3 GENERAL GEOCHEMISTRY OF THE RARE EARTH ELEMENTS

3.1 Geochemical and Cosmochemical Classification

The REE consist of the Group 3 transition elements $_{21}$Sc, $_{39}$Y, and $_{57}$La and the inner transition (lanthanide) elements $_{58}$Ce through $_{71}$Lu. As described in greater detail below, the REE are trivalent in all known geochemical systems with the exception of europium (which can also be divalent) and cerium (which can also be tetravalent). In geochemistry nomenclature, the term *rare earth elements* almost universally refers only to lanthanum, yttrium, and the lanthanides (i.e., La–Lu, Y), which differs from formal chemistry nomenclature, resulting in some confusion. Geochemists also subdivide REE into the light rare earths (LREE (La–Sm) and heavy rare earth elements (HREE; Gd–Lu) due to their contrasting geochemical behavior, with a natural break at the commonly anomalous europium (see below). In some geochemical literature, a group of middle REE, Nd–Tb, is also recognized.

Yttrium behavior is very similar to the HREE in the vicinity of Dy–Ho, which is why it is typically included with the other REEs in geochemical discussions. On the other hand, the geochemical behavior of scandium, especially in magmatic systems, is much more similar to the first row (ferromagnesian) transition elements, iron, vanadium, chromium, cobalt, and nickel, due to its smaller ionic radius and different coordination in mineral lattices.[7] Because of this, many geochemists do not consider scandium as a REE, but rather as a ferromagnesian trace element. However, McLennan[8], among others, has pointed out that in aqueous systems, scandium indeed has much more affinity for the other REE and so there is some inconsistency with REE terminology even within the geochemical literature (Figure 1).

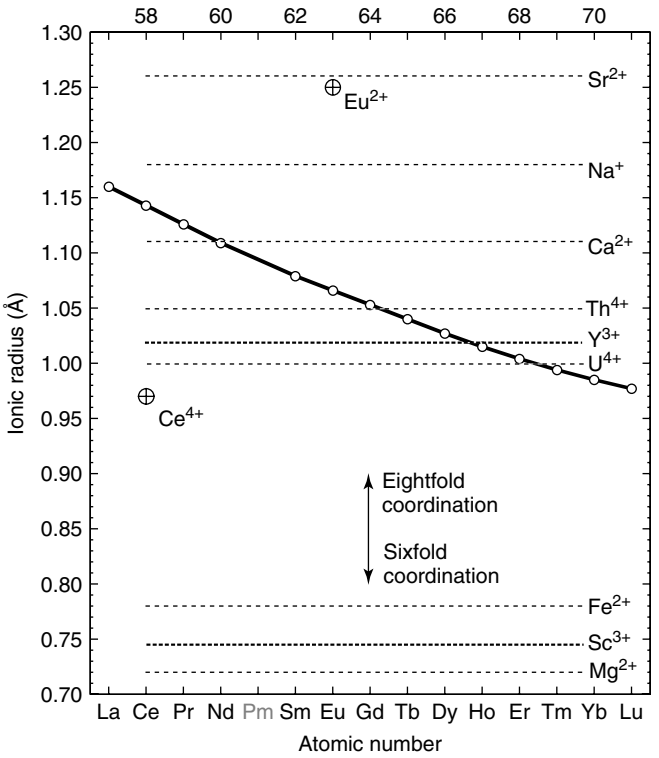


Figure 1 Plot of ionic radius versus atomic number for the trivalent lanthanide elements (La–Lu). Also shown are the ionic radii for trivalent Y and Sc, for the Eu^{2+} and Ce^{4+}, and for other selected cations. The regular decrease in the ionic radii of the trivalent lanthanides is part of the *lanthanide contraction*. Sc^{3+} is much smaller than the other rare earth elements and more similar in size to Fe^{2+} and Mg^{2+}

The development of the lanthanide series by filling of inner 4f orbitals, which poorly shield outer electrons from the increasing nuclear charge, is the underlying cause of the remarkably coherent geochemical behavior of the group (Table 1). Among other things, this results in the trivalent state being especially stable (with two notable exceptions) and the ionic radius decreasing in a remarkably systematic manner, part of the ''*lanthanide contraction*'' (Figure 1; Table 1). The dominant controls on the geochemical and cosmochemical behavior of the REE are their size (ionic radius), mineral site coordination (CN), redox behavior, volatility, and complexing behavior. An additional influence, termed the *tetrad* effect, is more controversial and discussed in greater detail below. Although the lanthanides bear some chemical properties that are similar to the Group 13 elements (boron, aluminum, gallium, etc.), their geochemical and cosmochemical distributions are not significantly influenced by this.

With rare exception, REE are lithophile (''rock-loving'') in igneous systems and with the exception of Sc, are incompatible (i.e., bulk solid-melt partition coefficients, $D < 1$) with the degree of incompatibility increasing with increasing size (and decreasing atomic number). Their ionic potentials (nominal charge/ionic radius) are ≥ 4.0 and so they are large-ion lithophile, rather than high field strength, incompatible elements. Accordingly, the lanthanides (and yttrium) tend to be concentrated in magmatic liquids and late crystallizing mineral phases. Only sodium and calcium come close in size to the REE (apart from scandium) among the major mineral-forming cations in the Earth's crust and mantle; however, substitution for these elements (especially sodium) leads to significant charge imbalances, thus limiting any such substitutions. In aqueous alteration systems, REE have very low fluid/rock partition coefficients and thus their primary abundances are only disturbed at relatively high fluid/rock ratios under most weathering, diagenetic, hydrothermal, and metamorphic conditions. This resistance to disturbance and remobilization is another important reason why REE are considered such valuable trace elements in geochemistry and cosmochemistry.

From a cosmochemical perspective, all of the REE are refractory elements (Table 1), with relatively high 50% condensation temperatures (≥ 1356 K at 10^{-4} bar), although significant variations in volatility are present (e.g., cerium, europium, and ytterbium being less refractory than other REE). These modest differences in volatility are important for interpreting certain early formed meteorite components (minerals and inclusions) in terms of the early thermal history of the solar nebula (see below).

Under aqueous conditions, the REE exist mostly in very low concentrations as a variety of complexes, with metals (REE^{3+}), carbonate species ($REECO_3^{+}$), and bicarbonate species ($REE(CO_3)_2^{-}$) dominating in seawater.[9] For a number of rare earth complexes that in nature can exist in magmatic, hydrothermal, and other fluid systems, such as fluorides, chlorides, sulfates, hydroxides, and carbonates, stability constants tend to increase with increasing temperature and decrease with increasing pressure. In general, there also tends to be an increase in stability of complexes with the heavier (smaller) REE.[10,11] In aqueous fluids, REE concentrations tend to increase with decreasing pH.

Table 1 provides some basic data for selected REE properties of geological interest, compiled from several sources, and a thorough compilation of the full range of REE chemical and physical properties is available in Emsley.[12]

3.2 Normalization of Lanthanide Abundances

The absolute concentrations of REE in geological materials follow the Oddo–Harkins, or odd–even, effect such that even atomic number elements are of higher concentrations than their adjacent odd atomic number counterparts. Since REE concentrations and relative distributions are also highly variable among rocks and minerals, it is difficult to compare absolute abundances graphically. Accordingly, it is customary to display REE data as a plot of normalized

Table 1 Selected rare earth element properties

	Symbol	Atomic number (Z)	Ground[12,13] state configuration	Trivalent[14] ionic radius (Å) (CN6)	Trivalent[14] ionic radius (Å) (CN8)	Atomic[12,13] weight	Pauling[12,13] electronegativity	50% Oxide[15] condensation (K at 10^{-4} bar)
Lanthanum	La	57	$[Xe]5\,d^1 6s^2$	1.032	1.160	138.9055	1.10	1578
Cerium	Ce	58	$[Xe]4f^1 5d^1 6s^2$	1.01	1.143	140.116	1.12	1478
Praseodymium	Pr	59	$[Xe]4f^3 6s^2$	0.99	1.126	140.90765	1.13	1582
Neodymium	Nd	60	$[Xe]4f^4 6s^2$	0.983	1.109	144.24	1.14	1602
Samarium	Sm	62	$[Xe]4f^6 6s^2$	0.958	1.079	150.36	1.17	1590
Europium	Eu	63	$[Xe]4f^7 6s^2$	0.947	1.066	151.964	—	1356
Gadolinium	Gd	64	$[Xe]4f^7 5d^1 6s^2$	0.938	1.053	157.25	1.20	1659
Terbium	Tb	65	$[Xe]4f^9 6s^2$	0.923	1.040	158.92534	—	1659
Dysprosium	Dy	66	$[Xe]4f^{10} 6s^2$	0.912	1.027	162.500	1.22	1659
Holmium	Ho	67	$[Xe]4f^{11} 6s^2$	0.901	1.015	164.93032	1.23	1659
Erbium	Er	68	$[Xe]4f^{12} 6s^2$	0.890	1.004	167.259	1.24	1659
Thulium	Tm	69	$[Xe]4f^{13} 6s^2$	0.880	0.994	168.93421	1.25	1659
Ytterbium	Yb	70	$[Xe]4f^{14} 6s^2$	0.868	0.985	173.04	—	1487
Lutetium	Lu	71	$[Xe]4f^{14} 5d^1 6s^2$	0.861	0.977	174.967	1.27	1659
Scandium	Sc	21	$[Ar]3d^1 4s^2$	0.745	0.870	44.955910	1.36	1659
Yttrium	Y	39	$[Kr]4d^1 5s^2$	0.900	1.019	88.90585	1.22	1659
	Eu^{2+}	—	—	1.17	1.25	—	—	—
	Ce^{4+}	—	—	0.87	0.97	—	—	—

Note: 50% oxide condensation temperatures are for REE oxide solid solution in pure compounds hibonite ($CaAl_{12}O_{19}$) ± Ca-titanate ($CaTiO_3$; $Ca_4Ti_3\,O_{10}$; $Ca_3Ti_2O_7$) ± feldspar ($CaAl_2Si_2O_8$).[15]

values (on a logarithmic scale) versus atomic number or reverse-order ionic radius (on a linear scale), termed *Coryell–Masuda plots* (Figure 2). On such diagrams, REE in rocks and minerals tend to follow smooth patterns (but with important exceptions discussed below). The two most commonly used data sets for normalization are average CI chondritic meteorites (usually on a volatile-free basis), reflecting solar and bulk Earth abundances, and average shale reflecting upper continental crust abundances (see below). Commonly used values for these two normalization sets are provided in the data tables discussed in more detail below. It should be noted that there are several different sets of chondrite values in use that differ by up to about 15% in absolute abundances (but with negligible differences in relative abundances) and so some care must be taken when comparing diagrams among different workers.

In addition to these normalization standards, it is not uncommon to normalize REE data to other compositions that are especially relevant to a specific problem. For example, in an igneous rock suite, it might be useful to normalize samples to the least petrologically evolved magmatic rock in the series. When studying weathering processes, it might be useful to normalize weathered samples to the unweathered parent rock. For authigenic minerals, insight might be gained by normalizing the mineral to the fluid from which they precipitated.

3.3 Europium and Cerium Redox Geochemistry

The existence of europium and cerium in other than trivalent states ($Eu^{2+/3+}$, $Ce^{3+/4+}$) is of considerable importance to geochemistry. Reduction of europium occurs under highly reducing conditions. Such conditions typically exist only within certain magmatic or hydrothermal environments but rarely if ever in environments found at the surface of the Earth. The ionic radius of Eu^{II} is about 17% larger than Eu^{III} and essentially identical to Sr^{II} (Figure 1). Accordingly, its substitution behavior differs greatly from the trivalent REE, resulting in anomalous REE patterns (Eu anomalies; see below). The most important geological example is that europium becomes highly concentrated in plagioclase feldspar (substituting into the calcium site). Plagioclase is only stable to about 10 kbars pressure or 40 km depth on Earth and so anomalous europium behavior in magmatic rocks is a clear sign of relatively shallow igneous partial melting or fractional crystallization processes. No example of europium reduction at surficial conditions has been convincingly documented but could potentially be present during diagenesis under highly reducing, high temperature, and alkaline conditions.[16]

In contrast, cerium is readily converted from Ce^{III} to Ce^{IV} under oxidizing surficial conditions. Especially notable examples are during formation of manganese oxide particles in the oceans and under certain surficial weathering conditions. Ce^{IV} is about 15% smaller than Ce^{III} and tends to form highly insoluble hydroxide complexes. These processes commonly

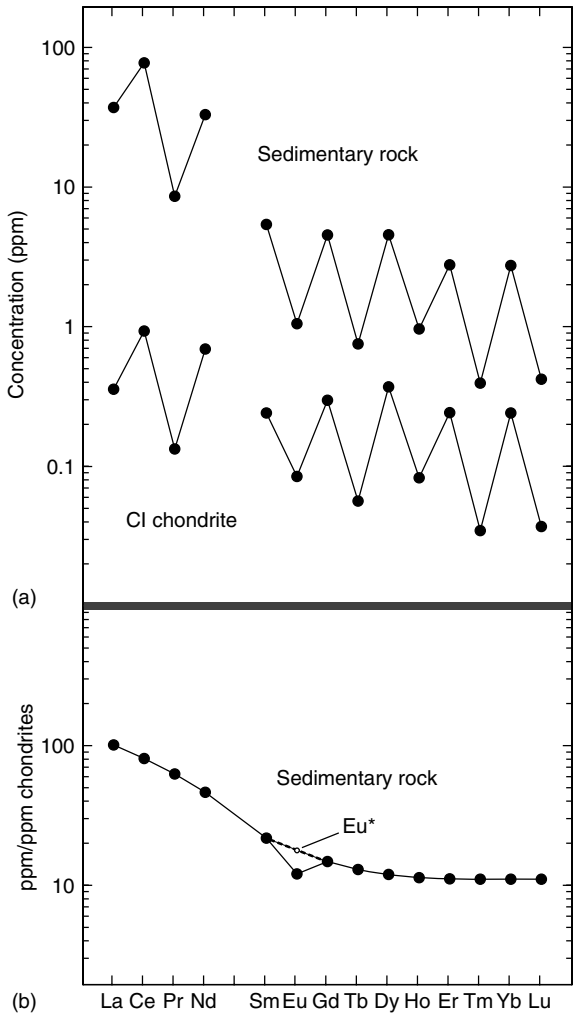


Figure 2 (a) Rare earth element abundance data for average shale and chondritic meteorites illustrating the Oddo–Harkins effect. (b) Masuda–Coryell diagram showing the average shale normalized to average chondrites. From such normalization, it is possible to readily observe the relative LREE enrichment and negative Eu anomaly in the shale. Eu* is the expected value for Eu on a smooth chondrite-normalized pattern and used to quantify the size of the Eu anomaly. A similar formulation can be used to characterize Ce anomalies

lead to separation of cerium from the other trivalent REE, again resulting in anomalous REE patterns (Ce anomalies). The anomalous depletion of cerium in seawater (see below) as a result of manganese oxide formation is a direct reflection of such redox controls. During most continental weathering, cerium is readily oxidized to Ce^{IV} and forms highly insoluble cerium hydroxide which may be locally precipitated while other trivalent REE are more readily mobilized. The effect of this is that Ce anomalies may also occur in weathering profiles.[8]

Anomalous europium and cerium behavior can be quantified using the parameter Eu/Eu* and Ce/Ce*. Eu* is the expected value for europium for a smooth chondrite-normalized REE pattern (Figure 2), such that

$$\frac{\mathrm{Eu}}{\mathrm{Eu}^*} = \frac{\mathrm{Eu}_N}{(\mathrm{Sm}_N \times \mathrm{Gd}_N)^{0.5}} \quad (1)$$

where the subscript ''N'' refers to the chondrite-normalized value. In the geochemical literature, arithmetic means (i.e., $(\mathrm{Sm}_N + \mathrm{Gd}_N)/2$) are sometimes used to calculate Eu* but this is incorrect because REE diagrams are plotted on a logarithmic scale and can lead to serious error especially for steep chondrite-normalized REE patterns. Cerium anomalies can be similarly calculated with

$$\frac{\mathrm{Ce}}{\mathrm{Ce}^*} = \frac{\mathrm{Ce}_N}{(\mathrm{La}_N \times \mathrm{Pr}_N)^{0.5}} \quad (2)$$

In some analytical methods, adjacent elements are not determined (e.g., gadolinium and/or praseodymium)[17] and in these instances, they are estimated assuming smooth chondrite-normalized REE patterns apart from europium and cerium.

3.4 The Tetrad Effect

As the lanthanide series develops, there appears to be increased stability (manifested by a variety of observations) associated with quarter (neodymium–praseodymium), half (gadolinium), three-quarter (holmium–erbium), and completely (lutetium) filled 4f shells. Resulting anomalous behavior in REE distribution patterns has been termed the *tetrad* or *double–double* effect.[18] The four tetrads are La–Ce–Pr–Nd, (Pm–)Sm–Eu–Gd, Gd–Tb–Dy–Ho, and Er–Tm–Yb–Lu. The effect was first noted in liquid/liquid partition coefficients and stability constants for organic compounds (e.g., log K of EDTA in aqueous solutions). A number of workers have also suggested that the effect can be seen in REE patterns of a wide variety of geological samples, especially those that have been influenced by aqueous interaction (e.g., seawater, marine phases) or by late-stage magmatic fluids (e.g., pegmatites). The observations that have been used to demonstrate the effect are apparent discontinuities in REE patterns at the tetrad boundaries generating either M-shaped or W-shaped REE patterns.[19] Although not directly related to the phenomena, significant deviations of the Y/Ho ratio from chondritic values are also thought to commonly accompany samples with the tetrad effect.[20]

McLennan[21] reviewed the geochemical literature on the tetrad effect and concluded that many of the cited examples could be explained as artifacts related to a variety of factors including incomplete analyses, analytical error, inappropriate choices for normalization, and complex mixing processes that resulted in apparent discontinuities. In addition, for many sample varieties (e.g., seawater, shales), the apparent effect is observed by some laboratories but not by others. The most

compelling examples of geological environments appear to involve igneous rocks associated with late-stage magmatic fluids (e.g., pegmatites, leucogranites). In our judgment, the question of whether or not the tetrad effect is truly a significant geochemical influence will remain clouded until there is a careful and systematic interlaboratory comparison of the same samples, preferably using a variety of analytical methods.

4 MINERALOGY AND GEOLOGY OF RARE EARTH ELEMENTS

Although REE are trace elements in most rocks and minerals, there are about 200 minerals in which REE are essential structural constituents, forming necessary structural cationic components of the mineral, or are major substituting cations in the structure. Reviews of REE mineralogy, geochemistry, and geology can be found in several multiauthored books edited by Henderson[22], Lipin and McKay[23], Möller *et al*.[24], and Jones *et al*.[25], the latter including a comprehensive appendix of REE minerals known to that date. Taylor and McLennan[26] also provided a comprehensive review of REE geochemistry.

Cation sites in most of the common igneous rock-forming minerals, such as olivines, pyroxenes, iron-titanium-oxides, feldspars, and micas, are characterized by highly variable coordination number and charge but with overall cation site conditions that are not particularly favorable to substantial REE substitution. This, of course, is the reason why the REE are usually incompatible elements. The abundances of REE consequently tend to be low (mostly less than 100–200 times CI values) but highly varied, ranging over about five orders of magnitude, from LREE enrichment to HREE enrichment and with highly variable Eu/Eu* (Figure 3). The major influences on the REE patterns in such minerals are the mineral-melt partition coefficients (K_d), the bulk composition and REE content of the parent magma, the major element chemistry (and thus coordination of cation sites) of the mineral, and the pressure–temperature conditions at which the mineral formed.

It is this variation and the distinctive REE abundances and patterns in a wide variety of common rock-forming minerals that make the REE such useful trace elements for evaluating most igneous and metamorphic petrogenetic

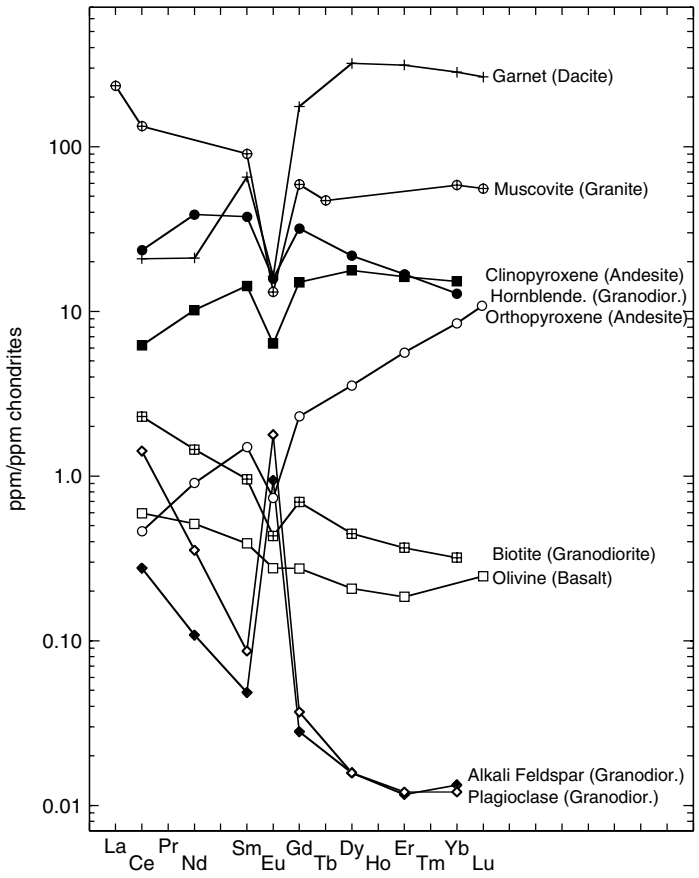


Figure 3 Chondrite-normalized REE patterns for common igneous rock-forming minerals. The igneous rock type from which the mineral was extracted is also listed. Data from compilation provided by Taylor and McLennan.[26] The extreme range of REE and the distinctive patterns for certain minerals is one of the reasons why REE are valuable trace elements for evaluating petrogenesis

processes. For example, Eu anomalies in magmatic rocks commonly indicate the involvement of plagioclase feldspar fractionation and HREE depletion commonly indicates a role for garnet fractionation in the history of their parent magmas. The stabilities of such minerals are sensitive to pressure, temperature, and bulk composition and thus REE patterns in rocks and minerals, coupled with an understanding of the partition coefficients, can be used to quantitatively constrain the origin and history of the magmas.

REE compounds tend to be relatively insoluble in aqueous fluids and fluid–rock partition coefficients tend to be very low during most fluid–rock interaction processes (e.g., weathering, diagenesis, hydrothermal activity). Accordingly, REE contents of most natural waters are very low, typically in the subpart per billion to subpart per trillion range. Only in high temperature, low pH hydrothermal environments do concentrations rise to near the part per million level.[8–11] REE patterns of aqueous fluids are also highly variable, reflecting among other things the ultimate crustal or mantle sources of the dissolved REE, the nature of fluid–rock interactions (e.g., fluid/rock ratio), redox conditions and history, the nature of REE complexing ligands, and the pressure–temperature-compositional history of the fluids. In turn, minerals precipitated directly from most natural waters (e.g., carbonates, silica, evaporites, sulfides) have very low REE contents. REE are also particle-reactive under marine conditions and accordingly are readily scavenged and adsorbed onto a number of marine sedimentary particles, such as clay minerals and iron-oxides.[27]

REE are highly electropositive (Table 1) resulting mostly in the formation of ionic compounds. REE mineral types thus include a wide variety of silicates, carbonates, oxides, phosphates, borates, halides, arsenates, sulfates, and vanadates. Among the most significant for geochemistry are lanthanite [$(La,Ce,Nd)_2(CO_3)_3{\cdot}8H_2O$], bastnäsite [$(Ce,La)(CO_3)F$], allanite [$(Ce,Y,Ca)_2(Al,Fe^{3+})_3(SiO_4)_3OH$], and the phosphates florencite [$(Ce,La)Al_3(PO_4)_2(OH)_6$], monazite [$(La,Ce,Th)(PO_4)$], rhabdophane [$(La,Ce)(PO_4){\cdot}H_2O$], and xenotime [$YPO_4$]. Of these, the most important REE ore minerals include bastnaesite, monazite, xenotime, as well as a rare form of REE-bearing clays.[28]

4.1 REE Ore Geology

Industrial uses of pure REE metals and compounds have expanded greatly from the early applications in incandescent gas light mantles, as polishing agents, and as glass coloring to being crucial components in a wide array modern technologies (e.g., computers, magnets, lasers, petroleum refining, alloys).[2,3] An underlying driver of industrial development was the fundamental research carried out on the REE because of their production as fission products in the nuclear fuel cycle. The past several decades have witnessed an explosion in industrial use, much of it having considerable strategic importance (e.g., precision guidance systems, stealth technology, night vision). Accordingly, the geological processes giving rise to ore-grade concentrations of REE are also of considerable and growing interest.

There are a number of recent reviews of the geology, geochemistry, and origin of REE ore deposits[28–35]. The most important types of REE ore deposits include sedimentary-hosted carbonate bodies of controversial origin, igneous carbonatite bodies, heavy mineral placer sands, and several types of regolith deposit. REE patterns of major REE ores are plotted in Figure 4. Minor REE ore deposits include those related to alkaline magmatism and to early Precambrian uraniferous/auriferous quartz-pebble conglomerate paleoplacers.

By far, the largest REE ore body in the world is the Bayan Obo REE-Nb–Fe deposit hosted in Early–Middle Proterozoic carbonate rocks in north China (inner Mongolia). The geology of the deposit is complex and there is no

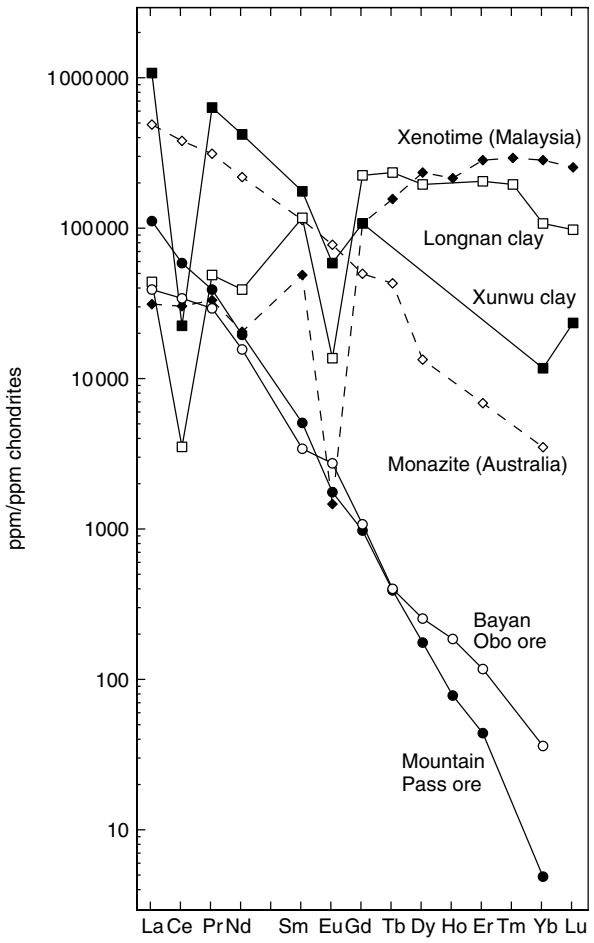


Figure 4 Chondrite-normalized REE patterns for selected REE ores from Bayan Obo and Mountain Pass; ion absorption clay ores from Longnan and Xunwu, China; and heavy mineral placer concentrates (monazite from Queensland Australia and xenotime from Malaysia)[32,35]. Note that the ion absorption clay REE patterns are normalized to 100%.

consensus on a genetic model. The REE ore, characterized by extreme LREE enrichment and no Eu anomalies, may be related either to carbonatite magmatism and/or hydrothermal activity. The dominant REE ore minerals are bastnäsite, a readily processed REE carbonate, and monazite. Ore grades are in the range of ~5–6% REE_2O_3.

The Middle Proterozoic Mountain Pass LREE-Ba deposit, located in eastern California, is the second largest known economical deposit and has been mined semicontinuously since 1954 (and currently under redevelopment). The deposit is closely related to mantle-derived carbonatite magmatism with the major REE ore mineral being igneous bastnäsite, with ore grades of about 9% REE_2O_3 (other minerals in the ore include calcite, dolomite, and barite). The ore is also extremely LREE enriched but with somewhat higher HREE abundances than at Bayan Obo.

Placers represent the third most important REE ore variety that has or is being mined and occur in widely dispersed unconsolidated Neogene and Quaternary beach sands, the most important being Ti-mineral-rich beach sands on the coasts of both western and eastern Australia. REE are by-products of these deposits and the main REE ore minerals are monazite ± xenotime. Xenotime is of special interest because unlike most other REE ore minerals that are highly LREE enriched, xenotime is enriched in the HREE (Figure 4).

The fourth variety of REE ore includes those associated with regoliths. One such deposit, exploited in China, is composed of ion absorption clays forming weathering profiles, up to ~10 m thick, on petrologically evolved igneous rocks such as granites. Deposits may be enriched in either LREE or HREE (and Y) and exhibit negative Eu anomalies and negative Ce anomalies. Negative Eu anomalies indicate an upper crustal source of REE and negative Ce anomalies suggest ion exchange from groundwaters depleted in cerium due to removal of insoluble Ce^{IV}-oxides during weathering. Although clays are enriched in REE, the overall grades are low (<0.5% REE_2O_3) and deposits are economical because of the ease of extraction and HREE enrichment. Another example is residual laterites that form on REE-rich rocks. The Mount Weld deposit of Western Australia, a laterite formed on a carbonatite, represents a major deposit that at the time of writing was about to go into production.[35]

5 DISTRIBUTION OF REE IN MAJOR SOLAR SYSTEM RESERVOIRS

5.1 Solar System Abundances

The sun comprises approximately 99.87% of the mass of the solar system and its composition is the most direct estimate of the composition of the current solar system and primordial solar nebula from which the planets were derived. The REE composition of the sun can be determined directly from spectral data for the solar atmosphere using both photospheric absorption lines and coronal emission lines. Concentration data are determined relative to some standardized concentration (typically silicon = 10^6 atoms or hydrogen = 10^{12} atoms) and one recent estimate is given in Table 2.[36]

The second approach to estimating the composition of the solar nebula is from average Ivuna-class carbonaceous chondritic meteorites, or CI chondrites (Type 1 carbonaceous chondrites using older terminology). This class of meteorites is the most volatile rich and thus considered to be the most primitive available. CI compositions are essentially identical to spectroscopically determined solar photosphere compositions for a broad array of elements, from the most refractory to the most volatile, within analytical uncertainty. Accordingly, the REE content of average CI chondrites is taken as the best estimate of the solid fraction (i.e., ''metal'' fraction) of the solar nebula. Table 2 also includes an estimate of average CI chondrites recalculated to a comparable concentration scale as the solar photosphere by assuming identical silicon atomic abundances. An advantage of meteorite data for determining the composition of the solar nebula is that abundances have been determined much more precisely than are direct spectral measurements of the sun (compare uncertainties in Table 2).

5.2 Meteorites

REE distributions in meteorites and their mineralogical–lithological components provide fundamental information about the origin and early history of the solar system. Reviews of meteorite chemistry, including REE chemistry,

Table 2 Log atomic concentration of rare earth elements in the solar photosphere and CI chondrites

	Solar abundance (H = 10^{12})	CI chondrite (Si = $10^{7.51}$)
H	12.00	8.22 ± 0.04
Si	7.51 ± 0.03	7.51 ± 0.01
La	1.10 ± 0.04	1.17 ± 0.02
Ce	1.58 ± 0.04	1.58 ± 0.02
Pr	0.72 ± 0.04	0.76 ± 0.03
Nd	1.42 ± 0.04	1.45 ± 0.02
Sm	0.96 ± 0.04	0.94 ± 0.02
Eu	0.52 ± 0.04	0.51 ± 0.02
Gd	1.07 ± 0.04	1.05 ± 0.02
Tb	0.30 ± 0.10	0.32 ± 0.03
Dy	1.10 ± 0.04	1.13 ± 0.02
Ho	0.48 ± 0.11	0.47 ± 0.03
Er	0.92 ± 0.05	0.92 ± 0.02
Tm	0.10 ± 0.04	0.12 ± 0.03
Yb	0.84 ± 0.11	0.92 ± 0.02
Lu	0.10 ± 0.09	0.09 ± 0.02
Sc	3.15 ± 0.04	3.05 ± 0.02
Y	2.21 ± 0.05	2.17 ± 0.04

can be found in Brearley and Jones[37], Mittlefehldt *et al*.[38], and McSween and Huss[39].

REE patterns in bulk carbonaceous chondrites are fairly uniform, parallel to CI, and show no dependence on volatility (e.g., no Eu or Yb anomalies). This uniformity also applies to the ordinary (H, L, LL classes) and enstatite (EL, EH classes) chondrite classes that show significant loss of their moderately and highly volatile elements (e.g., potassium, lead) and/or variations in their metal/silicate ratios. Accordingly, REE abundances in chondritic meteorites indicate no substantial cosmochemical fractionation (i.e., volatile related; redox related) during their formation in the early stages of solar system evolution and indicate broad homogeneity in the solar nebula.

On the other hand, millimeter to centimeter scale calcium–aluminum refractory inclusions (CAI) and individual refractory mineral inclusions (e.g., hibonite ($CaAl_{12}O_{19}$) and perovskite) from the Allende and Murchison carbonaceous chondrites provide evidence for local heterogeneity in the early solar nebula related to very high-temperature processes.[40,41] CAIs have been radiometrically dated as the oldest known objects in the solar system (4.567 billion years old) and exhibit highly variable REE patterns with variable Eu and Yb anomalies, in the case of CAIs, and Ce, Eu, and Yb anomalies in the case of hibonite grains (Figure 5). Such anomalies cannot be related to magmatic processes but instead are due to complex evaporation–condensation processes that fractionated the least refractory cerium, europium, and ytterbium from the other more refractory REE (Table 1). This veritable ''zoo'' of REE patterns calls for very high local temperatures, very complex histories of evaporation and condensation, and local compositional heterogeneity.

Silicate-bearing differentiated meteorites from the asteroid belt, including achondrites and stony-iron meteorites, are thought to represent fragments from asteroidal parent bodies that were melted very early in the history of the solar system and differentiated into core, mantle, and crust. REE data from these materials show significant variations, compared to chondrites, which reflect the magmatic histories of their parent bodies. For example, the howardite–eucrite–diogenite (HED) meteorites appear to be petrologically interrelated and probably are derived from the large asteroid 4-Vesta. REE patterns of the basaltic eucrites display variable positive and negative Eu anomalies that can be related to partial melting histories within Vesta.

Meteorites that do not come from the asteroid belt include the so-called SNC meteorites (for shergottites–nakhlites–chassignites) derived from Mars and the lunar meteorites. These were ejected from the planetary surfaces during impact processes and their REE compositions are highly variable, reflecting the magmatic evolution of these planetary bodies (see below).

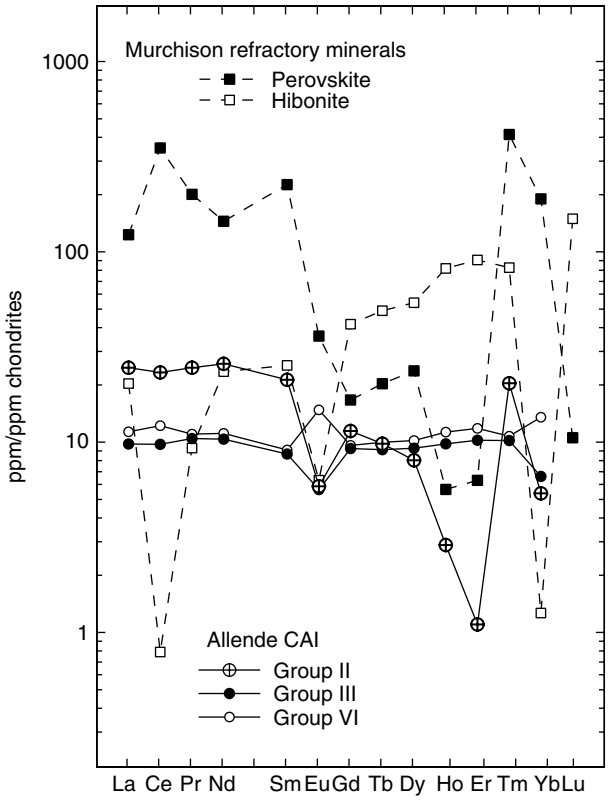


Figure 5 Chondrite-normalized REE patterns for selected calcium–aluminum inclusions (CAI) from the Allende carbonaceous chondrite and refractory mineral grains (perovskite, hibonite) from the Murchison carbonaceous chondrite.[40,41] The highly irregular REE patterns, including anomalies for the least refractory Ce, Eu, and Yb, are indicative of localized very high temperatures leading to complex REE evaporation/condensation processes

5.3 Planetary Compositions

As refractory lithophile elements, the REE play an important role in constraining the overall composition and history of the silicate fraction of planets, which for the terrestrial planets is also termed their *primitive mantle* (equivalent to the present-day crust plus mantle). Since there is no evidence for significant planetary-scale fractionation of refractory elements during the assembly and differentiation of planetary bodies, it is widely accepted that the primitive mantles of terrestrial planets and moon possess chondritic proportions of the REE. As such, the absolute concentrations of REE (and other refractory elements) in primitive mantles provide an important constraint on the proportions of volatile elements to refractory elements and on the oxidation state (i.e., metal/silicate ratio) of the body. To date, the only major planetary bodies for which REE data are directly available are the Earth, Moon, and Mars, and Taylor and McLennan[42] recently reviewed these data.

There is an enormous body of knowledge upon which to base estimates of the composition of the primitive mantle of

Table 3 Estimates of REE concentrations in the primitive mantles of Earth, Mars, and Moon and crusts of Mars and Moon[42]

	Average CI chondrite	Average volatile-free CI chondrite	Earth primitive mantle	Mars primitive mantle	Mars crust mantle	Moon primitive mantle	Moon highland crust
La	0.245	0.367	0.546	0.480	5.5	1.10	5.3
Ce	0.638	0.957	1.423	1.250	13.9	2.87	13
Pr	0.0964	0.137	0.215	0.180	1.9	0.411	1.8
Nd	0.474	0.711	1.057	0.930	9.4	2.13	7.4
Sm	0.154	0.231	0.343	0.300	2.7	0.69	2.0
Eu	0.058	0.087	0.129	0.114	0.95	0.26	1.0
Gd	0.204	0.306	0.454	0.400	3.1	0.92	2.3
Tb	0.0375	0.058	0.084	0.076	0.55	0.17	0.35
Dy	0.254	0.381	0.566	0.500	3.4	1.14	2.3
Ho	0.0567	0.0851	0.126	0.110	0.70	0.255	0.53
Er	0.166	0.249	0.370	0.325	1.9	0.75	1.51
Tm	0.0256	0.0356	0.057	0.047	0.25	0.11	0.22
Yb	0.165	0.248	0.368	0.325	1.7	0.74	1.4
Lu	0.0254	0.0381	0.057	0.050	0.26	0.11	0.21
Sc	5.90	8.64	13.0	11.3	-	19	5
Y	1.56	2.25	3.48	2.7	18	6.3	13.4

Concentrations in parts per million ($\mu g\ g^{-1}$).

the Earth. There are basically two approaches: (i) those based on the composition of xenoliths and high-degree partial melts from the upper mantle, and (ii) those based on fundamental cosmochemical principles. In practice, both lines of evidence are employed and models differ mostly in the relative weight given to each. As discussed above, it is generally assumed that refractory elements are not fractionated from each other in the primitive mantles of planetary bodies. Thus, for the Earth, the REE abundances can be derived by assuming that ratios such as REE/Ca and REE/Al are in chondritic proportions. In turn, absolute abundances of refractory elements depend on the diluting effects of (i) amount of relatively volatile elements in the primitive mantle and (ii) oxidation state of the planet, which controls the proportion of iron partitioned into the metal core and silicate primitive mantle. Table 3 lists estimates for the REE contents of the primitive mantles of Earth, Mars, and the Moon, and chondrite-normalized plots are given in Figure 6.

The terrestrial planets and other large silicate-rich planetary bodies (e.g., large asteroids, moons) typically are differentiated into metal cores, silicate mantles, and incompatible element-enriched silicate crusts. The mechanisms, scales, and timing of this process are extremely variable.[42] For REE, crust–mantle differentiation is the most important process in controlling abundances and distributions; REE are essentially excluded from planetary metal cores due to their lithophile character. In Table 3 and Figure 6, estimates of the REE distributions in planetary crusts (Earth's continental crust, lunar highland crust, Martian crust) are also given. In the following sections, we discuss the REE content of the Earth's crust in much greater detail.

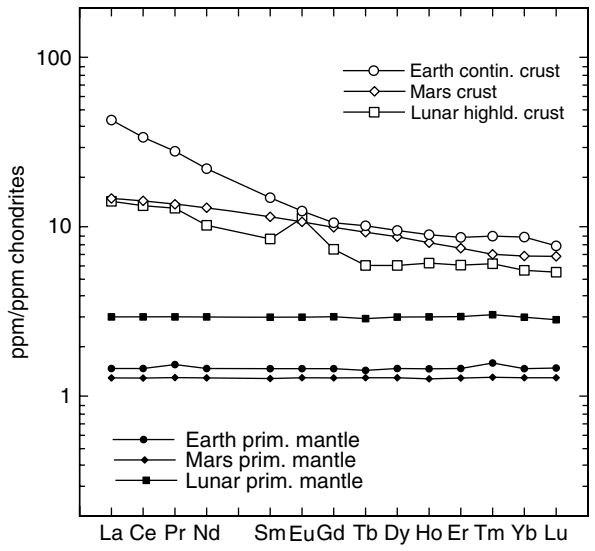


Figure 6 Chondrite-normalized REE patterns of the primitive mantles and crusts of Earth, Mars, and the Moon. For the Earth, the continental crust is shown; for the Moon, the highland crust is shown; and for Mars, the bulk crust is shown

6 DISTRIBUTION OF REE IN TERRESTRIAL RESERVOIRS

The major geochemical reservoirs of the Earth that are currently in existence—inner and outer core, upper and lower mantle, upper and lower continental crust, oceanic crust, sedimentary shell, oceans, and atmosphere—were established early in the planet's history. On the other hand, the sizes and compositions of these reservoirs have changed over

geological time through a variety of processes and on vastly differing timescales, but largely controlled by the history of crust–mantle evolution associated with plate tectonics.

For example, the continental crust is mostly very old (>2 billion years old on average) but has grown and internally differentiated (into upper and lower crust) episodically over geological time with the greatest activity occurring in the Late Archean (~2.5–3.2 billion years ago), resulting in a major change in composition (including for REE) at about that time. Today, the continental crust ultimately is derived from partial melting in the upper mantle initiated by fluids (depressing melting temperatures) that are released from the top of the downgoing plate during subduction. This magmatic activity expresses itself as the large island-arc and continental-arc volcanic chains (e.g., Japan, Andes) that form behind the great ocean trenches that mark the sites of subduction. Once formed, this continental crust rapidly differentiates into a relatively felsic upper crust and relatively mafic lower crust, a process that also causes a major fractionation of REE distributions. Recycling of this low-density crust back into the mantle is minimal and, accordingly, the composition of the mantle in turn evolves largely in response to this long-term extraction of continental crust. At present, the continents grow at ~1 km^3 per year on average but crustal growth rates were more rapid in the geological past.

The oceanic crust in contrast forms from high degrees of partial melting of the upper mantle beneath the mid-oceanic ridges, at the site of upwelling convecting mantle, giving rise to mid-oceanic ridge basalts (MORB) at a rate of about 20 km^3 per year. The oceanic lithosphere, comprising the oceanic crust and its attached rigid uppermost mantle, is recycled and lost back into the deeper mantle at subduction zones over short timescales, with no oceanic crust being older than ~0.2 billion years old. This continuous, geologically rapid recycling gives rise to a largely steady-state process that over geological time accounts for about 10% of the mantle being comprised of this recycled oceanic crust. Compositional changes in both oceanic crust and mantle, such as those resulting from the hydrothermal interaction of seawater with hot ocean-floor magmas, do occur but from the perspective of REE distributions are of second order importance.

Oceanic crust and, to a lesser degree continental crust, is also influenced by ''intraplate'' volcanism that occurs when relatively deep stationary plumes rise to the surface to form basaltic volcanoes; the best example being the Hawaiian chain of oceanic islands. Intraplate volcanism, giving rise to what is termed *oceanic island basalts* (OIB), results from a long and complex history within the mantle, giving rise to an average composition (including REE) quite distinct from MORB. Overall, intraplate volcanism accounts for about 1.5 km^3 per year and accordingly, while highly visible at the Earth's surface, comprises <5–10% of the oceanic crust and an even small component of the continental crust.

Although fundamentally different types of crust characterize other planetary bodies (e.g., the lunar highland crust and mare basalt crust of the Moon), the Earth is unique in having a mostly ancient continental crust and a mostly very young oceanic crust that are almost completely separated laterally. Within our solar system, plate tectonic processes, which gave rise to these distinct crustal types, appear to have only taken place on Earth.

6.1 Present-Day Mantle

The primitive mantle, discussed above, provides insight into the bulk composition of the silicate fraction of the Earth. However, over geological time, mantle compositions have evolved in a very complex manner due largely to plate tectonic processes. Among those processes are extraction of continental crust, recycling of oceanic crust back into the mantle, recycling of sedimentary components into the mantle, complex interactions of subducting lithosphere with the upper mantle–lower mantle boundary (at ~660 km depth), and so forth. The overall effect is that the mantle is heterogeneous on scales ranging from thousands of kilometers to just a few kilometers. Thus, for REE, upper mantle is likely distinct from lower mantle; lithospheric mantle beneath continents is distinct from lithospheric mantle beneath oceanic crust; mantle sources of MORB are distinct from those of OIB; broad regions of the upper mantle, identified by geophysics, may be distinct from other regions; and even along single segments of mid-oceanic ridges, basalts from one volcano can have distinct mantle REE sources from volcanoes just a few kilometers away.

Accordingly, it is difficult to identify and quantify the scales of significant mantle reservoirs and estimating average compositions is equally difficult. Since the oceanic crust is dominated by MORB, one useful concept is to define a mantle reservoir equivalent to the depleted mantle source of MORB (DMM). Since MORB are derived from high degrees of partial melting and the REE are incompatible, the DMM REE composition is roughly parallel to MORB but at lower absolute concentrations proportional to the average degree of partial melting. One such estimate is provided in Table 4 and plotted in Figure 7.

6.2 Oceanic Crust

The oceanic crust varies from 0 km (where magmas are erupting at the oceanic ridges) to >8 km thickness and averages ~7 km well away from the ridges. It is composed of three main parts:

1. **Layer 1:** sedimentary cover up to ~1 km thick but mostly ≤0.5 km thick. The ultimate source of most sediment is continental weathering and accordingly, the REE signature is similar to upper continental crust (see below). Biological activity supplies carbonate and siliceous sediment, derived from seawater, but these materials are very low in REE abundances.

Table 4 REE concentrations in major oceanic crust-related geochemical reservoirs[42]

	Depleted mantle (DMM)	Mid-oceanic ridge basalt (MORB)	Oceanic island basalt (OIB)	Average pelagic clay
La	0.23	1.9	19	42
Ce	0.77	6.0	43	80
Pr	0.13	0.99	4.9	10
Nd	0.71	6.1	21	41
Sm	0.27	2.22	5.4	8.0
Eu	0.11	0.90	1.8	1.8
Gd	0.40	3.5	5.5	8.3
Tb	0.08	0.70	0.9	1.3
Dy	0.53	4.5	5.3	7.4
Ho	0.12	1.1	1.0	1.5
Er	0.37	2.6	2.7	4.1
Tm	0.06	0.42	0.3	0.57
Yb	0.40	2.7	1.9	3.8
Lu	0.06	0.40	0.3	0.55
Sc	16	44	30	19
Y	4.1	25	23	40

Concentrations in parts per million ($\mu g\ g^{-1}$).

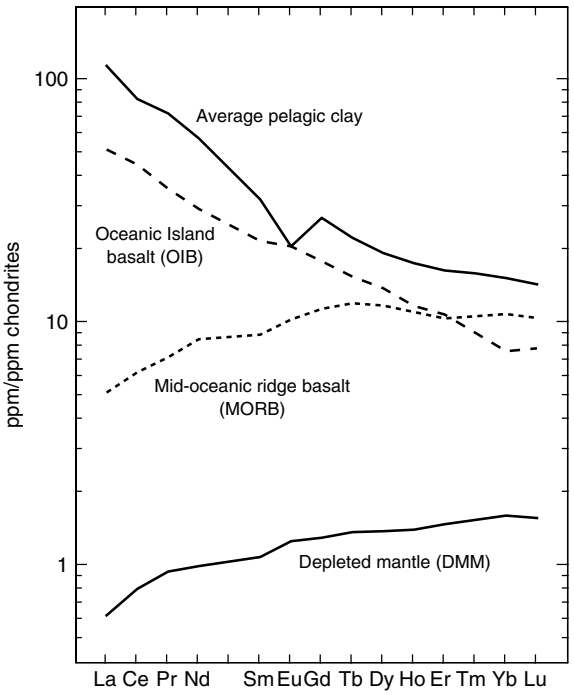


Figure 7 Chondrite-normalized REE patterns of selected rocks and reservoirs from oceanic crustal environments. Note that MORB and DMM have parallel REE patterns, a reflection that MORB is derived from DMM by high degrees (≥10%) of partial melting. Also note that pelagic clays have REE patterns similar to shales derived from the upper continental crust. The slight negative Ce anomaly is significant and reflects a small component of authigenic material derived from seawater

2. **Layer 2:** MORB-type basalt and intrusive equivalents with intercalated sediment lenses that varies in thickness, but on average is ~2.5 km.
3. **Layer 3:** MORB-type basalt and intrusive equivalents of up to about 4.5 km in thickness.

In Table 4, several relevant compositions are given, including average MORB, OIB, and pelagic clay. Any estimate of the bulk composition of the oceanic crust is dominated by the MORB component. The REE patterns of MORB basalts are typically depleted in the LREE with flat HREE patterns (Figure 7). OIB differ from MORB, being significantly enriched by large-ion lithophile elements, including the LREE (Figure 7). Thus, in addition to the depleted MORB, OIB contributes an uncertain amount of these elements to the overall composition of the oceanic crust that is eventually subducted back into the mantle. In addition to the OIB lavas, an additional minor component is variable amounts of deep-sea sediment, whose REE budget is dominated by deep-sea clays (Table 4; Figure 7).

6.3 Continental Crust

Continental crust (referred to hereafter simply as crust) comprises only about 0.4% of the mass of the Earth but its geochemical importance is far greater since it contains ~30–50% of the budget of the Earth's incompatible elements, including LREE. The crust has an average thickness of 41 km, ranging from 10 to 80 km, and has grown episodically over geological time with ~60% being in place by 2700 million years ago. A major difference in the style of crustal formation–evolution started in the Late Archean, beginning about 3200 million years ago.[43]

During the Archean, higher heat flow resulted in partial melting of the downgoing slab at relatively shallow depth (~50 km) in subduction zones. This produces the eruption of silica-rich magmas, leaving garnet as a residual

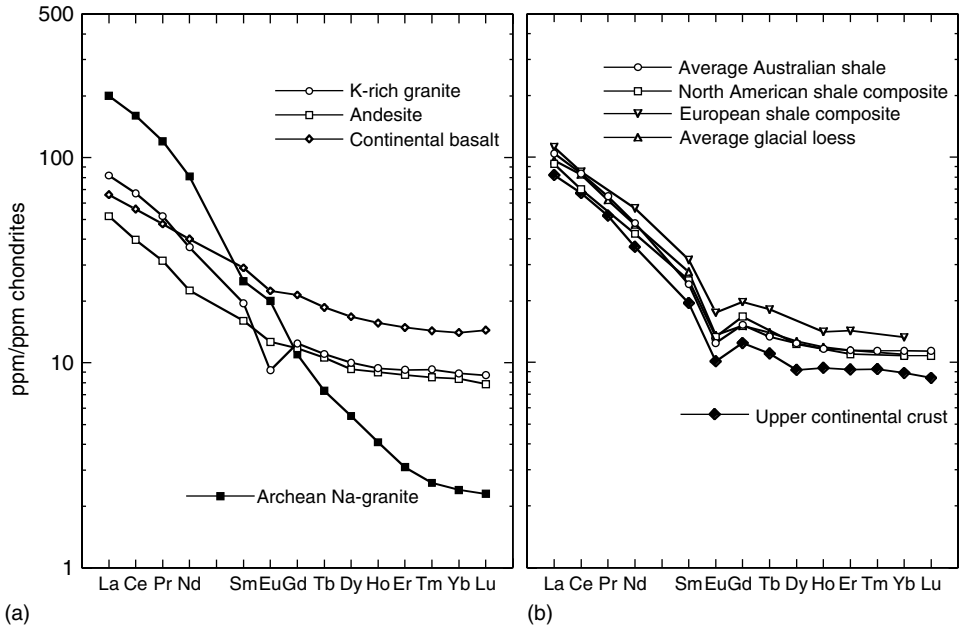


Figure 8 (a) Chondrite-normalized REE patterns of selected igneous rocks from the continental crust. Note the substantial negative Eu anomaly in K-rich granitic rocks and the very steep, HREE-depleted character of Archean Na-rich granites from the TTG suite discussed the text. (b) Chondrite-normalized REE patterns for various averages and composites of shales and for average glacial loess. The remarkable uniformity in these REE patterns is taken as compelling evidence that they reflect the REE pattern of the upper continental crust exposed to weathering and erosion. (Data from compilation given in Taylor and McLennan.[43])

phase. Garnet has REE patterns that are depleted in LREE and enriched in HREE (Figure 3). The erupting lavas in turn have a reciprocal pattern, enriched in LREE and depleted in HREE (Figure 8a), typically with no Eu anomaly. During the Late Archean (3.2–2.5 billion years ago), modern-style plate tectonics became established and oceanic crust was older and colder by the time it reached subduction zones. Under these conditions, the downgoing slab does not melt but does release fluids into the overlying mantle, which in turn partially melts to produce the present subduction-zone island-arc and continental-arc magma suite, which is added to the crust. Within 50–100 million years of crust formation, further partial melting within the crust results from high abundances of radioactive elements (potassium, thorium, uranium) and intrusions of basaltic plumes at the base of the crust. Partial melts produced in the lower crust rise and generate an upper crust dominated by granodiorites and granites (Figure 8a).

In summary, continental crust has grown in an episodic manner through geological time with a major increase in growth rate during the Late Archean. At present, the crust continues to grow by island-arc and continental-arc magmatism, followed by episodes of intracrustal melting that differentiates the upper from lower crust.

The average REE abundances of the bulk continental crust is model dependent and can be determined from the average composition of modern island-arc magmas and the composition of distinctive Archean igneous suites (see Refs 42 and 43 for details). The composition, so determined, is characterized by modest LREE enrichment and no Eu anomalies (Table 5; Figure 6).

For the upper continental crust, roughly the upper 10–12 km, highly reliable estimates of the average REE composition can be determined from sediments and sedimentary rocks. From the earliest days of REE analyses, the remarkable uniformity in sedimentary REE patterns throughout the post-Archean has been noted (Figure 8b) and this has been interpreted to reflect the average composition of the upper continental crust that erodes to produce clastic sediment. Such an interpretation is also consistent with the very low levels of REE in natural waters (see Section 6.4) and in chemical sediments precipitated from water (carbonates, evaporites). A major advantage of this approach is that sedimentary rocks can be used to evaluate the evolution of the upper crustal REE composition over geological time (see below).

Accordingly, REE in average shale (for this work, based on PAAS, post-Archean average Australian shale) is equated to the upper continental crust after a minor adjustment in total REE to account for low REE abundance sediments (sandstones, limestones). The derived pattern (Figure. 8b) differs from the bulk crust in having higher REE abundances, greater LREE enrichment, and a distinctive negative Eu anomaly (see Figure 9 for comparison). Elevated levels of the most incompatible LREE are consistent with intracrustal partial melting. The Eu anomaly indicates that partial melting to form the upper crust resulted in plagioclase being a stable

Table 5 REE concentrations in the major continental crust-related geochemical reservoirs[42]

	Average shale (PAAS)	Upper continental crust	Bulk continental crust	Lower continental crust	Archean upper crust	Archean bulk crust
La	38.2	30	16	11	20	15
Ce	79.6	64	33	23	42	31
Pr	8.83	7.1	3.9	2.8	4.9	3.7
Nd	33.9	26	16	12.7	20	16
Sm	5.55	4.5	3.5	3.17	4.0	3.4
Eu	1.08	0.88	1.1	1.17	1.2	1.1
Gd	4.66	3.8	3.3	3.13	3.4	3.2
Tb	0.774	0.64	0.60	0.59	0.57	0.59
Dy	4.68	3.5	3.7	3.6	3.4	3.6
Ho	0.991	0.80	0.78	0.77	0.74	0.77
Er	2.85	2.3	2.2	2.2	2.1	2.2
Tm	0.405	0.33	0.32	0.32	0.30	0.32
Yb	2.82	2.2	2.2	2.2	2.0	2.2
Lu	0.433	0.32	0.30	0.29	0.31	0.33
Sc	16	13.6	30	35	14	30
Y	27	22	20	19	18	19

Concentrations in parts per million ($\mu g\ g^{-1}$).

residual phase that sequestered europium into the lower crustal residue. Since plagioclase is only stable to depths of 40 km on Earth, the negative Eu anomaly provides compelling evidence that the crust differentiated through intracrustal (shallow) partial melting processes. This REE pattern is observed in virtually all sedimentary rocks dating back to the Archan–post-Archean boundary, at which time sedimentary patterns change (see below).

The simplest method for estimating the REE composition of the lower crust is through the mass balance of subtracting 25% of upper crustal composition from the bulk crust (Table 5; Figure 9). This composition is characterized by the complementary positive Eu anomaly. Although the upper crustal negative Eu anomaly indicates the importance of intracrustal partial melting in governing the composition of the lower crust, xenoliths and granulite facies rocks provide additional constraints. Lower crustal xenoliths are commonly mafic in composition, and frequently show a relative enrichment in Eu. However, this enrichment is mostly related to the accumulation of cumulate phases rather than being due to residual phases from partial melts and so these rocks may represent basaltic magmas that were later added to the base of the crust. Granulite facies regions also commonly possess positive Eu anomalies, but these are in the more felsic rocks rather than mafic rocks that could represent residues after partial melting. Many such terranes appear, on compositional grounds, to be upper crust that has been buried in Himalayan-type continental collisions, and so many regional granulites likely formed in mid-crust regions and are not a good model on which to base lower crustal compositions. In summary, the lower crust appears to be essentially the mafic residue left after extraction of the granodioritic upper crust together with additions from underplating by basaltic magmas.

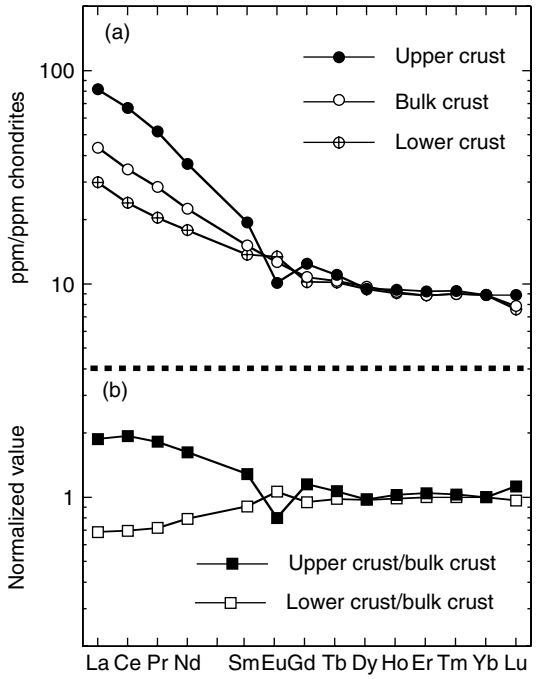


Figure 9 (a) Chondrite-normalized REE patterns for the upper, bulk, and lower continental crust reservoirs. (b) Upper and lower continental crust normalized to the bulk continental crust, highlighting the fractionation of europium and the more incompatible LREE during intracrustal differentiation

How far back in geological time can these crustal compositions be traced? The sedimentary record provides the most insight. Sedimentary REE patterns remain constant throughout the post-Archean; however, an abrupt change takes place at the Archean–Proterozoic boundary. Archean

sedimentary rocks, though more variable, have REE patterns that on average differ fundamentally from post-Archean sediments, being less enriched in LREE and lacking the negative Eu anomaly (Figure 10). This change reflects an episodic change in upper crustal composition and is related to large-scale emplacement of K-rich granitic rocks, depleted in europium, in the upper crust toward the close of the Archean. This process, termed *cratonization*, produces large volumes of granites derived from massive intracrustal melting, transfers heat-producing elements to the upper crust, and fundamentally ''stabilizes'' the crust. The changes in both upper crustal compositions and the REE patterns of derived sediment were nonsynchronous over the globe, and extended over several hundred million years.

This change is also consistent with the Archean igneous record. In the Archean, igneous rocks characteristic of modern island-arc magmatism are scarce and instead, a ''bimodal suite'' of Na-rich felsic igneous rocks (tonalites, trondhjemites, granodiorites or the ''TTG suite'' and their volcanic equivalents) and basaltic rocks dominate. Archean basalts typically have flat REE patterns, whereas the TTG suite is characterized by very steep REE patterns (see Figure 8a). Mixtures of these rocks bear a superficial resemblance to the REE patterns of island-arc magmatic rocks such as andesites. On average, the Archean bulk crust was probably similar to but slightly less LREE enriched than the post-Archean bulk continental crust, but this similarity in average REE patterns belies the very different geological processes that gave rise to Archean and post-Archean continental crust.

The Archean crust probably consisted of many small fast-spreading plates. As described above, the TTG suite was produced by subduction of young, warm basaltic crust. The steep REE patterns indicate that garnet was in the residue during partial melting, indicating a mantle origin since garnet is only stable in mafic–ultramafic systems at depths below about 40 km. The Archean crust thus formed as a mixture of piled-up basalts and related volcanic rocks and TTG intrusions and extrusives. Only minor intracrustal melting appears to have occurred in the earlier part of the Archean, since negative Eu anomalies are rare, and areas of the crust that underwent such melting (i.e., generating upper crustal negative Eu anomalies) formed only localized cratonic regions of limited global extent.

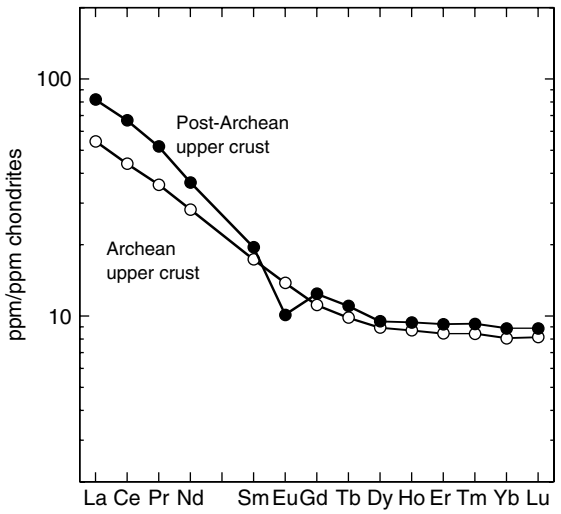


Figure 10 Comparison of chondrite-normalized REE patterns for the Archean and post-Archean upper continental crust, estimated from the sedimentary rock data. The absence of a negative Eu anomaly in the Archean upper crust indicates that intracrustal differentiation processes were not widespread at that time

6.4 The Hydrosphere

Oceans comprise 96.8% of the Earth's near-surface water and accordingly, completely dominate the REE mass balance in the global hydrosphere. A thorough review of the geochemistry of REE in natural waters can be found in Byrne and Sholkovitz.[27] Most REE in both terrestrial and marine waters are derived ultimately from the upper continental crust and accordingly, normalization to average shale is most informative. One notable exception is that REE in marine hydrothermal fluids are derived ultimately from interactions with oceanic basalts.

The abundances of REE in ocean water are vanishingly low, in the part per trillion range, due to their low solubility in natural waters and efficient scavenging by sediment particles (Table 6; Figure 11). For perspective, a column of ocean water of average depth (~4 km) contains about the same content of REE as 1 mm of clay-rich sediment on the seafloor. Relative to shales, the average ocean water REE pattern is characterized by a negative Ce anomaly and a trend of HREE enrichment. This pattern results from a variety of complex processes involving surface chemistry on sedimentary particles and solution chemistry. Ce anomalies form through a coupling with manganese redox chemistry. In the marine environment, Mn^{II} oxidizes to Mn^{IV} and forms Mn-oxide particles that sink; the process is biologically mediated. On Mn-oxide particles, cerium oxidation takes place and Ce^{IV} is adsorbed onto the particle surfaces and preferentially removed from the water column compared to the trivalent REE. One important sink for Ce^{IV} is in diagenetically formed Mn nodules in seafloor sediment. Enrichment of HREE results from the fact that stability constants for many REE complexes (mainly carbonate complexes in seawater) increase with increasing atomic number and accordingly, the LREE are preferentially scavenged by sediment particles.

In detail, REE abundances in marine waters are heterogeneous both laterally and vertically. This is largely a result of complex scavenging by particles as they sink through the ocean column and the low residence times of REE in seawater, ranging from about 50 years for cerium, 240–500 years for the LREE, and 520–2900 years for the HREE (Table 6). These residence times are less than or comparable to the ~1000 year mixing times of the oceans. It is this heterogeneity, especially for the LREE, which

Table 6 REE concentrations in selected natural waters and residence time in seawater[8,43–46]

	Average seawater	Residence time	River water (Luce R.)	Marine hydrothermal water	Continental high pH hydrothermal	Continental low pH hydrothermal
La	4.17	500	59.0	—	—	—
Ce	0.631	50	84.2	325	52	46 000
Pr	0.535	240	—	—	—	—
Nd	2.88	400	52.6	175	21.4	32 000
Sm	0.601	400	12.1	39	5.3	8400
Eu	0.152	410	3.15	158	0.6	1700
Gd	0.739	520	13.1	32	3.2	8170
Tb	0.175	570	—	—	—	—
Dy	1.06	740	15.9	22	2.8	6500
Ho	0.330	1820	—	—	—	—
Er	1.09	2420	10.8	8.0	1.7	2570
Tm	0.169	2430	—	—	—	—
Yb	1.12	2440	8.95	6.0	1.3	2700
Lu	0.227	2890	—	—	—	—
Sc	0.84	8000	—	—	—	—
Y	19.6	1670	—	—	—	—

Concentrations in parts per trillion (pg g^{-1}).

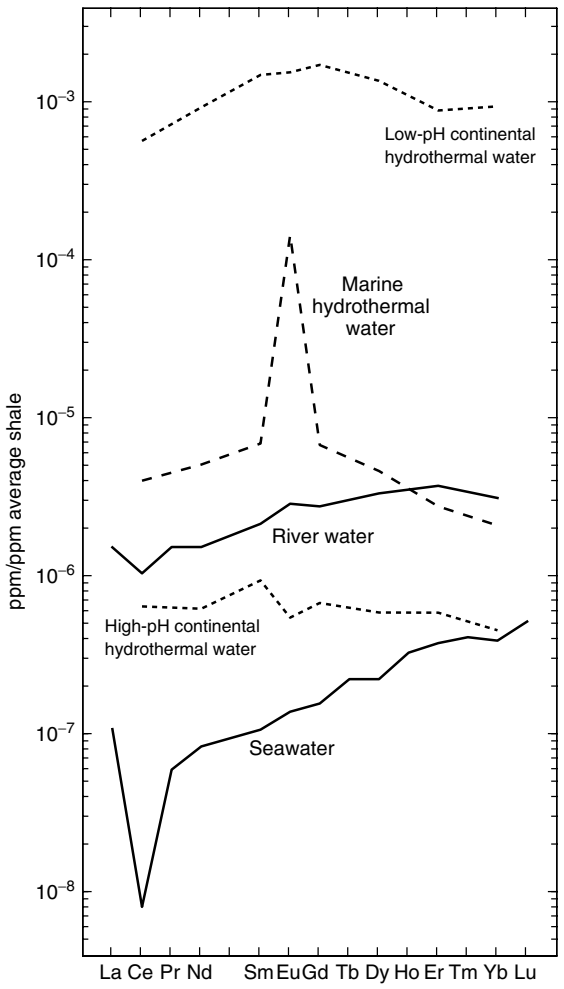


Figure 11 Chondrite-normalized REE patterns of selected natural waters

makes the use of the $^{147}Sm \Rightarrow ^{143}Nd$ isotope system very useful for paleoceanography because it is possible to trace distinctive water masses on the basis of their neodymium isotopic composition ($^{143}Nd/^{144}Nd$).

The REE contents in river waters are about an order of magnitude greater than in seawater but are also variable in detail (Figure 11). Patterns are mostly HREE enriched relative to average upper continental crust (and average shale) and the degree of fractionation and absolute concentrations are pH dependent such that higher pH results in lower absolute concentrations and more fractionated (HREE-enriched) patterns. Accordingly, the major controls on REE distributions in river waters are the upper crustal sources of REE coupled with preferential scavenging of LREE by particles and colloids (especially Fe colloids). Ce anomalies, where present, are more muted than those observed in seawater.

The final natural waters to be considered are hydrothermal waters that form by the circulation of warm surface waters (e.g., ocean water, groundwater) into the subsurface due to deep heat sources, such as magma chambers. In the marine setting, hydrothermal waters are mostly derived from the circulation of seawater through the oceanic crust in the vicinity of the ridges. These waters are surprisingly uniform from place to place and characterized by very large positive Eu anomalies (Figure 11) thought to reflect the dominance of plagioclase alteration in the subsurface basalt. Once vented onto the seafloor, the REE are rapidly scavenged and deposited in the sediment around the ridges. In terrestrial settings, hydrothermal waters commonly have relatively flat shale-normalized REE patterns, reflecting the upper crustal sources, with absolute abundances being pH dependent (Figure 11).

7 CONCLUSIONS

From the earliest foundations of geochemistry and cosmochemistry, the REE have proven to be crucial for understanding a myriad of processes that have influenced the origin and evolution of the solar system and Earth. REE data provided new and important constraints on wide-ranging topics as broad as constraining the earliest history of the solar system using refractory inclusions in meteorites to tracing the evolution of the Earth's crust using sedimentary rocks to understanding paleoceanography using ancient marine authigenic phases. After 50 years of concerted effort, REE geochemistry is now a fairly mature research field. For example, high-quality REE determinations in geological materials, once considered a major analytical challenge, can now be obtained fairly routinely mainly using argon plasma mass spectrometry. Most available geological and cosmochemical reservoirs and processes have now been evaluated at some significant level of understanding for their REE geochemistry.

Although high-quality data can now be relatively easily obtained, there are still issues with poor data that pass peer review and gets published, and data quality remains a lessening but still significant issue. Although there are many international standards available for comparisons (probably too many!), anomalous samples for which data quality may still be an issue (e.g., the tetrad effect) would benefit from international interlaboratory comparisons.

Research that is in need of increased attention by geologists and geochemists is in the field of the economic geology of REE. Increased use of REE in strategically sensitive applications, coupled with limited occurrences of ore deposits—in terms of both numbers and locations–indicates a need for further research in at least two areas. The first is better understanding of the geological relationships leading to ore-grade REE occurrences (e.g., the origin of the largest REE ore deposit on Earth remains controversial) and the second is to further study the fundamental geochemistry of REE, using experimental methods, to better understand processes that may lead to such occurrences.

8 GLOSSARY

Archean Eon: The period of time between the occurrence of the oldest rocks on the Earth (around 4000 million years ago; prior to which is called the *Hadean Eon*) and the base of the Proterozoic eon at about 2500 million years ago.

Authigenic: A mineral or other sedimentary rock component that forms in place, rather than having been transported. May form either at the time the sedimentary rock was deposited or sometime after deposition by diagenetic processes.

Carbonaceous Chondrites: Type of stony meteorite, characterized by the presence of hydrated, clay-type silicate minerals and abundant organic matter. They represent among the most primitive material known in the solar system, and are thought to approximate the bulk composition of the accreting solar nebula.

Carbonatite: A carbonate rock (calcite- and/or dolomite-rich) of magmatic origin typically associated with alkaline igneous rocks and kimberlites.

Crystal Fractionation: Separation of mineral crystals from a magma, typically by settling or flotation due to density differences, resulting in magmatic differentiation.

Diagenesis: Chemical, physical, mineralogical, and biological transformations undergone by a sediment between time of initial deposition and metamorphism.

Granulites: Metamorphic rocks, commonly with coarse grains and gneissic textures, formed at very high pressure and temperatures, typical of lower continental crust.

Leucogranite: A type of highly evolved granite characterized by light color due to a low content of dark mafic minerals.

Lithosphere: Cool outer rigid layer of the Earth, including crust and uppermost mantle. Separated from deeper convecting layers of the mantle by the asthenosphere, a relatively weak zone. Thickness varies from zero at active mid-ocean ridges to as much as 200 km or more beneath continents.

Partial Melting: Incomplete melting of a rock mass. The magma commonly separates from the site of melting.

Pegmatite: A very coarse grained igneous rock, typically of granitic composition, that forms during the latest stages of magma crystallization when volatile contents are high.

Placer and Paleoplacer: Mineral deposits resulting from mechanical concentration of mineral particles by sorting according to density during sedimentary transport (placer deposit), which may also be preserved in ancient sedimentary rock sequences (paleoplacer).

Primitive Mantle: The mantle of a planet prior to the extraction of any crust. Mostly used as a geochemical concept that is the sum of the present-day mantle and crust (but excluding the core) of a planet.

Proterozoic Eon: The period in Earth history between the Archean and the Phanerozoic eons (2500–542 million years ago).

Regolith: The general term for fragmental, unconsolidated material that forms a cover over more coherent bedrock. May be either a residual or transported deposit.

Solar Photosphere: The bright visible surface of the sun, resulting from a layer of strongly ionized gases.

Xenolith: An inclusion within an igneous rock that is genetically unrelated to the enclosing rock.

9 RELATED ARTICLES

Lanthanides: Luminescence Applications; Lanthanides in Living Systems; Lanthanide Oxide/Hydroxide Complexes; Lanthanides: Coordination Chemistry; Sustainability of Rare Earth Resources; The Electronic Structure of the Lanthanides; Variable Valency.

10 ABBREVIATIONS AND ACRONYMS

Ce/Ce*	The ratio of measured Ce divided by the expected Ce assuming a smooth chondrite-normalized REE pattern (Ce*). Values deviating significantly from 1.0 are termed positive Ce anomalies (Ce/Ce*>1) and negative Ce anomalies (Ce/Ce*<1).
CI	Refers to the family of carbonaceous chondritic meteroites named after the Ivuna meteorite. CI chondrites are volatile rich and chemically the most primitive known with compositions nearly identical to the solar photosphere for the nongaseous elements.
CN	Coordination number.
D	Bulk solid-melt partition coefficient, which is the ratio of the element concentration in the bulk rock divided by the concentration in the coexisting melt.
DMM	Depleted mantle source of mid-oceanic ridge basalts (MORB).
EH	The class of enstatite chondrites with relatively high enstatite content.
EL	The class of enstatite chondrites with relatively low enstatite content.
Eu/Eu*	The ratio of measured Eu divided by the expected Eu assuming a smooth chondrite-normalized REE pattern (Eu*). Values deviating significantly from 1.0 are termed positive Eu anomalies (Eu/Eu*>1) and negative Eu anomalies (Eu/Eu*<1).
H	Refers to H-type (high iron) ordinary chondrites.
HED	The meteorite association comprising howardite, eucrite, and diogenite types of meteorites thought to be derived from the asteroid 4-Vesta.
HREE	Heavy rare earth elements—Gd–Lu.
K_d	Mineral-melt partition coefficient, which is the ratio of the element concentration in a mineral divided by the concentration in the coexisting melt.
L	Refers to L-type (low iron) ordinary chondrites.
LL	Refers to LL-type (low iron, low metal) ordinary chondrites.
LREE	Light rare earth elements—La–Sm.
MORB	Mid-ocean ridge basalts.
N	Subscript ''*N*'' refers to a chondrite-normalized value.
OIB	Oceanic island basalts.
PAAS	Post-Archean Australian shale
REE	Rare earth element—in geochemistry nomenclature, this refers to La–Lu, typically also including Y, but excluding Sc.
SNC	The meteorite association comprising shergottite, nakhlite, and chassignite types of meteorites thought to be derived from the planet Mars.
TTG	Sodium-rich granitic rocks, including tonalites, trondhjemites, and granodiorites, typically present in Archean terrains (and in contrast with potassium-rich granitic rocks).

11 REFERENCES

1. L. A. Haskin and F. A. Frey, *Science*, 1966, **152**, 299.
2. E. Greinacher, in 'Industrial Applications of Rare Earth Elements', ed. K. Gschneidner, ACS Symposium Series, The American Chemical Society, Washington, 1981, p. 3.
3. G. B. Haxel, J. B. Hedrick, and G. R. Orris, Rare Earth Elements—Critical Resources for High Technology, U.S.G.S. Fact Sheet 087-02, 2005, p. 4.
4. E. Minami, *Nachr. Gess. Wiss. Göttingen, 2, Math-Physik Kl. IV*, 1935, **1**, 155.
5. R. A. Schmitt, A. W. Mosen, C. S. Siuffredini, J. E. Lasch, R. A. Sharp, and D. A. Olehy, *Nature*, 1960, **186**, 863.
6. L. A. Haskin and M. A. Gehl, *J. Geophys. Res.*, 1962, **67**, 2537.
7. J. C. Norman and L. A. Haskin, *Geochim. Cosmochim. Acta*, 1968, **32**, 93.
8. S. M. McLennan, *Rev. Mineral.*, 1989, **21**, 169.
9. R. H. Byrne, *Geochem. Trans.*, 2002, **3**, 11.
10. J. R. Haas, E. L. Schock, and D. C. Sassani, *Geochim. Cosmochim. Acta*, 1995, **59**, 4329.
11. R. Gieré, in 'Rare Earth Minerals: Chemistry, Origin and Ore Deposits', eds. A. P. Jones, F. Wall, and C. T. Williams, Chapman and Hall, London, 1996, p. 107.
12. J. Emsley, 'The Elements', 3rd edition, Oxford University Press, Oxford, 1998, p. 292.
13. R. A. Dragoset, A. Musgrove, C. W. Clark, and W. C. Martin, Periodic Table: Atomic Properties of the Elements, N.I.S.T., 2011, http://www.nist.gov/pml/data/periodic.cfm.

14. R. D. Shannon, *Acta Crystallogr.*, 1976, **A32**, 751.
15. K. Lodders, *Astrophys. J.*, 2003, **591**, 1220.
16. D. M. Sverjensky, *Earth Planet. Sci. Lett.*, 1984, **67**, 70.
17. C. T. Williams, in 'Rare Earth Minerals: Chemistry, Origin and Ore Deposits', eds. A. P. Jones, F. Wall, and C. T. Williams, Chapman and Hall, London, 1996, p. 327.
18. I. Kawabe, *Geochem. J.*, 1992, **26**, 309.
19. A. Masuda, O. Kawakami, Y. Dohmoto, T. Takenaka, *Geochem. J.*, 1987, **21**, 119.
20. M. Bau, *Geochim. Cosmochim. Acta*, 1999, **63**, 67.
21. S. M. McLennan, *Geochim. Cosmochim. Acta*, 1994, **58**, 2025.
22. P. Henderson ed., 'Rare Earth Element Geochemistry', Elsevier, Amsterdam, 1984, p. 510.
23. B. R. Lipin and G. A. McKay eds, 'Reviews in Mineralogy', Mineralogical Society of America, Washington, 1989, Vol. 21, p. 348.
24. P. Möller, P. Cerny, and F. Saupé, 'Lanthanides, Tantalum and Niobium: Mineralogy, Geochemistry, Characteristics of Primary Ore Deposits, Prospecting, Processing and Applications', Springer-Verlag, Berlin, 1989, p. 380.
25. A. P. Jones, F. Wall, and C. T. Williams eds, 'Rare Earth Minerals: Chemistry, Origin and Ore Deposits', Chapman and Hall, London, 1996, p. 372.
26. S. R. Taylor and S. M. McLennan, in 'Handbook on the Physics and Chemistry of Rare Earths', eds. K. A. Gschneidner Jr, and L. Eyring, Elsevier, Amsterdam, 1988, Vol. 11, p. 485.
27. R. H. Byrne and E. R. Sholkovitz, in 'Handbook on the Physics and Chemistry of Rare Earths', eds. K. A. Gschneidner Jr and L. Eyring, Elsevier, Amsterdam, 1996, Vol. 23, p. 497.
28. Y. Kanazawa and M. Kamitani, *J. Alloy Compd.*, 2006, **408–412**, 1339.
29. A. N. Mariano, *Rev. Mineral.*, 1989, **21**, 309.
30. C. Wu, Z. Yuan, and G. Bai, in 'Rare Earth Minerals: Chemistry, Origin and Ore Deposits', eds. A. P. Jones, F. Wall, and C. T. Williams, Chapman and Hall, London, 1996, p. 281.
31. G. B. Haxel, U.S.G.S. Open-File Report 2005-1219, 2005, 55.
32. S. B. Castor and J. B. Hedrick, in 'Industrial Minerals and Rocks', eds. J. E. Kogel, N. C. Trivedi, and J. M. Barker, Society for Mining, Metallurgy and Exploration, 2006, p. 769.
33. S. B. Castor, *Resour. Geol.*, 2008, **58**, 337.
34. X. -Y. Yang, W. -D. Sun, Y. -X. Zhang, and Y. -F. Zheng, *Geochim. Cosmochim. Acta*, 2009, **73**, 1417.
35. D. M. Hoatson, S. Jaireth, and Y. Miezitis, 'The Major Rare Earth-Element Deposits of Australia: Geological Setting, Exploration, and Resources', Geoscience Australia, 2011, p. 204.
36. M. Asplund, N. Grevesse, A. J. Sauva, and P. Scott, *Annu. Rev. Astron. Astrophys.*, 2009, **47**, 481.
37. A. J. Brearley and R. H. Jones, *Rev. Mineral.*, 1998, **36**, 3.1.
38. D. W. Mittlefehldt, T. J. McCoy, C. A. Goodrich, and A. Kuacher, *Rev. Mineral.*, 1998, **36**, 4.1.
39. H. Y. McSween, Jr and G. R. Huss, 'Cosmochemistry', Cambridge University Press, Cambridge, 2010, p. 549.
40. B. Mason and S. R. Taylor, *Smithsonian Contrib. Earth Sci.*, 1982, **25**, 30.
41. T. R. Ireland, A. J. Fahey, and E. K. Zinner, *Geochim. Cosmochim. Acta*, 1991, **55**, 367.
42. S. R. Taylor and S. M. McLennan, 'Planetary Crusts: Their Composition, Origin and Evolution', Cambridge University Press, Cambridge, 2009, p. 378.
43. S. R. Taylor and S. M. McLennan, 'The Continental Crust: Its Composition and Evolution', Blackwell Scientific Publications, Oxford, 1985, p. 312.
44. J. Hoyle, H. Elderfield, A. Gledhill, and M. Greaves, *Geochim. Cosmochim. Acta*, 1984, **48**, 143.
45. Y.-H. Li, 'A Compendium of Geochemistry: From Solar Nebula to Human Brain', Princeton University Press, Princeton, 2000, p. 475.
46. Y. Nozaki, in 'Encyclopedia of Ocean Sciences', eds. J. H. Steele, K. K. Turekian, and S. A. Thorpe, Academic Press, London, 2001, Vol. 4, p. 2354.

Sustainability of Rare Earth Resources

David A. Atwood

University of Kentucky, Lexington, KY, USA

1 Summary 21
2 Introduction 21
3 Endangered Elements 22
4 Resources and Consumption 23
5 Markets, Products, Applications 23
6 Reduced Use and Recycling 23
7 Fate and Disposition 24
8 Conclusions 24
9 Future Outlook 24
10 Glossary 24
11 End Notes 24
12 Related Articles 25
13 Abbreviations and Acronyms 25
14 References 25

1 SUMMARY

Modern society has come to rely on the incredible technological utility of rare earth elements (REEs). Many products and applications are based on the unique electronic, optical, and magnetic properties of REE. They are used in manufacturing, medicine and catalysis, and provide the foundation for many clean energy technologies. REEs are critically important in military components and therefore considered ''strategic'' with regards to national defense.

However, the widespread use of rare earths has developed with two false assumptions: (i) REEs will always be available, regardless of their location and the environmental costs associated with their extraction and (ii) rare earth resources are sufficiently vast that the elements can be incorporated into single-use commodities. Unfortunately, REE resources are finite and access to REE supplies is uncertain. If the current standards of living are to be maintained, and the ability of future generations to enjoy a similar quality of life is to be ensured, REEs need to be produced and used in a sustainable manner. This should involve reducing the amount of REEs in single-use products, recycling and reusing REEs that are currently being produced, and finding sustainable REE substitutes whenever possible. Ultimately, products containing REEs should be designed in a ''cradle-to-cradle''[1] manner, which is cost-effective and environmentally benign, and ensures a supply of REEs for future generations.

2 INTRODUCTION

Modern society, at the national and individual levels, has come to rely on the unique electronic (***The Electronic Structure of the Lanthanides***), optical, luminescent (***Lanthanides: Luminescence Applications***, ***Luminescence***), magnetic (***Magnetism***), and catalytic (***Homogeneous Catalysis***, ***Heterogeneous Catalysis***) properties of the REEs. REEs, the 17 lanthanoid elements, along with scandium (Sc) and yttrium (Y) are used in catalysts, metal alloys, and magnets, which accounts for about 60% of global REE consumption (approximately evenly divided among the three applications).[2] They are also used in glass, polishing, phosphors and pigments, ceramics, and other products and applications. REEs are also important in medicine, albeit in relatively small amounts, as shift reagents (***Lanthanide Shift Reagents***) and magnetic resonance imaging (***Lanthanides: Magnetic Resonance Imaging***). Significantly, REEs are essential in clean

The Rare Earth Elements. Edited by David A. Atwood. © 2012 John Wiley & Sons, Ltd. ISBN 978-1-119-95097-4

energy technologies for wind turbine generators, low-energy lighting, fuel cells, magnetic refrigeration, and rechargeable batteries in hybrid electric vehicles (HEV).[(a)] Furthermore, REEs are used in majority of military components and therefore considered ''strategic'' with regard to national defense. It has been noted that ''It is easier to find a defense system that has rare earths in it than to find one that does not use them.''[3] The use of REEs in this new, broad range of products and applications has increased significantly over the past decade and is expected to continue to increase in the coming decades.

The widespread use of rare earths has developed with two dangerous assumptions: (i) REEs will always be available, regardless of their location and the geopolitical implications and (ii) REE resources are sufficiently vast that the elements can be used indefinitely in products designed to be used only once.

This chapter does not address the political aspects of rare earth resources embodied in the first assumption. This is a complicated subject that includes how indigenous resources are managed by the countries where they are found and the environmental regulations associated with the mining and isolation of REEs. In addition, this chapter does not describe the substantial human impacts of REE extraction and use. Instead, it outlines the problems and potential solutions associated with the use of the earth's limited REE resources in products and applications.

3 ENDANGERED ELEMENTS

Essentially, all metal use is currently unsustainable, with the possible exception of those such as iron, aluminum, and silicon that comprise a significant fraction of the earth's crust (if the energy costs of their extraction and isolation are not considered). Warnings about the dwindling supplies are summarized for the REEs and other elements in an ''endangered elements periodic table'' (Figure 1).[4,5] Elements become ''endangered'' because of (i) limited supplies, (ii) use in dispersive technologies, (iii) rapid growth in use, (iv) environmental effects being sufficiently damaging to preclude extraction, (v) geopolitical limits to the resource, and (vi) the absence of recycling. On the basis of these criteria REEs are considered, at the least, as ''having limited availability with a future risk to the supply,'' and europium (Eu), terbium (Tb), dysprosium (Dy), and ytterbium (Yb) are listed as ''seriously threatened in the next 100 years.''[3] A complicating factor unique to REEs by comparison to other metals is that REEs are not mined as separate elements but as groups of elements. Increased production for a group of elements, such as dysprosium, praseodymium, and neodymium used in magnets, will lead to increased production of most of the other REEs. Ironically, the move to address climate change and create sustainable energy with HEV and wind turbines will result in increased ''endangerment'' of praseodymium (Pr),

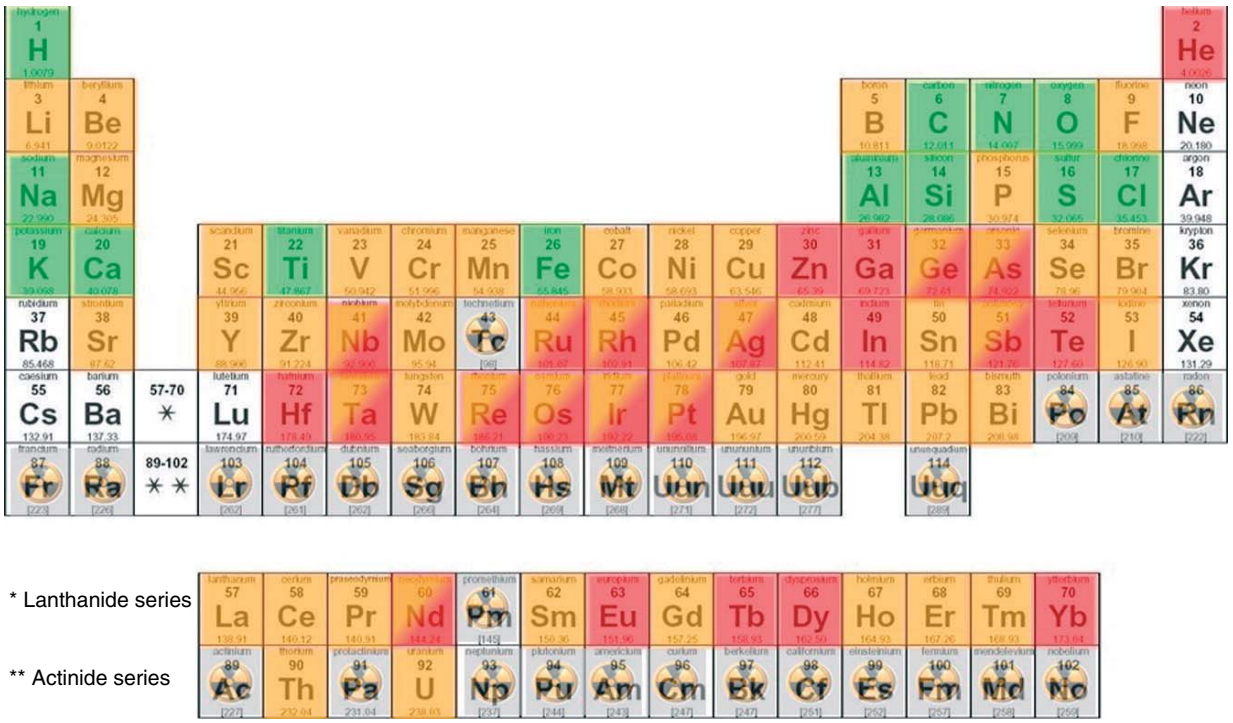


Figure 1 The ''endangered elements periodic table'' created by Mike Pitts, the sustainability manager for Chemistry Innovation. The periodic table and related information can be found at: https://connect.innovateuk.org/web/mike-pitts/blogs/-/blogs/update-to-the-endangered-elements-periodic-table. Reproduced with permission from Mike Pitts

neodymium (Nd), and Dy since these elements are used in wind turbine generators and HEV rechargeable batteries.

4 RESOURCES AND CONSUMPTION

REEs are classified as lithophiles and are partitioned into the earth's crust and mantle. The name ''rare earths'' originated over a century ago when the elements were first identified in minerals that, at the time, were ''rare.'' The elements are actually distributed widely over the earth and relatively accessible on the earth's surface. For a comprehensive description of REE geology, geochemistry, and natural abundances, see ***Geology, Geochemistry, and Natural Abundances of the Rare Earth Elements***. In 2010, the United States Geological Survey (USGS) estimated that there were REE reserves of 110 million metric tons (mt).[6] The static depletion index, the ratio of reserves to present-day production, for REEs is approximately 870 years.[7] Thus, the primary immediate consideration is whether REE production can match demand, and particularly whether it will be possible to increase the use of dysprosium and neodymium in wind turbines and the batteries of electric vehicles.

In 2008, the global production of rare earth oxides (REOs) was 129 000 mt, which corresponds to 109 000 mt of metallic elements. Global demand for REEs has been increasing over the past few years, and the demand has exceeded the amount that China was able to export (Table 1).

5 MARKETS, PRODUCTS, APPLICATIONS

The markets for REEs can be divided into those that are mature and those that are based on more recent technological advances and high growth.[8] Mature markets, accounting for ~60% of global consumption, include the use of REEs in catalysts, glassmaking, lighting, and metallurgy. High-growth markets, accounting for ~40% of global consumption, include battery alloys, ceramics, and permanent magnets (for use in electronics, for example). Some examples discussed below demonstrate the scale of REE consumption.

In 2008, automotive catalytic convertors utilized 6840 mt CeO_2, 380 mt of La_2O_3, and 228 mt of Nd_2O_3. However, more cerium was used as a glass additive and in glass polishing. The predominant use of La_2O_3, at 17 800 mt, is the refining of petroleum into lighter hydrocarbon fractions (called *fluid catalytic cracking*). The Prius nickel metal-hydride (NiMH) battery contains 22 kg of La and Ce. The ''metal'' in NiMH is lanthanum. Cerium and lanthanum accounted for about 63% of the total consumption of REEs in 2008. The Prius has 10 different components that contain, collectively, La, Ce, Eu, Y, Nd, Pr, Dy, and Tb.[9] Neodymium, and lesser amounts of Pr, Dy, and Gd, is the basis of the strong, permanent, and lightweight magnets that are a critical component of a wide variety of products such as wind turbine generators, electric motors, and cell phones. For example, a 3.5-MW wind turbine incorporates 600 kg of REEs. Each Prius HEV contains 22 kg. In 2008, the consumption of Nd_2O_3 was 23 900 mt. This makes Nd the third most consumed REE after cerium (Ce) and lanthanum (La).

6 REDUCED USE AND RECYCLING

In response to the recent high REE prices, manufacturers have begun reducing the amounts of the elements in their products. General Electric has reduced the amount of REEs used in the motors that power windmills. Toyota and other car manufacturers are exploring the possibility of replacing REE-containing magnetic motors with the induction motor used by Tesla motors. However, issues such as the increased weight of the induction motor in comparison to magnetic motors remain to be addressed.

Only about 20 of the 60 most economically valuable metals are currently being recycled at rates >50%. REEs are essentially not being recycled at all, with a recycling rate <1%.[10,11] The majority of the recycling that takes place is the recovery and reuse of material from the production of new magnets. However, Shin-Etsu plans to begin reclaiming the rare earths from used magnets.[12] New chemical and engineering technologies will be needed to recover and recycle

Table 1 Comparison of Chinese and world REE production and demand

	2008[(a)]	2009	2010	2011	2012[(b)]
Global demand	124	85	120	105	123
Production: China	125	120	109	98	na
Consumption: China	68	60	71	70	80
Export quota	56	50	30	30	30
Rest of world demand	56	25	49	35	45

[(a)] Amounts in 100 000 mt.
[(b)] Anticipated as of May 2012.

REEs already in circulation, if the use of REE resources is to eventually become sustainable. This is both a necessity and an opportunity.

7 FATE AND DISPOSITION

The absence of reuse, recovery, or recycling of REEs led to the majority, 58 700 mt, being ultimately disposed in landfills in 2008. Construction aggregate accounted for 21 000 mt. However, 38 800 mt remained in the ''consumer product reservoir,'' meaning that a significant fraction of 2008 production remained in durable products.

8 CONCLUSIONS

Future updates to this chapter will include separate sections to describe recent advances in material reduction, reuse, and recycling in mature markets (catalysts, glass industry, metallurgy, and phosphors) and developing markets (ceramics, Nd magnets, and battery alloys). Intense research and development is on to explore the possibility of replacing REEs with other elements and compounds.

Making REEs a sustainable resource will require a careful consideration of the economic, environmental, and societal implications of REE extraction and use. Sustainable practices in the REE industry must be instituted not only to preserve the quality of life in our current society but also to ensure that future generations may enjoy a similar quality of life.

In the words of Mike Pitts, the sustainability manager for Chemistry Innovation:[13]

> *The real problem is the way we obtain, use and discard rare earth elements. In our linear economy, getting hold of them depends on finding sufficiently concentrated sources. We then smash the ores of the ground, expend huge amounts of energy purifying them, use them and then discard them. The concentration of rare earth elements and other precious metals in our waste streams is often higher than in the ore. Ultimately, the scarcity of rare earth elements comes down to our own short-sightedness and the apparent low cost of business as usual—dig it up, use it, discard it. If we value modern society and want to build a better future, business as usual is no longer an option. We must treasure our rare resources.*

9 FUTURE OUTLOOK

The many new possibilities for REEs, and those that are sure to be discovered, are likely to be unrealized unless the elements can be produced and used in a sustainable manner. REEs should follow the example provided by industries using the platinum group metals (PGMs—Ru, Rh, Pd, Os, Ir, Pt), where recycling and reuse have been integrated into the applications. The cost of the PGMs has motivated this more sustainable approach. The PGMs are predominantly used as catalysts, which makes their isolation more cost-effective and relatively easier in comparison to the REEs that are predominantly used as components in complicated products. Nevertheless, availability and cost are likely to provide the motivation for similar strategies with the REEs. One potential advantage for REEs is that they will be, in effect, more ''concentrated'' in easily identified products compared to their mineral forms. There are significant possibilities for the development of new chemical and engineering technologies to isolate REEs and other ''endangered elements'' from the products that form the foundation of modern society. These must be developed given the impending scarcity of such critical elements. Otherwise, at some point in the not-so-distant future our massive landfills will become the next ''mine-sites'' to obtain the REEs.

10 GLOSSARY

Lithophiles: Elements located in the earth's crust and mantle that typically form ionic bonds and have a high affinity for oxygen. REEs are lithophiles, as are Na, K, Mg, Ca, Fe, and Al.

Sustainable resource: A resource where the rate of consumption is balanced by the rate at which the resource is replenished. An example is products made from wood when the rate at which the trees are harvested matches the rate at which new trees mature. Minerals are not a sustainable resource.

11 END NOTES

[a.] The role of REE in clean energy technology was the subject of a recent U.S. Senate Hearing: Rare Earths, hearing before the Subcommittee on Energy of the Committee on Energy and Natural Resources, United States Senate, 111th Congress, 2nd Session, to examine the role of strategic minerals in clean energy technologies and other applications, as well as a legislation to address the issue, including S. 3521, The Rare Earths Supply Technology and Resources Transformation Act of 2010; September 30, 2010 (62–707 PDF).

12 RELATED ARTICLES

Geology, Geochemistry, and Natural Abundances of the Rare Earth Elements; Heterogeneous Catalysis; Homogeneous Catalysis; Lanthanides: Luminescence Applications; Magnetism.

13 ABBREVIATIONS AND ACRONYMS

HEV = hybrid electric vehicle; PGMs = platinum group metals, Ru, Rh, Pd, Os, Ir, Pt; REEs = rare-earth elements; REOs = rare-earth oxides.

14 REFERENCES

1. W. McDonough and M. Braungart, 'Cradle to Cradle: Remaking the Way We Make Things', North Point Press, New York, 2002.
2. D. J. Kingsnorth, Rare Earths Supply Security: Dream or Possibility, Industrial Minerals Company of Australia (IMCOA) Presentation, Freiberg, FRG, April 2012, Available online at https://connect.innovateuk.org/c/document_library/get_file?p_l_id=3491474&folderId=7750109&name=DLFE-80274.pdf (Accessed May 5, 2012).
3. D. J. Hanson, 'Rare Earths for Security', Chemical & Engineering News, December 2011, p. 33.
4. Aversion of the Endangered Elements Periodic Table updated by Mike Pitts, May 1, 2012, is available online at https://connect.innovateuk.org/web/mike-pitts/blogs/-/blogs/update-to-the-endangered-elements-periodic-table (Accessed May 5, 2012).
5. E. Davies, 'Endangered Elements', Chemistry World, 2011, January, p. 50.
6. United States Geological Survey 'Mineral Yearbook and Mineral Commodity Summary', 2011, Available online at http://minerals.usgs.gov/minerals/ (Accessed April 20, 2012).
7. E. Alonso, A. M. Sherman, T. J. Wallington, M. P. Everson, F. R. Field, R. Roth, and R. E. Kirchain, *Environ. Sci. Technol.*, 2012, **46**, 3406.
8. T. G. Goonan, Rare Earth Elements-End Use and Recyclability, United States Geological Survey Scientific Investigations Report 2011–5094, United States Geological Survey, Denver, CO.
9. British Geological Survey and Natural Environment Research Council, 'Rare Earth Elements', November 2011, p. 21.
10. J. Kemsley, 'Metal Recycling Falls Short', Chemical & Engineering News, May 30, 2011, p. 9.
11. T. E. Graedel, J. Atwood, J.-P. Birate, B. K. Reck, S. F. Sibley, G. Sonnemann, M. Buchart, C. Hagelüken, and United Nations Environmental Programme (UNEP), 'Recycling Rates of Metals: A Status Report, A Report of the Working Group on the Global Metal Flows to the International Resource Panel', 2011.
12. J.-F. Tremblay, 'Managing a Dearth of Rare Earths', Chemical & Engineering News, April 2, 2012, p. 14.
13. M. Pitts, 'Let's Take Better Care of our Rare Earth Elements', New Scientist, February 15, 2011, (2799) p. 26.

The Electronic Structure of the Lanthanides

Ana de Bettencourt-Dias

University of Nevada, Reno, NV, USA

1	Summary	27
2	Introduction	27
3	Valence Configuration of the Metals	27
4	Term Symbols	29
5	Valence Configurations of the Ions	29
6	Ground and Excited State Configurations of the +III Oxidation States	29
7	Lifting of Degeneracies of Ground and Excited States	31
8	Conclusions	32
9	Glossary	33
10	Abbreviations and Acronyms	33
11	References	33

1 SUMMARY

This chapter covers the electronic configuration of the lanthanides as elements and as ions. The valence configurations of these elements are influenced by attractive interactions between the positively charged nucleus and the negatively charged electrons, and by repulsive interactions between negatively charged electrons. The configuration is further influenced by the mutual interaction of the angular momenta of each electron as well as interactions of these electrons with ligands surrounding the atom.

2 INTRODUCTION

The lanthanide ions are the first row of the f-block in the periodic table, often also called the inner transition elements, due to their placement between the s- and the d-block. In agreement with the Aufbau principle and Madelung's energy ordering rule,[1,2] it is for these elements that the 4f orbitals starting being filled. The filling order of the orbitals is greatly influenced by relativistic effects, as addressed below.[3] The 4f orbitals, while part of the valence configuration, are shielded from the coordination environment by the filled 5s and 5p orbitals, and that is the case for lanthanides in their atomic state as well as higher oxidation states, as shown in Figure 1. This greatly influences the chemistry as well as the spectroscopic and magnetic properties of these elements.[4–7]

3 VALENCE CONFIGURATION OF THE METALS

Owing to relativistic and nonrelativistic increased nuclear attraction, atoms with heavy nuclei, starting with the third row of the periodic table, experience contraction of the s and p orbitals, while the d and f orbitals, already diffuse and less penetrating, further expand owing to increased shielding from the nucleus.[3,10,11] This leads to an electron configuration in which all 15 lanthanide elements share the xenon core, [Xe], corresponding to $1s^2 2s^2 2p^6 3s^2 3p^6 3d^{10} 4s^2 4p^6 4d^{10} 5s^2 5p^6$. The remaining electrons, the valence electrons, are then placed in the 6s orbital and, with exception of La, Ce, Gd, and Lu, in the 4f orbital, since the energy difference between the 4f and 5d orbitals is large. Nonetheless, La, Gd, and Lu place one electron in the 5d orbital, a configuration which is favorable as it leads to an empty $4f^0$ (La), a half-filled $4f^7$ (Gd), and a fully filled $4f^{14}$ (Lu) orbital and is further supported by relativistic considerations, which also explains

The Rare Earth Elements. Edited by David A. Atwood. © 2012 John Wiley & Sons, Ltd. ISBN 978-1-119-95097-4

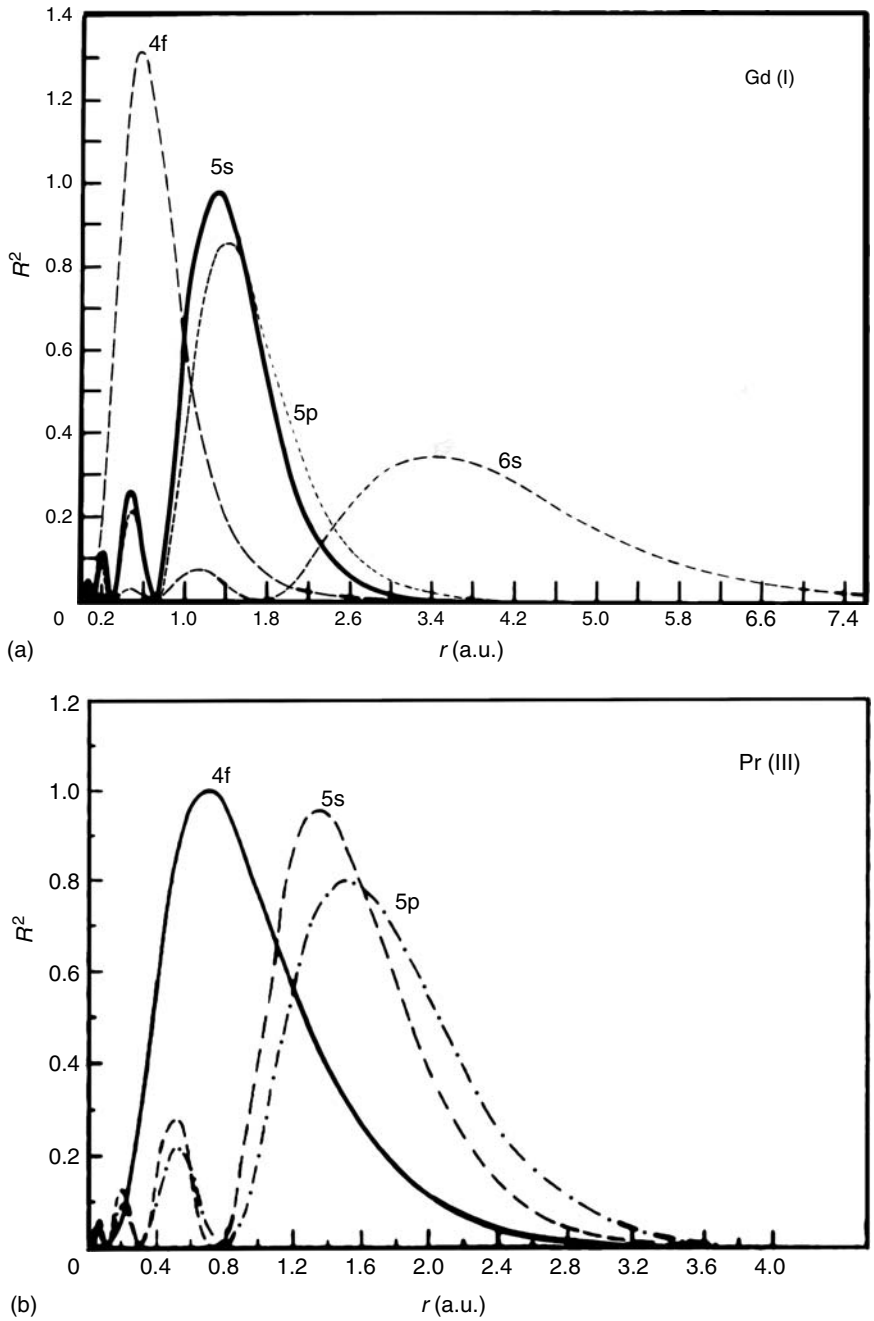


Figure 1 Radial charge density of the valence orbitals of Gd^+ (a) (This figure was published in Ref. 8, Copyright Elsevier (2003)) and Pr^{3+} (b). (Redrawn from B. G. Wybourne, Ref. 9)

the configuration of cerium.[3,6] However, it is found that for metallic lanthanides, the gas phase electronic configuration is $4f^{n+1}6s^2$.[7] The valence configurations for the metallic atoms are summarized in Table 1.

In these elements, the 4f electrons are highly localized, as the 5s and 5p are higher in energy and the orbitals are more spatially extended. Thus, while the 4f electrons convey the atoms and ions interesting magnetic and spectroscopic properties, in the metallic state, their chemical and physical behavior is dictated by the 5d and 6s valence electrons.[4,7] These electrons form the conduction band, along with some contribution from a 4f electron, with the remaining electrons forming the localized +III core. However, europium and ytterbium only donate two electrons to the conduction band, and therefore in the metallic state, a core with +II oxidation state exists for these two elements.[7,12,13]

Table 1 Valence electron configurations of the lanthanides La–Lu in the oxidation states 0, +II, +III, and +IV and corresponding term symbols

Atomic number	Element symbol and name	Valence configuration of element	Term symbol of element	Valence configuration of Ln^{III}	Term symbol of Ln^{III}	Valence configuration of Ln^{II}	Valence configuration of Ln^{IV}
57	La—lanthanum	$[Xe]5d^16s^2$	$^2D_{3/2}$	[Xe]	$^1S_0$	$[Xe]5d^1$	$[Kr]4d^{10}5s^25p^5$
58	Ce—cerium	$[Xe]4f^15d^16s^2$	$^3H_4$	$[Xe]4f^1$	$^2F_{5/2}$	$[Xe]4f^2$	[Xe]
59	Pr—praseodymium	$[Xe]4f^36s^2$	$^4I_{9/2}$	$[Xe]4f^2$	$^3H_4$	$[Xe]4f^3$	$[Xe]4f^1$
60	Nd—neodymium	$[Xe]4f^46s^2$	$^5I_4$	$[Xe]4f^3$	$^4I_{9/2}$	$[Xe]4f^4$	$[Xe]4f^2$
61	Pm—promethium	$[Xe]4f^56s^2$	$^6H_{5/2}$	$[Xe]4f^4$	$^5I_4$	$[Xe]4f^5$	$[Xe]4f^3$
62	Sm—samarium	$[Xe]4f^66s^2$	$^7F_0$	$[Xe]4f^5$	$^6H_{5/2}$	$[Xe]4f^6$	$[Xe]4f^4$
63	Eu—europium	$[Xe]4f^76s^2$	$^8S_{7/2}$	$[Xe]4f^6$	$^7F_0$	$[Xe]4f^7$	$[Xe]4f^5$
64	Gd—gadolinium	$[Xe]4f^75d^16s^2$	$^9D_2$	$[Xe]4f^7$	$^8S_{7/2}$	$[Xe]4f^75d^1$	$[Xe]4f^6$
65	Tb—terbium	$[Xe]4f^96s^2$	$^6H_{15/2}$	$[Xe]4f^8$	$^7F_6$	$[Xe]4f^9$	$[Xe]4f^7$
66	Dy—dysprosium	$[Xe]4f^{10}6s^2$	$^5I_8$	$[Xe]4f^9$	$^6H_{15/2}$	$[Xe]4f^{10}$	$[Xe]4f^8$
67	Ho—holmium	$[Xe]4f^{11}6s^2$	$^4I_{15/2}$	$[Xe]4f^{10}$	$^5I_8$	$[Xe]4f^{11}$	$[Xe]4f^9$
68	Er—erbium	$[Xe]4f^{12}6s^2$	$^3H_6$	$[Xe]4f^{11}$	$^4I_{15/2}$	$[Xe]4f^{12}$	$[Xe]4f^{10}$
69	Tm—thulium	$[Xe]4f1^36s^2$	$^2F_{7/2}$	$[Xe]4f^{12}$	$^3H_6$	$[Xe]4f^{13}$	$[Xe]4f^{11}$
70	Yb—ytterbium	$[Xe]4f^{14}6s^2$	$^1S_0$	$[Xe]4f^{13}$	$^2F_{7/2}$	$[Xe]4f^{14}$	$[Xe]4f^{12}$
71	Lu—lutetium	$[Xe]4f^{14}5d^16s^2$	$^2D_{5/2}$	$[Xe]4f^{14}$	$^1S_0$	$[Xe]4f^{14}6s^1$	$[Xe]4f^{13}$

4 TERM SYMBOLS

The electronic configuration of a polyelectronic atom in its ground or an excited state is given by the term symbol $^{2S+1}L_J$, where $2S + 1$ is the spin multiplicity, S the total spin quantum number ($S = \sum_i s_i$, with s_i the spin quantum number of electron i), and L is the total angular momentum quantum number ($L = \sum_i l_i$ with l_i the angular momentum quantum number of electron i). Instead of numbers, L is indicated by the letters S, P, D, F, G, H, etc., for $L = 0$, 1, 2, 3, 4, 5, etc. J is the total spin–orbit coupling quantum number ($J = L + S, \ldots |L - S|$) and is defined for elements in which spin–orbit coupling, also known as Russell–Saunders coupling, is valid, which is the case for the heavy lanthanides.[9] In Table 1, the ground state term symbols for the elemental lanthanides are indicated. The reader is referred to additional references for methods to determine the term symbols for ground and excited states.[14,15]

5 VALENCE CONFIGURATIONS OF THE IONS

Despite the presence of the $6s^2$ electrons in addition to the 4f and the Xe core for most lanthanides, the most common oxidation state is +III and not +II, as is seen for the alkaline-earth metals which have a similar configuration. The electronic configurations for this oxidation state, along with the corresponding term symbols, are summarized in Table 1. In the oxidation state +III, the configuration is $[Xe]4f^n$ for all of the ions, with $n = 0$ for La^{III} to $n = 14$ for Lu^{III}. The more common +III state is justified by the additional stabilization gained in interactions of the triply charged instead of doubly charged ions, which offsets the energy expended for the removal of an f electron.[16] For example, the hydration energies ΔG^0 of the divalent lanthanide ions average 1402 ± 68 kJ mol^{-1}, while for the trivalent lanthanide ions, the average is 3362 ± 126 kJ mol^{-1}.[17] Nonetheless, an oxidation state of +II is frequently attained by europium and ytterbium, since these ions will have configurations with half-filled and fully filled 4f shells, which translate, for example, into relatively mild reduction potentials of -0.34 and -1.18 V, respectively.[17] Similarly, samarium easily reaches the +II oxidation state, and its reduction potential is 1.50 V.[17] The extra stability of the half-filled and fully filled shells is seen for terbium and cerium, both of which are encountered in the +IV oxidation state, with reduction potentials of 1.7 and 3.3 V, respectively.[18] More recently, the unusual oxidation states, most notably +II, have been reported for several other lanthanides in organometallic compounds,[19–21] despite the large reduction potentials (< -2.22 V).[17] The +IV states, especially of terbium, are more frequently seen in solid-state inorganic compounds.[22–24]

6 GROUND AND EXCITED STATE CONFIGURATIONS OF THE +III OXIDATION STATES

The ground state electronic configurations summarized in Table 1 are indicated with their corresponding term symbols. In addition to the ground state, every lanthanide has excited states. The total degeneracy or number of microstates (D) for a given electronic configuration for an element with a $4f^n$ configuration, for which the angular momentum quantum

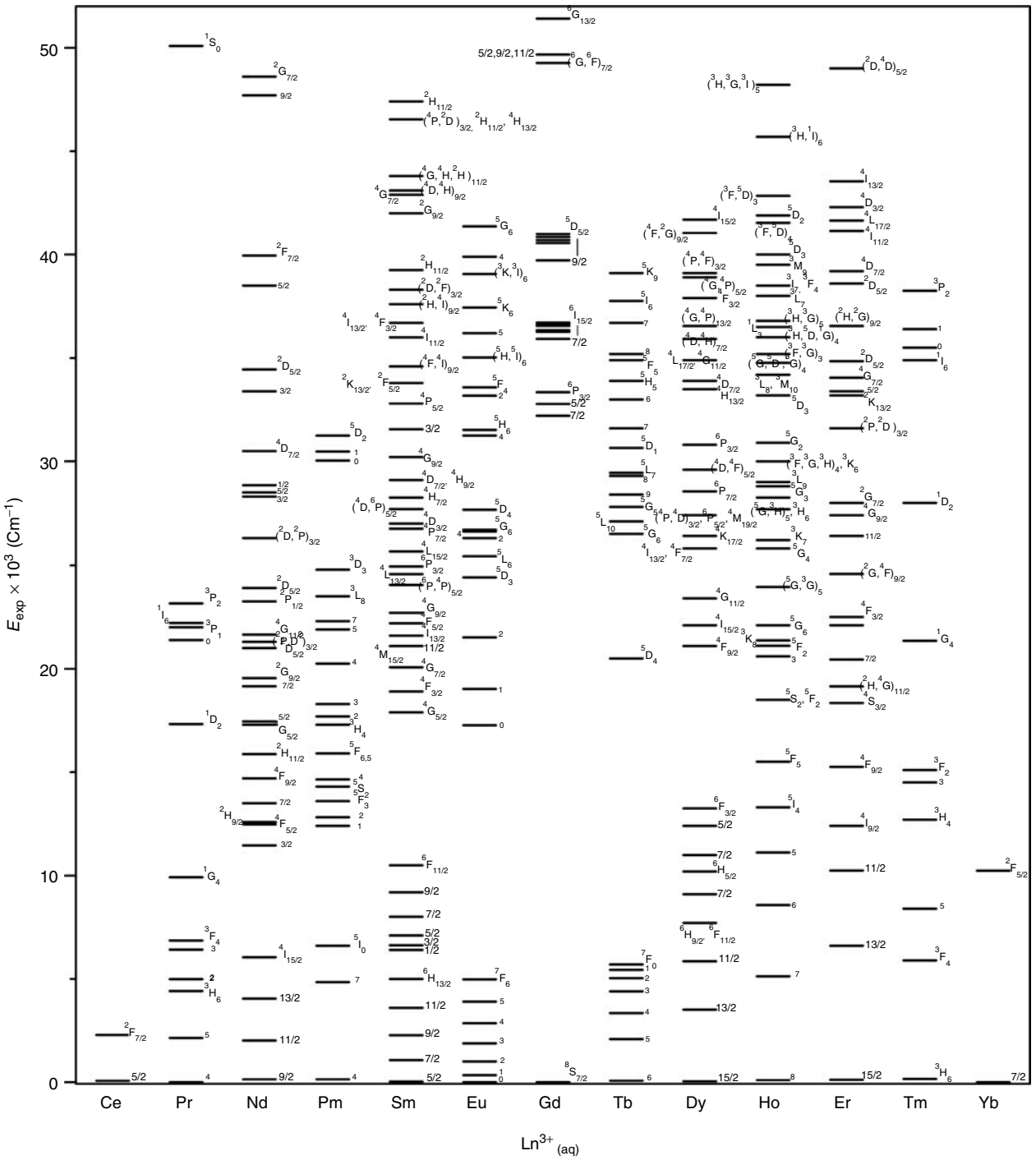


Figure 2 Observed energy levels of the Ln^{III} aqueous ions with term symbols[27–32]

number $l = 3$, is given by equation (1).

$$D = \frac{(4l+2)!}{(4l+2-n)!n!} = \frac{14!}{(14-n)!n!} \quad (1)$$

This degeneracy is lifted when electron–electron interactions are considered, as well as spin–orbit coupling, leading to a large number of nondegenerate levels for each lanthanide. Energies of these states can be calculated, and are also observed in absorption spectra of the atoms and ions.[25] The energy levels observed in absorption spectra of the $Ln^{3+}_{(aq)}$ ions are displayed in Figure 2. The large number of levels further splits when the ions are placed in a crystal field.

Table 2 Number of new M_J sublevels for a parent J term in a given group symmetry[8,33]

Symmetry	Integer J						
	0	1	2	3	4	5	6
Icosahedral I_h	1	1	1	2	2	3	4
Cubic O_h, O, T_d, T_h, T	1	1	2	3	4	4	6
Hexagonal D_{6h}, D_6, C_{6v}, C_{6h}, D_{3h}, C_{3h}, D_{3d}, D_3, C_{3v}, S_6, C_3	1	2	3	5	6	7	9
Pentagonal D_{5h}, C_{5h}, C_{5v}, C_5, D_5	1	2	3	4	5	7	8
Tetragonal D_{4h}, D_4, C_{4v}, C_{4h}, C_4, D_{2d}, S_4	1	2	4	5	7	8	10
Low D_{2h}, D_2, C_{2v}, C_{2h}, C_2, C_s, S_2, C_1	1	3	5	7	9	11	13
	Half-integer J						
	1/2	3/2	5/2	7/2	9/2	11/2	13/2	15/2	17/2
Cubic	1	1	2	3	3	4	5	6	6
Other symmetries	1	2	3	4	5	6	7	8	9

The crystal field has a similar effect on the f elements as on the transition metals, leading to symmetry-dependent splitting, but in the case of the f elements, the observed splittings are much smaller. While a d-block element experiences crystal field splitting energies in the range of 15 000 to 25 000 cm^{-1}, in the case of the lanthanides, the splitting is in the range 100–500 cm^{-1}.[26] In a crystal field, lifting of the $2J + 1$ degenerate J levels leads to up to $2J + 1$ new Stark levels, as summarized in Table 2, depending on the point group symmetry of the lanthanide ion.

These new states are assigned additional quantum numbers M_J.[34] A similar lifting of the degeneracy is seen when the ions are placed in a magnetic field and the Zeeman levels are observed.[9,34]

7 LIFTING OF DEGENERACIES OF GROUND AND EXCITED STATES

The behavior of the electrons in the atom or ion is given by a wave function, which is a solution of the Hamiltonian for the system. In the case of the lanthanides, the Hamiltonian H is given in equation (2).

$$H = H_o + H_{ee} + H_{so} + H_{cf} + H_z \quad (2)$$

H_o is the contribution to the Hamiltonian from the kinetic energy of all the electrons and their Coulomb interaction with the nucleus. The effect of H_o is equal on all electrons, not leading to a lifting of the degeneracy of the levels and can therefore be taken as a constant. H_{ee} is the contribution from electron–electron Coulomb interactions, given by equation (3a), H_{so} is the contribution from the coupling of the spin and orbital angular momentum of the electron, given by equation (3b). H_{cf} is the contribution from the crystal field, given by equation (3c), and H_z, the Hamiltonian due to the Zeeman effect or magnetic field interaction, is given by equation (3d).[8,9,34–36]

$$H_{ee} = \sum_{k=0}^{6} f^k F_k \quad (3a)$$

$$H_{so} = \zeta_{4f}\, S \times L \quad (3b)$$

$$H_{cf} = \sum_{i,k,q} B_q^k (C_q^k)_i \quad (3c)$$

$$H_z = g\, \beta\, B \times J \quad (3d)$$

F_k are Slater's radial integrals with coefficients f^k and k an even integer. The radial integrals can be fit to experimentally observed energy levels, and representative values are shown in Table 3. ζ_{4f}, the spin–orbit coupling constant, is a radial integral. It is a constant for any states with the same configuration and can be fit experimentally; its values range from approximately 600 to 3000 cm^{-1}, depending on the number of electrons in the 4f shell, as shown in Table 3.[9]

S, L, and J are the quantum numbers defined above, ${C_q}^k$ is a tensor operator, with the same symmetry properties as the angular integrals, and ${B_q}^k$ its expansion coefficient or crystal field parameter, g is Landé's value, B the external

Table 3 Parameters (cm^{-1}) for energy levels of solution absorption spectra of Ln^{III} with f^n configuration[8,36]

Ln^{III}	n	F_2	F_4	F_6	ζ_{4f}
Ce	—	—	—	—	644
Pr	2	304.7	50.82	5.16	714.5
Nd	3	333.6	48.06	5.450	874.1
Pm	4	351.0	47.70	5.9300	1030
Sm	5	371.8	54.02	6.027	1171
Eu	6	470.6	70.91	4.953	1297
Gd	7	488.4	46.28	6.219	1454
Tb	8	486.7	69.17	5.859	1681
Dy	9	420.0	58.00	6.346	1900
Ho	10	415.0	68.80	7.270	2163
Er	11	433.2	667.10	7.360	2393
Tm	12	447.6	67.12	7.336	2652
Yb	13	—	—	—	2882.7

Table 4 Nonvanishing crystal field parameters B_q^k for various symmetries[26]

Crystal symmetry	Site symmetry	B_q^k
Monoclinic	C_s, C_2, C_{2h}	B_0^2, B_0^4, B_0^6, Re(B_2^2), B_2^4, B_2^6, B_4^4, B_4^6, B_6^6
Rhombic	C_{2v}, D_2, D_{2h}	B_0^2, B_0^4, B_0^6, Re(B_2^2, B_2^4, B_2^6, B_4^4, B_4^6, B_6^6)
Trigonal	C_3, S_6	B_0^2, B_0^4, B_0^6, Re(B_3^4), B_3^6, B_6^6
	C_{3v}, D_3, D_{3d}	B_0^2, B_0^4, B_0^6, Re(B_3^4, B_3^6, B_6^6)
Tetragonal	C_4, S_4, C_{4h}	B_0^2, B_0^4, B_0^6, Re(B_4^4), B_4^6
	D_4, C_{4v}, D_{2d}, D_{4h}	B_0^2, B_0^4, B_0^6, Re(B_4^4, B_4^6)
Hexagonal	C_6, C_{3h}, C_{6h}, D_6, C_{6v}, D_{3h}, D_{6h}	B_0^2, B_0^4, B_0^6, Re(B_6^6)
Cubic	T, T_d, T_h, O, O_h	B_0^4, B_0^6, Re(B_4^4, B_4^6) ($B_4^4 = 5/\sqrt{70}\ B_0^4$, $B_4^6 = -\sqrt{(7/2)}B_0^6$)

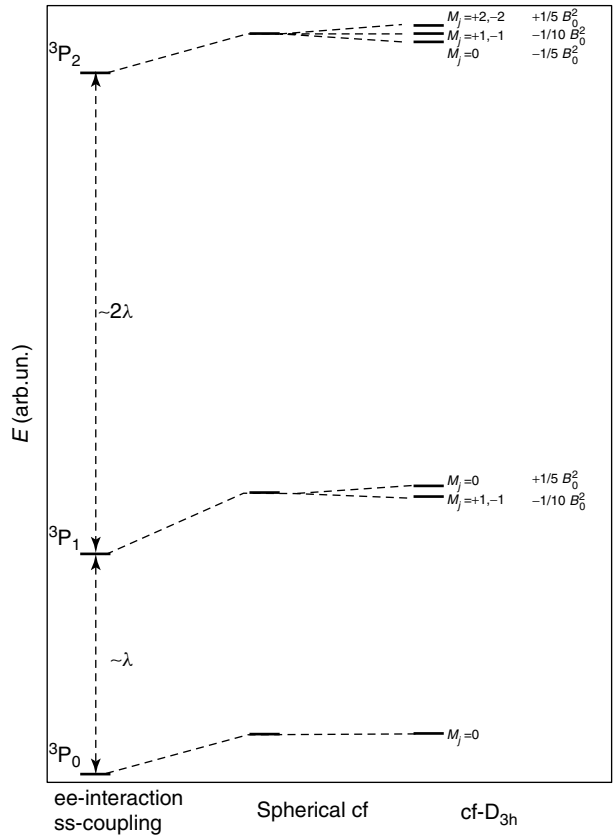


Figure 3 Effects of the electron–electron interaction, spin–orbit coupling (indicated by the spin–orbit constant λ), a spherical crystal field, and a crystal field of D_{3h} symmetry (indicated by the crystal field parameters B_0^2) on the energy levels of the ^3P term of Pr^{3+}.[8, 36]

magnetic field, and β is Bohr's magneton. For a 4f system, k has the values 2, 4, and 6, while $|q| \leq k$.[8] The B_q^k crystal field parameters can also be fit experimentally.[25,35,36] Their sign and magnitude depend on the symmetry of the crystal field around the lanthanide ion and equation (4), which includes an imaginary crystal field parameter, represents the crystal field Hamiltonian for trigonal C_{3h} symmetry.[37]

$$H_{cf} = B_0^2C_0^2 + B_0^4C_0^4 + B_0^6C_0^6 + B_6^6(C_6^6 + C_{-6}^6) + iB'^6_6(C_{-6}^6 - C_6^6) \quad (4)$$

Table 4 summarizes which B_q^k parameters are nonvanishing for other symmetries.

A many-electron spin–orbit constant for a $4f^n$ ion, the parameter λ, can be defined and is related to ζ_{4f} as shown in equation (5).[8]

$$\lambda = \frac{\zeta_{4f}}{n} \quad (5)$$

Landé's interval rule specifies that the energy of two neighboring levels with quantum numbers J and $J-1$ is proportional to J by the parameter λ,[9] as discussed below.

Considering a central field approximation, in which the electrons move independently in a spherically symmetric potential, it is possible to determine the energies of the different electronic configurations and inspect the lifting of the degeneracy through the electron–electron interactions, the spin–orbit coupling, as well as the crystal field effect. How these perturbations affect a given lanthanide ion is shown in Figure 3 for the ^3P level of Pr^{3+} in an environment of D_{3h} symmetry. The electron–electron interactions and spin–orbit coupling lead to the splitting of the ^3P level into $^3P_0$, $^3P_1$, and $^3P_2$. In the presence of a spherically symmetric crystal field, the energies of these levels are raised, but it is only in the presence of a different symmetry field, such as D_{3h}, that the splitting into Stark levels is observed.

8 CONCLUSIONS

The properties of the f elements are strongly influenced by the core nature of the 4f electrons. In the metallic state, in addition to the 4f electrons, the valence configuration contains 6s and, in some cases, 5d electrons. As ions, the oxidation state commonly seen is the +III state. The valence electron configuration then is composed only of 4f electrons. These f electrons display a large number of degenerate states in the absence of any interactions. However, perturbations such as electron–electron interactions, spin–orbit coupling, an external crystal field, or external magnetic field lead to lifting of the degeneracy and the appearance of numerous nondegenerate levels.

9 GLOSSARY

Coulomb interactions: Electrostatic interactions between charged particles. These interactions are attractive in the case of differently charged particles and repulsive for equally charged particles.

Crystal field: The static electric field generated by a group of ligands modeled as point charges surrounding a central atom or ion and which contributes to a differentiation of the energies of initially degenerate orbitals.

Degenerate levels: Levels with the same energy.

Relativistic effects: Difference in calculated properties of a system with electrons when considering and without considering relativity theory. In heavy atoms with highly positive nuclear charges, electrons near the nucleus are accelerated to close to the speed of light to avoid collapsing into the nucleus. As a result of the increased speed, they experience a relativistic mass increase and a relativistic contraction of the radius of their ''orbit'' around the nucleus.

Spin–orbit coupling: Interaction of the spin of the electron with its angular momentum of movement around the nucleus.

Stark effect: Lifting of the degeneracy of levels due to an external electric field.

Zeeman effect: Lifting of the degeneracy of levels due to an external magnetic field.

10 ABBREVIATIONS AND ACRONYMS

$^{2S+1}L_J$	term symbol of ground or excited state
$2S+1$	spin multiplicity
$S = \sigma_i s_i$	total spin quantum number
s_i	spin quantum number of electron i
$L = \sigma_i l_i$	total angular momentum quantum number
l_i	angular momentum quantum number of electron i
$J = L+S, \ldots, \lvert L-S \rvert$	spin –orbit coupling quantum number
D	total degeneracy of a state; number of microstates
l	one-electron angular momentum quantum number
n	principal quantum number
H	Hamiltonian
H_o	contribution to Hamiltonian from kinetic energy of all electrons and their Coulomb interaction with the nucleus
H_{ee}	contribution to Hamiltonian from electron–electron Coulomb interactions
H_{so}	contribution to Hamiltonian from spin–orbit coupling
H_{cf}	contribution to Hamiltonian from crystal field
H_z	contribution to Hamiltonian due to interaction with magnetic field
F_k	Slater's radial integrals
f^k	coefficient to Slater's radial integrals, k is even integer
ζ_{4f}	spin-orbit coupling constant, a radial integral
λ	many-electron spin–orbit constant
C_q^k	tensor operator
B_q^k	expansion coefficient of tensor operator; also, crystal field parameter
g	Landè's value
B	external magnetic field
β	Bohr's magneton

11 REFERENCES

1. V. N. Ostrovsky, *Ann. N. Y. Acad. Sci.*, 2003, **988**, 182.
2. E. Madelung, 'Die mathematischen Hilfsmittel des Physikers', 4th edition, Springer Verlag, Berlin, 1950.
3. J. Autschbach, S. Siekierski, M. Seth, P. Schwerdtfeger, and W. H. E. Schwarz, *J. Comput. Chem.*, 2002, **23**, 804.
4. M. R. Norman and D. D. Koelling, in 'Handbook on the Physics and Chemistry of Rare Earths', eds. Karl A. Gschneidner Jr., Gregory R. Choppin, and LeRoy Eyring, Elsevier, Amsterdam, 1993, Vol. 17, p. 1.
5. A. de Bettencourt-Dias, *Curr. Org. Chem.*, 2007, **11**, 1460.
6. N. M. Edelstein, *J. Alloys Compd.*, 1995, **223**, 197.
7. K. A. Gschneidner Jr., *J. Less-Common Met.*, 1971, **25**, 405.
8. V. S. Sastri, J. C. Bünzli, J. R. Perumareddi, V. R. Rao, and G. V. S. Rayudu eds, 'Modern Aspects of Rare Earths and their Complexes, Elsevier, Amsterdam, 2003.
9. B. G. Wybourne, 'Spectroscopic Properties of Rare Earths', Wiley Interscience, New York, 1965.
10. E. J. Baerends, W. H. E. Schwarz, P. Schwerdtfeger, and J. G. Snijders, *J. Phys. B: At. Mol. Opt. Phys.*, 1990, **23**, 3225.
11. E. Diemann, *Prax. Naturwiss. Chem.*, 1994, **43**, 36.
12. A. J. Freeman, *Physica B+C*, 1980, **102**, 3.
13. C. H. la Blanchetais and F. Trombe, *Compt. Rend.*, 1956, **243**, 707.
14. N. W. Gregory, *J. Chem. Educ.*, 1956, **33**, 144.

15. K. E. Hyde, *J. Chem. Educ.*, 1975, **52**, 87.
16. R. E. Connick, *J. Chem. Soc.*, 1949, S235. DOI: 10.1039/jr949000s235.
17. N. B. Mikheev, S. A. Kulyukhin, A. N. Kamenskaya, I. A. Rumer, and N. A. Konovalova, *Radiochemistry*, 2004, **46**, 521.
18. S. A. Cotton, 'Lanthanide and Actinide Chemistry', John Wiley & Sons, Chichester, 2006.
19. P. L. Arnold and I. J. Casely, *Chem. Rev.*, 2009, **109**, 3599.
20. J. G. Brennan and A. Sella, *Organomet. Chem.*, 2010, **36**, 121.
21. F. T. Edelmann, *Coord. Chem. Rev.*, 2011, **255**, 1834.
22. D. Avignant, E. Largeau, V. Gaumet, P. Dugat, and M. El-Ghozzi, *J. Alloys Compd.*, 1998, **275–277**, 1.
23. V. Nair and A. Deepthi, *Chem. Rev.*, 2007, **107**, 1862.
24. V. Sridharan and J. C. Menendez, *Chem. Rev.*, 2010, **110**, 3805.
25. P. S. Peijzel, A. Meijerink, R. T. Wegh, M. F. Reid, and G. W. Burdick, *J. Solid State Chem.*, 2005, **178**, 448.
26. G. Liu and B. Jacquier eds, 'Spectroscopic Properties of Rare Earths in Optical Materials', Springer Verlag, Heidelberg, 2005.
27. W. T. Carnall, P. R. Fields, and K. Rajnak, *J. Chem. Phys.*, 1968, **49**, 4450.
28. W. T. Carnall, P. R. Fields, and K. Rajnak, *J. Chem. Phys.*, 1968, **49**, 4447.
29. W. T. Carnall, P. R. Fields, and K. Rajnak, *J. Chem. Phys.*, 1968, **49**, 4443.
30. W. T. Carnall, P. R. Fields, and K. Rajnak, *J. Chem. Phys.*, 1968, **49**, 4424.
31. W. T. Carnall, *J. Phys. Chem.*, 1963, **67**, 1206.
32. N. Haage, K. H. Hellwege, J. Jaeger, and G. Schaack, *Phys. Kondens. Mater.*, 1969, **10**, 144.
33. J.-C. G. Bünzli and S. V. Eliseeva, *Springer Ser. Fluoresc.*, 2011, **7**, 1.
34. B. G. Wybourne and L. Smentek, 'Optical Spectroscopy of Lanthanides: Magnetic and Hyperfine Interactions', CRC Press, Boca Raton, FL, 2007.
35. W. T. Carnall, G. L. Goodman, K. Rajnak, and R. S. Rana, *J. Chem. Phys.*, 1989, **90**, 3443.
36. W. T. Carnall and P. R. Fields, *Adv. Chem. Ser.*, 1967, **71**, 86.
37. C. Görller-Walrand and K. Binnemans, in 'Handbook on the Physics and Chemistry of Rare Earths', eds. Karl A. Gschneidner Jr. and LeRoy Eyring, Elsevier, Amsterdam, 1996, Vol. 23, p. 121.

Variable Valency

Andrew W.G. Platt

Staffordshire University, Stoke-on-Trent, UK

1 Summary 35
2 Introduction 35
3 Zero Oxidation State Compounds 36
4 Distribution of Oxidation States 36
5 The +3 Oxidation State 39
6 Conclusion 42
7 Glossary 42
8 Related Articles 42
9 Abbreviations and Acronyms 42
10 References 42

1 SUMMARY

The most stable oxidation state for all lanthanide elements is the +3 state. This primarily arises as a result of the lack of covalent overlap, which stabilizes low and high oxidation states in the d-block metals by the formation of π bonds. While some zero-valent complexes are known, only the +2 and +4 oxidation states have an extensive chemistry and even this is restricted to a few of the elements. The reasons for the existence of compounds in the +4 and +2 oxidations states can be found in an analysis of the thermodynamics of their formation and decomposition reactions. For example, while the formation of all LnF_4 and LnX_2 is favorable with respect to the elements, there are favorable decomposition routes to Ln^{III} for the majority of them. As a result, relatively few are known as stable compounds. Thus LnX_4 decomposition to LnX_3 and X_2 is generally favorable, while most LnX_2 are unstable with respect to disproportionation to LnX_3 and Ln.

In aqueous solution, all Ln^{3+} ions are stable and the observation of Ln^{IV} and Ln^{II} species is only possible as decomposition by either oxidation or reduction of water is, in some cases, slow, e.g., in Ce^{IV} and Eu^{2+}. The redox potentials of Ce^{IV} are dependent, to some extent, on the ligands bonded to the ion and this may account for the existence of a few compounds with readily oxidizable groups bound to Ce^{4+} such as chloride and even iodide.

2 INTRODUCTION

The term *variable valency* is normally applied to transition metals and p-block elements where interconversions from one oxidation state to another are often easily achieved and several oxidation states of an element are readily accessible. For example, Fe^{II} and Fe^{III} are conveniently interconverted by use of mild oxidizing and reducing agents and many p-block elements have a large range of available oxidation states, e.g., S^{-II} to S^{VI} and Cl^{-I} to Cl^{VIII}.

For lanthanide metals, the situation is very different and the +3 oxidation state is by far the most stable in aqueous solution and in the solid state and the oxidation and reduction of the Ln^{3+} ion is usually very difficult. With the possible exceptions of cerium and europium transitions between oxidation states require forcing conditions. The products of these oxidations and reductions are almost always unstable with respect to the +3 oxidation state.

For lanthanide metals, the range of oxidation states is thus very limited and for many of the metals, the +3 state is the only significant one.

This limited range of oxidation states can be explained by the lack of covalent bonding, which plays a major role in the stabilization of transition metal compounds in both low and high oxidation states. For instance, in metal carbonyl complexes, such as $Fe(CO)_5$, the high electron density at the metal center is reduced by overlap between the filled metal d orbitals and the empty CO π* orbitals (Figure 1a). Similarly,

The Rare Earth Elements. Edited by David A. Atwood. © 2012 John Wiley & Sons, Ltd. ISBN 978-1-119-95097-4

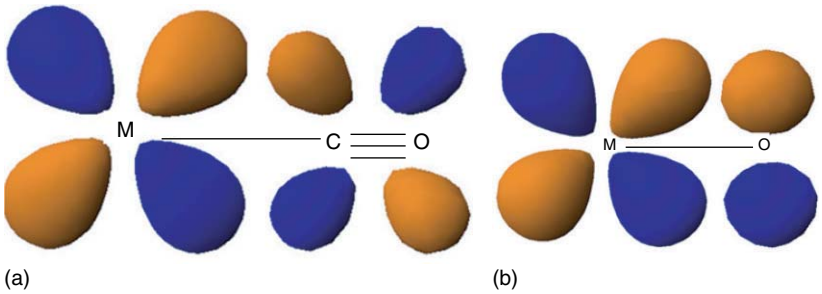


Figure 1 The π bonding in (a) low valent and (b) high valent transition metal complexes

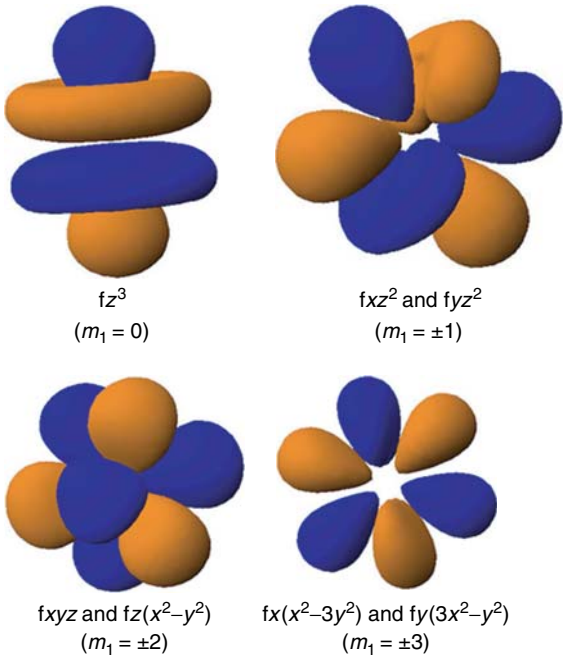


Figure 2 The shapes of the f orbitals

in high oxidation state complexes such as MnO_4^-, pπ–dπ bonding increases electron density at the Mn^{VII} center by donation of electron density from the filled oxygen 2p orbital into empty metal d orbitals as illustrated in Figure 1b.

The valence 4f orbitals on lanthanides do not possess the correct symmetry for such overlap as can be seen in the boundary surfaces shown in Figure 2. In addition to this, they are effectively embedded within the 5s and 5p core and do not extend to the bonding region on the periphery of the atom. Thus, covalent overlap and the stabilization it brings to high and low oxidation states are not possible for lanthanides, where bonding is essentially electrostatic in nature.

3 ZERO OXIDATION STATE COMPOUNDS

Compounds in the zero oxidation state[1] are represented mainly by a number of unstable carbonyl complexes that decompose well below room temperature and some better characterized zero-valent complexes with bulky aromatic hydrocarbons. Their stability depends in part on the low 4f → 5d promotion energies, which allow the formation of covalent bonds. Their synthesis requires special conditions and they are not further discussed here.

4 DISTRIBUTION OF OXIDATION STATES

While the +3 oxidation state is the most stable for all lanthanide elements, some do show a significant chemistry in +2 and +4 oxidation states as indicated in Table 1.

Simple thermodynamics in the form of thermochemical cycles can often shed light on the changes in stability of the +2 and +4 states.

4.1 The +4 Oxidation State: Solid State

The existence of compounds in the +4 oxidation states can be correlated to the relatively low ionization energies

Table 1 The distribution of oxidation states of lanthanides

+4		√	√	√					√	√					
+3	La	Ce	Pr	Nd	Pm	Sm	Eu	Gd	Tb	Dy	Ho	Er	Tm	Yb	Lu
+2	—	—	—	√	—	√	√	—	—	√	—	—	√	√	—

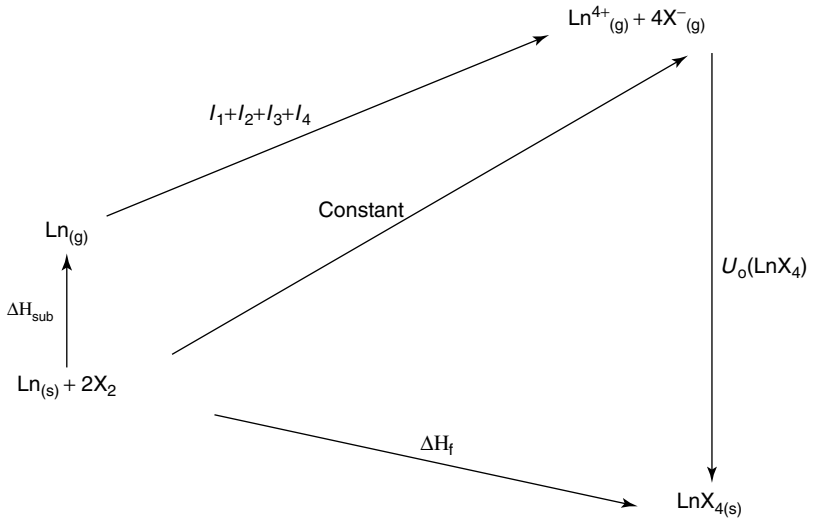


Figure 3 A thermochemical cycle for the formation of LnX_4

associated with the production of Ln^{4+}, e.g., when the Ln^{4+} ion has an especially stable electronic configuration as in Ce^{4+} ($4f^{0}$) and Tb^{4+} ($4f^{7}$). However, this does not fully explain the observation of +4 oxidation states for other lanthanides, some of which have a limited range of compounds in the +4 oxidation state without a stabilizing electronic configuration. Thus Pr^{IV}, Nd^{IV}, and Dy^{IV} can all be prepared albeit with some difficulty.

The accessibility of the +4 oxidation state can be examined by use of thermochemical cycles. For solid-state compounds, the enthalpy of formation of tetrahalides, LnX_4, can give an insight into the factors that influence the variation in the stability of oxidation states. A cycle for the estimation of the enthalpy of formation of LnX_4 is shown in Figure 3.

From this, the enthalpy of formation is as shown in equation (1)

$$\Delta H_f = \Delta H_{sub} + (I_1 + I_2 + I_3 + I_4) + U_o(LnX_4) + c \quad (1)$$

where I_n refers to the respective ionization energies (I_1 for $Ln_{(g)} \rightarrow Ln^{+}_{(g)} + e^{-}$ etc.) and $U_o(LnX_4)$ is the lattice energy of the tetrahalide and ''c'' is a constant that depends only on the properties of the halogen and thus does not affect the variation in stability of LnX_4 with lanthanide. The values for this constant are all exothermic with the value for fluorine, at about $-994\,kJ\,mol^{-1}$, being considerably more so than the others. Not surprisingly, this means that of all the tetrahalides, LnF_4 would be expected to be the most stable.

On inspecting the lanthanide-dependent terms, it can be seen that ΔH_f is governed primarily by the difference in two large quantities. The lattice energy of LnX_4 makes a large exothermic contribution to ΔH_f and the sum of the first four ionization energies a large endothermic contribution. The sum of ionization energies is known for all lanthanides and while LnF_4 are unknown for most Ln, a reasonable estimation of the lattice energy can be made from those of similar compounds. As the magnitude of ΔH_{sub} is in the order of hundreds of $kJ\,mol^{-1}$, it might be expected to have relatively little impact on the stability of LnX_4. However, in equation (1), ΔH_f can be seen to result from a potentially small difference between two large terms and so the influence of lower magnitude contributions such as ΔH_{sub} may well help to explain the observed stability of the +4 oxidation state for some of the lanthanides.

As the sum of ionization energies makes an endothermic contribution to ΔH_f of LnX_4, it would be expected that stable compounds are most likely to be found where these values are low or at a minimum.

The values of the sum of the first four ionization energies are shown in Figure 4 and from this, it can be seen that the minimum values correspond to Ce and Tb for which stable tetrafluorides are known. Relatively low values for Pr and Nd mean that the +4 oxidation state is at least accessible in the solid state for these elements. The fact that stable compounds of Tb and Dy can be made when the sum of ionization energies is higher than Pr and Nd is possibly due to their lattice energies. These would be expected to be higher in magnitude because of the smaller ionic radii of Tb^{4+} and Dy^{4+} compared to Ce^{4+}, Pr^{4+}, and Nd^{4+}. In the case of dysprosium, the observation of a +4 state also corresponds to a local minimum in the enthalpy of sublimation of the metal (see ***Group Trends***) which would be expected to make a small endothermic contribution to the stability of Dy^{IV} compared to Ho^{IV}.

To estimate the heat of formation of LaF_4, the lattice energy can be taken as being similar to the value for the known CeF_4 for which $U_o = -8391\,kJ\,mol^{-1}$ and the sum of ionization energies, $I_1 + I_2 + I_3 + I_4 =$

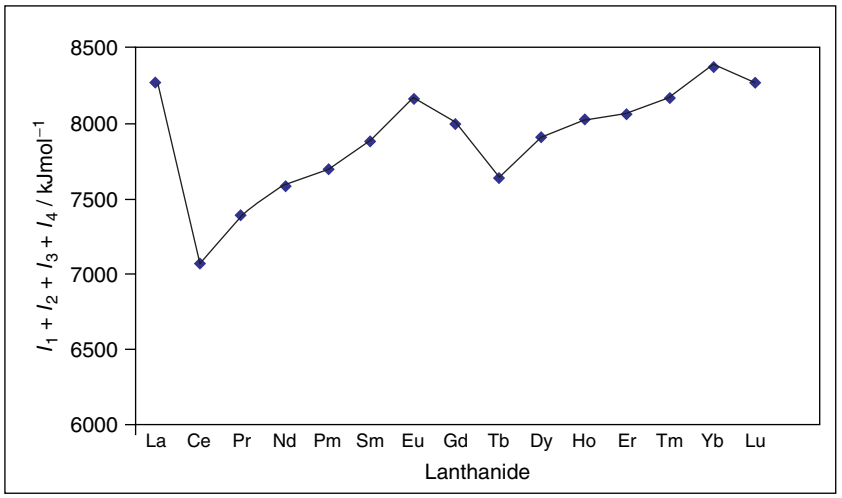


Figure 4 The sum of the first four ionization potentials

Table 2 Estimated values of Ln^{3+}/Ln^{2+} reduction potentials (V)

	Ce	Pr	Nd	Pm	Sm	Eu	Gd	Tb	Dy	Ho	Er	Tm	Yb	Lu
Thermochemical	1.76	3.9	4.9	5.4	5.2	6.2	7.4	—	4.5	5.7	5.7	5.6	6.8	8.1
Spectroscopic	1.8	3.2	5.0	4.9	5.2	6.4	7.9	3.1	5.2	6.2	6.1	6.1	7.1	8.5

8274 kJ mol^{-1}, which with a ΔH_{sub} of 402 kJ mol^{-1}, gives $\Delta H_f = -709$ kJ mol^{-1}. This strongly exothermic value occurs despite the sum of ionization energies being higher for La than any of the other lanthanides and at first glance, it might be expected that this and all the other tetrafluorides would thus be stable. A more complete analysis should, of course, consider possible decomposition routes and for LnX_4, the reduction to the +3 oxidation state is the most likely decomposition route (equation 2)

$$LnX_4 \longrightarrow LnX_3 + 1/2\ X_2 \qquad (2)$$

The enthalpy change for this reaction can easily be estimated if the heats of formation of LnX_4 and LnX_3 are known or can be estimated.

A compilation of the relevant values has been made[2] from which it can be seen that only CeF_4 and TbF_4 would be expected to be stable to this reaction with PrF_4 possibly having marginal stability. This analysis ignores entropy changes but these in any case will favor the forward reaction due to the formation of X_2. These calculations agree well with the experimental observations as CeF_4 and TbF_4 are the only thermodynamically stable tetrafluorides. Stable compounds do exist in which Ln^{IV} is present as complex ions such as $[LnF_7]^{3-}$.

4.2 The +4 Oxidation State: Solution

In aqueous solution, the most convenient way of judging the stability of oxidation states is by analysis of reduction potentials. For the +4 oxidation state, the relevant reduction potential is for $Ln^{4+}{}_{(aq)} + e^- \rightarrow Ln^{3+}{}_{(aq)}$ for which there is little experimental data. Thermochemical measurements based on Gibbs free energies of formation for $Ln^{3+}{}_{(aq)}$ and $Ln^{4+}{}_{(aq)}$ and spectroscopic measurements allow estimates to be made of the Ln^{4+}/Ln^{3+} reduction potentials.[3] Data are shown in Table 2.

The experimental data that exists confirms that the range of LnIV species is very limited. Given that the potential for the oxidation of water is −1.23 V, it would be expected that all of the tetravalent lanthanide ions should be unstable to reduction by water.

$$4Ln^{4+} + 2H_3O^+ \longrightarrow 4Ln^3 + O_2 + 6H^+$$

Only Ce^{IV} has any stability in aqueous acidic solution and this must therefore be of kinetic origin and a number of its salts are stable in aqueous solution as a result. Here, they act as powerful oxidants but are of sufficient kinetic stability to find use as analytical reagents.

Cerium(IV) is a strong Lewis acid (see ***Group Trends***) and readily forms complexes in aqueous solution. In a manner similar to some transition metals, the formation of complexes can have an appreciable effect on the oxidizing ability of the ion. For example, Co^{3+}/Co^{2+} has reduction potentials ranging from 1.83 V to −0.8 V depending on the ligands attached. While the range of reduction potentials for Ce^{IV} is not as great as this, the values do depend strongly

Table 3 Reduction potentials of Ce^{4+}/Ce^{3+} as a function of the nature of the acid and its concentration

	E^0/V			
Acid concentration/M	1	2	4	8
$HClO_4$	1.70	1.71	1.75	1.87
HNO_3	1.61	1.62	1.61	
H_2SO_4	1.44	1.44	1.43	1.42
HCl	1.28	—	—	—

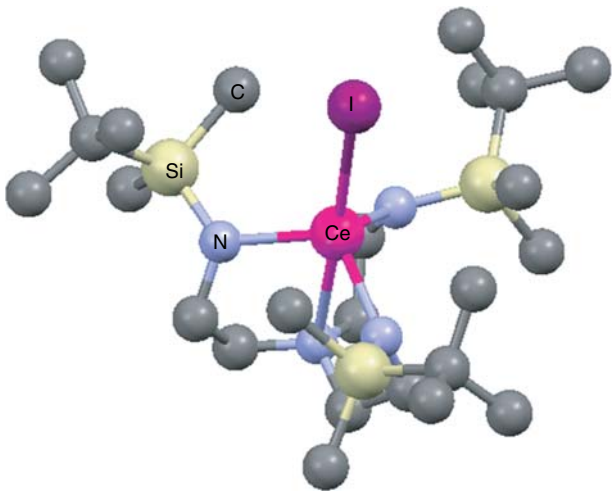


Figure 5 A stable Ce^{IV} iodide complex

on the nature of the acid and the complexes formed and, to a lesser extent, on the concentration of acid as shown in Table 3.

In perchloric acid, the complex formation is likely to be weak and the Ce^{IV} species present will be $[Ce(OH_2)_n]^{4+}$ or possibly $[Ce(OH_2)_nOClO_3]^{3+}$, while in other solutions, strong complexes such as $[Ce(SO_4)]^{2+}$ are known to exist.

The kinetic stability of Ce^{IV} complexes is seen in cases such as the $CeCl_6^{2-}$ ion which is readily isolated in the solid state and by the remarkable example of a Ce^{IV} iodide complex (Figure 5).[4] The kinetic stability is probably a result of using bulky R groups, ^{t}BuMe$_2$Si in this case, with the possibility that the Ce^{IV}/Ce^{III} reduction potential is lowered on complex formation.

Redox potentials for many elements are known to be pH dependent and electrochemical or ozone oxidation of Pr^{III} and Tb^{III} in alkaline conditions has been reported to give tetravalent species in the presence of carbonate ions.[5] Presumably, these Ln^{IV} species are carbonate complexes. Other complexes of Tb^{IV} have been reported with tellurate and periodate (both of which would be oxidation-resistant ligands) in both solution and solid state.[6,7]

5 THE +3 OXIDATION STATE

This is the most stable oxidation state for all lanthanides and a vast number of stable simple salts are known. The reduction potentials for Ln^{3+}/Ln are all negative, reflecting stability of the trivalent state as shown in Table 4.

In general, the Ln^{3+} ions can be considered to be essentially redox inactive under most conditions. Half-wave potentials are available in nonaqueous solvents and, as can be seen in Table 5, they are significantly solvent dependent.[8] The half-wave potentials are directly proportional to the reduction potential. The values are quoted relative to bis(biphenylchromium(I))/(0) as this can be used as an internal standard that eliminates problems with unknown junction potentials in systems where the reference electrode is in a different solvent.

The metals are strongly reducing in these solvents with a general trend of lower reducing ability in acetonitrile and acetone.

The data for reduction to Ln^{2+} are shown in Table 9 for Sm, Eu, and Yb where the relative oxidizing abilities of Ln^{3+} are Eu>Yb>Sm in all solvents as might be expected from the relative stabilities of the respective Ln^{2+} ions.

Table 4 Reduction potentials (V) for Ln^{3+}/Ln in acidic aqueous solution

La	Ce	Pr	Nd	Pm	Sm	Eu	Gd	Tb	Dy	Ho	Er	Tm	Yb	Lu
−2.38	−2.34	−2.35	−2.32	−2.29	−2.30	−1.99	−2.28	−2.31	−2.29	−2.33	−2.32	−2.32	−2.22	−2.30

Table 5 The solvent dependence of the half-wave potentials (V) for Ln^{3+}/Ln relative to bis(biphenylchromium(I))/(0) with 0.1 M Et_4NClO_4 supporting electrolyte

Solvent	La	Ce	Pr	Nd	Sm	Eu	Gd	Tb	Dy	Ho	Er	Tm	Yb
DMSO	−1.59	−1.57	−1.53	−1.53	−1.42	−1.01	−1.49	−1.52	−1.41	−1.42	−1.42	—	−1.30
DMF	−1.37	−1.37	−1.37	−1.37	−1.28	−0.91	−1.46	−1.46	−1.58	−1.5	−1.51	—	−1.19
Acetone	—	—	−0.81	−0.83	−0.85	−0.54	−0.83	−0.72	−0.78	−0.78	−0.77	−0.78	−0.72
CH_3CN	−0.7	—	−0.7	−0.7	−0.72	−0.28	−0.7	—	—	—	—	—	−0.53

5.1 The +2 Oxidation State: Solid State

As can be seen from Table 1, occurrence of the +2 oxidation state varies in an irregular manner similar to the +4 state. In the solid state, the relative stability of representative compounds such as the dihalides, LnX_2, can be assessed by thermochemical cycles. A reasonable decomposition route for LnX_2 is disproportionation to LnX_3 and Ln (equation (3)). The thermochemical cycle for this reaction is shown in Figure 6. This leads to the expression for ΔH for the disproportionation reaction shown in equation (4)

$$3\,LnX_{2(s)} \rightarrow Ln_{(s)} + 2LnX_{3(s)} \quad (3)$$

$$\Delta H = 2U_o(LnX_3) - 3U_o(LnX_2) - (I_1 + I_2) + 2I_3 - \Delta H_{sub} \quad (4)$$

Inspection of equation (4) leads to the expectation that high values of I_3 will tend to make ΔH less exothermic and thus favor the stability of LnX_2. Intuitively, this might be expected as high values for I_3 indicate that Ln^{3+} is formed with more difficulty. The plot of I_3 for the metals is shown in Figure 7. Peaks are found at Eu and Yb corresponding to the break up of stable $4f^7$ and $4f^{14}$ configurations involved in the production of Ln^{3+}.

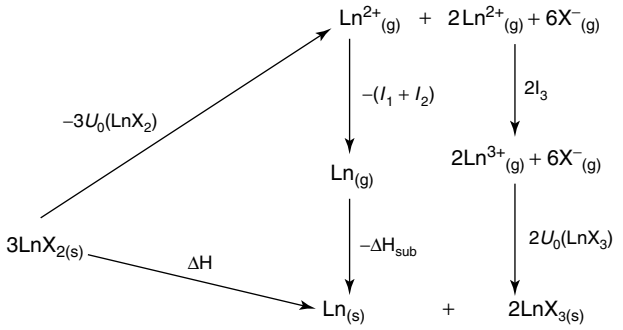


Figure 6 A thermochemical cycle to assess the stability of lanthanide dihalides with respect to disproportionation

Similarly, high values are found for Sm and Tm and all four of these elements have significant chemistry in the +2 oxidation state. It is also worth noting that I_3 for Dy is at a local maximum and DyX_2 might be expected to be more stable than TbX_2 and HoX_2 again in accord with observation. Equation (4) also implies that low values of ΔH_{sub} should also favor the divalent state. The plot of ΔH_{sub} (see ***Group Trends***) shows that Sm, Eu, Tm, and Yb all have low enthalpies of sublimation, which will further contribute to the stability of Ln^{II}. Similarly, the value for Dy lies at a local minimum imparting some stability to Dy^{II} compounds compared to the adjacent elements.

A more detailed analysis taking into account the lattice energy terms in equation (4) has been carried out[2] and leads to the prediction that the order of stability of $LnCl_2$ is Eu>Yb>Sm>Tm>Nd≈Pm>Dy>Ho≈Pr>Er>Tb>Ce>Gd>La>Lu.

This sequence matches well with the observed order of stabilities with dysprosium representing the limit for the formation of $LnCl_2$. ($PmCl_2$ has not been observed because of the radioactivity of all Pm isotopes.)

Values of the enthalpies of formation of all LnX_2 have been estimated[9] and are shown schematically in Figure 8.

These values together with the known ΔH_f for LnX_3 have been used to assess the stability of the dihalides with respect to disproportionation. The results are summarized in Table 6 as enthalpies of disproportionation. Only the values for the endothermic reactions are quoted as these imply stable LnX_2. The data in Table 6 broadly agree with the predictions of stability quoted above for $LnCl_2$ based on lattice energies.[2]

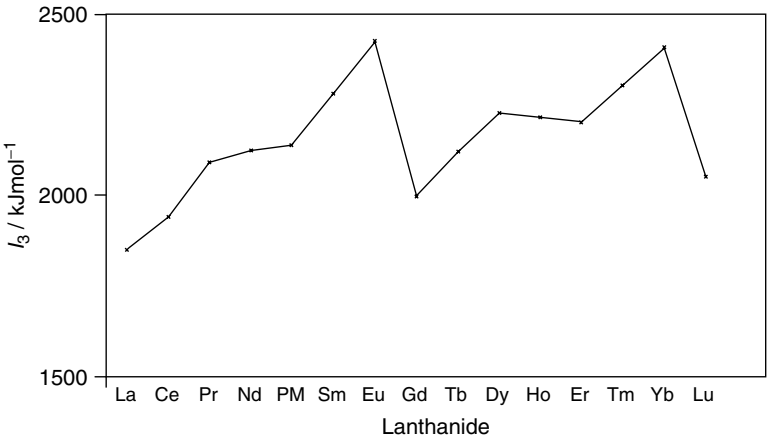


Figure 7 I_3 (kJ mol^{-1}) for lanthanide metals

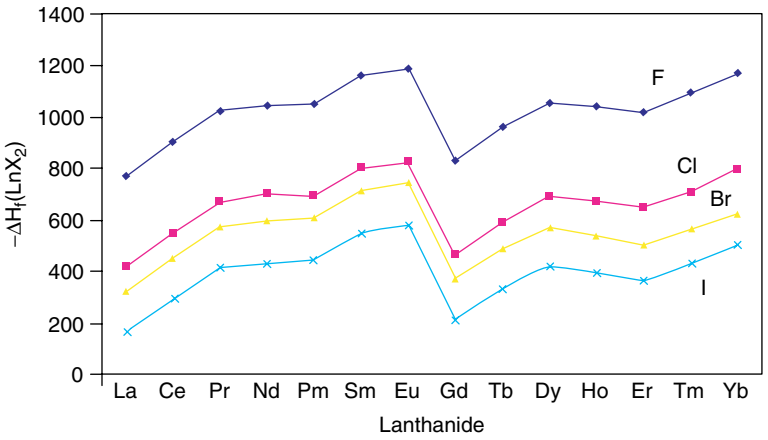


Figure 8 Enthalpies of formation of LnX_2 (X = F, Cl, Br, I)

Table 6 Enthalpies of disproportionation (kJ mol^{-1}) for the stable LnX_2

	La	Ce	Pr	Nd	Pm	Sm	Eu	Gd	Tb	Dy	Ho	Er	Tm	Yb
F	—	—	—	—	—	47	132	—	—	—	—	—	—	125
Cl	—	—	—	13	9	119	200	—	—	33	8	—	49	161
Br	—	—	—	21	43	153	226	—	—	16	—	—	10	97
I	—	—	—	11	27	137	229	—	—	15	—	—	35	146

5.2 The +2 Oxidation State: Solution

The existence of Ln^{2+} in aqueous solution is limited by the tendency of Ln^{2+} to reduce water as follows:

$$2Ln^{2} + 2H^{+} \longrightarrow 2Ln^{3+} + H_2$$

Thermochemical and spectroscopic measurements have been used to give estimates of the Ln^{3+}/Ln^{2+} reduction potentials for all Ln (Table 7).[3]

Available experimental reduction potential data shown in Table 8 agree well with these values and indicate that all Ln^{2+} are unstable with respect to this reaction. Only solutions of Eu^{2+} have significant kinetic stability in water while Sm^{II} and Yb^{II} can be fleetingly observed.

There is little information about the variation of Ln^{3+}/Ln^{2+} potential on complex formation. Variations in the value for Eu^{3+}/Eu^{2+} between different laboratories have been explained as being due to complex formation with formate ion.[3] In liquid ammonia, both Eu and Yb dissolve to give blue solutions of $2e^{-}$, again illustrating the stability of the +2 oxidation state for these metals. There are limited data available for the reduction of Ln^{3+} to Ln^{2+} in nonaqueous solvents, restricted to Sm, Eu, and Yb.[8] Data for selected solvents are shown in Table 9.

Table 8 Reduction potentials (V) for Ln^{3+}/Ln^{2+} in aqueous solution

	Sm	Eu	Yb
E^0Ln^{3+}/Ln^{2+}	−1.50	−0.34	−1.05

The reducing ability of the Ln^{2+} ion as a function of solvent generally decreases along the series DMSO>DMF>acetone>CH_3CN and hence it might be anticipated that acetonitrile would be the best solvent for the preparation of Ln^{II} species.

Table 7 Estimated Ln^{3+}/Ln^{2+} reduction potentials in aqueous acidic solution

	La	Ce	Pr	Nd	Pm	Sm	Eu	Gd	Tb	Dy	Ho	Er	Tm	Yb
Thermochemical	−3.7	−3.76	−3.03	−2.62	−2.67	−1.57	−0.35	−3.82	−3.47	−2.42	−2.80	−2.96	−2.27	−1.04
Spectroscopic	−3.1	−3.2	−2.7	−2.6	−2.6	−1.6	−0.3	−3.9	−3.7	−2.6	−2.9	−3.1	−2.3	−1.1

Table 9 Solvent-dependent half-wave potentials (V) for Ln^{3+}/Ln^{2+} relative to bis(biphenylchromium(I))/(0) with 0.1 M Et_4NClO_4 supporting electrolyte

	Sm	Eu	Yb
DMSO	−1.35	−0.143	−0.81
DMF	−1.17	0.002	−0.69
Acetone	−0.47	0.63	−0.05
CH_3CN	−0.84	0.93	0.21

6 CONCLUSION

The occurrence of Ln^{IV} and Ln^{II} seems to be well understood in both solid state and solution. In both cases, a balance between energetically unfavorable ionization energies and favorable lattice and hydration energies can rationalize the experimental observations and provide indications of where further study may prove fruitful.

While the stability of Ln^{III} means that access to compounds in higher and lower oxidation states will always be difficult, it appears that there may be scope for extending the range of compounds by suitable choice of ligand and/or solvent system. The existence of a Ce^{IV}–I complex makes the prospect of stabilizing Pr^{IV} by judicial choice of ligands seem enticing. Similarly, while many lanthanides form solid-state compounds in the +2 oxidation state, there is scope for increasing the range of compounds again perhaps by the use of stabilizing ligands.

7 GLOSSARY

Half-wave potential, $E_{1/2}$: $E_{1/2} = E^{o} + RT\ln\gamma_{ox}D_{R}^{1/2}$ nF $\gamma_{red}D_{o}{}^{1/2}$ where E^{o} is the standard reduction potential, n the number of electrons involved in the reduction, γ_{ox} and γ_{red} the activity coefficients of the oxidized and reduced forms and D their respective diffusion coefficients.

8 RELATED ARTICLES

Homogeneous Catalysis; Lanthanide Halides; Organometallic Chemistry Fundamental Properties; Tetravalent Chemistry: Inorganic; Tetravalent Chemistry: Organometallic; The Divalent State in Solid Rare Earth Metal Halides; The Electronic Structure of the Lanthanides.

9 ABBREVIATIONS AND ACRONYMS

DMSO = dimethylsulfoxide; DMF N,N = dimethylformamide.

10 REFERENCES

1. F. G. N. Cloke, *Chem. Soc. Rev.*, 1993, **22**, 17.
2. D. W. Smith, *J. Chem. Educ.*, 1986, **63**, 228.
3. L. R. Morss, *Chem. Rev.*, 1976, **76**, 827.
4. C. Morton, N. W. Alcock, M. R. Lees, I. J. Munslow, C. J. Sanders, and P. Scott, *J. Amer. Chem. Soc.*, 1999, **121**, 11255.
5. D. E. Hobartr, K. Samhoun, J. P. Young, V. E. Norvell, G. Mamantov, and J. R. Peterson, *Inorg. Nucl. Chem. Lett.*, 1980, **16**, 321.
6. Y. M. Kiselev and A. S. Baranov, *Russ. J. Inorg. Chem.*, 2002, **47**, 688.
7. Y. Ying and Y. Ru-Dong, *Polyhedron*, 1992, **11**, 963.
8. G. Gritzner, *Pure Appl. Chem.*, 1990, **62**, 1839.
9. Y. C. Kim and J. Oishi, *J. Less - Common Met.*, 1979, **65**, 199.

Group Trends

Andrew W.G. Platt

Staffordshire University, Stoke-on-Trent, UK

1 Summary 43
2 Introduction 43
3 The Lanthanide Contraction 44
4 Trends in the Properties of the Metals 44
5 Trends in Ionic Radii and their Effect on Compounds and Complexes 46
6 Formation Constants of Complexes 48
7 Hydration Enthalpies of Ln^{3+} Ions 50
8 Entropy of Hydration of Ln^{3+} 50
9 Enthalpies of Formation of Halides, Oxides, and $Ln^{3+}_{(aq)}$ 51
10 Conclusion 52
11 Glossary 53
12 Related Articles 53
13 Abbreviations and Acronyms 53
14 References 53

1 SUMMARY

The properties of lanthanide metals and their compounds and coordination complexes are influenced by the size of the lanthanide ion. The normal oxidation state for all of the metals in simple compounds is +3 and subtle changes in ionic radius are generally responsible for the changes in their properties. An understanding of the variation in the stability of oxidation states other than the +3 state can be obtained by analysis of the thermochemical properties such as ionization energies, enthalpies of vaporization of the metals, and hydration enthalpies, in addition to properties such as ionic radii. Thus a knowledge and understanding of these properties and how they vary across the lanthanide series is fundamental to an understanding of the chemistry of the 4f elements. Trends are often visualized as a function of the variation of a given property with atomic number but often this does not show uniform changes, even where there is no change in oxidation state. In some instances, good correlations can be found with the total electronic angular momentum L of the lanthanide metal or ion.

2 INTRODUCTION

The f-block metals form the longest continuous rows of elements in the periodic table. The metals are chemically very similar with the +3 oxidation state being the most stable for all of them. The only differences lie in rather subtle effects caused primarily by small incremental differences in the size of the ions. Trends in the physical and chemical properties of lanthanides are generally viewed as a function of the atomic number of a given property, the so-called Z plots. The inherent ease of construction and interpretation of such plots in terms of increasing charge density/decreasing ionic radius makes these the most popular means of presenting and analyzing trends across the series. While many trends can readily be rationalized in terms of Z plots, it has been noted that many properties do not show a consistent linear relationship to Z across the series of lanthanides, often with significant irregularities in the trends. This effect has been variously termed the *tetrad effect*, the *gadolinium break*, and *inner series* periodicity. Correlations of these properties with the ground-state total orbital angular momentum quantum number L frequently show a better relationship than correlation with

The Rare Earth Elements. Edited by David A. Atwood. © 2012 John Wiley & Sons, Ltd. ISBN 978-1-119-95097-4

atomic number.[1] The resulting graphical representations are termed *inclined W plots* on account of their visual appearance.

These frequently show four linear regions comprising groups of four elements, the so-called tetrads, within which trends are often easily interpreted as being due to changes with atomic number or effective nuclear charge.

A general principle of lanthanide chemistry stated by Johnson in 1980 is that in processes which do not involve changes in the number of f electrons, the lanthanides behave similarly.[2] While this holds for many properties of the lanthanides, there are some important exceptions where trends are not regular. For example, trends in the formation constants of complexes of Ln^{3+} ions often show irregularities when there is no change in oxidation state of the metal. Many seemingly irregular trends can be rationalized by a more detailed analysis of the processes involved.[3]

There are large irregularities in the trends in the stability of Ln^{IV} and Ln^{II}, and hence compounds containing these ions (see ***Variable Valency***, ***The Divalent State in Solid Rare Earth Metal Halides***, and ***Tetravalent Chemistry: Inorganic***).

3 THE LANTHANIDE CONTRACTION

In all rows of the periodic table, the valence electrons shield one another imperfectly from the nuclear charge and the result is an increase in effective nuclear charge moving from left to right. One result of this imperfect mutual shielding of the valence f orbitals is a reduction in the atomic and ionic radii of the lanthanides across the series, and as there are 14 elements in the series, this cumulative effect is more pronounced than for other rows of the periodic table. This is frequently termed the *lanthanide contraction* and this leads to an overall reduction of about 10% in the ionic radii from La to Lu. While the increasing effective nuclear charge/orbital penetration effects are primarily responsible for this contraction, it is thought that relativistic effects on the outer electrons also make a significant contribution (~10–15%) to the contraction.[4,5] The limited spatial extension of the 4f orbitals means that the outer boundary of lanthanide ions, and hence their size, is defined by their core 5s and 5p orbitals. The 5s electrons, in particular, are subject to relativistic effects as they have significant electron density at the nucleus. Electrons orbiting close to a highly charged nucleus can be expected to do so at high velocities and as these approach the speed of light, a significant increase in mass above the rest mass will occur according to equation (1)

$$m_v = \frac{m_o}{\sqrt{(1 - v^2/c^2)}} \quad (1)$$

where m_v is the relativistic mass at velocity v, m_o is the rest mass, and c *is* the velocity of light.

As the binding energy of the electron to a nucleus is directly proportional to its mass, the overall effect is to bind it more strongly and hence reduce the size of the ions further than might be expected from the increase in effective nuclear charge/orbital penetration effects alone.

The lack of spatial extension of the 4f orbitals means that they are not available to overlap with orbitals of surrounding ligands unlike the d-block metals where the d orbitals form the boundary surface of the ions (see ***Lanthanides: ''Comparison to 3d Metals''***). Thus covalent bonding in lanthanide complexes in their normal oxidation states does not occur to any significant extent except in zero-valent organometallic complexes with aromatic hydrocarbons. Thus the vast majority of complexes (see ***Lanthanides: Coordination Chemistry***) are bonded by ionic/electrostatic interactions with little to no covalent interaction between the metal and bound ligands.

4 TRENDS IN THE PROPERTIES OF THE METALS

4.1 Metallic Radii

Most of the metals have Ln^{3+} ions in the lattice with a $4f^n$ configuration with three electrons in the conduction band. The variation of the atomic radii as measured by the lanthanide–lanthanide distance in the solid metals, shown in Figure 1, displays the expected gradual decrease with increasing atomic number because of the increase in effective nuclear charge. The seemingly anomalously high values for europium and ytterbium are due to the presence of the larger divalent ions in the metal lattice resulting from the stability associated with the half-filled $4f^7$ and filled $4f^{14}$ electronic configurations for Eu^{2+} and Yb^{2+} respectively.

When metallic radii derived from metals with the same crystal structure are plotted against L, the results fall into four clearly distinguished lines as shown in Figure 2 (the points for Ce, Eu, and Yb are not included as these have different crystal structures, face-centered cubic (Ce and Yb), and body-centered cubic (Eu), while the other metals are hexagonal close packed).[1]

Within each tetrad, a trend of decreasing radius with increasing effective nuclear charge can be seen. For example, La–Nd and Gd–Ho show a decrease in radius, while the Gd–Pm and Lu–Er lines have a positive gradient. Thus it is possible that many irregular trends in properties of the lanthanides are due to the fact that the effect of electronic configuration is superimposed on that of the effective nuclear charge.

The metallic radii have significance in the chemistry of the bulk metals themselves—and in their chemistry in the gas phase—for instance, in the production of zero-valent complexes where synthesis involves atomic lanthanides. Generally, metallic radii do not directly influence the chemistry of the lanthanides.

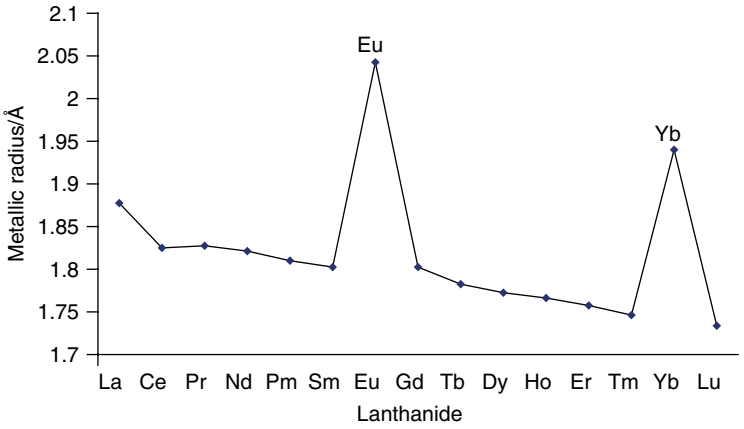


Figure 1 Metallic radii of lanthanides

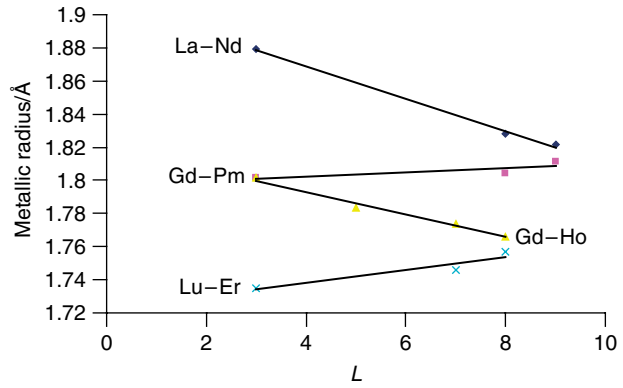


Figure 2 The plot of metallic radius vs *L*

4.2 Trends in Chemical Reactivity of the Metals

The rate of reaction with air seems to vary with atomic size—the lighter metals generally being more reactive than the heavier ones, which show no appreciable reaction with air at room temperature. The exceptions to this trend are Eu and Yb, which have the largest metallic radii and are considerably more reactive. At higher temperatures, most of the metals react with air to give the oxides Ln_2O_3. The exceptions are where the tetravalent state has reasonable stability (see ***Variable Valency*** and ***Tetravalent Chemistry: Inorganic***) and here oxides such as CeO_2 and mixed III/IV oxides Pr_6O_{11} and Tb_4O_7 are formed.

The elements themselves are all electropositive metals as would be expected from their position in the periodic table. Their values of electronegativity range from 1.10 (La) to 1.27 (Lu) on the Pauling scale and reduction potentials for Ln^{3+}/Ln have E^o values between −2.0 and −2.3 V, which are all consistent with high reducing ability.

As might be expected, they all react vigorously with halogens to give the expected LnX_3 (or LnF_4 for Ce and Tb).

All the metals react with hydrogen at elevated temperatures to produce LnH_2 and under high pressure, LnH_3. These are best formulated as $Ln^{III}{\cdot}2H^-{\cdot}e^-$ with the electron in a conduction band, and salt-like $Ln^{III}{\cdot}3H^-$ respectively.

4.3 Enthalpy of Vaporization of the Metals

The enthalpy of vaporization of the metals refers to the process $Ln_{(s)} \rightarrow Ln_{(g)}$. This has an influence in the stability of oxidation states of the lanthanides (see ***Variable Valency***, ***The Divalent State in Solid Rare Earth Metal Halides***, and ***Tetravalent Chemistry: Inorganic***) and the variation of ΔH_{vap} across the series is shown in Figure 3.

The general trend of a decrease from La to Eu is repeated from Gd to Lu. This could be associated with an increasingly stronger binding of the 4f electrons with increasing atomic number, making their promotion into the conduction band of the metals less favorable and reducing the overall cohesive forces within the metal. The minima at Eu and Yb and low values for Sm and Tm are generally associated with the presence of Ln^{2+} in the metallic lattice leading to weaker binding between the lanthanide ion and electrons in the conduction band. The irregularities in the trend are due to differences in the energies of the atomic lanthanides produced. Their energies differ as a result of differing electronic configurations of the atoms and when these are taken into account, a smooth trend as a function of atomic number is found.[3]

4.4 Ionization Energies of the Metals

The magnitude of ionization energies has an obvious influence on the ease of formation of various oxidation states. The trends for those of chemical significance are shown in Figure 4.

These trends show the expected increase in ionization energy with increasing atomic number. The breaks in the trends

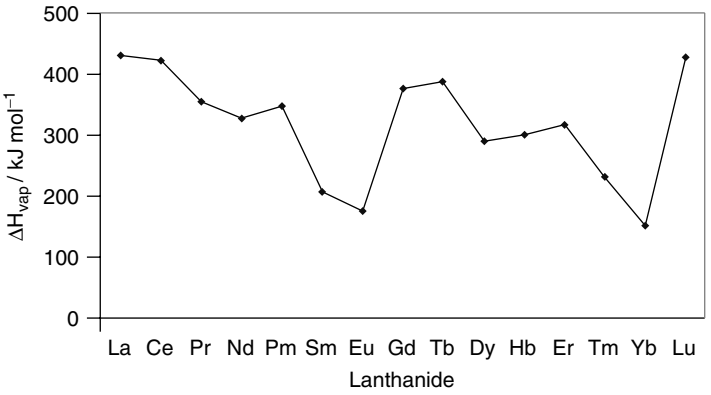


Figure 3 The enthalpies of vaporization of the lanthanide metals

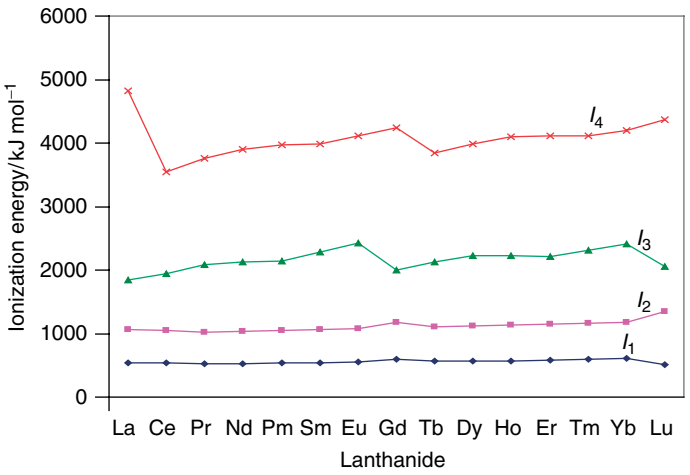


Figure 4 Trends in the first four ionization energies of the lanthanides

are as a result of particularly stable electron configurations associated with filled and half-filled 4f orbitals. These are particularly important for the third ionization energies where the high values due to the loss of stable $4f^7$ (Eu^{2+}) and $4f^{14}$(Yb^{2+}) help explain the occurrence of the +2 oxidation state from these metals (see ***Variable Valency***). The lower values at Gd and Lu are due to the $4f^7$ and $4f^{14}$ configurations, which are attained on the formation of Ln^{3+}. Similarly, the local minima found in I_4 are due to formation of the $4f^0$ and $4f^7$ configurations for Ce^{4+} and Tb^{4+}, respectively, with the peak at Gd being explained by the relatively less favorable $4f^7 \rightarrow 4f^6$ change on going from Gd^{3+} to Gd^{4+}.

5 TRENDS IN IONIC RADII AND THEIR EFFECT ON COMPOUNDS AND COMPLEXES

The ionic radii play an important role in determining the chemical properties of lanthanide compounds, as it is the small differences in these that are exploited in the separation of the metals and are responsible for gradual changes in other properties of families of lanthanide compounds. The plots of ionic radii of the +3 oxidation states for different coordination numbers determined from crystallographic data are shown in Figure 5(a). These are the so-called Shannon–Prewitt radii [6] which are derived from crystal structures of halides and chalcogenides and have been considered as the definitive ionic radii for lanthanide and other ions for a number of years. More recently, other compilations of radii have included solution data from EXAFS as these are free from crystal packing effects.[7] One set of such data are shown in Figure 5(b). The two series of values do differ, with the later values being significantly smaller than the original Shannon–Prewitt values. However, both sets of data show essentially the same trends with a more or less linear decrease with increasing atomic number of the metal. This is readily explained by the progressively increasing effective nuclear charge on the Ln^{3+} ions. The increase in ionic radius with coordination number is due to the increased steric congestion around the metal ion

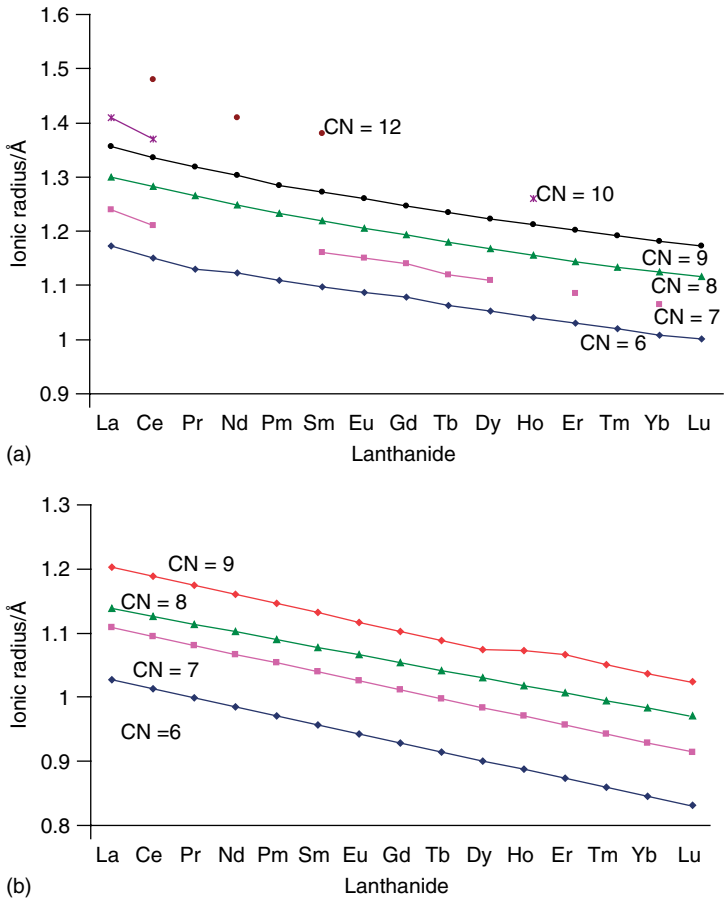


Figure 5 Ionic radii as a function of coordination number for Ln^{3+}. (a) Shannon ionic radii for lanthanide (III) ions. (b) Ionic radii according to Ref. 8

when more ligands are bonded to it. This effectively means that groups bonded to the metal move further away from each other and hence from the ion to reduce steric repulsions. This leads to an increase in the measured size of the ion. Regardless of the coordination number, the trend remains a smooth one.

The changes in ionic radii influence the structures of both simple salts and coordination complexes. For instance, in simple anhydrous salts such as the halides LnX_3 (X = halide) the coordination numbers of the metal ions decrease from La to Lu as a consequence of the lanthanide contraction: X = F from 11 to 9, X = Cl, Br from 9 to 6, X = I from 8 to 6. In more complex systems (see ***Lanthanides: Coordination Chemistry***), such as the hydrated nitrates, the coordination numbers of the metal ions decrease from 11 to 9 with a reduction in the number of coordinated water molecules. In the hydrated lanthanide nitrates, the structures $Ln(O_2NO)_3(OH_2)_x$ have been established by X-ray crystallography.[9] For Ln = La, Ce, the metals are 11-coordinate $Ln(O_2NO)_3(OH_2)_5$ with each nitrate acting as a bidentate ligand. For Ln = Pr to Yb, the metal coordination number is reduced to 10 in $Ln(O_2NO)_3(OH_2)_4$, while for Ln = Lu, a further water molecule is ejected from the primary coordination sphere to give $Lu(O_2NO)_3(OH_2)_3$. In other nitrate complexes, the increasing steric congestion caused as a result of the decrease in ionic radius is minimized by changes in the nitrate coordination mode from the normal bidentate to monodentate as in $Ln(NO_3)_3(OPCy_3)_3$ (Cy = cyclohexyl).[10] Here for Ln = La–Eu, the complexes are nine-coordinate with all three nitrates acting as bidentate ligands. The Er complex has two molecules in the unit cell, one with a nine-coordinate metal and the other with eight-coordination due to one of the nitrates being monodentate. The Tm and Yb complexes are likewise eight-coordinate with two bidentate and one monodentate nitrate. Another response to the reduction in ionic radius is removal of one of the nitrates from the primary coordination sphere by ionization. This is found in the series of complexes $Ln(NO_3)_3(OPPh_3)_4$ where the coordination number changes from nine (two bidentate and one monodentate nitrate) to eight (two bidentate and one ionic nitrate).[11]

Changes in the composition of complexes formed can also occur as a result of the lanthanide contraction. For example, lanthanide nitrate complexes of $(MeO)_2P(O)CH_2C(=CH_2)P(O)(OMe)_2$ = L form two

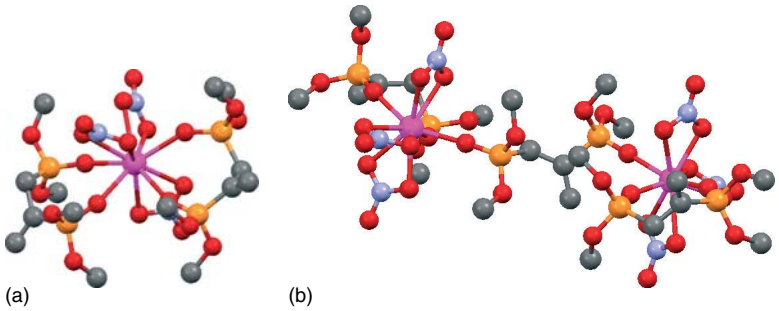


Figure 6 The change in structure of lanthanide nitrate complexes of $(MeO)_2P(O)CH_2C(=CH_2)P(O)(OMe)_2$ Pr complex (a), Yb complex (b). (C and H atoms omitted for clarity)

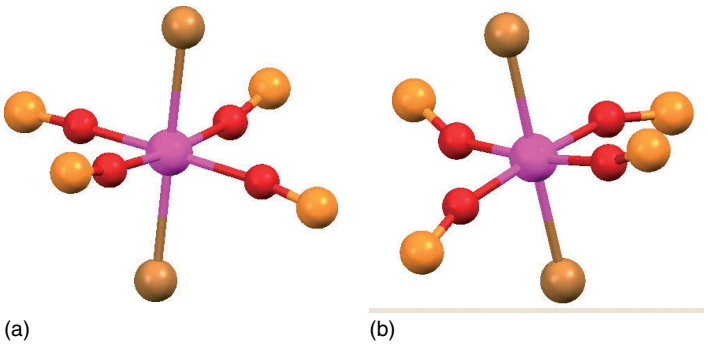


Figure 7 Schematic representations of $[trans\text{-}LnBr_2(OPPh_3)_4]^+$. (a) Ln = Nd, (b) Ln = Yb. (C and H atoms omitted for clarity)

distinct series: $Ln(NO_3)_3L_2$ for the larger lanthanide ions (La–Eu) with a coordination number of 10 and $LLn(NO_3)_3(\mu L)Ln(NO_3)_3L$ for the smaller ions where the coordination number is reduced to nine with one L bridging between two metal centers.[12] The structures are shown in Figure 6.

Changes in the peripheral structure of coordination complexes also appear to be influenced by the lanthanide contraction. For instance, the complexes of lanthanide bromides with triphenylphosphine oxide all have the structure $[trans\text{-}LnBr_2(OPPh_3)_4]^+$ $[Br]^-$.[13] The structures differ between the lighter and heavier lanthanides in the Ln–O–P angles. These are essentially linear for Ln = La–Gd, and probably reflect the minimization of electrostatic repulsions between the positively charged lanthanide ion and phosphorus atom in the $Ln^{3+}–O^{\delta-}–P^{\delta+}$ arrangement. By the end of the lanthanide series, however, these angles are significantly smaller than 180°. As the lanthanide ion becomes smaller, the unfavorable steric interactions between the phenyl groups on the adjacent ligands increase and by Yb, the Ln–O–P angle decreases to reduce the interactions between the mutually *cis* ligands. This is indicated schematically in Figure 7.

There are analogous changes in ionic radii for compounds in the +2 and +4 oxidation states with similar effects being apparent with changes in coordination number, but here the number of lanthanides which have accessible +2 and +4 oxidation states is more restricted and hence the data are much more limited.

6 FORMATION CONSTANTS OF COMPLEXES

It might also be anticipated that as the bonding in coordination complexes is predominantly either ion–ion or ion–dipole (see ***Lanthanides: Coordination Chemistry***), their thermodynamic stability will be related to the effective nuclear charge of the lanthanide ion. There have been many studies of the stability of lanthanide complexes, the stability being measured by formation constants or free energy of formation. The interpretation of data is often not straightforward as observed trends in data are subject to the exact nature of the starting material in the chosen reaction solvent, particularly in poor donor solvents[7].

A study of the formation constants of complexes between Ln^{3+} and Cl^- in dimethylformamide (DMF) showed that a series of complexes are formed according to the equilibrium in equation (2).

$$Ln^{3+} + nCl^- \rightleftharpoons LnCl_n^{(3-n)+} \qquad (2)$$

The distribution of species is strongly dependent on the lanthanide with heavier elements favoring the formation of the less sterically crowded $LnCl_4^-$ ion compared to species such as $[LnCl(DMF)_n]^{2+}$ and $[LnCl_2(DMF)_n]^+$ which predominate for lighter lanthanides. There was, however, no simple dependence between reaction enthalpies or entropies and atomic number of the lanthanide.[14]

Other properties of the ions are also affected in the same manner as a result of the lanthanide contraction. The formation constants of complexes between Ln^{3+} and

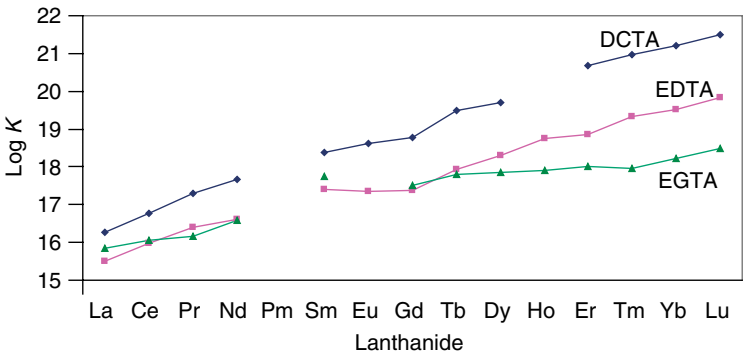


Figure 8 Formation constants of Ln^{3+} with some aminocarboxylic acids. DCTA, 1,2-diaminocyclohexanetetraacetic acid; EDTA, ethylenediaminetetraacetic acid; EGTA, 1,2-bis(di(carboxymethyl)aminoethoxy)ethane

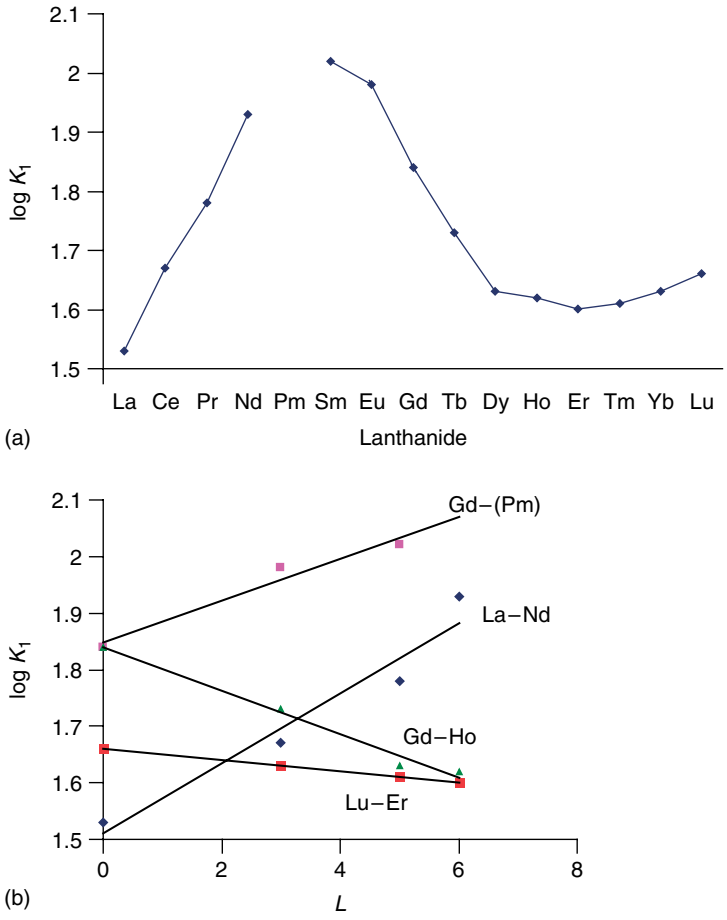


Figure 9 Examples of a Z plot (a) and an inclined W plot (b) for log K_1 for lanthanide complexes with propionate

aminocarboxylic acids such as EDTA increase consistently from La to Lu as shown in Figure 8. This general trend is again readily explained by the increasing electrostatic attraction of the ligand to ions of increasing charge density.

For other complexes, the trends are not so uniform. Formation constants for Ln^{3+} with carboxylic acids increase from lanthanum to a maximum in the region of europium followed by a decrease in stability to lutetium.[1] While there is no simple correlation between the atomic number of the lanthanide and the stability of the complexes, linear correlations are found with the orbital angular momentum. For example, the trend in the formation constants (as log K_1) for complexes of lanthanide ions with propionate is shown as a traditional Z plot in Figure 9(a) and an inclined W plot in Figure 9(b). There is no simple dependence of the stability of the complexes as a function of Z, which shows an increase between La and Nd as might be expected from the increase in effective nuclear charge, but a decrease from Sm to Er followed by a slight rise from Er to Lu. The plot of log K_1 vs L in Figure 9(b) shows four linear regions for the individual tetrads.

The tripositive lanthanide ions would be expected to be relatively acidic because of inductive effects on the coordinated water molecules with the equilibrium shown in equation (3) occurring to some extent.

$$[Ln{-}OH_2]^{3+} + H_2O \rightleftharpoons [Ln{-}OH]^{2+} + H_3O^+ \qquad (3)$$

However, owing to their large size, this effect is much smaller than that observed in transition metal ions such as Fe^{3+}, which are significantly acidic in aqueous solution (see ***Lanthanides: ''Comparison to 3d Metals''***). The pK_1 values for Ln^{3+} decrease more or less uniformly from 9.33 (La) to 8.17 (Lu) as expected from the decrease in ionic radii and consequent increase in charge density on the Ln^{3+} ion. There is an apparent break in the trend at Gd, which has a slightly higher value than Eu or Sm.

7 HYDRATION ENTHALPIES OF Ln^{3+} IONS

The hydration enthalpies, defined by equation (4), play an important role in determining the solution properties of the ions and the compounds that contain them.

$$Ln^{3+}{}_{(g)} \rightarrow Ln^{3+}{}_{(aq)} \quad \Delta H = \Delta H_{Hydr} \qquad (4)$$

The trend is shown in Figure 10 and shows a smooth increase in the exothermic nature of ΔH_{Hydr} from La to Lu. The $Ln^{3+}{}_{(aq)}$ ions are, of course, simply another class of lanthanide complex and the observed trend in ΔH_{Hydr} is entirely as expected from the increase in charge density on the ions, which dominates the trend in the stability of aminocarboxylate complexes noted earlier.

8 ENTROPY OF HYDRATION OF Ln^{3+}

The trend in partial molal entropies of hydration of Ln^{3+} is shown in Figure 11. The entropies of hydration are a balance between two competing factors. The ordering effect of water binding to the highly charged positive ion tends to decrease the entropy of the system, while the presence of a solute ion will disrupt the local structure of the bulk solvent thus increasing entropy. For highly charged ions, the solvation effect always dominates and the result is an overall decrease in entropy for the hydration process.

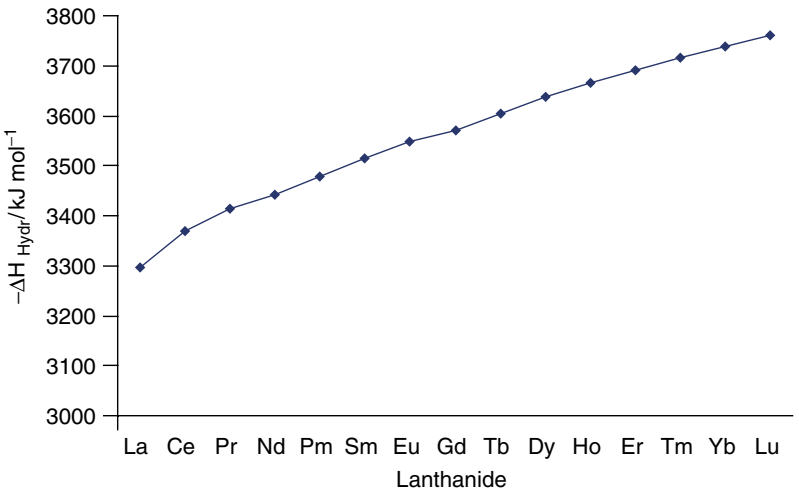


Figure 10 Enthalpies of hydration $-\Delta H_{Hydr}$ of Ln^{3+}

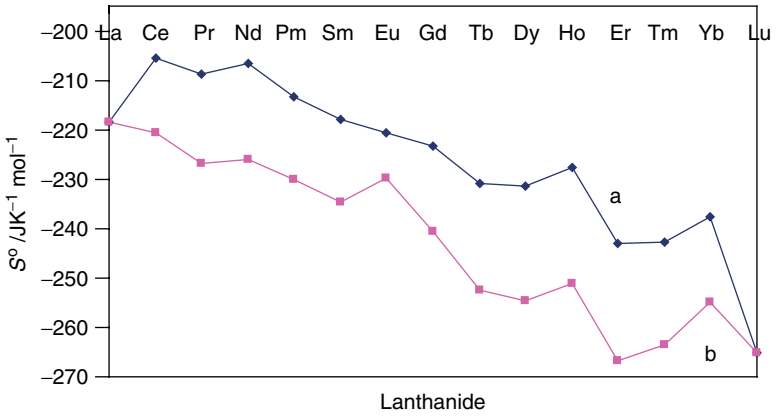


Figure 11 Partial molal entropies of hydration of Ln^{3+}

9 ENTHALPIES OF FORMATION OF HALIDES, OXIDES, AND $Ln^{3+}_{(aq)}$

The enthalpies of formation of LnX_3 (X = Cl, Br, I) have been reviewed and recommended values derived from the available data.[15] These show the expected dependence on the halide with order of stability being $LnCl_3 > LnBr_3 > LnI_3$ (Figure 12).

Across the series of compounds, the trend in ΔH_f^o is of a decrease in exothermic nature from LaX_3 to LuX_3 with ΔH_f varying from $-1071.6\,kJ\,mol^{-1}$ (La) to $-987.1\,kJ\,mol^{-1}$ (Lu). Simple thermochemical cycles for ΔH_f^o for LnX_3 lead to the expression shown in equation (5).

$$\Delta H_f^o = \Delta H_{vap} + I_1 + I_2 + I_3 + U_0 + K \qquad (5)$$

Where ΔH_{vap} is the enthalpy of vaporization of the metal, I_n the ionization energy, U_0 the lattice energy of LnX_3, and K a constant dependent on the halogen only. Breaks in the trend occur at Eu and Yb, which have less stable LnX_3 than those of the adjacent elements for all X. The reason for this is that the high values of I_3 for these metals (see Figure 4) increase the endothermic contribution to ΔH_f^0. Indeed this feature is seen in all the plots of enthalpy of formation of lanthanide(III) species (see below).

The trend observed for the enthalpies of formation of Ln_2O_3[16] shows a general increase in the exothermic nature of the oxides with atomic number as shown in Figure 13. Again, the large breaks in the overall trend at Eu and Yb reflect the high values of I_3 for these metals.

The gradual trend of increasing stability of Ln_2O_3 across the series is the opposite of that noted for LnX_3 with values of $\Delta H_f(Ln_2O_3)$ ranging from $-1791\,kJmol^{-1}$ (La) to $-1877\,kJmol^{-1}$ (Lu) although the trend is not entirely uniform even taking into account the expected low values for Eu and Yb. The fact that the underlying trends in enthalpy

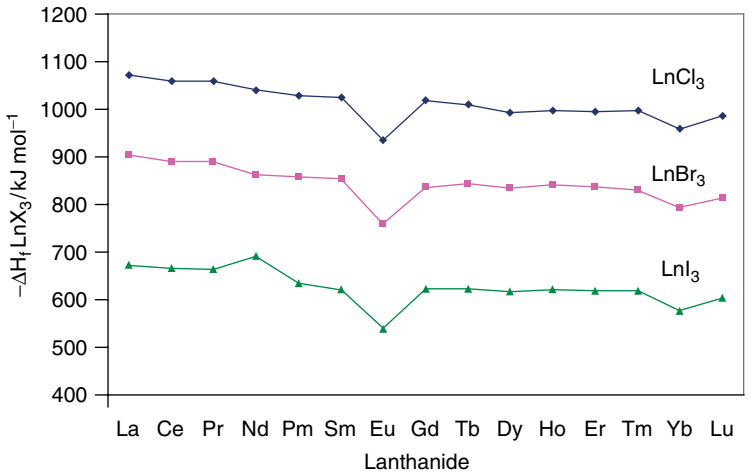


Figure 12 Enthalpies of formation of LnX_3

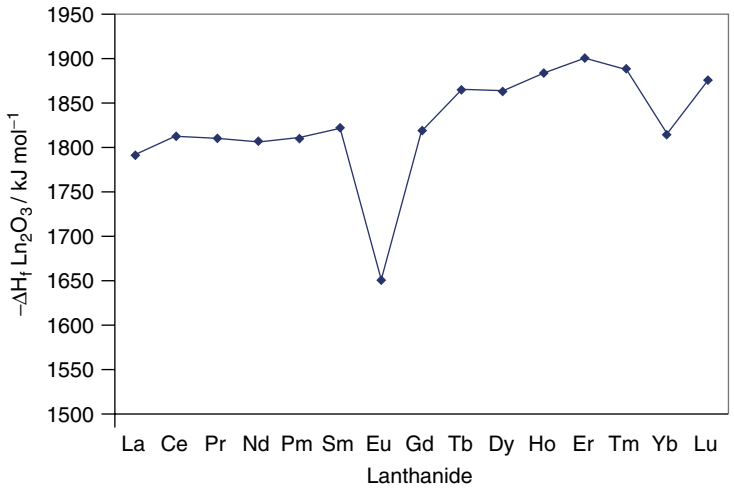


Figure 13 Enthalpies of formation of Ln_2O_3

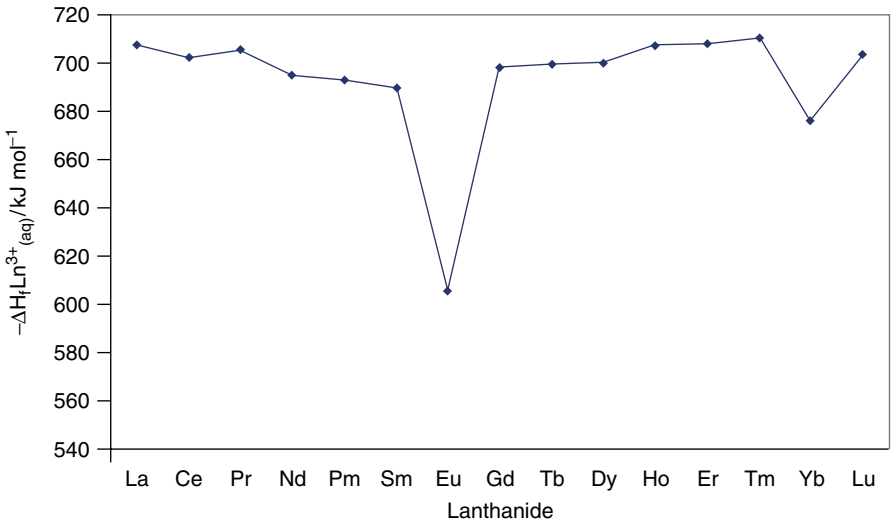


Figure 14 Enthalpies of formation $Ln^{3+}_{(aq)}$

of formation are different for LnX_3 and Ln_2O_3 can, in part, be explained by the balance between the lattice energies[17], enthalpy of vaporization, and sum of the first three ionization energies across the respective series. For LnX_3, this sum becomes less exothermic with values of $-377\,kJmol^{-1}$ (La) to $-313\,kJmol^{-1}$ (Yb) compared with an increase in its exothermic nature for the oxides, $-4680\,kJmol^{-1}$ (La) to $-4994\,kJmol^{-1}$ (Lu).

A similar trend is seen for the enthalpy of formation of $Ln^{3+}_{(aq)}$[18] which shows more or less constant values for all Ln^{3+} ions except Eu and Yb. The trend as a function of lanthanide is shown in Figure 14, which contrasts with the rather smoother trend seen in the enthalpy of hydration of the ions seen in Figure 10.

10 CONCLUSION

Trends in the properties of lanthanides are usually visualized as *Z* plots although in some cases, plots against orbital angular momentum show linear relationships where the more traditional *Z* plots are difficult to interpret. The thermodynamic parameters required for a firm underpinning of much of lanthanide chemistry are now in place and most of the important quantities have been determined or reliably estimated. Revised ionic radii are now available and it will be interesting to see whether these replace the ''classical'' Shannon–Prewitt radii which have been used for over 30 years.

11 GLOSSARY

Coordination number: The number of atoms directly bonded to another atom or ion.

Coordination sphere: The environment surrounding an atom or ion. This normally comprises atoms or groups of atoms immediately bonded to a central atom or ion and others in successive shells less strongly bonded to it.

Enthalpy change: The heat given to or taken from the surroundings during a process. Commonly applied to chemical processes. The unit is $kJ\,mol^{-1}$.

Enthalpy of formation: The heat change on forming one mole of substance from the elements in their standard states. The unit is $kJ\,mol^{-1}$.

Entropy: A measure of the disorder or randomness of a system. The unit is $JK^{-1}\,mol^{-1}$.

Formation constant: The equilibrium constant for the formation of a complex.

Ionization energy: The energy required to remove an electron from one mole of a gaseous atom or ion.

Molality: The number of moles of solute per kilogram of solvent.

Orbital penetration: The tendency of the outer electrons to be found closer to the nucleus than the core electrons. The greater the probability of this the more pronounced the effect.

12 RELATED ARTICLES

Lanthanide Complexes with Multidentate Ligands; Lanthanide Oxide/Hydroxide Complexes; Lanthanides: Coordination Chemistry; Solvento Complexes of the Lanthanide Ions; Trivalent Chemistry: Cyclopentadienyl.

13 ABBREVIATIONS AND ACRONYMS

DMF = *N*, *N* dimethylformamide; EDTA = ethylenediaminetetraacetic acid; EXAFS = extended X-ray absorption fine structure.

14 REFERENCES

1. S. P. Sinha ed., 'Systematics and the Properties of the Lanthanides', D. Reidel, Dordrecht, 1982.
2. D. A. Johnson, *J. Chem. Ed.*, 1980, **57**, 475.
3. L. R. Morss, *Chem. Rev.*, 1976, **76**, 27.
4. A. G. Massey, 'Main Group Chemistry', Ellis Horwood, London, 1990.
5. P. Pyykko, *Chem. Rev.*, 1988, **88**, 563.
6. R. D. Shannon, *Acta Crystallogr.*, 1976, **A 32**, 751.
7. P. DiBernado, A. Melchior, M. Tolazzi, and P. L. Zanonato, *Coord. Chem. Rev.*, 2012, **256**, 328.
8. D. Linberg, I. Persson, L. Erikson, P. D'Angelo, and S. De Panfils, *Inorg. Chem.*, 2010, **49**, 4420.
9. P. C. Junk, D. L. Kepert, B. W. Skeltern, and A. White, *Aust. J. Chem.*, 1999, **52**, 497.
10. A. P. Hunter, A. M. J. Lees, and A. W. G. Platt, *Polyhedron*, 2007, **26**, 4865.
11. W. Levason, E. H. Newnam, and M. Webster, *Polyhedron*, 2000, **19**, 2697.
12. R. A. Kresinski, A. M. J. Lees, and A. W. G. Platt, *Polyhedron*, 2012, **33**, 341.
13. A. Bowden, A. W. G. Platt, K. Singh, and R. Townsend, *Inorganica Chimica Acta*, 2010, **363**, 243.
14 S. Ishiguro and R. Takahashi, *Inorg. Chem.*, 1991, **30**, 1854.
15. E. H. P. Corfunke and R. J. M. Koonings, *Thermochim. Acta*, 2001, **375**, 17.
16. M. E. H. PCorfunke and R. J. M. Koonings, *Thermochim. Acta*, 2001, **375**, 65.
17 H. D. B. Jennings and H. K. Roobottom, in 'CRC Handbook Chemistry and Physics' ed. D. R. Lide, 84th edition, CRC Press, 2003.
18. M. E. H. P. Corfunke and R. J. M. Koonings, *Thermochim. Acta*, 2001, **375**, 51.

Solvento Complexes of the Lanthanide Ions

Simon A. Cotton

University of Birmingham, Birmingham, UK

and

Jack M. Harrowfield

Université de Strasbourg, Strasbourg, France

1 Summary 55
2 Introduction 55
3 Lanthanide(III) Ions in Aqueous Media—Overview 56
4 Individual Aqua Species and their Salts 57
5 Lanthanide(III) Ions in Nonaqueous Media 59
6 Conclusions 60
7 End Notes 61
8 Abbreviations and Acronyms 61
9 References 61

1 SUMMARY

As understanding of the chemistry of the lanthanides has grown, so have their applications in areas such as medicine and technology. Simple lanthanide complexes are often very soluble in water, and are very labile species, so the understanding of their speciation that relates to possible environmental impact becomes vital. Both diffraction and spectroscopic probes have been applied to the study of their coordination sphere, as the coordination number is not immediately apparent from the color of the aqua ion. Diffraction studies have been carried out on crystalline salts and more recently upon solutions; at present, knowledge is largely limited to the first coordination sphere. In aqueous solution, nine-coordinate $[Ln(OH_2)_9]^{3+}$ ions predominate for the early lanthanides and eight-coordinate $[Ln(OH_2)_8]^{3+}$ ions for yttrium and the later lanthanides. The scandium aqua ion has a coordination number greater than 6, either seven or eight. Several analogous ions present in nonaqueous solvents, such as $[Ln(dmf)_8]^{3+}$ and $[Ln(dmso)_8]^{3+}$, are also now recognized.

2 INTRODUCTION

The coordination chemistry of the lanthanides[a] (Ln) is a relatively recent development in chemistry since the laborious methods[1] required for separation of the elements available prior to these developed as part of the World War II Manhattan Project and made widely available only in the 1950s[2] severely restricted their study before the second half of the twentieth century. The many remarkable properties of both the elements themselves and their compounds now known[3,4] have led to the lanthanides being of considerable industrial,[5,6] technological,[5–7] (bio)analytical,[8,9] medical,[10] economic,[5,11] and even political[5,11] importance. One reflection of this is the anthropogenically induced increase in first-world countries in environmental levels of elements such as lanthanum[12] and gadolinium,[13] due in these particular cases to their use in catalyst systems[5–7,12] and magnetic resonance imaging[10,13] agents, respectively. Underlying these developments, as indeed it did the earliest chemistry concerning separation of the elements by fractional crystallisation of their salts,[1] is the increasingly sophisticated coordination chemistry of the lanthanides.

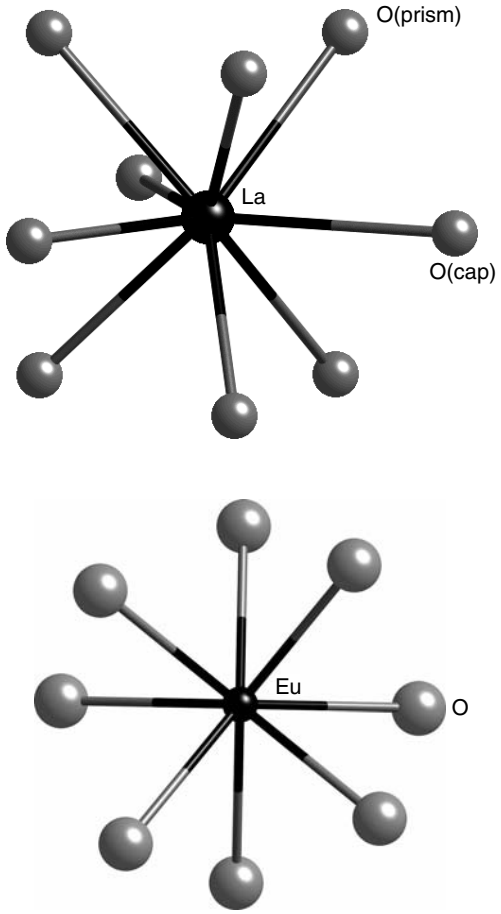
The Rare Earth Elements. Edited by David A. Atwood. © 2012 John Wiley & Sons, Ltd. ISBN 978-1-119-95097-4

A fundamental aspect of the discussion of the coordination chemistry of the lanthanides is to define exactly what is meant by the term ''coordination chemistry.''[14] Commonly, this is taken to be the chemistry associated with changes in the immediate environment of a metal (ion), this environment being considered to be composed of various (donor) atoms, which may be part of larger molecules. The high solubility of many lanthanide metal salts in water, however, is a factor favorable to the study of metal ion speciation in solution by X-ray diffraction[15–17] and such work has been important in establishing a model of metal ion coordination in terms of multiple ''coordination spheres'' expanded about the metal ion as center.[18] While such studies are relatively readily conducted on highly soluble materials, they are not generally applicable, so that in most instances very little is known about secondary and higher coordination spheres, and ''coordination chemistry'' in practice is interpreted in terms just of changes in the primary coordination sphere (nonetheless not always easily defined[19,20]). It is possible to perform sophisticated theoretical calculations, at least for simple species (ligands), such as water, found in proximity to a metal ion and so to define the structure of its extended environment.[21] For hydrated Ln^{III} species,[21] such calculations have shown that the primary coordination sphere consists of 8 or 9 water molecules surrounded by a secondary sphere of 12 water molecules, in essential agreement with experiment.[15,16] Higher coordination spheres presumably exist, though exchange between them must occur at diffusion-limited rates and it is only exchange between the primary coordination sphere and ''bulk'' solvent that is measurably slower.[22,23]

As indicated by the preceding remarks, the oxidation state +3 is important in lanthanide chemistry and is indeed so important that it is considered to typify the behavior of the elements, even though there are some very familiar examples of the chemistry of other oxidation states, such as +4 for Ce and +2 for Sm, Eu, and Yb.[3,4] A very well-known characteristic of many Ln^{III} species, though it is not one limited to this oxidation state, is that they may show very pale colors because of absorption arising from what are conventionally considered as f–f transitions.[24] These weak absorptions are very different to those described as d–d absorptions of transition metal ions in that they show little or no sensitivity to the nature of the donor atoms bound to the Ln center, meaning that a given color, such as pale green for Pr^{III}, is typical of all compounds of a given element and, unlike transition metal complexes, the structure of lanthanide ion complexes cannot generally be readily deduced by electronic absorption (or emission) spectroscopy (although, in certain instances, notably for Eu^{III}, both their donor atom sphere and its symmetry may be defined in detail by high-resolution measurements).[8,25] For this reason, characterization of the coordination chemistry of the lanthanides in the solid state by X-ray diffraction studies is particularly important. Interestingly, the perceived colors of many lanthanide complexes may be strongly influenced by emission,[26] so that Nd^{III} complexes, for example, are sometimes described as pale blue and sometimes as violet, and many Ho^{III} complexes show strikingly different colors under solar irradiation (pale yellow) and fluorescent lighting (bright pink).

3 LANTHANIDE(III) IONS IN AQUEOUS MEDIA—OVERVIEW

The aqua-Ln^{III} cations may be considered reference species in several regards[27] and for $[Ln(OH_2)_n]^{3+}$ complexes, measurements of water molecule exchange between the primary coordination sphere and the ''bulk,'' based largely on NMR measurements,[22,23] have established that all are extremely labile species, with exchange half-lives in the micro- to nanosecond range. Various measurements[22,23,28–37] have established that, in aqueous solution, $[Ln(OH_2)_9]^{3+}$ (**1**) is the dominant species for Ln = La–Nd and $[Ln(OH_2)_8]^{3+}$ and (**2**) for Ln = Gd–Lu, while for Ln = Pm–Eu a mixture of



both species is present. For the ''extra'' elements considered in this discussion, the primary coordination spheres in aqueous solutions of Sc^{III}[38] and Y^{III}[39] contain, respectively, seven or eight water molecules. Consistent with the facile

interconversion between eight- and nine-coordinate species in the Pm–Eu group, the rates of water exchange are greatest there (though not greatly different from that for Gd).[22,23] The great lability of all the lanthanide aqua ions means that their complex formation reactions are expected to be controlled by thermodynamic factors although, as with all metal ions, the use of multidentate and, in particular, macrocyclic ligands[40] can dramatically modify the kinetics of complexation and rates of exchange of aqua coligands.[28]

In the solid state, single crystal X-ray crystallography has been used to characterize $[Ln(OH_2)_n]^{3+}$ species in hexaqua-octahedral,[41] octa-aqua-square-antiprismatic (and octa-aqua-bicapped-trigonal-prismatic),[42–48] and nona-aqua-tricapped-trigonal-prismatic[49–56] forms. When seen in detail,[27] it is clear that H-bonding to the associated anion has a significant effect on the Ln–O bond lengths and indeed upon the primary coordination number of the metal ion (given that, for example, with La^{III} the octahedral species seen in the solid state with perchlorate anion becomes nine coordinate in solution[39]). Theoretical calculations also indicate that the nature of the primary coordination sphere depends upon that of the secondary coordination sphere.[21] That both eight- and nine-coordinate aqua complexes have been isolated for several Ln^{III} species and that both may indeed be present within one lattice[39,49] is consistent with the solution evidence for both species being present in equilibrium and supports the postulate[28] of an I_a mechanism for water exchange on all Ln^{III}.

The lanthanide(III) aqua ions are weak acids with pK_a values in the range 7–9[3] and this is one factor limiting the coordination chemistry observable in aqueous media since with basic ligands, such as amines, formation and precipitation of the rather insoluble hydroxides can occur to the exclusion of complexation. Even where this is not so, complexation may be accompanied by partial deprotonation of water ligands leading to the formation of hydroxo-bridged, oligomeric species, such as are found with amino acids.[57] Nonetheless, there are many systems involving multidentate ligands for which relatively simple complexation equilibria have been characterized, rather well-known examples being those involving EDTA (ethylenediaminetetra-acetate)[58,59] and dipicolinate (pyridine-2,6-dicarboxylate = dipic).[60] Note that the stability constants for the EDTA complexes show significant and consistent differences between consecutive pairs of Ln^{III} ions, with an overall difference (La–Lu) of approximately 10^5, explaining the utility of EDTA complexation in ion-exchange chromatographic separation of the lanthanides.[2] Some of the differences may be explained in part by changes in the coordination number (8 or 9) of the lanthanide ion depending upon the number of bound water molecules[61] but in general a major factor favoring binding of EDTA is the entropy of reaction,[58] consistent with the ligand displacing a large number of bound solvent (water) molecules. The elimination of water from the primary coordination sphere in complexes such as the $[Ln(dipic)_3]^{3-}$ anions, in which the Ln^{III} has N_3O_6 nine-coordination, in turn eliminates one mechanism of excited state deactivation[25] and results in certain species, such as those where Ln = Eu and Tb, showing bright visible luminescence under ultraviolet illumination.[62–64] Note that such complexes of very widely employed ligands involve five-membered chelate rings, but the principle that larger metal ions should prefer smaller chelate rings[65] is nicely illustrated by the lanthanides in their ready formation of nitrato and carbonato chelates.[4] Simple unidentate ligands (e.g., Cl^-), in contrast, especially as most are rather well solvated by water, form only exceedingly weak Ln^{III} complexes in water.[66]

4 INDIVIDUAL AQUA SPECIES AND THEIR SALTS

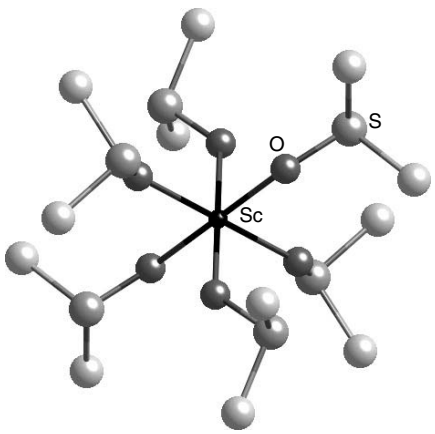
4.1 Scandium

In the periodic table, scandium immediately precedes the 3d transition elements Ti–Cu. Since these elements form octahedral $[M(H_2O)_6]^{n+}$ ($n = 2, 3$) aqua ions, it was assumed for many years that scandium also formed a $[Sc(H_2O)_6]^{3+}$ in aqueous solution. This assumption neglected the facts that the ionic radius of the Sc^{3+} ion (0.885 Å) is intermediate between those of Ti^{3+} (0.810 Å) and the lanthanide ions (La^{3+} = 1.172 Å; Lu^{3+} = 1.001 Å; all values quoted for six coordination). Thus, simply on steric grounds, a coordination number between 6 and 8 or 9 would be expected. Scandium forms a variety of hydrated salts, which in turn contain a variety of hydrated scandium ions, many of which have only been fully characterized in recent years. Of the perchlorates, $Sc(ClO_4)_3 \cdot nH_2O$ ($n = 6, 7$), the hexahydrate is isostructural with the lanthanide analogs, and so contains octahedral $[Sc(H_2O)_6]^{3+}$ ions, which are also found in $[Sc(H_2O)_6][Sc(CH_3SO_3)_6]$, with Sc–O 2.085 Å.[67] If aqueous $HC(SO_2CF_3)_3$ is refluxed with scandium oxide, it forms the triflide salt $[Sc(OH_2)_7](C(SO_2CF_3)_3)_3$, whose $[Sc(OH_2)_7]^{3+}$ ion is found in other salts;[44] recrystallizing scandium halides from acidified aqueous solution (to prevent hydrolysis) gives $ScX_3 \cdot 7H_2O$ (X = Cl, Br) and $ScI_3 \cdot 8H_2O$. All contain $[Sc(OH_2)_7]^{3+}$ ions; in the chloride and bromide, the coordination geometry is pentagonal bipyramidal.[68] Under different conditions, scandium chloride crystallizes as $ScCl_3 \cdot 6H_2O$, which is *trans*-$[ScCl_2(H_2O)_4]Cl \cdot 2H_2O$.[69] The very soluble scandium triflate is isostructural with the lanthanide analogs $Ln(O_3SCF_3)_3 \cdot 9H_2O$, but crystalline $[Sc(H_2O)_8](CF_3SO_3)_3$ actually contains eight-coordinated scandium with a distorted bicapped trigonal prismatic coordinating geometry. Hydrated scandium nitrate molecules are present as eight-coordinate $[Sc(NO_3)_3(H_2O)_2]$ and nine-coordinate $[Sc(NO_3)_3(H_2O)_3]$ in crown ether complexes, but crystalline $Sc(NO_3)_3 \cdot 5H_2O$ is $[Sc(NO_3)_2(H_2O)_4]^+ NO_3^- \cdot H_2O$.[69] Other salts containing coordinated anions include the sulfate $Sc_2(SO_4)_3 \cdot 5H_2O$, with six-coordinate scandium, and the

tosylate (*p*-toluenesulfonate) Sc(tosylate)$_3\cdot 6H_2O$, which contains six-coordinate $[Sc(H_2O)_4(tosylate)_2]^+$ ions. The oxalate $Sc_2(C_2O_4)_3\cdot 6H_2O$ has dodecahedral coordination of scandium by two water molecules and six oxygens from bridging oxalates.

Partial hydrolysis of the aqua ion produces a bridged dimeric species, the $[(H_2O)_5Sc(OH)_2Sc(H_2O)_5]^{4+}$ ion, which has been found in three salts, $[(H_2O)_5Sc(\mu\text{-}OH)_2Sc(H_2O)_5]$ $X_4.2H_2O$ (X = Cl, Br), and also a benzene sulfonate $[(H_2O)_5Sc(\mu\text{-}OH)_2Sc(H_2O)_5]$ $(C_6H_5SO_3)_4\cdot 4H_2O$. In view of the tendency of many of the hydrated lanthanide halides to contain coordinated halide ions, the chlorides in particular, the absence of halide from the coordination sphere of scandium in these compounds is remarkable.

Raman spectra of solutions and glasses of Sc^{3+} (aq) proved quite different from those of the octahedral $[Al(H_2O)_6]^{3+}$ ion, implying that the aqua ion of scandium was not a hexaqua species, and diffraction studies on both solutions and crystalline hydrates have settled the matter. The fact that six-, seven-, and eight-coordinate aqua ions $[Sc(OH_2)_x]^{3+}$ ($x = 6$, 7, 8) can be isolated in different salts suggests that it is the solubility of a particular salt that determines which compound crystallizes out from aqueous solution, and the data from reference compounds enables solution diffraction data to be interpreted. X-ray diffraction data for scandium perchlorate solutions indicated a Sc–O distance of 2.180(7) Å, with a coordination number of 7.4(4), and X-ray absorption fine structure (XAFS) data from scandium triflate solutions also indicate a Sc–O distance of 2.18(2) Å.[70] More recently, XAFS and large-angle X-ray scattering (LAXS) measurements showed that strongly acidic solutions of Sc^{3+} (aq) contain eight-coordinate $[Sc(H_2O)_8]^{3+}$ in a distorted bicapped trigonal prismatic arrangement similar to that in the crystalline triflate, with a mean Sc–O bond distance to the six waters at the angles of the trigonal prism of 2.17(1) Å, and two more capping oxygens at 2.32(4) and 2.5 Å.[67] The aqua complexes of scandium are exceptional; otherwise six coordination is found for species such as $[Sc(dmso)_6]^{3+}$ (**3**).



4.2 Yttrium and the Lanthanides

Reaction of lanthanide oxides or carbonates with acids gives a range of hydrated salts readily crystallized from solution. It was established[56] as early as 1939 that hydrated neodymium bromate was $[Nd(H_2O)_9]$ $(BrO_3)_3$, containing $[Nd(H_2O)_9]^{3+}$ ions. More recently, the tricapped trigonal prismatic (TTP) nonaaqua ion has been shown to occur in a wide range of salts, complete series $[Ln(OH_2)_9]X_3$ (X, e.g., bromate, triflate, ethylsulphate; Ln = La–Lu) as well as two incomplete series, the toluene *p*-sulfonates (tosylates) $[Ln(OH_2)_9](p\text{-}MeC_6H_4SO_3)_3$ (Ln = La–Nd) and the iodides $[Ln(OH_2)_9]$ I_3 (Ln = La–Ho). For the smaller later lanthanide ions, the tosylates $Ln(p\text{-}MeC_6H_4SO_3)_3\cdot 9H_2O$ contain $[Ln(OH_2)_6(p\text{-}MeC_6H_4SO_3)_2]^+$ ions (Ln = Sm, Gd, Dy, Ho, Er, Yb, Y) in distorted dodecahedral eight coordination,[54] while for the heavier lanthanides, $LnI_3\cdot 10H_2O$ (Ln = Er–Lu) contain square antiprismatic $[Ln(OH_2)_8]^{3+}$ ions.[42] In a more striking example of the influence of the counter ion, the perchlorates $Ln(ClO_4)_3\cdot 6H_2O$ contain octahedral $[Ln(H_2O)_6]^{3+}$ ions in the solid state (Ln, e.g., La, Er, Tb). Thus, even when anions do not enter the coordination sphere, they affect the structure of the hydrated lanthanide ion isolated in the crystalline form, presumably the least soluble species crystallizing. Some remarkably complicated solid-state structures incorporating lanthanide aqua ions are obtained when crystallized with calixarene sulfonates as the counteranions.[50] When anions do enter the coordination sphere, a range of structures is obtained. Thus, the chlorides $LnCl_3\cdot 7H_2O$ (Ln = La, Ce) are dimeric $[(H_2O)_7Ln(\mu\text{-}Cl)_2Ln(OH_2)_7]$ Cl_4, and $LnCl_3\cdot 6H_2O$ (Ln = Nd–Lu) contain antiprismatic $[LnCl_2(H_2O)_6]^+$ cations. The two lightest bromides, $LnBr_3\cdot 7H_2O$, resemble the chlorides in being dimeric $[(H_2O)_7Ln(\mu\text{-}Br)_2Ln(OH_2)_7]$ Br_4; $LnBr_3\cdot 6H_2O$ (Ln = Pr–Dy) are again similar to some chlorides in being $[LnBr_2(H_2O)_6]Br$, while $LnBr_3\cdot 8H_2O$ (Ln = Ho–Lu) resemble the heavy iodides in being $[Ln(H_2O)_8]$ Br_3. Nitrates have a variety of structures, but in all of them the nitrates are coordinated in a bidentate manner, and the coordination number decreases with decreasing ionic radius. Among $Ln(NO_3)_3\cdot 6H_2O$, the La and Ce compounds are $[Ln(NO_3)_3\cdot(H_2O)_5]\cdot H_2O$ (Ln = La, Ce; CN = 11), while the others are $[Ln(NO_3)_3\cdot(H_2O)_4]\cdot 2H_2O$ (Ln = Pr–Dy, Y; CN = 10). $Ln(NO_3)_3\cdot 5H_2O$ (Ln = Eu, Dy–Yb) have $[Ln(NO_3)_3\cdot(H_2O)_4]$ molecules (CN = 10). $Ln(NO_3)_3\cdot 4H_2O$ and $Ln(NO_3)_3\cdot 3H_2O$ both contain $[Lu(NO_3)_3\cdot(H_2O)_3]$ (CN = 9).

Again, it has been X-ray diffraction data on crystalline solid salts that has provided models for the species present in solution. Nd^{3+} is a lanthanide(III) ion whose 4f–4f absorption spectrum has spectral features sensitive to changes in coordination environment (''hypersensitivity''), and this was applied to studying the Nd^{3+} (aq) ion (1968). In the hypersensitive region of the spectrum around 8000 Å, the spectra of solid $[Nd(H_2O)_9]$ $(BrO_3)_3$ and of dilute aqueous solutions of Nd^{3+} are very similar; the spectrum of Nd^{3+} in concentrated HCl solution is quite different, resembling the

eight-coordinate Nd in solid $NdCl_3 \cdot 8H_2O$, which contains $[NdCl_2(H_2O)_6]^+$ ions.[71] This influential report has been followed by a number of studies, involving both spectroscopy and diffraction. A luminescence study of lanthanide complexes showed a linear correlation between the decay constant and the number of coordinated water molecules, which afforded first coordination sphere hydration numbers of 9.0, 9.1, 8.3, and 8.4 for Sm^{3+}, Eu^{3+}, Tb^{3+}, and Dy^{3+}, respectively. Another study that employed laser-induced fluorescence spectroscopy showed that the hydration number decreased from 9 to 8 in the Eu–Tb region of the series. A neutron diffraction study of the Ln^{3+} (aq) gave hydration numbers of 9.0 and 8.5 for Pr^{3+} and Sm^{3+}, respectively, and 7.9 for Dy^{3+} and Lu^{3+}, suggesting that both eight- and nine-coordinate species are present for samarium. Extended X-ray absorption fine structure (EXAFS) spectra of aqueous solutions of lanthanum perchlorate are very similar to those of solid $[Ln(H_2O)_9]$ $(CF_3SO_3)_3$, implying a coordination number of 9 for La^{3+} (aq), and incidentally showing that the six-coordinate species present in the crystalline perchlorate are not significant in solution. An EXAFS study of chloride complexation by Ln^{3+} (aq) also gave evidence of a drop in coordination number across the series, with hydration numbers being 9.2 (La); 9.3 (Ce); 9.5 (Nd); 9.3 (Eu); 8.7 (Yb); and 9.7 (Y). X-ray absorption near-edge structure (XANES) spectroscopy has been applied to this. The early lanthanides form TTP $[Ln(H_2O)_9]^{3+}$ ions; on crossing the series, two waters become more weakly bound until eventually one leaves the hydration sphere, forming distorted bicapped trigonal prismatic $[Ln(H_2O)_8]^{3+}$ ions.[72]

Overall, then, the nature of the hydrated lanthanide ion in solution now appears to be well understood. In summary, the coordination number of $[Ln(H_2O)_n]^{3+}$ (aq) is believed to be 9 for the early lanthanides (La–Nd or Sm) and 8 for the later metals (Dy–Lu, Y), with the intermediate metals exhibiting a mixture of eight- and nine-coordinate species. The nine-coordinate species are assigned TTP structures and the eight-coordinate species square antiprismatic coordination.

5 LANTHANIDE(III) IONS IN NONAQUEOUS MEDIA

While the coordination chemistry of lanthanide ions in water is extensive, it is of course not limited to this solvent. In the 1970s, considerable interest developed in the synthesis of lanthanide ion complexes soluble in apolar solvents for their use as ''lanthanide shift reagents'' in NMR spectroscopy.[73] Typically, such complexes were neutral and based on chelating 1,3-diketonate ligands, one of their attractive features being that not only did they cause normally overlapping resonances to be spread out and resolved but that they could readily be prepared from optically active ligands and thus used to distinguish enantiomers. The degree of shifting observed could also be used to deduce molecular structure. Such applications have, however, been largely surpassed by modern developments in NMR spectroscopy. In contrast, the effects of paramagnetic lanthanide(III) ions on the nuclear properties of other elements have become of increasing importance in medical diagnosis,[74] as discussed in detail in ***Lanthanides: Magnetic Resonance Imaging***.

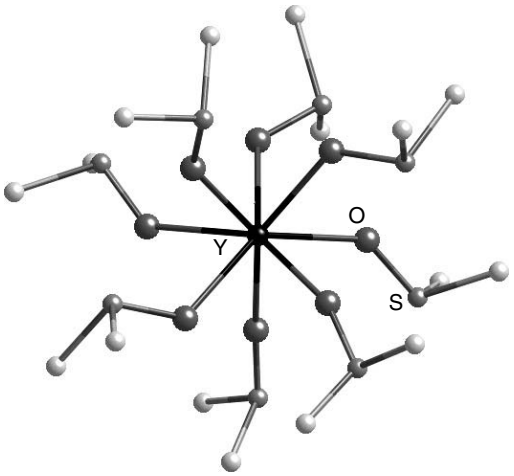
As for water, homoleptic solvento complexes can be regarded as reference species for the formation of complexes in nonaqueous media and there is a substantial body of thermodynamic data relating to this topic.[75] Chloride ion complexes, for example, are readily formed in dimethylformamide (dmf), with $[LnCl_n]^{(3-n)+}$, $n = 1–4$, detectable for all Ln^{III}, though K_1 has only a value close to 10^3 that varies but slightly across the Ln series. The poor anion solvating ability of dmf is considered one of the primary reasons for the enhanced stability relative to that in aqueous systems. Since dipolar, aprotic solvents do not protonate amines (to produce the conjugate base of the solvent), it is possible to study amine complexation of Ln^{III}, and in dimethylsulfoxide (dmso) reactions between $[Ln(dmso)_8]^{3+}$ (obtained by dissolution of $Ln(CF_3SO_3)_3$) and various polyamines of different denticity give complexes of moderate stability. Data summarized in Ref. 81 show that log K_1 varies from 1.48 for 1,2-diaminoethane to 4.13 for triethylenetetramine, for example, with evidence for some of the higher species formed that the ligands may be hypodentate.

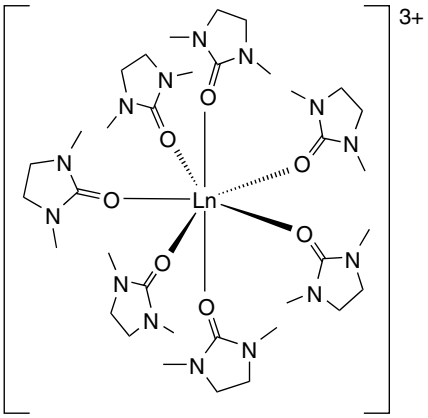
Very extensive studies have been made of crown ether complexation of the lanthanides (again carefully summarized in Ref. 81) in relatively weakly polar, aprotic solvents such as acetonitrile (MeCN) and propylene carbonate, and a problem recognized in this work is that in such solvents the Ln^{III} reactant, for example, $Ln(NO_3)_3$, may be incompletely dissociated. This may explain why crystal structure determinations on the products of these reactions[48] show stoichiometries such as $[Ln(crown)(NO_3)_2]_3[Ln(NO_3)_6]$, which in turn indicates that the speciation in solutions from which the crystals deposit may be somewhat more complicated than is commonly assumed. As noted above, anion binding is in part a reflection of the strength of anion solvation by the solvent and it is only for weakly coordinating anions such as perchlorate, triflate, and iodide and strongly coordinating solvents such as dmso and dmf that there is definitive and wide-ranging evidence for the formation of homoleptic solvento species on dissolution.[39,76] Note that studies in mixed solvents[77] and of solvent transfer thermodynamics[78] have shown that water is not the most strongly bound simple solvent on Ln^{III}, with an affinity order proposed for some common solvents being dmso > dmf $\sim H_2O$ > CH_3OH > $(CH_3)_2CO$ > THF (tetrahydrofuran) > MeCN.

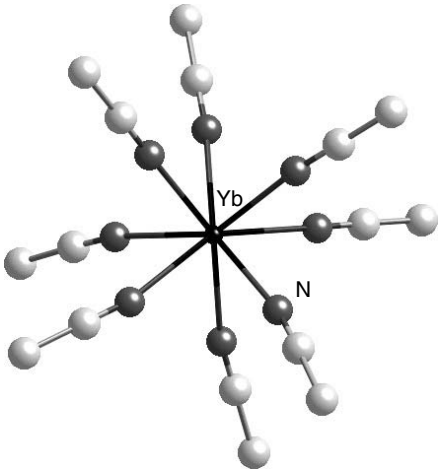
Again as for water, various lines of evidence[75] indicate that the energy difference between various forms of solvento complexes may be small and that more than one

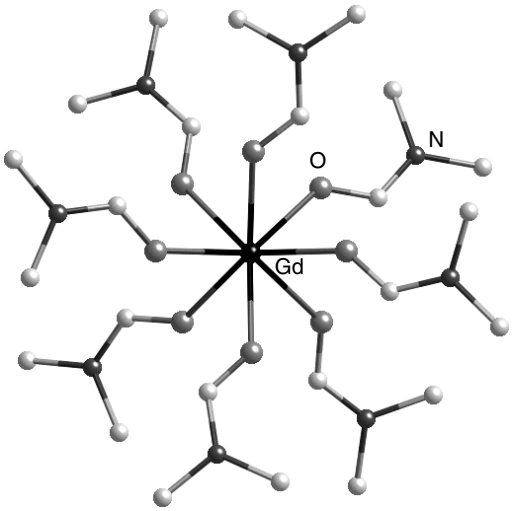
species may therefore be present in solution. For the solid state, X-ray structural studies have defined both $[Ln(MeCN)_8]^{3+}$ (**4**) and $[Ln(MeCN)_9]^{3+}$[79,80] as well as $[La(dmf)_8]^{3+}$ (**5**) and $[La(dmf)_9]^{3+}$[81–83] although for all other characterized dmf solvates,[27,84] as for dmso solvates (**6**),[27,85] only square-antiprismatic $[Ln(solvent)_8]^{3+}$ species have been found. In the interesting mixed solvento-species $[Nd(OH_2)_6(dmf)_3]^{3+}$,[86,87] the dmf-oxygen donors occupy the capping sites of a tricapped trigonal-prismatic unit but, unlike $[Nd(OH_2)_9]^{3+}$, bonds to the capping atoms are shorter than those to the prismatic site donors. Seven coordination is established for the *N*, *N*′-dimethylpropyleneurea complexes $[Ln(dmpu)_7]^{3+}$ (**7**) for all lanthanides except Lu.[17]

Although measurements of solvent exchange rates on Ln^{III} solvento complexes are rather limited, it appears that they are appreciably less labile than their aqua analogs and may involve dissociative activation.[28]









The donor atoms found in lanthanide shift reagents and in complexes stable in aqueous solution are in most cases O and/or N,[88] usually considered as ''hard'' base species and thus justifying the description of the lanthanide(III) ions as ''hard'' acids.[3] This classification is of importance in, for example, consideration of ligand design for the separation of lanthanides from actinides present in nuclear wastes.[89] That the same donor atom types are present in complexes soluble in both polar and apolar solvents should not, however, be taken to mean that the coordination chemistry of the lanthanides with ''soft'' donors is particularly limited and indeed the organometallic chemistry of the lanthanides, largely conducted in nonaqueous solvents, is both novel and important, so important in fact that it is discussed in ***Organometallic Chemistry Fundamental Properties***.

6 CONCLUSIONS

The nature of the first coordination sphere for the lanthanide aqua ions is now well understood, and studies in nonaqueous solvents are leading to identification of related

species with other ligands. It is hoped that future research will mean better knowledge of the second and further coordination spheres, with understanding of the process of complex formation. Clearly, there is already a considerable choice of simple complexes that can be used as reactants to solve particular problems arising in the synthesis of more sophisticated lanthanide complexes. Although the discussion above does not concern the nature of multidentate ligand complexes, several aspects of which are discussed in other chapters, it is worthy of note here that the lability characteristic of simple solvento species may not be shared by such complexes, even though there are many multidentate ligands where the donor sites are identical with those of simple solvents. Where the lanthanide ion and its donor sphere can be regarded as inert, kinetic control of the reactions of the complex can be envisaged and consequently, new applications for the lanthanide. Finally, it may be stated that, as a development from studies of solvento complexes and where any applications of multidentate ligand complexes involve solution chemistry, extended use of techniques such as EXAFS and LAXS as complements to more conventional spectroscopic techniques might be expected to lead to advances in the detailed general understanding of lanthanide ion coordination chemistry.

7 END NOTES

[a.] In its strictest sense, the term ''lanthanide'' applies to the 14 elements following La in the periodic table, although La itself is commonly taken to be a member of this group. The term ''rare earth,'' especially (translated) in languages other than English, is widely used to refer to the lanthanides and various other elements with certain chemical similarities, and in this chapter we adopt an intermediate posture of including Sc, Y, and La along with the ''true'' lanthanides for the purpose of analyzing their coordination chemistry.

8 ABBREVIATIONS AND ACRONYMS

dmpu = *N*, *N*′-dimethylpropyleneurea; dmf = dimethylformamide; dmso = dimethylsulfoxide; THF = tetrahydrofuran.

9 REFERENCES

1. C. James, *J. Am. Chem. Soc.*, 1908, **30**, 182.
2. F. H. Spedding and A. H. Daane, 'The Rare Earths', John Wiley & Sons, London, 1961.
3. K. A. Gschneidner, Jr., J.-C. Bünzli, and V. Pecharsky, eds, 'Handbook on the Chemistry and Physics of the Rare Earths', Elsevier, New York, 2011, Vol. 41 and preceding volumes.
4. S. A. Cotton, 'Lanthanide and Actinide Chemistry', Wiley-VCH, Weinheim, 2006.
5. K. A. Gschneidner, Jr., Rare Earth Minerals and 21st Century Industry (detailed responses to a US Government enquiry), Available online at www.gop.science.house.gov/Media/hearings/oversight10/mar16/Gschneidner.pdf (accessed 2011).
6. K. A. Gschneidner, Jr., *Mater. Matters (Aldrich)*, 2011, **6**, 32.
7. J.-C. G. Bünzli, *Acc. Chem. Res.*, 2006, **39**, 53.
8. S. V. Eliseeva and J.-C. G. Bünzli, *Chem. Soc. Rev.*, 2010, **39**, 189.
9. P. R. Selvin, *Annu. Rev. Biophys. Biomol. Struct.*, 2002, **31**, 275.
10. P. A. Caravan, *Acc. Chem. Res.*, 2009, **42**, 851.
11. R. G. Eggert, *Nat. Chem.*, 2011, **3**, 688.
12. S. Kulaksiz and M. Bau, *Environ. Int.*, 2011, **37**, 973.
13. M. Bau, A. Knappe, and P. Dulski, *Geochemistry*, 2006, **66**, 143.
14. J. M. Harrowfield and G. A. Koutsantonis, *C. R. Chim.*, 2005, **8**, 103.
15. G. Johanson, *Adv. Inorg. Chem.*, 1993, **39**, 159.
16. G. Johanson, *Pure Appl. Chem.*, 1988, **60**, 1773.
17. D. Lundberg, I. Persson, L. Eriksson, P. D'Angelo, and S. De Panfilis, *Inorg. Chem.*, 2010, **49**, 4420 and references therein.
18. L. Helm and A. E. Merbach, *Coord. Chem. Rev.*, 1999, **187**, 151.
19. J. M. Harrowfield, W. Lu, B. W. Skelton, and A. H. White, *Aust. J. Chem.*, 1994, **47**, 321.
20. A. A. Soudi, F. Marandi, A. Ramazani, E. Ahmadi, and A. Morsali, *C. R. Chim.*, 2005, **8**, 157.
21. J. Kuta and A. E. Clark, *Inorg. Chem.*, 2010, **49**, 7808.
22. L. Helm, G. M. Nicolle, and A. E. Merbach, *Adv. Inorg. Chem.*, 2005, **57**, 327.
23. S. F. Lincoln, *Helv. Chim. Acta*, 2005, **88**, 523.
24. A. Dossing, *Eur. J. Inorg. Chem.*, 2005, 1425 and references therein.
25. G. R. Choppin and D. R. Peterman, *Coord. Chem. Rev.*, 1998, **174**, 283 and references therein.
26. E. G. Moore, A. P. S. Samuel, and K. N. Raymond, *Acc. Chem. Res.*, 2009, **42**, 542 and references therein.
27. J. M. Harrowfield, *Met. Ions Biol. Syst.*, 2003, **40**, 105.
28. L. Helm and A. E. Merbach, *Chem. Rev.*, 2005, **105**, 1923.
29. L. Helm and A. E. Merbach, *Eur. J. Solid State Inorg. Chem.*, 1991, **28**, 245.
30. C. Cossy, A. C. Barnes, J. E. Enderby, and A. E. Merbach, *J. Chem. Phys.*, 1989, **90**, 3254.
31. E. N. Rizkalla and G. R. Choppin, in 'Handbook on the Chemistry and Physics of the Rare Earths', eds.

K. A. Gschneidner, Jr., L. Eyring, G. R. Choppin, G. H. Lander, Elsevier, Amsterdam, 1994, Vol. 18, Chap. 127, p. 591.

32. F. H. Spedding, P. F. Cullen, and A. Habenschuss, *J. Phys. Chem.*, 1974, **78**, 1106.
33. F. H. Spedding, L. E. Shiers, M. A. Brown, J. L. Derer, D. L. Swanson, and A. Habenschuss, *J. Chem. Eng. Data*, 1975, **20**, 81.
34. A. Habenschuss and F. H. Spedding, *J. Chem. Phys.*, 1979, **70**, 3758.
35. A. Habenschuss and F. H. Spedding, *J. Chem. Phys.*, 1980, **73**, 442.
36. T. Yamaguchi, M. Nomura, H. Wakita, and H. Ohtaki, *J. Chem. Phys.*, 1988, **89**, 5153.
37. K. Miyakawa, Y. Kaizu, and H. Kobayashi, *J. Chem. Soc. Faraday Trans.*, 1988, **84**, 1517.
38. S. A. Cotton, in 'Comprehensive Coordination Chemistry II', eds. J. A. McCleverty and T. J. Meyer, Elsevier, Amsterdam, 2004, Vol. 3, p. p. 93.
39. P. Lindqvist-Reis, K. Lamble, S. Pattanaik, I. Persson, and M. Sandström, *J. Phys. Chem. B*, 2000, **104**, 402.
40. V. Alexander, *Chem. Rev.*, 1995, **95**, 273.
41. J. Glaser and G. Johanson, *Acta Chem. Scand.*, 1981, **35A**, 639.
42. K. C. Lim, B. W. Skelton, and A. H. White, *Aust. J. Chem.*, 2000, **53**, 867.
43. P. C. Junk, L. I. Semenova, B. W. Skelton, and A. H. White, *Aust. J. Chem.*, 1999, **52**, 531.
44. F. J. Waller, A. G. M. Barrett, D. C. Braddock, D. Ramprasad, R. M. McKinnell, A. J. P. White, D. J. Williams, and R. Ducray, *J. Org. Chem.*, 1999, **64**, 2910.
45. T. Yamase, H. Naruke, and M. Kaneko, *Bull. Chem. Soc. Jpn.*, 1999, **72**, 1775.
46. T. Yamase, A. M. S. J. Wery, and M. Kaneko, *Chem. Lett.*, 1998, 1281.
47. H. Zhang, R. Wang, T. Jin, Z. Zhou, and X. Zhou, *J. Rare Earths*, 1998, **16**, 311.
48. R. D. Rogers and C. B. Bauer in 'Comprehensive Supramolecular Chemistry', eds. J. L. Atwood, J. E. D. Davies, D. D. MacNicol, and F. Vögtle, Pergamon, Oxford, 1996, Vol. 1, Chap. 8, p. p. 315.
49. A. Abassi, P. Lindqvist-Reis, L. Eriksson, D. Sandström, S. Lidin, and I. Persson, *Chem. Eur. J.*, 2005, **11**, 456.
50. J. L. Atwood, L. J. Barbour, M. J. Hardie, and C. L. Raston, *Coord. Chem. Rev.*, 2001, **222**, 3.
51. D. L. Faithfull, J. M. Harrowfield, M. I. Ogden, B. W. Skelton, and A. H. White, *Aust. J. Chem.*, 1992, **45**, 583.
52. R. D. Rogers, *Inorg. Chim. Acta*, 1988, **149**, 307.
53. A. Chatterjee, E. N. Maslen, and K. J. Watson, *Acta Crystallogr.*, 1988, **B44**,, 381, 386.
54. C. O. P. Santos, E. E. Castellano, L. C. Machado, and G. Vincentini, *Inorg. Chim. Acta*, 1985, **110**, 83.
55. J. M. Harrowfield, D. L. Kepert, J. M. Patrick, and A. H. White, *Aust. J. Chem.*, 1983, **36**, 483.
56. L. Helmholz, *J. Am. Chem. Soc.*, 1939, **61**, 1544.
57. R. Wang, H. D. Selby, H. Liu, M. D. Carducci, T. Jin, Z. Zheng, J. W. Anthis, and R. J. Staples, *Inorg. Chem.*, 2002, **41**, 278 and references therein.
58. R. H. Betts and O. F. Dahlinger, *Can. J. Chem.*, 1959, **37**, 91.
59. E. J. Wheelwright, F. H. Spedding, and G. Schwarzenbach, *J. Am. Chem. Soc.*, 1953, **75**, 4196.
60. R. M. Smith and A. E. Martell, *Sci. Total Environ.*, 1987, **64**, 125.
61. N. Sakagami, Y. Yamada, T. Konno, and K. Okamoto, *Inorg. Chim. Acta*, 1999, **288**, 7.
62. F. S. Richardson, *Chem. Rev.*, 1982, **82**, 541.
63. H. G. Brittain, *J. Coord. Chem.*, 1989, **20**, 331.
64. F. S. Richardson and J. P. Riehl, *Chem. Rev.*, 1986, **86**, 1.
65. R. D. Hancock and A. E. Martell, *Chem. Rev.*, 1989, **89**, 1875.
66. Y. Hasegawa, K. Takashima, and F. Watanabe, *Bull. Chem. Soc. Jpn.*, 1997, **70**, 1047.
67. P. Lindqvist-Reis, I. Persson, and M. Sandström, *Dalton Trans.*, 2006, 3868.
68. K. C. Lim, B. W. Skelton and A. H. White, *Aust. J. Chem.*, 2000, **53**, 875.
69. A. J. Rossini and R. W. Schurko, *J. Am. Chem. Soc.*, 2006, **128**, 10391.
70. T. Yamaguchi, M. Niihara, T. Takamuru, H. Wakita, and H. Kanno, *Chem. Phys. Lett.*, 1997, **274**, 485.
71. D. G. Karraker, *Inorg. Chem.*, 1968, **7**, 473.
72. P. D'Angelo, A. Zitolo, V. Migliorati, and I. Persson, *Chem. Eur. J.*, 2010, 684.
73. G. Otting, *J. Biomol. NMR*, 2008, **42**, 1.
74. P. Caravan, *Acc. Chem. Res.*, 2009, **42**, 851.
75. P. Di Bernardo, A. Melchior, M. Tolazzi, and P. L. Zanonato, *Coord. Chem. Rev.*, 2012, **256**, 328.
76. J. Näslund, P. Lindqvist-Reis, I. Persson, and M. Sandstrom, *Inorg. Chem.*, 2000, **39**, 4006 and references therein.
77. T. Kimura, R. Nagaishi, Y. Kato, and Z. Yoshida, *J. Alloys Compd.*, 2001, **323–324**, 164.
78. M. E. Clark and J. L. Bear, *J. Inorg. Nucl. Chem.*, 1969, **31**, 2619.
79. G. R. Willey, D. R. Aris, and W. Errington, *Inorg. Chim. Acta*, 2001, **318**, 97.
80. G. B. Deacon, B. Gortler, P. C. Junk, E. Lork, R. Mews, J. Petersen, and B. Zemva, *J. Chem. Soc., Dalton Trans.* 1998, 3887.
81. J. C. Berthet, P. Thuéry, and M. Ephritikine, *Polyhedron*, 2006, **25**, 1700.
82. S. S. Yarovoi, Y. V. Mironov, S. F. Solodovnikov, Z. A. Solodovnikova, D. Y. Naumov, and V. E. Fedorov, *Russ. J. Coord. Chem.*, 2006, **32**, 712.
83. S. M. Liu, C. E. Plecnik, E. A. Meyers, and S. G. Shore, *Inorg. Chem.*, 2005, **44**, 282.

84. J. M. Harrowfield, B. W. Skelton, A. H. White, and F. R. Wilner, *Inorg. Chim. Acta*, 2004, **357**, 2358.

85. E. J. Chan, B. G. Cox, J. M. Harrowfield, B. W. Skelton, and A. H. White, *Inorg. Chim. Acta*, 2004, **357**, 2365.

86. D. M. Araujo Melo, G. Vincentini, L. B. Zimmer, C. A. De Simone, and E. E. Castellano, *Inorg. Chim. Acta*, 1988, **146**, 123.

87. R. E. Marsh, *Inorg. Chim. Acta*, 1989, **161**, 1.

88. S. Mishra, *Coord. Chem. Rev.*, 2008, **252**, 1996.

89. P. Y. Cordier, C. Hill, P. Baron, C. Madic, M. J. Hudson, and J. O. Liljenzin, *J. Alloys Compd.*, 1998, **271–273**, 738.

Lanthanides in Living Systems

Simon A. Cotton

University of Birmingham, Birmingham, UK

and

Jack M. Harrowfield

Université de Strasbourg, Strasbourg, France

1	Summary	65
2	Introduction	65
3	Lanthanides in Biological Analysis	66
4	Lanthanides in Medical Diagnosis	67
5	Lanthanides in Medical Therapy	68
6	Conclusions	69
7	Glossary	69
8	Related Articles	69
9	Abbreviations	70
10	References	70

1 SUMMARY

Although considered as inessential elements for life, the lanthanides are certainly biologically active and have numerous applications of importance in biological analysis and in both diagnosis and therapy in medicine. These applications exploit not only the spectroscopic and magnetic properties of various naturally occurring lanthanides but also the activity of synthetic radioisotopes. This chapter is focused on recent developments in such areas and on the basic aspects of coordination chemistry, which underlie the use of lanthanide(III) species in particular.

2 INTRODUCTION

While the lanthanides do not appear to be biologically essential elements,[1,2] they are certainly biologically active and useful in many ways,[3–5] and their applications in medicine,[6,7] in particular, continue to expand. In a recent review[8] focussed on a broad range of applications of lanthanide ion luminescence, a detailed list is provided of the many particular applications of lanthanide complexes in biology and medicine. These extend from use, in the nineteenth century, of cerium oxalate in the treatment of nausea during pregnancy to two-photon luminescence microscopy developed in the 1990s. One result of such work has been the demonstration that nonradioactive lanthanide compounds are of relatively low toxicity for human beings,[1,2,8,9] though this may not be true for other organisms.[1,2,8,10] Nonetheless, since medical use as in magnetic resonance imaging (MRI)[11–20] can involve quite large (gram quantity) dosages, an important aspect of the coordination chemistry of the compounds exploited (largely Gd^{III} complexes) is that of ensuring that the lanthanide is not in a form where it may be retained within the body and in particular that it is bound to a ligand so strong that negligible amounts of the aqua ion may be released. Heavy metal ions are typically considered as toxic species[21] and the fact that there is an extensive coordination chemistry of the lanthanides with sugars[22–24] and aminoacids, See Ref. 25 and references therein,[26] for example, points to their capability of interacting with biomolecules including polysaccharides and proteins. In addition, Ln^{III} species are of a similar size to Ca^{II} and, largely

The Rare Earth Elements. Edited by David A. Atwood. © 2012 John Wiley & Sons, Ltd. ISBN 978-1-119-95097-4

because of their higher charge, will replace calcium bound to proteins, a property which has been exploited to produce spectroscopically active probes of calcium sites,[3–5,27,28] though the introduction of the lanthanide is not necessarily associated with retention of the same activity as the Ca protein (as is also true where Ln^{III} is substituted for Mn^{II} in various enzymes[29]). They will also replace Ca^{II} in bone, a property which has found therapeutic applications,[30–32] and the fact that they are not biologically essential elements thus appears to be a consequence of their relatively low natural abundance (with respect to Ca in particular) and the highly insoluble nature of their ores, among other factors. Monazite, one of the more common lanthanide ores,[33] is a phosphate and it is the insolubility of $LaPO_4$ which is in part the basis of the successful use of $La_2(CO_3)_3$ in treatment of phosphate overload[34] (see ahead).

True problems of toxicity are associated with the mining and treatment (including wastes disposal) of rare earth ores (See Ref. 35 and References therein) but these are largely due to the fact that the ores are typically contaminated with significant levels of radioactive elements, thorium and uranium being the most important of these.[36] The lanthanide promethium occurs only as radioisotopes of short half-life, the longest lived being ^{145}Pm, $t_{1/2}$17.7 years,[37] and thus its abundance is so low that it is not considered a health risk. Numerous radioactive lanthanide isotopes are present in nuclear wastes and their separation and disposal have been the subject of much research,[38] although efforts have also been directed at the synthesis of particular isotopes through neutron irradiation for use in medical treatments,[30,31] where indeed it is *selective toxicity* which is the important issue. Here, it may also be noted that some nonradioactive lanthanides have been studied as models for the chemical behavior of highly toxic actinide species present in nuclear wastes (Eu^{III} for Am^{III}[39], Ce^{IV} for Pu^{IV}[40]).

Since a full discussion of the nature and effects of lanthanides in living systems would pass well beyond the limits of a single chapter, what has been done in the present work is to focus largely on recent developments in some of the more important fields, most of which (excluding that of radiopharmaceuticals) are based on exploitation of the magnetic or luminescence properties of the lanthanide ions. In medical areas, in particular, these more recent developments have concerned efforts to achieve more efficient targeting of lanthanide-containing reagents to particular tissues and organs, work which generally has required sophisticated ligand design and careful exploitation of lanthanide coordination chemistry in order to make the most efficient and selective use possible of the inherent properties of the lanthanide ion centers. The various reviews cited herein provide extensive referencing to basic studies of lanthanide ion/biomolecule interactions and to the foundations of current applications, as well as to earlier substantial reviews with similar coverage.

3 LANTHANIDES IN BIOLOGICAL ANALYSIS

The first sophisticated bioanalytical application of lanthanide ion luminescence was that of (most commonly) Eu^{III} complexes in time-resolved fluoroimmunoassays.[3,4] See Ref. 41 and references therein. A basic requirement for any immunoassay is that it must be possible to label in some way an antibody or an antigen with a tag that is stable and readily detected under the conditions of the analysis. In the case of luminescent tags incorporating lanthanide ions,[3,4,8,9,42–49] the metal ion must be bound sufficiently strongly by a multidentate ligand to prevent its loss by coordination to the variety of other ligands present in (aqueous) biological media and the ligand itself must be such as to promote the most intense luminescence possible from the metal ion. A particular advantage of lanthanide ions as luminescent tags is their relatively long excited state lifetimes, enabling time gating to be used to eliminate the effects of short-lived background biological luminescence, although these lifetimes can be shortened by the presence, in particular, of aqua ligands, so that ideally the denticity of the binding ligand should be such as to exclude the availability of a site for water (in distinction to the situation for MRI[11–20] see ahead). A further requirement of the ligand is that it should incorporate a strongly absorbing chromophore which can act as an ''antenna'' to transfer excitation to the otherwise very weakly absorbing lanthanide ions. Further still, the ligand must be functionalized in a way that is suitable for its attachment (perhaps multiply) to proteins (antibodies) and antigens. While a considerable variety of ligands giving lanthanide ion complexes of high stability in biological media are now known,[47] satisfying all the criteria for use in an immunoassay system is not a readily obtained objective. Nonetheless, minor deficiencies can be tolerated and an example of a satisfactory case is provided in the Eu^{III} complex of the cryptand derivative shown in Figure 1.[45] Here, the macrobicyclic nature of the ligand inhibits access of water ligands to the metal ion center, the heteroaromatic coordinating units absorb strongly in the ultraviolet region and efficiently transfer their excitation to Eu^{III}, and the external functionalization can be used for efficient attachment to proteins.

Advances[4,8,42] in the application of luminescent lanthanide probes of the form just described both in the area of immunoassays and of general bioanalysis include the use of the lanthanide center as an excitation transfer agent (via Förster resonant energy transfer (FRET),[45] one of several possible sensing mechanisms for fluorescent chemosensors[50]) to produce emission from organic fluorophores at various wavelengths and the use of the external functionalization for specific reactions which ''switch on'' strong luminescence.[43] An example of the latter is provided in detection of singlet oxygen by the Eu^{III} complex of the anthracenyl-substituted terpyridine derivative shown in Figure 2, in which deactivation of the metal ion excited state by the anthracenyl substituent is excluded by the reaction of this unit to form an adduct

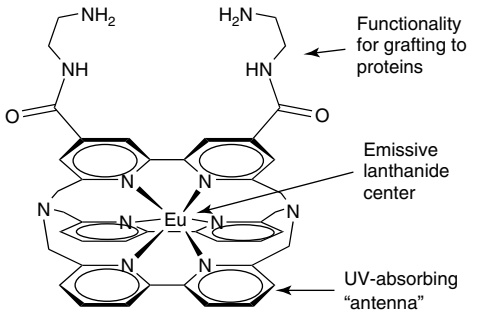


Figure 1 An europium(III) cryptand complex[45] satisfying the requirements for use in fluoroimmunoassays

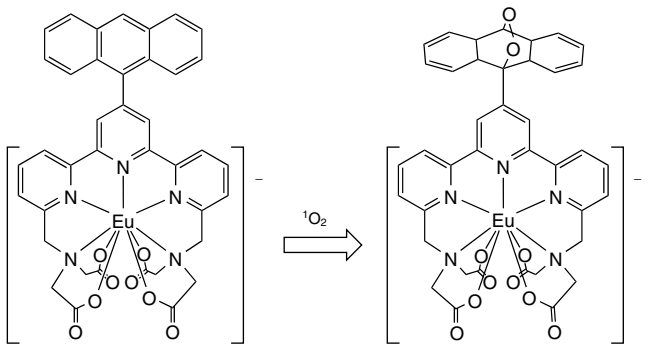


Figure 2 ''Switching on'' of Eu^{III} luminescence resulting from reaction of a pendent anthracenyl group with singlet oxygen

with the singlet oxygen.[51] This complex and related species which respond to a variety of other biological substrates can be used, through luminescence microscopy, to provide maps of the cellular locations and transport of the substrates,[42] thus providing both qualitative and quantitative bioanalysis. It is of course essential that the lanthanide complex used be not only luminescent but also noncytotoxic and stable in biological media, and there is in fact a considerable choice of species which satisfy these criteria,[8,9,42] their innocuous nature confirming the general supposition that toxicity is rarely likely to be an issue in the use of lanthanide complexes. Note that one means of enhancing the sensitivity of luminescence measurement is to use polynuclear complexes containing multiple emitters, even binuclear species having proved advantageous.[9]

Although the visible red and green, respectively, emissions from Eu^{III} and Tb^{III} complexes are particularly familiar due to their widespread exploitation,[8,42–45] they do occur and may be excited by absorption in spectral regions where biological tissues and structures may absorb. Consequently, considerable interest has developed in lanthanide ions which emit in the near-infrared (NIR) region (Nd^{III} being long exploited, in solid state lasers, in particular, because of this property), since, here, most biological tissues are transparent.[8,52] Hence, both excitation and emission may be achieved without complications associated with the medium. A development of the capacity to irradiate efficiently in a relatively low energy region is that of ''upconversion'' systems[53,54] where two absorbed NIR photons are converted into a single emitted visible photon. This in turn has been associated with the development of lanthanide emitters based on nanoparticles and various other aggregates,[8,46] materials which can also be exploited in other areas such as MRI (see ahead).

Hydrolysis of phosphate esters by lanthanide hydroxide gels was one of the earliest observations of metal ion catalysis of such reactions[55] and this, in fact, does provide a reason for considering that lanthanide ions might indeed be toxic under certain conditions. What has been shown, however, is that it is only Ce^{IV} which is a particularly efficient catalyst for hydrolysis of phosphate ester bonds in nucleic acids (as well as of peptide bonds in proteins)[56,57] and this property has been put to use in developing methods for excising small polynucleotide units from DNA.[58] Although $[NH_4]_2[Ce(NO_3)_6]$ is the reagent conventionally used as the source of Ce^{IV} in these reactions, due to the lability and facile hydrolysis of the $[Ce(NO_3)_6]^{4-}$ anion, the nature of the actual catalytically active species is somewhat obscure and the reaction process is probably heterogeneous. Hydrolytic oligomerization is a means of providing multiple metal centers in close proximity to engender bimetallic catalysis.

4 LANTHANIDES IN MEDICAL DIAGNOSIS

The development of gadolinium-based relaxivity enhancement agents to improve tissue contrast in MRI has been a crucial aspect of the now widespread use of this imaging technique.[11–20] An obvious reason for the use of Gd^{III} is that this ion has the greatest number of unpaired electrons of any simple metal ion and thus is a source of strong paramagnetism (although other Ln^{III}, Dy^{III}, and Ho^{III}, in particular, have higher magnetic moments[17]). Many other issues must, however, be considered in developing reagents suitable for medical use. A crucial requirement is stability in a biological environment and another the avoidance of possible toxic effects (of the reagent itself or of gadolinium aqua ion if released from the reagent[8]) by ensuring efficient elimination from the organism (usually a human being) after use. Since the basic effect of the reagent used is to enhance the nuclear relaxation rate of the protons of water molecules in tissue, an efficient mechanism for transfer of this relaxivity effect must operate and this requires the coordination of at least one water molecule to the metal center. The subtlety of the strategy necessary to realize just these objectives is illustrated by the fact that although both the macrocycle derivatives 1,4,8,11-tetra-azacyclotetradecane tetra-acetate (TETA) and 1,4,7,10-tetra-azacyclododecane

tetra-acetate (DOTA) (Figure 3) give Gd^{III} complexes of more than sufficient stability to be injected into and recovered intact from living tissues, only the DOTA complex is a useful relaxivity enhancement agent because of the ability of the bound Gd^{III} to pass from eight- to nine-coordination by coordinating a water molecule as well as the macrocycle.[11]

Numerous more subtle aspects of relaxivity agent design have been subjected to close scrutiny, various substitution patterns of the cyclen macrocycle which is the core of DOTA having been examined, for example, with the aim of producing just a trianionic derivative so that the Gd^{III} complex would be neutral,[59] minimizing osmotic shock associated with its injection. A major drawback to the use of mononuclear Gd^{III} complexes (despite the fact that it is the conventional procedure in current medical diagnosis[12,13]) is that relatively high concentrations, therefore high doses, are required to generate useful effects. Hence, various approaches[12–16] have been developed, for example, toward functionalization of the complex to achieve targeting to a particular tissue, an objective of broad importance in the application of lanthanide ion chemistry,[60,61] or toward formation of clusters in which (sometimes very large) numbers of Gd^{III} centers are present. The Gd^{III} complex of a derivative of diethylentetramine-penta-acetate (DTPA) known as MS-325 (Figure 4a) was designed

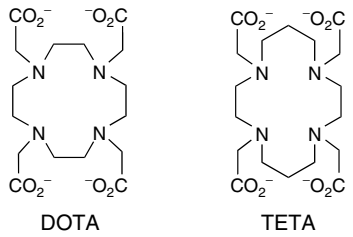


Figure 3 Tetrakis(carboxylatomethyl) derivatives of the tetra-azamacrocycles ''cyclen'' (1,4,7,10-tetra-azacyclododecane) and ''cyclam'' (1,4,8,11-tetra-azacyclotetradecane) which form Ln^{III} complexes of high stability in biological media

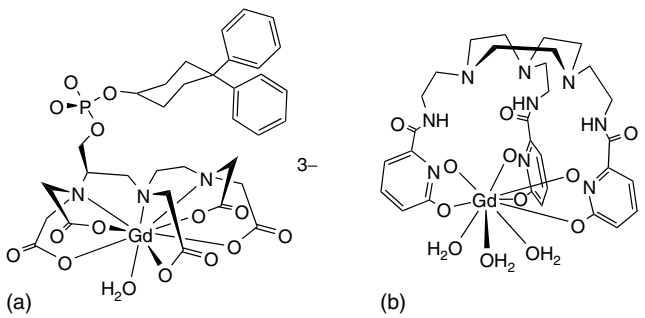


Figure 4 (a) The Gd^{III} complex termed MS-325 designed for binding to human serum albumin[13]. (b) The Gd^{III} complex of a sexidentate tripodal ligand in which three readily exchanged water molecules are also present[15]

to target binding to serum albumin and has been shown to be useful, for this reason, for blood vessel imaging.[13] Gadonanotubes are an example of a high-performance contrast agent in which chlorogadolinium(III) clusters are encapsulated in single-walled carbon nanotubes.[18,20] Other means of controlled aggregation such as the formation of micelles with appropriately functionalized mononuclear complexes[14,18,20] are a further source of potentially useful multimetallic agents. An alternative strategy to enhance the relaxivity of mononuclear species is the use of a tripodal ligand occupying six-coordination sites about Gd^{III} (Figure 4b), thus allowing up to three water molecules to also be coordinated and, because of their high exchange rates, to enhance the nuclear relaxation rates of solvent protons considerably more effectively than does $[Gd(DOTA)(OH_2)]^-$ or its relatives.[15] Note also that the lowered tumbling rate of a simple complex resulting from its attachment to a biopolymer can be another important influence on relaxivity.[13,15]

The similarity in coordinating properties of all the lanthanides means that, broadly speaking, all that has been learnt about binding and targeting of Gd^{III} can be applied to the other cations.[60,61] In the case of radioactive lanthanides, most such applications concern therapy[34,61] but certainly positron-emitting radiolanthanides[31] could also be used in imagery (PET, positron emission tomography). Indeed, the increasing trend to use one species for both imaging and therapy[61] has led to the definition of the field of ''theranostics''[62] as the combination of these applications.

5 LANTHANIDES IN MEDICAL THERAPY

The use of radiolanthanides in both treatment and palliation of cancer has been long established[34,63] and methods for the production of radioisotopes with optimal properties for different uses continue to be a matter of research interest.[30,31,64] The rare earth species ^{90}Y has also been long known for its medical use in cancer treatment.[65] In the alleviation of the severe pain associated with bone cancer, the targeting of bone by exchange with Ca^{II} of, for example, $^{153}Sm^{III}$ delivered as its complex with phosphonate analogs of DOTA (and other multidentate ligands) is a fundamental aspect of the therapy.[66] Certain nonradioactive Ln^{III} complexes have been extensively investigated for cancer treatment.[34] The Gd^{III} complex of the expanded porphyrin ''texaphyrin,'' for example, having a long wavelength absorption suited to its excitation by tissue-penetrating NIR radiation gives a species deactivated by conversion of triplet oxygen to its cytotoxic singlet form.[67] Nonradioactive lanthanides have also proven useful in the treatment of bone disorders such as osteoporosis, the substitution of Ln^{III} for Ca^{II} in various enzymes enabling modification of the imbalance between bone resorption and bone formation.[32] Here, an important aspect of the therapy is the use of ligands bound to Ln^{III} which overcome the incapacity of simple Ln salts to be absorbed from the intestinal

tract (this being in fact another reason to those noted previously for their low toxicity).

As noted previously, therapeutic applications of Ce, in particular, were developed in the nineteenth century[8,34] and indeed the early recognition of the antibacterial properties of both Ce^{III} and Ce^{IV} compounds led to their quite extensive and continuing use in treatment of burn patients to avoid infection, although it may be that their influence on the immune response is more important than their bacteriocide properties.[34] The effect of Ln^{III} species, in general, on immune function is well established but seemingly rather complicated biochemically.[34]

A fascinating illustration of the issues involved in the development of a lanthanide-based therapeutic agent is provided by the use of lanthanum carbonate in the treatment of hypophosphatemia.[34] This is an overload illness commonly arising in patients with renal disease, with an apparently simple solution being to inhibit phosphate absorption from the gut. While various metal ions give exceedingly insoluble phosphates, which are not absorbed, problems may arise from absorption of any excess metal ion (for example, Al^{III}, for which toxic effects are well established) and thus the fact that simple Ln^{III} species do not cross intestinal membranes makes them of unique utility. $La_2(CO_3)_3$ will dissolve in stomach acid to give a species which will bind phosphate both at low pH and at higher pH values found in other parts of the intestine. Any excess of La^{III} is excreted efficiently along with insoluble $LaPO_4$.

6 CONCLUSIONS

Despite their inessential nature, the lanthanide elements in their compounds can be involved in and influence the functioning of biological systems in a remarkable variety of ways. There are certainly reasons to expect that this variety may increase, especially in the areas of medical diagnosis and imaging.[34,62] An index of just how important such applications have already become is the anthropogenically induced augmentation of environmental Gd levels due to the use of MRI procedures.[68] The present report provides no more than a brief glimpse of the fascinating coordination chemistry which underlies the development of known applications of the lanthanides, and this is chemistry which no doubt will further evolve in the future. Many of the issues which are touched upon only briefly in the present chapter are discussed in much greater detail in other chapters of this encyclopedia, in particular ***Lanthanides: Coordination Chemistry***, ***Luminescence***, ***Lanthanide Complexes with Multidentate Ligands***, ***Near-Infrared Materials***, ***Lanthanides: Magnetic Resonance Imaging***, ***Luminescent Bioprobes***, and ***Sensors for Lanthanides and Actinides***.

7 GLOSSARY

Multidentate ligand: A single molecule containing multiple donor-atoms, such that it can occupy all or most of the coordination sites of single metal ion, thus forming a complex of high stability. Macrocyclic ligands, where several donor atoms are found within the large ring, are a particularly useful class of multidentate ligands for lanthanide chemistry.

Antenna ligand: A ligand containing a chromophore capable of strong light absorption and of then transferring the energy of excitation to a bound metal ion.

Radiolanthanide: Usually, a synthetic radioisotope of a lanthanide produced by neutron irradiation of a stable species, although radiolanthanides are also found as nuclear fission products and promethium is only known in the form of radioactive species.

Relaxivity: A measure of the effect of a paramagnetic ion, such as gadolinium(III) on the nuclear excited state lifetime of any adjacent nucleus, that of the proton being most important in current applications of the lanthanides.

Luminescence: In general, the loss of the energy of an electronic excited state by the emission of light, a particularly important aspect of lanthanide ion behaviour being that this energy loss occurs relatively slowly. In some cases, luminescence can be switched ''on'' or ''off'' by chemical reactions of the lanthanide complex.

Imaging: Any technique making use of relaxivity effects or luminescence to provide a three-dimensional map of the structure of a micro- or macro-scopic system.

Immunoassay: A bioanalytical technique based on the use of antibody–antigen interactions and where either the antibody or the antigen can be ''tagged'' by grafting on a luminescent or radioactive lanthanide complex.

Toxicity: Any deleterious effect of a lanthanide on the living body, usually considered to be a result of the lanthanide ion interfering with enzyme function.

Cancer palliation: Reduction of the pain associated with certain cancers resulting from the targeting of radiolanthanides to particular cells.

Hypophosphatemia: An overload illness commonly arising in patients with renal disease, with an apparently simple solution being to inhibit phosphate absorption from the gut.

8 RELATED ARTICLES

Lanthanides: Coordination Chemistry; Luminescence; Lanthanide Complexes with Multidentate

Ligands; Near-Infrared Materials; Lanthanides: Magnetic Resonance Imaging; Luminescent Bioprobes; Sensors for Lanthanides and Actinides.

9 ABBREVIATIONS

DTPA = diethylentetramine-penta-acetate; FRET = Förster resonant energy transfer; MRI = magnetic resonance imaging; NIR = near infra-red; PET = positron emission tomography.

10 REFERENCES

1. C. H. Evans, 'Biochemistry of the Lanthanides', Plenum Press, New York, 1990.
2. R. A. Bulman, *Met. Ions Biol. Syst.*, 2003, **40**, 39.
3. J.-C. G. Bünzli and G. R. Choppin eds, 'Lanthanide Probes in Life, Chemical and Earth Sciences', Elsevier, Amsterdam, 1989.
4. P. Häminnen and H. Härmä eds, 'Lanthanide Luminescence : Photophysical, Analytical and Biological Aspects', Springer-Verlag, Berlin, 2011.
5. K. A. Gschneidner Jr., *et al*., 'Handbook on the Chemistry and Physics of the Rare Earths, Elsevier, Amsterdam.
6. K. H. Thompson and C. Orvig, *Chem. Soc. Rev.*, 2006, **35**, 499.
7. T. J. Meade and S. Aime, *Acc. Chem. Res.*, 2009, **42**, 821.
8. S. V. Eliseeva and J. C. G. Bünzli, *Chem. Soc. Rev.*, 2010, **39**, 189.
9. J.-C. G. Bünzli, A.-S. Chauvin, C. D. B. Vandevyver, S. Bo, and S. Comby, *Ann. N.Y. Acad. Sci.*, 2008, **1130**, 97.
10. P. Tai, Q. Zhao, D. Su, P. Li, and F. Stagnitti, *Chemosphere*, 2010, **80**, 1031.
11. A. E. Merbach and É. Toth eds, 'The Chemistry of Contrast Agents in Medical Magnetic Resonance Imaging', Wiley-VCH, Weinheim, 2001.
12. P. Caravan, J. J. Ellison, T. J. McMurry, and R. B. Lauffer, *Chem. Rev.*, 1999, **99**, 2293.
13. P. Caravan, *Acc. Chem. Res.*, 2009, **42**, 851.
14. S. Aime, D. Delli Castelli, S. G. Crich, E. Gianolio, and E. Terreno, *Acc. Chem. Res.*, 2009, **42**, 822.
15. A. Datta and K. N. Raymond, *Acc. Chem. Res.*, 2009, **42**, 938.
16. L. M. De Leon-Rodriguez, A. J. M. Lubag, C. R. Malloy, G. V. Martinez, R. J. Gillies, and A. D. Sherry, *Acc. Chem. Res.*, 2009, **42**, 948.
17. M. Norek and J. A. Peters, *Prog. Nucl. Magn. Reson. Spectrosc.*, 2011, **59**, 64.
18. A. J. Surman, G. D. Kenny, D. K. Kumar, J. D. Bell, D. R. Casey, and R. Vilar, *Chem. Commun.*, 2011, **47**, 10245.
19. C. Vanasschen, N. Bouslimani, D. Thonon, and J. F. Desreux, *Inorg. Chem.*, 2011, **50**, 8946.
20. K. B. Hartmann, S. Laus, R. D. Bolskar, R. Muthupillai, L. Helm, E. Toth, A. E. Merbach, and L. J. Wilson, *Nano Lett.*, 2008, **8**, 415.
21. J. J. R. Frausto Da Silva and R. J. P. Williams, 'Biological Chemistry of the Elements: The Inorganic Chemistry of Life', 2nd edition, Oxford University Press, Oxford, 2001.
22. S. J. Angyal, *Carbohydr. Res.*, 1974, **35**, 165.
23. S. J. Angyal, *Adv. Carbohydr. Chem. Biochem.*, 1989, **47**, 1.
24. B. Gyurscik and L. Nagy, *Coord. Chem. Rev.*, 2000, **203**, 81.
25. R. Wang, H. D. Selby, H. Liu, M. D. Carducci, T. Jin, Z. Zheng, J. W. Anthis, and R. J. Staples, *Inorg. Chem.*, 2002, **41**, 278.
26. R. Wang, Z. Zheng, T. Jin, and R. J. Staples, *Angew. Chem. Int. Ed.*, 1999, **38**, 1813.
27. E. Pidcock and G. R. Moore, *J. Biol. Inorg. Chem.*, 2001, **6**, 479.
28. C. H. Evans, *Trends Biochem. Sci.*, 1983, **8**, 445.
29. Z. R. Yang, R. Batra, D. L. Floyd, H. C. Hung, G. G. Chang, and L. Tong, *Biochem. Biophys. Res. Commun.*, 2000, **274**, 440.
30. D. Ma, A. R. Ketring, G. J. Ehrhardt, and W. Jia, *J. Radioanal. Nucl. Chem.*, 1996, **206**, 119.
31. H. Uusijärvi, P. Bernhardt, F. Rösch, H. R. Maecke, and E. Forssell-Aronsson, *J. Nucl. Med.*, 2006, **47**, 807.
32. C. A. Barta, K. Sachs-Barrable, J. Jia, K. H. Thompson, K. M. Wasan, and C. Orvig, *Dalton Trans.*, 2007, **2007**, 5019.
33. N. N. Greenwood and E. A. Earnshaw, 'Chemistry of the Elements', Pergamon, Oxford, 1987, Chap. 20, p. 1102.
34. S. P. Fricker, *Chem. Soc. Rev.*, 2006, **35**, 524.
35. A. Peltier, J. M. Elhabache, and C. Guillemin, *Cahiers de Notes Documentaires*, 1992, **147**, 227.
36. R. van Emden, M. R. Thornber, J. Graham, and F. J. Lincoln, *Can. Mineral.*, 1997, **35**, 95.
37. J. Emsley, 'The Elements', Clarendon Press, Oxford, 1989, p. 150.
38. M. Nilsson and K. L. Nash, *Solvent Extr. Ion Exch.*, 2007, **25**, 665.
39. G. R. Choppin and M. P. Jensen, in 'The Chemistry of the Actinide and Transactinide Elements', eds. L. R. Morss, N. M. Edelstein, J. Fuger, and J. J. Katz, Springer, Dordrecht, 2006, Vols. 4 & 5, p. 2524.
40. A. E. V. Gordon, J. Xu, K. N. Raymond, and P. W. Durbin, *Chem. Rev.*, 2003, **103**, 4207.
41. J. Yuan and G. Wang, *Trends Anal. Chem.*, 2006, **25**, 490.
42. C. P. Montgomery, B. S. Murray, E. J. New, R. Pal, and D. Parker, *Acc. Chem. Res.*, 2009, **42**, 925.
43. D. Parker, R. S. Dickins, H. Puschmann, C. Crossland, and J. A. K. Howard, *Chem. Rev.*, 2002, **102**, 1977.
44. I. Hemmilä and V. Laitala, *J. Fluorescence*, 2005, **15**, 529.

45. P. R. Selvin, *Annu. Rev. Biophys. Biomol. Struct.*, 2002, **31**, 275.

46. C. Lincheneau, F. Stomeo, S. Comby, and T. Gunnlaugsson, *Aust. J. Chem.*, 2011, **64**, 1315.

47. N. N. Katia, A. Lecointre, M. Rigueiro-Figueroa, C. Platas-Iglesias, and L. J. Charbonnière, *Inorg. Chem.*, 2011, **50**, 1689.

48. B. Alpha, J.-M. Lehn, and G. Mathis, *Angew. Chem. Int. Ed.*, 1987, **26**, 266.

49. G. Mathis, *Clin. Chem.*, 1995, **41**, 1391.

50. J. Wu, W. Liu, J. Ge, H. Zhang, and P. Wang, *Chem. Soc. Rev.*, 2011, **40**, 3483.

51. R. Song, G. Wang, M. Tan, and J. Yuan, *New J. Chem.*, 2005, **29**, 1431.

52. S. Comby and J.-C. G. Bünzli, in 'Handbook on the Physics and Chemistry of Rare Earths', eds. K. A. Gschneidner Jr., J.-C. G. Bünzli, and V. K. Pecharsky, Elsevier, Amsterdam, 2007, Vol. 37, Chap. 235, p. 217.

53. F. Auzel, *Chem. Rev.*, 2004, **104**, 139.

54. A. Meijerink, *Mater. Matters (Aldrich)*, 2011, **6**(4), 113.

55. W. W. Butcher and F. H. Westheimer, *J. Am. Chem. Soc.*, 1955, **77**, 2420.

56. M. Komiyama, *Met. Ions Biol. Syst.*, 2003, **40**, 463.

57. T. Takarada, M. Yashiro, and M. Komiyama, *Chem. Eur. J.*, 2000, **6**, 3906.

58. J. Sumaoka, Y. Yamamoto, Y. Kitamura, and M. Komiyama, *Curr. Org. Chem.*, 2007, **11**, 463.

59. E. J. Shiells, L. N. Natrajan, D. Sykes, M. Tropiano, P. Cooper, A. M. Kenwright, and S. Faulkner, *Dalton Trans.*, 2011, **40**, 11451.

60. T. Storr, K. H. Thompson, and C. Orvig, *Chem. Soc. Rev.*, 2006, **35**, 534.

61. M. F. Tweedle, *Acc. Chem. Res.*, 2009, **42**, 958.

62. H. Cabral, N. Nishiyama, and K. Kataoka, *Acc. Chem. Res.*, 2011, **44**, 999.

63. S. Z. Lever, J. D. Lydon, C. S. Cutler, and S. S. Jurisson, in 'Comprehensive Coordination Chemistry II', eds. J. A. McCleverty and T. Meyer, Elsevier Science, Oxford, 2004, Vol. 9, p. 883.

64. H. Mohsin, F. Jia, J. N. Bryan, G. Sivaguru, C. S. Cutler, A. R. Ketring, W. H. Miller, J. Simon, R. K. Frank, L. J. Theodore, D. B. Axworthy, S. S. Jurisson, and M. R. Lewis, *Bioconj. Chem.*, 2011, **22**, 2444.

65. S. Liu, *Chem. Soc. Rev.*, 2004, **33**, 445.

66. J. N. Bryan, D. Bommarito, D. Y. Kim, L. M. Berent, M. E. Bryan, J. C. Lattimer, C. J. Henry, H. Engelbrecht, A. Ketring, and C. Cutler, *J. Nuc. Med. Technol.*, 2009, **37**, 45.

67. T. D. Mody, L. Fu, and J. L. Sessler, *Prog. Inorg. Chem.*, 2001, **49**, 551.

68. M. Bau, A. Knappe, and P. Dulski, *Geochemistry*, 2006, **66**, 143.

Lanthanides: Coordination Chemistry

Simon A. Cotton

University of Birmingham, Birmingham, UK

and

Jack M. Harrowfield

Université de Strasbourg, Strasbourg, France

1	Summary	73
2	Introduction	73
3	Choice of Donor Atoms	74
4	Coordination Numbers	74
5	The Lanthanide Contraction and Coordination Numbers	77
6	The Need for X-Ray Diffraction Studies	77
7	Complexes with Simple Monodentate O-Donor Ligands	78
8	Conclusions	80
9	Related Articles	80
10	Abbreviations and Acronyms	80
11	Further Reading	80
12	References	80

1 SUMMARY

In their coordination chemistry, the lanthanides are typified by complexes of Ln^{3+}, species that exhibit significant differences from analogous transition metal ions such as Cr^{3+} and Co^{3+}. Not only do they not form readily isolable complexes with basic N-donors such as ammonia, but also they do not have a characteristic coordination number in their complexes. Their characteristics are shared by the much less commonly encountered complexes of Ln^{2+} and Ln^{4+} ions. Coordination numbers are determined by the size of the ligand, either by the number of donor atoms that may pack round the metal, or, in the case of bulky ligands, the interactions between distant groups that decide how many ligands may bind to the metal ion. Coordination numbers up to 8 or 9 are the norm with monodentate ligands, though using multidentate ligands may produce values as high as 12. Yttrium behaves in a way similar to the later lanthanides, while scandium can behave differently from either the lanthanides or the earlier transition metals.

2 INTRODUCTION

Apart from simple hydrated salts, little was known about the coordination chemistry of the lanthanides until the 1960s. It was generally assumed that complexes of the Ln^{3+} ions resembled those of the transition metals, though there was little hard evidence to support that view, in particular, the assumption that six-coordination would be the norm. It was known that ligand-field effects were weak in lanthanide chemistry, and so that, combined with the knowledge that lanthanide ions were substantially bigger than typical transition metals, it could have been predicted that coordination numbers greater than 6 would be the norm. Verification of this, however, had to wait for the renaissance

The Rare Earth Elements. Edited by David A. Atwood. © 2012 John Wiley & Sons, Ltd. ISBN 978-1-119-95097-4

of coordination chemistry and also for the rise in rapid crystal structure determination.

3 CHOICE OF DONOR ATOMS

The large, highly charged, Ln^{3+} ions are ''hard'' Lewis acids, and therefore favor ''hard'' donor atoms, binding to oxygen and nitrogen in preference to sulfur and phosphorus. Such character is largely determined by solvation effects so that an important factor is the high hydration energy of the Ln^{3+} ion, meaning that syntheses of complexes with mono- and bidentate ligands must often be carried out in weakly coordinating nonpolar solvents such as MeCN to minimize competition. Complexes with the more basic amine ligands such as ammonia or aliphatic amines are less well known, and tend to have been prepared by reaction in supercritical ammonia or by reactions under anhydrous conditions involving solvento complexes, rather than by direct reaction of a hydrated metal salt and a ligand in an organic solvent, to avoid precipitation of the lanthanide hydroxide in the presence of water. The high electronegativity of oxygen and the consequent polar nature of ligands such as phosphine oxides $R_3P^{\delta+} = O^{\delta-}$ is also a factor.

4 COORDINATION NUMBERS

Because of ligand-field factors, certain transition metal ions, notably Cr^{3+} and Co^{3+}, almost exclusively exhibit a coordination number of six in their complexes.[1–2] The kinetically inert nature of Cr^{III} and Co^{III} complexes, dramatically different from that of the extremely labile lanthanide solvento ions, facilitates the isolation of isomeric species and was crucial in enabling Alfred Werner to formulate the fundamental tenets of coordination chemistry. For simple lanthanide ion complexes, their lability and the lack of a marked sensitivity of their visually observed colors to the nature of the coordination sphere renders Wernerian procedures inapplicable, such that the establishment of high and variable coordination numbers as a characteristic of lanthanide ions has depended largely on modern spectroscopic and crystallographic measurements.

In delineating the factors determining these coordination characteristics, chemists have introduced the concepts of first-order and second-order steric effects.

First-order effects are those that arise from crowding involving the ligand donor atoms in the immediate vicinity of the metal ion, the primary coordination sphere. Interatomic repulsions involving the donor atoms make it impossible for more atoms to be ''in contact'' with the lanthanide ion. This is particularly applicable to ligands consisting of a single donor such as halide (or oxide) ions, or those of small, uncongested ions or molecules, such as H_2O, NCS^-, and OH^-.

Second-order effects apply to situations where there are bulky groups attached to the donor atom. The donor atom may be small (C, N, O) but it is the repulsions between the bulky substituent groups that determine how many ligands may pack round the lanthanide ion, not the repulsions between the donor atoms. Ligands of this type are exemplified by bulky amides, notably $N(SiMe_3)_2$, as well as the isoelectronic alkyl-$CH(SiMe_3)_2$ and bulky alkoxides and aryloxides. Such ligands are associated with compounds with unusually low coordination numbers.

So, first-order effects determine the coordination number in species such as $LnCl_6^{3-}$ and $[Ln(H_2O)_9]^{3+}$, whereas bulky ligands with high second-order steric effects lead to crowding and impose low coordination numbers in $[Ln\{(CH(SiMe_3)_2\}_3]$ and $[Ln\{(N(SiMe_3)_2\}_3]$.

4.1 Examples of Coordination Numbers

Despite the 1939 report of the crystal structure of $[Nd(H_2O)_9](BrO_3)_3$, which showed that a coordination number of nine was possible for Ln^{III}, it was generally believed right into the 1960s that yttrium and the lanthanides would be six coordinate in their complexes. A breakthrough came in the mid-1960s, with the determination of structures of compounds such as $[Eu(terpy)_3](ClO_4)_3$ and $[La(edta)(OH_2)_3]\cdot 5H_2O$ (both nine coordinate) and $[La(Hedta)(OH_2)_4]$ (10 coordinate). In fact, coordination numbers up to 12 can be obtained using ligands such as nitrate and 1,8-naphthyridine, in $[Pr(naph)_6](ClO_4)_3$ and salts of the $[Ln(NO_3)_6]^{3-}$ ion (Ln = La, Ce, Pr, Nd and the Ce^{IV} analog), where the small ''bite angle'' of the bidentate ligand is responsible. It was subsequently shown that use of bulky ligands (discussed earlier) made very low coordination numbers possible, as in three-coordinate $[Ln\{N(SiMe_3)_2\}_3]$ (Ln = Y; La–Lu except Pm) and four-coordinate $[Li(thf)_4]^+$ $[Lu(2,6\text{-}Me_2C_6H_3)_4]^-$. Eight and nine coordination are probably the most frequently encountered, although in broad terms the earlier (larger) Ln^{III} tend to be associated with higher coordination numbers than the heavier (see below).

Representative examples of each coordination number follow. Coordination numbers below six are so far found only in σ-bonded organometallics, amides, and the like, which employ bulky ligands. Note that most precise information on lanthanide coordination comes from crystallographic studies, so that it is necessary to state the caveat that what is best known concerns the solid state, even though much is also known of solution behavior.

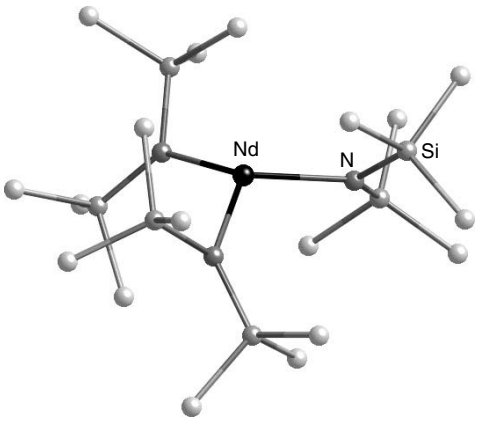
4.2 Coordination Number 2

The only two-coordinate compounds are the volatile two-coordinate bent Ln^{II} alkyls $[Ln(C(SiMe_3)_3)_2]$ (Ln = Yb, Eu). These contain just two Ln–C σ bonds, but are bent

(C–Yb–C 137°) because of additional agostic Yb···H–C interactions.

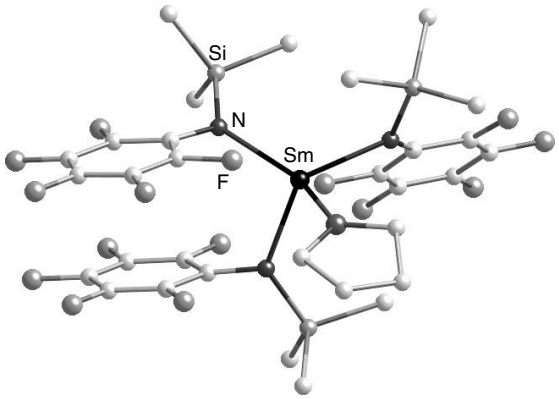
4.3 Coordination Number 3

This was first observed in the amides $Ln\{N(SiMe_3)_2\}_3$, (**1**; Ln = Y, all lanthanides). These are planar in the gas phase and in solution (they have zero dipole moment) but have pyramidal structures in the solid state, again probably caused by agostic interactions. The alkyls $Ln\{CH(SiMe_3)_2\}_3$ (e.g., Ln = Y, La, Pr, Nd, Sm, Lu) appear to be similar.



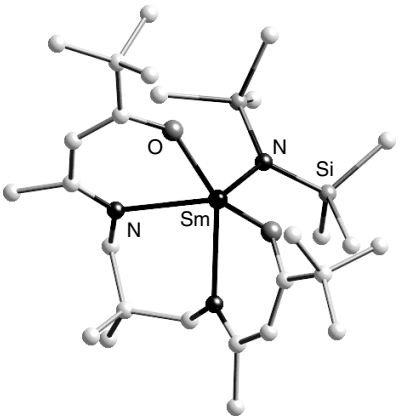
4.4 Coordination Number 4

Both organometallics $[Li(thf)_4]$ [Lu(2,6-dimethylphenyl)$_4$] and $[Li(thf)_4]$ $[Ln(CH_2SiMe_3)_4]$ (Ln = Y, Er, Tb, Yb), and the amides $Ln[(N(SiMe_3)_2]_3{\cdot}(Ph_3PO)$ and $[Li(thf)_4]$ $[Ln(NPh_2)_4]$ (Ln = Er, Yb) are examples of tetrahedral structures, as is the amide $[Sm\{(C_6F_5)(Me_3Si)N\}_3(thf)]$ (**2**).



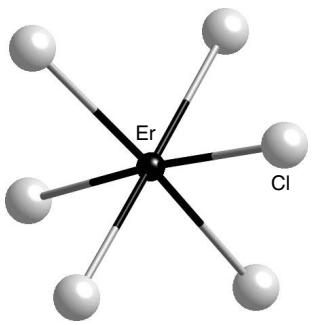
4.5 Coordination Number 5

The few cases of trigonal bipyramidal coordination are mainly represented by the adducts of the amides with slender nitriles, $Ln[(N(SiMe_3)_2]_3(NCMe)_2$, and by a few σ-bonded organometallics, e.g., $[ScPh_3(thf)_2]$ and $[Yb(CH_2^tBu)_3(thf)_2]$. A few complexes of bulky Schiff bases also exhibit this coordination number (**3**).



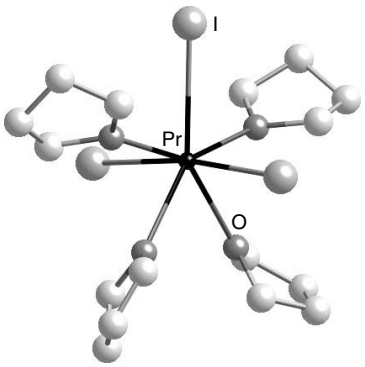
4.6 Coordination Number 6

For the transition metals, most M^{III} tris(β-diketonate) complexes have octahedral coordination, but for the lanthanides this is only realized for a few Ln(diketonate)$_3$ with very bulky ligands, e.g., $[Ln(^tBuCOCHCO^tBu)_3]$ (Ln = Tb–Lu). Other notable examples of octahedral coordination include the alkyls $[Li(L–L)_3]{\cdot}[Ln(CH_3)_6]$ (L–L = $MeOCH_2CH_2OMe$ or $Me_2NCH_2CH_2NMe_2$; Ln = La–Sm, Gd–Lu, Y). Salts $Cs_2LiLnCl_6$ (Ln = La–Lu) have the elpasolite structure with $[LnCl_6]^{3-}$ anions (**4**) on cubic sites; these have been widely used to study optical properties of Ln^{3+} ions. A few cases are known of salts with $[LnCl_7]^{4-}$ ions. Some thiocyanate complexes $(Bu_4N)_3$ $[M(NCS)_6]$ (M = Y, Pr–Yb) have octahedral coordination, but other counterions produce seven and eight coordination with anionic thiocyanate complexes. Similarly, while crystalline hydrated lanthanide ion perchlorates appear to contain octahedral $[Ln(OH_2)_6]^{3+}$, this is not the case for the analogous bromates, triflates, or iodides. A very few cases are known of nonoctahedral six coordination, with distortion to trigonal prismatic because of steric interactions between ligands in $[Ln(S_2P(cyclohexyl)_2)_3]$.



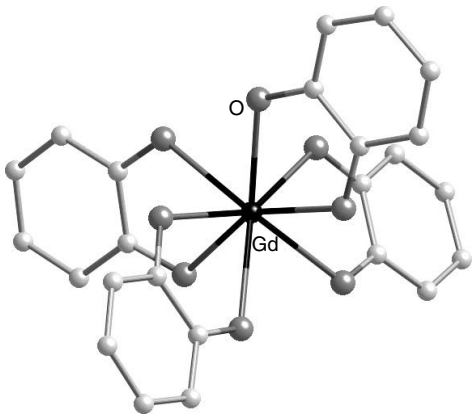
4.7 Coordination Number 7

Among simple complexes, the best examples are thf complexes of the type $Ln(thf)_4X_3$ (X = halogen (**5**), NCS) with pentagonal bipyramidal geometries, while many adducts of the β-diketonate complexes of the type $Ln(diketonate)_3 \cdot L$ (L = Lewis base, e.g., H_2O, py) also have seven–coordinate structures. Capped trigonal prismatic $[EuCl_7]^{4-}$ ions are found in Ba_2EuCl_7.



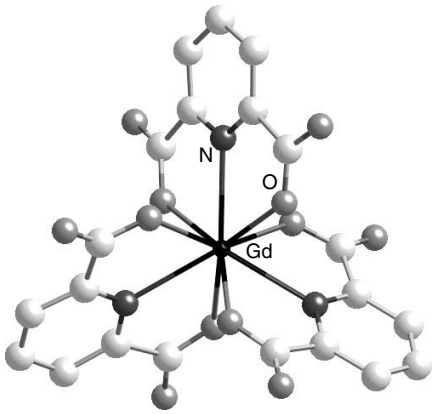
4.8 Coordination Number 8

Again, two geometries predominate here, dodecahedral or square antiprismatic, with the choice of geometry often dictated by minor factors, as with dodecahedral $(Ph_4As)[Ln(S_2PEt_2)_4]$, and square antiprismatic $(Ph_4P)[Pr(S_2PMe_2)_4]$. Dodecahedral coordination is also illustrated by the $[Gd(catecholate)_4]^{5-}$ ion (**6**).



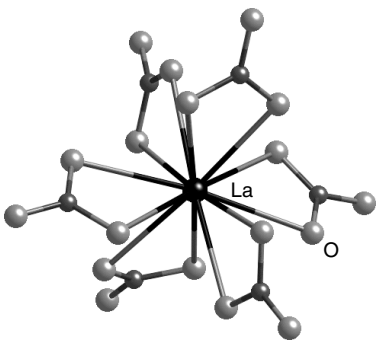
4.9 Coordination Number 9

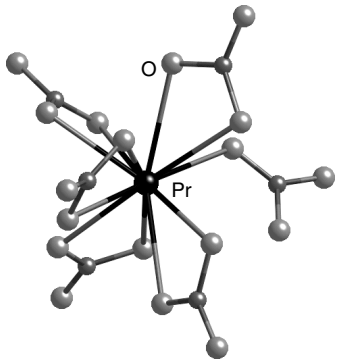
Several classic examples of tricapped trigonal prismatic geometry can be noted in the chloride $LnCl_3$ (Ln = La–Gd) and bromides $LnBr_3$ (Ln = La–Pr), as well as in the aqua ions $[Ln(H_2O)_9]^{3+}$ ions and the complexes $[Ln(terpy)_3]^{3+}$ (e.g., Ln = Eu) and $[Ln(dipic)_3]^{3-}$ (e.g., Ln = Gd (**7**)).



4.10 Coordination Numbers 10–12

Because of interligand repulsions, it is hard to get coordination numbers greater than nine with monodentate ligands. Interdonor atom repulsions (''first-order'' effects) can be minimized with donor atoms in the first short period, such as oxygen or nitrogen, and there are bidentate ligands such as nitrate or 2,2′-bipyridyl that do take up relatively little space in the coordination sphere—they are often referred to as having a small ''bite angle.'' Multidentate crown ether ligands also tend to be associated with high coordination numbers. Polyhedra in these high coordination numbers are often necessarily irregular, but when all the ligands are identical, near-icosahedral geometries occur for the 12-coordinate complexes. Examples of such high coordination numbers are, for 10 coordinate: $(Ph_4As)_2$ $[Eu(NO_3)_5]$, $Ln(bipy)_2(NO_3)_3$ (Ln = La–Lu, Y), $Ln(terpy)(NO_3)_3(H_2O)$ (Ln = Ce–Ho); 11 coordinate: $Eu(15\text{-crown-}5)(NO_3)_3$ (Ln = Nd–Lu); 12 coordinate: $Ln(18\text{-crown-}6)(NO_3)_3$ (Ln = La, Nd); $[Pr(naph)_6]$ $(ClO_4)_3$ and $[Ln(NO_3)_6]^{3-}$ ions (Ln = La (**8**), Ce, Pr, Nd) in crystalline salts. Counter-ions can be influential as 11-coordinate $[Pr(O_2NO)_5(ONO_2)]^{3-}$ ions can also be obtained (**9**).

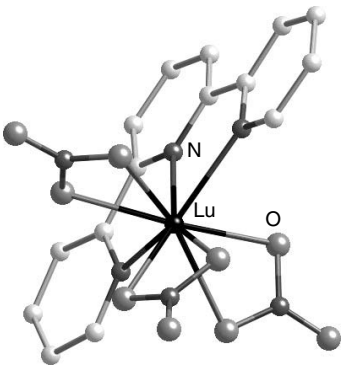




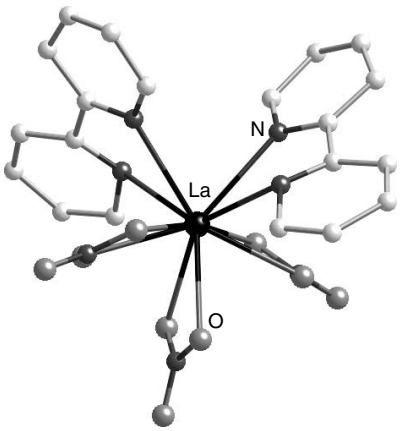
5 THE LANTHANIDE CONTRACTION AND COORDINATION NUMBERS

On crossing the lanthanide series from La to Lu, there is a 16% decrease in the ionic radius of the La^{3+} ion for a fixed coordination number. If coordination numbers were purely determined by the packing of spheres round a central ion, then a decrease in coordination number would be expected on crossing the series. This expectation is realized in the halides; thus for the fluorides, the coordination number (CN) decreases from 11 to 9; in both the chlorides and bromides, the CN decreases from 9 to 6; and in the iodides, the CN decreases from 8 to 6.

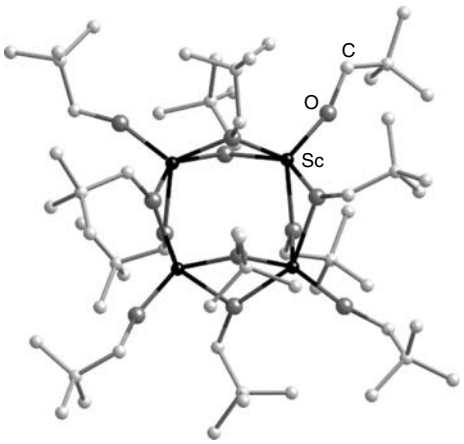
In those cases where it has been possible to make a study across the whole series for a family of complexes involving the same ligands, a similar situation often arises. Thus, for the complexes of the terdentate ligand 2,2′:6′,2″-terpyridyl, it is the heaviest and smallest lanthanide ions that form water-free nine-coordinate $[Ln(terpy)(NO_3)_3]$ (Ln = Ho–Lu (**10**)), the slightly larger lanthanides form 10-coordinate $[Ln(terpy)(NO_3)_3(H_2O)]$ (Ln = Ce–Dy) and only the largest, lanthanum, forms 11-coordinate $[La(terpy)(NO_3)_3(H_2O)_2]$.



There are, however, a few cases where the coordination number remains constant, possibly because the ligands ''mesh.'' Thus, using the bidentate ligands 2,2′-bipyridyl and 1,10-phenanthroline, the complexes $[Ln(bipy)_2(NO_3)_3]$ ((**11**), Ln = La) and $[Ln(phen)_2(NO_3)_3]$ (Ln = La–Lu, Y) are obtained in isomorphous and isostructural series. Both series have 10-coordinate lanthanides with all nitrates present as bidentate ligands. A few other cases are known. Thus, a family of isostructural eight-coordinate lanthanide complexes [Ln(TREN-1,2-HOIQO)] (Ln = La–Lu, except Pm), utilizing a hexadentate tripod ligand based on hydroxamic acid donors, has shown them to be isostructural.[3]



The same phenomenon appears to exist in the alkylamides $[Ln((N(SiMe_3)_2)_3]$ (Ln = La–Lu) and alkyls $[Ln((CH(SiMe_3)_2)_3]$ (Ln = Y, La–Lu), which are all believed to have three-coordinate trigonal pyramidal structures in the solid state. Here, however, the constant coordination number is probably due to the ''second-order effects'' of the bulky ligands'; this factor may also be the cause of isostructurality in the neopentoxides $Ln(ONp)_3$ (Ln = Sc (**12**), Y, La–Lu except Pm), where the tetrameric structure $[\{Ln(\mu\text{-}ONp)_2(ONp)\}_4]$ is maintained in toluene solution.[4]



6 THE NEED FOR X-RAY DIFFRACTION STUDIES

As already noted, for the lanthanides, there is no characteristic coordination number as there is for transition

metals. Furthermore, coordination numbers can generally not be deduced from the color of the compound, or even the absorption spectrum, as a majority of the Ln^{3+} ions are colorless to the eye and have very weak absorption spectra, which are scarcely influenced by their environment. Exceptions do arise in the case of Eu^{III}, for example, where the narrowness of the absorption lines in its visible absorption spectrum can allow detailed information on the coordination sphere to be extracted from high resolution measurements.[5] Nonetheless, X-ray diffraction studies are often the only way of determining which ligands form the coordination sphere of the metal.

Among many examples that could be given, two types of complex of the terdentate ligand 2,2′:6′,2″-terpyridyl may be cited. Reaction of lanthanide chlorides with terpy in ethanolic solution gives complexes such as Ln(terpy) $Cl_3 \cdot x H_2O$ (e.g., Ln = La–Nd, $x = 8$). They contain $[Ln(terpy)Cl(H_2O)_n]^{2+}$ ions (Ln = La–Nd, $n = 5$; Ln = Sm–Lu, $n = 4$), and there was no way of predicting this or indeed obtaining it from any spectroscopic measurement.[6] Reaction of hydrated lanthanide nitrates with terpy in ethanol affords $Ln(terpy)(NO_3)_3 \cdot C_2H_5OH$ (Ln = Dy–Lu, Y). These have nine-coordinate lanthanides, with two bidentate nitrates, one monodentate nitrate, and a coordinated ethanol. Again, neither the denticity of the nitrates nor the coordination of the ethanol molecule could easily have been foreseen.[7] In another example, X-ray diffraction revealed that the complex $Nd(NO_3)_3 \cdot 3$ bipy (bipy = 2, 2′-bipyridyl) had the structure $[Nd(bipy)_2(NO_3)_3] \cdot bipy$.

The counterion can also affect coordination numbers; for example, in the edta complexes $M[Ln(edta)(H_2O)_x]$, nine-coordinate $[Ho(edta)(H_2O)_3]^-$ ions are found in the crystal when M = K, while eight-coordinate $[Ho(edta)(H_2O)_2]^-$ ions are found when M = Cs. Similarly, a wide range of simple thiocyanate complexes have been isolated, again showing dependence upon the cation and solvent employed as well as the ionic radius of the metal. Examples are $(Bu_4N)_3[M(NCS)_6]$ (M = Y, Pr–Yb; octahedral); $(Et_4N)_4[M(NCS)_7] \cdot$benzene (M = La, Pr: capped trigonal prismatic) and $(Me_4N)_4[M(NCS)_7] \cdot$benzene (M = Dy, Er, Tb: pentagonal bipyramidal) and $(Me_4N)_5[M(NCS)_8] \cdot$benzene (M = La–Dy: intermediate between square antiprism and cubic).

Sometimes, small differences in stoichiometry that would not readily be detected by analysis are revealed by crystallography. For example, crystals of two lanthanum nitrate complexes of the terdentate 4-amino-bis(2,6-(2-pyridyl))-1,3,5-triazine, 10- and 11-coordinate $[La(abptz)(NO_3)_3(H_2O)_n]$ ($n = 1$, 2), can be isolated from the same reaction mixture, evidently because of similar solubilities. This subtle difference in stoichiometry leads to significant differences in the molecular geometry. Thus, the increase in coordination number of the lanthanum from 10 to 11 is accompanied by a sharp increase in La–O (water) distance from 2.483 (5) Å to 2.589 (4) and 2.610 (4) Å.[8]

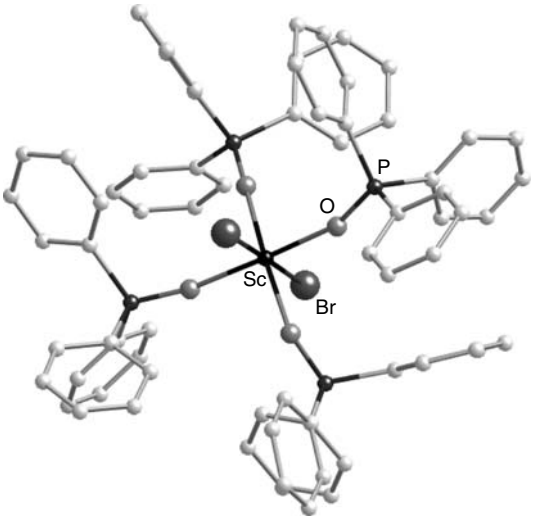
7 COMPLEXES WITH SIMPLE MONODENTATE O-DONOR LIGANDS

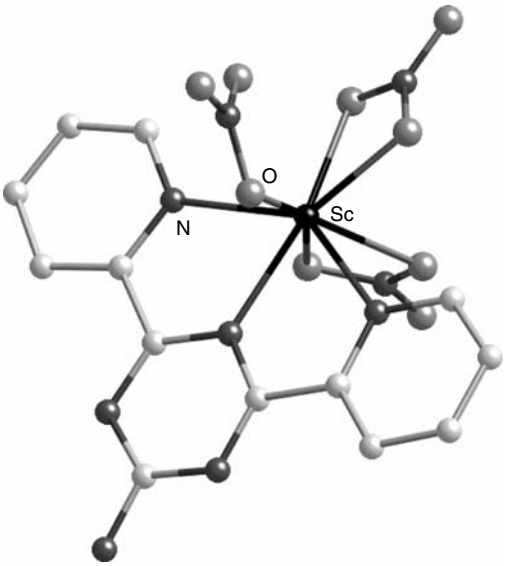
7.1 Simple Scandium Complexes

It might be expected that, since the Sc^{3+} ion has a considerably greater crystal radius than the corresponding tripositive ions of the 3d metals (compare Sc^{3+} at 0.885 Å with Ti^{3+}, Cr^{3+}, and Fe^{3+} at 0.810, 0.755, and 0.785 Å, respectively), coordination numbers greater than six might be common in scandium complexes. With the exception of the aqua ion (and nitrate complexes), this has not been realized, but studies of scandium chemistry are still relatively rare (partly on account of cost). Aqua complexes and simple hydrates have been discussed in ***Solvento Complexes of the Lanthanide Ions***.

The widest range of complexes to have been studied is with monodentate O-donor ligands (e.g., dmso, hmpa, R_3PO, pyO). Complexes isolated typically fall into two types: ScL_3X_3 (where X is a coordinating anion such as chloride) and ScL_6X_3 (with noncoordinating anions such as perchlorate). In addition, nitrate complexes exhibit higher coordination numbers because of the small ''bite angle'' of bidentate nitrate. Even with the small O-donor ligand dimethylsulfoxide, scandium is six coordinate in $[Sc(dmso)_6](ClO_4)_3$ and in $[Sc(dmso)_6]I_3$; X-ray diffraction studies on crystals and extended X-ray absorption fine structure (EXAFS) studies on solutions indicate similar Sc–O distances (2.069(3) Å and 2.09(1) Å, respectively).[9,10]

It is possible for six of the sterically relatively undemanding phosphine and arsine oxide ligands Me_3PO and Me_3AsO to coordinate to scandium, whereas for Ph_3PO the maximum is four. Of the many compounds reported: $[ScCl(Me_3PO)_5]$ Cl_2; $[Sc(Me_3PO)_6]$ X_3 (X = Br, I); $[ScX_2(Ph_3PO)_4]$ X (X = Cl, Br, I); $[ScX_2(Ph_3AsO)_4]$ X; $[Sc(Me_3AsO)_6]$ X_3 (X = Cl, Br, I); $[ScCl_3(Ph_2MePO)_3]$; and $[ScBr_2(Ph_2MePO)_4]$ Br (**13**), structures have been determined for $[ScBr_2(Ph_3PO)_4]$ Br, $[ScCl_2(Ph_3AsO)_4]$ Cl, and $[Sc(Me_3AsO)_6]$ Br_3. Me_3PO and Me_3AsO are both likewise capable of completely displacing nitrate from the coordination sphere, in the octahedral $[Sc(Me_3PO)_6](NO_3)_3$ and $[Sc(Me_3AsO)_6](NO_3)_3$. This is not found for the lanthanides. Nitrate coordination is found in the eight-coordinate $[Sc(abptz)(NO_3)_3]$ (**14**; one nitrate monodentate), $[Sc(NO_3)_3(Ph_3PO)_2]$ and $[Sc(NO_3)_2(Ph_2MePO)_4]$ (NO_3) as well as in the seven-coordinate $[Sc(NO_3)_2(Ph_3AsO)_3]$ NO_3. The triflate complex $Sc(CF_3SO_3)_3(Ph_3PO)_4$ has two monodentate triflates, and is *trans*-$[Sc(CF_3SO_3)_2(Ph_3PO)_4]$ CF_3SO_3.[11,12]





7.2 Complexes of Yttrium and the Lanthanides with Simple Ligands

The Y^{3+} ion is comparable in size with heavier lanthanides, and its coordination chemistry therefore resembles them. Aqua complexes and simple hydrates have been discussed in ***Solvento Complexes of the Lanthanide Ions***. Fewer solution studies of solvated species with other donors have been made for these metals, but an examination of the Y^{3+} ion in O-donor solvents using X-ray absorption fine structure (XAFS) and large angle X-ray scattering shows that the metal is eight coordinate in dimethylformamide and dimethylsulfoxide, but seven coordinate in *N*, *N*′-dimethylpropyleneurea (dmpu), as are other lanthanides. It should be noted that in the solid state, six-coordinate $[Ln(dmpu)_6]I_3$ (Ln = La, Pr, Nd, Gd, Tb, Er, Yb, Lu) are isolated.[13,14]

In the solid state, lanthanides form $[Ln(dmso)_8]I_3$ with noncoordinating ions (X = I, CF_3SO_3)[15], but nitrate can coordinate. The earlier metals (La–Sm) form 10-coordinate $[Ln(dmso)_4(NO_3)_3]$ complexes, while smaller metal ions (Eu–Lu, Y) form nine-coordinate $[Ln(dmso)_3(NO_3)_3]$ complexes, in both cases with all nitrates bidentate.[16]

The best known complexes are those of ligands such as phosphine and arsine oxides, where the high electronegativity of oxygen and consequent polarity of the molecule ($R_3P^{\delta+} = O^{\delta-}$) make them good donors.[17] The most systematic results are with yttrium halides, where complexes isolated include $[Y(Me_3PO)_6]X_3$ (X = Cl, Br, I); $[YX_2(Ph_3PO)_4]Z$ (X = Cl, Br, or I; Z = X or PF_6); $[YX_3(Ph_2MePO)_3]$; and $[Y(Me_3AsO)_6]Cl_3$. Although the bulk of the ligand affects the number of phosphine oxides coordinating it is not the only one responsible for the stoichiometry of the complex isolated. Ph_2MePO is less bulky than Ph_3PO, and yet only three of these molecules coordinate in the presence of halide, but in the presence of NH_4PF_6, $[YCl_2(Ph_2MePO)_4]PF_6$ was isolated (and in other circumstances $[YCl(Ph_3PO)_5](SbCl_6)_2$ can be made). Solubility is important too. Less systematic study has been made with lanthanide halides, but compounds reported and characterized in the solid state include *mer*-$[LnCl_3(Ph_3PO)_3]\cdot 0.5Me_2CO$ (Ln = La, Ce); *trans*-$[LnCl_2(Ph_3PO)_4]Cl\cdot x$EtOH (Ln = Tb, Yb); *trans*-$[LnBr_2(Ph_3PO)_4]Br$ (Ln = Pr, Nd, Gd, Tb, Er, Yb, Lu)[18]; and *trans*-$[LnI_2(Ph_3PO)_4]I$, Ln = La, Ce, Nd).

A good deal more is known about nitrate complexes; ^{31}P NMR studies on solutions show that several species often coexist, and complexes with different stoichiometries can be isolated by changing the reaction conditions. Thus, $[Y(NO_3)_3(Ph_3PO)_2(EtOH)]$; $[Y(NO_3)_3(Ph_3PO)_3]$; and $[Y(NO_3)_2(Ph_3PO)_4]NO_3$ can all be isolated from the reaction of yttrium nitrate with Ph_3PO by changing solvent and temperature. $[Y(NO_3)_3(R_3PO)_3]$ is the most common stoichiometry, but with the less bulky Ph_2MePO, 10-coordinate $[La(\eta^2\text{-}NO_3)_3(Ph_2MePO)_4]$ has all nitrates bidentate. With the bulky tricyclohexylphosphine oxide, periodic trends are clearly illustrated in $[Ln(NO_3)_3(Cy_3PO)_3]$. For La–Eu, there are three bidentate nitrates; in the Tm and Yb complexes, one nitrate is monodentate. The Er complex displays an interesting example of isomerism, as one molecule present in the crystal has three bidentate nitrates and another has two bidentate and one monodentate nitrate.[19] Similarly, in the complexes of Ph_3PO with the lanthanide triflates, they all have the structure $[Ln(OTf)_2(Ph_3PO)_4]OTf$. While the Sc, Er, and Lu complexes all have two monodentate triflates completing octahedral six coordination, the complexes of the larger La and Nd have seven coordination with one triflate being bidentate.

In the case of hexamethylphosphoramide ($(Me_2N)_3PO$), a maximum of six of these ligands coordinate to a lanthanide, as in $[Ln(hmpa)_6]X_3$ (Ln = La–Lu; X = ClO_4, BrO_4, ReO_4). The most interesting hmpa complexes are the chlorides, where both *fac*- and *mer*-$[LnCl_3(hmpa)_3]$ can be isolated; they isomerize in solution by an associative mechanism.[20] $[La(hmpa)_3(NO_3)_3]$ is nine coordinate and

$[Ln(hmpa)_4(NCS)_3]$ is seven coordinate, while $La(hmpa)_4Br_3$ is six-coordinate $[LaBr_2(hmpa)_4]Br$.[21]

Tetrahydrofuran complexes of the lanthanide chlorides have been intensively studied for two reasons. They are essentially soluble forms of the anhydrous chlorides, and as such are very useful starting materials in the synthesis of compounds such as alkoxides, aryloxides, alkylamides, and organometallic compounds in general. Second, six different types of structure have been reported for these compounds, with formulae $LnCl_3(thf)_x$ (e.g., $x = 2$, 2.5, 3, 3.5, 4) representing a decrease in coordination number across the lanthanide series from 8 (La) to 6 (Lu). $[LaCl_3(thf)_2]$ is a single-stranded polymer $\cdots La(\mu\text{-}Cl)_3(thf)_2La(\mu\text{-}Cl)_3(thf)_2La\cdots$ with eight-coordinate La, while $[LnCl_3(thf)_2]$ (Ce–Nd) have seven-coordinate metals in $\ldots LaCl(thf)_2(\mu\text{-}Cl)_2LaCl(thf)_2(\mu\text{-}Cl)_2\cdots$chains. Nd–Gd form 4 : 1 complexes, monomeric $[LnCl_3(thf)_4]$; $[LnCl_3(thf)_{3.5}]$, found for Gd–Tm, are ''self-ionized'' $[LnCl_2(thf)_5]^+$ $[LnCl_4(thf)_2]^-$, with seven and six coordination. $[YbCl_3(thf)_2]$ is a six-coordinate dimer, $[Cl_2(thf)_2Yb(\mu\text{-}Cl)_2Yb(thf)_2Cl_2]$, and *mer*-$[LnCl_3(thf)_3]$ (Ln = Yb, Lu) resemble the Sc analog.[22] The bromide complexes $[LnBr_3(thf)_4]$ (Ln = La,[23] Pr,[24] Nd,[25] Sm[24]), $[EuBr_3(thf)_{3.5}]$,[24] and $[YbBr_3(thf)_3]$[23], as well as the iodide complexes $[PrI_3(thf)_4]$ (**5**), $[LnI_3(thf)_{3.5}]$ (Ln = Nd, Gd, Y)[26] and $[YbI_3(thf)_3]$[27] have structures analogous to chlorides of corresponding formulae. In contrast, only one stoichiometry is observed for the thiocyanates, $[Ln(NCS)_3(thf)_4]$, where the Yb complex is a pentagonal bipyramidal monomer. With larger metals, however, these units associate via Ln···SNC–Ln bridges to produce dimers with eight-coordinate square antiprismatic coordination.[28]

8 CONCLUSIONS

Our knowledge of simple lanthanide complexes has blossomed over the past half-century, but there are still many opportunities for its development. More still needs to be known about scandium chemistry; it is still too often regarded as a 3d transition metal, even though it is now clear that it is quite unlike 3+ transition metal species. For reasons of size, it would be expected that coordination numbers greater than six should occur in simple scandium complexes, but at present this is confined to the aqua ion. Now that crystal structure determination has become a routine and very rapid technique (far faster than ''sporting methods'') it is to be hoped that many more studies will be made where a whole family of complexes right across the lanthanide series is studied. This will give an idea of the host of often subtle factors at work in determining coordination number, deciding the point at which a discontinuity may occur. Enough studies have now been made to show that the coordination number can depend on factors such as solvent, solubility, and counter ion, as well as the coordination number not being the same in solution as in the solid state. Assumptions were made over half a century ago by assuming that the lanthanides would resemble the 3d transition metals; different assumptions remain and have to be challenged. There is of course a vast and expanding coordination chemistry of the lanthanides and scandium with highly sophisticated multidentate ligands that depends for its full interpretation upon the detailed understanding of simple systems as presently surveyed.

9 RELATED ARTICLES

Solvento Complexes of the Lanthanide Ions.

10 ABBREVIATIONS AND ACRONYMS

abptz = 4-amino-bis(2,6-(2-pyridyl))-1,3,5-triazine; bipy = 2,2′-bipyridyl; dipic = 2,6-pyridinedicarboxylate; dmpu = *N*, *N*′-dimethylpropyleneurea; dmf = dimethylformamide; dmso = dimethylsulfoxide; edta = ethylenediaminetetraacetic acid; hmpa = hexamethylphosphoramide; naph = 1,8-naphthyridine; phen = 1,10-phenanthroline; terpy = 2, 2′:6′,2″-terpyridyl; pyO = pyridine *N*-oxide; thf = tetrahydrofuran.

11 FURTHER READING

S. A. Cotton, in J. A. McCleverty, and T. J. Meyer, eds., 'Comprehensive Coordination Chemistry II', Elsevier, Amsterdam, 2004, Vol. 3, p. 93.

F. A. Hart in G. Wilkinson, eds., 'Comprehensive Coordination Chemistry', Pergamon Press, Oxford, 1987, Vol. 3, p. 1059.

S. Mishra, *Coord. Chem. Rev.*, 2008, **252**, 1996 (lanthanide complexes with O- and N-donors).

12 REFERENCES

1. S. A. Cotton, *C. R. Chim.*, 2005, **8**, 129.
2. S. A. Cotton, 'Lanthanide and Actinide Chemistry', Wiley-VCH: Chichester, 2006.
3. M. Seitz, A. G. Oliver, and K. N. Raymond, *J. Am. Chem. Soc.*, 2007, **129**, 11153.
4. T. J. Boyle, L. A. M. Ottley, S. D. Daniel-Taylor, L. J. Tribby, S. D. Bunge, A. L. Costello, T. M. Alam, J. C. Gordon, and T. M. McCleskey, *Inorg. Chem.*, 2007, **46**, 3705.

5. S. V. Eliseeva and J. C. G. Bünzli, *Chem. Soc. Rev.*, 2010, **39**, 189.
6. C. J. Kepert, W. M. Lu, B. W. Skelton, and A. H. White, *Aust. J. Chem.*, 1994, **47**, 365.
7. B. Ahrens, S. A. Cotton, N. Feeder, O. E. Noy, P. R. Raithby, and S. J. Teat, *J. Chem. Soc., Dalton Trans.*, 2002, 2027.
8. M. G. B. Drew, M. J. Hudson, P. B. Iveson, C. Madic, and M. L. Russell, *J. Chem. Soc., Dalton Trans.*, 2000, 2711.
9. E. J. Chan, B. G. Cox, J. M. Harrowfield, M. I. Ogden, B. W. Skelton, and A. H. White, *Inorg. Chim. Acta*, 2004, **357**, 2365.
10. M. Y. Skripkin, P. Lindqvist-Reis, A. Abbasi, J. Mink, I. Persson, and M. Sandström, *Dalton Trans.*, 2004, 4038.
11. N. J. Hill, W. Levason, M. C. Popham, G. Reid, and M. Webster, *Polyhedron*, 2002, **21**, 1579.
12. J. Fawcett, A. W. G. Platt, and D. R. Russell, *Polyhedron*, 2002, **21**, 287.
13. P. Lindqvist-Reis, J. Näslund, I. Persson, and M. Sandström, *Dalton Trans.*, 2000, 2703.
14. D. Lundberg, I. Persson, L. Eriksson, P. D'Angelo, and S. De Panfilis, *Inorg. Chem.*, 2010, **49**, 4420.
15. I. Persson, E. D. Risberg, P. D'Angelo, S. De Panfilis, M. Sandström, and A. Abbasi, *Inorg. Chem.*, 2007, **46**, 7742.
16. L. I. Semenova, B. W. Skelton, and A. H. White, *Aust. J. Chem.*, 1996, **49**, 997.
17. M. J. Glazier, W. Levason, M. L. Matthews, P. L. Thornton, and M. Webster, *Inorg. Chim. Acta*, 2004, **357**, 1083.
18. A. Bowden, A. W. G. Platt, K. Singh, and R. Townsend, *Inorg. Chim. Acta*, 2010, **363**, 243.
19. A. P. Hunter, A. M. J. Lees, and A. W. G. Platt, *Polyhedron*, 2007, **26**, 4865.
20. S. Petricek, A. Demsar, L. Golic, and J. Kosmrlj, *Polyhedron*, 2000, **19**, 199.
21. S. Petrièek, *Z. Anorg. Allg. Chem.*, 2005, **631**, 1947 and references therein.
22. G. B. Deacon, T. Feng, P. C. Junk, B. W. Skelton, and A. H. White, *Aust. J. Chem.*, 1998, **51**, 75.
23. G. B. Deacon, T. Feng, P. C. Junk, G. Meyer, N. M. Scott, B. W. Skelton, and A. H. White, *Aust. J. Chem.*, 2000, **53**, 851.
24. S. Petricek, *Polyhedron*, 2004, **23**, 2293.
25. M. Gallazzi, F. Bianchi, L. Depero, and M. Zocchi, *Polymer*, 1988, **29**, 1516.
26. K. Izod, S. T. Liddle, and W. Clegg, *Inorg. Chem.*, 2004, **43**, 214.
27. T. J. Emge, A. Kornienko, and J. G. Brennan, *Acta Crystallogr. Sect. C*, 2009, **C65**, m422.
28. J. M. Bakker, G. B. Deacon, C. M. Forsyth, P. C. Junk and M. Wiecko, *Eur. J. Inorg. Chem.*, 2010, 2813 and references therein.

Organometallic Chemistry Fundamental Properties

Stephen T. Liddle

University of Nottingham, Nottingham, UK

1	Summary	83
2	Introduction	83
3	Bonding	84
4	Thermodynamic and Kinetic Considerations	88
5	Solvation, Salt Occlusion, and Aggregation	89
6	Stability	90
7	Methods of Preparation and Principal Reaction Types	95
8	Conclusions	100
9	Related Articles	100
10	Glossary	100
11	Acknowledgments	101
12	Abbreviations and Acronyms	101
13	References	101

1 SUMMARY

This chapter describes the fundamental properties of organometallic rare earth chemistry. The history and importance of the field are described from its tentative inception in 1902 to its firm establishment in 1954 and continuance to the present day. The bonding in this area is outlined with reference to (i) the covalency observed in zero-valent compounds; (ii) the highly ionic bonding in the more common rare earth(II) and (III) complexes; (iii) the general dearth of π-acid derivatives such as carbonyls and olefins and the known rare earth carbonyl chemistry in matrix isolation experiments; (iv) the general paucity of rare earth–ligand multiple bond linkages and advances made in that area. The basic physicochemical properties of the area are discussed in terms of (i) thermodynamic and kinetic considerations which show that rare earth organometallic linkages are not inherently weak but the ionic bonding renders them labile; (ii) salvation at vacant coordination sites by ethers; (iii) salt occlusion of lithium salts; (iv) aggregation as a result of the electron-deficient nature of the rare earths. The stability of organometallic rare earth complexes is detailed in terms of (i) handling and utilizing inert atmosphere techniques; (ii) elimination reactions and design features of commonly employed hydrocarbyl ligands; (iii) saturation of the coordination sphere through ligand design; (iv) the use of donor-functionalized ligands. Methods of preparation and reaction types are surveyed including (i) salt elimination; (ii) metathesis; (iii) oxidation and transmetallation; (iv) acid–base chemistry; (v) metal vapor synthesis; (vi) donor cleavage and adduct formation; (vii) σ-bond metathesis; (viii) classical reactivity patterns including the lack of oxidative addition and reductive elimination chemistry; (ix) one-electron redox chemistry.

2 INTRODUCTION

The first hint of organometallic rare earth (RE) chemistry to appear in the literature was the attempted synthesis of trimethyl cerium which appeared as a footnote in a paper in 1902 concerned with the reactivity of metallic cerium and lanthanum toward hydrogen and ethylene.[1] Following subsequent attempts reported in 1935 to prepare RE alkyls through the exposure of a lanthanum mirror to methyl radicals,[2] triethyl scandium and yttrium were claimed in 1938.[3] However, this was before the advent of the seminal

The Rare Earth Elements. Edited by David A. Atwood. © 2012 John Wiley & Sons, Ltd. ISBN 978-1-119-95097-4

molecule ferrocene and the establishment and understanding of organometallic chemistry as it is now known. Owing to the low kinetic stability of triethyl scandium and yttrium and the limited characterization techniques and synthetic methods at that time, such compounds remained curiosities.

The field of organometallic RE chemistry became firmly established in 1954 when Wilkinson and Birmingham reported the synthesis of π-bonded *tris*(cyclopentadienyl) RE complexes for the first time.[4] Generally speaking, cyclopentadienyl ligands can be regarded as ''spectator'' ancillary ligands that stabilize and solubilize RE centers but which do not themselves become directly involved in subsequent reactivity. The report of *tris*(cyclopentadienyl) RE complexes extended a broad drive to investigate the properties of all metal cyclopentadienyl complexes in an era when organometallic chemistry itself was still being established. Therefore, the importance of the *tris*(cyclopentadienyl) RE complexes was their synthesis and existence, rather than their reactivity.

In 1968, the first σ-bonded organometallic RE complex $[Sc(C_6H_5)_3]$ was reported by Hart and Saran.[5] However, organometallic RE chemistry developed slowly, mainly because of the limitations of synthetic and analytical techniques. However, in the late 1970s and early 1980s, modern preparative methods and characterization techniques began to become widely available which spurred renewed interest in the area. In particular, advances in single-crystal X-ray crystallography made it possible to structurally authenticate these highly air- and moisture-sensitive complexes in order to fully understand their structures. Organometallic RE chemistry gained real momentum in the 1980s which has been maintained to this day.[6,7] For a number of years, cyclopentadienyl complexes dominated the literature.[8–12] However, by searching for new applications and reactivity patterns, researchers have in recent years focused more on utilizing ''noncyclopentadienyl'' ligand environments.[13–35] Thus, in this so-called post-metallocene era, other organometallic RE linkages such as alkyls, aryls, arenes, heteroallyls, and carbenes have come to the fore.

The area has flourished in part not only from a desire to understand the bonding of organometallic RE complexes and delineate structure–reactivity relationships but also due to the numerous applications of such compounds which are academically and technologically important. Such complexes find utility in organic synthesis through redox and σ-bond metathesis chemistries which can be conducted enantioselectively with the appropriate choice and combination of ancillary ligands. Furthermore, many organometallic RE complexes are highly active in catalysis/polymerization chemistry and are very attractive because they do not require expensive activating cocatalysts as group 4 congeners require.[36–40] Lastly, organometallic RE complexes find use as metal organic chemical vapor deposition (MOCVD) precursors in the synthesis of semiconductors and superconductors, and as dopants for opto-electronic materials.[41,42] This chapter details a general overview of the fundamental properties of organometallic RE chemistry. Selected examples of complexes are given to highlight pertinent points—the reader is directed to chapters ***Trivalent Chemistry: CyclopentadienylAlkyl***, ***Aryls***, ***Tetravalent Chemistry: Organometallic***, ***Organic Synthesis***, and ***Homogeneous Catalysis*** and a series of excellent reviews elsewhere for more detailed and comprehensive discussions of the organometallic chemistry of the REs.[6–42]

3 BONDING

3.1 General Considerations

The bonding of organometallic RE complexes is classified as predominantly ionic in character. This is a result of the valence 4f orbitals being ''core-like'' in RE(II) and (III) complexes due to poor radial extension which results from the greater effective nuclear charge and poor shielding of the 4f orbitals following oxidation from the zero-valent metal state. Thus, the highly angular 4f orbitals show little or no appreciable overlap with ligand orbitals. Additionally, the 5d orbitals are vacant and can generally be considered to be too high in energy to interact with ligand-based orbitals in di- and trivalent RE complexes. The bonding picture is uniquely different in zero-valent RE complexes and this is discussed in Section 3.2.3. The generally ionic nature of organometallic RE bonding manifests itself in

- high reactivities which make organometallic RE complexes attractive candidates for applications in catalysis;
- labile ligands giving facile ligand scrambling for sterically unencumbered systems;
- irregular coordination geometries through little orbital control of geometry;
- a general paucity of bonding to neutral π-acid ligands such as carbon monoxide (CO), olefins, and arenes;
- a general paucity of RE–ligand multiple bond linkages.

For organometallic transition metal chemistry, the 18-electron rule is well established; no such rule exists for the REs since electrostatics dominate the bonding picture and thus the steric demands of ligands are of paramount importance. The REs are large metal centers with ionic radii in the range 1.27–0.75 Å and thus the use of sterically demanding ligands is necessary to limit coordination numbers, solubilize the RE centers, and to retard the inherent sensitivity of these metals toward oxygen and moisture. The RE ions are hard, electropositive elements, and hard soft acid base (HSAB) considerations suggest a preference for bonding of RE centers to oxo and halide ligands which renders organometallic RE complexes very reactive. Such complexes are frequently pyrophoric and react with oxygen or moisture to rapidly form oxides. The absence of covalency in di- and

trivalent RE organometallic bonding and a preference for bonding to halides is underscored by the reactivity of the *tris*(cyclopentadienyl) RE complexes with iron(II) chloride to give covalent ferrocene and ionic RE trichlorides. Studies of trivalent RE chemistry dominate the literature, and only a small number of cerium(IV) organometallic derivatives are known[43] due to the inherently reducing nature of hydrocarbyl ligands, but significant progress has been made in divalent RE chemistry in recent years.[44–47]

3.2 The General Paucity of Neutral π-Acid Derivatives

3.2.1 Neutral Carbonyl Derivatives

The paucity of isolable RE carbonyl complexes, perhaps more than any other aspect of organometallic RE chemistry, underscores the highly ionic nature of the bonding in this area. The standard bonding picture for a transition metal carbonyl bonding interaction, neglecting the possible but less significant π-donation from carbonyl to metal, is illustrated in Figure 1. From this synergic bonding scheme, it is evident that a metal center with accessible valence electrons for π-backbonding is required and that the metal be preferentially in a low oxidation state to maximize orbital overlap. Considering the ionic nature of RE bonding and the chemical inaccessibility of the 4f electrons, it is clear that synergic bonding of carbon monoxide to REs is not realistic under standard conditions. Indeed, the paucity of isolable molecular RE carbonyls contrasts even to the actinides where molecular uranium carbonyls, $[L_3UCO]$ (L = cyclopentadienyl ligand), have been isolated.[48–50]

However, while RE carbonyl complexes are not ''bottleable,'' they have been detected under matrix isolation conditions in frozen argon matrixes or in CO atmosphere high-pressure studies.[51] Binary RE carbonyls, $[M(CO)_n]$ ($n = 1–6$), have been observed with some evidence for the formation of $M(CO)_n$ ($n = 7$ or 8) species. These binary RE carbonyl adducts typically exhibit a single carbonyl stretch which is $\sim$145–195 cm^{-1} lower than the stretching frequency of 2134 cm^{-1} for free CO. Backbonding could be assumed to operate, which is reasonable for RE metals in a formal zero-oxidation state where valence orbitals are more chemically accessible. However, it has been noted that the infrared (IR) spectra of all binary RE carbonyls across the RE series

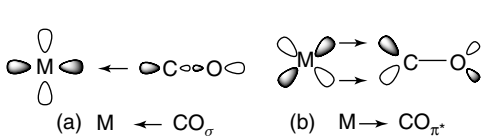


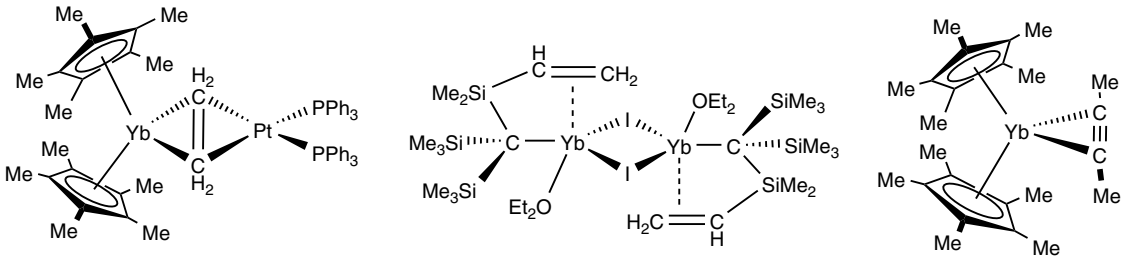
Figure 1 Bonding scheme for transition metal carbonyl bonding. (a) σ-donation from carbon lone pair to vacant metal orbital. (b) π-backbonding from filled metal orbital to vacant π^* orbital of CO

are remarkably similar even though the number of 4f electrons varies, which implies that the 4f orbitals/electrons do not significantly participate in the bonding. In contrast, CO adducts of RE trifluorides exhibit carbonyl stretches that are higher than free carbon monoxide. This may be rationalized on the basis that for an RE(II) or (III) centers, the 4f electrons will be core-like and unavailable for backbonding. When CO is placed in an electrostatic field, with the carbon atom directed toward a positive charge, then coupling of the CO oscillator to this field will result in the CO stretching frequency increasing, i.e., CO is acting purely as a σ-donor ligand. Divalent RE carbonyl complexes have been investigated and whereas the CO adduct of $[Eu(C_5H_5)_2]$ exhibits a carbonyl stretching band at 2150 cm^{-1}, the analogous ytterbium complex $[Yb(C_5H_5)_2]$ shows a carbonyl stretching band at 2114 cm^{-1}.[52] The former observation with europium may be explained as described above, but for the latter result, computational work suggests that in fact an O-bound CO adduct, not a C-bound CO adduct, is formed.[53] Compared to molecular transition metal carbonyl complexes which may routinely be isolated, RE carbonyl bonding is clearly very weak, which is supported by experimentally determined M–CO bond enthalpies of only $\sim$20 kJ mol^{-1} and the fact the $[M(CO)_n]$ compounds decompose above 40 K.[51]

3.2.2 Neutral Olefin and Alkyne Derivatives

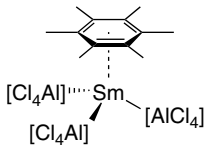
Neutral olefin–RE complexes are still rare, which is consistent with the ionic nature of the bonding which precludes the standard synergic Dewar–Chatt–Duncanson bonding model of olefins with electron-rich transition metals. The first reported example was $[(C_5Me_5)_2Yb(\mu\text{-}C_2H_4)Pt(PPh_3)_2]$ (**1**, Figure 2).[54] The $Pt(PPh_3)_2$ fragment is a good π-donor which renders the ethylene electron rich and thus more π-basic. This complex is regarded as having minimal Yb-ethylene π-backbonding and this interaction is thus best described as a donor–acceptor interaction. One notable example of a RE–alkene interaction was reported in the dimeric complex $[\{(Me_3Si)_2C(SiMe_2CH{=}CH_2)Yb(OEt_2)(\mu\text{-}I)\}_2]$ (**2**) where the pendant olefin datively coordinates to the ytterbium center.[55]

A similar strategy to that employed for (**1**) afforded the first example of an η^2-alkyne RE derivative $[(C_5Me_5)_2Yb(\eta^2\text{-}MeC{\equiv}CMe)]$ (**3**)[56] (Figure 2) utilizing the π-basic alkyne MeC≡CMe. Nuclear magnetic resonance (NMR) and IR spectroscopic analysis of the acetylene fragment in (**3**) showed little perturbation of the MeC≡CMe on coordination to ytterbium. Since acetylenes bind to transition metals in a similar way to olefins, the essentially negligible change of the MeC≡CMe ligand upon coordination suggests that it is behaving as a Lewis base donor with little or no π-backbonding.



(**1**) (**2**) (**3**)

Figure 2 Neutral olefin and alkyne rare earth complexes



(**4**)

Figure 3 A samarium neutral arene complex

3.2.3 Neutral Arene Derivatives

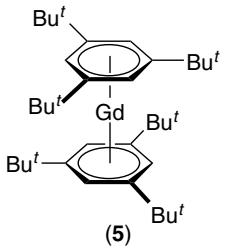
Neutral arene derivatives of the REs such as [Sm(η^6-C_6Me_6)($AlCl_4$)$_3$] (**4**, Figure 3)[57] are known but are not common. This is a direct consequence of the ionic bonding giving negligible orbital overlap between the arene π- and RE 4f-orbitals. Electrostatics dominate the bonding, and to impart the necessary stability to conveniently prepare and isolate neutral arene RE complexes, it is usual to employ the very electron-rich Lewis base arene hexamethylbenzene and generate a highly Lewis acidic and electron-deficient RE center by utilizing aluminate groups.

3.2.4 Neutral Bis(Arene) Derivatives of Zero-Valent Rare Earths

Although the bonding in di- and trivalent RE organometallic complexes is predominantly ionic, the bonding picture is dramatically changed when zero-valent RE*bis*(arene) complexes are considered.[58] The first structurally characterized example was the *bis*(1,3,5-*tert*-butylbenzene) gadolinium complex (**5**)[59] (Figure 4), which revealed a staggered arrangement of the two arene rings and a gadolinium center kinetically shielded by the close approach of 12 *tert*-butyl methyl groups. A standard bonding model for *bis*(arene) metal complexes principally invokes a_{1g} (s-arene), a_{2u} (p_z-arene), e_{1u} (p_x- and p_y-π-arene), e_{1g} (d_{xz}- and d_{yz}-arene), e_{2g} (d_{xy}- and d_{x2-y2}-arene), and a'_{1g} (d_{z2}-arene) molecular orbital bonding combinations where the z axis resides along the metal-arene-centroid axis. The e_{1u} and e_{1g} molecular orbitals are predominantly arene in character, whereas the a'_{1g} and e_{2g} are principally metal in character. However, the e_{2g} orbitals are lower in energy compared to the a'_{1g} and more delocalized onto the arene rings. By applying the same bonding scheme to the 15 valence electron [M(η^6-$C_6H_3Bu^t_3$)$_2$] (M = Sc or Y), it can be seen that by filling the energy levels successively, there are three electrons in the degenerate e_{2g} orbitals. Extension of this across the RE series leads to the conclusion that three electrons are required from the metal. Thus, to a first approximation, a ground d^1s^2 or easily accessible excited d^1s^2 state is required and it can be seen that arene → RE π-donation and 5d-orbital → arene δ-backbonding is prevalent. The stability of these complexes correlates very well as to whether the promotion energy for the $f^ns^2 \rightarrow f^{n-1}d^1s^2$ transition can be sufficiently offset by the metal–arene bond energy. For Eu, Tm, and Yb, the promotion energies are $\geq$12000 cm^{-1} and the corresponding *bis*(arene) complexes are not accessible at any convenient temperature. The Sm analog, which possesses an $f^6s^2 \rightarrow f^5d^1s^2$ promotion energy of ~12000 cm^{-1}, decomposes above −30°C. Notably, gadolinium, terbium, dysprosium, holmium, erbium, and yttrium *bis*(arene) complexes are all isolable and exhibit much smaller promotion energies. However, the corresponding lanthanum and cerium complexes are not isolable and do not fit this trend since their promotion energies are actually small. These two apparent inconsistencies are rationalized on the basis that the $C_6H_3Bu^t_3$ ligand is of insufficient steric bulk to kinetically stabilize these large metal centers. The implied covalency in the RE–arene bonding is supported experimentally by impressive thermal stabilities and many of the accessible *bis*(arene) RE complexes are sublimable at ~100 °C. Additionally, thermochemical studies[60] reported metal–arene bond enthalpies of ~300–430 kJ mol^{-1} which must be considered strong and these values are comparable to *bis*(benzene) tungsten and nearly twice as large as for bis-benzene chromium. Thus, in the zero-valent state, organometallic RE complexes exhibit covalency but in higher oxidation states, the bonding is predominantly ionic.

3.3 The General Paucity of Rare Earth–Ligand Multiple Bond Linkages in an Organometallic Context

The ionic nature of RE bonding, the limited radial extension of the 4f orbitals, and the high-lying nature of



(**5**)

Figure 4 The first structurally authenticated rare earth bis(arene) complex

the 5d orbitals for the RE metals preclude the formation of covalent π-bonds with ligand orbitals, and therefore formal organometallic RE–ligand multiple bond linkages are comparatively rare.[61] As early as 1979, the formation of RE alkylidenes in $[Lu(=CHSiMe_3)(CH_2SiMe_3)_2]Li$ and $[Er(=CHSiMe_3)(CH_2SiMe_3)]$ was proposed,[62] but definitive structural authentication has remained elusive and since γ- as well as α-elimination is plausible in the parent alkyls, the structures of these compounds cannot be known for sure. This has prompted the use of pincer ligands where carbene/alkylidene centers are pinned to an RE metal center and forced to coordinate and a representative selection of ligand combinations which have met with success are illustrated in Figure 5.[35] Notably, structural and computational studies have shown that in these systems, which employ geminal dianions, e.g., methanediides, the formal RE carbon double bond is in fact highly polarized and bond orders of ~0.6–0.7 have been calculated. It is germane to observe that this is experimentally borne out in as much as when methanediide-stabilizing substituents, such as the phosphanyl groups in (**6**–**8**) and aluminum groups in (**9**) and (**10**), are absent, clusters such as $[\{La(\eta^5\text{-}C_5Me_5)(THF)\}_4(\mu\text{-}Cl)_4(\mu_3\text{-}CH_2)]$[63] result; this is in order to stabilize the formal dianionic charge on the ''carbene'' centers through contact with several metal centers. Although not strictly organometallic, it should be noted that it was as recently as 2010 that the isolation of the first terminal imido RE complex (**11**)[64] was accomplished. Therefore, it is reasonable to propose that with suitable co-ligands, a terminal RE carbene/alkylidene that does not exhibit stabilizing pincer substituents might eventually be prepared.

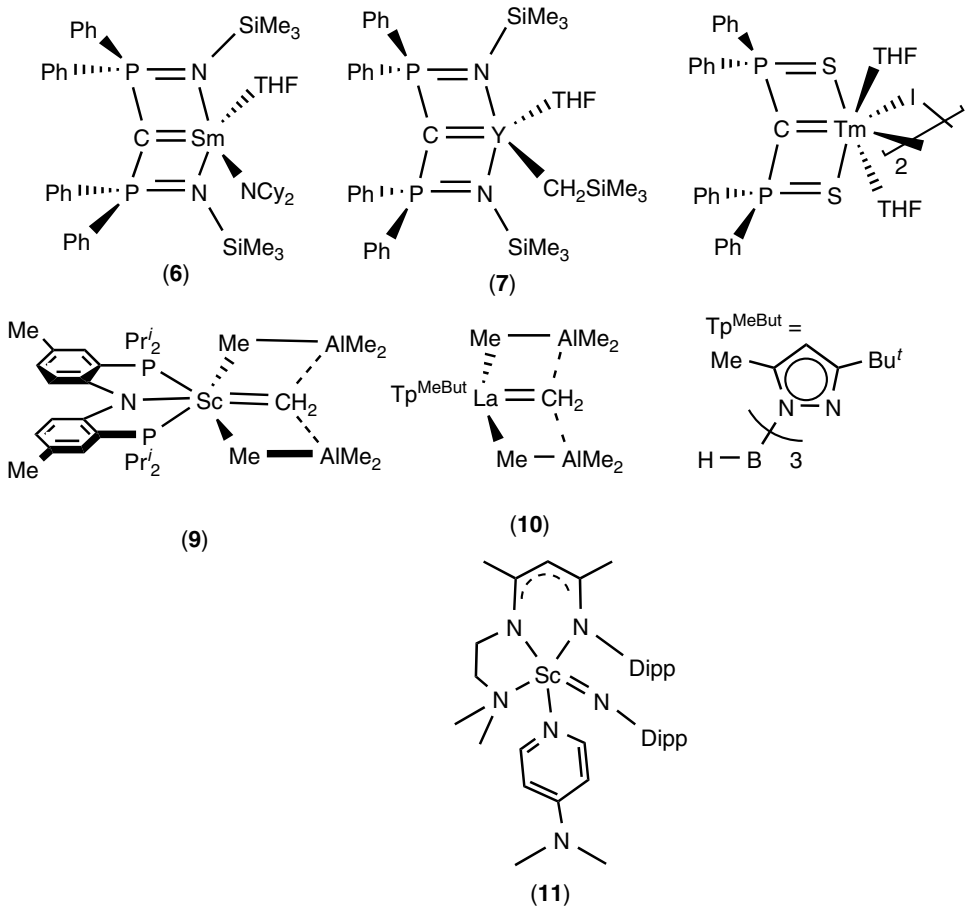


Figure 5 Selected rare earth carbenes with formal metal–carbon multiple bond linkages

4 THERMODYNAMIC AND KINETIC CONSIDERATIONS

4.1 Thermodynamic Considerations

A key contribution to the stability of organometallic RE complexes is the inherent and underlying thermodynamic aspects. Elegant thermochemical investigations of *bis*(pentamethylcyclopentadienyl) samarium have enabled a rigorous assessment of the thermodynamic aspects of organometallic RE chemistry and given experimental credence to the theoretical framework.[65] The data were obtained by anionic iodinolytic and alcoholytic titration calorimetry conducted in toluene. Accordingly, consideration of equations (1–4) enables calculation of the absolute bond disruption enthalpies according to equation (5). Such calculations enable a better understanding of the thermodynamics of archetypal reaction types in organometallic RE chemistry and also for predicting viable catalytic mechanisms.

$$[(C_5Me_5)_2Sm-R] + X_2 \rightarrow [(C_5Me_5)_2Sm-X] + RX \quad \Delta H_{rxn}(1) \tag{1}$$

$$[(C_5Me_5)_2Sm-X] \rightarrow [(C_5Me_5)_2Sm] + 0.5\,X_2 \quad \Delta H_{rxn}(2) \tag{2}$$

$$X^{\cdot} \rightarrow 0.5\,X_2 \quad -0.5\,D(X-X) \tag{3}$$

$$R-X \rightarrow R^{\cdot} + X^{\cdot} \quad D(R-X) \tag{4}$$

$$D([(C_5Me_5)_2Sm-R]) = \Delta H_{rxn}(1) + \Delta H_{rxn}(2) - 0.5\,D(X-X) + D(R-X) \tag{5}$$

These calorimetric investigations have generated the series illustrated in Figure 6. As would be anticipated, THF, which binds datively to RE centers, forms the weakest bond in the series. Conversely, chloride forms a polarized covalent bond to RE centers and makes the strongest bond, a feature whose origins can be traced back to the ionic nature of the bonding and the hard, electropositive character of the REs. As expected from hard–soft arguments, the corresponding bromide and iodide bonds become progressively weaker compared to chloride, although as halides, they still form relatively strong bonds. Chalcogenide bonding is also notably strong, even for the softer, more polarizable sulfur, which directly contrasts to a representative phosphide dialkyl which is the weakest of the anionic ligand series. Alkyl, amide, and hydride ligands fall in the middle of this series which is to be expected from hard–soft considerations. This thermodynamic series also sets the air- and moisture-sensitive nature of organometallic RE complexes into context in as much as it demonstrates the strength of RE–O bonds, and when the insolubility of RE hydroxides and oxides, which will provide a strong driving force to the reaction, is taken into account, it is clear that RE oxides represent thermodynamic sinks.

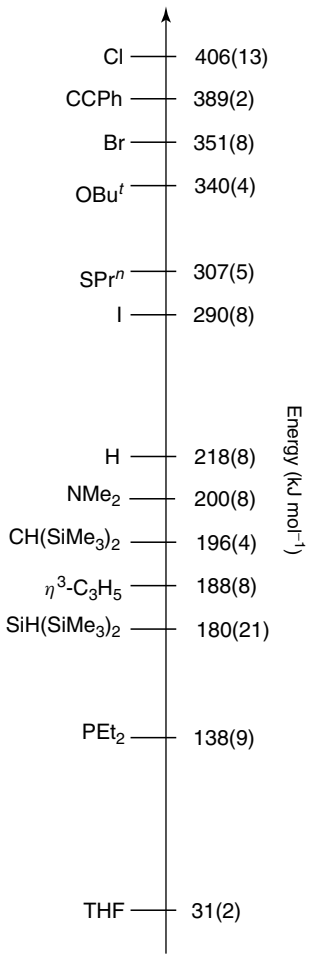


Figure 6 Bond disruption enthalpies for $[(C_5Me_5)_2Sm\text{-}R]$ (kJ mol^{-1}) where R = THF, PEt_2, $SiH(SiMe_3)_2$, η^3-C_3H_5, $CH(SiMe_3)_2$, NMe_2, H, I, SPr^n, OBu^t, Br, CCPh, and Cl

4.2 Kinetic Considerations

Although Figure 6 demonstrates the relative weakness of organometallic RE linkages in comparison to RE halide and oxo bonds, it does show that RE–R bonds are in fact reasonably stable from a thermodynamic perspective. In fact, when considering the bond energies of group 14 element methyl bonds ($CMe_4 = 358$; $SiMe_4 = 311$; $GeMe_4 = 249$; $SnMe_4 = 217$; $PbMe_4 = 152$ kJ mol^{-1}) which are all air- and moisture-stable, it becomes clear that the high reactivity of RE organometallics is not due to an inherent thermodynamic weakness in the bonding. Instead, the highly reactive nature of organometallic RE complexes derives from the ionic nature of the bonding which gives highly polar and labile bonds that are easily cleaved due to kinetically facile reaction routes. This is both beneficial and detrimental because on the one hand this gives high reactivities in catalytic reactions, and on the other hand, it also means that organometallic RE complexes are easily poisoned and decomposed by traces of oxygen, moisture, halides, and sulfur impurities.

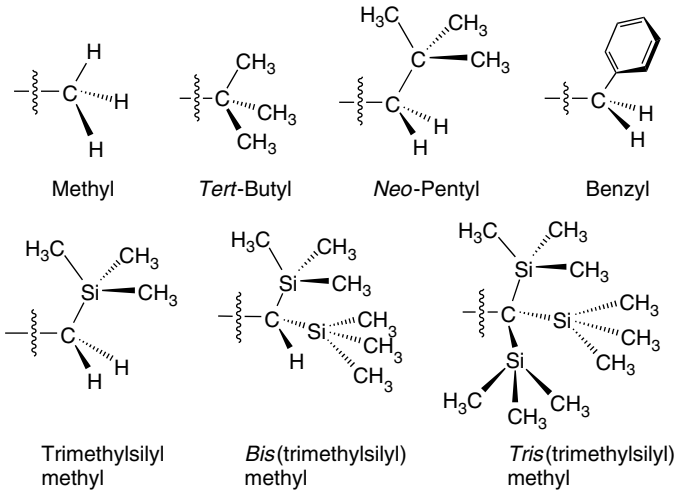


Figure 7 Commonly employed classes of alkyl ligands in organometallic rare earth chemistry

5 SOLVATION, SALT OCCLUSION, AND AGGREGATION

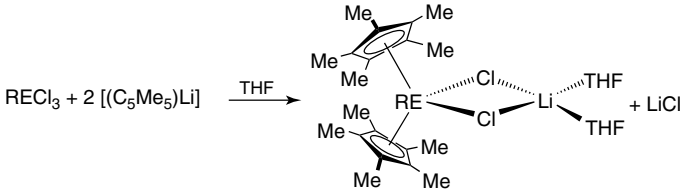
The ionic nature of the bonding in organometallic RE complexes results in some phenomena which must be taken into account when designing the synthesis of new complexes. The steric demands of ligands play a principal role in determining the coordination sphere of the metal, since they will arrange themselves to minimize steric clashes, but once anions are coordinated, the highly electropositive and Lewis acidic REs will fill any remaining unoccupied coordination sites with any available ligand which provides additional electron density to the RE center and which is sterically suited to coordinate in the remaining space. This typically manifests through the coordination of Lewis bases or any available halides.

5.1 Solvation

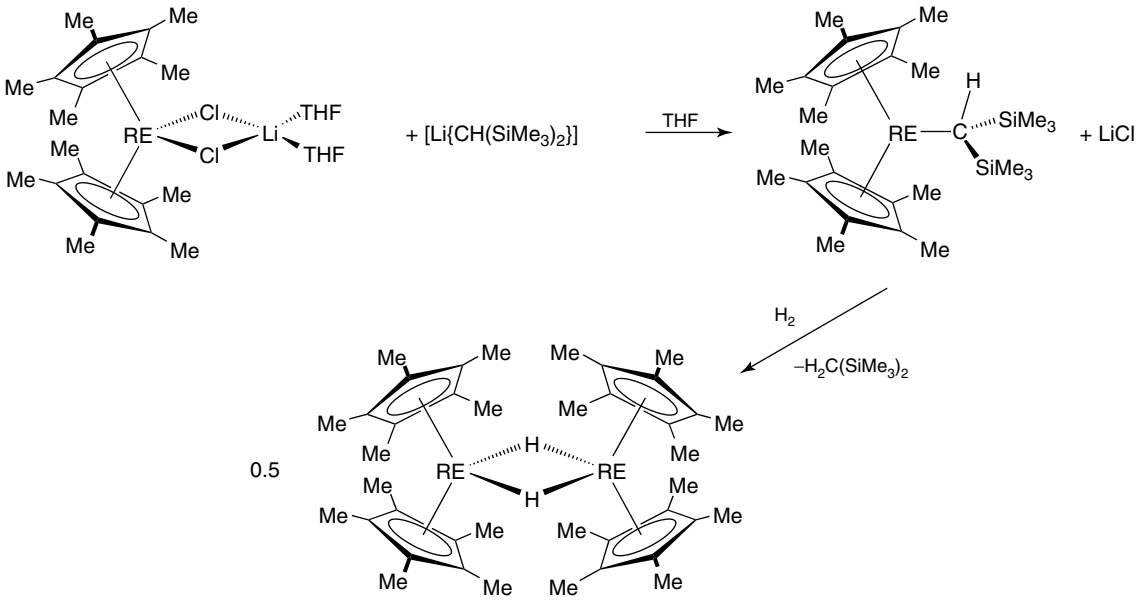
Many polar solvents, e.g., ethers, possess lone pairs and are therefore capable of acting as dative ligands to RE centers. Many organometallic RE complexes are either prepared in ethers to aid the salt-elimination reactions employed in their synthesis through provision of a polar reaction medium or utilize RE halides which incorporate ethers to aid their solubility. Thus, if coordinated organometallic ligands are not sufficiently sterically demanding, space may be left in the coordination sphere of RE centers allowing Lewis bases to coordinate. Commonly coordinated ligands include diethyl ether, THF, DME, and pyridine. In principle, the coordination of these ligands may not pose a problem in terms of subsequent reactivity, but they may block otherwise accessible reaction sites, become involved in deleterious ether cleavage reactions, and/or engage in C–H activation reactions so there are often scenarios where the exclusion of ethers is necessary.

5.2 Occlusion

Another direct consequence of the highly electropositive nature of RE bonding is that if the coordination sphere of a newly formed organometallic complex is sufficiently open, certain alkali metal halides may remain within the primary coordination sphere of the RE if salt elimination is the synthetic method employed. Lithium chloride is soluble in THF, but not diethyl ether, and the lithium cation is sufficiently small such that during salt elimination, a formal MX fragment may not be eliminated and instead the halide remains bound to the RE center and bridges to the alkali metal. An example of this is the generic reaction of an RE trichloride with 2 equiv. of $Li(C_5Me_5)$ to afford $[(C_5Me_5)_2RE(\mu\text{-}Cl_2)Li(THF)_2]$ and LiCl (Scheme 1) instead of $[(C_5Me_5)_2M(Cl)(THF)_n]$ and 2 equiv. of



Scheme 1 Generic reaction for the formation of *bis*(cyclopentadienyl) rare earth ''ate'' complexes



Scheme 2 Utility of *bis*(cyclopentadienyl) rare earth ''ate'' complexes in the synthesis of alkyl and hydride derivatives

LiCl.[9] Examples of $[(C_5Me_5)_2RE(\mu\text{-}Cl_2)M(THF)_2]$ (M = Li, Na, K), which are often referred to as ''ate'' complexes, are known across the entire RE series and these complexes are surprisingly soluble in organic solvents, despite the presence of alkali metal halide, and can be easily recrystallized. It should be noted, however, while it is necessary to realize that the formation of ''ate'' complexes is a possibility in organometallic RE chemistry, they are not necessarily undesirable since they are excellent precursors for subsequent derivatization. For example, for a wide range of REs, the ''ate'' complexes can be converted into hydrocarbyl derivatives which find use as precatalysts or precursors to solvent-free hydrides (Scheme 2). Should it be desirable to avoid occlusion, but salt elimination is a necessary synthetic methodology, generally utilizing potassium bromide or iodide elimination is the tactic of choice since KBr and KI are generally too large to remain coordinated to the RE center and they are insoluble in THF.

5.3 Aggregation

A reoccurring theme for all electropositive, electron-deficient metals, such as the REs, is the formation of aggregates. This occurs when co-ligands are not sterically demanding enough to fill the metal coordination sphere, ancillary Lewis bases are not available to reduce the extent of oligomerization/polymerization, and/or occlusion has been avoided. This is driven by the requirement of the RE centers to maximize the amount of electron density they receive since they are electropositive and electron deficient. In order to prevent this, solvated, lower order aggregates can be prepared, or sterically demanding ligands need to be employed which block access to or occupy multiple coordination sites.

6 STABILITY

6.1 Employ Anhydrous and Anaerobic Conditions

Given that organometallic RE complexes are air- and moisture sensitive, it is necessary to prepare and handle such complexes under a dry and inert atmosphere such as nitrogen or argon using Schlenk line and/or glove box techniques. It should be noted, however, that RE(II) complexes are often strongly reducing and may reduce and incorporate dinitrogen into complexes as N_2^{2-}, so this is an important consideration which must be taken into account when choosing an ''inert'' atmosphere. Solvents and reagents must be rigorously dried and degassed before use and inert atmosphere gases should be passed through drying/deoxygenation columns to remove parts per million level traces of oxygen and moisture. Even organometallic RE derivatives with phenolic ligands which exhibit pK_a values lower than water are generally vulnerable to hydrolysis because the resulting hydroxides and oxides form insoluble precipitates which generates a strong driving force to the reactions.

6.2 Avoid β-Hydrogens

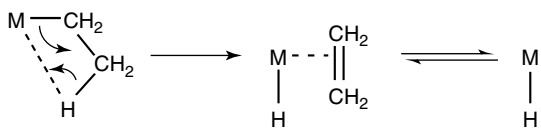
Conversion of metal alkyl complexes to a metal hydride and an alkene by β-hydride elimination represents a fundamental decomposition route for organometallic RE complexes (Scheme 3). Main group organometallics, such as tetraethyl lead, show good stability up to around 100 °C because with a filled 5d-shell, a full octet, and high-lying, energetically inaccessible σ^*-orbitals, M–C bond homolysis is a high energy process. For transition metals, vacant d-orbitals

provide low energy routes to decomposition. Although the RE metals are ionic and orbital considerations can be largely set to one side, the kinetic lability of ligands, and the ability of the highly electropositive RE centers to polarize bonds, thus making them more reactive, enables σ-bond metathesis reactions to occur, and thus RE alkyls with β-hydrogens may easily decompose.

Therefore, in organometallic RE chemistry, alkyl ligands, which do not possess β-hydrogens, have become workhorse ligands as a result of the greater thermal stability that they engender to complexes. It should be noted that many RE alkyl complexes are still thermally sensitive due to the labile nature of RE–alkyl bonds, but a variety of ligands have been developed which afford organometallic RE complexes which are sufficiently stable to be routinely prepared and handled. Figure 7 shows some commonly employed alkyl ligands in organometallic RE chemistry; these ligands can be sourced as alkali metal reagents commercially or are generally straightforward to synthesize.[66] These ligands can easily be functionalized to incorporate bulky substituents and/or Lewis base donor groups to improve stability. The benzyl ligand is depicted as a σ-ligand but it should be noted that benzyl can also bind to metal centers in an η^2-mode, an allyl-like η^3-mode, and also has the capacity to bind η^6.

A selection of archetypal RE nonsilyl alkyls are illustrated in Figure 8.[33] Although methyl has no β-hydrogens, it is not very sterically demanding. Early attempts to prepare the simplest homoleptic RE trimethyl complexes proved unsuccessful, but it was found that hexamethyl ''ate'' complexes such as $[Nd(\mu\text{-}Me)_6\{Li(TMEDA)\}_3]$ (**12**) could instead be obtained in the presence of suitable co-ligands such as TMEDA. More recently, it has been found that RE tetramethyl aluminates $[RE(AlMe_4)_3]$ can be converted to polymeric $[\{RE(Me)_3\}_\infty]$ by treatment with stoichiometric amounts of diethyl ether, THF, or PMe_3. *Tert*-butyl ligands are more sterically demanding than methyl, but even here, ''ate'' complexes such as $[Sm(Bu^t)_4][Li(THF)_4]$ (**13**) dominate. There are surprisingly few examples of *neo*-pentyl derivatives of the REs. One notable example is the ytterbium complex $[Yb(CH_2Bu^t)_3(THF)_2]$ (**14**) which was prepared from ytterbium metal and *neo*-pentyl iodide. Representative examples of tribenzyl complexes for most RE metals are now known with a variety of substitution patterns. As described above, benzyl can adopt a variety of coordination modes and the lanthanide contraction can be seen in the series of benzyls $[RE(Bn)_3(THF)_3]$ where for Ce, Pr, and Nd (**15a**–**c**), three η^2-benzyls are observed in the solid state; for Sm (**15d**), only one η^2-benzyl is observed; and for Gd, Dy, Er, Lu, and Y (**15e**–**i**), all benzyl groups are η^1-bound.[67]

Organosilyl ligands have played a pivotal role in the development of organometallic RE chemistry and



Scheme 3 General scheme for the decomposition of a metal alkyl complex by β-hydride elimination

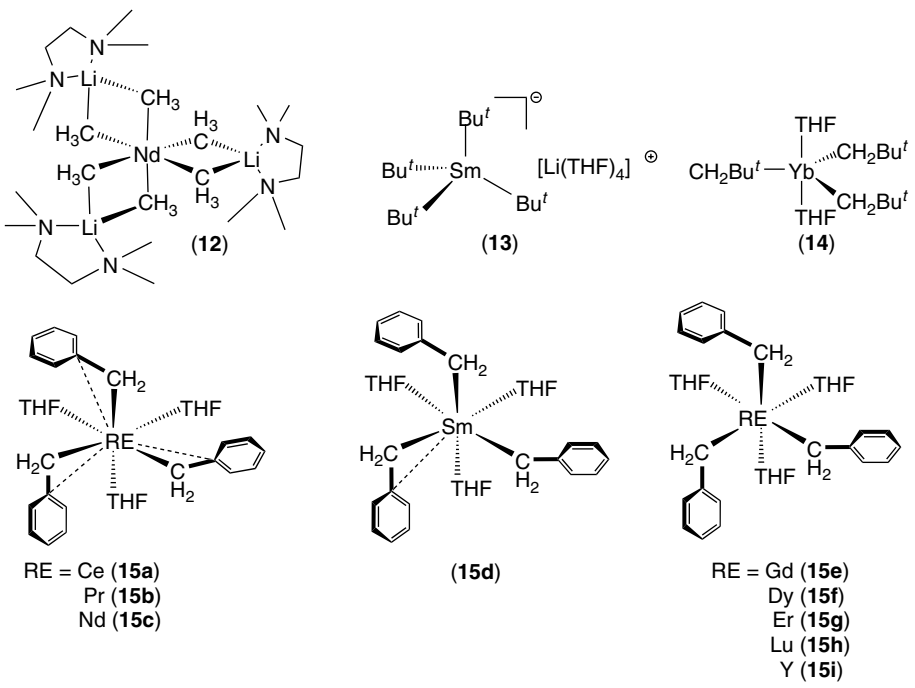


Figure 8 Selected examples of β-hydride-free rare earth nonsilyl alkyls

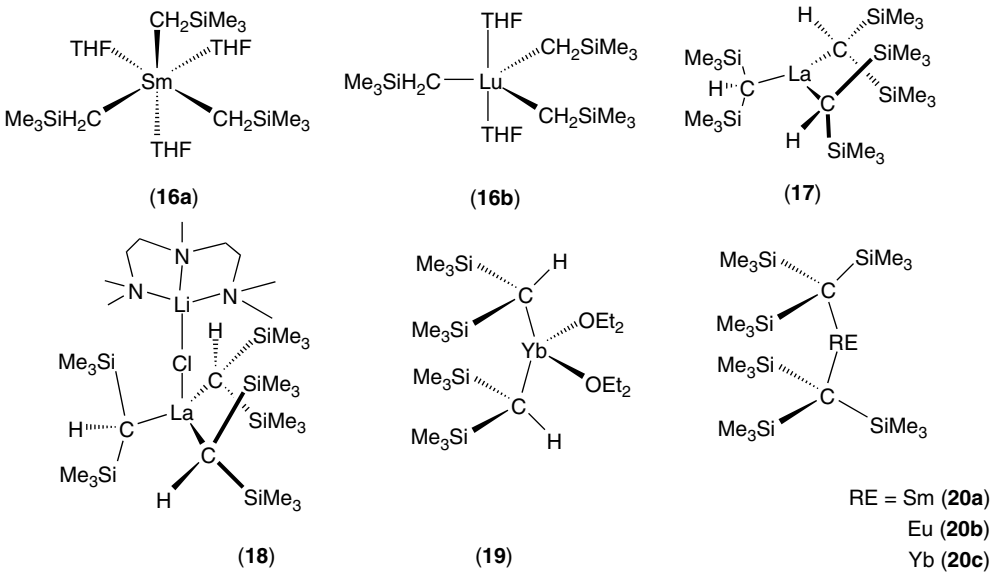


Figure 9 Selected examples of β-hydride-free rare earth silyl alkyls

some of the key compounds are shown in Figure 9.[33] It was recognized as early as 1969 that trimethylsilylmethyl represents a valuable ligand because it imparts thermal stability, solubility, and a lipophilic nature to its metal derivatives. Two structural types have been identified, namely $[RE(CH_2SiMe_3)_3(THF)_3]$ (RE = Sm, **16a**) and, for example, $[Lu(CH_2SiMe_3)_3(THF)_2]$ (**16b**); the former adopts a mutually *fac* geometry, whereas the latter adopts trigonal bipyramidal geometries for scandium, yttrium, terbium, erbium, thulium, ytterbium, and lutetium.[68,69] However, the trimethylsilylmethyl ligand does not saturate the coordination sphere of RE metals as evidenced from coordination of THF and that metals larger than samarium are generally inaccessible as they decompose through either α- or γ-elimination. This spurred interest in the bulkier *bis*(trimethylsilyl)methyl ligand, which is much more sterically demanding, and this marked a new era in organometallic RE chemistry. For trivalent REs, the use of the *bis*(trimethylsilyl)methyl ligand enabled the remarkable isolation of solvent-free RE trialkyls such as $[La\{CH(SiMe_3)_2\}_3]$ (**17**).[70] However, even *bis*(trimethylsilyl)methyl is not of sufficient steric bulk to prevent the formation of ''ate'' complexes such as $[La\{CH(SiMe_3)_2\}_3(\mu\text{-Cl})Li(PMDETA)]$ (**18**) where the early, larger RE metals are concerned. This necessitates the use of $[RE(OC_6H_2Bu^t{}_2\text{-}2,6\text{-}Me\text{-}4)_3]$ and $[Li\{CH(SiMe_3)_2\}]$ since the by-product $[Li(OC_6H_2Bu^t{}_2\text{-}2,6\text{-}Me\text{-}4)]$ is insoluble in hexanes, allowing easy separation, and it does not coordinate to (**17**). For divalent ytterbium, $[Yb\{CH(SiMe_3)_2\}_2(OEt_2)_2]$ (**19**) has been isolated but ytterbium(II) is large and the *bis*(trimethylsilyl)methyl group is of insufficient steric bulk to prevent the coordination of ethers. Finally, in order to prepare stable and ether-free RE(II) alkyls, it was found to be necessary to employ *tris*(trimethylsilyl)methyl as a ligand. This is a very sterically demanding ligand, so demanding that three of them cannot be accommodated around any RE center. However, use of the *tris*(trimethylsilyl)methyl ligand allowed the synthesis of the bent, solvent-free RE dialkyls $[RE\{C(SiMe_3)_3\}_2]$ (RE = Sm, Eu, Yb, **20a**–**c**)[71] which are remarkably stable.

6.3 Saturate the Coordination Sphere

A number of strategies exist for increasing the stability of organometallic RE complexes but all reply on closing down the coordination environment at a metal center thus precluding kinetically facile decomposition reactions. It is salient to highlight the difference between actually directly occupying coordination sites, using sterically demanding ligands which protect vacant coordination sites by placing bulky groups in close proximity, and using bulky ligands which block access to these sites but do not actually occupy space close to them.

6.3.1 Directly Occupying Coordination Sites

One reason that the cyclopentadienyl ligand has been so successful in organometallic RE chemistry is that formally it occupies three coordination sites at a metal. Thus *bis*- and *tris*(cyclopentadienyl) complexes can be considered to be six- and nine-coordinate before any other ligands are taken into account. Thus, such complexes possess high formal coordination numbers and are therefore stabilized.

A second strategy in this area involves the use of multidentate ligands which can datively bind to metal centers. Thus, DME, TMEDA, and phosphines such as

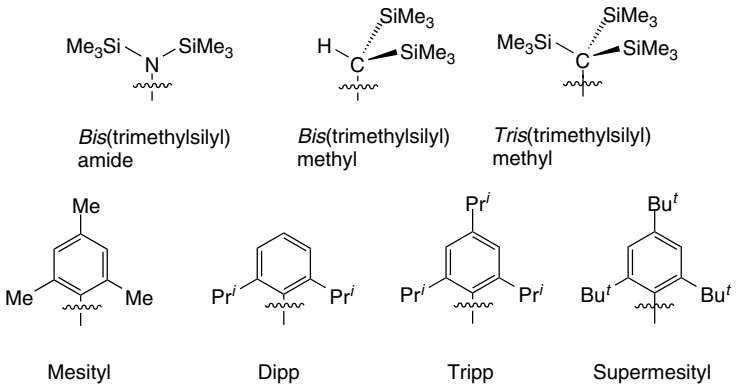


Figure 10 Classical sterically demanding ligands

$Me_2PCH_2CH_2PMe_2$ may directly coordinate to RE metal centers to occupy coordination sites. Since these ligands form stable five-membered ring chelates, they are entropically favored and bring kinetic stabilization through their steric bulk. However, although this method has clear advantages, the very act of stabilization inherently reduces the subsequent reactivity of a given complex since potential sites of reactivity are blocked which may preclude any further utility.

6.3.2 Using Sterically Demanding Ligands to Protect Vacant Coordination Sites

Classical organometallic ligands which are sterically demanding and can protect vacant coordination sites are illustrated in Figure 10. The *bis*(trimethylsilyl)amido ligand is not organometallic, but has been used extensively in organometallic RE chemistry as a sterically demanding ancillary ligand. The size of the *bis*(trimethylsilyl)amido ligand and silyl substituents ensures that low-coordinate complexes are formed and imparts enhanced solubility and crystallinity to complexes. The *bis*- and *tris*(trimethylsilyl)methyls were introduced in Section 6.2. It should be noted that these silyl ligands place silyl–methyl groups close to the metal centers and thus C–H activation reactions must be considered. This is also the case for the mesityl, dipp, tripp, and supermesityl ligands which all employ steric bulk to shield metal centers, but in all cases, the *ortho*-substituents come into close proximity to the metal and thus become vulnerable to C–H activation. The silyl and alkyl C–H bonds in the ligands in Figure 7 are relatively robust, but less-stabilized RE alkyl linkages can effect deprotonation, and the resulting metallocycles can be stabilized through negative hyperconjugation, the chelate effect, and/or resonance delocalization.

6.3.3 Blocking Access to Vacant Coordination Sites

Given that the ligands discussed in Section 6.3.2 are useful but not immune to decomposition reactions, ligands which protect the vacant coordination sites but do not place any reactive groups close to them have been developed. One particularly successful ligand in this regard is the terphenyl ligand class (Figure 11).[72] Terphenyl ligands can be made straightforwardly with a wide, almost inexhaustible, range of substituents. The *bis*(phenyl) derivative is likely to have coplanar aryl rings to maximize conjugation. However, simple addition of *ortho*-methyls, or bulkier substituents, to the *ortho*-phenyl rings forces them to reside orthogonal to the central ring. Thus, coordination of a metal to the *ipso*-carbon creates a pocket around the metal without actually placing potentially reactive groups directly next to metal coordination sites (Figure 12).

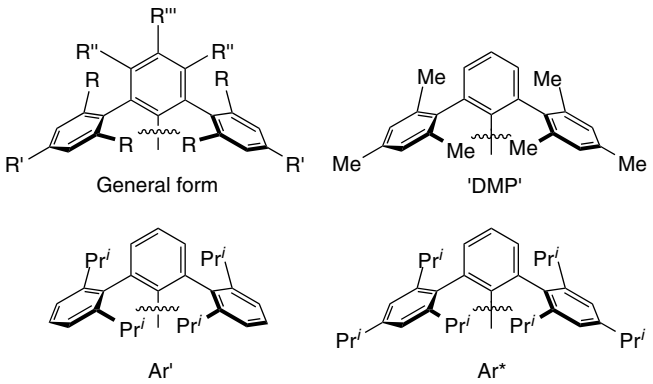


Figure 11 The generic structure of terphenyl ligands and some representative examples

6.4 Use of Donor-Functionalized Chelating Ligands

As organometallic RE chemistry developed in the 1980s and 1990s and progressed into a ''post-metallocene'' phase, the use of ligands with donor-functionalized chelating pendant donor groups became more popular (Figure 13).[73] The benefits of employing this approach are manifold:

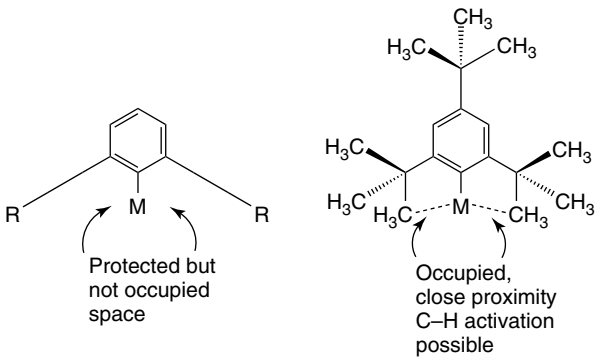


Figure 12 Comparison of blocking versus preventing access to coordination sites at a metal M in terphenyl and supermesityl complexes viewed from above

- Pendant donor groups can occupy otherwise vacant coordination sites, thus precluding oligomerization/polymerization, salt occlusion, and coordination of solvent molecules.
- Donor-functionalized ligands can enforce monomeric formulations rendering the resulting complexes volatile and suitable for sublimation in materials applications.
- Such ligands can incorporate chiral centers to enforce a given ligand conformation which can be exploited in enantioselective reactions and catalysis.
- These donor groups may be hemilabile and thus block kinetically facile decomposition routes but enable desirable reactivity to occur.
- Such donor groups form relatively stable and entropically favorable chelate rings increasing the stability of complexes.
- Many donor-functionalized ligands are straightforward to prepare and substitution patterns can be easily modified giving flexibility over control of sterics which are of paramount importance.
- The length of the tether to pendant donor groups in donor-functionalized ligands can be controlled and fine-tuned to tailor the resulting properties of complexes.

With the prevalence of cyclopentadienyl ligands, a natural step forward was to tether two of these ligands together to produce a class of ligand known as *ansa*.[33] For ansa ligands, a wide variety of substitution patterns are easily accessible, and because the two cyclopentadienyl ligands are ''tied back' in the resulting RE complexes, the coordination sphere of the metal is more open which brings greater reactivity. Such ligands, and especially chiral variants, have found extensive use in hydroamination and can effect impressive enantiomeric excesses.[39] A closely related ligand type, the so-called constrained geometry class, also forms part of a larger field of mono-cyclopentadienyl complexes. The use of methoxy-substituted ligands has proven to be an effective strategy for the *bis*- and *tris*(silyl)methyls (Figure 14). As noted above with (**18**) (Figure 9),[33] the larger REs are prone to ''ate'' complex formation when $(Me_3Si)_2CH$ is employed. However, utilizing $(Me_3Si)(MeOSiMe_2)CH$ results in intramolecular ''solvation'' (**21**) preventing the formation of ''ate'' complexes. When this strategy is applied to *tris*(silyl)methyls, complexes such as (**22**) result which is notable for the fact it is a formally five-coordinate samarium(II) center. Donor-functionalized benzyl complexes have also been investigated (**23**). Whereas the unsubstituted benzyls (**15**, Figure 7) incorporate three-coordinated THF molecules, the *N*, *N*-dimethylaminobenzyl congeners are solvent free as the coordinating NMe_2 groups block coordination of THF. Finally, complex (**24**) represents a useful ytterbium dialkyl precursor to a range of derivatives and this

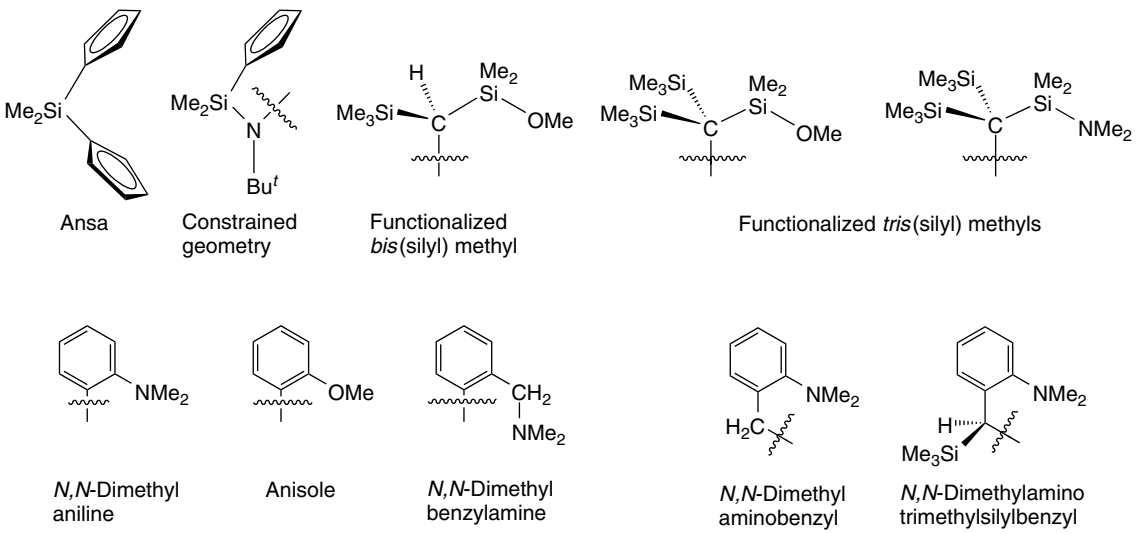
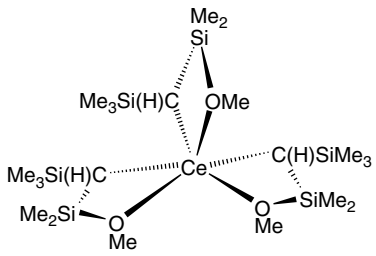
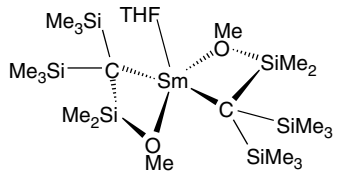


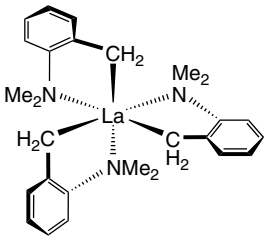
Figure 13 Classical examples of donor-functionalized ligands used in organometallic rare earth chemistry



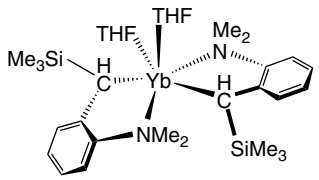
(**21**)



(**22**)



(**23**)



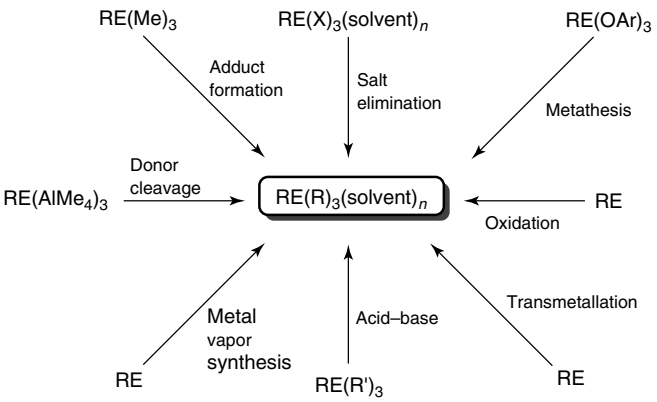
(**24**)

Figure 14 Selected examples of organometallic rare earth donor-functionalized alkyls

complex exemplifies all of the design features of bulky, donor-functionalized ligands discussed in this section.

7 METHODS OF PREPARATION AND PRINCIPAL REACTION TYPES

As the field of RE organometallic chemistry has progressed, the number of synthetic methods has increased and this is summarized in Scheme 4. This has been in order to provide higher yielding reactions or open up otherwise inaccessible avenues of chemistry. The methods of preparation typically involve all of the principal reaction types and there is significant overlap between the two concepts so they are described jointly in this section.



Scheme 4 Synthetic strategies for the synthesis of organometallic rare earth complexes

7.1 Salt Elimination

$$REX_3 + n\,MR \rightarrow REX_{3-n}R_n + n\,MX \quad (6)$$

$$REX_3 + n\,MgRX \rightarrow REX_{3-n}R_n + n\,MX_2 \quad (7)$$

$$REX_3 + n\,TlR \rightarrow REX_{3-n}R_n + n\,TlX \quad (8)$$

Salt elimination of MX (M = alkali metal, magnesium, thallium; X = halide) represents a powerful tool for introducing organometallic ligands to the coordination spheres of RE metals (equations 6–8). The general insolubility of alkali metal halide salts and their high lattice enthalpies render this methodology straightforward and convenient although the prospect of salt occlusion (Section 5.2) should be considered. Thus, organometallic alkali metal reagents are commonly employed in the preparation of organometallic RE complexes. Grignard reagents also find utility in this area, but this does not always lead to clean elimination of magnesium dichloride; however, the addition of 1,4-dioxane precipitates the magnesium halide as an insoluble polymer. The insolubility of thallium(I) halides renders organothallium reagents effective reagents in the preparation of organometallic RE complexes. However, thallium is toxic which has made the use of organometallic thallium reagents less prevalent than the corresponding alkali metal complexes.

7.2 Metathesis

Metathesis represents an excellent method for introducing organometallic ligands to RE centers. The normal trend, based on HSAB principles would be that RE centers would exchange hydrocarbyl ligands in favor of amides, which would subsequently be exchanged in favor of alk-/aryloxide ligands. However, by employing RE *tris*(aryloxides) and lithium alkyls, complexes such as $[La\{CH(SiMe_3)_2\}_3]$ (**17**, Figure 8) can be prepared because the small and highly polarized lithium preferentially binds to the aryloxide over lanthanum. This method also has the added advantage of avoiding salt occlusion ''ate'' complexes.

7.3 Oxidation and Transmetallation

The direct oxidation or transmetallation of REs represents an elegant and direct method of preparing RE organometallic complexes such as $[Yb(CH_2Bu^t)_3(THF)_2]$ (**14**, Figure 8) which was prepared from ytterbium chips and ICH_2Bu^t. Furthermore, employing organomercury reagents such as $[Hg(C_6F_5)_2]$ affords complexes such as $[Yb(C_6F_5)_2(THF)_4]$ (**25**, Figure 15).[74] However, these reactions suffer from two drawbacks. Firstly, these methods are currently limited to RE metals with readily available divalent states such as samarium, europium, and ytterbium. Secondly, these reactions generate mercury which has to be disposed of and recent years have witnessed a drive to remove toxic heavy metals from synthetic protocols.

7.4 Acid–Base

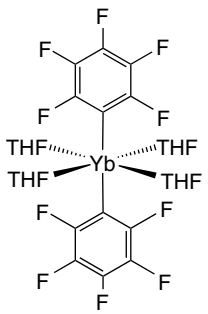
The polar and labile nature of RE ligand linkages lends itself to facile acid–base chemistry. pK_a considerations play an important role, and since most hydrocarbyl ligands possess relatively high pK_a values, it follows that in an acid–base reaction, a proligand with a low pK_a will displace a coordinated hydrocarbyl ligand whose conjugate acid displays a higher pK_a. Of course, kinetic and thermodynamic factors play a role, but pK_a provides a useful guide as to organometallic RE reactivity. Naturally it is possible to encourage reactions through appropriate design including elimination of a gas or solid to force the equilibrium through Le Chateliers principle, and the introduction of a chelating ligand will favor product formation through entropic effects. It should be noted that the pK_a values of hydrocarbyls cover a wide range and it is entirely feasible to use RE amides to deprotonate hydrocarbyl proligands if the resulting carbanion is sufficiently stabilized. Thus, RE amides and hydrocarbyls often form the basis for the synthesis of organometallic RE complexes.

7.5 Metal Vapor Synthesis

Metal vapor synthesis represents a highly specialized method of synthesis but it provides unique opportunities to access compounds inaccessible by other methods. The method involves condensation of metal atoms, vaporized under high vacuum, with potential ligands onto a cold (~77 K) surface.[58] This method has been particularly successful at accessing *bis*(arene) RE organometallic complexes. For example, co-condensation of gadolinium metal with 1,3,5-tri-*tert*-butylbenzene at 77 K gave a purple matrix from which $[Gd(\eta^6\text{-}C_6H_3Bu^t_3)_2]$ (**5**, Figure 4),[59] the first structurally authenticated RE*bis*(arene) complex, could be isolated. The method is not limited to metal(0) derivatives; co-condensation of scandium with *tert*-butylphosphaalkyne resulted in the isolation of the novel 22-electron triple decker complex $[\{Sc(\eta^5\text{-}C_2P_3Bu^t_2)\}_2(\mu\text{-}\eta^6\text{:}\ \eta^6\text{-}C_3P_3Bu^t_3)]$ (**26**, Figure 16)[75] which contains formal scandium(I) centers.

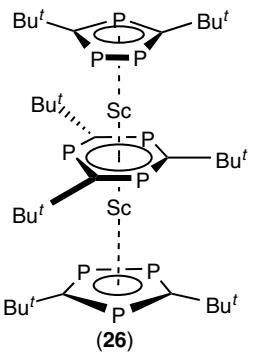
7.6 Donor Cleavage and Adduct Formation

Homoleptic *tris*(aluminate) RE complexes have a diverse and fascinating chemistry, especially when the



(**25**)

Figure 15 The σ-bound *bis*(pentafluorophenyl) ytterbium(II) complex $[Yb(C_6F_5)_2(THF)_4]$ (**25**) prepared by transmetallation from $[Hg(C_6F_5)_2]$



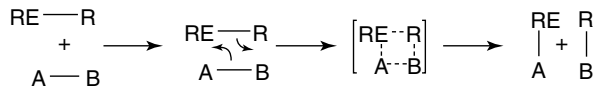
(**26**)

Figure 16 A triple decker scandium(I) complex prepared by metal vapor synthesis

aluminate substituents are alkyl groups due to the agostic interactions to the RE centers that these hydrocarbyl fragments exhibit. Such complexes have also uniquely afforded access to the archetypal solvent-free RE trimethyls which are otherwise inaccessible.[33] Adduct formation is an important, but easily overlooked, fundamental synthesis pathway for the REs and represents a convenient method of introducing ancillary ligands into the metal coordination sphere, especially when the ligands are multidentate such as crown ethers.

7.7 σ-Bond Metathesis

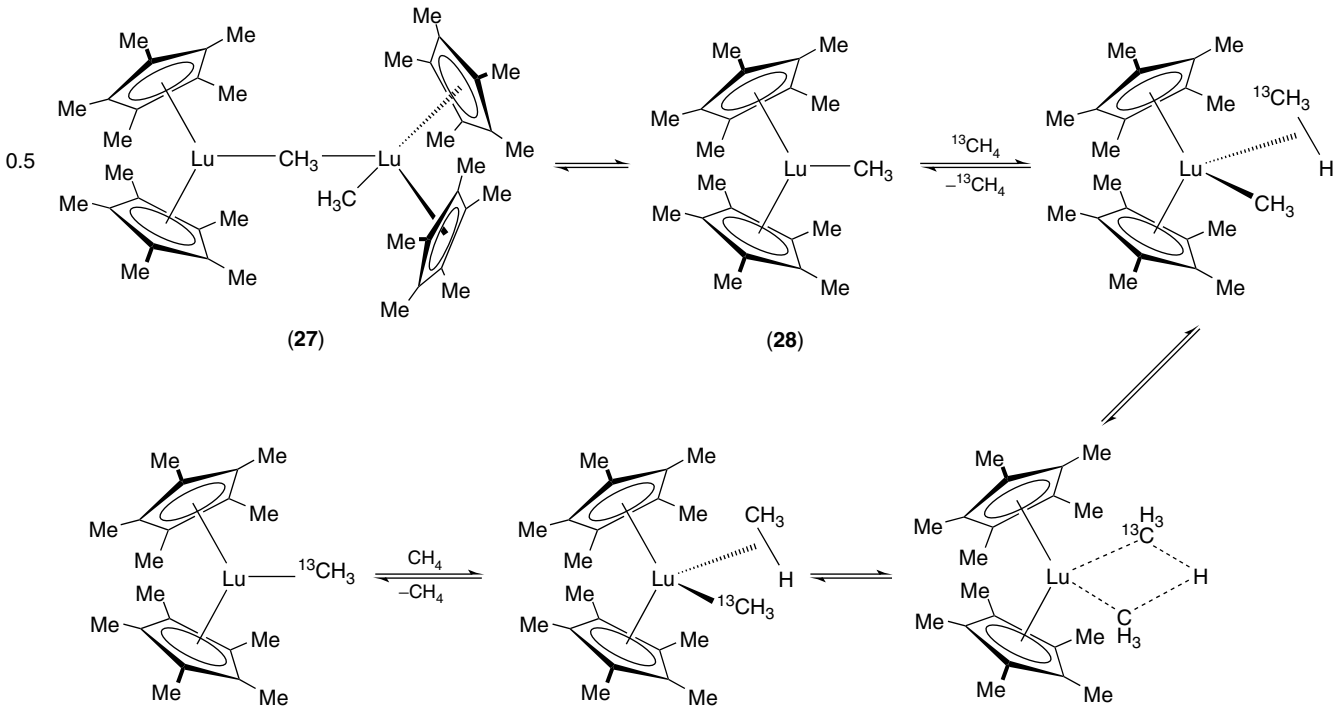
As noted in Section 6.2, σ-bond metathesis reactions of the generic form illustrated in Scheme 5 are often facile for organometallic RE complexes. The highly polarizing nature of the REs engenders their derivatives with high reactivities because substrate bonds which would otherwise be unreactive or inert can be sufficiently polarized and hence activated in the presence of RE centers to undergo subsequent reactions.



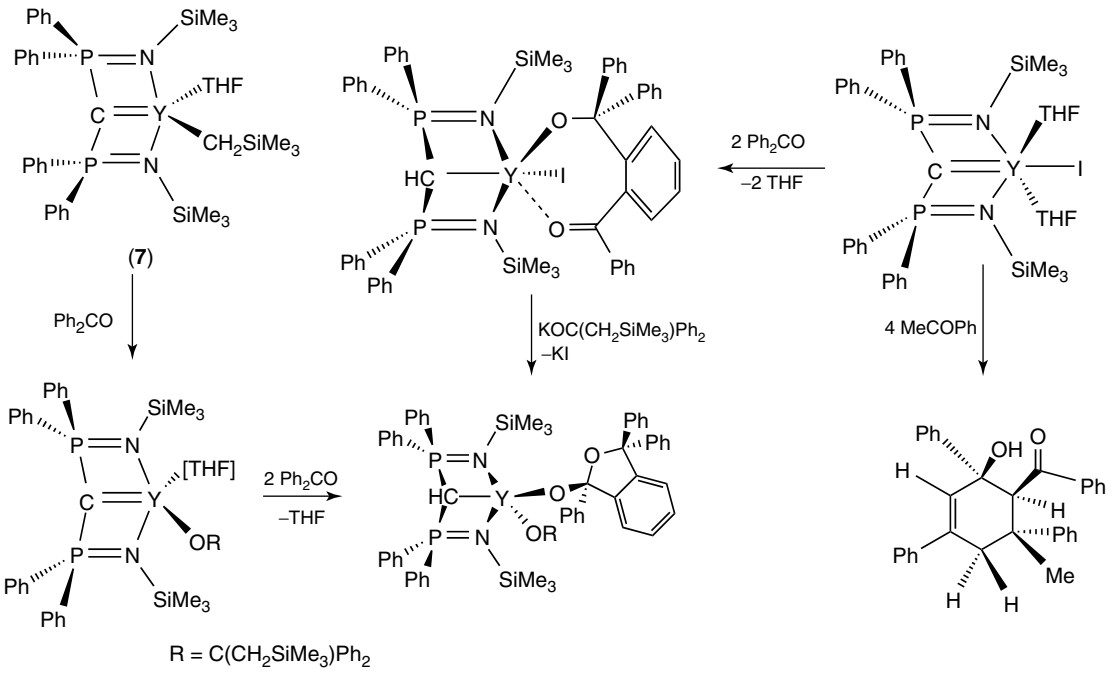
Scheme 5 Generic steps for σ-bond metathesis. Note the reaction as portrayed implies irreversibility but such reactions can be and often are in equilibrium

The remarkable σ-bond metathesis chemistry which can be effected by the REs was first recognized fully in the chemistry of $[(C_5Me_5)_2LuCH_3]$ (Scheme 6).[76] This methyl metallocene is a methyl bridged dimer in the solid state[26], but in solution, it is in equilibrium with its monomeric form (**28**). Complex (**28**) effects σ-bond metathesis of methane, and this can be elegantly demonstrated through the use of isotopically ^{13}C-labeled methane which generates ^{13}C-labeled (**27**/**28**). The reaction is in equilibrium, but the importance of this reaction derives from the fact that methane is an industrially important C_1 feedstock so its C–H activation offers the tantalizing prospect of C–H activation and functionalization of this molecule. Complex (**28**) also undergoes σ-bond metathesis with benzene and hydrogen to eliminate methane in both cases. The latter reaction affords a hydride and this hydrogenolysis reaction is analogous to that covered in Section 5.2 and Scheme 2. A comprehensive treatment of the σ-bond metathesis chemistry of the closely related complex $[(C_5Me_5)_2ScCH_3]$[77] demonstrated the broadly applicable nature of σ-bond metathesis chemistry to the REs. Similar to (**28**), this complex can activate dihydrogen to give the corresponding scandium hydride, and it activates a variety of C–H bonds to give α-metallated pyridine, methane, vinyl, and aryl derivatives.

The limited number of RE carbene complexes reported to date have established two principal types of reactivity.[35] Complexes such as (**8**), the scandium analog of (**8**), (**9**), and (**10**) exhibit metallo-Wittig reactivity with benzophenone via [2 + 2]-cycloaddition followed by σ-bond



Scheme 6 σ-Bond metathesis of methane with *bis*(pentamethylcyclopentadienyl) lutetium methyl



Scheme 7 C–H activation and C–C and C–O bond forming reactions promoted by yttrium carbenes.

metathesis; this affords the corresponding terminal alkenes with concomitant elimination of metal oxide derivatives.[78–80] Alternatively, complex (**7**) and derivative thereof attack the *ortho*-C–H bonds of aryl ketones as outlined in Scheme 7 to afford substituted ring-closed *iso*-benzofurans and ring-opened oxymethylbenzophenones,[81] the latter of which is a mechanistic precursor to the former and this chemistry invokes σ-bond metathesis.

7.8 Other Classical Reactivity Patterns

Similar to their early d-block cousins, RE organometallic complexes with σ-bound hydrocarbyl ligands can generally engage in α-, β-, and γ-hydride elimination reactions where the corresponding hydrogens are present in the alkyl groups. Indeed, these reactions constitute the principal decomposition routes for homoleptic alkyls in general. α-Hydrogen abstraction represents the principal method for the formation of alkylidene complexes in transition metal chemistry and this is the case for the REs. However, the formation of RE carbenes is considerably more difficult and rare than for the d-block due to the lack of covalency in the bonding of the former compared to the latter. β-Hydride elimination is of course the reverse reaction of 1,2-migratory insertion and the RE metals accomplish both with ease and indeed the latter is the basis for extremely efficient RE catalysts in homogeneous catalysis. 1,1-migratory insertion reactions are also a basic reaction type for organometallic RE chemistry.

Unlike the d-block, oxidative addition and reductive elimination do not play a role in organometallic RE chemistry and thus catalytic cycles cannot be constructed using these two reactions as they commonly are in the d-block. This is because none of the RE elements exhibits a pair of oxidation states that are (i) separated by two units; (ii) routinely accessible; and (iii) relatively close in energy with respect to each other. Arguably, cerium represents the best opportunity for this scenario due to the accessibility of cerium(IV)[43]; however, the conditions described above are not met. For example, although cerium(IV) is isolable and is employed as an oxidation reagent, most notably as cerium ammonium nitrate (CAN) in organic synthesis, it is easily reduced to cerium(III) and cerium(II) is not a routinely accessible oxidation state.[46] Thus, organometallic RE chemistry is known more for the chemistry described in this section above, and also for one-electron redox chemistry described below.

7.9 One-Electron Redox Chemistry

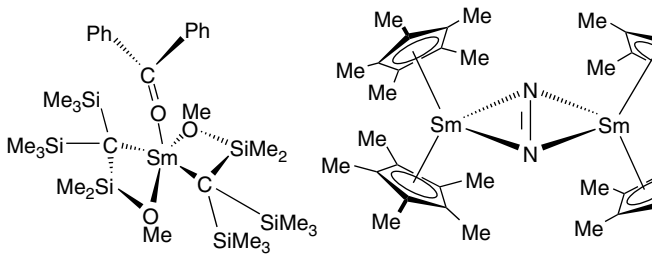
For ninety years samarium, europium, and ytterbium were the only accessible divalent rare earths in molecular organometallic chemistry. However, the past two decades have witnessed the addition of scandium(II), yttrium(II), lanthanum(II), cerium(II), neodymium(II), dysprosium(II), holmium(II), erbium(II) and thulium(II) in a molecular context.[44–47,82,83] Thus 12 of the 17 rare earths are now known in the divalent state in an organometallic context and no other area of chemistry has seen such a dramatic expansion in the number of available oxidation states. It would therefore seem to be only a matter of time before divalent states are extended to the remaining REs. An extensive palate of

RE one-electron redox chemistry is now emerging, driven by the highly reducing nature of the $RE^{2+} \rightarrow RE^{3+} + e^-$ couple (Table 1), and some examples of one-electron redox chemistry in organometallic RE chemistry are described below and illustrated in Figure 17 in order to give a flavor of the area and to demonstrate its breadth and potential capability.

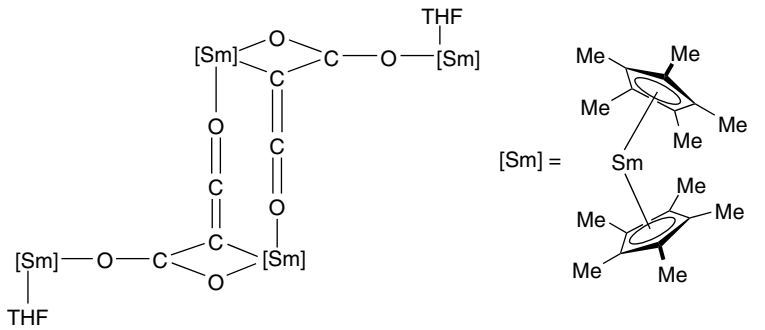
A classical use of samarium diiodide is in pinacol couplings of carbonyl compounds to give 1,2-diols after aqueous work-up. In an organometallic context, RE complexes are also capable of effecting pinacol coupling; however, one notable example which diverges from this pattern of reactivity is complex (**22**) from Figure 14 in Section 6.4, which reacts with benzophenone to afford a stable ketyl radical anion complex $[Sm(OCPh_2)\{C(SiMe_3)_2(SiMe_2OMe\}_2]$ (**29**) instead of a pinacol-coupled product.[84] The organometallic samarium(II) complex $[(C_5Me_5)_2Sm]$ reacts with dinitrogen to give $[\{(C_5Me_5)_2Sm\}_2(N_2)]$ (**30**),[85] and carbon monoxide at 90 psi to afford a reductively homologated ketenecarboxylate complex $[\{(C_5Me_5)_2Sm(O_2CCCO)Sm(THF)(C_5Me_5)_2\}_2]$ (**31**).[86] When $[(C_5Me_5)_2Sm]$ is reacted first with PhC=CPh, then carbon monoxide the remarkable complex (**32**) is formed.[87]

Table 1 Known RE(III)/RE(II) reduction potentials (versus NHE) in volts

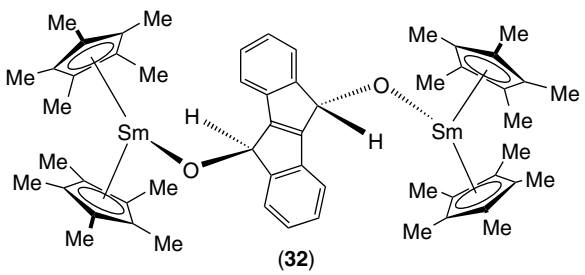
RE	$RE^{3+} + e^- \rightarrow RE^{2+}$ $E_{1/2}$ vs NHE (V)
Sc	—
Y	—
La	−3.1
Ce	−3.2
Pr	−2.7
Nd	−2.6
Pm	—
Sm	−1.55
Eu	−0.35
Gd	−3.9
Tb	−3.7
Dy	−2.6
Ho	−2.9
Er	−3.1
Tm	−2.3
Yb	−1.15
Lu	—



(**29**) (**30**)



(**31**)



(**32**)

Figure 17 samarium-mediated one-electron reduction reactions of unsaturated molecules.

Complexes (**31**) and (**32**) underscore the potential utility of low-valent organometallic RE complexes in accessing unusual radicals and/or syntheses that, for the latter, provide routes to functionalizing small molecules and potentially converting them into higher order derivatives in a straightforward manner.

8 CONCLUSIONS

The bonding in organometallic di- and trivalent RE chemistry is highly ionic as a consequence of the ''core-like'' nature of the 4f orbitals and this has resulted in a paucity of neutral π-acid ligands, such as carbonyls and olefins, and relatively few RE–ligand multiple bond linkages. However, significant advances have been made in recent years and this gives promise to eventually accessing RE carbonyls under ambient conditions[88] and expanding the range of RE–ligand multiple bond linkages. The bonding is not inherently weak, but it is highly polarized which results in kinetically facile ligand scrambling and high reactivities. This is exemplified by elegant σ-bond metathesis chemistry and an ongoing challenge will be to harness this facet of RE chemistry for new catalytic cycles which will undoubtedly require new ligand designs. The lack of accessible two-electron redox couples results in no oxidative addition and reductive elimination chemistry. However, the RE metals are strong one-electron redox reagents and in recent years, there has been a dramatic increase in the number of isolable divalent REs. Such complexes exhibit novel redox chemistries and this, together with a drive to expand the number of isolable divalent RE complexes, represents exciting avenues for future developments.

9 RELATED ARTICLES

Aryls; Alkyl; Homogeneous Catalysis; The Electronic Structure of the Lanthanides; Variable Valency; Solvento Complexes of the Lanthanide Ions; Lanthanides: Coordination Chemistry; The Divalent State in Solid Rare Earth Metal Halides; Lanthanides: ''Comparison to 3d Metals''; Trivalent Chemistry: Cyclopentadienyl; Tetravalent Chemistry: Organometallic; Organic Synthesis.

10 GLOSSARY

Allyl: C_3H_5

α: Alpha

Å: Angstrom

Benzophenone: Ph_2CO

Benzyl: $C_6H_5CH_2-$

β: Beta

Bu^t: *tert*-butyl, $-C(CH_3)_3$

cm^{-1}: Wavenumber

CO: Carbon monoxide

Cyclopentadienyl: C_5H_5

Diethyl ether: $(CH_3CH_2)_2O$

DME: Dimethoxyethane, $CH_3OCH_2CH_2OCH_3$

1,4-Dioxane: $O(CH_2CH_2)_2O$

η: Eta

Et: Ethyl, CH_3CH_2-

Fac: Facially coordinated

Ferrocene: $[Fe(\eta^5\text{-}C_5H_5)_2]$

γ: Gamma

HSAB: Hard soft acid base

Ipso: 1-position of aryl rings

IR: Infrared

J: Joule

K: Kelvin

Me: Methyl, CH_3

MOCVD: Metal organic chemical vapor deposition

Mol: Mole

μ: Mu

MVS: Metal vapor synthesis

Ortho: 2-position of aryl rings

Neo-pentyl: $(CH_3)_3CCH_2-$

NHE: Normal hydrogen electrode

NMR: Nuclear magnetic resonance

Ph: Phenyl

pK_a: Acid dissociation constant

PMDETA: Pentamethyldiethylenetriamine

π*:* pi

Pr^n: Propyl, $CH_3CH_2CH_2-$

Pyridine: C_5H_5N

RE: Rare earth

σ*:* Sigma

σ^**:* Sigma antibonding

THF: Tetrahydrofuran, C_4H_8O

TMEDA: Tetramethylethylenediamine

11 ACKNOWLEDGMENTS

The author gratefully acknowledges the continued support of the Royal Society through a University Research Fellowship.

12 ABBREVIATIONS AND ACRONYMS

CAN = cerium ammonium nitrate; HSAB = hard soft acid base; IR = infrared; MOCVD = metal organic chemical vapor deposition; NMR = Nuclear magnetic resonance; RE = rare-earth; HSAB = hard soft acid base; Allyl = C_3H_5; α = Alpha; Å = Angstrom; Benzophenone = Ph_2CO; Benzyl = $C_6H_5CH_2-$; β = Beta; Bu^t = *tert*-butyl, $-C(CH_3)_3$; cm^{-1} = Wavenumber; CO = Carbon monoxide; Cyclopentadienyl = C_5H_5; Diethyl ether = $(CH_3CH_2)_2O$; DME = Dimethoxye- thane, $CH_3OCH_2CH_2OCH_3$; 1, 4 − Dioxane = $O(CH_2CH_2)_2O$; η = Eta; Et = Ethyl, CH_3CH_2-; *Fac* = Facially coordinated; Ferrocene = $[Fe(\eta^5\text{-}C_5H_5)_2]$; γ = Gamma; *Ipso* = 1-position of aryl rings; IR = Infrared; J = Joule; K = Kelvin; Me = Methyl, CH_3; Mol = Mole; μ = Mu; MVS = Metal vapor synthesis; *Ortho* = 2-position of aryl rings; *Neo*-pentyl = $(CH_3)_3CCH_2-$; NHE = Normal hydrogen electrode; Ph = Phenyl; pK_a = Acid dissociation constant; PMDETA = Pentamethyldiethylenetriamine; π = pi; Pr^n = Propyl, $CH_3CH_2CH_2-$; Pyridine = C_5H_5N; σ = Sigma; σ^* = Sigma antibonding; THF = Tetrahydrofuran, C_4H_8O; TMEDA = Tetramethylethylene-diamine; DME = appears to be clashing/not formatted.

13 REFERENCES

1. W. Muthmann and K. Kraft, *Liebigs Ann. Chem.*, 1902, **325**, 261.
2. F. O. Rice and K. K. Rice, 'The Aliphatic Free Radicals', The John Hopkins Press, Baltimore, MD, 1935.
3. V. M. Plets, *Dokl. Akad. Nauk. SSSR*, 1938, **20**, 27.
4. G. Wilkinson and J. M. Birmingham, *J. Am. Chem. Soc.*, 1954, **76**, 6210.
5. F. A. Hart and M. S. Saran, *J. Chem. Soc., Chem. Commun.*, 1968, 1614.
6. S. Cotton, 'Lanthanide and Actinide Chemistry', John Wiley & Sons, Chichester, 2006.
7. N. Kaltosyannis and P. Scott, 'The f Elements', Oxford University Press, Oxford, 1999.
8. T. J. Marks and R. D. Ernst, 'Comprehensive Organometallic Chemistry', eds. E. W. Abel, F. G. A. Stone, and G. Wilkinson, Pergamon Press, Oxford, 1982 Vol. 3, p. 173.
9. C. J. Schaverien, 'Advances in Organometallic Chemistry', eds F. G. A. Stone and R. West, Elsevier, 1994 Vol. 36, p. 283.
10. H. Schumann, J. A. Meese-Marktscheffel, and L. Esser, *Chem. Rev.*, 1995, **95**, 865.
11. S. Arndt and J. Okuda, *Chem. Rev.*, 2002, **102**, 1953.
12. W. J. Evans and B. L. Davis, *Chem. Rev.*, 2002, **102**, 2119.
13. F. T. Edelmann, *Angew. Chem. Int. Ed.*, 1995, **34**, 2466.
14. C. Eaborn, K. Izod, and J. D. Smith, *J. Organomet. Chem.*, 1995, **500**, 89.
15. W. J. Evans, *New J. Chem.*, 1995, **19**, 525.
16. M. P. Hogerheide, J. Boersma, and G. van Koten, *Coord. Chem. Rev.*, 1996, **155**, 87.
17. F. T. Edelmann, *Top. Curr. Chem.*, 1996, **179**, 113.
18. L. N. Zakharov and Y. T. Struchkov, *J. Organomet. Chem.*, 1997, **536–537**, 65.
19. S. A. Cotton, *Coord. Chem. Rev.*, 1997, **160**, 93.
20. F. Nief, *Coord. Chem. Rev.*, 1998, **178–180**, 13.
21. M. N. Bochkarev, *Russ. Chem. Rev.*, 2000, **69**, 783.
22. F. T. Edelmann, D. M. M. Freckmann, and H. Schumann, *Chem. Rev.*, 2002, **102**, 1851.
23. W. E. Piers and D. J. H. Emslie, *Coord. Chem. Rev.*, 2002, **233–234**, 131.
24. M. N. Bochkarev, *Chem. Rev.*, 2002, **102**, 2089.
25. N. Marques, A. Sella, and J. Takats, *Chem. Rev.*, 2002, **102**, 2137.
26. P. Mountford and B. D. Ward, *Chem. Commun.*, 2003, 1797.
27. P. M. Zeimentz, S. Arndt, B. R. Elvidge, and J. Okuda, *Chem. Rev.*, 2006, **106**, 2404.
28. T. Cantat, N. Mézailles, A. Auffrant, and P. Le Floch, *Dalton Trans.*, 2008, **15**, 1957.
29. S. T. Liddle, *Philos. Trans. R. Soc. London, Ser. A*, 2009, **465**, 1673.

30. F. T. Edelmann, *Chem. Soc. Rev.*, 2009, **38**, 2253.
31. P. L. Arnold and I. J. Casely, *Chem. Rev.*, 2009, **109**, 3599.
32. S. T. Liddle and D. P. Mills, *Dalton Trans.*, 2009, 5569.
33. M. Zimmermann and R. Anwander, *Chem. Rev.*, 2010, **110**, 6194.
34. J.-F. Carpentier, S. M. Guillaume, E. Kirillov, and Y. Sarazin, *Compt. Rend. Chim.*, 2010, **13**, 608.
35. S. T. Liddle, D. P. Mills, and A. J. Wooles, *Chem. Soc. Rev.*, 2011, **40**, 2164.
36. P. L. Watson and G. W. Parshall, *Acc. Chem. Res.*, 1985, **18**, 51.
37. F. T. Edelmann, *Top. Curr. Chem.*, 1996, **179**, 247.
38. G. A. Molander and J. A. C. Romero, *Chem. Rev.*, 2002, **102**, 2161.
39. S. Hong and T. J. Marks, *Acc. Chem. Res.*, 2004, **37**, 673.
40. C. J. Weiss and T. J. Marks, *Dalton Trans.*, 2010, **39**, 6576.
41. Y. K. Gun'ko and F. T. Edelmann, *Comments Inorg. Chem.*, 1997, **19**, 153.
42. J. Kido and Y. Okamoto, *Chem. Rev.*, 2002, **102**, 2357.
43. M. C. Cassani, Y. K. Gun'ko, P. B. Hitchcock, A. G. Hulkes, A. V. Khvostov, M. F. Lappert, and A. V. Protchenko, *J. Organomet. Chem.*, 2002, **647**, 71.
44. W. J. Evans, *J. Organomet. Chem.*, 2002, **647**, 2.
45. W. J. Evans, *J. Organomet. Chem.*, 2002, **652**, 61.
46. M. N. Bochkarev, *Coord. Chem. Rev.*, 2004, **248**, 835.
47. F. Nief, *Dalton Trans.*, 2010, **39**, 6589.
48. J. G. brennan, R. A. Andersen, and J. L. Robbins, *J. Am. Chem. Soc.*, 1986, **108**, 335.
49. J. Parry, E. Carmona, S. Coles, and M. Hursthouse, *J. Am. Chem. Soc.*, 1995, **117**, 2649.
50. W. J. Evans, S. A. Kozimor, G. W. Nyce, and J. W. Ziller, *J. Am. Chem. Soc.*, 2003, **125**, 13831.
51. R. K. Sheline and J. L. Slater, *Angew. Chem. Int. Ed.*, 1975, **14**, 309.
52. P. Selg, H. H. Brintzinger, M. Schultz, and R. A. Andersen, *Organometallics*, 2002, **21**, 3100.
53. L. Maron, L. Perrin, O. Eisenstein, and R. A. Andersen, *J. Am. Chem. Soc.*, 2002, **124**, 5614.
54. C. J. Burns and R. A. Andersen, *J. Am. Chem. Soc.*, 1987, **109**, 915.
55. C. Eaborn, P. B. Hitchcock, K. Izod, Z.-R. Lu, and J. D. Smith, *Organometallics*, 1996, **15**, 4783.
56. C. J. Burns and R. A. Andersen, *J. Am. Chem. Soc.*, 1987, **109**, 941.
57. F. A. Cotton and W. Schwotzer, *J. Am. Chem. Soc.*, 1986, **108**, 4657.
58. F. G. N. Cloke, *Chem. Soc. Rev.*, 1993, **22**, 17.
59. J. G. Brennan, F. G. N. Cloke, A. A. Sameh, and A. Zalkin, *J. Chem. Soc., Chem. Commun.*, 1987, 1668.
60. W. A. King, S. D. Bella, G. Lanza, K. Khan, D. J. Duncalf, F. G. N. Cloke, I. L. Fragala, and T. J. Marks, *J. Am. Chem. Soc.*, 1996, **118**, 627.
61. G. R. Giesbrecht and J. C. Gordon, *Dalton Trans.*, 2004, **16**, 2387.
62. H. Schumann and J. Müller, *J. Organomet. Chem.*, 1979, **169**, C1.
63. H. M. Dietrich, K. W. Törnroos, and R. Anwander, *J. Am. Chem. Soc.*, 2006, **128**, 9298.
64. E. Lu, Y. Li, and Y. Chen, *Chem. Commun.*, 2010, **46**, 4469.
65. S. P. Nolan, D. Stern, and T. J. Marks, *J. Am. Chem. Soc.*, 1989, **111**, 7844.
66. P. J. Davidson, M. F. Lappert, and R. Pearce, *Chem. Rev.*, 1976, **76**, 219.
67. A. J. Wooles, D. P. Mills, W. Lewis, A. J. Blake, and S. T. Liddle, *Dalton Trans.*, 2010, **39**, 500.
68. M. F. Lappert and R. Pearce, *J. Chem. Soc., Chem. Commun.*, 1973, 126.
69. H. Schumann, D. M. M. Freckmann, and S. Dechert, *Z. Anorg. Allg. Chem.*, 2002, **628**, 2422.
70. P. B. Hitchcock, M. F. Lappert, R. G. Smith, R. A. Bartlett, and P. P. Power, *J. Chem. Soc., Chem. Commun.*, 1988, 1007.
71. C. Eaborn, P. B. Hitchcock, and K. Izod, *J. Am. Chem. Soc.*, 1994, **116**, 12071.
72. J. A. C. Clyburne and N. McMullen, *Coord. Chem. Rev.*, 2000, **210**, 73.
73. R. Anwander and W. A. Herrmann, *Top. Curr. Chem.*, 1996, **179**, 2.
74. G. B. Deacon and C. M. Forsyth, *Organometallics*, 2003, **22**, 1349.
75. P. L. Arnold, F. G. N. Cloke, P. B. Hitchcock, and J. F. Nixon, *J. Am. Chem. Soc.*, 1996, **118**, 7630.
76. P. L. Watson, *J. Am. Chem. Soc.*, 1983, **105**, 6491.
77. M. E. Thompson, S. M. Baxter, A. R. Bulls, B. J. Burger, M. C. Nolan, B. D. Santarsiero, W. P. Schaefer, and J. E. Bercaw, *J. Am. Chem. Soc.*, 1987, **109**, 203.
78. J. Scott, H. Fan, B. F. Wicker, A. R. Fout, M.-H. Baik, and D. J. Mindiola, *J. Am. Chem. Soc.*, 2008, **130**, 14438.
79. R. Litlabø, M. Zimmermann, K. Saliu, J. Takats, K. W. Törnroos, and R. Anwander, *Angew. Chem. Int. Ed.*, 2008, **47**, 9560.
80. M. Fustier, X. F. Le Goff, P. Le Floch, and N. Mézailles, *J. Am. Chem. Soc.*, 2010, **132**, 13108.
81. D. P. Mills, L. Soutar, W. Lewis, A. J. Blake, and S. T. Liddle, *J. Am. Chem. Soc.*, 2010, **132**, 14379.
82. M. R. MacDonald, J. W. Ziller, and W. J. Evans, *J. Am. Chem. Soc.*, 2011, **133**, 15915.
83. M. R. MacDonald, J. E.Bates, M. E.Fieser, J. W.Ziller, F. Furche, and W. J. Evans, *J. Am. Chem. Soc.*, 2012, **134**, 8420.
84. W. Clegg, C. Eaborn, K. Izod, P. O'Shaughnessy, and J. D. Smith, *Angew. Chem. Int. Ed.*, 1997, **36**, 2815.

85. W. J. Evans, T. A. Ulibarri, and J. W. Ziller, *J. Am. Chem. Soc.*, 1988, **110**, 6877.

86. W. J. Evans, J. W. Grate, L. A. Hughes, H. Zhang, and J. L. Atwood, *J. Am. Chem. Soc.*, 1985, **107**, 3728.

87. W. J. Evans, L. A. Hughes, D. K. Drummond, H. Zhang, and J. L. Atwood, *J. Am. Chem. Soc.*, 1986, **108**, 1722.

88. M. Fang, J. H. Farnaby, J. W. Ziller, J. E. Bates, F. Furche, and W. J. Evans, *J. Am. Chem. Soc.*, 2012, **134**, 6064.

Lanthanides: ‘‘Comparison to 3d Metals’’

Simon A. Cotton

University of Birmingham, Birmingham, UK

1	Summary	105
2	Introduction	105
3	Reactivity of the Elements	105
4	Oxidation States	105
5	Coordination Numbers in Complexes	106
6	Organometallic Compounds	106
7	Electronic Properties	107
8	Electronic Spectra	107
9	Magnetic Properties	108
10	Conclusions	108
11	End Notes	108
12	Related Articles	108
13	Abbreviations and Acronyms	108
14	Further Reading	108
15	References	109

1 SUMMARY

Although lanthanides share certain characteristics with elements such as the 3d metals in the form of a detailed coordination chemistry, and numerous coloured compounds, there are very significant differences between lanthanides and the lighter transition elements. Not only are the lanthanides significantly the more electropositive metals but their chemistry, particularly in aqueous solution, is primarily that of the (+3) oxidation state and their complexes are more labile. Their developing organometallic chemistry lacks the compounds with π-acceptor ligands familiar from the 3d metals. These differences originate primarily in the nature of the 4f orbitals, occupied by electrons that are well shielded from surrounding ligands, with which they have little interaction, notably an inability to form π-bonds with oxygen or other ligands, which could stabilize both high and low oxidation states.

2 INTRODUCTION

At first sight of the Periodic Table, lanthanides form a slightly longer version of the d-block elements, an impression perhaps reinforced by the sight of coloured aqua ions and complexes of metals such as praseodymium or erbium. In fact, the 4f and 3d metals have many points of difference.

3 REACTIVITY OF THE ELEMENTS

Lanthanides readily tarnish in air, reacting slowly with cold water and rapidly with dilute acid. The reactivity of the elements is greater than that of the transition metals, akin to the Group II metals. Typical reduction potentials are:- $-E^{o}Sc^{3+}/Sc = -2.03$ V; $E^{o}Y^{3+}/Y = -2.37$ V; $E^{o}La^{3+}/La = -2.38$ V; and $E^{o}Lu^{3+}/Lu = -2.30$ V. These may be compared with $E^{o}Ca^{2+}/Ca = -2.87$ V and $E^{o}Mg^{2+}/Mg = -2.37$ V for Group II metals, and with values for 3d transition elements of $E^{o}V^{2+}/V = -1.13$ V; $E^{o}Fe^{2+}/Fe = -0.44$ V; and $E^{o}Cu^{2+}/Cu = +0.34$ V.[1]

4 OXIDATION STATES

A significant difference between the lanthanides and the 3d metals lies in the oxidation states adopted. In

The Rare Earth Elements. Edited by David A. Atwood. © 2012 John Wiley & Sons, Ltd. ISBN 978-1-119-95097-4

comparison with the transition metals, even those of the 3d series, lanthanides exhibit a greatly reduced range of oxidation states. In aqueous solution, the most stable ion for all lanthanides is the $Ln^{3+}(aq)$ ion, with the $Eu^{2+}(aq)$ ion the only other aqua ion at all long-lived (in the absence of air), apart from cerium(IV) whose aqua ion is thermodynamically unstable. Within the 3d series in contrast, manganese exhibits oxidation states in aqueous solution from +2 to +7, ranging from $Mn^{2+}(aq)$ to $MnO_4^-(aq)$. Likewise, iron forms both $Fe^{2+}(aq)$ and $Fe^{3+}(aq)$ as well as the FeO_4^{2-} ion.[2,3] Lanthanides do not form these ''high-valent'' oxy species analogous to CrO_4^{2-}, MnO_4^-, and $FeO_4{}^{2-}$, owing to their unwillingness to form multiple bonds such as Ln=O, reflecting the contracted nature of 4f orbitals and their nonavailability to participate in Ln–O π bonds. Of course, several early actinides do form such bonds, best exemplified by the uranyl ion $UO_2{}^{2+}$, reflecting the greater radial extension of uranium 5f (or 6d) orbitals.[4,5]

The pattern with the early transition metals—in the 3d series up to Mn, and for the 4d, 5d metals up to Ru and Os—is that the maximum oxidation state corresponds to the number of ''outer shell'' electrons. There is no trace of this behavior for lanthanides. The highest oxidation states of the 3d metals may depend upon complex formation (e.g., the stabilization of Co^{3+} by ammonia) or upon the pH (thus $MnO_4^{2-}(aq)$ is prone to disproportionation in acidic solution). Within the 3d series, there is considerable variation in relative stability of oxidation states, sometimes on moving from one metal to a neighbor; thus, for iron, Fe^{3+} is more stable than Fe^{2+}, especially in alkaline conditions, while the reverse is true for cobalt.

The ability of transition metals to exhibit a wide range of oxidation states is marked with metals such as vanadium, where the standard potentials can be rather small, making a switch between states relatively easy. Thus successive reduction potentials of vanadium (values for acidic solution) are: $-VO_2^+ + e \rightarrow VO^{2+}(E = 1.0V)$; $VO^{2+} + e \rightarrow V^{3+}(E = 0.337V)$; $V^{3+} + e \rightarrow V^{2+}(E = -0.255V)$. In contrast, for lanthanides, the reduction potentials for $Ln^{3+} + e \rightarrow Ln^{2+}$ are greater than −2.3 V, except for Eu (−0.34 V); Sm (−1.55 V); and Yb (−1.05 V); similarly all the potentials for $Ln^{4+} + e \rightarrow Ln^{3+}$ are greater than + 3.3 V, except for cerium (+1.7 V). These are the only lanthanides with any tendency to adopt other oxidation states in their aqueous chemistry.

The consistent adoption of the (+3) state as the stable one for the lanthanides can be contrasted with the 3d series, as here the heaviest stable triiodide is MnI_3, and there is no stable M^{3+} aqua ion after $[Fe(H_2O)_6]^{3+}$. This can be correlated with the much sharper increase in the value of the third ionization energy, I_3, on traversing the 3d series as compared with crossing the 4f series, which favors the adoption of the (+2) state for the later 3d elements.[6]

5 COORDINATION NUMBERS IN COMPLEXES

In comparison with the 3d metals, lanthanides exhibit a much greater range of coordination numbers in their compounds. On grounds of size alone, it would be expected that coordination numbers would be greater for lanthanides than for the 3d metals, but typical values lie between 6 and 12, but with values of 3 and 4 when some bulky groups such as $-N(SiMe_3)_2$ and $-CH(SiMe_3)_2$ are used. In contrast, the norm for the 3d metals is 4–6, but with cases known of 3 (and very rarely 2).[7]

In general and without exception as a function of f^n electron configuration, lanthanides form labile ''ionic'' complexes that undergo facile exchange of ligand. With transition metals, the lability of complexes varies with electron configuration; some being labile, some kinetically very inert, such as d^3 species exemplified by $[Cr(H_2O)_6]^{3+}$ and low-spin d^6 species exemplified by $[Co(NH_3)_6]^{3+}$ with high crystal field stabilization energies and correspondingly high activation energies for ligand substitution. However, using multidentate ligands, such as the polyamino carboxylic acid H_5dtpa (diethylene triamine pentaacetic acid) or the tetracarboxylic acid H_4dota (1,4,7,10-tetraazacyclododecane-1,4,7,10-tetraacetic acid), affords very stable complexes of the lanthanides with particularly high stability constants; this is of particular importance in magnetic resonance imaging (MRI) agents, where the presence of free $Gd^{3+}(aq)$ is to be avoided. One consequence of the lability of simple lanthanide complexes is the extreme rarity of isomerism, in contrast to transition metals, where isomers of cobalt(III) complexes helped Werner establish his coordination theory. Thus two isomers exist for the compound with the formula $CoCl_3 \cdot 4\,NH_3$, one containing violet *cis*-$[CoCl_2(NH_3)_4]^+$ ions, the other green *trans*-$[CoCl_2(NH_3)_4]^+$ ions. Likewise, $[CoCl_2en_2]^+$ has cis/trans isomers, while the optical isomers of $[Coen_3]^{3+}$ can be isolated. However, both *fac*- and *mer*- complexes have been authenticated[8] for $[LnCl_3(hmpa)_3]$ (hmpa = $(OP(NMe_2)_3)$, with a reversible *fac*–*mer* isomerization (via an associative mechanism) observable by variable temperature ^1H NMR spectroscopy.[a]

6 ORGANOMETALLIC COMPOUNDS

The lanthanides are now known to have a rich and developing organometallic chemistry in normal oxidation states, but in comparison with the transition metals, these compounds tend to have greater sensitivity to traces of oxygen and moisture. In general, there are very few or none of the compounds with familiar π-acceptor ligands (e.g., CO, NO^+, RNC, N_2). In the case of transition metal organometallics featuring π-acceptor ligands, the 18-electron rule (effective atomic number rule) applies. For a 3d metal, use of the 4s, 4p, and 3d orbitals means that 9 orbitals are available for bonding,

corresponding to 18 electrons; these are supplied by the metal and the associated ligands. Thus, many stable compounds such as $[Cr(CO)_6]$, $[Fe(CO)_5]$, $[Ni(PF_3)_4]$, and $[Fe(C_5H_5)_2]$ exemplify this rule, which can be extended to polynuclear compounds. Contrastingly, in the case of lanthanides, formulae and coordination numbers are primarily dictated by steric effects.

A particular difference lies in the organometallic chemistry in low oxidation states. Transition metals form stable binary carbonyls—for example, $Fe(CO)_5$ and $Ni(CO)_4$ are volatile liquids, stable at elevated temperatures, and $Os_3(CO)_{12}$ decomposes at 190 °C to other carbonyls such as $Os_6(CO)_{18}$. In contrast, lanthanide carbonyls, prepared by cocondensation of lanthanide atoms with Ar/CO mixtures at 4.2 K, are only stable at these very low temperatures, decomposing above 20 K.[9] The ability of metals in the middle of the d block to form carbonyls is related to their possessing vacant d orbitals that can accept electron pairs from the σ-donor CO ligand, and also some filled d orbitals that can participate in π back-donations (back-bonding). In fact, CO is not a strong enough σ-donor to bind well to lanthanides, and the lanthanide 4f orbitals are not suitable to π-bond to carbon monoxide. Molecular orbital (MO) calculations indicate that the bonds in these compounds are very weak indeed.[10]

A more stable and defined family of zerovalent compounds is provided by the bis(tri-*tert*-butylbenzene) compounds $[Ln(\eta^6\text{-}C_6H_3\text{-}^tBu_3\text{-}1,3,5)_2]$ (Ln = Y, Nd, Gd, Tb, Dy, Ho, Er, and Lu), synthesized by codeposition of lanthanide vapor and tri-*tert*-butylbenzene onto a surface at 77 K.[11] For these metals, the compounds are stable enough to be sublimed at 100 °C in vacuo; other lanthanides form less-stable compounds. Attempts to form similar compounds between yttrium and less-hindered arenes such as toluene and mesitylene give extremely unstable products, suggesting that the stability of $[Ln(\eta^6\text{-}C_6H_3\text{-}^tBu_3\text{-}1,3,5)_2]$ is due to the bulk of the substituted arene ligand, as well as to the inductive effect of the *t*-butyl groups causing an increase in the strength of the metal–arene bond.[12] Metal–ligand bond disruption enthalpies have been measured for $[Ln(\eta^6\text{-}C_6H_3\text{-}^tBu_3\text{-}1,3,5)_2]$ (Ln = Y, Gd, Dy, Ho, Er) and fall in the range 47–72 kcal mol^{-1}, closely comparable with the values for $[Cr(\eta^6\text{-}C_6H_6)_2]$, $[Cr(\eta^6\text{-}C_6H_5Et)_2]$, $[Cr(\eta^6\text{-}C_6H_3Me_3)_2]$, $[Mo(\eta^6\text{-}C_6H_6)_2]$, and $[W(\eta^6\text{-}C_6H_5Me)_2]$. Some similar zerovalent compounds with heteroarenes, such as $[Ho(\eta\text{-}PC_5H_2Bu^t{}_3\text{-}2,4,6)_2]$, have also been made.[13,14] As far as 3d metals are concerned, these compounds may be contrasted with di(benzene)chromium, which, though air sensitive, is stable to high temperatures (melting point 284 °C). $[Cr(\eta^6\text{-}C_6H_6)_2]$ obeys the 18-electron rule, and similar compounds are not obtained with the metals to either side.

As already noted, unlike the 3d metals (and, indeed early actinides), lanthanides do not form Ln = O or Ln ≡ N multiple bonds, so that they do not yield analogs to the rich vein of species exemplified by MnO_4^-, CrO_4^{2-}, or $Cr_2O_7^{2-}$; *cis*-$[MoO_2]^{2+}$, *trans*-$[OsO_2]^{2+}$, or *trans*-$[UO_2]^{2+}$; and $[ReNCl_2(PEt_2Ph)_3]$ or $[OsNCl_4]^-$. This is generally attributed to the inability of electrons in the contracted and core-like lanthanide 4f orbitals to participate in the bonding, supported by a density functional theory (DFT) study of the silylamides $[Ln\{N(SiMe_3)_2\}_3]$. Calculations upon $[Ce(h^5\text{-}C_5H_5)_3]$ and its Th analog indicated that in $[Ce(h^5\text{-}C_5H_5)_3]$, the 4f-based MOs were little changed from those of free Ce^{III}.[15–17]

7 ELECTRONIC PROPERTIES

The optical and magnetic properties of lanthanide ions are very different to those of the 3d transition metals. The 4f electrons are well shielded by the $5s^2$ and $5p^6$ orbitals, so that these electrons are largely uninvolved in bonding. Shielding from ligands means that there is no quenching of the orbital moment and their spectroscopic and magnetic properties are thus largely uninfluenced by the ligand.[18–21]

8 ELECTRONIC SPECTRA

Many of the lanthanide(III) ions in solution are so weakly coloured as to appear colourless, the three principal exceptions being Pr^{3+}, Nd^{3+}, and Er^{3+}. In comparison with the d–d transitions in the electronic spectra of complexes of the 3d metals, lanthanide complexes have much weaker f–f transitions. Thus extinction coefficients in the spectra of the octahedral $[Co(H_2O)_6]^{2+}$ ion are ~5, while values for tetrahedral complexes such as $[CoCl_4]^{2-}$ often exceed 500. Contrasting values for Pr^{3+}(aq) ion are of the region of 0.1. Both d–d and f–f transitions are Laporte forbidden, but can acquire intensity through vibrational interactions introducing p or d character into the transitions respectively. However, because of the contracted nature of the 4f orbitals, f electrons are only weakly perturbed by their ligands, so lanthanide ions are less successful in this mechanism than ions of the 3d metals. These vibrations are also responsible for broadening the absorption lines; this is again less marked for the lanthanides. The absorptions due to f–f transitions are much sharper than the absorptions in the spectra of 3d complex ions.

The crystal field splitting of f orbitals is around $1/100^{th}$ that of d orbitals. This means that the position and intensity of the absorption lines are also very weakly affected by ligands, in contrast with complexes of a given transition metal, such as nickel, where the change in colour from green to violet as H_2O molecules are replaced by NH_3 on adding ammonia to $[Ni(H_2O)_6]^{2+}$ is clearly visible to the naked eye. In a few cases, notably Nd^{3+}, certain transitions are influenced by ligand and environment (the ''hypersensitive transitions''),

showing small shifts in their position and variations in splitting and intensity, but these are altogether exceptional.

9 MAGNETIC PROPERTIES

For the transition metals of the 3d series, magnetic moments are given by the expression $\mu = [4S(S+1) + L(L+1)]^{1/2}$, where S is the total spin quantum number and L the total orbital momentum quantum number. In practice for these metals, the orbital angular momentum is frequently quenched by the crystal field, so that only spin orbital momentum need be considered, and the expression reduces to $\mu = [4S(S+1)]^{1/2}$, or $\mu = [n(n+2)]^{1/2}$ where n is the number of unpaired electrons, the so-called spin-only formula. However, in those cases where an orbital contribution to the moment is possible, there can be considerable variation in magnetic moment, even for a given ion. Thus high-spin complexes of Co^{2+} have magnetic moments μ_{eff} greater than the spin-only value of 3.87 μ_B, covering a range of 4.3 to 5.2 μ_B, with tetrahedral complexes often having values of 4.3 to 4.8 μ_B, and octahedral complexes tending to have a greater orbital contribution and frequently having μ_{eff} values of 4.8 to 5.2 μ_B at room temperature, thus sometimes permitting diagnosis of geometry. Complexes of Fe^{3+} can have μ_{eff} values $\sim 2\mu_B$ or 5.9 μ_B, depending upon whether the complex is high or low spin.

In contrast to the transition metals, which have weak spin–orbit coupling and strong ligand-field splitting, lanthanides have strong spin–orbit coupling but weak ligand-field effects. In the case of lanthanides, the magnetic properties are described using the Russell–Saunders coupling scheme. Magnetic moments are given by the expression $\mu = g_J[J(J+1)]^{1/2}$, where $g_J = 1 + [(S(S+1) + J(J+1) - L(L+1)/2J(J+1)]$. $J = (L+S)$ for a shell more than half-filled and $J = (L-S)$ for a shell less than half-filled.[22]

In general, the strong spin–orbit coupling means that excited states are well above the ground state, so that the properties of the ground state are usually an accurate representation of the magnetic behavior of lanthanide ions. Magnetic moments are also independent of the coordination environment, so that deductions of the type sometimes made about the geometry of Co^{II} complexes are not possible. In the cases of Sm^{III} and Eu^{III} compounds, there are low-lying excited states that are thermally accessible at room temperature. Thus the $^7F_0$ ground state of Eu^{3+} is diamagnetic, but contributions from the $^7F_1$ and $^7F_2$ states lead to moments of around 3.5 μ_B at room temperature. A similar effect is observed for samarium, where contributions from the $^6H_{7/2}$ excited state cause room temperature moments to be greater than those expected from a $^6H_{7/2}$ ground state. This effect also means that the moments of Sm^{III} and Eu^{III} compounds are temperature dependent, decreasing on cooling.

10 CONCLUSIONS

There are similarities between the 3d and 4f metals arising from their metallic nature; the differences can usually be traced to the profoundly different character of electrons in 3d orbitals, which are more free to interact with the groups bound to the metal, and those in 4f orbitals which are shielded by the electrons in 5s and 5p orbitals. Nevertheless, the lanthanides have provided many surprises as their chemistry has unfolded, in the past half century in particular, and much remains to be discovered.

11 END NOTES

[a.] This is discussed in more detail in ''Coordination Chemistry'' (***Lanthanides: Coordination Chemistry***).

12 RELATED ARTICLES

Lanthanides: Coordination Chemistry; Organometallic Chemistry Fundamental Properties; Tetravalent Chemistry: Inorganic; Variable Valency.

13 ABBREVIATIONS AND ACRONYMS

DFT = density functional theory; MO = molecular orbital; MRI = magnetic resonance imaging.

14 FURTHER READING

H. C. Aspinall, 'Chemistry of the f-Block Elements', CRC Press (Gordon and Breach), Amsterdam, 2001, esp. p. 15, 33, 61, 109.

J.-C. G. Bünzli and G. R. Choppin, 'Lanthanide Probes in Life, Chemical and Earth Sciences: Theory and Practice', Elsevier, Amsterdam, 1989.

S. A. Cotton, 'Lanthanide and Actinide Chemistry', John Wiley & Sons, Chichester, 2006, esp. p. 9, 35, 61, 89, 105.

N. Kaltsoyannis and P. Scott, 'The f Elements (Oxford Chemistry Primers)', Oxford University Press, Oxford, 1999, esp. p. 21, 30, 46, 68.

R. Saez and P. Caro, 'Rare Earths', Editorial Complutense, Madrid, 1998, esp. p. 43, 223.

15 REFERENCES

1. A. J. Bard, R. Parsons, and J. Jordan, 'Standard Potentials in Aqueous Solutions', IUPAC (Marcel Dekker), New York, 1985.
2. S. Riedel and M. Kaupp, *Coord. Chem. Rev.*, 2009, **253**, 606.
3. D. A. Johnson, 'Some Thermodynamic Aspects of Inorganic Chemistry', 2nd edition, Cambridge, Cambridge University Press, 1982, p. 158.
4. K. G. Dyall, *Chem. Phys.*, 2005, **311**, 19.
5. N. Kaltsoyannis, *Inorg. Chem.*, 2000, **39**, 6009.
6. D. W. Smith, 'Inorganic Substances', Cambridge, Cambridge University Press, 1990, esp. 145, p. 163.
7. S. A. Cotton, *C. R. Chim.*, 2005, **8**, 129.
8. S. Petriček, A. Demšar, L. Golič, and J. Košmrlj, *Polyhedron*, 2000, **19**, 199.
9. R. K. Sheline and J. L. Slater, *Angew. Chem. Int. Ed.*, 1975, **14**, 309.
10. E. A. Boudreaux, *Int. J. Quantum Chem.*, 1996, **60**, 1673.
11. F. G. N. Cloke, *Chem. Soc. Rev.*, 1993, **22**, 17.
12. P. L. Arnold, F. G. N. Cloke, and P. B. Hitchcock, *Chem. Commun.*, 1997, 481.
13. P. L. Arnold, M. A. Petrukhina, V. E. Bochenkov, T. I. Shabatina, V. V. Zagorskii, G. B. Sergeev, and F. G. N. Cloke, *J. Organomet. Chem.*, 2003, **688**, 49.
14. W. A. King, T. J. Marks, D. M. Anderson, D. J. Duncalf, and F. G. N. Cloke, *J. Am. Chem. Soc.*, 1992, **114**, 9221.
15. L. Maron and O. Eisenstein, *J. Phys. Chem. A*, 2000, **104**, 7140.
16. M. Dolg and H. Stoll, 'Handbook of the Physics and Chemistry of Rare Earths', Elsevier Science, Amsterdam, 1996, Vol. 22, p. 607.
17. N. Kaltsoyannis and B. E. Bursten, *J. Organomet. Chem.*, 1997, **528**, 19.
18. D. Nicholls, 'Complexes and First-Row Transition Elements', Macmillan, Basingstoke, 1974.
19. S. F. A. Kettle, 'Physical Inorganic Chemistry: A Coordination Chemistry Approach', Oxford University Press, Oxford, 1998.
20. B. N. Figgis and M. A. Hitchman, 'Ligand Field Theory and Its Applications', Wiley-VCH, New York, 2000.
21. J.-C. G. Bünzli and G. R. Choppin, 'Lanthanide Probes in Life, Chemical, and Earth Sciences: Theory and Practice', Elsevier, Amsterdam, 1989.
22. N. Kaltsoyannis and P. Scott, 'The f Elements (Oxford Chemistry Primers)', Oxford University Press, Oxford, 1999, p. 30.

Luminescence

Julien Andres and Anne-Sophie Chauvin

École Polytechnique Fédérale de Lausanne, Vaud, Switzerland

1 Summary 111
2 Introduction 111
3 Electronic Structure of the f-Elements 112
4 Interaction of Light with Matter 117
5 Luminescence 123
6 Conclusions 131
7 Glossary 132
8 Related Articles 132
9 End Notes 132
10 Abbreviations and Acronyms 133
11 Further Readings 133
12 References 133

1 SUMMARY

At the end of this chapter, the reader should be able to describe the basic principles and the mechanisms responsible for the emission from a lanthanide ion. Because lanthanide ions are poorly absorbing compounds, many interesting luminescent lanthanide compounds are also made of strong light-harvesting organic molecules (ligands) that will absorb light and sensitize the lanthanide ion. The key concepts to understand both the ligand-centered properties and the lanthanide-centered properties are presented here. The general idea was to start from basic photophysics that is commonly related to organic molecules and then to expand those concepts toward the photophysics of the lanthanide ions. In this way, the reader should be able to understand not only how lanthanide ions emit light but also why lanthanides are so special emitters.

In a first part, all the concepts needed to understand the luminescence of lanthanides are clarified. It encloses a brief overview or summary of the electronic structure of 4f-elements that then extend toward the absorption of light, the formation of excited states, and the emission of light, in other words, the luminescence phenomena. Notions such as fluorescence, phosphorescence, sensitization, and charge transfer (CT) are detailed. Again, the intent is to provide the reader with the essential tools to understand and develop photophysical systems, and then apply these fundamental notions to the particular case of the lanthanide ions. Quantum mechanics is avoided as much as possible (the mathematical description that often scares the reader). We have chosen to simplify quantum mechanics by showing what the results often found in textbooks may imply in a concrete manner. Those simplifications are not intended to represent the true nature of the physical world, but we believe them to be as good as the fancy equations from which they are inspired. To support them and help clarify basic notions, physics remainders are given. Finally, the photophysics is developed using rate equations similar to the description of chemical dynamics (or kinetics).

2 INTRODUCTION

2.1 A Brief History of Luminescence

Luminescence is a general term introduced in 1888 by Eilhard Wiedemann, a German physicist and historian. It originated from the Latin ‘‘lumen’’ (light) and expresses the emission of light from ‘‘cold matter.’’ It has to be distinguished from incandescence, which expresses the emission of light from ‘‘hot matter’’ (with $T > 800\,^{\circ}\mathrm{C}$, also known as black body radiation). The light emitted from the sun or from a

The Rare Earth Elements. Edited by David A. Atwood. © 2012 John Wiley & Sons, Ltd. ISBN 978-1-119-95097-4

tungsten light bulb is thus not considered as a luminescent emission, but as an incandescent emission.

Luminescence includes phenomena such as fluorescence and phosphorescence. It comes from the radiative deactivation of excited matter following an excitation (the mechanism of the excitation, as well as fluorescence and phosphorescence is explained below). The excitation can come from light (photoluminescence), electricity (electroluminescence), a chemical reaction (chemoluminescence or bioluminescence, if the reaction takes place in a biological system), or a mechanical stress (triboluminescence). We focus on photoluminescence, because most of the other excitation sources require special conditions and are, with the exception of electroluminescence, quite rare, especially when dealing with the luminescence of the lanthanides.

Luminescent materials have been observed in nature since ancient times. The obvious example is glow-in-the-dark minerals or phosphors as they were called at that time (from the Greek ''$\varphi\omega\sigma\varphi\acute{o}\rho o\varsigma$'' meaning bearer of light). Other luminescent materials were also observed, but not identified as light carriers because the luminescence does not carry on after the excitation. For example, some plant infusions were identified by their particular bluish tint when exposed to sunlight, which is nowadays known to be a blue emission from a fluorescent organic compound absorbing some of the ultraviolet (UV) light of sunlight. Back then, no purely UV light source (black light) was known, so that the luminescence was only identified as a special color property in sunlight. The oldest accounts for luminescent materials can be traced back to the sixteenth century, but the scientific investigation of luminescence phenomena began in the nineteenth century with the English physicist Sir George Gabriel Stokes (1819–1903) and the French physicist Edmond Becquerel (1820–1891). For more details on the history of luminescence, see the article of Valeur and Berberan.[1]

2.2 Nowadays Omnipresence of Luminescent Materials

Currently, luminescent materials are ever-present in modern life. From lighting applications, to color displays, optical brightener for a washing powder, a paper or a detergent, security markings, highlighter pens, embedded in plastics, textiles, watches, and banknotes among other things. Luminescent materials based on lanthanide compounds are present in many of those examples. Among the numerous examples to be mentioned, one can cite organic light emitting diode (OLED), cathode ray tube (CRT), and plasma displays, fluorescent light bulbs, security inks for banknotes, lasers for surgery, or new medical analysis that are based on luminescence bioassays.

2.3 Lanthanide Elements

The lanthanide or lanthanoid series is composed of 15 elements with atomic numbers ranging from 57 to 71. They have very close chemical properties with scandium and yttrium and the whole series is often referred as rare earth elements, since lanthanides were historically isolated from uncommon oxide-type minerals. However this term is not totally adequate, the lanthanides are not to be considered as rare, because even a scarce 4f-element such as lutetium is more abundant than silver (see ***Geology, Geochemistry, and Natural Abundances of the Rare Earth Elements***).

2.4 Separation and Purification of Lanthanides

The separation of the different lanthanides from their mineral source took more than a hundred years. The difficulty to extract and characterize each different lanthanide ion is due to the chemical similarity of these ions. Even though having similar chemical properties make them hard to be distinguished within the series, each lanthanide is well defined by its spectroscopic properties. The introduction of spectroscopy in the mid-nineteenth century was then essential for the discovery of the new elements and the luminescence of these ions was important for the development of many technological applications derived from luminescent materials.

3 ELECTRONIC STRUCTURE OF THE f-ELEMENTS

3.1 Atomic Orbitals

When an electron is trapped around a nucleus, a quantization of its energy and therefore of many of its physical quantities occurs. As a result, the electron cannot be found anywhere around the nucleus, but has to be located in quantized spaces. An atomic orbital (AO) is a quantized volume of space around the nucleus in which the probability of presence of the electron is more than 90%. Inside an orbital, the electron has defined properties such as a defined energy and a defined angular momentum[a]. As a consequence, the idea that an orbital has a defined energy and angular momentum is often encountered, even though it is the electron which it encloses that possesses this property.

The shapes of those orbitals were calculated for the hydrogen atom (by solving the so-called time-independent Schrödinger equation). For polyelectronic atoms, because the calculation is too complex to yield an exact solution, the solutions of the hydrogen atom are used as approximations of the orbitals. Owing to this approximation, the AOs are usually called hydrogenoid orbitals.

The hydrogenoid orbitals have precise shapes that depend on the level of quantization of the angular momentum of the electron inside those orbitals. The angular momentum is a vector quantity. The quantization of a vector quantity is dual: its intensity is quantized (takes noncontinuous absolute values), and its direction in space is quantized (takes noncontinuous orientation in space). The orbitals inside which

the electrons have the same intensity of their angular momenta can be grouped together in a structure called a *subshell*. In a subshell, the angular momenta of the electrons are then simply pointing toward different directions with the same absolute intensity.

Looking at the subshell electronic structure of the atom, subshells can be grouped together according to their size. An orbital, and thus a subshell extend from the nucleus to a certain distance. This distance is finite and quantized, so that the increase in this maximal distance to the nucleus is not continuous, but takes discrete values. The subshells that expend up to a same distance are said to be in a same shell. It is important to understand that this layered structure of the atom only arises because no electron can have all its quantized physical quantities that are exactly the same as another electron in the same atom. We say that each electron in an atom must have its own quantum state. This crucial law of nature is known as the *Pauli exclusion principle*. Such an electronic quantum state can be described by quantum mechanics using four quantum numbers (n, ℓ, m_ℓ, and m_s) that fully characterize all the quantized physical properties of the electrons within the atom.

The principal quantum number n defines the shell into which the electron is located ($n = 1, 2, 3, \ldots$). The electrons in a same shell are all contained in a sphere between the nucleus and a threshold distance (the radius of the sphere) defined by the extent of n. An electron in a higher n shell is, in average, further away from the nucleus than it is in a lower shell.

The azimuthal quantum number ℓ defines the subshells in a shell that are associated with the orbital angular momentum of the electron ($\ell = 0, 1, \ldots, n-1$). All the electrons in an ℓ subshell have an orbital angular momentum of the same intensity. The intensity of the angular momentum is defined by $\sqrt{\ell(\ell+1)}$. The subshells are represented with the letters s, p, d, f, g, h, etc. that correspond to the values of $\ell = 0, 1, 2, 3, 4, 5$, etc. respectively.

The magnetic quantum number m_ℓ defines the orbitals in a subshell and arises because of the space quantization of the angular momentum ($m_\ell = -\ell, -\ell+1, \ldots, 0, \ldots, \ell-1, \ell$). This means that the angular momentum cannot point toward any directions, but is restricted to a few angles around the nucleus. The m_ℓ values then represent orbitals pointing toward different directions. Inside an ℓ subshell, there are $2{\cdot}\ell{+}1 m_\ell$ values and therefore, $2{\cdot}\ell{+}1$ orbitals. The electrons inside any of those orbitals have an angular momentum whose intensity is identical to any other electron in the same subshell (with the same ℓ). Nevertheless, each angular momentum vector $\boldsymbol{\ell}$ points toward different directions. Those directions are quantized and translate into quantized projections of the angular momenta onto an arbitrary direction (for example, on the z axis).

In summary, the n, ℓ, and m_ℓ quantum numbers are defining the size, the shape, and the orientation in space of the AOs, respectively. In addition to those three quantum numbers, the spin quantum number s defines the intrinsic angular momentum of the electron ($s = \frac{1}{2}$). This spin quantum number is an intrinsic property of the electron. Similar to the orbital angular momentum ℓ, the spin angular momentum s has quantized projections onto an arbitrary direction (for example, on the z axis), which is commonly represented as spin-up and spin-down with up and down arrows ($m_s = -\frac{1}{2}, +\frac{1}{2}$). The m_s value is the fourth quantum number of the electron (the s quantum number is fixed anyway to a single value). Because of this spin quantization value, the Pauli exclusion principle allows two electrons with opposite spins (opposite m_s values) in the same orbital (i.e., with the first three quantum numbers that are identical).

3.2 f Atomic Orbitals

The lanthanides are f-elements and the lanthanide ions have all their valence electrons that fill 4f orbitals. The f orbitals are depicted in Figure 1. There are seven f orbitals; each can accept two electrons with an opposite spin. Electrons in the 4f subshell have their principal quantum number $n = 4$, their azimuthal quantum number $\ell = 3$, can have their

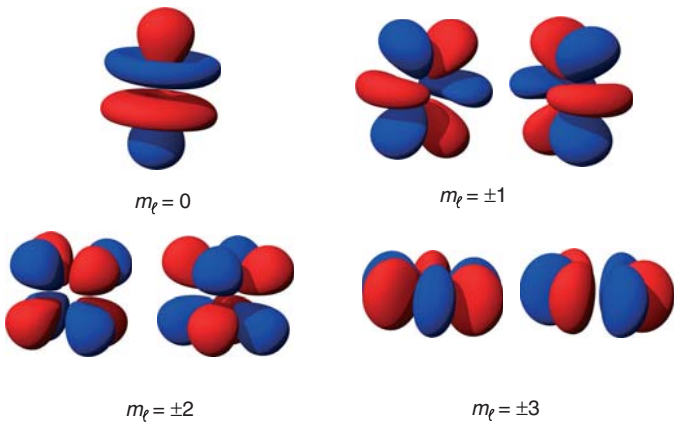


Figure 1 3D representation of the seven f orbitals associated with the seven *ml* quantum numbers. (Images from Wikipedia, 2012.)

magnetic quantum number $m_\ell = -3, -2, -1, 0, +1, +2, +3$ depending on the orbital into which they are located, and because their spin is fixed by nature as $s = \frac{1}{2}$, they can have either $m_s = -\frac{1}{2}$ or $m_s = +\frac{1}{2}$.

The lanthanide elements differ from the main group elements and the transition metals because of the nature of the 4f orbitals, which are shielded by the presence of the $5s^2$ and $5p^6$ electrons (the Xe core). Consequently, 4f electrons possess the interesting characteristic to be inner electrons, i.e., they are closer to the nucleus than the electrons in the 5s and 5p orbitals. This exceptional property fairly screens the 4f electrons from the exterior, so that they are very few affected by the chemical environment. This is the reason why the chemical properties of the series are closely similar, with the exception of the so-called lanthanide contraction (see ***The Electronic Structure of the Lanthanides***).

Finally, note that lanthanides are naturally occurring in their oxidized form. Their oxidation state is usually +3, i.e., it is the most stable one. Therefore, the electronic structure of the lanthanide ions have no electron in the 5d or 6s subshell. In the following sections of this chapter, lanthanides should then be understood as lanthanide ions or lanthanide(III) unless stated otherwise.

3.3 Filling f Orbitals

Seven f orbitals can contain two electrons per orbital, so a maximum of 14 electrons will fill these orbitals (the subshell). One can picture 14 boxes that represent the 14 possible positions of the electrons (two boxes per orbital). By using a simple statistical approach, one finds out that there are 14 possibilities to put a single electron in one of these boxes. One box being filled, there are 13 possibilities for the second electron, but because both electrons are undistinguishable, the permutation of the two electrons should not be taken into account, so there are $(14 \times 13)/2$ possibilities to fill the boxes. For three electrons, and taking into account the removal of the six permutations of the three electrons, $(14 \times 13 \times 12)/(3 \times 2)$ combinations are achievable.

Applying this principle to any subshell, the number of configurations that can be generated by placing N indistinguishable electrons in $N_{\max}$ boxes is defined by equation (1). This number of boxes $N_{\max}$ corresponds to the maximum number of electrons in the subshell, i.e., $2 \cdot (2 \cdot \ell + 1)$.

$$\frac{N_{\max}!}{N! \cdot (N_{\max} - N)!} \tag{1}$$

The maximal number of configurations is obtained when the subshell is half filled. For the 4f subshell, the seven electrons of Gd^{3+} yield 3432 possible electronic configurations. In comparison, the half-filled 3d subshell and its 5 electrons in 10 boxes maximum (e.g., Fe^{3+}, $[Ar]3d^5$) yields ''only'' 252 electronic configurations.

3.4 Degeneracy of the Atomic Orbitals

We explained earlier that the electrons in an atom have quantized energies, but no further details were given so far. The calculation of the energy of an electron in an atom can be divided into four parts. First, the attraction of the negatively charged electron toward the positively charged nucleus induces an electrostatic potential that depends on the distance between the electron and the nucleus, and on the effective charge of the nucleus felt by the electron. Second, the electron has a mass and a velocity, thus a linear momentum that defines its kinetic energy.[b] Third, if more than one electron is present around the nucleus, an electrostatic repulsion between the electrons is expected. This part depends on the position of each electron relative to every other electron. Finally, an interaction between the orbital angular momentum and the spin angular momentum occurs. This phenomenon is called the *spin–orbit coupling*. It is a magnetic interaction between the spin of the electron and a magnetic field generated on each electron by the apparent circulation of the nuclear charge around the electron. This magnetic field is in the same direction as the angular momentum of the electron. When the spin of the electron is in the opposite direction relative to this induced magnetic field, and thus in the opposite direction relative to the orbital angular momentum, there is a stabilization of the electron (lowering of its energy). On the other hand, when the spin is in the same direction as the orbital angular momentum, there is a destabilization of the electron.[c]

For the hydrogen atom (one proton and one electron), the energy depends only on the attractive electrostatic potential energy between the electron and the proton, and on the kinetic energy of the electron. The quantization of the energy results in discrete energy levels that depend only on the n quantum number, so on the shell into which the electron is located.

From the point of view of the hydrogenoid energy levels, all the electronic levels that result in the different arrangement of the electrons in a subshell are equivalent. The hydrogenoid subshell is therefore degenerate and the degeneracy corresponds to the number of electronic levels as calculated by equation (1).

Nevertheless, the hydrogenoid energy levels are only valid in absence of electronic repulsion. As soon as more than one electron is present in the atom, the electronic repulsion shifts the energy levels according to the orbital angular momentum of the electrons. The energy of the electronic levels thus depends on the distribution of the electrons in the different orbitals.

Furthermore, there are some combinations of spin and orbital angular momentum that are stabilized relative to the uncoupled situation, whereas others are destabilized. As a consequence, the energy also depends on the orientation of the spin angular momentum relative to the orbital angular momentum.

All electronic levels are yet not fully separated. There are still some combinations that have the same energy. This remaining degeneracy arises because the AO has a spherical

symmetry, so that all directions are identical. In order to further break the degeneracy, the atom has to be placed in an environment where an external field makes the orientation of the atom relative to that field significant.

The ''natural'' way to do this is to put the atom in a chemical environment. For example, put a metal cation, such as a lanthanide ion, in solution. In this state, the atom is surrounded by other atoms forming a coordination sphere. This coordination sphere may have different geometries or symmetries, which breaks the spherical arrangement of the free ion. The ligand induces a ligand field around the metal ion. The symmetry of this ligand field further modifies the energy of the electrons in the metal ion. This modification depends on the position of the electron relative to the ligand field and therefore, on the orbital into which the electron is located relative to the orientation and symmetry of the ligand field.

The other way to break the remaining degeneracy of the free atom is to apply an external magnetic field in one direction. In such a field, the energy depends on the position relative to the direction of the magnetic field, so on the orientation of the orbital relative to the direction of the magnetic field. Therefore, each orbital in a subshell, which inherently points toward different directions, will have a different energy shift. An external magnetic field is actually the only way to fully remove the degeneracy of the electronic levels.

In the case of the lanthanide ions, the electronic repulsion induces the higher shift relative to the hydrogenoid energy level of the subshell. The shift due to the spin–orbit coupling comes next (~10 times lower than the electronic repulsion), whereas the shift due to the ligand field is weak (~ a thousand times lower than the electronic repulsion). As a result, a remarkable property of the lanthanide ions is that the splitting of these electronic levels remains fairly constant whatever the environment around the lanthanide ion. The reason for this behavior is the inner character of the 4f orbitals.

3.5 Classification of an Electronic Level

First, let us define three new quantum numbers L, S, and J representing the overall quantum state of the subshell. Those quantum numbers are associated with the overall orbital, spin, and spin–orbit angular momentum of the subshell, respectively. The idea behind those overall quantum numbers is that for an unfilled subshell, the sum of the orbital angular momentum $\boldsymbol{\ell}$ of each electron, as well as the sum of the spin angular momentum $\mathbf{s}$ of each electron may be different from zero. The sum of the total angular momentum $\mathbf{j} = \boldsymbol{\ell} + \mathbf{s}$ of each electron may thus also be different from zero. These new vectors are overall vectors because they enclose the contribution of all the electrons (it is a vector sum). The overall quantum numbers are easily calculated from the filling of the subshell by summing the m_ℓ values of each electron and then keeping the absolute value for L, by summing the m_s values of each electron and then keeping the absolute value for S, and by summing the m_ℓ with the m_s values of each electron and then keeping the absolute value for J.

Being the sum of quantized angular momenta, the overall angular momenta are also quantized. The number of orientation they can posses is called the *multiplicity*. The spin multiplicity is calculated by $2 \cdot S + 1$, whereas the orbital multiplicity is calculated by $2 \cdot L + 1$. The total angular momentum then can have $2 \cdot J + 1$ orientations.

Instead of using directly a sequence of quantum numbers to characterize an electronic level, the overall quantum numbers are usually expressed using a specific notation called *spectroscopic terms, spectroscopic levels*, and *spectroscopic sublevels*. A spectroscopic term ${}^{(2S+1)}\Gamma$ is determined by the S and L overall quantum numbers. It defines the multiplicity of the overall spin angular momentum and represents the overall orbital quantum number as a capital letter Γ = S, P, D, F, G, H, etc. that corresponds to values of L = 0, 1, 2, 3, 4, 5, etc.

In the case of the lanthanide ions, the spectroscopic term is associated with the energy shift of the hydrogenoid energy level of the subshell due to the electronic repulsion. The degeneracy of a spectroscopic term is given by the product of the spin and orbital multiplicities $(2 \cdot S + 1) \cdot (2 \cdot L + 1)$.

The introduction of the spin–orbit coupling then further splits each spectroscopic term into spectroscopic levels. A spectroscopic level ${}^{(2S+1)}\Gamma_J$ introduces the spin–orbit quantum number J. The J quantum number represents a particular combination of the spin and orbital angular momentum. The possible combinations of the spin and orbital quantum numbers are $J = |L - S|, |L - S + 1|, \ldots, L + S$. One of these particular combinations can have $2 \cdot J + 1$ orientations, so that the multiplicity of a spectroscopic level is now $2 \cdot J + 1$.

The splitting of the $2 \cdot J + 1$ sublevels enclosed in a spectroscopic level requires either a ligand field, which may partly break the degeneracy, or an external magnetic field in one direction, which completely breaks the degeneracy.

Examples of spectroscopic terms and levels are found in the next section when illustrating the lower energy level or ground state of the 4f subshell.

3.6 How to Find the Electronic Ground State of a Subshell?

Finding the energy of an electronic level is not easily accessible. Nevertheless, there are three rules, known as *Hund's rules*, that allow finding the ground-state arrangement of the electrons in an unfilled subshell.

The first Hund's rule states that the lower energy level should have the higher spin multiplicity. This implies that a maximum number of electrons have to be unpaired. Therefore, electrons first fill individual orbitals and only when no more free orbitals are available do the additional electrons

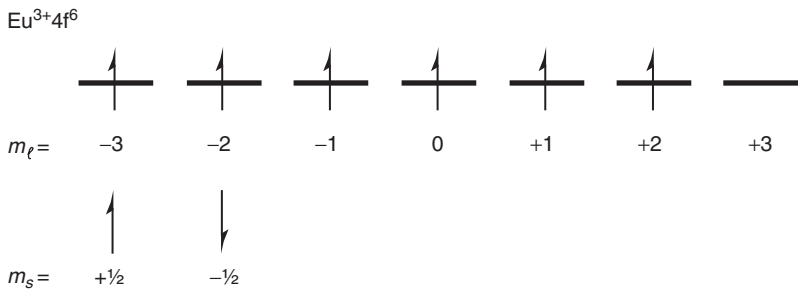


Figure 2 Electronic configuration of the electronic ground state of Eu^{3+}

fill singly occupied orbitals. The reason is that when two electrons are in the same orbitals, the effective charge of the nucleus is lower because one electron tends to screen the charge of the nucleus for the other electron. Consequently, the electrostatic attraction is lower and the electrostatic potential increases.

The second Hund's rule states that the lower energy level should then have the higher orbital angular momentum multiplicity. This means that the electron should rather be orbiting all in the same direction than equally clockwise and anticlockwise. The reason is here that the electrostatic repulsion is lower when the electrons orbit in the same direction because they ''see each other'' less.

As a consequence of the second Hund's rule, electrons are sequentially placed into the m_ℓ orbitals starting from either the negative or positive higher end of the m_ℓ range (e.g., for the lanthanide ions either from the -3 or from the $+3 m_\ell$ orbital) and filling from that end to the other (e.g., -3, -2, -1, 0, $+1$, $+2$, $+3$, or $+3$, $+2$, $+1$, 0, -1, -2, -3) and then again pairing either from one side or the other.

The third Hund's rule states that the total angular momentum or spin–orbit angular momentum, which is the sum of the spin angular momentum and the orbital angular momentum, has the lower multiplicity when the subshell is less than half filled and the higher multiplicity when the subshell is more than half filled.

This comes from the stabilization of the spin–orbit that requires a spin angular momentum that is opposite to the orbital angular momentum. As a consequence, electrons with a positive m_s (spin-up) tends to go in orbitals with a negative m_ℓ, and vice versa. But because the spin has to be maximized first (first Hund's rule), the subshell is first half filled with all spin-up or all spin-down electrons before changing a single spin orientation. When the subshell is then more than half filled, the electrons are forced to pair and the spin–orbit stabilization again favors a pairing in the orbital with an m_ℓ opposite to the m_s. This results in a lower energy electronic level for the more than half-filled subshells that has a $J = L + S$ value in terms of overall quantum numbers, so the highest spin–orbit multiplicity. The examples below might help better visualize this change of lower energy spin–orbit multiplicity between the less and more than half-filled subshell.

The spectroscopic level of the ground state of each lanthanide can be easily determined by applying Hund's rules and finding the corresponding L, S, and J overall quantum numbers. The excited states (higher energy levels), on the other hand, are not straightforward. To calculate the spectroscopic term of the ground state, the electronic configuration of the ion, i.e., for lanthanide ions, the number of f electrons has to be known. As an example, the electronic structure of elemental europium is $[Xe]4f^7 6s^2$. The removal of three electrons thus yields the $[Xe]4f^6$ electronic configuration of Eu^{3+}. The ground state is the lower energy state. Hund's rules states that it corresponds to the largest value of S and L. Practically, it corresponds to the filling of each f orbitals before pairing electrons (see Figure 2).

According to this filling, the L and S values are calculated as following: $L = |(-3) + (-2) + (-1) + 0 + 1 + 2| = |-3| = 3$ and $S = 6 \cdot (+\frac{1}{2}) = 3$, which correspond to the spectroscopic term ${}^{(2S+1)}\Gamma = {}^7\mathrm{F}$

The spin–orbit coupling J can range from $|3 - 3|$ to $(3 + 3)$, so can take values such as 0, 1, 2, 3, 4, 5, 6. The third Hund's rule states that the ground state has the $|L - S|J$ value if the subshell is less than half filled (<7 electrons), and the $(L + S)$ J value if it is half filled or more than half filled (≥ 7 electrons). Since europium(III) is less than half filled with 6 electrons (<7 electrons), the ground state J value is $|L - S| = |3 - 3| = 0$. The electronic ground state of Eu^{3+} is thus the ${}^7\mathrm{F}_0$ spectroscopic level. This level represents a single electronic level since the degeneracy $(2 \cdot J + 1) = 1$. On the other hand, the higher spectroscopic levels of the ${}^7\mathrm{F}$ spectroscopic term represent more than one electronic level per spectroscopic level because $J \neq 0$. The ${}^7\mathrm{F}_1$ spectroscopic level is a triplet, with three electronic levels; the ${}^7\mathrm{F}_2$ level is a quintet with five electronic levels; and so on until the ${}^7\mathrm{F}_6$ level, which encloses 13 electronic levels. The sum of all the electronic levels in the ${}^7\mathrm{F}_J$ levels is then $1 + 3 + 5 + 7 + 9 + 11 + 13 = (2 \cdot S + 1) \times (2 \cdot L + 1) = 7 \times 7 = 49$, which is the degeneracy of the spectroscopic term.

Terbium(III) is another example where the electronic configuration is more than half filled (see Figure 3).

Here, the spectroscopic term of the ground state is also ${}^7\mathrm{F}$. Nevertheless, because the subshell is more than half filled, the pairing of the $-\frac{1}{2}$ spin electron occurs in the

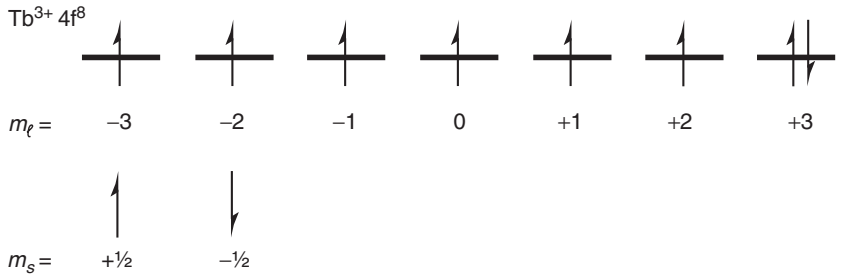


Figure 3 Electronic configuration of the electronic ground state of Tb^{3+}

$m_\ell = +3$ orbital to ensure the best stabilization due to an antiparallel spin–orbit coupling. The spin–orbit coupling with the lowest energy is $J = L + S = 3 + 3 = 6$. The spectroscopic level of the ground state is then $^7F_6$.

The spectroscopic levels will be essential in the next sections, when dealing with the interaction of light with matter. Spectroscopy is actually defined as the study of this particular interaction. The interaction of light with an atom, or the spectroscopy of an atom is then a way to probe its electronic structure by measuring the energy difference between two of those electronic level.

3.7 Effect of the Coordination

The spectroscopic levels correspond to the electronic levels for the free ion in a spherical symmetry. When this ion is coordinated to a ligand, all directions are not identical anymore, but depends on the symmetry of the coordination sphere. The coordination sites of the ligands can be represented as point charges around the lanthanide ion generating a static electrostatic ligand field around the metal ion. The spectroscopic levels are then further split into spectroscopic sublevels due to the ligand field. A $^{(2S+1)}\Gamma_J$ level can be split into $(2 \cdot J + 1)$ sublevels. But not all sublevels are uncovered upon coordination. The number of sublevels that a spectroscopic level exhibits actually depends on the symmetry of the coordination sphere. Therefore, the fine structure of the spectroscopic levels (i.e., the sublevels) is a tool to determine the symmetry around the ion.

If all the spectroscopic levels were split into sublevels, the number of spectroscopic sublevels would be equal to the number of electronic levels calculated according to equation (1). Hence, the number of electronic levels is a maximal number. The only way to uncover all electronic levels for sure and for any metal ion is to apply an actual external magnetic field.

Further details about the electronic structure of the lanthanides are available in ***The Electronic Structure of the Lanthanides***.

4 INTERACTION OF LIGHT WITH MATTER

In order to understand the photophysical properties of the lanthanide ions, it is necessary to have a clear knowledge about the different kinds of interactions that light can have with matter as well as about light itself.

In addition, the lanthanide ions are always embedded in a chemical environment. This environment might be either inorganic or organic. Both types of compounds may be stoichiometric compounds where a lanthanide ion represents at least 1 equiv. of the total composition, or doped compounds where the lanthanide ions are only present as impurities in a defined matrix (thus representing a small percentage of the total composition). A typical example of a lanthanide-doped material is an inorganic phosphor. On the other hand, a typical example of a stoichiometric lanthanide compounds is a lanthanide complex where ideally all the lanthanide ions are surrounded by the same coordination sphere.

An essential part of the luminescent lanthanide compounds is composed of lanthanide complexes where the ligands are organic molecules. The reason is that organic molecules might be very good light-absorbing compounds, whereas lanthanide ions are not as it will be shown later. Consequently, the photophysical properties of luminescent lanthanide complexes with organic ligands need to investigate the photophysics of the organic ligands, as well as the photophysics of the lanthanide ion. The terms *ligand-centered photophysics* and *metal-centered photophysics* are often encountered in literature. Basic photophysical concepts enabling the understanding of organic ligands and lanthanide ions are developed hereafter.

4.1 What is Light?

From a physical point of view, light is an electromagnetic radiation. Actually, the mere fact that electromagnetic waves travels at the speed of light was used to demonstrate that light is an electromagnetic wave. It can be shown from Maxwell's equations that a localized perturbation of an electromagnetic field yields a wave equation that travels through space at the speed of light. By extension, light can

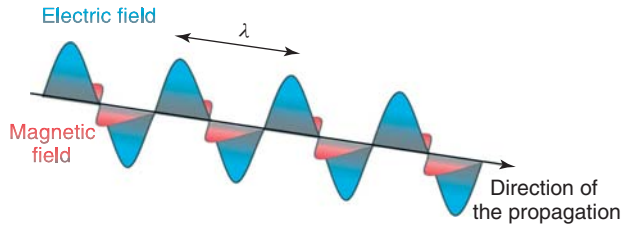


Figure 4 Representation of a monochromatic electromagnetic wave propagating at the speed of light in one direction transverse to the oscillation of the electric and magnetic fields

thus be defined not only to what we can see with our naked eyes, but to any electromagnetic radiations: γ rays, X rays, UV light, visible light, infrared (IR) light, microwaves, and radio waves. All these radiations are characterized by the frequency of the oscillations of the electromagnetic field, also related to the wavelength of its oscillation (γ rays are oscillating very fast whereas radio waves are oscillating very slowly). If a monochromatic ray of light were frozen in time, the distance (called wavelength λ) between two consecutive peaks of intensity of the oscillating electric or magnetic field spreads over a length that can be calculated from the frequency ν of the oscillation and the speed of light c by using the equation $\lambda = c/\nu$. Such apparently ''frozen'' waves can be produced by two waves of the same frequency traveling in opposite directions. The standing wave resulting from the interference of the two other waves is a wave oscillating in time at a stationary position in space (Figure 4).

There are three types of light that are almost constantly appearing in luminescence studies: UV light, visible light, and to a lesser extent IR light. The UV light covers the wavelengths from 100 nm to 380 nm, the visible light from 380 nm to 780 nm, and the IR light from 780 nm up to 1 000 000 nm (the nanometer unit is usually preferred at least for the UV and visible light spectral range). The near-IR (or NIR) is often encountered for the luminescence of the lanthanide ions; it ranges from 780 nm up to 2500 nm.

The interaction of these three kinds of light with matter at a microscopic scale (atomic or molecular scale) is affecting the following two parameters of the atom or molecule:

1. The electronic state or how the electrons are filling the atomic or molecular orbitals (MO) of the atom or molecule.
2. The vibrational state or how the atoms of a molecule are oscillating relative to each other.

When dealing with atoms and molecules, the classical wave nature of light is not very useful. The electromagnetic picture derived from Maxwell's equations fails to predict the interaction of light with matter. One of the most important discoveries of the twentieth century, i.e., the quantized nature of light when interacting with matter was highlighted with the photoelectric effect. To account for this particular effect, Albert Einstein proposed the introduction of light quanta. This explanation earned him the Nobel Prize in 1921.

Light quanta, nowadays known as *photons*, are often visualized as particles of light, but they should be seen as energy packets. The energy of a photon (of one of these packets) depends on the wavelength of the radiation it is part of. A monochromatic radiation (only one frequency of oscillation of the electromagnetic field) will be constituted of photons whose energies are all the same and that is directly proportional to the frequency. It is the well-known Planck's relation $E = h\nu$, where E is the energy of the photon (in Joule) for a wave at frequency ν (in s^{-1} or Hz) and h is Planck constant ($h \approx 6.626 \times 10^{-34}$ J·s). This photonic picture of light is usually used to describe the interaction of light with matter.

4.2 What Happens When Light and Matter Interact?

What do photons interact with? As already stated, light is affecting the electronic and vibrational states of matter. The justification of this interaction is straightforward, since light is also an electromagnetic wave; the interaction has to affect the electric charges of matters, which are the electrons and protons of the nucleus. The electronic excitation needs energies in the UV or visible range; on the other hand, the vibrational excitation is taking place in molecules that are susceptible to experience a variation of a dipole moment upon vibration (a net separation in the distribution of the positive and the negative charges) and needs energies in the IR range. The absorption of light thus induces both a displacement of electrons and nuclei in matter. However, the location and the energy in matter of both an electron and a vibrational motion of nuclei are quantized. These displacements can consequently only occur to quantized states. There are therefore two primary parameters that have to overlap in order to yield an absorption: the energy of a photon, and a difference between two electronic or vibrational levels that corresponds to this energy.

Hereafter, we focus on the electronic absorptions that occur with UV or visible light. A compound or part of a compound that absorbs UV or visible light is called a *chromophore* (from the Greek $\chi\rho\tilde{\omega}\mu\alpha$ meaning color and $\varphi\acute{\varepsilon}\rho\omega$ bear, carry). However, electronic absorptions in molecules are usually concomitant with vibrational excitations. Both the electronic ground state and excited state have vibrational levels. Usually, the electronic excitation changes the nature of the chemical bonds, a double bond might, for example, become a single bond in the excited state, so that the average distance between two bonded nuclei (the bond length) may be altered. Some electronic excited states are even dissociative, meaning that they yield to a cleavage of a chemical bond. The vibrational levels are very important even for electronic absorptions.

The promotion of an electron by absorption of a photon occurs in the femtosecond timescale ($fs = 10^{-15}$ s). Just after the absorption, the absorbing compound (the

chromophore) is said to be excited, or to be in an excited state. Photophysical processes are often illustrated with a so-called Jablonski diagram (Figure 7). In such a diagram, the electronic levels are represented with thick horizontal lines one of top of the other. The bottom line is the ground state (the most stable one) whereas the higher lines are excited states. The vibrational excited states are represented as thinner horizontal lines on top of each electronic level. They are responsible for the structured shape observed in the absorption or the emission spectra. The intensities of those absorption and emission bands are a result of the difference between the vibrational motions in the ground state and in the excited state.

Sometimes, rotational levels are also represented on top of the vibrational levels. The rotations of molecules are also quantized, but their observation is only possible in gas phase. In liquids or solids, the numerous collisions destroy the fine rotational structure.

4.3 Electronic Absorptions

The electronic structure of the lanthanides has just been presented earlier. Many of these aspects are useful for the general description of the interaction of light with atoms. The interaction with the electronic structure of an atom takes place with AOs. One electron is promoted to a higher AO or higher electronic level. A higher electronic level might be a higher shell or a higher subshell. A promotion inside a subshell (as in the case of the 4f subshell) requires special conditions as already foreseen. It will be clarified in the next section.

In the case of a molecule such as an organic chromophore, the absorption takes place between MOs. A promotion of an electron from the highest occupied molecular orbital (HOMO) to the lowest unoccupied molecular orbital (LUMO) is always the lowest in energy and will define the threshold of absorption. Other absorptions usually occur at higher energies yet, either from orbitals lower in energy, or to orbitals higher in energy, or even both. If a photon whose energy matches exactly the difference in energy between the LUMO and the HOMO meets the molecule, it shall be absorbed and promote one of the electrons from the HOMO to the LUMO. The excited state thus has one electron in the HOMO and one electron in the LUMO. MOs are normally described by a linear combination of atomic orbitals (LCAO theory): x AO of the same or close energy level (for example, 2s and 2p in most organic molecules) will combine to give x MO. End-on interaction between two 2p AOs yields sigma MOs with bonding σ and antibonding σ^* orbitals, while parallel overlap forms the bonding π and antibonding π^* orbitals. Nonbonding residual orbitals such as the n orbital of oxygen (actually a filled 2p orbital) might also be encountered.

4.4 Description of the Vibrational Modes of a Molecule

Since vibrational levels are so important in photophysics, a brief description about how molecular vibrations are described is certainly helpful. A vibration is an oscillating motion of an object between two positions in space without a change of its global position (without a translational motion). There are two types of vibrations, the free vibration where the system is given an initial impulse and allowed to freely vibrate according to its vibrational modes, and the forced vibration where the system is maintained under vibration by a continuous external force. After the force is removed, the system evolves as a free vibration. If the system encounters no loss in energy, it remains in the vibrational state that was defined by the external impulse; otherwise, it loses the energy and goes back to its equilibrium state.

The two classical examples of vibrational motions are a mass suspended at the end of a spring and a pendulum. These examples are described by classical mechanics as harmonic oscillators. The energy stored in a harmonic oscillator is described as a parabolic function of the energy as a function of the distance of the oscillation with a minimum at the equilibrium distance.

At an atomic scale, a vibration is an oscillation of the entire atom (both the electrons and the nucleus), but since the movement of the electrons is much faster than those of the nuclei, it is more a consequence of the movement of the nucleus (the electrons adapt continuously as the nucleus moves). Because a free vibration is not possible for a single object, vibrations are only relevant in molecular systems. It thus corresponds to oscillations of the nuclei of the molecule along or around the chemical bonds. We have seen that such vibrations are quantized. It means that the nuclei of a molecule are not free to go and vibrate continuously through space, but that their positions (similar to that of the electrons around the nucleus) are restricted to defined locations of defined energies. It gives rise to a quantization of the vibrational energy that is defined as vibrational levels of defined energies. The lowest vibrational energy level corresponds to the minimal vibration induced by the Heisenberg uncertainty principle of the ''frozen'' nuclei. The Heisenberg uncertainty principle is a quantum mechanical principle that states that the position and momentum of a particle cannot be measured with an infinite precision. If we try to ''freeze'', i.e., to know with a great precision, the position of an atom, it induces a great uncertainty on the momentum of the particle, and if we try to ''freeze'' the momentum, the position becomes blurry. The harmonic oscillator is used as an approximation of a vibrational motion of a molecule. It works well for the first vibrational states, but then fails because at higher energies, a chemical bond starts to get loose and eventually breaks. This behavior is anharmonic and is described classically with a Morse potential curve. Furthermore, the higher the vibrational states are in energy, the less quantized the states are. Near the dissociation limit, the vibrational levels are a nearly continuum as in the classical description.

The vibrational motion of a simple harmonic oscillating homodiatomic molecule (two identical atoms) might be represented as shown in Figure 5.

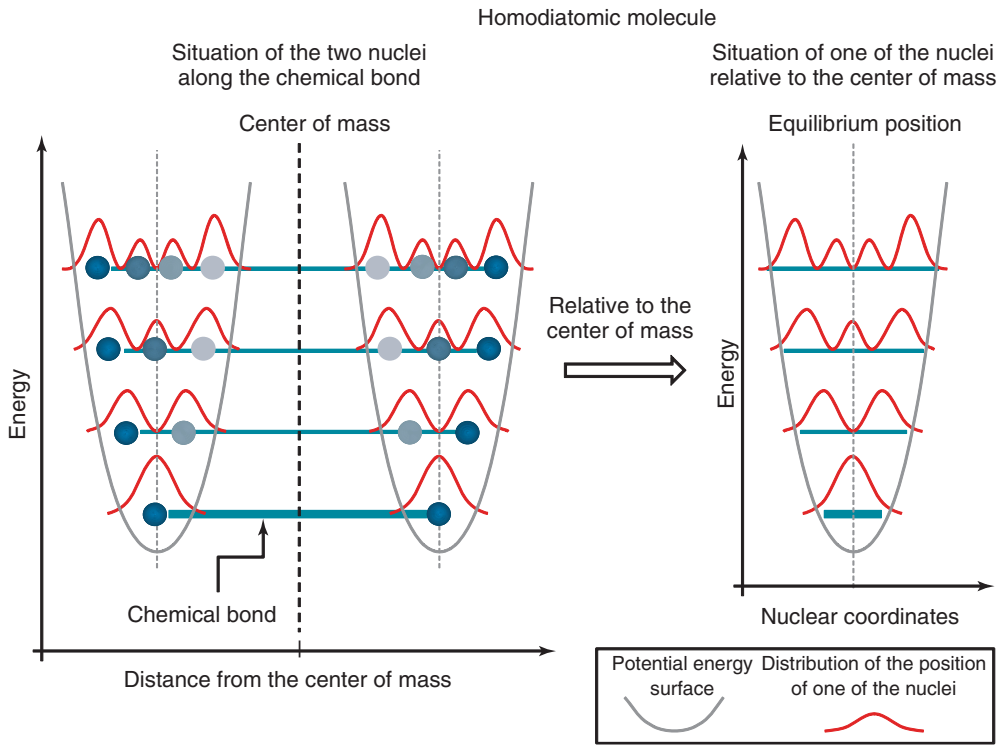


Figure 5 Illustration of the quantized vibrational motion in a homodiatomic molecule using the harmonic oscillator approximation

The oscillation can be symmetric or antisymmetric relative to the center of mass. In the case of a diatomic molecule, only the stretching of the bond is relevant, but as soon as the number of atoms and their conformation allow the formation of angles between the chemical bonds, some additional modes appear. Bendings such as scissoring, rocking, twisting, and wagging are possible in nonlinear molecules. They are correlated with the movement of a pendulum, whereas a stretching is more of a string oscillation.

4.5 Interaction of Light with the Vibronic Levels of a Molecule

As briefly introduced earlier, both the electronic ground state and electronic excited state have vibrational levels. Actually, a vibrationally and electronically excited molecule can be generated by absorption of a photon in the UV visible range. In order to excite only the vibrational state of a molecule, IR light is needed (lower energy photons). When both vibrations and electronic levels are excited, the term *vibronic excitation* is used (contraction of vibration and electronic). The jump from one state to another (either vibrational, electronic or vibronic) is called a *transition*.

The so-called Frank–Condon principle (Figure 6) explains how the change in nuclear coordinates (the vibrational excitation) during a transition dictates the probability of such an event. Because the movement of an electron (an electronic transition, absorption, or emission) is much faster than the movement of a nuclei (a vibration), a transition is said to be vertical relative to the nuclear coordinates. Absorption or emission then occurs at a constant nuclear coordinates. The best absorptions and emissions occur when the overlaps between the density distributions in the initial and in the final states are maximal. If there is no overlap between two states, for example, because the nuclear coordinates change a lot in the excited states, there is no absorption because the nuclear coordinates in the excited states have to immediately match the coordinates of the electronic ground state. The probability of the absorption or emission expresses the strength of the absorption or of the emission at a defined energy. This strength is called the *oscillator strength* between the two states. In practice, it is correlated to the intensity of the absorption as shown by the spectra (intensity as a function of the energy) in Figure 6. It can be related to the extinction coefficient $\varepsilon(\lambda)$ of the Beer–Lambert law of absorption.

The two slightly different figures shown in Figure 6 illustrate two cases of vibronic spectra. First, on the left side, the nuclear coordinates in the electronic excited state remains unchanged. As a result, the best overlap is for the $S_1{}^{(v=0)} \leftarrow S_0{}^{(v=0)}$ transition (the $(v = 0)$ superscripts indicate that it is from the 0 vibrational level of the S_0 electronic state to the 0 vibrational level of the S_1 electronic state). Hence, the $0 \leftarrow 0$ transition in the spectrum has the maximal intensity, which keeps decreasing for the other transitions. The left-pointing arrow indicates here that the transition is an

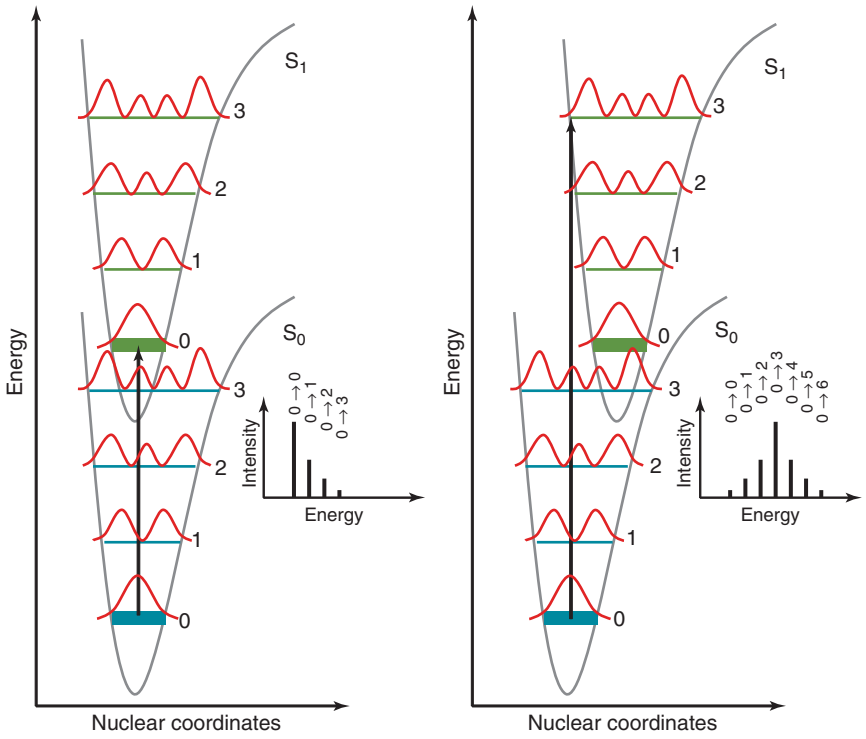


Figure 6 Frank-Condon principle applied to the absorption of light (emission is a downward version of this figure with arrows starting from the 0 vibrational state of the S_1 excited states). The red sinusoid curves are the density distributions (or probability functions) of the position of the nucleus at the defined vibrational states

upward transition from the lower S_0 state to the higher S_1 state. By convention, the higher energy state is written first and connected with an arrow to the lowest energy state. The direction of the arrow defines if it is an upward (left-pointing arrow) or a downward (right-pointing arrow) transition, so an absorption or an emission, respectively. This convention still holds with lanthanide ions. The higher spectroscopic level is written first and connected with an arrow to the lower spectroscopic level.

The second case on the right-hand side of Figure 6 shows a shift of the equilibrium position toward a longer distance. The nuclear distributions are thus not vertical to each other anymore. The best overlap is now between the ${S_0}^{(v=0)}$ and the ${S_1}^{(v=3)}$ levels, which therefore give rise to the transition with the maximal intensity in the spectrum.

The Frank–Condon principle is particularly well suited for the rationalization of the absorption spectra of organic chromophores. The electronic absorptions of organic molecules are considerably widened by a quite large vibronic coupling. Concerning the lanthanide ions, even though some vibrations between the ion and the atoms of the ligands may be observed, the required energies for exciting a Ln–L bond are much smaller than for the vibrations in the ligands. The vibration of the coordination sphere relative to the lanthanide ion is neglected most of the time. The electronic absorptions of the lanthanide ions are thus narrow because they are not widened by the vibrations between the lanthanide and the coordination sphere.

4.6 Selection Rules

An important point about a transition is that, even though a photon might have the correct energy to be absorbed or emitted, there are some forbidden transitions that are defined by quantum mechanics and its so-called selection rules. There are two major selection rules that are of great importance for the luminescence of lanthanides. First, an electron cannot change its spin during a transition: a singlet spin state has to remain a singlet spin state, whereas a triplet spin state has to remain a triplet spin state. In theory, a singlet–triplet transition is forbidden. Then, transitions inside the same atomic subshell are also forbidden (the electron has to jump to another subshell). The electrons cannot rearrange in the orbitals from the same subshell, so d–d and f–f transitions are forbidden, whereas d–f transitions are allowed.

This last point comes from symmetry considerations. The transition has to occur according to the symmetry of the absorbing or emitting compound. If no translational (vertical) transition with a symmetry that belongs to those of the chromophore transforms the AOs or MOs from the symmetry in the initial state to the symmetry in the final state, the transition is forbidden by symmetry. In

organic chromophores, $\pi - \pi*$ transitions are usually allowed by the symmetry selection rule, whereas $n - \pi*$ transitions are forbidden, therefore very weak, because of symmetry concerns. Other transitions involving the σ or $\sigma*$ orbitals are usually too energetic to be observed under usual conditions, so that they will not be discussed here. Because of this symmetry selection rule, the most intense transitions from an organic chromophore are usually attributed to $\pi - \pi*$ transitions (some computational chemistry calculations are available to support the attribution of the electronic transitions).

The selection rules that dictates the probability (or strength) of a transition can be summarized in three terms, the spin selection rule, which is the most important one; the symmetry selection rule; and finally, the vibrational selection rule or Frank–Condon principle.

In practice, those selection rules are not strict, and some couplings can make forbidden transitions happen. However, they remain weak, slow, or of low probability. Phosphorescence, for example, is a manifestation of a forbidden singlet–triplet transition favored by a spin–orbit coupling, whereas the luminescence of the trivalent lanthanide ions is a manifestation of forbidden f–f transitions favored by the disruption of the spherical (centrosymmetric) symmetry of the free ion once coupled to ligands.

The transitions involved up to now were electric dipole (ED) transitions involving ED moments. It means that the transitions were induced by the interaction of the oscillating electric field of light quanta with the ED moments of the compound. But it has been shown that the electrons in AOs, and by extension in MOs, also have magnetic dipole (MD) moments. For example, the spin–orbit coupling is an interaction between a magnetic field and the spin MD moment. Therefore, an oscillating magnetic field of an electromagnetic radiation may also induce MD transitions by interacting with the MD moment of matter.

The selection rules for MD transitions are different from the ED transitions. An MD transition is related to a rotational movement of the electron under the torque generated by the magnetic field. As a consequence, the symmetry selection rule that was valid for the translational movement of the electron under the force generated by the electric field is changed upon MD transition. An MD transition allows the inner subshell transitions, so that f–f transitions are allowed by MD transitions. Nevertheless, the intensities of the MD transitions are usually weaker than the intensities of the ED transitions. In lanthanide ions, partly allowed ED transitions are usually still more intense than allowed MD transitions, except when the symmetry of the complex is very high, meaning that the ion is little disrupted from its centrosymmetric geometry by the ligand field, and therefore that the ED transitions are very little relaxed from their forbidden character. Because an f–f MD transition is allowed, its intensity is fairly independent on the chemical environment. An ED transition on the other hand is a forced transition that is induced by the symmetry of the ligand field, so that its intensity depends on the chemical environment. Finally, MD transitions are usually neglected in the photophysical properties of organic chromophores. Any transition in an organic chromophore can thus fairly be stated as a pure ED transition.

4.7 What Happens After the Interaction of Light with Matter?

In a Jablonski diagram (Figure 7), an excitation is represented as an arrow from the ground state to the excited state (pointing up). But this excitation does not last forever. After the interaction of light (a photon) with matter (an electronic or vibronic level of the chromophoric part of matter) has occurred, the excess in energy given by the incoming photon has a tendency to be released in order to form again the most stable state (the lowest in energy). Many processes can deactivate the excited state. The term *relaxation* is often found to account for a deactivation. Collisions with other atoms or molecules can ''cool'' the excited state, or a process called *internal conversion* can transform the electronic excitation into vibrational excitation resulting in a hot electronic lower state. All these processes are called *nonradiative* or *radiationless deactivations* because they do not emit photons. In the Jablonski diagram, the nonradiative deactivations are represented as wavy arrows from an excited state to a lower state (pointing down). When the deactivation occurs through a second atom or molecule, the deactivating atom or molecule is known as a *quencher* and the deactivation as a *quenching*.

The Jablonski diagram of a lanthanide ion is different from the Jablonski diagram of an organic chromophore in two points. First, there is no vibrational level depicted above each electronic level since the vibrations of the lanthanide ion relative to the coordination sphere are neglected. Then the labeling of the ground and excited states is not S_0, S_1, and T_1 (that stand for singlet spin ground state, singlet spin first excited state, and triplet spin first excited state, respectively), but the spectroscopic levels corresponding to the quantum state of the subshell (the spectroscopic level of the ground state is straightforward as explained earlier, whereas the spectroscopic levels of the excited states were calculated for all the lanthanide ions). The electronic levels of all the lanthanide ions are illustrated in the energy diagram in Figure 12. The energy diagram of a lanthanide ion can be used in the same way as a Jablonski diagram.

The most important consequence of the absence of vibrational levels between the spectroscopic levels of a lanthanide ion is that the deactivation cannot occur via an internal conversion, but only via a quenching from a ligand state, a quenching from an external quencher such as a solvent molecule, or a radiative deactivation.

5 LUMINESCENCE

The phenomenon of interest here is the deactivations that will emit a photon and thus give rise to a luminescence of the compound. The radiative deactivation is represented in the Jablonski diagram (Figure 7) as an arrow from the excited state to a lower state (pointing down).

According to Kasha's rule, the emission always occurs from the vibrational ground state of the electronic excited state. It means that the deactivation of the vibrational excited states of an electronic excited state is much quicker than the emission. The vibrational relaxation occurs in the picoseconds timescale ($ps = 10^{-12}$ s). Here again, from a lanthanide point of view, Kasha's rule is somehow irrelevant because lanthanide ions have no vibrational structure as understood for an organic molecule. However, the emission seems generally to occur mainly from defined spectroscopic levels, so that despite an excitation to a higher level might happen, a relaxation down to one of these luminescent levels is often observed. But this rule is not as strict as Kasha's rule, so that it extensively depends on the lanthanide ion and on its chemical environment.

Back to the basic photophysics of organic chromophore, it has been stated earlier that an electronic transition is very fast, much faster than the vibrational motion. Why then is the vibrational relaxation occurring first? Actually, it is not the transition itself that takes longer than the vibrational deactivation of the excited electronic state, but the probability of occurrence of this emissive transition that is much lower than the rate of the vibrational relaxation. The excited state is not so unstable that the electron has to immediately return to its original location. It can wait sometimes in the excited states. In fact, the notion of rates of deactivation is a statistical concept. In average, the electron stays excited for a certain time before releasing the excessive energy. Some transitions happen faster, others slower, but in average, the lifetime of the electron in the excited state is quite defined for each compound and every excited state.

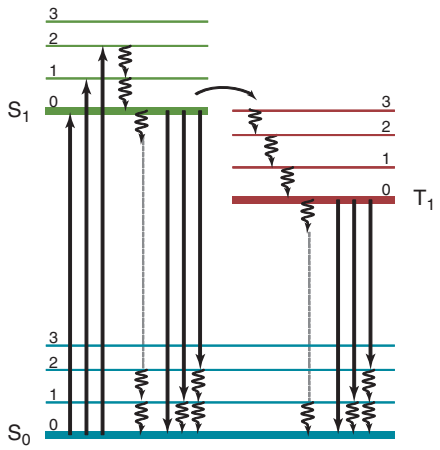


Figure 7 Typical Jablonski diagram of an organic chromophore showing the electronic ground state S_0, radiative transitions (thick vertical arrows), nonradiative deactivations (wavy arrows), and intersystem crossing (ISC, curved thick arrow) from the first singlet excited state (S_1) to the first triplet excited state (T_1)

The efficiency of luminescence depends then on the kinetics (or dynamics) of the deactivation. If the radiative deactivation is much quicker than the nonradiative ones, the compound has a good efficiency. On the other hand, if the radiative deactivation is slow compared to the other processes, the efficiency then entirely depends on the occurrence of nonradiative deactivations. Therefore, the efficiency of luminescence is a competition between nonradiative and radiative deactivation of the excited state.

5.1 Fluorescence, Phosphorescence, and Luminescence

Most of what has just been stated for the interaction of light with matter (the absorption or excitation) still holds for the radiative deactivations (the luminescence mechanisms). The Frank–Condon principle is applicable for downward radiative transitions, and all the other selection rules (spin and symmetry) are as valid for the absorption as for the emission of a photon.

So, what is the difference between fluorescence, phosphorescence, and the luminescence of the lanthanide ions? In fact, the mechanism is not the same. The fluorescence is an allowed transition without a change of the total spin. The fluorescent emission is quick because the transition is allowed, usually in the nanosecond timescale ($ns = 10^{-9}$ s).

For example, in an organic fluorophore, the transition from a singlet excited state S_1 to the singlet ground state S_0 (a $S_1 \rightarrow S_0$ transition) is a fluorescent emission. Usually, these transitions correspond to $\pi - \pi^*$ transitions. During such a fluorescent transition, an electron in a π^* orbital falls down back to the π orbital, the two electrons in the π^* and π orbitals having opposite spins all along. It then corresponds to a $^1\pi\pi^*$ excited state (one electron in a π orbital, the other with an opposite spin in a $\pi*$ orbital) and a $^1\pi\pi$ ground state (two paired electrons, both in the same π orbital), so a $^1\pi\pi* \rightarrow {}^1\pi\pi$ transition. The notation $^1\pi\pi^*$ is often encountered in literature to account for a fluorescent emission of an organic chromophore originating from a $^1\pi\pi^*$ excited state and so from a $\pi - \pi^*$ transition.

The phosphorescence on the other hand is forbidden since it requires a change of the total spin. The phosphorescence is slow because the transition is forbidden, usually in the microsecond ($\mu s = 10^{-6}$ s) up to the second timescale.

For example, in an organic chromophore, the transition from a triplet excited state T_1 to the singlet ground state S_0 (a $T_1 \rightarrow S_0$ transition) is a phosphorescent emission. These transitions also correspond to $\pi - \pi^*$ transitions most of the time. During such a phosphorescent transition, an electron in a π^* orbital falls down back to the π orbital, the two electrons in the π^* and π orbitals having the same spins

in the excited state. It then corresponds to a $^3\pi\pi^*$ excited state (one electron in a π orbital, the other with the same spin in a π^* orbital) and a $^1\pi\pi$ ground state (two paired electrons, both in the same π orbital), so a $^3\pi\pi^* \rightarrow ^1\pi\pi$ transition. The notation $^3\pi\pi^*$ is often encountered in literature to account for a phosphorescent emission of an organic chromophore originating from a $^3\pi\pi^*$ excited state and so from a $\pi - \pi^*$ transition.

In order to generate the triplet state, or any other spin state that is different from the ground spin state, one electron has to change its spin. This process is only achievable if there is at least one unpaired electron in the excited state (yielding a paramagnetic compound). Otherwise, the spin is constrained by the Pauli exclusion principle, so that it cannot change without a concomitant change in the spin of the electron in the same orbital (which yields no net spin change). For organic chromophores, this condition is fulfilled in the excited state where the electrons are no longer in the same orbital.

The switch of the spin quantum number is called the *intersystem crossing*. An intersystem crossing is only possible if it results in a lower energy state. According to Hund's rule, a lower energy state usually corresponds to a higher spin, so that intersystem crossing usually results in a higher spin state. In an organic chromophore, the triplet state is a higher spin state than the singlet spin state and is then lower in energy than the corresponding singlet excited state. Hund's spin multiplicity rule is even reinforced in organic molecules where the unpaired electrons in the excited states occupy different orbitals that may be spatially far away. The apparently paradoxical result of a transition that moves the electron over a longer distance but needs less energy to do so than over a shorter distance can be explained by the oscillating nature of a transition. A transition is not immediate but rather a transitional state between two other states. The Jablonski diagram tends to misguide us in that way, but a transition corresponds to an oscillation of the electron between the initial and final state, or between the initial and final location. And we have seen that electromagnetic oscillations with large amplitudes and thus low frequencies correspond to photons of low energies and vice versa oscillations with low amplitudes and high frequencies correspond to photons of high energies.

Concerning the luminescence of the lanthanides, the f–f transitions are actually described by the spectroscopic levels of the ion, either down to the ground state or down to an intermediate level. Usually, the visible emissions of the lanthanide ions have transitions that change the total spin number of the ion, i.e., the $(2 \cdot S + 1)$ multiplicity, whereas the NIR emissions do not change the spin. Since several lanthanides exhibit both mechanisms, the term luminescence is preferred over fluorescence or phosphorescence for the lanthanide ions. In this way, the common mistake of calling fluorescence all kind of emissions is avoided. Because of their forbidden character, f–f transitions are slow and the lanthanide luminescence may take up to a few milliseconds ($ms = 10^{-3}$ s).

5.2 Sensitization

Now, how to excite a lanthanide ion so that it would emit light? We have seen that the luminescence of the lanthanides comes from the forbidden f–f transitions between two $^{(2S+1)}\Gamma_J$ spectroscopic levels. Unlike phosphorescence, which is available through the intersystem crossing from an allowed excited state, to populate excited f levels, we cannot rely on the absorption of the lanthanide ion. The direct f–f absorption is very weak, with extinction coefficients (ε_λ) of a few $L \cdot mol^{-1} \cdot cm^{-1}$, more than a few thousand times less than an average organic chromophore. In order to excite a lanthanide ion, we need to use another compound that will efficiently absorb light and that may then transfer the energy to the lanthanide cation. This phenomenon is called *photosensitization* (or simply sensitization, or antenna effect) and the compound that absorbs and transfers the energy is the *photosensitizer* (or simply sensitizer).

The general picture of lanthanide-sensitized emission is illustrated in the Jablonski diagram in Figure 8.

Likewise any chromophore, a lanthanide ion can be de-excited via nonradiative deactivations (k_{nr}^{Ln}). Depending on the excited states of the sensitizer, a back-transfer from the lanthanide ion back to the sensitizer might also be possible. The sensitizer can thus partly act as a quencher, as well as molecules of solvent or any other compound near the lanthanide ion.

There are two mechanisms for the energy transfer from a donor to an acceptor (see Figure 9). The Dexter

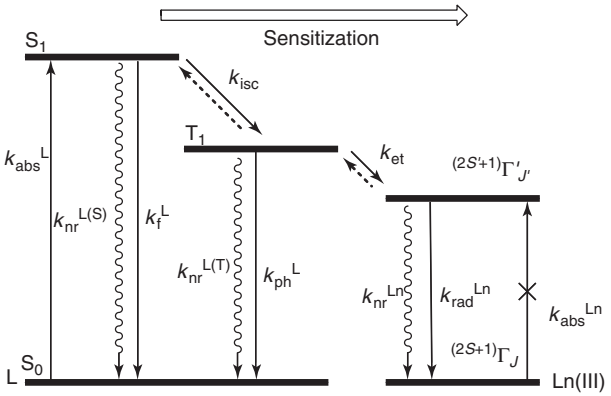


Figure 8 Simplified Jablonski diagram showing the sensitization pathway from the chromophoric ligand L to the lanthanide ion Ln^{III} via the triplet state T_1 of the sensitizer. The k values are the rate constants for all photophysical phenomena involved. Absorption k_{abs}^{L} by the sensitizer, intersystem crossing k_{isc} of the sensitizer, and energy transfer k_{et} from the triplet state of the sensitizer to the lanthanide ion (to one of its $^{(2S'+1)}\Gamma'_{j'}$ excited spectroscopic level) resulting in an excited lanthanide ion that can undergo a radiative deactivation k_{rad}^{Ln}, which yields to its luminescence. The nonradiative deactivations are shown with ''nr'' subscripts. The radiative deactivations of the ligand occur either via fluorescence k_f^L or phosphorescence k_{ph}^L. This figure is to be compared with Figure10, which illustrates the sensitization pathway in a lanthanide coordination complex

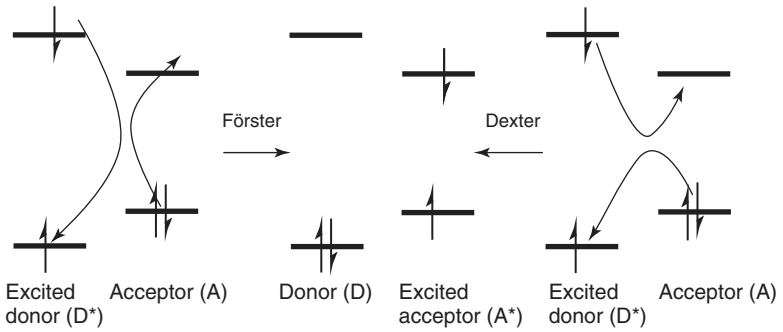


Figure 9 Mechanisms for the photoinduced energy transfer from a donor (D) to an acceptor (A)

mechanism involves an exchange of electrons between the donor and acceptor, whereas the Förster mechanism relies on the Coulombic interactions and a dipole–dipole coupling to promote an electron in the acceptor when the electron of the excited donor falls back to the ground state (nonradiative transition). Figure 9 also introduces the ''chemical'' notation for a compound in an excited state. Here, a donor D is excited and forms D*. The excited donor D* can then transfer its excitation (thus becoming the unexcited D again) to an acceptor A, which becomes an excited acceptor A*. This notation is useful when writing the equations for the kinetics of photochemical reactions or photophysical processes.

Both the Dexter and the Förster mechanisms depend on the overlap between the donor and acceptor energy levels and the distance between the donor and the acceptor. The Dexter mechanism has an exponential decay of the energy transfer rate as a function of the separation distance r, whereas the efficiency of the Förster mechanism depends on $1/r^6$. Let us not forget that the thick lines in Figure 9 represents the lowest vibrational state of the considered electronic level, the difference in energy between the donor excitation and the acceptor excitation is thus not lost, but converted into vibrational energy. Thinner lines should be pictured above the thick ones as illustrated in Figure 7. The electron hop from one level to the other then occurs rather horizontally from a thick line to a thinner one and is then deactivated by vibrational quenching down to the next thick line.

In the case of lanthanide coordination complexes, two kinds of chromophoric ligands are generally designed as follows:

1. The chromophore is directly coordinated to the lanthanide ion (see Figure 10a). Chromophores are thus designed to ensure an efficient positioning of the triplet energy, which would allow the photosensitization of the lanthanide ion, and enclose adequate coordination sites to guarantee a stable complexation of the cation. For further details, see ***Lanthanides: Luminescence Applications*** and ***Luminescent Bioprobes***.
2. The chromophore is not directly coordinated to the lanthanide ion, but is part of the ligand and can also work as a sensitizer (see Figure 10b). In that case, a coordinating unit such as a diethylenetriamine pentaacetate (DTPA) or a cyclen moiety has one or more positions substituted by the chromophore. The longer distance somewhat lowers the efficiency of the energy transfer which ought then rather to occur via a Förster mechanism (no close contact that would enable an electronic exchange), but such ligand designs introduce more versatility regarding the choice of the chromophore.

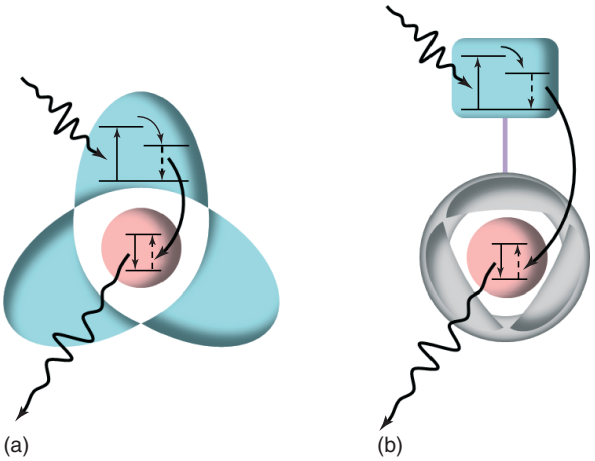


Figure 10 Illustration of the sensitization of a coordinated lanthanide ion by absorption of a directly coordinated chromophore (a) or by absorption of a distant coordinated chromophore (b)

5.3 Charge Transfer

In special cases, a CT between the ligand (sensitizer) and the metallic coordinated acceptor can take place. This CT state is sometimes encountered in lanthanide complexes as a ligand to metal charge transfer (LMCT) transition. The opposite charge transfer, i.e., the metal to ligand charge transfer (MLCT), is generally not observed due to the large ionization energy of the Ln^{3+}. The reduced lanthanide ion is usually oxidized back to the stable oxidation state by electron

transfer from the reduced excited lanthanide to the oxidized ligand. In a way, an LMCT is very similar to that of the Dexter mechanism where no charge separation is carried out to avoid a recombination of the electron with the oxidized ligand.

In solids, because ligands tend to interact together through π-stacking, H-bonding, and Van der Waals interactions, some transitions may occur between two ligands, bound to two different complexes. Such transitions are called ligand to ligand charge transfer (LLCT). LLCT transitions may also occur in solution between two ligands (or two chromophores) of the same complex, but the attribution of this kind of transition would be complicated.

Because the electron has to jump over a long distance in LLCT, LMCT, and MLCT, the energy of these transitions is typically lower than the intraligand (IL) absorption. It is often observed as a bathochromic shift (toward the red region of the spectrum) of the absorption or excitation spectrum of the IL transition. CT transitions are also often in the same energy range, so that the exact attribution of the additional band might be difficult. A certain amount of confusion exists in the literature about the luminescence of lanthanide ions between LMCT, MLCT, ILCT (intraligand charge transfer), and LLCT. In principle, only LLCT is relevant for lanthanide ions coordinated to organic chromophores. LMCT may occur with the most easily reduced ions (Eu^{3+}, Yb^{3+}, or Sm^{3+}), but true LMCT transitions are rare, except in inorganic materials such as phosphors where their energy is also high enough to provide an efficient sensitization pathway. Concerning MLCT, it may only really occur with Ce^{3+}, which has the lowest oxidation potential. LLCT, on the other hand, depends on the ligand and is favored in solid states. A sensitization through an LLCT is possible and often provides an additional mechanism for the emission from solid-state compounds.

5.4 Solvatochromism

A chromophore in the solid state does not exhibit the same photophysical properties as in solution. It comes principally from the different chemical environment of the chromophore.

In solid state, the chromophores tend to be tightly packed together in a quite rigid structure. Sometimes, CTs between the chromophores occur. This may even yield to a conductive solid or to a semiconductor-type material. The vibrational modes may also be altered because they couple with the neighboring molecules. The term *phonon* is often encountered in material science to account for a collective excitation involving the concomitant vibration of lattice structures in the solid (in crystals).

In diluted solution (up to a few millimolar), the chromophore is in average only surrounded by solvent molecules. As the concentration increases, the frequency of collision with other chromophoric molecules increases, but providing that there is no specific interaction between the chromophores, they will not remain together. Special cases may occur when an excited molecule forms a dimer with another (excited or not) molecule. It yields an exciplex or an excimer when the dimer is a homodimer that possesses particular photophysical properties compared to the monomers.

A dissolved chromophore is surrounded by a solvation sphere. The solvent molecules are oriented around the chromophore so that their ED moments align with the dipole moment of the chromophore. The charge distribution, as well as the polarity of both the chromophore and the solvent molecules, hence plays a major role in the solvation of the chromophore. Since the charge density is related to the MOs of the chromophore, the solvation influences the energy of the electrons in the MOs. The solvation sphere may be compared with the coordination sphere of a metal ion (in the case of a metal ion, sometimes the coordination sphere is a solvation sphere). The solvation sphere generates a solvation field around the chromophore, which perturbs the electronic levels of the chromophore.

In the excited state, the charge distribution changes, since an electron moves from an orbital to another. An excited chromophore then requires a different arrangement of the solvent molecules in its solvation sphere to maximize its stabilization compared to the best stabilization in the ground state. Therefore, after an excitation, the solvent molecules have to reorient themselves to accommodate the newly formed excited state of the chromophore. This reorientation takes time (several picoseconds) and is much slower than the transition. This implies that after the excitation, the chromophore is in a higher solvation energy state which then relaxes down to a more stabilizing arrangement of the solvent molecules. The same is also true for a radiative deactivation. This phenomenon yields Figure 11, which somehow resembles the figure of the Franck–Condon principle, except that, since the orientation of the solvent molecules in the liquid is not quantized but continuous, the stabilization is also continuous. The right-hand part of Figure 11 illustrates an ideal situation where the solvent molecules are perfectly aligned with the dipole moment of the chromophore. This situation is the lowest in energy. However, because a solution is highly dynamic, other slightly misaligned situations are also present due to the thermal agitation of the solvent molecules in a liquid phase. A distribution of solvation coordinates with different energies is thus expected, but the major part of this distribution is centered at the ideal situation.

Solvatochromism is the variation of the absorption and emission spectra depending on the solvent. An important solvatochromism yields a high Stokes shift between the emission and the absorption. The speed of this relaxation depends on the viscosity of the solvent, so that in certain cases, an emission can take place before the relaxation is complete. The Stokes shift may thus be adjusted by tuning the viscosity of the solvent.

Changing the solvent may have either a better stabilizing effect on the excited state, in which case,

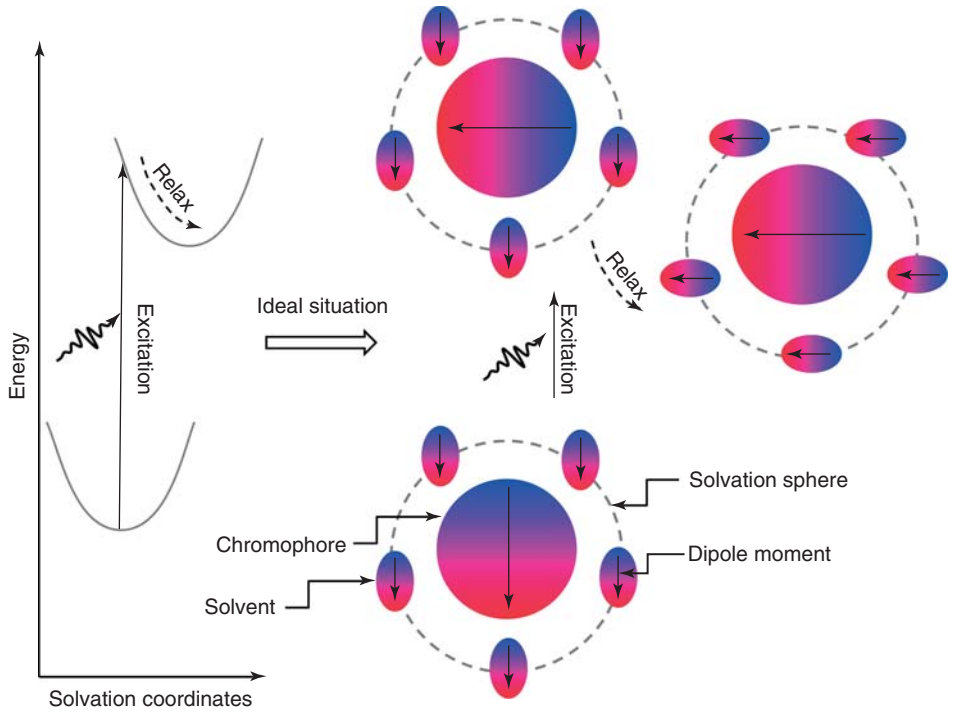


Figure 11 Solvation effect on the energy of the excited state

the emission is shifted toward lower energies or higher wavelengths (bathochromic shift), or a lower stabilizing effect on the excited state, in which case, the emission is shifted toward higher energies or lower wavelengths (hypsochromic shift).

Solvatochromism is important for lanthanide coordination complexes because it may tune the energy of the triplet state of the ligand relative to the electronic level of the lanthanide ion that is, as already pointed earlier, quite independent on the chemical environment.

5.5 Quantum Yield

It is not because the emission spectrum of a luminescent compound can be measured that it necessarily means the compound is a good emitter. There are different criteria to be taken into account before concluding on the efficiency of the luminescence. In the case of lanthanide complexes, it is not because the luminescence of the ion is measured that either the sensitization or the luminescence of the ion is efficient. The luminescence needs to be further investigated to evaluate the efficiency of each step yielding to the emission of the lanthanide ion.

We have seen that once excited, a molecule or an atom such as a lanthanide ion does not stay so forever. The electron tends naturally to lose the excess of energy and form the most stable configuration. If this excessive energy is not intercepted by another molecule, or not transformed into vibrational excitations, the deactivation will be radiative and reemit a photon. The competition between all nonradiative deactivations and the radiative one is at the center of all luminescence phenomena. The quantum yield (Φ_{em}) is used to characterize the luminescence of the compound and gives the efficiency of the emission process. It is defined as the ratio of the number of emitted photons (N_{em}^{photon}) over the number of absorbed photons (N_{abs}^{photon}) as shown in equation (2).

$$\Phi_{em} = \frac{N_{em}^{photon}}{N_{abs}^{photon}} \tag{2}$$

A compound having a purely radiative deactivation (meaning that all absorbed photons are reemitted) would then exhibit a quantum yield of 100%. In fact, there are no purely emissive compounds. Some of the most efficient fluorophores are rhodamine dyes. Rhodamine 101 is one of the few examples that may exhibit in the proper solvent, pH, temperature, and concentration range, a near unity quantum yield (0.98 ± 0.02 as an average literature data). To the opposite, a low quantum yield points to most of the absorbed photons being lost by nonradiative deactivations.

The quantum yield of the ligand-sensitized lanthanide luminescence (sometimes called overall quantum yield) is the ratio of the number of photons emitted by the lanthanide per number of photons absorbed by the ligand. It is generally written as Φ_L^{Ln}. It is not to confuse with the intrinsic quantum yield Φ_{Ln}^{Ln}, which is defined as the number of photons emitted

by the lanthanide per number of photons directly absorbed by the lanthanide (through a very weak f–f absorption band). The intrinsic quantum yield does not take into account the loss of energy due to the ligand sensitization pathway, but does take into account all the deactivation of the lanthanide, included the ones that are due to the presence of the ligand such as a back-transfer (transfer from the lanthanide to the ligand triplet state) or some kind of quenching phenomena. The intrinsic quantum yield is related to the ligand-sensitized quantum yield by the sensitization efficiency (η_{sens}), which is a percentage of the number of absorbed photons that yield to a transfer of the energy onto the lanthanide (some definitions state that it is the number of photons transferred onto the lanthanide ion per number of photons absorbed by the ligand, but it is the energy that is transferred and not the photons).

$$\Phi_{\text{L}}^{\text{Ln}} = \eta_{\text{sens}} \cdot \Phi_{\text{Ln}}^{\text{Ln}} \tag{3}$$

This sensitization efficiency is composed of the efficiency of the intersystem crossing (isc) and of the energy transfer (et).

$$\eta_{\text{sens}} = \eta_{\text{isc}} \cdot \eta_{\text{et}} \tag{4}$$

The isc efficiency is the percentage of the number of absorbed photons that actually yields a triplet state, whereas the et efficiency is the percentage of the number of triplet-state ligands that transfer their energy onto the lanthanide ion. The product is thus the number of triplets formed per absorbed photon multiplied by the number of transfers from a triplet onto the lanthanide per triplet formed, which results in the number of transfers from a triplet onto the lanthanide per photon absorbed by the ligand.

5.6 Lifetime

Some other important characteristics of the emission are the rate of the deactivation of the excited state and the rate of the radiative deactivation. If we measure a time-resolved emission spectrum of the emission, we will observe that the emission spectrum loses some intensity as a function of time after a pulsed excitation. This emission decay is usually monoexponential and corresponds to the rate constant of the deactivation of the excited state, or observed deactivation rate constant k_{obs}. It is important here not to confuse this rate constant with the rate constant of the radiative deactivation k_{rad} (in Figure 8, k_{f}^{L} and k_{ph}^{L} for the fluorescence and phosphorescence rate constants of the ligand, respectively, $k_{\text{rad}}^{\text{Ln}}$ for the radiative rate constant of the lanthanide). Despite the fact that this method measures the decay of the emission, between each time step, the nonradiative processes (the k_{nr} deactivation rate constants in Figure 8) also deactivate the excited state. To better visualize the decay rates, some equations are helpful.

First, upon absorption, the excited state S_1 is formed. If we use the chemical notation for a compound D, it gives equation (5).

$$\text{D} + \text{photon} \rightarrow \text{D}^* \tag{5}$$

The rate of the absorption is related to the extinction coefficient or to the absorption cross-section. It obeys the law of Lambert–Bouguer and Lambert–Beer. The density of the photons [photon], and the concentration or density of the chromophore [D], thus define the rate of the concentration or density change of the excited chromophore [D^*], here appearing during the excitation (equation 6).

$$\left(\frac{\text{d}[\text{D}^*]}{\text{d}t}\right)_{\text{abs}} = k_{\text{abs}} \cdot [\text{photon}] \cdot [\text{D}] \tag{6}$$

Just after absorption, when no other process has already taken place, the number of excited chromophore will depend on the duration of the excitation, the density of the exciting photons, the rate constant of absorption k_{abs} for the defined energy of the photons and thus of the absorptions, and the initial number of chromophore $[\text{D}]_0$ (before excitation). The maximum number of excited chromophore is of course the initial number of chromophore, so that $[\text{D*}]_{\text{max}} = [\text{D}]_0$.

The density of the photons [photon] is related to the intensity of the incoming light I_0. Equation (6) can be developed to yield the famous Lambert–Beer law of absorption, $A(\lambda) = \varepsilon(\lambda) \cdot l \cdot c = -\log T(\lambda)$. $A(\lambda)$ is the absorbance at wavelength λ (no unit), $T(\lambda)$ is the transmittance at that same wavelength (no unit), $\varepsilon(\lambda)$ is the molar (decadic, because in log base 10) extinction coefficient of the absorbing compound at wavelength λ (in $\text{L} \cdot \text{mol}^{-1} \cdot \text{cm}^{-1}$), l is the length of the light path through the absorbing medium (in cm), and c is the concentration (in $\text{mol} \cdot \text{L}^{-1}$) of the absorbing compound in the medium.

After the absorption (one absorbed photon yields necessarily one excited chromophore), the deactivation of the excited state will decrease its concentration following a rate law that depends on the different deactivation pathways as shown by the equations (7–10) (either radiative or nonradiative, referred as rad and nr subscripts, respectively). The k_{q}, rate constants correspond to a quenching process involving the quencher or acceptor A, and the k_{d} rate constant to a deactivation such as an internal conversion or any other radiationless relaxation. The k_{d} rate constant may thus be a sum of different contributions to the nonradiative deactivation.

$$\text{D}^* \xrightarrow{k_{\text{rad}}} \text{D} + \text{photon}_{\text{em}} \tag{7}$$

$$\text{D}^* \xrightarrow{k_{\text{d}}} \text{D} \tag{8}$$

$$\text{D}^* + \text{A} \xrightarrow{k_q} \text{D} + \text{A}^* \tag{9}$$

$$k_{\text{nr}} = k_{\text{q}} \cdot [\text{A}] + k_{\text{d}} \tag{10}$$

These equations yield the following rate laws for the relaxation (*relax*) of the excited state:

$$\left(\frac{\mathrm{d}[\mathrm{D}^*]}{\mathrm{d}t}\right)_{\mathrm{rad}} = -k_{\mathrm{rad}} \cdot [\mathrm{D}^*] \tag{11}$$

$$\left(\frac{\mathrm{d}[\mathrm{D}^*]}{\mathrm{d}t}\right)_{\mathrm{nr}} = -k_{\mathrm{nr}} \cdot [\mathrm{D}^*] \tag{12}$$

$$\left(\frac{\mathrm{d}[\mathrm{D}^*]}{\mathrm{d}t}\right)_{\mathrm{relax}} = \left(\frac{\mathrm{d}[\mathrm{D}^*]}{\mathrm{d}t}\right)_{\mathrm{rad}} + \left(\frac{\mathrm{d}[\mathrm{D}^*]}{\mathrm{d}t}\right)_{\mathrm{nr}} \tag{13}$$

$$\left(\frac{\mathrm{d}[\mathrm{D}^*]}{\mathrm{d}t}\right)_{\mathrm{relax}} = -(k_{\mathrm{rad}} + k_{\mathrm{nr}}) \cdot [\mathrm{D}^*] = -k_{\mathrm{obs}} \cdot [\mathrm{D}^*] \tag{14}$$

After the integration of equation (14) (shown in equation 15), the expression in equation (16) is found.

$$\int_{[\mathrm{D}^*]_0}^{[\mathrm{D}^*]_t} \frac{\mathrm{d}[\mathrm{D}^*]}{[\mathrm{D}^*]} = \int_{t_0}^{t} -k_{\mathrm{obs}} \cdot \mathrm{d}t \tag{15}$$

$$\ln\left(\frac{[\mathrm{D}^*]_t}{[\mathrm{D}^*]_0}\right) = -k_{\mathrm{obs}} \cdot (t - t_0) \tag{16}$$

The time t_0 can be set to 0. Equation (16) is generally shown in its exponential form (equation 17), which is a usual expression for an exponential decay.

$$[\mathrm{D}^*]t = [\mathrm{D}^*]_0 \cdot \exp(-k_{\mathrm{obs}} \cdot t) \tag{17}$$

The rate of the radiative deactivation (equation 11) that yields the photons used to measure the emission as a function of time depends on $[D\mathrm{D}^*]_{\mathrm{t}}$. Since $[D\mathrm{D}^*]_{\mathrm{t}}$ depends on the observed rate constant, the decay of the emission depends on the decay of the excited state and thus on the observed rate constant and not only on the radiative rate constant.

The rate constant is normally expressed as lifetimes $\tau_{\mathrm{obs}} = 1/k_{\mathrm{obs}}$. The unit of a rate constant is s^{-1} or *Hz*. The unit of a lifetime is thus in seconds (s).

The quantum yield and the observed rate constant are related one to each other. Under continuous excitation, an equilibrium between the absorption (formation of the excited state) and the deactivations is established so that the change of the concentration of the excited state is zero (steady state, equations 18–20).

$$\left(\frac{\mathrm{d}[\mathrm{D}^*]}{\mathrm{d}t}\right)_{\mathrm{eq}} = 0 = \left(\frac{\mathrm{d}[\mathrm{D}^*]}{\mathrm{d}t}\right)_{\mathrm{abs}} + \left(\frac{\mathrm{d}[\mathrm{D}^*]}{\mathrm{d}t}\right)_{\mathrm{relax}} \tag{18}$$

$$\left(\frac{\mathrm{d}[\mathrm{D}^*]}{\mathrm{d}t}\right)_{\mathrm{abs}} = +k_{\mathrm{abs}} \cdot [\mathrm{photon}] \cdot [\mathrm{D}] = N_{\mathrm{abs}}^{\mathrm{photon}} \tag{19}$$

$$\left(\frac{\mathrm{d}[\mathrm{D}^*]}{\mathrm{d}t}\right)_{\mathrm{relax}} = -k_{\mathrm{obs}} \cdot [\mathrm{D}^*] = -(k_{\mathrm{rad}} + k_{\mathrm{nr}}) \cdot [\mathrm{D}^*] \tag{20}$$

By combining the increase of the excited state population due to the absorption of photons with the decay of the excited state population due to the radiative and nonradiative relaxations, and by defining the number of emitted photons with the quantum yield, the quantum yield then expresses as a ratio of rate constants or lifetimes.

$$N_{\mathrm{abs}}^{\mathrm{photon}} - k_{\mathrm{obs}} \cdot [\mathrm{D}^*] = N_{\mathrm{abs}}^{\mathrm{photon}} - (k_{\mathrm{rad}} + k_{\mathrm{nr}}) \cdot [\mathrm{D}^*] = 0 \tag{21}$$

$$\Leftrightarrow N_{\mathrm{abs}}^{\mathrm{photon}} = k_{\mathrm{obs}} \cdot [\mathrm{D}^*] \tag{22}$$

$$N_{\mathrm{em}}^{\mathrm{photon}} = k_{\mathrm{rad}} \cdot [\mathrm{D}^*] = \Phi_{\mathrm{em}} \cdot N_{\mathrm{abs}}^{\mathrm{photon}} \tag{23}$$

$$\Rightarrow \Phi_{\mathrm{em}} = \frac{N_{\mathrm{em}}^{\mathrm{photon}}}{N_{\mathrm{abs}}^{\mathrm{photon}}} = \frac{k_{\mathrm{rad}}}{k_{\mathrm{obs}}} = \frac{\tau_{\mathrm{obs}}}{\tau_{\mathrm{rad}}} \tag{24}$$

By measuring both the quantum yield and the lifetime, the radiative lifetime of the chromophore can then be calculated.

Now, what about a lanthanide-sensitized emission? In that case, other steps that occur in the sensitization process have to be considered and additional equations will refer to a sensitization through the triplet state of the ligand.

First, the sensitizer or ligand L absorbs a photon, forms a singlet excited state that can eventually experience an intersystem crossing (isc) to obtain the triplet excited state.

$$\begin{aligned} \mathrm{L} + \mathrm{photon} &\xrightarrow{k_{\mathrm{abs}}} {}^1\mathrm{L}^* \\ {}^1\mathrm{L}* &\xrightarrow{k_{\mathrm{isc}}} {}^3\mathrm{L}^* \end{aligned} \tag{25}$$

From the triplet state, the energy transfer (et) from the ligand to the lanthanide ion (Ln) can occur.

$${}^3\mathrm{L}^* + \mathrm{Ln} \xrightarrow{k_{\mathrm{et}}} \mathrm{L} + \mathrm{Ln}^* \tag{26}$$

This step is similar to that of the donor acceptor energy transfer shown in equation (9) ($\mathrm{D}^* + \mathrm{A} \rightarrow \mathrm{D} + \mathrm{A}^*$). It is a nonradiative deactivation of the ligand, which yields to the excitation of the lanthanide ion. The ligand is thus the excited donor D* and the lanthanide ion the acceptor A.

The excited lanthanide may then emit a photon through an f–f forbidden transition.

$$\mathrm{Ln}^* \xrightarrow{k_{\mathrm{rad}}} \mathrm{Ln} + \mathrm{photon}_{\mathrm{em}} \tag{27}$$

But both the ligand and the lanthanide can also be deactivated. The ligand can emit a photon by fluorescence from its singlet state or by phosphorescence from its triplet state, or can be deactivated (also from either its singlet or triplet excited state) by internal conversion, quenching, or any other nonradiative possibility. Even if the sensitization is efficient, i.e., if the isc and et is quick relative to the undesired deactivations, the lanthanide can also experience some nonradiative deactivations, so that the rate of the radiative deactivation of the lanthanide is in competition with nonradiative processes.

The sensitization efficiency is calculated by measuring the observed lifetime of the lanthanide excited state, the

sensitized quantum yield, and the intrinsic quantum yield. The ratio of the observed and radiative lifetime gives the intrinsic quantum yield.

$$\Phi_{Ln}^{Ln} = \frac{\tau_{obs}}{\tau_{rad}} \tag{28}$$

Since the measurement of the intrinsic quantum yield is very hard to perform, it is usually replaced by the calculation of the radiative lifetime. However, this calculation is also very complicated, except for the special case of europium where approximations yield a simple convenient formula. It comes from the very rare property of europium to exhibit a purely MD transition, the $^5D_0 \rightarrow {}^7F_1$, the intensity of which is practically independent on the chemical environment. The calculation then only needs the emission spectrum (corrected to take into account the sensitivity function of the detector) and uses the ratio of the total intensity of the lanthanide emission over the intensity of the MD transition, as well as the refractive index of the medium n, and a parameter $A_{MD,0}$ that defines the strength of the MD transition. For Eu^{3+}, $A_{MD,0} = 14.65\, s^{-1}$.

$$\frac{1}{\tau_{rad}} = k_{rad} = A_{MD,0} \cdot n^3 \cdot \left(\frac{I_{tot}}{I_{MD}}\right) \tag{29}$$

By knowing either the radiative lifetime and the observed lifetime, or the intrinsic quantum yield and the observed lifetime, one can calculate the missing parameter (see ***Lanthanides: Luminescence Applications***).

The observed lifetime usually significantly depends on the temperature (whereas the radiative lifetime only depends on the small variation of the refractive index as a function of temperature if the coordination is unaffected by the lower temperature). This dependence comes from the fact that some nonradiative deactivations of the lanthanide ion are vibrationally assisted (i.e., needs some heat to take place, e.g., back-transfer to the triplet state of the ligand). Nevertheless, the observed lifetime of the lanthanide does not depend on the excitation wavelength. A direct excitation through an f–f transition or through a sensitizer results in the same observed lifetime. In other words, this lifetime, and thus the deactivation of the lanthanide excited state only depends on the chemical environment and on the temperature, not on how this excitation was achieved.

5.7 Solvent Effect and q Numbers

The photophysical properties also depend on the form of the compound. A solid will not exhibit the same properties as a solution, and in solution, the presence of other solute can affect the luminescence as much as a different solvent. Even by changing a solvent for its deuterated analog has a drastic effect. This effect is even used in aqueous solutions. By measuring the observed lifetime in H_2O and in D_2O, one can retrieve the number of water molecules q in the first coordination sphere of the lanthanide ion. This is the work of Supkowski and Horrocks for the determination of the number of water molecule in the first coordination sphere of the europium complexes.

$$q = A \cdot [\tau_{obs}^{-1}(H_2O) - \tau_{obs}^{-1}(D_2O) - k_{XH}]$$
$$k_{XH} = \alpha + \beta \cdot n_{OH} + \gamma \cdot n_{NH} + \delta \cdot n_{O=CNH} \tag{30}$$

where τ_{obs} (H_2O) is the lifetime in water, τ_{obs} (D_2O) the lifetime in deuterated water and n_{XH} the number of XH oscillators in the first coordination sphere, α the contribution of the water molecules in the outer coordination sphere, β the contribution of an OH oscillator in the first coordination sphere, γ the contribution of an NH oscillator in the first coordination sphere, and δ the contribution of a O=CNH oscillator in the first coordination sphere. Similar formula were developed then using the same idea.

The lower vibrational energy of the OD bond relative to the OH bond is responsible for the lower quenching of the excited lanthanide in the deuterated solvent (more OD than OH vibrations are needed to deactivate the same excited state). The vibrational relaxation needs several vibrational quanta of the quenching molecule in order to deactivate an excited state and particularly a lanthanide excited state. Both the match between the vibrational quanta and the excitation energy, and the number of vibrational quanta required to achieve such a relaxation define the efficiency of this nonradiative process. The more quanta, the less efficient the deactivation, because of the selection rules for vibrational transitions.

5.8 Luminescence of the Different Lanthanide Ions

The nonradiative deactivations a lanthanide ion can undergo are actually very lanthanide dependent. If we have a look at the spectroscopic levels of the lanthanide ions, we can notice that some have a lot of close levels whereas some have higher gaps (Figure 12).

The higher the gap between two levels, the better it is for the emission of the lanthanide. This is due to the easier deactivation of the excited state by transfer of the energy to the vibrational modes of other molecules when the energy difference better matches the energy of a vibration. Hence it explains also why it is very difficult to obtain highly luminescent NIR emitters.

As already pointed out earlier, the electronic levels of the lanthanide ions are fairly independent on the environment. This corresponds to emission lines that are never really shifted. This apparent unexciting property of lanthanide ions are actually one of their most interesting properties. The luminescence is always expected in the same region and thus gives always nearly the same color. It also confers high Stokes shifts on them (difference between the excitation and the emission wavelength) in contrast to organic fluorophores where the emission is usually next to the absorption with an overlapping area in between.

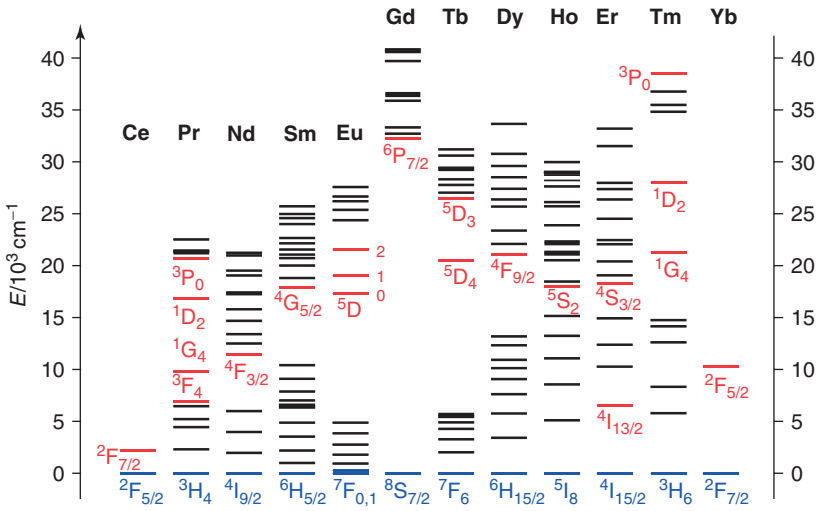


Figure 12 Energy diagram of the Ln^{III} ions. (Modified and reprinted with permission from Ref. 2. Copyright 1990, American Institute of Physics.)

5.9 Hypersensitive Transitions as Probes

We have just seen that the spectroscopic levels of the lanthanides are not affected by the chemical environment. But actually, the splitting of each spectroscopic level depends on the geometry of the coordination sphere of the lanthanide ion (its symmetry). This is referred to as the *ligand field effect* and induces splittings of a few cm^{-1}. Some transitions are particularly sensitive to changes around the lanthanide ions, both in shape and intensity. Such transitions are called *hypersensitive transitions*. For example, the emission from the $^5D_0 \rightarrow {}^7F_2$ transition of europium is hypersensitive. It is the only true hypersensitive transition in emission. All other hypersensitive transitions are absorptions. The $^5D_4 \rightarrow {}^7F_5$ transition of terbium is sometimes called pseudo-hypersensitive because it exhibits a hypersensitive character with some ligands. Hypersensitive transitions are used in many applications in order to probe the environment. Unfilled coordination spheres are required in order for the environment to interact with the lanthanide ion.

6 CONCLUSIONS

Most of the basic principles needed to approach the luminescence of the lanthanide ions have been described. Luminescence is a fascinating phenomenon, but as it was shown, very intricate because many processes are involved. Therefore, the design of highly luminescent lanthanide compounds and especially of highly luminescent-sensitized lanthanide complexes is quite unpredictable. From a theoretical point of view, the efficiency of the luminescence can always be associated with one particular feature of the environment of the lanthanide ion. It may be solvent molecules that are present in the coordination sphere; the ligands that are not rigid enough; or the sensitizer that absorbs unexpectedly high wavelengths, which also shifts its triplet state toward inefficient for energy transfer lower energies. Sometimes the sensitizer is also quickly deactivated even before the energy can be transferred to the lanthanide ions, so that the sensitization efficiency is very low. Nevertheless, few of those effects can be accurately predicted. That is said, some general trends are known to be detrimental to the luminescence properties of the lanthanide complex, such as inserting on the ligand backbone specific functional organic groups or deactivating oscillators. Complex models based on quantum mechanics, including the Judd–Ofelt theory, were developed to calculate the intensity of each f–f transition. But such models are usually too complex to be readily applied, so that the development of such theories is somehow restricted to a limited specialist's audience. Theoretical calculations still need further developments and therefore, the experimental approach remains the main tool to appreciate the interest of a given complex regarding its photophysical properties.

The luminescence of the lanthanide ions is particularly attractive because the energies of their electronic transitions are fairly constant whatever the chemical environment. Furthermore, the forbidden character of their electronic transitions yield long lifetimes which enable, for example, time-resolved imaging. The lifetime, as the quantum yield is on the other hand very sensitive to the chemical environment. The luminescence of the lanthanide complexes are thus good probes and are even used in biomedicine for some diagnosis and analytical methods.

The investigation of the luminescence properties of a lanthanide compound actually depends on the ion, on the type of compounds, and on the application to which the compound is intended. But usually, the common feature of all

photophysical measurements and mainly of the luminescence of the lanthanide ion is to collect pieces of information about the structure around the lanthanide ion. If the symmetry is rather high or low, if solvent molecules are coordinated to the ion, if the radiative deactivation is slow or quick relative to the nonradiative relaxations, etc. Luminescence thus often provides a unique method to probe the structure of matter. The choice of the authors was to restrict the presentation of the fundamentals concepts of luminescence to a minimum set of equations. After reading this chapter, the reader has accumulated enough knowledge to understand the photophysical discussions in the next chapters and in most of the publications. The next level would be to formulate the photophysical concepts with mathematical expressions. Nice books and reviews are dealing with these formulations and we recommend their lecture (see for example, Chapter 1 of Ref. 3).

Some examples are emphasized in the next chapter (***Lanthanides: Luminescence Applications***). The luminescence spectra of various lanthanide ions will be given and several applications using luminescent lanthanide complexes will be presented. In ***Luminescent Bioprobes***, some practical data and a case of study will be presented. The properties of a series of lanthanide complexes (i.e., with ligands that share a common architecture) will be explicated both from a physicochemical and from a photophysical point of view. It will be demonstrated that these complexes are highly stable and present interesting photophysical properties, so that their application as bioprobe can be undertaken.

7 GLOSSARY

Photophysic: Study of the laws and processes arising from the interaction of light with matter.

Spectroscopy: Study of the interaction of light with matter.

Photon: Quantum of light defining the minimal energy packet of a light radiation at a given frequency.

Quantization: Restriction of a continuum quantity into a discrete set of values.

Luminescence: Emission of light from a nonincandescent object as a result of a radiative deactivation of matter arising after an electronic excitation of matter.

Fluorescence: Luminescence phenomenon involving no variation of the spin of the electron during the electronic transition.

Phosphorescence: Luminescence phenomenon involving a variation of the spin of the electron during the electronic transition.

Excitation: Transition from a lower energy state to a higher energy state.

Sensitization: (Photosensitization) Transfer of energy from a sensitizer to an acceptor energy level of the sensitized compound that is not populated without the presence of the sensitizer (no direct sensitivity).

Quenching/Quencher: Nonradiative deactivation of an excited state by transfer of the energy to a quencher molecule that deactivates nonradiatively.

Charge transfer: Electronic transition to a long distance exhibiting a high extinction coefficient ($> 10\,000\ \mathrm{L \cdot mol^{-1} \cdot cm^{-1}}$).

Solvatochromism: Shift in the absorption or emission spectra when changing the composition of the solvent.

Degeneracy: Number of microstates at the same energy.

Chromophore: Compound, or parts of a compound that absorb UV or visible light.

Fluorophore: Compound, or parts of a compound that emit UV or visible light.

Stokes shift: Difference between the maximum of absorption and the maximum of emission (either wavelength, energy, wavenumber, or frequency).

Rate law/Kinetics/Dynamics: Laws describing the variation of the composition of a chemical or physical system as a function of time.

Selection rules: Set of rules derived from quantum mechanics that describes the probability of a given transition (absorption and emission).

8 RELATED ARTICLES

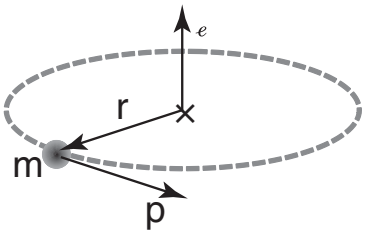
Lanthanides: Luminescence Applications; Luminescent Bioprobes; Near-Infrared Materials; The Electronic Structure of the Lanthanides; Upconversion Nanoparticles for Bioimaging Applications.

9 END NOTES

[a]**Physics reminder**

The orbital angular momentum defines the relation between the position of the electron around the nucleus and its momentum, so its velocity. An angular momentum $\boldsymbol{\ell} = \mathbf{r} \times \mathbf{p}$, where $\mathbf{r}$ is the position relative to the nucleus and

p is the momentum. The momentum (or linear momentum) $\mathbf{p} = m \cdot \mathbf{v}$. The bold notation is used to indicate that those quantities are vectors. The angular momentum $\boldsymbol{\ell}$ is a vector perpendicular to the plane formed by **r** and **p**.



[b]**Physics reminder**

The electrostatic potential energy U_{AB} between two charged particles is defined by Coulomb's law.

$$U_{AB} = \frac{1}{4 \cdot \pi \cdot \varepsilon_0} \cdot \frac{q_A \cdot q_B}{r_{AB}}$$

where ε_0 is the vacuum permittivity, q_A and q_B the electric charge of particles A and B, respectively, and r_{AB} the distance between particle A and B.

The kinetic energy of an object of mass m and velocity v or momentum p is defined by

$$E_{kin} = \frac{1}{2} \cdot m \cdot v^2 = \frac{p^2}{2 \cdot m}$$

[c]**Physics reminder**

$$\Delta E = -\boldsymbol{\mu} \cdot \mathbf{B}$$

$$\boldsymbol{\mu}_{spin} = -g_s \cdot \mu_B \cdot \mathbf{S}/\hbar$$

$$\mathbf{B} = \boldsymbol{\ell} \cdot |\mathbf{E}|/(|\mathbf{r}| \cdot m_e \cdot c^2)$$

ΔE is the energy shift due to the spin orbit interaction; $\boldsymbol{\mu}$ is the magnetic dipole moment of the electron or spin dipole moment $\boldsymbol{\mu}_{spin}$; **B** is the magnetic field induced by the apparent circulation of the nuclear magnetic charge; $\hbar$ is the reduced Planck constant, $\hbar = h/(2 \cdot \pi)$; **S** is the spin angular momentum; g_s is the electron g-factor ($g_s = 2$); μ_B is the Bohr magneton (a physical constant given by $e \cdot \hbar/(2 \cdot m_e)$, where e is the elementary charge and m_e is the mass of the electron); $|\mathbf{E}|$ is the intensity of the electric field of the nucleus (a radial electric field, $E = |\mathbf{E}|/|\mathbf{r}| \cdot \mathbf{r}$) at a distance $|\mathbf{r}|$ from the nucleus; and $\boldsymbol{\ell}$ is the orbital angular momentum of the electron.

10 ABBREVIATIONS AND ACRONYMS

AO = atomic orbital; CT = charge transfer; ED = electric dipole; HOMO = highest occupied molecular orbital; IR = infrared; ICT = intraligand charge transfer; IL = intraligand; LLCT = ligand to ligand charge transfer; LMCT = ligand to metal charge transfer; LCAO = linear combination of atomic orbitals; LUMO = lowest unoccupied molecular orbital; MD = magnetic dipole; MLCT = metal to ligand charge transfer; MO = molecular orbitals; NIR = near-IR; UV = ultraviolet

11 FURTHER READINGS

The choice of the authors was to restrict the presentation of the fundamentals concepts of luminescence to a minimum of equations. After reading this chapter, the reader has accumulated enough knowledge to understand the photophysical discussions in the next chapters and in most of the publications. The next level would be to formulate the photophysical concepts with mathematical expressions. Nice books and reviews are dealing with these formulations and we recommend their lecture (see for example, Chapter 1 of Ref. 3).

12 REFERENCES

1. B. Valeur and M. N. Berberan, *J. Chem. Educ.*, 2011, **88**,, 731.
2. J.-C. G. Bünzli and C. Piguet, *Chem. Soc. Rev.*, 2005, **34**,, 1048.
3. P. Hänninen and H. Härmä, in 'Springer Series on Fluorescence', eds. O. S. Wolfbeis and M. Hof, Springer-Verlag, Berlin, 2011, Vol. 7, particular Chap. 1.
4. S. Cotton, Lanthanide and Actinide Chemistry, John Wiley & Sons, Chichester, 2006.
5. J. R. Lakowicz, 'Principles of Fluorescence Spectroscopy', Springer Science, New York, 2006.
6. B. Valeur, M. N. Berberan-Santos, 'Molecular Fluorescence, 2nd Edition', Wiley-VCH Verlag & Co., Weinheim, 2012.

Lanthanides: Luminescence Applications

Julien Andres and Anne-Sophie Chauvin

École Polytechnique Fédérale de Lausanne, Vaud, Switzerland

1 Summary 135
2 Introduction 135
3 The Colorful Potential of the Luminescent Lanthanide Ions 136
4 How to Characterize the Color from a Luminescent Emission? 140
5 Upconversion with Lanthanide Compounds 142
6 Light Amplification by Stimulated Emission of Lanthanide Radiation—Laser 142
7 Design of An Efficient Sensitizer for a Lanthanide Ion 143
8 Designing a Complex Emitting in the Near-Infrared (NIR) Range 150
9 Conclusions 151
10 Glossary 151
11 End Notes 151
12 Related Articles 151
13 Abbreviations and Acronyms 151
14 References 151

1 SUMMARY

The forthcoming chapter gives many examples where the luminescence of the lanthanide ions has a significant impact. It provides a description of the fundamental concepts related to the luminescence of lanthanide ions such as upconversion, laser, near-infrared (NIR) emission, and particularly, colorimetry, an important way to characterize emission in the visible range of the spectrum. Selected examples of sensitizing ligands from the literature are also discussed, starting from simple ligands such as β-diketonates and explain how a modification or a derivatization can alter the photophysical properties. The discussion is then extended toward the correlation of the triplet state energy of the ligand and the quantum yield of the complex and also argues about the quest for the highest quantum yield. More complex structures are finally shown in order to introduce special features, selective binding sites, and additional coordination sites forming polynuclear complexes and bimetallic complexes with d- and f-elements in the same complex.

2 INTRODUCTION

If there were only one example of application that should be remembered where the luminescence of the lanthanide ions is ever present, it would certainly be lighting. Nowadays, most of the so-called fluorescent lamps, light-emitting devices (LEDs), and display devices are made of phosphors-containing luminescent lanthanide ions. The reason is mainly the purity of the emitted color, particularly the red emission from europium(III) and green emission from terbium(III). The old CRT (cathode ray tube) display devices previously used in color televisions and computer monitors have now been replaced with LCDs (liquid crystal displays) and LEDs, but the light source still contains lanthanide ions. The technology changes but the building blocks remain the same. Since color science is never really addressed in chemistry textbooks, although the luminescence of the lanthanide ion is widely used in many applications that deal with color reproduction, an introduction to colorimetry is given in this chapter. We hope it may inspire readers to have a look

The Rare Earth Elements. Edited by David A. Atwood. © 2012 John Wiley & Sons, Ltd. ISBN 978-1-119-95097-4

at this fascinating domain, among which the luminescence of the lanthanide ions is extensively present.

Apart from the applications derived from lighting and color reproduction, the next important application is laser. The Nd:YAG laser is certainly one of the most widespread laser. The emission of Nd^{3+} in the NIR region thus also gives a good example of a lanthanide ion with an NIR emission, but as it will be shown, many other lanthanide ions have a transition in the NIR. When it comes to NIR emission, one could also wonder if an NIR absorption is achievable, and foremost, if such an absorption may yield a visible emission. Such an excitation is counterintuitive because it does not conserve the photon energy. Nevertheless, if two or more photons were absorbed, a conversion of two or more NIR photons to one visible photon may occur. The phenomenon (called *upconversion*) is indeed observed under special conditions that will be discussed.

Finally, some illustrative examples of sensitizing ligands are examined. The intent here is to provide, with a few structures, a broad overview of the trends and strategies used to improve or modulate the properties of a luminescent lanthanide complex. The examples are used to point at important considerations when attempting to design a ligand. This chapter is not a review of the whole complexes and applications which can be found in literature or patents, but aims at illustrating some of the aspects of the luminescent complexes, with arbitrary chosen examples. The fundamental concepts of photophysics and luminescence explained in ***Luminescence*** are a prerequisite to fully understand the notions presented here.

3 THE COLORFUL POTENTIAL OF THE LUMINESCENT LANTHANIDE IONS

The luminescence of the lanthanide ions spreads from the UV spectral range up to the NIR, and many lanthanide ions have unique spectral characteristics in the visible region of the spectrum, which also give them distinctive luminescent colors. A lot of applications take advantage of those characteristic emissions for color reproduction and lighting. Phosphors, nanomaterials made of lanthanide complexes or enclosing lanthanide compounds, as well as LEDs based on lanthanide complexes are extensively investigated.

Another growing field of research in luminescent lanthanide compounds is for energy conversion. The lanthanide ion is used as a converter that transforms one type of excitation energy, either UV light or IR light, into a visible energy that can be easily absorbed by a photosensitive device such as a solar cell. The process where the excitation energy is higher than the emission energy is well known and has been extensively described in the previous chapter (see ***Luminescence***). This process is called *downconversion* because it converts a high-energy photon light source into a lower energy photon light source. Nevertheless, the conversion of a low-energy photon light source into a higher energy photon light source is also possible if multiphoton absorptions or other special excitation mechanisms are taking place. This phenomenon is called upconversion and is briefly discussed later on. The upconversion materials are not to be confused with NIR emitters, which are downconversion materials, that are excited by UV or visible light and emit in the lower energy NIR spectral range.

Finally, the very important case of laser or light amplification by stimulated emission of radiation is briefly described, since lanthanide ions, and particularly neodymium, are among the most significant sources of laser medium.

3.1 The Lanthanide Ions and Their Color Characteristics

The most used lanthanides, relative to their luminescence, are europium and terbium. They have red and green emissions, respectively, that are very attractive for color reproduction (in an additive color synthesis, all colors can be reproduced by combinations of red, green, and blue primary colors). Their photophysical properties are further detailed in Sections 3.1.1 and 3.1.2.

Dysprosium (yellow emission) and samarium (orange emission) are also interesting for their luminescence, but their emission is usually weaker than europium and terbium. The luminescence of thulium (blue, red, and NIR emissions) is sometimes observed, but since several levels are present between the highest luminescent level (giving rise to the blue emission) and the ground state, nonradiative deactivations usually prevail. Praseodymium is less investigated compared to the other ions except for upconverting materials as shown later (Section 5). Its main transitions are two peaks in the red.

In the NIR side, the best lanthanides are ytterbium, erbium, and neodymium (it is used in the Nd:YAG laser, see Section 3.1.5). Holmium is less investigated but shows a very interesting emission spectrum with a red peak and an NIR peak.

A summary of the main visible transition of each lanthanide ion that has visible transitions, together with their typical emission intensity, can be found in Table 1.

To finish with this inventory, some lanthanides such as cerium, praseodymium, and terbium have allowed 4f–5d transitions whose energies are accessible using conventional instruments (between 220 and 330 nm). The extinction coefficients range from 100 to 1000 $l\,mol^{-1}\,cm^{-1}$.

The major nontrivalent lanthanide ion that is encountered for its luminescence property is Eu^{2+}. Europium(II) is mostly found in inorganic materials for its broad blue emission that comes from d–f transitions. The most well-known material is $BaMgAl_{10}O_{17}$: Eu^{2+} (BAM) that is used in blue-emitting phosphors (Figure 1).

Table 1 Summary of the main visible transition of the lanthanide ions having visible emissions and typical intensity of their visible emission

Trivalent lanthanide ion	Color of the visible luminescence due to the main transitions	Intensity of the emission
Europium	Red $^5D_0 \rightarrow {}^7F_2$ (615 nm) or Red-orange when $^5D_0 \rightarrow {}^7F_1$ (590 nm) as important as the $^5D_0 \rightarrow {}^7F_2$	Strong
Terbium	Green, $^5D_4 \rightarrow {}^7F_5$ (545 nm)	Strong
Dysprosium	Yellow, $^4F_{9/2} \rightarrow {}^6H_{13/2}$ (575 nm)	Medium
Samarium	Orange- red, $^4G_{5/2} \rightarrow {}^6H_{7/2}$ (600 nm)	Medium
Praseodymium	Red, $^1D_2 \rightarrow {}^3H_4$ (600 nm) and $^3P_0 \rightarrow {}^3F_2$ (650 nm)	Weak
Erbium	Green, $^4S_{3/2} \rightarrow {}^4I_{15/2}$ (545 nm)	Weak
Holmium	Red, $^5F_5 \rightarrow {}^5I_8$ (650 nm)	Weak
Thulium	Blue, $^1G_4 \rightarrow {}^3H_6$ (480 nm)	Weak

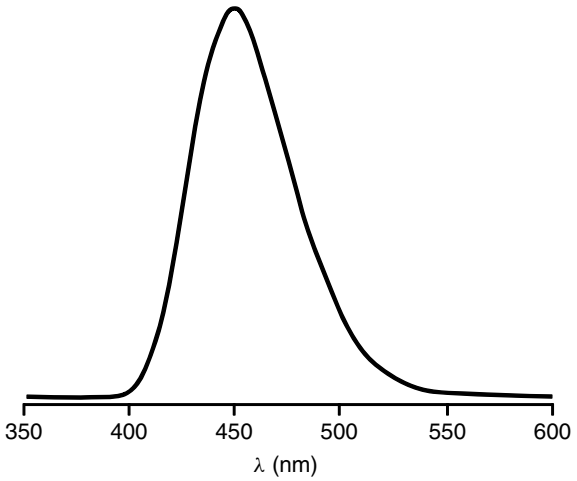


Figure 1 Emission spectrum of $BaMgAl_{10}O_{17}:Eu^{2+}$ (λ_{ex} = 254 nm)

Examples of typical emission spectra are presented in Figure 2, with the ligand H_2L^{C2} forming 2 : 3 complexes with Ln ions. For more details regarding this ligand and the applications of its 2 : 3 Ln:L complexes, the reader is referred to ***Luminescent Bioprobes***. The luminescence is originating from the $^5D_0 \rightarrow {}^7F_J$ transitions for Eu^{3+} ($J = 0$–6) and $^5D_4 \rightarrow {}^7F_J$ for Tb^{3+} ($J = 6$–0), and from the $^4G_{5/2} \rightarrow {}^6H_J$ (J = 5/2, 7/2, 9/2, and 11/2) transitions for Sm^{3+}. A residual fluorescent emission from the ligand is also observed for the samarium complex.

3.1.1 The Very Special Case of Europium

Europium is certainly the most versatile lanthanide. Its luminescence can be used to reproduce blue ($BaMgAl_{10}O_{17}:Eu^{2+}$), green ($SrGa_2S_4:Eu^{2+}$), or red (any sensitized Eu^{3+} complex). The presence of such europium compounds in the luminescent inks used on the euro banknote is suspected for the blue and the green luminescent colors, undoubted for the red-emitting one. Eu^{2+} is produced and stabilized in phosphors under reducing atmospheres.

Regarding the luminescence of the trivalent ion, the visible emission spectrum from Eu^{3+} is composed of the $^5D_0 \rightarrow {}^7F_J$ transitions. Three transitions are particularly useful: the $^5D_0 \rightarrow {}^7F_2$, $^5D_0 \rightarrow {}^7F_1$, and $^5D_0 \leftarrow {}^7F_0$.

The so-called hypersensitive transition ($^5D_0 \rightarrow {}^7F_2$) found around 615 nm enables detecting changes in the coordination sphere. This perturbation can be caused by the addition of another molecule (for example, a competitive ligand) by a variation of the ionic strength of the solution (addition of a salt), by a variation of the polarity of the solvent (addition of another solvent), or by a variation of the pH value of the solution (addition of an acid or a base) when working in aqueous solutions.

The purely magnetic dipole transition ($^5D_0 \rightarrow {}^7F_1$) has an intensity that is practically independent of the chemical environment and that provides an estimate of the radiative lifetime of the europium ion (see ***Luminescence*** and ***Luminescent Bioprobes***). Furthermore, the ratio between the intensity of the $^5D_0 \rightarrow {}^7F_2$ and the $^5D_0 \rightarrow {}^7F_1$ is a good indicator of the resulting emission color. The more intense the $^5D_0 \rightarrow {}^7F_1$ relative to the $^5D_0 \rightarrow {}^7F_2$, the more orange the luminescence looks like (the emission in Figure 2 is an example of an orange-shifted luminescence from Eu^{3+}). The purest red emissions are achieved when the $^5D_0 \rightarrow {}^7F_2$ is by far the most intense transition. This ratio is however not an indicator of the quantum yield, but a rough approximation of the ratio used to calculate the radiative lifetime: the higher the $^5D_0 \rightarrow {}^7F_1$ relative to the $^5D_0 \rightarrow {}^7F_2$, the higher the radiative lifetime. The intrinsic quantum yield also depends on the observed lifetime.

Finally, the $^5D_0 \leftarrow {}^7F_0$ transition is unsplit by the ligand field due to the multiplicity of one ($2J + 1 = 1$) of both the final and the initial state. This transition is usually measured by scanning at low temperature the excitation wavelength with a laser source and recording of the emission intensity of the $^5D_0 \rightarrow {}^7F_2$ transition. Since any splitting of the 0–0 transition is due to a different europium environment, because a single europium species has only one peak, the number of peaks in the 0–0 transition shown in the excitation spectrum indicates the number of differently coordinated europium species.

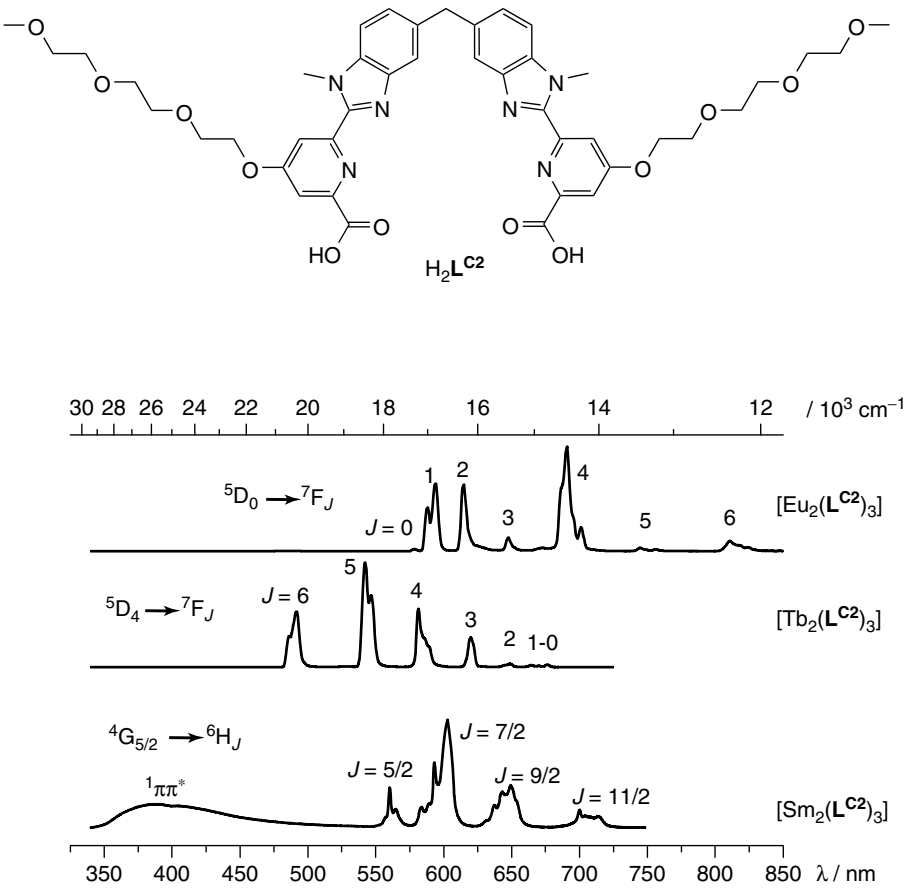


Figure 2 Emission spectra of H_2L^{C2} and its Eu^{3+}, Tb^{3+}, and Sm^{3+} helicates in Tris-HCl 0.1 M pH 7.4, with $[H_2L^{C2}]_t = 4.5 \times 10^{-5}$ M under ligand excitation at and 323 nm (Eu, Tb). All spectra have been recorded without delay at room temperature

3.1.2 The Special Case of Terbium

Terbium is, besides europium, a remarkable lanthanide ion. All the emission peaks come from $^5D_4 \rightarrow {}^7F_J$ transitions, with $J = 6, 5, 4, 3, 2, 1, 0$. Its major emission peak is the $^5D_4 \rightarrow {}^7F_5$ centered around 545 nm, which gives it a green shade. Three other peaks, at 490 nm ($^5D_4 \rightarrow {}^7F_6$), 590 nm ($^5D_4 \rightarrow {}^7F_4$), 620 nm ($^5D_4 \rightarrow {}^7F_3$) are also present, but they usually have a lower intensity and are well balanced around the 545 nm peak, so that the color is little disrupted from the green. Actually, they can be seen as if they would add some white to the green so that it looks brighter. Besides, the $^5D_4 \rightarrow {}^7F_2$, $^5D_4 \rightarrow {}^7F_1$, and $^5D_4 \rightarrow {}^7F_0$ are typically very weak and consequently their contribution to the color of the emission can be neglected.

In addition to the $^5D_4$ luminescent excited state, the higher $^5D_3$ spectroscopic level is also luminescent. The luminescence from this level down to the ground state shows emission peaks in the blue region of the spectrum around 400 nm. In some inorganic materials, the blue emission peaks might become important, but a fast relaxation from the $^5D_3$ down to the $^5D_4$ level usually prevails. In coordination complexes with organic sensitizers, the triplet state has to be high enough in energy in order to populate the $^5D_3$ level, but the relaxation down to the $^5D_4$ level is here even favored by the vibrations of the ligands and of the solvent molecules.

Terbium also has an accessible 4f–5d transition around 220 nm. This property is yet not often encountered in a common photophysical investigation that spreads from 250 nm to 1100 nm. An energy migration from the 4f–5d state down to the $^5D_3$ and then down to the $^5D_4$ is however possible.

Finally, note that terbium has the second highest energy gap (after gadolinium) between its excited state and the lower energy states from its ground spectroscopic term (the ^7F term). As a result, the luminescence of terbium is, providing an appropriate triplet state of the ligand, in general more easily efficient than the luminescence of europium. The terbium ion is indeed not as sensitive to the vibrationally assisted deactivations as the other lanthanide ions. The lifetime of a terbium complex does hence not change very much as a function of temperature. A few examples of nearly quantitative quantum yields (between 94% and 98%) are encountered in literature with chromophores derived from 2,6-bis(*N*-pyrazolyl)pyridine, even in aqueous solution, but

such examples are truly exceptional.[1] Usually, the quantum yields of terbium complexes in aqueous solution are lower than 40%. The observed lifetime of terbium complexes are also higher than those of the other lanthanide ions: lifetimes higher than 2 ms are not rare.

3.1.3 *The Special Case of Gadolinium*

On the other side of the visible spectrum, gadolinium has a very high gap between its ground state and the first excited state. It comes from the particular stabilization of the half-filled 4f subshell. Its luminescence would be in the UV region. Its possibility to emit UV light is very attractive for the lighting industry (particularly for compact fluorescent lamps or CFL) because the nearly exclusive excitation light source used nowadays to excite phosphors contains mercury (mercury have strong UV transitions at 254 and 366 nm). An alternative efficient UV light source without such a toxic element would have a considerable positive impact.

Under usual UV excitation and with an organic sensitizer, the UV transition of Gd^{3+} is never observed. Gadolinium is thus commonly considered as nonluminescent in coordination complexes. Nevertheless, it has the highest number of unpaired electrons (a half-filled 4f subshell yields seven unpaired electrons), and thus possesses a very high paramagnetism which favors the intersystem crossing of the sensitizer even more than the other lanthanides. Therefore, gadolinium is often used as a nonemissive ion to investigate the triplet state of the coordinated sensitizer by the measurement of the phosphorescence spectrum of the gadolinium complex. The gadolinium complexes also show a better vibronic structure of the phosphorescence than the other nonemissive lanthanide ions. The two other nonemissive lanthanide ions are lanthanum and lutetium. They have, respectively, no electron (empty subshell) and 14 electrons (full subshell) in the 4f subshell, so that they do not possess any electronic levels and thus have no photophysical properties that are due to their 4f electrons.

3.1.4 *The Case of Lanthanide Ions Emitting Both in Visible and Near-IR Range*

Some lanthanide ions emit light in both the visible and the NIR range (Pr^{3+}, Sm^{3+}, Dy^{3+}, Ho^{3+}, Tm^{3+}). The emission spectra given in Figure 3 are examples of such faint and sharp Ln^{3+}-centered emission bands in the visible range with a same ligand (H_2L^{C2}).

- For Pr^{3+}, both $^1D_2 \rightarrow {}^3H_4$ and $^3P_0 \rightarrow {}^3H_6$ transitions are observed at 602 and 615 nm, respectively[2,3].
- For Dy^{3+}, two bands are displayed at 476 and 572 nm, corresponding to the $^4F_{9/2} \rightarrow {}^6H_J$ ($J = 15/2$ and 13/2) transitions, respectively[2].
- For Ho^{3+}, only the $^5F_5 \rightarrow {}^5I_8$ is seen around 650 nm[2,4].
- On the other hand, the emission of the Tm^{3+} helicate does not exhibit any metal-centered luminescence at room temperature.

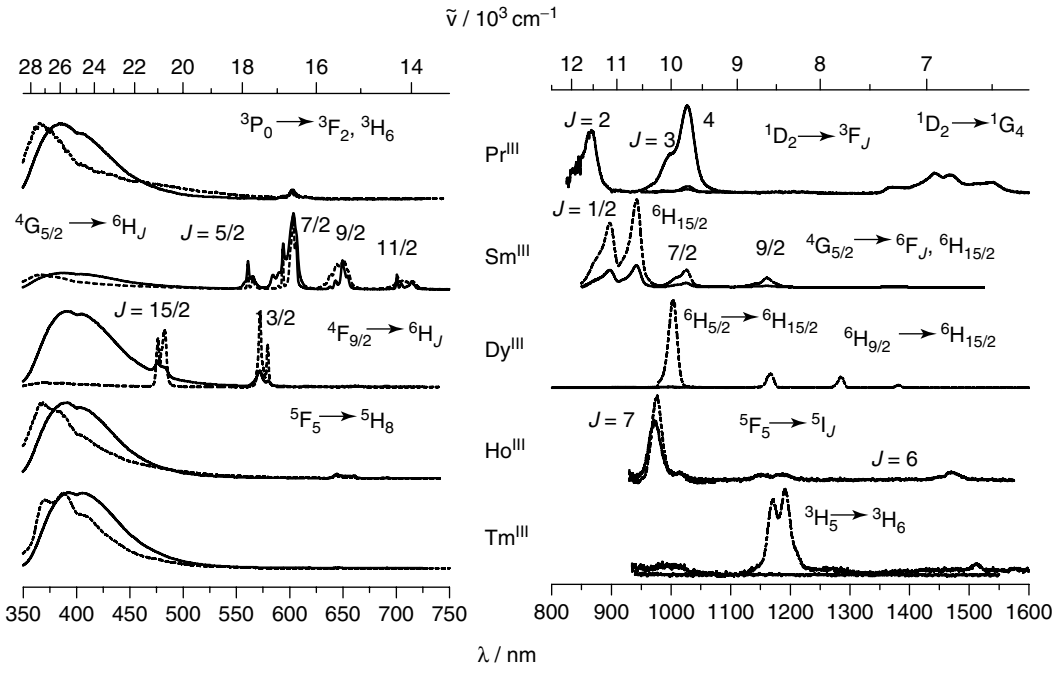


Figure 3 Emission spectra upon excitation at 323 nm of Ln^{3+} helicates (Ln = Pr, Sm, Dy, Ho, and Tm) with ligand H_2L^{C2} pH 7.4 (Tris-HCl 0.1 M), $[H_2L^{C2}]_t = 4.5 \times 10^{-5}$ M. (Left) emission in the visible range at 298K (black line) and 77 K (dashed line). (Right) emission in the NIR range at 298K, in H_2O (black line) or D_2O (dashed line). $\lambda_{ex} = 323$ nm. (Taken from Ref. 5.)

For these helicates emitting in both spectral ranges, a change in temperature (in particular for Dy^{3+}, Ho^{3+}, Tm^{3+}) or a deuteration of the solution (Pr^{3+}, Sm^{3+}) both lead to a sizeable enhancement of the luminescence. These techniques are often used to increase the photophysical properties of the complexes.

3.1.5 The Case of the ''Standard'' NIR-Emitting Lanthanide Ions

There are three NIR-emitting ions, whose emissions in the NIR are more efficient than the other ions: Yb^{3+}, Nd^{3+}, and Er^{3+}. The two main difficulties to develop ligands able to sensitize these lanthanide ions consist in (i) the numerous deactivating oscillators present in the ligand backbone and (ii) the large energy gap ($>10\ 000\ cm^{-1}$) separating the 0–0 vibronic transition of the triplet state of the ligand (H_2L^{C2} ligand in the example depicted in Figure 4) from the Nd($^4F_{3/2}$), Er($^4I_{13/2}$), and Yb($^2F_{5/2}$) levels lying at 11 500, 6500, and 10 400 cm^{-1}, respectively.

The $[Nd_2(L^{C2})_3]$ helicate displays one main band between 1020 and 1130 nm ($^4F_{3/2} \rightarrow {}^4I_{11/2}$) with a maximum at 1064 nm, and two other ones between 845 and 940 ($^4F_{3/2} \rightarrow {}^4I_{9/2}$) and 1275–1400 nm ($^4F_{3/2} \rightarrow {}^4I_{13/2}$). The Yb^{3+} emission is characterized by a band in the 920–1090 nm range, which is assigned to the $^2F_{5/2} \rightarrow {}^4F_{7/2}$ transition. Finally, one transition at 1450–1650 nm is observed for the $[Er_2(L^{C2})_3]$ helicate, corresponding to the $^4I_{13/2} \rightarrow {}^4I_{15/2}$ transition, but this later is detected in deuterated water only.

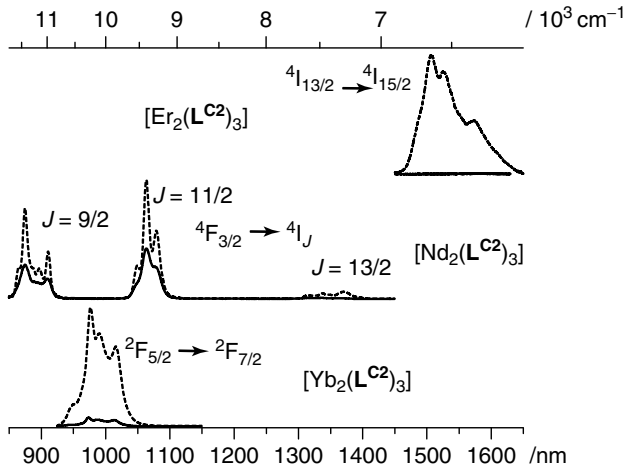


Figure 4 Emission spectra upon excitation at 323 nm of Ln^{3+} helicates (Ln = Nd, Er, and Yb) with H_2L^{C2} at room temperature in H_2O (—, full line) and D_2O (---, dashed line); $[H_2L^{C2}]_t = 4.5 \times 10^{-5}$ M. $\lambda_{ex} = 323$ nm. (Taken from Ref. 5.)

4 HOW TO CHARACTERIZE THE COLOR FROM A LUMINESCENT EMISSION?

Luminescent materials or compounds that have an emission in the visible spectrum (anywhere from 380 to 730 nm) appear colored to the naked human eye. The color property, beyond the subjective designation of colors by words, is described scientifically by colorimetry. Because the photosensitive cells in the eyes are sensitive either to red, green, or blue, any color can be described by a combination of red (R), green (G), and blue (B) primary colors. The combination of the primary colors then gives other colors that are named cyan (C) for the combination of green and blue, magenta (M) for the combination of red and blue, and yellow (Y) for the combination of red and green. The combination of the three primary colors then yields the white (W) color, whereas the absence of any light is seen as black (K). This mode is called the *additive synthesis of color* because it adds primary colors coming from a colored light source.[a] The additive mode is suitable for emissive compounds. The color of the luminescence of lanthanide complexes are often characterized when they are applied in LEDs. More generally, in any field of research dealing with the color resulting from a luminescence phenomenon, one should consider the special case of the colorimetry of emissive compounds. A brief description of what is a color space and a presentation of two of the most widespread color spaces follows.

An important feature of the color perception is that, besides the raw sensing of the color world, the brain processes the information. One of these signal processings deals with the chromatic adaptation to what the brain perceives as the more intense and pleasant white. This is similar to what is known in digital photography as the white balance. This aspect is important as soon as we compare colors together, because a color coordinate is always defined relative to a reference stimulus that is processed as the white color. The reference white depends on the color space that is used to measure the color.

A color space is a three-dimensional representation of the colors as a combination of three other color coordinates chosen as primaries. For example, the *RGB* color space is represented as a cubic space with a red, green, and blue axis (primaries) growing from the black up to the red, green, and blue color, and then from the red to the magenta, yellow and white, from the green to the cyan, yellow and white, and from the blue to the cyan, magenta and white. The diagonal from the black corner to the white corner is then the grayscale. This color space is simple, but rarely used directly to characterize a color.

Since 1931, the most widespread color spaces for colorimetry of luminescent materials are based on the CIE XYZ color space. The CIE (commission internationale de l'éclairage) is an organization that standardizes all the color sciences. Here, X, Y, and Z coordinates represent a defined combination of R, G, and B so that the sensitivity function that defines the Y coordinate fits the photopic sensitivity of the eye (average sensitivity function of the

cone cells). The sensitivity functions associated with the X, Y, and Z coordinates are called *color-matching functions* (see equations 1–4). The integration over the whole visible spectrum of the multiplication of a stimulus $S(\lambda)$ (e.g., a spectrum from a visible light source) with each color-matching function $\bar{x}(\lambda)$, $\bar{y}(\lambda)$, and $\bar{z}(\lambda)$ gives the tristimulus value XYZ that are usually scaled relative to a constant factor K that depends on the luminance of a reference spectrum $S_{\text{ref}}(\lambda)$ (luminance is defined as the photometric counterpart of radiance, producing the visual sensation called brightness). The XYZ values depend on the spectral power distribution and on the intensity of the stimulus. They can also be normalized relative to the sum of the X, Y, and Z values to yield the xyz values. Usually, the Y value is retained to account for the intensity or luminance of the color relative to the luminescence of the reference stimulus, whereas the x and y values give the chromaticity of the stimulus that is independent of the reference stimulus chromaticity.

$$X = K \cdot \int_{\lambda} S(\lambda) \cdot \bar{x}(\lambda) \cdot \mathrm{d}\lambda \tag{1}$$

$$Y = K \cdot \int_{\lambda} S(\lambda) \cdot \bar{y}(\lambda) \cdot \mathrm{d}\lambda \tag{2}$$

$$Z = K \cdot \int_{\lambda} S(\lambda) \cdot \bar{z}(\lambda) \cdot \mathrm{d}\lambda \tag{3}$$

$$K = \frac{100}{\int_{\lambda} S_{\text{ref}}(\lambda) \cdot \bar{y}(\lambda) \cdot \mathrm{d}\lambda} \tag{4}$$

The xyY color space is the predominant color space for the characterization of luminescent materials because it enables a convenient visualization of the chromaticity of the emitted light that is independent of the visualization condition (no chromatic adaptation). A chromaticity diagram represents all perceivable colors in the xy plane. The border of this diagram is the monochromatic visible spectrum from 380 to 700 nm and what is called the purple axis from red to violet via magenta (Figure 5).

Nevertheless, the chromaticity diagram has the main disadvantage to exhibit nonuniform color differences between the different regions. A chromaticity difference in the green part is not perceived as the same difference in the red or in the blue for example. We can still see a very similar green over a large area of the chromaticity diagram, whereas the red and blue regions are much smaller. More advanced color spaces tend to minimize this color difference so that the color space is as homogeneous as possible. The typical example is the CIELAB color space. Here, the chromaticity is expressed as a^* and b^* coordinates and the luminance (the grayscale axis) as L^*. This color space also performs a chromatic adaptation to a reference white so that the 100, 0, 0 $L^*a^*b^*$ point represent the reference white color. Color differences are much easier to calculate using, for example, ΔE_{94} values.[6] This color space is particularly suited when reproducing color images. For more

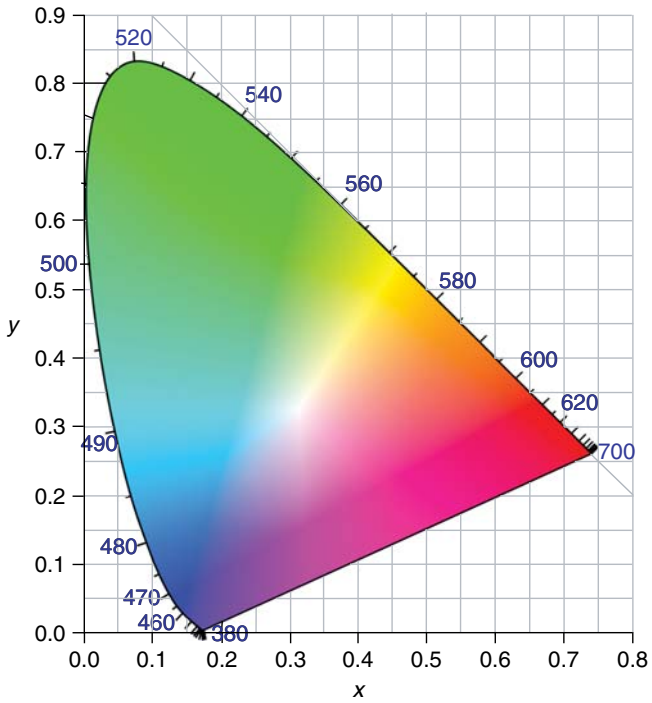


Figure 5 xyY chromaticity diagram. (Reproduced from Wikipedia, 2012.)

information about color science, see the book of Wyszecki and Stiles.[7]

The best suited color space then depends on the intent of the colorimetry. If it is only to provide an absolute chromaticity indication because the luminescent emission is not compared in an environment that is relevant for color reproduction, the simple chromaticity diagram is sufficient. For example, literature about LEDs, several of which have lanthanide ions, usually expresses the chromaticity of the emitted light on a chromaticity diagram (xyY). For white light sources, the correlated color temperature ((CCT), representing the temperature of a black body radiator that would have a similar color) gives similar information. On the other hand, if the luminescent emissions are combined to reproduce white lights or to yield an image, or if color differences are calculated, the quite uniform CIELAB color space should be preferred. In the above white LED example, the quality of the white emission is often tested by calculating its color-rendering index (CRI). The CRI is a measurement of the average color difference calculated on a set of standard reference color patches (reflective color samples generating colors by reflection of part of the white light) viewed under the tested light source relative to the color that would be seen under its CCT emission. Nevertheless, the color space used in the determination of the CRI is outdated and this metric quite criticized. Another quality metric called *color quality scale* (CQS) has been developed by the National Institute of Standards and Technology (NIST) using CIELAB and

provides a better appreciation of the quality of a white light source, especially for LEDs.[8]

Besides the sole lighting domain where lanthanide ions are extensively used, all applications that intent to reproduce colors need colorimetry. The most obvious ''color-rendering example'' that also widely consumes luminescent lanthanide ions is a display device where the emissions from different phosphors are combined to obtain all the colors that can be generated by the device. The subset of colors that a system can reproduce is called a *gamut* and represents a region of the color space. Another domain where the luminescence of lanthanide ions is extensively present is in document security. Apart from the color reproduction of color images similar to a display but with printed luminescent security inks that can be excited by UV light, the luminescence in the document security domain can be used to hide or reveal patterns, encrypt information, and thus secure genuine valuable documents or objects to prevent counterfeiting. Banknotes are the most prominent example of such applications.

An important point about colorimetry is that all the standard color spaces use relative radiometric units and not relative photon counts. This is important because a spectrophotometer usually measures counts that are proportional to the number of received photons at a defined wavelength. A correction function that performs at the same time the correction of the detector sensitivity at each wavelength as well as the conversion to radiometric units is then needed

5 UPCONVERSION WITH LANTHANIDE COMPOUNDS

Upconversion refers to the emission of light at lower wavelength (higher energy) than the excitation light source. There are two distinct mechanisms that enable this phenomenon. The first one takes advantage of the higher excited states that lies higher than the first excited state. An absorption from the excited state to generate a multiply excited compound may emit then a photon of higher energy from this higher excited state. This is called *excited state absorption*. The second mechanism has no intermediate excited state and simply requires a sufficient photon density for a simultaneous interaction of two photons of lower energy to an excited state at twice the photon energy; therefore, this process is defined as two-photon absorption.

Both mechanisms depend on the photon density, which translates into the light intensity (power) and thus on the square of the electromagnetic field. The requirement for an excited state absorption is a metastable excited state. The photon density should then be sufficient to ensure that during the lifetime of the excited state, another photon has a high probability of interacting with excited chromophore. The limit when the state is very unstable tends toward the case of a two-photon absorption. The two-photon absorption is also characterized by a two-photon absorption cross section that is related to the two-photon absorption rate constant.

Another process derived from excited state absorption is an energy transfer from one excited compound to another excited compound to form the doubly excited state. In this transfer, the energy stored in the two excited states of low energy is combined to form a high-energy excited state that can give back the energy in the form of a higher energy photon.

Two-photon absorption is certainly the main process in coordination complexes with organic chromophores. A tuning of the two-photon cross section can be apprehended by a derivatization of the ligands. By the two-photon excitation process, the excited ligand transfers the energy onto the lanthanide ion similar to a downconversion mechanism.

The other upconversion pathways are foremost relevant in doped inorganic materials. Multiionic mechanisms can be developed based on those fundamental principles. The most frequent lanthanide ions for upconversion in inorganic materials are Pr^{3+}, Er^{3+}, and Tm^{3+}. Most of those inorganic materials use f–f transitions to achieve excited state absorptions. Lanthanide ions having both NIR and visible emission are thus needed. This limitation does not occur for two-photon absorption, which may use any lanthanide ion. For more details, the reader can refer to specific reviews.[9,10]

6 LIGHT AMPLIFICATION BY STIMULATED EMISSION OF LANTHANIDE RADIATION—LASER

A laser is the result of a stimulated emission. Such an emission mechanism is similar to that of a spontaneous emission as described in ***Luminescence***, except that the emission of the photon is triggered by an incoming photon at the same energy.

$$\text{photon} + D^* \rightarrow 2\ \text{photon} + D \qquad (1)$$

When the emissive component D^* is more abundant than the absorbing component D, the flux of emitted photons is more important than the flux of absorbed photons. This condition is called an *inversion population* and is the requirement for a laser to have a net gain, or a real amplification.

A laser is composed of a laser medium enclosed in a cavity between two mirrors, and of an excitation light source that is used to excite the laser medium, which is often referred as pumping of the laser medium. The excited medium then emits photons in all directions. Along the axis of the cavity, the photons will bounce back on the mirrors through the laser medium and might trigger a stimulated emission from an excited active compound in the laser medium. This stimulated emission is also along the axis of the cavity so that the photon

flux along the axis rapidly builds up in intensity. The laser then reaches a steady state when the flux of emitted photon in the cavity is constant, and therefore the radiative rate of the laser medium compensates the excitation rate and the nonradiative deactivation rate.

There are many types of laser media, either gas, liquid, or solid. Furthermore, there are different electronic structures that can be used to facilitate an inversion population. A simple two-level scheme is indeed not optimal. A four-level scheme where two levels are used to excite the medium and two others are used to emit light is much better. In such a conformation, the excitation takes place between the ground state and an upper excited state with two other available levels in between the initial and final state. The excited compound then quickly relaxes nonradiatively down to the closer lower excited state where the emission takes place down to the first excited state. The first excited state finally relaxes down to the ground state similar to the relaxation between the fourth and third level. This way, the emission process always occurs to a statistically empty level (provided that the relaxation is fast enough). The inversion population is therefore maximized.

Owing to their narrow line emission, lanthanide ions are very attractive for lasers. The numerous electronic levels also provide many possible output wavelengths, even for a same ion, and are appropriate for an efficient four-level laser medium. The most common laser made of lanthanide ions is the Nd:YAG laser. Here, the neodymium is the active ion, whereas YAG is a solid host material with the proper physical characteristics to yield an efficient laser. The laser medium can be excited by various light sources (halogen–tungsten, krypton lamp, LED, etc.). The excitation of the laser medium is taking place at 808 nm. It corresponds to the $^4F_{5/2}$, $^2H_{9/2} \leftarrow {}^4I_{9/2}$ transitions of the Nd^{3+} ions. In Nd:YAG, the absorption coefficient at 808 nm is lower than 10 cm^{-1}, which is low and comes from the forbidden character of the f–f transitions. Nevertheless, it enables an excitation through the whole laser. A highly absorbing material would indeed not be transparent enough to allow the excitation light source to penetrate through the laser medium. The classical output wavelength of the Nd:YAG laser is 1064 nm (NIR). It corresponds to a $^4F_{3/2} \rightarrow {}^4I_{11/2}$ transition. The Nd:YAG laser is a good example of a four-level laser as shown in Figure 6.

Other modes are possible with a Nd:YAG laser (other output wavelengths). They correspond to transitions to the higher ^4I_J states (represented in gray in Figure 6), or to the ground state if working as a three-level laser.

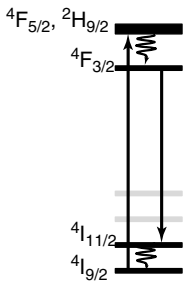


Figure 6 Main transition of the Nd^{3+} ion involved in a Nd:YAG laser lasing at 1064 nm

7 DESIGN OF AN EFFICIENT SENSITIZER FOR A LANTHANIDE ION

Up to now, some basic applications have been presented which apply in some cases to lanthanide complexes and in other cases to lanthanide phosphors or inorganic materials. We now exclusively focus on luminescent lanthanide complexes, and how to design, improve, or adjust the photophysical properties of such complexes.

Lanthanide ions can form complexes with various organic molecules such as β-diketones, polyaminopolycarboxylic acids (EDTA and the like), (poly)pyridines, and calixarenes. As already explained in ***Luminescence***, there are two parts in a ligand: the coordination site and the chromophore. Some have a coordination site that is part of the chromophore (e.g., β-diketones, pyridine derivatives), while others have a more separate architecture where the chromophore may even not be involved in the coordination (e.g., polyaminocarboxylates). The design of a ligand then firstly aims at combining a proper coordination site and a suitable chromophore so that the complex forms, is stable, and has a luminescence high enough to be useful for a particular application. On a first approach, the higher the luminescence, the better the ligand. The characterization of the photophysical properties of a luminescent lanthanide complex includes the determination of the quantum yield, the excitation wavelength and the associated extinction coefficient, the location of the triplet state of the ligand (the energy of its 0–0 vibronic transition), the observed lifetime of the excited state of the lanthanide ion, the radiative lifetime of the lanthanide ion and its intrinsic quantum yield if possible, and the hydration number q in the first coordination sphere. The investigation of a complex also required physicochemical characterization though, in order to check its stability. Some of the requirements to make a good luminescent probe are the following:

1. The ligand should strongly coordinate to the lanthanide ions. The highest stability constant ensures that no dissociation of the complex occurs, which may lead to a decline of the luminescent properties. The stability of the complex has to be established from a thermodynamic as well as a kinetic point of view, which implies that the complex should be stable over time.
2. A full coordination sphere with coordination number CN>8 in solution is required. The full coordination sphere prevents any solvent molecule, especially the presence of water molecules (which are known to be

strong quenchers), to come in the first coordination sphere and coordinate to the lanthanide ion. Their presence is determined by the determination of the hydration number q.

3. The presence of OH, NH oscillators should be avoided, especially in case of NIR sensitization, to prevent the quenching of luminescence. Ideally, even C–H oscillators should be replaced by lower energy oscillators such as C–F groups.
4. Ligands should possess chromophores exhibiting high extinction coefficients to maximize the number of absorbed photons and thus decrease the ratio of unused photons. The distance between the chromophore and the lanthanide ion and also its orientation should be taken into account since dipole–dipole transfer varies as $1/r^6$ (where r refers to the distance between the two entities).
5. The triplet state of the ligand has to be located not too far in energy from one of the excited state of the lanthanide ions, in order to have an optimal rate of the energy transfer; yet not too close to avoid energy back transfer from the lanthanide excited state to the triplet state, which would drastically decrease the luminescence intensity.

The limiting point is often (5). A sensitizer must possess the correct triplet energy in order to sensitize the desired lanthanide ion. It requires then a triplet emission or phosphorescence of the ligand that is higher in energy than a threshold limit fixed by the energy of the lower luminescent excited spectroscopic level of the lanthanide ion.

The phosphorescence is usually measured at 77 K to limit the temperature-dependent nonradiative deactivations, and a time delay is added between a pulsed excitation and the measurement to discard any residual fluorescence. The phosphorescence is typically located at the lower energy end of the fluorescence spectrum.

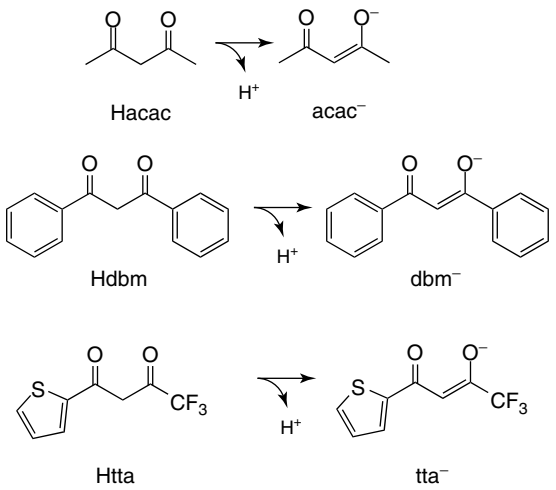
There are no precise rules that guarantee a proper energy of the triplet state. Some computational methods exist to predict the photophysical properties of an organic molecule, but their accuracy is not always satisfactory. Some empirical rules have been developed by Woodward in order to determine the absorption wavelength by an incremental method, but even if the absorption is known, there is little way to find out where the triplet state will be located relative to the absorption. The best method is then to study known structures and compare already used chromophores. The purpose of the forthcoming discussion is to have a look at different structures, how they can be altered to modify their photophysical properties, what are the similar patterns that they might share, and ultimately how to rationalize their efficiency by structural and comparative considerations. To finish, a new interest for computational chemistry dealing with lanthanide complexes has recently emerged with the development of new models, in particular based on density functional theory (DFT); it has been successfully applied to the determination of structure, vibrational spectra, nuclear magnetic resonance (NMR) chemical shifts, hyperfine interactions, excited states, and on the conformational properties of some lanthanide(III) polyaminocarboxylate complexes.[11]

7.1 Chromophores, Conjugation, and Auxochromes

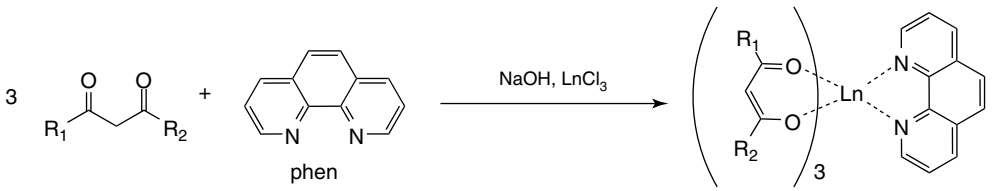
7.1.1 β-Diketonate Ligands

To illustrate the common motifs or chromophores, sensitizing luminescent lanthanide ions, one should begin with β-diketones. They are very simple and yet highly derivatizable so that many chromophores can be formed. β-Diketones are based on two keto groups as presented in Scheme 1, which form six-membered metal-containing rings. Most of the times, the ligand is stabilized as its monodeprotonated form and can easily coordinate a given metal cation. Although coordination compounds from β-diketonate ligands are reported for nearly all groups of the periodic classification, the lanthanide-containing ones are of great interest and yields several highly luminescent lanthanide complexes. The simplest β-diketone is acetylacetone (Hacac, see Scheme 1). Once coordinated to a lanthanide ion, one of the two protons between the two ketones is removed and the negative charge is delocalized between those two ketones. The limit structure is a diketonate ($acac^-$) with one ketone and an enolate (Scheme 1).

The delocalization also induces a higher conjugation of the chromophore (resonance over a longer distance): In the protonated form, the chromophore has only a C=O double bond, whereas in the deprotonated form, the chromophore now extends through four bonds O=C–C=C–O. The increase of the delocalization, conjugation, or resonance also increases the absorption wavelength (lower the energy of the excitation, see ***Luminescence***). The triplet state of acac once complexed with a lanthanide ion is well located to efficiently sensitize terbium. Nevertheless, an additional neutral ligand has to be added to complete the coordination sphere and yield a



Scheme 1



Scheme 2

coordination number of at least eight; phenanthroline (phen) is a typical example (Scheme 1) of such a ligand forming a ternary complex.

Acetylacetone is one of the few β-diketone that can sensitize terbium because more extended β-diketones usually have a triplet state lower than the emissive level of Tb^{3+}. Dibenzoylmethane (Hdbm) is an example of such an extended β-diketone. Here, two phenyl moieties are replacing the methyl group of Hacac (Scheme 1). The deprotonation joins the two acetophenone chromophore together. The absorption of dbm^- then goes up to the visible spectrum. The absorption of some blue light yields a yellow solution under daylight. The triplet state is well suited for europium, which is well sensitized by dbm^-, provided that an additional neutral molecule such as phenanthroline is added to complete the coordination sphere.

The most efficient europium complex up to now is made of thenoyltrifluoroacetone (Htta, see Scheme 1) as a β-diketone and phen as the additional neutral ligand. $[Eu(tta)_3phen]$ has an absorption up to 400 nm. The β-diketone has a thenoyl moiety on one side of the β-diketone and a trifluoromethyl group on the other side. The introduction of C–F bonds instead of C–H bonds has two main effects: it decreases the vibrational deactivation due to the C–H vibrations because C–F vibrations are much lower in energy, and it pulls the electrons toward the CF_3 group (electron-withdrawing group). The introduction of an electron-withdrawing or electron-donating group on a chromophore usually lowers its transition energy, so that the absorption occurs at higher wavelengths. Such substituents are called *auxochromes* (from the Greek *αὐξώ* increase). Usually, the lowest wavelength (highest energy transition) is obtained from the unsubstituted chromophore (hydrogen at position R). Nevertheless, the exact effect depends on the structure of the chromophore, and on the position at which the auxochrome is added. An auxochrome may also induce solvatochromic effect, so that unexpected results are sometimes observed.

The tta^- ligand (Scheme 1) is a typical example of a push–pull chromophore where one extremity is electron rich (the thenoyl part) and the other electron poor (the $O{=}CCF_3$). Push–pull systems are convenient designs where the absorption wavelength can be well predicted according to the distance between the push and pull moieties. Further derivatizations introducing electron-withdrawing or electron-donating groups on the chromophore can then finely tune the photophysical properties of the chromophore or fluorophore.[12]

Those preliminary considerations are good basis in chromophore design to tune the absorption and emission properties. The chromophore usually directly coordinates to the lanthanide ion, as depicted in Scheme 2 for β-diketonate complexes. Without the phen ligand (or any other coordinating ligand), the β-diketonate complexes generally forms hydrated complexes $[Ln(\beta\text{-diketonate})_3(H_2O)_2]$. The shielding provided by the phen ligand (or any nondeactivating coordinating ligand) then greatly improves the luminescence properties.

Steric hindrance is also very important in ligand design. An extended ligand may not coordinate properly, or may decrease the stability of the complex so that the lanthanide ion may be exposed to the solvent molecules. Such phenomena are less relevant when the coordination moieties are not part of the chromophore. A separate configuration thus allows more flexibility in the chromophore design, but lowers the efficiency of the energy transfer.

The same problem of complex stability may happen when electron-withdrawing groups are conjugated with the coordination moieties. The coordination sites should be good hard electron donor to yield the best ionic interaction with the lanthanide ion. Because electron-withdrawing groups withdraw part of the electronic density from the coordination sites, the stability of the coordination bonds are weakened by this kind of derivatization. This effect is experienced in the case of the fluorinated ligand such as tta^-. However, the photophysical properties of the europium complexes are impressive, with a quantum yield of 0.72 (to be compared to ~0.48–0.50 with other cited complexes) and a nearly quantitative sensitization efficiency (η_{sens} ~95–100%). The limit is here the stability of the complex that may also be weakened in the excited state (photobleaching).

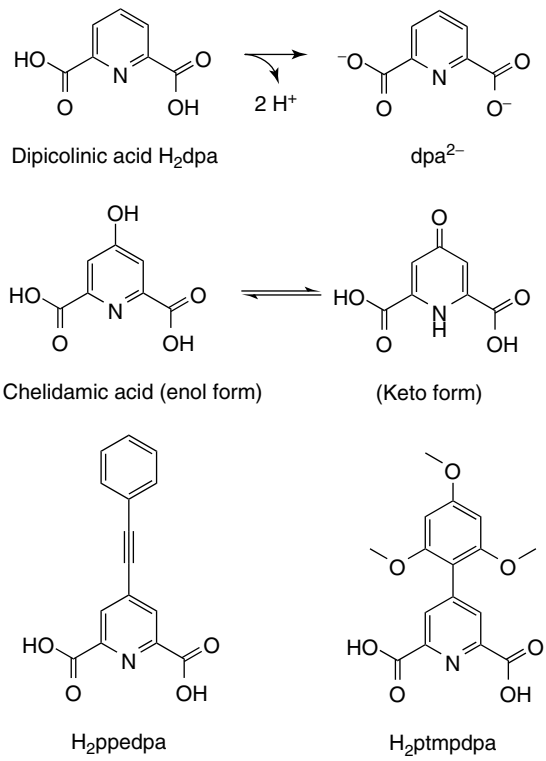
7.1.2 Dipicolinic-Acid-Based-Ligands

The next ligand that will be discussed is one of the most studied ligand in the photophysics of the lanthanide coordination complexes. Its versatility and its efficiency with a broad range of lanthanide ions are impressive and very useful. It is also the representative of a whole family of ligand, the tridentate chelates forming 1 : 3 nonacoordinated complexes. Such complexes have a full coordination sphere

and do not require any additional ligand to enhance their luminescence. This ligand is the dipicolinic acid (H_2dpa) also known as 2,6-pyridinedicarboxylic acid (Scheme 3) that forms trisdipicolinate complexes (1 : 3 Ln:L) with the lanthanide ions.

The chromophore in this ligand is not very extended. It encloses only a pyridine ring and the two carboxy groups. The ligand absorbs below 300 nm, in the UVC region. It exhibits no fluorescence, but at low temperature, its phosphorescence is observed between 360 and 500 nm with a maximum at 395 nm. The first band is called the 0–0 transition because it involves no vibrational quantum (from the 0 vibrational state of the triplet excited state down to the 0 vibrational state of the single ground state). In the $[Gd(dpa)_3]^{3-}$ complex, it is clearly seen at 370 nm (around 27 000 cm^{-1} in wavenumber units usually preferred for spectroscopy). The 0–0 phosphorescence transition is the value reported in literature to characterize the location of the triplet state of the ligand.

Such a high triplet state is efficient for a sensitization of terbium, but also shows a very good efficiency with europium (even better than with terbium), and interesting efficiencies with dysprosium and samarium. Even the NIR emitters are quite fairly luminescent relative to other structures. The complex is very stable in aqueous solutions due to the tridentate effect and overall negative charge of the edifice. It is also well soluble and can be crystallized under certain conditions. The terbium and europium complexes are often used as standards for quantum yield measurements. They exhibit 22% and 24% quantum yields, respectively.[13]



Scheme 3

An extensive derivatization of this framework is still running nowadays. The starting material is then often chelidamic acid (commercially available, obtained from chelidonic acid and ammonia) rather than dipicolinic acid. The para position of the chelidamic acid is substituted by a hydroxyl substituent, leading to a keto-enolic tautomerism forming either the 4-hydroxypyridine or 4-pyridinone forms. This confers different photophysical properties of the 1 : 3 Ln:L complexes. Numerous substitutions can be undertaken at this para position. The most extensive work was performed by Latva *et al*. in an attempt to correlate the triplet state location with the efficiency of the complex.[14] The best result considering the increase of the quantum yield for an addition of a phenylethynyl group for europium and a trimethoxyphenyl for terbium. However, the solubility should be greatly affected by those substitutions. Another advantage yet is that the excitation wavelength was increased up to 320 nm. The extinction coefficient is also higher, particularly for the para-phenylethynyl derivative.

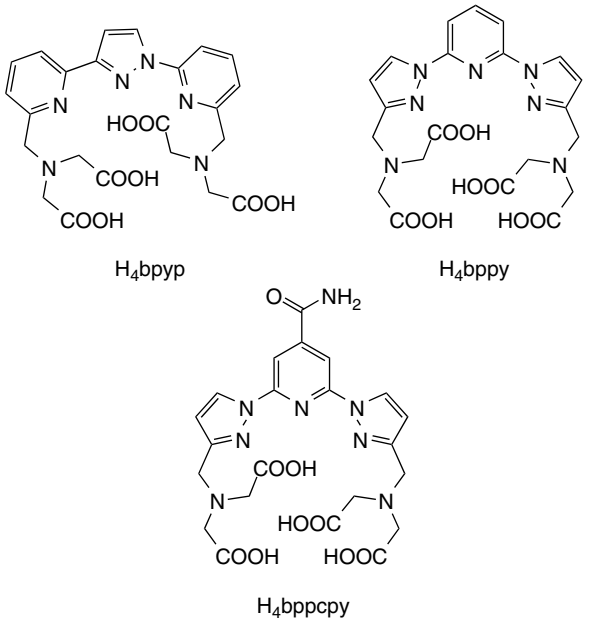
One strategy to keep the water solubility of these complexes is to introduce in this para position polyoxyethylene arms fitted by different functions, such as alcohol, amine, or carboxylic acid. This later can be coupled to a second chromophore, such as a coumarin, with a higher excitation wavelength, which enables a double sensitization of the lanthanide ions (dominated by the efficient sensitization of the pyridine chromophore under 300 nm and by the sole absorption, and hence sensitization, of the coumarin moiety above 300 nm).[15]

The H_2ppedpa (see Scheme 3) architecture was then further investigated and derivatized to a whole new series of dpa derivatives with a triple bond at its para position. It was shown that such ligands have very interesting two-photon absorption abilities. For further details about these lanthanide complexes, the reader should refer to the work of Andraud and Maury.[16]

7.1.3 Polyaminocarboxylate Ligands

Another significant derivatization of the pyridine structure from the work of Latva *et al*. is the replacement of the tridentate coordinating moieties by polyaminocarboxylates that add six-coordination sites. The best result for europium and terbium are a bis(pyridine)pyrazolyl (H_4bpyp) and a bis(N-pyrazolyl)pyridine (H_4bppy) derivative, respectively (see Scheme 4).

The important points to retain here are that the complexes have a 1 : 1 stoichiometry (one ligand per lanthanide ion), are mononegatively charged, and have a quite rigid coordination site on the chromophore. The extension of the absorption wavelength is here up to 330 nm for both ligands, but the extinction coefficient is quite low. A



Scheme 4

derivatization of H_4bppy with a carbamoyl substituent at the para position of the pyridine ring yielding H_4bppcpy resulted in the most efficient terbium complex with a near unity quantum yield.[1]

The pyridine core is found in many other chromophores such as bipyridines, terpyridines, and, as already seen, phenanthroline ligands.

7.2 Correlation Between the Energy of the Triplet State and the Quantum Yield of the Sensitized Lanthanide Luminescence

Europium and terbium have emission peaks originating from a single excited spectroscopic level (i.e., the $^5D_0$ and the $^5D_4$, respectively). Those levels are then threshold limits for an energy transfer from a triplet state to occur. It means that the triplet state has to be located higher in energy than the $^5D_0$ ($>17\,500\,cm^{-1}$) to yield a sensitization of europium, and higher than the $^5D_4$ ($>20\,200\,cm^{-1}$) to yield a sensitization of terbium. The rate of the energy transfer depends on the Franck–Condon factor between the initial and final state, so approximately on the overlap between the absorption spectrum of the acceptor and the emission spectrum of the donor for a donor–acceptor energy transfer. The closest the match, the higher the rate, but this is also true for the back energy transfer from the acceptor back to the donor. A certain amount of energy difference between the energy state of the donor and of the acceptor is thus required to have a net energy transfer in the forward direction. If this difference is yet too important, the spectral overlap integral diminishes, so that the rate of the energy transfer falls down. In a lanthanide complex, we then need to find a phosphorescence spectrum that overlaps with an excited spectroscopic level of the lanthanide ion, yet keeps a sufficient energy gap between the spectroscopic levels of the lanthanide ion and the 0–0 triplet state to prevent back transfers.

As seen in ***Luminescence***, the sensitized quantum yield depends on three parameters: the intrinsic quantum yield of the lanthanide ion, which defines how efficient the radiative pathway is compared to the other relaxations; the intersystem crossing efficiency, which describes the percentage of excited ligand that are converted to their triplet state; and the energy transfer efficiency, which determines how many ligands transfer their energy onto the lanthanide ion. The energy transfer efficiency is of course directly related to the energy transfer rate. The quantum yield should thus be correlated to the energy difference between the triplet state and the spectroscopic levels of the lanthanide ions (for example, of the europium or terbium ions shown in Figure 7).

Experimentally, this correlation between the energy of the triplet state of the ligand and the quantum yield is well established.[14] Terbium shows the most dramatic effect. A triplet state lower than 465 nm is required (or higher than $21\,500\,cm^{-1}$) to ensure a good terbium sensitized quantum yield. For europium, the correlation is somehow less clear (maybe because of the hypersensitive transition and because of the greater number of levels onto which the energy can be transferred). An investigation with a series of similar ligands (benzymidazolpicolinic acid derivatives, Hbpa, see Scheme 5) coordinating in an identical way revealed a much better correlation.[17] The quantum yield seems to increase as the triplet state grows higher than the $^5D_0$ spectroscopic level at least up to the $^5D_2$. The work by Latva *et al*.

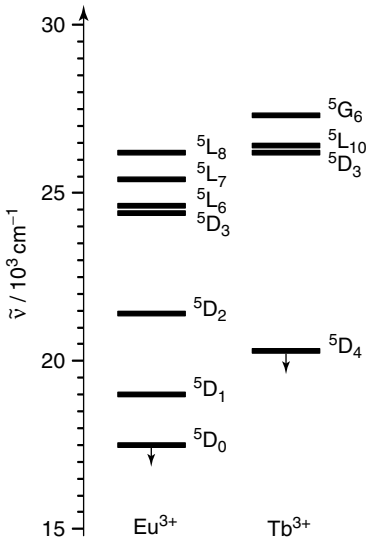
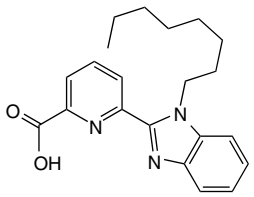


Figure 7 Spectroscopic levels of the excited states of Eu^{3+} and Tb^{3+} that might be sensitized by a ligand. The levels with an underneath arrow are the levels from which the main transitions of the luminescence are observed



Hbpa

Scheme 5

had already shown that the optimal triplet state should be located somewhere just above the $^5D_2$ (around 455 nm or 22 000 cm^{-1}). The chromophore quite similar to Hbpa is described in ***Luminescent Bioprobes*** to illustrate the huge scope of applications of a good lanthanide complex.

7.3 Solubility, Stability, and Additional Features

The highest quantum yield is quite attractive, but other considerations are also to be taken into account. Solubility is the most obvious one, because depending on the application, a solid state complex, an organic solvent, or an aqueous solution might be needed. Stability is also a very important point and depends on the medium. Most of the β-diketones are not soluble in water and β-diketonate complexes would even not be stable in water because the coordination is not strong enough to compete with the water molecules. However, β-diketonates are extensively used when incorporating lanthanide complexes in host materials. Nanoparticles are particularly well investigated because they may efficiently protect the sensitive complex inside their core, yet be functionalized on their shells to be soluble or to interact with the desired target. A lot of these nanoparticles containing β-diketonate lanthanide complexes have been tested as electroluminescent devices.

Another argument against a too high quantum yield is to take advantage of the residual emission (fluorescence) of the ligand that is often encountered when the chromophore also exhibits a strong fluorescence (usually a blue emission). A dual mode emission may thus be interesting. The fact that the fluorescence of the ligand is much quicker than the luminescence of the lanthanide ion is also very attractive for discriminating the two emissions in a time-resolved experiment. If the ligand is composed of several chromophores, a multimodal and excitation-wavelength-dependent emission is even achievable, as long as one chromophore does not quench the whole luminescence.

7.4 Sensing Ability of a Lanthanide Complex

A growing field of research nowadays is to design ligands for probing or sensing. A group is often grafted to quench or activate the luminescence of the complex or of the ligand and be sensitive to an analyte. The analyte may either induce a change of the configuration of the sensitive group, or a cleavage of part of the moiety that would change the emissive state of the complex. The easiest probe is a pH-sensitive ligand that undergoes a protonation that quenches the luminescence of the complex. Some Förster resonance energy transfers (FRETs, sometimes also known as fluorescence resonance energy transfers or donor–acceptor energy transfers) are also possible between lanthanide complexes and other complexes or other organic fluorophores.

In such complex applications, 1 : 1 complexes are sometimes needed because the ligand is to be stoichiometrically attached to another material, whereas for other purposes, a branched or polymeric architecture requires a maximum number of ligand per lanthanide ion.

The problem with many ligand designs is to obtain a soluble complex, and particularly when water solubility is needed. Apart from the coordination moieties, the chromophores are generally quite hydrophobic. They tend to remain together and interact through π-stackings and Van der Waals interactions. Some functional groups are known to confer some water solubility, for example, sulfonates, quaternary amines, or polyethylene glycols, but the functionalization has to take place at a position that would neither affect the photophysical properties of the chromophore too drastically nor prevent a proper coordination with the lanthanide ion because of the steric hindrance or the coordinating ability of the solubilizing group. The reader is referred to ***Sensors for Lanthanides and Actinides*** dealing with sensors for more details.

7.5 Coordination Moieties, Flexibility, and Complex Architectures

The choice of the coordinating moieties is critical in ligand design because it dictates where the lanthanide ion is located relative to the chromophore, how it is linked to ligand, and how many ligands may be coordinated to it. Good coordinating groups are carboxylates, phosphonates, aromatic nitrogens (such as in pyridine, bipyridine, terpyridine, pyrazol, and benzimidazol), amines, carbonyls, and ethers. When they compete with water molecules, the softer groups such as ethers, carbonyls, and amines are only appropriate to fill a few coordination sites near strong coordinating groups, which prevent the complex from disassembling.

The flexibility of the coordination sites is also an important feature. A rigid structure with multiple directional coordination sites does not enable binding a single ion, but rather forms polymeric-type structures. Terephthalic acid, for example, is a bidentate ligand with two carboxylic moieties in a para position. A single ligand hence cannot bind to a single ion with both sides, but must coordinate to at least two different ions. The ligand geometry thus set up many coordination modes that all tends toward a polymeric structure rather than a molecular complex. Depending on the

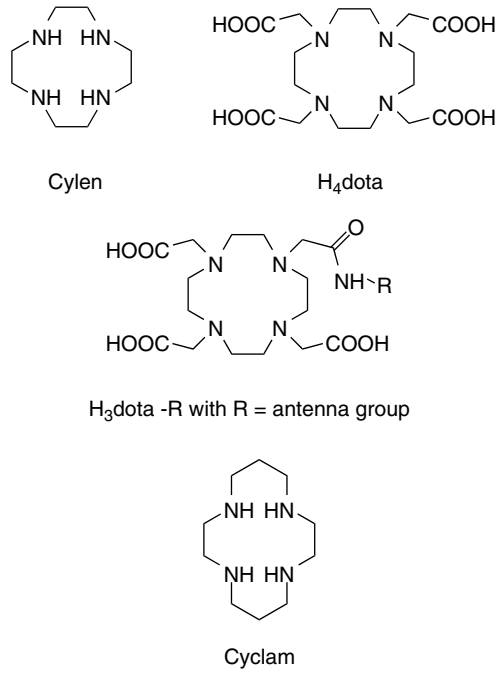
choice of the binding ligand, supramolecular edifices with various 2D and 3D architectures are obtained. For further reading, one can refer to the book of Jean-Marie Lehn dealing with supramolecular chemistry, and which contain application with lanthanide ions.[18] Some metallopolymers containing lanthanide ions were also successfully used for applications in photovoltaics, electro, and photoluminescent materials.[19]

On the other hand, when a selective flexibility is introduced in a rigid structure, a molecular complex with several lanthanide ions can be designed. For example, helix structures formed by a 2 : 3 stoichiometry (2 Ln^{3+} and 3 L) are achieved by taking two rigid tridentate ligand such as a Hbpa derivative, and fuse them together with a flexible bridge such as a methylene ($-CH_2-$). The resulting structure will be thoroughly discussed in ***Luminescent Bioprobes***, and an example of emission of various Ln complexes has been illustrated in Section 3.1, with the ligand depicted in Figure 2.

Macrocyclic coordination moieties are also a very important way to coordinate a ligand to a lanthanide ion. They usually form highly stable complexes even though the coordination may take a very long time relative to the other structures. A very well used ligand is the 1,4,7,10-tetraazacyclododecane-1,4,7,10- tetraacetic acid, for which the acronym is dota (see Scheme 6). It comes from the cylen (1,4,7,10-tetrazacyclododecane which is the aza analog of the crown ether 12-crown-4), the amines of which have been fitted by N-CH_2CO_2H substituents. The dota ligand (H_4dota is the fully protonated form containing four carboxylic acid moieties) is then an octadentate ligand. Having a strong binding constant for lanthanide ions ($\log\beta_{11} = 23.5$ for Gd^{3+}) and with a at least one water molecule in the first coordination sphere, the dota-containing gadolinium complex has proved to be a great magnetic resonance imaging (MRI) contrast agents. For more information about MRI and contrast agents, see ***Lanthanides: Magnetic Resonance Imaging***.

This ligand being devoid of an antenna group is, however, not a good one for sensitizing the lanthanide ions (see ***Luminescent Bioprobes*** for an application of these complexes for competitive titrations experiments). The interest is then to modify at least one of the four carboxylic acid substituents and to selectively introduce the antenna group (=chromophoric unit) through an amide function. The organic chemistry with these compounds in not trivial and require a thoughtful planning. Bulky chromophores or chromophores with two coordinating groups may however effectively shield the lanthanide ion. This kind of substitution has offered many possibility of derivatization, leading to lanthanide complexes with ability for bioimaging (see, for example, the bioprobes responsive to cellular events developed by Parker and coworkers[20] and for acting as sensors see ***Sensors for Lanthanides and Actinides***) among other applications.

A similar structure based on a cyclam macrocycle (two opposite bridges between the four nitrogen atoms are one carbon longer) is also commonly encountered. The presence of the carboxylic moieties ensures the high stability,



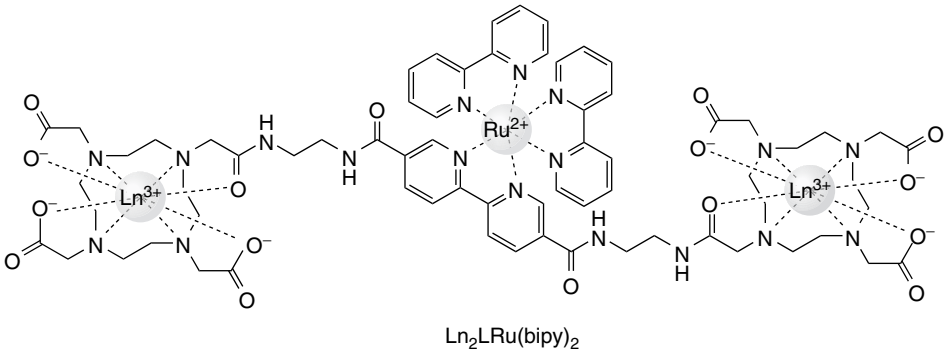
Scheme 6

but phosphonic acids or phosphoryl-containing coordination moieties are also very efficient.

The cyclen/cyclam architecture also allows uncoordinated chromophores, additional probing groups, and even biological materials to be ''easily'' grafted on a lanthanide complex. Such systems are therefore, and also due to their higher stability, often chosen for biological applications.

Cyclen/cyclam-type ligands are also very useful to introduce several coordination sites in a same ligand, thus enabling polynuclear complexes. Ultimately, polyheteronuclear complexes can be constructed, combining the luminescence properties of many lanthanide ions (e.g., Eu^{3+} and Tb^{3+}) on a same ligand. Actually, any ligand (coordination site) forming a 1 : 1 complex with a lanthanide ion is well suited for such designs. The introduction of coordination sites for d-elements is even feasible. The sensitization of a lanthanide ion by a d-element complex such as a ruthenium complex or a platinum complex has been observed on many occasions.

In the example of $Ln_2LRu(bipy)_2$ (Scheme 7), the complex is obtained by first coordinating the lanthanide ions, which bind to the cyclen-based coordination sites, and then coordinating the ruthenium(II) on the bipyridine moiety at the center of the ligand.[17] The bipyridine is not strong enough for an efficient coordination of a lanthanide ion when no strong electron donors are in the coordination site, but is a typical good coordinating site for ruthenium(II) which then requires two other bipyridine to reach its octahedral geometry. A sensitization of Nd^{3+} by the ruthenium moiety was shown in this case. The lanthanide ions have a coordination number of



$Ln_2LRu(bipy)_2$

Scheme 7

eight in this architecture; the hydration number q is consistent with one water molecule in the first coordination sphere, the quantum yields are thus low with either Tb^{3+} or Eu^{3+} and very low with the NIR-emitting lanthanide ions.

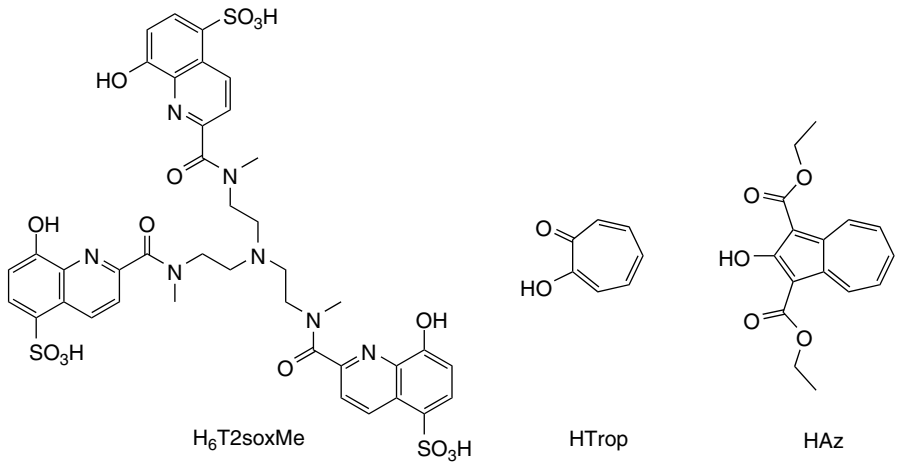
8 DESIGNING A COMPLEX EMITTING IN THE NEAR-INFRARED (NIR) RANGE

Most of the lanthanide ions are NIR emitters, sometimes alongside visible emissions and sometimes purely in the NIR region. Obtaining an efficient NIR emission is quite challenging and nowadays, the best sensitized NIR emitters do not exceed 4% quantum yields with ytterbium complexes. For other lanthanide ions, the quantum yield is usually below 1%, especially in aqueous solution where the deactivation is favored by the OH vibrations of the solvent molecules.

NIR emitters are important because their applications in biomedicine and photomedicine are very attractive. Biological tissues are indeed quite transparent in the NIR region, which may enable a deep visualization of biological materials.

Among selected examples with a quantum yield considered as high for an NIR emission, one can cite ligands with a quinoline chromophore such as [YbT2soxMe] (0.13% in H_2O, pH 7.4);[21] ligands with a chromophore that has a seven-membered ring such as tropolonate, which give a very good quantum yield in the ytterbium complex (1.9% in DMSO) but that also efficiently sensitize all the other NIR-emitting lanthanide ions; or such as azulene derivatives (up to 3.8% in CH_3CN) (see Scheme 8).[22]

Common strategies to have a better efficiency include the deuteration of the ligand (CH, OH, and NH bonds) and of the solvent, as well as the halogenation, principally of the CH bonds of the ligand into CF bonds. Such modifications aim at decreasing the energy of the vibrational quanta so that more quanta are needed to deactivate the excited state of the lanthanide ion, thus decreasing the efficiency of the nonradiative relaxation. The encapsulation of the complex inside solid matrices such as nanoparticles or the development of functionalizable NIR-emitting doped phosphors at a



$H_6T2soxMe$ HTrop HAz

Scheme 8

nanoscale are other efficient ways to have an NIR emitter in solution where the sensitive lanthanide ions are yet shielded from the deactivation from the solvent molecules.

9 CONCLUSIONS

After a survey of the photophysical properties exhibited by lanthanide complexes emitting in the visible or the NIR range, including their emission properties, we have focused on the important field of applications for these complexes, with a particular interest for the lanthanide ions emitting in the visible range, and which are so important for color reproduction. We then emphasized some of the requirements needed to design a complex with highly luminescent properties, and we introduced some of the families of ligands commonly used for an efficient sensitization of the lanthanide ions. We illustrated that the choice and design of the chromophores allow a fine tuning of the photophysical properties, but also takes into account the requirements for a specific application (electroluminescence, biological applications including bioimaging or sensing) such as solubility, stability, absorption in a specific spectral domain, high conversion rate, and presence of a targeting group.

Several new interests have emerged for lanthanide chemistry over the last years. Many exciting applications are reported in literature every month, presenting numerous examples of elegant ligand designs and complex architectures. The chapters in the session ''advances topics'' present several applications in the domain of ionic liquids, sensors, medical applications (including MRI agents), etc. In particular, ***Luminescent Bioprobes*** will present a case study of a lanthanide-containing complex from its physicochemical properties and photophysical properties to its application as a probe for biological materials.

10 GLOSSARY

Auxochrome: Electron-withdrawing or electron-donating groups added on a chromophore to modulate its photophysical properties.

Helicate: Ligands that wraps around metal ions in a helical way.

Color space: Mathematical representation of the colors in a three-dimensional space by three color components or color primaries.

Conjugation, resonance: A conjugated molecule is composed of interacting p orbitals forming a long range π molecular orbital. Organic molecules with alternate single and double bonds are conjugated molecules. The electrons in a conjugated system are delocalized through the whole conjugated structure. A conjugation is shown by a resonance structure.

11 END NOTES

[a.] To the contrary, in every day life, most of the colors that we see are composed of absorbing materials that reflect or transmit the ambient white light source such as daylight. The color then comes from the reflected and transmitted white light that has been more or less attenuated by the absorbing surfaces in different part of the spectrum. The colors are in this case made by subtractive color synthesis, starting from the white light or illuminant that represent the white color and then removing red, green, blue, to yield respectively cyan, magenta, and yellow, or removing cyan, magenta, yellow or white to yield red, green, blue or black.

12 RELATED ARTICLES

Luminescence; Near-Infrared Materials; Upconversion Nanoparticles for Bioimaging Applications; Luminescent Bioprobes.

13 ABBREVIATIONS AND ACRONYMS

CCT = correlated color temperature; CFL=compact fluorescent lamps; CIE = commission internationale de l'éclairage; CQS=color quality scale; CRI=color-rendering index; CRTcathode ray tube; DFT = density functional theory; FRETs = Förster resonance energy transfers; LCDs = liquid crystal displays; LEDs = light-emitting devices; MRI = magnetic resonance imaging; NIR = near-infrared; NIST = National Institute of Standards and Technology; NMR = nuclear magnetic resonance.

14 REFERENCES

1. E. Brunet, O. Juanes, R. Sedano, and J.-C. Rodriguez-Ubis, *Photochem. Photobiol. Sci.*, 2002, **1**, 613.
2. W. T. Carnall, P. R. Fields, and K. Rajnak, *J. Chem. Phys.*, 1968, **49**, 4424.
3. A. I. Voloshin, N. M. Shavaleev, and V. P. Kazakov, *J. Lumin.*, 2001, **93**, 199.

4. T. Zhang, J. Wang, J. Jiang, R. Pan, and B. Zhang, *Thin Solid Films*, 2007, **515**, 7721.
5. S. Comby, 'Luminescent Lanthanide Bioprobes Emitting in the Visible and/or Near-Infrared Ranges' Ph. D. dissertation, École Polytechnique Fédérale de Lausanne, 2008.
6. R. Jacobson, *Color. Technol.*, 2003, **119**(6), 359.
7. G. Wyszecki and W. S. Stiles, 'Color Science: Concepts and Methods, Quantitative Data, and Formulae', Wiley classics library ed., John Wiley & Sons, New York, 2000, p. xv, p. 950.
8. W. Davis and Y. Ohno, *Opt. Eng. (Bellingham, WA)*, 2010, **49**(3),. 033602-1-033602/16.
9. F. Auzel, *Chem. Rev.(Washington, DC)*, 2004, **104**(1), 139.
10. G. S. He, L. S. Tan, Q. Zheng, and P. N. Prasad, *Chem. Rev.(Washington, DC)*, 2008, **108**(4), 1245.
11. C. Platas-Iglesias, A. Roca-Sabio, M. Regueiro-Figueroa, D. Esteban-Gómez, A. de Blas, and T. Rodríguez-Blas, *Curr. Inorg. Chem.*, 2011, **1**, 91.
12. C. Freund, W. Porzio, U. Giovanella, F. Vignali, M. Pasini, S. Destri, A. Mech, S. Di Pietro, L. Di Bari, and P. Mineo, *Inorg. Chem.*, 2011, **50**, 5417.
13. A.-S. Chauvin, F. Gumy, D. Imbert, and J.-C. G. Bünzli, *Spectrosc. Lett.*, 2004, **37**, 517. Erratum, 2007, **40**, 193.
14. M. Latva, H. Takalo, V. M. Mukkala, C. Matachescu, J.-C. Rodriguez-Ubis, and J. Kankare, *J. Lumin.*, 1997, **75**, 149.
15. J. Andres and A.-S. Chauvin, *Eur. J. Inorg. Chem.*, 2010, **2010**, 2700.
16. C. Andraud and O. Maury, *Eur. J. Inorg. Chem.*, 2009, **29–30**, 4357.
17. N. M. Shavaleev, S. V. Eliseeva, R. Scopelliti, and J.-C. G. Bünzli, *Chem.—Eur. J.*, 2009, **15**, 10790.
18. J.-M. Lehn, 'Supramolecular Chemistry: Concepts and Perspectives', VCH Weinheim, New York, Basel, Cambridge, Tokyo, 1995.
19. G. R. Whittell, M. D. Hager, U. S. Schubert, and I. Manners, *Nat. Mater.*, 2011, **10**, 176.
20. E. J. New, D. Parker, D. G. Smith, and J. W. Walton, *Curr. Opin. Chem. Biol.*, 2010, **14**, 238.
21. S. Comby, D. Imbert, C. D. B. Vandevyver, and J.-C. G. Bünzli, *Chem.—Eur. J.*, 2007, **13**, 936.
22. H. Uh and S. Petoud, *C. R. Chim.*, 2010, **13**, 668.

Magnetism

Bing-Wu Wang and Song Gao

Peking University, Beijing, People's Republic of China

1 Summary 153
2 Introduction 153
3 Magnetic Coupling Interactions 155
4 Conclusions 158
5 Acknowledgments 158
6 Related Articles 158
7 Abbreviations and Acronyms 158
8 References 158

1 SUMMARY

Rare earths are among the most important magnetic sources in the modern industry. Owing to their large spin–orbital coupling and unquenched angular momentum, many magnetic materials nowadays contain rare earth elements as magnetic carriers. For example, neodymium–iron–boron magnets are the most commonly manufactured and commercially available high-strength permanent magnets. They are widely used in modern technology and can be found almost everywhere, from cell phones, disc drives, computers, and household appliances to magnetic resonance imaging (MRI) imaging, hybrid cars, satellites, and wind-power generators. In this chapter, the magnetic properties and exchange-coupling interactions between rare earth ions and radicals and 3d transition metal ions are introduced briefly. These are the fundamental concepts for understanding the magnetic behavior of rare earth containing systems.

2 INTRODUCTION

Rare earth elements are widely used in traditional magnet technology and in the new field of molecular magnets owing to their intrinsic large atomic magnetic moment. As important sources of magnetism, the magnetic properties of rare earth elements are dominated mainly by the spin, orbital angular momentum, and the interactions of their f electrons. Their magnetic properties are quite different from those of the transition metal ions, whose magnetism mainly comes from spin magnetic moment, the orbital contributions being quenched by the ligand field. Normally, the trivalent rare earth ions are characterized by f^n configurations, termed ^{2S+1}L *multiplets*, which are further split by spin–orbit coupling to give J states. The corresponding energy spectrum of the states can be calculated as

$$E(^{2S+1}L_J) = (\lambda/2)[J(J+1) - L(L+1) - S(S+1)] \quad (1)$$

where J is defined by the angular momentum summation rules $|L - S| \leq J \leq |L + S|$, and λ is the spin–orbit coupling constant. According to the number of f electrons n, the sign of λ implies that in the ground state $J = L - S$ for $n < 7$ and $J = L + S$ for $n > 7$.

The Landé factor g of a given J multiplet is given by

$$g_J = \frac{3}{2} + \frac{S(S+1) - L(L+1)}{2J(J+1)} \quad (2)$$

Within this multiplet, the total angular moment of rare earth ion can be expressed as

$$L + 2S = gJ \quad (3)$$

and corresponding effective moment on the atom is

$$\mu = g\mu_B J \quad (4)$$

The Rare Earth Elements. Edited by David A. Atwood. © 2012 John Wiley & Sons, Ltd. ISBN 978-1-119-95097-4

where μ_B is Bohr magneton. If J is nonzero, the magnetization for the ground-state multiplet will be

$$M(H,T) = \frac{N}{V} g\mu_B J B_J(\beta g \mu_B J H) \tag{5}$$

where the Brillouin function B_J is

$$B_J(x) = \frac{2J+1}{2J}\coth\left(\frac{2J+1}{2J}x\right) - \frac{1}{2J}\coth\left(\frac{1}{2J}x\right) \quad x = g\mu_B J H/k_B T \tag{6}$$

If $g\mu_B J H$ is small compared with $k_B T$, the theoretical magnetic susceptibility can be calculated as

$$\chi = \frac{M}{H} = \frac{g^2\mu_B^2 J(J+1)}{3k_B T}\frac{N}{V} \equiv \frac{C}{T} \tag{7}$$

where C is the Curie constant and the equation is known as *Curie's law*.

Combined with the J and g values mentioned above, the basic physical chemistry parameters and the calculated, experimental χT values at room temperature for the rare earth ions are listed in Table 1.

Besides the spin and orbital contribution to the total magnetic moment, the ligand field can also affect the magnetic properties of rare earth elements-containing compounds. For the inorganic or organic ligands surrounding the rare earth ion, this can be simplified as a normal charge distribution with definite local point symmetry. The electric field produced by these charges acts on the 4f electrons, affects the ground and low-excited energy spectra of the ions, and induces large magnetic anisotropies and versatile magnetic properties. This electric field, often called a *crystal field*, contributes to the potential energy of a 4f electron in the form

$$V_{cf}(r) = -\int \frac{e\rho(R)}{|r-R|}\mathrm{d}R \tag{8}$$

where $\rho(R)$ is the charge density surrounding the ion. For a pure electrostatic treatment, the crystal field can be solved from Laplace's equation and expanded in spherical harmonics as

$$V_{cf}(r) = \sum_{lm} A_l^m r^l Y_{lm}(\hat{r}) \tag{9}$$

where $Y_{lm}(r)$ is the corresponding spherical harmonics and

$$A_l^m = -(-1)^m \frac{4\pi}{2l+1}\int \frac{e\rho(R)}{R^{l+1}} Y_{l-m}(\hat{R})\mathrm{d}R \tag{10}$$

Because the wave functions of the 4f electron are highly contracted, the crystal field is much smaller than the interelectronic repulsion and also smaller than the spin–orbit coupling term. For the electron configurations of a rare earth ion, the degenerated ground states are split by interelectronic repulsion in spectroscopic terms, the one with the highest spin multiplicity $(2S+1)$ has the lowest energy according to Hund's rule of maximum spin multiplicity (Figure 1). Each of these terms is further split by the spin–orbit interaction into ${}^{2S+1}L_J$ spectroscopic levels, with $|L-S| \le J \le L+S$. These energy levels are in the range of $10^4\,\mathrm{cm}^{-1}$ for a rare earth ion. The ligand-field effect can be weaker than the interelectronic repulsion and spin–orbit coupling, and split the levels into Stark sublevels in the range of $10^2\,\mathrm{cm}^{-1}$ for the shielding of the 4f orbitals, which are much smaller than those for the 3d orbitals of transition metal ions. The magnitude of these energy levels is comparable to the $k_B T$ value, so the population of sublevels can be changed when the temperature decreases. At the same time, the orbital moment makes a non-negligible contribution to $\chi_{Ln}T$ values. As a result, the temperature dependence of χ_{Ln} deviates from the Curie law at low temperatures.

As mentioned above, the magnetic sources of magnetic materials containing rare earth ions not only come

Table 1 Electron configuration, ground-state spectral term, g values, calculated and experimental χT values at room temperature for Ln^{III} ions

Ln^{III}	Configuration	Ground state	g_J	χT_{cal} (emu mol^{-1} K)	χT_{exp} (emu mol^{-1} K)
Ce	f^1	${}^2F_{5/2}$	6/7	0.80	0.66–0.78
Pr	f^2	${}^3H_4$	4/5	1.60	1.45–1.62
Nd	f^3	${}^4I_{9/2}$	8/11	1.64	1.45–1.53
Pm	f^4	${}^5I_4$	3/5	0.90	1.05
Sm	f^5	${}^6H_{5/2}$	2/7	0.09	0.32
Eu	f^6	${}^7F_0$	—	—	1.53
Gd	f^7	${}^8S_{7/2}$	2	7.88	7.61–7.80
Tb	f^8	${}^7F_6$	3/2	11.82	11.76–12.01
Dy	f^9	${}^6H_{15/2}$	4/3	14.17	13.01–14.05
Ho	f^{10}	${}^5I_8$	5/4	14.07	13.26–13.78
Er	f^{11}	${}^4I_{15/2}$	6/5	11.48	11.05–11.28
Tm	f^{12}	${}^3H_6$	7/6	7.15	7.03
Yb	f^{13}	${}^2F_{7/2}$	8.7	2.57	2.53

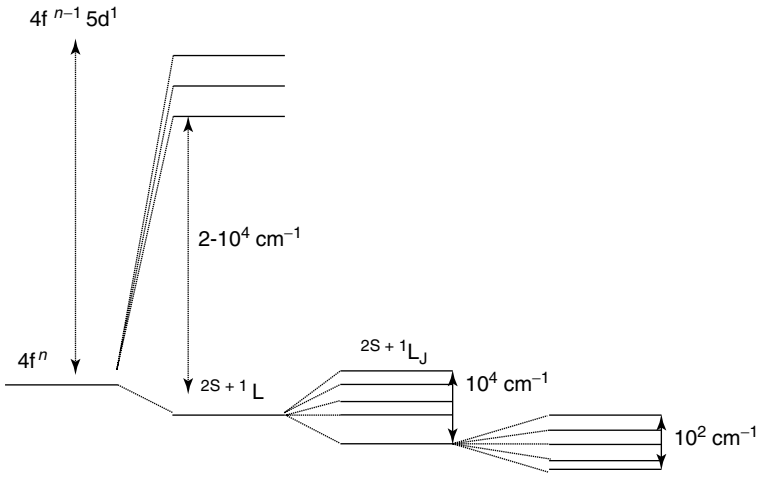


Figure 1 A schematic energy diagram showing the relative magnitude of the interelectronic repulsion, the spin–orbit coupling, and ligand-field effect. (Reproduced from Ref. 1. © Wiley-VCH Verlag GmbH & Co. KGaA, 2005.)

from possible large magnetic moments associated with spin and large orbital moments, both of which originate from the internal nature of the f electrons, but also from the exchange-coupling interactions between lanthanide ions and transition metal ions, radicals, or lanthanide itself. Comparing these magnetic materials with magnetic materials composed of transition metals ions and radicals, it is observed that the magnetic properties of all paramagnetic lanthanide ions except for Gd^{III} and Eu^{II} with f^7 electron configuration are considerably influenced by the large spin–orbit coupling and ligand-field effect. So the introduction of magnetic coupling between lanthanide ions and other paramagnetic centers of exchange-coupling systems can be divided into two parts, namely, Gd^{III} containing systems and other Ln^{III} ions with first-order orbital momentum, respectively.

3 MAGNETIC COUPLING INTERACTIONS

The orbital model to understand the exchange-coupling interactions was developed by Anderson about 50 years ago. He reduced the complex theory to only take account of simplified magnetic orbitals, which contain one unpaired electron. The magnetic interaction is antiferromagnetic when the two magnetic orbitals on different centers have nonzero overlap. On the other hand, the magnetic interaction will be ferromagnetic and the electron spin allies will be parallel if the magnetic orbitals are orthogonal to each other and overlap such that integral S tends to 0. There are also some other theoretical models to understand the magnetic properties of molecular magnetic materials, but almost all simplified models regard the exchange or superexchange interaction as a form of weak bonding between two paramagnetic centers including rare earth element containing compounds.

For a $4f^7$, rare earth ion such as gadolinium(III), its magnetic behavior is contributed only by a pure spin state $S = 7/2$. The exchange coupling interaction with other paramagnetic centers can be described by the well-known Heisenberg-Dirac-Van Vleck (HDVV) spin Hamiltonian

$$H = -J\, S_{Gd} \cdot S_s \tag{11}$$

where S_{Gd} is the spin operator associated with gadolinium(III) and S_s is the spin operator associated with the other magnetic center. A positive J value means ferromagnetic coupling and a negative value, antiferromagnetic coupling.

Distinguished from the unpaired d electrons of transition metal ions and s, p electrons of organic radicals, the unpaired f electrons of rare earth ions are highly contracted and energetically shielded deeply by the outer 5d, 6s shells. So the direct magnetic interaction between $4f^7$–$4f^7$ electrons is very weak, the value of the coupling constant J is normally smaller than $1\,cm^{-1}$[2]. The situation is quite different from the indirect pathway involving the 4f localized electrons and conduction electrons responsible for the magnetic ordering of rare earth intermetallic compounds.

Because the f electrons of gadolinium(III) are highly contracted, the magnetic interaction is mediated by the spin-polarized 5d, 6s valence electrons. To a good approximation, the $4f^7$ exchange field can be viewed as a kind of contact effect[3], which only exerts its influence on the orbitals centered on the Gd atom. Both the valence 5d and 6s electrons can penetrate to some extent and experience the $4f^7$ exchange field of the atom core, only the more contracted 5d electrons experience greater exchange interaction with the $4f^7$ core. Consequently, the valence 5d, 6s electrons are spin-polarized and the 5d orbital possesses larger spin density in ab initio

or density functional theory (DFT) calculations. This local character of the $4f^7$ exchange field can be treated by a simple perturbative molecular orbital (PMO) model that accounts for the perturbation of the $4f^7$ cores exerted on electrons that reside in 5d and 6s molecular orbitals.

Figure 2 illustrates how the potential from the $4f^7$ core affects the spin character of the 5d and 6s electrons. On the left side of the figure, the valence d electron in an ''unperturbed'' system experiences an average exchange potential from the half-filled 4f shell, so it has no preferred spin orientation. Upon application of the exchange field of $4f^7$ electrons, the spin aligned with (or against) the 4f spins is stabilized (or destabilized) by an energy δ. These exchange interactions are intrinsically ''ferromagnetic,'' favoring parallel alignment of the 4f and 5d spins.

Mixed 3d–4f compounds are the most studied molecular magnetic materials containing rare earth ions owing to their attracting properties in the field of molecular magnetism and coordination chemistry. Gd^{III}-3d systems, especially, are widely studied by experimentalists and theoretician because of the presence of the largest possible spin magnetic moment $S = 7/2$ and the lack of orbital contribution that facilitates the analysis of the magnetic properties. Among these clusters, a large number of binuclear and polynuclear complexes containing Gd^{III}–Cu^{II} unit have pronounced magnetostructural correlations and exhibit the widespread ferromagnetic coupling between Gd^{III} and Cu^{II} ion with only a few exceptions.

Gatteschi *et al.*[4] proposed a spin polarization mechanism that is due to the orbital interaction between the 6s orbital of Gd and delocalization tails of the 3d orbital of Cu on the ligand. In this scheme, it is considered that the most important contribution comes from the overlap of the magnetic orbital of copper(II) with the empty d or s orbitals of gadolinium(III). Therefore, a fraction of unpaired electrons is transferred into the empty orbitals and the electrons have spins that are parallel to each other according to the Hund's rule. In fact, this is a generalization of the Goodenough–Kanamori rule for Gd^{III}–Cu^{II} system, which suggests that ferromagnetic coupling takes place when a magnetic orbital of one site has nonzero overlap with an empty orbital of the other site. This idea is consistent with the theoretical PMO model treatment of Hughbanks, except that the contribution of 6s orbitals is replaced by that of 5d orbitals, as shown in Figure 2 above.

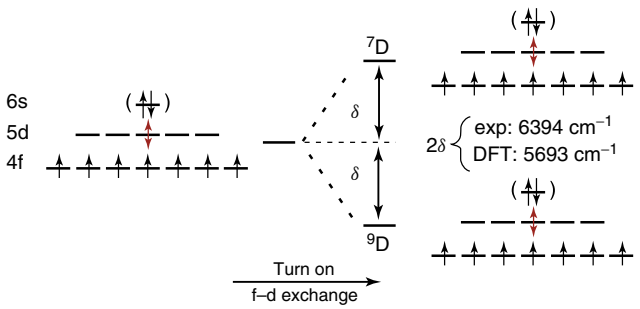
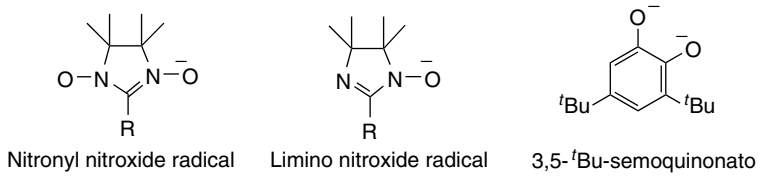


Figure 2 Orbital energy splitting of the Gd atom as a function of 4f–5d exchange perturbation. (Reprinted with permission from Ref. 3. Copyright (2006) American Chemical Society)

Also inspired by the general schemes of Goodenough, Kahn[5] gave an alternate explanation that attributes the ferromagnetic coupling to the interaction between the Gd^{III}–Cu^{II} ground-state and excited-state configurations arising from the occupied 3d (Cu) → vacant 5d (Gd) electron transfer. They used the extended Hückel approach to check the efficiency of the mechanism by the calculation of the electron charge transfer integral β_{5d-3d}, but were limited because they could not offer a proper account for the subtle configuration interaction problems at that time. Chen[6] reported the spin density maps and Mulliken-type population analysis based on the calculations of DFT-combined broken symmetry method, and reached an interpretation of the magnetic coupling as the spin delocalization from the copper center and the spin polarization from the gadolinium center.

More detailed magnetic coupling mechanisms are further discussed by Hirao using state-of-the-art CASSCF and CASPT2 calculations[7]. They concluded that the ferromagnetic gap is intrinsic to the Cu^{II}–Gd^{III} pair but appears with a low magnitude for the naked dimer. The pure ligand field with only electrostatic and polarization effects slightly increases the ferromagnetic gap. Within an appropriate definition of magnetic orbitals, Kahn's proposal can be certified as an effective mechanism of ferromagnetic coupling, involving orbitals not genuine Cu (3d) and Gd (5d) atomic orbitals (AOs), but molecular orbitals (MOs) already containing a small tail of Gd-origin on the orbital located mainly on the [CuL] side as well as a slight mixing between 4f and 5d AOs of Gd^{III}. The spin polarization picture is supported by the computation experiments based on the CASSCF method, involving the ligand and the 5d orbitals of Gd^{III}. From the view of state-of-the-art calculation, the polarization mechanisms of Kahn and Gatteschi are not mutually contradictory, but are even interconvertible by appropriate transformations of the magnetic orbitals, thereby adjusting the portion of pure Cu (3d) and ligand tails, in the active orbital that interacts with Gd (6s) or Gd (5d). In general, the contribution of 5d orbitals of Gd^{III} is larger than that of the 6s orbital and plays a more important role in the magnetic coupling of Gd^{III}–Cu^{II} compounds. The magnetic orbital analysis shows that the orbital orthogonal exchange pathway transmits ferromagnetic interaction in complexes of this kind. In fact, the important effect of 6s, 5d orbitals for rare earth magnetism is also widely accepted in the magnetic studies on rare earth metals, alloys, and oxides.

Other Gd^{III}-3d compounds are less documented and characterized, and have no strong tendency to be ferromagnetic or antiferromagnetic like the obvious magnetostructural correlation of Gd^{III}–Cu^{II} systems. It seems that the magnetic coupling properties are mainly governed by the nature of the chemical linker between the spin carriers, but this is



Scheme 1 Geometry structures of nitronyl nitroxide radical, imino nitroxide radical, and semoquinonato

not always right. For example, ferromagnetic couplings are found for Mn^{III}, Fe^{II}, Co^{II}, and Ni^{II} when the bridges are the oxygen atom of Schiff base derivatives, but both ferro- and antiferromagnetic interactions were found for $Gd^{III}-V^{IV}$ system. When the CN ligand is the linker, antiferromagnetic interactions are favorable for $Gd^{III}-Cr^{III}$ and $Gd^{III}-Fe^{III}$ compounds.

Organic radicals can also be linked to paramagnetic rare earth ions. This is because the direct bonding can shorten the interacting distance of the spin carriers, and the strength of the exchange interaction is improved to approach the 4f–3d system. Nitronyl nitroxide radical, imino nitroxide radical, and semiquinone derivatives are often selected for their stability and ease of coordinatation with rare earths. The structures of the radicals concerned are depicted in Scheme 1. For example, the exchange interactions of nitronyl nitroxide radical and Gd^{III} are mainly ferromagnetic and can be as large as $6.1\,cm^{-1}$.[8] For compound Gd $(Tp)_2(SQ)$ (Tp stands for hydro-trispyrazolyl borate and SQ stands for 3,5-di-*tert*-butylsemiquinonato), the coupling constant $J = -11.4\,cm^{-1}$ of the Gd–semiquinone interaction is the maximum value for the magnetic coupling intensity between Gd^{III} and other paramagnetic centers including lanthanide ions,

Owing to the highly contracted character of 4f electrons, the magnetic interactions of 4f–4f electrons are commonly very weak. Some oxygen (from carboxylate, phenoxide ligand, and so on)-bridged dinuclear Gd^{III} complexes are reported and they exhibit weak antiferromagnetic and ferromagnetic interactions. The exchange coupling constants range from -0.2 to $0.2\,cm^{-1}$, all values being much smaller than the values from Gd^{III}–TM compounds. It turns to nearly 0 in some compounds. If it turns to other rare earth ions

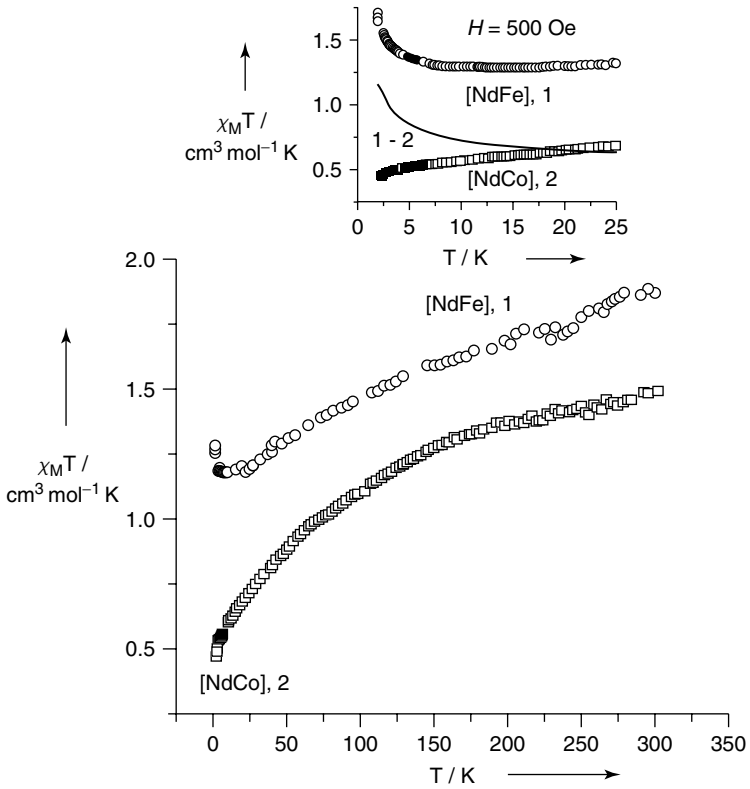


Figure 3 Temperature dependence of $\chi_M T$ for [NdFe] 1 (◯) and [NdCo] 2(□) at 10 kOe. Inset is the curve of $\chi_M T$ versus T at 500 Oe. (Reproduced from Ref. 9. © Wiley-VCH Verlag GmbH & Co. KGaA, 2001.)

with orbital moment contribution, the analysis of the magnetic properties will be much more complicated for the ligand-field effect and orbital part have overlapped contribution to the overall magnetic properties and no general analytical model can well simulate the rare earth magnetism at low temperature. Fortunately, knowledge of the periodic table provides a rather simple experimental approach to overcome the problem and can give some qualitative insight into the interactions between rare earths and other spin carriers. In general, this approach requires two compounds, one being a cluster-type molecule including a rare earth ion and the other an exchange-coupled spin carrier; the other molecule is an isostructural compound in which the coordination sphere of the rare earth ion is identical but corresponding coupled spin carrier is replaced by a diamagnetic ion. Then, the comparison of the magnetic behaviors of the two compounds could reveal the nature of the magnetic interaction in the exchange-coupled system.

The magnetic studies on $[NdM(bpym)(H_2O)_4-(CN)_6]\cdot 3H_2O$ (M = Fe, Co) coordination polymers by Gao *et al*. provide a good example to show the strength of this method[9]. The temperature dependence of the $\chi_M T$ for crystalline samples Nd–Fe^{III} and Nd–Co^{III} measured at 10 kOe and 500 Oe fields are shown in Figure 3. To exclude the magnetic contribution of the single Nd^{III} ion, the $\chi_M T$ of Nd–Co^{III} was subtracted from that of Nd–Fe^{III}. It was found that the difference (solid line in the inset of Figure 3) increased steadily with cooling, indicated ferromagnetic interactions occurred between the Nd^{III} and Fe^{III} ions.

The strongest exchange-coupling interaction between rare earths and other spin carriers yet reported was found in a dinuclear Ln^{III} complexes, $[K(18\text{-crown-}6)]\{[(Me_3Si)_2N]_2(THF)Ln\}_2$ (μ-η^2:η^2-N_2) Ln = Gd, Dy).[10] The N_2^{3-} radical bridged two rare earth ions and transferred the large antiferromagnetic-coupling interaction. The exchange-coupling constant J is as large as -27 cm^{-1} assuming spin-only Hamiltonian $H = -2\cdot J\cdot S_{radical}\cdot(S_{Gd(1)} + S_{Gd(2)})$. The unprecedented strength of the coupling is attributed to the diffuse spin orbital of the N_2^{3-} radical, which generates an unusually effective direct exchange pathway between the rare earth ion and the radical, despite the contracted nature of the Gd ^{III}4f orbitals. It is a promising method for enhancing the exchange-coupling interactions of rare earths.

Some other examples have been also reported for Ln^{III}-3d and Ln^{III}-radical systems. But there is no general magnetostructural correlation deduced from the reported compounds owing to the limited number of studies. These studies are still restricted by the difficulties of theoretical modeling and calculation for electronic structure of rare earths.

4 CONCLUSIONS

Magnetism of rare earths is briefly introduced in this chapter. The large unquenched orbital momentum and spin–orbital coupling of rare earths are the key points in determining the rich magnetic properties of rare earth containing compounds. Because the contracted nature of rare earth 4f orbitals, the exchange-coupling interactions are usually weak compared with those of 3d transition metals. For the same reason, the spin-polarized 6s, 5d orbitals are responsible for the superexchange interactions in the rare earth complexes.

5 ACKNOWLEDGMENTS

The authors thank the National Natural Science Foundation of China and the National Basic Research Program of China for the financial support. The authors also thank Ms. Ye Bi for the discussions.

6 RELATED ARTICLES

Molecular Magnetic Materials.

7 ABBREVIATIONS AND ACRONYMS

AO = atomic orbital; DFT = density functional theory; MO = molecular orbital; MRI = magnetic resonance imaging; HDVV = Heisenberg-Dirac-Van Vleck; PMO = perturbative molecular orbital.

8 REFERENCES

1. J. S. Miller and M. Drillon, 'Magnetism: Molecules to Materials', Wiley-VCH, Weinheim, 2005, Vol. V.
2. L. E. Sweet, L. E. Roy, F. Meng, and T. Hughbanks, *J. Am. Chem. Soc.*, 2006, **128**, 10193.
3. L. E. Roy and T. Hughbanks, *J. Am. Chem. Soc.*, 2006, **128**, 568.
4. C. Benelli, A. Caneschi, D. Gatteschi, O. Guillou, and L. Pardi, *Inorg. Chem.*, 1990, **29**, 1750.
5. M. Andruh, I. Ramade, E. Codjovi, O. Guillou, O. Kahn, and J. C. Trombe, *J. Am. Chem. Soc.*, 1993, **115**, 1822.
6. F. Yan and Z. Chen, *J. Phys. Chem. A*, 2000, **104**, 6295.

7. J. Paulovic, F. Cimpoesu, M. Ferbinteanu, and K. Hirao, *J. Am. Chem. Soc.*, 2004, **126**, 3321.

8. J. P. Sutter, M. L. Kahn, S. Golhen, J. P. Sutter, M.L. Kahn, S. Golhen, L. Ouahab, and O. Kahn, *Chem. Eur. J.*, 1998, **4**, 571.

9. B. Ma, S. Gao, G. Su, and G. Xu, *Angew. Chem. Int. Ed.*, 2001, **40**, 434.

10 J. D. Rinehart1, M. Fang, W. J. Evans, and J. R. Long, *Nat. Chem.*, 2011, **3**, 538.

The Divalent State in Solid Rare Earth Metal Halides

Gerd Meyer

Universität zu Köln, Köln, Germany

1 Summary 161
2 Introduction 161
3 Synthesis 162
4 Binary Halides 163
5 Ternary Halides 168
6 Oxide Halides 171
7 Glossary 172
8 Abbreviations and Acronyms 173
9 References 173

1 SUMMARY

Lanthanide compounds with the lanthanide in the +2 oxidation are known for chalcogenides and halides. Binary examples are EuO and TmS as well as LaI_2 and $NdCl_2$. Two cases of electronic configurations have to be distinguished, $[Xe]6s^05d^04f^n$ and $[Xe]6s^05d^14f^{n-1}$. The former with electrons occupying only 4f orbitals are salt-like insulators and their crystal chemical behavior is very similar to that of the respective alkaline-earth compounds. In the latter, there is one voluminous, outer-shell 5d orbital occupied. This 5d electron might be localized and involved in chemical bonding in cluster complexes (these are the subject of chapter ***Rare Earth Metal Cluster Complexes***). It may also be delocalized into a 5d band causing semiconducting or metallic behavior. In this chapter, only halides of both classes of compounds are discussed.

2 INTRODUCTION

The lanthanides (R, lanthanum through lutetium) have, as atoms in the oxidation state ± 0, the general electronic configuration $[Xe]6s^25d^14f^n$ with $n = 0$ for La and $n = 14$ for Lu. In the trivalent state, as R^{3+} ions, their electronic configuration is, accordingly, $[Xe]6s^05d^04f^n$. In the divalent state, the $6s^0$ electrons are released but the electronic configuration may be $[Xe]6s^05d^04f^n$ or $[Xe]6s^05d^14f^{n-1}$. This phenomenon is called *(electronic) configuration crossover*; symbolically, the first configuration is addressed as R^{2+} and the second one as $R^{3+}(e^-)$. Structurally, lanthanides with the R^{2+} configuration act as pseudo alkaline-earth ions; Eu^{2+} has, for example, the same ionic radius as Sr^{2+}. The $R^{3+}(e^-)$ configuration leads to metallic or half-metallic compounds or to cluster complexes. The latter is discussed in ***Rare Earth Metal Cluster Complexes***.

Halides of the lanthanides in the oxidation state +2 have been known since the early decades of the twentieth century. $EuCl_2$, $SmCl_2$, and $YbCl_2$ were the first to be reported.[1–5] For these 3 elements, all 12 possible halides are known. This is not the case for the elements thulium, dysprosium, and neodymium for which only the halides of the triad chlorine, bromine, and iodine have been synthesized and crystallographically characterized. They structurally bear close resemblance to the respective alkaline-earth metal halides.[6,7] The electronic configurations of the M^{2+} ions of these six elements are $6s^05d^04f^n$ with $n = 4$ (Nd), 6 (Sm), 7 (Eu), 10 (Dy), 13 (Tm), and 14 (Yb).

Diiodides RI_2 of the elements lanthanum, cerium, praseodymium, and gadolinium are also known. These were once called *metallic diiodides*;[8] in these the electronic configuration of the respective lanthanide is $[Xe]6s^05d^14f^{n-1}$ and the 5d electron is delocalized in a 5d band.[9–12]

Although scandium is not a lanthanide element, it belongs to the group of rare earth elements. Scandium diiodide should be mentioned in this connection. It is a special case as it is a scandium-deficient compound, $Sc_{0.9}I_2$. It does, however, qualify as a member of the $R^{3+}(e^-)$ group, at sufficiently high temperatures.[13,14]

The Rare Earth Elements. Edited by David A. Atwood. © 2012 John Wiley & Sons, Ltd. ISBN 978-1-119-95097-4

All of the dihalides, insulators or metallic, are produced as solids either by comproportionation reactions[15,16] or by *Wöhler*'s metallothermic reduction from the trihalides with alkali metals.[7,17]

3 SYNTHESIS

3.1 Reduction Methods in General

The reduction of rare earth metal trihalides, RX_3, is in principle possible with all kinds of reducing agents as long as they have standard electrode potentials E° that can overcome that of the respective potentials of E° ($R^{3+} \rightarrow R^{2+}$). This is discussed below in more detail. Therefore, the classical reducing agents, nonmetals such as hydrogen or carbon, or like metals (comproportionation route) and unlike metals (metallothermic reduction) are all possible but (may) lead to different products. Cathodic reduction of appropriate melts is also an option.

Metal oxides or halides may be reduced to the respective metal by a number of reductants; hydrogen and carbon are the most easily available and are inexpensive for large scales. When pure compounds or even metals are desired, the use of carbon as reductant is disadvantageous because the rare earth metals form carbide halides and carbides. These are in fact metallic carbides with carbon atoms occupying octahedral or tetrahedral voids in the metal's lattice. Hydrogen is more advantageous, although hydrides are also ubiquitous with the rare earth metals. However, with sufficient care, hydrogen can be pumped off at elevated temperatures and, subsequently, the metals or compounds may be sublimed or distilled, whatever is possible and feasible.

Indeed, hydrogen has been used in the early days as a reductant, for example, for the trichlorides RCl_3, when the rare earth metals for comproportionation reactions were either not available or were too valuable. As it is a solid–gas reaction, temperature and surface blocking are always a big issue, as also time. Only for europium, ytterbium, and samarium, the dichlorides RCl_2 are stable enough and can be produced at reasonably low temperatures. At higher temperatures and with all the other trichlorides, the metals are produced, actually as hydrides, the hydrogen content depending upon hydrogen pressure and cooling procedures.

The comproportionation reaction is straightforward whenever the respective phase diagrams are known. One can also make use of a melt of some kind. If properly carried out, pure products will be obtained. This method can also be used to prepare ternary and quaternary compounds with the proper choice of starting materials. The only problem here is that the phase diagrams are in most cases not known. This research is, therefore, exploratory and rather serendipitous.

The reduction of rare earth metal halides with unlike metals, Wöhler's metallothermic reduction, has originally been used to produce the rare earth metals. When used properly, intermediates with oxidation states between +3 and 0 can be obtained.

Cathodic reduction of appropriate halide melts (mostly chlorides) is an important process to produce rare earth metals, unless in certain cases, lower-valent halides have not been obtained or did not form during the cooling process.

In the following sections, only the comproportionation route and the metallothermic reduction route are discussed as the two most commonly used synthetic methods.

3.2 The Comproportionation Route

The comproportionation route[15,16] is widely used and is very efficient when pure phases are desired, especially when the phase relationships are known. It led to a great variety of ''reduced'' rare earth halides, binary, ternary, and higher, simple and complex salts and such that incorporate metal clusters interstitially stabilized by a nonmetal atom or by a (transition) metal atom; for example,

$$2EuCl_3 + Eu = 3\ EuCl_2$$

$$GdCl_3 + Gd = Gd_2Cl_3$$

$$3CsCl + 2\ SmCl_3 + Sm = 3\ CsSmCl_3$$

$$11\ ScI_3 + 7\ Sc + 6\ C = 3\ \{C_2Sc_6\}I_{11}$$

$$RbCl + 3\ PrCl_3 + 2\ Pr + 2\ C = [\{C_2Pr_5\}_2Cl_{10}]Rb$$

One disadvantage of this route is the often high reaction temperatures and unknown phase equilibria. Especially when it comes to ''higher'' systems, phase diagrams are not known at all.

It was a great thrust for reduced rare earth metal chemistry when it was discovered that sealed metal ampoules (mostly produced from niobium and tantalum tubing by He arc welding) were reaction containers inert enough to the corrosive molten salts to allow for pure products.[18] Still, all constituents of air need to be excluded, which is possible, thanks to modern dry box techniques. The unintended incorporation of ubiquitous hydrogen or carbon led to a whole new world of cluster complexes with endohedral atoms, mostly with extended structures, as in $\{H_xLu\}Cl$ or in $\{CLu_2\}Cl_2$ (see ***Rare Earth Metal Cluster Complexes***).

3.3 The Metallothermic Reduction Route

The metallothermic reduction of $SmCl_3$ designed for the preparation of samarium metal with an (apparently) insufficient quantity of sodium, resulting in the formation of $SmCl_2$,[5]

$$SmCl_3 + Na = SmCl_2 + NaCl$$

gave birth to a new approach to ''reduced'' rare earth metal halides that were previously synthesized only by the

comproportionation route or by reduction with hydrogen, namely,

$$2\ SmCl_3 + Sm = 3\ SmCl_2$$

$$2\ SmCl_3 + H_2 = 2\ SmCl_2 + 2\ HCl$$

In principle, the same experimental techniques as outlined above for the comproportionation route may be used for the reduction of rare earth metal halides with unlike metals, i.e., the metallothermic reduction route,[7,17] with low melting and highly electropositive metals, alkali, and alkaline-earth metals in particular. The low melting points of these metals are certainly an advantage, as the reaction temperatures may be much lower than for comparable comproportionation reactions. The most obvious disadvantage is that pure products are in most cases (but note the reaction $Cs + SmCl_3 = CsSmCl_3$) not available as one of the driving forces of this route is the production of high-lattice-energy alkali-metal halides.

The separation of the products is not easy, although not impossible. For the exploration of the respective systems and their phase contents, it is, however, often not necessary to obtain pure products because modern, fast X-ray crystallography is an easy means to analyze even multiproduct reactions. Afterwards, when the respective compounds are known, care has to be taken to produce the new compounds in pure phase by whatever route is desirable. One major advantage of the metallothermic reduction route is the fairly low reaction temperatures as these allow for the synthesis and crystal growth of compounds that decompose in the solid state, melt incongruently, or even form and decompose in the solid state at fairly low temperatures. Also, low-temperature modifications may be grown as single crystals below the transition temperature.

4 BINARY HALIDES

Dihalides of the rare earth elements became known shortly after the turn of the twentieth century. A first picture was completed in the late 1920s when it was thought that only the ''classical four,'' europium, ytterbium, samarium, and thulium, could be obtained in the divalent state. *Klemm*

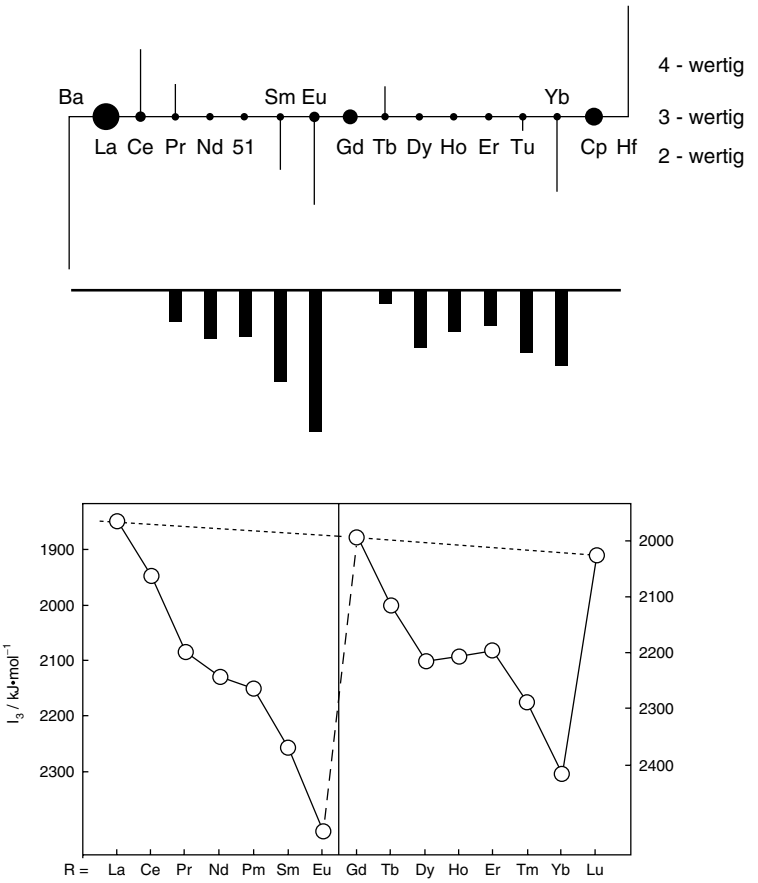


Figure 1 *Klemm*'s graph of 1929/1930 (top) exhibiting lanthanide elements with stable di- and tetravalent compounds; a modern version of this graph for the divalent state is shown in the middle: the difference $\Delta E^\circ = E^\circ\ (Gd^{3+}/Gd^{2+})$ -$E^\circ\ (R^{3+}/R^{2+})$ is plotted to parallel *Klemm*'s graph. Bottom: The third ionization potentials of the lanthanides, $I_3 = \Delta H^\circ$ (3), in kJ mol^{-1}

incorporated this knowledge in his famous graph, which is displayed in Figure 1.[19]

The picture became more complete (but also much more complicated) through the seminal phase diagram determinations by *Corbett* in the third quarter of the twentieth century. These made clear that in a number of other systems, dihalides can be thermodynamically stable under certain conditions; see Figure 2 for the system PrI_3/Pr. The picture as of today, verified by X-ray crystallographic studies, is summarized in Table 1.

Corbett also discovered a number of other binary reduced lanthanide chlorides, bromides, and iodides through phase diagram determinations and through further exploratory research. For example, there is the scandium-deficient ''scandium diiodide,'' with a composition around $Sc_{0.89}I_2$, and the praseodymium excess $PrCl_{2.31} = Pr_{0.29}PrCl_3$, with

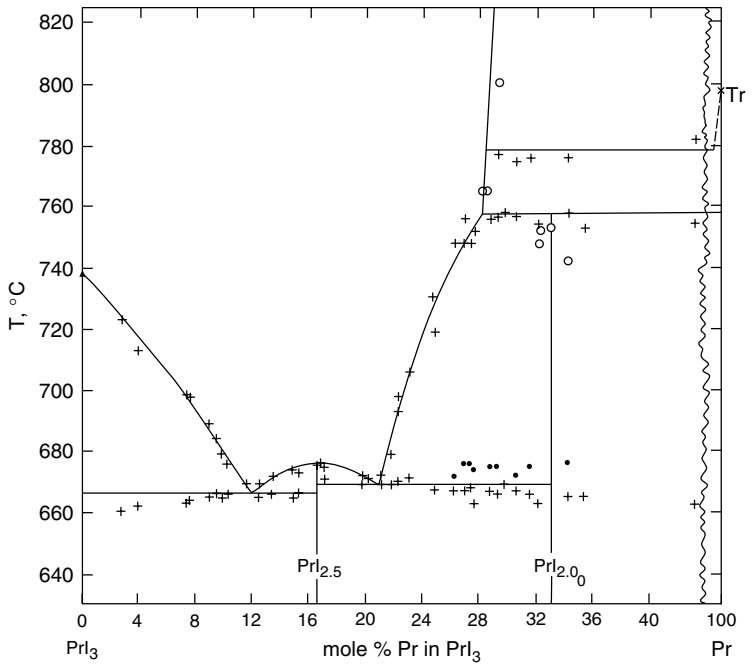


Figure 2 The temperature/composition phase diagram for the system PrI_3/Pr exhibiting the existence of two intermediate compounds, $PrI_{2.5} = Pr_2I_5$ and PrI_2, respectively. (Reprinted from Ref. 9. Reproduced by permission of The Royal Society of Chemistry. DOI: http://dx.doi.org/10.1039/DF9613200079.)

Table 1 Salt-like and ''metallic'' (bold-type) dihalides of the rare earth elements

	Fluoride	Chloride	Bromide	Iodide
Scandium	—	—	—	**$Sc_{0.9}I_2$**
Yttrium	—	—	—	—
Lanthanum	—	—	—	**LaI_2**
Cerium	—	—	—	**CeI_2**
Praseodymium	—	—	—	**PrI_2**
Neodymium	—	$NdCl_2$	$NdBr_2$	NdI_2, **NdI_2**
Promethium	—	—	—	—
Samarium	SmF_2	$SmCl_2$	$SmBr_2$	SmI_2
Europium	EuF_2	$EuCl_2$	$EuBr_2$	EuI_2
Gadolinium	—	—	—	**GdI_2**
Terbium	—	—	—	—
Dysprosium	—	$DyCl_2$	$DyBr_2$	DyI_2
Holmium	—	—	—	—
Erbium	—	—	—	—
Thulium	—	$TmCl_2$	$TmBr_2$	TmI_2
Ytterbium	YbF_2	$YbCl_2$	$YbBr_2$	YbI_2
Lutetium	—	—	—	—

additional praseodymium atoms incorporated in voids of the UCl_3-type structure of $PrCl_3$.[20] A number of sesquichlorides were discovered following Gd_2Cl_3, the ''seventh wonder of the rare earth world,''[21,22] with scandium, yttrium, lanthanum, cerium, terbium, and erbium. And there are R_2X_5-type halides with R = La, Ce, Pr and X = Br, I which have interesting magnetic properties.[23] Finally, there are class I mixed-valence halides, i.e., with R^{2+} (large) and R^{3+} (smaller) ordered in defined positions in their crystal structures for the elements R = Nd, Sm, Eu, Dy, Ho, Tm, Yb, for example, $Dy_5Cl_{11} = (Dy^{2+})_4(Dy^{3+})\,(Cl^-)_{11}$.[24]

Although this seems to be rather confusing, there are, of course, reasons. The relative stabilities of the di- and trivalent states of the respective lanthanides throughout the series follow, more or less, the third ionization potentials of the elements, $\Delta H°(3)$ (Figure 1). With a standard electrode potential of $E°(Eu^{2+}/Eu^{3+}) = -0.35$ V (which can be measured in aqueous solution), the ionization potentials or disproportionation enthalpies can be used to calculate standard electrode potentials $E°(R^{2+}/R^{3+})$ for the whole series. This work has essentially been put forward by *Johnson* and *Morss*.[25–27] These results may be summarized graphically as shown in Figure 1. It is evident that the standard electrode potentials perfectly parallel *Klemm*'s chemical intuition and observations. And, of course, the data explain why there are two further elements, neodymium and dysprosium, which form salt-like dihalides. In all of these halides, the rare earth ion R^{2+} has the electronic configuration $[Xe]6s^05d^04f^n$ with $n = 4$ (Nd^{2+}), 6 (Sm^{2+}), 7 (Eu^{2+}), 10 (Dy^{2+}), 13 (Tm^{2+}), and 14(Yb^{2+}).

These dihalides have crystal structures that are also observed for the respective alkaline-earth halides (see Table 2). Neodymium(II) iodide, NdI_2, undergoes a high-pressure phase transition from salt-like ($SrBr_2$ type of structure) to metallic ($CuTi_2$ type of structure) subject to the configuration crossover $4f^45d^0 \rightarrow 4f^35d^1$.[28] The 5d electron delocalizes into a 5d band with no volume such that the molar volume of $(Nd^{3+})(e^-)(I^-)_2$ is smaller than that of $(Nd^{2+})(I^-)_2$, a transition which is triggered by pressure.

As can be seen from Table 2, most of the crystal structures that are observed for the rare earth metal dihalides are classical structure types which are known for salts, purely ionic or with some admixture of covalency, with coordination numbers of 9 ($PbCl_2$), 8 (CaF_2, $SrBr_2$), 7 (SrI_2, EuI_2), and 6 ($CdCl_2$, CdI_2). Halides crystallizing in these structure types are insulating salts. The 2H- and 3R-MoS_2 types of structure are intermediate as these layered compounds may generally be insulating or semiconducting and may have very special properties as seen in GdI_2. This is a ferromagnet with a Curie temperature of 313 K, and shows collosal magnetoresistance.[12] The structural chemistry of all of these halides is quite straightforward and classical and shall not be discussed further.

There are the four diiodides LaI_2, CeI_2, PrI_2-I, and HP-NdI_2 that crystallize with the $CuTi_2$ type of structure. These halides are two-dimensional metals that becomes obvious by an inspection of their crystal structure (Figure 3). It is built from 4^4 nets of metal atoms and of iodide ions which are stacked in the [001] direction of the tetragonal unit cell such that the metal atoms are eight-coordinate. R-R distances are between 393 and 386 pm (R = La → Pr) at ambient temperature. The metal atoms R, which are in

Table 2 Crystal structures of the rare earth metal dihalides, structure types (ST), coordination numbers (CN), and shortest R–R distances (wherever known)

Salt-like $(R^{2+})(X^-)_2$			''Metallic'' $(R^{3+})(e^-)(X^-)_2$		
RX_2	**ST, CN**	**d(R–R)/pm**	**RX_2**	**ST, CN**	**d(R–R)/pm**
$NdCl_2$	$PbCl_2$, 9	451	LaI_2	$CuTi_2$, 8	393.6(1)
$NdBr_2$	$PbCl_2$, 9	—	CeI_2	$CuTi_2$, 8	388.8(1)
SmF_2	CaF_2, 8	415	PrI_2-I	$CuTi_2$, 8	386.4(2)
$SmCl_2$	$PbCl_2$, 9	449	PrI_2-II	2H-MoS_2, 6	—
$SmBr_2$	$SrBr_2$, 8	—	PrI_2-III	3R-MoS_2, 6	—
SmI_2	EuI_2, 7	501	PrI_2-IV	$CdCl_2$, 6	426.5(1)
EuF_2	CaF_2, 8	413	PrI_2-V	own, 6	391.3(2)
$EuCl_2$	$PbCl_2$, 9	448	HP-NdI_2	$CuTi_2$, 8	384.3(1)
$EuBr_2$	$SrBr_2$, 8	—	GdI_2	2H-MoS_2, 6	407.5
EuI_2-I	own, 7	486	$Sc_{0.89}I_2$	CdI_2, 6	410.2(1)
EuI_2-II	SrI_2, 7	—	—	—	—
$DyCl_2$	$SrBr_2$, 8	—	—	—	—
$DyBr_2$	SrI_2, 7	457	—	—	—
DyI_2	$CdCl_2$, 6	462	—	—	—
$TmCl_2$	SrI_2, 7	432	—	—	—
$TmBr_2$	SrI_2, 7	—	—	—	—
TmI_2	CdI_2, 6	452	—	—	—
YbF_2	CaF_2, 8	396	—	—	—
$YbCl_2$	SrI_2, 7	432	—	—	—
$YbBr_2$	SrI_2, 7	437	—	—	—
YbI_2	CdI_2, 6	450	—	—	—

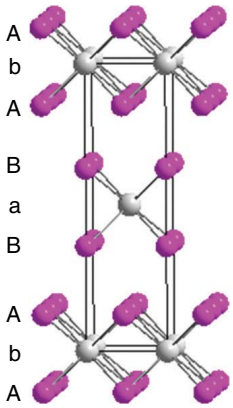


Figure 3 Crystal structure (tetragonal) of the rare earth metal diiodides LaI_2, CeI_2, PrI_2-I, and HP-NdI_2; projection approximately down [100]

the oxidation state +2, have the electronic configuration $[Xe]4f^n5d^1$ with $n = 0$ (La), 1 (Ce), 2 (Pr), and 3 (Nd). There is the paramagnetism of one to three core-like 4f electrons in CeI_2, PrI_2-I, and HP-NdI_2, respectively. The 5d electron is, however, not localized; rather it is delocalized in a two-dimensional 5d band which makes these compounds two-dimensional metals, similar to graphite. LaI_2 is a special case because here lanthanum has just one valence electron left. CeI_2 has one 4f and one 5d electron. It therefore is not only a metal but it also exhibits antiferromagnetism at temperatures below 10 K.[29]

Unfortunately, PrI_2-I has never been obtained as a pure phase except for single crystals suitable for structure determination by X-ray diffraction. PrI_2-IV, which exists only at high temperatures, crystallizes in principle with the $CdCl_2$ structure and appears to incorporate an additional 10% of praseodymium atoms in octahedral voids between the layers which are empty in the parent structure. On cooling, the surplus metal can be released either from the additionally occupied voids or from regular interstices. The layers of 3^6 nets as found in all of the structures of PrI_2-II, -III, -D, -IV, and -V may be arranged differently. The transition from a 3^6 to a 4^4 net as observed in PrI_2-I is an easy task. Structurally, it is a shear process (see Figure 4).[11]

Nucleation probabilities and enthalpies for the transition from PrI_2-IV on cooling to all the others must be very similar. The temperatures for the beginning of the nucleation in equilibrium are not known. Therefore, when cooling PrI_2-IV from, say, 700 °C to ambient temperature, a mixture of I–V (except IV), depending on the cooling process, is always obtained. Hydrogen stabilizes PrI_2-D (D for disorder), which is a polytype of II and III. PrI_2-V is unique among the rare earth metal diiodides. It is a perfectly ordered variant of the $CdCl_2$ type of structure in which iodide layers are stacked in the cubic face-centered . . .ABC. . . manner and octahedral holes between these layers are either all occupied (1) or all empty (0). In PrI_2-V, they are filled to 0.75 and 0.25, and in α-ZrI_2, another derivative, the ratio is 0.5/0.5.[11]

The only rare earth metal diiodides that crystallize in the $CdCl_2$ type of structure are PrI_2-IV and DyI_2. Interestingly enough, the elements praseodymium and dysprosium are homologs (see Figure 5) with electronic configurations for Pr^{2+} of $[Xe]4f^35d^0$ or $[Xe]4f^25d^1$ and Dy^{2+} of $[Xe]4f^{10}5d^0$ (or $[Xe]4f^95d^1$).

An idea about the electronic structures of PrI_2 and DyI_2 can be obtained from band structure calculations.[30]

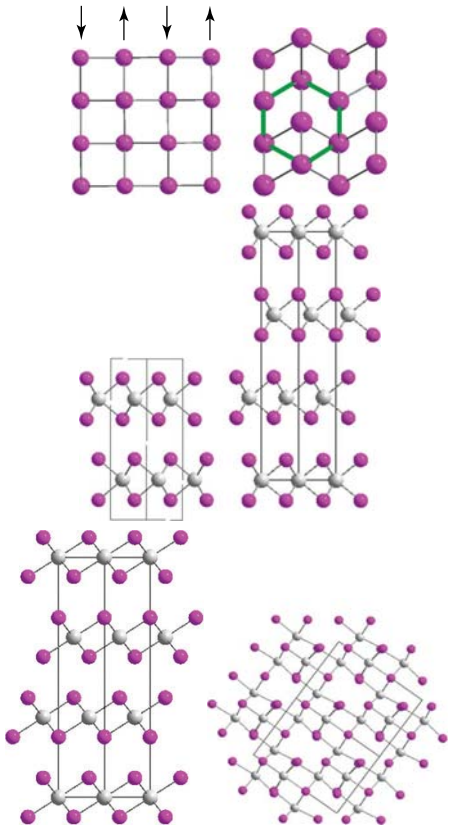


Figure 4 The shear transition from a 4^4 to a 3^6 net (above), the crystal structures of PrI_2-II and -III (middle), as well as of (bottom) PrI_2-IV and -V in equivalent projections showing the layer sequences

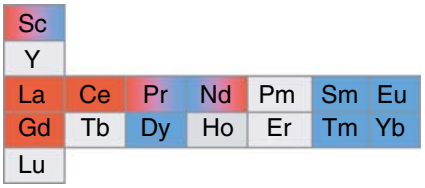


Figure 5 A periodic system of the rare earth elements, colored for the examples of the diiodides RI_2. Blue, $5d^04f^n$ configuration; red, $5d^14f^{n-1}$ configuration

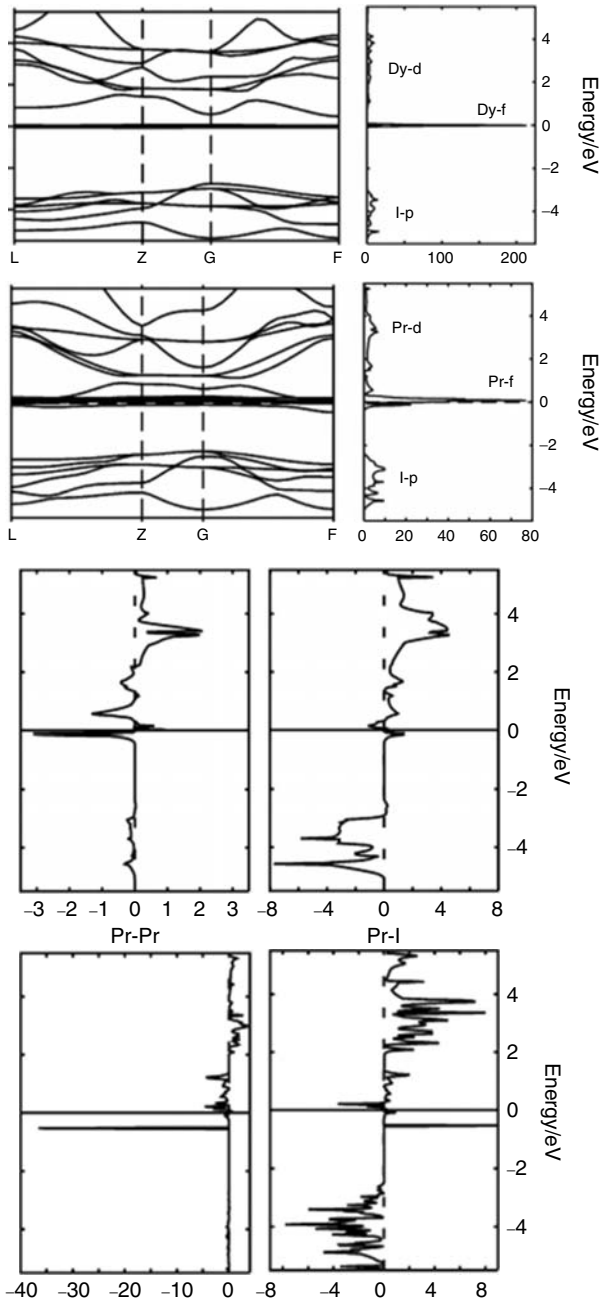


Figure 6 The electronic structures of DyI_2 and PrI_2-IV and -V. Shown are from top to bottom, the band structures of DyI_2 and PrI_2-IV and 5d densities of states (DOS) derived therefrom. Crystal overlap Hamiltonian population (COHP) curves for PrI_2-IV and -V) for Pr–Pr and Pr–I bonding (to the left, negative signs) and antibonding interactions (to the right) are exhibited

From these, the density of states (DOS) can be derived, either for the whole unit cell content or for certain atoms or atom types. This is shown in Figure 6. The DOS curves for the isostructural DyI_2 and PrI_2-IV show that the 4f and 5d states are much more separated for DyI_2; for PrI_2-IV, they overlap and, more importantly, the 5d state is considerably lower in energy and touches the Fermi level. The crystal orbital Hamiltonian population (COHP) curves, also derived from band structure calculations, show furthermore that there are considerable Pr–Pr bonding interactions just below the Fermi level (lower left of Figure 6). They outweigh the Pr–I antibonding interactions that also appear in this energy region. Hence, for PrI_2-IV, the rather large 5d orbitals can interact and contribute further to the stabilization of the compound. This is apparently not possible for the smaller 5d orbitals in DyI_2 (seven additional protons). As a result, DyI_2 is a salt under ambient conditions. This result is also reflected in the R–R distances in PrI_2-IV (426 pm) and DyI_2 (462 pm), which are against the trend of the lanthanide contraction.

Further stabilization of PrI_2 is possible through the transition IV $\rightarrow$ V on cooling, which results in the formation of tetrahedral $\{Pr_4\}$ clusters. This stabilization can be ''seen'' through the shrinkage of the Pr–Pr distances to 392 pm. In the COHP curves, bonding interactions are considerably lower in energy.

The diiodides of thulium and ytterbium, TmI_2 and YbI_2, crystallize with the CdI_2 type of structure and are salts. Scandium diiodide crystallizes also with this structure but is scandium deficient, Sc_xI_2 ($x = 0.87$, 0.93 from different structure determinations; we refer to it with a $Sc_{0.89}I_2$ in the following).[14] $Sc_{0.89}I_2$ is interesting because 4f electrons cannot be involved. It is the first 3d element, and the 3d orbitals are the most expanded in the fourth period. $Sc_{0.89}I_2$ is a metal above about 100 K, hence the electronic configurations are $[Ar]4s^03d^1$ and $[Ar]4s^03d^0$, above and below 100 K. According to the formulation $Sc_{0.89}I_2 \times 9 = Sc_8I_{18} = (Sc^{3+})_8(e^-)_6(I^-)_{18}$ (see Figure 7), there are only six electrons for eight scandium atoms which occupy

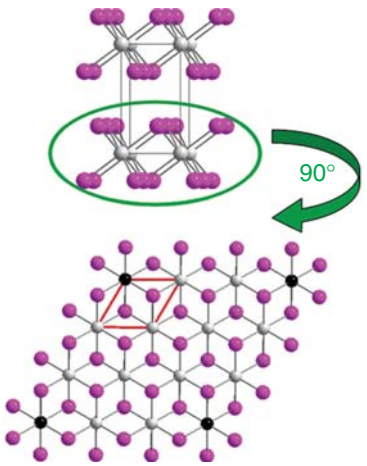


Figure 7 Crystal structure of $Sc_{0.89}I_2$. (a) CdI_2 type of structure. (b) A model for the under-occupation of one out of nine octahedral voids, leading, in principle, to a 3 × 3 larger unit cell

statistically the nine octahedral holes provided in the CdI_2-like structure of $Sc_{0.89}I_2$. At temperatures above 100 K, these electrons delocalize and (partly) fill the 3d band. The underoccupation of the scandium sites lowers the Fermi level and thereby appears to stabilize the whole structure (fighting the antibonding Sc–I interactions around the Fermi level). Below 100 K, the six electrons localize and $Sc_{0.89}I_2$ becomes an insulating, paramagnetic, mixed valent iodide according to $(Sc^{2+})_6(Sc^{3+})_2(I^-)_{18}$.

5 TERNARY HALIDES

Complex halides are generally obtained from the binary components; for example,

$$CsCl + TmCl_2 = CsTmCl_3$$

To avoid the tedious production of thulium(II) chloride, $TmCl_2$, by the comproportionation reaction

$$2TmCl_3 + Tm = 3TmCl_2$$

a ''one-pot'' reaction can also be carried out.

$$Cs + TmCl_3 = CsTmCl_3$$

This works in principle for the rare earth elements R = Nd, Sm, Eu, Dy, Tm, and Yb. In the case of the other rare earth elements which have much higher third ionization potentials I_3, partial reduction to the metals and the formation of ternary rare earth metal(III) halides is observed; for example,

$$3\ Li + 4\ GdCl_3 = 3\ GdLiCl_4 + Gd$$

The structural chemistry of $GdLiCl_4$ and other ternary lanthanide(III) halides such as Na_3GdCl_6 is not the subject of this chapter, but is discussed in a handbook article.[31] There are a few reduced ternary compounds, however, with R = La, Ce, Pr, which have similar behavior as the respective dihalides.

The metallothermic reduction with sodium appears to be special, as Na^+ has an ionic radius very similar to that of the large trivalent lanthanides, R^{3+}. Therefore, the reduction of all of the trichlorides RCl_3 that crystallize with the UCl_3 type of structure with sodium produces stuffed derivatives of this structure, $Na_{0.5}RCl_3$ or NaR_2Cl_6. These have been crystallographically characterized for R = Ce, Pr, Nd, Sm, Eu (see Figure 8).[5] Two classes need to be considered: Those with R = Ce, Pr are one-dimensional metals, in accord with the formulation $(Na^+)(R^{3+})_2(e^-)(Cl^-)_6$. The others with R = Nd, Sm, Eu are mixed-valent chlorides, $(Na^+)(R^{2+})\ (R^{3+})(Cl^-)_6$.

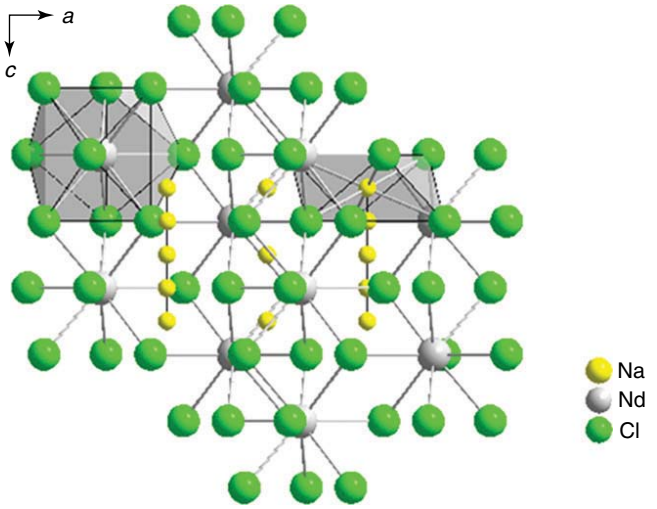


Figure 8 Crystal structure of the stuffed derivatives of the UCl_3 type of structure: additional (yellow) sites along the hexagonal *c* axis are occupied statistically by Na^+ in NaR_2Cl_6 and by Pr^{3+} in $PrCl_{2.31}$ (= $Pr_{0.58}Pr_2Cl_6$)

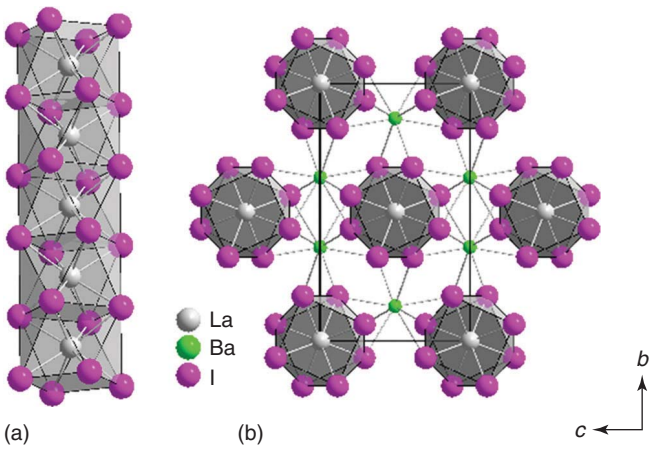


Figure 9 Crystal structure of ARI_4-type iodides exhibiting chains of face-sharing $[RI_{8/2}]$ square antiprisms (a) and their connection via A^{2+} cations (b), A = Sr, Ba, Nd, Sm, Eu; R = La, Ce

The enigmatic black $PrCl_{2.31}$ falls in the first class too, i.e., $(Pr^{3+})_{0.58}(Pr^{3+})_2(e^-)_{1.74}(Cl^-)_6$, with 58% of the additional sites occupied.[20]

Lanthanum and **cerium** triiodide, LaI_3 and CeI_3, when reduced with strontium or barium or with the *pseudo* alkaline-earth metals neodymium, samarium, and europium, yield ARI_4-type iodides, A = Sr, Ba, Nd, Sm, Eu; R = La, Ce.[32] These are built from square-antiprismatic $[MI_8]$ polyhedra sharing common faces to columns running parallel [100] (Figure 9). Although these iodides have one excess electron per formula unit, e.g., $(Ba^{2+})(La^{3+})(e^-)(I^-)_4$,

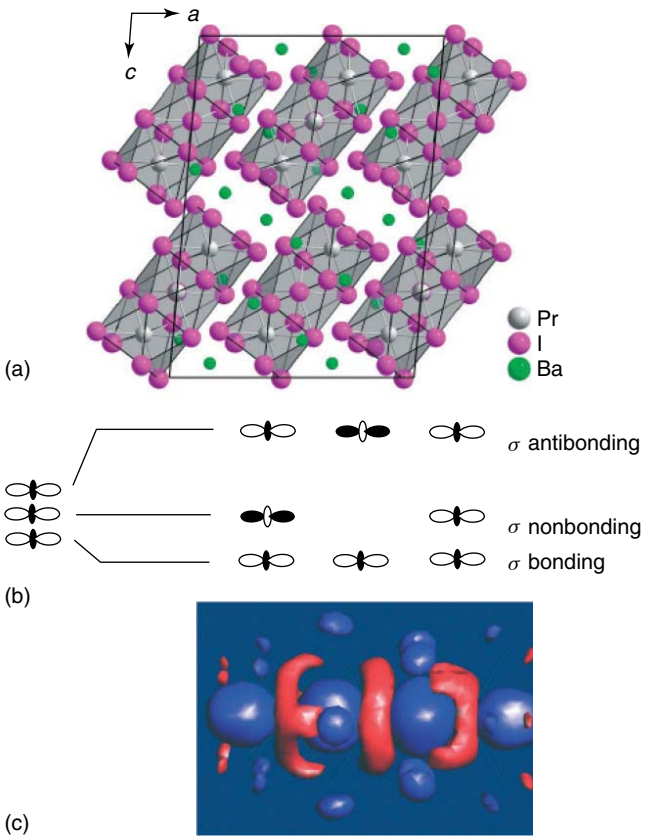


Figure 10 Crystal structure of $Ba_6Pr_3I_{19}$ (a) and the interaction scheme of three linearly oriented d_{z2} orbitals as well as the σ bonding three-center-two-electron orbital (b)

a *Peierls* distortion could not be detected, perhaps subject to matrix constraints. The structures are one-dimensional derivatives of the $CuTi_2$-type rare earth diiodides RI_2 (R = La, Ce) where $[RI_8]$ cubes are connected via four common faces to layers (see Figure 9).

Surprisingly, with *praseodymium*, an analogous iodide could not be synthesized. Rather, $Ba_6Pr_3I_{19}$ was obtained as single crystals from a reduction of PrI_3 with barium. This compound contains linear trimers, $[Pr_3I_{16}]$, consisting of three PrI_8 square antiprisms sharing two common faces (Figure 10). According to $(Ba^{2+})_6(Pr^{3+})_3(e^-)_2(I^-)_{19}$, there are two electrons available for an open two-electron-three-center bond.[33]

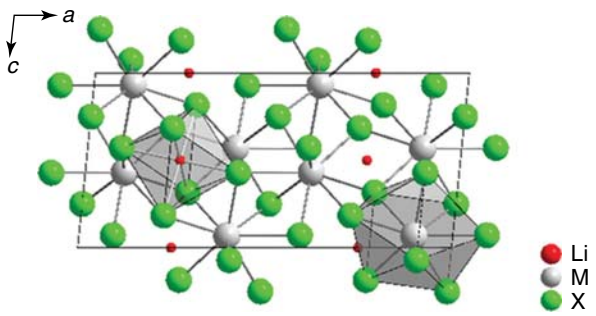


Figure 11 Crystal structure of LiR_2X_5 (R = Dy, Tm, Yb; X = Cl, Br)

With the smaller, harder rare earth elements (Gd through Lu), such compounds have never been seen, except for *scandium* where scandium-deficient hexagonal perovskites, ASc_xX_3 (A = Rb, Cs; X = Cl, Br, I), have been observed.[14] These are discussed together with the perovskite-type halides of R = Sm, Eu, Dy, Tm, Yb below. All other complex halides with reduced rare earth metals contain clusters and are discussed in ***Rare Earth Metal Cluster Complexes***.

Divalent *europium, ytterbium, samarium, thulium, dysprosium, and neodymium* can be incorporated in ternary AX/RX_2 compounds.[6,24,31] With the larger rare earth elements, R = Nd, Sm, Eu, mixed-valent $Na[R_2Cl_6]$ chlorides are obtained, which crystallize with a stuffed UCl_3-type structure, as described above. In the systems LiX/RX_2 with the smaller rare earth elements R = Dy, Tm, Yb, the ternary halides LiR_2Cl_5 and $LiDy_2Br_5$ are obtained as single crystals. In this crystal structure, which is known also from FeU_2S_5, R^{2+} is eight-coordinate (bicapped trigonal prism) and the polyhedra are connected to a three-dimensional network (Figure 11).

With the larger alkali metals, potassium, rubidium, and cesium, the perovskite-type structure with its variants plays an important role.[6,31,34] The usual concepts, radius ratios including *Goldschmidt*'s tolerance factor, structure field diagrams, or volume considerations derived from *Biltz*'s concept of volume increments may be used to classify these compounds and their behavior at different temperatures.[34] For example, $CsTmCl_3$ crystallizes with *the* (cubic) perovskite type of structure (Figure 12); $CsTmBr_3$ and $CsTmI_3$ with tetragonal and orthorhombic variants with octahedral tilts; and $CsSc_{0.71}Cl_3$ with the so-called hexagonal perovskite structure (Figure 12), isostructural with, for example, $CsNiCl_3$. In the ''perovskites,'' the R^{2+} cations are surrounded octahedrally by halide ions (in the variants symmetry elements as the four- and the threefold axes are given up), and common vertices or faces are shared to ensure the *Niggli* notation $A[RX_{6/2}]$. Variants with edge-sharing octahedra were also observed; $KTmI_3$ ($FeUS_3$ type) and $RbTmI_3$ (NH_4CdCl_3 type) are examples (Figure 12). Isolated octahedra occur in $Rb_4[YbI_6]$, K_4CdCl_6 type of structure, which is the only example of that kind in rare earth halide chemistry.

With the larger lanthanides, with neodymium, samarium, and europium, a structure type was observed which may envelope many different compositions as K_2SmCl_5, KSm_2Cl_5, $K_3Nd_3Br_{10}$, and $K_8Nd_7I_{25}$.[31] The parent crystal structures are $U_3Se_5/PbU_2S_5/Y_2HfS_5/K_2PrCl_5$ and $TlPb_2Cl_5/NH_4Pb_2Cl_5$. They have unit cells of the same shape. However, the first are orthorhombic (*Pnma*) and the latter monoclinic ($P2_1/c$, with a β angle very close

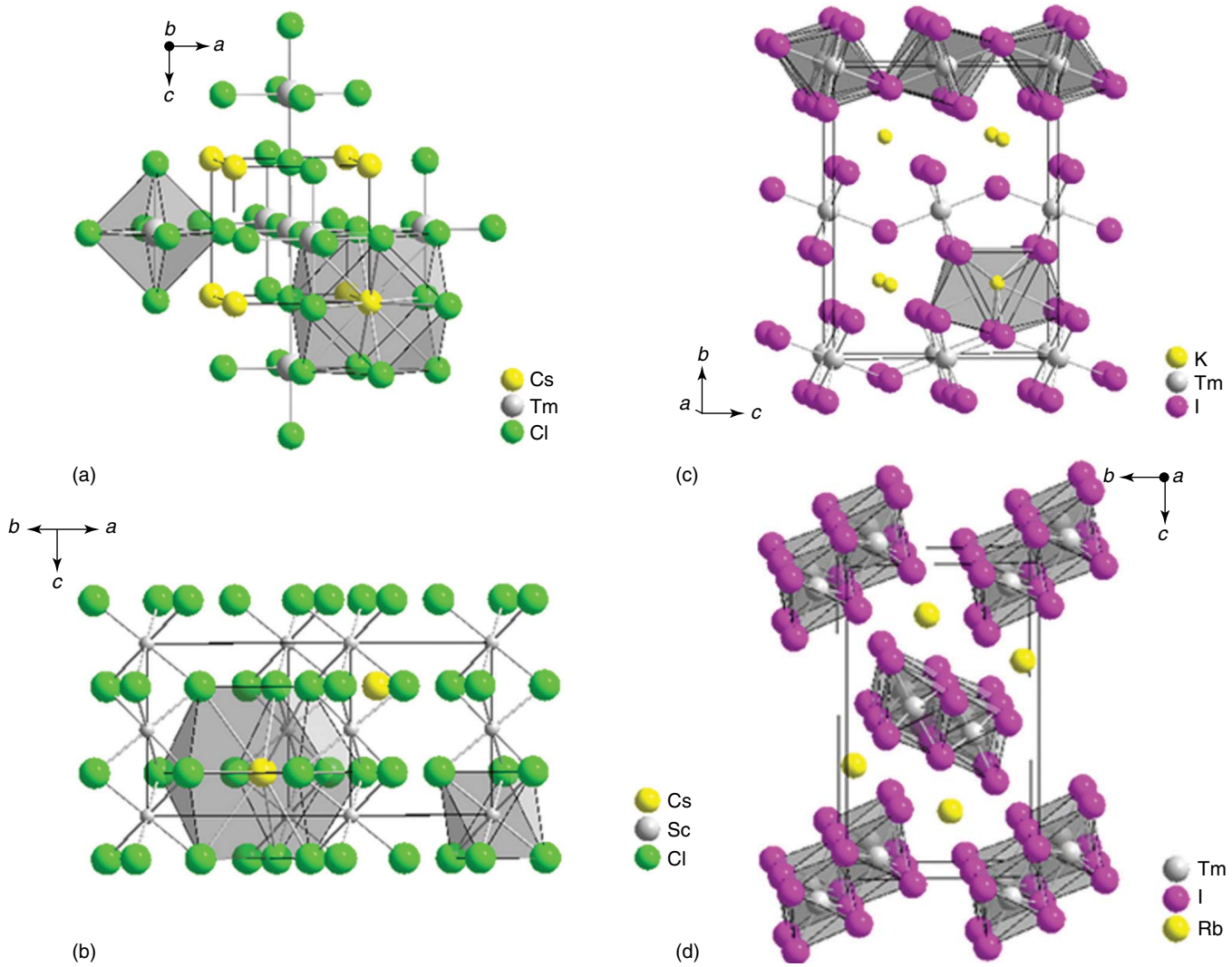


Figure 12 Crystal structures of AMX_3-type compounds. (a–d) The cubic perovskite type of structure, e.g., $CsTmCl_3$; the so-called hexagonal perovskite, e.g., $CsSc_{0.71}Cl_3$; the stuffed $PuBr_3$ or $FeUS_3$ type of structure, e.g., $KTmI_3$; the NH_4CdCl_3 type of structure, e.g., $RbTmI_3$

to 90°) by symmetry. For a general formula $ABRX_5$, the A_2RX_5 type is generated with A = B, eight- and seven-coordinate, and with B = R, the AR_2X_5 type with A and one R eight-coordinate and the other R seven-coordinate. The $RX_5 = RX_{3/1}X_{4/2}$ part of the structure is built from monocapped trigonal prisms that are edge-connected to chains (see Figure 13). For $K_8Nd_7I_{25}$, for example, a mixed-valent iodide, the formula must be understood as follows: $K_{1.6}Nd^{II}_{0.4}[Nd^{II}_{0.2}Nd^{III}_{0.8}I_5]$. Needless to say that many other compositions are possible because neodymium(II) and -(III) can afford both coordination numbers, seven and eight, in these halides.

Another interesting structure was found in the AX/RX_3 (A = K, Rb; X = Br, I) systems with dysprosium and thulium for the composition $A_5R_3X_{12}$. These

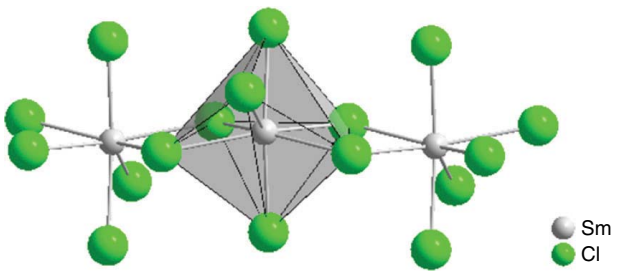


Figure 13 Part of the $RX_5 = RX_{3/1}X_{4/2}$ chain of trans edge-connected monocapped trigonal prisms as an important structural feature of the A_2RX_5/AR_2X_5 family

are mixed-valent halides, too; for example, $K_5Dy_3I_{12} = (K^+)_5(Dy^{2+})_2(Dy^{3+})(I^-)_{12}$. The anionic structure consists

of chains of edge-sharing octahedra, $Dy_3I_{12} = DyI_4 = DyI_{2/1}I_{4/2}$ (Figure 14) in which the Dy^{II}/Dy^{III} cations are statistically distributed. Antiferromagnetic coupling is observed at low temperatures.[35]

6 OXIDE HALIDES

Accidental oxide ''impurities'' or the deliberate addition of rare earths, R_2O_3, with europium, samarium, and ytterbium leads to the formation of $\{OR_4\}X_6$-type oxide halides with isolated oxide-centered R^{2+} tetrahedra (Figure 15). This structure type was first observed with the rare earth metals europium and ytterbium, as $\{OEu_4\}Cl_6$ and $\{OYb_4\}Cl_6$, and is the antitype of K_6HgS_4/Na_6ZnO_4. The oxide chlorides $\{OR_4\}Cl_6$ are now all known with Ae, R = Ca, Sr, Ba, Sm, Eu, Yb, for $\{OR_4\}Br_6$ (R = Sm, Eu) as well as for $\{OR_4\}I_6$ (Ae, R = Sr, Ba, Sm, Eu).[36] Isostructural compounds with neodymium, dysprosium, and thulium are elusive. This cannot be a size effect. If it is not an experimental disability, it must have thermodynamic reasons. Indeed, in systems where such $\{OR_4\}X_6$ compounds are usually obtained, for example, in the system $Na/EuCl_3/Eu_2O_3$, elements with higher reduction potentials form oxide chlorides such as NdOCl or even oxides such as Sc_2O_3 as single crystals under reducing conditions.[37,38]

In an attempt to prepare a large sample of $\{OEu_4\}Br_6$ and during the reduction of a mixture of EuI_2 and $\{OEu_4\}I_6$ with barium metal, two new oxide halides of europium

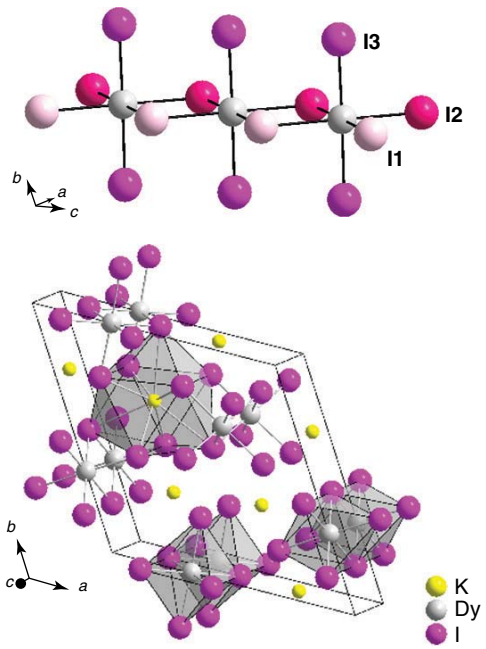


Figure 14 Crystal structure of $K_5Dy_3I_{12}$. (a) Part of the trans-edge connected $DyI_{4/2}I_{2/1}$ chains; (b) a projection down the chains

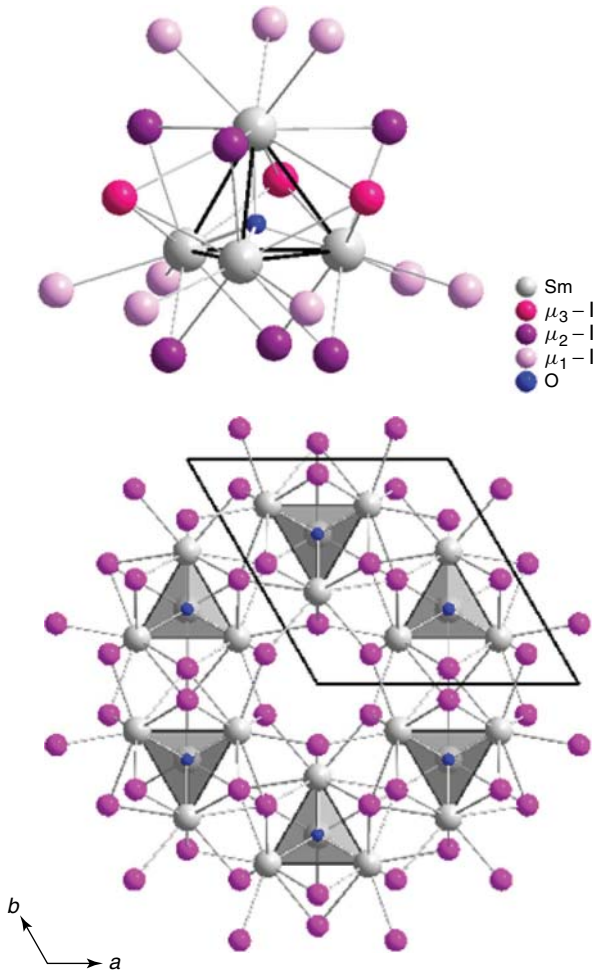


Figure 15 Crystal structure of $\{OSm_4\}I_6$ as an example of $\{OR_4\}X_6$-type oxide halides

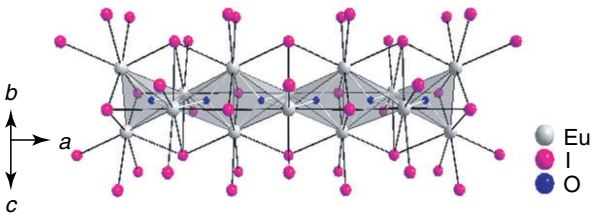


Figure 16 A chain of trans-edge-connected $\{OEu_{4/2}\}$ chains in the crystal structure of Eu_2OI_2

were obtained, the mixed-valent $Eu_2O_2Br = (Eu^{2+})(Eu^{3+})(O^{2-})_2(Br^-)$ and the Eu(II) oxide iodide Eu_2OI_2.[39,40] In both $\{OEu_4\}$ tetrahedra occur. They are edge-connected, just as in SiS_2, in $Eu_2OI_2 = \{OEu_{4/2}\}I_2$, surrounded by and connected through iodide anions (Figure 16). In Eu_2O_2Br, the $\{OEu_4\}$ tetrahedra are connected to two kinds of chains that combine to corrugated layers $[O_2Eu_2]^+$ and sheath likewise corrugated

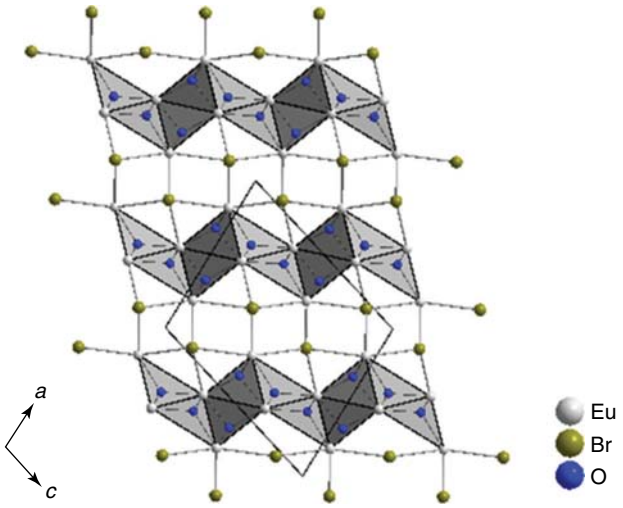


Figure 17 Corrugated layers built from two types of edge-connected chains $\{OEu_{4/4}\}$ in the crystal structure of Eu_2O_2Br

layers of Br^- ions (Figure 17). The Eu^{2+} and Eu^{3+} cations can be clearly distinguished in the crystal structure of Eu_2O_2Br, likewise in the isostructural Sm_2O_2I.[41]

7 GLOSSARY

Band structure: *k*-space-dependent energy level diagram for an extended solid, similar to the molecular orbital diagram at the gamma point

Binary halides: Compounds of two elements, one typically a metal and the other a halogen

Cathodic reduction: Electrochemical reduction at the cathode

Configuration crossover: Transition from one electronic configuration to another

Comproportionation: Compounds with higher and lower oxidation states of one element react to a compound with an oxidation state in between

Coordination number (CN): The number of atoms surrounding a central (metal) atom in a coordination complex

Cluster: According to Cotton, ''a group of two or more metal atoms in which there are substantial and direct bonds between the metal atoms'', put in waved brackets {. . .} in this chapter

Cluster complex: A cluster surrounded by ligands, $\{R_x\}X_z$

Crystal orbital Hamiltonian population (COHP): From the density of states of band structure calculations, showing the degree of bonding and antibonding interactions between atom types in a solid

Density of states (DOS): Number of states per interval of energy at each energy level that are available to be occupied by electrons in a solid

Electronic configuration: Energy levels in the shell of an atom which are occupied with electrons; symbolized by quantum numbers

Endohedral atom: Atom *Z* in the center of a cluster, $\{ZR_x\}X_z$

Extended structures: Crystal structures with polyhedra connected to a one-, two-, or three-dimensional arrangement

Fermi level: Highest occupied energy level in a solid

Incongruent melting: A compound decomposes at an elevated temperature yielding at least one liquid phase

Lanthanides: The elements La, Ce–Lu

Metallothermic reduction: Reduction of a metal oxide or halide with a highly reductive metal

Mixed valence halide: A metal halide in which the metal atoms are in two different oxidation states (class I: the oxidation states can be clearly distinguished)

Nucleation: Process of forming a crystal nucleus

Oxidation state (. . . number): According to Pauling (1949), the ''number which represents the electrical charge which an atom would have if the electrons in a compound were assigned to the atoms''

Peierls distortion: Distortion that occurs to break the symmetry in order to avoid a degeneracy of states at the Fermi level, similar to the Jahn–Teller distortion in molecular compounds

rare earth elements (metals): The elements Sc, Y, La, and the lanthanoids Ce through Lu

Rare earths: Oxides of the rare earth elements, in most cases of the composition R_2O_3

Ternary halides: Compounds of three elements, of which two are metals and the third a halogen

Valence: According to Pauling (1949) ''the number of other atoms with which an atom of a certain element can combine''

Valence electron(s): Electron(s) constituting the valence shell beyond the core (usually a noble gas configuration)

8 ABBREVIATIONS AND ACRONYMS

[. . .] = square brackets indicate a Werner-type complex; {. . .} = waved brackets indicate a cluster; A = alkali metal atom; Ae = alkaline-earth metal atom; [Ar] = electronic configuration of an argon atom; °C = degrees Celsius; temperature scale after Celsius; CN = coordination number; COHP = crystal orbital Hamiltonian population; d = distance (between the nuclei of two atoms); DOS = density of states; $E°$ = standard electrode potential (in V); $\Delta H°(3)$ = third ionization potential (in $kJ\,mol^{-1}$); HP = high pressure; I_3 = third ionization potential (in eV or $kJ\,mol^{-1}$); K = Kelvin; absolute temperature scale; pm = picometer, 10^{-12} m; R = rare-earth and lanthanide element (Sc, Y, La, Ce–Lu); ST = structure type; X = halogen atom, X^- halide ion; [Xe] = electronic configuration of a xenon atom; V = Volt; unit of voltage.

9 REFERENCES

1. C. Matignon and E. C. Cazes, *Ann. Chim. Phys.*, 1906, **8**, 417.
2. W. Klemm, *Z. Anorg. Allg. Chem.*, 1929, **184**, 345.
3. W. Klemm and W. Schüth, *Z. Anorg. Allg. Chem.*, 1929, **184**, 352.
4. G. Jantsch and W. Klemm, *Z. Anorg. Allg. Chem.*, 1933, **216**, 80.
5. W. Klemm and H. Bommer, *Z. Anorg. Allg. Chem.*, 1937, **231**, 138.
6. G. Meyer, *Chem. Rev.*, 1988, **88**, 93.
7. G. Meyer, *Z. Anorg. Allg. Chem.*, 2007, **633**, 2537.
8. J. D. Corbett, *Rev. Chim. Miner.*, 1973, **10**, 239.
9. J. D. Corbett, L. F. Druding, W. J. Burkhard, and C. B. Lindahl, *Discuss. Faraday Soc.*, 1961, **32**, 79.
10. L. F. Druding and J. D. Corbett, *J. Am. Chem. Soc.*, 1961, **83**, 2462.
11. G. Meyer and A. Palasyuk, in 'Inorganic Chemistry in Focus', eds. G. Meyer, D. Naumann, and L. Wesemann, WILEY-VCH, Weinheim, 2006, Vol. 3, p. 45.
12. C. Felser, K. Ahn, R. K. Kremer, R. Seshadri, and A. Simon, *J. Solid State Chem.*, 1999, **147**, 19.
13. B. C. McCollum, D. J. Dudis, A. Lachgar, and J. D. Corbett, *Inorg. Chem.*, 1990, **29**, 2030.
14. G. Meyer, L. Jongen, A.-V. Mudring, and A. Möller, in 'Inorganic Chemistry in Focus', eds. G. Meyer, D. Naumann, and L. Wesemann, WILEY-VCH, Weinheim, 2005, Vol. 2, p. 105.
15. J. D. Corbett, *Inorg. Synth.*, 1983, **22**, 15.
16. J. D. Corbett, in 'Synthesis of Lanthanide and Actinide Compounds', eds. G. Meyer and L. R. Morss, Kluwer Acad. Publ., Dordrecht, 1991, p. 159.
17. G. Meyer and T. Schleid, in 'Synthesis of Lanthanide and Actinide Compounds', eds. G. Meyer and L. R. Morss, Kluwer Acad. Publ., Dordrecht, 1991, p. 175.
18. J. D. Corbett, *Inorg. Synth.*, 1983, **22**, 31.
19. W. Klemm, *Z. Anorg. Chem.*, 1929, 1930, **184, 187**, 345, 29.
20. G. Meyer, T. Schleid, and K. Krämer, *J. Less-Common Met.*, 1989, **149**, 67.
21. J. D. Mee and J. D. Corbett, *Inorg. Chem.*, 1965, **4**, 88.
22. D. A. Lokken and J. D. Corbett, *Inorg. Chem.*, 1973, **12**, 556.
23. K. Krämer, G. Meyer, P. Fischer, A. Hewat, and H.-U. Güdel, *J. Solid State Chem.*, 1991, **95**, 1.
24. G. Meyer, *Prog. Solid State Chem.*, 1982, **14**, 141.
25. D. A. Johnson, 'Some Thermodynamik Aspects of Inorganic Chemistry', 2nd edition, Cambridge University Press, 1982.
26. L. R. Morss, *Chem. Rev.*, 1976, **76**, 827.
27. D. A. Johnson, in 'Inorganic Chemistry in Focus', eds. G. Meyer, D. Naumann, and L. Wesemann, WILEY-VCH, Weinheim, 2006, Vol. 3, p. 1.
28. H. P. Beck, *Z. Naturforsch.*, 1976, **31b**, 1548.
29. K. W. Krämer, H. U. Güdel, P. Fischer, and L. Keller, *Appl. Phys.*, 2002, **A 74**, S595.
30. N. Gerlitzki, G. Meyer, A.-V. Mudring, and J. D. Corbett, *J. Alloys Comp.*, 2004, **380**, 211.
31. G. Meyer and M. S. Wickleder, in 'Handbook on the Physics and Chemistry of Rare Earths', eds. K. A. Gschneidner Jr. and L. Eyring, North Holland, Amsterdam, 2000, Vol. 28, p. 53.
32. N. Gerlitzki, S. Hammerich, and G. Meyer, *Z. Anorg. Allg. Chem.*, 2004, **630**, 2431.
33. N. Gerlitzki, A.-V. Mudring, and G. Meyer, *Z. Anorg. Allg. Chem.*, 2005, **631**, 381.
34. G. Schilling and G. Meyer, *Z. Anorg. Allg. Chem.*, 1996, **622**, 759.
35. G. Schilling, M. Böcker, A. Möller, and G. Meyer, *Z. Anorg. Allg. Chem.*, 2001, **627**, 1309.
36. S. Hammerich, I. Pantenburg, and G. Meyer, *Z. Anorg. Allg. Chem.*, 2006, **632**, 2181.
37. G. Meyer and T. Schleid, *Z. Anorg. Allg. Chem.*, 1986, **533**, 181.
38. T. Schleid and G. Meyer, *J. Less-Common Met.*, 1989, **149**, 73.
39. S. Hammerich and G. Meyer, *Z. Anorg. Allg. Chem.*, 2006, **632**, 1244.
40. S. Hammerich, I. Pantenburg, and G. Meyer, *Z. Anorg. Allg. Chem.*, 2006, **632**, 1487.
41. M. Ryazanov, C. Hoch, H. Mattausch, and A. Simon, *Z. Anorg. Allg. Chem.*, 2006, **632**, 2385.

Lanthanide Halides

Timothy J. Boyle and Leigh Anna M. Steele

Sandia National Laboratories, Albuquerque, NM, USA

1	Summary	175
2	Introduction	175
3	Hydrates	176
4	Anhydrides	177
5	Alcohols	178
6	Other Solvates	179
7	Conclusion	181
8	Glossary	181
9	Related Articles	181
10	Abbreviations and Acronyms	181
11	References	181

1 SUMMARY

The lanthanide halide compounds represent one of the key precursors that are used to develop the chemistry of lanthanide cations. There are numerous researchers who have contributed to characterizing and understanding these amazing precursors, including the founding father of lanthanide chemistry F. H. Spedding, as well as G. Deacon, M. G. B. Drew, K. Izod, and J. C. Gordon, to mention just a few. Their efforts and many others have led to the development and structural understanding of these extremely important lanthanide halides. This chapter covers some of the synthesis and structural properties of lanthanide halides and solvates reported in the literature. This is not meant to be a comprehensive review but a description of some of the structural properties reported for this unusual family of compounds.

2 INTRODUCTION

Lanthanide halide (LnX_n where X = F, Cl, Br, I) precursors are some of the most important and versatile compounds available for anyone interested in using lanthanide cations. Researchers have found use for this family of compounds in an extensive range of applications, such as for catalyst in organic transformation processes (see ***Tetravalent Chemistry: Inorganic***), biomedical applications for the determination of cellular activity, contrast agents for magnetic resonance imaging (MRI) studies (see ***Lanthanide Shift Reagents***), nuclear magnetic resonance (NMR) shift reagents (see ***Lanthanide Shift Reagents***), scintillators for detection of nuclear materials, pyroreprocessing of spent nuclear fuel, and many other efforts. The increased utility of Ln cations is driven by the diverse metathesis chemistry of LnX_3 that has made a wide range of important organometallic and metalloraganic precursors. All of the LnX_3 derivatives (i.e., F, Cl, Br, and I) are commercially available; however, the promethium (Pm) adducts are notably absent from all discussions because of its radioactive nature and omitted from all discussion below for the lack of available research on this element.

In order to fully understand the crystal chemistry of the anhydrous LnX_3 and their solvates ($[LnX_3(solv)_n]$), the Ln atomic properties of these species must be considered. The predominant oxidation state for LnX_n species is the +3 state; however, for a number of these cations, the +2 (see ***The Divalent State in Solid Rare Earth Metal Halides***) and +4 (see ***Tetravalent Chemistry: Inorganic***) states are available. Since the bonding in these compounds is mainly ionic, the cation size and sterics of the binding solvent play a significant role in determining the final crystal structures isolated. The ionic nature of the LnX_n complexes makes

The Rare Earth Elements. Edited by David A. Atwood. © 2012 John Wiley & Sons, Ltd. ISBN 978-1-119-95097-4

Fourier transform infrared spectroscopy (FTIR) data less useful for identifying the structural properties. Further, owing to the paramagnetic nature of the majority of cations in the family, NMR data is also not typically of use for characterizing these compounds. The limited number of analytical handles for these compounds results in single crystal[1] and powder X-ray diffraction (XRD) being the tools of choice to characterize these useful precursors. Therefore, the following sections focus on the specific structural aspects of LnX_3 species reported; however, for more details, several reviews are available.[2–6]

3 HYDRATES

Hydrates are probably the most widely used LnX_3 precursors (albeit most researchers remove the water prior to use). The production of the anhydrous LnX_3 species has been approached from a wide variety of synthetic pathways, but typically, the hydrate species have been isolated. In fact, at one time, it was feared that there would be no reasonable route to anhydrous LnX_3 materials (the only known route at the time to generate Ln(0) employed LnX_3) and thus it was claimed that Ln would only be a laboratory curiosity; obviously, this proved unfounded. However, the hydrates have demonstrated novel properties that make this family of compounds unique. Two of the more common routes that are employed to generate these materials are the reaction of a halide acid with lanthanide oxide (Ln_2O_3) (equation 1) or metal (equation 2). Other halogen-containing reagents such as ammonium halides or carbon tetrachloride have also been successfully employed to generate the halide derivatives.

$$Ln_2O_3 + HX_{(aq)} \rightarrow 2[LnX_3(H_2O)_n] + H_2O \quad (1)$$

$$Ln^0 + HX_{(aq)} \rightarrow [LnX_3(H_2O)_n] + H_2 \quad (2)$$

Little information pertaining to structural aspects of the $LnX_3(H_2O)_n$ compounds was available until the early 2000s.[7–11] By the late 2000s, the entire $[LnCl_3(H_2O)_n]$ (X = Cl, Br, I) series was structurally identified from the dissolution of the metal in the specific halide acids in water.[12] Table 1

Table 1 Structural arrangements for (i) $[LnCl_3(H_2O)_n]$ and (ii) $[LnCl_3(MeOH)_n]$

(i)	Chloride				Bromide				Iodide			
H_2O	Solv	IS	OS	Nu	Solv	IS	OS	Nu	Solv	IS	OS	Nu
La	7	2(μ)	4	2	7	2(μ)	4	2	9	0	3	1
Ce	7	2(μ)	4	2	7	2(μ)	4	2	9	0	3	1
Pr	7	2(μ)	4	2	7	2(μ)	4	2	9	0	3	1
Nd	6	2	1	1	6	2	1	1	9	0	3	1
Sm	6	2	1	1	6	2	1	1	9	0	3	1
Eu	6	2	1	1	6	2	1	1	9	0	3	1
Gd	6	2	1	1	6	2	1	1	9	0	3	1
Tb	6	2	1	1	6	2	1	1	9	0	3	1
Dy	6	2	1	1	6	2	1	1	9	0	3	1
Ho	6	2	1	1	8	0	3	1	9	0	3	1
Er	6	2	1	1	8	0	3	1	9	0	3	1
Tm	6	2	1	1	8	0	3	1	8	0	3	1
Yb	6	2	1	1	8	0	3	1	8	0	3	1
Lu	6	2	1	1	8	0	3	1	8	0	3	1
(ii)	**Chloride**				**Bromide**				**Iodide**			
MeOH	**Solv**	**IS**	**OS**	**Nu**	**Solv**	**IS**	**OS**	**Nu**	**Solv**	**IS**	**OS**	**Nu**
La	4	3	0	2	5	3	0	1	9	0	3	1
Ce	4	3	0	2	5	3	0	1	9	0	3	1
Pr	4	3	0	2	5	3	0	1	—	—	—	—
Nd	4	3	0	2	5	3	0	1	9	0	3	1
Sm	4	3	0	2	—	—	—	—	8	0	3	1
Eu	4	3	0	2	—	—	—	—	2	2	0	∞
Gd	4	3	0	2	5	2	1	1	—	—	—	—
Tb	4	3	0	1	5	2	1	1	—	—	—	—
Dy	4	3	0	1	5	2	1	1	8	0	3	1
Ho	4	3	0	1	5	2	1	1	—	—	—	—
Er	4	3	0	1	5	2	1	1	—	—	—	—
Tm	—	—	—	—	5	2	1	1	8	0	3	1
Yb	—	—	—	—	5	2	1	1	—	—	—	—
Lu	—	—	—	—	5	2	1	1	—	—	—	—

(i) H_2O color key: Green (1IS/2OS-dimer) $[Ln(\mu\text{-}X)(H_2O)_7]_2(X)_4$; brown (2IS/1OS) $[LnX_2(H_2O)_6](X)$; Blue (3OS) $[Ln(H_2O)_n](X)_3$.

(ii) MeOH color key: Red (3IS-dimer) $[(MeOH)_n(X)_2Ln(\mu\text{-}X)]_2$, (3IS) $[Ln(X)_3(MeOH)_x]_n$; brown (2IS/1OS) $[LnX_2(MeOH)_6](X)$; blue = (3OS) $[Ln(MeOH)_n](X)_3$; purple for $[(MeOH)_2Eu(\mu\text{-}I)_2]_n$.

Different shades indicate slight structural variations.
Ln, lanthanide; Solv, number of solvent molecules bound per metal; IS, innersphere; OS, outersphere; Nu, nuclearity; "—" no structure.

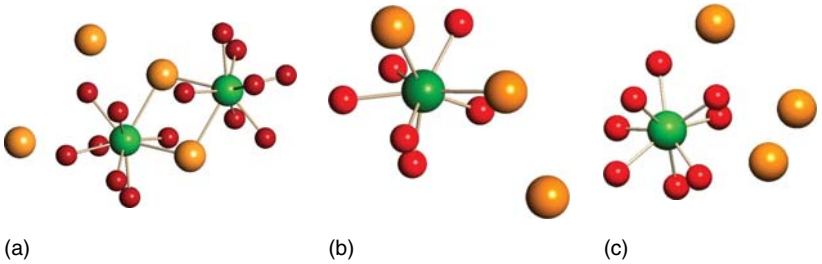


Figure 1 Schematic structure plots of hydrate species (a) $[\{(H_2O)_7Ln(\mu-X)\}_2]_2[X]$ referred to as *1IS/2OS-dimer* shown in $[Ce(\mu\text{-}Br)(H_2O)_6]_22[Br]$, (b) $[(H_2O)_8Ln(X)_2][X]$ termed *2IS/1OS* as observed for $[GdBr_2(H_2O)_6][Br]$, and (c) $[Ln(H_2O)_n]3[X]$ called *3OS* adopted by $[Yb(H_2O)_8]_3[Br]$. (Obtained from Cambridge Structural Database. Obtained from Ref. 12)

lists the structurally characterized $[LnX_3(H_2O)_n]$ species arranged by cation (i). Combined, these reports illustrate the different structures available to the $[LnX_3(H_2O)n]$ family of compounds; however, information concerning the structures of the fluorides is limited to the crystal structure of $[LnF_3(H_2O)_{1/2}]$, which is highly insoluble in water.[6] The wide range of structure types noted for the other hydrates are shown in Figure 1 (Ln in green, O from water in red, and halide in orange throughout the chapter unless otherwise stated) and involve halide atoms directly bound to the metal (referred to as *innersphere* (IS)) and halide anions not bound to the metal but in close proximity (referred to as *outersphere* (OS)). The three structure types shown in Figure 1 are abbreviated, based on the number of IS and OS halide ligands and are referred to as (a) *1IS/2OS dimer*, (b) *2IS/1OS*, and (c) *3OS*.

$[LnCl_3(H_2O)_n]$ family of compounds was found to adopt two general structure types. The first was identified as the *1IS/2OS dimer* (Figure 1a), which was solved for the Ln cations ranging from La to Pr. This structure consists of two IS bridging chloride (μ-Cl) atoms that connect the Ln cations. The two remaining anions are located in the OS of the Ln cation. The metals finish their coordination sphere by binding various numbers of water molecules. Structural ''cross-over'' points were clearly established for the $[LnCl_3(H_2O)_n]$ species to occur from Pr to Nd. The structure from Nd to Lu was shown to adopt a monomeric structure with two IS and one OS Cl atoms (or *2IS/1OS*), as shown in Figure 1b. The degree of hydration varies on the basis of the size of the cation. Switching to the bromide anion, the same two structure types were noted for the early lanthanide cations: the 1IS/2OS dimer was observed through the Pr cation followed by the 2IS/1OS structure, which was isolated up to the Dy cation. After this, a different structure type was adopted, where all of the Br anions were located in the OS with the cation being coordinated *only* by water. This was termed the *3OS* and is shown in Figure 1c. The iodide derivatives, independent of the Ln cation, were all found to adopt a 3OS arrangement with the degree of solvation changing on the basis of the decreased cation size. As can be determined, the size of the Ln^0 and the X atoms directs the final structure, with water filling in open coordination sites.

4 ANHYDRIDES

Attempts to generate the anhydrous LnX_3 species have dominated research efforts for decades since they are widely used to generate Ln metals. Typically, it is reported that heating of the hydrates to drive off the water will result in oxide formation through the preferential elimination of HX. The most common method to circumvent this problem is to heat $[LnCl_3(H_2O)_n]$ in the presence of NH_4Cl under a vacuum. Removal of the residual NH_4Cl is easily achieved through sublimation. Generating HX species *in situ* from the reaction of the desired precursor such as Ln_2O_3 or $Ln_2(CO_3)_3$ in the presence of thionyl chloride or halosilanes have also been demonstrated. In contrast to earlier reports, it has been shown that $[LnCl_3(H_2O)_n]$, under vacuum with careful heating can also yield anhydrous material.[12] Once isolated, however, the LnX_3 compounds are extremely deliquescent and require careful handling under inert atmospheres.

$$[LnCl_3(H_2O)_n] + HX_{(g)} \longrightarrow LnX_3 \qquad (3)$$

The structures of the anhydrous LnX_3 have been characterized by powder XRD phase identification.[6,13] Figure 2 shows the $(2 \times 2 \times 2)$ unit cell observed for the various LnX_3 anhydrous species. Dimorphism (or two different atomic arrangements) based on cation size is reported for the LnF_3 series, with the preferred phases identified as either tysonite (YF_3: Ln = La to Nd) or β-YF_3 (Ln = Sm to Lu). Tysonite is an 11-coordinated fully capped distorted trigonal prismatic coordination of the Y by F atoms, whereas, the β-phase of YF_3 is a nine-coordinated tricapped trigonal prismatic coordinated Y metal center. The size of the cation dictates the degree of coordinated F atoms. For the chlorides, the UCl_3 structure is noted for La through Gd, while Tb adopts the $PuBr_3$ structure, and the rest form the $AlCl_3$ (or YCl_3) phase. Again, cation size controls the coordination numbers achieved by the lanthanide cation. For the UCl_3 structure, the central cation adopts a tricapped trigonal prismatic arrangement using nine equidistant Cl atoms. As the Ln series is transversed, the PBr_3 structures are reported for the $TbCl_3$ species, which forms an eight-coordinated bicapped trigonal

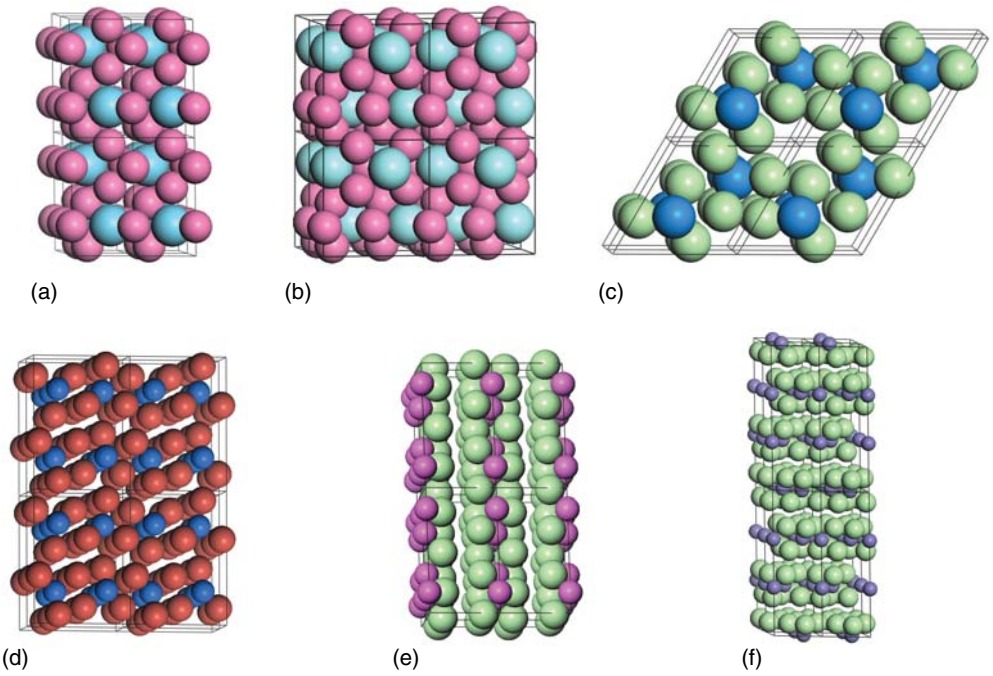


Figure 2 $2 \times 2 \times 2$ unit cell drawing of (a) tysonite, (b) β-YF_3, (c) UCl_3, (d) $PuBr_3$, (e) $AlCl_3$, and (f) $FeCl_3$. Y atoms are shown as blue spheres, F is pink, U is blue, Cl is green, Pu is blue, Br is brown, Al is pink, and Fe is dark blue. (Pictures courtesy of R. Cygan (Sandia National Laboratories))

prismatic structure. The remaining Cl derivatives adopt the $AlCl_3$ or YCl_3 structure with each cation surrounded by an octahedron of Cl atoms. For the bromides, three structure types have been identified: UCl_3 (La to Pr), $PuBr_3$ (Nd to Eu), and the $FeCl_3$ (Gd to Lu). The UCl_3 and $PuBr_3$ phases have been described (vide infra). Some reports indicate that the $PuBr_3$ structure is retained upto Lu, while others state that the $FeCl_3$ structure is predominant. The $FeCl_3$ phase is a simple octahedral arrangement of the Br atoms around the metal center. The early iodides (La to Pm) have been isolated in the $PuBr_3$ structure with the remainder crystallizing in the $FeCl_3$ phase.

Lower (LnX_2, see ***The Divalent State in Solid Rare Earth Metal Halides***) and higher (LnX_4) oxidation states are available for a number of lanthanide halides. For the +4 species, the anion is typically the fluoride and they are mainly synthesized by the fluorination of the metal or LnF_3. Of particular interest for organic transformations are the +2 derivatives, which can be generated from several routes: thermal decomposition, iodination of metals from organic species, or comproportionation of the metal with the +3. Of these, SmI_2 has found particular use as a catalyst in organic chemical processes. While structures of these species may be limited, complexometric titration techniques have been of use to verify the composition of the bulk materials.

5 ALCOHOLS

The next largest set of structurally characterized $[LnX_3(solv)_n]$ species are the alcohol-coordinated compounds. These species are typically generated by the crystallization of the anhydride materials out of an alcohol (ROH) solvent (see ***Lanthanides: Coordination Chemistry***).[7,12] Or, more often than not, these have been the result of an accidental crystallization of a by-product.

The methanol (MeOH) derivatives have found a great deal of attention since LnX_3 precursors are readily soluble in this alcohol and the Ce adduct has demonstrated use as a molecular scintillator material. The structure types noted for these compounds were similar to those observed for the hydrates and are shown in Figure 3 and in (ii) Table 1. Again, no fluoride structures are reported. For the chlorides, a *3IS dimer* (Figure 3a) was observed for the La through Gd cations. This species is an edge-shared complex with μ-Cl, two terminal Cl atoms, and four -coordinated MeOH solvent molecules filling in the remainder of the Ln cation's coordination sphere. After this, a *3IS* monomeric species (Figure 3b) forms with various MeOH degrees of solvation and appears to extend to the end of the Ln series; however, the final three (Tm, Yb, and Lu) structures were not isolated. Switching to the Br derivative, only monomeric species were isolated. Up to the Nd metal, the MeOH derivatives were identified as *3IS* species, which then converted to a *3OS* (Figure 3c)

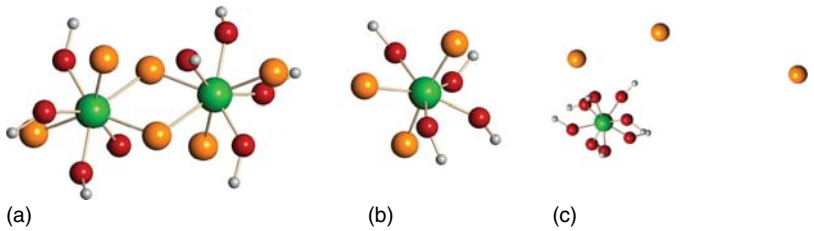


Figure 3 Structure types for MeOH: (a) 3IS dimer shown in $[Sm(\mu\text{-}Cl)(Cl)_2(MeOH)_4]_2$, (b) 3IS as found in $[DyCl_3(MeOH)_4]$, and (c) 3OS as noted for $[Tm(MeOH)_8 3[I]]$. (Obtained from Cambridge Structural Database. Obtained from Ref. 12)

monomer; however, the structure cross-over point was not established since the Sm and Eu derivatives were not isolated. Of the sporadic iodide derivatives, only the *3OS* complexes were observed with variations in the number of bound solvent species. Comparison of the MeOH derivatives to the H_2O species reveals different structures for the same Ln cations. In addition to the anion and the cation size controlling the final structure, the size of the coordinating solvent appears to play a role as well. So, tuning the structure for the desired ligand set should be achievable on the basis of the solvents employed.

6 OTHER SOLVATES

With this in mind, it is of interest to understand how other solvents affect the final LnX_3 structure. Few structurally characterized $[LnX_3(solv)_n]$ species of the complete lanthanide series are available or have been reported.[7] A comprehensive review of complex $[LnX_3(solv)_n]$ with neutral oxygen and nitrogen donor ligands has been reported that covers complex Lewis basic ligands (i.e., lactones, gyms, polyethylene glycols, crown ethers, pyridine and pyridine-based polydentate ligands, and mixed O-, N-donor ligands).[4] Below, the more simple solvents are discussed.

Single crystal X-ray structural characterization is again the predominate methodology to identify these $[LnX_3(solv)_n]$ species. From this family of compounds, a number of different structure types have been identified. For the chlorides, there are more than 160 solvated compounds that contain three Cl for each Ln. For the more than 50 monodentate solvated $LnCl_3$ species, the majority adopt either six- or seven-coordination geometries. Of the few eight-coordinated $[LnX_3(solv)_n]$ species reported, two of these compounds possess six μ-Cl along with one tetrahydrofuran (THF) and one H_2O solvent, forming polymeric structures. Four additional noncharged species were isolated as dinuclear species adopting the general 3IS dimer structure $[(solv)_n(Cl)Ln(\mu\text{-}Cl)]$. In addition, several salts have also been isolated. An analysis of the $LnBr_3$ system reveals that only 20 compounds have been reported but only one of these is a dinuclear species, $[Br_2(DME)_2La(\mu\text{-}Br)]$ (DME), and no polymeric compounds have been observed. As noted for the Cl derivatives, a number of *salt* derivatives with all IS anions have been characterized. The LnI_3 system has more than 80 structures available in the literature[7] which include (i) monomeric 3IS LnI_3 species that utilize combinations of bulky neutral ligands, solvent, or both to fill the coordination sphere; (ii) 2IS/1OS $[LnI_2][I]$ that utilize bulky ligands, solvents such as $HOPr^i$, THF, py, other complex solvents, or mixture of solvents; (iii) *salts*; and (iv) *polymers*. The following section discusses the solvated structure types noted from above. While the structure of these compounds are varied, there are a few general structure types that they can be grouped in *(i) dimers, (ii) monomers, (iii) salts,* and *(iv) polymers*.[1] Representative molecules for each of these species are shown in Figure 4 and discussed in the following sections.

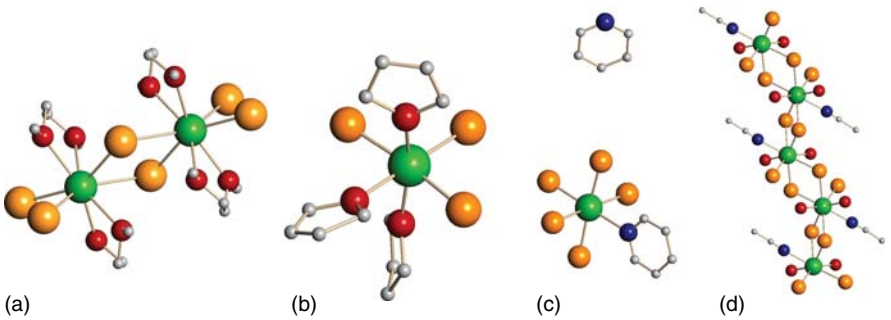


Figure 4 Representative structures observed as (a) 3IS dimer observed for $[La(\mu\text{-}Br)(Br)_2(DME)_2]$, (b) 3IS monomer as reported for $[LuCl_3(THF)_3]$, (c) salts noted for $[EuCl_3Cl(Py)\cdot H^+$ py], and (d) polymers as shown for $[Gd(CH_3CN)(H_2O)(\mu\text{-}Cl)_2Cl]_\infty$. (Obtained from Cambridge Structural Database. Obtained from Ref. 7)

6.1 Monomers

For this set of compounds, there are three general substructure types observed, which is determined by the number of bound solvents. The number of solvents vary for such solvents as THF, *iso*-propanol ($HOPr^i$), acetonitrile (CH_3CN), pyridine (py), and dimethoxyethane (DME). Some examples of these systems are as follows:

1. The three-solvent coordinated species forming a $[LnX_3(solv)_3]$ (where Ln = Lu, Yb; X = Cl, I; solv = THF). All of these compounds adopt an octahedral (Oh) coordination geometry.
2. The four-solvent coordinate system adopting $[LnX_3(THF)_4]$ when X = Cl, then Ln = Nd, Gd, Eu, Sm; when X = Br, then Ln = La, Ce, Pr, Sm; and when X = I, then Ln = La, Ce, Pr, Nd. As can be noted, the higher coordination is typically observed for the larger cations, such as when $[LnX_3(HOPr^i)_4]$ forms using X = Br and Ln = Sm or when X = I, then Ln = La or Ce. However, when stronger Lewis bases are employed, smaller cations can adopt this structures as observed for $[LnX_3(py)_4]$ when X = Cl and Ln = La, Eu, Er, Yb. Other bidentate solvents also are included in this section since they fill four coordination sites, such as in the $[LnX_3(DME)_4]$ system when X = Cl and Ln = Nd, Sm, Eu, Gd, Er, Yb or when X = Br, then Ln = Pr, Nd, Sm, Eu, Yb. As can be garnered, the smaller cations can easily accommodate the seven-coordinated species because of the chelation effect of the solvent.
3. A slight variation of the four-coordinated species is one cation with two different solvents $[LnX_3(solv)_2(solv')_2]$ such as is noted for the $[ErCl_3(CH_3CN)_2(H_2O)_2]$ or $[NdBr_3(THF)_2(HOPr^i)_2]$. One system that has generated large families of mixed solvated compounds includes the $[LnX_3(MeOH)_n(H_2O)_m]$ where two structure types were isolated for these coordination compounds:
   (a) $[(solv)_n(X)_2Ln(\mu\text{-}X)]_2$ or 3IS-dimer
   (b) $[(solv)_nLn]3[X]$ (or 3OS), solv = H_2O:MeOH).

More regular stoichiometries were noted for $[LnX_3(solv)_2(solv')_2]$ systems such as $[ErCl_3(CH_3CN)_2(H_2O)_2]$ or $[NdCBr_3(THF)_2(HOPr^i)_2]$. Of course mixed solvents systems that employ bidentate solvents exist as well such as for the $[LnCl_3(THF)_2(DME)_2]$ identified for Ln = Sm, Tb, Ho, Tm, Lu.

6.2 Dimers

The family of dimeric-substituted LnX_3 species also have been found to utilize a wide range of coordinating solvents around the general core constructs of $[X_2Ln(\mu\text{-}X)]_2$. For the Lewis base THF, only two solvents per metal center are reported for $[(THF)_2Cl_2Yb(\mu\text{-}Cl)]_2$. Interestingly, the larger $HOPr^i$ allows for three solvents coordinating per metal for the chloride derivatives of Ln = La, Nd, Ce. Not surprising is the increased coordination for 1-methyl imidazole (MeIm) derivatives for the iodides of Ln = Sm and Eu due to its increase Lewis basicity in comparison to the other solvents. Retention of the dinuclear structure indicates the stability of this arrangement since MeIm typically yields monomeric species. It is not unreasonable to observe even higher coordination numbers for the sterically smaller but strong Lewis base for the pyridine derivative of $[(py)_4Cl_2La(\mu\text{-}Cl)]_2$. Also, the tetrasubstituted HOEt derivative has been reported and is most likely due to the smaller size of the alcohol. The bidentate species fill the same number of coordination sites and are included here as well for the DME chloride derivatives of Ln = La, Ce, Nd, Pr and the DME bromide derivatives of Ln = La, Sm.

6.3 Salts

Interestingly, some of the species isolated have formed salt (or charge-separated species located in the same crystal structure) generated by solvent charging or halide ligand exchange. Of the former, most are isolated in the presence of pyridine. For example, in some of the structures, a bis-pyridinium cation is formed, yielding $[LnX_5(py)]_2[pyH]$ for Ln = Eu, Er, Yb. In other instances, two py bind to the Ln as noted for $[YbCl_4(py)_2][pyH]$. Other salts result from segregation of the halide ligands and are mainly observed for the THF species. The general structure reported is $[(THF)_5LnX_2][(THF)_2LnX_4]$ where the chlorides have been identified for Ln = Gd, Dy, Er, Eu, Tb; the bromides for Eu; and the iodides for Sm. Another chloride salt species adopts the general structure type $[CH_3CN)_5YbCl_2][(CH_3CN)Yb(\mu\text{-}Cl)(Cl)_3]_2$. Obviously, the shigher the halide coordination, the lower the solvation coordination.

6.4 Polymers

Only three structure types were available for the polymeric arrangements that employed coordinated solvents. Interestingly, these were all for the chloride species. For one of the polymers, the central seven-coordinated cation has two solvent molecules and one terminal Cl anion and four bridging (μ-Cl) atoms. The μ-Cl links to the neighboring lanthanide atoms and forms a continuous chain. This occurs for the THF adducts of Ln = Ce, Pr, Nd. In contrast, the THF derivative of $LaCl_3$ as well as the mixed solvent species THF/H_2O derivatives of Ln = La, Ce, Nd does not possess a terminal Cl atom but instead forms a branched polymer using μ-Cl for each link. This leaves the central cation as an eight-coordinated species with six μ-Cl ligands. Another derivation of the four μ-Cl arrangement has an eight-coordinated metal center with a terminal Cl and three bound solvents. The two examples of this are for La using two $HOPr^i$ and water and for Gd using two H_2O and CH_3CN. While the majority of these polymeric structures have been isolated for the larger cations, the smaller cations may also adopt this structure but further work is necessary to verify this.

In addition to the Ln^{+3} species, some of the Ln^{+2} halide derivative's structures have also been disseminated but these are typically a compartmentalized group of anions and solvated species. All of the +2 species isolated utilized I ligands with the Lewis basic solvents THF, DME, or a combination of *only* these two solvents. The structure isolated was the monomeric $[LnI_2(solv)_n]$ arrangement. The pentasolvated species includes THF adduct for Nd, Eu, and Sm yielding a seven-coordinated metal center. The only lower solvate species of this family of compounds is Yb, which binds four THF molecules, achieving Oh geometry. Two species (Tm and Sm) use two chelating DME and one THF to achieve the seven-coordination. In contrast, Sm uses three THF and one chelating DME to achieve the same coordination number. For the DME-only solvated species, an eight-coordination was achieved through the chelation of each DME as noted for Dy, Sm, and Eu. Also, a seven-coordination occurred for Tm and Yb because of the monochelation of one of the DME solvates, presumably due to the smaller cation size.

7 CONCLUSION

LnX_3 are very versatile sets of precursors that have been incorporated in materials applications such as catalyst for organic transformations, biomedical applications, NMR studies, scintillators, and pyro-reprocessing of used nuclear fuel. The most common oxidation state for these compounds is +3; however, there are reports of +2 and +4 species. Since the lanthanides tend to be highly paramagnetic and FTIR analysis gives limited structural information for these mainly ionic compounds, single-crystal X-ray structures and powder XRD analysis help identify the structure types as well as the phase of these materials. Synthesis of these LnX_3 often starts with the preparation of the LnX_3 hydrate. The hydrates have been shown to adopt three structure types:1IS/2OS dimer, 2IS/1OS, and 3OS depending on which lanthanide and halide combination is used. To isolate the anhydrous LnX_3, heating of the hydrated compound can be done but it often results in the formation of oxide; therefore, the most successful route is to heat the hydrate in the presence of NH_4Cl under vacuum, followed by sublimation for purification. These tend to rehydrate, so inert atmosphere synthesis is vital. In addition, other solvated LnX_3 have been reported including the MeOH, which was found to adopt a3IS dimer, 3IS, and 3OS structure type based on the anion and size of the cation employed. Other neutral oxygen and nitrogen donor solvated LnX_3 are available as well representing a wide range of solvents. Lanthanide compounds have the ability to possess a wide range of coordination numbers as well as structure types which are displayed in LnX_3, $[LnX(H_2O)_n]$, and $[LnX_3(solv)_n]$ that have been reported. The cation, anion, and solvent employed tend to direct the final structure adopted. As more systematic studies are undertaken to understand the fundamental nature of these types of compounds, new structure types will undoubtedly be uncovered and fine-tuning the final structure will be realized.

8 GLOSSARY

Comproportionation: A mixture of two compounds of the same element but in different oxidation states that react to form a product with an intermediate oxidation state. Example: Sm^0 reacted with Sm^{III} complex to form a Sm^{II} species.

Halide: A halogen (F, Cl, Br, I or At) bearing a negative charge.

Innersphere: Ligand bound directly to the metal.

Ligand: Anything bound to a metal center.

Metallorganic: Broadly used term to refer to compounds that possess both a metal and an organic ligand but does not contain a metal carbon bond (see Organometallic). A typical example would be a metal alkoxide.

Organometallic: Broadly used term to refer to a compound that is a metal with an organic ligand but contains a metal carbon bond. An example would be a Grignard reagent.

Outersphere: Ligand not bound directly to the metal but present in the unit cell.

Scintillator: A material that luminesces (or glows) when exposed to ionizing radiation.

9 RELATED ARTICLES

Geology, Geochemistry, and Natural Abundances of the Rare Earth Elements; Lanthanides: Coordination Chemistry; Lanthanide Alkoxides.

10 ABBREVIATIONS AND ACRONYMS

FTIR = Fourier transform infrared spectroscopy; MRI = magnetic resonance imaging; NMR = nuclear magnetic resonance; THF = tetrahydrofuran; XRD = X-ray diffraction.

11 REFERENCES

1. S. Anfang, K. Dehnicke, and J. Magull, *Z. Naturforsch., B: Chem. Sci.*, 1996, **51**, 531.

2. J. Burgess and J. Kijowski, *J. Inorg. Nucl. Chem.*, 1981, **43**, 2389.
3. M. Hargittai, *Acc. Chem. Res.*, 2009, **42**, 453.
4. S. Mishra, *Coord. Chem. Rev.*, 2008, **252**, 1996.
5. H. J. Seifert, *J. Therm. Anal. Calorim.*, 2006, **83**, 479.
6. H. C. Aspinall, 'Chemistry of the f-Block Elements', Gordon and Breach Science Publishers, Canada, 2001.
7. Conquest Version 1.14, Cambridge Crystallographic Data Centre: support@ccdc.cam.ac.uk or http://www.ccdc.cam.ac.uk (V 5.33 Nov 2011).
8. E. H. P. Cordfunke and R. J. M. Konings, *Thermochim. Acta*, 2001, **375**, 17.
9. A. Habenschuss and F. H. Spedding, *J. Chem. Phys.*, 1980, **73**, 442.
10. P. C. Junk, L. I. Semenova, B. W. Skelton, and A. H. White, *Aust. J. Chem.*, 1999, **52**, 531.
11. K. C. Lim, B. W. Skelton, and A. H. White, *Aust. J. Chem.* **53**, 2000, 867.
12. T. J. Boyle, L. A. M. Ottley, T. M. Alam, M. A. Rodriguez, P. Yang, and S. K. Mcintyre, *Polyhedron*, 2010, **29**, 1784.
13. G. B. Deacon, T. Feng, P. C. Junk, B. W. Skelton, and A. N. Sobolev, *Aust. J. Chem.*, 1998, **51**, 75.

Lanthanide Oxide/Hydroxide Complexes

Zhiping Zheng

Xi'an Jiaotong University, Xi'an, Shanxi, People's Republic of China and University of Arizona, Tucson, AZ, USA

1	Summary	183
2	Introduction	183
3	General Comments about Lanthanide Oxide/Hydroxide Complexes	184
4	Properties and Possible Applications	190
5	Conclusions	192
6	Glossary	193
7	Acknowledgment	193
8	Related Articles	193
9	Abbreviations and Acronyms	193
10	Further Reading	193
11	References	193

1 SUMMARY

The coordination chemistry of lanthanide oxides and hydroxides originates from the hard Lewis acidity and oxophilicity of the lanthanide ions. Once considered limited in scope and generally undesirable, the rational synthesis, structural characterization, and property investigation of lanthanide oxide/hydroxide (Ln-O/OH) complexes have attracted much recent interest, stimulated by the steadily increasing number of such species that are nevertheless synthetic serendipities. A breakthrough came about in the late 1990s when the approach of controlled hydrolysis of the lanthanide ions was developed; the degree of lanthanide hydrolysis and the subsequent olation reaction of the resulting hydroxo species are limited due to the limited number of sites for aqua coordination as a result of the preoccupation by inorganic and organic ancillary ligands of the lanthanide coordination sphere. A large number of structurally pleasing polynuclear lanthanide oxide/hydroxide complexes characterized by distinct cluster-type Ln-O/OH core motifs have since been prepared. Significant chemical, biomedical, and advanced technological applications are envisioned for these new members of the lanthanide complex family, which serve to further this niche sub field of lanthanide coordination chemistry.

2 INTRODUCTION

Lanthanides are a unique group of elements. Their f electronic configurations, hard Lewis character of their ions, and their large ionic radii render their coordination chemistry distinctly different from that of transition metal elements. Specifically, because of the large ionic size, a high coordination number is required unless sterically bulky ligands are utilized. As an alternative to satisfy this requirement, formation of polynuclear species featuring bridging ligands is a familiar scenario. The insignificant involvement of f orbitals in chemical bonding means that lanthanide–ligand interactions are primarily ionic, leading to generally labile lanthanide complexes with flexible and irregular coordination environment. For this very reason, the use of multidentate ligands is a general practice in the making of stable lanthanide complexes.

Because of their hard Lewis acid character, lanthanide coordination toward O-based ligands is strongly preferred, with water being the one arguably most prevalent even mundane. Ironically, although the $Ln\text{-}OH_2$ motif is ubiquitous in lanthanide complexes, the scope of this particular chemistry has always been viewed as limited at best. A dogma is that only within a narrow, low-pH range can aqua complexes of the lanthanide ions be stabilized; at higher pH, deprotonation of the aqua ligands occurs, leading to intractable

The Rare Earth Elements. Edited by David A. Atwood. © 2012 John Wiley & Sons, Ltd. ISBN 978-1-119-95097-4

precipitates of lanthanide oxide/hydroxides. Instead, the major players in lanthanide coordination chemistry are alkoxides, aryloxides, as well as multidentate ligands featuring both O and other non-O coordinating atoms.[1–4] A hiatus clearly exists between the chemistry of this branch of lanthanide chemistry and that of lanthanide oxide/hydroxide complexes. Although less developed, an increasing number of lanthanide oxide/hydroxide complexes have appeared in the literature, most of which have been structurally characterized.[5–8] In addition, many exciting applications have been realized or envisioned of these interesting chemical species.[5] The rapid development certainly warrants a separate discussion of this topical research.

The materials presented below are primarily concerned with lanthanide complexes whose central motifs are characterized by Ln–O, Ln–OH, or a combination of both. The common structural features of such complexes are summarized first, together with the various coordination modes of the oxo and hydroxo ligands. The rational synthesis of these otherwise elusive substances is then discussed after a presentation of the historical context of how this particular chemistry is developed in the light of the widespread belief that its scope is limited. Salient structural features of selected examples are then discussed, based on which certain general principles for the design and synthesis of polynuclear lanthanide oxide/hydroxide complexes may be developed. Interesting physical properties and chemical reactivity of these complexes are detailed toward the end of the discussion, based on which, useful applications, realized or envisioned, are presented. This chapter is concluded with a brief summary of the current status of the research of Ln–O/OH complexes, followed by an account of the challenging issues ahead and suggestions as to toward what directions this chemistry may be heading.

3 GENERAL COMMENTS ABOUT LANTHANIDE OXIDE/HYDROXIDE COMPLEXES

Three general observations are of particular note regarding the structure and composition of lanthanide oxide/hydroxide complexes. *First*, the presence of OH ligand is much more prevalent than O group. The latter may be viewed as formally derived from an OH upon deprotonation. Unambiguous assignment in crystallographic work is not always possible, but can generally be made on the basis of the different Ln–O distances in combination with charge balancing consideration. *Second*, only one lanthanide hydroxide complex has been verified to be mononuclear;[9] the core Ln–O/OH motifs are otherwise exclusively dinuclear and polynuclear. For complexes of nuclearities >4, cluster-type structures featuring the lanthanide atoms bridged by O/OH groups are frequently observed.[5] The ease of cluster formation may be understood in terms of the unique coordination behaviors of the lanthanide ions and the O/OH ligands. On the one hand, the large size of the lanthanide ions requires a high coordination number. On the other hand, the negatively charged O/OH ligands are electrically and ''coordinatively insatiate,'' and therefore, in need of additional metal ions. As such, a number of lanthanide ions are coordinatively stabilized by a number of O/OH ligands, and its assembly into a cluster type of core is presumably facilitated by the ready structural reorganization of the Ln–O/OH arrangement as a result of the primarily ionic nature of the bonding interactions involving lanthanide ions. To keep an easy line of discussion, the present discussion is arranged according to the core nuclearity of the complexes. *Third*, a small number of oxide/hydroxide complexes have been prepared by the direct hydrolysis of lanthanide iodides,[10] nitrates,[11–14] perchlorates,[14] and triflates,[15] but most oxide and hydroxide complexes feature organic multidentate ligands in addition to the O/OH ligands.[6–8] They are believed to control or limit the degree of hydrolysis of the lanthanide ions to avoid the formation of intractable precipitates of lanthanide oxide/hydroxides due to extensive hydrolysis. Ligands that are successfully applied in this capacity include α-amino acids, polyaminopolycarboxylates, functionalized carboxylates, β-diketonates, Schiff bases, and some other less-commonly used ligands.[5] *Lastly*, just as with most lanthanide-containing compounds, the solid-state structures of lanthanide oxide/hydroxide complexes generally do not represent their solution behaviors. Thus, our discussion of salient structural features of selected examples obtained by single-crystal X-ray diffraction studies should not be extrapolated for the identification of corresponding solution species.

3.1 Coordination Modes of OH Ligands

The hydroxo ligand displays a number of coordination modes, collected in Figure 1. Although there are only three and four lone pairs of electrons on the OH^- and O^{2-} group, respectively, thanks to the primarily ionic nature of bonding of the lanthanide ions, up to five lanthanide ions can be bridged simultaneously by the same OH ligand, and complexes featuring μ_6-O ligands have also been reported.

3.2 Rational Synthesis of Lanthanide Oxide/Hydroxide Complexes

As O/OH groups are formally derived from deprotonation of an aqua ligand, which is greatly enhanced by coordination with the Lewis acidic lanthanide ion, conducting lanthanide coordination chemistry in aqueous solutions at low pH (often below 4) is a common practice in order not to produce precipitates of lanthanide oxide/hydroxides due to extensive hydrolysis of the metal ion. This concern is easily understandable, and analogous chemistry is well established in the precipitation of gel-like oxide/hydroxides of Fe^{III} and Al^{III} when salts

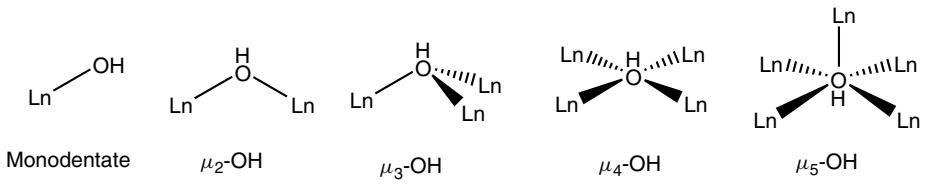


Figure 1 Coordination modes displayed by OH in lanthanide hydroxide complexes

of these Lewis acidic metal ions are left in an aqueous solution for an extended period of time. One may find the situation somewhat similar to sol–gel synthesis in which a metal alkoxide precursor hydrolyzes first to afford metal–OH (MOH). Following the condensation of the MOH species, M–O–M is formed. As the sequential process of hydrolysis and condensation progresses, more extensive networks of the M–O–M are formed, eventually producing a wet-gel material. Instead of a similar condensation of the Ln–OH units, ''olation'' occurs in which one OH ligand participates in bridging interactions with additional lanthanide ions as shown in Figure 2. If the degree of olation is not controlled, an intractable mixture characterized by extensive Ln–OH bridging and undesirable for the making of compositionally definitive and structurally well-defined complexes would be obtained.

The first insight into the prospect of developing an equally rich and exciting chemistry of the lanthanide oxide/hydroxide complexes as that of lanthanide alkoxides was provided by Evan and coworkers.[16] Having isolated and structurally characterized three unexpected polynuclear Sm^{III} hydroxide complexes, they made the note that although ''in the past, polymetallic lanthanide chemistry involved primarily alkoxide ligands, an accessible hydroxide-based polymetallic chemistry may now be available to the lanthanides.'' In the meantime, more examples of polynuclear lanthanide oxide/hydroxide complexes featuring cluster-type Ln–O/OH cores have appeared in the literature.[17–19] Although adventitious hydrolysis was suspected to be responsible for the assembly of these serendipitous discoveries, no systematic studies were available until Zheng and coworkers developed the rational synthesis of polynuclear lanthanide oxide/hydroxide complexes using the approach of ligand-controlled hydrolysis of the lanthanide ions.[6–8] The essence of this approach is that the ligands pre-occupy part of the lanthanide coordination sphere, thus leaving only a small number of sites for aqua coordination. Upon deliberate pH enhancement, the aqua ligands, bound to and activated by the metal ion, undergo deprotonation, affording the corresponding hydroxo complex. Olation reaction ensues because the OH group is unsaturated, both coordinatively and electrically, leading to polynuclear hydroxo-bridged species. Clearly, it is the preoccupation of the coordination sphere by the supporting ligands with different numbers of coordinating atoms and steric bulk that controls the number of sites available for aqua coordination and in turn, the degree of hydrolysis and the structure of the cluster eventually assembled.

3.3 Lanthanide Oxide/Hydroxide Complexes of Different Nuclearities

Significant advancement has been made in the development of the chemistry of lanthanide oxide/hydroxide complexes. A great variety of species with different nuclearity and often aesthetically pleasing core structures (Figure 3) have been reported in which the O/OH groups are engaged in extensive bridging interactions with the lanthanide ions. We note that only one structurally characterized mononuclear lanthanide hydroxide complex exists in the literature.[9] The crystal structure of $Sm(Tp^{Me_2})_2(OH)$ (Tp^{Me_2} — tris(dimethylpyrazolyl)borate, a sterically cumbersome ligand) is shown in Figure 4. The steric protection of the Sm^{III} ion by the two extremely bulky ligands clearly prevents the hydroxo group from participating in any bridging interactions with other lanthanide complex unit(s).

If one takes the various supporting ligands into consideration, a detailed discussion of these interesting compounds becomes a challenge. The following discussion is thus limited to selected and representative examples according to the nuclearity of the cluster core. It is noted that many higher nuclearity cores such as those shown in the bottom portion of

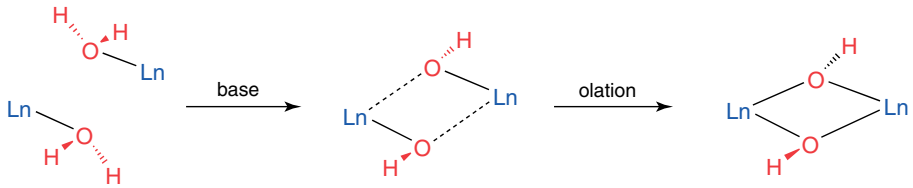


Figure 2 Hydrolysis of aqua lanthanide complexes via olation of the intermediate Ln–OH species, affording lanthanide hydroxide complexes

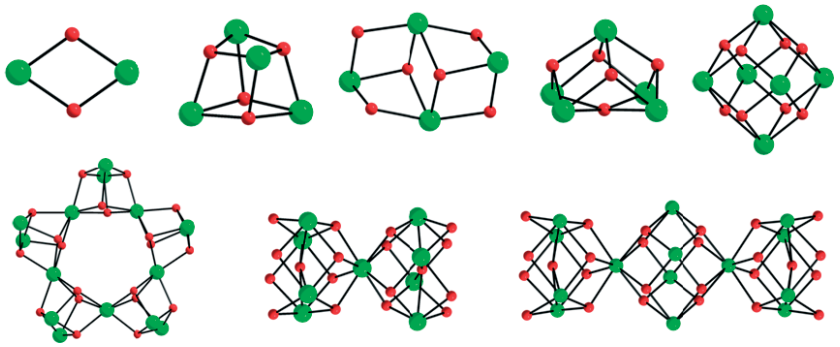


Figure 3 Core structures of representative polynuclear Ln–O/OH complexes. Ln (green), O (red)

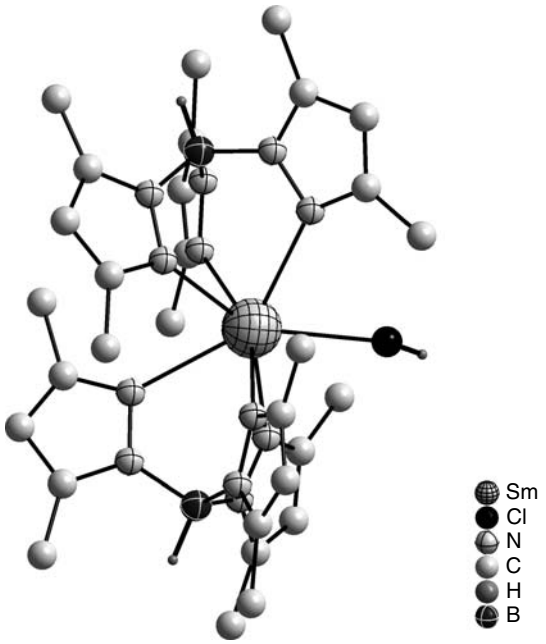


Figure 4 The crystal structure of $Sm(Tp^{Me2})_2(OH)$. (Reprinted with permission from Ref. 9. Copyright (2002) American Chemical Society.)

Figure 3 can be formally constructed by using smaller well-defined Ln–OH building blocks shown in the top portion of the same figure.

3.3.1 *Dinuclear Complexes*

A large number of lanthanide hydroxide complexes featuring a diamond-shaped dinuclear core doubly bridged by two μ_2-OH groups have been reported, most of which are products of adventitious lanthanide hydrolysis, and are not reproducible.[16,20–24] With the ligand-controlled hydrolytic approach, they can now be rationally synthesized starting from a mononuclear aqua complex. Shown in Figure 5 is the synthesis of $[(EDTA)Er(\mu\text{-}OH)_2Er(EDTA)]^{4-}$;[6] the dinuclear core structurally resembles the active site of many naturally occurring nucleases. In fact, dinuclear lanthanide hydroxide complexes bearing such a core motif have been shown to catalyze the hydrolytic cleavage of DNA and RNA analogs,[25–27] which is of significance in the model studies of these very important metalloenzymes.

3.3.2 *Trinuclear Complexes*

The first trinuclear lanthanide hydroxide complex structurally characterized was reported by Evans and coworkers,[16] based on which the insightful suggestion of accessible chemistry of lanthanide hydroxides was made. Additional examples, though much fewer than dinuclear or tetranuclear complexes, have since appeared in the literature.[28–30] A triangular arrangement of the metal atoms face-capped by one or two μ_3-OH ligands, above and/or below the Ln_3 plane, is a prevalent motif found in these complexes. This hydroxide core is then encapsulated and stabilized by the organic supporting ligands through bridging interactions along the sides of the trimetallic array.

3.3.3 *Tetranuclear Complexes*

Lanthanide oxide/hydroxide complexes featuring discrete and recognizable tetranuclear Ln–O/OH units are most abundant among all reported lanthanide hydroxides. Three distinct core motifs, the distorted cubane, the rhombus, and the square, have been found, with the cubane-like structure being dominant.

The cubane motif, consisting of four metal atoms and four μ_3-OH groups occupying the alternate vertices of the cube, was reported as early as in 1968 in the crystal structure of lanthanide-containing zeolites.[31] The prevalence of this motif was subsequently suggested by a number of unexpected complexes that share the same cubane core structure, despite the fact that they were obtained under markedly different reaction conditions and with the use of distinctly different organic ligands.[17–19] Most extensive and

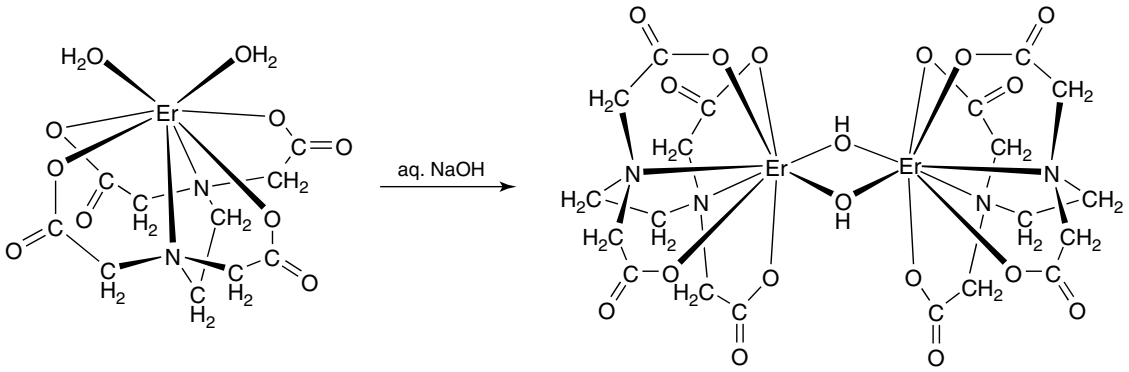


Figure 5 Synthesis of the dinuclear hydroxide complex $[(EDTA)Er(\mu\text{-}OH)_2Er(EDTA)]^{4-}$ by deliberately hydrolyzing $[(EDTA)Er(H_2O)_2]^-$ with aqueous NaOH

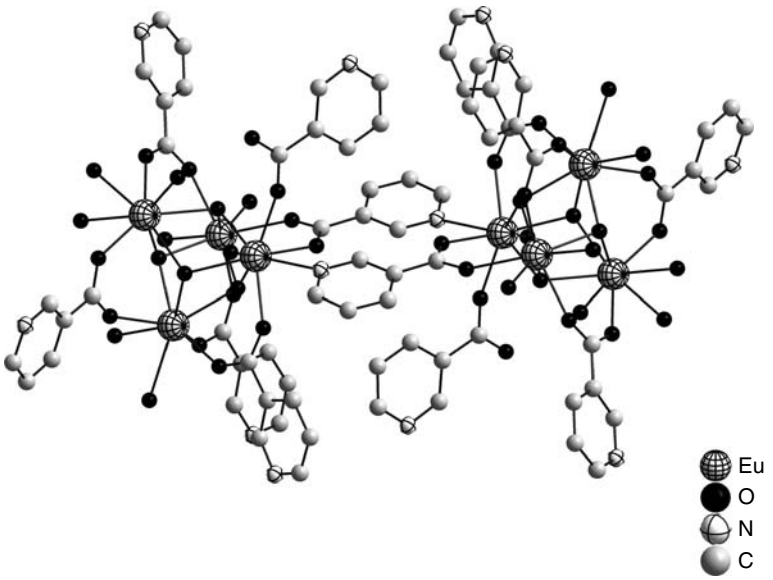


Figure 6 Crystal structure of $\{[Eu_4(\mu_3\text{-}OH)_4\ (nic)_6(H_2O)_8]_2\}^{4+}$ (nic = nicotinate) featuring two-bridge tetranuclear $[Eu_4(\mu_3\text{-}OH)_4]$ units. (Reproduced with permission from Ref. 5. © John Wiley & Sons (Asia) Pte Ltd, 2010.)

systematic work to rationally produce complexes bearing such a core motif was accomplished by Zheng and coworkers who developed the so-called high-pH coordination chemistry of the lanthanide ions by employing ligands such as α-amino acids, polyaminopolycarboxylates, and β-diketonate ligands to control the hydrolysis of these unique metal ions.[6–8,32] In such an approach, the deliberate enhancement of the pH of the reaction mixture ensures complete hydrolysis, as opposed to adventitious hydrolysis suspected for the formation of the serendipitous literature precedents, while the organic supporting ligands prevent extensive hydrolysis from occurring and thus avoiding the intractable precipitates of oxide/hydroxides.

The prevalence of the cubane motif has now been well established. In addition to being seen in complexes with ligands derived from the aforementioned conventional ligands, they are also found in complexes with rather sophisticated or even unusual ligands including polyoxometalate and cucurbit[6]uril.[33] Furthermore, higher nuclearity complexes can be assembled by using the cubanes as building blocks, either through bridging ligands to produce linked cluster arrays or networks or by directly sharing metal vertices to generate fused multiclusters.[34–38] Shown in Figure 6 is the crystal structure of the cationic cluster complex $\{[Eu_4(\mu_3\text{-}OH)_4(nic)_6(H_2O)_8]_2\}^{4+}$(nic = nicotinate) consisting of two tetranuclear units of $[Eu_4(\mu_3\text{-}OH)_4(nic)_6(H_2O)_8]^{2+}$ bridged by two nicotinate ligands using the ligand's carboxylate group for two lanthanide ions of one of the cubanes while using its pyridyl N atom to coordinate a lanthanide ion within the other tetranuclear cluster core.[34]

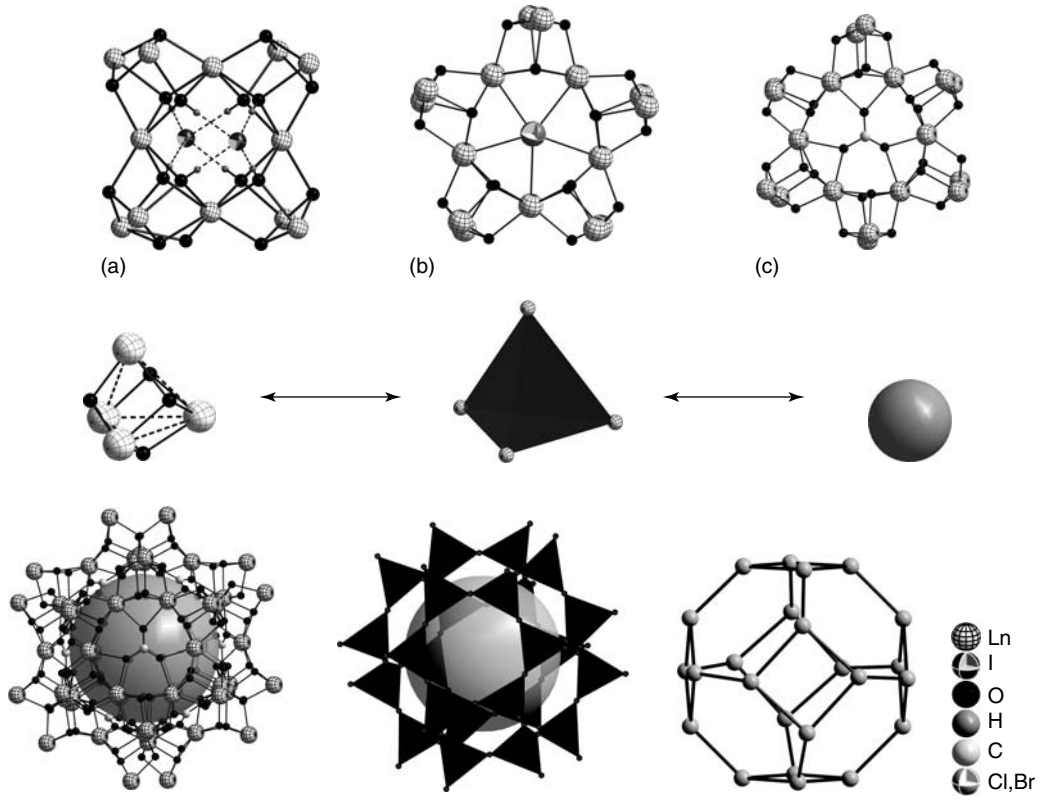


Figure 7 The structures of (a) dodeca-, (b) pentadeca-, and (c) octadecanuclear clusters templated by two μ_4-I^- ions, a μ_5-X^- (X = Cl, Br) ion, and $\mu_6:\eta^1:\eta^1:\eta^1:\eta^1:\eta^1:\eta^1CO_3^{2-}$, respectively. Formal assembly of a 60-metal hydroxide complex featuring 24 vertex-sharing $[Ln_4(\mu_3\text{-}OH)_4]$ cubane units. These cubane building blocks form six dodecanuclear squares and eight octadecanuclear hexagons that are further assembled into the sodalite cage. (Reproduced with permission from Ref. 5. © John Wiley & Sons (Asia) Pte Ltd, 2010.)

With four, five, and six vertex-sharing cubanes, wheel-like cyclic structures (Figure 7), templated by anionic entities such as halide and carbonate ions, have been obtained.[36–38] Even more sophisticated complexes can be formed by using these wheel-like secondary building units, for example, the 60-metal hydroxide cluster core composed of 24 vertex-sharing cubanes organized into a giant cage of the well-known sodalite structure.[38]

Although not nearly prevalent as the cubane motif, the rhombus-shaped tetranuclear core of $Ln_4(\mu_3\text{-}OH)_2$ (Figure 3) is found in a number of lanthanide hydroxide complexes. Such an arrangement can be viewed as two edge-sharing equilateral triangles, each being face-capped by a μ_3-OH group, one above and the other below the tetrametallic plane. As an example, the crystal structure of $Ln_4(\mu_3\text{-}OH)_2(\mu,\eta^2\text{-acac})_6(\eta^2\text{-acac})_4$ (Ln = Y, Nd; acac = acetylacetonate) containing such a core is shown in Figure 8.[39,40]

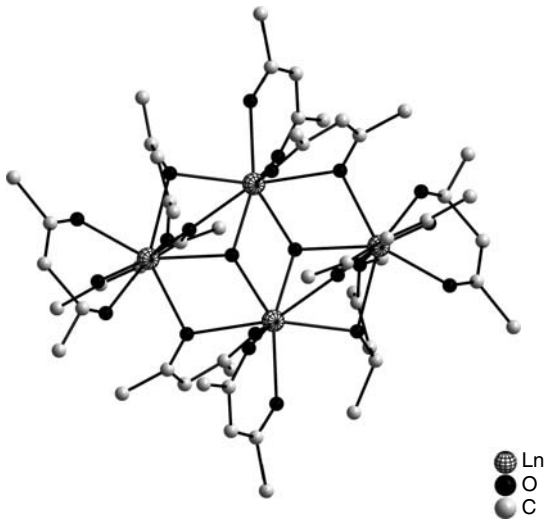


Figure 8 Crystal structure of $Ln_4(\mu_3\text{-}OH)_2(\mu,\eta^2\text{-acac})_6(\eta^2\text{-acac})_4$ (Ln = Y, Nd). (Reproduced with permission from O. Poncelet and L.G. Hubert-Pfalzgraf, ''Reactivity of neodymium(III) isopropoxide derivatives: Synthesis, characterization and crystal structure of $[Nd_4(\mu_3\text{-}OH)_2(\mu_2,\mu_1\text{-acac})_6(acac)_4]$,'' *Polyhedron*, 1989, **8**, 2183–2188. Reproduced from Ref. 39, Copyright (1989), with permission from Elsevier.)

3.3.4 Pentanuclear Complexes

A square pyramidal arrangement of lanthanide ions face-capped by triply bridging OH groups constitutes another



Figure 9 Crystal structure of $[Dy_5(\mu_4\text{-}OH)(\mu_3\text{-}OH)_4(\mu,\eta^2\text{-}Ph_2acac)_4(\eta^2\text{-}Ph_2acac)_6]$. (Reproduced with permission from Ref. 5. © John Wiley & Sons (Asia) Pte Ltd, 2010.)

common motif for lanthanide hydroxide complexes. The basal plane generally features a μ_4-O/OH ligand. Shown in Figure 9 is the crystal structure of $[Dy_5(\mu_4\text{-}OH)(\mu_3\text{-}OH)_4(\mu,\eta^2\text{-}Ph_2acac)_4(\eta^2\text{-}Ph_2acac)_6]$, one such example with 1,3-diphenyl-1,3-propanedionate (Ph_2acac) as the supporting ligand encapsulating the pentanuclear core of $[Dy_5(\mu_4\text{-}OH)(\mu_3\text{-}OH)_4]$.[41]

Joining two such pentanuclear units by sharing the nonbasal lanthanide atom affords an hourglass-like nonanuclear motif whose basal planes are twisted by 90° with respect to each other. As such, the eight basal lanthanide atoms form a square antiprism. A number of hydroxide complexes containing such a core have been reported, including $[Ln_9(\mu_4\text{-}OH)_2(\mu_3\text{-}OH)_8(acac)_{16}]^+[Mo_2(CO)_{10}(\mu\text{-}H)]^-$ (Ln = Sm, Eu, Gd, Dy, Yb) and $[Sm_9(\mu_4\text{-}OH)_2(\mu_3\text{-}OH)_8(acac)_{16}]^+$ $[CrW(CO)_{10}(\mu\text{-}H)]^-$, obtained by the hydrolysis of $Ln(acac)_3{\cdot}2H_2O$ promoted by homo or heterodinuclear decacarbonyl hydrides.[42–44] The crystal structure of $[Sm_9(\mu_4\text{-}OH)_2(\mu_3\text{-}OH)_8(acac)_{16}]^+$ is shown in Figure 10.[45] It is interesting to note that in the very first series of complexes containing the nonanuclear core, $[Ln_9(\mu_4\text{-}O)_2(\mu_3\text{-}OH)_8L_{16}]^-$ [Ln = Y; L = $MeC(O)CHC(O)OCH_2CH{=}CH_2$ or $MeC(O)CHC(O)OCH_2CH_3$, Ln = Sm, Eu, Gd, Dy, Er, L = $C_6H_5C(O)CHC(O)CH_3$], μ_4-O rather than μ_4-OH is the end-capping ligand, an assignment consistent with the noticeably different Ln–O distances and corroborated by the number of counterions.[46] That two different forms of the O-based ligands are present in closely related core structures indicates the subtlety of this class of lanthanide-containing compounds and the coordination chemistry of lanthanide hydroxides in general.

3.3.5 *Hexanuclear Complexes*

By sharing the basal plane, two pentanuclear units would make an octahedral, hexanuclear cluster core, with or without an interstitial μ_6-oxo group. Such a core can also be viewed as capping the above pentanuclear unit with an additional and sixth lanthanide atom. The first lanthanide complex containing one such discrete octahedral core is $[Ce_6(\mu_3\text{-}O)_6(\mu_3\text{-}OH)_4(acac)_{12}]$, isolated from the hydrolysis of $Ce(OCHMe_2)_2(acac)_2$.[47] It is interesting to note that only four of the eight face-capping ligands are hydroxo groups of this ''hollow'' hexanuclear cluster core while the remaining four are μ_3-oxo ligands. This combination is mandated by the Ce^{IV} ions. In a recent report, a similar hollow octahedral core of $[Gd_6(\mu_3\text{-}OH)_8]$ has been found in a heterometallic 3d–4f cluster assembly.[47] An almost identical hexanuclear cluster motif with an interstitial μ_6-O group is more frequently observed. Complexes containing such a core were obtained by the direct hydrolysis of lanthanide perchlorates,[14] nitrates,[11–14] iodides,[10] and most recently by lanthanide hydrolysis in the presence of a trivacant Wells–Dawson polyoxo-anion α-$[P_2W_{15}O_{56}]^{12-}$.[48] The crystal structure of $[Nd_6(\mu_6\text{-}O)(\mu_3\text{-}OH)_8(H_2O)_{24}]^{8+}$ obtained by base-promoted direct hydrolysis of $Nd(ClO_4)_3$ is shown in Figure 11.[14]

There exist a number of tetradecanuclear lanthanide hydroxide complexes whose core can be viewed as formally constructed by combining two square pyramids of $[Ln_5(\mu_4\text{-}OH)(\mu_3\text{-}OH)_4]$ with one ''hollow'' octahedron of $[Ln_6(\mu_3\text{-}OH)_8]$ by vertex sharing. The structural relationship between the penta-, hexa-, nona-, and tetradecanuclear species

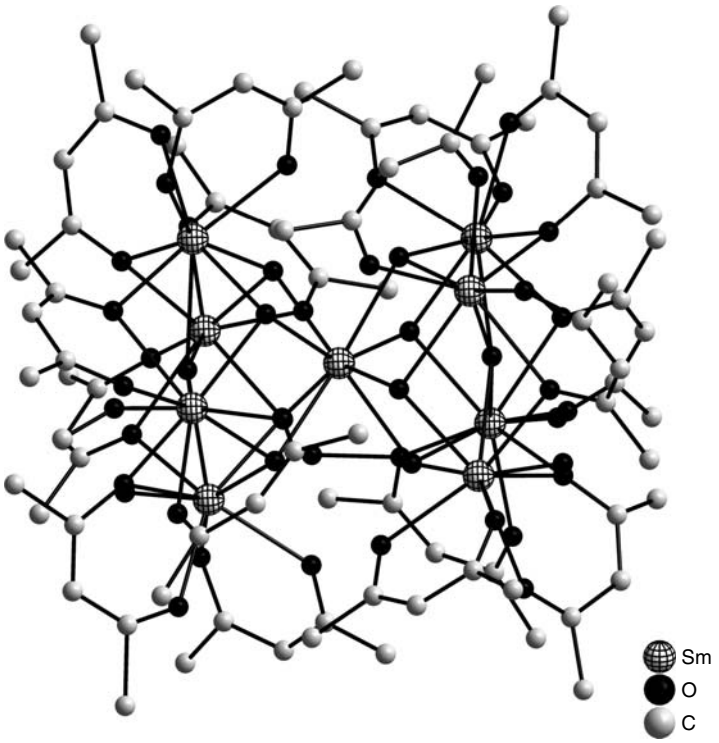


Figure 10 Crystal structure of nonanuclear complex $[Sm_9(\mu_4\text{-}OH)_2(\mu_3\text{-}OH)_8(acac)_{16}]^+$. (Reproduced from Ref. 44, Copyright (2006), with permission from Elsevier.)

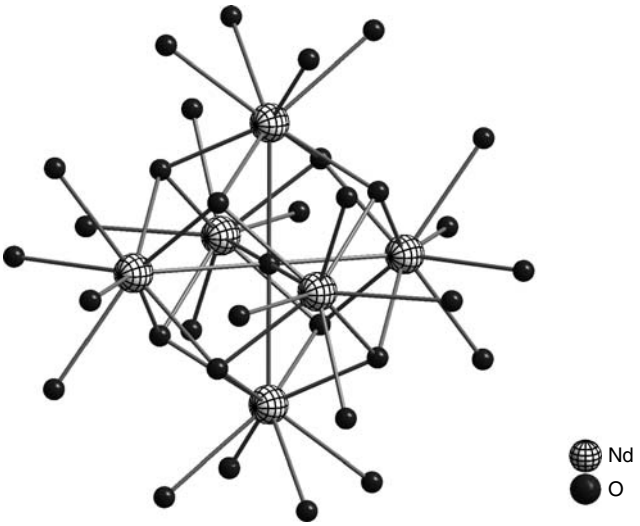


Figure 11 Crystal structure of $[Nd_6(\mu_6\text{-}O)(\mu_3\text{-}OH)_8(H_2O)_{24}]^{8+}$. (Reprinted with permission from Ref. 10. Copyright (2006) American Chemical Society.)

can be easily discerned from the relevant structures presented in Figure 3.[49–51]

In addition to the regular octahedral cluster core structure, a rare example of an open, chair-like hexanuclear lanthanide hydroxide motif (Figure 12) was identified in the structure of $[Ln_3(\mu_3\text{-}OH)_2(BDC)_{3.5}(H_2O)_2]\cdot H_2O$ (Ln = Y, Yb, Er; BDC = 1,4-benzenedicarboxylate) coordination polymer obtained under hydrothermal conditions.[52] The hexanuclear building block, consisting of six lanthanide ions and four μ_3-OH groups, can be conveniently described as four edge-sharing units of $[Ln_3(\mu_3\text{-}OH)]$.

3.3.6 Octanuclear Complexes

The octanuclear lanthanide hydroxide cluster core was first identified in $Er_8(\mu_4\text{-}O)(\mu_3\text{-}OH)_{12}(THD)_8$ (THD = 2,2,6,6-tetramethylheptane-3,5-dionate).[53] It is a triangulated dodecahedron with an interstitial oxo group; each of its triangular faces is capped by a μ_3-OH group. The same cluster core has also been found in $[Eu_8(\mu_6\text{-}O)(\mu_3\text{-}OH)_{12}(\mu_2\text{-}OTf)_{16}(OTf)_2]$ (Figure 13)[15] and $[Eu_8(\mu_4\text{-}O)(\mu_3\text{-}OH)_{12}(DMF)_8(Se_3)(Se_4)_3(Se_5)_2]$.[54,55] That the same cluster core is obtained with different ancillary ligands suggests the prevalence of this motif in the lanthanide hydroxide coordination chemistry.

4 PROPERTIES AND POSSIBLE APPLICATIONS

Lanthanide oxide/hydroxide complexes are a class of intriguing lanthanide-containing compounds, not just because

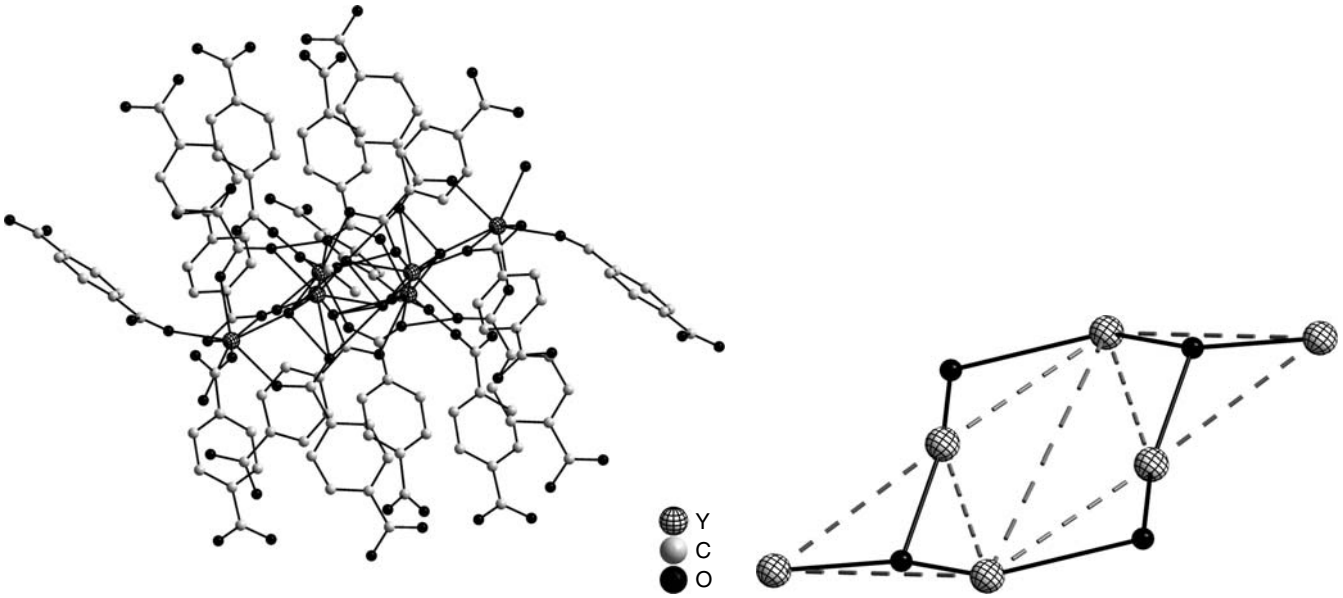


Figure 12 Crystal structure of $[Y_3(\mu_3\text{-}OH)_2(BDC)_{3.5}(H_2O)_2]\cdot H_2O$ with its chair-like core motif. (Reproduced with permission from Ref. 5. © John Wiley & Sons (Asia) Pte Ltd, 2010.)

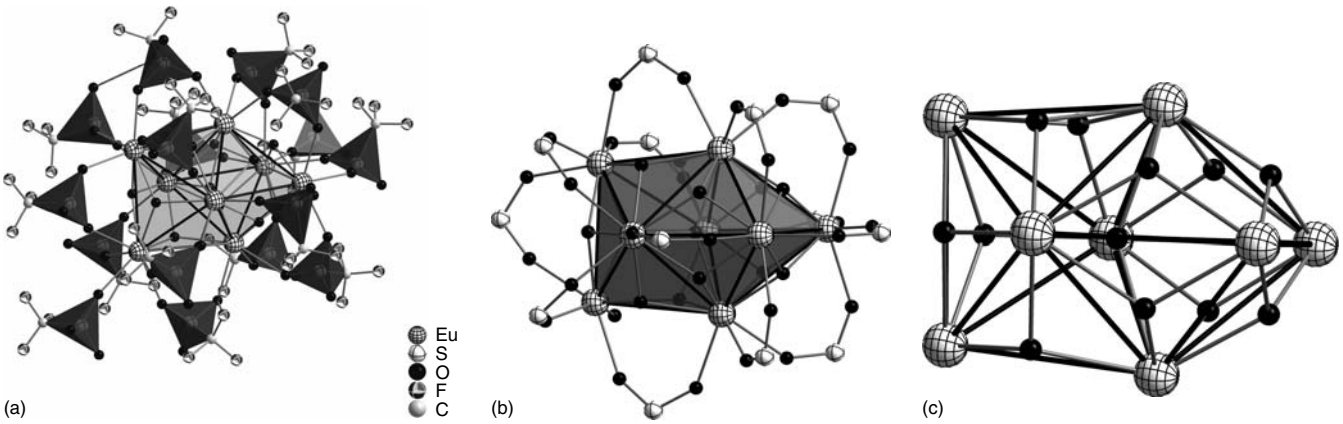


Figure 13 (a) Crystal structure of $[Eu_8(\mu_4\text{-}O)(\mu_3\text{-}OH)_{12}(\mu_2\text{-}OTf)_{14}(OTf)_2]$ with its coordination sphere (b) and cluster core (c). (Reproduced with permission from Ref. 5. © John Wiley & Sons (Asia) Pte Ltd, 2010.)

of the beautiful Ln–O/OH core structures, but because of the inherent Lewis acidity of the trivalent metal ions, unique magnetic properties, and luminescence characteristics. Diverse applications in developing novel catalysts, hybrid materials, molecular magnetic materials, and bioimaging contrast agents are envisioned.

4.1 Catalysis

The ability of lanthanide hydroxide complexes to catalyze the hydrolytic cleavage of DNA and RNA analogs, mimicking the function of natural nucleases, has long been recognized.[25–27] Many dinuclear complexes have been prepared for model studies. A possible mechanism as suggested by the crystallographic studies of natural nucleases entails first the coordination of the phosphate group of a nucleic acid by the Lewis acidic lanthanide ion, followed by nucleophilic attack by the metal-bound OH group. The lanthanide ion is believed to (i) activate the substrate by removing part of the electron density from the negatively charged phosphate O atom; (ii) enhance the nucleophilicity of an OH group; and (iii) facilitate the departure of the leaving group following the nucleophilic attack. Other propitious traits include the large size of the metal ion to accommodate both the substrate and nucleophile in the same coordination sphere and the primarily ionic nature of the bonding interactions

that would facilitate any necessary structural reorganization in order to achieve an optimal substrate/nucleophile arrangement for reaction.

The catalytic potential of lanthanide hydroxide complexes have also been shown in more chemistry-oriented schemes. For example, the air- and moisture-stable pentanuclear complex, $[Y_5(\mu_4\text{-OH})(\mu_3\text{-OH})_4(\mu, \eta^2\text{-Ph}_2\text{acac})_4(\eta^2\text{-Ph}_2\text{acac})_6]$, has been found to catalyze the oxidation of aldehydes to the corresponding carboxylic acids in the presence of air.[56]

4.2 Cluster–Polymer Hybrids with Enhanced Properties

Three-dimensional cationic frameworks featuring lanthanide hydroxide clusters as building blocks have been prepared by using amino acids or other types of bridging ligands.[35] As-prepared materials possess nanosized pores that are occupied by water and counterions from the original synthesis. These substances may find zeolitic applications for anion exchange or occlusion and activation of electron-rich substrates.

In addition, hybrid materials have been made by doping diketonate cluster complexes of lanthanide hydroxide into organic polymers. The resulting materials exhibit lowered coefficients of thermal expansion, increased moduli, reduced solvent sensitivity while preserving acceptable thermal and mechanical properties.[57]

4.3 Lanthanide-Containing Molecular Magnetic Materials

Possessing a large number of unpaired electrons and magnetic anisotropy, lanthanide complexes are particularly attractive for developing single-molecule magnets for information storage. As an example, trinuclear Dy^{III} hydroxide complexes have been shown to exhibit single molecular magnet-like slow relaxation behavior within its excited states, even though it possesses an almost diamagnetic ground spin state.[28,58] This peculiar magnetic showing has been ascribed to noncolinearity of the easy axes of magnetization of the Dy^{III} ions that lie in the Dy_3 triangular plane, but are disposed at 120° with respect to each other. Clearly, the trimetallic arrangement bridged by two μ_3-OH groups is critical in determining the observed magnetic properties. A more recent report describes an anion-dependent slow magnetic relaxation behavior in two tetranuclear Dy^{III} hydroxide complexes. Thus, it appears that there is a real possibility to realize novel molecule-based magnetic materials whose properties may be tuned by altering the core structure of the magnetic clusters.

Magnetically active lanthanide oxide/hydroxide complexes are also of potential applications in developing magnetic refrigeration, an energy-efficient and environmentally friendly technology operating on the magnetocaloric effect (MCE).[59] MCE is an intrinsic property to a magnetic solid, and it has been shown that a molecule exhibiting a large MCE usually possesses a large spin ground state, negligible magnetic anisotropy, existence of low-lying excited spin states, dominant ferromagnetic exchange, and a large metal/ligand mass ratio. Recent literature reports clearly point to the potential use of high-nuclearity Gd^{III} clusters in this capacity, in particular those featuring extensive bridging interactions via O/OH ligands.

4.4 New Paradigms of Biomedical Imaging Contrast Agents

Mononuclear aqua complexes of Gd^{III} with stabilizing ligands such as DTPA and DOTA are valuable in enhancing the contrast of clinical magnetic resonance imaging (MRI).[60,61] The greater the contrast, the higher the quality of the images, and the greater their value to the physician performing the diagnosis. Moreover, the greater the contrast, the smaller the body structures that may be visualized in the imaging procedure. In other words, enhanced contrast can lead to improved resolution. As a result, much effort has been devoted to identifying methods of enhancing contrast in diagnostic imaging. Gd^{III}-based contrast agents work on the principle of shortening the relaxation time (T_1) of water molecules in the vicinity of the complex via exchange of the body fluid water molecules with the aqua ligand. In other words, the higher the number of aqua ligands on a contrast complex, the higher the efficiency of the agent. However, there is only one aqua ligand in the current clinically used contrast agents, and their uses are not based on their efficiency. Rather, it is out of the consideration of costs and stability/clearance profile. In principle, the efficiency as judged by the contrast agent's relaxivity can be increased if a complex with a large number of exchangeable aqua ligands is used. Indeed, with the use of $[Gd_{16}(\mu_6\text{-OH})_2(\mu_3\text{-OH})_{16}(H_2O)_8(\text{L-serine})_{20}]^{3+}$,[51] a tetradecanuclear cluster with serine as supporting ligand, a significantly increased relaxivity over the clinically utilized Gd^{III} contrast reagent has been achieved, portending the significant applications of high-nuclearity lanthanide oxide/hydroxide complexes as MRI contrast agents. Furthermore, the high content of lanthanide elements, heavy atoms capable of effectively attenuating X-ray radiation, makes such complexes potential new paradigms of contrast agents for radiographic imaging.[62] The key roadblock to further development appears to be the stability (or lack thereof) of the currently available complexes.

5 CONCLUSIONS

The development of the chemistry of lanthanide oxide/hydroxide complexes has come a long way, from the dogma of such chemistry being limited and not interesting, to academic prerogative stimulated by the unexpected isolation

of structurally pleasing cluster complexes, and finally to systematic and rational synthetic studies toward the reliable production of potentially useful materials. The number of reports dealing with their preparation, physical properties, and potential applications of practical significance is steadily increasing, and it appears that tremendous opportunities exist for further development.

Significant progresses notwithstanding, there is still a tremendous potential for further development of this research field, but significant challenges remain. For example, a large number of complexes displaying diverse and often pleasing structures have been obtained, but reliable reproduction of many of these species remains elusive, in particular for polynuclear hydroxide complexes. As such, ''the 'rational design' of polynuclear lanthanide (cluster) complexes with specific properties is currently an inexact science, and exploratory syntheses, with the hope of discovering new materials with useful properties, has been a common alternative.''[63] On the other hand, interesting properties and potentially significant applications of many lanthanide oxide/hydroxide complexes have been demonstrated. For example, some of these clusters have been used as precursors for oxide materials in advanced technologies. Efficient synthetic nucleases have been developed that show superior catalytic properties in the hydrolytic cleavage of nucleic acids. Potential applications of certain cluster species as new paradigms of contrast-enhancing agents in biomedical imaging have also been demonstrated. Fixation of atmospheric CO_2 has also been observed in a number of cluster species, which carries significant ramifications from the environmental viewpoint.[64,65] More fundamentally, many novel chemical transformations have been found to be facilitated by lanthanide-containing clusters. It is entirely reasonable to predict that this particular research will continue to grow with high possibility of producing many new species with novel structures and realizing useful applications that may not even have been contemplated.

6 GLOSSARY

Cluster: A chemical species containing three or more metal atoms that are directly metal-metal bonded, or within normal bonding distances and with significant inter-metal interaction, or bridged by some nonmetal atoms.

Contrast agents: Contrast agents are a class of pharmaceuticals that when administered to a patient, enter and pass through anatomic regions of interest to provide transient enhancement of contrast in medical imaging procedures.

Hydrolysis: A chemical reaction in which a substance reacts with water to be converted into one or more other substances.

Nuclearity: The number of metal atoms in a polynuclear complex.

Nucleases: Enzymes that hydrolyze nucleic acids.

Olation: The process by which metal ions form polymeric oxo or hydroxo species in aqueous solution.

7 ACKNOWLEDGMENT

The author acknowledges the US National Science Foundation and Xi'an Jiaotong University (China) for support.

8 RELATED ARTICLES

Carboxylate; β-Diketonate; Lanthanide Complexes with Amino Acids; Lanthanides: Luminescence Applications; Lanthanides: ''Comparison to 3d Metals''; Lanthanide Alkoxides; Lanthanides: Coordination Chemistry; Lanthanides: Magnetic Resonance Imaging; Lanthanide Complexes with Multidentate Ligands; Molecular Magnetic Materials; Magnetism; Metal–Organic Frameworks; Rare Earth Metal Cluster Complexes; Supramolecular Chemistry: from Sensors and Imaging Agents to Functional Mononuclear and Polynuclear Self-Assembly Lanthanide Complexes;

9 ABBREVIATIONS AND ACRONYMS

MCE = magnetocaloric effect; MOH = metal–OH; MRI = magnetic resonance imaging.

10 FURTHER READING

S. Xiang, S. Hu, T. Sheng, R. Fu, X. Wu, and X. Zhang, *J. Am. Chem. Soc.*, 2007, **129**, 15144.

11 REFERENCES

1. R. C. Mehrotra, A. Singh, and U. M. Tripathi, *Chem. Rev.*, 1991, **91**, 1287.
2. R. Anwander and W. A. Herrmann, *Top. Curr. Chem.*, 1996, **179**, 1.
3. T. J. Boyle and L. A. M. Ottley, *Chem. Rev.*, 2008, **108**, 1896.

4. L. G. Hubert-Pfalzgraf, *N. J. Chem.*, 1995, **19**, 727.
5. Z. Zheng, in 'Handbook on the Physics and Chemistry of Rare Earths', eds. K. A. Gschneidner Jr., J. C. G. Bünzli, and V. K. Pecharsky, Elsevier, Amsterdam, 2009, Vol. 40 Chap. 245.
6. Z. Zheng, *Chem. Commun.*, 2001, 2521.
7. Z. Zheng, *Chemtracts*, 2003, **16**, 1.
8. Z. Zheng and R. Wang, *Comments Inorg. Chem.*, 2000, **22**, 1.
9. N. Marques, A. Sella, and J. Takats, *Chem. Rev.*, 2002, **102**, 2137.
10. A. Mudring, T. Timofte, and A. Babai, *Inorg. Chem.*, 2006, **45**, 5162.
11. Z. Zák, P. Unfried, and G. Giester, *J. Alloys Compd.*, 1996, **205**, 235.
12. G. Giester, P. Unfried, and Z. Zák, *J. Alloys Compd.*, 1997, **257**, 175.
13. G. Calvez, O. Guillou, C. Daiguebonne, P.-E. Car, V. Guillerm, Y. Gérault, F. Le Dret, and N. Mahé, *Inorg. Chim. Acta*, 2008, **361**, 2369.
14. R. Wang, M. D. Carducci, and Z. Zheng, *Inorg. Chem.*, 2000, **39**, 1836.
15. A. Babai and A. Mudring, *Z. Anorg. Allg. Chem.*, 2006, **632**, 1956.
16. W. J. Evans, G. W. Rabe, and J. W. Ziller, *Inorg. Chem.*, 1994, **33**, 3072.
17. J. C. Plakatouras, I. Baxter, M. B. Hursthouse, M. K. M. Abdul, J. McAleese, and S. R. Drake, *J. Chem. Soc., Chem. Commun.*, 1994, 2455.
18. X. Chen, Y. Wu, Y. Tong, Z. Sun, and D. N. Hendrickson, *Polyhedron*, 1997, **162**, 4265.
19. T. Dube, S. Gambarotta, and G. Yap, *Organometallics*, 1998, **17**, 3967.
20. D. Wei, Y. Zheng, and J. Lin, *Z. Naturforsch., B: Chem. Sci.*, 2002, **57**, 625.
21. E. Baraniak, R. S. L. Bruce, H. C. Freeman, N. J. Hair, and J. James, *Inorg. Chem.*, 1976, **15**, 2226.
22. M. D. Grillone, F. Benetollo, and G. Bombieri, *Polyhedron*, 1991, **10**, 2171.
23. V. Ripert, L. G. Hubert-Pfalzgraf, and J. Vaissermann, *Polyhedron*, 1999, **18**, 1845.
24. R. Wang, J. Zhao, T. Jin, G. Xu, Z. Zhou, and X. Zhou, *Polyhedron*, 1998, **17**, 43.
25. E. R. Farquhar, J. P. Richard, and J. R. Morrow, *Inorg. Chem.*, 2007, **46**, 7169.
26. S. J. Franklin, *Curr. Opin. Chem. Biol.*, 2001, **5**, 201.
27. M. Komiyama, N. Takeda, and H. Shigekawa, *Chem. Commun.*, 1999, 1443.
28. J. Tang, I. Hewitt, N. T. Madhu, G. Chastanet, W. Wernsdorfer, C. E. Anson, C. Benelli, R. Sessoli, and A. K. Powell, *Angew. Chem. Int. Ed.*, 2006, **45**, 1729.
29. J. P. Costes, F. Dahan, and F. Nicodeme, *Inorg. Chem.*, 2001, **40**, 5285.
30. M. Lama, O. Mamula, G. S. Kottas, L. De Cola, H. Stoeckli-Evans, and S. Shova, *Inorg. Chem.*, 2008, **47**, 8000.
31. D. H. Olson, G. T. Kokotailo, and J. F. Charnell, *J. Colloid Interface Sci.*, 1968, **28**, 305.
32. Y. Wu, S. Morton, X. Kong, G. S. Nichol, and Z. Zheng, *Dalton Trans.*, 2011, **40**, 1041.
33. O. A. Gerasko, E. A. Mainicheva, M. I. Naumova, M. Neumaier, M. M. Kappes, S. Lebedkin, D. Fenske, V. P. Fedin, *Inorg. Chem.*, 2008, **47**, 8869.
34. X. Kong, L. Long, L. Zheng, R. Wang, and Z. Zheng, *Inorg. Chem.*, 2009, **48**, 3268.
35. B. Ma, D. Zhang, S. Gao, T. Jin, C. Yan, and G. Xu, *Angew. Chem. Int. Ed.*, 2000, **39**, 3644.
36. R. Wang, Z. Zheng, T. Jin, and R. J. Staples, *Angew. Chem. Int. Ed.*, 1999, **38**, 1813.
37. R. Wang, H. D. Selby, H. Liu, M. D. Carducci, T. Jin, Z. Zheng, and R. J. Staples, *Inorg. Chem.*, 2002, **41**, 278.
38. X. Kong, Y. Wu, L. Long, L. Zheng, and Z. Zheng, *J. Am. Chem. Soc.*, 2009, **131**, 6918.
39. O. Poncelet and L. G. Hubert-Pfalzgraf, *Polyhedron*, 1989, **8**, 2183.
40. E. H. Barash, P. S. Coan, E. B. Lobkovsky, W. E. Streib, and K. G. Caulton, *Inorg. Chem.*, 1993, **32**, 697.
41. M. T. Gamer, Y. Lan, P. W. Roesky, A. K. Powell, and R. Clerac, *Inorg. Chem.*, 2008, **47**, 6581.
42. M. Addamo, G. Bombieri, E. Foresti, M. D. Grillone, and M. Volpe, *Inorg. Chem.*, 2004, **43**, 1603.
43. M. Volpe, G. Bombieri, and N. Marchini, *J. Alloys Compd.*, 2006, **608–612**, 1066.
44. M. Volpe, G. Bombieri, D. A. Clemente, E. Foresti, and M. D. Grillone, *J. Alloys Compd.*, 2004, **374**, 382.
45. G. Xu, Z. Wang, Z. He, Z. Lu, C. Liao, and C. Yan, *Inorg. Chem.*, 2002, **41**, 6802.
46. L. G. Hubert-Pfalzgraf, N. Miele-Pajot, R. Papiernik, and J. Vaissermann, *J. Chem. Soc., Dalton Trans.*, 1999, 6127.
47. P. Toledano, F. Ribot, and C. Sanchez, *Comptes Rendus de l'Academie des Sciences Serie II: Mecanique Physique Chimie Sciences de la Terre et de l'Univers*, 1990, **311**, 1315.
48. X. Fang, T. M. Anderson, C. Benelli, and C. L. Hill, *Chem. Eur. J.*, 2005, **11**, 712.
49. M. R. Burgstein and P. W. Roesky, *Angew. Chem. Int. Ed.*, 2000, **39**, 549.
50. M. R. Buergstein, M. T. Gamer, and P. W. Roesky, *J. Am. Chem. Soc.*, 2004, **126**, 5213.
51. L. Messerle, D. Nolting, L. Bolinger, A. H. Stolpen, B. F. Mullan, D. Swenson, and M. Madsen, *Acad. Raiol.*, 2005, **12**, S46.
52. D. Weng, X. Zheng, and L. Jin, *Eur. J. Inorg. Chem.*, 2006, **20**, 4184.

53. J. C. A. Boeyens and J. P. R. De Villiers, *J. Cryst. Mol. Struct.*, 1972, **24**, 197.

54. C. G. Pernin and J. A. Ibers, *J Cluster Sci.*, 1999, **10**, 71.

55. C. G. Pernin and J. A. Ibers, *Inorg. Chem.*, 1997, **36**, 3802.

56. P. W. Roesky, C. Canseco-Melchor and A. Zulys, *Chem. Commun.*, 2004, 738.

57. D. S. Thompson, D. W. Thompson, and R. E. Southward, *Chem. Mater.*, 2002, **14**, 30.

58. C. Benelli and D. Gatteschi, *Chem. Rev.*, 2002,, **102**, 2369.

59. J.-B. Peng, Q.-C. Zhang, X. Kong, Y. Ren, L. Long, R. Huang, L. Zheng, and Z. Zheng, *Angew. Chem. Int. Ed.*, 2011, **50**, 10649.

60. S. Aime, M. Botta, and E. Terreno, *Adv. Inorg. Chem.*, 2005, **57**, 173.

61. P. Caravan, J. J. Ellison, T. J. McMurry, and R. B. Lauffer, *Chem. Rev.*, 1999, **99**, 2293.

62. S. B. Yu and A. D. Watson, *Chem. Rev.*, 1999, **99**, 2353.

63. M. K. Thompson, A. J. Lough, A. J. P. White, D. J. Ws, and I. A. Kahwa, *Inorg. Chem.*, 2003, **42**, 4828.

64. P. C. Andrews, T. Beck, C. M. Forsyth, B. H. Fraser, P. C. Junk, M. Massi, and P. W. Roesky, *Dalton Trans.*, 2007, 5651.

65. L. Natrajan, J. Pecaut, and M. Mazzanti, *Dalton Trans.*, 2006, 1002.

Lanthanide Alkoxides

Timothy J. Boyle and Leigh Anna M. Steele

Sandia National Laboratories, Albuquerque, NM, USA

1	Summary	197
2	Introduction	197
3	Synthetic Routes	197
4	Characterization	199
5	Conclusions	202
6	Glossary	203
7	Related Articles	203
8	Abbreviations and Acronyms	203
9	References	203

1 SUMMARY

The use of metal alkoxide [$M(OR)_x$] precursors continues to grow, driven mainly by their use in the development of complex ceramic materials (i.e., electroceramics, superconductors, and computer memories) but also as catalysts supports, biological applications, power sources, and many other research efforts. Of this particular family of compounds, the lanthanide alkoxides ([$Ln(OR)_3$]) have been found to be of interest because of a number of the inherent properties of these unique cations. In particular, the systematic changes in the cation size that the lanthanide contraction delivers without changing the charge allows for the fine-tuning of material systems. The first [$Ln(OR)_3$] was reported in 1958 and their study was greatly accelerated in the 1980s as they proved to be excellent precursors to luminescent materials. Since that time, there has been substantial effort to further develop this family of compounds; however, only a handful of reviews are available concerning the properties of [$Ln(OR)_3$] compounds.[1–4] This section details some of the general trends noted in these and other literature reports with a particular emphasis on the structural properties of the [$Ln(OR)_3$].

2 INTRODUCTION

A [$M(OR)_x$] is a derivative of an alcohol (HOR), where the proton has been replaced by a metal. The bonds of the M−O are typically considered to be polarized with the $\delta+$ residing on the metal and the δ- on the OR ligand. The degree of polarization is heavily dependent on the metal and the OR ligand. Therefore, it is not surprising that [$Ln(OR)_3$] is considered to be highly ionic in nature because of the high electropositive nature of the Ln and the high electronegativity of the oxygen. This polarization greatly reduces their solubility and volatility in comparison to other tervalent alkoxides. The molecular complexity of these precursors has been thoroughly investigated using a number of analytical tools. However, NMR data is often limited because of the paramagnetic nature of the Ln cations and results in a heavy effort associated with single crystal X-ray diffraction studies to elucidate the solid-state structure of these compounds. Therefore, the following discussion focuses on the homoleptic [$Ln(OR)_x$] species that have been crystallographically characterized.

A brief discussion of the synthetic routes to the [$Ln(OR)_x$] is presented in the following sections. The reader is urged to find the original literature that detail the different efforts necessary to successfully isolate the compounds discussed. The various problems/limitations associated with these strategies are addressed below.

3 SYNTHETIC ROUTES

The syntheses of [$Ln(OR)_x$] are air-sensitive because of their susceptibility to hydrolysis. Therefore, most work is performed under strict anhydrous conditions using glovebox and Schlenk line techniques. While the +2 and +4 states have

The Rare Earth Elements. Edited by David A. Atwood. © 2012 John Wiley & Sons, Ltd. ISBN 978-1-119-95097-4

been reported for the $[Ln(OR)_x]$ species, the general chemistry of the lanthanide elements is dominated by the tervalent oxidation state (Ln^{3+}). A number of synthetic routes are available to prepare the +3 homoleptic lanthanide alkoxides along with their Lewis base adducts. The majority of these pathways involve the reaction of various anionic ligands (i.e., alkoxide, halide, amide) with the alcohol of choice. Detailed descriptions of synthetic methodologies are available in the literature but a general description is provided below along with the various problems and limitations associated with these strategies.[1]

The simplest method for generating $[Ln(OR)_x]$ is termed *metal alcoholysis* (equation (1)). In this effort, the metal is dissolved in the alcohol (often in the presence of a catalysts (i.e., $HgCl_2$ or $Hg(C_6F_5)_2$). However, the effectiveness of the reaction between the Ln^0 and excess HOR is limited by the general nonreactivity of both precursors. The surface oxide layer that readily forms on the bulk metal significantly reduces the utility of this pathway. Of the diverse, readily available alcohols, the *iso*-propoxide ($OCHMe_2$ or OPr^i) derivatives are the most commonly reported product. Using the above methodology (equation (1)), ligand decomposition or adventitious water caused by the difficulties in drying alcohols often leads to alkoxy, oxo clusters, as evidenced by the numerous structurally characterized examples of $Ln_5(\mu_5\text{-O})(OCHMe_2)_{13}$ (Ln = Eu, Nd, Gd, Er, Yb). While equation (1) is the preferred route since this will avoid any number of other side products that plague other metal alkoxide synthesis routes (equations (2–4), it is often not effective because of the reduced reactivity based on oxide coatings or low acidity of the ROH employed.

Additional solventless, inert fluxes, or transmetalation/ligand metatheses have also become established routes for the synthesis of $La(OAr)_3$ derivatives and the more favored of these (equations (2–4)) are briefly discussed.

$$Ln^0 + 3\,HOR \longrightarrow \text{``}Ln(OR)_3\text{''} + 3/2\,H_2(g) \quad (1)$$

$$Ln(OR')_3 + 3\,H\text{-}OR \longrightarrow \text{``}Ln(OR)_3\text{''} + 3\,H\text{-}OR' \quad (2)$$

$$LnX_3 + 3\,A(OR) \longrightarrow \text{``}Ln(OR)_3\text{''} + 3\,AX \quad (3)$$

$$LnX_3 + 3\,ANR_2 \xrightarrow[-3\,AX]{} Ln(NR_2)_3 \xrightarrow[+3\,HOR]{} \text{``}Ln(OR)_3\text{''} + 3\,H\text{-}NR_2 \quad (4)$$

If the $[Ln(OR)_3]$ of interest are commercially available, one of the easiest syntheses is to react the precursor with the desired alcohol. The alcoholysis methodology involves a protonolysis reaction (exchange) of one or more coordinated alkoxide ligands (*alcohol exchange,* equation (2)) with another alcohol of interest. The extent of ligand substitution is dependent on numerous conditions, so an excess of alcohol followed by heating is typically used to induce complete exchange. However, this is not always successful and care must be taken to fully characterize the final product. Unfortunately, few $[Ln(OR)_3]$ are commercially available and their limited solubility often leads to solutions at low molarities being sold, which greatly restricts the use of equation (2).

The *halide metathesis* route (equation (3)) utilizes anhydrous lanthanide halides, LnX_3 complexes (X = Cl, Br, I), in exchange with alkali metal or thallium alkoxides. The general metathesis reaction (equation (3)) is often frustrated by the reduced solubility of the base-free LnX_3 compounds, as well as the retention of the halide, the metathesis metal, and/or oxo-group formation. An ammoniacal synthesis is sometimes employed to circumvent the low solubility of LnX_3. For this route, ammonia gas is condensed at low temperatures (i.e., dry ice/acetone bath) onto the LnX_3 precursor. The appropriate alkali metal (A°) is then added to precipitate the AX by-product, yielding a blue solution believed to be a short lived ''$Ln(NH_2)_x$'' species. After this, the desired HOR is added and the reaction allowed to stir, and the $[Ln(OR)_3]$ obtained by allowing the ammonia to slowly boil off as the reaction warms. This approach is similar to the aminoloysis route (equation (4)) with the amide generated *in situ*. Some reports indicate that the use of simple alkyl-substituted groups can lead to the incorporation of the alkali metal but a wide number of solvent-free aryloxides have been successfully generated by this method. However, there are some instances where the NH_3 was found to bind to the Ln metal center.

Of all the routes reported, the most useful, versatile, and reproducible for the production of $[Ln(OR)_x]$ compounds is the *aminolysis route* shown in equation (4). This is particularly true if the tris-amido ''$Ln(NR_2)_3$'' complex produced in step (i) is adequately purified by multiple recrystallizations or sublimation. The most common $Ln(NR_2)_3$ precursor is the trimethylsilyl amide [$NR_2 = N(SiMe_3)_2$] derivative, which has been crystallographically characterized as monomeric species supported via a distorted trigonal planar arrangement of amide ligands. The reaction with alcohols (step ii) usually proceeds rapidly in a variety of solvents and is often performed at low temperatures.

While the +3 oxidation state dominates the chemistry of the $[Ln(OR)_x]$, other oxidation states are available. Divalent lanthanide alkoxides $[Ln(OR)_2]$ are the next most abundant for the $[Ln(OR)_x]$ family. In general, two specific routes are favored for production of $[Ln(OR)_2]$ species: (i) metal alcoholysis or (ii) divalent precursors. Following equation (1) sometimes yields the +2 derivative; however, the conditions that favor this oxidation state have not been explained. Other routes to divalent $[Ln(OR)_2]$ that use the bulk metal include redox transmetallation/ligand exchange reactions, which employ either $Hg(C_6F_5)_2$ or thallium(I) phenolate reagents. The other often-used approach to synthesize $[Ln(OR)_2]$ species is to undertake the direct metathesis with [A(OR)] or aminolysis using Ln +2 derivatives. As can be discerned while synthetic routes to $[Ln(OR)_2]$ species are available, additional research is necessary to develop rational methods that yield $[Ln(OR)_2]$. For the +4 species, the Ln^{4+} cation is typically part of a charge separated (i.e., salt) system.

4 CHARACTERIZATION

As discussed previously, $[Ln(OR)_3]$ compounds are frustratingly difficult to identify using common analytical methodologies. This is due to several factors, including their tendency to retain spurious atoms or molecules (i.e., halides, alkali metals, solvents), the large cation to small charge on the alkoxide, and the ionic nature of the Ln–O bond. $[Ln(OR)_3]$ can easily decompose upon exposure to air or heat, making elemental analyses vary considerably from sample to sample. Further, these compounds often burn before melting, making classical melting point determinations difficult. In addition, most of the Ln cations possess a high degree of paramagnetism, rendering NMR spectroscopic investigations difficult. FTIR spectroscopic data is useful in determining some compositional information but distinguishing the various constructions is difficult. Therefore, single crystal X-ray diffraction studies have led the way in terms of understanding the solid state structural properties of this family of compounds.[5] The rest of the chapter discusses some of the

Table 1 General list of crystallographically identified $[Ln(OR)_3]$

Type	Ligand	Formula	Lanthanide	Nu	Coord.
Alkyl	OPr^i	$OCH(CH_3)_2$	Ce, Nd, Yb	2	O_h
			Eu(III, II)	4	6
	OBu^t	$OC(CH_3)_3$	La, Ce, Nd, Dy, Er	3	O_h
	ONep	$OCH_2C(CH_3)_3$	La, Ce, Pr, Nd, Sm, Eu(II), Gd, Tb, Dy, Ho, Er, Tm, Yb, Lu	4	sbp
	TBM	$OC(C(CH_3)_3)_3$	Ce, Nd	2	T_d
			Yb(II)	1	T_d
Di-substituted OPh	DMP	$OC_6H_3(CH_3)_2$-2,6	La	1	8
			Ce, Nd, Eu(II), Pr	2	O_h
			Dy, Er		O_h
			Dy	3	tbp
	DIP	$OC_6H_3(CH(CH_3)_2)$-2,6	La, Pr, Sm, Gd, Dy, Ho, Er, Lu	1	Varied
			La, Eu, Nd, Sm, Er, Dy, Pr	2	3LPS
	DBP	$OC_6H_3(C(CH_3)_3)_2$-2,6	Ce, Pr, Nd, Eu, Dy, Er, Sm, Yb, Lu	1	Varied
	DPhP	$OC_6H_3(C_6H_5)_2$-2,6	La, Ce, Pr, Nd, Yb, Lu, Yb, Tm, Sm, Ho, Eu(II)	1	Varied
			Yb(II/III), Yb(II), Eu(II/III)	2	Varied
	DBP-3,5	$OC_6H_3(C(CH_3)_3)$-3,5	La	4	tbp
			Nd	3	O_h/pbp
			Er, Yb, La	2	O_h, tp
	DBzP	$OC_6H_3(CH_2C_6H_5)_2$-2,6	La, Eu(II), Yb	2	sbp
Tri-substituted OPh	OMes	$OC_6H_2(CH_3)_3$-2,4,6	Nd, Eu, Yb	2	O_h
			Sm, Er, Yb	1	O_h
			Eu	3	O_h
			Er	4	tbp
	DBP-Me-4	$OC_6H_3(C(CH_3)_3)_2$-2,6-(CH_3)-4	Yb	2	Varied
			Sm, Eu(II), Yb(II/III)	1	tbp
			Nd, Er, Yb(II)	1	Td
	TBP	$OC_6H_2(C(CH_3)_3)_3$-2,4,6	Sm(II)	1	5
			Sm(II)	1	6
			Yb	1	sbp
			Yb(II)	1	sbp
	DBP-OMe	$OC_6H_2(C(CH_3)_3)_2$-2,6-(OCH_3)-4	Nd, Ho	1	T_d
			Sm, Yb	1	sbp
Tetra-substituted OPh	DPP-3,5-Me	$OC_6H(C_6H_5)_2$-2,6-$(CH_3)_2$-3,5	Yb	1	Tp
			Yb(II)	1	tbp
	$DPP-3,5-Bu^t$	$OC_6H(C_6H_5)_2$-2,6-$(C(CH_3)_3)_2$-3,5	Yb	1	Tp
			—	—	—
	DPP-3,5-Ph	$OC_6H(C_6H_5)_4$-2,3,5,6	Yb	1	sbp
Siloxides	TMS	$OSi(CH_3)_3$	Nd	4	O_h
	TPS	$OSi(C_6H_5)_3$	La, Ce, Pr, Sm, Dy, Er	1	O_h
			Ce, Dy, Er	2	Varied

O_h, octahedral; sbp, square base pyramidal; T_d, tetrahedral; 3LPS, 3-legged piano stool; tbp, trigonal bipyramidal; pbp, pentagonal bipyramidal; tp, trigonal pyramidal; sbp, square base pyramidal.

more general trends noted for the various sub-groups of $[Ln(OR)_3]$.

Table 1 gives an abbreviated listing of the crystallographically characterized homoleptic $[Ln(OR)_3]$ reported.[1] Again, this is not meant to be a complete listing of the numerous ligand variations but to give an overview of the existing structures. There are two major groups that these alkoxide ligand sets can be broken down into: (i) alkyl and (ii) aryloxides, with the latter being the predominant section. The rest of this chapter describes some of the rich and diverse structures observed for the $[Ln(OR)_3]$ species.

4.1 Alkyl Compounds

For the numerous alkyl alkoxides isolated for $[Ln(OR)_3]$, only a handful of ligands have been investigated for a majority of the different Ln cations, including (i) OPr^i, (ii) *tert*-butoxides ($OC(CH_3)_3$ or OBu^t), (iii) *neo*-pentoxides ($OCH_2C(CH_3)_3$ or ONep), and (iv) tri-*t*-butyl methoxide ($OC(C(CH_3)_3)_3$ or TBM). This list omits the oxo species that are prevalent throughout the development of alkoxide compounds.

For the OPr^i homoleptic species, dinuclear complexes have been generated always with bound Lewis basic solvents (i.e., $HOPr^i$, THF, DME). The coordination of the Ln metals with a homoleptic OPr^i ligand set was found to adopt an octahedral (O_h) arrangement. The number of OPr^i derivatives increases dramatically when the oxo species are included. An unusual tetranuclear Eu(II/III) OPr^i species has been reported with seven-coordinated metal centers adopting a ''butterfly'' arrangement. Figure 1 shows the structure plot of this complex. For all the figures in this section, the O and C atoms are drawn as red and white spheres, respectively. Each Ln cation has its own particular colored sphere. For example, in Figure 1, Er is pink with red O and white C atoms for the $HOPr^i$ ligand—the same color scheme is used for Figure 4(d).

Typically for transition metal complexes, as the steric bulk is increased on the ligand, both nuclearity and the number of uncharged bound ligands (i.e., solvents) decrease because of steric hindrance. For Ln, increasing the steric bulk from the OPr^i to the OBu^t ligand set results in a surprising increase in nuclearity but a reduction in the number of bound solvent ligands. These species have all been identified as trinuclear solvated species with O_h geometries around the metal centers.

The *neo*-pentoxide (ONep) ligand is often found to be more sterically demanding than most primary and even some secondary alcohols. This is thought to be due to an increased steric hindrance caused by rotation of the *t*-butyl groups around the methylene carbon. When the ONep ligand was introduced to the Ln cations, a tetranuclear species was isolated, independent of the size of the cation. For each of these compounds, the metal centers are oriented in a square arrangement and inter-connected via eight bridging μ-ONep ligands (four above and four below the plane of the Ln_4 fragment). Figure 2 shows the general structure type. The four remaining terminal ONep ligands radiate outward from each metal center (i.e., one per Ln ion). Each metal is therefore penta-coordinated, adopting a distorted square-based pyramidal geometry with a terminal alkoxide ligand occupying the apical position. This is surprising, since independent of the size of the cation (including Sc and Y—often added as a part of the Ln series), the general structure type is not varied; however, metrical data does show the changes wrought from the cation contraction. Further, no solvents were found bound to these metal centers. The only member of the $Ln(OR)_3$ that has every member crystallographically characterized is the neopentoxide derivative (ONep).[6]

The final dominant alkyl alkoxides are the tris(*tert*-butyl)methoxide (TBM) derivatives. These were found for the $+3$ to adopt a dimer structure with the bound solvents. For the Yb^{2+} cation, a monomer with the bound solvent was isolated. It is of note that other alkyl alkoxide ligands have been sporadically structurally investigated with the majority of these compounds yielding solvated dinuclear complexes. One interesting species is the methoxyethoxide (OEtOMe) derivative of Dy[7], which forms an unusual decanuclear star-shaped species (see Figure 3).

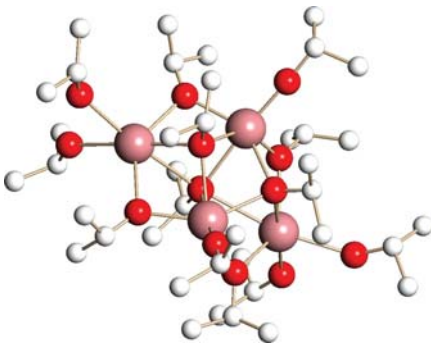


Figure 1 Structure plot of $Eu_4(\mu_4\text{-}OPr^i)(\mu_3\text{-}OPr^i)_2(\mu\text{-}OPr^i)_2(OPr^i)_3(H{-}OPr^i)_2{\cdot}H{-}OPr^i$

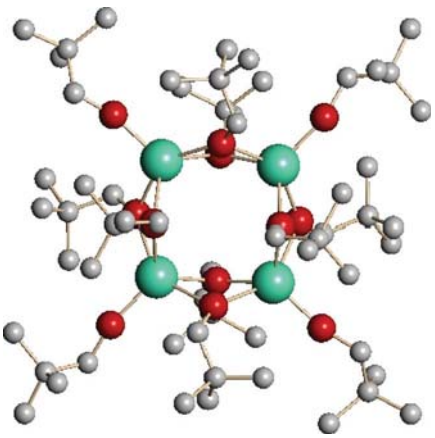


Figure 2 Structure plot of $[Ln(\mu\text{-}ONep)_2(ONep)]_4$

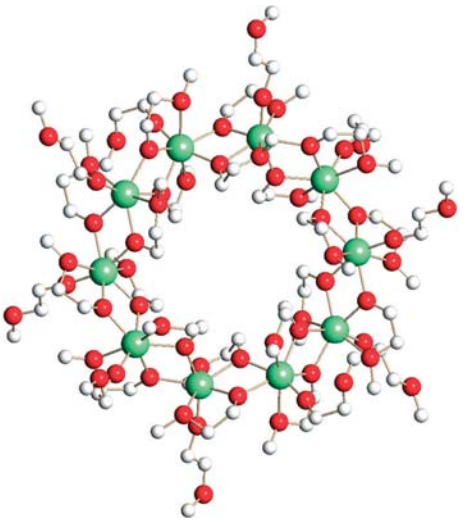


Figure 3 Structure plot of $[Dy(\mu\text{-OEtOMe})_2(OEtOMe)]_{10}$

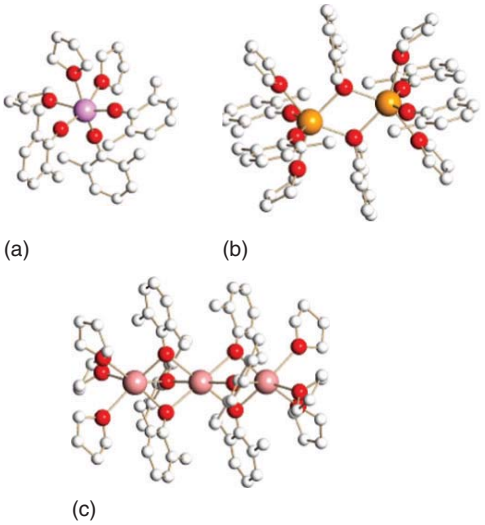


Figure 4 Structure plots of $Ln(DMP)_3(THF)_x$ derivatives showing the diverse arrangements available: (a) monomer for $Er(DMP)_3(THF)_3$, (b) dimer for $[Nd(\mu\text{-DMP})(DMP)_2(THF)_2]_2$, and (c) linear trimer for $Eu[(\mu\text{-DMP})_3\ Eu(THF)_3]_2$

4.2 Aryloxide Compounds

For the aryloxide derivatives, numerous substituents on the ring have been reported. This section focuses on the homoleptic alkyl derivatives of phenol (H−OPh or $H-OC_6H_5$). It is of note that no unsubstituted OPh species have been reported for the Ln compounds, which is most likely due to uncontrolled oligomerization causing low solubility. Further, only one monosubsituted alkyl species has been structurally characterized, the O_h bound monomeric $Ce(oBP)_3(THF)_3$, where ($oBP = OC_6H_4(Me)$-2). However, a great deal more effort has been put forth for the 2,6-disubstituted species.[5]

For the 2,6-dimethylphenoxide (DMP) species, a wide range of nuclearities are observed for the final species characterized, ranging from mono to di to tri (linear). All of these compounds have coordinated solvents that assist in minimizing oligomerization with all of the metal centers adopting either a five- or a six-coordination geometry. Shown in Figure 4 are some of the THF adducts and the structure types observed for these compounds.

Increasing the steric bulk of the 2,6-substituents on the OPh ring to an *iso*-propyl group or the 2,6-di (*iso*-propyl) phenoxide (DIP) species results in a reduced number of structure types—only monomeric and dinuclear species are observed as shown in Figure 5. All of the monomers were coordinated by a Lewis basic solvent such as THF, py, or NH_3; however, the degree of solvation varies based on the size of the Ln cation, which leads to a number of different coordination environments available. The observed dinuclear species are π-bound by the phenyl ring of the DIP ligand to the neighboring Ln cation. The increased steric bulk prevents isolation of any trinuclear complexes as of now.

Finally, the di-*tert*-butyl or DBP derivatives are all found to be monomeric, adopting 3−5 coordination environments. These derivatives are the few that can be isolated without solvents; however, they can be easily solvated by simple dissolution in a Lewis basic solvent. The monomeric nature is not solely due to the 2,6-*t*-butyl substituents, since the mesityloxide (OMes) species have been found to form both monomeric and dinuclear complexes. Figure 6 shows

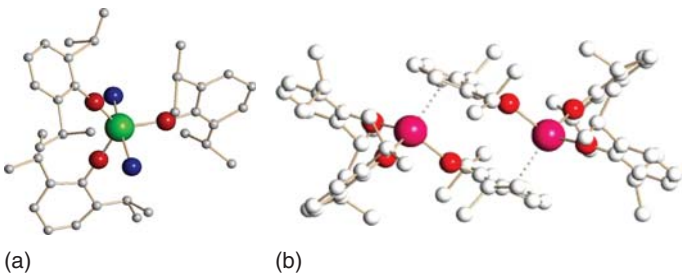


Figure 5 Structure plots of $Ln(DIP)_{3x}$ derivatives: (a) monomer as for $Dy(DIP)_3(NH_3)_2$ and (b) dinuclear shown for $[Nd(\eta\text{-DIP})(DIP)_2]_2$

representative monomeric DBP compound structures and the monomeric and dinuclear OMes compounds. Other alkyl derivatives are available but most involve a sterically hindering ligand (i.e., *t*-Bu groups) that results in monomeric species with bound solvents.

Additional 2,6-substitutents that possess phenyl rings are also available and have unusual interactions. These diphenyl (DPHP) and dibenzyl (DBzP) phenoxide ligands tend to reduce nuclearity using π-interactions to form unusual mono- and di-nuclear complexes. These can be simple monomers with no π-interactions to unsolvated monomers with a phenyl ring π-bound to the metal center. In addition, dinuclear species where the pendant phenyl rings of a μ-DPhP ligand of one metal center binds to that of the other. As expected, with the large cation size of the Ln cations, the various arrangements of these compounds can become quite complex with salt species being frequently reported. Figure 7 shows some of the structure types noted for the DPhP species. The 2,6-benzyl derivatives (DBzP) have been fully explored and were found to form dinuclear species that utilize bridging μ-DBzP ligands that π-bind back to one of the metal centers and/or the terminal DBzP π-binding to the metal center.[8] The various structural binding modes can be observed in Figure 8 for the Eu derivative. It is of note, once again, that this just scratches the surface of ''simple'' aryloxide species. Bi-, tri-, and tetra-dentate polysubstituted aryloxides have been successfully reacted with the various Ln cations. The reader should delve further into the existing literature to get specific structural information on any alcohol of interest.

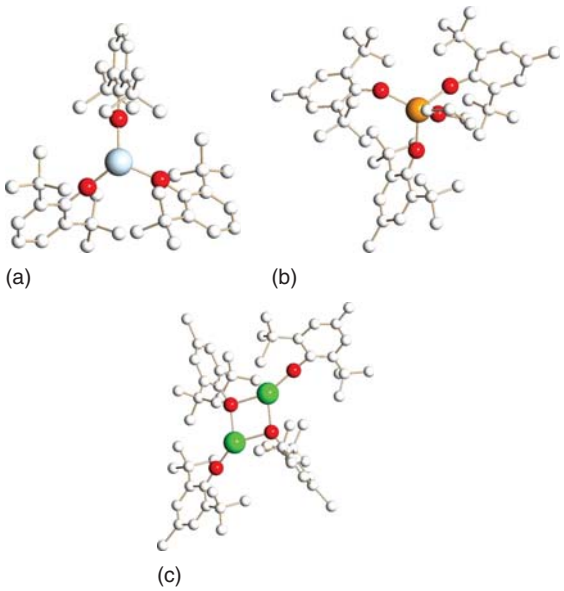


Figure 6 Structure plots of DBP and OMes derivatives shown for (a) $Pr(DBP)_3$, (b) $Nd(DBP\text{-}Me\text{-}4)_3(THF)$, and (c) $[Yb(\mu\text{-}DBP\text{-}Me\text{-}4)(DBP\text{-}Me\text{-}4)]_2$

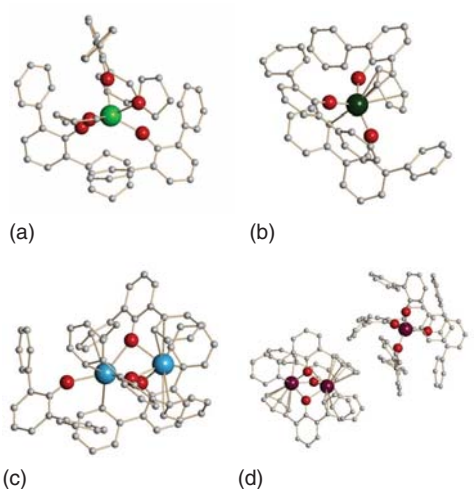


Figure 7 Structure plots of DPhP derivatives: (a) solvated monomer with no π-bonds shown for $[La(DPhP)_3(THF)_2]$, (b) monomer with π-bonds as in $[Tm(DPhP)_3]$, (c) dimer with π-bonds noted in $[Eu_2(\mu\text{-}DPhP)_3(DPhP)]$, and (d) salts as shown for $[Tb_2(\mu\text{-}DPhP)_3]^+\text{-}[Yb(DPhP)_4]$

4.3 Siloxides

One alternative set of ligands that have been explored are the siloxides ($OSiR_3$). These species induce a slight electronic variation in the alkoxide ligand from the introduction of Si in place of the C. The commercially available trimethyl and phenyl derivatives appear to give structural species that resemble their alkoxide analogs. A wide variety of silanols are available and more diverse structure species are expected as work with these ligands increases (see ***Rare Earth Siloxides***).

5 CONCLUSIONS

The lanthanide contraction allows for a controlled, systematic study of the inclusion of lanthanide cations

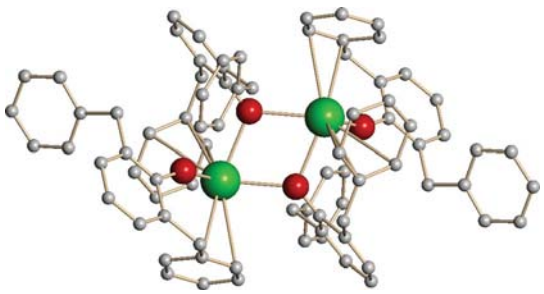


Figure 8 Structure plot of $[Eu(\eta, \mu\text{-}DBzP)(\eta\text{-}DBzP)(DBzP)]_2$

in materials to fine-tune their final properties. Because of this tenability, $[Ln(OR)_3]$ species have been used as precursors to a variety of ceramic oxide materials for use in such applications as scintillators, magnets, nanoparticles, bioimaging agents, luminescent, and thermal materials. The Ln cations typically adopt the +3 oxidation state; however, the +2 and +4 are accessible for a number of these metals. Synthesis of the $[Ln(OR)_x]$ compounds requires inert atmosphere conditions to avoid hydrolysis through circumjacent water. There are several synthetic routes to obtain useful precursors, with the aminolysis route yielding the highest purity compound. To characterize these often-paramagnetic $[Ln(OR)_3]$ compounds, NMR is typically of little use and FTIR mainly gives information about the ligand, so single crystal X-ray structure analysis has dominated this area of research. Both alkyl and aryl alkoxides have been studied crystallographically and are summarized in Table 1. The structure types range from mononuclear to tetranuclear, with a wide range of coordination numbers. Many $[Ln(OR)_3]$ contain irregular geometric arrangements in addition to a wide range of coordination numbers, which necessitates the need for crystallographic characterization to fully understand the structure before it is employed in materials systems. It is important to note that this chapter discusses *only* a few of the many homoleptic, homocationic $[Ln(OR)_3]$ species, and none of the heteroleptic or heterocationic species that are available. The existing work on $[Ln(OR)_x]$ should lay the groundwork for an understanding of the exciting and diverse structure types that are possible with this family of compounds. Further, control over the nuclearity and arrangement can be achieved using steric substituents and solvents, which will lead to greater tailored materials.

6 GLOSSARY

Electroceramic: a group of metal oxide (ceramic) materials that are of interest due to their electrical properties, such as computer memories, high dielectric materials, and capacitors.

7 RELATED ARTICLES

Lanthanides: Coordination Chemistry; Luminescence; Lanthanide Oxide/Hydroxide Complexes; Rare Earth Siloxides; Organic Synthesis.

8 ABBREVIATIONS AND ACRONYMS

*o*MP = 2-methylphenoxide; DMP = 2,6-di-methyl phenoxide; DIP = 2,6-di-*iso*-propyl phenoxide; DBP = 2,6-di-*t*-butyl phenoxide; TBM = tri(*t*-butyl)methoxide; ONep = *neo*-pentoxide; [Ln(OR)x] = lanthanide alkoxide.

9 REFERENCES

1. T. J. Boyle and L. A. M. Ottley, *Chem. Rev.*, 2008, **108**, 1896.
2. L. G. Hubert-Pfalzgraf, *New J. Chem.*, 1995, **19**, 727.
3. R. C. Mehrotra, A. Singh, and U. M. Tripathi, *Chem. Rev.*, 1991, **91**, 1287.
4. R. Anwander, *Top. Curr. Chem.*, 1996, **79**, 149.
5. Conquest Version 1.14, Cambridge Crystallographic Data Centre: support@ccdc.cam.ac.uk or http://www.ccdc.cam.ac.uk (Version 5.32 Nov 2010).
6. T. J. Boyle, L. A. M. Ottley, S. D. Daniel-Taylor, L. J. Tribby, S. D. Bunge, A. L. Costello, T. M. Alam, J. C. Gordon, and T. M. McCleskey, *Inorg. Chem.*, 2007, **46**, 3705.
7. L. G. Westin, M. Kritikos, and A. Caneschi, *Chem. Commun.*, 2003, 1012.
8. M. L. Cole, G. B. Deacon, P. C. Junk, K. M. Proctor, J. L. Scott, and C. R. Strauss, *Eur. J. Inorg. Chem.*, 2005, 4138.

Rare Earth Siloxides

Clemens Krempner and Brian McNerney

Texas Tech University, Lubbock, TX, USA

1	Summary	205
2	Introduction	205
3	Properties of the Siloxide Ligand	206
4	Ln^{II} Siloxides	206
5	Ln^{III} Siloxides	206
6	Ln^{IV} Siloxides	211
7	Conclusions	211
8	Related Articles	212
9	Glossary	212
10	Acknowledgment	212
11	Abbreviations and Acronyms	212
12	References	212

1 SUMMARY

Rare earth siloxides, also referred to as rare earth silanolates or silyloxides, are molecular compounds of the general bond sequence Ln–O–SiR_3, where R = alkyl, aryl, silyl, alkoxy, or siloxy. These well-defined species are believed to be useful as precursor for silicate materials and heterogeneous catalysts as well as homogeneous catalysts in organic transformations. A brief discussion of the electronic and steric properties of various siloxide ligands used in the chemistry of rare earth siloxides is followed by a representation of important synthetic and structural aspects of divalent, trivalent, and tetravalent rare earth siloxides along with selected reactivity studies. Special emphasis is given to the chemistry of trivalent rare earth siloxides and involves a discussion of synthetic methods, structures, coordination modes, and important bond parameters of the Ln–O–Si bond sequence. Applications of some heteroleptic rare earth siloxides as homogeneous catalysts in the polymerization of isoprene and hydrosilylation of olefins are discussed briefly.

2 INTRODUCTION

The chemistry of rare earth siloxides, also referred to as rare earth silanolates or silyloxides, dates back to 1970, when Batwara and Mehrotra[1] reported the first synthesis of homoleptic and heteroleptic erbium and gadolinium trimethylsiloxides of the general formula $Ln(OSiMe_3)_n(OPr^i)_{3-n}$. These compounds were prepared by reacting trimethylsilylacetate with $Ln(OPr^i)_3$ via transesterification and were characterized by elemental analysis and infrared (IR) spectroscopy. The molecular complexities of the homoleptic siloxides $[Gd(OSiMe_3)_3]_n$ ($n = 3–4$) and $[Er(OSiMe_3)_3]_n$ ($n = 3–5$) in benzene were measured, but their solid-state structures were not determined by X-ray crystallography. It took until 1989 for the first crystal structure of the octahedral cerium(IV) triphenylsiloxide, $(Ph_3SiO)_4Ce(DME)$, to be reported by Gradeff and coworkers.[2] Soon after the synthesis and structural characterization of further rare earth siloxides, the field developed rapidly, in part driven by the belief that rare earth siloxides have the potential of being useful as homogeneous catalysts in organic transformations (see ***Homogeneous Catalysis***), as molecular precursors for novel silicate materials, and as model compounds for silica-supported rare earth metal catalysts. The commercial availability of various stable organosilanols and rare earth metal precursor compounds has helped generate further progress in the field.[3–5] This chapter aims to take a more general view of the synthetic and structural aspects of rare earth metal siloxides in different oxidation states. Particular emphasis is given to the steric and electronic

eject

The Rare Earth Elements. Edited by David A. Atwood. © 2012 John Wiley & Sons, Ltd. ISBN 978-1-119-95097-4

influence of siloxide ligands on the structure, stability, and reactivity of the supported rare earth metals.

3 PROPERTIES OF THE SILOXIDE LIGAND

By far, the most popular siloxides employed as supporting ligands for rare earth metal ions are monoanionic Ph_3SiO^-, bidentate monoanionic $(Bu^tO)_3SiO^-$, dianionic $[(OSiPh_2)_2O]^{2-}$, and trianionic $[R_7Si_7O_9(O)_3]^{3-}$ formally derived from the silanols Ph_3SiOH, (**1**); $(Bu^tO)_3SiOH$, (**2**); $(HO)SiPh_2OSiPh_2(OH)$, (**3**); and the ''incompletely condensed'' POSS $R_7Si_7O_9(OH)_3$, (**4**), respectively. (Scheme 1). The structure and chemistry of these synthetically readily available silanols are well documented in the literature and have been reviewed thoroughly.[6–8]

Siloxides (R_3SiO^-) are electronically analogous to alkoxides (RO^-); they may act as $\sigma + 2\pi$ donors for metal ions and can formally be described as monoanionic $6e^-$ donors.[9] However, the $O_{p\pi}$-to-$M_{p\pi}$ back-bonding is reduced compared to aliphatic alkoxides owing to back-bonding of the O_p orbitals into fairly low lying and vacant silicon–carbon σ^* orbitals of the SiR_3 group. This in turn decreases the overall electron-donating power of siloxides and further increases the Lewis acidity of the metal center. However, the electronic and steric properties of R have a significant impact on the electron-donating property of R_3SiO^-. A good estimate of the electron-releasing properties of R_3SiO^- can be obtained from the relative acidity of its protonated form, R_3SiOH, which progressively decreases as R becomes more electropositive. This is consistent with the following order: $(siloxy)_3SiOH > (alkoxy)_3SiOH > (aryl)_3SiOH > (alkyl)_3SiOH > (silyl)_3SiOH$. As pointed out by Wolczanski,[10] siloxides behave electronically very similar to phenoxides, as both bind with somewhat more ionic character to early transition metals than aliphatic alkoxides. There is even more ionic character in the Ln–$OSiR_3$ bond than in the early TM–$OSiR_3$ bond because of the much larger ionic radii of the highly Lewis acidic rare earth metal ions and the fact that the 4f electrons are effectively shielded toward the influence of σ, π-donor ligands (see ***The Electronic Structure of the Lanthanides***).

4 LN^{II} SILOXIDES

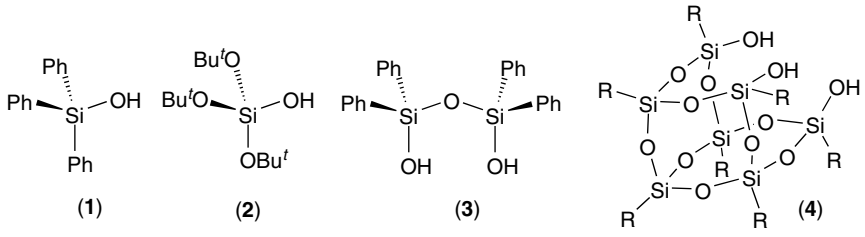
Relatively little is known about the chemistry of divalent rare earth siloxides, primarily because of the sensitivity of these cations to oxidation as reflected in their highly negative standard reduction potentials [$E^\circ_{(Ln^{3+}/Ln^{2+})} = -0.35$ V (Eu), -1.05 V (Yb), -1.55 V (Sm), -2.30 V (Tm), -2.50 V (Dy), and -2.6 V (Nd)]. The first report on a divalent rare earth siloxide dates back to 1996, when Hitchcock *et al.*[11] reported the synthesis and X-ray structure of dimeric $[(Bu^tMe_2SiO)_2Yb(DME)]_2$. The compound was prepared in 70% yield from the reaction of elemental ytterbium with Bu^tMe_2SiOH and DME in liquid ammonia.

The synthesis and chemistry of the first structurally characterized samarium(II) complexes supported by the bidentate monanionic siloxide, $(Bu^tO)_3SiO^-$, are shown in Scheme 2.[12] Reaction of $(Cp^*)_2Sm(THF)_2$ with $(Bu^tO)_3SiOH$ gave the dinuclear samarium(II) trisiloxide (**5**) in 93% yield, which served as a useful precursor for a variety of chemical transformations at both the Sm^{II} centers and the Cp* ligand. Most remarkable are reactions of (**5**) with the trivalent rare earth siloxides, $(Ph_3SiO)_3Sm(THF)_3$, $[(Bu^tO)_3SiO]_3Sm(THF)_2$, and $[(Bu^tO)_3SiO]_3Gd(THF)_2$, which with loss of THF gave the Cp*-bridged trinuclear Ln^{III}–Sm^{II} siloxides (**6**) in excellent yields. Treatment of (**5**) with divalent $Sm[N(SiMe_3)_2]_2(THF)_2$ generated the ionic samarium(II) hexasiloxide (**7**). X-ray analysis revealed that the two dinuclear samarium(II) trisiloxide subunits are bridged via the Cp* ligand to form a tetranuclear samarium(II) hexasiloxide cation.

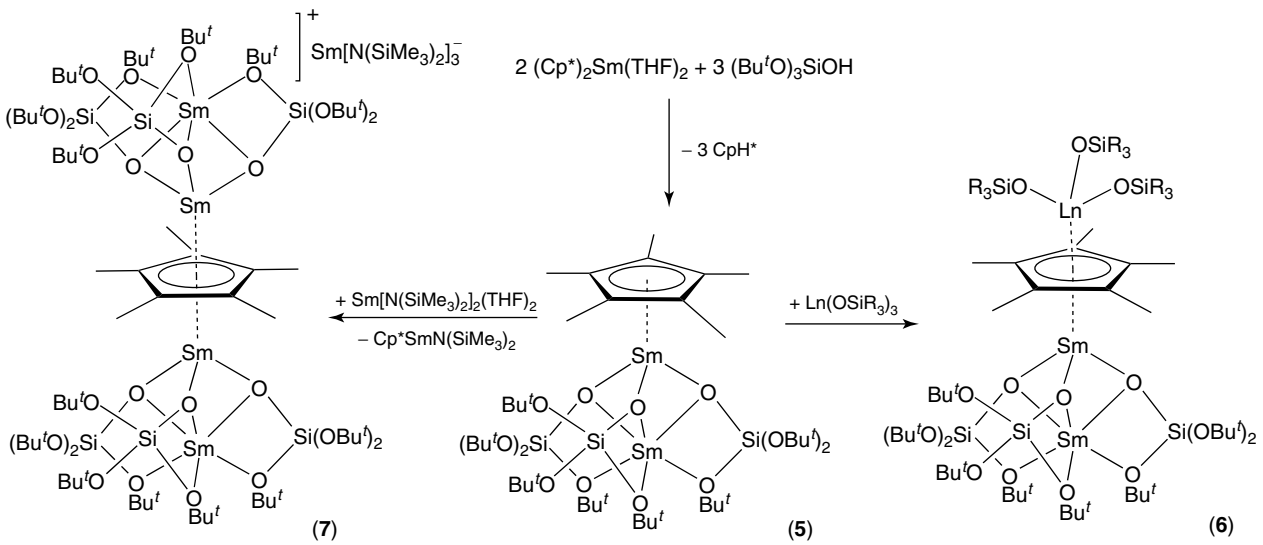
5 Ln^{III} SILOXIDES

5.1 Synthetic Methods

There are a number of synthetic pathways to trivalent rare earth siloxides and their Lewis base adducts such as salt metathesis, transesterification, acid–base chemistry, and silanolysis. Less frequently used are insertions of organo rare earth complexes into cyclic and linear siloxanes[13–15] and CO_2 insertion into rare earth silylamides.[16] Transesterification is a common route for the preparation of sterically less-hindered early transition metal trialkyl siloxides and involves



Scheme 1 Most commonly used silanols in the synthesis of rare earth siloxides



Scheme 2 Synthesis and reactivity of dinuclear samarium(II) siloxide (**5**)

treatment of transition metal alkoxides with trialkylsilyl acetates [17]. This method requires elevated temperatures but can be applied to rare earth metals and provides easy access to homoleptic trimethyl and triethyl siloxides in very high purities (equation 1). Deprotonation of silanols with rare earth metal alkyls, hydrides, alkoxides, or silylamides provides a second important and convenient synthetic route to homo- and heteroleptic siloxides in high yields and purities useful for metal organic chemical vapor deposition (MOCVD) applications.[18] These reactions often proceed smoothly at room temperature with elimination of highly volatile and easily removable by-products such as H_2, RH, ROH, or $HN(SiMe_3)_2$ (equations 3–5). This synthetic protocol also avoids separation of salts by filtration.

$$n\ R_3SiOAc + Ln(OR)_3 \rightarrow (R_3SiO)_nLn(OR)_{3-n} + n\,ROAc \quad (1)$$

$$n\ R_3SiOM + LnX_3 \rightarrow (R_3SiO)_nLnX_{3-n} + n\,MX \quad (2)$$

$$n\ R_3SiOH + LnR_3 \rightarrow (R_3SiO)_nLnR_{3-n} + n\,RH \quad (3)$$

$$n\ R_3SiOH + Ln(OR)_3 \rightarrow (R_3SiO)_nLn(OR)_{3-n} + n\,ROH \quad (4)$$

$$n\ R_3SiOH + Ln[N(SiMe_3)_2]_3 \rightarrow (R_3SiO)_nLn[N(SiMe_3)_2]_{3-n} + n\ HN(SiMe_3)_2 \quad (5)$$

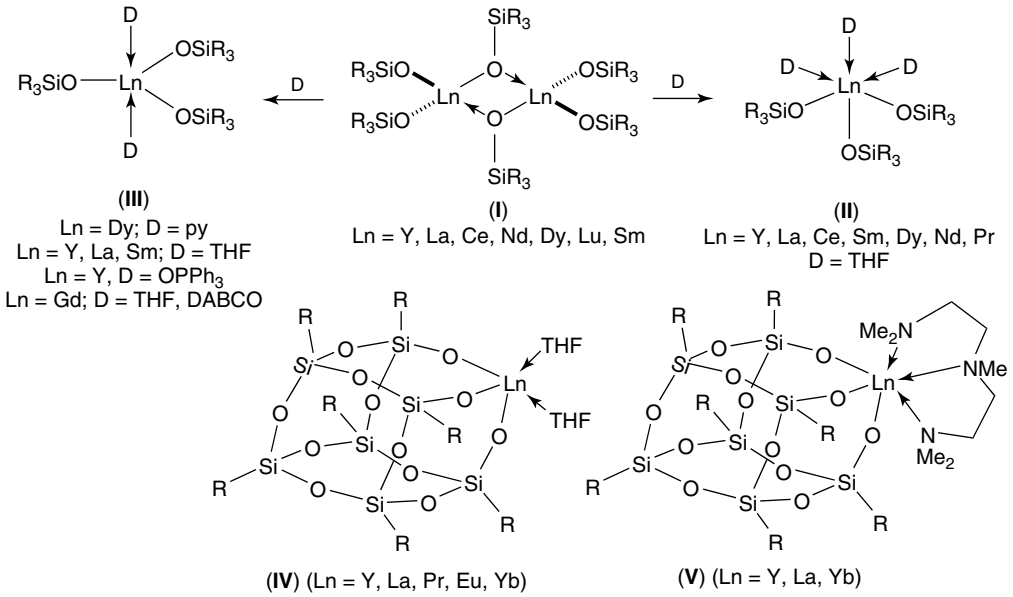
Reactions of anhydrous rare earth halides with alkali metal siloxides, R_3SiOM, yield hetero- and homoleptic rare earth siloxides via salt metathesis (equation 2). The aforementioned alkali metal siloxides can be conveniently generated from deprotonation of silanols with Bu^nLi or MH. However, these reactions require donor solvents such as THF and Et_2O and are often accompanied by solvent coordination to the final product or lead to the formation of salt adducts and ''ate'' complexes.[3–5]

5.2 Structure and Aggregation

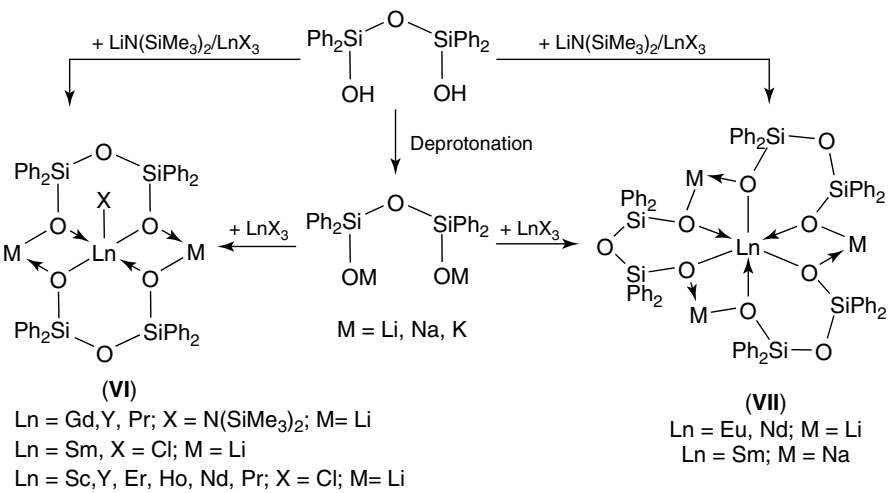
The structural chemistry of homoleptic trivalent rare earth siloxide shows striking similarities to that of rare earth alkoxides (see ***Lanthanide Alkoxides***).[19] Both classes of compounds form aggregated structures in the solid state and in solution, particularly when the metal ion is sterically accessible and coordinatively unsaturated (Scheme 3). Aggregation preferentially occurs via bridging; each of the bridging R_3SiO^- ligands may coordinate to two or more metal ions, which typically results in the formation of dimers or highly aggregated clusters. For example, the sterically less-hindered siloxide, $[Nd(OSiMe_3)_3]_4$, forms a tetramer in the solid state.[20]

All bridged dimers feature a central Ln_2O_2 core (type **I**), which in the presence of strong donor molecules such as THF, DME, $OPPh_3$, or pyridine dissociate into mononuclear species with either octahedral (type **II**) or trigonal bipyramidal structures (type **III**). Similar structural motifs are found in cyclic silsesquioxane-based rare earth siloxides. In the presence of donors, distorted octahedral (**V**) or distorted trigonal bipyramidal complexes (**IV**) are formed, which in solution through loss of donor solvent may be in equilibrium with their respective dimers (see ***Lanthanides: Coordination Chemistry***).[3]

The structural chemistry of the dianionic disiloxide ligand, $[(OSiPh_2)_2O]^{2-}$, is somewhat different from the aforementioned systems as in all cases either spirocyclic ''ate'' complexes (type **VII**) or spirocyclic salt adducts (type **VI**) are formed with rare earth metal ions.[21–23] The formation of these two structural types is heavily dependent on the size of the rare earth ion and synthetic protocol applied (Scheme 4). Thus, the smaller ions Y^{3+} and Sc^{3+} preferentially form salt



Scheme 3 Common coordination modes for homoleptic rare earth siloxides



Scheme 4 Synthesis and structure of rare earth tetraphenyldisiloxane-1,3-diolates

adducts, whereas the larger ions Sm^{3+} and Nd^{3+} can form both types of siloxide complexes.

5.3 Ln–O–Si Bond Parameters

It is generally accepted that M–O distances are shorter for M–O–R groups that have M–O–C angles approaching 180° owing to ligand to metal π-bonding. The case of rare earth siloxides, however, should be approached with caution, since silicon is more electropositive than carbon, and siloxides bind with somewhat more ionic character to rare earth metal ions. Table 1 displays the average Ln–O and Si–O distances and Ln–O–Si angles of selected dimeric and monomeric Ln^{III} triphenylsiloxides (**9–18**) along with cerium(IV) siloxide (**19**) and aluminum(III) siloxide (**8**). From a comparison of these data, some general trends can be discerned. (i) All triphenylsiloxides have large average Ln–O–Si angles ranging from 164 to 178°. (ii) The terminal Ln–O distances of the bridging dimers (**9–11**) and the Ln–O distances of the monomeric species (**12**–**17**) follow the expected size-dependent trend; as the size of Ln^{3+} decreases across the series, the Ln–O distance decreases monotonically. (iii) Owing to their lower coordination number, (**9–11**) have terminal Ln–O distance that are 5–7 pm shorter than the average Ln–O distances for (**12**), (**14**), and (**16**), respectively.

Table 1 Selected average atom distances (pm) and angles (°) of various rare earth siloxides

	Compound	Oxidation state	CN	M–O	Si–O	M–O–Si
(**8**)	$(Ph_3SiO)_3Al(THF)$	+3	4	170	161	153
(**9**)	$[(Ph_3SiO)_3Y]_2$	+3	4	206	161	178
(**10**)	$[(Ph_3SiO)_3Ce]_2$	+3	4	217	163	164
(**11**)	$[(Ph_3SiO)_3Dy]_2$	+3	4	207	161	169
(**12**)	$(Ph_3SiO)_3Y(THF)_3$	+3	6	213	158	172
(**13**)	$(Ph_3SiO)_3La(THF)_3$	+3	6	223	160	173
(**14**)	$(Ph_3SiO)_3Ce(THF)_3$	+3	6	222	160	174
(**15**)	$(Ph_3SiO)_3Sm(THF)_3$	+3	6	217	159	175
(**16**)	$(Ph_3SiO)_3Dy(THF)_3$	+3	6	213	159	174
(**17**)	$(Ph_3SiO)_3Dy(py)_2$	+3	5	214	157	178
(**18**)	$[(Ph_3SiO)_4Y(DME)][K(DME)_4]$	+3	6	217	158	169
(**19**)	$(Ph_3SiO)_4Ce(DME)$	+4	6	211	162	174

(iv) Upon increasing the formal oxidation state of Ce from (III) in (**14**) to (IV) in (**19**), the Ce–O distance significantly shortens from 222 to 211 pm, while the Si–O distance slightly elongates from 160 to 162 pm. (v) The Ln–O distance increases if the formal oxidation state does not change but the number of triphenylsiloxides bound to the metal ion increases, as is seen from a comparison of the Y–O distances of yttrium siloxide (**12**) with anionic species (**18**).

A comparison of the Ln–O distances of rare earth siloxides and alkoxides is complicated by a lack of structural information on alkoxides that have similar steric properties to triphenylsiloxides. However, according to a search in the **Cambridge Database**, the Ln-O distances of aliphatic rare earth alkoxides appear to be somewhat smaller, consistent with the increased overall electron-releasing properties of alkoxides relative to siloxides.

5.4 Reactions Involving Ln–OSiR$_3$ Bond Cleavage

Mehrotra *et al*.[1] studied the hydrolytic cleavage of the Ln–O bond of rare earth trimethylsiloxides and found that these compounds hydrolyze at a much lower rate than aliphatic rare earth alkoxides (see ***Lanthanide Oxide/Hydroxide Complexes***). This was attributed by the authors to the water-repellent properties of the hydrophobic trimethylsilyl group. Similar observations have been made by Bradley *et al*., who investigated the partial hydrolysis of early transition metal alkoxides and trimethylsiloxides to soluble, oligomeric, and polymeric oxo(alkoxide)s and oxo(siloxide)s.[24] Kornev *et al*. studied reactions of the homoleptic lanthanum and gadolinium siloxides (**20**) and (**21**) with CO_2 (equations 6 and 7).[25] Clean formation of the monosilyl and trisilyl carbonate complexes (**22**) and (**23**) resulting from insertion of CO_2 into Ln–O bonds was observed in high yields. Carbonate formation via CO_2 insertion does not seem to appear in the homoleptic siloxides $[Pr(OSiMe_3)]_n$ and $[Nd(OSiMe_3)]$ generated from reactions of excess CO_2 with $Pr[N(SiMe_3)_2]_3$ and $Nd[N(SiMe_3)_2]_3$, respectively[16] The propensity of (**20**) and (**21**) to readily incorporate CO_2 may arise from the better electron-releasing properties of $(Me_3Si)_3SiO^-$ as opposed to Me_3SiO^-. This in turn might facilitate nucleophilic attack of CO_2 by the siloxide ligand (see section 5.3). It should be noted that CO_2 readily inserts into rare earth phenoxides to generate stable carbonate complexes. These species could be involved as the actual catalysts in the copolymerization of CO_2 with epoxides.[26]

$$[(Me_3Si)_3SiO]_3La(THF)_2(\mathbf{20}) + 3CO_2 \rightarrow [(Me_3Si)_3SiOCO_2]_3La(THF)_2(\mathbf{22}) \quad (6)$$

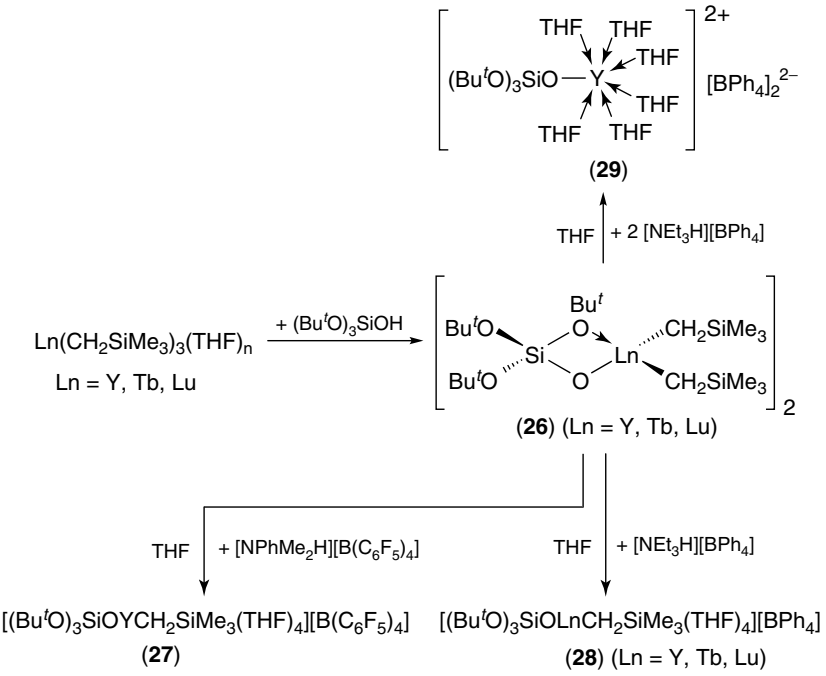
$$[(Me_3Si)_3SiO]_3Gd(THF)_2(\mathbf{21}) + CO_2 \rightarrow [(Me_3Si)_3SiO]_2Gd[O_2COSi(SiMe_3)_3](THF)_2(\mathbf{23}) \quad (7)$$

$$[(R_3SiO)_3Ln]_2(\mathbf{24}) + 6A1Me_3 \rightarrow (R_3SiO)Ln(AlMe_4)_2(AlMe_3)(\mathbf{25}) \quad (8)$$

Anwander and coworkers investigated reactions of various dimeric Ln siloxides (**24**) (Ln = Y, La, Nd, Lu) with excess $AlMe_3$. The formation of a multitude of products arising from Ln–OSiR$_3$ bond cleavage was noted. Only in the case of $\{[(Bu^tO)_3SiO]_3La\}_2$, (**24**), could a single product, $[(Bu^tO)_3SiOLa(AlMe_4)_2(AlMe_3)]$, (**25**), be isolated and structurally fully characterized.[27] A selective and more convenient route to (**25**), with Ln = La, Ce, Pr, Nd, is provided via reactions of $[Ln(AlMe_4)_3]$ with 1 equiv. of $(Bu^tO)_3SiOH$. Complexes (**25**) (Ln = Ce, Pr, Nd) in combination with Et_2AlCl as cocatalyst showed high catalytic activities in the polymerization of isoprene but exhibited an inferior performance compared to its counterpart, $Ln(AlMe_4)_3$ (Ln = Ce, Pr, Nd) (see ***Homogeneous Catalysis***).[28,29]

5.5 Siloxides as Spectator Ligands

There are only a few studies of siloxides serving as spectator ligands in the chemistry of trivalent rare earth metal complexes. In an attempt to design robust precatalysts for the hydrosilylation of olefins, Okuda *et al*. prepared several rare earth complexes supported by the siloxide ligand, $(Bu^tO)_3SiO^-$ (Scheme 5).[30] Reaction of $[Ln(CH_2SiMe_3)_3(THF)_n]$ (Ln = Y, Tb, Lu) with $(Bu^tO)_3SiOH$ afforded the dimeric siloxides (**26**). Addition



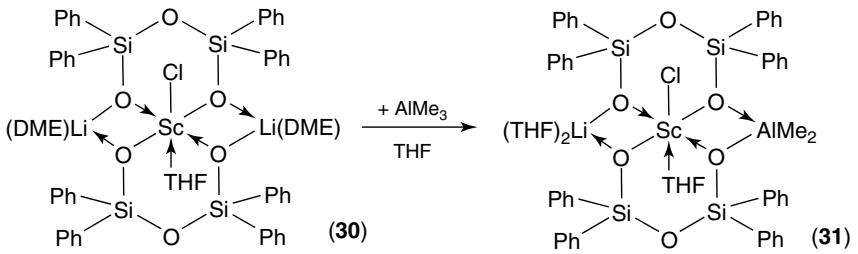
Scheme 5 Synthesis of neutral and cationic rare earth siloxides

of 1 equiv. of $[NMe_2PhH][B(C_6F_5)_4]$ and $[NEt_3H][BPh_4]$ allowed for the synthesis of the monocationic species (**27**) and (**28**), respectively, in good yields. Treatment of (**26**) (Ln = Y) with 2 equiv. of $[NEt_3H][BPh_4]$ gave the dicationic yttrium siloxide (**29**), of which the solid-state structure was determined. X-ray data revealed that none of the Bu^{t}O groups bridge to the central yttrium dication and that the Y–O distance (207 pm) of (**29**) is somewhat shorter than that of the bridging dimer (**26**) (Ln = Y) with 211 pm.

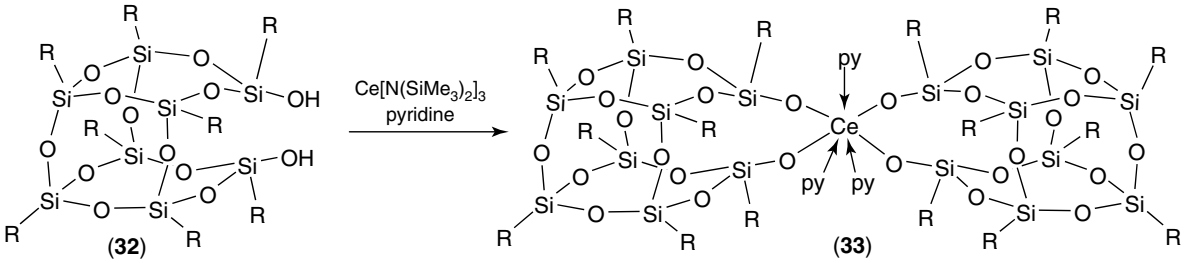
The yttrium siloxides (**26**) and (**27**) showed catalytic activity in the hydrosilylation of 1-decene. However, the neutral complex, $\{[(Bu^tO)_3SiO]Y(CH_2SiMe_3)_2\}_2$, (**26**), was far superior to their cationic counterpart (**26**) as it completely catalyzed the hydrosilylation of 1-decene by $PhSiH_3$ at room temperature within 2 h. Cationic (**27**), under similar conditions, only gave a 30% conversion after 20 h and (**28**) did not show any activity at all. The poor performance of the cationic yttrium siloxide species was presumed to be due to their rapid decomposition during the catalytic process (see ***Homogeneous Catalysis***).

Edelmann *et al*. recently reported **the** reaction behavior of the heterotrimetallic lithium–scandium–lithium siloxide (**30**) toward $AlMe_3$, $GaMe_3$, and $InMe_3$, respectively (Scheme 6).[31] In case of excess $AlMe_3$, selective replacement of one of the lithium ions by a cationic $AlMe_2$ **unit** occurred, rather than nucleophilic displacement of the chloride bound to scandium by a methyl group was observed.

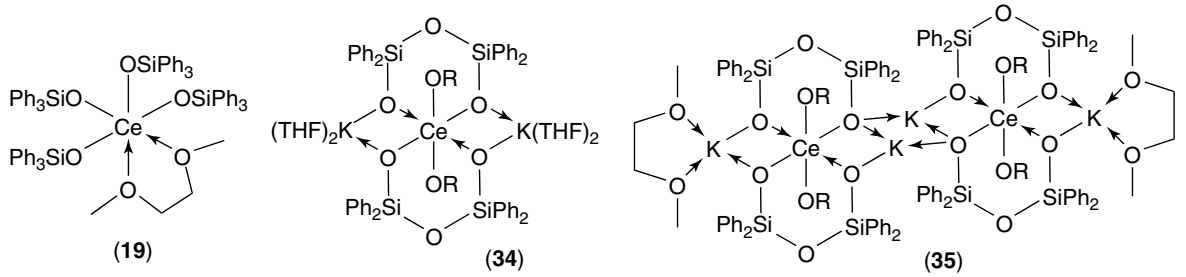
The molecular structure of the isolated product could unambiguously be identified by X-ray analysis as the heterotrimetallic lithium–scandium–aluminum siloxide (**31**). The selective formation of (**31**) is promising insofar as this synthetic strategy may open the door to the preparation of a wide variety of heterotrimetallic siloxides with perhaps interesting electronic and magnetic properties, from readily available salt adducts of rare earth siloxides.



Scheme 6 Reaction of heterotrimetallic scandium siloxide (**30**) with $AlMe_3$



Scheme 7 Synthesis of cerium(IV) siloxide (**33**)



Scheme 8 Coordination modes of cerium(IV) siloxides characterized by X-ray analysis

6 Ln^{IV} SILOXIDES

Similar to alkoxide ligands, siloxides stabilize oxophilic metals in high oxidation states most likely via additional ligand to metal π-bonding of the two O_p lone pair orbitals. Therefore, it is not surprising that cerium, the only rare earth metal that can exist in oxidation state (IV) in aqueous solution, forms stable tetravalent complexes even with less sterically hindered siloxides (see ***Tetravalent Chemistry: Inorganic***).[2,32,33] For example, $(Ph_3SiO)_4Ce(DME)$, (**19**), derived from the reaction of $Ce(OPr^i)_4$ with Ph_3SiOH, is an air and thermally stable compound being resistant to hydrolysis.[32] The remarkable stability of (**19**) parallels some titanium(IV) siloxides, which have also shown high thermal and hydrolytic resistances.[9] Synthetic routes to cerium(IV) siloxides are displayed in equations (9) and (10), and involve the use of either $(NH_4)Ce(NO_3)_6$ or cerium tetraalkoxides as precursor compounds in classical salt metathesis or silanolysis reactions.

$$6\,R_3SiOM + (NH_4)_2\,Ce(NO_3)_6 \rightarrow (R_3SiO)_4\,Ce + 2NH_3 + 2R_3SiOH + 6MNO_3 \quad (9)$$

$$n\,R_3SiOH + Ce(OR)_4 \rightarrow (R_3SiO)_n\,Ce(OR)_{4-n} + n\,ROH \quad (10)$$

Edelmann *et al*. recently reported the reaction of disilanol (**32**) with $Ce^{III}[N(SiMe_3)_2]_3$ in the presence of excess pyridine to surprisingly produce the product of oxidation, heptacoordinate cerium(IV) siloxide (**33**), in yields of 67% (Scheme 7).[33] Interestingly, the low oxidation state uranium precursors, $(COT)_2U$ (COT = η_8-C_8H_8), and UCl_4 react with $R_7Si_7O_9(OH)_3$, (**4**), to generate the homoleptic uranium(VI) siloxide $[R_7Si_7O_{12}]_2U$ exclusively upon oxidation.[3] Although the identity of the oxidizing agent remained unclear (no elemental oxygen was present), this type of oxidative silanolysis of cerium(III) precursor compounds could provide a convenient synthetic alternative in the synthesis of various homo- and heteroleptic cerium(IV) siloxides.

Scheme 8 displays all cerium(IV) siloxides characterized in the solid state by X-ray crystallography. In the presence of strong donor molecules such as THF, DME, or pyridine, monomeric and dimeric species with either octahedral (**19, 34, 35**) or distorted pentagonal bipyramidal structures (**33**) are formed (see ***Lanthanides: Coordination Chemistry***).[34]

7 CONCLUSIONS

Siloxide ligands are able to coordinate to rare earth metals in various oxidation states and coordination numbers to primarily form mono- and dinuclear complexes. In particular, the synthetic and structural chemistry of trivalent rare earth siloxides are well documented in the literature and show analogies with rare earth alkoxides. It is fair to state, however, that the field of divalent and tetravalent rare earth siloxides is poorly developed and that applications pertaining to the design of siloxide-based homogeneous and heterogeneous rare earth metal catalysts as well as the development of novel silicate-based materials are scarce. Although the few results of the catalytic activity of some of the rare earth siloxides in olefin

hydrosilylation and isoprene polymerization are promising, further research on the design of new robust siloxide ligands that help stabilize the active rare earth metal center is needed.

8 RELATED ARTICLES

Homogeneous Catalysis; Lanthanides: Coordination Chemistry; Lanthanide Alkoxides; Lanthanides: Coordination Chemistry; Tetravalent Chemistry: Inorganic; The Electronic Structure of the Lanthanides.

9 GLOSSARY

Homoleptic: A metal compound with all ligands identical.

Heteroleptic: A metal compound with at least two different ligands.

Ate complex: A salt formed by reaction of a Lewis acid with a base in which the central atom increases its coordination number.

10 ACKNOWLEDGMENT

The support by Texas Tech University is greatly acknowledged.

11 ABBREVIATIONS AND ACRONYMS

Ac = acetyl; Bu^t = tertiary butyl; CN = coordination number; Cp* = pentamethylcyclopentadienyl; DME = 1,2-dimethoxyethane; DABCO = 1,4-diazabicyclo[2.2.2] octane; Eq. = equation; equiv = equivalent(s); Et = ethyl; IR = infrared (spectroscopy); Ln = rare earth metal (Sc, Y, La; Ce–Lu); M = metal; MOCVD = metal organic chemical vapor deposition; Pr^i = isopropyl; Py = pyridine; R = alkyl; Ar = aryl; THF = tetrahydrofuran; TM = transition metal; X = halide.

12 REFERENCES

1. J. M. Batwara and R. C. Mehrotra, *J. Inorg. Nucl. Chem.*, 1970, **32**, 411.
2. P. S. Gradeff and K. Yunlu, *Polyhedron*, 1989, **8**, 1001.
3. V. Lorenz, A. Fischer, S. Gießmann, J. W. Gilje, Y. Gun'ko, K. Jacob, and F. T. Edelmann, *Coord. Chem. Rev.*, 2000, **206–207**, 321.
4. V. Lorenz and F. T. Edelmann, *Adv. Organomet. Chem.*, 2005, **53**, 101.
5. V. Lorenz, A. Edelmann, S. Giessmann, C. G. Hrib, S. Blaurock, and F. T. Edelmann, *Z. Anorg. Allg. Chem.*, 2010, **636**, 2172.
6. P. D. Lickiss, *Adv. Inorg. Chem.*, 1995, **42**, 147.
7. P. D. Lickiss, in 'The Chemistry of Organo Silicon Compounds', eds. Z. Rappoport and Y. Apeloig, John Wiley & Sons, New York, 2001, Vol. 3 p. 695.
8. V. Chandrasekhar, R. Boomishankar, and S. Nagendran, *Chem. Rev.*, 2004, **104**, 5847.
9. C. Krempner, *Eur. J. Inorg. Chem.*, 2011, **11**, 1689.
10. P. T. Wolczanski, *Polyhedron*, 1995, **14**, 3335.
11. D. J. Duncalf, P. B. Hitchcock, and G. A. Lawless, *J. Organomet. Chem.*, 1996, **506**, 347.
12. M. Nishiura, Z. Hou, and Y. Wakatsuki, *Organometallics*, 2004, **23**, 1359.
13. X. Zhou, Z. Huang, R. Cai, L. Zhang, L. Zhang, and X. Huang, *Organometallics*, 1999, **18**, 4128.
14. W. J. Evans, T. A. Ulibarri, and J. W. Ziller, *Organometallics*, 1991, **10**, 134.
15. X. Zhou, W. Ma, Z. Huang, R. Cai, X. You, and X. Huang, *J. Organomet. Chem.*, 1997, **545–546**, 309.
16. Y. F. Radkov, E. A. Fedorova, S. Y. Khorshev, G. S. Kalinina, M. N. Bochkarev, and G. A. Razuvaev, *Zh. Obshch. Khim.*, 1986, **56**, 386.
17. D. C. Bradley and I. M. Thomas, *J. Chem. Soc.*, 1959, 3404.
18. R. D. Clark and A. K. Hochberg, U.S. Pat. Appl. Publ. US 20040044163 A 120040304 2004.
19. T. J. Boyle and L. A. M. Ottley, *Chem. Rev.*, 2008, **108**, 1896.
20. D. Mansfeld and M. Mehring, *Z. Anorg. Allg. Chem.*, 2005, **631**, 2429.
21. S. Giessmann, S. Blaurock, V. Lorenz, and F. T. Edelmann, *Inorg. Chem.*, 2007, **46**, 10383.
22. V. Lorenz, A. Edelmann, S. Blaurock, C. Hrib, and F. T. Edelmann, *C. R. Chimie*, 2010, **13**, 577.
23. V. Lorenz, A. Fischer, K. Jacob, W. Bruser, and F. T. Edelmann, *Chem.—Eur. J.*, 2001, **7**(4), 848.
24. D. C. Bradley, *Coord. Chem. Rev.*, 1967, **2**, 299.
25. A. N. Kornev, T. A. Chesnokova, E. V. Zhezlova, L. N. Zakharov, G. K. Fukin, Y. A. Kursky, G. A. Domrachev, and P. D. Lickiss, *J. Organomet. Chem.*, 1999, **587**, 113.
26. D. Cui, M. Nishiura, O. Tardif, and Z. Hou, *Organometallics*, 2008, **27**, 2428.
27. A. Fischbach, G. Eickerling, W. Scherer, E. Herdtweck, and R. Anwander, *Z. Naturforsch., B*, 2004, **59**, 1353.

28. M. Zimmermann, N. A. Froystein, A. Fischbach, P. Sirsch, H. M. Dietrich, K. W. Tornroos, E. Herdtweck, and R. Anwander, *Chem.—Eur. J.*, 2007, **13**, 8784.

29. A. Fischbach, M. G. Klimpel, M. Widenmeyer, E. Herdtweck, W. Scherer, and R. Anwander, *Angew. Chem. Int. Ed.*, 2004, **43**, 2234.

30. B. R. Elvidge, S. Arndt, T. P. Spaniol, and J. Okuda, *Dalton Trans.*, 2006, 890.

31. S. Giessmann, S. Blaurock, V. Lorenz, and F. T. Edelmann, *Inorg. Chem.*, 2007, **46**, 10956.

32. P. S. Gradeff, K. Yunlu, T. J. Deming, J. M. Olofson, R. J. Doedens, and W. J. Evans, *Inorg. Chem.*, 1990, **29**, 420.

33. Y. K. Gun'ko, R. Reilly, F. T. Edelmann, and H. Schmidt, *Angew. Chem. Int. Ed.*, 2001, **40**(7), 1279.

34. S. Giessmann, S. Blaurock, V. Lorenz, and F. T. Edelmann, *Inorg. Chem.*, 2007, **46**, 8100.

Thiolates, Selenolates, and Tellurolates

John G. Brennan

Rutgers, The State University of New Jersey, Piscataway, NJ, USA

1	Summary	215
2	Introduction	215
3	Organometallics	215
4	$Ln(ER)_2$ and $Ln(ER)_3$	216
5	Chalcogen-Based Cluster Chemistry	217
6	Molecular Approaches to Solid-State Materials	219
7	Notable Physical Properties	220
8	Glossary	221
9	Related Articles	221
10	Abbreviations And Acronyms	221
11	Conclusions	221
12	References	221

1 SUMMARY

This chapter summarizes, with examples, the fundamental types of compounds having bonds between lanthanides and the heavier group 16 elements (S, Se, and Te). It will include a description of organometallic compounds that have Ln–C bonds in addition to Ln–E bonds and ''homoleptic'' divalent ($Ln(ER)_2$) and trivalent ($Ln(ER)_3$) compounds. Polynuclear lanthanide compounds containing chalcogenido anions (E^{2-}, EE^{2-}, E_n^{2-}) are also described. These have grown in importance with the possibility of controlling and optimizing the near infrared (NIR) emission properties of Ln cluster materials. Molecular lanthanide chalcogenolates can also be used to prepare a wide assortment of solid state materials, from LnTe and $Ln_4Cd_2Se_8$ to LnF_3 or LnN.

2 INTRODUCTION

The chemistry of the lanthanide elements bound to the more electronegative chalcogen elements (E; E = S, Se, Te) has been investigated extensively, particularly in the past decade, because this unconventional combination of highly ionic metals and highly covalent ligands leads to materials with unique chemical and physical properties. What was once thought to be chemically impossible (at least in the absence of sterically saturating ancillary ligands) has since blossomed into an area in which the physical properties and the chemistry of compounds with Ln–E bonds can be controlled by varying Ln, E, and the steric/electronic properties of R. This subject was reviewed exhaustively in 1997,[1] and a review outlining the utility of these compounds in organic synthesis has also appeared.[2]

3 ORGANOMETALLICS

The first compounds with lanthanide–chalcogen bonds were prepared with ancillary Cp or Cp* ligands (see ***Trivalent Chemistry: Cyclopentadienyl***), because at the time it was believed that Cp steric demands were necessary to control chemical reactivity, and because the solubility of products in hydrocarbon solvents limited potential side reactions. Metathesis reactions[3] governed by the insolubility of alkali halides were initially investigated (Reaction 1), but eventually a host of synthetic approaches were successfully employed. Compounds have been prepared by reduction of RE-ER with divalent Ln (Reaction 2),[4–6] where the driving force of the reaction is increased stability associated

The Rare Earth Elements. Edited by David A. Atwood. © 2012 John Wiley & Sons, Ltd. ISBN 978-1-119-95097-4

with the greater electrostatic interaction of anions with trivalent Ln. Alternatively, there are examples in which elemental chalcogen inserts into a preformed Ln–C bond[7,8] of an organometallic species, for which the driving force is presumably the stability of the chalcogen-based anion (Reaction 3). Similar σ-bond metathesis (proton transfer) reactions[9–12] of lanthanide organometallics or hydrides with thiols proceed for the same reason, forming stable C–H bonds and chalcogen-based anions (Reaction 4) with a wide range of R (i.e., CH_3, C_5H_5).

$$Cp^*_2LnCl + NaER \rightarrow Cp^*_2Ln - ER + NaCl \quad (1)$$

$$Cp^*_2Ln + RE-ER \rightarrow Cp^*_2Ln - ER \quad (2)$$

$$Cp^*_2LnR + E \rightarrow Cp^*_2Ln - ER \quad (3)$$

$$Cp^*_2LnR + HER' \rightarrow Cp^*_2Ln - ER' + H - R \quad (4)$$

Compounds with Ln–E bonds were originally prepared in order to probe the nature of the Ln–E chemical bond, but it quickly became apparent that the overwhelming steric demands of the ancillary ligands made it impossible to extract bonding information, and so eventually a number of groups began to investigate the synthesis of ''homoleptic'' $Ln(ER)_2$ and $Ln(ER)_3$ chalcogenolate compounds.

4 $Ln(ER)_2$ AND $Ln(ER)_3$

The first report outlining the synthesis of a homoleptic product was the synthesis by Bochkarev of the divalent compound ($Yb(EBu)_2$; E = S, Se), prepared by a proton-transfer reaction of an amido precursor with HEBu.[13] This was followed by the metathetical synthesis[14] of $Ln(SR)_6^{3-}$ and compounds of the heavier chalcogenolates ($Ln(EC_6H_3R_3)_2$ (E = Se, Te; R = Me).[15–17] The structure of the thiolate compound was described, but structural characterization of selenolate and tellurolate compounds did not appear until later, when the $E-Si(SiMe_3)_3$ ligand[18–20] was introduced to the Ln field, and new synthetic approaches to complexes of the EPh ligand[21] were developed.

A number of chemically distinct R groups have also been introduced, with each R imparting unique chemical or physical properties to the resultant molecular complex. By far, the most useful ligand system is the EPh series,[21–30] because the ligand imparts adequate solubility in organic solvents and is commercially available for E = (S, Se), with TePh being easily prepared. With R = Ph, all Ln form stable $Ln(EPh)_3$ (E = S, Se), with the exception of Eu. The trivalent compounds are easily prepared in high yield by reduction of PhEEPh with elemental Ln (Reaction 5), and in Eu chemistry this reactivity stops at the stable divalent oxidation state for S, Se, and Te.[21,27] The instability of ''homoleptic'' Eu^{III} compounds was confirmed in metathesis chemistry, where reductive elimination of REER was observed (Reaction 6).

$$Ln + \frac{3}{2}PhEEPh \rightarrow Ln(EPh)_3 \quad (Ln = La - Lu, \text{ not Eu}) \quad (5)$$

$$Eu + PhEEPh \leftarrow Eu(EPh)_2 \leftarrow EuCl_3 + NaEPh \quad (6)$$

This chemistry is relatively straightforward, and the ability to span the entire lanthanide series provided an opportunity to establish how Ln and E influenced physical properties. It is clear that the larger Ln tend to form oligomeric species, while the smaller Ln favor the formation of molecular products, and that increasing the basicity of the chalcogen donor favors the formation of products in which the ER ligand bridged metal ions rather than adopting terminal bonding modes. In all of this work, the minimal steric requirements of the Ph group do not inhibit oligomerization, and so this chemistry always involves the presence of Lewis base solvents that saturate the Ln coordination sphere. While these products unfortunately never led to the observation of any interesting magnetic behavior (the magnetic characteristics of coordination polymers and discrete molecular compounds were indistinguishable), structural characterization of $(py)_3Yb(SPh)_3$ (Figure 1) revealed anomalous bond lengths[26] that are discussed later.

Trisubstituted arylchalcogenolates have also been investigated, with some very distinctive products. The first selenolates and tellurolates were prepared with metathesis using Yb, and more recently, there have been interesting descriptions of base-free compounds.[31,32] Here, the tendency of the R groups to increase solubility was used to prepare a compound with no solubilizing Lewis base solvents and because there are no alternative sources of electron density, the chalcogenolate ligands respond by coordinating to the Ln through the arene carbons.

Similar solubility can be obtained with the silylated chalcogenolates, for which there exist thoroughly characterized examples of bidentate phosphine stabilized

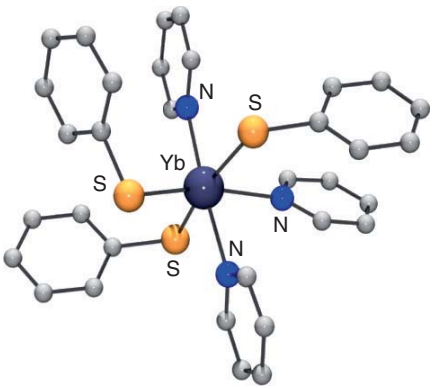


Figure 1 Bond distances in *mer*-octahedral LnA_3B_3 compounds such as $(py)_3Yb(SPh)_3$ pictured here reveal a trans influence that is thought to originate from a covalent interaction involving the Ln 5d orbitals

$Ln(ESi(SiMe_3)_3)_2$ and $Ln(ESi(SiMe_3)_3)_3$ (E = Se, Te) coordination compounds. Surprisingly, the steric ''bulk'' of this silylated chalcogenolate did not dramatically change the structural coordination chemistry, with $Ln(ER)_3$ still readily forming Lewis base coordination compounds[20] having coordination numbers that were little changed from related $Ln(EPh)_3$ products. In these E–Si–R_3 compounds, the potential energy surfaces that determine Ln–E–R bond angles are relatively shallow, and so the Ln–E–R angle simply increases to reduce ligand–ligand repulsions and permit the coordination of additional donor ligands. The solubilizing nature of this ligand was particularly useful in subsequent thermolysis chemistry, as discussed in the cluster section.

Fluorinated chalcogenolates have been investigated as an alternative approach to the synthesis of soluble products. The Teflon-like character of the C_6F_5 moiety reduces intermolecular attractions and leads to the formation of hydrocarbon-soluble products. Thiolates[33,34] have been investigated most extensively, and there are descriptions of both $Ln(SC_6F_5)_2$ and $Ln(SC_6F_5)_3$. These compounds have to be prepared with transmetallation reactions (Reaction 7), because attempts to reductively cleave disulfide bonds with elemental Ln leads to the formation of metal sources that appear to be passivated with a fluoride film.

$$2\ Ln + 3\ Hg(SC_6F_5)_2 \rightarrow Ln(SC_6F_5)_3 + Hg \qquad (7)$$

The fluorine substituents impact the structure of coordination compounds in two ways. First, by polarizing electron density away from the sulfur-based anion, the sulfur becomes less basic, and this lengthens the Ln–S bond relative to Ln–SPh. This reduced basicity also leads to the formation of fewer oligomeric structures because the sulfur anion cannot compete as effectively for access to Ln coordination spheres. Second, these compounds form dative Ln–F bonds for all but the smallest Ln. These interactions are absent in the analogous fluorinated alkoxide compounds,[35] and presumably originate with the electropositive character of the sulfur, which allows for more electron density to be located on the fluorine atoms. Similar dative interactions have been noted in other fluorinated systems,[36] but this is the only example that allows for comparisons of related donor atoms within a given row of the periodic chart. The analogous selenolates have been prepared recently,[37] and here the tendency for dative fluoride interactions is even more pronounced than in the isomorphous thiolates.

In order to probe the chemistry of the electronically important Eu^{III} ion, resonance-stabilized thiolates were explored. Of the simple chalcogenolates, only the pyridinethiolate (S-2-NC_5H_4, SPy) ligand has been used successfully in Eu(III) chemistry. Compounds with SPy have been prepared across the lanthanide series,[38] and again there is a tendency for the larger Ln to form more complicated species, while the smaller Ln readily form discrete uncharged species. Most significant here is the chemistry of Eu, for which divalent and trivalent compounds could be isolated from transmetallation reactions of Eu with $Hg(SPy)_2$ in pyridine.[39] Divalent $(py)_4Eu(Spy)_2$ and $(BIPY)(THF)Eu(Spy)_2$ were isolated as deep orange crystals, with the color attributed to the existence of an allowed Eu-to-ligand charge-transfer absorption. The Eu^{II} oxidized further and reduced Py–S–S–Py to form salts with $Eu(SPy)_4$ anions. These were also intensely colored, this time because of an allowed S-to-Eu charge-transfer excitation.[30] The redox-inactive Ln^{III} all formed compounds with colors that were characteristic of the Ln ion.

Similar resonance stability can be introduced with thiocarbamate (S_2CNR_2)[40–44] and thiocarboxylate (S_2CR)[45] compounds, which have garnered a significant amount of attention in recent years. These ligands, while not formally chalcogenolates (Ln–E–R, where R = $(S)CNR'_2$), have been included here because they produce compounds that are useful in materials synthesis. There are various approaches to the synthesis of thiocarbamates. These compounds can be isolated either as discrete molecular compounds or as salts, with the molecular species more desirable because they are relatively volatile. These ligands invariably adopt η^2 interactions with Ln, all with the negative charge equally delocalized over the two sulfur atoms.

5 CHALCOGEN-BASED CLUSTER CHEMISTRY

The chemistry of polynuclear lanthanide compounds (see ***Rare Earth Metal Cluster Complexes***) constructed with chalcogenido anions (E^{2-}, EE^{2-}, E_n^{2-}) has been evolving dramatically in the past decade, motivated by a fundamental interest in understanding how the physical properties of lanthanide compounds depend on particle size, and more recently, because of an interest in controlling and optimizing the NIR emission properties of Ln cluster materials.

The first example of this chemistry came from an investigation into the reactions of Cp^*_2Sm with elemental Se, which initially forms a triselenido product that eventually proceeds to give the ''spherical'' cluster $Cp^*_6Sm_6Se_{21}$ (Reaction 8).[46] This product is the result of multiple ligand redistribution reactions, and the serendipity with which the final product precipitates from hydrocarbon solution reflects one of the more frustrating aspects of this field, namely, the absence of control in determining the precise formulation of a product. The identify of a crystalline product is governed primarily by the relative solubility of the reaction products.

$$[Cp^*_2Sm]_2Se_3 \rightarrow Cp^*_6Sm_6Se_{11} + \cdots \qquad (8)$$

A second cluster description soon followed this original report, namely, the synthesis of $Ce_5Te_3(TeS(SiMe_3)_3$ via cleavage of a Te–Si bond and subsequent ligand redistribution in hexane.[18,20] This compound was isolated

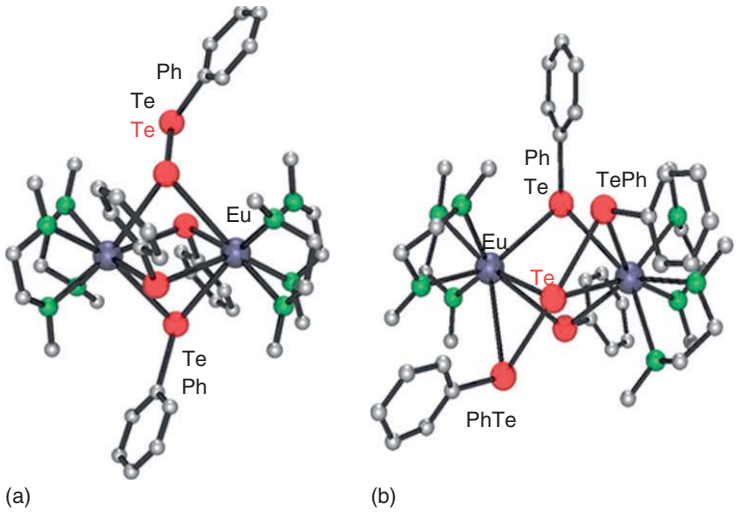


Figure 2 Divalent $Eu(TePh)_2$ reacts with elemental Te, first inserting Te into a Ln–Te bond (a) to form a TeTePh ligand, and then coupling to form $(PhTe–Te–TePh)^{2-}$ (b) that bridges two Eu^{II} ions

and structurally characterized, but the extreme instability of the products inhibited further work.

A more general approach to the synthesis and characterization of chalcogenido cluster compounds was subsequently developed in reactions of homoleptic lanthanide chalcogenolates with elemental chalcogen. Mechanistic insight into these reactions can be obtained in divalent Eu chemistry (Figure 2). Reactions of $Eu(TePh)_2$ with elemental Te results first in insertion of E to form a compound with an Eu–Te–Te–Ph connectivity, and heating this product results in migration of a second EPh to give a dimeric product with two Eu bridged by $(Ph–Te–Te–Te–Ph)^{2-}$. Further heating results in the elimination of Ph_2Te_2 to give chalcogenido clusters in what is formally a reduction of elemental Te and oxidation of TePh (Freedman *et al.*, unpublished results).

This ligand-based redox route represents the broadest available synthetic approach to LnE_x clusters, with the most commonly found structure being $(solvent)_8Ln_8E_6(E'Ph)_{12}$ materials (Figure 3),[47–56] which are adopted by La–Er with all possible combinations of E, E′, and solvent (E/E′ = S, Se, and solvent = THF or pyridine). These compounds have a cube of Ln, with the six faces of the cube caped by μ_4E, the 12 edges of the cube bridged by EPh, and a neutral donor solvent completing the primary coordination sphere. The smaller Ln form cubanes (i.e., $[(py)_2YbSe(SePh)]_4$) or derivatives (i.e., $(py)_8Yb_6Se_6(SePh)_6$), in which the Ln adopt octahedral geometries.[53]

In this chemistry, the identity of the resultant chalcogen anion depends on the ratio of Ln:E. Addition of E to a solution of $Ln(EPh)_3$ results first in the formation of clusters with E^{2-} ligands, with the further addition of E resulting in the formation of compounds with $(EE)^{2-}$ anions (Reaction 9). This reactivity is seemingly governed by electrostatic considerations favoring the formation of

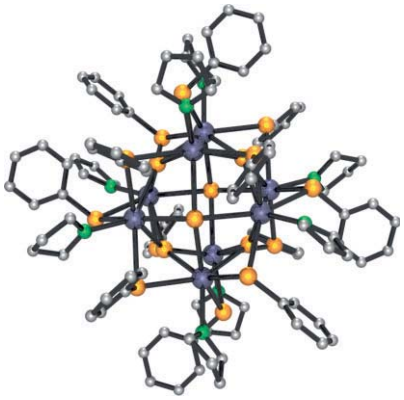


Figure 3 The octanuclear $(solvent)_3Ln_8E_6(EPh)_{12}$ clusters form in high yield for Ln = La–Er, E = S or Se, and solvent = THF or pyridine [grey, Ln; orange, Se; green, O(THF)]. The structures contain a cube of Ln, with the six faces capped by E^{2-} and the 12 edges bridged by EPh

divalent anions, with charge delocalized over two E a more stable configuration given the absence of significant covalent interactions that would effectively stabilize E^{2-}. This chemistry was found to be reversible,[49] as illustrated in Yb chemistry where the lanthanide cubanes and polyselenide species could be interconverted by adjusting the Ln:Se:SePh ratios.

$$Yb(SePh)_3 \leftarrow Yb_4Se_4(SePh)_4 \longleftrightarrow Yb_4Se(ScSe)_4(SePh)_2 \qquad (9)$$

Attempts to prepare larger cluster materials so as to study the evolution of size-dependent properties has led to the synthesis of two compounds with internal chalcogen-encapsulated Ln. The first, $(THF)_{14}Er_{10}S_6(SeSe)_6I_6$, contained

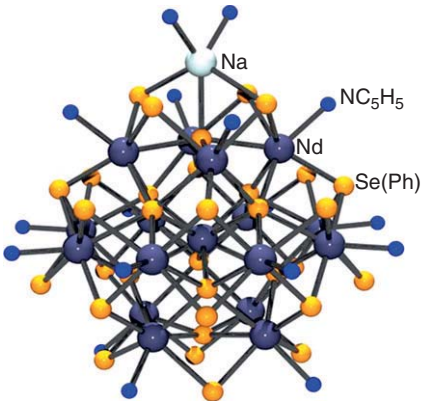


Figure 4 ORTEP diagram of the core atoms in$(py)_{16}Ln_{17}NaSe_{16}(SePh)_{17}$, a crystalline cluster with a 2 nm diameter. This compound downconverts 800 nm light with a 35% quantum efficiency

a cluster with two chalcogen-encapsulated Er, a sulfido core bound to the Er that are then encapsulated with (SeSe) and iodide ligands that decorate the cluster surface.[57] The second, $(py)_{16}Ln_{17}NaSe_{16}(SePh)_{17}$ (Figure 4, Ln = Pr, Nd)[58] is a more straightforward cluster compound with an internal, eight-coordinate Nd surrounded by a shell of Se dianions that are next enveloped with a layer of Nd^{III} ions that bond to SePh and pyridine ligands that saturate the cluster surface. The chalcogen-encapsulated Nd coordination spheres are different from the Nd environments found in solid-state Nd_2Se_3.

Chalcogenolate ligands have also been used to prepare clusters with more electronegative anion cores (see ***Lanthanide Oxide/Hydroxide Complexes***). Extension of this redox approach to the synthesis of oxide clusters[59–61] led, for Nd, to the preparation of two oxo clusters with Nd_8O_2 and $Nd_{12}O_6$ cores (Reaction 10). In these two clusters, all the Nd are coordinated to neutral donors and so there is no relevant comparison with the Nd in Nd_2O_3, but bond distances and angles around the oxo ligands are indistinguishable from the geometries of the oxo ligands in Nd_2O_3.

$$Nd(SePh)_3 + SeO_2 \rightarrow (THF)_8Nd_8O_2Se_2(SePh)_{16} \rightarrow [(py)_{18}Nd_{12}O_6Se_4(Se_2)_4(SePh)_4(Se_2Ph)_2Hg_2(SePh)_4]^{2+} \quad (10)$$

Fluoride clusters were also stabilized with chalcogenolate ligands.[62] When $Ln(EPh)_3$ react with a variety of fluoride sources (NaF, AgF, NR_4F, CaF_2, HgF_2), metathesis reactions clearly occur, but only with the ammonium fluoride reactions in a specific F:Ln ratio could crystalline fluoride clusters of $(py)_{24}Ln_{28}F_{68}(SePh)_{16}$ be isolated and structurally characterized (Reaction 11). These compounds have four internal fluoride-encapsulated Ln with 10-coordinate geometries that are different from the Ln environments in LnF_3.

$$Ln(SePh)_3 + 2\,NH_4F \rightarrow (py)_{24}Ln_{28}F_{68}(SePh)_{16} + NH_4SePh \quad (11)$$

In addition to atomically defined cluster chemistry, there is also an emerging interest in the preparation of larger submicron-sized Ln particles, motivated by the potentially useful magnetic properties of divalent Eu (see ***Oxide and Sulfide Nanomaterials***). Much of this work focuses on EuS using a variety of dithiocarbamate derivatives with an arsenal of chelating ligands (i.e., BIPY, phen). A number of groups have been investigating the solution thermolysis of these single-source precursors (Reaction 12).[63–70] To date, EuS particles have been prepared with a range of particle sizes, from sub-2 nm, 5–6 nm, and 20 nm, to reports detailing a range of particle sizes with narrow distributions. These efforts are devoted to understanding the effect of particle size on ferromagnetic interactions, with Curie temperatures lower than the temperature reported for the analogous bulk EuS, or glasslike behavior. There are considerable challenges to the data interpretation here because smaller particles have nonnegligible concentrations of surface Eu that influence the data. Heterometallic approaches to Gd-doped EuS particles formed lattices with Gd^{III} that had Curie temperatures above 29 K for materials with 5.3% Gd.

$$Eu(S_2CNR_2)_3 \rightarrow EuS + S(CNR_2)_2 + \cdots \quad (12)$$

Similar chemistry was used to approach 10–30 nm particles of La_2S_3,[71] via the solution thermolysis of $La(S_2CNEt_2)_3$-phen. In this work, changes in the energy of the bandgap were attributed to a quantum size effect. When solution thermolyses of these trivalent materials were approached in the presence of air, nanoplates or nanorods of Ln_2O_2S were instead observed (Ln = Eu, Gd).[72]

Nanomaterials based on Ln-doped semiconductors are also known. This chemistry is complicated by the fact that molecular approaches to these materials can lead either to materials with Ln–E–M connectivities,[73] or to heterogeneous materials such as $[(THF)_8Sm_4Se(SePh)_8][Zn_8Se(SePh)_{16}]$,[74] where there are $LnSe_x$ and MSe_x clusters that exist as discrete Ln cations and M anions. Recently, spherical EuS clusters were grown on CdE nanorods, using the same single-source thermolysis approach, and the EuS was shown to have a dramatic impact on the semiconductor luminescence.[75]

6 MOLECULAR APPROACHES TO SOLID-STATE MATERIALS

Molecular thermolysis is a well-established approach to materials synthesis, offering the advantage of exceptionally low reaction temperatures that are useful either in the synthesis of metastable solids or in the fabrication of layered materials where atomic diffusion is not desirable. Chalcogenolate compounds have been used for decades as low-temperature sources of solid-state chalcogenido materials. With Ln, the earliest thermolysis investigation outlined

the synthesis of YbE from the thermal decomposition of aryl chalcogenolates (Reaction 13),[15,16] and this work rapidly expanded to the synthesis of trivalent chalcogenides (Reactions 14 and 15).[26,30]

More complicated ternary solids have also been approached. Solid-state oxychalcogenides were prepared from solution pyrolysis in the presence of air,[72] although there is a report describing the thermal conversion of an oxy-selenido cluster into separate oxide and selenido phases (Reaction 16). Similarly, precursor identity was shown to be important to product identity in the thermolysis of heterometallic chalcogenido compounds. The heterometallic cluster $(py)_8Yb_4Cd_2Se_6(SePh)_4$ decomposes to give Ln_2CdSe_4 (Reaction 17),[73] while the related telluride cluster $(py)_3Ln_3HgTe_4(TePh)_3$ gave LnTe[76] (Reaction 18).

$$Yb(TeC_6H_3\text{-}2,4,6,Me_3)_2 \rightarrow YbTe + Te(C_6H_3\text{-}2,4,6,Me_3)_2 \quad (13)$$

$$Ln(SPh)_3 \rightarrow Ln_2S_3 + 2\ SPh_2 \quad (14)$$

$$Ho(SePh)_3 \rightarrow HoSe + HoSe_2 + SePh_2 \quad (15)$$

$$Ln_8O_2Se_2(SePh)_{16} \rightarrow Ln_2O_3 + Ln_2Se_3 + SePh_2 \quad (16)$$

$$Yb_4Cd_2Se_6(SePh)_4 \rightarrow Yb_4Cd_2Se_8 + SePh_2 \quad (17)$$

$$(py)_3Ln_3HgTe_4(TePh)_3 \rightarrow LnTe + Hg + TePh_2 \quad (18)$$

Finally, chalcogenolate compounds have also been used to deliver lattices with more electronegative anions, reflecting the relative instability of Ln ions bound only to chalcogenides. Solid-state LnN[77] forms via the thermolysis of azobenzene compounds (Reaction 19). Similarly, in the thermolysis of $Ln(SC_6F_5)_3$, fluoride abstraction leads to the formation of LnF_3 and fluorinated sulfur crowns[33] (Reaction 20).

$$Yb(PhNNPh)(EPh) \rightarrow YbN \quad (19)$$

$$Ln(SeC_6F_5)_3 \rightarrow LnF_3 + (SC_6F_4)_n \quad (20)$$

7 NOTABLE PHYSICAL PROPERTIES

The nature of the Ln–E bond was probed with a number of different ligand systems. The most readily visualized indication that covalent bonding can contribute to complex stability is seen in a series of *mer*-octahedral (Lewis base)$_3$Ln(ER)$_3$ compounds, for which it was noted that there is always a small, but statistically significant dependence of Ln–E bond lengths on the identity of the trans ligands. In every case, Ln–E bonds trans to Ln–ER were longer than Ln–E bonds trans to neutral donor ligands, and a DFT analysis identified the origin of the trans influence as a covalent interaction between the Ln 5d orbitals and the orbitals on the chalcogenolates.[78] This bond length pattern is noted with virtually all ligand combinations that form *mer*-LnA_3B_3 structures. Similar conclusions were drawn from calculations on other molecules with sulfur-based anions, although in these structures, a clear geometric influence on bond lengths is not apparent.[31,32]

In addition to structural properties, compounds with Ln–E bonds also have distinctly unconventional electronic properties (see ***Near-Infrared Materials***). NIR emission properties from an extensive series of molecules and clusters with Ln–E bonds has been examined,[57,58,79–83] and the results indicate that incorporation of E-based anions has a dramatic influence on the stability of excited-state Ln lifetimes, and thus quantum efficiencies. The low-phonon-energy character of the Ln–E bond effectively decouples ligand vibrational modes from a lanthanide-localized excited state, both because of the low phonon energy of a Ln–E stretching frequency and because the longer Ln–E bonds effectively distance the organic group from the metal center. The effects are dramatic, with $(DME)_2Ln(SeC_6F_5)_3$ compounds (Ln = Nd,[60] Tm,[80] Er[57]) having quantum efficiencies that are 2–10 times greater than conventional molecular sources. Further, emission measurements on Nd^{III} compounds have a transition at 1.8 mu that is observed only from low-phonon solid-state materials (Figure 5). A study of related fluorinated alkoxides[35] further confirmed the hypothesis that the low-phonon character of the Ln–S bond is responsible for these extraordinary emission properties.

The same remarkable emission intensity is observed with cluster compounds, which benefit further from the fact that there is a greater ratio of emissive Ln:NIR quenching ligands. A series of both chalcogenido compounds and oxo clusters have been studied to explore the influence of particle size on emission properties, and each system reveals a dependence that reflects the phonon characteristics of the anions. For the chalcogenido clusters, it becomes clear that increasing the nuclearity of the system, going from $(DME)_2Nd(SeC_6F_5)_3$ to $(py)_{16}Nd_{17}NaSe_{16}(SePh)_{17}$ to $Nd{:}La_2Se_3$ leads to an increase in quantum efficiency (9%,

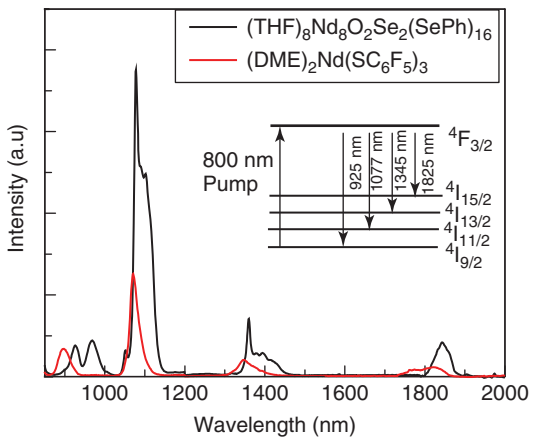


Figure 5 Emission spectra of chalcogen bound Nd compounds, with the 1.8 μm emissions clearly evident. These are the only molecules for which this low energy transition is not quenched

35%, and 100%, respectively), in this case because the ratio of fluorescence quenching C−H:Nd is reduced. In contrast, with oxo clusters, the high phonon energy Ln−O bonds quench NIR emission, and so given the previously described clusters with Nd_8O_2 and $Nd_{12}O_6$ cores and solid-state Nd_2O_3, the quantum efficiency decreases (16%, 12%, and 5×10^{-3}%, respectively) as the concentration of Nd−O bonds increases.

8 GLOSSARY

py: pyridine

THF: tetrahydrofuran

BIPY: bipyridine

Phen: phenanthrolene

Cp:* C_5Me_5

9 RELATED ARTICLES

Trivalent Chemistry: Cyclopentadienyl; Rare Earth Metal Cluster Complexes; Lanthanide Oxide/Hydroxide Complexes; Oxide and Sulfide Nanomaterials; Near-Infrared Materials.

10 ABBREVIATIONS AND ACRONYMS

NIR = near infrared.

11 CONCLUSIONS

The Chemistry of the lanthanides with chalcogen based anions continues to evolve, with the synthesis and characterization of increasingly large and complicated materials that help us understand the relationships between molecular and solid state materials. This combination of ionic Ln with covalent ligand systems leads to materials with extraordinary physical properties.

This work was supported by the NSF (CHE-0747165).

12 REFERENCES

1. F. Nief, *Coord. Chem. Rev.*, 1998, **178–180**, 13.
2. H. X. Li, Y. J. Zhu, M. L. Cheng, Z. G. Ren, J. P. Lang, and Q. Shen, *Coord. Chem. Rev.*, 2006, **250**, 2059.
3. T. D. Tilley, R. A. Andersen, A. Zalkin, and D. H. Templeton, *Inorg. Chem.*, 1982, **21**, 2644.
4. D. J. Berg, R. A. Andersen, and A. Zalkin, *Organometallics*, 1988, **7**, 1858.
5. A. Recknagle, M. Noltemeyer, D. Stalke, U. Pieper, H. G. Schmidt, and F. T. Edelmann, *J. Organomet. Chem.*, 1991, **411**, 347.
6. W. J. Evans, K. A. Miller, D. S. Lee, and J. W. Ziller, *Inorg. Chem.*, 2005, **44**, 4326.
7. I. P. Beletskaya, A. Z. Voskoboynikov, A. K. Shestakova, and H. Schumann, *J. Organomet. Chem.*, 1993, **463**, C1.
8. Z. X. Zhang, Y. R. Li, R. T. liu, Z. X. Chen, L. H. Weng, and X. Z. Zhou, *Polyhedron*, 2007, **26**, 4986.
9. S. D. Stults and R. Andersen, *Organometallics*, 1989, **9**, 1623.
10. H. Schumann, I. Albrecht, M. Galagher, E. Hahn, C. Muchmore, and J. Pickardt, *J. Organomet. Chem.*, 1988, **349**, 103.
11. H. Schumann, I. Albrecht, and E. Hahn, *Angew. Chem. Int. Ed. Engl.*, 1985, **24**, 985.
12. T. J. Mueller, J. W. Ziller, and W. J. Evans, *Dalton Trans.*, 2010, **39**, 6767.
13. Y. F. Rad'kov, E. A. Fedorova, S. I. Khorchev, G. S. Kalinina, M. N. Bochkarev, and G. A. Razuvaev, *Zh. Obshch.*, 1985, **55**, 2153.
14. K. Tatsumi, T. Ememiya, H. Kawaguchi, and K. Tani, *J. Chem. Soc. Chem. Commun.*, 1993, 773.
15. A. R. Strzelecki, P. A. Timinski, B. A. Hesel, and P. A. Bianconi, *J. Am. Chem. Soc.*, 1992, **114**, 3159.
16. A. R. Strzelecki, C. Likar, B. A. Hesel, T. Utz, M. Lin, and P. A. Bianconi, *Inorg. Chem.*, 1994, **33**, 5188.
17. K. Mashima, Y. Nakayama, H. Fukumoto, N. Kanehisa, Y. Kai, and A. Nakamura, *J. Chem. Soc. Chem. Commun.*, 1994, 2523.
18. D. R. Cary and J. Arnold, *J. Am. Chem. Soc.*, 1993, **115**, 2520.
19. D. R. Cary, G. E. Ball, and J. Arnold, *J. Am. Chem. Soc.*, 1995, **117**, 3492.
20. D. Cary and J. Arnold, *Inorg. Chem.*, 1994, **33**, 1791.
21. M. Berardini, T. J. Emge, and J. G. Brennan, *J. Am. Chem. Soc.*, 1993, **115**, 8501.
22. D. Khasnis, J. Lee, M. Brewer, T. Emge, and J. Brennan, *J. Am. Chem. Soc.*, 1994, **116**, 7129.
23. J. Lee, T. Emge, and J. Brennan, *Inorg. Chem.*, 1997, **36**, 5064.
24. M. Berardini, T. Emge, and J. Brennan, *Inorg. Chem.*, 1995, **34**, 5327.
25. M. Brewer, J. Lee, and J. Brennan, *Inorg. Chem.*, 1995, **34**, 5919.
26. J. Lee, M. Brewer, M. Berardini, and J. Brennan, *Inorg. Chem.*, 1995, **34**, 3215.
27. M. Berardini, T. Emge, and J. Brennan, *J. Am. Chem. Soc.*, 1994, **116**, 6941.

28. M. Brewer, D. Khasnis, M. Buretea, M. Berardini, T. Emge, and J. Brennan, *Inorg. Chem.*, 1994, **33**, 2743.
29. D. Freedman, A. Kornienko, T. Emge, and J. Brennan, *Inorg. Chem.*, 2000, **39**, 2168.
30. J. Lee, D. Freedman, J. Melman, M. Brewer, L. Sun, T. Emge, F. Long, and J. Brennan, *Inorg. Chem.*, 1998, **37**, 2512.
31. M. Niemeyer, *Eur. J. Inorg. Chem.*, 2001, **8**, 1969.
32. M. Roger, N. Barros, T. Arliguie, P. Thuery, L. Maron, and M. Ephritikhine, *J. Am. Chem. Soc.*, 2006, **128**, 8790.
33. J. Melman, T. Emge, and J. Brennan, *Inorg. Chem.*, 2001, **40**, 1078.
34. J. Melman, C. Rhode, T. Emge, and J. Brennan, *Inorg. Chem.*, 2002, **41**, 28.
35. K. Norton, A. Kumar, J. Dilks, R. E. Riman, T. J. Emge, and J. G. Brennan, *Inorg. Chem.*, 2009, **48**, 3573.
36. D. R. Click, B. L. Scott, and J. G. Watkin, *Chem. Commun.*, 1999, 633.
37. M. Romanelli, Molecular lanthanide fluorides:photoluminescence from novel architectures, PhD thesis, Rutgers University, 2009.
38. M. Berardini, J. Lee, D. Freedman, J. Lee, and J. Brennan, *Inorg. Chem.*, 1997, **36**, 5772.
39. M. Berardini and J. Brennan, *Inorg. Chem.*, 1995, **34**, 6179.
40. M. D. Regulacio, N. Tomson, and S. L. Stoll, *Chem. Mater.*, 2005, **17**, 3114.
41. C. Su, M. Tan, N. Tang, X. Gan, Z. Zhang, Q. Xue, and K. Yu, *Polyhedron*, 1997, **16**, 1643.
42. M. D. Regulacio, M. H. Pablico, V. Acay, P. Myers, S. Gentry, M. Prushan, S. Tam-Chang, and S. L. Stoll, *Inorg. Chem.*, 2008, **47**, 1512.
43. C. Su, N. Tang, M. Tan, and K. Yu, *Polyhedron*, 1996, **15**, 233.
44. J. F. Bower, S. A. Cotton, J. Fawcett, R. S. Hughes, and D. R. Russell, *Polyhedron*, 2003, **22**, 347.
45. T. Kanda, M. Ibi, K. Mochizuki, and S. Kato, *Chem. Lett.*, 1998, **9**, 957.
46. W. Evans, G. W. Rabe, M. A. Ansari, and J. W. Ziller, *Angew. Chem., Int. Ed. Engl.*, 1994, **33**, 2110.
47. J. Melman, T. J. Emge, and J. Brennan, *Chem. Commun.*, 1997, 2269.
48. D. Freedman, T. J. Emge, and J. G. Brennan, *J. Am. Chem. Soc.*, 1997, **119**, 11112.
49. A. Kornienko, T. Emge, and J. Brennan, *J. Am. Chem. Soc.*, 2001, **123**, 11933.
50. J. Melman, M. Fitzgerald, D. Freedman, T. Emge, and J. Brennan, *J. Am. Chem. Soc.*, 1999, **121**, 10247.
51. D. Freedman, T. Emge, and J. Brennan, *Inorg. Chem.*, 1999, **38**, 4400.
52. J. Melman, T. Emge, and J. Brennan, *Inorg. Chem.*, 1999, **38**, 2117.
53. D. Freedman, J. Melman, T. Emge, and J. Brennan, *Inorg. Chem.*, 1998, **37**, 4162.
54. M. Fitzgerald, T. Emge, and J. Brennan, *Inorg. Chem.*, 2002, **41**, 3528.
55. D. Freedman, T. Emge, and J. Brennan, *Inorg. Chem.*, 2002, **41**, 492.
56. A. Kornienko, T. Emge, G. Hall, and J. Brennan, *Inorg. Chem.*, 2002, **41**, 121.
57. A. Kornienko, T. Emge, A. Kumar, R. Riman, and J. Brennan, *J. Am. Chem. Soc.*, 2005, **127**, 3501.
58. B. F. Moore, G. A. Kumar, M. C. Tan, J. Kohl, R. E. Riman, M. G. Brik, T. J. Emge, and J. G. Brennan, *J. Am. Chem. Soc.*, 2011, **132**, 373.
59. S. Banerjee, G. A. Kumar, R. Riman, T. J. Emge, and J. Brennan, *J. Am. Chem. Soc.*, 2007, **129**, 5926.
60. S. Banerjee, L. Huebner., M. D. Romanelli, G. A. Kumar, R. E. Riman, T. J. Emge, and J. G. Brennan, *J. Am. Chem. Soc.*, 2005, **127**, 15900.
61. K. Norton, S. Banerjee, L. Huebner, S. Das, T. J. Emge, and J. G. Brennan, *JCS Dalton Trans.*, 2010, **39**, 6794.
62. M. Romanelli, G. A. Kumar, R. E. Riman, T. J. Emge, and J. G. Brennan, *Angew. Chem.*, 2008, **47**, 6049.
63. Y. Hasegawa, M. Afzaal, P. O'Brien, Y. Wada, and S. Yanagida, *Chem. Commun.*, 2005, 242.
64. S. Thongchant, Y. Hasegawa, Y. Wada, and S. Yanagida, *Chem. Lett.*, 2003, **32**, 706.
65. T. Kataoka, Y. Tsukahara, Y. Hasegawa, and Y. Wada, *Chem. Commun.*, 2005, 6038.
66. M. D. Regulacio, K. Bussmann, B. Lewis, and S. L. Stoll, *J. Am. Chem. Soc.*, 2006, **128**, 11173.
67. W. L. Boncher, M. D. Regulacio, and S. L. Stoll, *J. Solid State Chem.*, 2010, **183**, 52.
68. R. S. Selinsky, J. H. Han, E. A. M. Perez, I. A. Guzei, and S. Jin, *J. Am. Chem. Soc.*, 2010, **132**, 15997.
69. R. S. Selinsky, D. J. Keavney, M. J. Bierman, and S. Jin, *Appl. Phys. Lett.*, 2009, **95**, 202501/1.
70. S. Kar, W. L. Boncher, D. Olszewski, N. Dollahon, R. Ash, and S. L. Stoll, *J. Am. Chem. Soc.*, 2010, **132**, 13960.
71. P. Guo, B. Jiao, S. Chen, R. Hu, S. Gao, and Q. Shi, *Sci. China B Chem.*, 2005, **48**, 83.
72. F. Zhao and S. Gao, *J. Mater. Chem.*, 2008, **18**, 949.
73. A. Kornienko, S. Banerjee, A. Kumar, R. Riman, T. Emge, and J. Brennan, *J. Am. Chem. Soc.*, 2005, **127**, 14008.
74. A. Kornienko, L. Huebner, D. Freedman, T. Emge, and J. Brennan, *Inorg. Chem.*, 2003, **42**, 8476.
75. T. Mirkovic, D. Rossouw, G. Botton, and G. D. Scholes, *Chem. Mater.*, 2008, **23**, 181.
76. S. Banerjee, J. Sheckelton, T. J. Emge, and J. G. Brennan, *Inorg. Chem.*, 2010, **49**, 1728.
77. A. Kornienko, D. Freedman, T. Emge, and J. Brennan, *Inorg. Chem.*, 2001, **40**, 140.
78. K. Krogh-Jespersen, M. D. Romanelli, J. H. Melman, T. J. Emge, and J. G. Brennan, *Inorg. Chem.*, 2010, **49**, 552.

79. A. Kornienko, B. F. Moore, G. A. Kumar, M. C. Tan, R. E. Riman, M. G. Brik, T. J. Emge, and J. G. Brennan, *Inorg. Chem.*, 2011, **50**, 9184.

80. S. Banerjee, A. Kumar, T. Emge, R. Riman, and J. G. Brennan, *Chem. Mater.*, 2008, **20**, 4367.

81. G. A. Kumar, R. Riman, S. Banerjee, A. Kornienko, and J. G. Brennan, *Chem. Mater.*, 2005, **17**, 5130.

82. G. A. Kumar, R. Riman, S. Chen, D. Smith, J. Ballato, S. Banerjee, A. Kornienko, and J. G. Brennan, *Appl. Phys. Lett.*, 2006, **88**, 91902.

83. G. A. Kumar, R. E. Riman, L. A. Diaz Torres, S. Banerjee, M. D. Romanelli, T. J. Emge, and J. G. Brennan, *Chem. Mater.*, 2007, **19**, 2937.

Carboxylate

Jia-sheng Lu and Ruiyao Wang

Queen's University, Kingston, ON, Canada

1 Summary 225
2 Introduction 225
3 Synthesis of Rare Earth Carboxylates 225
4 Structural Chemistry of Rare Earth Carboxylates 227
5 Conclusions 235
6 Glossary 235
7 Acknowledgments 235
8 Abbreviations and Acronyms 235
9 References 235

1 SUMMARY

Rare earth carboxylates are also called rare earth complexes with carboxylic acids, including rare earth monocarboxylates and rare earth polycarboxylates. They have been attracting research interests for several decades due to their unique and fascinating structural chemistry (high coordination numbers (CN), diverse coordination modes, and structures) and their applications as advanced materials (such as catalysts, light emitters, optical sensors, magnets, and storage materials). A variety of structures with intriguing topology and coordination modes and compounds having potential applications as storage materials, magnetic materials, Lewis acid catalysts, optical sensors, etc. have been reported. But challenges still remain to ''engineer'' rare earth carboxylates of special functions or to predict a priori the structure of a given compound, due to the ionic nature of the RE(III)–O(carboxylate) bonds.

2 INTRODUCTION

Characterized as hard Lewis acids and with large ionic radii, RE(III) ions prefer to coordinate to hard Lewis base donors, such as F, O, or N, and to have high CNs. With O as coordinating atoms and diverse structures to satisfy the high CN requirement, carboxylic acids, including monocarboxylic acids and polycarboxylic acids, are among the most suitable ligands for RE(III) ions. Studies on rare earth carboxylates can be traced back to 60 years ago when citrate and polyaminopolycarboxylates were used as the initial eluents for separating rare earth using cation-exchange resin.[1,2] Since then, research on rare earth carboxylates has been active driven by both their versatile and intriguing structural modes and varieties of applications on biology, clinics, and advanced function materials, such as catalysts, magnets, nonlinear optics (NLO), organic light-emitting diode (OLED), and metal–organic frameworks (MOF)[3–5] and even as greener corrosion inhibitors to replace the traditional and toxic chromate-based compounds.[6] This chapter covers the synthetic and structural chemistry of rare earth carboxylates and special efforts have been made to review the types of the structures and the controls over their syntheses.

3 SYNTHESIS OF RARE EARTH CARBOXYLATES

Either rare earth oxides or salts can be used to prepare rare earth carboxylates:

$$3\,R{-}COOH + 1/2RE_2O_3(s) \longrightarrow RE(R{-}COO)_3 + 3/2H_2O \quad (1)$$

$$MOH + R{-}COOH \longrightarrow R{-}COOM + H_2O\ (M = NH_4^+, Na^+, K^+) \quad (2)$$

$$3\,R{-}COOM + REX_3 \longrightarrow RE(R{-}COO)_3 + 3MX\ (X = NO_3^-, Cl^-, ClO_4^-;\ M = NH_4^+, Na^+, K^+) \quad (3)$$

The Rare Earth Elements. Edited by David A. Atwood. © 2012 John Wiley & Sons, Ltd. ISBN 978-1-119-95097-4

While the chemistry for the synthesis of rare earth carboxylates is relatively simple, challenges remain to obtain the compounds with high purity and good yield due to the low solubility of the compounds arisen by their high nuclearity and structural complexity. On the basis of the types of synthetic conditions, the methods can be put into three categories: (i) synthesis under ambient conditions, (ii) hydro(solvo)thermal synthesis, and (iii) gel synthesis. While, in principle, both insoluble and soluble-starting materials such as rare earth oxides, salts, or acids can be used as the starting materials for (i) and (ii), only soluble-starting materials are acceptable for (iii). Synthesis can be done in aqueous solutions, organic media, or the mixtures of the two, depending on the solubility and the nature of the acids and the products. Carboxylates with good solubility are usually synthesized under ambient, but those with low solubility can only be obtainable with high purity by hydro(solvo)thermal synthesis or by gel synthesis.

3.1 Synthesis under Ambient Conditions

By heating and/or refluxing the mixture of RE_2O_3 with a stoichiometric amount of R−COOH in water or an organic solvent, such as MeOH, EtOH, DMF, or DMSO, or mixtures of water and organic solvents under atmospheric pressure, a clear solution of the complex can be obtained (equation 1). The solvent is removed by evaporation after a filtration, and the pure product can be obtained after recrystallization. About 5% in excess of RE_2O_3 are typically used to avoid the possible contamination from the unreacted R−COOH, and the unused RE_2O_3 can then be removed by filtration after the reaction is completed.

Starting from inorganic salts and corresponding carboxylic acids, a two-step preparation will be employed according to reactions (2) and (3). The rare earth carboxylates, $RE(R{-}COO)_3$, can then be separated from MX ($X = NO_3^-$, Cl^-, ClO_4^-; $M = NH_4^+, Na^+, K^+$) through recrystallization with good yields.

3.2 Hydro(solvo)thermal Synthesis

The first hydro(solvo)thermal synthesis was accomplished in 1839 by a German chemist, Robert Bunsen. By heating aqueous solutions in sealed thick-walled glass tubes at temperature above 200 °C and at pressure above 100 bars, Bunsen obtained the crystals of barium carbonate and strontium carbonate.[7] The modern form of hydro(solvo)thermal synthesis device, a sealed glass ampoule in an autoclave, was developed by de Senarmont in 1851.[8] Hydro(solvo)thermal synthesis is the heterogeneous reaction in aqueous or nonaqueous media with temperature above the boiling point of the solvent and pressure higher than 1 bar. It has many advantages over conventional synthesis, and one of them is the single-crystal growth of low solubility compounds such as rare earth polycarboxylates. The starting materials can be carboxylic acids and rare earth oxides or salts (nitrates, chlorides, or perchlorates) with or without base. The medium can be water or organic solvents such as methanol, ethanol, THF, or mixtures of different solvents. Many MOF materials have been synthesized through hydro(solvo)thermal synthesis. However, for most hydro(solvo)thermal syntheses, the structures of the products are still unpredictable. The reaction conditions for different syntheses, such as the solvents, the concentrations of the starting materials, the reaction temperature, the controls of the heating and cooling process, may vary greatly, and a slight change may result in different products.

3.3 Gel Synthesis—Crystal Growth in Gel

Owing to the high thermal stability and porosity, rare earth polycarboxylates are considered to be very promising MOF materials. However, their limited solubility in water or organic solvents makes growing single crystals a great obstacle for detailed structural characterization. Hydro(solvo)thermal synthesis has been proved to be very effective in solving this problem, but the inherently demanding experimental requirements (100 °C or higher) and the unpredictability prevents this method from being widely used. Gel synthesis, operating under ambient conditions, is a good alternative for hydro(solvo)thermal synthesis.

Gel synthesis was introduced by Liesegang a century ago.[9] A gel is a two-component system that is semisolid and is particularly rich in liquid and has fine pores in it. This media prevents turbulence and helps in the formation of crystal by providing a framework of nucleation site. Silica gels are the most widely used media for single-crystal preparations. Under pH 4 ∼ 5, silicate ion starts to gel by reacting with itself to produce Si−O−Si bonds and form cross-linked 3D framework with the channels or pockets filled by water molecules. To prepare single crystals of rare earth polycarboxylates in a gel, a common practice is to first dissolve a polycarboxylic acid in the gel and the gel is then allowed to set in a test tube or beaker, then a solution of the rare earth salt, usually, chloride, nitrate, or perchlorate, is added to the top of the gel. The solution slowly diffuses through the pockets in the gel allowing the reaction to take place between the rare earth ions and the polycarboxylic acid, and well-shaped crystals may be observed in the gel after a certain period of time (days to months). Crystals obtained by gel synthesis usually contain more lattice water, and rare earth polycarboxylic acid complexes with larger channels have been prepared efficiently by this method. In addition, several other gels such as oleates, gelatin, polyvinyl alcohol, and agar have been used for crystal growth.[10,11]

4 STRUCTURAL CHEMISTRY OF RARE EARTH CARBOXYLATES

RE(III) ions are characterized by their high CNs and flexible coordination geometries, owing to the high positive charge and large ionic radii, hard Lewis acid character of RE(III), as well as the ionic nature of the RE(III)–O bonds. In addition, rare earth carboxylates have also been found with intriguing coordination modes and instinct bridging modes.

4.1 Coordination Numbers and Coordination Modes

The CNs of RE(III) in the compounds are in the range of 6–10, achieved by the formation of dimeric or polymeric structures and/or with high degree of solvation. But the most popular CNs for carboxylates are 8 and 9, with square antiprism, monocapped square antiprism, or tricapped trigonal prism geometries. The light and mid-lanthanide ions (La^{3+}–Tb^{3+}) prefer CN = 9, while the heavy lanthanide ions (Dy^{3+}–Lu^{3+}) prefer CN = 8. For the Y^{III} carboxylates, they usually fall into the heavy lanthanide group with CN = 8, while a few Sc^{III} carboxylates stand out with CN = 6 and an octahedral coordination geometry.[12]

Compared with carboxylates of 3d metals, where the carboxylate groups are usually unidentate, the coordination modes in rare earth carboxylates are far more versatile. As shown in Figure 1, nine typical coordination modes adopted by carboxylates are found in rare earth carboxylates. The nine different modes can be put into three groups, i.e., the nonbridging modes (modes (a) and (b)), dinuclear bridging (modes (c–g)), and trinuclear bridging (modes (h) and (i)). Owing to the large size of RE(III) ions and the ionic nature of the RE–O bonds, the carboxylato groups can approach the RE(III) ions without any geometrical limit, which makes

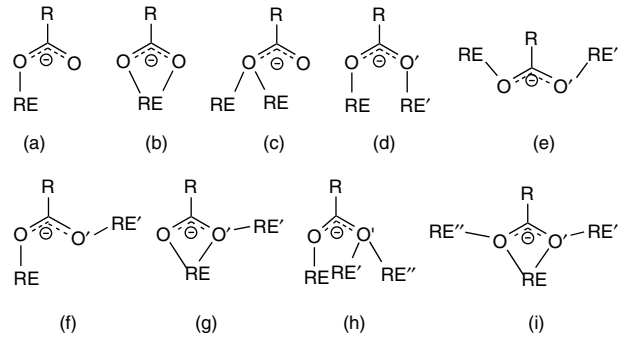


Figure 1 Coordination modes adopted by carboxylate groups in rare earth carboxylates: (a) η^1; (b) η^2; (c) μ_2-$\eta^1\eta^1$ (O, O); (d) μ_2-$\eta^1\eta^1$ *ZZ*; (e) μ_2-$\eta^1\eta^1$ *EE*; (f) μ_2-$\eta^1\eta^1$ *ZE*; (g) μ_2-$\eta^2\eta^1$; (h) μ_3-$\eta^2\eta^1$; (i) μ_3-$\eta^2\eta^2$. (Reproduced from R. Wang and Z. Zheng, ''Rare Earth Complexes with Carboxylic Acids, Polyaminopolycarboxylic Acids and Amino Acids'' in Chun-Hui Huang, Rare Earth Coordination Chemistry: Fundamentals and Applications, © John Wiley & Sons (Asia) Pte Ltd, 2010.)

bidentate, tridentate, or chelating coordination modes possible in the structures. Meanwhile, the large size of RE(III) ions also makes the 4-member chelating ring (Figure 1b, g, and i) more stable than those in 3d metal carboxylates. The most common coordination modes for rare earth carboxylates are unidentate: η^1; simple chelating: η^2; bridging bidentates: μ_2-$\eta^1\eta^1$ *ZZ*, μ_2-$\eta^1\eta^1$ *EE*, and μ_2-$\eta^1\eta^1$ *ZE*; and the chelating tridentate: μ_2-$\eta^2\eta^1$. In mononuclear rare earth carboxylates, carboxylato groups usually adopt unidentate (Figure 1a) and the simple chelating (Figure 1b), while in dinuclear or polynuclear carboxylates, the most popular coordination modes for carboxylato groups are bridging bidentate: μ_2-$\eta^1\eta^1$ *ZZ*, chelating tridentate: μ_2-$\eta^2\eta^1$, and the simple chelating: η^2. However, as indicated by Ouchi,[12] these modes are only the typical forms. It is not uncommon to see the intermediate mode between the two distinct types. For example, a chelating tridentate mode: μ_2-$\eta^2\eta^1$ (Figure 1g), when the RE–O′ distance is much longer than those of the RE–O and RE′–O′ bonds, is regarded as the intermediate between the chelating tridentate (μ_2-$\eta^2\eta^1$) (Figure 1g) and the bidentate mode (μ_2-$\eta^1\eta^1$ *ZE*) (Figure 1f).

4.2 Bridging Modes

In addition to high CN and the variety of coordination modes, dinuclear and polynuclear rare earth carboxylates are also featured with the ways how two neighboring RE(III) ions are linked together by the carboxylato groups, i.e., the bridging modes of carboxylato groups. Figure 2 shows the 12 bridging modes found from the studies reported so far. The numbers of the bridges between two adjacent metal centers can be 1, 2, 3, or 4, and bridging carboxylato groups can be any one of the five-coordination modes (Figure 1c–g). While only 4 (b, d, g, and j) out of the 12 bridging modes in Figure 2 were found in the structures of the dinuclear carboxylates, all of the 12 bridging modes were found in the polynuclear rare earth carboxylates, where the two adjacent RE(III) can be held together by 1–4 bridging carboxylates, and up to 4 bridging modes can occur in one structure. Among the different bridging modes, μ_2-$\eta^2\eta^1$ bridging mode makes the shortest RE···RE distances, while μ_2-$\eta^1\eta^1$ *EE* gives the longest, and with the same bridging mode, the more the bridges, the shorter the RE···RE distances.[13]

4.3 Polynuclearity and the Controls

Owing to the high positive charge, large ionic radii of RE(III) ions, and the ionic nature of the RE(III)–oxygen bonds, RE(III) ions tend to share the carboxylato groups and form dinuclear or polynuclear structures. We have found that the nuclearity of rare earth carboxylates vary with the change of the bulkiness of the carboxylate ligands, the ratio of the molar ratio of carboxylate/RE(III), and the availability of the auxiliary ligands such as phen, bipy, or terp. Mononuclear or dinuclear carboxylates can be obtained by using bulky ligands,

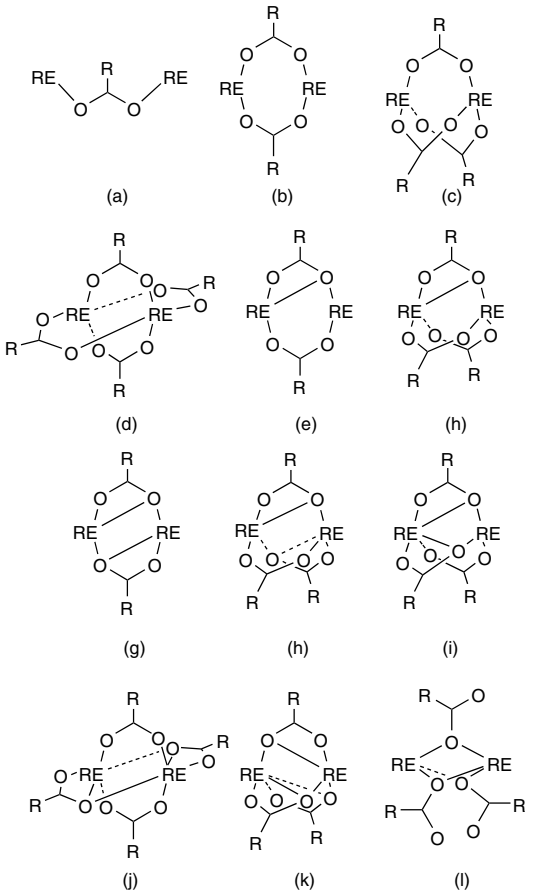


Figure 2 Bridging modes observed in dinuclear and polynuclear rare earth carboxylates. (Reproduced with permission from from R. Wang and Z. Zheng, ''Rare Earth Complexes with Carboxylic Acids, Polyaminopolycarboxylic Acids and Amino Acids'' in Chun-Hui Huang, Rare Earth Coordination Chemistry: Fundamentals and Applications. © John Wiley & Sons (Asia) Pte Ltd, 2010.)

raising the molar ratio of carboxylate/RE(III), or introducing auxiliary ligands to the RE(III)–carboxylate systems.

When a carboxylate anion is bulky enough, compared to the sizes of RE(III) ions, the ligand itself can prevent the compound from polymerizing. As such, dimeric or monomeric complexes can be obtained. Formate anion is the smallest member of the carboxylate family. Its compounds with RE(III) are not surprisingly all polymeric. Two series of RE(III) formates have been structurally characterized, i.e., the anhydrous series with the general formula $[REL_3]_n$ (RE = La, Ce, Gd, Tb, Tm, and Gd) and the hydrated series $[REL_3(H_2O)_2]_n$ (RE = Gd, Tb, Dy, Ho Er, Tm, and Y). For the second smallest carboxylic acid, acetic acid, the structures are polymeric for La–Nd, dimeric for Sm–Lu.[14] While propionates behave very similar to acetates, the steric effect from pivalate anions is effective enough to form stable mononuclear and dinuclear dysprosium pivalate.[15,16] Meanwhile, the planar-shaped benzoate anion was found to perform very similarly to acetate and propionate.

The molar ratio of coordinating carboxylate to RE(III) is usually noted as ''carboxylate/RE.'' rare earth formates are polymeric from La to Lu when carboxylate/RE = 3. They become mononuclear when carboxylate/RE increases from 3 to 6 or 8, where the metal centers are eight-coordinated either by 4 unidentate(η^1) and 2 bidentate(η^2) formates, or by 8 unidentate(η^1) formates.[17,18]

Some N-containing neutral chelating ligands, such as 1, 10-phenanthroline (phen), 2,2′-bipyridine (bippy) or 2,2′:6′,2″-terpyridine (terp), can compete with carboxylate anions to form stable coordination bonds with RE(III), which prevent the carboxylates from dimerizing or polymerizing. For example, $[RE_2L_6(phen)_2]$ (HL = acetic acid; RE = Ce, Ho, and Lu) is dimeric, where the two RE(III) ions are bridged by four acetates, and each of the two RE(III) is chelated by an acetate and a phen. With 4-aminobenzonic acid, a bulkier ligand, three types of ternary complexes with monomeric structures are isolated: (i) $[LaL_3(HL)(phen)_2(H_2O)]\cdot H_2O$), (ii) $[REL_3(phen)(H_2O)]\cdot 2H_2O$ (RE = Eu, Tb), and (iii) $[TbL_2(phen)_2(H_2O)_2]\cdot(L)(phen)\cdot 4H_2O$. The use of bipy or terp as the auxiliary ligand can also lead to the formation of the monomeric or dimeric structures.

4.4 Structures of Rare Earth Monocarboxylates

Extensive studies have been done for the structures of rare earth monocarboxylates. Most of them are found to be polynuclear, although mononuclear, dinuclear, and tetranuclear rare earth monocarboxylates do exist. So far, only four types (two with double bridging and two with quadruple bridging) of dinuclear carboxylates and two types of tetranuclear carboxylates have been reported. But the structures of the polymeric complexes are much more complicated: the bridging modes between two neighboring metals range from single, double, triple to quadruple, and up to three different bridging modes can be present in one structure. In this chapter, only polymers with one and two bridging modes in the structures are discussed.

4.4.1 Mononuclear Carboxylates

As discussed in Section 4.2, mononuclear rare earth carboxylates are only obtainable in three cases, i.e., the use of bulky carboxylate anions, the application of the high carboxylate/RE ratio, and the presence of the auxiliary ligands.

With bulky carboxylate anions, the mononuclear compound formed can be expressed $[REL_3(sol)_n]$, where sol is a coordinating solvent, such as H_2O, EtOH, MeOH, DMF, or DMSO. In most cases, the three carboxylates are in the chelating (η^2) mode, and n is 2 or 3, CN = 8 or 9. However, when the ligand is too bulky, there would be not enough room for all of the three carboxylates to be in the chelating mode, and one or two of them have to be in the monodentate(η^1) mode, and the number of the solvent molecules (n) becomes 3 or 4. Figure 3 shows the structures

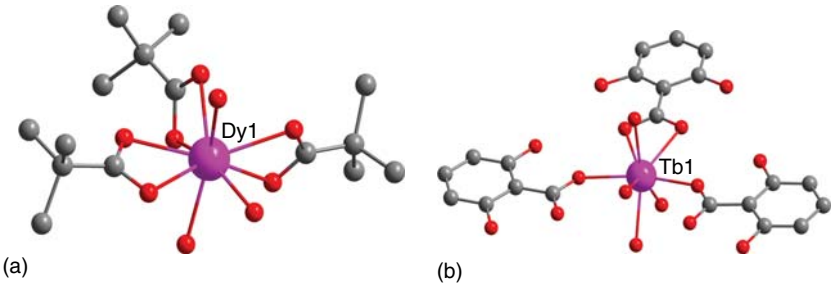


Figure 3 Structures of $[DyL_3(H_2O)_3]$ (a) and $[TbL'_3(H_2O)_4]$ (b) (HL = pivalic acid and HL′ = 2,6-dihydroxybenzoic acid) (RE, black; O, gray; C, white; H, omitted). (Reproduced with permission from from R. Wang and Z. Zheng, ''Rare Earth Complexes with Carboxylic Acids, Polyaminopolycarboxylic Acids and Amino Acids'' in Chun-Hui Huang, Rare Earth Coordination Chemistry: Fundamentals and Applications. © John Wiley & Sons (Asia) Pte Ltd, 2010.)

of $[DyL_3(H_2O)_3]$ (a) and $[TbL'_3(H_2O)_4]$ (b) (L = pivalate, L′ = 2,6-dihydroxybenzate).

When the carboxylate/RE ratio is high (≥4), anionic monomeric complexes can be formed. Only four structures in this category have been reported: $K_3[ErL_6] \cdot 2H_2O$, $K_5[TbL_8]$, $(NH_4)_2[LaL'_6]{\cdot}0.5H_2O$, and $K_3[YbL'_6]] \cdot 4H_2O$ (L = formate and L′ = acetate). While all of the eight formate anions in the structure of $K_5[TbL_8]$ are unidentate, only three or four ligands in the other three compounds are unidentate, with the rest of the ligands chelating to the metal centers, CN = 8 or 9.[4,17,18]

With bipy as auxiliary ligand, RE(III) ions form two types of mononuclear trichloroacetates (L = trichloroacetate): (i) $[RE(bipy)_2L_3]$ (RE = Pr or Nd) and (ii) $[RE(H_2O)(bipy)_2L_3]$ (RE = Tb or Er). All of the three trichloroacetate anions in (i) are in the simple chelating mode (η^2), CN = 10, while all of the trichloroacetate anions are unidentate (η^1), CN = 8. The cases for mononuclear carboxylates with phen as auxiliary ligand are more complicated. They can be formulated as $[REL_3(phen)_m\ (sol)_n]$ (m = 1 or 2, n = 0, 1, or 2, and sol = solvent molecule). The carboxylate ligands in the structure can be simple chelating (η^2), or unidentate (η^1). The CNs are 8 or 9, depending on the size of the RE(III) ions and the bulkiness of the carboxylate ligands.

4.4.2 Dinuclear Carboxylates

Although hundreds of dinuclear rare earth carboxylates have been structurally characterized, the bridging numbers between the two metal centers are only found to be either 2 or 4, and in only 4 bridging modes out of 12 from Figure 2: (i) double bidentate bridging, $(\mu_2\text{-}\eta^1\eta^1)_2$ (Figure 2b); (ii) double chelating tridentate bridging, $(\mu_2\text{-}\eta^2\eta^1)_2$ (Figure 2g); (iii) quadruple simple bridging, $(\mu_2\text{-}\eta^1\eta^1)_4$ (Figure 2d)); and (iv) quadruple chelating bridging, $(\mu_2\text{-}\eta^2\eta^1)_2 + (\mu_2\text{-}\eta^1\eta^1)_2$ (Figure 2j).

While most of the monocarboxylic acids can form quadruply-bridged dinuclear carboxylates with RE(III), with a bridging mode (III) or (IV), only a few monocarboxylic acids have been found to form double-bridged dinuclear carboxylates: with acetic acid, propionic acid, benzoic acid, as well as some *para*-substituted derivatives of benzoic acid (p-RC_6H_4COOH) (R = $-NH_2$,$-OCH_3$,–CN, etc.) for type (I) and acetic acid, methacrylic acid, 3-(2-hydroxyphenyl) acrylic acid, 2-thiophene carboxylic acid, 2-methoxybenozoic acid, 3-hydroxybenzoic acid, 4-hydroxy-3-methoxybenzoic acid, and 2,6-dichlorobenzoic acid for type (II). Although one can imagine the steric hindrance and the solubility of the ligands or the carboxylates may play roles for this phenomena, it is still too early to have any clear answer about it. As examples for bridging mode (I), the structure of $[TbL_3(H_2O)_2]_2 \cdot 2H_2O$ (L = p-aminobenzoate) is shown in Figure 4(a).[19] The bridging mode (II) is found in the structure of rare earth acetates for RE = Sm–Lu. The structure of $[SmL_3(H_2O)_2]_2$ (L = acetate) is shown in Figure 4(b).[20]

While most of the monocarboxylic acids can only form dinuclear carboxylates in bridging mode (III), i.e., $(\mu_2\text{-}\eta^1\eta^1)_4$, with the help of auxiliary ligands such as phen, terp, bipy, DMSO, DMF, ethanol, methanol, NO_3^-, and even the carboxylate (L^-) or the carboxylic acid (HL), trifluoroacetic acid is the only one so far, which can form dinuclear rare earth carboxylates in this mode without any auxiliary ligands. The structure of $[GdL_3(H_2O)_3]_2$ (L = trifluoroacetate) is shown in Figure 5(a).[21] This may be due to the unique geometry and the nucleophilicity of the trifluoroacetate ligand.

Almost all of the monocarboxylic acids can form dinuclear carboxylates in bridging mode (IV) with or without auxiliary ligands. The structures of $[CeL_3(phen)]_2$ (L = acetate) are shown in Figure 5(b).[22] The two Ce^{III} ions are bridged in mode (IV), i.e., $((\mu_2\text{-}\eta^2\eta^1)_2 + (\mu_2\text{-}\eta^1\eta^1)_2)$. Each of the two Ce^{III} ions is then chelated by one simple chelating (η^2) carboxylate ligand and one phen, CN = 9.

By comparing the structures of the four types of dinuclear carboxylates, we can see the following trends: (i) large RE(III) ions prefer bridging modes (II) and (IV), while smaller RE(III) ions prefer modes (I) and (III); (ii) without auxiliary ligands, RE(III) ions tend to form double-bridged structures, i.e., type (I) and (II), whereas with auxiliary ligands, such as phen, bipy, and even other carboxylate anions,

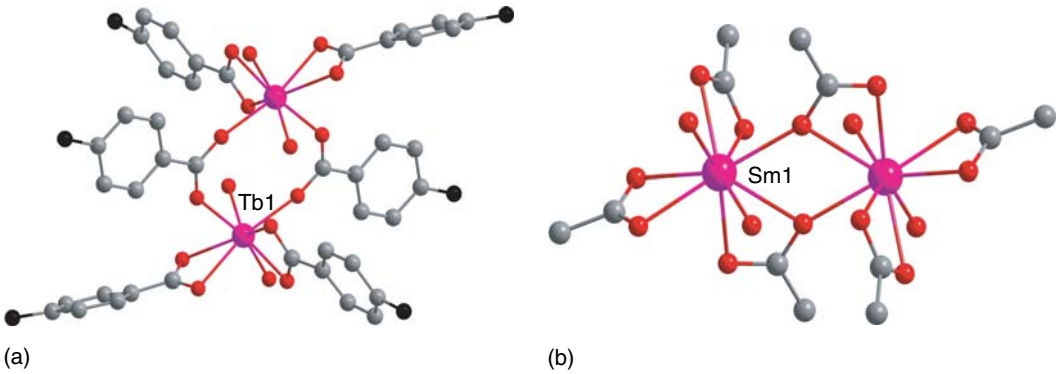


Figure 4 Structures of $[TbL_3(H_2O)_2]_2$ (L = *p*-aminobenzonate) (a) and $[SmL'_3(H_2O)_2]_2$ (L′ = acetate) (b) (RE, black (large balls); O, gray; N, black (small balls); C, white; H, omitted). (Reproduced with permission from from R. Wang and Z. Zheng, ''Rare Earth Complexes with Carboxylic Acids, Polyaminopolycarboxylic Acids and Amino Acids'' in Chun-Hui Huang, Rare Earth Coordination Chemistry: Fundamentals and Applications. © John Wiley & Sons (Asia) Pte Ltd, 2010.)

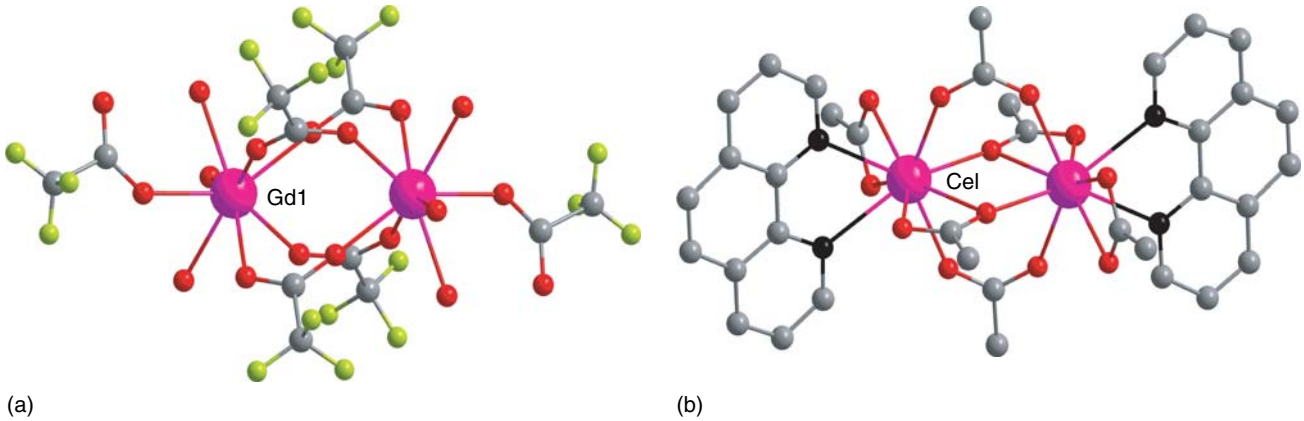


Figure 5 Structures of $[GdL_3(H_2O)_3]_2$ (L = trifluoroacetate) (a) and $[CeL'_3(phen)]_2$ (L′ = acetate) (b) (RE, black (large balls); O, gray; N and F, black (small balls); C, white; H, omitted). (Reproduced with permission from from R. Wang and Z. Zheng, ''Rare Earth Complexes with Carboxylic Acids, Polyaminopolycarboxylic Acids and Amino Acids'' in Chun-Hui Huang, Rare Earth Coordination Chemistry: Fundamentals and Applications. © John Wiley & Sons (Asia) Pte Ltd, 2010.)

the compounds will adopt the modes (III) or (IV), where the auxiliary ligands push one nonbridging carboxylate from each end to form two new bridges. Apparently, chelating tridentate coordination mode, μ_2-$\eta^2\eta^1$, which supplies three dentates, is more appreciated by large RE(III) ions, and the trends are in good consistence with the ionic nature of the RE(III)−O bonds and the trend of lanthanide contraction.

4.4.3 Tetranuclear Carboxylates

Only four tetranuclear carboxylates have been reported so far, and they only involve small RE(III) (RE = Y, Dy, Tm, and Lu). Their structures are all centrosymmetric and fall into two types. The structure of linear tetramer, $[YL_3(H_2O)_2]_4$ (L = *p*-hydroxybenzoate), is shown in Figure 6(a).[23] The four Y^{III} ions are linked together by simple double bridges ($(\mu_2$-$\eta^1\eta^1)_2$). Each of the two terminal Y^{III} are then coordinated by two chelating(η^2) ligands and two water molecules, and each of the two internal Y^{III} are coordinated by one chelating(η^2) ligands and two water molecules, CN = 8.

$Cs_4[LuL_4]_4$ (HL = acetic acid) is a closed square, and only half of the structure is unique.[24] This is also the only example of its type. In the structure, Lu1 and Lu2 or Lu1a and Lu2a are linked together by a mixed triple bridge ($(\mu_2$-$\eta^2\eta^1)_2 + (\mu_2$-$\eta^1\eta^1)$), while Lu1 and Lu2a or Lu2 and Lu1a, on the other hand, are bridged by an acetate in the bidentate bridging (μ_2-$\eta^1\eta^1$) mode, resulting a square with four Lu^{III} at the corners. Lu1 or Lu1a is then coordinated by two chelating (η^2) carboxylates, CN = 9. Lu2 or Lu2a has a very similar coordination environment, except that only one carboxylate is in the chelating (η^2) mode, and the other one is unidentate(η^1), CN = 8 (Figure 6b).

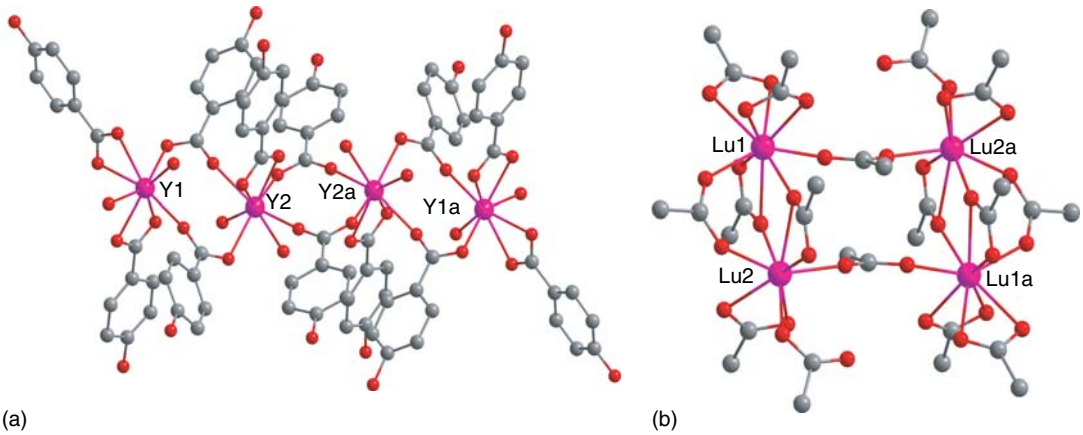


Figure 6 Structures of $[YL_3(H_2O)_2]_4$ (HL = *p*-hydroxybenzoic acid) (a) and $[LuL_4]_4^{4-}$ (HL = acetic acid) (b) (RE, black; O, gray; C, white; H, omitted). (Reproduced with permission from from R. Wang and Z. Zheng, ''Rare Earth Complexes with Carboxylic Acids, Polyaminopolycarboxylic Acids and Amino Acids'' in Chun-Hui Huang, Rare Earth Coordination Chemistry: Fundamentals and Applications. © John Wiley & Sons (Asia) Pte Ltd, 2010.)

The formation mechanism of the tetramers is still not clear, although the sizes of the metals may play important roles there.

4.4.4 *Polynuclear Carboxylates with One Bridging Mode*

The polynuclear carboxylates in this category have the same bridging modes repeating in between the two neighboring metal ions. So far, seven (a, b, c, g, h, i, and k) out of the twelve bridging modes in Figure 2 have been observed: (i) single bidentate bridging: μ_2-$\eta^1\eta^1$; (ii) double bidentate bridging $(\mu_2$-$\eta^1\eta^1)_2$; (iii) double tridentate bridging $(\mu_2$-$\eta^2\eta^1)_2$; (iv) triple bidentate bridging $(\mu_2$-$\eta^1\eta^1)_3$; (v) mixed triple bridging (Figure 2a) $((\mu_2$-$\eta^1\eta^1)_2 + (\mu_2$-$\eta^2\eta^1))$; (vi) mixed triple bridging (Figure 2b) $((\mu_2$-$\eta^1\eta^1 + (\mu_2$-$\eta^2\eta^1)_2)$, and (vii) triple tridentate bridging $(\mu_2$-$\eta^2\eta^1)_3$.

Single bidentate bridging $(\mu_2$-$\eta^1\eta^1)$ modes are very rare, and are only found with small RE(III) ions. In $[YbL_3(H_2O)_2]_n$ (HL = formic acid), the two neighboring Yb^{III} ions are linked together via a single bidentate bridging $(\mu_2$-$\eta^1\eta^1)$ formate, and each of the Yb^{III} ions are then coordinated by two chelating(η^2) formates and two aqua ligands, CN = 8.[25] The same connectivity is also observed in $[YbL_3(H_2O)_2]_n$ (HL = methylthioacetate) and $[DyL_3(H_2O)_4]_n \cdot nH_2O$(L = benzoate).[26,27]

Figure 7 shows the structures with double bridging modes $(\mu_2$-$\eta^1\eta^1)_2$ and $(\mu_2$-$\eta^2\eta^1)_2$. The double bidentate mode, $(\mu_2$-$\eta^1\eta^1)_2$, is only found in the benzoate and some of its derivatives. As shown in Figure 7(a), the neighboring RE(III) ions in $[REL_3(MeOH)_2]_n$ (RE = Sm, Eu, Gd, and Tb; L = benzoate) are bridged by the two bidentate benzoate ligands, and each of the RE(III) centers is coordinated further by one chelating (η^2) benzoate and two methanol with CN = 8.[28] On the other hand, reports show that aliphatic ligands, for example, acetates or propionates, prefer the double tridente bridging mode $(\mu_2$-$\eta^2\eta^1)_2$. Figure 7(b) shows the structure of $[Pr_2L_6(H_2O)_3]_n \cdot 3nH_2O$ (HL = propionic acid).[29] In the structure, the Pr^{III} ions are linked together by two tridentate chelating propionate ligands. With the chelating (η^2) propionate and three water molecules, each Pr^{III} is nine-coordinated.

The four triple bridging modes are the result of the combinations out of the two coordination modes, i.e., bidentate bridging and tridentate bridging. Of the four bridging modes, three of them are observed in anhydrous rare earth acetates ($[REL_3]_n$): with triple bidentate bridging mode, $(\mu_2$-$\eta^1\eta^1)_3$, for RE = Sc;[30] with mixed triple bridging mode (a), $(\mu_2$-$\eta^1\eta^1)_2 + (\mu_2$-$\eta^2\eta^1)$ for RE = Tm–Lu; and with mixed triple bridging mode (b), $(\mu_2$-$\eta^1\eta^1) + (\mu_2$-$\eta^2\eta^1)_2$ for RE = Sm–Er, Y.[31] The mixed triple bridging mode (b) are also found for hydrated larger rare earth acetates, $[RE_2L_6(H_2O)]_n$ (L = acetate, RE = Sm and Eu), $[Ln_2L_6(H_2O)_3]_n \cdot 2.25nH_2O$ (L = 2-thiopheneacetate, RE = Ce–Sm), and $[RE_3L_9(DMSO)_4]_n$ (L = chloroacetate, RE = La, Pr, and Nd). Triple tridentate bridging mode, $(\mu_2$-$\eta^2\eta^1)_3$, is only found with very few anhydrous rare earth carboxylates such as $[EuL_3]_n$ (L = *p*-methylbenzoate) and $[NdL_3]_n$ (L = *m*-methylbenzoate), where CN = 9.

4.4.5 *Polynuclear Carboxylates with Two Bridging Modes Alternated*

Polynuclear carboxylates with two bridging modes alternated form the largest family of rare earth polynuclear carboxylates. At least six bridging modes have been identified within this family.[13] The three most often observed structure types with two bridging modes are the alternating double bidentate bridging and double tridentate bridging, referred as

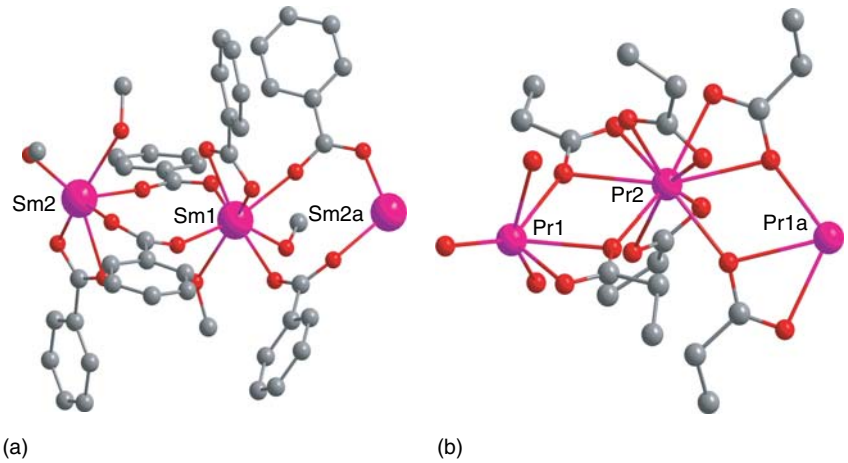


Figure 7 Structures of $[Sm_2L_6(MeOH)_4]_n$ (HL = benzoic acid) (a) and $[Pr_2L'_6(H_2O)_3]_n$ (HL′ = propanoic acid) (b) (RE, black; O, gray; C, white; H, omitted). (Reproduced with permission from from R. Wang and Z. Zheng, ''Rare Earth Complexes with Carboxylic Acids, Polyaminopolycarboxylic Acids and Amino Acids'' in Chun-Hui Huang, Rare Earth Coordination Chemistry: Fundamentals and Applications. © John Wiley & Sons (Asia) Pte Ltd, 2010.)

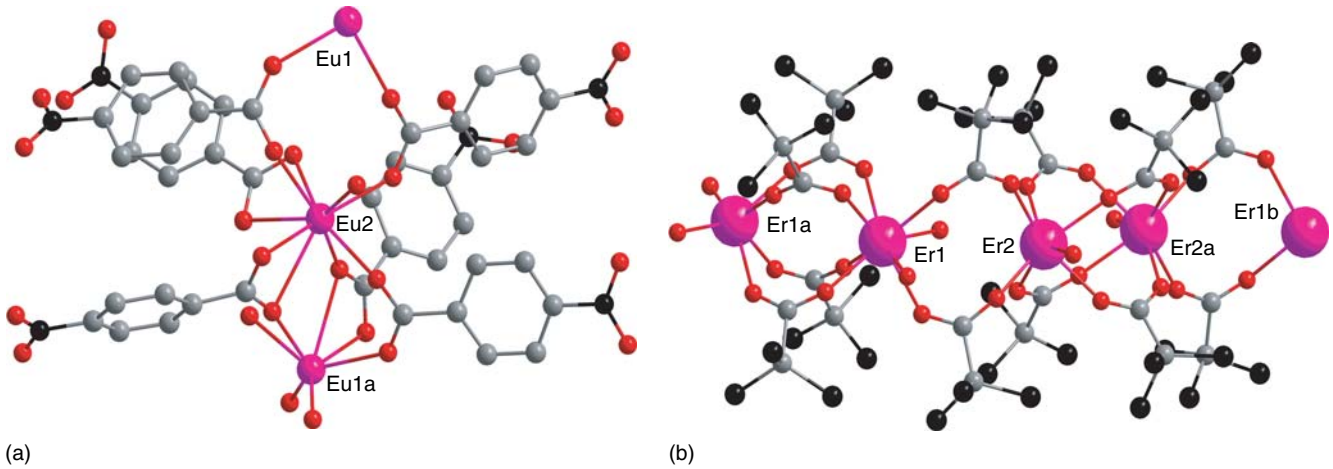


Figure 8 Structures of $[Eu_2L_6(H_2O)_4]_n$ (HL = *p*-nitrobenzoic acid) (a) and $[Er_2L'_6(H_2O)_3]_n$ (HL′ = trichloroacetic acid) (b) (RE, black (large balls); N and Cl (black (small balls); O, gray; C, white; H, omitted). (Reproduced with permission from from R. Wang and Z. Zheng, ''Rare Earth Complexes with Carboxylic Acids, Polyaminopolycarboxylic Acids and Amino Acids'' in Chun-Hui Huang, Rare Earth Coordination Chemistry: Fundamentals and Applications. © John Wiley & Sons (Asia) Pte Ltd, 2010.)

$(\mu_2\text{-}\eta^1\eta^1)_2//(\mu_2\text{-}\eta^2\eta^1)_2$; alternating double bridging and triple bridging, referred as $(\mu_2\text{-}\eta^1\eta^1)_2//(\mu_2\text{-}\eta^1\eta^1)(\mu_2\text{-}\eta^2\eta^1)_2$; and alternating double bridging and quadruple bridging, referred as $(\mu_2\text{-}\eta^1\eta^1)_2//(\mu_2\text{-}\eta^1\eta^1)_4$ or $(\mu_2\text{-}\eta^1\eta^1)_2//(\mu_2\text{-}\eta^1\eta^1)_2(\mu_2\text{-}\eta^2\eta^1)_2$.

The bridging mode $(\mu_2\text{-}\eta^1\eta^1)_2//(\mu_2\text{-}\eta^2\eta^1)_2$ is found in $[La(L)_3(CH_3OH)_2(H_2O)]_n \cdot nCH_3OH$ (L = *E*-3-(4-hydroxyl-phenyl)-acrylic acid).[32] Two La^{III} are linked together through the double tridentate bridging $(\mu_2\text{-}\eta^2\eta^1)_2$, and the double tridentate bridging pairs connect to each other through the double bidentate bridging. Meanwhile, each La^{III} is also coordinated by a monodentate (η^1) carboxylate, two methanol molecules, and one water, CN = 10.

Figure 8(a) shows the structure of $[Eu_2L_6(H_2O)_4]_n \cdot 2nH_2O$ (L = *p*-nitrobenzoate).[33] The structure is of alternating double bridging and triple bridging mode: $(\mu_2\text{-}\eta^1\eta^1)_2//(\mu_2\text{-}\eta^1\eta^1)(\mu_2\text{-}\eta^2\eta^1)_2$, with Eu2 and Eu1a linked by the double bridging $(\mu_2\text{-}\eta^1\eta^1)_2$ and Eu1 and Eu2 bridged by a triple bridging $(\mu_2\text{-}\eta^1\eta^1)(\mu_2\text{-}\eta^2\eta^1)_2$.

The bridging mode, $(\mu_2\text{-}\eta^1\eta^1)_2//(\mu_2\text{-}\eta^1\eta^1)_4$, is found in $[Er_2L_6(H_2O)_3]_n nH_2O$ (L = trichloroacetate) (Figure 8b).[34] The two independent RE(III) ions are joined together by the quadruple bridge, i.e., $(\mu_2\text{-}\eta^1\eta^1)_4$, and each of them are then linked to the neighboring RE(III) ions with a double bridge $(\mu_2\text{-}\eta^1\eta^1)_2$.

The second form of alternating double bridging and quadruple bridging is $(\mu_2\text{-}\eta^1\eta^1)_2//(\mu_2\text{-}\eta^1\eta^1)_2(\mu_2\text{-}\eta^2\eta^1)_2$, where the quadruple bridging consists of a double bidentate bridge and double tridentate bridge. Terbium *m*-nitrobenzoate obtained from DMF, $[Tb_2L_6(DMF)_2]_n$, exhibits this type of bridging, while its lanthanum analog is of a bridging mode, $(\mu_2\text{-}\eta^1\eta^1)_2//(\mu_2\text{-}\eta^1\eta^1)_4$.

4.5 Structures of Rare Earth Polycarboxylates

As discussed in Section 4.4, monocarboxylate ligands tend to bridge RE(III) ions through various coordination modes to form coordination polymers or polynuclear compounds. This feature can certainly be translated to polycarboxylate ligands. Thus, two or more carboxylato groups in the same polycarboxylate can bridge the RE(III) ions in a similar manner, resulting in 2D or 3D polymeric structures. They are insoluble in most solvents, such as water, THF, DMF, or DMSO, and thus are very hard to crystallize as single crystals, which hinder the full structural characterization of the compounds. This may be why rare earth polycarboxylates received much less attention in the past decades than the rare earth monocarboxylates did. However, attracted by the fascinating structures and their potential applications, and with the help hydro(solvo)thermal synthesis techniques, research activities in this area have been increasing exponentially in recent years, and many fascinating 2D and 3D structures have been obtained.

All of the coordination modes shown in Figure 1 have been observed in the structures of rare earth polycarboxylates reported so far, although only limited number of rare earth polycarboxylates have been structurally characterized compared to monocarboxylates. The carboxylate groups within the same ligand are found to display the same or distinctly different coordination modes. The four most frequently observed coordination modes are $\mu_2\text{-}\eta^2\eta^1$, η^2, $\mu_2\text{-}\eta^1\eta^1ZZ$, and $\mu_2\text{-}\eta^1\eta^1ZE$. In a structure, the two adjacent RE(III) ions are generally joined together by up to four carboxylate groups from different ligands to form a chain of edge-sharing rare earth-oxygen polyhedra REO_m ($m = 7$ to 10), and the ligands then use the remaining carboxylate groups to construct more identical or similar chains and to link them together. When all the ligands around the REO_m polyhedron stretch out in the same plane, they will hold the chains in the same plane, and the compound is of a 2D layered structure. And if the ligands around the REO_m polyhedron stretch out in different planes to join the chains of rare earth-oxygen polyhedra, the compound will be a 3D network structure. Therefore, RE(III)–polycarboxylic acid complexes can be considered as polymeric structures made by edge-sharing rare earth-oxygen polyhedra REO_m ($m = 7$ to 10) linked together by carbon chains.[35]

Despite the efforts devoted to the area, very few rare earth polycarboxylates obtained so far can be potentially used for gas storage, liquid absorption, magnetic materials, fluorescent probe, or Lewis acid catalyst. Among them are $[Tb_2(bdc)_3(H_2O)_4]_n$, $[Tb(btc)(H_2O)]_n \cdot 0.5nH_2O{\cdot}n$DMF, and $[Tb(bpdc)_{1.5}(H_2O)]_n \cdot 0.5n$DMF. It is worthy of note that $[Tb_2(bdc)_3(H_2O)_4]_n$ reported by Yaghi *et al*. was the first rare earth-based MOF material. The work was the very first attempt to seek open MOF materials beyond transition metal compounds, and it was also the first time to examine rare earth-carboxylic acid complex as porous materials.[36]

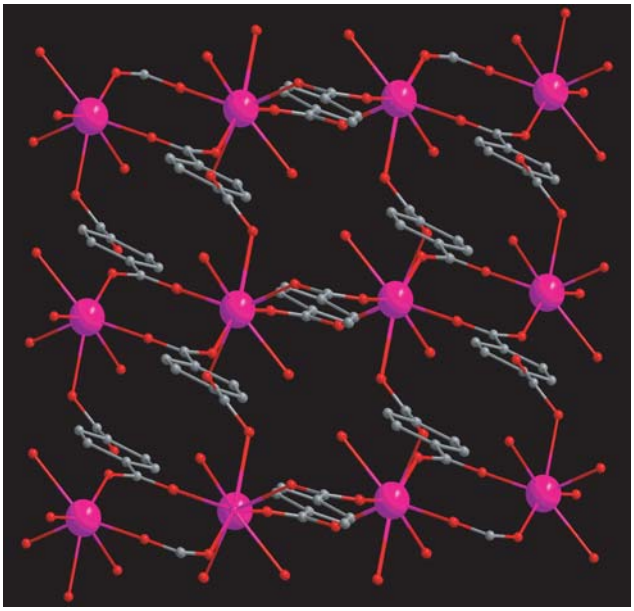


Figure 9 The crystal structure of $[Tb_2(dbc)_3{\cdot}(H_2O)_4]_n$ shown approximately down the crystallographic *b*-axis, where aqua ligands are found to point toward the center of the 1D channels (Tb, black; O, gray; C, white; H, omitted). (Reproduced with permission from from R. Wang and Z. Zheng, ''Rare Earth Complexes with Carboxylic Acids, Polyaminopolycarboxylic Acids and Amino Acids'' in Chun-Hui Huang, Rare Earth Coordination Chemistry: Fundamentals and Applications. (c) John Wiley & Sons (Asia) Pte Ltd, 2010.)

$[Tb_2(bdc)_3(H_2O)_4]_n$ was prepared by hydrothermal synthesis using an aqueous mixture of $Tb(NO_3)_3 \cdot nH_2O$; 1,4-benzodicarboxylic acid(H_2bdc); and triethylamine. In the structure, each Tb^{III} ion is coordinated by six oxygens of bdc^{2-} in a monodentate manner and two water molecules, CN = 8 (Figure 9). The overall structure can be described as a parallelepipedal motif with a terbium center on each of its eight corners and a bdc^{2-} on its four faces (the *ab* and *bc* crystallographic planes and their symmetry-equivalent counterparts), leaving a 1D channel (5.1×6.1 Å^2) running in *b* direction filled with coordination water. Experiments showed that the aqua ligands were removed at 115 °C without framework collapsing, and reintroduction of water to the dehydrated sample restored the original porous structure. The dehydrated porous solid with coordinatively unsaturated metal sites may be useful as fluorescent probe and Lewis acid catalyst.

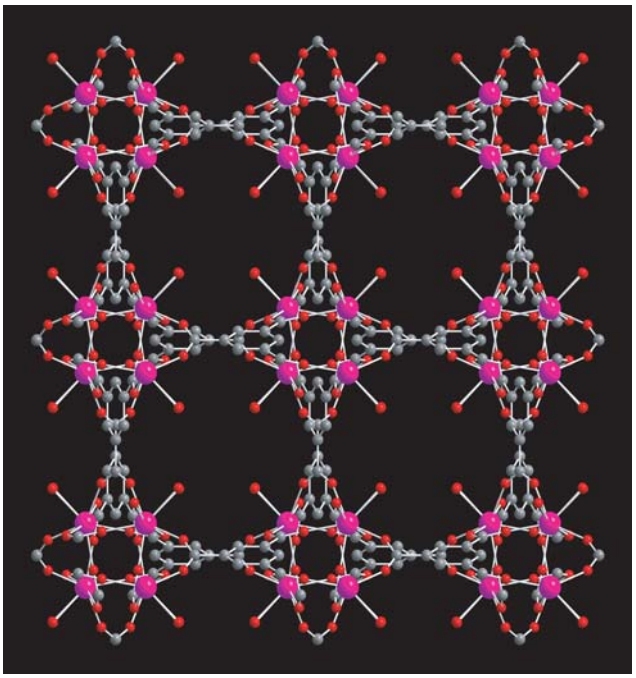


Figure 10 The structure of MOF-76 showing the 6.6 × 6.6 Å^2 square channels in the *c* direction with the ''rod-like'' chains of rare earth-oxygen polyhedra REO_7 linked together via the benzene ring of 1,3,5-benzenetricarboxylate (RE, black; O, gray; C, white; H, omitted; DMF and H_2O guest molecules have been removed for clarity). (Reproduced with permission from from R. Wang and Z. Zheng, ''Rare Earth Complexes with Carboxylic Acids, Polyaminopolycarboxylic Acids and Amino Acids'' in Chun-Hui Huang, Rare Earth Coordination Chemistry: Fundamentals and Applications. (c) John Wiley & Sons (Asia) Pte Ltd, 2010.)

$[Tb(btc)(H_2O)]_n \cdot 0.5nH_2O{\cdot}nDMF$ (H_3btc = 1,3,5-benzenetricarboxylic acid), dubbed as MOF-76, was obtained by solvothermal synthesis.[37] The structure is shown in Figure 10. Each Tb^{III} ion is linked to each of its two Tb^{III} neighbors through three carboxylates with a mode of μ_2-$\eta^1\eta^1ZZ$ to form an edge-sharing infinite chain of rare earth-oxygen polyhedra REO_7. They may be viewed as ''rod-like'' building units in the construction of the overall framework structure. Each rod is then connected to four neighboring rods through the ligand benzene ring. The rods pack in a tetragonal manner, resulting in 6.6 × 6.6 Å^2 square channels along *c* direction, filled with solvent molecules.

$[Tb(bpdc)_{1.5}(H_2O)]_n \cdot 0.5n$DMF was synthesized by diffusion of triethylamine into the mixture of $Tb(NO_3)_3 \cdot nH_2O$ and 4,4′-biphenyldicarboxylic acid(H_2bpdc) (molar ratio 2 : 1) in DMF/EtOH at 4 °C and then at 55 °C.[38] Its crystal structure is shown in Figure 11(a). The terbium atom is coordinated by six oxygen atoms from six $bpdc^{2-}$ and one oxygen atom from a terminal aqua ligand, CN = 7. The crystallographically equivalent Tb^{III} ions are bridged by $bpdc^{2-}$ with a mode of alternating double bidentate bridging and quadruple bidentate bridging: $(\mu_2\text{-}\eta^1\eta^1)_2//(\mu_2\text{-}\eta^1\eta^1)_4$ to give an edge-sharing infinite chain of rare earth-oxygen polyhedra REO_7 in the [001] direction. The 1D chains are linked by biphenyl groups in the [110] and [$\bar{1}$10] directions to form a 3D framework with remarkably large rhombic channels sized 25.2 × 17.1 Å^2 along the diagonals (calculated from the distances of metal ion centers) (Figure 11b).

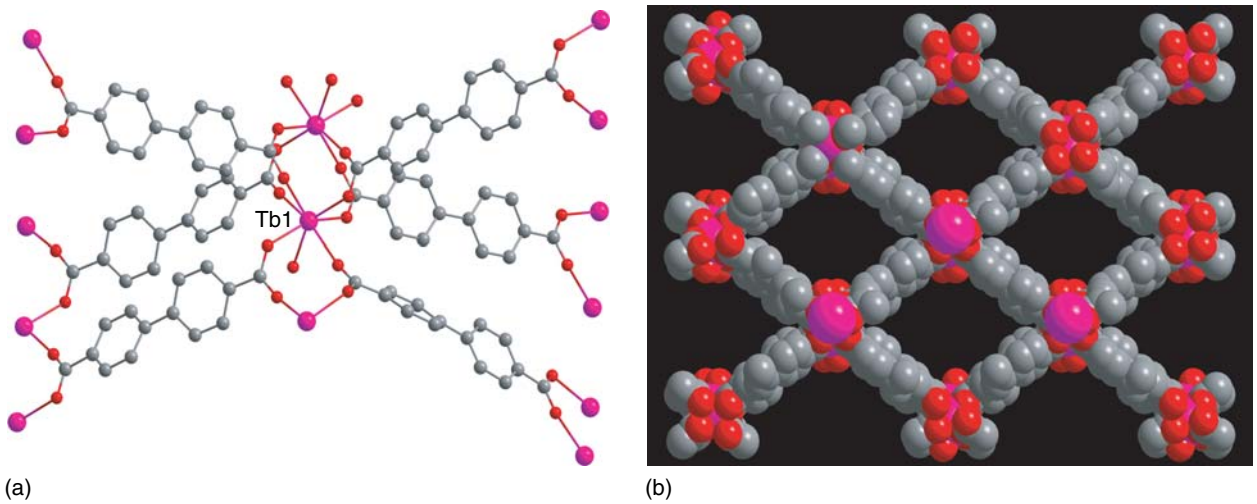


Figure 11 The structure of $[Tb(bpdc)_{1.5}(H_2O)]_n \cdot 0.5n$DMF: (a) The paddle-wheel building block; (b) the 3D framework showing the large rhombic channels (Tb, black; O, gray; C, white; H, omitted; DMF guest molecules in (b) have been removed for clarity). (Reproduced with permission from from R. Wang and Z. Zheng, ''Rare Earth Complexes with Carboxylic Acids, Polyaminopolycarboxylic Acids and Amino Acids'' in Chun-Hui Huang, Rare Earth Coordination Chemistry: Fundamentals and Applications. © John Wiley & Sons (Asia) Pte Ltd, 2010.)

5 CONCLUSIONS

Numerous RE(III) carboxylates, including monocarboxylate and polycarboxylates, with intriguing topologies, diverse nuclearity, fascinating structures, and coordination modes have been reported, and their applications as catalysts, light emitters, optical sensors, porous materials, and magnets have been established. The rare earth carboxylates reported so far reveal 9 coordination modes and 12 bridging modes adopted by carboxylato groups, and are characterized by coordination modes, bridging modes, and their nuclearity. Special efforts have been made to design and synthesize RE(III) polycarboxylates of potential applications, taking advantage of their high thermal stability and high porosity. However, due to the ionic nature of the RE(III)–O(carboxylate) bonds, it remains a challenge to predict a priori the structure of any given compounds. Meanwhile, due to their low solubilities, it is hard to obtain good quality single crystals for rare earth polycarboxylates, which is still the biggest obstacle for rare earth polycarboxylates studies.

6 GLOSSARY

Coordination number(CN): the total number of the atoms coordinate directly to the central atom

Dinuclear compound: a coordination compound containing two metal centers

Monocarboxylic acid: an organic molecule with only one–COOH group

Mononuclear compound: a coordination compound containing only one metal center

Polycarboxylic acid: an organic molecule with more than one–COOH groups

Polynuclear compound: a coordination compound containing two metal centers

7 ACKNOWLEDGMENTS

This chapter is dedicated to my rare earth chemistry mentor, Professor Jia-Zuan Ni on the occasion of his 80th birthday.

8 ABBREVIATIONS AND ACRONYMS

CN = coordination numbers; MOF = metal–organic frameworks; NLO = nonlinear optics; OLED = organic light-emitting diode.

9 REFERENCES

1. B. H. Ketelle and G. E. Boyd, *J. Am. Chem. Soc.*, 1947, **69**, 2800.
2. G. Schwarzenbach, E. Kampitsch, and R. Steiner, *Helv. Chim. Acta*, 1945, **28**, 828.
3. H. Li, M. Eddaoudi, M. O'Keefe, and O. M. Yaghi, *Nature*, 1999, **402**, 276.
4. J. Perles, M. Iglesias, C. Ruiz-Valero, and N. Snejko, *J. Mater. Chem.*, 2004, **14**, 2683.
5. J.-C. G. Bunzli, *Chem. Lett.*, 2009, **38**, 104.
6. G. B. Deacon, M. Forsyth, P. C. Junk, and W. W. Leeb, *Chem. Aust.*, 2008, **75**, 18.
7. R. A. Laudise, *Chem. Eng. News*, 1987, **65**, 30.
8. A. Rabenau, *Angew. Chem. Int. Ed.*, 1985, **24**, 1026.
9. R. E. Liesegang, *Z. Anorg. Chem.*, 1905, **48**, 364.
10. H. K. Henisch, 'Nucleation Sites in Gels', Pennsylvania State University Press, University Park, 1970.
11. N. S. Patil, P. A. Savale, S. K. Bachhav, and S. T. Pawar, *Arch. Phys. Res.*, 2011, **2**, 39.
12. A. Ouchi, Y. Suzuki, Y. Ohki, and Y. Koizumi, *Coord. Chem. Rev.*, 1988, **92**, 29.
13. J. Ma and J. Ni, *Huaxue Jinzhan*, 1996, **8**, 259.
14. P. C. Junk, C. J. Kepert, L. Wei-Min, B. W. Skelton, and A. H. White, *Aust. J. Chem.*, 1999, **52**, 437.
15. Y.-Z. Zheng, M. Evangelisti, and R. E. P. Winpenny, *Angew. Chem. Int. Ed.*, 2011, **50**, 3692.
16. C. Huang, H. Sun, D. Zhang, G. Xu, Y. Han, and N. Shi, *Prog. Nat. Sci.*, 1992, **2**, 113.
17. A. S. Antsyshkina, M. A. Porai-Koshits, and V. N. Ostrikova, *Koord. Khim.*, 1988, **14**, 850.
18. G. Meyer and D. Gieseke-Vollmer, *Z. Anorg. Allg. Chem.*, 1993, **619**, 1603.
19. L. Oyang, L. H.-L. Sun, X.-Y. Wang, J.-R. Li, D.-B. Nie, W.-F. Fu, S. Gao, and Yu. Kai-Bei, *J. Mol. Struct.*, 2005, **740**, 175.
20. R. Vadura and J. Kvapil, *Mater. Res. Bull.*, 1971, **6**, 865.
21. D. John, A. Rohde, and W. Urland, *Z. Naturforsch., B: Chem. Sci.*, 2006, **61**, 699.
22. A. Panagiotopoulos, T. F. Zafiropoulos, S. P. Perlepes, E. Bakalbassis, I. Masson-Ramade, O. Kahn, A. Terzis, and C. P. Raptopoulou, *Inorg. Chem.*, 1995, **34**, 4918.

23. M. S. Khiyalov, I. R. Amiraslanov, K. S. Mamedov, and E. M. Movsumov, *Koord. Khim. (Russ.)(Coord. Chem.)*, 1981, **7**, 1255.

24. A. Lossin and G. Meyer, *Z. Anorg. Allg. Chem.*, 1993, **619**, 1465.

25. N. G. Furmanova, L. V. Soboleva, L. I. Khapaeva, and N. V. Belov, *Kristallografiya (Russ.) (Crystallogr. Rep.)*, 1983, **28**, 62.

26. A. Ouchi, M. Shimoi, and S. Kondo, *Bull. Chem. Soc. Jpn.*, 1985, **58**, 1053.

27. M. S. Khiyalov, I. R. Amiraslanov, F. N. Musaev, and K. S. Mamedov, *Koord. Khim.*, 1982, **8**, 548.

28. U. P. Singh, R. Kumar, and S. Upreti, *J. Mol. Struct.*, 2007, **831**, 97.

29. D. Deiters and G. Meyer, *Z. Anorg. Allg. Chem.*, 1996, **622**, 325.

30. R. Fuchs and J. Strahle, *Z. Naturforsch., Teil B: Anorg. Chem., Org. Chem.*, 1984, **39B**, 1662.

31. A. Lossin and G. Meyer, *Z. Anorg. Allg. Chem.*, 1993, **619**, 1609.

32. H. Li and C. W. Hu, *J. Solid State Chem.*, 2004, **177**, 4501.

33. A. Bettencourt-Dias and S. Viswanathan, *Dalton Trans.*, 2006, 4093.

34. T. Imai and A. Ouchi, *Bull. Chem. Soc. Jpn.*, 1987, **60**, 408.

35. C. L. Cahill, D. T. Lill, and M. Frisch, *CrystEngComm*, 2007, **9**, 15.

36. T. M. Reineke, M. Eddaoudi, M. Fehr, D. Kelley, and O. M. Yaghi, *J. Am. Chem. Soc.*, 1999, **121**, 1651.

37. N. L. Rosi, J. Kim, M. Eddaoudi, B. Chen, M. O'Keeffe, and O. M. Yaghi, *J. Am. Chem. Soc.*, 2005, **127**, 1504.

38. X. D. Guo, G. S. Zhu, Q. R. Fang, M. Xue, G. Tian, J. Y. Sun, X. T. Li, and S. L. Qiu, *Inorg. Chem.* 2005, **44**, 3850.

Lanthanide Complexes with Amino Acids

Zhiping Zheng

Xi'an Jiaotong University, Xi'an, Shanxi, People's Republic of China and University of Arizona, Tucson, AZ, USA

1	Summary	237
2	Introduction	238
3	Proteinogenic (Standard) Amino Acids	238
4	Lanthanide–Amino Acid Complexes Obtained Under Low-pH Conditions	239
5	Lanthanide–Amino Acid Complexes Obtained Under Hydrolytic Conditions	241
6	Conclusions	247
7	Glossary	247
8	Related Articles	247
9	Abbreviations and Acronyms	247
10	References	247

1 SUMMARY

An understanding of the interactions between amino acids and the lanthanide (Ln) ions is of biological and biomedical significance, in particular, under physiological conditions, for example, for the development of spectroscopic probes for the studies of biological systems, artificial nucleases, and new paradigms of contrast agents for magnetic resonance imaging (MRI). Such efforts will also provide an understanding of the metabolism of lanthanide complexes that go into the food chain by way of lanthanide-containing fertilizers.

Out of the concern of lanthanide hydrolysis to produce intractable precipitates of lanthanide oxides and/or hydroxides, the coordination of the lanthanide ions with amino acids has historically been carried out under rather acidic conditions. A large number of such complexes have been obtained under low-pH (1–4) conditions and structurally characterized. Following a summary of the unique features of lanthanide coordination chemistry and the structural and functional characteristics of amino acids, the coordination modes of the amino acid ligands and the salient structural features of the complexes prepared under acidic conditions are discussed.

Recognizing that the low-pH lanthanide–amino acid coordination chemistry is not particularly useful in getting insights into the interactions of these unique metal ions with biological environments, chemists have turned their interest to the lanthanide–amino acid interactions under higher-pH conditions, and sometimes near physiological pH or even higher. Complexes distinctly different from their low-pH counterparts have been discovered, frequently characterized by their polynuclear nature and the presence of structurally well-defined cluster motifs within the complexes. The second part of this article highlights the development of the rational synthetic approach of ligand-controlled hydrolysis of the lanthanide ions for the assembly of these otherwise elusive cluster complexes. Of particular note are the dual function of the amino acid ligands; they not only coordinate the lanthanide ions, they are also critical in serving to limit the degree of lanthanide hydrolysis so that ''oligomeric'' cluster species are formed as opposed to the ''polymeric'' precipitates of lanthanide oxides and/or hydroxides. It has been found that the controlled hydrolysis approach is generally applicable to all readily accessible lanthanide ions, though the reaction outcome appears to be dependent more on the nature of the supporting amino acid ligands. For most of the amino acids studied, discrete complexes featuring a distorted cubane-like core of $[Ln_4(\mu_3\text{-}OH)_4]^{8+}$ were obtained. However, the use of amino acids equipped with polar side chains tends to produce higher-nuclearity clusters whose cores contain up to 60 metal atoms.

The Rare Earth Elements. Edited by David A. Atwood. © 2012 John Wiley & Sons, Ltd. ISBN 978-1-119-95097-4

2 INTRODUCTION

Lanthanides are a family of unique metal elements. With a few exceptions, their ions are predominantly trivalent. All unique features of the coordination chemistry of the lanthanide ions are originated from their large size and characteristic f-electronic configurations.[1,2] There is the requirement of high coordination number (CN) due to the large ionic radius of a lanthanide ion. Its hard Lewis acidic nature makes a lanthanide ion strongly prefer coordination with a hard Lewis base ligand (L). The insignificant involvement of f electrons in chemical bonding leads to the primarily ionic nature of the Ln–L bond, and the general lability of lanthanide complexes. These characteristics of lanthanide coordination chemistry lead to a number of general observations. First of all, the coordination sphere is not well defined, and is dictated by the steric requirement of the ligands for a given lanthanide ion. In addition, multidentate ligands are generally employed in order to obtain thermodynamically and kinetically stable complexes. Furthermore, complexes with ligands containing hard donor atoms, in particular O, are prevalent, with aqua ligand being the one arguably most mundane and frequently observed. Last but not least, upon coordination, an aqua ligand is activated by the Lewis acidic lanthanide ion toward deprotonation, resulting in the formation of the Ln–OH species. If this process is not properly controlled or limited, olation of the Ln–OH species, that is the aggregation of multiple Ln–OH units via bridging interactions of the OH group, occurs, leading eventually to the intractable precipitates of lanthanide oxides/hydroxides. Largely out of this concern, a high pH is considered as detrimental to the realization of well-defined lanthanide complexes; a low-pH condition, typically below 4, is generally adopted when lanthanide complexes are prepared.

The coordination chemistry of the lanthanide ions has leapt from the mere synthesis of structurally interesting complexes to the study of their physical properties and exploration of their potential applications, in particular, toward biologically and biomedically significant problems.[3] For example, $[Gd(DTPA)]^{2-}$ (DTPA: diethylenetriaminepentaacetate) has been used as a contrast-enhancing agent in clinical MRI.[4–6] Luminescent lanthanide complexes have long been used as probes for time-resolved immunoassays.[7–10] Owing to the similar sizes of Ca^{II} and Ln^{III} and their common preference for oxygen donors in complex formation, lanthanide ions have been used as a substitute for the spectroscopically silent Ca^{II} in studies of biological systems; such studies have yielded valuable information about the interaction of metal ions with peptides and proteins. Lanthanide complexes have also been investigated as artificial nucleases to catalyze the hydrolytic cleavage of DNA and RNA;[11,12] amino acids in the protein's peptide linkage serve to coordinate the metal ion, affecting the enzyme's structure and resulting in its active conformation. Lanthanide complexes have also been developed as additives in fertilizers.[13] But anticipated entry of these nonendogenous metal ions into the food chain of mankind is a potential concern as little is known about their subsequent metabolism.

It is clear that a detailed understanding of the interactions between the lanthanide ions and amino acids is critical to the evaluation of how these unique metal ions may impact biological systems and human life. The study of the coordination chemistry of the lanthanides thus becomes not only necessary but also significant.

In this chapter, a review of the progress in the study of lanthanide complexes with amino acids is provided. It should be noted that this article is meant to draw to the attention of interested readers, the interesting coordination chemistry of the lanthanide ions with the all-important amino acid ligands and their potential applications. An exhaustive citation of the large amount of research activities on the subject is not intended and in fact, not possible owing to length limit. Instead, only selected but representative examples from primary literatures are used to highlight the key features of the chemistry. In addition, the chemistry involving ''amino acid-like'' ligands,[14] for example, carboxylates functionalized with N-containing groups, such as (iso)nicotinic acid, are not included. In addition, the discussions of the complexes with (poly)aminopolycarboxylate[15] and nonstandard amino acids are beyond the scope of this chapter. Interested readers are referred to relevant chapters in this volume or review articles published elsewhere ***Carboxylate***; ***Lanthanide Complexes with Multidentate Ligands***.

Our discussion starts with a brief account of the structure and properties of proteinogenic amino acids,[16] those naturally incorporated into polypeptides, in particular, the features that are relevant to metal complexation. The coordination chemistry of the lanthanide ions with amino acids under different pH conditions is then reviewed with emphasis being placed on the discussion of the synthetic and structural chemistry of this important class of lanthanide-containing compounds. This chapter concludes with a summary of the salient features of this research, followed by some personal perspectives pertinent to the current status including the challenging issues ahead, and suggestions regarding the directions toward which the chemistries may be heading.

3 PROTEINOGENIC (STANDARD) AMINO ACIDS

Amino acids discussed in this chapter refer specifically to α-amino acids that are naturally incorporated in proteins. They are molecules containing an amino group and a carboxylic acid group attached to the same C atom with the generic formula $H_2NCHRCOOH$ (Figure 1(a)), where R is a substituent typically referred to as the *side chain* of an amino acid. It is the identity of the R group that determines the structural variety and properties of these unique ligands. Properties important to the coordination of the lanthanide ions

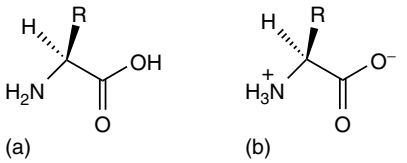


Figure 1 A generic structure of an amino acid (a) and its zwitterionic form (b)

include an amino acid's steric bulk, solubility, hydrophilicity or hydrophobicity, chirality, and acidity/basicity.

The presence of an amine and a carboxylic acid group allow an amino acid to have amphiprotic properties, that is, the carboxylic acid group ($-CO_2H$) can be deprotonated to become a carboxylate ($-CO_2^-$), while the *a*-amino group (NH_2-) can be protonated to become an ammonium group ($-NH_3^+$). The pK_a of the carboxylic acid group in different amino acids has a narrow range between 1.7 and 2.4, with an average of about 2.2, below which, the predominant form contains a neutral carboxylic acid group and an ammonium ion, the protonated amino group. The pK_a range of the *a*-ammonium group is slightly bigger, between 8.8 and 10.8, with an average of 9.4, above which the negatively charged form with an electrically neutral amino group and a -1 charged carboxylate dominates. These different forms of a particular amino acid coexist in a dynamic equilibrium, but at pH between these two pK_a values, the predominant form is zwitterionic (Figure 1(b),), of net zero charge but with the carboxylate and ammonium groups, negatively and positively charged, respectively.

Several amino acids possess ionizable R groups. These include aspartate (Asp), glutamate (Glu), histidine (HHis), lysine (HLys), and arginine (HArg), each with a charged group, and cysteine (HCys) and tyrosine (HTyr), each with a neutral polar side chain. These side chains are potentially involved in the coordination of the same lanthanide ion, together with the skeleton carboxylate and amino groups or in bridging interactions with neighboring complex unit(s).

One last note regarding the coordination behavior of an amino acid toward metal coordination is that except for HGly being nonchiral and HCys being *R*-configured, all standard amino acids are *S*-configured. Coordination of lanthanide ions using optically pure amino acids results in the production of optically active complexes, and possibly homochiral bulk materials that are useful for separation and catalysis where discrimination based on chirality plays a significant role.

Clearly, the coordination ability of an amino acid depends on its specific form, with carboxylate and amino groups, and the side chain each potentially coordinating. This feature in turn is critically dependent on the pH condition. It is thus convenient to present the chemistry of lanthanide–amino acid complexes according to the pH conditions under which the synthesis is carried out. Specifically, the synthetic and structural chemistry of lanthanide complexes with amino acids in two distinct pH ranges is presented, one employed in traditional studies of such complexes and typically below pH 4 and the other, 6 or higher, including physiological pH when hydrolysis of the lanthanide ions are observed to give polynuclear oxide/hydroxide species. With amino acid ligands limiting the degree of hydrolysis, structurally and compositionally well-defined cluster-type complexes are generally obtained rather than the intractable precipitates of lanthanide oxide/hydroxides.

4 LANTHANIDE–AMINO ACID COMPLEXES OBTAINED UNDER LOW-pH CONDITIONS

The development of the synthetic and structural chemistry of lanthanide complexes with amino acids has come a long way since the early 1970s when the role of lanthanide ions in substituting spectroscopically but biologically significant Ca^{II} ion was recognized in the studies of biological systems and functions. A large number of lanthanide–amino acid complexes have since been synthesized, generally by mixing amino acids with readily available and water-soluble lanthanide salts, usually, perchlorates, nitrates, or chlorides. Slow evaporation of the reaction mixture affords solid products whose stoichiometry and structure do not generally show dependence on the initial Ln:L ratio. But in some cases, different products were isolated from the same reaction mixture. However, by adjusting the Ln:L ratio of the starting material, the purity of the products can be improved, which in turn, facilitates the growth of single crystals for structure determination by X-ray diffraction. Today, hundreds of such complexes with crystallographically determined structures have appeared in the literature.[17]

Out of the concern of lanthanide hydrolysis as alluded to above, preparation of lanthanide complexes with amino acids have traditionally been carried out under acidic conditions (typically between pH 1–4). Metal coordination is exclusively through the interaction with the carboxylate group(s) as the amino group remains protonated and therefore, noncoordinating. As such, it is adequate to describe the coordination of amino acid ligands with lanthanide ions by simply commenting on the interactions between the carboxylate group and the lanthanide ion.[18] The various modes of a carboxylate group ''extracted'' from published crystal structures featuring lanthanide–carboxylate coordination, regardless of the origin of the carboxylate group, are collected in Figure 2.

In addition to the diverse coordination modes exhibited by a *single* carboxylate group, a wide range of fascinating dimeric motifs via various bridging interactions (Figure 3) have been identified in the crystal structures of lanthanide–amino acid complexes. In such dimeric units, the lanthanide ions are held together by bridging carboxylato ligands of the same or different modes. Among the different bridging modes, the chelating/bridging unidentate (μ_2-η^2,η^1)

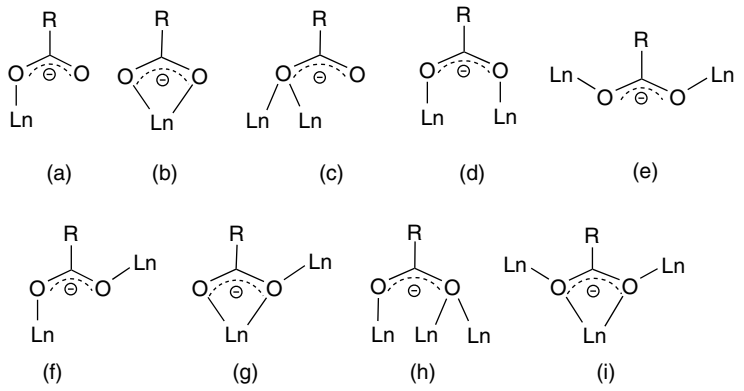


Figure 2 Diverse coordination modes displayed by a carboxylate group toward lanthanide coordination: (a) η^1 (unidentate); (b) η^2 (chelating); (c) μ_2-η^1, η^1 (O, O) (bridging unidentate); (d) μ_2-η^1, η^1 *ZZ* (bridging bidentate); (e) μ_2-η^1, η^1 *EE* (bridging bidentate); (f) μ_2-η^1, η^1 *ZE* (bridging bidentate); (g) μ_2-η^2, η^1 (chelating/bridging unidentate); (h) μ_3-η^2, η^1 (unidentate and unidentate bridging); (i) μ_3-η^2, η^2 (unidentate bridging, chelating, and unidentate bridging)

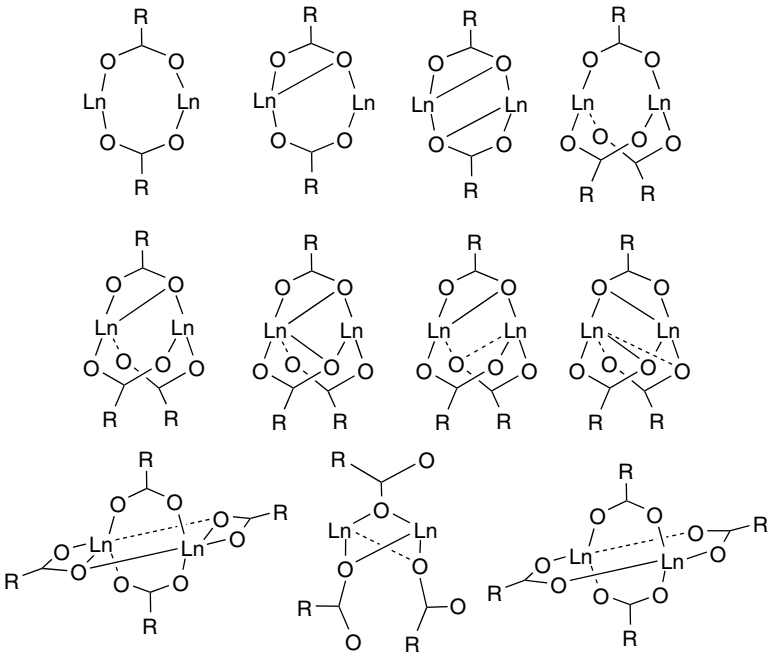


Figure 3 Bridging modes observed in dimeric and polymeric lanthanide complexes with carboxylate ligands

mode makes the shortest Ln···Ln distances, while the bridging bidentate mode (μ_2-η^1,η^1: *EE*) makes the longest. With the same type(s) of bridging interactions, the more such bridging interactions, the shorter is the Ln···Ln separation. The bridged dimeric units are formal secondary building blocks with which the structures of discrete or polymeric lanthanide–carboxylate complexes are constructed.

Different modes are frequently present in the same complex, adding complexity to the lanthanide–carboxylate coordination. The large size, flexible coordination geometry, and oxophilicity of the lanthanide ions are responsible for such observations as chelating and bridging interactions, by contributing more coordinating O atoms, help satisfy the requirement for high CN. Any necessary structural adjustment in order to accommodate the large number of coordinating O atoms is easily achieved largely because of the primarily ionic nature of lanthanide bonding. The hard Lewis acidity of the lanthanide ions, and therefore their strong oxophilicity, helps stabilize the overall structure characterized by such extensive Ln–O bonding.

The situation is actually not as complicated when the coordination of a carboxylate group of an amino acid ligand is

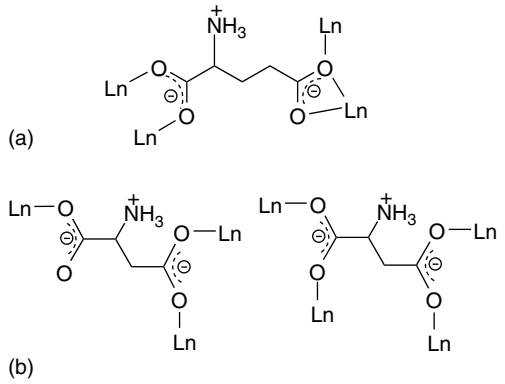


Figure 4 Coordination modes of HGlu (a) and HAsp (b) found in their lanthanide complexes obtained under low-pH conditions

considered.[17] Although far more diverse than the unidentate mode observed in their transition metal complexes, the carboxylate group only shows five modes in lanthanide–amino acid complexes. These include unidentate (η^1), chelating (η^2), bridging bidentate (μ_2-η^1, η^1: *ZZ* and *ZE*), and chelating/bridging unidentate (μ_2-η^2, η^1) modes. However, HAsp and HGlu each possess a side-chain carboxylic group, which deprotonates and participates in the coordination of the lanthanide ions, adding sophistication to the structure of their complexes. The bridging modes observed are shown in Figure 4. Clearly, extensive bridging interactions of both the skeletal and side-chain carboxylate groups are responsible for the polymeric structures observed. The structure of a two-dimensional polymeric complex built from repeating dinuclear units of $[Gd_2(L\text{-Glu})_2(H_2O)_8]^{4+}$ is shown in Figure 5.[19]

Together with other smaller-molecule ligands, such as H_2O and O-containing solvent molecules, high CNs ranging from 6 to 10 are achieved, with CN = 8 and the coordination geometry of a distorted square antiprism being most frequently observed. As for the composition of the complexes, compounds with Ln:L ratios 1 : 1, 1 : 2, or 1 : 3 have been obtained,[20–29] depending on the nature of the amino acids. HGly and proline (HPro) are found to form complexes of all three different Ln:L ratios, while both alanine (HAla) and serine (HSer) can form two different types of complexes, with Ln:L = 1:1 and 1 : 2 for HAla and Ln:L = 1:2 and 2 : 3 for HSer.[30] For complexes with other amino acid ligands, the Ln:L ratio is either 1 : 1 or 1 : 2. It is also of note that structurally characterized mononuclear complexes are not yet known; all published structures of lanthanide–amino acid complexes are either dimeric and discrete or polymeric. Crystal structures of representative complexes, one for each of Ln:L ratios 1 : 1,[26] 1 : 2,[23] and 1 : 3,[27] are shown in Figure 6. A comprehensive discussion of the structural features of various lanthanide complexes with amino acids obtained under low-pH conditions can be found elsewhere.[17]

While studies on the crystal structures of Ln–amino acid complexes offer a clear picture of how the lanthanide ions interact with amino acids, such static snapshots do not present the complete picture of the complex's behavior in solution, which is probably more important if one considers the primarily ionic nature of lanthanide bonding and the anticipated lability of many of these complexes.[1,2] Studying the solution chemistry of lanthanide–amino acid complexes and identifying various species possibly in dynamic equilibria in solution under physiological conditions can better our understanding of the interaction of the lanthanide ions with biological systems where amino acids are the most fundamental building blocks. Extensive efforts along this line of research since half a century ago have garnered valuable information and knowledge.[31] It has been found that the amino acids studied behave very similarly to one another toward lanthanide coordination in solutions, just as we have learned from their structural chemistry in the solid state. Mononuclear species with Ln:L ratios 1 : 1 and 1 : 2 have been found for all the amino acids. Mononuclear species with Ln:L ratio 1 : 3 and dinuclear species with Ln:L ratios 2 : 4 and 2 : 6 have also been confirmed.

5 LANTHANIDE–AMINO ACID COMPLEXES OBTAINED UNDER HYDROLYTIC CONDITIONS

In the solution studies of lanthanide complexation with amino acids discussed above, the presence of hydrolyzed species such as $[Ln(OH)L]^+$ has been identified when the pH of the reaction mixture was raised to above the upper limit of the range (pH 1–4) typically used.[31] It has also been found that complexation of lanthanide ions by neutral and basic amino acids takes place when pH is higher than 6, and that precipitation, presumably due to the formation of lanthanide oxide/hydroxides, occurs when pH is higher than 8.

There was the need to develop lanthanide coordination chemistry with amino acid ligands under physiological pH conditions as the knowledge of how the lanthanide ions interact with amino acids is critical to the understanding of how lanthanide complexes are metabolized if they ever get into our food chain by way of lanthanide-containing fertilizers. The long-term stability and possibly toxicity of these compounds can then be assessed. Despite the fact that the lanthanide ions are highly prone to hydrolysis even at relatively low pH and the dogma that high-pH lanthanide coordination chemistry is limited in scope, the reports of a number of lanthanide complexes with amino acid-like ligands characterized by dinuclear and polynuclear Ln–OH core motifs are encouraging.[32,33] Adventitious hydrolysis was suspected to be responsible for their unexpected formation. The recurring appearance of these motifs suggested that such complexes may not be as elusive as originally thought, and more importantly, may be produced rationally by deliberate hydrolysis. Most importantly, the amino acid-like ligands in these complexes suggest the use of standard amino acids in the same capacity.

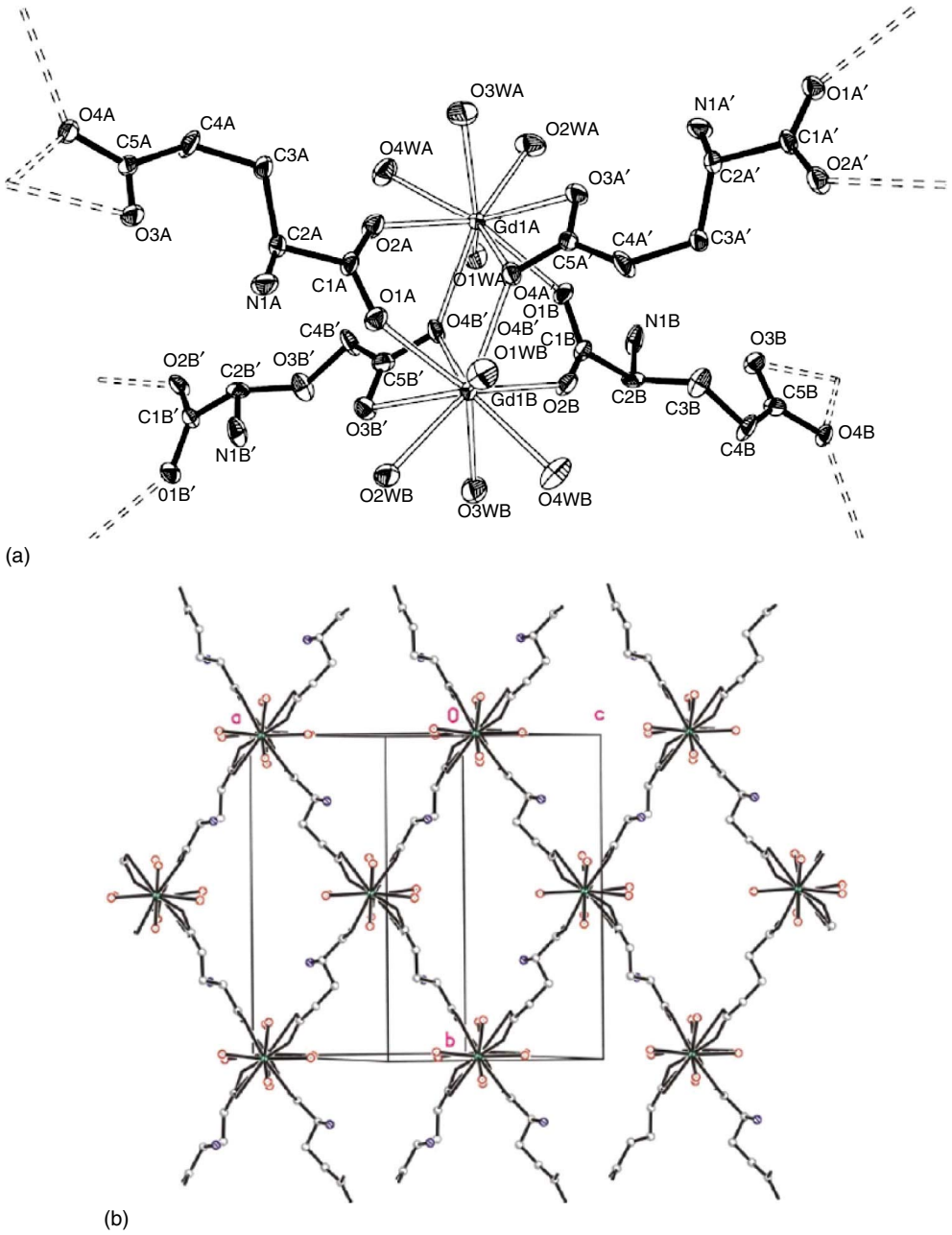


Figure 5 The structure of $[Gd_2(L\text{-}Glu)_2(H_2O)_8]^{4+}$ (a), the building unit of the two-dimensional polymeric structure (b) (Reproduced from Ref. 19, Copyright (2006), with permission from Elsevier)

Adding to the excitement of this research is the observation that the diamond-shaped dinuclear motif of $[Ln(\mu\text{-}OH)_2Ln]$ in some of these unintended discoveries structurally resembles the active-site structure of nucleases, metalloenzymes capable of catalyzing the hydrolytic cleavage of DNA and RNA.[11,12] Later research has found that complexes with this core structure and/or their kinetic equivalents are indeed catalytically active and mimic nicely the functions of naturally occurring nucleases. In fact, the choice of amino acids in making such complexes is natural, as the protein-based ligand environment for the active site of nucleases is constructed by using amino acids as building blocks. From a chemical perspective, the extensive research on lanthanide–amino acid complexes at low pH provides a valuable reference point to compare the coordination modes of the ligands and the structure of the complexes obtained under higher-pH conditions.

By adopting a straightforward procedure but with careful control of pH conditions, structurally well-defined lanthanide complexes with amino acid ligands were obtained.[34,35] As compared with their counterparts synthesized under acidic

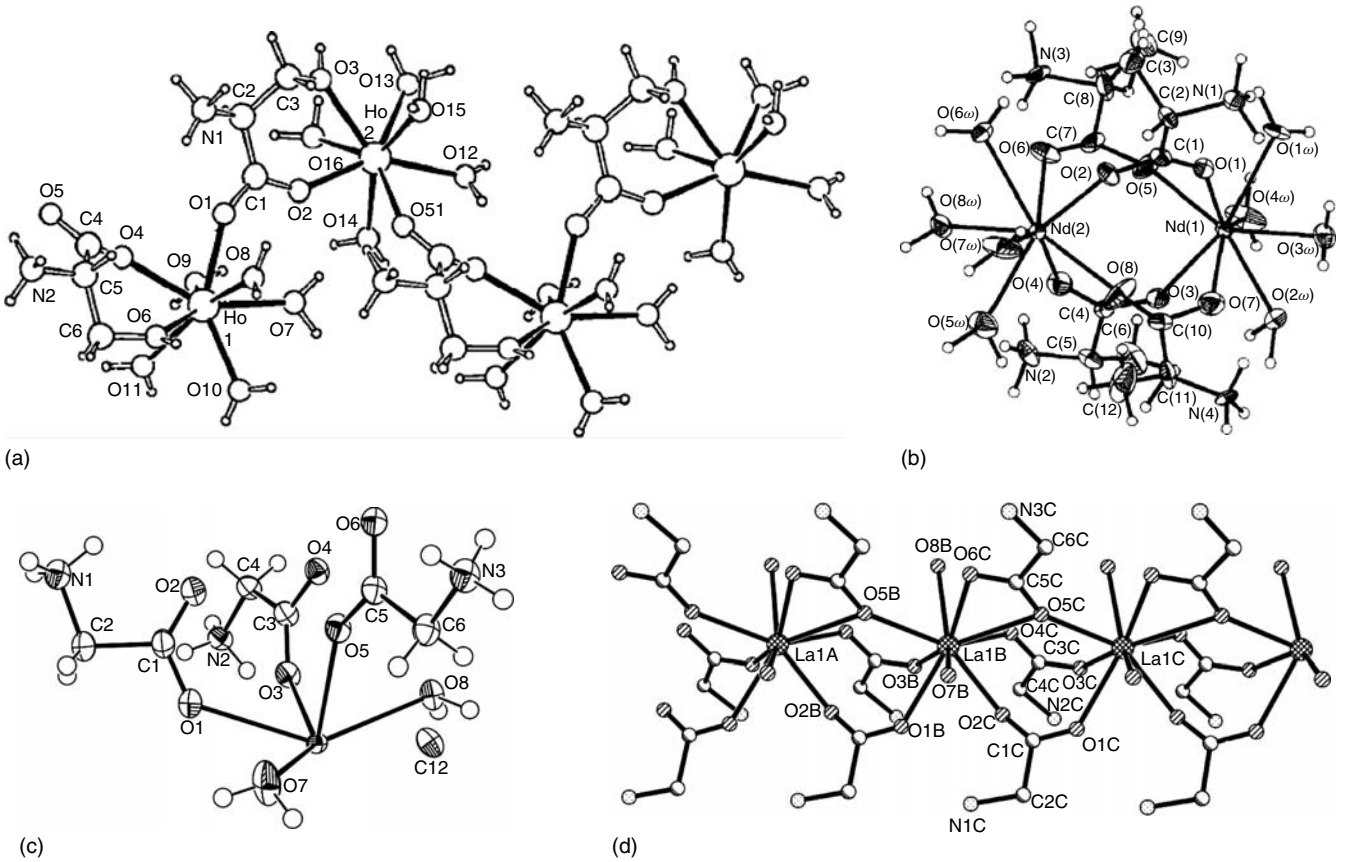


Figure 6 The crystal structures of (a) $[Ho(HSer)(H_2O)_5]^{3+}$; (b) $[Nd_2(HAla)_4(H_2O)_8]^{6+}$; (c) the basic repeating unit of $[La(Gly)_3(H_2O)_2]^{3+}$ and (d) the one-dimensional chain structure (Reproduced with permissions from Ref. 26. © International Union of Crystallographers (IUCr) (published by John Wiley & Sons), 1993; Ref. 23, © (1996), with permission from Elsevier; and Ref. 27, Copyright International Union of Crystallography (published by John Wiley & Sons), 2002)

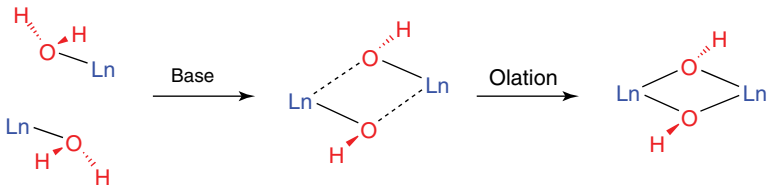


Figure 7 Hydrolysis of aqua lanthanide complexes via olation of the Ln–OH intermediate, affording lanthanide hydroxide complexes

pH conditions, these new complexes were synthesized at pH several orders higher, at about 6.5. Moreover, rather than being dimeric or polymeric with recognizable bridged building units of lanthanide–carboxylate, these new complexes are distinct by the presence of polyhedral cluster-type Ln–OH cores encapsulated by amino acid-based coordination spheres.

The synthetic approach is schematically shown in Figure 7. The essence of this methodology is to limit the extent of lanthanide hydrolysis by using amino acid ligands (not shown) to pre-occupy part of the metal's coordination sphere, leaving only a limited number of sites for aqua coordination. Note that such aqua complexes are the products obtained under low-pH conditions as detailed above. A base is added to raise the pH of the reaction mixture and to promote deliberate hydrolysis of the lanthanide ion. As such, the uncertainty associated with adventitious hydrolysis can be removed. Deprotonation of the aqua complex affords the corresponding hydroxo species. Because of its coordinative and electrical unsaturation, there is a natural tendency for the hydroxo group to seek interaction with additional lanthanide ions. Such a process, often referred to as *olation*

reaction, leads eventually to the assembly of finite-sized and well-defined polynuclear complexes with [Ln(μ-OH)$_2$Ln], the aforementioned nuclease's active site-like diamond-shaped dinuclear species being the smallest member of this type of motifs. If one views the low-pH aqua complexes as monomers, the cluster species can be considered as oligomers with the precipitates of oxide/hydroxides being the undesired intractable polymeric products of the lanthanide hydrolysis.

It has been found that this approach is generally applicable to all the lanthanide ions, and to the most part, to the supporting amino acids.[35–37] It appears that a tetranuclear motif formulated as $[Ln_4(\mu_3\text{-}OH)_4]^{8+}$ with four lanthanide atoms and four triply bridging hydroxo (μ_3-OH) groups occupying the alternate vertices of a distorted cubane is prevalent. Linking the four metal atoms gives a perfect tetrahedron each of whose six edges is bridged by the carboxylate group of an amino acid; the Ln:L ratio is therefore 4 : 6. As a representative, the crystal structure of $[Nd_4(\mu_3\text{-}OH)_4(HAla)_6(H_2O)_8]^{8+}$, the cluster cation of the complex prepared by using alanine as supporting ligand under hydrolytic conditions,[38] is shown in Figure 8.

Discrete cluster complexes with such a single-cubane core were obtained by using HAla, HGly, phenylalanine (HPhen), HPro, HSer, and HVal as ligands.[38–41] Minor discrepancies exist among these complexes, however. Although in most of these complexes, the amino acid ligands are zwitterionic with the amino group remaining protonated, there are examples such as $[Gd_4(\mu_3\text{-}OH)_4(HPro)_4(Pro)_2(H_2O)_7]^{6+}$,[39] $[Gd_4(\mu_3\text{-}OH)_4(HVal)_3(Val)_3(H_2O)_8]^{5+}$,[40] and $[Eu_4(\mu_3\text{-}OH)_4(Asp)_2(HAsp)_3(H_2O)_7]^{11+}$,[41] wherein the ligands are present in both the zwitterionic and the deprotonated and negatively charged forms. In addition, not in all tetranuclear complexes are all six edges of the Ln_4 tetrahedron bridged by carboxylate groups of the ligand. Examples include $[Eu_4(\mu_3\text{-}OH)_4(Asp)_2(HAsp)_3(H_2O)_7]^{11+}$,[41] $[Sm_4(\mu_3\text{-}OH)_4(Gly)_5(H_2O)_{11}(ClO_4)]^{7+}$,[38] and $[Er_4(\mu_3\text{-}OH)_4(Val)_5(H_2O)_{10}]^{8+}$.[38] The coordination sphere is completed with terminal aqua ligands. Coexistence of hydroxo and aqua ligands in the same complex suggests that the pH condition needs to be carefully controlled. In fact, a solution prepared by dissolving the crystals of $[Nd_4(\mu_3\text{-}OH)_4(Ala)_6(H_2O)_8](ClO_4)_8$ in deionized water turned turbid upon standing at room temperature for about 24 h, presumably due to the formation of insoluble lanthanide oxide/hydroxides when further hydrolysis of the terminal aqua ligands occurred.[38] These observations, together with the aforementioned differences in the specific forms of the amino acid ligands and the Ln:L ratio, point to the subtlety of the lanthanide coordination chemistry with amino acid ligands under hydrolytic conditions.

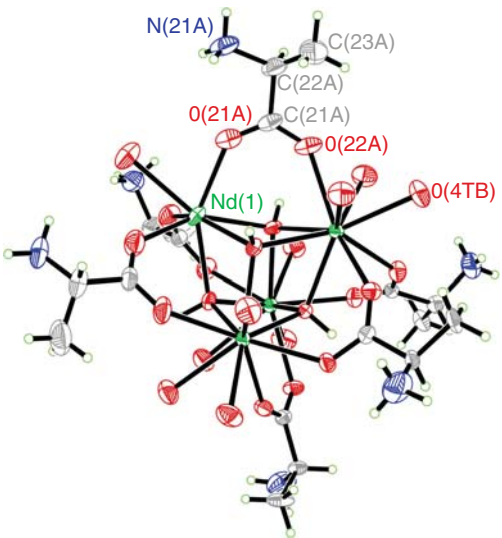


Figure 8 Crystal structure of the cationic complex $[Nd_4(\mu_3\text{-}OH)_4(Ala)_6(H_2O)_8]^{8+}$ (Nd, shaded sphere; O, black sphere; N, crossed gray sphere; C, gray sphere) (Reprinted with permission from Ref. 38. Copyright (2001) American Chemical Society)

In the single-cubane complexes described above, the carboxylate group of the amino acid is used for metal coordination. It is entirely reasonable to anticipate that the side-chain carboxylate group acts in the same capacity. Indeed, the use of Asp and Glu afforded respectively $[Dy_4(\mu_3\text{-}OH)_4(Asp)_3(H_2O)_8]^{2+}$[39] and $[Er_4(\mu_3\text{-}OH)_4(Glu)_3(H_2O)_8]^{2+}$;[38] both possess a three-dimensional (3D) porous structure, featuring discrete cubane units of $[Ln_4(\mu_3\text{-}OH)_4]^{8+}$ (Ln = Dy, Er) interlinked by the skeletal and side-chain carboxylate groups. The formal use of the cubane units as secondary building blocks in the construction of these extended networks further reflects the prevalence of this fundamental lanthanide hydroxide motif. The structures of the building unit (a) and the overall network of $[Dy_4(\mu_3\text{-}OH)_4(Asp)_3(H_2O)_8]^{2+}$ (b) are shown in Figure 9.

Amino acids with polar side chains, neutral or charged, produce most intriguing results in terms of the nuclearity and overall structure of the complexes. These ligands include HSer, threonine (HThre), HTyr, HAsp, HGlu, and HHis. In the synthetic scheme shown in Figure 7, a base is added with heating of the reaction mixture to promote the hydrolysis of the lanthanide ion. The addition of base is stopped when incipient but permanent precipitation of lanthanide oxide/hydroxides is evident; an excess of lanthanide ion in the starting mixture thus serves as the indicator. Using a lower Ln:L ratio and at room temperature, a discrete, single-cubane complex $[Eu_4(\mu_3\text{-}OH)_4(Asp)_2(HAsp)_3(H_2O)_7](ClO_4)_{11}$ (Figure 10)[41] was the isolated product, distinctly different from the 3D network structure shown in Figure 9. The side-chain carboxylic acid groups in three of the five amino acids remain protonated; the other two are deprotonated, but neither participates in the coordination of the metal ions. In addition, different from the bridging mode usually observed for the skeletal carboxylate group, only three of the five are bridging; the other two are unidentate.

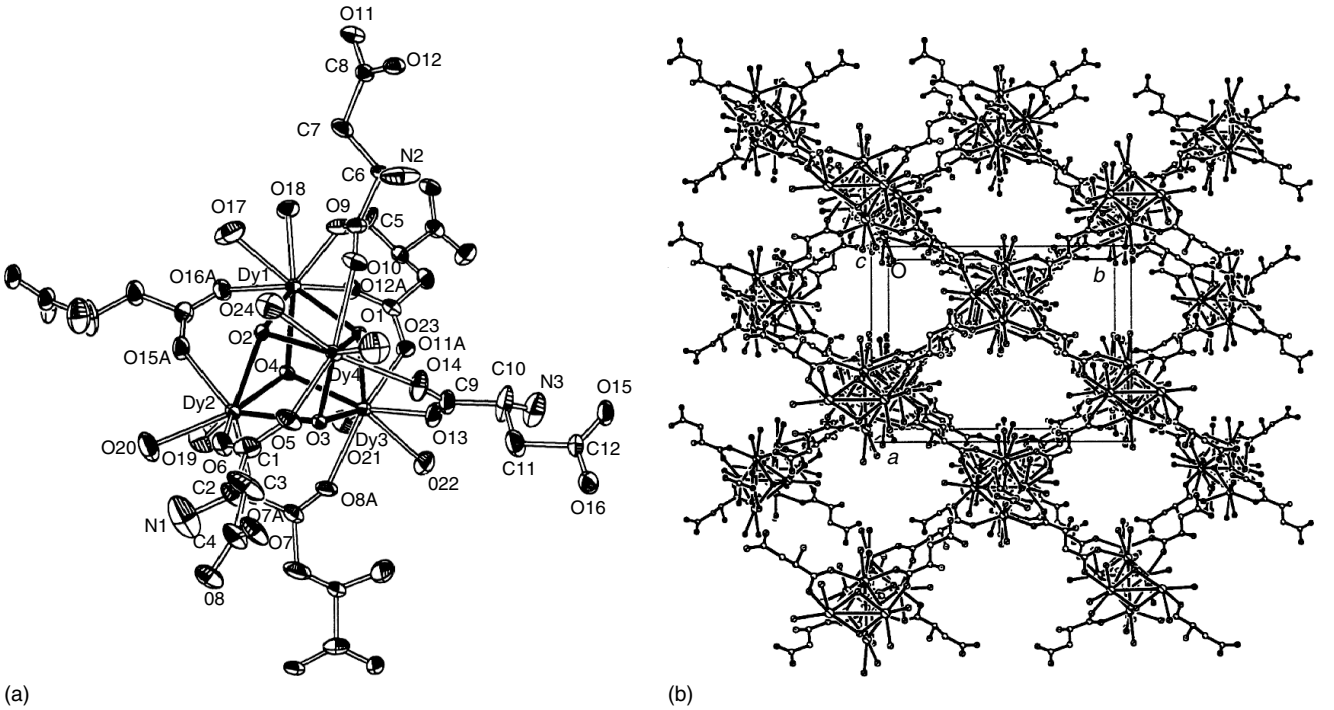


Figure 9 Structure of one repeating unit (a) in the extended network (b) of $[Dy_4(\mu_3\text{-}OH)_4(Asp)_3(H_2O)_8]^{2+}$ (Reproduced with permission from Ref. 39. © Wiley-VCH Verlag GmbH & Co. KGaA, 2000)

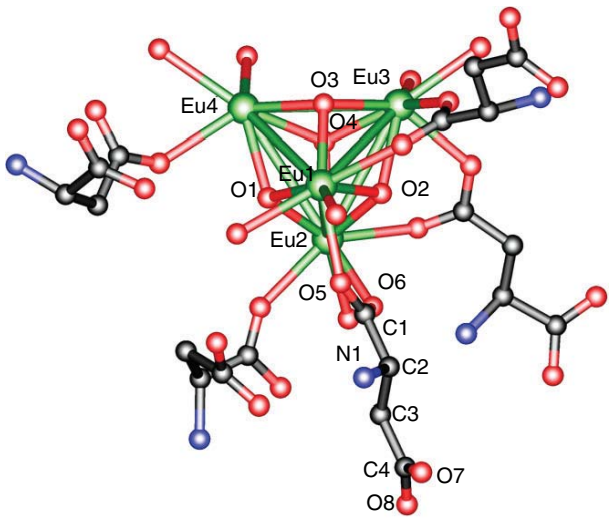


Figure 10 Crystal structure of the cationic cluster complex $[Eu_4(\mu_3\text{-}OH)_4(Asp)_2(HAsp)_3(H_2O)_7]^{11+}$ (Eu, shaded sphere; O/N, black sphere; C, gray sphere) (Reproduced from Ref. 41, Copyright (2007), with permission from Elsevier)

Even more intriguing is the assembly of $[Gd_{14}(\mu_4\text{-}OH)_2(\mu_3\text{-}OH)_{16}(H_2O)_8(Ser)_{20}]^{4+}$[42], a tetradecanuclear complex with HSer. The cluster core (Figure 11), reported first by using nitrophenolate as the supporting ligand,[43] may be viewed as three fused Gd_6 octahedrons into a linear arrangement by sharing opposite vertices, but with the outer two vertices missing. Every Gd_3 triangular face is capped by a triply bridging hydroxo group, while each of the two terminal Gd_4 faces is capped by a μ_4-OH. Alternatively, the structure may be viewed as a ''triple-deckered'' structure with two Gd atoms being sandwiched between the three decks of square-shaped Gd_4 units. These three decks are rotated by 45° with respect to their neighbors. The Ser ligands (not shown) form a protective sheath, rendering the cluster water soluble. This complex has been shown to have superb proton relaxivity and great potential as a highly efficient contrast agent for MRI.

Surprisingly, an analogous reaction using serine to limit the hydrolysis of $Ln(ClO_4)_3$ (Ln = Nd, Gd) produced

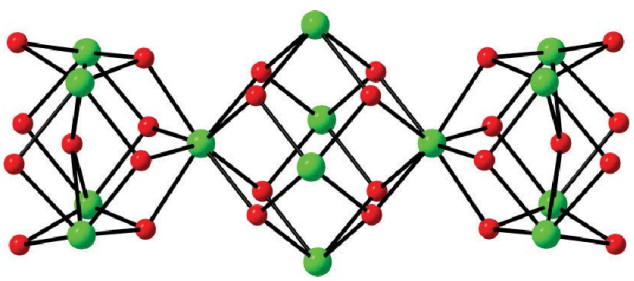


Figure 11 The structure of the tetranuclear cluster core of $[Gd_{14}(\mu_4\text{-}OH)_2(\mu_3\text{-}OH)_{16}]^{24+}$ (Gd, green sphere; O, red sphere)

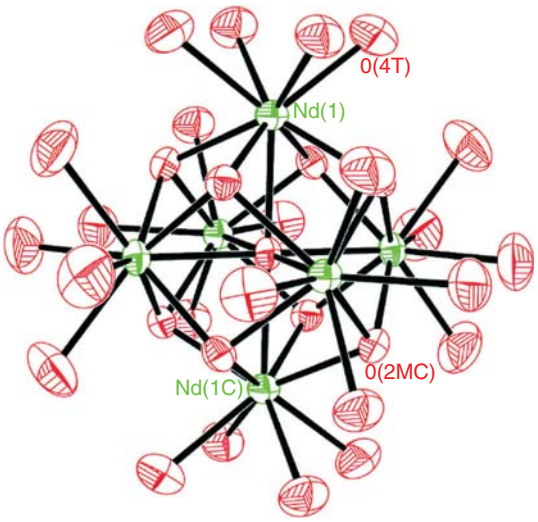


Figure 12 ORTEP drawing of $[Nd_6(\mu_6\text{-}O)(\mu_3\text{-}OH)_8(H_2O)_{24}]^{8+}$. (Reprinted with permission from Ref. 45. Copyright (2000) American Chemical Society).

hexanuclear aqua clusters $[Ln_6(\mu_6\text{-}O)(\mu_3\text{-}OH)_8(H_2O)_{24}]^{8+}$ with no HSer ligands;[44] the structure of the Nd cluster that had already been obtained from the direct hydrolysis of $Nd(ClO_4)_3$ is shown in Figure 12.[45]

Arguably the most interesting series of lanthanide hydroxide complexes are those obtained with HTyr, HHis, and HThre as ligands. Using HTyr as the supporting ligand, pentadecanuclear lanthanide hydroxide clusters were first isolated.[46,47] The isostructural complexes each contain a wheel-like cluster core featuring five vertex-sharing $[Ln_4(\mu_3\text{-}OH)_4]$ cubane units (Figure 13(a)). The unshared vertices are coordinated with Tyr ligands whose amino groups are part of the coordination sphere; the ligand is thus in its deprotonated form as opposed to being zwitterionic. A salient feature of the core motif is the presence of a halide ion (Cl^- or Br^-) situated in the middle of the cluster wheel, coordinating simultaneously the five shared lanthanide atoms. The templating role of the halide ion was subsequently verified. Analogous complexes were subsequently obtained with the use of His as ligand.

In exploring the templating roles of other anionic species, a dodecanuclear complex composed of four vertex-sharing cubane units was isolated, in which two presumably templating iodide ions are found above and below the plane of the wheel-like structure (Figure 13(b)).[46,47] A recent development with Thre as ligand significantly increases the cluster nuclearity along the same series of complexes.

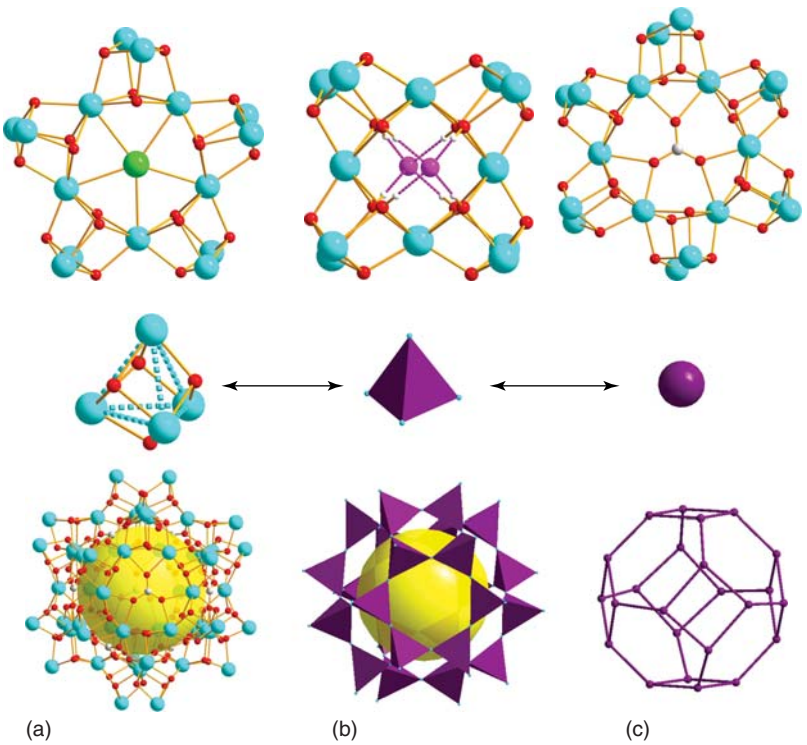


Figure 13 Upper portion: The structures of (a) pentadeca, (b) dodeca, and (c) octadecanuclear clusters templated by a $\mu_5\text{-}X^-$ (X = Cl, Br) ion, two $\mu_4\text{-}I^-$ ions, and a $\mu_6\text{-}CO_3^{2-}$, respectively (Ln, cyan; O, red; Cl or Br, green; I, purple; C, gray). Bottom box: Formal assembly of a 60-metal hydroxide complex featuring 24 vertex-sharing cubane units, represented as dark tetrahedron in the middle structure. These cubane units form six squares and eight hexagons, organized into a sodalite cage structure (Reprinted with permission from Ref. 48. Copyright (2009) American Chemical Society)

A 60-metal cationic complex $[Er_{60}(Thre)_{34}(\mu_6\text{-}CO_3)_8(\mu_3\text{-}OH)_{96}(\mu_2\text{-}O)_2(H_2O)_{18}]^{30+}$ was isolated and structurally characterized.[48] The giant cluster core is composed of 24 vertex-sharing cubane units organized into a beautiful discrete sodalite cage (Figure 13d, bottom box). Two types of secondary building blocks in the overall structure are evident, a 4-cubane wheel and a 6-cubane wheel, the latter being templated by a $\mu_6\text{-}CO_3^{2-}$ ion (Figure 13(c)).

The above discussion suggests that the identity of the lanthanide–amino acid complexes, more specifically, the structure of the core motif, is dependent more on the nature of the ligands than on that of the metal ions. With the assistance of small-molecule entities, cluster-type complexes with amino acid ligands with unprecedented structures may be realized.[49]

6 CONCLUSIONS

Through the extensive coordination chemistry of the lanthanide ions with amino acids under both low- and high-pH conditions, a great variety of coordination modes have been identified for these biologically significant ligands. Extensive bridging interactions by the carboxylate groups, be it in the skeleton or in the side chain, are key to the formation of these complexes; the amino group remains protonated at low pH, and affects a complex's solid-state structure by participating in hydrogen-bonding interactions between different complex units. At higher pH, however, lanthanide coordination by the neutral amino group has been found, in addition to the expected coordination by the carboxylate group(s). It is probably the synergetic coordination of the carboxylate and amino groups that leads to the assembly of these highly sophisticated and aesthetically pleasing cluster complexes.

Extensive research and significant progresses notwithstanding, it remains to be seen how this chemistry will lead to practically significant applications. The key obstacle is the solution stability of such complexes, which is particularly important for the development of clinically viable contrast agents for biomedical imaging. Fundamentally, the synthesis of such complexes remains a challenge as the structures of these species are hard to predict if at all possible, largely due to the ionic character of the bonding interactions, the diverse coordination modes of the amino acid ligands, and the sensitive dependence of the specific forms of the ligands on pH conditions. Exactly because of this gamut of factors, solution studies aiming at the delineation of the different species at equilibrium have been difficult, and therefore, far from being systematic and definitive. These challenges should constitute the major tasks for future studies of these unique lanthanide complexes.

7 GLOSSARY

Cluster: A chemical species containing three or more metal atoms that are directly metal–metal bonded, or within normal bonding distances and with significant intermetal interaction, or bridged by some nonmetal atoms.

Contrast agents: A class of pharmaceuticals that when administered to a patient, enter and pass through anatomic regions of interest to provide transient enhancement of contrast in medical imaging procedures.

Hydrolysis: A chemical reaction in which a substance reacts with water to be converted into one or more other substances.

Nuclearity: The number of metal atoms in a polynuclear complex.

Nucleases: Enzymes that hydrolyze nucleic acids.

Olation: The process by which metal ions form polymeric oxo or hydroxo species in aqueous solution.

Proteinogenic amino acids: Amino acids found in proteins and produced by cellular machinery coded for in the genetic code of any organism.

Zwitterion: A chemical species carrying both positive and negative charges in the same entity.

8 RELATED ARTICLES

Lanthanides in Living Systems; Lanthanides: Coordination Chemistry; Lanthanides: Luminescence Applications; Luminescence; Lanthanides: Magnetic Resonance Imaging; Lanthanide Oxide/Hydroxide Complexes; Carboxylate; Lanthanide Complexes with Multidentate Ligands; Rare Earth Metal Cluster Complexes; Supramolecular Chemistry: from Sensors and Imaging Agents to Functional Mononuclear and Polynuclear Self-Assembly Lanthanide Complexes.

9 ABBREVIATIONS AND ACRONYMS

CN = coordination number; DTPA = diethylenetriaminepentaacetate; MRI = magnetic resonance imaging.

10 REFERENCES

1. C. Huang, 'Rare Earth Coordination Chemistry: Fundamentals and Applications', John Wiley & Sons, Inc., West Sussex, 2010.

2. S. Cotton, 'Lanthanide and Actinide Chemistry', John Wiley & Sons, Inc., West Sussex, 2006.
3. S. N. Misra, M. A. Gagnani, and R. S. Shukla, *Bioinorg. Chem. Appl.*, 2004, **2**, 155.
4. P. Hermann, J. Kotek, V. Kubicek, and I. Lukes, *Dalton Trans.*, 2008, 3027.
5. S. Aime, M. Botta, and E. Terreno, *Adv. Inorg. Chem.*, 2005, **57**, 173.
6. P. Caravan, J. J. Ellison, T. J. McMurry, and R. B. Lauffer, *Chem. Rev.*, 1999, **99**, 2293.
7. J.-C. G. Bünzli, *Chem. Lett.*, 2009, **38**, 104.
8. I. Hemmila and V. Laitala, *J. Fluor.*, 2005, **15**, 529.
9. A.-S. Chauvin, F. Gumy, D. Imbert, and J.-C. G. Bünzli, *Spectr. Lett.*, 2004, **37**, 517.
10. N. Chatterton, Y. Bretonnière, J. Pécaut, and M. Mazzanti, *Angew. Chem. Intl. Ed.*, 2005, **44**, 7595.
11. S. J. Franklin, *Curr. Opin. Chem. Bio.*, 2001, **5**, 201.
12. M. Komiyama, N. Takeda, and H. Shigekawa, *Chem. Commun.*, 1999, 1443.
13. G. Xu, 'Rare Earths', Metallurgical Industry Inc, Beijing, 1995.
14. X. Kong, L. Long, L. Zheng, R. Wang, and Z. Zheng, *Inorg. Chem.*, 2009, **48**, 3268.
15. G. R. Choppin, *J. Alloys Compd.*, 1993, **192**, 256.
16. U. Meierhenrich, 'Amino Acids and the Asymmetry of Life', Springer, Berlin, 2008.
17. R. Wang and Z. Zheng, in 'Rare Earth Coordination Chemistry: Fundamentals and Applications', ed. C. Huang, John Wiley & Sons, Inc., West Sussex, 2010, p. 91.
18. A. Ouchi, Y. Suzuki, Y. Ohki, and Y. Koizumi, *Coord. Chem. Rev.*, 1988, **92**, 29.
19. B. Barja, R. Baggio, R. Calvo, M. T. Garland, M. Perec, and A. Rizzi, *Inorg. Chim. Acta*, 2006, **359**, 3921.
20. E. Huskowska, I. Turowska-Tyrk, J. Legendziewicz, and T. Glowiak, *J. Alloys Compd.*, 1998, **275–277**, 852.
21. J. Torres, C. Kremer, E. Kremer, H. Pardo, L. Suescun, Á. Mombrú, S. Domínguez, A. Mederos, R. Herbst-Irmer, and J. M. Arrieta, *J. Chem. Soc., Dalton Trans.*, 2002, 4035.
22. T. Glowiak, J. Legendziewicz, C. N. Dao, and E. Huskowska, *J. Less Common Met.*, 1991, **168**, 237.
23. T. Glowiak, J. Legendziewicz, E. Huskowska, and P. Gawryszewska, *Polyhedron*, 1996, **15**, 2939.
24. A.-Z. Ma, L.-M. Li, Y.-H. Lin, and S.-Q. Xi, *Acta Cryst.*, 1993, **C49**, 865.
25. T. Glowiak, C. N. Dao, J. Legendziewicz, and E. Huskowska, *Acta Cryst.*, 1991, **C47**, 78.
26. T. Glowiak and C. N. Dao, *Acta Cryst.*, 1993, **C49**, 1171.
27. S. Gao, Y. Li, Q. Ren, Q. Shi, and L. Wang, *Acta Cryst.*, 2002, **E58**, m234.
28. I. Csöeregh, P. Kierkegaard, J. Legendziewicz, and E. Huskowska, *Acta Chem. Scand.*, 1989, **43**, 636.
29. J. Torres, C. Kremer, E. Kremer, H. Pardo, L. Suescun, Á. Mombrú, S. Domínguez, and A. Mederos, *J. Less Common Met.*, 2001, **323–324**, 119.
30. Q. Jin, X. Wang, T. Z. Jin, G. Xu, N. Shi, and Z. Ma, *Acta Sci. Nat. Univ. Pekinensis*, 1995, **31**, 218.
31. C. Kremer, J. Torres, S. Dominguezb, and A. Mederos, *Coord. Chem. Rev.*, 2005, **249**, 567.
32. X. Chen, Y. Wu, Y. Tong, Z. Sun, and D. N. Hendrickson, *Polyhedron*, 1997, **162**, 4265.
33. T. Dube, S. Gambarotta, and G. Yap, *Organometallics*, 1998, **17**, 3967.
34. Z. Zheng and R. Wang, in 'Rare Earth Coordination Chemistry: Fundamentals and Applications', ed. C. Huang, John Wiley & Sons, Inc., West Sussex, 2010, p. 229.
35. Z. Zheng and R. Wang, *Comments Inorg. Chem.*, 2000, **22**, 1.
36. Z. Zheng, *Chem. Commun.*, 2001, 2521.
37. Z. Zheng, *Chemtracts*, 2003, **16**, 1.
38. R. Wang, H. Liu, M. D. Carducci, T. Jin, C. Zheng, and Z. Zheng, *Inorg. Chem.*, 2001, **40**, 2743.
39. B. Ma, D. Zhang, S. Gao, T. Jin, C. Yan, and G. Xu, *Angew. Chem. Int. Ed.*, 2000, **39**, 3644.
40. B. Ma, D. Zhang, S. Gao, T. Jin, and C. Yan, *New J. Chem.*, 2000, **24**, 251.
41. H. Zhang, H. Yu, H. Xu, J. Ren, and X. Qu, *Polyhedron*, 2007, **26**, 5250.
42. L. Messerle, D. Nolting, L. Bolinger, A. H. Stolpen, B. F. Mullan, D. Swenson, and M. Madsen, *Acad. Radiol.*, 2005, **12**, S46.
43. M. R. Burgstein and P. W. Roesky, *Angew. Chem. Int. Ed.*, 2000, **39**, 549.
44. D. Zhang, B. Ma, S. Gao, T. Jin, C. Yan, and T. C. W. Mak, *New J. Chem.*, 2000, **24**, 61.
45. R. Wang, M. D. Carducci, and Z. Zheng, *Inorg. Chem.*, 2000, **39**, 1836.
46. R. Wang, Z. Zheng, T. Jin, and R. J. Staples, *Angew. Chem. Int. Ed.*, 1999, **38**, 1813.
47. R. Wang, H. D. Selby, H. Liu, M. D. Carducci, T. Jin, Z. Zheng, J. W. Anthis, and R. J. Staples, *Inorg. Chem.*, 2002, **41**, 278.
48. X. Kong, Y. Wu, L. Long, L. Zheng, and Z. Zheng, *J. Am. Chem. Soc.*, 2009, **131**, 6918.
49. Z. Zheng, in 'Handbook on the Physics and Chemistry of Rare Earths', eds. K. A. Gschneidner Jr., J.-C. G. Bünzli, and V. K. Pecharsky, Elsevier, Amsterdam, 2009, Chap. 245, Vol. 40.

β-Diketonate

Ke-Zhi Wang

Beijing Normal University, Beijing, People's Republic of China

1 Summary 249
2 Introduction 249
3 Types of β-Diketones used for Lanthanide Complexes 250
4 Crystal Structural Studies of β-Diketonate Lanthanide Complexes 253
5 Polynuclear β-Diketonate Lanthanide Complexes 257
6 Conclusions 260
7 Glossary 260
8 Acknowledgments 260
9 Abbreviations and Acronyms 260
10 References 260

1 SUMMARY

1,3-Diketones, which are frequently called β-diketones, are a family of the most intensively investigated ligands for lanthanide complexes.[1] This chapter outlines the types of β-diketones according to mono(β-diketone), bis(β-diketones), and dendritic β-diketone, and summarizes the types of β-diketone lanthanide complexes according to mononuclear and polynuclear lanthanide complexes. The mononuclear complexes are subclassified according to coordination numbers from 6 to 10, while the polynuclear complexes are divided into f–f and d–f polynuclear lanthanide complexes subcategories. Owing to potential practical applications and synthetic flexibility, numbers of β-diketone lanthanide complexes have been rapidly expanding every year. But many important references have to be omitted because of space limitations and because many topics of β-diketone lanthanide complexes have been covered in two elegant reviews.[2,3] The more extensive citations can be found in a previous review.[4] This chapter focuses on the recent typical examples of crystal structures rather than on optical or other applications of β-diketonate lanthanide complexes. The structural characterizations have played a key role in the development of the chemistry of β-diketonate lanthanide complexes.

2 INTRODUCTION

1,3-Diketones usually occur as prototropic tautomerisms, so called keto-enol tautomerisms, in the solutions and the solids. Figure 1 shows the keto-enol tautomerism equilibria among three species of β-diketo, β-keto-enol, and β-enol-keto as the substitutes R_1 and R_2 are different. The positions of the keto-enol tautomerism equilibria are determined by the solvent polarities and substituents, and the presence of bulkier substituents seems to be the driving force able to shift the tautomeric equilibrium toward the less-stabilized β-diketo form. β-Diketones occur as only a few percent of the β-diketo tautomer in the solution, while otherwise almost exclusively as β-keto-enol form in the solid.

A β-diketone behaves as a monobasic acid as the proton on the α-carbon of its β-diketo form or the enol proton of β-keto enol form can readily be deprotonated at an appropriate pH range depending on the acidity constant values of β-diketones. Thus, the β-diketone acts as a mononegative O–O′ bidentate ligand to strongly coordinate to a lanthanide ion, and forming stable lanthanide complexes. However, the double–single and single–double bond characteristic of the keto-enol and enol-keto forms of free β-diketone are unified upon ligandation. Since tris(β-diketonate) lanthanide(III) complexes are electrically neutral, and can dissolve in some water-immiscible organic solvents

The Rare Earth Elements. Edited by David A. Atwood. © 2012 John Wiley & Sons, Ltd. ISBN 978-1-119-95097-4

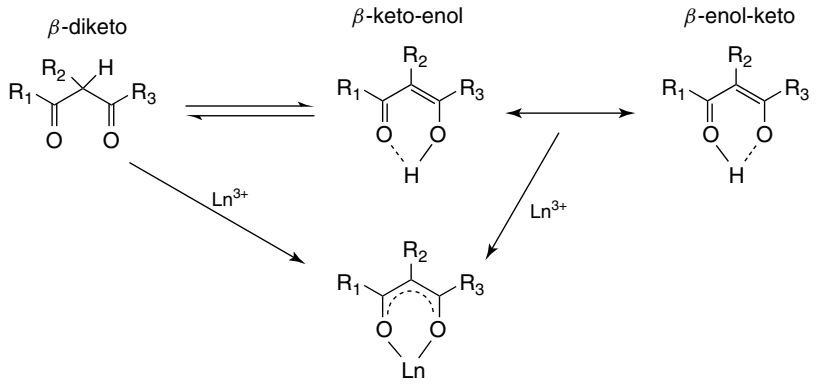


Figure 1 Keto-enol tautomerism equilibrium and equalization of the keto-enol bond lengths upon ligandation for acetylacetone derivatives

such as chloroform and benzene, in early time, many β-diketones were synthesized as lanthanide extractants. Since β-diketones were recognized as efficient sensitizers, so called antennas (see ***Near-Infrared Materials***), to achieve high harvest lanthanide emissions due to the effectiveness of the energy transfer from β-diketonate to the Ln^{3+} cation, this family of complexes have being rapidly developed, and attracted long-lasting interest due partially to their easy synthesis, but mainly to their promising prospects of widespread applications ranging from materials science to biomedical analysis. In the past few decades, many intriguing applications of lanthanide β-diketonates envisioned include light conversion molecular devices; nuclear resonance shift reagents; organic–inorganic hybrid photonic and nanobiophotonic devices; molecular switching and sensing devices; organic electroluminescent devices; liquid-crystalline materials; stains and labels for immunoassays; and the imaging of biological cells, diode lasers and optical fibers, and supramolecular assemblies.

3 TYPES OF β-DIKETONES USED FOR LANTHANIDE COMPLEXES

3.1 Mono(β-Diketone) Ligands

2,4-Pentanedione (HL^1) (also known as acetylacetone), which was prepared by Claisen more than 100 years ago, is the simplest aliphatic (mono)β-diketone ligand. Its development and important properties and applications have recently elagantly reviewed by Reedijk.[3] Many HL^1 derivatives have so far been synthesized. Among them, fluorinated β-diketones have received special attention, and are summarized in Figure 2. These ligands were developed with the purposes of enhancing extraction power by reducing β-diketone acidities, and of improving photoluminescence and electroluminescence properties by reducing the degree of a higher energy frequency oscillator C–H vibrational quenching, and of enhancing thermal stability and volatility of their lanthanide complexes, which are of significance for practical applications.

Although lanthanide emitters have potential advantages of sharp emission bands with high purities of colors ranging from blue to red over fluorescent organic emitters in photonic electroluminescent (EL) applications, the emission intensity of lanthanide ions is usually very weak due to poor charge-transporting capabilities of the lanthanide complexes, hindering their applications in EL displays. In order to improve the performance, many lanthanide β-diketonates grafted with hole-transporting carbazole and triphenylamine or electron-transporting 1,3,4-oxadiazole groups were reported. Some representative nonfluorinated β-diketones based on parent 1,3-propanedione are shown in Figure 3. If the β-diketones were grafted with H-bond-forming group such as hydroxyl, e.g., H_2L^{27}, high-dimensional supramolecular network could be formed. If the β-diketones with additional coordination groups such as pyridine, e.g., $HL^{31,32,35}$, they often could function as useful building blocks for the construction of supramolecular assemblies.

Next category of β-diketones are 1-phenyl-3-methyl-4-acyl-5-pyrazolones 4-acyl-l-phenyl-3-methyl-5-pyrazolones (see Figure 4) and their analogs of 3-phenyl-4-acyl-5-isoxazolones (Figure 5) with the latter kind of β-diketones being stronger acidities (lower acidity constant values) than the former, and have recently been studied as promising light conversion molecular devices.

Figure 6 shows a family of inorganic analogs of β-diketonates, aryl-functionalized imidodiphosphinate ligands (HL^{46-48}), which are bulky ligands around the lanthanide ion, providing shell-type protection of the ion from coordinated solvent molecules. HL^{48} is made of fully fluorinated N-{P,P-di(pentafluorophinoyl)}-P,P-dipentafluorophenylphosphinimidic acid, and can form ideal fluorinated shells about all visible- and near-infrared (NIR)-emitting lanthanides.

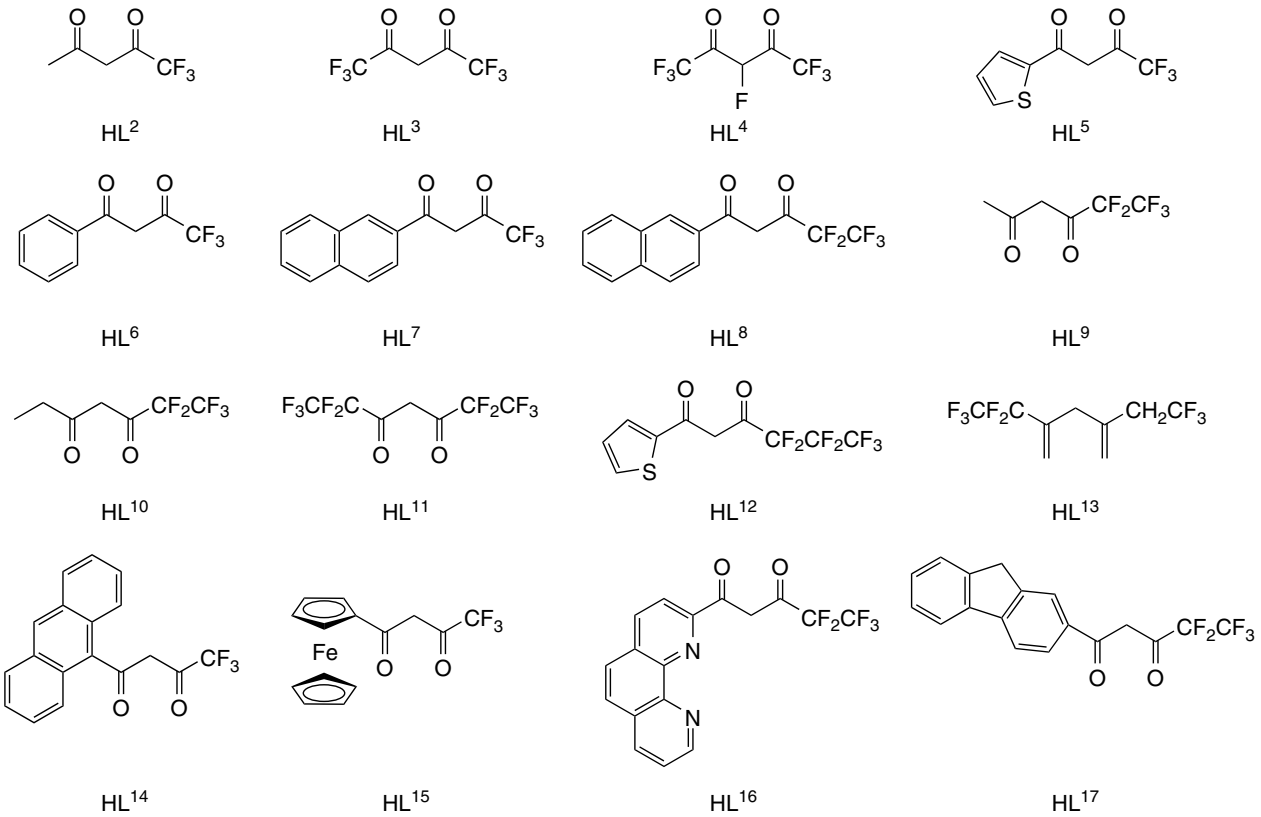


Figure 2 Some representative fluorinated β-diketones

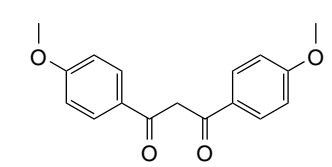
3.2 Bis(β-Diketones) Ligands

Molecular structures of some representative bis(β-diketones) ligands are shown in Figure 7.

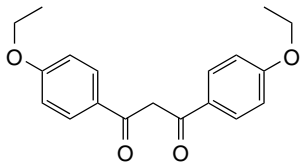
Bis(β-diketones) ligands were proved to be efficient motifs or structural elements for self-assembling highly luminescent metallo-supramolecular lanthanide complexes, and representative ones (H_2L^{49-57}) are shown in Figure 7. Special attention has also been paid to the use of enantiomerically pure bis-β-diketones of H_2L^{54-56}.

3.3 Dendritic β-Diketones Ligands

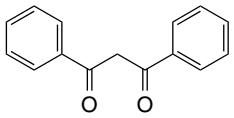
Dendrimers are tree-like branched macromolecules that consist of a core, one or more dendrons, and surface groups. Several dendrimer β-diketones recently reported are shown in Figure 8. They have attracted special interest due to their unique structures and properties. The tree-like shape of dendrimers provides a large surface area that can be grafted with such chromophores as carbazole, resulting in a large absorption cross section and accordingly efficient capture of photons, as well as tuning of carrier-transporting capability and site-isolation effect. The other interesting properties of dendritic molecules are the site-isolation effect of dendrons to create a microenvironment to prevent the intermolecular interaction and avoid self-quenching effect. Indeed, it was found that the dendritic shell could achieve site isolation of the Ln^{3+} cation and maximize their luminescent characteristics. The introduction of such functional groups as carrier-transporting carbazole group into the dentrimer diketone lanthanide complexes would be an attractive aspect of dentrimer chemistry. The dendritic β-diketonate ligands consisting of dibenzoylmethane cores, Fréchet-type poly(aryl ether) dendrons, and the carrier-transporting group-grafted peripheral functional groups may not only tune triplet energy level but also exhibit strong light-harvesting potential, resulting in a strong intense emission from the central lanthanide(III) ion via sensitization. Therefore, some dendritic β-diketonates (see Figure 8) and their corresponding lanthanide complexes were synthesized. Among such very wide range of applications as drug delivery, light harvesting, solar cells, organic light-emitting diode (OLED), and sensors, the application of β-diketone lanthanide dendrimer as OLED materials has attracted particular attention due to their being controllable key features such as intermolecular interactions and charge transport, which are important for all OLED.



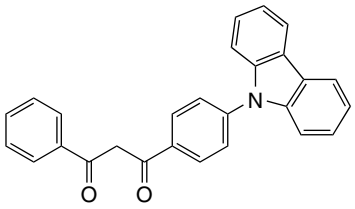
HL^{18}



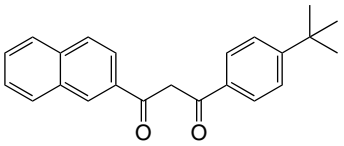
HL^{19}



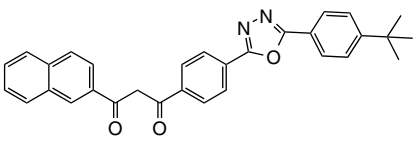
HL^{20}



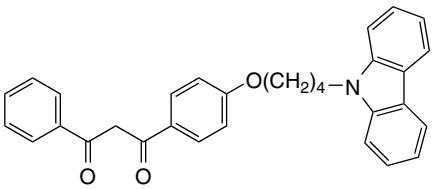
HL^{21}



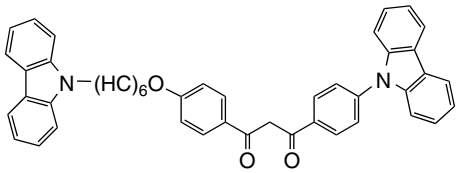
HL^{22}



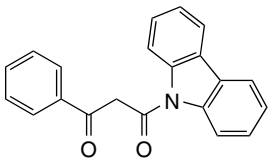
HL^{23}



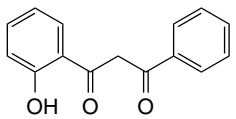
HL^{24}



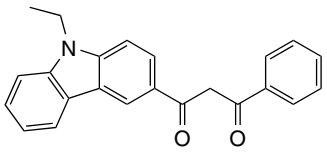
HL^{25}



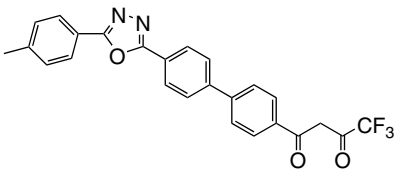
HL^{26}



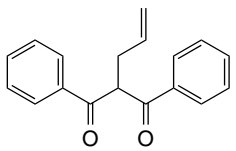
H_2L^{27}



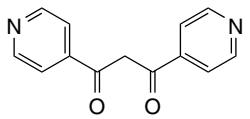
HL^{28}



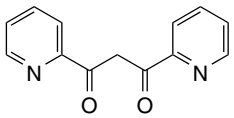
HL^{29}



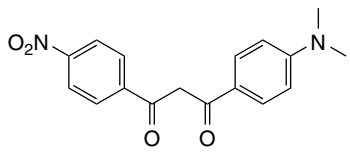
HL^{30}



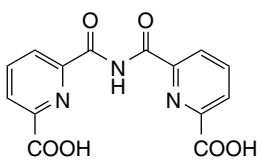
HL^{31}



HL^{32}



HL^{34}



H_3L^{35}

Figure 3 Some representative nonfluorinated β-diketones based on parent 1,3-propanedione

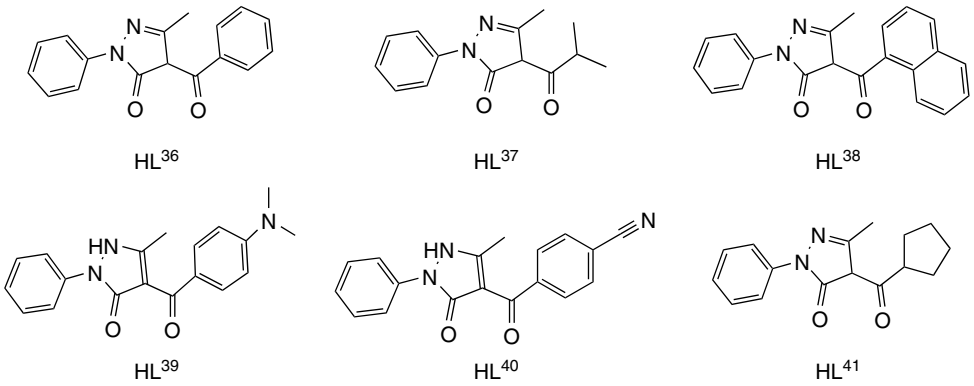


Figure 4 Molecular structures of 1-phenyl-3-methyl-4-acyl-5-pyrazolones

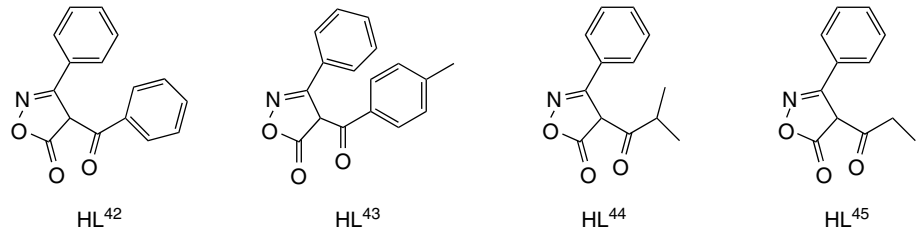


Figure 5 Molecular structures of 3-phenyl-4-acyl-5-isoxazolones

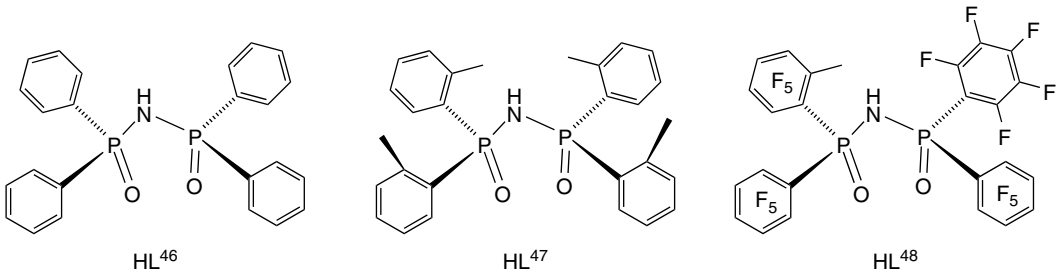


Figure 6 Aryl-functionalized imidodiphosphinate ligands

4 CRYSTAL STRUCTURAL STUDIES OF β-DIKETONATE LANTHANIDE COMPLEXES

4.1 Mononuclear Lanthanide Complexes with β-Diketones

Coordination numbers of mononuclear β-diketonate lanthanides complexes are generally high, varying from six to ten, and strictly depend on the ion radii of lanthanide ions, β-diketones, and the reaction medium and conditions such as temperature or ligand to metal ratio. Since lanthanide ions have large ionic radii, and are typical hard Lewis acids, thus the bonding in their complexes is electrostatic and nondirectional. As a result, the coordination geometries are often irregular, and are governed by steric factors. In the following section, mian attention will be paid to the crystal structural studies on some representative mononuclear β-diketonate lanthanide complexes recently reported.

4.2 Six-Coordinate Lanthanide Complexes with β-Diketones

Generally, six-coordinate lanthanide complexes with β-diketones are coordinatively unsaturated, and thus particularly difficult to synthesize because water or other solvent molecules are particularly prone to occupy extra coordination positions. However, the anionic ligands of L^{46-48} adopt a bidentate coordination mode to produce a six-coordinate

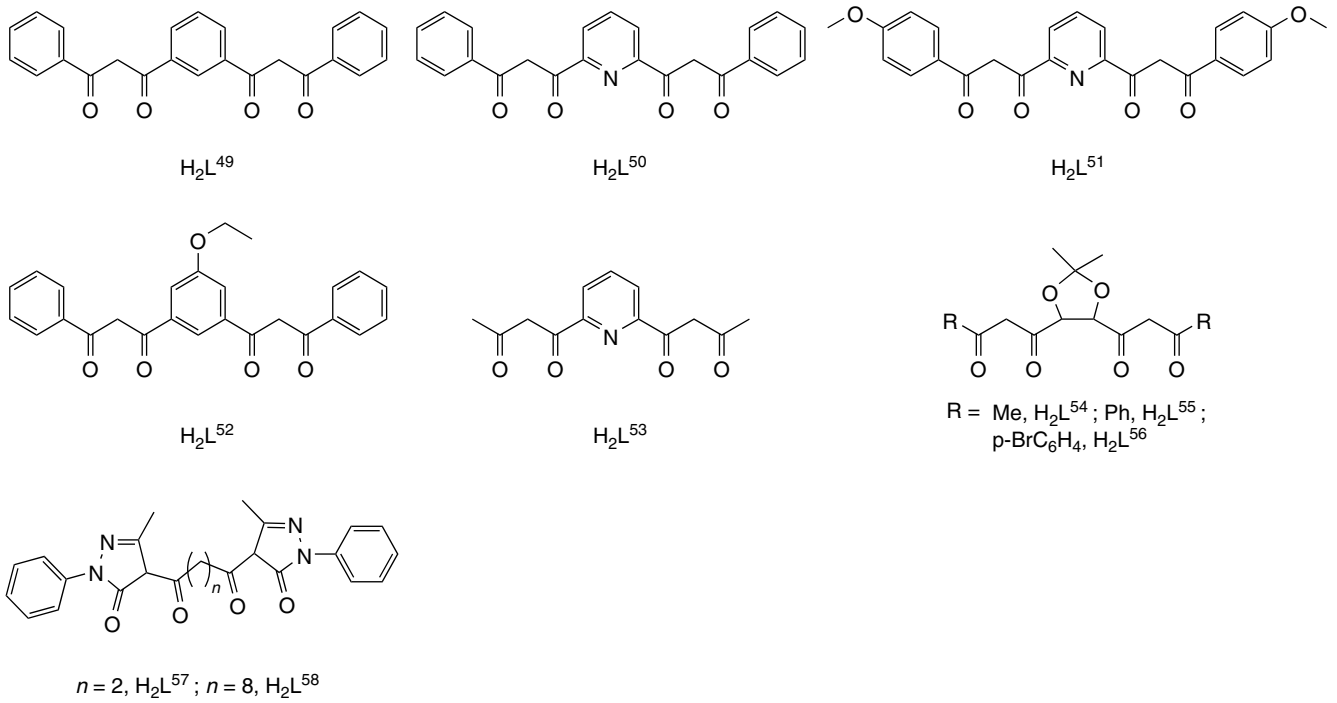


Figure 7 Molecular structures of some representative bis(β-diketones) ligands

metal ion as there are no coordinated solvent molecules.[5] The low coordination number is stabilized by a hydrophobic shell around the central metal ion formed by the 12 *o*-tolyl groups with 6 of the 12 methyl groups being located above the faces of the distorted octahedron defined by the oxygen atoms, shielding the approach of any solvent molecules.

Due to elimination of potential quenching oscillators of N–H and C–H by the fluorination of alkyl chains, lanthanide complexes with HL^{48}, $[Ln(L^{48})_3]$ (in which Ln = Nd, Sm, Eu, Gd, Tb, Dy, Er, Yb, Y, Gd (see Figure 9 for molecular structure of $[Nd(L^{48})_3]$), exhibited enhanced visible or NIR emission with increased luminescence lifetimes.

4.3 Seven-Coordinate Lanthanide Complexes with β-Diketones

Seven-coordinate lanthanide complexes with β-diketones are lacking, such an example is $[Yb(TFPP)(L^1)(H_2O)]$ (see Figure 10)[6] where H_2TFPP = 5,10,15,20-tetra(4-fluorophenyl)porphyrin. Water that binds to ytterbium(III) ion quenches the NIR emission of Yb^{3+}, resulting a shorter lifetime of ~2.4 μs.

4.4 Eight-Coordinate Lanthanide Complexes with β-Diketones

Eight-coordinate β-diketonate lanthanides are one-family of the most widely studied complexes, since the complexes are coordinatively saturated, or almost coordinatively saturated, the emissive properties should be optimized if the appropriate ligands are chosen. A number of lanthanide complexes with compositions of Ln(β-diketonate)$_3$(L) (L = N,N- or N,O-bidentate ligand), Ln(β-diketonate)$_3$(L′)$_x$(sol)$_{2-x}$ (where L′ = monodentate O-containing ligand, sol = O-containing solvent molecule, x = 0, 1, 2), and C^+ [Ln(β-diketonate)$_4$]$^-$ (in which C^+ = inorganic or organic countercation) were structurally characterized. An ORTEP molecular structure diagram for $Eu(L^{40})_3(TPPO)(H_2O)$ (TPPO = triphenylphosphine oxide) is shown in Figure 11.[7] The coordination geometry of the metal center is best described as a distorted bicapped trigonal prism with the trigonal prism being composed of six oxygen atoms (O1, O2, O3, O5, O6, O8). Of them, O1, O2 and O5, O6 are from two β-diketones, and O3 and O8 are from the third diketone and a water molecule, respectively. Another two oxygen atoms (O4, O7) cap the two quadrilateral faces O3–O5–O8–O1 and O2–O6–O3–O1, respectively.

Figure 12 shows ORTEP diagram of N,O-bidentate ligand-containing $[Eu(L^5)_3(PBO)]$ (PBO = 2-(2′-pyridyl)-1,3-benzoxazole).[8] It is eight-coordinated by three bidentate L^5 anions and one bidentate N,O-chelated PBO molecule. This is a rare example of preference of N–O coordination rather than N–N coordination by a lanthanide ion.

By using a bis(β-diketone) of 4-sebacoylbis(1-phenyl-3-methyl-5-pyrazolone (H_2L^{58}) as ligand, sodium di-benzo-18-crown-6 [Na(DB18C6)] as countercation, $[Tb(L^{58})_2]$

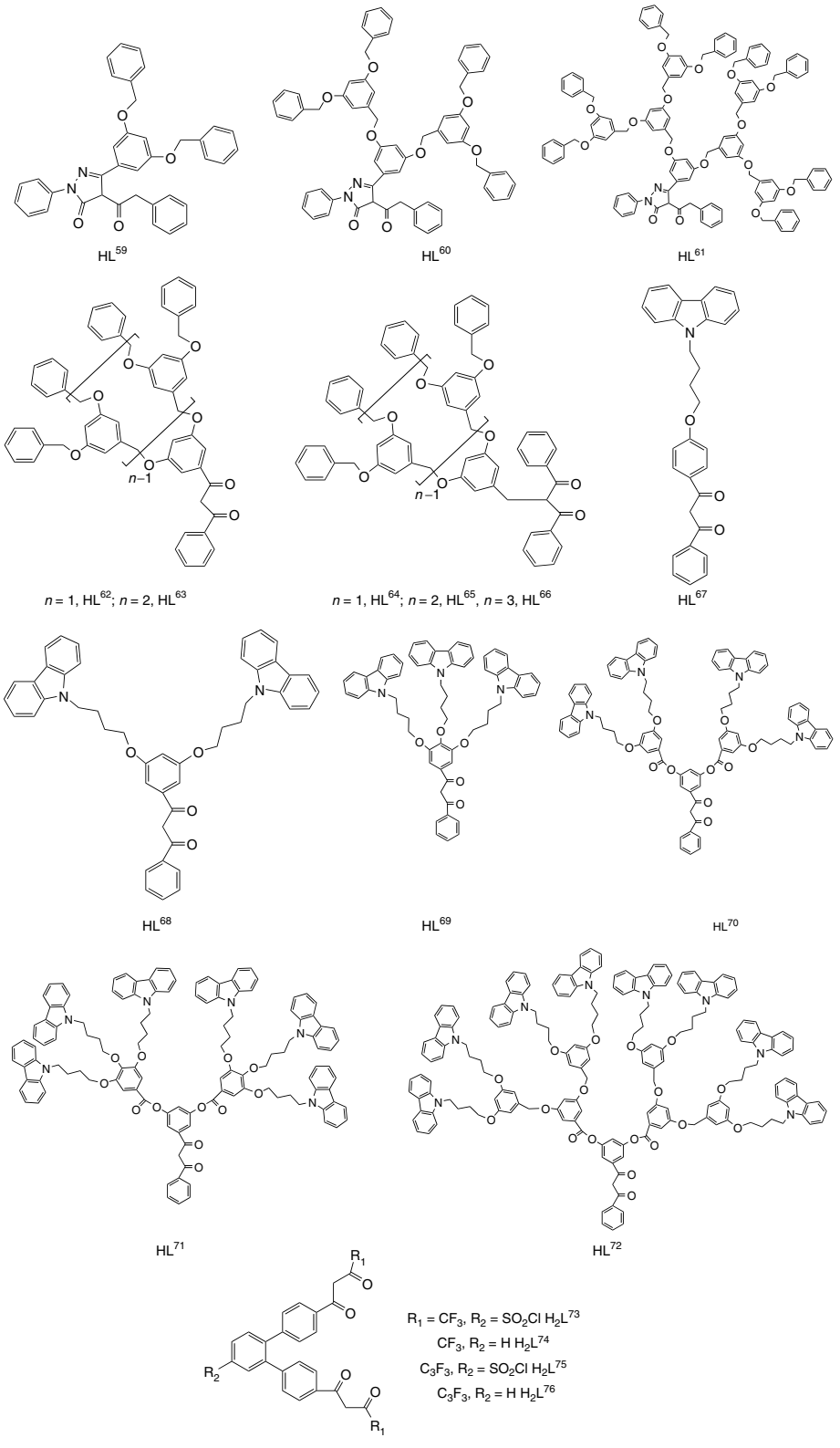


Figure 8 The molecular structures of some representative bis(β-diketones) ligands

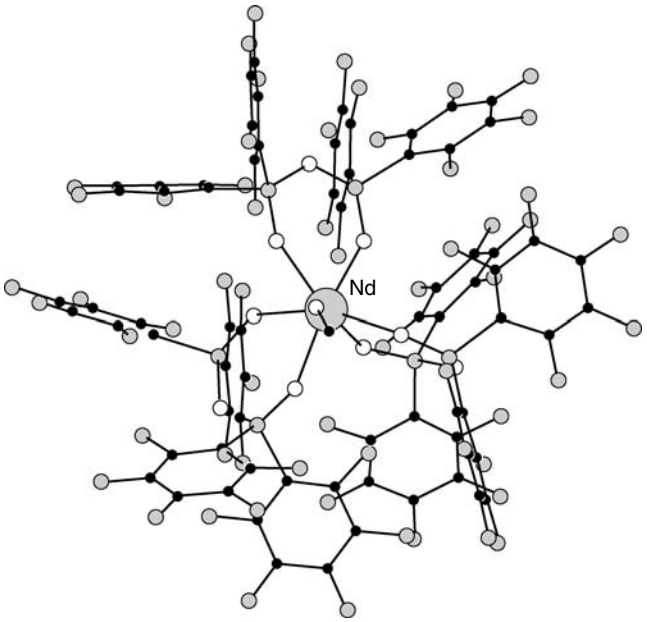


Figure 9 Crystal structure of $[Nd(L^{48})_3]$. (Reproduced from Ref. 5. © Wiley-VCH Verlag GmbH & Co. KGaA, 2007.)

$[Na(DB18C6)H_2O]$ was synthesized and structurally characterized (see Figure 13).[9] The crystal structure of $[Tb(L^{58})_2][Na(DB18C6)H_2O]$ is a one-dimensional molecular ladder structure based on C–H/π, intra- and intermolecular hydrogen-bonding interactions featuring with a Tb^{3+} center surrounded by two tetradentate bispyrazolone L^{57} in a somewhat distorted square antiprismatic coordination geometry. The Na^+ coordination environment is distorted hexagonal pyramidal and involves six oxygen atoms furnished by DB18C6 and one oxygen atom from a water molecule. The quantum yields and $^5D_4$ lifetimes for $[Tb(L^{58})_2][Na(DB18C6)H_2O]$ in solid state were found to be 18.13% and and 2.82 ms, respectively.

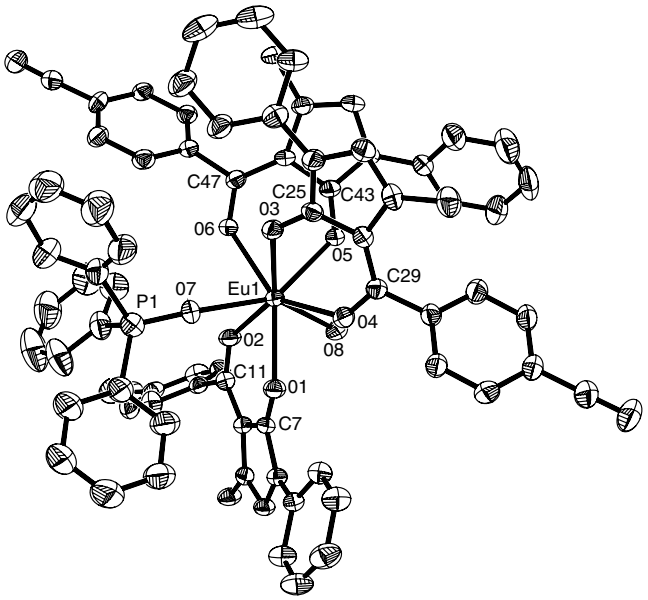


Figure 11 ORTEP diagram of $Eu(L^{40})_3(TPPO)(H_2O)$ and the H atoms removed for clarity. (Reprinted with permission from Ref. 7. Copyright (2005) American Chemical Society.)

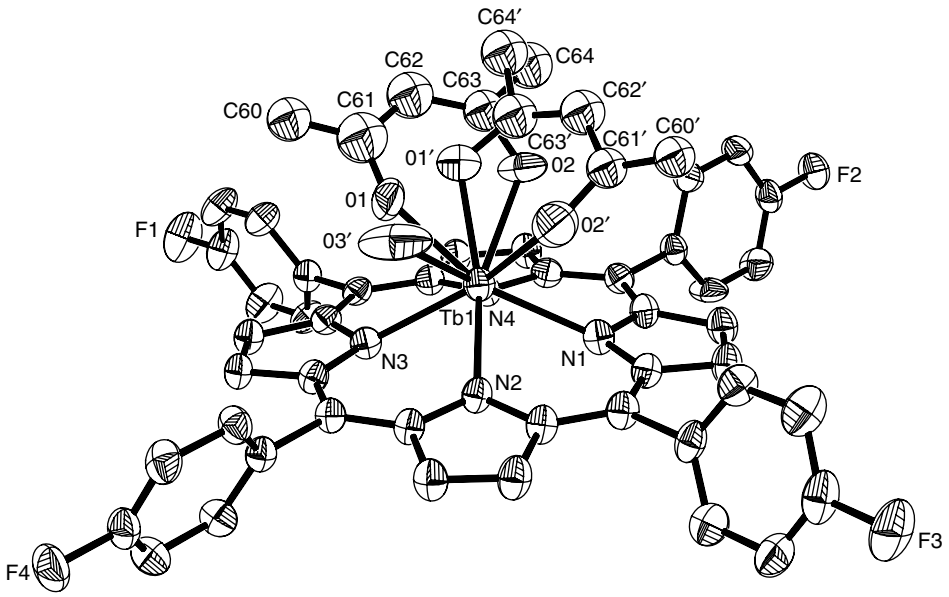


Figure 10 The ORTEP diagram of $[Yb(TFPP)(L^1)(H_2O)]$. All hydrogen atoms are omitted for clarity. (Reproduced from Ref. 6. © Elsevier, 2008.)

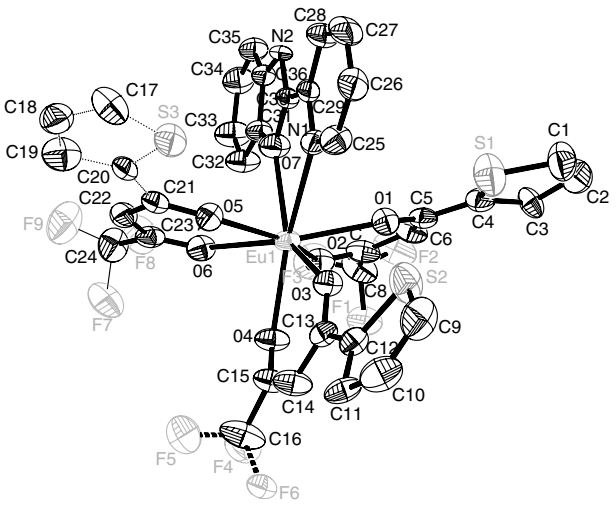


Figure 12 Asymmetric unit of $[Eu(L^5)_3(PBO)]$ with atom numbering scheme and thermal ellipsoids (30%). (Reproduced from Ref. 8. © Wiley-VCH Verlag GmbH & Co. KGaA, 2006.)

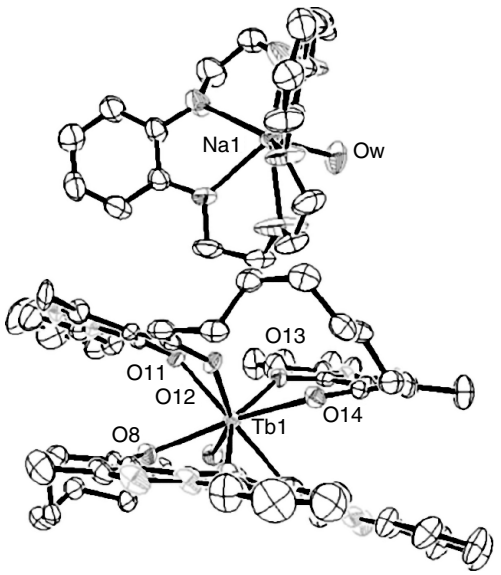


Figure 13 ORTEP diagram of $[Na(DB18C6)H_2O][Tb(L^{58})_2]$ and the hydrogen atoms removed for clarity. (Reprinted with permission from Ref. 9. Copyright (2008) American Chemical Society.)

4.5 Nine-Coordinate Lanthanide Complexes with β-Diketones

Nine-coordinate lanthanide complexes with β-diketones having the compositions of Ln(β-diketonate)$_4$(sol) and Ln(β-diketonate)$_3$(L)(sol)$_x$ (L = N,N,N-tridentate ligand, $x = 0$; L = N,N,-bidentate ligand, $x = 1$), have recently been structurally characterized. The molecular structure of $Eu(L^5)_3$(TPTZ) (TPTZ = 2,4,6-tri(2-pyridyl)-1,3,5-triazine) isis shown in Figure 14.[10] The lanthanide ion in each of these complexes is with six β-diketonate oxygen atoms and three TPTZ nitrogen atoms, forming a monocapped square antiprism coordination polyhedron.

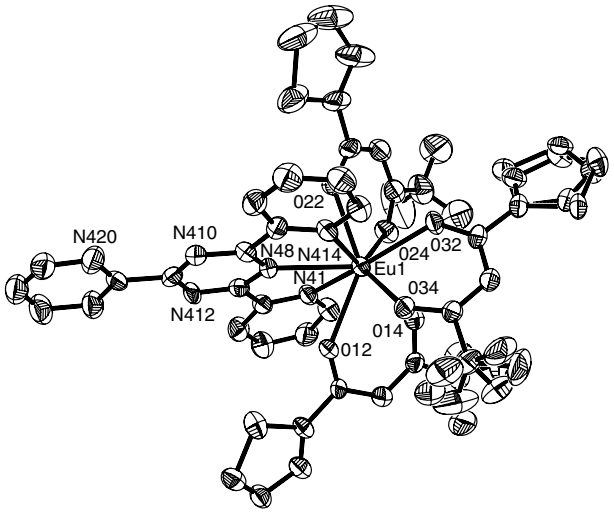


Figure 14 An ORTEP view of the crystal structure of $Eu(L^5)_3$(TPTZ). (Reproduced from Ref. 10. © Elsevier, 2007.)

4.6 10-Coordinate Lanthanide Complexes with β-Diketones

Using HL^3 and bpm as ligands, 10-coordinate complexes of $Ln(L^3)_3$bpm (Ln = Nd^{III}, Gd^{III}, or Tb^{III}; bpm = 2, 2′-bipyrimidine) were synthesized and structurally characterized.[11] The Nd and Gd complexes are with repeating Ln-bpm units, forming one-dimensional arrays. However, on the contrary, the Tb complex does not form a one-dimensional array with its structure being nine-coordinate with the ninth position occupied by a covalently bonded H_2O molecule, which is H-bonded to the bpm group from another complex in solution.

A 10-coordinate La^{III} complex of $\{[La(L^3)_5][(TTF–CH=CH–Py^{+})]_2\}$ was also structurally characterized (Figure 15).[12] The La^{III} ion is coordinated by 10 oxygen atoms from 5 bis-chelating L^3 ligands. The arrangement of the 10-coordinated oxygen atoms leads to a tetradecahedral polyhedron around the lanthanum.

5 POLYNUCLEAR β-DIKETONATE LANTHANIDE COMPLEXES

5.1 f–f Polynuclear β-Diketonate Lanthanide Complexes

HL^{31} was reported to form a monodimensional polymeric chain $\{[Gd(L^{31})_3(H_2O)]\cdot 4H_2O\}_\infty$, while HL^{32} yielded

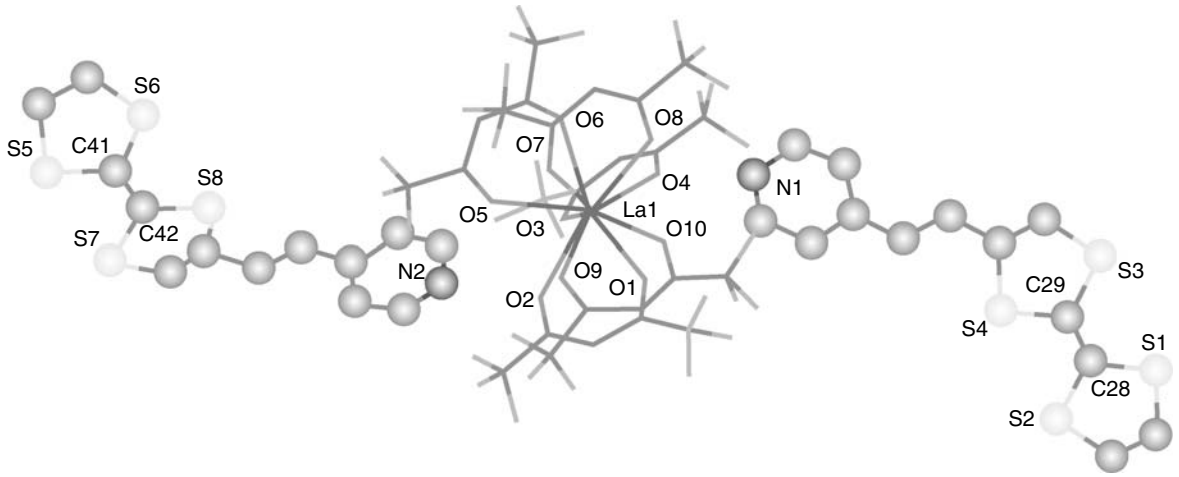


Figure 15 The asymmetric unit of $\{[La(L^3)_5][(TTF–CH{=}CH–Py^{\cdot+})]_2\}$. The radical cation donors are drawn as balls and sticks; the anionic coordination complex of La(III) is drawn as capped sticks. (Reprinted with permission from Ref.12. Copyright (2009) American Chemical Society.)

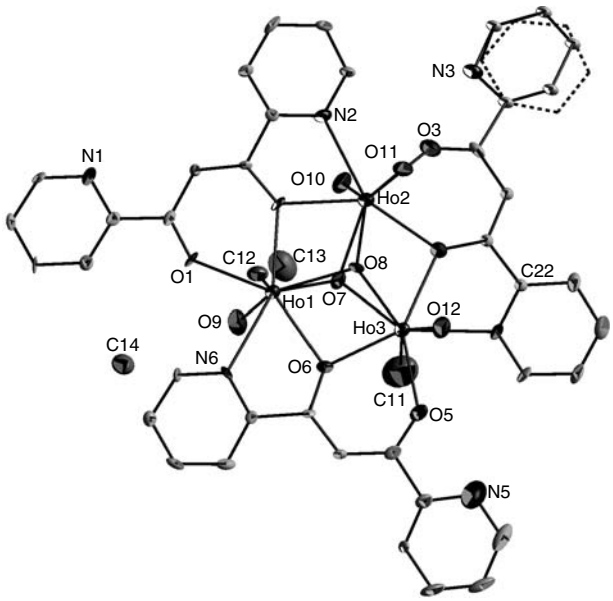


Figure 16 Molecular structure of $[Ho_3(L^{32})_3(\mu_3\text{-}OH)_2(H_2O)_4Cl_2]Cl_2$ showing 30% ellipsoids with all H atoms and lattice solvent molecules removed. (Reproduced from Ref. 13. © Wiley-VCH Verlag GmbH & Co. KGaA, 2009.)

a trinuclear cluster $[Ho_3(L^{32})_3(\mu_3\text{-}OH)_2(H_2O)_4Cl_2]Cl_2$ (see Figure 16).[13]

By using a bis-acylpyrazolone ligand H_2L^{57}, triple-stranded helical complexes of $Tb_2(L^{57})_3(H_2O)_2$ and $Tb_2(L^{57})_3(DMF)_2$ were formed,[14] which, were then reacted with a bridging ligand diphenylphosphinethane dioxide ($dppeO_2$), affording final polymeric product $[Tb_2(L^{57})_3(dppeO_2)]_n$. The crystal structure revealed that $[Tb_2(L^{57})_3(dppeO_2)]_n$ consists of infinite parallel chains

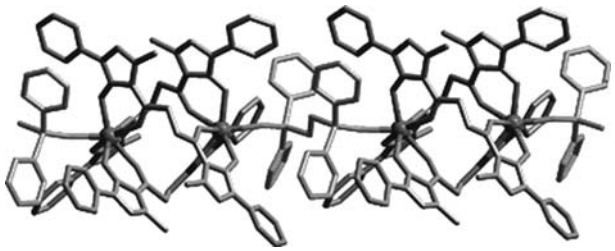


Figure 17 Fragment of the polymeric chain in $[Tb_2(L^{57})_3(dppeO_2)]_n$. Ligands forming helices. (Reproduced from Ref. 14 with permission of The Royal Society of Chemistry.)

formed by bridging the helical units $\{Tb_2(L^{57})_3\}$ with $dppeO_2$ ligands (see Figure 17).

By using an α-NH substituted β-diketone ligand carrying two carboxylic acid groups, H_3L^{35}, a trinuclear discrete complex $[Eu_3(L^{35})_3(H_2O)_6]$ was synthesized,[15] in which nine-coordinate cations are linked by ligands to provide a triangular complex (see Figure 18).

5.2 d–f Polynuclear β-Diketonate Lanthanide Complexes

Many efforts have been made on using ferrocene derivatives, optically active transition metal Re^{I}, Au^{I}, Ru^{II}, Pt^{II}, and Os^{III} complexes as the energy donors, in order to shift the excitation wavelength of lanthanide β-diketonate complexes to visible light region and enhance luminescent efficiencies by efficient energy transfers. The molecular structure of a ferrocene-containing $[Eu(L^5)_3(Fc_2phen)]$ (Fc_2phen = bis(ferrocenyl-ethynyl)-1,10-phenanthroline) is shown in Figure 19.[16] The visible light with a wavelength up to 420 nm

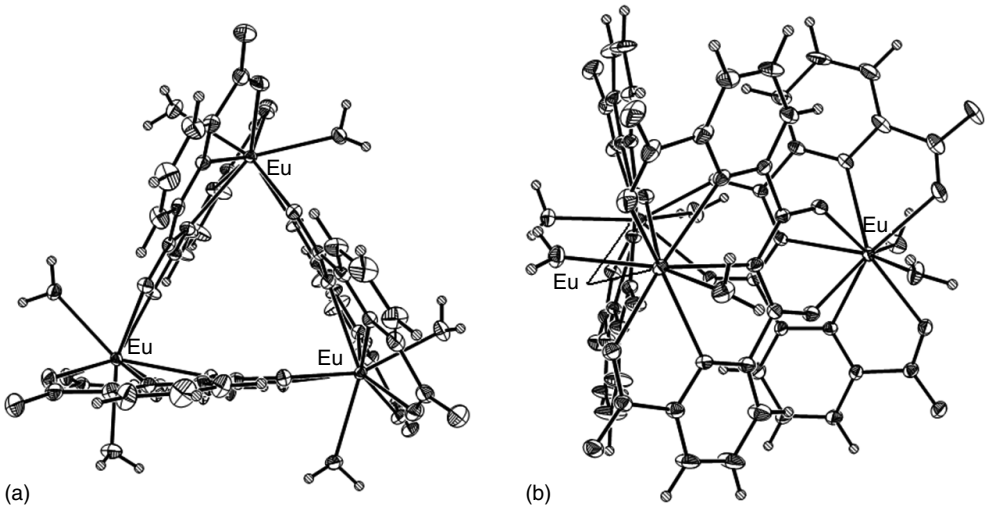


Figure 18 Crystal structure of $[Eu_3(L^{35})_3(H_2O)_6]$. View of the trinuclear complex (a) along and (b) perpendicular to the threefold axis. (Reproduced from Ref. 15. © Wiley-VCH Verlag GmbH & Co. KGaA, 2009.)

(blue light) could be used for excitation of europium(III) to observe the red emission of the Eu^{III} complex.

Main efforts have been devoted to sensitize NIR lanthanide luminescence by using d-block transition metal complexes as energy donors, but studies on sensitized visible lanthanide luminescence are relatively rare. By using a 1,10-phenanthroline-substituted β-diketone of HL^{16} as ligand, an intermediate Ir^{III} complex-substituted β-diketone of $Ir(dfppy)_2(L^{16})$ [dfppy = 2-(4′,6′-difluorophenyl)-pyridinato-N,C^2] could be made, which was used as a ligand, two novel iridium-europium bimetallic complexes of $\{[(dfppy)_2Ir(\mu\text{-}L^{16})]_3EuCl\}Cl_2$ and $(dfppy)_2Ir(\mu\text{-}L^{16})\,Eu(L^2)_3$ were also synthesized.[17] The molecular and crystal structure of $\{[(dfppy)_2Ir(\mu\text{-}L^{16})]_3EuCl\}Cl_2$ is shown in Figure 20. In $\{[(dfppy)_2Ir(\mu\text{-}L^{16})]_3EuCl\}Cl_2$, the Eu^{III} ion is seven-coordinated by six oxygen atoms from the three β-diketones and one chloride ion from the starting material $EuCl_3 \cdot 6H_2O$.

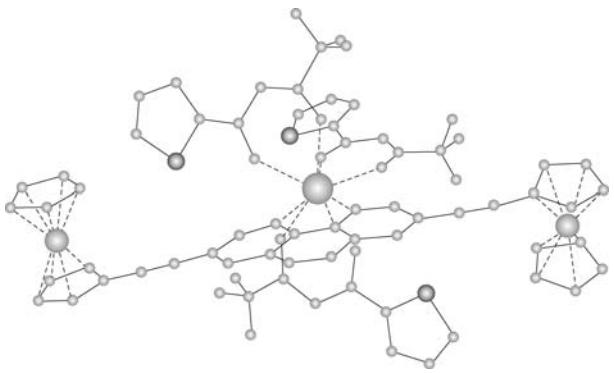


Figure 19 Molecular structure of $[Nd(L^5)_3(Fc_2phen)]$. (Reprinted with permission from Ref. 16. Copyright (2007) American Chemical Society.)

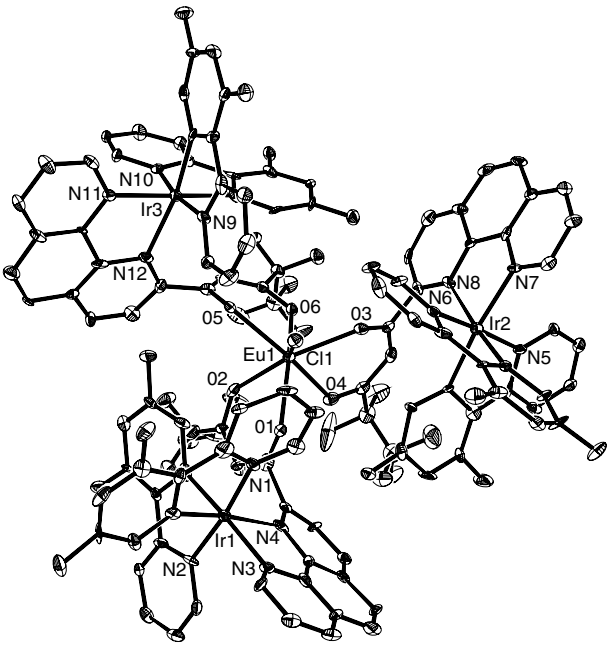


Figure 20 ORTEP diagrams of complexes $\{[(dfppy)_2Ir(\mu\text{-}L^{16})]_3EuCl\}Cl_2$. The hydrogen atoms, counterions, and solvent molecules are omitted for clarity. (Reprinted with permission from Ref. 17. Copyright (2008) American Chemical Society.)

The nonbonding distances for Eu···Ir are 6.028, 5.907, and 6.100 Å, ensuring effective energy transfer from Ir^{III} center to the Eu^{III} emissive states since the effective energy transfer distances were reported to be around 6 Å (<10 Å).

Ziessel and Charbonnière *et al*. reported a bimetallic nine-coordinate Pt–Eu complex (^{t}Buterpy)Pt(C≡Ctpy)$Eu(L^3)_3$ (^{t}Buterpy = 4, 4′,4″-*tert*-butyl-2,2′:6′,2″-terpyridine,

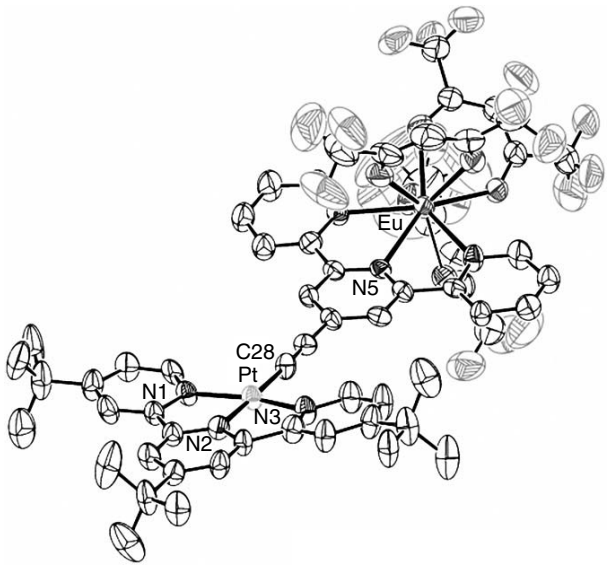


Figure 21 ORTEP view of (^{t}Buterpy)Pt(C≡Ctpy)Eu(hfc)$_3$, with hydrogen atoms omitted for clarity. (Reproduced from Ref. 18. © Wiley-VCH Verlag GmbH & Co. KGaA, 2007.)

C≡Ctpy = 4′-ethynyl-2,2′:6′,2″-terpyridine) and its crystal structure (see Figure 21).[18] They interestingly found that a strong Eu^{III} luminescence with a lifetime of 868 μs and a luminescence quantum yield of 38% independent of the presence of oxygen was generated by quantitative energy transfer from the Pt^{II} complex to the Eu^{III} complex upon visible light irradiation at 460 nm.

6 CONCLUSIONS

The β-diketonate lanthanide complexes have been evidenced to have variable coordination numbers ranging from 6 to 10, and diverse structural motifs. This family of complexes with desiring luminescent properties in the visible and NIR regions holds great potential for widespread practical applications. The poly-β-diketones have gained bright prospects in supramolecular chemistry in recent years, although they have particularly been ill explored and in their infancy. Current challenges are the synthesis and structural characterization of lanthanide β-diketonate complexes with tailoring properties not only at the molecular level but also at nanometer dimensional level, such as the supramolecular assemblies at nanomaterials or other underlying surface, fulfilling smart and controllable functionalities for high-technological applications in the borderlines of chemistry, materials chemistry, chemistry biology, and medicine. The fascinating crystal structural chemistry of lanthanide complexes will certainly greatly promote the rapid developments of these interdisciplinary sciences.

7 GLOSSARY

Crystal structure: The arrangement of atoms within a crystal. The structure is composed of a pattern, a set of atoms arranged in a particular way, and a lattice exhibiting long-range order and symmetry. The structure is solved by a special device called.

Dendrimer diketone: A repetitively branched diketone molecule, which is typically symmetric around the core, and often adopts a spherical three-dimensional morphology, being of a shape like a tree.

Lanthanide: Often called as lanthanoid. It comprised the 15 metallic chemical elements with atomic numbers 57–71, from lanthanum to lutetium. These 15 lanthanide elements, along with the chemically similar elements of scandium and yttrium, are often termed the rare earth elements.

ORTEP diagram: A kind of graphical illustrations of a molecular structure in a crystalline solid, which is created by ORTEP, a crystal structure resolution software program.

8 ACKNOWLEDGMENTS

This work was financially supported by National Natural Science Foundation of China (21171022, 20971016, and 90922004).

9 ABBREVIATIONS AND ACRONYMS

EL = electroluminescent; NIR = near-infrared; OLED = organic light-emitting diode; TPTZ = 2,4,6-tri(2-pyridyl)-1,3,5-triazine.

10 REFERENCES

1. C. H. Huang, 'Rare Earth Coordination Chemistry: Fundamentals and Applications', John Wiley & Sons, Singapore, 2010, p. 41.
2. K. Binnemans, in 'Handbook on the Physics and Chemistry of Rare Earths', eds. K. A. Gschneidner, J. C. G. Bünzli, and V. K. Pecharsky, Elsevier Science, North Holland, 2005, Vol. 35, p. 107.
3. G. Aromí, P. Gamez, and J. Reedijk, *Coord. Chem. Rev.*, 2008, **252**, 964.
4. K. Z. Wang, in 'Rare Earth Coordination Chemistry: Fundamentals and Applications', ed. C. H. Huang, John Wiley & Sons, Singapore, 2010, p. 41.

5. P. B. Glover, A. P. Bassett, P. Nockemann, B. M. Kariuki, R. Van Deun, and Z. Pikramenou, *Chem.—Eur. J.*, 2007, **13**, 6308.
6. H. He, A. G. Sykes, D. Ng, S. W. Galipeau, and M. Ropp, *Inorg. Chem. Commun.*, 2008, **11**, 1051.
7. M. Shi, F. Li, T. Yi, D. Zhang, H. Hu, and C. Huang, *Inorg. Chem.*, 2005, **44**, 8929.
8. L. H. Gao, M. Guan, K. Z. Wang, L. P. Jin, and C. H. Huang, *Eur. J. Inorg. Chem.*, 2006, (18), 3731.
9. P. N. Remya, S. Biju, M. L. P. Reddy, A. H. Cowley, and M. Findlater, *Inorg. Chem.*, 2008, **47**, 7396.
10. C. R. De Silvaa, J. R. Maeyera, A. Dawsona, and Z. Zheng, *Polyhedron*, 2007, **26**, 1229.
11. A. Fratini, G. Richards, E. Larder, and S. Swavey, *Inorg. Chem.*, 2008, **47**, 1030.
12. F. Pointillart, O. Maury, G. Y. Le, S. Golhen, O. Cador, and L. Ouahab, *Inorg. Chem.*, 2009, **48**, 7421.
13. P. C. Andrews, G. B. Deacon, R. Frank, B. H. Fraser, P. C. Junk, J. G. MacLellan, M. Massi, B. Moubaraki, K. S. Murray, and S. Morrystein, *Eur. J. Inorg. Chem.*, 2009, (6), 744.
14. S. N. Semenov, A. Y. Rogachev, S. V. Eliseeva, C. Pettinari, F. Marchetti, A. A. Drozdov, and S. I. Troyanov, *Chem. Commun.*, 2008, (17), 1992.
15. S. Zebret, N. Dupont, G. Bernardinelli, and J. Hamacek, *Chem.–Eur. J.*, 2009, **15**, 3355.
16. Y. F. Yuan, T. Cardinaels, K. Lunstroot, K. Van Hecke, L. Van Meervelt, C. Goerller-Walrand, K. Binnemans, and P. Nockemann, *Inorg. Chem.*, 2007, **46**, 5302.
17. F. F. Chen, Z. Q. Bian, Z. W. Liu, D. B. Nie, Z. Q. Chen, and C. H. Huang, *Inorg. Chem.* 2008, **47**, 2507.
18. R. Ziessel, S. Diring, P. Kadjane, L. Charbonniere, P. Retailleau, and C. Philouze, *Chem. Asian J.* 2007, **2**, 975.

Rare Earth Borides, Carbides and Nitrides

Takao Mori

National Institute for Materials Science (NIMS), Namiki 1-1, Tsukuba, Japan

1	Summary	263
2	Introduction	264
3	Rare Earth Borides	264
4	Rare Earth Carbides	271
5	Rare Earth Borocarbides	272
6	Rare Earth Transition Metal Borocarbides (Rare Earth Transition Metal Boronitrides)	274
7	Rare Earth Nitrides	274
8	Rare Earth Boronitrides	275
9	Rare Earth Carbonitrides	275
10	Rare Earth Borocarbonitrides	275
11	Conclusions	276
12	Related Articles	276
13	Abbreviations and Acronyms	276
14	References	277

1 SUMMARY

This chapter briefly reviews what is known of the rare earth borides, carbides, and nitrides. This review would particularly like to showcase interesting features of the crystal structure and intriguing physical properties ranging from the fundamental to the very applicable, with an emphasis on recent emerging results in important functionalities such as magnetism, thermoelectricity, and superconductivity.

The interest in magnetism of f-electron rare earth compounds is clear, and in the case of borides, carbides, and nitrides, it ranges from fundamental phenomena such as magnetic transitions, heavy fermion physics, and valence fluctuation to applications as permanent magnets and spintronics. The borides, carbides, and nitrides are interesting in terms of thermoelectrics (TEs) for their general high thermal stability, and intrinsic low thermal conductivity in the case of some borides. Since the main atomic network framework of the borides, carbides, and nitrides are constructed with relatively light elements, they are attractive systems to induce superconductivity because of the strong phonon coupling, leading to relatively high transition temperatures. In addition, as a general feature of the compounds described in this chapter, they are attractive in terms of physical property control because of easy variation of the containing rare earth atoms and relatively easy substitution of the host network atoms (B, C, and N). This also can lead to variations in the crystal structure (i.e., new compounds) which are described in this chapter, and which have significant effect on the physical properties. A rich variety of rare earth borocarbides, boronitrides, carbonitrides, and borocarbonitrides have also been discovered and will be reviewed.

Striking applications have been realized for the rare earth borides, carbides, and nitrides such as for permanent magnetic materials, electron emitters, monochromators, contrast agents for magnetic resonance imaging (MRI), phosphor materials, and exciting new possibilities have emerged in TE, spintronics, battery-related materials new graphite intercalation compounds (GICs), etc.

While there are myriad helpful reviews, there has previously been no up-to-date, one-stop review article available for any one of the rare earth borides, carbides, and nitrides, and in this sense I feel this chapter, which contains brief summaries, valuable references as gateways to further detailed information, and a focus on timely topics of all three systems, will be particularly useful. A section is included at the end summarizing the particularly notable physical properties described in each section.

The Rare Earth Elements. Edited by David A. Atwood. © 2012 John Wiley & Sons, Ltd. ISBN 978-1-119-95097-4

2 INTRODUCTION

Rare earth elements form a rich variety of compounds with boron, carbon, and nitrogen. The rare earth borides, carbides, and nitrides tend to be highly refractory compounds, typically with melting points above 2300 K. One way of looking at the less metal-rich compounds is that the boron, carbon, and nitrogen atoms, respectively, form strongly covalent atomic networks in which rare earth atoms reside. The strong covalent bonding among the network atoms is the origin for the high-temperature stability, while the rare earth elements typically play a critical role in the physical properties, namely, functionalization of the material.

For example, especially in the case of boron, boron has one less electron than carbon and therefore it is electron deficient when forming atomic networks compared to carbon networks such as graphite and fullerenes. However, this causes boron to have an especially good affinity with the rare earth elements, which are localized and can occupy voids in the boron network while readily supplying electrons to stabilize novel structures, providing a wide variety of compounds that are introduced in this chapter together with carbides and nitrides. Furthermore, the shell of f electrons can provide interesting physical properties such as magnetism and luminescence, and also provide possible tuning of the electronic properties. In this sense as functional materials, the rare earth elements play a critical role in the functionalization, even although their content may be low in the higher borides, carbides, and nitrides. This is one important direction to strive in the current world where natural resources are limited, namely, to highly functionalize materials that are mainly composed of abundant light elements through the innovative use of a small amount of a rare element.

3 RARE EARTH BORIDES

3.1 Binary Rare Earth Borides

The binary borides can be divided into two groups by focusing on the rare earth to boron ratio in the chemical composition: for [B]/[R] = n, when $n \leq 12$, the compounds are metallic for trivalent rare earth elements; and for RB_n with $n > 12$, the compounds are insulators.

The crystal structures of the binary rare earth borides RB_n; RB_2, RB_4, RB_6, RB_{12}, RB_{25}, RB_{50}, RB_{66}, are depicted in Figure 1. As can be seen, when the boron content is relatively low, the boron network forms a 2D planar atomic net in the case of RB_2. As the boron content increases, the basic unit of the boron network becomes a cluster, namely, the B_6 octahedron, for RB_4 and RB_6. As the boron content is increased further, the boron cluster becomes larger and is the B_{12} cuboctahedron for RB_{12}, and for RB_n with $n > 12$, the basic structural unit becomes the B_{12} icosahedron.

There have been several reviews written on boron and borides, which include various reports on the well-known rare earth borides, such as RB_2, RB_4, RB_6, RB_{12}, and RB_{66} which were first synthesized over a half century ago.[1–4] The novel higher borides discovered in the past decade with [B]/[R] = n, with $n > 12$[5] have been included in a review.

I have briefly summarized essential information known on the rare earth borides and updated with exciting new developments in their chemistry and physics.

3.1.1 RB_2 (Rare Earth Diborides)

RB_2 takes the AlB_2-type crystal structure (space group *P6/mmm*), where rare earth atoms are sandwiched between 2D graphitic boron nets (Figure 1(a)). RB_2 has been reported to form for the rare earth elements of R = Sc, Y, Sm, Gd, Tb, Dy, Ho, Er, Tm, Yb, Lu.

With regard to synthesis, it appears that it is harder to grow single crystals for the rare earth diborides compared to other systems such as the tetraborides and hexaborides. Therefore, there have been relatively fewer investigations into its physical properties despite its simple crystal structure and composition.

With regard to notable physical properties, the diboride system is unusual since it is the only rare earth boron-rich boride that is mainly ferromagnetic. TbB_2, DyB_2, HoB_2, and ErB_2 exhibit ferromagnetic transitions at T_C = 151, 55, 15, and 16 K, respectively,[4,6] while YbB_2 was reported to be antiferromagnetic at T_N = 5.6 K.[7] Recently, it was found that the TmB_2 compound that lies in between is also ferromagnetic at T_C = 7.2 K.[8]

Superconductivity has not been reported for any of the rare earth diborides. This may have also contributed to the overlooking of the superconductivity in magnesium diboride, where the compound was known for 50 years but its superconductivity was only discovered in 2001, creating worldwide excitement.[9] In general, boron compounds have been much less studied than carbon-based materials, for example, despite having interesting structural and chemical features, and other striking properties that are most likely awaiting discovery.

3.1.2 RB_4 (Rare Earth Tetraborides)

RB_4 takes the UB_4-type crystal structure (space group *P4/mbm*), where rare earth atoms and B_6 octahedra are arranged in a tetragonal configuration (Figure 1(b)). RB_4 has been reported to form for the rare earth elements of R = Y, La, Ce, Pr, Nd, Sm, Gd, Tb, Dy, Ho, Er, Tm, Yb, Lu. Interestingly, it does not form for europium, which may be due to the divalent nature and subsequently large size of europium, however, it does form for another frequently divalent rare earth element, samarium.

Regarding the physical properties, the magnetism of the rare earth tetraborides has been investigated extensively.[10]

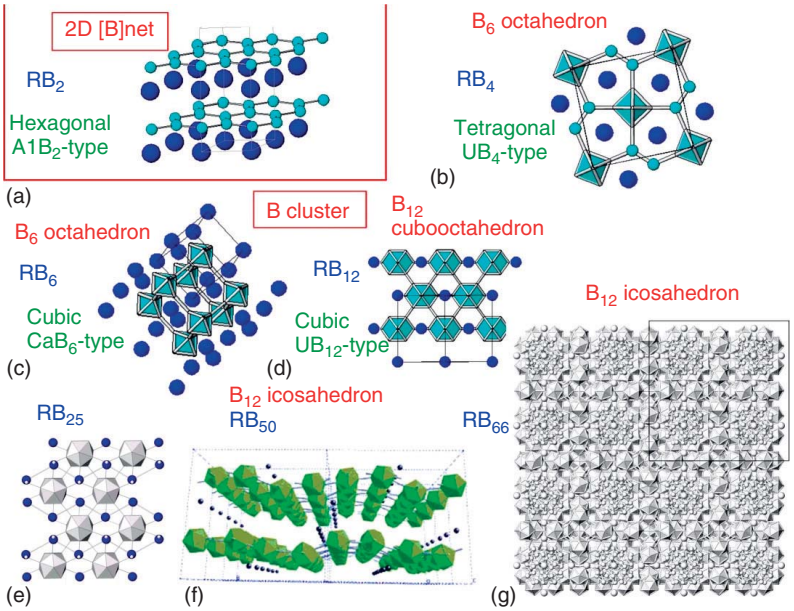


Figure 1 View of structures of binary borides (a) MB_2, (b) RB_4, (c) RB_6, (d) RB_{12}, (e) RB_{25}, (f) RB_{50}, and (g) RB_{66}

RB_4 mainly exhibits antiferromagnetism, with PrB_4 initially thought to be the only ferromagnet with $T_C = 24$ K. However, recently it has also been claimed that there is actually an antiferromagnetic transition at $T_N = 19.5$ K with a further ferromagnetic transition at $T_C = 15.9$ K.[11] The disparate temperatures indicate that sample dependence probably plays a large role in the magnetism of PrB_4.

The antiferromagnetic transition temperatures are $T_N = 42$, 15.4, and 10 K for GdB_4, ErB_4, and YbB_4, respectively. TbB_4, DyB_4, HoB_4, and TmB_4 exhibit multiple transitions with temperatures of $T_N = 44$ and 24 K, 20.4 and 12.8 K, 7.1 and 5.7 K, and 11.7 and 9.7 K, respectively.[12,13] The specific heat has also been analyzed to identify the electronic, lattice, and magnetic contributions to the total heat capacity.[14]

Relatively recently, one interesting feature that has been pointed out is that the configuration in RB_4 of the rare earth atoms is actually that of the Shastry–Sutherland lattice.[15,16] The Shastry–Sutherland lattice had theoretically been raised as an interesting frustrated magnetic system,[17] but with not so many examples in actual physical systems. Hence, the antiferromagnetic behavior in some of the RB_4 compounds noted above have been observed to be quite complex, exhibiting multiple magnetization plateaus, multiple transitions, etc.

LaB_4 has been reported to be a good electron emitter similar to the well-known LaB_6.[18] Superconductivity has not been reported for any of the rare earth tetraborides.

3.1.3 *RB_6 (Rare Earth Hexaborides)*

RB_6 take the CaB_6-type crystal structure (space group $Pm3m$), where rare earth atoms and B_6 octahedra are arranged in a simple cubic CsCl-like packing (Figure 1(c)). The RB_6 structure is quite robust, meaning that the space in which the rare earth atom resides among the boron octahedral network is rather large and can accommodate a wide range of atom sizes. Therefore, RB_6 has been reported to form for all the rare earth elements dealt with in this chapter, namely, R = Sc, Y, La, Ce, Pr, Nd, Sm, Eu, Gd, Tb, Dy, Ho, Er, Tm, Yb, Lu.

A note about the bonding and electron requirements is that the B_6 octahedron has been calculated to be two-electron deficient when bonding in solids, namely, it lacks two electrons to satisfy the bonding orbitals.[19] Therefore, for trivalent rare earth atoms, which supply three electrons, there is one extra electron in the conduction band, and RB_6 for trivalent rare earths can be well understood to be good metals. When the metal atom is divalent, such as for europium in the divalent state and calcium, the hexaboride becomes semiconducting or similar to a semimetal.

A rich variety of interesting physical phenomena has been observed in the hexaborides. I will briefly review them.

Regarding the magnetism, the hexaborides are dominantly antiferromagnetic, but EuB_6 was found to be ferromagnetic by Geballe around 40 years ago.[20] However, the detailed magnetism of EuB_6 was only elucidated recently, because of large sample dependence and large effect of impurities. For example, it has been demonstrated that the ferromagnetism in EuB_6 disappears with the existence of a small amount of impurities.[21] Strikingly, it was shown that two ferromagnetic transitions with very close transition temperatures occur in EuB_6 at $T_{C1} = 15.3$ K and $T_{C2} = 12.5$ K. Furthermore, the ferromagnetism is indicated to be induced by magnetic polarons. At high temperatures, EuB_6 is a semiconductor but upon approaching the ferromagnetic

transition temperatures, the number of carriers sharply increases and it turns into a metal.[21]

With regard to the antiferromagnetism, multiple transitions have been observed at $T_N = 7$ and 4.3 K for PrB_6 and $T_N = 16$ and 11 K for GdB_6. $T_N = 8.45$, 19.5, 25.6, and 5.6 K have been reported for NdB_6, TbB_6, DyB_6, and HoB_6, respectively.[20]

Striking behavior has been observed for CeB_6, SmB_6, and YbB_6. CeB_6 was first pointed out by Kasuya and others to be a heavy electron system.[22,23] It is a so-called Kondo lattice system with the Kondo effect from the localized f-electrons and conduction electrons playing a large role in the determination of the physical properties. Complex phases have been reported and quadrupole and octupole coupling are also indicated to be effective. SmB_6 exhibits valence fluctuation and is a Kondo insulator with a gap temperature of $\Delta = 27$ K. YbB_6 has been reported to exhibit valence fluctuation also.

In one topic related to the magnetism in hexaborides, high temperature ferromagnetism was reported previously when CaB_6 was substitutionally doped with La and electrons injected into the system.[24] This report gained much attention because of the possibilities for spintronics. However, it was later clearly proved that the ferromagnetism originated from iron impurities.[25] The tendency to observe ferromagnetism for only the doped samples was also explained by a picture in which iron impurities are attached onto crystals during the metal-flux-removal procedure through an electrochemical reaction. The doped samples have lower electrical resistivity and therefore, the electrochemical plating is enhanced. CaB_2C_2 which has similarities in the band structure to $Ca_{1-x}La_xB_6$ was also reported to exhibit high-temperature ferromagnetism,[26] but this was also revealed to be nonintrinsic.[27]

YB_6 is a superconductor with a transition temperature of $T_C = 8.4$ K.[28,29] Strong coupling features of the superconductivity have been directly revealed through point-contact spectroscopy.[30]

LaB_6 and CeB_6 are well known for being excellent field emitters,[31] and have actually been commercialized as thermionic cathode materials. With low work functions around 2.6 eV, they can provide greater brightness and lower operation temperatures (longer service life) than tungsten cathodes, for example. A simple method to grow high-quality physical vapour deposition (PVD) films of CeB_6 was recently reported.[32]

3.1.4 RB_{12} (Rare Earth Dodecaborides)

RB_{12} takes the UB_{12}-type crystal structure (space group $Fm3m$), where rare earth atoms and B_{12} cuboctahedra are arranged in a simple cubic NaCl-like packing (Figure 1(d)). RB_{12} has been reported to form for R = Sc, Y, Gd, Tb, Dy, Ho, Er, Tm, Yb, Lu, but not for the light lanthanides, R = La, Ce, Pr, Nd, Sm, and Eu, because the atoms of these elements are too large. It is interesting that the 12-boron atom cluster formed in RB_{12} is a cuboctahedron in RB_{12} versus the B_{12} icosahedron cluster that is predominant in the other higher borides. Owing to the small size of scandium, scandium borides have sometimes taken different crystal structures than that of the other rare earth phases. ScB_{12} has been reported to take a tetragonal modification of the UB_{12}-type structure with space group of $I4/mmm$.[33,34] A small amount (e.g., 10%) of replacement doping of scandium has resulted in ScB_{12} being stabilized to the normal cubic UB_{12}-type structure.

For the magnetic rare earths, aside from ytterbium, antiferromagnetic transitions were found to occur[28,35,36] with transition temperatures for TbB_{12}, DyB_{12}, HoB_{12}, ErB_{12}, and TmB_{12} of $T_N = 19.2$, 16.5, 7.5, 6.7, and 3.4 K, respectively. The f-electron dependence of the magnetic coupling is consistent with the deGennes factor.[37] Despite the simple cubic structure of RB_{12}, recent interesting results showing more complex behavior of the magnetism have been obtained.[38,39] YbB_{12} is a Kondo insulator system, and similar to CeB_6, SmB_6, and YbB_6 described above, embodies heavy electron physics.[40]

Superconductivity has been observed for the non-magnetic dodecaborides; ScB_{12} and LuB_{12}, with transition temperatures of $T_C = 0.39$ and 0.48 K, respectively. Superconductivity was initially reported with a partial volume fraction for YB_{12} also, but subsequent investigations have not found intrinsic superconductivity above 2.5 K.[41]

3.1.5 ScB_{19}

As noted in the previous Section 3.1.4 on dodecaborides, the scandium phase of a series of rare earth compounds sometimes take different structures because of the small size of scandium compared to the other rare earths. Various scandium higher borides have been observed that do not form for other rare earth phases,[5] One such phase is the ScB_{19} compound, which is tetragonal (space group $P4_12_12$ or $P4_32_12$).[42] It is isostructural with the structure type α-AlB_{12}.

3.1.6 RB_{25}

The crystal structure of RB_{25} is a new type discovered in the past decade, and can be described as a monoclinic distortion of the $MgAlB_{14}$-type structure with space group of $I12/m1$ (Figure 1(e)).[43] An interesting structural feature of RB_{25} is that with the addition of carbon atoms, it has been observed that superstructures of the compound can form.[44]

RB_{25} has been reported for R = Y, Gd, Tb, Dy, Ho, Er, Tm, Yb, Lu. The only magnetic transition observed above 2 K is the antiferromagnetic transition at $T_N = 2.1$ K in TbB_{25}.[43]

3.1.7 RB_{50} ($RB_{44}Si_2$)

Crystal Structure. Similar to RB_{25} above, the crystal structure of RB_{50} is a new type discovered in the

past decade or so. The structure is orthorhombic with space group of *Pbam*. The structure is composed of five structurally independent B_{12} icosahedra and a B_{15} icosahedron. As a particular structural feature, there is an infinite chain of boron icosahedra running along the *c*-axis, along which a bond-alternating chain of rare earth atoms also lies.[45]

RB_{50} has been reported to form for R = Y, Tb, Dy, Ho, Er, Tm, Yb, Lu. GdB_{50} does not form owing to the size of gadolinium. In an interesting example of actual material design, a gadolinium RB_{50}-type compound was synthesized.[46] Addition of a small amount of silicon to YB_{50} was found to result in an isostructural compound $YB_{44}Si_2$, which is possible to melt stably unlike YB_{50}.[47] In a subsequent work, the fact that the silicon addition has a side effect to make the lattice constants larger was focused on, and in this way the RB_{50}-type $GdB_{44}Si_2$ was successfully obtained.[46]

Magnetic Properties (Novel Mediator of Magnetic Interaction). In a striking discovery regarding the physical properties, it was found that TbB_{50}, which is an insulating, relatively magnetic-dilute, localized f-electron system, exhibits an antiferromagnetic transition at an unexpectedly high transition temperature,[48] that is, it was found to manifest unexpectedly strong magnetic coupling. Magnetic transitions were observed for the other magnetic rare earths also.[49] From the crystal structure, it was hypothesized that the B_{12} icosahedron, which is the basic building block of the higher borides, functions as a novel mediator of magnetic interaction.[48]

An interesting effect was observed upon magnetically diluting $TbB_{44}Si_2$. The critical magnetic field of the antiferromagnetic transition, H_C, which is a measure of the strength of the magnetic coupling, was observed to show no variation for $Tb_{1-x}Lu_xB_{44}Si_2$, even for $x = 0.50$ (Figure 2). The number of free Tb spins, N, and doping level x was also shown to have a correlation of $N \propto x(1-x)$. These results, namely, the imperviousness of H_C versus dilution, indicate that the transition in $TbB_{44}Si_2$ is dimer-like.[50] An ESR study on $GdB_{44}Si_2$ revealed 1D features.[51]

These results indicate that in $RB_{44}Si_2$ the rare earth ions magnetically form pairs along the bond-alternating ladder, which happens to be the second-nearest-neighbor direction. This result is consistent with the idea that the B_{12} icosahedra function as novel mediators of magnetic interaction since the icosahedra form a chain along the *c*-axis adjacent to the magnetic ion pairs.

Regarding the mechanism of the magnetic interaction of the B_{12} icosahedral compounds, Figure 3 shows a plot of some of the characteristic temperatures of the magnetism plotted versus f-electron number, together with expected dependencies in the case of conventional f-electron magnetism mechanisms such as the RKKY interaction and the dipole–dipole interaction (normalized with the value for Er arbitrarily set as 4.5 K). It can be seen that the f-electron dependencies for the higher borides do not simply follow

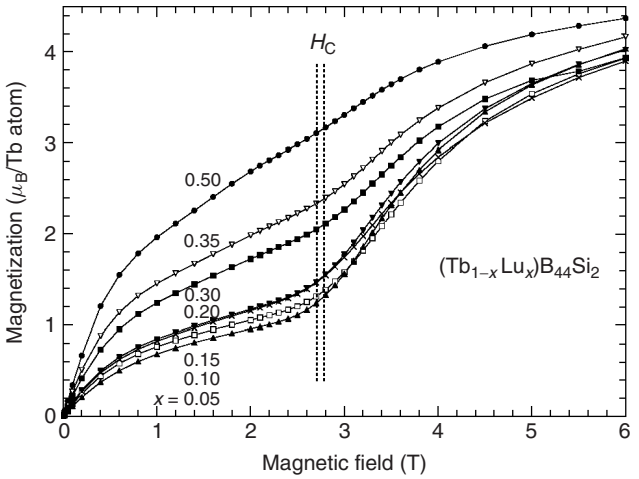


Figure 2 Magnetization curves of diluted $TbB_{44}Si_2$[50]

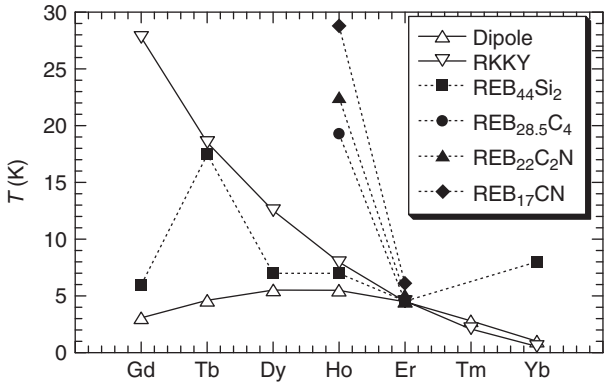


Figure 3 Rare earth (f-electron) dependence of the characteristic magnetic temperatures

either mechanism. This is also underlined by the fact that the Tb phase has the highest T_N for RB_{25},[43] while as described in a following section, Gd has the highest for $RB_{18}Si_5$.[52] Furthermore, the RKKY interaction is not expected to be effective for these insulating higher borides. The magnetism indicated to be mediated by the B_{12} icosahedra is still an interesting problem.

Thermoelectric Properties. Another attractive feature of the physical properties of RB_{50} ($RB_{44}Si_2$) is that they have been found to be promising systems for high-temperature TEs.

One of the great challenges that modern society faces is to find ways to use energy more efficiently. As depicted in Figure 4, approximately two-thirds of all primary energy, such as fossil fuels, being consumed in the world, sadly turns out to be unutilized, with much of it being waste heat. The useful and direct conversion of waste heat to electricity is a large incentive to find viable TE materials. One need exists to

develop materials that can function at high temperature, for applications utilizing high-temperature waste heat (such as in factories, incinerators, and piping in thermal power plants), focused solar power, radioisotope thermoelectric generator (RTG), etc.

Boron-rich compounds are attractive materials for their stability, exhibiting melting points above 2200 K. Furthermore, they have been found to possess intrinsic low thermal conductivity,[53–55] which is a ''built-in'' advantage as TE materials. The low thermal conductivity of boron is quite anomalous considering its neighbors in the periodic table, which have similar strongly covalent bond networks—carbon (diamond and graphite) and beryllium, for example; and this can give the keys to novel mechanisms to control the thermal conductivity.[56] Some interesting mechanisms that have been suggested are (i) crystal complexity, (ii) ''rattling'' of rare earth atoms in the boron framework, (iii) disorder, (iv) ''symmetry mismatch effect,'' and (v) particular features of the crystal structures, such as boron dumbbells, which are found to reduce thermal conductivity.[56]

Boron carbide was previously found to be an excellent high-temperature p-type TE material.[57,58] It is one of the few TE materials with a history of commercialization (by the Hi-Z company of the USA). However, a viable n-type counterpart
boride material was not found for over 20 years. A new series of higher borides, the rare earth borocarbides, $RB_{17}CN$, $RB_{22}C_2N$, and $RB_{28.5}C_4$, was discovered to exhibit intrinsic n-type behavior[59] and are described later in this chapter.

The TE properties of the RB_{50}-type compounds, $RB_{44}Si_2$, are p-type similar to boron carbide and also exhibit attractive properties with Seebeck coefficients exceeding 200 $\mu V\,K^{-1}$ observed above 1000 K, and low values of thermal conductivity around $\sim 0.02\ W\,cm^{-1}\,K^{-1}$ for crystals.[60]

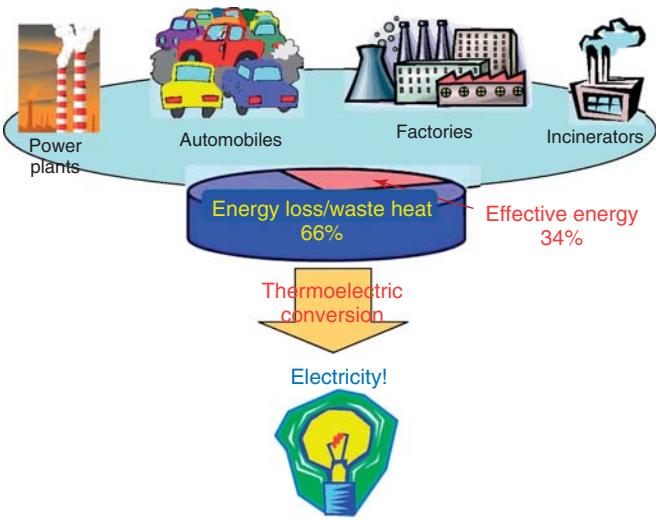


Figure 4 Depiction of the merits of thermoelectrics

These compounds have melting points above 2300 K and extrapolation to 1500 K leads to starting figure of merit ZT (where $ZT = \alpha^2 \cdot \sigma \cdot \kappa^{-1} \cdot T$, with α = Seebeck coefficient, σ = electrical conductivity, and κ = thermal conductivity) values of ~ 0.2, for nondoped and nonoptimized materials[55] (T. Mori, unpublished result).

This is a good starting point as a TE material. There are aspects of the borosilicide in the processing (significantly lower melting temperatures) that may make it an attractive new replacement of boron carbide.

In general, doping of foreign atoms and control of the microstructure are routes to significantly modifying the TE properties. Doping work on this new system is in progress, and crystal structure studies have revealed that transition metal atoms can be intrinsically doped into the crystal structure[61] to yield large modifications in the physical properties. Furthermore, a ''zinc doping effect'' was found to modify the microstructure (i.e., crystallinity) and lead to a dramatic 30% enhancement of the power factor. This zinc doping effect is an easy, inexpensive, nonobtrusive (i.e., zinc does not remain in the final product) method, which may be applicable for other high-temperature materials also.[62]

3.1.8 RB_{66}

The crystal structure of RB_{66} is cubic with space group of *Fm*3*c*. The most striking feature is that it is a complex compound with more than 1600 atoms in the unit cell (Figure 1(f)).[63] However, as depicted in Figure 5(a), we can see the structure can be grasped simply as cubic packing of just three structural components, namely, the ''super-icosahedron'' $B_{12}(B_{12})_{12}$, where 12 icosahedra are connected to all the apexes of an icosahedra (Figure 5(b)), B_{80} cluster (Figure 5(c)), and yttrium atoms.

As a notable feature of the physical properties, Slack first observed that the thermal conductivity of RB_{66}, a crystalline compound, is similar to that of a glass.[53]

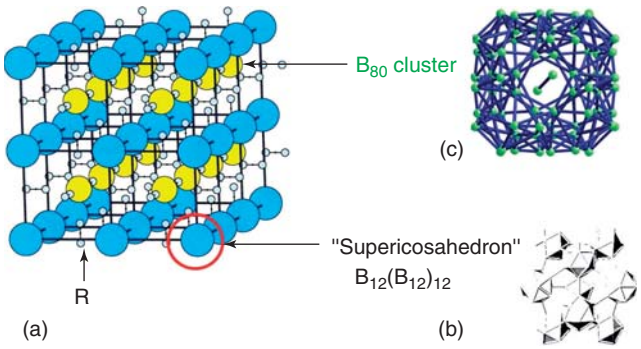


Figure 5 Schematic view of (a) crystal structure of RB_{66}, (b) ''supericosahedron'' $B_{12}(B)_{12}$, and (c) B_{80} cluster

The TE properties of RB_{66} are inferior to the RB_{50}-type borosilicide described above, but interesting effects have been observed upon doping with transition metals.[64]

A novel application of the YB_{66} was found by utilizing its large unit cell (a = 23.52 Å) and strong reflection at $2d = 11.76$ Å (the 400 index), to use it as a soft X-ray (1–2 keV) monochromator for dispersing synchrotron radiation.[65]

3.2 Ternary Rare Earth Boride Compounds

In this section, I focus on the ternary rare earth boride compounds that have particular interest for their structural features or physical properties. Rare earth borocarbides are described in a separate section, after the section on rare earth carbides.

3.2.1 Rare Earth Borosilicides

rare earth borosilicides have been systematically investigated mainly by the Rennes group for relatively metal-rich phases, and the NIMS group for relatively boron-rich phases.

For example, $R_2Si_5B_8$ was discovered in the past decade, and has a tetragonal crystal structure (space group *P4/mbm*).[66] It has been reported to form for R = Y, Sm, Gd, Tb, Dy, and Ho. This compound is interesting in that it does not form either for the large, light lanthanides of R = La, Ce, Pr, and Nd or for the small, heavy rare earths, R = Er, Tm. Yb, and Lu. The structure can be described as intergrowth of two independent boron and silicon substructures, formed of RB_4 and R_3Si_2, respectively.

Regarding the physical properties, $Tb_5Si_2B_8$ and $Dy_5Si_2B_8$ are antiferromagnets with $T_N = 45$ and 28 K, respectively. $Gd_5Si_2B_8$ shows weak ferromagnetism at $T_C =$ 70 K followed by a collinear antiferromagnetic spin ordering at 44 K.[67]

For the higher borides, a new compound $RB_{18}Si_5$ was discovered by the flux-growth method using silicon flux.[52,68] At the same time, the compound $R_{1.8}B_{36}C_2Si_8$ was also reported.[69] The crystal structures are basically the same (rhombohedral with space group $R-3m$), but the Kanatzidis group have reported that the presence of carbon is necessary for the formation of this compound. In this sense, strictly speaking, it should be considered to be a quaternary compound, but for this review we have included it in this section on rare earth borosilicides. $RB_{18}Si_5$ forms for R = Gd, Tb, Dy, Ho, Er, Tm, Yb, Lu, and Y, $R_{1.8}B_{36}C_2Si_8$ was reported to form for at least Tb, Dy, Er, Tm, Y, and Sc.

An interesting feature of the crystal structure of $RB_{18}Si_5$ is that the boron icosahedra are arranged in 2D layers. The boron icosahedra have a trigonal configuration within the layers, and there are hexagonal rings of icosahedra with voids in the middle. The boron cluster layers are linked by Si–Si bridges, which have a Si–Si separation similar to to elemental cubic silicon.

The electrical conductivity of $GdB_{18}Si_5$ follows the 3D variable range hopping (VRH) dependence that is typical of the icosahedral higher borides, and it exhibits a 3D long-range-order antiferromagnetic transition at $T_N = 3.2$ K.[52]

Differing from the compounds described above, a second group of R–B–Si compounds are found to form when silicon atoms are inserted or replace boron atoms in rare earth boride structures, or boron is inserted or replaces silicon in rare earth silicides.

Regarding the former case, solid solutions of $RB_{2-x}Si_x$ were studied for R = Dy and Ho. A striking marked effect in the physical properties was that magnetocrystalline anisotropy and magnetic hardness were enhanced for $DyB_{2-x}Si_x$ compared to DyB_2, while silicon caused the ferromagnetic behavior of HoB_2 transform into antiferromagnetic behavior for $HoB_{2-x}Si_x$.[70]

As we have described in a previous Subsection 3.1.7, a modification of the RB_{50} compound was obtained when silicon replaced some boron sites, partially occupying them to yield the $RB_{44}Si_2$ compound.

In regard to the latter case, the Mn_5Si_3-type structure has yielded a very large variety of compounds up to now.[71] There are binary compounds and also interstitial compounds of which some have been called the *Nowotny phases*.[72,73] Regarding the R–B–Si compounds, $R_5Si_3B_x$ have been studied for R = Y, Gd, Dy, Ho, Lu. The structure is basically boron atom insertion into interstitial octahedral sites of R_5Si_3 and is hexagonal with space group *P63/mcm*. As an interesting feature, the lattice constants shrink when boron is introduced into the crystal structure. Conversely, the magnetic transition temperatures exhibit a decrease for $R_5Si_3B_x$ compared to R_5Si_3.[74]

3.2.2 Rare Earth Transition Metal Borides

Magnets. For a man-made compound, not naturally found, the $Nd_2Fe_{14}B$ permanent magnet probably has had the most impact in terms of applications, for a boride. I will not go into detail here, since this topic is handled in detail in the article ***Magnetism*** of this book, but the discovery by Sagawa of Sumitomo Special Metals Co. in 1983 changed the landscape of permanent magnets. He synthesized a $Nd_{15}Fe_{77}B_8$ compound which exhibited a remanence of 1.23 T, coercivity of 880 kA m^{-1}, and energy product of 290 kJ m^{-3} which were a large jump up from anything previously known.[75] Subsequent processing of $Nd_2Fe_{14}B$ magnets have improved the properties and reduced costs, leading to wide-ranging applications. It should be noted that the boron content of $Nd_2Fe_{14}B$ is relatively low, but boron was the critical component to realize the new crystal structure (tetragonal with space group of *P42/mnm*) from which the excellent magnetic properties originated.

AlB_2-Type Analogous Tiling Compounds. A series of layered graphitic boride compounds (AlB_2-type analogous

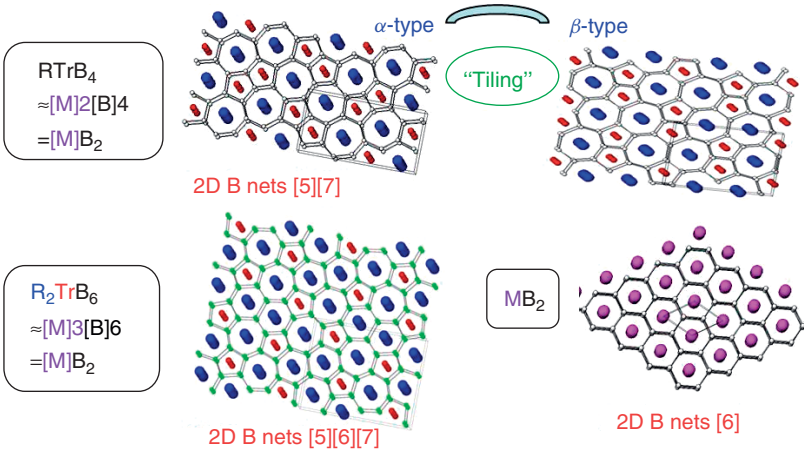


Figure 6 Schematic view of AlB_2-type ''tiling'' compounds[76–78]

''tiling'' compounds) are recently found to be of increasing interest for their structural and physical properties. As described in Figure 6, a systematic approach can be taken regarding these rare earth transition metal (or aluminum) borides, which are composed of 2D boron atomic sheets (based on the hexagonal graphitic structure) sandwiching rare earth and transition metal (or aluminum) atoms.[76–78]

This can be done by considering first the $RTrB_4$ compound, which can be approximated as M_2B_4, namely, two metal atoms and four boron atoms, which is equivalent to MB_2, i.e., the AlB_2-type structure. However, since R and Tr are different, instead of homogeneous hexagon B[6] rings sandwiching the metals, the compound forms B[5] and B[7] rings to accommodate the different-sized R and Tr atoms. The [5] and [7] rings can be arranged in two different ''tiling'' patterns, namely, the $YCrB_4$-type structure[79] and $ThMoB_4$-type structure,[80] otherwise known as ''α-'' and ''β-'' type structures, respectively. Of course these structures do not form for all combinations of rare earth and transition metals, just some combinations, of which several have been synthesized by Kuzma's group,[79] Rogl,[80] Okada, Mori, and collaborators,[76–78,81,82] and others. However, not all combinations have been investigated and synthesis of many new compounds of these structure types can be envisioned upon viewing them in this systematic way.[76–78] For example, the R_2TrB_6 compound can also be imagined and has been previously individually synthesized.[83] This can also be approximated as M_3B_6, namely, MB_2, and because it is more uniform (closer to RB_2) than $RTrB_4$, B[5], B[6], and B[7] rings form in this compound. Recently, the Tm_2AlB_6 compound was newly synthesized and properties investigated to reveal that it has a magnetic-field-induced state with extreme field stability.[77]

The physical properties of the $RAlB_4$ compounds have been recently found to show striking behavior. Frustrated magnetism has been observed in α-$HoAlB_4$ and α-$ErAlB_4$,[76] and multiple magnetic anomalies in α-$TmAlB_4$ were found to manifest below the Neel temperature T_N.[78] Intrinsic tiling variations in the boron layer (building defects) were conjectured to play a large role in the physical properties of α-$TmAlB_4$. Recently, with a counterintuitive approach to crystal growth, single crystals of α-$TmAlB_4$ were successfully grown, which were indicated from transmission electron microscopy (TEM) and advanced XRD analysis to be virtually free from the ubiquitous building defects. The physical properties show a striking difference from those of conventional α-$TmAlB_4$ crystals, and the large effect of the building defects on the physical properties could be directly confirmed, such as the origin of ''missing entropy.'' These building defects are quite subtle and may, in some cases, be unperceived, and might possibly be the origin of anomalous behavior in other layered systems also.[84]

Rare Earth Transition Metal Borides with Structures Related to the $CaCu_5$-Type. There are a series of rare earth transition metal borides that have their structure derived from the $CaCu_5$-type: RTr_4B, $R_3Tr_{11}B_4$, $R_2Tr_7B_3$, and RTr_3B_2. A comprehensive review on their magnetic properties is given in the *Handbook of Magnetic Materials Series*.[85] The compounds are mainly ferromagnetic, with RTr_4B exhibiting transition temperatures well above room temperature for transition metals of Fe and Co, for example. A study on the Gd and Co series, $GdCo_4B$, $Gd_3Co_{11}B_4$, $Gd_2Co_7B_3$, and GdCo3B_3, showed that the transition temperatures decreased linear as a function of increasing boron ratio, x, in Gd $(Co_{1-x}B_x)_5$.[86]

Others. There is a large body of work on the rare earth transition metal borides especially following the discovery of the excellent permanent magnet $Nd_2Fe_{14}B$ described at the beginning of this Section 3.2.2, with the majority of investigations being focused on Tr = Fe and Co.[85]

In addition to the phases related to the $CaCu_5$-type structure described above, there are also compounds such as $RTr_{12}B_6$, $R_2Tr_{23}B_3$, and $R_{1+x}Tr_4B_4$ that have been synthesized and investigated for their magnetic properties. There have also been metastable compounds discovered such as $R_3Fe_{63}B_{14}$ and $NdFe_{12}B_6$.[87]

4 RARE EARTH CARBIDES

While perhaps with not as wide variety as the borides, the rare earth elements also form interesting compounds with carbon to form the rare earth carbides. The phases are particularly rich for the relatively metal-rich carbide compounds. Adachi *et al*. have written a detailed, 129-page long review on the rare earth carbides,[88] while Gschneidner and Calderwood have comprehensively reviewed phase diagrams and lattice constants of binary rare earth carbides.[89]

In this review, I briefly summarize important points about these compounds and especially focus on some new developments, such as the enhanced superconductivity recently discovered for yttrium sesquicarbide, and also new discoveries for the rare earth intercalated carbon compounds.

4.1 Binary Rare Earth Carbides

4.1.1 RC_2

The striking feature of the crystal structure of RC_2 dicarbides is that they exhibit a tetragonal to cubic transformation at high temperatures.[90] Although there has been some scattering of the data reported by different groups, the transition temperatures tend to increase along the lanthanide series and range from around 1000–1500° C, for the whole variation from LaC_2 to LuC_2. Gschneidner and Calderwood have made a tabulation where they averaged the various data, and find that the transition temperature dependence versus atomic number appears to follow two straight lines for the light rare earths and heavy rare earths, respectively.[89] The tetragonal phase and cubic phase are sometimes labeled as α-RC_2 and β-RC_2, respectively.

The room-temperature tetragonal structure was first solved by Atoji and Medrud for LaC_2 and takes the CaC_2-type crystal structure (space group $I4/mmm$).[91] The high-temperature cubic phase structure is that of the KCN-type (space group $Fm3m$). RC_2 has been reported to form for the rare earth elements of R = Y, La, Ce, Pr, Nd, Sm, Eu, Gd, Tb, Dy, Ho, Er, Tm, Yb, Lu.

While the rare earth diborides RB_2 were predominantly ferromagnetic, the rare earth dicarbides RC_2 are predominantly antiferromagnetic. CeC_2, NdC_2, SmC_2, GdC_2, TbC_2, DyC_2, HoC_2, and ErC_2 are reported to exhibit antiferromagnetic transitions at 30, 24, 21, 42, 67, 61, 25, and 8 K, respectively. It has been noted that CeC_2 and GdC_2 deviate from the deGennes factor dependence expected from the RKKY interaction. This has been attributed to effect of crystal field and deviation of the crystal structure, respectively.[88,92]

In contrast to the other magnetic rare earth carbides, EuC_2 is ferromagnetic at 20 K, while PrC_2 also exhibits anomalous behavior. This rare earth dependence is somewhat similar to the case of the tetraborides RB_4 and hexaborides RB_6, mentioned in previous Sections 3.1.2 and 3.1.3, respectively, where PrB_4 and EuB_6 were the anomalously ferromagnetic systems.

4.1.2 R_2C_3

The rare earth sesquicarbide R_2C_3 takes the body-centered cubic Pu_2C_3-type crystal structure (space group $I43d$). R_2C_3 has been reported to form for R = Y, La, Ce, Pr, Nd, Sm, Eu, Gd, Tb, Dy, Ho, Er, Tm, Yb, and Lu. However, the stability of the sesquicarbides to take the cubic Pu_2C_3-type crystal structure decreases along the series of heavy rare earths, and Er_2C_3, Tm_2C_3, Yb_2C_3, and Lu_2C_3 can only be formed through high-temperature and high-pressure methods.

As for striking physical properties, Krupka *et al*. first reported superconductivity in Y_2C_3, which was synthesized through a high-pressure (1.5–2.5 GPa), high-temperature method, with a relatively high transition temperature of $T_C = 11.5$ K.[93] La_2C_3 was also found to be superconducting with T_C of 11 K.[94]

In a recent development, it was reported that this superconductivity could be enhanced to 18 K for the same Y_2C_3 compound.[95] The origin for the high T_C behavior appearing is not clear, but the recent compound was synthesized at higher pressures (4–5.5 GPa) and the lattice constants happen to be smaller, i.e., in the range 8.181–8.226 Å, versus 8.2142–8.2514 Å, for the previous work, so this difference in lattice constant may be playing a role.

4.1.3 R_2C and R_3C (RC_x; $0.25 < x < 0.65$)

R_2C takes the trigonal anti-$CdCl_2$-type crystal structure (space group $R3m$), while R_3C (RC_x; $0.25 < x < 0.65$) takes the cubic Fe_4N-type crystal structure (space group $Fm3m$). A close relationship between the crystal structures exist, with a transformation from the cubic to trigonal structure that can be understood through a transfer (filling/ordering) of carbon atoms.[96] In more detail, the crystal structure of R_3C (RC_x; $0.25 < x < 0.65$) viewed along the (1, 1, 1) axis is basically a sequence of rare earth layers and partially occupied carbon layers. At the same time, the crystal structure of R_2C can be viewed as a sequence of rare earth layers, fully occupied carbon layers, and vacant layers. These structures are translated through the transfer (filling/ordering) of carbon atoms.[96]

R_2C has been reported to form for R = Gd, Tb, Dy, Ho, Er, Yb, Sc, while R_3C forms for R = Sm, Eu, Gd, Tb, Dy, Ho, Er, Tm, Yb, Lu.

R_2C and R_3C are mainly ferromagnetic systems with recent detailed measurements showing that Gd_2C exhibits a transition above room temperature at $T_C = 351$ K.[97] As a novel application, nanoparticles of Gd_2C have been investigated as candidates to use for hyperthermia treatment of cancer.[98]

4.1.4 $R_{15}C_{19}$

$R_{15}C_{19}$ forms for the smaller-sized rare earth elements of R = Sc, Y, Ho, Er, Tm, Yb, Lu, and takes a tetragonal structure with space group of $P4_21$. The structure can be described as built of two building blocks of apexes sharing $[Sc_6C]$ octahedra and a distorted octahedral encapsulating a C_2 carbon pair, $[Sc_6C_2]$.[99]

4.1.5 Rare Earth Intercalated Carbides

Rare Earth Graphite Intercalation Compounds (GICs). GICs, in which intercalants (atoms and compounds) are inserted between the surfaces of graphite, have been intensively studied since the 1980s.[100,101] There have been hundreds of different GICs reported. As for notable properties, LiC_6 is still used as a good electrode material for some lithium batteries and superconductivity has been created by intercalating potassium, for example, into graphite.

In regard to the rare earth intercalants, rare earths in the divalent state have been reported to form GICs, namely, EuC_6 and YbC_6 have been reported. The properties of both are interesting, with EuC_6 exhibiting an antiferromagnetic transition at $T_N = 40$ K, and displaying complex magnetic structures evidenced by the magnetization behavior.[102] The properties of YbC_6 are even more dramatic, with superconductivity being observed at $T_C = 6.5$ K.[103] Incidentally, CaC_6 also exhibits superconductivity at a transition temperature of 11.5 K. These temperatures are significantly higher than those observed for the alkali intercalant GICs and have attracted a lot of attention.

Despite the wide range of possible intercalant atoms demonstrated in GICs, and despite the behavior of divalent rare earths, for a long time, it was not considered possible for the trivalent rare earth elements to form GICs. However, rare earth intercalated graphite thin-film samples were shown to be possibly synthesized by the thermally driven surface reaction of an ultra-high-vacuum deposited overlayer of rare earth atoms with a graphite (0001) substrate.[104]

Magnetic measurements revealed for Gd–GIC that the Gd atoms were indicated to be in the trivalent state. Furthermore, the intrinsic magnetism of Gd–GIC was demonstrated to not have large anisotropy, in marked contrast to graphite, and as further proof of transfer of electron density from the intercalant RE layers to graphite layers.[105]

Rare Earth Encapsulated Fullerenes. Alkali metal encapsulated fullerenes have attracted interest since some of them such as K_3C_{60} exhibit superconductivity at relatively high temperatures. Interesting applications have been found for rare earth metal encapsulated fullerene. For example, $Gd@C_{82}$ was reported to show enhanced properties as a contrast agent for MRIs.[106] The Gd^{3+} ions act as a relaxation mechanism for the proton in water molecules in bodies and strengthen the contrast of MRI images.

The near-infrared luminescence of Er^{3+} at 1.5 μm is of interest since this is the wavelength of least loss in optical fibers. An interesting effect was observed when $(Er_2C_2)@C_{82}$ was observed to show more than a 100 times strong luminescence compared to $Er_2@C_{82}$.[107]

Another interesting effect was observed when $Gd@C_{82}$ were encapsulated in nanotubes, to form so-called ''peapods.'' These peapods of $Gd@C_{82}$ were proposed to act as 1D quantum dots.[108]

A review detailing recent developments in metallofullerenes is also given in Ref. 109 and also the article ***Endohedral Fullerenes***. While MRI is described in article ***Lanthanides: Magnetic Resonance Imaging***.

4.2 Ternary Rare Earth Carbide Compounds

In regard to ternary rare earth carbides, I will review the rare earth borocarbides and rare earth carbonitrides in separate sections.

4.2.1 Rare Earth Transition Metal Carbides

Following the discoveries of the excellent magnetic properties of the rare earth transition metal borides, the rare earth transition metal carbides have also been investigated extensively. For example, an early review and detailed comparative study have been given by Buschow.[110] A more recent review on particular developments has been given for Sm–Fe–C systems, for example. [111]

While the magnetic performances have not been found yet to exceed the best rare earth transition metal borides, the rare earth transition metal carbides also have variation in properties and are interesting systems to study.

5 RARE EARTH BOROCARBIDES

Excellent reviews and compilations on the rare earth borocarbides have been written by Bauer *et al.*[112] and Rogl.[113]

The rare earth borocarbides can be basically classified into three groups. The first group of compounds contains finite chains of carbon and boron located in voids created by the arrangement of the metal atoms. This includes compounds

such as Sc_2BC_2, $R_5B_2C_6$ (R = La, Ce, Gd, Ho), $R_{10}B_9C_{12}$ (R = La, Ce, Nd), $Gd_5B_2C_5$, $Ce_5B_4C_5$, and $La_{15}B_{14}C_{19}$.

The second group of compounds contains infinite zigzag chains of boron atoms bonded with carbon atoms that occupy channels created by the metal atom configuration. This includes compounds such as RBC (R = Y, Dy, Ho, Er).

The third group is 2D planar borocarbides that have boron and carbon 2D layers sandwiching metal layers. In this review, I will focus in more detail on these 2D planar compounds which have shown aspects of particular interest, such as the recent first [B/C] GIC discovery.

5.1 2D Planar Borocarbides

5.1.1 RB_2C_2

Metal borocarbide compounds containing boron and carbon mixed 2D layers are structurally interesting. A variation in the atomic rings and coordination of the [B/C] layer is exhibited depending on type/size of the metal atoms sandwiched in between, even for compounds with the same stoichiometry. For example, for the rare earth borocarbides, there are two structure types shown in Figure 7. The structures are RB_2C_2 (R = La, Ce, Pr, Nd, Sm, Y, Gd, Tb, Dy, Ho, Er, Tm, Yb, Lu) which have [4], [8] rings and are tetragonal (space group *P4/mbm*), while ScB_2C_2 takes a different structure because of its small size and has [5], [7] rings and is orthorhombic with space group of *Pbam*. Incidentally, expanding to other metals, MgB_2C_2 has puckered graphitic [6] ring layers.

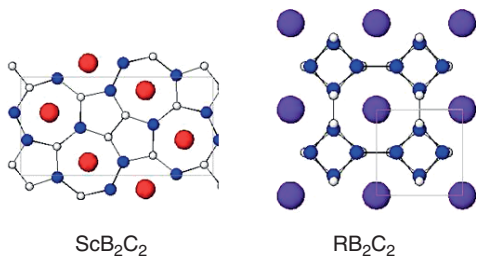


Figure 7 View of crystal structure of RB_2C_2

In regard to the physical properties, the magnetic properties have been studied extensively by Adachi and Shiokawa groups.[114] RB_2C_2 for R = Ce, Nd, Sm, Gd, Tb, Er, and Tm have antiferromagnetic transitions, while PrB_2C_2 exhibits Van Vleck paramagnetism. DyB_2C_2, HoB_2C_2 were first thought to be ferromagnetic, but it was elucidated that they are actually antiferromagnetic. As an interesting development, TbB_2C_2, DyB_2C_2, HoB_2C_2 were revealed to additionally have antiferromagnetic quadrupole ordering as well. The magnetic behavior is quite complex, owing to a competition between conventional antiferromagnetic coupling from the RKKY interaction, and antiferromagnetic quadrupole coupling.[115]

5.1.2 RB_2C

For the RB_2C compounds the structure depends on the rare earth size, similar to the RB_2C_2 compounds. RB_2C (R = Sc, Tb, Dy, Ho, Er, Tm, Yb, Lu) have four to seven rings, while CeB_2C has six to nine rings.[112] The configuration of the Ce atoms in CeB_2C is triangular and therefore frustrated behavior is observed, with the magnetic order depressed.[116]

These compounds form for the actinides also, but we note again that in this review we focus on the lanthanides.

5.1.3 First [B/C] Graphite Intercalation Compound

As a striking development, the first [B/C] GIC was discovered.[117] This is quite interesting, since as noted for just carbon-based GICs, hundreds of compounds have been extensively studied and have yielded interesting properties as battery materials, and superconductivity, etc., as noted in Section 4.1.5.

$Sc_2B_{1.1}C_{3.2}$ takes a trigonal crystal structure (space group *P*3*m*1). As shown in Figure 8, the structure is composed of alternate $-[B_{1/3}C_{2/3}]_\infty-Sc-C-Sc-[B_{1/3}C_{2/3}]_\infty-$layers, namely, boron and carbon mixed graphitic layers are sandwiching Sc_2C. Only three compounds have previously been reported with the $[BC]_\infty$ graphite like framework: LiBC, MgB_2C_2, and BC_3. The physical properties of $Sc_2B_{1.1}C_{3.2}$ are anomalously interesting, as briefly reviewed below.

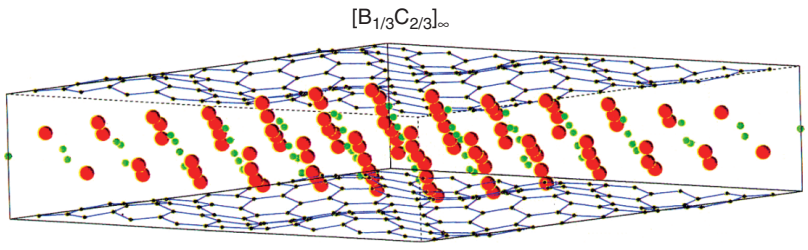


Figure 8 Schematic view of the crystal structure of the [B/C] GIC, $Sc_2B_{1.1}C_{3.2}$. Large dark circles represent scandium atoms, while smaller circles represent boron and carbon atoms

(1) A large anisotropy in the electrical conductivity exists between the in-plane (metallic) and *c*-axis (nonmetallic) directions.
(2) The in-plane resistivity shows a quadratic temperature dependence: $\rho = \rho_0 + \rho_1 T^n$, where the best fit is $n = 2$. Such quadratic dependence is one of the signatures observed in some GICs and has been attributed to interpocket electron–phonon scattering.[101] From the fitting result, it is indicated that the major temperature-dependent scattering mechanism of carriers is not the typical electron–phonon scattering of 3D systems, but rather such an interpocket transition, which reflects the 2D nature of $Sc_2B_{1.1}C_{3.2}$.
(3) The Sc_2C layers could be removed from the compound with oxydic agents, reminiscent of intercalants in GICs.
(4) The orbital susceptibility χ_{orb} of $Sc_2B_{1.1}C_{3.2}$ is determined to be paramagnetic. Although it is not exactly a signature of a GIC, orbital paramagnetism, which has been attributed to both interband and intraband effects, it has previously been observed in GICs.

To summarize, $Sc_2B_{1.1}C_{3.2}$ exhibits properties characteristic of GICs, and it can be considered to be the first boron and carbon mixed GIC with a $[B_{1/3}C_{2/3}]$ graphitic layer. Up to now, hundreds of GIC's with conventional carbon graphite layers have been researched over the years, and this can be the start of new exploration. The intercalant atomic density in the [B/C] GIC is quite high, which may have potential for battery applications. Replacement by other intercalants besides scandium-based ones should be explored.

6 RARE EARTH TRANSITION METAL BOROCARBIDES (RARE EARTH TRANSITION METAL BORONITRIDES)

I will focus on the most interesting system and review it briefly here, since this topic has been extensively dealt with in many reviews.[118,119]

The striking aspect of the rare earth transition metal borocarbides (or boronitrides) is the superconductivity observed in some of the RTr_2B_2C compounds. The RTr_2B_2C compounds are tetragonal (space group *I4/mmm*), and the structure has been described[120] as a ''filled'' version of the $ThCr_2Si_2$-type structure where Tr_2B_2 layers are separated by RC layers. An expanded version of this structure can be envisioned, namely, $(RC)_nTr_2B_2$, where Tr_2B_2 layers are separated by an *n* number of RC layers. A boronitride analog also exists, $(RN)_nTr_2B_2$, where Tr_2B_2 layers are separated by an *n* number of RN layers.

There have been relatively high transition temperatures reported like $T_C = 23$ K for YPd_2B_2C, and 16.5, 15, and 12 K for $LuNi_2B_2C$, YNi_2B_2C, and $(LaN)_3Ni_2B_2$, respectively.[121–123]

But the most fascinating feature is the coexistence of magnetism and superconductivity observed in RTr_2B_2C (R = Dy, Ho, Er, Tm). These compounds display an intricate interplay between magnetic ordering and superconductivity and the study of this has deepened understanding of superconductivity itself and vortex formation, for example.[118]

7 RARE EARTH NITRIDES

The rare earth nitrides are not as varied as the rare earth carbides and rare earth borides in the sense that the only binary phase is the RN compound, but they are interesting materials, nonetheless. For example, RN has recently been proposed as a material usable for spintronics. The preparation of high-quality samples of some of the rare earth nitrides has traditionally been reported to be difficult, because of problems with controlling the stoichiometry and high sensitivity versus oxygen and moisture. However, preparation techniques have become advanced over the years to enable higher-quality, pure, stoichiometric samples, and compounds such as the rare earth boron silicon nitrides are quite stable. As for previous reviews on rare earth nitrides, the basics of the binary rare earth nitrides have been covered by Hulliger in an early review on rare earth pnictides,[124] while ternary and higher-order nitrides have been reviewed in detail by Marchand.[125]

7.1 Binary Rare Earth Nitrides, RN

The only binary rare earth nitride known is the RN phase with cubic structure (space group *Fm*3*m*). RN has been reported to form for R = Sc, Y, La, Ce, Pr, Nd, Sm, Eu, Gd, Tb, Dy, Ho, Er, Tm, Yb, Lu.

As noted above, the preparation of pure and stoichiometric samples has been found to be difficult and this led to varying reports on the physical properties. Marchand has reviewed various synthesis methods for obtaining good-quality samples.[125] In the case of RN, high-quality single crystals have been obtained by Kaldis *et al*.[126]

An interesting feature in the physical properties of RN is that many of them are ferromagnetic for the magnetic rare earths. The rare earth–rare earth separations in RN are similar to the rare earth metals and Hulliger attributes the ferromagnetism to the direct coupling being dominant over the indirect coupling. Among the rare earth nitrides, Ce is anomalous, having tetravalency.

As a striking recent possible application for rare earth nitrides, they have been proposed as possible spintronics material. Aerts *et al*. have made a theoretical study where they report that the RN compounds can take a wide spectrum of properties over the different rare earths, from insulating to half-metallic to metallic behavior.[127] SmN and EuN are

reported as half-metallic compounds. In combination with the ferromagnetism, it is proposed that these materials can be used as spin-filtering materials, for example.[127]

7.2 Ternary and Higher Rare Earth Nitrides

The rare earth boron nitrides, carbonitrides, and borocarbonitrides are described in separate sections. The transition metal boronitrides that have been described in a previous section are interesting compounds in which superconductivity manifests.

7.2.1 Rare Earth Silicon Nitrides

RSi_3N_5 (R = La, Ce, Pr, Nd), which has an orthorhombic structure (space group $P2_12_12_1$), and $R_3Si_6N_{11}$ (R = La, Ce, Pr, Nd, Sm), which has a tetragonal structure (space group $P4bm$), are well established. The basic building blocks of these structures are corner-sharing SiN_4 tetrahedra, where the rare earth atoms occupy voids created by the tetrahedral coordination. These rare earth silicon nitrides exhibit very good stability both thermally and chemically.

7.2.2 Rare Earth Sialons

This topic should be described in detail elsewhere in the book, but rare earth-containing sialon (Si–Al–O–N) have been developed as excellent phosphor materials with applications as white-light-emitting diodes used in high-end liquid-crystal televisions and displays.[128]

8 RARE EARTH BORONITRIDES

Klesnar and Rogl have investigated the thermodynamic phase diagrams and found that no rare earth boronitrides exist for Sc or Y or the heavy rare earths from Tb to Lu. The lighter rare earths have been reported to form several phases.[129]

8.1 RBN_2

RBN_2 has been reported to form for R = Pr, Nd, Sm, Gd, and takes the so-called $PrBN_2$-type structure which is rhombohedral with space group $R3c$. The structure is formed of hexagonal BN planes where the rare earth is coordinated in an irregular bypyramidal [R_5B] unit, which is centered by additional N atoms.

8.2 $R_3B_2N_4$

The crystal structure of $R_3B_2N_4$ ($R_3B_2N_4$-type) is orthorhombic with space group $Immm$. $R_3B_2N_4$ forms for R = La, Ce, Pr, Nd.

9 RARE EARTH CARBONITRIDES

The existence of rare earth carbonitrides has been reviewed by Adachi *et al*.,[88] but one aspect was that nitrogen was thought to perhaps stabilize the elusive rare earth monocarbide RC phase.

It appears that two groups of face-centered-cubic structure compounds RC_xN_y exist, which are both nonequilibrium phases. For the former, compounds such as $CeN_{0.74}C_{0.60}$, $CeN_{0.65}C_{0.86}$, and $PrN_{0.73}C_{0.69}$ have been reported with $x + y$ significantly larger than 1. A second group appears to exist with $x + y$ smaller than 1 and has methanide carbon units.

Owing to the unstable nature of these compounds, work on physical properties, etc., have not advanced. In any case, nitrogen is indicated to be critical for a rare earth monocarbide-like phase to appear.

10 RARE EARTH BOROCARBONITRIDES

The most striking discovery is the series of rare earth borocarbonitrides (or R–B–C(N)) compounds which are found to be the long awaited n-type counterpart to p-type boron carbide as high-temperature TE materials.[59]

The homologous series of rare earth borocarbonitrides; $RB_{17}CN$, $RB_{22}C_2N$, and $RB_{28.5}C_4$, as shown in Figure 9, have a layered structure along the c-axis. Layers of B_{12} icosahedra and C–B–C chains reside between layers of B_6 octahedra and the rare earth atoms. The number of layers of B_{12} icosahedra and C–B–C chain layers increases successively along the series of $RB_{17}CN$, $RB_{22}C_2N$, and $RB_{28.5}C_4$, and in the infinite limit of no rare earth-containing layers, it is analogous to boron carbide.[130]

p-Type boron carbide is one of the few TE materials to have a previous history of being commercialized (by the company Hi-Z Technology in the USA), and these rare earth borocarbonitrides can embody the long-awaited n-type counterpart.[59]

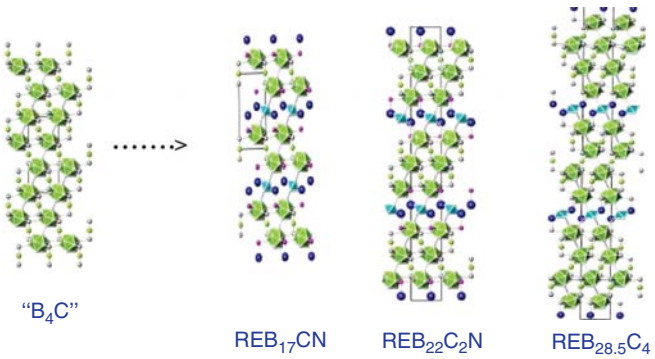


Figure 9 View of crystal structure of the rare earth borocarbonitrides[59]

Various results to further develop these materials as TE materials have been obtained such as the densification of these materials through usage of sintering additives,[131,132] doping with transition metals,[133] and modification of the [B]/[C] composition,[134] which previously had led to significant improvement in the TE properties of boron carbide.

11 CONCLUSIONS

The rare earth borides, carbides, and nitrides have yielded compounds very interesting for their chemical and physical aspects. One way of viewing the crystal structure of the less metal-rich compounds is to see them as compounds where the boron, carbon, and nitrogen atoms basically form a strong refractory atomic network (with such examples like atomic clusters or nets in some cases) inside which rare earth atoms occupy particular spaces/voids. In ways, some of these systems are particularly amenable to material design, considering it is possible to have a systematic view of the possible arrangements of basic building blocks of the structure, such as configuration of atomic polyhedra in the cluster-based compounds and atomic polygons in the layered compounds (''tiling'').

I would like to briefly sum up some of the notable physical properties of the rare earth borides, carbides, and nitrides described in the previous sections.

The rare earth borides, carbides, and nitrides all have compounds that manifest superconductivity, fundamental magnetic transitions, and other interesting phenomena such as strongly correlated heavy fermion behavior. Some of the rare earth transition metal borocarbides such as RTr_2B_2C have shown fascinating properties where magnetism and superconductivity phenomena coexist.

One interesting result in the magnetic behavior is the discovery of unexpectedly strong magnetic interactions and wide range of magnetic behavior (1D and dimer-like transition, 2D spin-glass behavior, and 3D long-range order) in some higher borides, which are insulating, magnetically dilute, localized f-electron systems. It has been indicated that the B_{12} icosahedral clusters play an important role in mediating the magnetic interaction. Another possibility is that of rare earth nitrides being used as materials for spintronics.

The AlB_2-type analogous layered rare earth transition metal (or aluminum) borides have interesting structural features where myriad unexplored layered compounds can be envisioned, and where the physical properties have been found to be strongly influenced by the ''tiling'' of atomic hexagons,[6] pentagons,[5] and heptagons.[7] For example, tiling building defects were shown to have a large effect on the physics in $TmAlB_4$, and Tm_2AlB_6 has exhibited an interesting magnetic field induced field stable state. In the borocarbide-layered compounds, the first [B/C] GIC was discovered.

One increasingly important aspect in present society regarding application of physical properties is the development of viable TE materials, namely, materials that can effectively convert waste heat into electricity. Borides are attractive as high-temperature TE materials because of their excellent stability under high temperature and because the thermal conductivity of boron icosahedra cluster-containing systems has generally been found to be intrinsically low. As new developments, the RB_{50} system ($RB_{44}Si_2$) was found to be a good p-type high-temperature TE material with Seebeck coefficients exceeding $200\,\mu V\ K^{-1}$ and the figure of merit trending higher at temperatures above 1000 K. The rare earth borocarbonitride series, $RB_{17}CN$, $RB_{22}C_2N$, and $RB_{28.5}C_4$, are found to embody the long-awaited n-type counterpart to boron carbide.

Regarding other notable physical properties of the rare earth borides, carbides, and nitrides, with successful applications, high-performance permanent magnetic materials have been discovered in the rare earth transition metal borides and carbides, such as $Nd_2Fe_{14}B$. LaB_6 and CeB_6 have been established as excellent electron emitters, while RB_{66} has been applied as a novel monochromator material. Nanoparticles of Gd_2C have been investigated for use for hyperthermia treatment of cancer, for example. $Gd@C_{82}$ was reported to show enhanced properties as a contrast agent for MRIs, while $(Er_2C_2)@C_{82}$ shows strong luminescence in the near-infrared range at $1.5\,\mu m$. Rare earth sialon compounds have been developed as excellent phosphor materials.

To summarize, the rare earth borides, carbides, and nitrides have yielded interesting compounds with striking features in their crystal structures and physical properties, and also successful applications. They also appear to be systems that are amenable to materials design. This is an important direction to strive for in the current world where natural resources are limited, namely, to highly functionalize materials that are mainly composed of abundant light elements through the innovative use of a small amount of rare element.

12 RELATED ARTICLES

Magnetism; Endohedral Fullerenes; Lanthanides: Magnetic Resonance Imaging.

13 ABBREVIATIONS AND ACRONYMS

GICs = graphite intercalation compounds; TEs = thermoelectrics.

14 REFERENCES

1. J. Etourneau, *J. Less Common Met.*, 1985, **110**, 267.
2. O. A. Golikova, *Phys. Status Solidi A*, 1987, **101**, 277.
3. T. Mori, in 'Boron Rich Solids, Sensors, Ultra High Temperature Ceramics, Thermoelectrics, Armor', eds. N. Orlovskaya and M. Lugovy, Springer: New York, 2010, p. 63.
4. D. Gignoux and D. Schmitt, in 'Handbook of Magnetic Materials', ed. K. H. J. Buschow, North-Holland, Amsterdam, 1997, Vol. 10, p. 239.
5. T. Mori, in 'Handbook on the Physics and Chemistry of Rare-Earths', eds. K. A. Gschneidner, Jr., J.-C. Bunzli, and V. Pecharsky, Elsevier, Amsterdam, 2008, Vol. 38, p. 105.
6. K. H. J. Buschow, in 'Boron and Refractory Borides', Heidelberg, Berlin, 1977, p. 494.
7. M. A. Avila, S. L. Bud'ko, C. Petrovic, R. A. Ribeiro, P. C. Canfield, A. V. Tsvyashchenko, and L. N. Fomicheva, *J. Alloys Compd.*, 2003, **358**, 56.
8. T. Mori, T. Takimoto, A. Leithe-Jasper, R. Cardoso-Gil, W. Schnelle, G. Auffermann, H. Rosner, and Y. Grin, *Phys. Rev. B*, 2009, **79**, 104418.
9. J. Nagamatsu, N. Nakagawa, T. Muranaka, Y. Zenitani, and J. Akimitsu, *Nature*, 2001, **410**, 63.
10. Yu. B. Paderno and S. Pokrzywnicki, *Phys. Status Sol.*, 1967, **24**, K11.
11. G. A. Wigger, E. Felder, R. Monnier, H. R. Ott, L. Pham, and Z. Fisk, *Phys. Rev. B*, 2005, **72**, 14419.
12. K. H. J. Buschow and J. H. N. Croyghton, *J. Chem. Phys.*, 1972, **57**, 3910.
13. Z. Fisk, M. B. Maple, D. C. Johnston and L. D. Woolf, *Solid State Commun.*, 1981, **39**, 1189.
14. V. V. Novikov, A. V. Morozov, A. V. Matovnikov, D. V. Avdashenko, Y. N. Polesskaya, N. V. Sahoshko, B. I. Kornev, V. D. Solomennik, and V. V. Novikova, *Phys. Solid State*, 2011, **53**, 1743.
15. D. Okuyama, T. Matsumura, H. Nakao, and Y. Murakami, *J. Phys. Soc. Jpn.*, 2005, **74**, 2434.
16. R. Watanuki, G. Sato, K. Suzuki, M. Ishihara, T. Yanagisawa, Y. Nemoto, and T. Goto, *J. Phys. Soc. Jpn.*, 2005, **74**, 2169.
17. B. S. Shastry and B. Sutherland, *Physica*, 1981, **108B**, 1069.
18. J. A. Deacon and S. E. R. Hiscocks, *J. Mater. Sci.*, 1971, **6**, 309.
19. H. C. Longuet, M. De, and V. Roberts, *Proc. R. Soc.*, 1955, **A230**, 110.
20. T. H. Geballe, B. T. Matthias, K. Andres, J. P. Maita, A. S. Cooper, and E. Corenzwit, *Science*, 1968, **160**, 1443.
21. S. Sullow, I. Prasad, M. C. Aronson, J. L. Sarrao, Z. Fisk, D. Hristova, A. H. Lacerda, M. F. Hundley, A. Vigliante, and D. Gibbs, *Phys. Rev. B*, 1998, **57**, 5860.
22. T. Kasuya, *Prog. Theor. Phys. Suppl.*, 1992, **108**, 1.
23. T. Kasuya, K. Takegahara, Y. Aoki, T. Suzuki, S. Kunii, M. Sera, N. Sato, T. Fujita, T. Goto, A. Tamaki, and T. Komatsubara,'Valence Instabilities', North-Holland, Amsterdam, 1982, p. 359.
24. D. P. Young, D. Hall, M. E. Torelli, Z. Fisk, J. L. Sarrao, J. D. Thompson, H. R. Ott, S. B. Oseroff, R. G. Goodrich, and R. Zysler, *Nature*, 1999, **397**, 412.
25. T. Mori and S. Otani, *Solid State Commun.*, 2002, **123**, 287.
26. J. Akimitsu, K. Takenawa, K. Suzuki, H. Harima, and Y. Kuramoto, *Science*, 2001, **293**, 1125.
27. T. Mori and S. Otani, *J. Phys. Soc. Jpn.*, 2002, **71**, 1789.
28. B. T. Matthias, T. H. Geballe, K. Andres, E. Corenzwit, G. Hull, and J. P. Maita, *Science*, 1968, **159**, 530.
29. Z. Fisk, P. Schmidt, and L. Longinotti, *Mater. Res. Bull.*, 1976, **11**, 1019.
30. P. Szabo, J. Kaemareik, P. Samuely, J. Girovsky, S. Gabani, K. Flachbart, and T. Mori, *Physica C*, 2007, **460–462**, 626.
31. C. Oshima, E. Bannai, T. Tanaka, and S. Kawai, *J. Appl. Phys.*, 1977, **48**, 3925.
32. J. Xu, T. Mori, Y. Bando, D. Golberg, D. Berthebaud, and A. Prytuliak, *Mater. Sci. Eng. B*, 2012, **177**, 117.
33. K. Hamada, M. Wakata, N. Sugii, K. Matsuura, K. Kubo, and H. Yamauchi, *Phys. Rev. B*, 1993, **48**, 6892.
34. Y. Paderno, N. Shitsevalova, I. Batko, K. Flahbart, H. Misiorek, J. Mucha, and A. Jezowski, *J. Alloys Compd.*, 1995a, **219**, 215.
35. Y. Paderno and N. Shitsevalova, *J. Alloys Compd.*, 1995b, **219**, 119.
36. S. Gabani, I. Bat'ko, K. Flachbart, T. Herrmannsdoerfer, R. Koenig, Y. Paderno, and N. Shitsevalova, *J. Magn. Magn. Mater.*, 1999, **207**, 131.
37. P. G. deGennes, *C.R.*, 1958, **247**, 1836.
38. K. Siemensmeyer, K. Flachbart, S. Gabani, S. Mat'as, Y. Paderno, and N. Shitsevalova, *J. Solid State Chem.*, 2006, **179**, 2748.
39. N. Sluchanko, L. Bogomolov, V. Glushkov, S. Demishev, M. Ignatov, E. Khayrullin, N. Samarin, D. Sluchanko, A. Levchenko, N. Shitsevalova, and K. Flachbart, *Phys Status Solidi B*, 2006, **243**, R63.
40. F. Iga, Y. Takakuwa, Y. Takahashi, M. Kasaya, T. Kasuya, and T. Sagawa, *Solid State Commun.*, 1984, **50**, 903.
41. A. Czopnik, N. Shitsevalova, V. Pluzhnikov, A. Krivchikov, Yu. B. Paderno, and Y. Onuki, *J. Phys.: Condens. Matter.*, 2005, **17**, 5971.
42. T. Tanaka, S. Okada, and V. N. Gurin, *J. Alloys Compd.*, 1998, **67**, 211.
43. T. Mori, F. Zhang, and T. Tanaka, *J. Phys. Condens. Matter*, 2001, **13**, L423.
44. F. Zhang, F. Xu, A. Leithe-Jasper, T. Mori, T. Tanaka, A. Sato, P. Salamakha, and Y. Bando, *J. Alloys Compd.*, 2002, **337**, 120.

45. I. Higashi, T. Tanaka, K. Kobayashi, Y. Ishizawa, and M. Takami, *J. Solid State Chem.*, 1997a, **133**, 11.
46. T. Mori and T. Tanaka, *Mater. Res. Bull.*, 2001, **36**, 2463.
47. T. Tanaka, S. Okada, and Y. Ishizawa, *J. Solid State Chem.* 1997, **133**, 55.
48. T. Mori and T. Tanaka, *J. Phys. Soc. Jpn.*, 1999, **68**, 2033.
49. T. Mori and T. Tanaka, *J. Phys. Soc. Jpn.*, 2000, **69**, 579.
50. T. Mori, *J. Appl. Phys.*, 2004, **95**, 7204.
51. T. Mori, *J. Appl. Phys.*, 2006, **99**, 08J309.
52. T. Mori and F. Zhang, *J. Phys. Condens. Matter*, 2002, **14**, 11831.
53. G. A. Slack, D. W. Oliver, and F. H. Horn, *Phys. Rev. B*, 1971, **4**, 1714.
54. D. G. Cahill, H. E. Fischer, S. K. Watson, R. O. Pohl, and G. A. Slack, *Phys. Rev. B*, 1989, **40**, 3254.
55. T. Mori, *Physica B*, 2006, **383**, 120.
56. T. Mori, 'Boride Thermoelectrics; High temperature thermoelectric materials' in 'Modules, Systems and Applications', ed. D. M. Rowe, CRC Press, London, 2012, pp. 14-1 – 14-18.
57. C. Wood and D. Emin, *Phys. Rev. B*, 1984, **29**, 4582.
58. D. Emin, *Phys Today*, 1987, **40**, 55.
59. T. Mori and T. Nishimura, *J. Solid State Chem.*, 2006, **179**, 2908.
60. T. Mori, *J. Appl. Phys.*, 2005, **97**, 093703.
61. D. Berthebaud, A. Sato, Y. Michiue, T. Mori, A. Nomura, T. Shishido, and K. Nakajima, *J. Solid State Chem.*, 2011, **184**, 1682.
62. T. Mori, D. Berthebaud, T. Nishimura, A. Nomura, T. Shishido, and K. Nakajima, *Dalton Trans.*, 2010, **39**, 1027.
63. S. M. Richards and J. S. Kasper, *Acta Crystallogr. B*, 1969, **25**, 237.
64. T. Mori and T. Tanaka, *J. Solid State Chem.*, 2006, **179**, 2889.
65. J. Wong, G. Shimkaveg, W. Goldstein, M. Eckart, T. Tanaka, Z. U. Rek, and H. Tompkins, *Nucl. Instrum. Methods A*, 1990, **291**, 243.
66. V. Babizhetskyy, J. Roger, S. D'eputier, R. Jardin, J. Bauer, and R. Gu'erin, *J. Solid State Chem.*, 2004, **177**, 415.
67. J. Roger, V. Babizhetskyy, S. Cordier, J. Bauer, K. Hiebl, L. LePoll'es, S. H. Ashbrook, J. F. Halet, and R. Gu'erin, *J. Solid State Chem.*, 2005, **178**, 1851.
68. F. Zhang, A. Sato, and T. Tanaka, *J. Solid State Chem.*, 2002, **164**, 361.
69. J. R. Salvadore, D. Bilc, S. D. Mahanti, and M. G. Kanatzidis, *Angew. Chem. Int. Ed.*, 2002, **41**, 844.
70. J. Roger, V. Babizhetskyy, T. Guizouarn, K. Hiebl, R. Guérien, and J.-F. Halet, *J. Alloys Compd.* 2006, **417**, 72.
71. J. D. Corbett, E. Garcia, A. M. Guloy, W. M. Hurng, Y. U. Kwon, and E. A. Leon-Escarmilla, *Chem. Mater.*, 1998, **10**, 2824.
72. H. Nowotny, B. Lux, and H. Kudielka, *Monatsh. Chem.*, 1956, **87**, 447.
73. W. Jeitschko, H. Nowotny, and F. Benesovsky, *Monatsh. Chem.*, 1964, **95**, 1242.
74. J. Roger, M. Ben Yahia, V. Babizhetskyy, S. Cordier, R. Guérin, J. Bauer, K. Hiebl, X. Rocquefelte, J.-Y. Saillard, and J.-F. Halet, *J. Solid State Chem.*, 2006, **179**, 2310.
75. M. Sagawa, S. Fujimori, N. Togawa, and Y. Matuura, *J. Appl. Phys.*, 1984, **55**, 2083.
76. T. Mori, K. Kudou, T. Shishido, and S. Okada, *J. Appl. Phys.*, 2011, **109**, 07E111.
77. T. Mori, T. Shishido, K. Nakajima, K. Kieffer, and K. Siemensmeyer, *J. Appl. Phys.*, 2009, **105**, 07E124.
78. T. Mori, H. Borrmann, S. Okada, K. Kudou, A. Leithe-Jasper, U. Burkhardt, and Y. Grin, *Phys. Rev. B*, 2007, **76**, 064404.
79. Y. B. Kuzma, *Sov. Phys. Crystallogr.*, 1970, **15**, 312.
80. P. Rogl and H. Nowotny, *Monatsh. Chem.*, 1974, **105**, 1082.
81. S. Okada, T. Shishido, T. Mori, K. Kudou, K. Iizumi, T. Lundstrom, and K. Nakajima, *J. Alloys Compd.*, 2006, **408–412**, 547.
82. I. Veremchuk, T. Mori, Yu. Prots, W. Schnelle, A. Leithe-Jasper, M. Kohout, and Y. Grin, *J. Solid State Chem.*, 2008, **181**, 1983.
83. Y. B. Kuzma and S. I. Svarichevskaya, *Sov. Phys. Crystallogr.*, 1972, **17**, 569.
84. T. Mori, I. Kuzmych-Ianchuk, K. Yubuta, T. Shishido, S. Okada, K. Kudou, and Y. Grin, *J. Appl. Phys.*, 2012, **111**, 07E127.
85. H. S. Li and J. M. D. Coey, in 'Handbook of Magnetic Materials', ed. K. H. J. Buschow, Elsevier, Amsterdam, 1991, Vol. 6, p. 1.
86. H. H. A. Smit, R. C. Thiel, and K. H. J. Buschow, *J. Phys. F*, 1988, **18**, 295.
87. D. B. de Mooij and K. H. J. Buschow, *Philips J. Res.*, 1987, **41**, 400.
88. G. Adachi, N. Imanaka, and Z. Fuzhong, in 'Handbook on the Physics and Chemistry of Rare-Earths', eds. K. A. Gschneidner, Jr. and L. Eyring, Elsevier, Amsterdam, 1991, Vol. 15, p. 61.
89. K. A. Gschneidner and F. W. Calderwood, *Bull. Alloy Phase Diagrams*, 1986, 7.
90. A. L. Bowman, N. H. Krikorian, G. R. Arnold, T. C. Wallace, and N. G. Nereson, *Acta Crystallogr. B*, 1968, **24**, 459.
91. M. Atoji and R. C. Medrud, *J. Chem. Phys.*, 1959, **31**, 332.
92. T. Sakai, G. Adachi, and J. Shiokawa, *J. Appl. Phys.*, 1979a, **50**, 3592.
93. M. C. Krupka, A. L. Giorgi, N. H. Krikorian, and E. G. Szklarz, *J. Less-Common Met.*, 1969a, **17**, 91.
94. A. L. Giorgi, E. G. Szklarz, M. C. Krupka, and N. H. Krikorian, *J. Less-Common Met.*, 1969, **17**, 121.
95. G. Amano, S. Akutagawa, T. Muranaka, Y. Zenitani, and J. Akimitsu, *J. Phys. Soc. Jpn.*, 2004, **73**, 530.

96. M. Atoji and M. Kikuchi, *J. Chem. Phys.*, 1969, **81**, 3863.
97. Y. Mudryk1, Durga Paudyal1, V. K. Pecharsky1, 2, and K. A. Gschneidner, *J. Appl. Phys.*, 2011, **109**, 07A924.
98. S. N. Ahmad, Y. Akin, and S. A. Shaheen, *J. Appl. Phys.*, 2005, **97**, 10Q902.
99. J. Bauer and D. Ansel, *J. Less-Common Met.*, 1985, **109**, L9.
100. M. S. Dresselhaus and G. Dresselhaus, *Adv. Phys.*, 1981, **30**, 139.
101. H. Kamimura and T. Ohno, 'Exotic Metal GIC', Butsurigaku Saizensen, Vol. 7, Kyoritsu Publishing, Tokyo, Japan, 1984.
102. H. Suematsu, K. Ohmatsu, K. Sugiyama, T. Sakakibara, M. Motokawa, and M. Date, *Solid State Commun.*, 1981, **40**, 241.
103. T. E. Weller, M. Ellerby, S. S. Saxena, R. P. Smith, and N. T. Skipper, *Nat. Phys.*, 2005, **1**, 39.
104. I. I. Mazin and S. L. Molodtsov, *Phys. Rev. B*, 2005, **72**, 1.
105. T. Mori, T. Tanaka, S. A. Gorovikov, and S. L. Molodtsov, *J. Phys. Soc. Jpn.*, 2000, **69**, 3051.
106. H. Kato, Y. Kanazawa, M. Okumura, A. Taninaka, T. Yokawa, and H. Shinohara, *J. Am. Chem. Soc.*, 2003, **125**, 4391.
107. Y. Ito, T. Okazaki, S. Okubo, M. Akachi, Y. Ohno, T. Mizutani, T. Nakamura, R. Kitaura, T. Sugai, and H. Shinohara, *ACS Nano*, 2007, **1**, (5), 456.
108. J. Lee, H. Kim, S.-J. Kahng, Y.-W. Son, J. Ihm, H. Kato, Z. W. Wang, T. Okazaki, H. Shinohara, and Y. Kuk, *Nature*, 2002, **415**, 1005.
109. H. Shinohara and Y. Saito, in 'Handbook on the Physics and Chemistry of Rare-Earths', eds. K. A. Gschneidner, Jr., J.-C. Bunzli, and V. Pecharsky, Elsevier, Amsterdam, 2010, Vol. 41, p. 95.
110. K. H. J. Buschow, in 'Handbook on Ferromagnetic Materials', eds. E. P. Wohlfarth and K. H. J. Buschow, North-Holland, Amsterdam, 1988c, Vol. 4, p. 1.
111. G. C. Hadjipanayis, Y. H. Zheng, A. S. Murthy, W. Gong, and F. M. Yang, *J. Alloys Compd.*, 1995, **222**, 49.
112. J. Bauer, J. F. Halet, and J. Y. Saillard, *Coord. Chem. Rev.*, 1998, **178**, 723.
113. P. Rogl, 'Phase Diagrams of Ternary Metal-Boron-Carbon Systems', ASM International, Ohio, 1998.
114. T. Sakai, G. Adachi, and J. Shiokawa, *Solid State Commun.*, 1981, **40**, 445.
115. H. Onodera, K. Kaneko, T. Onimaru, K. Ohoyama, Y. Yamaguchi, H. Kobayashi, Y. Nemoto, and T. Goto, *J. Magn. Magn. Mater.*, 2000, **221**, 293.
116. K. Hirota and M. Ishikawa, *Physica B*, 1993, **186–188**, 478.
117. T. Mori, M. Tansho, Y. Onoda, Y. Shi, and T. Tanaka, *Phys. Rev. B*, 2000, **62**, 7587.
118. K.-H. Müller, M. Schneider, G. Fuchs, and S.-L. Drechsler, in 'Handbook on the Physics and Chemistry of Rare-Earths', eds. K. A. Gschneidner, Jr., J.-C. Bunzli, and V. Pecharsky, Elsevier, Amsterdam, 2008, Vol. 38, p. 174.
119. K.-H. Müller, G. Fuchs, S.-L. Drechsler, and V. N. Narozhnyi, in 'Handbook of Magnetic Materials', ed. K. H. J. Buschow, Elsevier, Amsterdam, 2002, Vol. 14, p. 199.
120. T. Siegrist, R. J. Cava, J. J. Krajewski, and W. F. Peck, Jr., *J. Alloys Compd.* 1994, **216**, 135.
121. C. Mazumdar, R. Nagarajan, C. Godart, L. C. Gupta, M. Latroche, S. K. Dhar, C. Levy-Clement, B. D. Padalia, and R. Vijayaraghavan, *Solid State Commun.*, 1993, **87**, 413.
122. R. J. Cava, H. Takagi, H. W. Zandbergen, J. J. Krajewski, W. F. Peck Jr., T. Siegrist, B. Batlogg, R. B. van Dover, R. J. Felder, K. Mizuhashi, J. O. Lee, H. Eisaki, and S. Uchida, *Nature* 1994, **367**, 254.
123. R. J. Cava, H. W. Zandbergen, B. Batlogg, H. Eisaki, H. Takagi, J. J. Krajewski, W. F. Peck, Jr., E. M. Gyorgy, and S. Uchida, *Nature (London)* 1994, **372**, 245.
124. F. Hulliger, in 'Handbook on the Physics and Chemistry of Rare-Earths', eds. K. A. Gschneidner, Jr. and L. Eyring, Elsevier, Amsterdam, 1979, Vol. 4, p. 153.
125. R. Marchand, in 'Handbook on the Physics and Chemistry of Rare-Earths', eds. K. A. Gschneidner Jr., J.-C. Bunzli, and V. Pecharsky, Elsevier, Amsterdam, 1998, Vol. 25, p. 51.
126. Kaldis, E., B. Steinmann, B. Fritzler, E. Jilek, and A. Wizard, in 'Modern Science and Technology', The Rare Earths, eds. J. McCarthy, *et al*., Plenum, New York, 1982, Vol. 3, p. 224.
127. C. M. Aerts, P. Strange, M. Horne, W. H. Temmermann, Z. Szotek, and A. Svane, *Phys. Rev. B*, 2004, **69**, 045115.
128. N. Hirosaki, R. Xie, and S. Ken, *OYO BUTURI*, 2005, **74**, 1449.
129. H. Klesnar and E. Rogl, *High Temp. High Pressures*, 1990, **22**, 453.
130. E. L. Belokoneva and T. Mori, *Cryst. Res. Technol.*, 2009, **44**, 19.
131. T. Mori, T. Nishimura, K. Yamaura, and E. Takayama-Muromachi, *J. Appl. Phys.*, 2007, **101**, 093714.
132. D. Berthebaud, T. Nishimura, and T. Mori, *J. Mater. Res.*, 2010, **25**, 665.
133. A. Prytuliak and T. Mori, *J. Electron. Mater.*, **40**, 920.
134. O. Sologub and T. Mori, to be submitted.

Lanthanide Complexes with Multidentate Ligands

Xiaoping Yang and Richard A. Jones

University of Texas at Austin, Austin, TX, USA

and

Wai-Kwok Wong

Hong Kong Baptist University, Kowloon Tong, Hong Kong, People's Republic of China

1	Summary	281
2	Introduction	281
3	Polynuclear Lanthanide Complexes with Conjugated Schiff-Base Ligands	282
4	Polynuclear Lanthanide Complexes and Lanthanide Coordination Polymers with Flexible Schiff-Base Ligands	286
5	Construction of High Nuclearity Lanthanide Complexes Using Small Linkers	291
6	Conclusions	295
7	Glossary	296
8	Acknowledgments	296
9	Related Articles	296
10	Abbreviations and Acronyms	297
11	References	297

1 SUMMARY

The synthesis, structures, and luminescence properties of polynuclear lanthanide complexes and lanthanide coordination polymers, which are formed from multidentate oxygen and nitrogen-containing Schiff-base ligands, are described in this chapter.

2 INTRODUCTION

Polynuclear lanthanide complexes and lanthanide coordination polymers with distinct magnetic and luminescent properties are currently of interest for the use in applications involving the fabrication of novel materials and as probes in biological systems.[1,2] However, compared to polynuclear complexes of the d-block transition metals, the design and synthesis of polynuclear lanthanide complexes, as well as lanthanide coordination polymers, are more challenging and far less developed. This may be due to the difficulty in controlling the coordination environment of Ln^{III} ions which often display high and variable coordination numbers. Many lanthanide systems reported have involved the use of oxygen- and nitrogen-containing ligands such as carboxylates, amino acidates, and pyridones.[3,4] Schiff-base ligands are among the most widely studied chelators for metal ions owing to their relatively easy synthesis and versatility in the formation of stable complexes.[5,6] For example, they can show various coordination modes with metal ions in the construction of supramolecular frameworks. Here we describe the synthesis, crystal structures, and luminescence properties of 25 polynuclear lanthanide complexes and lanthanide coordination polymers based on multidentate ''salen''-style Schiff-base ligands. Two kinds of salen-style Schiff-base ligands have been employed in the synthesis: one kind is a

The Rare Earth Elements. Edited by David A. Atwood. © 2012 John Wiley & Sons, Ltd. ISBN 978-1-119-95097-4

conjugated Schiff-base type of ligand and the other is a more flexible Schiff-base ligand (Scheme 1). In these lanthanide complexes, the ligands not only stabilize lanthanide centers in the formation of polynuclear assemblies but also act as antennas that sensitize the luminescence of lanthanide ions.

3 POLYNUCLEAR LANTHANIDE COMPLEXES WITH CONJUGATED SCHIFF-BASE LIGANDS

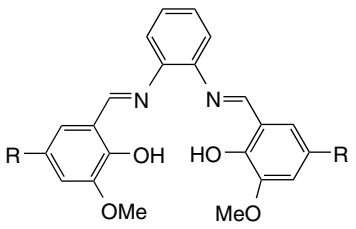
Recently, the use of pthalocyanines and porphyrins by Ishikawa and coworkers enabled the synthesis of several so-called double-decker or triple-decker lanthanide complexes, described as ''stacked π-conjugate molecules.''[7,8] The photophysical properties of lanthanide ions depend markedly on their coordination environments. Since a multidecker framework can effectively keep solvent molecules away from Ln^{III} centers, it is assumed that enhanced luminescent properties can be achieved with these types of architectures. We discovered that the use of two conjugated Schiff-base ligands H_2L[1,2] can stabilize novel multidecker frameworks (Scheme 1).

3.1 ''Multidecker'' Lanthanide Complexes

''Multidecker'' lanthanide complexes (**1**–**5**) have been synthesized from the reactions of lanthanide salts with conjugated Schiff-base ligands H_2L[1,2]. An interesting emerging feature exhibited by these complexes is the self-assembly of stacked multidecker structures in which Ln^{III} ions are sandwiched between alternating layers of the Schiff-base ligands.

Reaction of H_2L^1 (*N*,*N*′-bis(5-bromo-3-methoxy-salicylidene)phenylene-1,2-diamine) with $LnCl_3 \cdot 6H_2O$ (Ln = Tb and Yb) in the presence of $Zn(OAc)_2 \cdot 2H_2O$ resulted in the formation of the triple-decker complexes $[Ln_3(L^1)_3(OAc)_2Cl]$ (Ln = Tb (**1**) and Yb (**2**)).[9,10] A view of the cationic moiety of (**1**) and skeletal view of the N, O donor framework is shown in Figure 1. In (**1**), one terminal Tb^{3+} ion (Tb(1)) is coordinated to two N_2O_2 donor sets of two L^1 ligands. The two inner L^1 ligands create a coordination environment for the central Tb(Tb(2)) which consists of two phenolic oxygen atoms and one OMe from one ligand in addition to the N_2O_2 donor set of the other. A bridging acetate unit spans Tb(2)–Tb(3) and gives Tb(2) an eight-coordinate environment. The third Tb^{3+} ion (Tb(3)) is also eight-coordinate and is virtually coplanar with the O_2O_2 donor set of one inner L^1 group. The coordination environment of Tb(3) is completed by a terminal chloride and a chelating acetate ligand. The distances for Tb(3)–Tb(2) and Tb(1)–Tb(2) are 3.676 and 3.819 Å, respectively. The solid-state structure of (**2**) reveals the presence of two independent, chiral $Yb_3L_3^1$ units of the complex (Figure 2). Each chiral $Yb_3L_3^1$ unit has a similar structure to (**1**). In the $Yb_3L_3^1$ unit, each Yb^{III} ion is eight-coordinate bound by the N_2O_2 donor sets of two L groups, and intermetallic distances range between 3.7 and 3.8 Å.

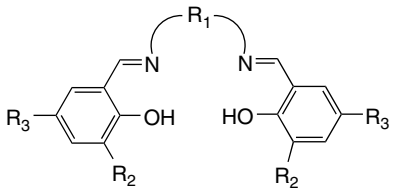
Reaction of H_2L^1 with $TbCl_3 \cdot 6H_2O$ in an acetonitrile/methanol mixture resulted in the formation of the trimetallic tetradecker complex $[Tb_3(L^1)_4(H_2O)_2]Cl$ (**3**).[9] As shown in Figure 3, the two outer Tb^{3+} ions, Tb(1) and Tb(3), have similar nine-coordinate environments comprising the N_2O_2 donor set of the outer L^1 group, the O_2O_2 set of one inner L^1 group, and one H_2O molecule. The central Tb(2) ion has an eight-coordinate pseudo-square-based antiprismatic geometry formed by the two N_2O_2 donor sets of the internal L^1 ligands. The phenolic oxygen atoms of the interior L^1 group are bridging, while those of the outer L^1 are monodentate. The Tb–Tb separations are similar at 3.884 and 3.872 Å for Tb(1)–Tb(2) and Tb(2)–Tb(3), respectively. The valence



H_2L^1: R = Br

H_2L^2: R = H

(a)



H_2L^3: $R_1 = CH_2CH_2$, $R_2 = R_3 = H$

H_2L^4: $R_1 = CH_2CH_2CH_2$, $R_2 = OMe$, $R_3 = Br$

H_2L^5: $R_1 = CH_2CH_2$, $R_2 = OMe$, $R_3 = H$

H_2L^6: $R_1 = CH_2CH_2CH_2CH_2$, $R_2 = OMe$, $R_3 = H$

(b)

Scheme 1 Conjugate (a) and flexible (b) Schiff-base ligands H_2L[1–6]

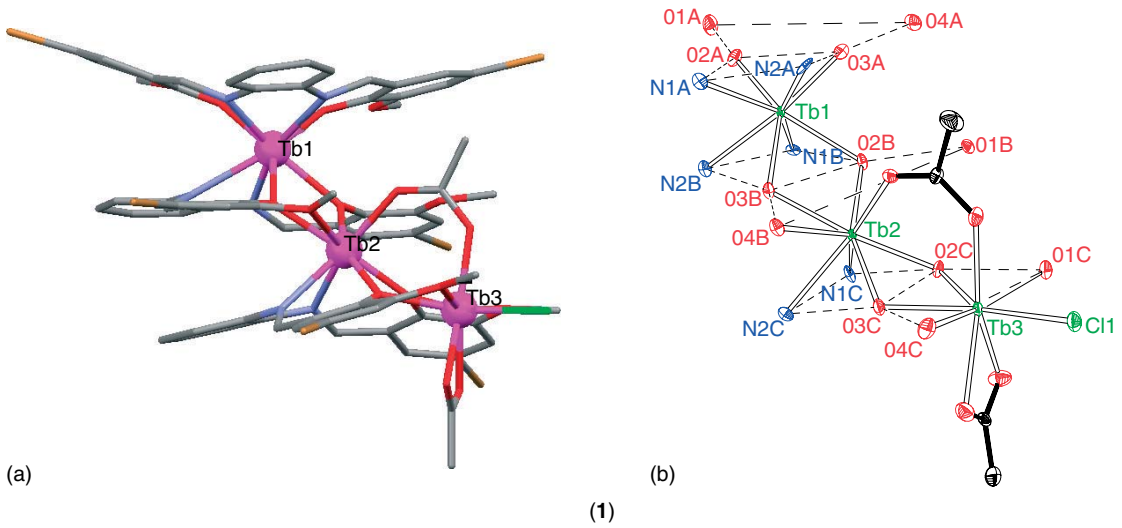


Figure 1 (a) Crystal structure of (**1**) showing ligand configurations. (b) Cut-away view of (**1**) showing locations of donor atoms. (Reprinted with permission from Ref. 9. Copyright (2005), American Chemical Society.)

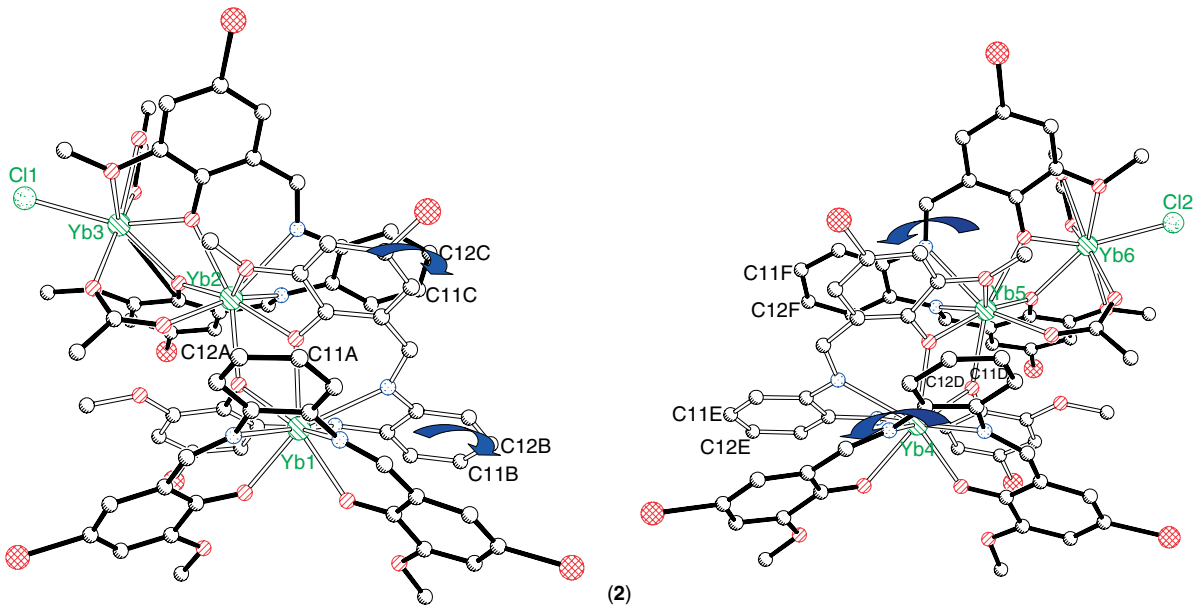


Figure 2 View of the two independent molecules of (**2**) present in the asymmetric unit. (Reprinted with permission from Ref. 10. Copyright (2006), American Chemical Society.)

requirements for (**3**) are satisfied by the presence of a single uncoordinated Cl^- ion.

Interestingly, the reaction conditions and the nature of counteranions used for the synthesis of these kinds of materials are critical. With the addition of Et_3N, the reaction of H_2L^1 with $Ln(NO_3)_3{\cdot}6H_2O$ (Ln = Eu, Nd) and $Eu(CF_3SO_3)_3$ in refluxing MeOH gave the pentanuclear tetradecker lanthanide Schiff-base complexes $[Eu_5(L^1)_4(OH)_2(NO_3)_4(H_2O)_2]{\cdot}NO_3$ (**4**), $[Nd_5(L^1)_4(OH)_2(NO_3)_5MeOH]$ (**5**), and $[Eu_5(L^1)_4(CF_3SO_3)_4\ (MeO)_2(H_2O)_4]{\cdot}CF_3SO_3$ (**6**) (Scheme 2). [11] A view of the cationic moiety of (**4**) is shown in Figure 4. The two outer Eu^{3+} ions, Eu(1) and Eu(5), have similar nine-coordinate environments and each is bound to the O_2O_2 cavities of the outer Schiff-base ligand and surrounded by nine oxygen atoms from one L^1 group, one bidentate NO_3^- anion, one bridged NO_3^- anion, one OH^- anion, and one H_2O molecule. The two inner Eu^{3+} ions, Eu(2) and Eu(4), also have similar nine-coordinate environments comprising the N_2O_2 donor set of one outer L^1 group, the O_2O_2 set of one inner L^1 group, and one bridged NO_3^- anion. The central Eu(3)

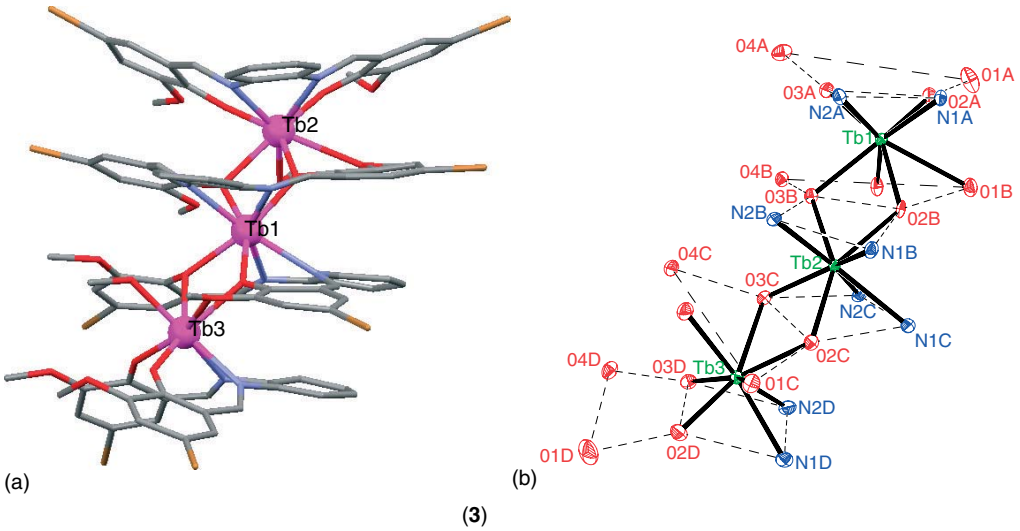
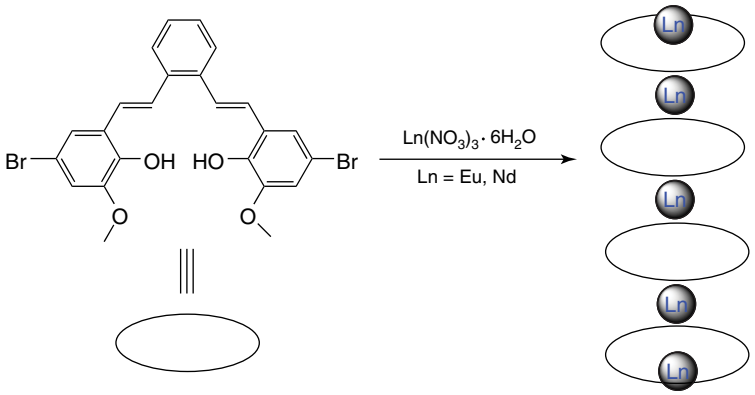


Figure 3 (a) Crystal structure of (**3**) showing general ligand configurations. (b) Cut-away view of (**3**) showing locations of the N and O donor atoms. (Reprinted with permission from Ref. 9. Copyright (2005), American Chemical Society.)



Scheme 2 Formation of pentanuclear tetradecker lanthanide complexes. (Reproduced from Ref. 11. © Royal Society of Chemistry, 2008.)

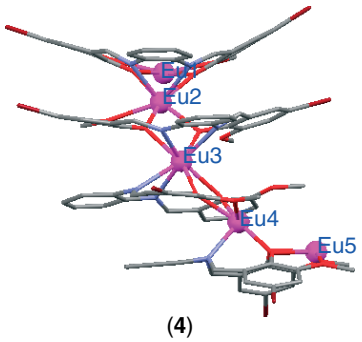


Figure 4 Crystal structure of (**4**) showing general ligand configurations. Coordinated NO_3^- and OH^- anions, H_2O molecules, and H atoms have been omitted for clarity. (Reprinted with permission from Ref. 11. Copyright (2008), American Chemical Society.)

ion has an eight-coordinate pseudo-square-based antiprismatic geometry formed by the two N_2O_2 donor sets of the internal L^1 ligands. The Eu–Eu separations range from 3.700 to 3.925 Å. In (**5**), the three inner Nd^{3+} ions (Nd(2), Nd(3), and Nd(4)) have coordination environments similar to the inner Eu^{3+} ions in (**4**), while the two outer Nd^{3+} ions (Nd(1) and Nd(5)) have slightly different sets of coordinating ligands (Figure 5). For Nd(1), one methanol molecule replaces the coordinated H_2O molecule in (**4**), and for Nd(5), an additional bidentate NO_3^- anion, results in a coordination number of 10. The differences between (**4**) and (**5**) could be due to the larger ionic radius of Nd^{3+} vs Eu^{3+}. The Nd–Nd separations range from 3.660 to 3.940 Å. A view of the structure of (**6**) is shown in Figure 6. The two outer Nd^{3+} ions, Nd(1) and Nd(5), have similar coordinate environments and each is bound to the O_2O_2 cavities of the outer Schiff-base ligand. Nd(1) is nine-coordinate, surrounded by nine O atoms from one L^1 group, two NO_3^- and one

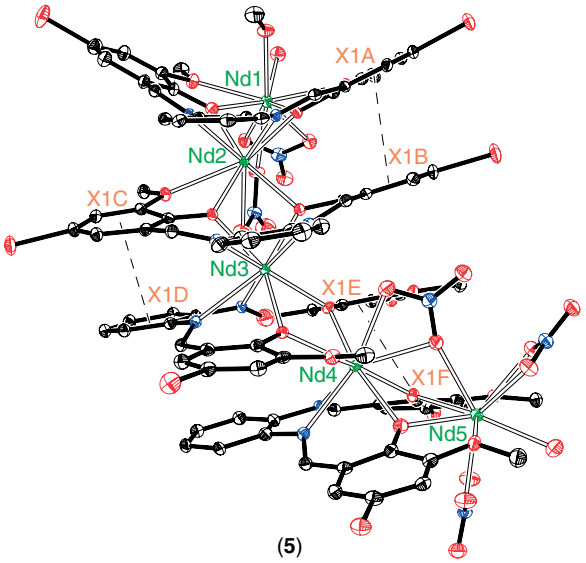


Figure 5 A view of the molecular structure of (**5**). Hydrogen atoms are omitted for clarity. Intramolecular π–π stacking interactions: X1A···X1B: 3.705 Å, X1C···X1D: 3.619 Å, X1E···X1F: 3.731 Å. (Reprinted with permission from Ref. 11. Copyright (2008), American Chemical Society.)

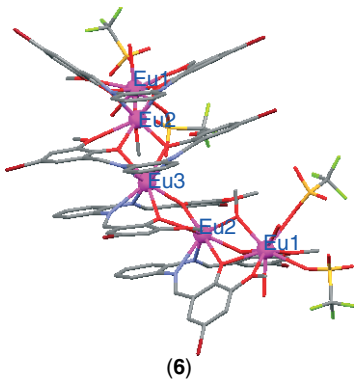


Figure 6 A view of the molecular structure of (**6**). Hydrogen atoms are omitted for clarity. Intramolecular π–π stacking interactions: X1A···X1B: 3.705 Å, X1C···X1D: 3.619 Å, X1E···X1F: 3.731 Å. (Reprinted with permission from Ref. 11. Copyright (2008), American Chemical Society.)

OH^- anions, and one MeOH molecule. For Nd(5), an additional bidentate NO_3^- anion results in a coordination number of 10. The two inner Nd^{3+} ions, Nd(2) and Nd(4), have similar nine-coordinate environments comprising the N_2O_2 donor set of one outer L^1 group, the O_2O_2 set of one inner L^1 group, and one bridged NO_3^- anion. The central Nd(3) ion has an eight-coordinate pseudo-square-based antiprismatic geometry formed by the two N_2O_2 donor sets of the internal L^1 ligands. The Nd–Nd separations range from 3.660 to 3.940 Å.

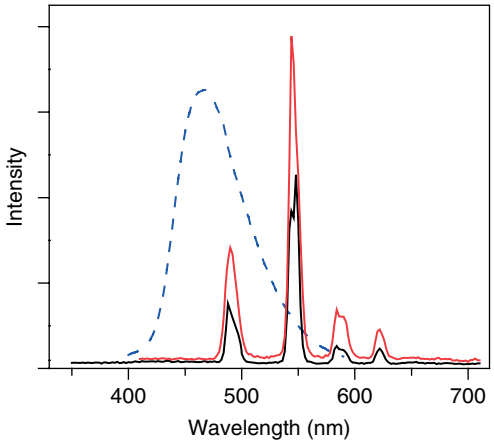


Figure 7 The emission spectra of the free ligand H_2L^1 (——), (**1**) (red line) and (**3**) (black line) in CH_3CN at room temperature. (Reprinted with permission from Ref. 9. Copyright (2005), American Chemical Society.)

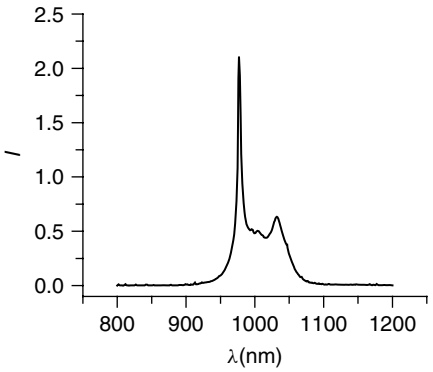


Figure 8 The NIR luminescence of (**2**) in CH_3CN at room temperature. (Reprinted with permission from Ref. 10. Copyright (2006), American Chemical Society.)

In complexes (**1**–**6**), the outer two Schiff-base ligands display a curved bowl-like configuration, while the inner Schiff-base ligands are virtually planar. Intramolecular π–π stacking interactions between phenylene units are found in all these multidecker structures, which may further add to the stability of the complexes (Figures 1–6). The photophysical properties of complexes (**1**–**6**) have been studied in solution. Upon excitation of the ligand-centered absorption band, (**1**) and (**3**) show visible emission bands typical of the Tb^{3+} ion ($^5D_4 \rightarrow {}^7F_n$ transitions; $n = 6$, 5, 4, and 3), (**2**) shows near infra-red (NIR) luminescence of Yb^{3+} ion ($^2F_{5/2} \rightarrow {}^2F_{7/2}$ transition), (**4**) and (**6**) show visible emission bands typical of the Eu^{3+} ion ($^5D_0 \rightarrow {}^7F_j$ transitions; $j = 1$, 2, 3, and 4), and (**5**) shows NIR luminescence of Nd^{3+} ion ($^4F_{3/2} \rightarrow {}^4I_{j/2}$ transitions; $j = 9$, 11, 13). The emission spectra of (**1**–**5**) are shown in Figures 7–10. The fluorescence quantum yields (Φ_{em}) of (**1**), (**3**), (**4**), and (**6**) in CH_3CN are 0.181, 0.153, 0.084,

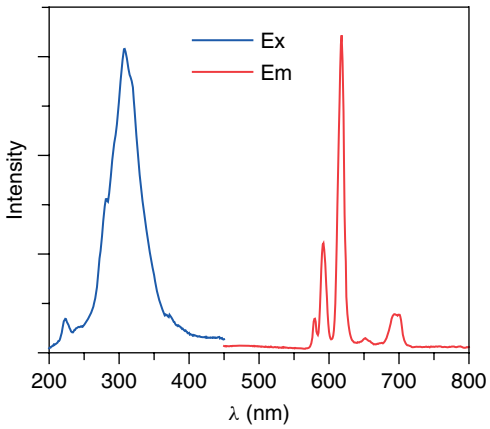


Figure 9 The excitation and emission spectra of (**4**) in CH_3CN at room temperature. (Reprinted with permission from Ref. 11. Copyright (2008), American Chemical Society.)

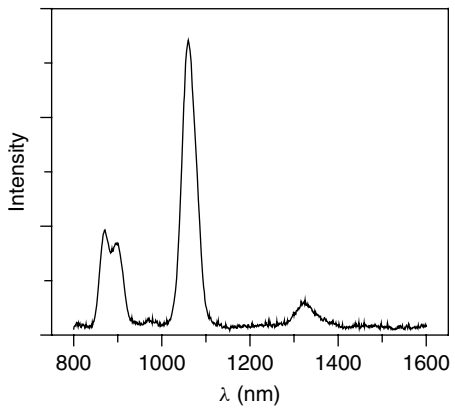


Figure 10 NIR luminescence of (**5**) in CH_3CN at room temperature. (Reprinted with permission from Ref. 11. Copyright 2008, American Chemical Society.)

and 0.077, respectively. For the Tb^{3+} and Eu^{3+} complexes, the absence of typical Tb^{3+} and Eu^{3+} ion excitation bands in their excitation spectra and the ligand-centered (L^1) luminescence in their emission spectra indicates that the ligand-to-metal energy transfer takes place efficiently.[12]

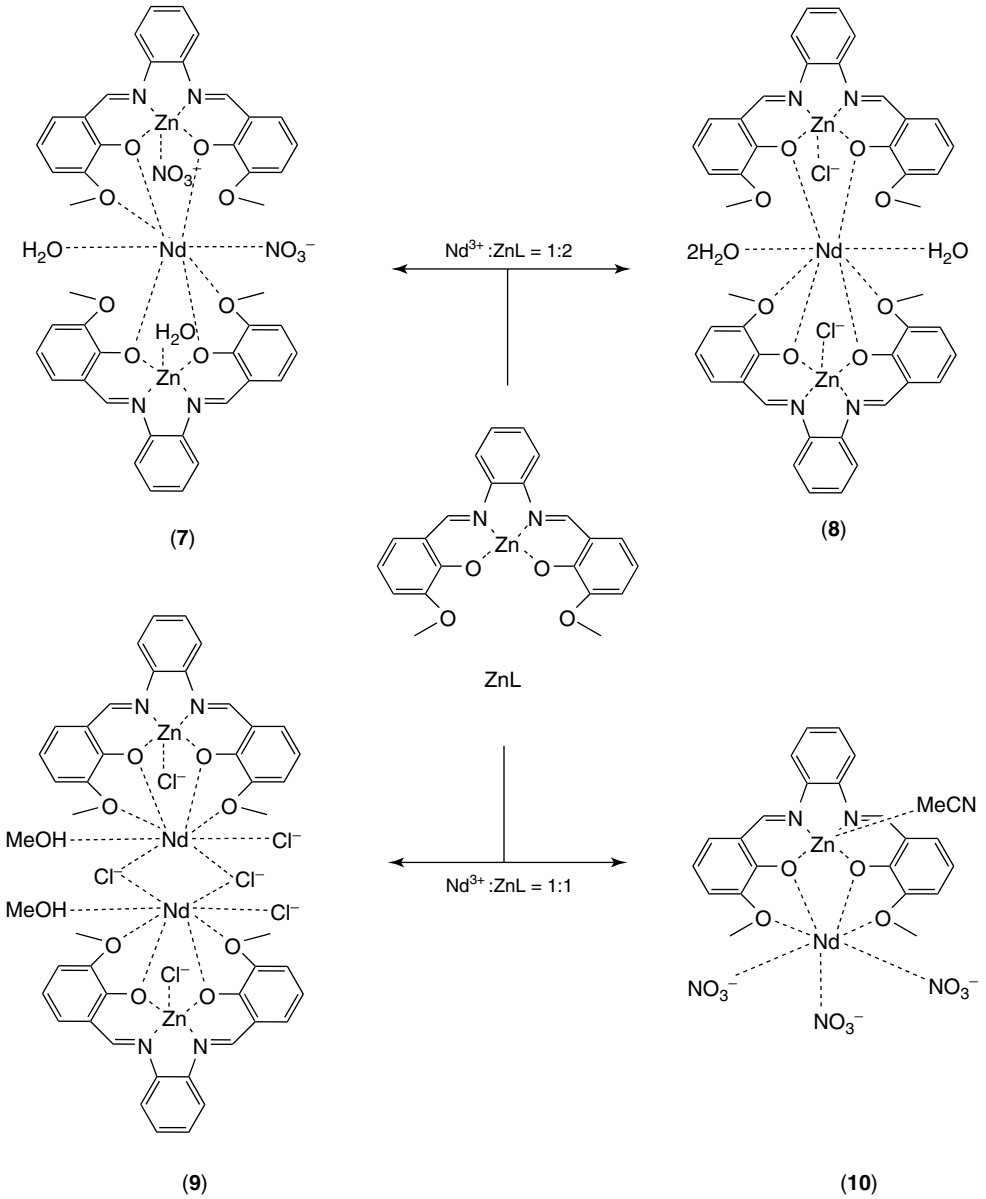
3.2 ''Double-decker'' Zn–Nd Complexes

The use of strongly absorbing d-block chromophores as sensitizers for the NIR emissions from lanthanide ions has attracted increasing attention since the first report by van Veggel and coworkers on the Nd^{3+} and Yb^{3+} luminescence sensitized by $Ru(bpy)_3^{2+}$ and ferrocene in 2000.[13] Subsequently, many d-block chromophores, based on related transition metals, such as Pt^{2+}, Ru^{2+}, Re^{+}, Os^{2+}, Pd^{2+}, Zn^{2+}, Cr^{3+}, and Co^{3+}, have been extensively studied in sensitizing the NIR emissions of lanthanide ions (i.e., Nd^{3+}, Yb^{3+}, and Er^{3+}). Specifically, zinc(II) Schiff-base complexes, which are known to be effective emitters, can act as effective antenna chromophores for lanthanide ion sensitization.

As shown in Scheme 3, four multinuclear Zn–Nd Schiff-base complexes $[Nd(ZnL^2)_2(NO_3)_2(H_2O)_2]\cdot NO_3$ (**7**), $[Nd(ZnL^2)_2Cl_2(H_2O)_3]\cdot Cl$ (**8**), $[Nd_2(ZnL^2)_2Cl_6(MeOH)_2]$ (**9**), and $[NdZnL^2(NO_3)_3MeCN]$ (**10**) have been prepared from the reactions of ZnL^2 ($L^2 = N,N'$-bis(3-methoxy-salicylidene)phenylene-1,2-diamine) with $Nd(NO_3)_3\cdot 6H_2O$ and $NdCl_3\cdot 6H_2O$.[14] Complexes (**7**–**9**) show interesting ''double-decker'' structures, while (**10**) has a more common heterodinuclear structure. The stoichiometry and structures of these complexes are dependent on the ZnL^2:Nd ratio employed in their syntheses as well as the nature of the anion present (Cl^- vs NO_3^-). In trinuclear Zn_2Nd complexes (**7**) and (**8**), the Nd^{3+} ion is sandwiched between the two ZnL^2 units which are virtually parallel to each other (Figures 11 and 12). Although there is a Nd^{3+} ion sandwiched between two ZnL^2 moieties, the planar aromatic groups of each ligand are sufficiently close to each other to form intramolecular π–π stacking interactions in both molecules (the shortest distance between aryl units is 3.498 Å). The structure of the tetranuclear Zn_2Nd_2 complex (**9**) comprises of two $ZnNdL^2$ units linked together by two bridging Cl atoms bound to both Nd^{3+} ions (Figure 13). The Zn^{2+} and Nd^{3+} ions in this complex are located in the inner N_2O_2 and O_2O_2 cavities of each Schiff-base ligand, respectively. The Nd–Nd separation is 4.477 Å which effectively rules out the possibility of any π–π stacking between the aromatic groups of the ligands. For all these complexes, excitation of the ligand-centered absorption bands results in Nd^{3+} NIR emission bands assigned to the $^4F_{3/2} \rightarrow {}^4I_{j/2}$ ($j = 9$, 11, 13) transitions (Figure 14). The luminescence properties of lanthanide complexes are dependent on both coordination structures and outside solvent environment. In these double-decker structures, the Nd^{3+} ion is sandwiched between two ZnL^2 units and protected from outside solvent environment, so their photophysical properties are less affected by outside solvent molecules. As a result, the relative emission intensities of (**7**–**9**) are higher than that of the comparable heterodinuclear complex (**10**) in MeOH.[14]

4 POLYNUCLEAR LANTHANIDE COMPLEXES AND LANTHANIDE COORDINATION POLYMERS WITH FLEXIBLE SCHIFF-BASE LIGANDS

While the majority of polynuclear lanthanide complexes and coordination polymers have been synthesized by the use of rigid ligands, such as multicarboxylic acids and carboxyphenyl porphyrin, relatively few studies involving more flexible ligands have been reported. However, the skeletal adaptability of flexible ligands enables them to form many different molecular systems and extended network

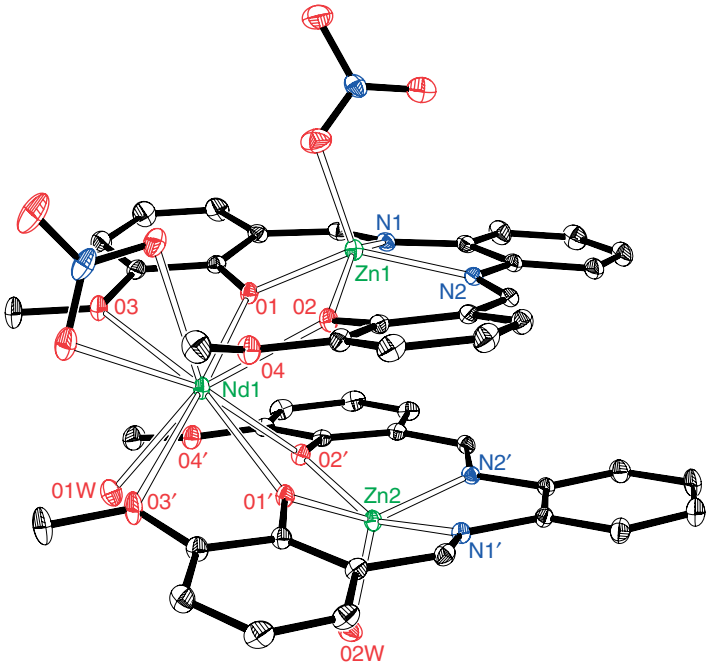


Scheme 3 Syntheses of Zn–Nd complexes (**7**–**10**)

materials. It should be noted that some flexible ligands featuring S, N, or O atom donors have been employed in the construction of d-block transition metal frameworks.[15] Here we introduce the use of some flexible Schiff-base ligands (Scheme 1) to synthesize polynuclear lanthanide complexes and lanthanide coordination polymers.

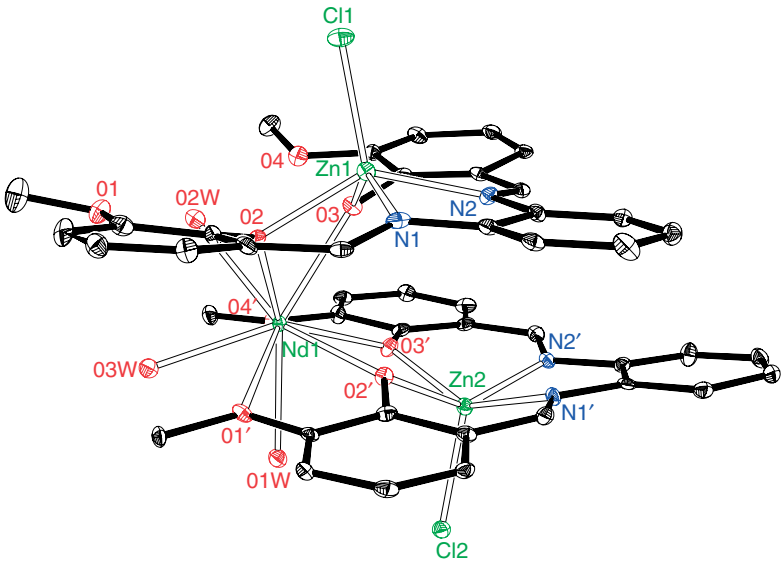
4.1 Polynuclear 4f and 3d–4f Complexes

The neutral homoleptic lanthanide salen complex $[Tb_4(L^3)_6]$ (**11**) has been prepared from the reaction of H_2L^3 (*N*, *N*′-ethylene bis(salicylideneimine)) with $Tb(OAc)_3{\cdot}4H_2O$.[16] A view of the crystal structure of (**11**) is shown in Figure 15, and reveals a tetranuclear centrosymmetric core with two equivalent $Tb_2(L^3)_3$ moieties linked by two μ–O phenoxide atoms. Interestingly, none of the MeOH or H_2O molecules found in the structure are bound to a metal center. The unique outer Tb ion (Tb(1)) is eight-coordinate and bound by the inner N_2O_2 cavities of two salen groups. The inner Tb ion (Tb(2)) is bound by the N_2O_2 core of just one salen group in addition to phenoxide O atoms from three other ligands resulting in a seven-coordinate geometry. The two unique Tb–Tb distances are similar at 3.857 and 3.869 Å for Tb(1)–Tb(2) and Tb(2)–Tb(2A), respectively. It is noted that each salen group is bound to a Tb^{III} center through its N_2O_2 core with only one of its phenoxide O atoms adopting



(**7**)

Figure 11 Crystal structure of trinuclear $[Nd(ZnL^2)_2(NO_3)_2(H_2O)_2]\cdot NO_3$ (**7**). (Reprinted with permission from Ref. 14. Copyright 2006, American Chemical Society.)

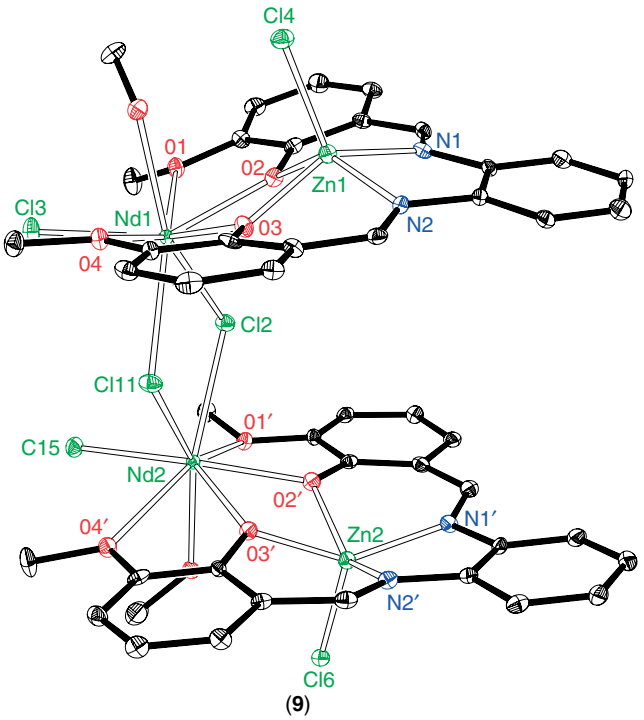


(**8**)

Figure 12 Crystal structure of trinuclear $[Nd(ZnL^2)_2Cl_2(H_2O)_3]\cdot Cl$ (**8**). (Reprinted with permission from Ref. 14. Copyright 2006, American Chemical Society.)

a bridging role. The molecular structure of (**11**) also features $\pi-\pi$ stacking between aryl groups which may add to the overall stability of the compound. The distances between adjacent aryl units range from 3.805 to 3.994 Å.

The use of the acetate derivative $Tb(OAc)_3\cdot 4H_2O$ for the preparation of (**11**) is critical to the formation of the homoleptic complex. Reactions of H_2L^3 with $Tb(NO_3)_3\cdot 6H_2O$ and $LnCl_3\cdot 6H_2O$ (Ln = Tb, Nd, and Yb) under similar



(**9**)

Figure 13 Crystal structure of tetranuclear Zn_2Nd_2 complex $[Nd_2(ZnL^2)_2Cl_6(MeOH)_2]$ (**9**). (Reprinted with permission from Ref. 14. Copyright 2006, American Chemical Society.)

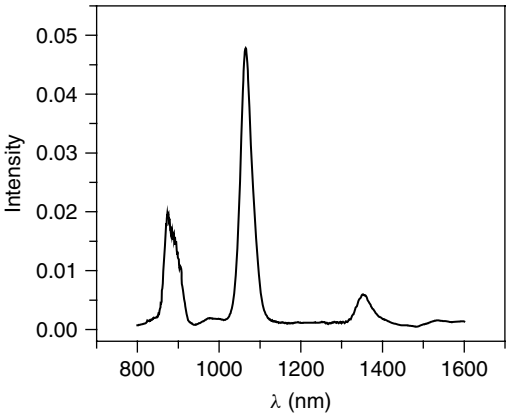
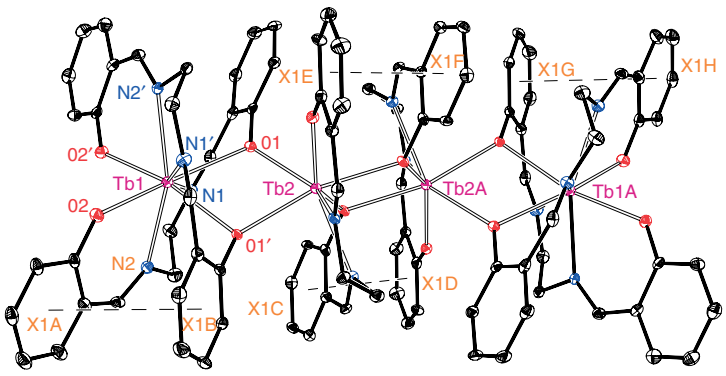


Figure 14 NIR luminescence of (**7**) in CH_3OH at room temperature. (Reprinted with permission from Ref. 14. Copyright 2006, American Chemical Society.)

conditions gave complexes $[TbL^3(NO_3)(MeOH)]_2(\mu\text{-}H_2L^3)$ (**12**) and $[LnL^3(Cl)(MeOH)]_2(\mu\text{-}H_2L^3)$ (Ln = Tb (**13**), Nd (**14**), and Yb (**15**)).[16] Views of the Tb complexes (**12**) and (**13**) are shown in Figures 16 and 17, respectively. Compounds (**13**–**15**) are isomorphous and their structures are similar to that of (**12**). The common feature in both structures is the retention of one Cl^- or NO_3^- per Ln^{3+} ion which is bound to the central N_2O_2 core of a salen ligand. Two Ln^{3+} centers are also bridged by a single neutral molecule of H_2L^3, each bound to one of the two phenolic OH groups. The imine N atoms of these groups do not participate in bonding.

The photophysical properties of these complexes have been studied in solution. The emission and excitation spectra of both H_2L^3 and (**11**) are shown in Figure 18. Excitation of the absorption band at 366 nm in the free ligand H_2L^3 produces a broad emission band at $\lambda_{max} = 455$ nm. Excitation of the ligand-centered absorption bands (at 237, 266, and 246 nm for (**11**–**13**), respectively) in all three complexes results in typical visible emission bands for the Tb^{3+} ion ($^5D_4 \rightarrow {}^7F_n$ transitions; $n = 6$, 5, 4, and 3), while the ligand-centered $^1\pi$–π^* emissions are not detected. The fluorescence quantum yields (Φ_{em}) for (**11**–**13**) are 0.230, 0.127, and 0.096, respectively. In (**11**), the Tb^{3+} ions are completely encapsulated by the Schiff-base ligands and protected from solvent molecules, as a result, it has a noticeably higher quantum yield than (**12**) and (**13**).[16]

Increasing the number of CH_2 units in the backbone of the salen ligand from 2 to 3 results in the formation



(**11**)

Figure 15 A view of the molecular structure of (**11**). Intramolecular π–π stacking interactions: X1A···X1B and X1G···X1H: 3.805 Å, X1C···X1D and X1E···X1F: 3.994 Å. (From Ref. 16. Reproduced by permission of The Royal Society of Chemistry.)

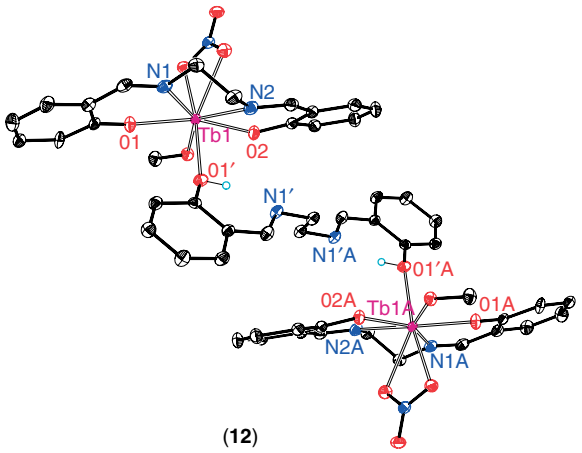


Figure 16 A view of the molecular structure of (**12**). (From Ref. 16. Reproduced by permission of The Royal Society of Chemistry.)

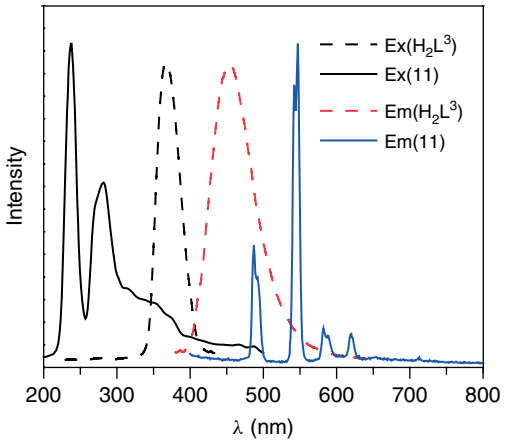


Figure 18 Excitation and emission spectra of free H_2L^3 (—) and (**11**) (—) in CH_3OH. (From Ref. 16. Reproduced by permission of The Royal Society of Chemistry.)

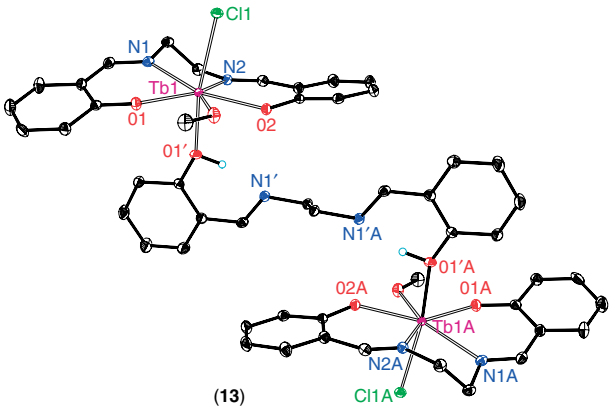


Figure 17 A view of the molecular structure of (**13**). (From Ref. 16. Reproduced by permission of The Royal Society of Chemistry.)

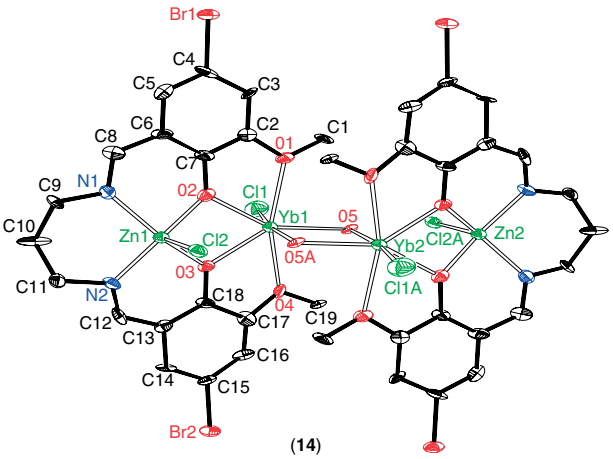


Figure 19 A view of the molecular structure of (**14**). (Reprinted with permission from Ref. 17. Copyright (2005), American Chemical Society.)

of a tetrametallic Zn–Yb complex $[Zn_2Yb_2(L^4)_2(OH)_2Cl_4]$ (**14**). This complex may be synthesized from the reaction of H_2L^4 (*N*,*N*′-bis(5-bromo-3-methoxysalicylidene)propylene-1,3-diamine) with $Zn(NO_3)_2{\cdot}6H_2O$ and $YbCl_3{\cdot}6H_2O$ in the presence of Et_3N.[17] A view of the crystal structure of (**14**) is shown in Figure 19. Each Zn atom is five-coordinate and sits slightly above the N_2O_2 plane of each ligand by 0.555 Å. The Yb–Yb separation is 3.588 Å, and each Yb^{3+} ion is seven-coordinate from the four oxygen atoms of L^4, two bridging hydroxides, and a terminal chloride. The molecule sits on a crystallographically imposed inversion center. The unique Zn–Yb distance is 3.481 Å. The two central bridging hydroxides give the molecule an overall slipped sandwich configuration. The typical emission band of Yb^{3+} assigned to the $^2F_{5/2} \rightarrow {}^2F_{7/2}$ transition is observed at 977 nm upon excitation of the ligand-centered absorption band either at 275 or 350 nm (Figure 20).

4.2 4f and 3d–4f Coordination Polymers

Seven 1D coordination lanthanide polymers $\{[Ln_2(L^3)_2(CF_3SO_3)(H_2L^3)_4(MeOH)]{\cdot}CF_3SO_3\}_n$ (Ln = Eu (**15**), Nd (**16**), and Er (**17**)), $[Yb_2(L^3)_2(OAc)_2(MeOH)_2]_n$ (**18**), $\{[Tb_3(L^5)_2(OAc)_5]{\cdot}Et_2O{\cdot}(MeOH)_{0.5}\}_n$ (**19**), and $[Ln_2(H_2L^6)(OAc)_6]_n$ (Ln = Eu (**20**), Er (**21**)) have been prepared from the reactions of flexible Schiff-base ligands (H_2L^3 and $H_2L^{5,6}$) and lanthanide salts.[18] H_2L^5 and H_2L^6 are *N*, *N*′-bis(3-methoxysalicylidene)ethylene-1,2-diamine and *N*, *N*′-bis(3-methoxysalicylidene)butane-1,4-diamine, respectively. The stoichiometry and structures of these complexes are dependent on the Schiff-base ligand employed in their syntheses as well as the nature of the anion present (i.e., $CF_3SO_3^-$ vs OAc^-). Complexes (**15–17**) are isomorphous. As shown in Figure 21,

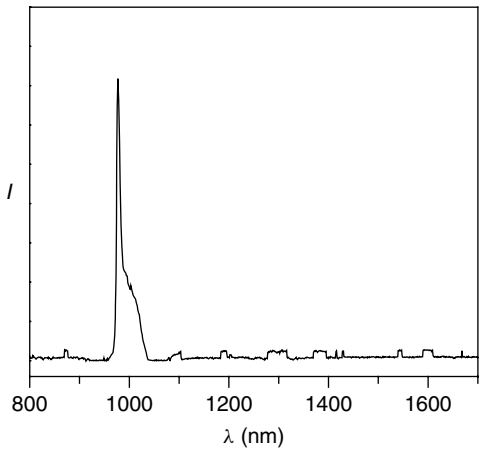


Figure 20 The NIR luminescence of (**14**) in CH_3CN at room temperature. (Reprinted with permission from Ref. 17. Copyright 2005, American Chemical Society.)

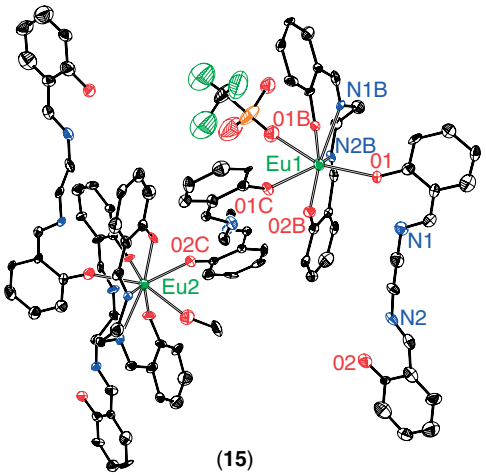


Figure 21 A view of the molecular structure of (**15**). (Reprinted with permission from Ref. 18. Copyright (2009), American Chemical Society.)

in (**15**), each Eu(1) ion is coordinated to a deprotonated salen group $(L^3)^{2-}$ and two neutral salen ligands H_2L^3, while Eu(2) is coordinated to three salen ligands and one $(L^3)^{2-}$. Eu(1) and Eu(2) are bridged by a neutral salen ligand with a separation of 10.171 Å, forming a 1D polymeric structure. In (**18**), each Yb^{III} ion is bound by the N_2O_2 cavity of a deprotonated salen ligand and is eight-coordinate (Figure 22). The acetate (OAc^-) is employed as a linker in the formation of 1D polymeric structure. In (**19**), the central Tb_3 core of this material contains two L^5 groups bound to the two terminal Tb^{3+} ions via the conventional N_2O_2-binding pocket as well as one chelating acetate and are eight-coordinate. The 1D polymeric framework is also completed by OAc^- units which link the Tb_3 clusters (Figure 23). In (**20**), each Eu atom is coordinated to one bidentate OAc^- anion (Figure 24). They

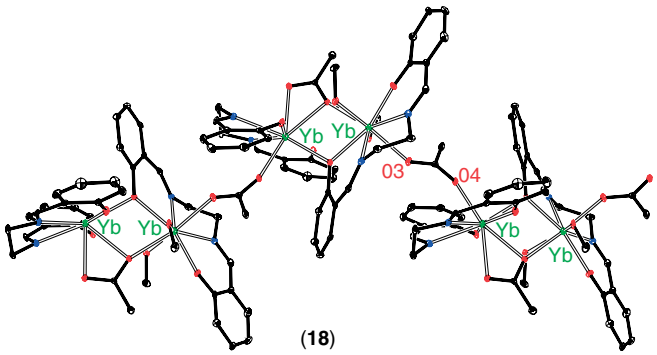


Figure 22 A view of the 1D polymeric chain in (**18**). (Reprinted with permission from Ref. 18. Copyright (2009), American Chemical Society.)

are bridged by other four OAc^- anions with a separation of 3.985 Å. The 1D polymeric framework is completed by neutral Schiff-base ligands (H_2L^6) which link the Eu_2 units via phenolic and methoxy O atoms.

The photophysical properties of Eu^{III} complexes (**15**) and (**20**) and Tb^{III} complex (**19**) have been studied in solution. Upon excitation of the ligand-centered absorption band, (**15**) and (**20**) show visible emission bands typical of the Eu^{3+} ion ($^5D_0 \rightarrow {}^7F_j$ transitions; $j = 1, 2, 3,$ and 4) and (**19**) shows visible emission bands typical of the Tb^{3+} ion ($^5D_4 \rightarrow {}^7F_n$ transitions; $n = 6, 5, 4,$ and 3). The emission spectra of (**15**) and (**19**) are shown in Figures 25 and 26, respectively. The fluorescence of (**15**) is very weak with a quantum yield (Φ_{em}) less than 10^{-3}, while the quantum yield of (**20**) was determined as 0.015. The fluorescence quantum yield (Φ_{em}) for (**19**) is 0.21.

One 1D Ni–Yb coordination polymer $\{YbNiL^6Cl(OAc)_2(H_2O)\}_n$ (**22**) has been prepared from the reaction of H_2L^6 with $NiCl_2{\cdot}6H_2O$ and $YbCl_3{\cdot}6H_2O$.[19] As shown in Figure 27, the Ni^{2+} and Yb^{3+} ions are located in the inner N_2O_2 and O_2O_2 cavities of the Schiff-base ligand, respectively. Within each Yb–Ni–L^6 moiety, the Ni^{2+} and Yb^{3+} ions are bridged by a single bidentate OAc^- group in addition to the phenolic oxygen atoms of the Schiff-base ligand. The Ni–Yb separation is 3.356 Å. The Ni^{2+} ion forms pseudo octahedral geometry with one chlorine anion and one oxygen atom from the bidentate OAc^- anion occupying axial positions. The 1D polymeric framework is formed by OAc^- units which link the Yb–Ni–L^6 moieties.

5 CONSTRUCTION OF HIGH NUCLEARITY LANTHANIDE COMPLEXES USING SMALL LINKERS

As shown in Scheme 4, the nuclearity of 4f and 3d–4f Schiff-base complexes can be manipulated by bridging 4f and 3d–4f building blocks with small

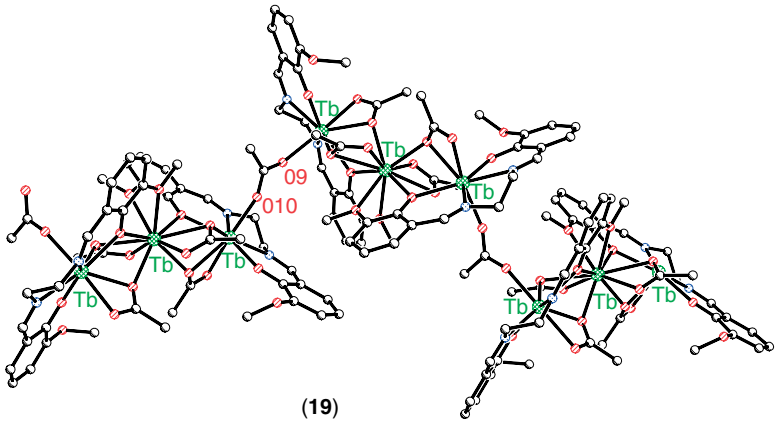


Figure 23 A view of the 1D polymeric chain in (**19**). (Reprinted with permission from Ref. 18. Copyright (2009), American Chemical Society.)

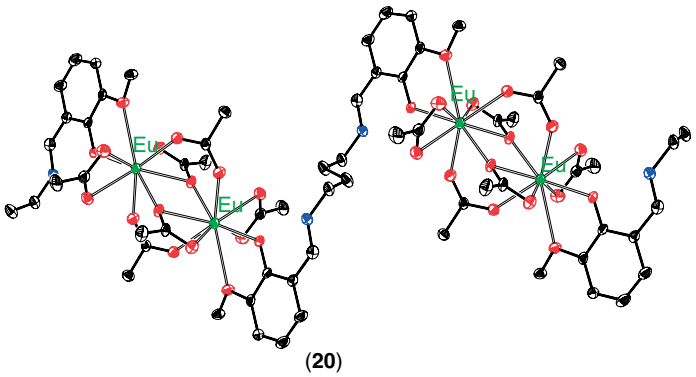


Figure 24 A view of the molecular structure of (**20**). (Reprinted with permission from Ref. 18. Copyright (2009), American Chemical Society.)

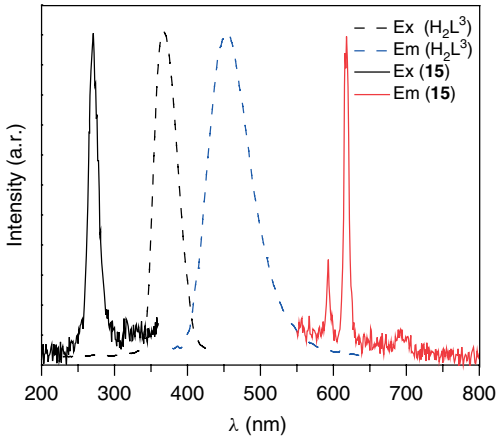


Figure 25 The excitation and emission spectra of free H_2L^3 (---) and (**15**) (—) in CH_3OH. (Reprinted with permission from Ref. 18. Copyright (2009), American Chemical Society.)

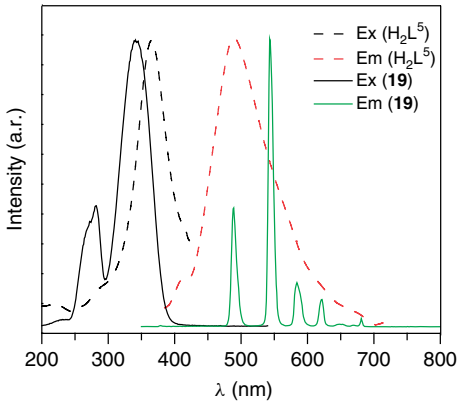


Figure 26 The excitation and emission spectra of free H_2L^5 (---) and (**19**) (—) in CH_3OH. (Reprinted with permission from Ref. 18. Copyright (2009), American Chemical Society.)

rigid linkers such as 1,4-benzene dicarboxylate (1,4-BDC) and 4,4′-bipyridyl. Two higher nuclearity 4f and 3d–4f assemblies $[Eu_8(L^1)_4(1,4\text{-BDC})_2Cl_8(MeOH)_{12}]\cdot 4Cl$ (**23**) and $[Zn_4Nd_2(L^1)_4(1,4\text{-BDC})_2]\cdot[Nd(NO_3)_5(H_2O)]$ (**24**) have been constructed by the use of the linker 1,4-BDC.[20,21] The overall

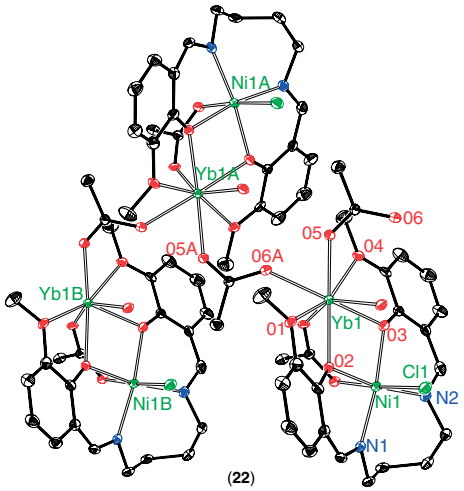
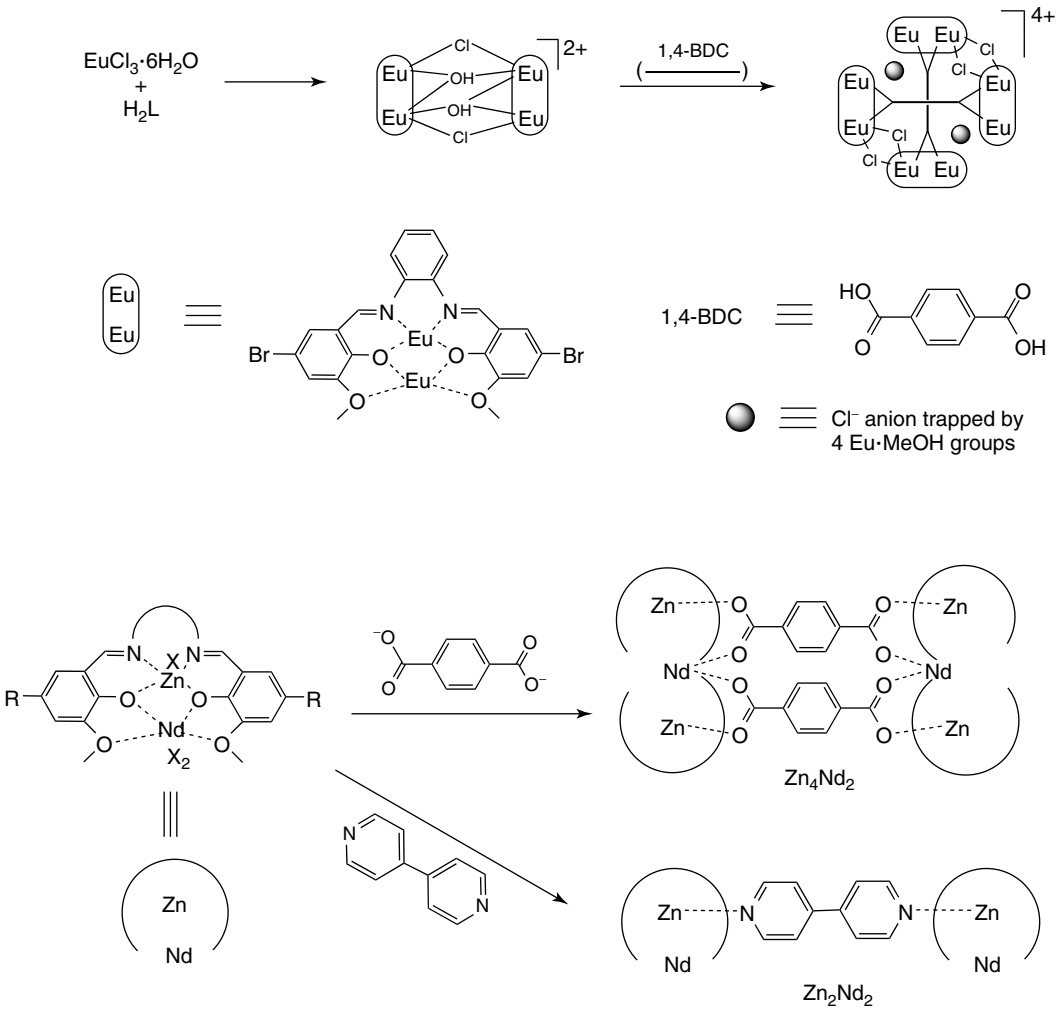
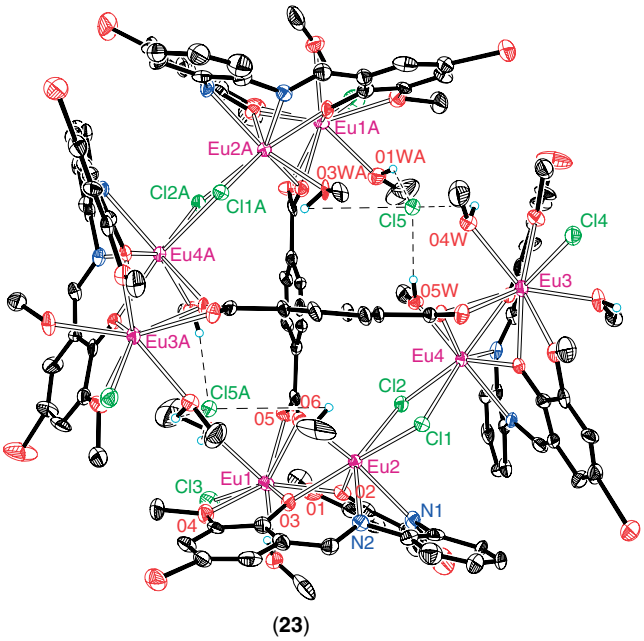


Figure 27 A view of the molecular structure of (**22**). (Reprinted with permission from Ref. 19. Copyright (2011), American Chemical Society.)

structure of the octa-nuclear Eu^{III} complex (**23**) comprises two crystallographically equivalent $Eu_4(L^1)_2$ units related by a center of symmetry and linked by two 1,4-BDC groups (Figure 28). The 1,4-BDC units are virtually perpendicular to each other which results in the cage-like structure. The complex is of nanoscale proportions (17.5 × 17.3 × 10.8 Å). In the solid state, (**23**) has an open, porous 3D metal–organic framework architecture formed by supramolecular interactions between neighboring $Eu_8(L^1)_4$ moieties (Figure 29). The porous structure has extended channels running along both *a*- and *c*-axes. These channels measure approximately 8 × 15 Å and 7 × 18 Å, respectively and accommodate guest molecules of MeOH and H_2O. The reversible host–guest binding of MeOH by (**23**) has been studied using the gas-phase quartz crystal microbalance (QCM) technique. Figure 30 is a plot of the apparent partition coefficient vs normalized partial pressure and shows binding-site saturation, qualitatively consistent with the Langmuir isotherm model. The partition coefficient of (**23**) at saturation is approximately 13.7 which is significantly



Scheme 4 Controlled design of high nuclearity 4f and heterometallic 3d–4f complexes



(**23**)

Figure 28 A view of the molecular structure of (**23**). (Reprinted with permission from Ref. 20. Copyright (2007), American Chemical Society.)

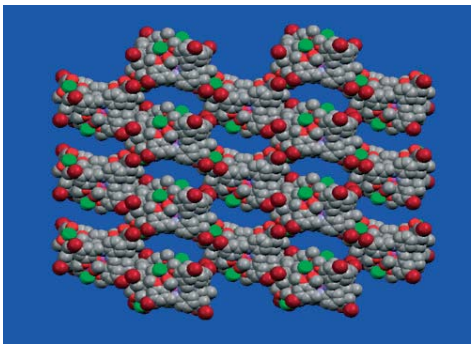


Figure 29 Space filling view of (**23**) along the *a*-axis showing the open mesoporous structure. (Reprinted with permission from Ref. 20. Copyright (2007), American Chemical Society.)

lower than K_{app} values of many other host materials. The photophysical properties of (**23**) have been studied in solution. The emission spectrum of the free ligand H_2L^1 and the excitation and emission spectra of (**23**) are shown in Figure 31. Excitation of the absorption band at 279 nm of the free H_2L^1 produces a broad emission band at $\lambda_{max} = 468$ nm. Upon excitation of ligand-centered absorption bands, (**23**) shows typical visible emission bands of the Eu^{3+} ion ($^5D_0 \rightarrow {}^7F_j$ transitions; $j = 0$, 1, 2, 3, and 4), while the ligand-centered (L^1 or 1,4-BDC) $^1\pi$–π^* emissions are not detected.

In the hexanuclear Zn–Nd complex (**24**), the use of the bridging ligand 1,4-BDC results in the stabilization of two trimetallic $Zn_2Nd(L^1)_2$ fragments (Figure 32). The

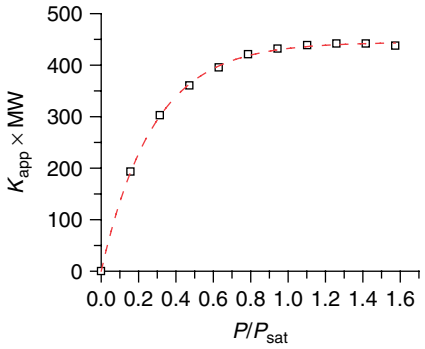


Figure 30 Apparent partition coefficient vs normalized partial pressure of MeOH for (**23**). (Reprinted with permission from Ref. 20. Copyright (2007), American Chemical Society.)

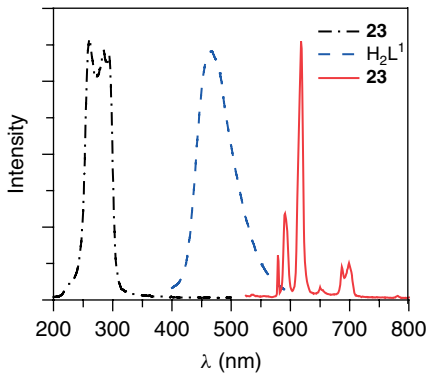


Figure 31 Excitation spectrum of (**23**) (-.-.-.-) and emission spectra of the free ligand H_2L^1 (— –) and (**23**) (—) in CH_3OH. (Reprinted with permission from Ref. 20. Copyright (2007), American Chemical Society.)

Zn^{2+} ions are bound inside the N_2O_2 cavities of each L^1 group, while the Nd ion is bound by the outer O_2O_2 sets of both L^1 groups. Two BDC groups bridge the Zn_2Nd moieties such that each carboxylate group spans a Zn–Nd set. The ^1H NMR spectrum of this complex is consistent with the complex retaining the same bridged structure in solution as in the solid state (Figure 33). This complex shows typical NIR emission bands of Nd^{3+} assigned to the $^4F_{3/2} \rightarrow {}^4I_{j/2}$ ($j = 9$, 11, 13) transition upon excitation of the ligand-centered absorption band (Figure 34). With the central metal ion encapsulated by four chromophoric ligands and shielded from solvent interactions, this complex has superior luminescence properties as compared to the related simple dinuclear Zn–Nd complex $[ZnNdL^1(OAc)(NO_3)_2]$.[21]

A tetranuclear Zn–Nd complex $[Zn_2Nd_2(L^5)_2(4,4'\text{-bpy})(NO_3)_6]$ (**25**) has been synthesized from the reaction of $Nd(NO_3)_3{\cdot}6H_2O$ with the Schiff-base ligand H_2L^5 and 4,4′-bpy.[22] As shown in Figure 35, in (**25**), two independent Zn–Nd dimers are linked by one 4,4′-bipyridyl group. NIR luminescence studies show that the use of 4,4′-bipyridyl

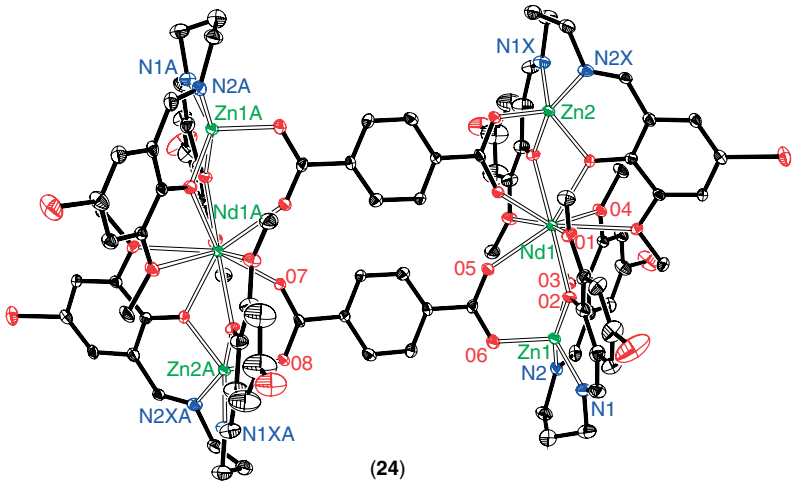


Figure 32 A view of the Zn_4Nd_2 core structure of (**24**). (From Ref. 21. Reproduced by permission of The Royal Society of Chemistry.)

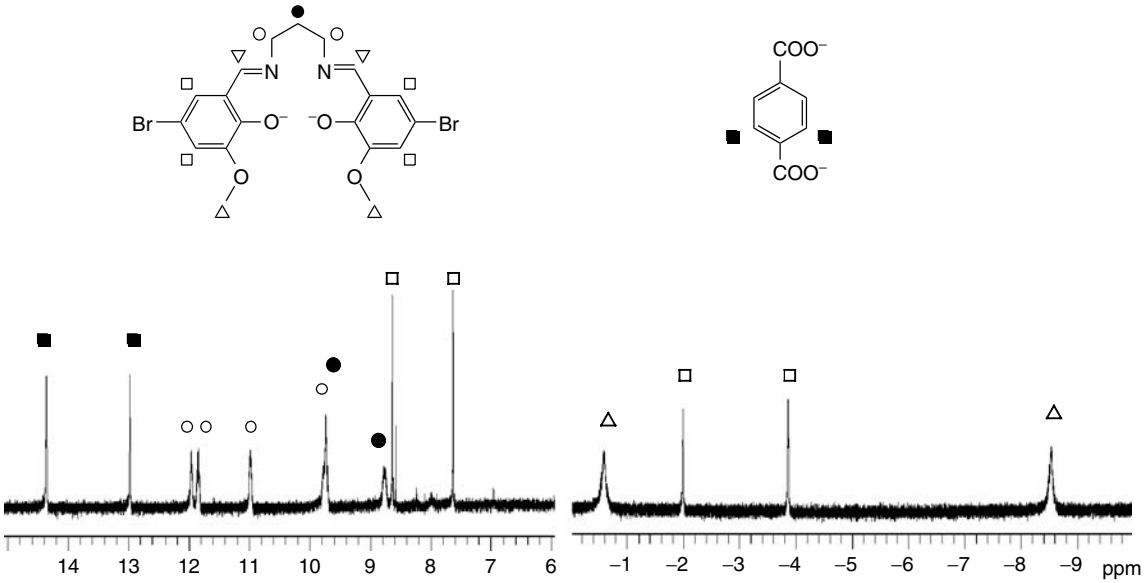


Figure 33 ^{1}H NMR spectrum of the Zn_4Nd_2 complex in CD_3OD. (From Ref. 21. Reproduced by permission of The Royal Society of Chemistry.)

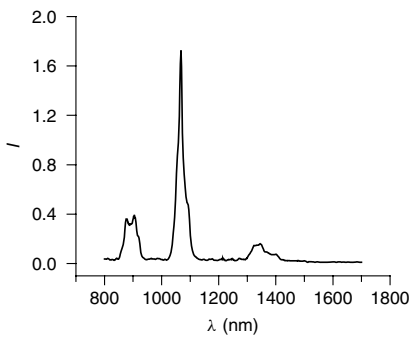


Figure 34 NIR luminescence of the Zn_4Nd_6 complex in CH_3OH. (From Ref. 21. Reproduced by permission of The Royal Society of Chemistry.)

linkers not only facilitates the construction of higher nuclearity Zn–Nd complexes but also improves their luminescence properties.

6 CONCLUSIONS

Two kinds of salen-type Schiff-base ligands, conjugated and flexible, have been used in the synthesis of polynuclear lanthanide complexes and lanthanide coordination polymers ***Lanthanides: Coordination Chemistry***, ***Rare Earth Metal Cluster Complexes***. The stoichiometry and structures of these complexes are dependent on the Schiff-base

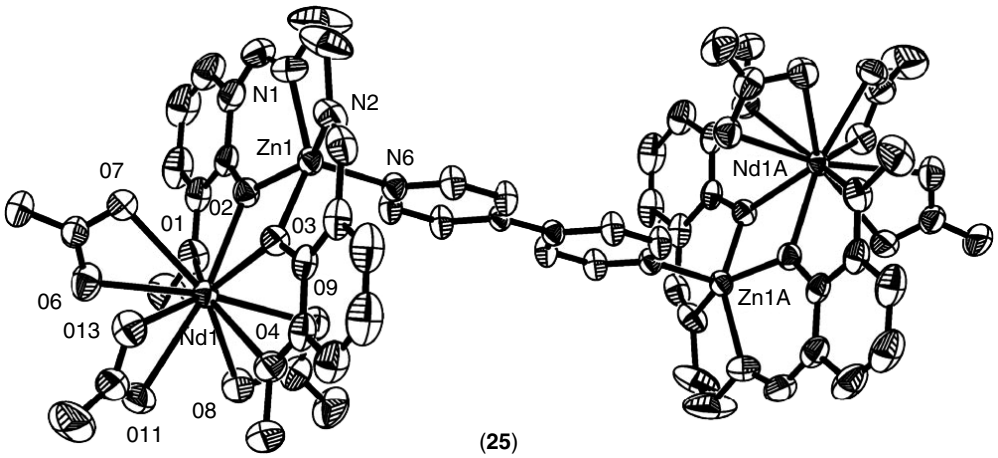


Figure 35 A view of the molecular structure of (**25**). (Reproduced from Ref. 22. © Elsevier, 2009.)

ligand employed in their syntheses as well as the nature of the anion present. Most of these multimetallic lanthanide complexes have interesting multidecker, cage-like, and polymeric structures. Of the complexes described in this chapter, three high nuclearity 4f and 3d–4f assemblies have been described which are formed by the use of two different ligands (one a Schiff-base ligand and the other a bridging ligand 1,4-BDC or 4,4′-bipyridyl).

In these lanthanide complexes, the multidentate Schiff-base ligands can stabilize Ln^{III} centers and act as antenna sensors for lanthanide luminescence. With the Ln^{3+} centers protected by the Schiff-base ligands from solvent and water molecules, those lanthanide complexes with multidecker and cage-like structures show improved luminescence properties.

7 GLOSSARY

Multidentate ligand: A ligand capable of donating two or more pairs of electrons in a complexation reaction to form coordinate bonds.

Conjugated ligand: A ligand which contains alternating single and multiple *bonds*, and has connected *p-orbitals* with *delocalized electrons*.

Flexible ligand: A ligand which can rotate freely.

Schiff-base: It is a compound with a *functional group* that contains a *carbon–nitrogen double bond* with the nitrogen atom connected to an *aryl* or *alkyl* group, not *hydrogen*.

Polynuclear: A metal complex which contains multiple metal atoms.

Coordination polymer: An *inorganic* or *organometallic polymer* structure containing metal cation centers linked by *ligands*, extending in an array. It can also be described as a polymer whose repeat units are *coordination complexes*.

Multi-decker: A structure formed by multiple layers.

Cage-like structure: A structure that looks like a cage.

High nuclearity: A complex containing many metal atoms.

Luminescence: A process by which light is produced by a substance other than by heating.

8 ACKNOWLEDGMENTS

We thank the Welch Foundation (Grant F-816, RAJ) and the Hong Kong Research Grants Council (HKBU 2038/02P and HKBU 202407, WKW) for financial support. Single-crystal X-ray data were collected using instrumentation purchased with funds provided by the National Science Foundation (CHE-0741973), USA.

9 RELATED ARTICLES

Lanthanides: Luminescence Applications; Luminescence; Near-Infrared Materials; Luminescent Bioprobes.

10 ABBREVIATIONS AND ACRONYMS

1,4-BDC = 1,4-benzene dicarboxylate; NIR = near infra-red; QCM = quartz crystal microbalance.

11 REFERENCES

1. J.-M. Lehn, *Supramolecular Chemistry*, VCH, Weinheim, 1995.
2. C. Piguet and J.-C. G. Bünzli, *Chem. Soc. Rev.*, 1999, **28**, 347.
3. N. Sabbatini, M. Guardigli, and J. M. Lehn, *Coord. Chem. Rev.*, 1993, **123**, 201.
4. P. Guerriero, S. Tamburini, and P. A. Vigato, *Coord. Chem. Rev.*, 1995, **139**, 17.
5. M. Sakamoto, K. Manseki, and H. Okawa, *Coord. Chem. Rev.*, 2001, **219**, 379.
6. R. E. P. Winpenny, *Chem. Soc. Rev.*, 1998, **27**, 447.
7. N. Ishikawa, T. Iino, and Y. J. Kaizu, *Am. Chem. Soc.*, 2002, **124**, 11440.
8. N. Ishikawa and Y. Kaizu, *J. Phys. Chem.*, 1996, **100**, 8722.
9. X.-P. Yang and R. A. Jones, *J. Am. Chem. Soc.*, 2005, **127**, 7686.
10. X.-P. Yang, R. A. Jones, M. M. Oye, A. Holmes, and W.-K. Wong, *Cryst. Growth Des.*, 2006, **6**, 2122.
11. X.-P. Yang, R. A. Jones, and W.-K. Wong, *Dalton Trans.*, 2008, 1676.
12. S. Petoud, S. M. Cohen, J.-G. Bünzli, and K. N. Raymond, *J. Am. Chem. Soc.*, 2003, **125**, 13324.
13. S. I. Klink, H. Keizer, and F. C. J. M. van Veggel, *Angew. Chem. Int. Ed.*, 2000, **39**, 4319.
14. W.-K. Wong, X.-P. Yang, R. A. Jones, J. Rivers, V. Lynch, W.-K. Lo, D. Xiao, M. M. Oye, and A. Holmes, *Inorg. Chem.*, 2006, **45**, 4340.
15. A. Y. Robin and K. M. Fromm, *Coord. Chem. Rev.*, 2006, **250**, 2127.
16. X.-P. Yang, R. A. Jones, and W.-K. Wong, *Chem. Commun.*, 2008, 3266.
17. X.-P. Yang, R. A. Jones, V. Lynch, M. M. Oye, and L. H. Archie, *J. Chem. Soc., Dalton Trans.*, 2005, 849.
18. X.-P. Yang, R. A. Jones, J. Rivers, and W.-K. Wong, *Dalton Trans.*, 2009, **47**, 10505.
19. X.-P. Yang, D. Lam, C. Chan, J. M. Stanley, R. A. Jones, B. J. Holliday, and W. K. Wong, *Dalton Trans.*, 2011, **40**, 9795.
20. X.-P. Yang, B. Hahn, R. A. Jones, W.-K. Wong, and K. Stevenson, *Inorg. Chem.*, 2007, **46**, 7050.
21. X.-P. Yang, R. A. Jones, W.-K. Wong, V. Lynch, M. M. Oye, and A. Holmes, *Chem. Commun.*, 2006, 1836.
22. X. Q. Lu, W. Y. Bi, W. L. Chai, J. R. Song, J. X. Meng, W. Y. Wong, W. K. Wong, X. P. Yang, and R. A. Jones, *Polyhedron*, 2009, **28**, 27.

Alkyl

Simon A. Cotton

University of Birmingham, Birmingham, UK

1	Summary	299
2	Introduction	299
3	Methyls	299
4	Benzyls	300
5	Trimethylsilylmethyl and Neopentyl Compounds	300
6	Bis(Trimethylsilylmethyl) Compounds	301
7	Conclusions	301
8	Related Articles	302
9	Abbreviations and Acronyms	302
10	Further Reading	302
11	References	302

1 SUMMARY

Lanthanide alkyls are relatively few in number at present. Only two simple methyls $Ln(CH_3)_3$ have been isolated; they are oligomeric, unlike the alkyls of the main-group elements, due to the desire of lanthanides for coordinative saturation. By using bulkier hydrocarbyl ligands, solvated molecular species $[Ln(CH_2Ph)_3(THF)_x]$ have been isolated for most lanthanides, though $[Ln(CH_2SiMe_3)_3(THF)_x]$ are only stable for the smaller, heavier, elements. Employing very bulky ligands such as $–CH(SiMe_3)_2$ and $–C(SiHMe_2)_3$ means that unsolvated three-coordinate compounds $[Ln\{CH(SiMe_3)_2\}_3]$ and $[Y(C(SiHMe_2)_3)_3]$ are isolable. Different synthetic routes have been devised for each family of compounds, which are generally very air and moisture sensitive, though mostly soluble in organic solvents, and of limited thermal stability.

2 INTRODUCTION

Frankland discovered the first main-group alkyl, diethylzinc, in 1849 and other compounds such as dimethylmercury and tetraethyllead soon followed. These are very volatile and reactive liquids, though thermally stable at room temperature. At a time when little was known about lanthanide chemistry, it was natural to assume that lanthanide alkyls might be similar. A brave attempt was made in 1902 to synthesize $CeMe_3$ by heating cerium with $HgMe_2$, but the pyrophoric product was not characterized. A later report of the reaction between $LnCl_3$ and EtMgBr producing $LnEt_3$ (Ln = Sc, Y) as etherates distilling unchanged at 200 °C has never been substantiated. The successful isolation of the first lanthanide alkyls in 1973 had to await other developments, as in many cases, alkyls cannot be obtained by direct synthesis from a lanthanide halide and a metal alkyl (e.g., RLi).

3 METHYLS

The lanthanides do not form simple molecular methyls, unlike many main-group elements, and the successful synthesis of the oligomeric methyls that have been described was a drawn-out and indirect affair.

In 1978, the first methyl compounds of the lanthanides were definitely characterized as anionic species, in which the lanthanide is octahedrally coordinated.[1]

$$LnCl_3 + 6\ LiMe \longrightarrow [Li(L–L)_3][LnMe_6] + 3LiCl$$

(L–L = tmed; Ln = Y, La, Pr, Nd, Sm, Gd–Lu;

L–L = dme, Ln = Ho–Lu)

The Rare Earth Elements. Edited by David A. Atwood. © 2012 John Wiley & Sons, Ltd. ISBN 978-1-119-95097-4

Subsequently, reaction of the LiCl adducts of the dimethylamides, $Ln(NMe_2)_3.3LiCl$, with excess trimethylaluminum was discovered to give lanthanide tetramethylaluminates, $Ln(AlMe_4)_3$, also accessible by other routes.[2] These compounds have the structure $[Ln((\mu\text{-}Me)_2AlMe_2)_3]$ (Ln = Y, La–Nd, Sm, Gd, Ho, Tm–Lu).[3]

On treating $Ln(AlMe_4)_3$ (Ln = Y, Lu) with Et_2O, cleavage of the bridges occurs, forming the binary alkyls $LnMe_3$ (Ln = Lu, Y), which are hydrocarbon insoluble and thought to be polymeric.[4] PMe_3 performs a similar cleavage reaction, but affording a less pure $LnMe_3$ product. Attempts to extend this reaction to other $Ln(AlMe_4)_3$ (Ln = La, Ce, Pr, Nd, Sm, Gd, Ho) were unsuccessful; a detailed study of attempts to make $LaMe_3$ from $La(AlMe_4)_3$ showed that instead of $LaMe_3$ being formed, extensive methyl group degradation occurred, resulting instead in the formation of heterobimetallic clusters featuring methylene, methine, or carbide groupings such as $[La_4Al_8(CH)_4(CH_2)_2(CH_3)_{20}(PMe_3)]$.[5]

4 BENZYLS

Stable monomeric benzyls can be made in solvated form, simply by the reaction of lanthanide halides (either in anhydrous form or the THF solvates) with an alkali metal benzyl. Best results are obtained with the iodide.[6–8]

$$[ScCl_3(thf)_3] + 3\ PhCH_2K \longrightarrow [Sc(CH_2Ph)_3(thf)_3] + 3\ KCl$$

$$[CeI_3(thf)_4] + 3\ PhCH_2K \longrightarrow [Ce(CH_2Ph)_3(thf)_3] + 3\ KI + thf$$

Compounds *fac*-$[Ln(CH_2Ph)_3(THF)_3]$ (Ln = Sc, Y, La–Sm, Gd, Dy, Er, and Lu) have all been synthesized; they are soluble in THF but insoluble in alkanes. The coordination polyhedron is not a perfect octahedron; the O–Ln–O angles are around 80°, similar to those in the triphenyls.

While the compounds of the smaller metals (Sc, Y, Gd, Dy, Er, Lu) all feature three σ-(h^1)-benzyls, $[Ln(CH_2Ph)_3(THF)_3]$ (Ln = La–Nd) all feature three h^2-benzyls, while in $[Sm(CH_2Ph)_3(THF)_3]$, there are one h^2-benzyl and two h^1-benzyl groups.[8] This desire for additional coordination thus relates strictly to the size of the lanthanide concerned, reflecting the characteristic wish of the lanthanides for coordinative saturation.

When the scandium and lutetium compounds are triturated with toluene, one THF molecule is lost, resulting in $[Ln(CH_2Ph)_3(THF)_2]$ (Ln = Sc, Lu) of which the scandium compound has a trigonal bipyramidal structure. There is no evidence for $[Yb(Bz)_3(THF)_3]$; when $C_6H_5CH_2K$ reacts with $[YbI_3(THF)_3]$, the mixed-valence compound $[Yb^{II}(CH_2Ph)(THF)_5]^+$ $[Yb^{III}(CH_2Ph)_4(THF)_2]$- results.[8] As a family of σ-alkyls obtainable for most lanthanides, the benzyls have promise as synthetic precursors, notably for phosphorus-stabilized carbenes.[8]

5 TRIMETHYLSILYLMETHYL AND NEOPENTYL COMPOUNDS

The first well-characterized σ-alkyls reported[9] (1973) were the (trimethylsilyl)methyl compounds of scandium and yttrium, $[Sc(CH_2SiMe_3)_3(THF)_2]$ and $[Y(CH_2SiMe_3)_3(THF)_2]$, as well as the analogous neopentyls $[Ln(CH_2CMe_3)_3(THF)_2]$ (Ln = Sc, Y). At that time, bulky ligands that were proof against β-elimination were thought most likely to afford simple binary alkyls of the transition metals. Lanthanide analogs $[Ln(CH_2SiMe_3)_3(THF)_2]$ (Ln = Tb, Er, Yb) were reported shortly afterward, all were prepared by reaction of the salt-elimination reaction between $LnCl_3$ (or $LnCl_3(THF)_x$) and $LiCH_2SiMe_3$.[10]

Attempts to extend the range of compounds to the early lanthanides showed[11] that the alkyls $[Ln(CH_2SiMe_3)_3(THF)_n]$ ($n \sim 3$) are very unstable for lanthanides larger than samarium. The isolation of $[Sm(CH_2SiMe_3)_3(THF)_3]$ required low-temperature work-up and crystallization, but this approach was unsuccessful with larger lanthanides. Both five- and six-coordinate compounds are known, with structures confirmed for *fac*-$[Sm(CH_2SiMe_3)_3(THF)_3]$ and *fac*-$[Y(CH_2SiMe_3)_3(THF)_3]$. Smaller lanthanides form $[Ln(CH_2SiMe_3)_3(THF)_2]$ (Ln = Tb, Er–Lu) with the Er, Yb, Lu compounds known to have five-coordinate trigonal bipyramidal structures, having two THF molecules in axial positions. The yttrium compound normally obtained by crystallization from solvents such as pentane is five-coordinate $[Y(CH_2SiMe_3)_3(THF)_2]$, but crystallization from THF yields six-coordinate $[Y(CH_2SiMe_3)_3(THF)_2]$. This has one Y–O distance some 0.04 Å greater than the others, possibly corresponding to the more labile THF molecule.[12] Attempts to stabilize $Ln(CH_2SiMe_3)_3$ by forming adducts with Lewis bases have met with varying success. With terpy (2,2′;6′, 2″-terpyridine), instability manifests itself in facile 1,3-alkyl migration, causing dearomatization and functionalization of the terpyridine ligand. On the other hand, 4,4′-di-*tert*-butyl-2,2′-bipyridyl ($^tBu_2bpy$) forms the stable $[Lu(CH_2SiMe_3)_3(^tBu_2bpy)]$.[13] By using a crown ether ligand, thermally stable seven-coordinate adducts $[Ln(CH_2SiMe_3)_3(12\text{-crown-}4)]$ (Ln = Sc, Y, Sm, Gd, Tb, Dy, Ho, Er, Tm, Yb, Lu) are formed over much of the series, though the initial $Ln(CH_2SiMe_3)_3$ compounds of the earlier lanthanides (La–Nd) are too unstable for their adducts to be isolated.[14] Other supporting groups have been employed.[15,16]

The alkyls $[Ln(CH_2SiMe_3)_3(THF)_n]$ ($n = 2, 3$) are widely used in syntheses, having a high reactivity toward organic molecules;[17] cationic species are readily formed and have been widely examined for their roles, e.g., in ethene polymerization.[18] Thus, $[Y(CH_2SiMe_3)_3(THF)_2]$ reacts with $Al(CH_2SiMe_3)_3$ forming $[Y(CH_2SiMe_3)_2(THF)_4]^+$ $[Al(CH_2SiMe_3)_4]^-$; $[Lu(CH_2SiMe_3)_3(THF)_2]$ reacts with $B(C_6XF_5)_3$ forming $[Lu(CH_2SiMe_3)_2(THF)_n]^+$ $[B(CH_2SiMe_3)(C_6F_5)_3]^-$ and with BPh_3 forming $[Lu(CH_2SiMe_3)_2$

$(THF)_3]^+$ $[B(CH_2SiMe_3)Ph_3]^-$. Adding aluminum alkyls such as $Al(CH_2SiMe_3)_3$ to $[Y(CH_2SiMe_3)_3(THF)_2]$/$[NMe_2HPh]$ $[B(C_6F_5)_4]$ mixtures generates very effective catalysts with high ethylene polymerization activity, believed to involve dicationic mono(alkyl) complexes of the type $[Ln(CH_2SiMe_3)(solvent)_z]^{2+}$. A few anionic species such as $[Li(tmed)_2]$ $[Ln(CH_2SiMe_3)_4]$ (Ln = Y, Er, Yb, Lu) appear to feature four-coordinate lanthanides[10,19,20] as do the similar *t*-butylates $[Li(solvent)_n]^+$ $[LnBu^t_4]^-$, (Ln = Y, Sm, Tb, Er, Yb, Lu), with the tetrahedral geometry confirmed in $[Li(tmed)_2]^+$ $[LnBu^t_4]^-$ and $[Li(dme)_3]^+$ $[ErBu^t_4]^-$.[21,22]

In contrast with the trimethylsilylmethyls, since the report of $[Ln(CH_2CMe_3)_3(THF)_2]$ (Ln = Sc, Y),[9] little study has been made of the neopentyls or of compounds with related ligands, though trigonal bipyramidal $[Yb(CH_2CMe_3)_3(THF)_2]$ has been made by reaction of ytterbium chips with ICH_2CMe_3 by a disproportionation reaction in THF.[23]

This reaction is noteworthy, in view of the fact that tribenzylytterbium has defied isolation, though $[Yb(CH_2SiMe_3)_3(THF)_2]$ also exists (vide supra), and demonstrates the small factors that may affect the stability of these compounds.

$$4Yb + 6\ {}^tBuCH_2I \rightarrow 3\ YbI_2 + Yb(CH_2{}^tBu)_3(thf)_2$$

Employing a sterically more demanding group means that the alkyls $[Ln(CH_2\text{-}SiMe_2Ph)_3(THF)_2]$ (Ln = Sc, Y) have greater stability, but as yet, there are no reports of alkyls of early lanthanides using this alkyl group.[24]

6 BIS(TRIMETHYLSILYLMETHYL) COMPOUNDS

Using the even bulkier $(Me_3Si)_2CH$ group leads to unsolvated alkyls. $[Ln\{CH(SiMe_3)_2\}_3]$ (Ln = La, Sm) were reported in 1988.[25] Because $LnCl_3$ react with $LiCH(SiMe_3)_2$ forming chloride-containing ''ate'' complexes including $[Li(THF)_4][LnClR_3]$ (Ln = Er or Yb),[10] an aryloxide was used as a chloride-free precursor

$$[Ln(OC_6H_3Bu^t_2\text{-}2,6)_3] + 3\ LiCH(SiMe_3)_2 \rightarrow$$
$$[Ln\{CH(SiMe_3)_2\}_3] + 3\ HOC_6H_3But^t_2\text{-}2,6$$

Subsequently, other $[Ln\{CH(SiMe_3)_2\}_3]$ (Ln = Y, Ce, Lu) have been synthesized by the same route, and there appears no reason why the others can be made, except possibly the Eu and Yb compounds.[26–28] These pentane-soluble compounds have trigonal pyramidal coordination geometries. One short $Ln\cdots CH_3$ contact is observed in the crystal structure of each molecule, ascribed to an agostic $Si\cdots C_\beta$ interaction (rather than $\gamma C\cdots H\cdots Ln$ interaction). Reactions of some of these compounds with protic molecules have been used synthetically. Although these alkyls do not coordinate THF, the use of slender nitrile ligands has permitted isolation of the adducts $[Y\{CH(SiMe_3)_2\}_3(NCBu^t)_2]$ and $[Ce\{CH(SiMe_3)_2\}_3(NCPh)]$; there is no evidence for nitrile insertion into the metal–carbon bond. Reactions of some of these compounds with protic molecules have been used synthetically.[25–27]

In addition to these compounds, the three-coordinate alkyl $[Y(C(SiHMe_2)_3)_3]$ has additionally 6 β-agostic $Y\cdots(H-Si)$ interactions, to judge from its nuclear magnetic resonance (NMR) spectrum.[29]

While lanthanide alkyls are generally involatile, this compound gives a detectable mass spectrum, as does $[Y\{CH(SiMe_3)_2\}_3]$. These hydrocarbyls are more stable than the Me_3SiCH_2-based alkyls; it is likely that, besides preventing attachment of molecules such as THF, the bulky alkyl groups also block decomposition pathways.

7 CONCLUSIONS

As yet, relatively few lanthanide alkyls have been isolated. Although LnR_3 (R = alkyl) systems would superficially be expected to be similar to main-group compounds such as aluminum alkyls, this is not observed in practice. The comparatively large size of the lanthanides is one factor in their not forming simple molecular alkyls, as their desire for coordinative saturation means that unsolvated species do not exist and that in fact decomposition pathways are facilitated.

The successful isolation of the first lanthanide alkyls reported in 1973 had to await recognition that bulky alkyl groups such as CH_2Ph, CH_2SiMe_3, and $CH(SiMe_3)_2$, which also blocked β-elimination pathways, were necessary. Even so, it has not always been possible to isolate compounds of these groups across the lanthanide series. A further key step has involved the recognition that in many cases, alkyls cannot be obtained by direct synthesis from a lanthanide halide and a metal alkyl (e.g., RLi), in some cases, because of chloride retention in the reaction product, so that alternative synthetic pathways have been devised, often unique to each family of alkyls.

Lanthanide alkyls are in general air- and moisture-sensitive compounds—sometimes pyrophoric to even traces of oxygen—that are not robust enough to be sublimed in vacuo (unlike the cyclopentadienyls and the silylamides). They are usually soluble in organic solvents such as THF, while those with greatest shielding of the metal, such as $[Ln\{CH(SiMe_3)_2\}_3]$, are hydrocarbon soluble.

Despite the narrowness of the field, several of the compounds have found real synthetic utility on account of their reactivity, notably but not exclusively with protic molecules.

8 RELATED ARTICLES

Aryls.

9 ABBREVIATIONS AND ACRONYMS

NMR = nuclear magnetic resonance.

10 FURTHER READING

M. Zimmermann and R. Anwander, *Chem. Rev.*, 2010, **110**, 6194.

11 REFERENCES

1. H. Schumann, J. Mueller, N. Bruncks, H. Lauke, J. Pickardt, H. Schwarz, and K. Eckart, *Organometallics*, 1984, **3**, 69.
2. W. J. Evans, R. Anwander, and J. W. Ziller, *Organometallics*, 1995, **14**, 1107.
3. G. Occhipinti, C. Meermann, H. M. Dietrich, R. Litlabø, F. Auras, K. W. Törnroos, C. Maichle-Mössmer, V. R. Jensen, and R. Anwander, *J. Am. Chem. Soc.*, 2011, **133**, 6323.
4. H. M. Dietrich, G. Raudaschl-Sieber, and R. Anwander, *Angew. Chem. Int. Ed.*, 2005, **44**, 5303.
5. L. C. H. Gerber, E. Le Roux, K. W. Törnroos, and R. Anwander, *Chem. Eur. J.*, 2008, **14**, 9555.
6. S. Bambirra, A. Meetsma, and B. Hessen, *Organometallics*, 2006, **25**, 3454.
7. N. Meyer, P. W. Roesky, S. Bambirra, A. Meetsma, B. Hessen, K. Saliu, and J. Takats, *Organometallics*, 2008, **27**, 1501.
8. A. J. Wooles, D. P. Mills, W. Lewis, A. J. Blake, and S. T. Liddle, *Dalton Trans.*, 2010, **39**, 500.
9. M. F. Lappert and R. Pearce, *J. Chem. Soc., Chem. Commun.*, 1973, 126.
10. J. L. Atwood, W. E. Hunter, R. D. Rogers, J. Holton, J. McMeeking, R. Pearce, and M. F. Lappert, *J. Chem. Soc., Chem. Commun.*, 1978, 140.
11. H. Schumann, D. M. M. Freckmann, and S. Dechert, *Z. Anorg. Allg. Chem.*, 2002, **628**, 2422.
12. W. J. Evans, J. C. Brady, and J. W. Ziller, *J. Am Chem. Soc.*, 2001, **123**, 7711.
13. J. D. Masuda,K. C. Jantunen, B. L. Scott, and J. L. Kiplinger, *Organometallics*, 2008, **27**, 1299.
14. S. Arndt, P. M. Zeimentz, T. P. Spaniol, J. Okuda, M. Honda, and K. Tatsumi, *Dalton Trans.*, 2003, 3622.
15. C. S. Tredget, E. Clot, and P. Mountford, *Organometallics*, 2008, **27**, 3458.
16. B. D. Ward, L. Lukešová, H. Wadepohl, S. Bellemin-Laponnaz, and L. H. Gade, *Eur. J. Inorg. Chem.*, 2009, 866.
17. Y. Nakajima and J. Okuda, *Organometallics*, 2007, **26**, 1270.
18. S. Arndt, T. P. Spaniol, and J. Okuda, *Angew. Chem. Int. Ed.*, 2003, **42**, 5075.
19. H. Schumann and J. Müller, *J. Organomet. Chem.*, 1979, **169**, C1.
20. W. J. Evans, J. L. Shreeve, R. N. R. Broomhall-Dillard, and J. W. Ziller, *J. Organomet. Chem.*, 1995, **501**, 7.
21. H. Schumann, W. Genthe, E. Hahn, J. Pickardt, H. Schwarz, and K. Eckart, *J. Organomet. Chem.*, 1986, **306**, 215.
22. W. Noh and G. S. Girolami, *Polyhedron*, 2007, **26**, 3865.
23. M. Niemeyer, *Z. Anorg. Allg. Chem*, 2000, **626**, 1027.
24. D. J. H. Emslie, W. E. Piers, M. Parvez, and R. McDonald, *Organometallics*, 2002, **21**, 4226.
25. P. B. Hitchcock, M. F. Lappert, R. G. Smith, R. A. Bartlett, and P. P. Power, *J. Chem. Soc., Chem. Commun.*, 1988, 1007.
26. C. J. Schaverien and A. G. Orpen, *Inorg. Chem.*, 1991, **30**, 4968.
27. M. Westerhausen, M. Hartmann, and W. Schwarz, *Inorg. Chim. Acta*, 1998, **269**, 91.
28. A. G. Avent, C. F. Caro, P. B. Hitchcock, M. F. Lappert, Z. Li, and X.-H. Wei, *Dalton Trans.*, 2004, 1567.
29. K.-K. Yan, A. V. Pawlikowski, C. Ebert, and A. D. Sadow, *Chem. Commun.*, 2009, 656.

Aryls

Simon A. Cotton

University of Birmingham, Birmingham, UK

1 Summary 303
2 Introduction 303
3 Triaryls 303
4 Monoaryls 304
5 Conclusions 304
6 Related Articles 305
7 Abbreviations and Acronyms 305
8 Further Reading 305
9 References 305

1 SUMMARY

Little exploration of lanthanide aryls has occurred, and unsolvated molecular species are not known. Phenyls $LnAr_3$ are only established for the heavier (and smaller) lanthanides, as well as scandium, in the form of solvates $[Ln(C_6H_5)_3(THF)_3]$ (Ln = Ho, Er, Tm, Lu) and $[Ln(C_6H_5)_3(THF)_2]$ (Ln = Lu, Sc). Some monophenyls $[Ln(Ar)Cl_2(THF)_x]$ are known, with the number of attached tetrahydrofuran (THF) molecules varying with the steric bulk of the phenyl (Ar = Ph, $n = 3$; Ar = 2,6-dimesitylphenyl or 2,6-di(1-naphthyl)phenyl, $n = 2$ or 3). The only unsolvated aryls are the anionic species $[Li(THF)_4]$ $[Ln(2,6\text{-dimethylphenyl})_4]$ (Ln = Yb, Lu). The known compounds are generally very air and moisture sensitive, though soluble in some organic solvents.

2 INTRODUCTION

For many years, it was not clear whether simple lanthanide alkyls or aryls could exist, and some researchers thought that they might be molecular species resembling diphenylmercury. Aryls have been made, but are not simple volatile molecules, and although the first aryls were synthesized slightly earlier than the alkyls, much less activity has been directed to their study subsequently.

3 TRIARYLS

The first simple alkyl or aryl of these metals to be reported was triphenylscandium (1968), soon to be followed by $Y(C_6H_5)_3$ and $LiLn(C_6H_5)_4$ (Ln = La, Pr).[1] These were obtained by conventional salt-elimination reactions from the anhydrous chlorides and phenyllithium in THF solvent.

$$ScCl_3 + 3\ C_6H_5Li \longrightarrow Sc(C_6H_5)_3 + 3\ LiCl$$

Initially, the phenyls are soluble in benzene, unlike the lithium chloride; after removal of lithium chloride, they are precipitated from THF solution by addition of hexane. The resulting dried solids are insoluble in benzene and other hydrocarbons; they are involatile, decomposed instantly by water, and are pyrophoric in air. The infrared spectra of these solids show rather broad bands in comparison with known σ-phenyls such as $Hg(C_6H_5)_2$, suggesting polymeric structures, as does their insolubility in hydrocarbons; the initial products were suggested to be THF adducts, but further elucidation was not obtained for over two decades.

It was another two decades before their nature was elucidated. In a different synthetic approach, lanthanide filings (Ln = Ho, Er, Tm, Lu) were found to react with diphenylmercury or triphenylbismuth by a transmetallation reaction in the presence of catalytic amounts of LnI_3, forming

The Rare Earth Elements. Edited by David A. Atwood. © 2012 John Wiley & Sons, Ltd. ISBN 978-1-119-95097-4

$[Ln(C_6H_5)_3(THF)_3]$.[2]

$$3\ (C_6H_5)_2Hg + 2\ Ln \longrightarrow 2\ Ln(C_6H_5)_3(THF)_3 + 3\ Hg$$

$$(C_6H_5)_3Bi + Ln \longrightarrow Ln(C_6H_5)_3(THF)_3 + Bi$$

The erbium and thulium compounds, $[Er(C_6H_5)_3(THF)_3]$ and $[Tm(C_6H_5)_3(THF)_3]$, both exist in the crystal as the *fac*-isomer, the octahedron being distorted with C–Ln–C angles ~100° and O–Ln–O angles ~80°, demonstrating the greater bulk of phenyl. The phenyl groups are monohapto.[2] The corresponding syntheses using an excess of Eu and Yb result in Ln^{II} compounds $[Ln(C_6H_5)_2(THF)_2]$ (Ln = Eu, Yb), but when an excess of diphenylmercury or triphenylbismuth is used in the reaction of ytterbium, in the presence of a catalytic amount of $YbI_2(THF)_4$, the product was $[Yb(C_6H_5)_3(THF)_3]$, with a structure very similar to Er and Tm analogs. It can also be made by oxidation of $[Yb(C_6H_5)_2(THF)_2]$.[3]

$$n\ Yb(C_6H_5)_2(THF)_2 + (C_6H_5)_nM \longrightarrow n\ Yb(C_6H_5)_3(THF)_3 + M$$

$$(M = Hg,\ n = 2;\ M = Bi,\ n = 3)$$

No further characterization of $Ln(C_6H_5)_3(THF)_3$ (Ln = Ho, Lu) has been published, but reaction of anhydrous $LuCl_3$ with a slight excess of aryl lithium resulted in $[Lu(C_6H_4\text{-}p\text{-}R)_3(THF)_2]$ (R = H, CH_3). The scandium analogs have been made similarly,[4] and $[Sc(C_6H_5)_3(THF)_2]$ has a trigonal bipyramidal structure, with THF ligands occupying the axial positions and phenyl groups the equatorial ones, as expected since phenyl groups are bulkier than THF.[5] On steric grounds, it might be expected that the phenyl groups in $[Sc(C_6H_5)_3(THF)_2]$ might adopt a propeller-like arrangement by twisting the phenyl rings out of the ScC3 plane to relieve close contacts involving *ortho*-hydrogen atoms; but in fact, they only twist slightly is (the torsion angles out of the ScC3 plane are 0°, 8°, and 18°).

In addition to these binary aryls, cationic and anionic species exist. Treatment of $[Ln(C_6H_4\text{-}p\text{-}R)_3(THF)_2]$ (Ln = Lu, Sc; R = H, CH_3) with stoichiometric amounts of $[NR'_3H]$ BPh_4 (R′ = Et; R'_3 = $PhMe_2$) results in protonolysis of metal–aryl bonds leading to the di(aryl) complexes $[Ln(C_6H_4\text{-}p\text{-}R)_2(THF)_4]^+[BPh_4]^-$ and mono(aryl) complexes $[Ln(C_6H_4\text{-}p\text{-}R)(THF)_5]^{2+}[BPh_4^-]_2$, which contain octahedrally coordinated metals.[4] When dissolved in pyridine, the dicationic monoaryl species $[Lu(C_6H_4\text{-}p\text{-}CH_3)(THF)_5]^{2+}[BPh_4^-]_2$ instantly exchanges the THF for pyridine, generating the $[Lu(C_6H_4\text{-}p\text{-}CH_3)(pyridine)_5]^{2+}$ ion, followed by two competing processes. One involves C–H activation of a pyridine molecule, resulting in loss of the aryl group as toluene and the formation of a η^2-(*C*, *N*)-pyridyl complex such as $[Lu(\eta^2\text{-}(C, N)\text{-}(C_5H_3N)py_5]^{2+}$ which undergoes a further insertion of pyridine into the Lu–C bond and the formation of a 2,2′-bipyridyl molecule. The second pathway involves attack of the coordinated *p*-tolyl group on a pyridine ligand, resulting in 2-*p*-tolylpyridine.

There is other evidence that aryls can be involved in processes involving C–H bond activation, in view of the side products observed in the synthesis of $[Sc(Dmp)Cl_2(THF)_2]$ in THF solution[6] or the limited stability of solutions of $[Sc(C_6H_5)_3(THF)_2]$.[5]

Since the initial report of $LiLn(C_6H_5)_4$ (Ln = La, Pr)[1], which probably contain solvated $[Ln(C_6H_5)_4]^-$ ions in THF solution, the only anionic arylates to be mentioned are $[Li(THF)_4]$ $[Lu(2,6\text{-dimethylphenyl})_4]$ and its ytterbium analog. Synthesized from anhydrous $LuCl_3$ and 2,6-dimethylphenyl-lithium in THF at −78°, it resulted from a conscious attempt to introduce crowding into lanthanide aryls and reduce the chance of polymerization. The Yb analog is isostructural, but similar mononuclear species could not be isolated for lighter (and larger) lanthanides. This compound is historically important as both the first crystallographically characterized example of a σ-bonded f-transition-metal organometallic and the first four-coordinate lanthanide compound.[7]

There are no reports of attempts to employ slightly bulkier substituted phenyls as a way of obtaining a neutral three-coordinate species.

4 MONOARYLS

In addition to neutral triaryls, some neutral species with one aryl group have been identified. Reaction of anhydrous $LnCl_3$ with 0.5 mol phenyl lithium in THF gives $Ln(C_6H_5)Cl_2{\cdot}n$ THF (Ln = Pr; n = 3; Ln = Sm, Gd; n = 3, 4); $[Gd(C_6H_5)Cl_2(THF)_4]$ has a monomeric structure with seven-coordinate gadolinium.[8]

Using bulkier-substituted phenyls such as 2,6-dimesitylphenyl (Dmp) and 2,6-di(1-naphthyl)phenyl (Dnp), 1 : 1 species with similar formulae are obtained, $[Y(Dmp)Cl_2(THF)_3]$, $[Ln(Dmp)Cl_2(THF)_2]$ (Ln = Sc, Yb), and $[Ln(Dnp)Cl_2(THF)_2]$ (Ln = Y, Tm, Yb). These adopt five- and six-coordinate structures. In these cases, however, it appears that further substitution of chloride is not possible because of the bulk of the substituents in the 2,6-positions of the benzene ring.[6,9]

5 CONCLUSIONS

Lanthanide aryls do exist, though none are not the simple volatile molecular species resembling main group aryls such as $Hg(C_6H_5)_2$ that some early researchers assumed. Lanthanide aryls are in general air- and moisture-sensitive

compounds, sometimes pyrophoric to even traces of oxygen. Even the neutral species reported so far cannot be sublimed in vacuo (unlike the cyclopentadienyls), not least because they lose solvent and oligomerize readily on warming. Apart from one study using the 2,6-dimethylphenyl group, the aryl groups employed so far have been either phenyl, which has the lowest steric requirements, or the very bulky 2,6-dimesitylphenyl or 2,6-di(1-naphthyl)phenyl groups; it is possible to envisage a situation where molecular $Ln(aryl)_3$ species could be synthesized. Even though very few compounds have been described, some of the cationic species described have shown potential in C−H bond activation.

6 RELATED ARTICLES

Alkyl.

7 ABBREVIATIONS AND ACRONYMS

Dmp = 2,6-dimesitylphenyl; Dnp = 2,6-di(1-naphthyl) phenyl; THF = tetrahydrofuran.

8 FURTHER READING

M. Zimmermann and R. Anwander, *Chem. Rev.*, 2010, **110**, 6194.

9 REFERENCES

1. F. A. Hart, A. G. Massey, and M. S. Saran, *J. Organomet. Chem.*, 1970, **21**, 147.
2. L. N. Bochkarev, T. A. Stepantseva, L. N. Zakharov, G. K. Fukin, A. I. Yanovsky, and Y. T. Struchkov, *Organometallics*, 1995, **14**, 2127.
3. L. N. Bochkarev, T. A. Zheleznova, A. V. Safronova, M. S. Drozdov, S. F. Zhil'tsov, L. N. Zakharov, G. K. Fukin, and S. Y. Khorshev, *Russ. Chem. Bull.*, 1997, **47**, 165.
4. P. M. Zeimentz and J. Okuda, *Organometallics*, 2007, **26**, 6388.
5. M. A. Putzer and G. P. Bartholomew, *Z. Anorg. Allg. Chem.*, 1999, **625**, 1777.
6. G. W. Rabe, C. D. Bérubé, G. P. A. Yap, K.-C. Lam, T. E. Concolino, and A. L. Rheingold, *Inorg. Chem.*, 2002, **41**, 1446.
7. S. A. Cotton, F. A. Hart. M. B. Hursthouse, and A. J. Welch, *Chem. Commun.*, 1972, 1225.
8. G. Lin, Z. Jin, Y. Zhang, and W. Chen, *J. Organomet. Chem.*, 1990, **396**, 307.
9. G. W. Rabe, C. D. Bérubé, and G. P. A. Yap, *Inorg. Chem.*, 2001, **40**, 2682.

Trivalent Chemistry: Cyclopentadienyl

Roman A. Kresinski

Kingston University, Kingston-upon-Thames, UK

1 Summary 307
2 Introduction 307
3 Synthesis 308
4 Structure and Reactivity 308
5 Conclusions 310
6 Glossary 310
7 Related Articles 310
8 Abbreviations and Acronyms 310
9 References 311

1 SUMMARY

This chapter outlines briefly the theory underlying the bonding between the cyclopentadienyl ligand and a typical rare earth ion, going on to discuss the relevance of structural studies; then to mention in more detail some of the synthetic methods available and the general reactivity of the title complexes; and then to present a more detailed discussion of structural, chemical, and catalytic behavior of the cyclopentadienyl complexes of rare earths.

The detailed discussion is split into three sections, dealing with complexes containing three, two, and one Cp rings, respectively. Since, steric considerations are paramount in this field, the assumption is made throughout that the Cp ligand is sterically equivalent, in the primary coordination sphere, to about three ''typical'' ligands. Hence, the coordination number below may not be the same as the number of atoms attached to the metal. Thus, since the rare earth metals generally decrease in size on moving from lighter to heavier metals, the narrative also tends to begin with the earlier, lighter metals and move generally toward the heavier.

Throughout the chapter, substitution of cyclopentadienyl ligands or groups is denoted by concatenation of abbreviations: for example, ''Cp'' denotes $\{C_5H_5\}$, ''CpMe'' denotes $\{C_5H_4CH_3\}$, and ''Cp-1,2-Et_2'' denotes $\{C_5H_3\text{-}1,2\text{-}(CH_2CH_3)_2\}$. This chapter is by no means exhaustive: more detailed information is available from the publications of W. J. Evans and H. Schumann, inter alia. The current literature is reviewed regularly in Royal Society of Chemistry publications.[1]

2 INTRODUCTION

The electronic structure of the rare earth ions is such as to afford them outermost electronic subshells that are fully occupied, with their unfilled subshells being relatively inaccessible to any ligands associated with the metal ions (see ***The Electronic Structure of the Lanthanides***). The resulting metal–ligand interactions are overwhelmingly electrostatic in nature (see ***Lanthanides: ''Comparison to 3d Metals''***, ***Organometallic Chemistry Fundamental Properties***). At the time of writing, just short of 1500 crystal structures are reported in the Cambridge Crystallographic Database,[2,3] containing the central motif of an aromatic five-carbon fragment bound facially to Ln (Ln = La–Lu) in all oxidation states. These are distributed rather unevenly throughout the rare earth series, with Yb- and Sm-containing structures being over-represented, at over 300 ''hits'' each. This gives some indication as to the relative research interest directed at each of these metals in the recent half-century. Pm reports only one ''hit,'' which is a determination of the unit cell parameters of $[Cp_3Pm]$ and reporting no further structural detail.[4] In almost all of the reports, the five-membered ring is bound near-symmetrically to the metals, maximal differences in bond distance from the metal to the C atoms of the Cp rings seldom exceeding 0.3 Å, or barely about 10% of the mean Ln–C distance. Exceptions to this rule number fewer than 10.[3] The most common form of distortion from a symmetrical ligation is a ''slippage'' of the ring so as largely to retain its planarity, but to move the metal away from a point normal to the ring centroid. This seems to be prompted

The Rare Earth Elements. Edited by David A. Atwood. © 2012 John Wiley & Sons, Ltd. ISBN 978-1-119-95097-4

by steric crowding, and examples are $[Cp_3Ce(thf)]$[5] or $[\{Cp\text{-}1,3\text{-}(^tBu)_2\}_3Yb]$,[6] both of which are likely to be approaching steric saturation. Still fewer reports are known for the rare earth metals wherein the rings are puckered: the report of dimeric $[\{Cp\text{-}1,3\text{-}(^tBu)_2\}_2Sm(\mu\text{-}BH_4)]_2$ is one[7] of the very few examples.

Owing to the electrostatic dominance in the bonding between the rare earths and their ligands, orbital overlap considerations are less important than they might be in the case of the transition metals. Hence, rare earth–ligand interactions tend to be ambidirectional and dependent largely on gross steric factors. In that regard, one ligand is much like another and the Cp and Cp-derived ligands are not in themselves special among ligands, as can be seen in the binuclear $[Cp_2Nd(\mu\text{-}NPPh_3)_2Nd(Cp)NPPh_3]$, which distributes Cp and $NPPh_3$ groups asymmetrically between metals.[8] Furthermore, the notion that complexes comprise negative ligands surrounding a positively charged metal undergoes occasional reversal, since efficient interaction might sometimes be achieved by alternative ordering of positive and negative charges, as seen in the remarkable stacked structure $[(dme)_2Na(\mu\text{-}Cp^*)TmCp^*(\mu\text{-}OMe)_2Na(\mu\text{-}Cp^*)Na(\mu\text{-}OMe)_2TmCp_2]$.[9]

3 SYNTHESIS

The cyclopentadienide complexes of the rare earths were among the first organo rare earths to be produced. Since this time,[10] their synthesis still generally requires the exclusion of oxygen, because the ligands are pyrophoric, and the exclusion of moisture, because the metal ions are prone to hydrolysis. To date, synthesis is commonly by means of direct replacement of halide or triflate[11] counterions using agents such as alkali metal cyclopentadienides. This reaction being sterically limiting, 1 equiv. of cyclopentadienide usually results in the replacement of 1 equiv. of halide or triflate; further equivalents usually result in the sequential introduction of a second (and then third) ring. Space permitting, the halide might be retained, as seen in the bimetallic complex $[Cp^*_2La(\mu\text{-}Cl)_2K(dme)_2]$.[12] Still further donor ligands may, if sufficient coordination space remains, be added simply by direct treatment with, or by recrystallization directly from, the said ligand.[13] Such adduct formation may often be reversed simply by vacuum treatment or sublimation,[14] but an ingenious approach to the removal of the thf ligand is by reaction with Me_3SiI, the resulting ring-opening product $Me_3SiO(CH_2)_4I$ being too bulky to coordinate. By this means $[Cp^*La\{CH(SiMe_3)_2\}_2]$ has been produced from its thf adduct, and proven to possess agostic Si–C interactions.[15] Alane intermediates might be used generically to create Cp–Ln bonds, as in the reaction between $La(AlMe_4)_3$ and HCp*, affording $Cp^*La(AlMe_4)_2$.[16] An ingenious method of producing mixed-ring complexes is metathesis of Cp^*_2Ca with $[Cp_3Ln]$ to give $[Cp^*_2NdCp]$ and the toluene-insoluble Cp_2Ca.[17] Occasionally, direct metal–atom reactions are preparatively feasible: $[Cp_2Sm(thf)_2]$ was first produced by vaporization of Sm directly into dicyclopentadiene followed by thf extraction,[18] lending itself to further oxidative derivatization.[19] Lastly, steric ''relaxation'' probably also underlies the ligand redistribution reactions which allow, for example, 3 equiv. of $[Cp_2CeN(SiMe_3)_2]$ to be formed from 2 equiv. of $[Cp_3Ce]$ and one of $[Ce\{N(SiMe_3)_2\}_3]$, a general principle allowing the synthesis of many bis-Cp heteroleptic complexes.[20]

4 STRUCTURE AND REACTIVITY

4.1 General

Strongly protic agents will tend to result in the removal of Cp rings by protonation and in this way they can be replaced by ligands for which rare earths have a high affinity. Accordingly, $[Cp_3Yb]$ reacts with ROH ($R = CH_2Bu$, CH^i_2Bu) to afford dimeric $[Cp_2Yb(\mu\text{-}OR)]_2$[21] and $[(Cp^tBu)_3Ce]$ reacts with 1 equiv. of HE^iPr to give $[(Cp^tBu)_2Ce(\mu\text{-}E^iPr)]_2$ (E = S, O). As is frequently the case in Ln chemistry, steric factors control this replacement, which can be seen from the fact that $[(Cp^tBu)_3Ce]$ seems inert to ^tBuOH, yet reacts with MeOH to give unreacted $[(Cp^tBu)_3Ce]$ and what is presumably $Ce(OMe)_3$.[22]

4.2 Structural Chemistry and Detailed Reactivity

4.2.1 Tris-Cp Complexes

The effects of steric strain on the general properties of these complexes might be seen in that homoleptic $[Cp_3Ln]$ complexes can be strongly associated into chains for the earlier rare earth metals,[23] and even examples from the middle of the series (Dy, Ho) possess some degree of intermolecular interaction.[20] Larger ligands lend a monomeric nature to early analogs such as $[(Me_4Cp)_3Pr]$.[24] Looking to the smaller metals, the steric strain in $[Cp^*_2Lu(Me_4Cp)]$ is such that the unique ligand adopts an η^3-coordination mode involving one of the methyl groups.[25]

An idea of the limit of steric bulk that can be accommodated around Ln^{III} in general might be obtained from $[\{Cp^*(CH_2)_2SEt\}_3La]$, whose Cp* ligands possess pendent sulfaethyl functionalities. Only two pendent groups are found to bind to the La ion[26] as is the case in $[(CpCH_2CH_2PMe_2)_3La]$.[11] Steric strain in tris-Cp complexes was explored in a single study[27], which observed that, similarly to $[Cp_3La(MeCN)_2]$,[28] trigonal bipyramidal bis(*t*-butyl cyanide) adducts $[Cp^*_3Ln(NC^tBu)_2]$ could be made for Ln = La–Pr, but only $[Cp^*_3Nd(NC^tBu)]$ could be formed.

With still smaller metal ions, insertions of the cyanide ligand into the Ln–Cp* bonds were promoted. Steric strain might on occasion result in Cp ring replacement by other ligands slightly less bulky in the primary coordination sphere but nevertheless bulky in their extremities. In this way, [Cp_3Ln] (Ln = Sm, Eu) and [$(MeCp)_3Yb$] undergo a simple translithiation with (LiPh-2,4,6-mes_3) to afford [Cp_2Ln-Ph-2,4,6-mes_3) and its Eu analog.[29] [$(CpMe)_2Er$(Ph-2,4,6-mes_3)] is similarly produced.[30] Many adducts are known to complete the steric saturation of the {Cp_3Ln} unit, among these esters,[31] ylides,[32] and chloride.[33] NMR and molecular orbital calculation evidence also exists for the weak adducts [$(CpSiMe_3)_3CeECp^*$] (E = Al, Ga).[34]

4.2.2 Bis-Cp Complexes

Hydride complexes, which in their turn might be made through hydrogenolysis of alkyl complexes,[35] are direct precursors for the formation of a variety of heteroleptic complexes. Methane elimination occurs on reaction of [(Cp-1,2,4-$Me_3)_2$CeH] with MeX to afford [(Cp-1,2,4-$Me_3)_2$CeX] (X = Cl, Br, I). Instead, treatment with Me_2O gives [(Cp-1,2,4-$Me_3)_2$Ce(η^2-CH_2OMe)] by hydrogen elimination.[36] Allene complexes can be made similarly: [Cp^*_2LnH] reacts with MeC≡CPh to afford [Cp^*_2Ln(η^3-CH_2CCPh)] (Ln = La, Ce).[37]

Treatment of [$Cp^*_2Ln(C_3H_5)$] with $Me_3SiCHNN$ affords [Cp^*_2Ln(μ-$Me_3SiCHNNCH_2CH{=}CH_2$)]$_2$ (Ln = La, Sm),[38] a symmetrical binuclear species. This binuclear pattern is very common in bis-Cp complexes and is repeated with a plethora of bridging ligands such as benzoates,[39] alkyls,[30,40] oximes,[41] thiol-substituted enolates,[42] diazotates,[43] thiolates,[44] acetylides,[45] halides,[30,46] $\{Cl_2AlMe_2\}^-$ anion[47] or amidopyrimidines.[48] Even dinitrogen complexes such as [{$(Cp')_2$Ln}(μ^2-η^2:η^2-N_2)] (Cp′ = Me_4Cp, Cp*; Ln = La, Nd) can be made under strongly reducing conditions.[24,49] The formation of such bridging complexes might find its useful steric limit before the end of the rare earth series, since [Cp_2YbCl(thf)] is mononuclear.[50] Arguably, such proximity of metals allows subtler control of coordination space, and also cooperative behavior between metals. To illustrate, hydrogen bond derivatizations are potentially of wider interest, especially if they might be catalytic or C–C bond forming. An interesting example occurs on treatment of the bulky [$Cp^*_2LnCH(SiMe_3)_2$] with acetonitrile, resulting in the eight-membered lanthanabicycle [Cp^*_2Ln(μ-CH_2CN)]$_2$ (Ln = La, Ce).[51] Treatment instead with alkynes RC≡CH results initially in the dimeric [Cp^*_2Ln(μ-C≡CR)]$_2$, which transform to [$(Cp^*_2Ln)_2$(μ-η^4:η^4-RC_4R)] (R = Me, Ln = La, Ce; R = ^{t}Bu, Ln = Ce). Interestingly the bridging ligand coupling product can be displaced by reaction with phenoxide ligands to give statistical distributions of RC_4H_2R products.[52] Complexes [$(Cp^tBu)_2$Ln(μ-C≡CR)]$_2$ (Ln = Nd, Gd) are also known but not reported to transform further.[53] Kindred interesting coupling reactions can arise from the treatment of [$Cp^*_2Ln(BPh_4)$] with Me_3SiCNN^- Li^+ to give [Cp^*_2Ln{μ-N($SiMe_3$)NC}]$_2$ (Ln = La, Sm). The bridging ligand in this dimer couples with organic cyanides to form appropriately substituted bridging triazole ligands.[54] Generally speaking, insertion reactions into Ln–ligand bonds in binuclear complexes occur frequently, all these reactions being driven in some way by a relief of strain. Thus, monomeric [$Cp_2Sm(CH_2Ph)$(thf)] reacts with N_2O to afford [Cp_2Sm(μ-$ONNCH_2Ph$)]$_2$.[43] If the energy involved in the relief of strain is as little as to make a local equilibrium measurable, a catalytic cycle might be feasible, driven by bulk energetics of reagents and products: indeed, pendent phenyl complexes [$(PhCMe_2Cp)_2ErCl$] and [$(PhCH_2CMe_2Cp)_2ErCl]_2$ possess, on treatment with $AlEt_3$, polymerization activity toward methyl methacrylate.[55] Other complexes with pendent-arm ligands relevant to this section are the cationic [{$Cp(CH_2)_2OMe$}$_2$Yb(thf)]$^+$, which is formally nine-coordinate[56] while the closely related [Cp*{$Cp(CH_2)_2SR$}LuCl] (R = Me, Et,[57] Ph[26]) are eight-coordinate. This again allows a qualitative idea of the limits of steric accommodation in complexes of this type.

A wide variety of heterobimetallic structures exist bridged by halides as in [$Cp^*_2Sm(\mu$-$Cl)_2Li(Et_2O)_2$],[58] alkyls as in [$Cp^*_2Sm(\mu$-$Et)_2AlEt_2$][59] or [$Cp_2Yb(\mu$-$Me)_2AlMe_2$],[60] and sulfide as in [{Cp^*_2Sm}$_2$(μ-$S)_4Mo]^-$ or[61] [{Cp^*_2Sm}$_2$(μ-$S)_2WS_2]^-$. Single bridges might arise in the case of the larger iodide: divalent [(Cp-1,2,4-^{t}$Bu_3)_2$Nd(μ-I)K{[18]crown-6}] is notable since it activates its own butyl C–H bond to give trivalent [(Cp-1,2,4-^{t}Bu_3)(Cp-1,2-^{t}Bu_2-4-CH_2)Nd(μ-I)K{[18]crown-6}].[62] The monomeric nature of the starting material might be contrasted with the polymeric nature of [$Cp_2Yb(NCS)_2$K{[18]crown-6}], wherein two bridges can be accommodated.[43]

4.2.3 Single-Cp Complexes

With single-Cp complexes the issue with applications, or even synthesis, is controlling unwanted or unknown guests within the coordination sphere. With one or two sizable ''hosts,'' this is more controllable than with just one. One way in which this might be achieved is, as seen above, by use of pendent-arm ligands. The ligands {Cp-1,*x*-$(CH_2CH_2NH_2)_2$} (*x* = 2, 3) give rise to several interesting complexes, namely, [{Cp-1,*x*-$(CH_2CH_2NH_2)_2$}LaI_2(thf)] (octahedral *fac*- and *mer*-isomers, if the Cp ring is taken as a single site), [{Cp-1,2-$(CH_2CH_2NH_2)_2$}Yb(Cp′)] (Cp′ = Cp^{t}Bu, Cp*), [{Cp-1,2-$(CH_2CH_2NH_2)_2$}YbI$(thf)_2$], and [Cp*{Cp-1,3-$(CH_2CH_2NH_2)_2$}Yb(η-I)Na]. The former two complexes are divalent and the last is polymeric.[63] Other pendent-arm stabilized complexes are the $cote^{2-}$-containing [{$Cp(CH_2)_2OMe$}Nd(cote)(thf)] and [{$Cp(CH_2)_2O(C_4H_7O)$}La(cote)(thf)].[64] Where the pendent group is noncoordinating, additional small ligands might be incorporated, such as in [$(CpCH_2Ph)Gd$(cote)$(dme)_2$].[65] Contrastingly, steric bulk allows [(^{i}Pr_4Cp)Nd(cote)] an unsolvated

structure[66] and allows [(^{i}Pr$_4$Cp)Nd(BH$_4$)$_2$(thf)] a reportedly open structure, which affords it styrene polymerization ability when treated with BuLi.[67]

The implied relative lack of steric control in single-Cp systems often allows for a degree of serendipitous formation of unusual bridging structures, including an example of a small cluster stabilizing a rare pyrene trianion, as found in [(Cp*La)$_3$(μ-Cl)$_3$(thf)(μ^3-η^2:η^6:η^6-C$_{16}$H$_{10}$)].[68] The cluster [{CpDy(μ-I)$_2$}$_7$Cp$_2$V(μ-I)] contains triply bridging iodides[69] and the anion [(CpYb)$_6$Cl$_{13}$]$^-$ contains a fully sextuply bridging chloride ion at its center.[70] Oxygen can similarly be persuaded into hypervalency by surrounding LnCp fragments.[46]

As is the case for some bis-Cp examples above, subtle changes in ligand bulk may induce or prevent dimerization: monomeric [CpSmBr$_2$(thf)$_3$][71] might be contrasted with [Cp*Sm(μ-I)(thf)$_2$]$_2$ in this regard.[72] Certain synthetic approaches have focused on the production of single-Cp complexes by the adoption of ligands that are bulky in the secondary coordination sphere: the {^{t}Pr$_4$Cp} ligand is interesting since, with a small metal, steric saturation might be reached before the accommodation of two Cp ligands halfway across the rare earth series: a contrast can be drawn between [{(^{i}Pr$_4$Cp)$_2$Nd}$_2${μ-Cl$_2$Na(Et$_2$O)}$_2$], a dimer with a complex bridging ligand but otherwise quite conventional, and [(^{i}Pr$_4$Cp)YbCl$_2$(dme)]. Attempts to synthesize two-ring complexes of this ligand reportedly failed with Yb.[73]

4.2.4 Related Metals and Ligands

A wholly analogous chemistry exists for Y as does for the rare earths.[60,74] Y^{3+} is believed to be similar to Ho in size.[75] Sc^{3+} is rather smaller and prone to covalent bonding, one of the rings in [Cp$_3$Sc] thus adopting an η^1 coordination mode.[25]

Ansa-Cp$_2$ complexes, namely, those with two Cp rings linked by a bridging group, are known.[76] The indenyl ligand (C$_9$H$_8$ = Ind) is naturally more sterically demanding than Cp but finds rare earth metals coordinating principally to its putatively anionic five-membered ring, rather than the arene functionality.[77,78] Bis- and tris-indenyl complexes are nevertheless known, even with bulky substituents.[79] Several studies are known comparing tris-indenyl complexes to their ''parent'' cyclopentadienyls, including some chiral, natural product adducts.[80,81] Fluorene ligands also coordinate in a η^5-fashion and result in a wide variety of complexes.[82,83] Examples are known of fluorenyl ring systems *ansa*-coupled to cyclopentadienyl.[74]

5 CONCLUSIONS

The field is developing rapidly as improved handling techniques become more widely used, and, this is likely to continue apace. More synthetic avenues might become available through the increasingly common divalent cyclopentadienide species. For example, [Cp*$_2$Yb] reacts with TlN$_2$C$_3$HPh$_2$ to give the mononuclear η^2-chelating trivalent diphenylpyrazolyl complex and metallic thallium.[84] Similar oxidations are available using silver salts.[19]

Just as binuclear examples mentioned above appeared to possess the greater activity in terms of catalytic or small molecule activation, it may be that heterobinuclear compounds might offer promise of cooperative behavior between metals of disparate character. The rare earth ions having little affinity for phosphine ligands, these moieties are pendent in complexes such as [CpLa(CpPPh$_2$)$_2$],[11]; this property might provide a means of forming bimetallic complexes with late transition series ions in future.

6 GLOSSARY

centroid: In this chapter, an imaginary location defined as the mean location of all five C atoms of a Cp ligand.

hypervalent: In this chapter, the state of bonding which involves formally possessing more outer or bonding electrons than accepted by the Lewis Octet Rule, or the state involving the formal removal of inner electrons, similarly violating the Lewis Octet Rule.

pendent: Reminiscent of something 'hanging down' from the cyclopentadienyl ligand. Usually used in the context of a secondary putatively coordinating substituent thereon.

7 RELATED ARTICLES

The Electronic Structure of the Lanthanides; Variable Valency; Group Trends; Lanthanides: ''Comparison to 3d Metals''; Organometallic Chemistry Fundamental Properties.

8 ABBREVIATIONS AND ACRONYMS

^{t}Bu = Tertiary butyl; ^{i}Bu = Secondary butyl; Bu = Butyl; Cote = Cyclooctatetraene; Me = Methyl; Mes = Mesityl; Dme = Dimethoxyethylene, MeOCH$_2$CH$_2$OMe; Cp = Cyclopentadienyl; Cp* = Permethylcyclopentadienyl; Ln = Generic rare earth element; thf = Tetrahydrofuran; Ph = Phenyl.

9 REFERENCES

1. J. G. Brennan and A. Sella, in 'Specialist Periodical Reports, Organometallic Chemistry', Vol. 36, eds. I. J. S. Fairlamb and J. M. Lynam, RSC Publishing, 2010.
2. D. A. Fletcher, R. F. McMeeking, and D. Parkin, *J. Chem. Inf. Comput. Sci.*, 1996, **36**, 746.
3. F. H. Allen, *Acta Crystallogr.*, 2002, **B58**, 380.
4. P. G. Lauberau and J. H. Burns, *Inorg. Chem.*, 1970, **9**, 1091.
5. W.-Q. Chen, G.-Y. Yang, J.-S. Xia, G.-C. Wei, Y. Zhang, and Z.-S. Jin, *Huaxue Xuebao*, 1994, **52**, 261.
6. A. V. Khvostov, B. M. Bulychev, V. K. Belsky, and A. I. Sizov, *J. Organomet. Chem.*, 1998, **568**, 113.
7. Y. K. Gun'ko, B. M. Bulychev, G. L. Soloveichik, and V. K. Belsky, *J. Organomet. Chem.*, 1992, **424**, 289.
8. S. Anfang, K. Harms, F. Weller, O. Borgmeier, H. Lueken, H. Schilder, and H. Dehnicke, *Z. Anorg. Allg. Chem.*, 1998, **624**, 159.
9. I. L. Fedushkin, F. Girgsdies, H. Schumann, and M. N. Bochkarev, *Eur. J. Inorg. Chem.*, 2001, 2405.
10. J. M. Birmingham and G. Wilkinson, *J. Am. Chem. Soc.*, 1956, **78**, 42.
11. H. H. Karsch, V. Graf, M. Reisky, and E. Witt, *Eur. J. Inorg. Chem.*, 1998, 1403.
12. K.-H. Thiele, A. Scholz, J. Scholz, U. Bohme, R. Kempe, and J. Sieler, *Z. Naturforsch.*, 1993, **B48**, 1753.
13. U. Baisch, S. Pagano, M. Zeuner, N. Barros, L. Maron, and W. Schnick, *Chem. Eur. J.*, 2006, **12**, 4785.
14. H. Schumann, M. Glanz, J. Winterfeld, and H. Hemling, *J. Organomet. Chem.*, 1993, **456**, 77.
15. H. van der Heijden, C. J. Schavieren, and A. G. Orpen, *Organometallics*, 1989, **8**, 255.
16. H. M. Dietrich, C. Zapilko, E. Herdtweck, and R. Anwander, *Organometallics*, 2005, **24**, 5767.
17. P. S. Tanner, D. J. Burkey, and T. P. Hanusa, *Polyhedron*, 1995, **14**, 331.
18. W. J. Evans, I. Bloom, W. E. Hunter, and J. L. Atwood, *J. Am. Chem. Soc.*, 1981, **103**, 6507.
19. Z. Xie, Z. Liu, Z.-Y. Zhou, and T. C. W. Mak, *J. Chem. Soc. Dalton Trans.*, 1998, 3367.
20. U. Baisch, S. Pagano, M. Zeuner, J. Schmedt auf der Guenne, O. Oeckler, and W. Schnick, *Organometallics*, 2006, **25**, 3027.
21. Z.-Z. Wu, Z.-E. Huang, R.-F. Cai, X. Xu, X.-Z. You, and X.-Y. Huang, *Polyhedron*, 1996, **15**, 13.
22. S. D. Stults, R. A. Andersen, and A. Zalkin, *Organometallics*, 1990, **9**, 1623.
23. S. H. Eggers, W. Hinrichs, J. Kopf, W. Jahn, and R. D. Fischer, *J. Organomet. Chem.*, 1986, **311**, 313.
24. W. J. Evans, D. B. Rego, and J. W. Ziller, *Inorg. Chem.*, 2006, **45**, 10790.
25. S. Demir, T. J. Mueller, J. W. Ziller, and W. J. Evans, *Angew. Chem. Int. Ed.*, 2011, **50**, 515.
26. H. Schumann, K. Herrmann, S. H. Muehle, and S. Dechert, *Z. Anorg. Allg. Chem.*, 2003, **629**, 1184.
27. W. J. Evans, T. J. Mueller, and J. W. Ziller, *Chem. Eur. J.*, 2010, **16**, 964.
28. M. R. Spirlet, J. Rebizant, C. Apostolidis, and B. Kanellakopulos, *Acta Crystallogr.*, 1987, **C43**, 2322.
29. M. Niemeyer and S.-O. Hauber, *Z. Anorg. Allg. Chem.*, 1999, **625**, 137.
30. H. Schumann, M. R. Keitsch, and S. H. Muehle, *Z. Anorg. Allg. Chem.*, 2002, **628**, 1311.
31. H. Schultz and H.-D. Amberger, *J. Organomet. Chem.*, 1993, **443**, 71.
32. W.-K. Wong, J. Guan, Q. Shen, L. Zhang, Y. Lin, and W.-T. Wong, *Polyhedron*, 1995, **14**, 277.
33. C. Quian, B. Wang, Y. Xin, and Y. Lin, *J. Chem. Soc. Dalton Trans.*, 1994, 2109.
34. J. L. Krinski, S. G. Minasian, and J. Arnold, *Inorg. Chem.*, 2011, **50**, 345.
35. W. J. Evans, J. H. Meadows, A. L. Wayda, W. E. Hunter, and J. L. Atwood., *J. Am. Chem. Soc.*, 1984, **106**, 4270.
36. E. L. Werkema, R. A. Andersen, A. Yahia, L. Maron, and O. Eisenstein, *Organometallics*, 2009, **28**, 3173.
37. V. F. Quiroga Norambuena, A. Heeres, H. J. Heeres, A. Meetsma, J. H. Teuben, and B. Hessen, *Organometallics*, 2008, **27**, 5672.
38. W. J. Evans, E. Montalvo, T. J. Champagne, J. W. Ziller, A. G. DiPasquale, and A. L. Rheingold, *Organometallics*, 2008, **27**, 3582.
39. G. B. Deacon, C. C. Quitmann, K. Mueller-Buschbaum, and G. Meyer, *Z. Anorg. Allg. Chem.*, 2003, **629**, 589.
40. J. Holton, M. F. Lappert, D. G. H. Ballard, R. Pearce, J. L. Atwood and W. E. Hunter, *J. Chem. Soc. Dalton Trans.*, 1979, 45.
41. Z.-Z. Wu, D.-M. Fan, Z.-E. Huang, and Z.-E. Cai, *Polyhedron*, 1996, **15**, 127.
42. C.-M. Zhang, R.-T. Lui, X.-Z. Chen, and X.-G. Zhou., *Chin. J. Chem.*, 2006, **24**, 231.
43. T. Labahn, A. Mandel, and J. Magull, *Z. Anorg. Allg. Chem.*, 1999, **625**, 1273.
44. Q. Lui, M. Ding, L. Lin, and Y. Xing, *Polyhedron*, 1998, **17**, 555.
45. J. Ren, J. Hu, Y. Lin, X. Yan, and Q. Shen, *Polyhedron*, 1996, **15**, 2165.
46. W. J. Evans, S. Allen, N. T. Greci, and J. W. Ziller, *Organometallics*, 2001, **20**, 2936.
47. M. Glanz, S. Dechert, H. Schumann, D. Wolff, and D. Springer, *Z. Anorg. Allg. Chem.*, 2000, **626**, 2467.
48. R. A. Layfield, A. Bashall, M. McPartlin, J. M. Rawson and D. S. Wright, *J. Chem. Soc. Dalton Trans.*, 2006, 1660.

49. W. J. Evans, D. S. Lee, C. Lie, and J. W. Ziller, *Angew. Chem. Int. Ed.*, 2004, **43**, 5517.
50. D. Stellfeldt, G. Meyer, and G. B. Deacon, *Z. Anorg. Allg. Chem.*, 2001, **627**, 1659.
51. H. J. Heeres, A. Meetsma, and J. H. Teuben, *Angew. Chem. Int. Ed.*, 1990, **29**, 420.
52. H. J. Heeres, J. Nijhoff, J. H. Teuben, and R. D. Rogers, *Organometallics*, 1993, **12**, 2609.
53. J. Ren, J. Hu, Y. Lin, Y. Xing, and Q. Shen, *Polyhedron*, 1996, **15**, 2165.
54. W. J. Evans, E. Montalvo, T. J. Champagne, J. W. Ziller, A. G. DiPasquale, and A. L. Rheingold, *Organometallics*, 2009, **28**, 2897.
55. X. Xie and J. Huang, *Appl. Organomet. Chem.*, 2004, **18**, 282.
56. D. Deng, X. Zheng, C. Quian, J. Sun, A. Dormond, D. Baudry and M. Visseaux, *J. Chem. Soc. Dalton Trans.*, 1994, 1665.
57. H. Schumann, K. Herrmann, J. Demtschuk, and S. H. Muehle, *Z. Anorg. Allg. Chem.*, 1999, **625**, 1107.
58. P. C. Junk and M. K. Smith, *Appl. Organomet. Chem.*, 2004, **18**, 252.
59. W. J. Evans, L. R. Chamberlain, and J. W. Ziller, *J. Am. Chem. Soc.*, 1987, **109**, 7209.
60. J. Holton, M. F. Lappert, D. G. H. Ballard, R. Pearce, J. L. Atwood and W. E. Hunter, *J. Chem. Soc. Dalton Trans.*, 1979, 54.
61. W. J. Evans, M. A. Ansari, J. W. Ziller, and S. I. Khan, *Organometallics*, 1995, **14**, 3.
62. F. Jaroschik, A. Momin, F. Nief, X.-F. Le Goff, G. B. Deacon, and P. C. Junk, *Angew. Chem. Int. Ed.*, 2009, **48**, 1117.
63. I. L. Fedushkin, S. Dechert, and H. Schumann, *Organometallics*, 2000, **19**, 4066.
64. Q. Liu, X. Shen, J. Huang, Y. Qian, A. S.-C. Chan, and W.-K. Wong, *Polyhedron*, 2000, **19**, 453.
65. J. Xia, S. Jin, and W. Chen, *Chin. J. Chem*, 1996, **14**, 31.
66. M. Visseaux, D. Barbier-Baudry, O. Blacque, A. Hafid, P. Richard, and F. Weber, *New J. Chem.*, 2000, **24**, 939.
67. D. Barbier-Baudry, O. Blacque, A. Hafid, A. Nyassi, H. Sitzmann and M. Visseaux, *Eur. J. Inorg. Chem.*, 2000, 2333.
68. K.-H. Thiele, S. Bambirra, J. Sieler, and S. Yelonek, *Angew. Chem. Int. Ed.*, 1998, **37**, 2886.
69. M. E. Burin, M. V. Smirnova, G. K. Fukin, E. V. Baranov and M. N. Bochkarev, *Eur. J. Inorg. Chem.*, 2006, 351.
70. W. P. Kretschmer, J. H. Teuben, and S. I. Troyanov, *Angew. Chem. Int. Ed.*, 1998, **37**, 88.
71. D. Stellfeldt, G. Meyer, and G. B. Deacon, *Z. Anorg. Allg. Chem.*, 1999, **625**, 1252.
72. W. J. Evans, J. W. Grate, H. W. Choi, I. Bloom, W. E. Hunter, and J. L. Atwood, *J. Am. Chem. Soc.*, 1985, **107**, 941.
73. H. Sitzmann, O. Schmitt, F. Weber, and G. Wolmershaeuser, *Z. Anorg. Allg. Chem.*, 2001, **627**, 12.
74. E. Kirillov, L. Toupet, C. W. Lehmann, A. Razavi, S. Kaklal, J.-Y. Saillard, and J.-F. Carpentier, *Organometallics*, 2003, **22**, 4038.
75. R. D. Shannon, *Acta Crystallogr.*, 1976, **A32**, 751.
76. H. Schumann, F. Erbstein, J. Demtschuk, and R. Weimann, *Z. Anorg. Allg. Chem.*, 1999, **625**, 1457.
77. J. Cheng, D. Cui, W. Chen, T. Tang, and B. Huang, *Polyhedron*, 2004, **23**, 1075.
78. A. A. Trifonov, E. N. Kirillov, S. Dechert, H. Schumann and M. N. Bochkarev, *Eur. J. Inorg. Chem.*, 2001, 3055.
79. H. Schumann, D. F. Karasiak, and S. H. Muehle, *Z. Anorg. Allg. Chem.*, 2000, **626**, 1434.
80. J. L. Atwood, J. H. Burns, and P. G. Laubereau, *J. Am. Chem. Soc.*, 1973, **95**, 1830.
81. J. Guan and R. D. Fischer, *Eur. J. Inorg. Chem.*, 2001, 2497.
82. G. R. Giesbrecht, J. C. Gordon, D. L. Clark, and B. L. Scott, *Appl. Organomet. Chem.*, 2005, **19**, 98.
83. K. Schierwater, H. Hanika-Heidl, M. Bollmann, R. D. Fischer, R. K. Harris, and D. C. Apperley, *Coord. Chem. Rev.*, 2003, **242**, 15.
84. G. B. Deacon, E. E. Delbridge, G. D. Fallon, C. Jones, D. E. Hibbs, M. B. Hursthouse, B. W. Skelton, and A. H. White, *Organometallics*, 2000, **19**, 1713.

Tetravalent Chemistry: Inorganic

Farid M.A. Sroor and Frank T. Edelmann

Chemisches Institut der Otto-von-Guericke-Universität Magdeburg, Magdeburg, Germany

1	Summary	313
1	Introduction	313
2	Lanthanide(IV) Tetrahalides	313
3	Lanthanide(IV) Dioxides	314
4	Other Lanthanide(IV) Salts	315
5	Coordination Compounds of Tetravalent Lanthanides	315
6	Conclusions and Future Outlook	320
7	Abbreviations and Acronyms	320
8	References	320

1 SUMMARY

This chapter gives an overview on the chemistry of tetravalent lanthanide compounds, especially those of tetravalent cerium. Following a brief introduction, it covers the tetrahalides, dioxides, and other lanthanides(IV) salts. Coordination compounds of cerium in the oxidation state +4 include halogeno complexes and complexes of oxo acids, β-diketonates and related Schiff-base complexes, as well as porphyrinates and related complexes.

1 INTRODUCTION

Besides the ubiquitous oxidation state Ln^{3+}, the higher oxidation state Ln^{4+} is also encountered with some lanthanoids, for example, in the case of the ions Ce^{4+} (f^0, orange–yellow), Pr^{4+} (f^1, colorless), Nd^{4+} (f^2, blue–violet), Tb^{4+} (f^7, colorless), and Dy^{4+} (f^8, orange–yellow) (Table 1). However, all three states $Ln^{2+,3+,4+}$ are never encountered for the same element. Thus, the highly important mechanistic steps of oxidative addition and reductive elimination typical for the d-block metals cannot occur with the f-block metals as they would involve M^{2+} or M^{4+} transformations, respectively.[1]

Among the tetravalent lanthanide ions, only Ce^{4+} is readily available in aqueous solution (E $Ce^{3+}/Ce^{4+} = +1.44$ V in 2M H_2SO_4, 1.61 V in 1M HNO_3, 1.70 V in 1M $HClO_4$). The different values for the reduction potentials indicate that stable complexes are formed in these acidic media. Thermodynamically, the oxidation of water by the Ce^{4+} aqua ion should be possible, but the system is kinetically stable. In contrast, the much more positive normal potentials of the other tetravalent lanthanide ions Pr^{4+}, Nd^{4+}, Tb^{4+}, and Dy^{4+} (e.g., Pr: +2.86 V) make them very strong oxidizing agents, which readily decompose water under evolution of O_2. The oxidation of Ce^{3+} to Ce^{4+} with the use of strong oxidizing agents such as MnO_4^- or $S_2O_8^{2-}$ (Scheme 1) enables the selective separation of cerium from lanthanide mixtures. The resulting Ce^{4+} can be precipitated from aqueous nitric acid solution in the form of ceric ammonium nitrate (CAN), $(NH_4)_2[Ce(NO_3)_6]$.[1]

The readily occurring transition from colorless Ce^{3+} to bright yellow or orange Ce^{4+} forms the basis for the use of cerium(IV) sulfate solutions in redox titrations (''cerimetric'' analysis). The ease of access to various tetravalent cerium compounds makes cerium(IV) most valuable in research as well as in various practical applications. Important fields of application for cerium(IV) compounds include organic syntheses, bioinorganic chemistry, materials science, and industrial catalysis (e.g., vehicle emissions control, oxygen storage).[1]

2 LANTHANIDE(IV) TETRAHALIDES

Only the tetrafluorides of Ce, Pr, and Tb exist, the three lanthanides with the most stable +4 oxidation state. Fluorine is most likely to support a high oxidation state,

The Rare Earth Elements. Edited by David A. Atwood. © 2012 John Wiley & Sons, Ltd. ISBN 978-1-119-95097-4

Table 1 Possible oxidation states for rare earth metals

Ce	Pr	Nd	Pm	Sm	Eu	Gd	Tb	Dy	Ho	Er	Tm	Yb	Lu
—	—	—	—	+2	+2	—	—	—	—	—	+2	+2	—
+3	+3	+3	+3	+3	+3	+3	+3	+3	+3	+3	+3	+3	+3
+4	+4	+4	—	—	—	—	+4	+4	—	—	—	—	—

$$2\,Ce^{3+} + S_2O_8^{2-} \longrightarrow 2\,Ce^{4+} + 2\,SO_4^{2-}$$

Scheme 1

and even though salts of ions such as $[CeCl_6]^{2-}$ are known, no binary tetrachlorides have ever been isolated as pure materials. Anhydrous LnF_4 (Ln = Ce, Pr, Nd, Tb, Dy) can be made by fluorination of the trifluorides or, in the case of Ce, by fluorination of metallic Ce, $CeCl_3$, or CeO_2. The method employing cerium dioxide appears to be the most straightforward one. CeF_4 can be crystallized from aqueous solution as a monohydrate. In the solid state, all tetrafluorides adopt the MF_4 structure with dodecahedral eight-coordination and are thus isomorphous with UF_4. Factors that favor formation of the tetrafluorides include a low value of I_4 for the metal and a high lattice energy. This is most likely to be found with the smallest halide, i.e., fluoride. The low bond energy of F_2 is an additional supporting factor.

Other tetrahalides do not exist. Thus, although both $CeCl_3$ and salts of the $[CeCl_6]^{2-}$ ion are quite stable, $CeCl_4$ cannot be made. The reasons for this are those that enable fluorine to support high oxidation states. Similar factors indicate that tetrabromides and tetraiodides are much less likely to be isolated.[1]

3 LANTHANIDE(IV) DIOXIDES

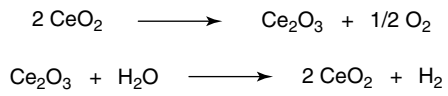
Rare earth metals generally react with dioxygen under formation of the lanthanide(III) oxides, Ln_2O_3, with the exception of cerium, praseodymium, and terbium. In these cases, CeO_2, Pr_6O_{11}, and Tb_4O_7 are formed, respectively. Lanthanide dioxides, LnO_2 (Ln = Ce, Pr, Tb), crystallize in the fluorite (CaF_2) structure. Defects in the oxygen positions lead to various mixed Ln^{3+}/Ln^{4+} oxides of the type (for praseodymium) $Pr_{12}O_{22}$, $Pr_{11}O_{20}$, $Pr_{10}O_{18}$, Pr_9O_{16}, Pr_8O_{14}, Pr_7O_{12}, and Pr_6O_{10} before the row ends with Pr_2O_3.[1] Under forcing conditions, e.g., heating in pure oxygen under pressure, these will eventually yield PrO_2 (or TbO_2 in the case of terbium).[1]

Among these materials, *cerium dioxide* (ceria) is of particular importance. Very pure ceria forms a white powder, but more often, it appears pale yellow, and less pure samples can even be brownish. A brownish coloration could be an indicative for the presence of impurities such as praseodymium and neodymium. Nevertheless, impure ceria can be used for applications where purity is not critical, e.g., for polishing glass or stones. Ceria can be prepared by calcination of suitable precursors such as cerium nitrate, $Ce(NO_3)_3$, cerium oxalate, $Ce_2(C_2O_4)_3$, or cerium hydroxide, $Ce(OH)_3$, in air. At room temperature and under atmospheric pressure, it is more stable than the Ce_2O_3 phase. Cerium dioxide is basic and can be dissolved in acids (although with some difficulty).[1]

Cerium dioxide has found numerous practical applications, e.g., as oxidation catalyst and as catalyst support (e.g., for gold nanoparticles), in ceramics, self-cleaning ovens, and catalytic converters, for sensitizing photosensitive glasses and for polishing glass and stones. Ceria is also being used in infrared (IR) filters and as a replacement for radioactive thorium dioxide in incandescent mantles. While cerium dioxide is transparent for visible light, it is a strong ultraviolet light absorber. Thus it has been envisaged as a prospective replacement for ZnO and TiO_2 in sunscreens, although its photocatalytic activity is somewhat lower.

Most of the practical uses of cerium dioxide in organic synthesis and catalysis are based on its oxidizing properties. For example, its use in the walls of so-called self-cleaning ovens makes use of the fact that it assists oxidation of sticky hydrocarbon deposits during the high-temperature cleaning process. Ceria is also of great current interest as a material for solid oxide fuel cells (SOFCs) because of its relatively high oxygen ion conductivity.[2] Another very important application of ceria is its use in catalytic converters in automotive applications. Cerium dioxide is able to release or store oxygen in the exhaust stream of an automotive engine because the material is able to become nonstoichiometric in its oxygen content. The catalytic activity of ceria has been found to depend directly on the number of oxygen. It is able to effectively reduce the NO_x emissions and also to oxidize toxic carbon monoxide to nontoxic CO_2. The use of inexpensive ceria in such catalysts also presents an economic advantage as it reduces the amount of platinum needed for reducing NO_x emissions and achieving complete combustion of harmful exhaust gases. In addition, ceria has been found to be a useful cocatalyst in a variety of industrially important reactions including various oxidation reactions, the Fischer–Tropsch reaction, as well as the water–gas shift reaction and steam reforming of diesel fuel to give hydrogen gas and carbon dioxide (in combination with various transition metal or metal oxide catalysts).

Furthermore, a laboratory demonstration of thermochemical water-splitting cycles based on the CeO_2/Ce_2O_3 pair (Scheme 2) has been reported. Thermal reduction of Ce^{4+} to



Scheme 2

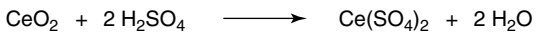
Ce^{3+} (endothermic step) has been performed in a solar reactor featuring a controlled inert atmosphere. The feasibility of this first step has been demonstrated and the operating conditions have been defined ($T = 2000\,^{\circ}C$, $P = 100-200$ mbar). The subsequent hydrogen generation step (water splitting with Ce_2O_3) carried out in a fixed bed reactor was complete with a fast kinetic in the studied temperature range 400–600 °C. The recovered CeO_2 was then recycled in the first step. In this process, water is the only material input and heat is the only energy input. The only outputs are hydrogen and oxygen, and these two gases are obtained in different steps avoiding a high-temperature energy-consuming gas-phase separation. Furthermore, pure hydrogen is produced which can be used directly in fuel cells. These results have shown that the two-step thermochemical cycle of cerium oxide is a promising process for hydrogen production.[3]

Finally, a surprising application of cerium dioxide in nanomedicine has been reported. It was discovered that cerium dioxide nanoparticles can scavenge reactive molecules in the eye and prevent degenerative retinal disorders in rats. The results suggested that nanoceria particles could be used to treat a variety of problems that cause blindness.[4]

4 OTHER LANTHANIDE(IV) SALTS

Pale yellow *cerium(IV) hydroxide* can be prepared by addition of bases, such as aqueous ammonia, to solutions of cerium(IV) salts, e.g., cerium(IV) nitrate or CAN. Nanocrystalline *cerium(IV) hydroxide* (NCs-$Ce(OH)_4$) is an intermediate in the production of cerium dioxide, which has been synthesized successfully using a novel and simple wet chemical route at ambient temperature for the preparation of nanocrystalline CeO_2 powder and films on mass scale for various purposes. The average crystallite size of NCs-$Ce(OH)_4$ has been estimated by the Scherrer equation to be 3–4 nm. Absorption and luminescence spectroscopic studies have been examined for future application in the development of optical devices.[5]

Cerium(IV) nitrate can be crystallized in the form of its pentahydrate, $Ce(NO_3)_4 \cdot 5H_2O$, which presumably contains 11-coordinate $Ce(NO_3)_4(H_2O)_3$ molecules with all four nitrato units acting as chelating ligands as in the corresponding thorium nitrate complex. *Cerium(IV) sulfate*, also called ceric sulfate, is a yellow to yellow–orange commercially available Ce^{4+} compound. It can be prepared by heating of cerium dioxide with concentrated sulfuric acid (Scheme 3).



Scheme 3

Cerium(IV) sulfate exists as the anhydrous salt $Ce(SO_4)_2$, but a few hydrated forms are also known: $Ce(SO_4)_2 \cdot nH_2O$ ($n = 4$, 8, or 12). It is moderately soluble in water and dilute acids. Its neutral solutions slowly decompose, depositing light yellow CeO_2. Solutions of ceric sulfate have an intense yellow color. The tetrahydrate will lose the water when heated to 180–200 °C. The Ce^{4+} ion is a strong oxidizer, especially under acidic conditions. If ceric sulfate is added to dilute hydrochloric acid, then elemental chlorine is formed, albeit slowly. With stronger reducing agents, it reacts much faster. For example, with sulfite in acidic solutions, it reacts quickly and completely. Ceric sulfate is frequently used in analytical chemistry for redox titrations, often together with a redox indicator. Cerium(IV) sulfate is also one of the reagents in the oscillating Belousov–Zhabotinsky reaction. In this reaction mixture consisting of potassium bromate, cerium(IV) sulfate, malonic acid, and citric acid in dilute sulfuric acid, the concentration ratio of the Ce^{4+} and Ce^{3+} ions oscillates, causing the color of the solution to oscillate between yellow and colorless. This is due to the Ce^{4+} ions being reduced by malonic acid to Ce^{3+} ions, which are then oxidized back to Ce^{4+} ions by bromate(V) ions.

Cerium(IV) acetate, $Ce(OAc)_4$, has been synthesized by first heating a solution of $Ce(OAc)_3$ and anhydrous $Ce(NO_3)_3$ in a mixture of glacial acetic acid and acetic anhydride until NO_2 evolution was complete. The resulting solution of $Ce(OAc)_3$ was ozonized at 70 °C to form $Ce(OAc)_4$ in quantitative yield and excellent purity. The presence of nitrate was essential for obtaining such good yield and purity. IR and X-ray diffraction measurements showed that $Ce(OAc)_4$ is isomorphous with $Th(OAc)_4$ and $U(OAc)_4$.[6] *Cerium(IV) trifluoromethanesulfonate* has been prepared by the reaction of cerium(IV) carbonate with trifluoromethanesulfonic acid. The powerful oxidizing ability of this compound was observed in the oxidation of benzyl alcohols and alkylbenzenes.[7] Further cerium(IV) salts include, among others, the hydrated *cerium(IV) chromates* $Ce(CrO_4)_2 \cdot H_2O$ and $Ce(CrO_4)_2 \cdot 2H_2O$. *Cerium(IV) perchlorate* is readily formed by the reaction of cerium(IV) hydroxide with $HClO_4$, but this process is complicated by hydrolysis and partial reduction of Ce^{4+}.

5 COORDINATION COMPOUNDS OF TETRAVALENT LANTHANIDES

With only a few exceptions, the coordination chemistry of rare earth elements in the oxidation state is basically the coordination chemistry of tetravalent cerium.

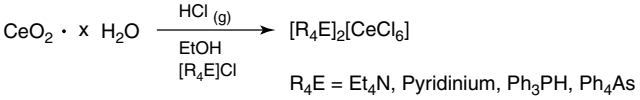
Even then well-characterized coordination compounds are limited to only a few classes of compounds. Notable are, e.g., halogeno complexes and complexes of oxo acids, β-diketonates and related Schiff-base complexes, as well as porphyrinates and related complexes.[1] Two other important classes of cerium(IV) compounds, the alkoxides and amides of Ce^{4+}, can be regarded as ''*pseudo*-organometallics'' and are discussed together with the organocerium(IV) complexes in ***Tetravalent Chemistry: Organometallic***.

5.1 Halogeno Complexes

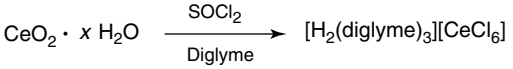
Several halogeno complexes of tetravalent lanthanides are known. For example, the tetrafluorides form three series of fluoro complexes, $[LnF_6]^{2-}$ (e.g., in $K_2[PrF_6]$), $[LnF_7]^{3-}$ (e.g., in $Cs_3[NdF_7]$), and $[LnF_8]^{4-}$ (e.g., in $(NH_4)_4[CeF_8]$). In the case of the fluorocerates(IV), ammonium salts such as $(NH_4)_4[CeF_8]$ (square antiprismatic coordination) and $(NH_4)_3[CeF_7(H_2O)]$ can be isolated by crystallization from aqueous solution. The synthesis of alkali metal derivatives of the types M_2CeF_6 and M_3CeF_7 (M = Na, K, Rb, Cs) requires the use of solid-state methods such as the reaction of CeO_2/MCl mixtures with elemental fluorine.[8] The same is true for the fluoro metallates of other lanthanides in the oxidation state +4, for which the alkali metal fluoro complexes M_2LnF_6 (M = Na, K, Rb, Cs; Ln = Tb, Pr) and Cs_3LnF_7 (Ln = Pr, Nd, Tb, Dy) are known. All these materials can only be prepared by anhydrous solid-state methods such as the fluorination of Ln_2O_3/MCl mixtures using elemental fluorine or fluorination of Cs_3LnCl_6 with XeF_2.[1]

Hexachlorocerates(IV) stabilized by bulky Group 15 cations are easily prepared as shown in Scheme 4 starting with hydrated cerium dioxide.[1] Among these, especially the bright yellow pyridinium salt $(pyH)_2[CeCl_6]$ has frequently been employed as alternative Ce(IV) precursor.[9]

The corresponding hexachloroceric acid has been isolated in the form of its adduct with diglyme (diglyme = diethyleneglycol dimethylether) by treatment of hydrated ceria with thionyl chloride in the presence of diglyme according to Scheme 5.



Scheme 4



Scheme 5

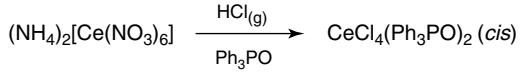
The diglyme-stabilized hexachloroceric acid also served as starting material for a series of stable adducts of cerium(IV) tetrachloride with *O*-donor ligands (Scheme 6). Similar to their uranium(IV) congeners, these complexes adopt an octahedral coordination geometry with the *O*-donor ligands arranged in the *trans*-positions.

In contrast, the closely related bis(triphenylphosphine oxide) adduct comprises the *cis*-configuration. This compound was prepared according to Scheme 7.

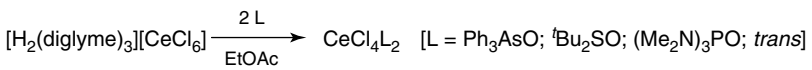
While pure cerium(IV) tetrahalides other than CeF_4 have never been isolated, it has been possible to convert hexachlorocerates (*cf.* Scheme 4) into the homologous salts containing the $[CeBr_6]^{2-}$ anion. These purple hexabromocerates(IV) can be prepared by treatment of the hexachloro precursors with gaseous HBr. It was not possible to make the corresponding hexaiodocerates(IV), most likely due to internal redox reactions.

5.2 Complexes of Oxo Acids

Ceric ammonium nitrate, $(NH_4)_2[Ce(NO_3)_6]$ (= CAN), is perhaps the most common Ce^{4+} precursor. This bright orange, water-soluble salt is widely used as a standard oxidant in quantitative analysis as well as an oxidizing agent in organic synthesis. The hexanitratocerate anion forms directly upon dissolution of cerium(III) oxide in nitric acid. Thus CAN can be prepared by dissolving Ce_2O_3 in hot concentrated nitric acid, followed by precipitation with ammonia. In the hexanitratocerate(IV) anion, the bite angle of the nitrato ligands is so small that they can all act as bidentate ligands, giving rise to an icosahedral coordination geometry (coordination number 12) around cerium.[10] Starting from CAN, some 10-coordinate neutral nitrato complexes containing additional *O*-donor ligands have been prepared, such as the bis(triphenylphosphine oxide) derivative shown in Scheme 8.



Scheme 7



Scheme 6

$$(NH_4)_2[Ce(NO_3)_6] \xrightarrow[Me_2CO]{Ph_3PO} Ce(NO_3)_4(Ph_3PO)_2\ (trans)$$

Scheme 8

CAN also served as a useful precursor for the synthesis of cerium(IV) alkoxides and mixed-ligand alkoxide/nitrato complexes.[11] Practical applications include its use as a component of chrome etchant, a material that is used in the production of liquid crystal displays and photomasks. The most important and versatile applications of CAN, however, are those in organic synthesis, where it is used as a strong oxidizing agent, as catalyst in the synthesis of heterocycles (e.g., quinolines, quinoxalines), and as a deprotection agent.

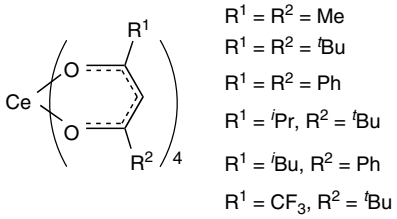
Ceric ammonium sulfate, $(NH_4)_2[Ce(SO_4)_3]$, is frequently used as a safe and nontoxic oxidizing agent in redox titrations (color change from orange Ce^{4+} to colorless Ce^{3+}). Monohydrated *ceric ammonium phosphate*, $(NH_4)_2[Ce(PO_4)_2]\cdot H_2O$, was hydrothermally synthesized from the system $NH_3/CeO_2/H_3PO_4$ and characterized by powder X-ray diffraction and various other analytical techniques.[12] Several interesting complexes containing the bis-μ-peroxo-hexacarbonatodicerate(IV) anion, $[(CO_3)_3Ce(\mu\text{-}O_2)_2Ce(CO_3)_3]^{8-}$, have been isolated and structurally characterized. Examples include $K_2Na_6[(CO_3)_3Ce(\mu\text{-}O_2)_2Ce(CO_3)_3]\cdot 13H_2O$, $Rb_8[(CO_3)_3Ce(\mu\text{-}O_2)_2Ce(CO_3)_3]\cdot 12H_2O$, and $Cs_8[(CO_3)_3Ce(\mu\text{-}O_2)_2Ce(CO_3)_3]\cdot 10H_2O$.[13,14] A $Ce(\mu\text{-}O_2)_2Ce$ unit with bridging, doubly bidentate peroxy groups has also been found in the the *N*, *N*, *N*′, *N*′-ethylenediaminetetraacetato (= EDTA) derivative $Na_2K_2[(EDTA)Ce(\mu\text{-}O_2)_2Ce(EDTA)]$.[13]

5.3 Cerium(IV) β-Diketonates and Related Complexes

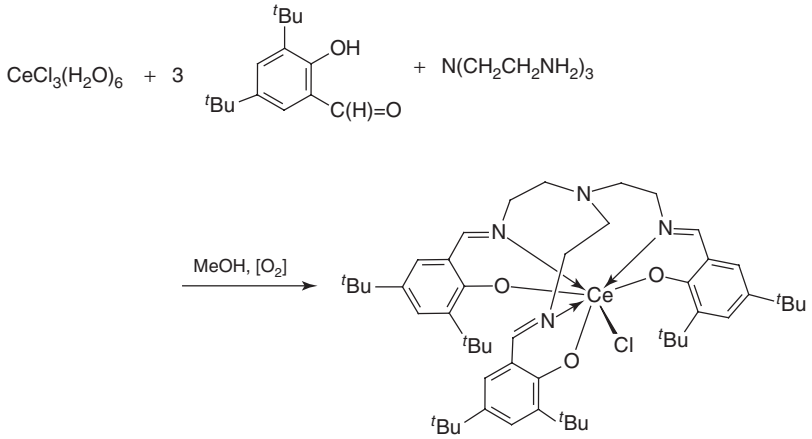
Homoleptic β-diketonate complexes of tetravalent cerium, $Ce[R^1C(O)CHC(O)R^2]_4$, are easily accessible and form a well-investigated class of cerium(IV) complexes.[15,16] Scheme 9 lists a small selection of known complexes of this type.

Most remarkably, the corresponding homoleptic β-diketonate complexes of trivalent cerium, $Ce[R^1C(O)CHC(O)R^2]_3$, tend to be readily oxidized in the presence of air. Thus a typical synthetic procedure for preparing the more stable Ce^{4+} derivatives involves the reaction of the Na salt of the diketonate with $Ce(NO_3)_3\cdot 6H_2O$ in aqueous EtOH solution. When the reaction is carried out in air, oxidation will easily take place and the cerium(IV) product is formed directly. Alternatively, the cerium(IV) precursor $(NH_4)_2[Ce(NO_3)_6]$ (= CAN) can be treated with the sodium β-diketonate in ethanol. The homoleptic $Ce[R^1C(O)CHC(O)R^2]_4$ complexes form dark red or purple crystalline solids, which are soluble in organic solvents such as toluene or CH_2Cl_2. The coordination geometry around cerium is in most cases square antiprismatic, but distorted dodecahedral and distorted bicapped trigonal prismatic geometries have also occasionally been found.[15,16]

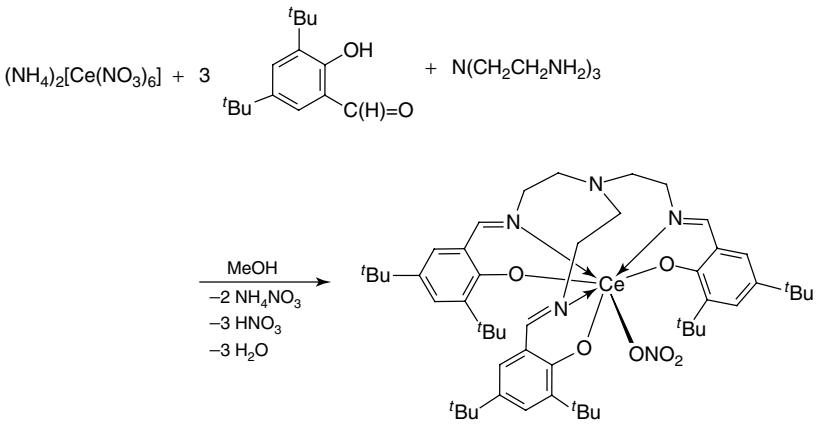
Mixed-ligand complexes containing chelating β-diketonate ligands are also known. For example, $Ce(OPPh_3)_2(TTA)_2(NO_3)_2$ (HTTA = thenoyltrifluoroacetone) has been prepared from $Ce(OPPh_3)_2(NO_3)_4$ (*cf.* Scheme 6) and HTTA. Owing to their relatively high volatility, homoleptic cerium(IV) tetrakis(β-diketonates) have been successfully



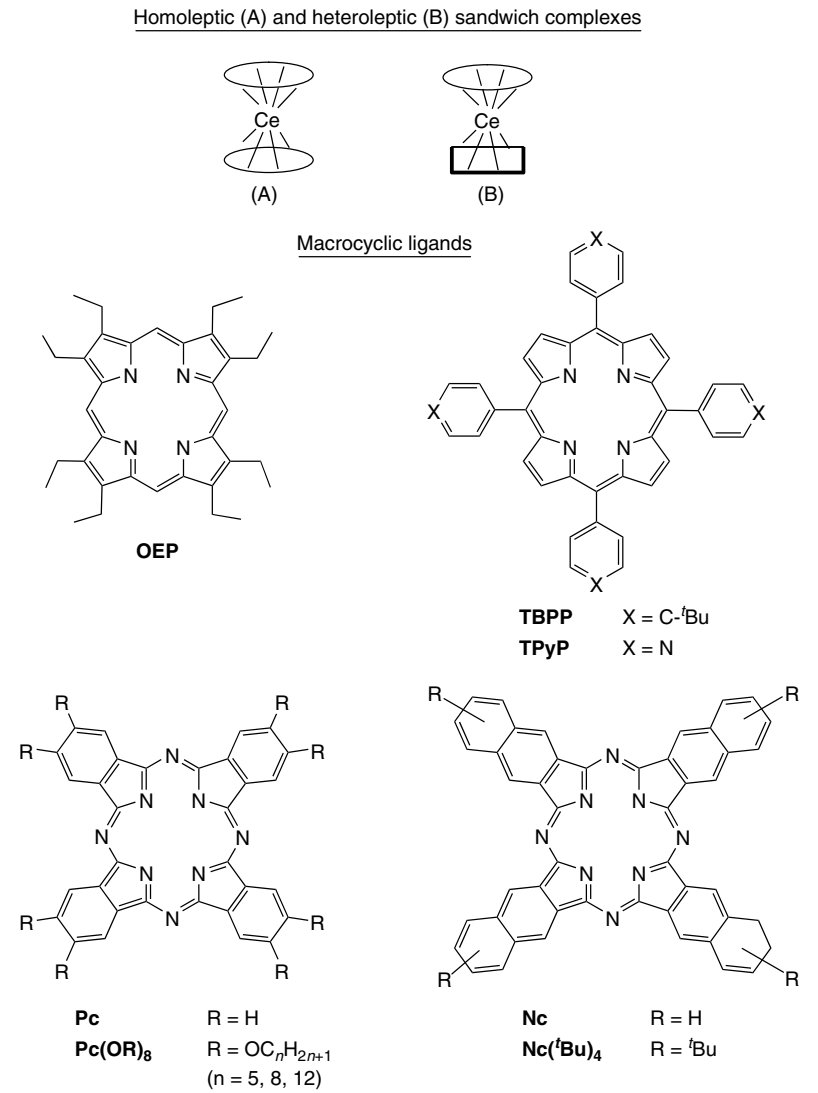
Scheme 9



Scheme 10



Scheme 11



Scheme 12

employed as molecular precursors for the MOCVD (= metal-organic chemical vapor deposition) production of pure CeO_2 and yttria-doped CeO_2 thin films.[17,18]

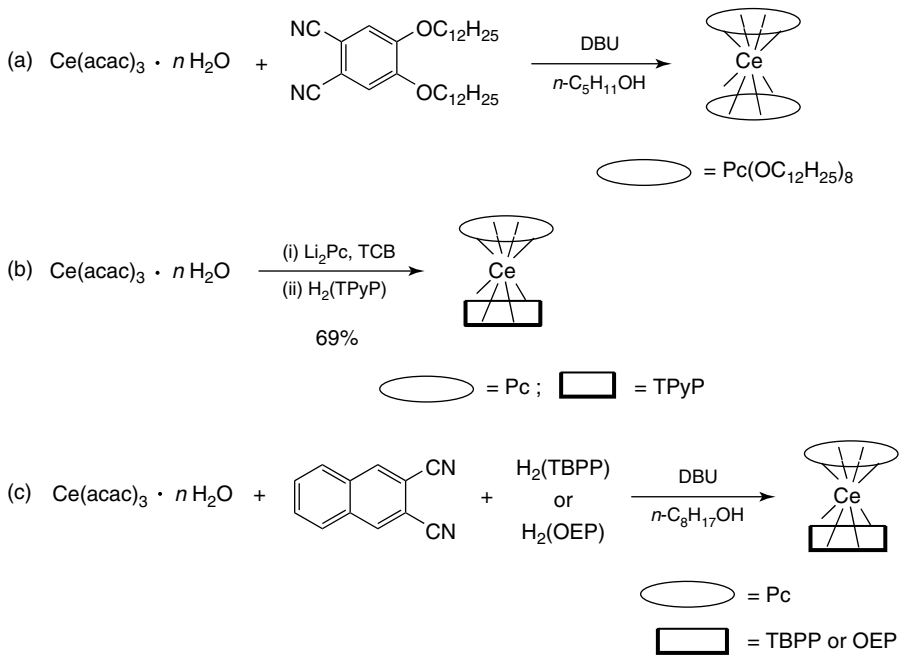
Recently, the very bulky tripodal Schiff-base ligand $N[CH_2CH_2N{=}CH(C_6H_2{}^tBu_2\text{-}3,5\text{-}OH\text{-}2]_3$ (= H_3TRENDSAL) has also been found to form very stable complexes with tetravalent cerium. As with the β-diketonates, it was found that the cerium(III) derivative Ce(TRENDSAL) is quite air sensitive. Thus a straightforward preparation of the cerium(IV) chloro derivative involves treatment of hydrated cerium trichloride with the *in situ*-prepared ligand in the presence of oxygen as illustrated in Scheme 10.[19] Halide abstraction from (TRENDSAL)CeCl upon reaction with $Na[BPh_4]$ in acetonitrile afforded the first cationic complex of tetravalent cerium, $[Ce(TRENDSAL)][BPh_4]$, which was isolated as a black, crystalline solid.[20]

The use of ceric ammonium nitrate (= CAN) as precursor allowed the synthesis of the corresponding nitrato complex according to Scheme 11.[19]

5.4 Cerium(IV) Sandwich Complexes with Tetrapyrrole-Type Ligands

Formally, tetravalent cerium is long known to form stable sandwich complexes with tetrapyrrole-type macrocyclic ligands such as porphyrines, phthalocyanines, and 2,3,-naphthalocyanines (Scheme 12).[21–23] For the rare earth sandwich complex series, virtually all the neutral complexes can be formulated as Ln^{III}(ring-1^{2-}) (ring-$2^{\bullet-}$), in which a trivalent rare earth metal center is sandwiched between a dianionic macrocycle and a radical anionic ligand, having different extent of electron delocalization. Among the entire lanthanide series, cerium is the only exception. Having an electronic configuration of $[Xe]4f^15d^16s^2$, cerium may also utilize the electron in the extended 4f orbital, leading to predominantly tetravalent neutral sandwich complexes.

Several synthetic methods have been established for the preparation of cerium sandwich complexes. Scheme 13 illustrates some typical preparations. For example, the homoleptic bis(phthalocyaninato) complex $Ce[Pc(OC_{12}H_{25})_8]_2$ was prepared by treatment of $Ce(acac)_3{\cdot}nH_2O$ with 4,5-bis(dodecyloxy)phthalonitrile in the presence of 1,8-diazabicyclo[5.4.0]undec-7-ene (DBU) (Scheme 13a). This represents a general procedure which has been employed previously to prepare the pentyloxy $Ce[Pc(OC_5H_{11})_8]_2$ and octyloxy $Ce[Pc(OC_8H_{17})_8]_2$ analogs as well as other bis(phthalocyaninato) rare earth complexes. The bis(naphthalocyaninato) analogs $Ln[Nc(^tBu)_4]_2$ (Ln = La, Ce, Pr, Nd, Eu, Gd, Tb, Y, Er) have also been synthesized in a similar manner using 6-*tert*-butylnaphthalonitrile as the starting material. The yield of the cerium sandwich complex $Ce[Nc(^tBu)_4]_2$ (71%) was much higher than those of the phthalocyanine counterparts mentioned above (9–49%), following the trend observed for the $Ln[Nc(^tBu)_4]_2$ series, the yield of which decreases gradually with decreasing the size of the metal center.[23] Neutral cerium(IV) sandwich complexes can also be obtained by deliberate oxidation of the anionic cerium(III) precursors. For example, anodic or chemical oxidation with dibenzoylperoxide of solutions of bis(phthalocyaninato)cerate(III) in dichloromethane yielded selectively the sparingly soluble



Scheme 13

bis(phthalocyaninato)cerium(IV), $Ce(Pc)_2$ as green, needle-like crystals. $Ce(Pc)_2$ is a sandwich complex in which the cerium atom is eight-coordinated by the isoindole nitrogens of the two staggered convex Pc-rings.[22]

The mixed-ring double-decker Ce(Pc)(TPyP) was prepared by a stepwise procedure as shown in Scheme 13b. Reaction of $Ce(acac)_3 \cdot nH_2O$ with Li_2Pc in 1,2,4-trichlorobenzene (TCB) followed by the addition of H_2(TPyP) led to Ce(Pc)(TPyP) in 69% yield together with a substantial amount of the tripledeckers $Ce_2(Pc)(TPyP)_2$ and $Ce_2(Pc)_2(TPyP)$. This procedure is one of the most common synthetic methods to prepare mixed double-deckers M(Pc)(Por). By using a convenient one-pot procedure, the mixed sandwich complexes Ce(Nc)(TBPP) and Ce(Nc)(OEP) were also synthesized. As shown in Scheme 13c, treatment of $Ce(acac)_3 \cdot nH_2O$ with the corresponding metal-free porphyrin and naphthalonitrile in the presence of DBU in *n*-octanol afforded these complexes in ~20% yield. It has been found that the cerium sandwich complexes always show different electronic absorption and electrochemical properties from the whole series of tetravalent rare earth analogs. To resolve and clarify this issue, a series of cerium double-deckers using a range of tetrapyrrole ligands with different electronic properties have been synthesized according to Scheme 13 and studied systematically with respect to their electrochemical and spectroscopic properties. The results showed that the oxidation state of the cerium center varies from +3 to +4 depending on the electronic nature of the two tetrapyrrole ligands. As revealed by X-ray absorption near-edge structure (XANES) study, the valence of the cerium center is 3.59 for $Ce[Pc(OC_5H_{11})_8]_2$ and 3.68 for Ce(Pc)(TPyP) [TPyP = *meso*-tetra(4-pyridyl)porphyrinate] and Ce(Nc)(OEP), while that in $Ce[Nc(^tBu)_4]_2$ is virtually 3.[23]

6 CONCLUSIONS AND FUTURE OUTLOOK

The chemistry of tetravalent lanthanide compounds is mainly restricted to cerium. Perhaps the most important material in this field is cerium dioxide (ceria), especially in the form of nanoparticles. Coordination compounds of cerium in the oxidation state +4 include halogeno complexes and complexes of oxo acids, β-diketonates and related Schiff-base complexes as well as porphyrinates and related complexes. An extension of this chemistry to nonclassical tetravalent lanthanide ions such as Pr^{4+}, Nd^{4+}, Tb^{4+}, or Dy^{4+} certainly presents one of the major challenges for future work in this area.

7 ABBREVIATIONS AND ACRONYMS

CAN = ceric ammonium nitrate; IR = infrared; SOFCs = solid oxide fuel cells; XANES = X-ray absorption near-edge structure.

8 REFERENCES

1. S. Cotton, 'Lanthanide and Actinide Chemistry', John Wiley & Sons, Ltd., Chichester, 2006.
2. S. Deshpande, S. Patil, S. Kuchibatla, and S. Seal, *Appl. Phys. Lett.*, 2005, **87**, 133113/1.
3. S. Abanades and G. Flamant, *Solar Energy*, 2006, **80**, 1611.
4. G. A. Silva, *Nat. Nanotechnol.*, 2006, **1**, 92.
5. A. A. Ansari and A. Kaushik, *J. Semicond.*, 2010, **31**, 033001/1.
6. N. E. Hay and J. K. Kochi, *J. Inorg. Nucl. Chem.*, 1968, **30**, 884.
7. T. Imamoto, Y. Koide, and S. Hiyama, *Chem. Lett.*, 1990, **19**, 1445.
8. Z. Hu, G. Kaindl, and B. G. Müller, *J. Alloys Compd.*, 1997, **246**, 177.
9. K. Jacob and K.-H. Thiele, *Z. Anorg. Allg. Chem.*, 1986, **536**, 147.
10. T. A. Beineke and J. Delgaudion, *Inorg. Chem.*, 1968, **7**, 715.
11. W. J. Evans, T. J. Deeming, J. M. Olofson., and J. W. Ziller, *Inorg. Chem.*, 1989, **28**, 4027.
12. Y. Xu, S. Feng, W. Pang, and G. Pang, *Chem. Commun.*, 1996, 1305.
13. J. C. Barnes, C. S. Blyth, J. D. Paton, and I. G. B. Smith, *Lanth. Actin. Res.*, 1990, **3**, 181.
14. N.-P. Pook and A. Adam, *Cryst. Res. Technol.*, 2008, **43**, 1197.
15. M. Ciampolini, F. Mani, and N. Nardi, *J. Chem. Soc., Dalton Trans.*, 1977, 1325.
16. M. J. Delarosa, K. S. Bousman, J. T. Welch, and P. J. Toscano, *J. Coord. Chem.*, 2002, **55**, 781.
17. M. Becht, T. Gerfin, and K. H. Dahmen, *Chem. Mater.*, 1993, **5**, 137.
18. M. Pan, G. Y. Meng, H. W. Xin, C. S. Chen, D. K. Peng, and Y. S. Lin, *Thin Solid Films*, 1998, **324**, 89.
19. P. Dröse and J. Gottfriedsen, *Z. Anorg. Allg. Chem.*, 2008, **634**, 87.
20. P. Dröse, J. Gottfriedsen, C. G. Hrib, P. G. Jones, and F. T. Edelmann, *Z. Anorg. Allg. Chem.*, 2011, **637**, 369.
21. J. W. Buchler, A. De Cian, J. Fischer, M. Kihn-Botulinski, H. Paulus, and R. Weiss, *J. Am. Chem. Soc.*, 1986, **108**, 3652.
22. J. Jiang and D. K. P. Ng, *Acc. Chem. Res.*, 2009, **42**, 79.
23. Y. Bian, J. Jiang, Y. Tao, M. T. M. Choi, R. Li, A. C. H. Ng, P. Zhu, N. Pan, X. Sun, D. P. Arnold, Z.-Y. Zhou, H.-W. Li, T. C. W. Mak, and D. K. P. Ng, *J. Am. Chem. Soc.*, 2003, **125**, 12257.

Tetravalent Chemistry: Organometallic

Farid M.A. Sroor and Frank T. Edelmann

Chemisches Institut der Otto-von-Guericke-Universität Magdeburg, Magdeburg, Germany

1	Summary	321
2	Introduction	321
3	Alkoxides	322
4	Amides	325
5	Amidinates	327
6	Cyclopentadienyl Complexes	328
7	Carbene Complexes	329
8	Cerocenes	330
9	Conclusions and Future Outlook	332
10	Glossary	333
11	Abbreviations and Acronyms	333
12	References	333

1 SUMMARY

The synthesis and full characterization of organolanthanide(IV) complexes are very difficult and often an unpredictable task. Thus far, organolanthanide chemistry in the oxidation state +4 remains entirely limited to cerium. This can be traced back to the very highly positive normal potentials of the other tetravalent lanthanide ions Pr^{4+}, Nd^{4+}, Tb^{4+}, and Dy^{4+} (e.g., Pr: +2.86 V) which make them very strong oxidizing agents. Not even well-defined ''pseudo-organometallics'' (i.e., alkoxides, amides, and related compounds) of tetravalent lanthanide ions other than Ce^{4+} have ever been isolated. Only the alkoxides and amides of tetravalent cerium form fairly well-investigated classes of compounds. In contrast, true organocerium(IV) containing Ce–C bonds remain scarce. The oldest compounds of this type are cerocene and its derivatives. The chemistry of cerium(IV) complexes containing *N*-heterocyclic carbene ligands is just emerging, and even cyclopentadienyl complexes of the type Cp_3CeX (X = Cl, OR) are limited to a handful of compounds.

2 INTRODUCTION

Organometallic chemistry of the lanthanide elements in the oxidation state +4 basically means organocerium(IV) chemistry, as no organometallic compounds have ever been synthesized for other Ln^{4+} ions. Among the tetravalent rare earth metal ions, only Ce^{4+} is readily available in aqueous solution (E Ce^{3+}/Ce^{4+} = +1.44 V in 2M H_2SO_4, 1.61 V in 1M HNO_3, 1.70 V in 1M $HClO_4$). The different values for the reported reduction potentials indicate that stable complexes are formed in these acidic media. Thermodynamically, oxidation of water by the hydrated Ce^{4+} ion should be possible, but the system is kinetically stable. In contrast, the much more positive normal potentials of the other tetravalent lanthanide ions Pr^{4+}, Nd^{4+}, Tb^{4+}, and Dy^{4+} (e.g., Pr: +2.86 V) make them very strong oxidizing agents which readily decompose water under evolution of O_2. This is the main reason why no organometallic compounds have ever been reported for lanthanide(IV) ions other than Ce^{4+}. In this chapter, we discuss not only ''real'' organocerium(IV) compounds, i.e., those containing direct Ce–C bonds but also several classes of *pseudo*-organometallics, which resemble true organolanthanide complexes in their solubility in organic solvents and/or enhanced volatility. In particular, these include the alkoxides, siloxides, amides, and amidinates of tetravalent cerium. Thus organocerium(IV) complexes can be divided into three classes of compounds: cyclopentadienyl complexes, complexes containing *N*-heterocyclic carbene ligands, and cerocenes, i.e., bis(cyclooctatetraenyl) sandwich complexes.

The Rare Earth Elements. Edited by David A. Atwood. © 2012 John Wiley & Sons, Ltd. ISBN 978-1-119-95097-4

$$(NH_4)_2Ce(NO_3)_6 + 4\ ROH + 6\ NaOMe \longrightarrow Ce(OR)_4 + 2\ NH_3 + 6\ NaNO_3 + 6\ MeOH$$

Scheme 1

$$(NH_4)_2[Ce(NO_3)_6] + n\ NaO^tBu \xrightarrow[n = 2\text{–}6]{THF} (^tBuO)_{n-2}Ce(NO_3)_{6-n}(THF)_2 + 2\ NH_3 + n\ NaNO_3 + 2\ HO^tBu$$

Scheme 2

3 ALKOXIDES

Tetraalkoxides of cerium form a long known and well-established class of lanthanide(IV) compounds which can be considered as pseudo-organometallic. The effect of difference in both size and charge should favor the formation of monomeric Ce(IV) alkoxides rather than their trivalent analogs. Ce^{4+} is smaller than Ce^{3+} (0.87 Å vs 1.01 Å effective ionic radii for six-coordination according to Shannon[1]) and can accommodate four alkoxide ligands as counterions. In addition, ''hard'' ligands such as the alkoxide ligands should stabilize the high oxidation state Ce^{4+}. Lanthanide alkoxides have been widely used as molecular precursors in materials science. Although Ce(IV) alkoxides have been known for many years, their preparation was often laborious and time consuming,[2] until the readily available and inexpensive tetravalent cerium reagent, ceric ammonium nitrate $(NH_4)_2[Ce(NO_3)_6]$ (= CAN), was utilized for their synthesis. Scheme 1 illustrates how CAN can be successfully employed as starting material for the preparation of homoleptic cerium(IV) alkoxides.[3]

Not only can the homoleptic tetraalkoxides be made using this synthetic approach but also a range of Ce^{4+} nitrate, mixed nitrate alkoxide, and alkoxide complexes have become available by careful control of the reaction stoichiometry. Scheme 2 illustrates this approach. The low costs of the starting materials and control of the functionalities present rendered this method an appealing route into further Ce^{4+} chemistry.[3]

Another access to cerium(IV) tetraalkoxides involves treatment of the readily available hexachlorocerate(IV) precursor with 4 equiv. of an appropriate alcohol followed by reaction with ammonia (Scheme 3).[2]

There is also one interesting report about Ce^{4+} alkoxides being formed via controlled oxidation reaction of cerium(III) alkoxide precursors, e.g., by reactions of cerium(III) tris[tri(*tert*-butyl)methoxide] with either an organic peroxide or benzoquinone. For example, treatment of $Ce(OC^tBu_3)_3$ with dibenzoylperoxide according to Scheme 4 afforded a mixed cerium(IV) alkoxide carboxylate, which was, however, stable only in solution and decomposed to cerium(III) species when the reaction was carried out on a preparative scale.[4]

Inherent instability was also observed for the mixed alkoxide derivative $Ce(OC^tBu_3)_2(O^tBu)_2$ which could be generated by treatment of $Ce(OC^tBu_3)_3$ with 2 equiv. of di-*tert*-butyl peroxide (Scheme 5). The mixed cerium(IV) alkoxide decomposed on attempted isolation under formation of the dimeric cerium(III) alkoxide product $[Ce(OC^tBu_3)_2(O^tBu)]_2$, highlighting the potential instability of the Ce^{4+} state in these cases.[4]

The titration of $Ce(OC^tBu_3)_3$ with benzoquinone was the cleanest and most easily characterized oxidation of

$$(pyH)_2[CeCl_6] + 4\ ROH + 6\ NH_3 \longrightarrow Ce(OR)_4 + 2\ py + 6\ NH_4Cl$$

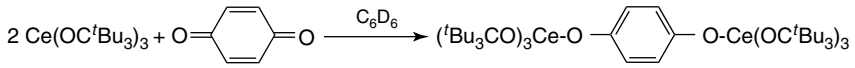
Scheme 3

$$2\ Ce(OC^tBu_3)_3 + PhC(O)OOC(O)Ph \xrightarrow[25\ ^\circ C]{C_6D_6} 2\ Ce(OC^tBu_3)_3[O\ C(O)Ph]$$

Scheme 4

$$Ce(OC^tBu_3)_3 + 2\ ^tBuOO^tBu \xrightarrow{C_6H_6} Ce(OC^tBu_3)_2(O^tBu)_2 + [^tBu_3COOC^tBu_3]$$

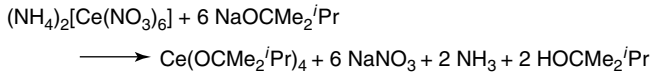
Scheme 5



Scheme 6

any in this study. The stoichiometry and nuclear magnetic resonance (NMR) spectra were consistent with formation of a binuclear complex bridged by a hydroquinonediolate as shown in Scheme 6. The resultant complex was somewhat less soluble than the starting alkoxide and precipitated from solution as single, well-formed, medium-brown plates suitable for X-ray diffraction. The crystals, once isolated, gave back purple solutions in C_6D_6 that yielded the same NMR data as seen in the titration.[4]

Simple homoleptic cerium(IV) tetraalkoxides normally comprise oligomeric structures in the solid state. Lower aggregates are formed upon adduct formation with *O*-donor ligands.[2] For example, the tetra(isopropoxide) forms a dinuclear adduct with propan-2-ol. In the dimer $Ce_2(O^iPr)_8(HO^iPr_2)_2$, each cerium is octahedrally coordinated. Thermolysis of $Ce_2(O^iPr)_8(HO^iPr_2)_2$ afforded the tetranuclear oxo-cluster $Ce_4(\mu_4\text{-}O)(\mu_3\text{-}O^iPr_2)_2(\mu\text{-}O^iPr)_8(O^iPr_3)_{14}$. Owing to their oligomeric structures, most of the homoleptic cerium(IV) tetraalkoxides are nonvolatile and do not sublime without decomposition. A notable exception is the tetraisopropoxide, which can be sublimed under vacuum at ~200 °C. The cerium(IV) alkoxide complex $Ce(OCMe_2{}^iPr)_4$, a volatile, nonfluorinated source of cerium, was used as a chemical vapor deposition (CVD) precursor to cerium oxide films. This complex was prepared according to Scheme 7 and isolated as a yellow liquid on a multigram scale in 50–60% yield after vacuum distillation.[5]



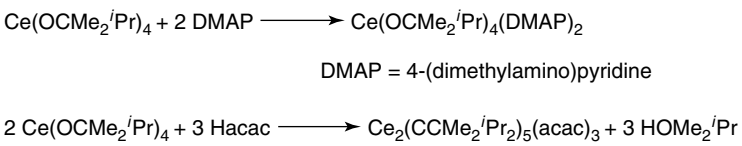
Scheme 7

A conventional thermal CVD process deposited cerium(IV) oxide films from $Ce(OCMe_2{}^iPr)_4$ on silicon, glass, quartz, lanthanum aluminum oxide (001), and nickel (001) substrates at low substrate temperatures (<550 °C). The films were highly oriented when the depositions were carried out on lanthanum aluminum oxide and textured nickel substrates. An X-ray crystallographic study of $Ce(OCMe_2^iPr)_4$, which melts at just below room temperature, shows that it is a loosely bound dimer in the solid state with five-coordinate cerium centers and two bridging alkoxide ligands. The synthesis and X-ray crystal structures of $Ce(OCMe_2{}^iPr)_4(DMAP)_2$ (DMAP = 4-(dimethylamino)pyridine) and $Ce_2(OCMe_2{}^iPr)_5(acac)_3$ have also been reported (Scheme 8). The cerium atoms in $Ce(OCMe_2{}^iPr)_4(DMAP)_2$ and $Ce_2(OCMe_2{}^iPr)_5(acac)_3$ have, respectively, distorted octahedral and pentagonal bipyramidal coordination geometries.[5]

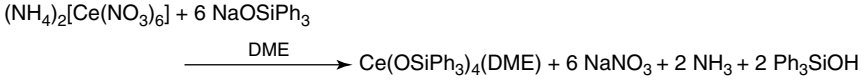
The same synthetic route starting with CAN as precursor has been employed for the preparation of the first homoleptic triorganosiloxides of tetravalent cerium. The reaction shown in Scheme 9 proceeded in the way that gas (NH_3) evolved, a white precipitate ($NaNO_3$) formed, and the product was isolated in about 70% yield as a light yellow powder. The reaction was carried out in DME to facilitate isolation of the product as the DME adduct, $Ce(OSiPh_3)_4(DME)$, and the product was identical with the crystallographically characterized product isolated by reaction of Ph_3SiOH with $Ce(O^iPr)_4$.[6]

The same preparative route also allowed the synthesis of the corresponding cerium(IV) tetrakis(triethylsiloxide) (Scheme 10). This compound was isolated as a yellow-brown powder in 83% yield.[6]

Quite in contrast to the alkoxides and simple siloxides, related disiloxanediolate complexes of cerium(IV) form spontaneously upon treatment of cerium(III) precursors with



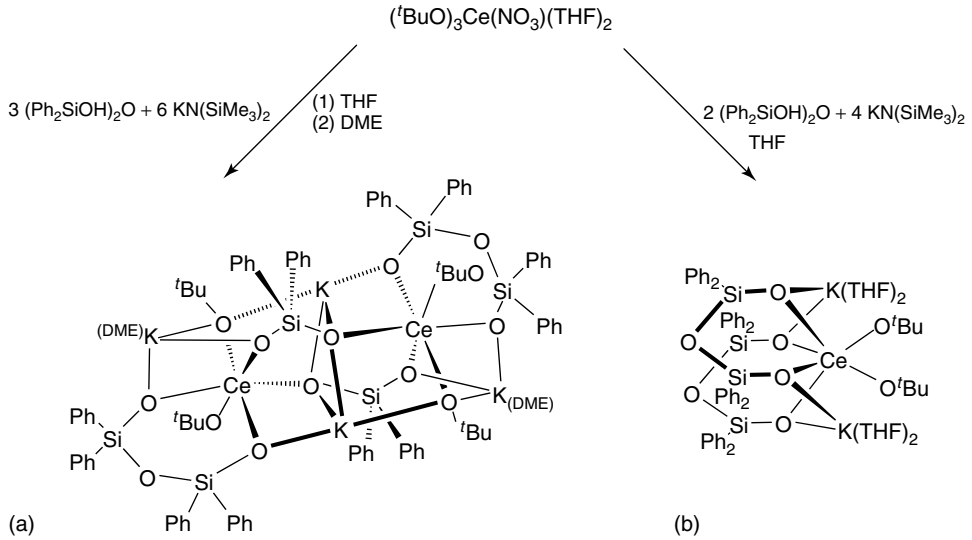
Scheme 8



Scheme 9

$$(NH_4)_2[Ce(NO_3)_6] + 6\ NaOSiEt_3 \xrightarrow{CH_3CN} Ce(OSiEt_3)_4 + 6\ NaNO_3 + 2\ NH_3 + 2\ Et_3SiOH$$

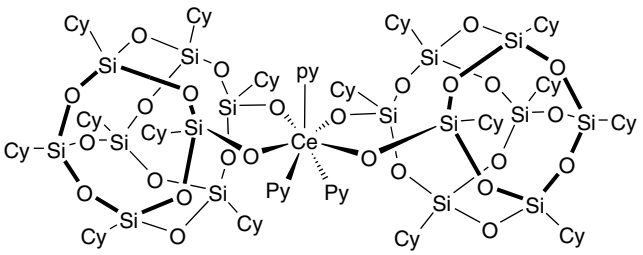
Scheme 10



Scheme 11

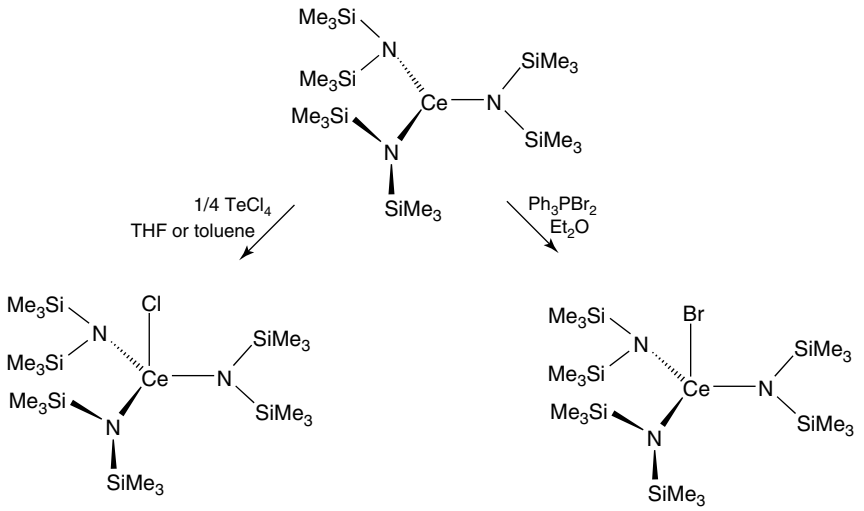
1,1,3,3-tetraphenyl disiloxanediol (Scheme 11). As a suitable cerium(IV) precursor, the readily available alkoxide nitrate complex $(^t BuO)_3Ce(NO_3)(THF)_2$ was chosen and treated with $(Ph_2SiOK)_2O$ (made *in situ* by deprotonation of 1,1,3,3-tetraphenyl-1,3-disiloxanediol with $KN(SiMe_3)_2$) in a molar ratio of 1 : 2 according to Scheme 11b. From this reaction, the novel heterobimetallic potassium/cerium(IV) disiloxanediolate complex $[\{(Ph_2SiO)_2O\}\{K(THF)_2\}]_2Ce(O^tBu)_2$ was isolated in the form of yellow, block-shaped crystals in 81% yield. Its structure was studied by single-crystal X-ray diffraction.[7]

The same reaction carried out in a molar ratio of 1 : 3 took a completely different course (Scheme 11a). In this case, a light yellow compound could be isolated in high yield (70%), which was shown by X-ray crystallography to be the novel heterobinuclear potassium/cerium(IV) disiloxanediolate cluster $[\{(Ph_2SiO)_2O\}_2\{(DME)KO^tBu\}\{(Ph_2SiO_2)K\}Ce]_2$. The X-ray study revealed that in this compound not only the expected dianions of 1,1,3,3-tetraphenyl-1,3-disiloxanediol act as ligands but also the dianions of diphenyl-1,1-silanediol, which originate from cleavage of the disiloxanediolate. Such transformations are not uncommon in the chemistry of silanediolates, disiloxanediolates, and trisiloxanediolates.[7]



Scheme 12

In a similar manner, the isolation of an unprecedented cerium(IV) silsesquioxane complex (Scheme 12) has been achieved. Treatment of $Ce[N(SiMe_3)_2]_3$ with 2 equiv. of the incompletely condensed silsesquioxane disilanol derivative $Cy_8Si_8O_{11}(OH)_2$ in diethyl ether in the presence of an excess of pyridine exclusively afforded the diamagnetic complex $(Cy_8Si_8O_{13})_2Ce(py)_3$. The same compound, albeit in somewhat lower yield, could also be prepared by direct reaction of anhydrous $CeCl_3$ with 2 equiv. of $Cy_8Si_8O_{11}(OH)_2$ in THF/pyridine mixture. Quite surprisingly in both cases, cerium was quantitatively oxidized to the tetravalent oxidation state. An X-ray diffraction study revealed the presence of the first example of a metallasilsesquioxane derived from the octameric disilanol ligand $[(c\text{-}C_6H_{11})_8Si_8O_{13}]^{2-}$. The central Ce atom is coordinated by four oxygen atoms of two siloxane ligands and three nitrogens of three pyridine molecules resulting in a distorted pentagonal bipyramidal arrangement.[8]



Scheme 13

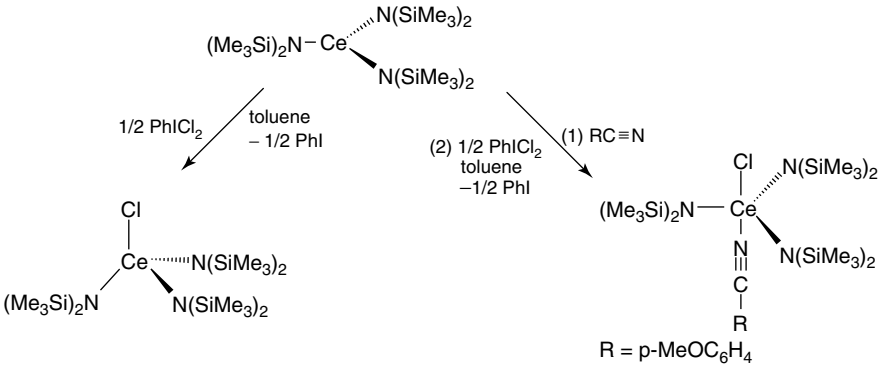
4 AMIDES

Amido complexes were among the first pseudo-organometallic compounds of tetravalent cerium to be reported in the literature. In the course of the synthesis of the first tri-coordinate tris(amido)lanthanides in 1972, it had been noted that the yellow $Ce[N(SiMe_3)_2]_3$ was readily oxidized by minute traces of air as evident by a formation of a brown material on the surface of the yellow crystals.[9] $Ce[N(SiMe_3)_2]_3$ was by far the most air-sensitive compound in the entire series of $Ln[N(SiMe_3)_2]_3$ derivatives. Thus this compound appeared to be a logical choice as starting material for the synthesis of cerium(IV) silylamido complexes. However, various oxidizing agents including elemental chlorine or bromine only led to the formation of decomposition products. The list of other failed alternative oxidants that have been compiled for this cerium amide is quite lengthy: I_2, *N*-bromosuccinimide, *N*-chlorosuccinimide, $AgBF_4$, AgCN, $Hg(C_6F_5)_2$, $PbCl_2$, and $^tBuOO^tBu$ were all tried and in all cases only unreacted $Ce[N(SiMe_3)_2]_3$ was recovered. Only the use of the uncommon reagent $TeCl_4$ allowed for the first time, the isolation of $[(Me_3Si)_2N]_3CeCl$. It furnished well-formed purple/black needles, although the workup procedure had to be carried out rapidly as delays resulted in the deposition of colorless blocks of $[Ce\{N(SiMe_3)_2\}_2(\mu\text{-Cl})(THF)]_2$ as a by-product in significant amounts. The analogous bromo-derivative $[(Me_3Si)_2N]_3CeBr$ was made by treatment of the cerium(III) silylamide with Ph_3PBr_2 (Scheme 13).[10,11]

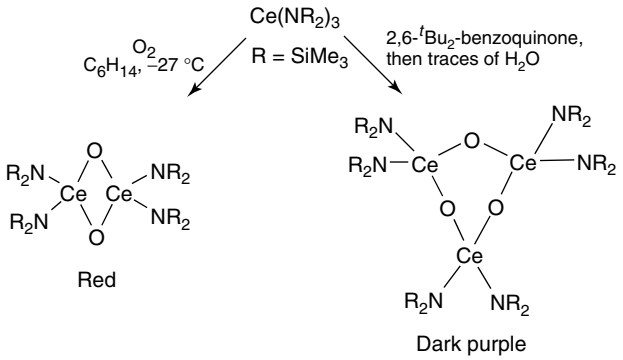
Most recently, it has been reported that phenyliodine(III) dichloride, $PhICl_2$, can be successfully employed as an innovative and superior reagent for the one-electron oxidation of cerium(III) precursors. The hypervalent organoiodine(III) compound $PhICl_2$ has several significant advantages: (i) it is readily accessible from inexpensive, commercially available starting materials; (ii) solid $PhICl_2$ can easily be employed in exact stoichiometric amounts; and (iii) liquid, highly soluble, and volatile iodobenzene is the only iodine-containing by-product. All these assumptions could be verified by a test reaction with the silylamide $Ce[N(SiMe_3)_2]_3$. Treatment of a toluene solution of $Ce[N(SiMe_3)_2]_3$ with the calculated amount of $PhICl_2$ in toluene (Scheme 14) resulted in an immediate color change from orange to purple. Pure $[(Me_3Si)_2N]_3CeCl$ could be isolated in 10% yield in a very simple manner by crystallization from the concentrated reaction mixture at $-20\,^\circ C$. The organoiodine(III) route could be also utilized to access novel five-coordinate cerium(IV) amido species. Dark red-brown $[(Me_3Si)_2N]_3CeCl(N{\equiv}CC_6H_4OMe\text{-}p)$ was isolated in 45% yield by adding *p*-anisonitrile to a toluene solution of $Ce[N(SiMe_3)_2]_3$ prior to treatment with $PhICl_2$.[12] Trityl chloride, Ph_3CCl, has also been found to be a very convenient reagent for the oxidative halogenation of cerium(III) amide precursors such as $Ce[N(SiMe_3)_2]_3$.[13]

Unprecedented crystalline cerium(IV) bis(amides) containing a cyclic $(Ce{-}O)_n$ core ($n = 2$, 3, or 4) have been prepared by oxidation of $Ce[N(SiMe_3)_2]_3$ or $Ce(NR''_2)_3$ ($NR''_2 = NC(Me)_2(CH_2)_3CMe_2$). The bis(trimethylsilyl)amides were prepared using oxygen gas or 2,6-di(*tert*-butyl)-1,4-benzoquinone/a trace H_2O at low temperature as illustrated in Scheme 15. These complexes were obtained as X-ray quality crystals in modest (38% for the dimer) or low (10% for the trimer) yield; ^1H and $^{13}C\{^1H\}$ NMR spectra in C_6D_6 showed each complex to be diamagnetic. However, the solutions decomposed after a few hours at ambient temperature.[14]

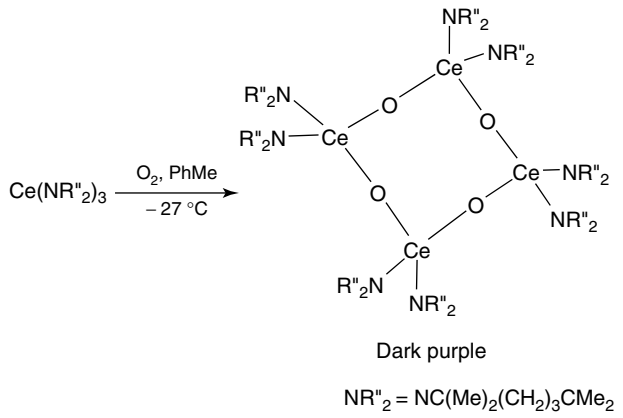
In a similar manner, oxidation of the tetramethylpiperidide derivative $Ce(NR''_2)_3$ ($NR''_2 = NC(Me)_2(CH_2)_3CMe_2$) with elemental oxygen as shown in Scheme 16 produced a tetrameric bis(amido)cerium(IV) oxide, although only a few single crystals of this compound could be isolated.[14]



Scheme 14



Scheme 15



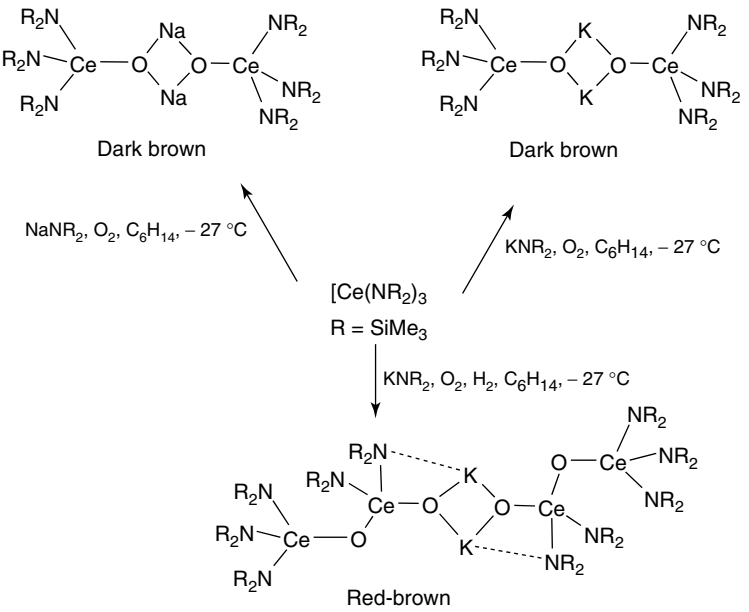
Scheme 16

The black binuclear complexes (μ-η^2:η^2-O_2)[Ce{N(SiMe$_3$)$_2$}$_2$]$_2$·2C$_n$H$_{2n+2}$ (n = 5, 6), obtained in a similar manner from Ce[N(SiMe$_3$)$_2$]$_3$ and dry oxygen, have either a bridging peroxide or superoxide ligand, but the O–O bond length data were not definitive. The preparation of related novel sodium and potassium bis(trimethylsilyl)amido (oxo)cerates(IV) is outlined in Scheme 17. Each of these compounds was obtained from a mixture of the cerium(III) amide Ce[N(SiMe$_3$)$_2$]$_3$ and the appropriate metal amide MN(SiMe$_3$)$_2$ (M = Na, K).[14]

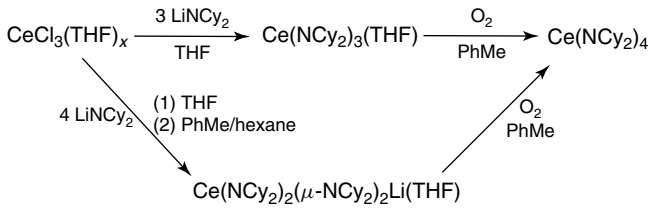
Facile oxidation of Ce(NCy$_2$)$_3$(THF) or Ce(NCy$_2$)$_2$ (μ-NCy$_2$)$_2$Li(THF) (Cy = cyclohexyl) with dry air produced the first homoleptic Ce(IV) amide Ce(NCy$_2$)$_4$ as illustrated in Scheme 18. Both cerium(III) precursors were extremely air sensitive in solution and if the smallest amount of air was accidentally introduced during the workup, a blue coloration appeared in the solution immediately, later yielding black microcrystals. When a measured amount of dry air was added to toluene or THF solutions of Ce(NCy$_2$)$_3$(THF) or Ce(NCy$_2$)$_2$(μ-NCy$_2$)$_2$Li(THF), the diamagnetic Ce(IV) amide Ce(NCy$_2$)$_4$ was isolated in a moderate yield. Ce(NCy$_2$)$_4$ is only sparingly soluble in hexane, benzene, toluene, or THF, producing deep blue solutions, which could be stored in a vacuum-sealed tube without decomposition for several months at room temperature (in contrast to the solution instability of Ce[N(SiMe$_3$)$_2$]$_3$(X (X = Cl, Br)). The solubility increased upon heating to 70 °C thus allowing recrystallization of Ce(NCy$_2$)$_4$ without noticeable decomposition even at this temperature.[15]

The synthesis and characterization of the related first neutral cerium dialkyl dithiocarbamate complexes, using a novel oxidative displacement of the amido ligands of Ce[N(SiMe$_3$)$_2$]$_3$ by tetraalkylthiuram disulfides [R$_2$NC(S)S]$_2$ (R = Me, Et) in THF solution, has also been reported. The crystalline, toluene-soluble cerium(IV) dithiocarbamate Ce(κ^2-S$_2$CNEt$_2$)$_4$ was made by briefly bubbling oxygen gas through a suspension of the yellow Ce(κ^2-S$_2$CNEt$_2$)$_3$ in toluene at ambient temperature. The reaction was rapid, as evident from the almost immediate color change to the black tetravalent complex.[16]

Particularly remarkable was the stabilization of cerium(IV) in the presence of an iodide ligand, as neither CeI$_4$ nor stable salts containing the hexaiodocerate(IV) anion, $[CeI_6]^{2-}$, have ever been isolated. This was achieved by reaction of triamidoamine complex Ce(NN′$_3$) [NN′$_3$ = N(CH$_2$CH$_2$NSiMe$_2$^{t}Bu)$_3$] with iodine to give (NN′$_3$)CeI. The base-free trivalent precursor complex Ce(NN′$_3$) was

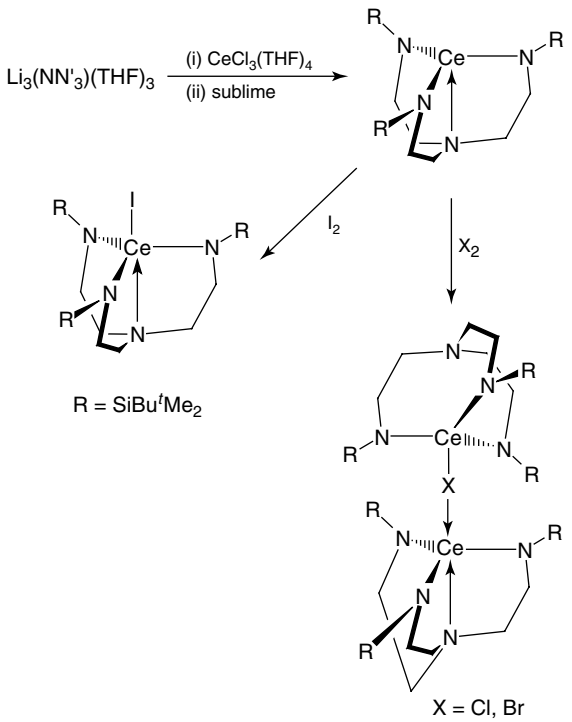


Scheme 17



Scheme 18

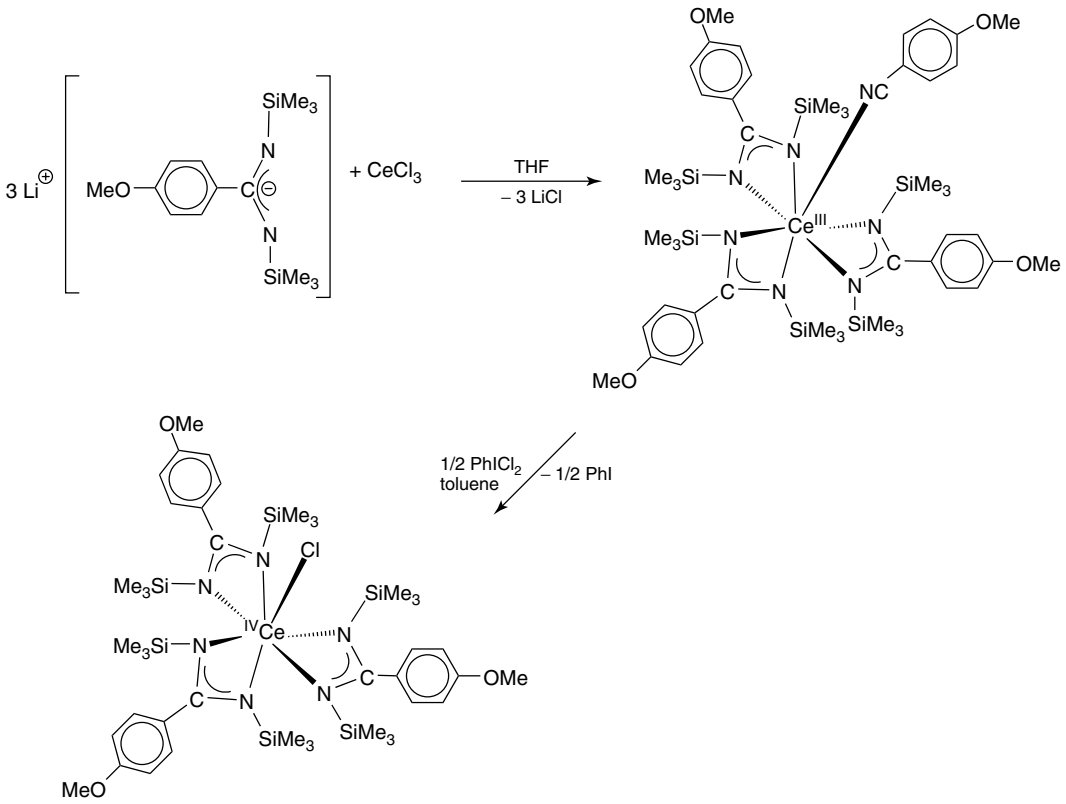
readily synthesized according to Scheme 19 by treatment of $CeCl_3(THF)_4$ with $Li_3(THF)_3(NN'_3)$ in dry THF followed by sublimation in vacuo. This bright yellow-orange complex decomposes rapidly in air but is otherwise quite stable. The reaction of $Ce(NN'_3)$ as a solution in pentane with 0.5–1.5 equiv. of elemental chlorine led to an immediate color change to purple and deposition of large purple crystals of the fascinating mixed valence $Ce^{3+/4+}$ complex (μ-Cl)[$Ce(NN'_3)_2$]. Similarly, reaction of $Ce(NN'_3)$ with bromine gave purple (μ-Br)[$Ce(NN'_3)_2$]. Most unexpectedly, however, the weakest oxidizing agent iodine gave the purple cerium(IV) iodide complex, $(NN'_3)CeI$ (Scheme 19).[17]



Scheme 19

5 AMIDINATES

Amidinate and guanidinate anions are nitrogen analogs of the carboxylates. They have been widely employed as spectator ligands in main group and transition metal coordination chemistry, with the latter encompassing both early and late transition metals as well as the lanthanides and actinides. These chelating anions are generally readily accessible using commercially available or easily prepared starting materials. Furthermore, their steric and electronic properties can be readily modified in a wide range through variation



Scheme 20

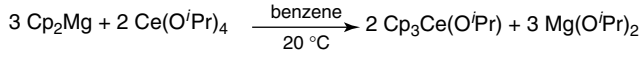
of the substituents on the carbon and nitrogen atoms. These properties combined make the amidinate anions clearly almost as versatile as the ubiquitous cyclopentadienyl ligands.[18]

Most recently, it was discovered that amidinate ligands are also capable of stabilizing novel cerium(IV) species. Thus they belong to the limited number of organic ligands, which allow the stabilization of lanthanide complexes in all possible oxidation states (+2, +3, and +4). For example, treatment of anhydrous cerium(III) trichloride with 3 equiv. of the lithium amidinate precursor Li[*p*-$MeOC_6H_4C(NSiMe_3)_2$] first afforded the bright yellow *p*-anisonitrile adduct of the cerium(III) amidinate (Scheme 20). Oxidation to the corresponding cerium(IV) amidinate [*p*-$MeOC_6H_4C(NSiMe_3)_2]_3CeCl$ was readily achieved using the reagent phenyliodine(III) dichloride (vide supra). This way the almost black cerium(IV) species could be isolated by simple crystallization directly from the concentrated reaction mixture. A single-crystal X-ray analysis clearly established the presence of the first amidinate complex of tetravalent cerium.[12]

6 CYCLOPENTADIENYL COMPLEXES

For cerium, the oxidation state +4 is remarkably stable because Ce^{4+} has the electronic configuration of xenon. Thus cerium should be by far the best candidate for making stable organolanthanide(IV) complexes. Historically, however, this was a notoriously difficult task, and it was a fundamental question persisting for decades in organolanthanide chemistry whether tetravalent organocerium complexes would exist at all. It is interesting to note that early reports on the synthesis of organometallic cerium(IV) complexes published in the 1970s were all found to be irreproducible or were shown to yield Ce^{3+} species. In particular, reactions of $(pyH)_2[CeCl_6]$ with cyclopentadienyl or indenyl reagents invariably led to reduction processes and formation of Ce^{3+} products. Even until today, well-characterized organocerium(IV) complexes remain scarce. Early reports[19] about the synthesis of $CeCp_4$ and $Ce(C_9H_7)_4$ (C_9H_7 = indenyl) have later been refuted.[20] The same is true for many other compounds of the types Cp_3CeX and $(C_9H_7)_2CeX_2$ (X = H, alkyl, aryl, BH_4, Cl, NH_2, N_3, CN, NCO, NCS, NO_2, NO_3, SR, and O_2CR).

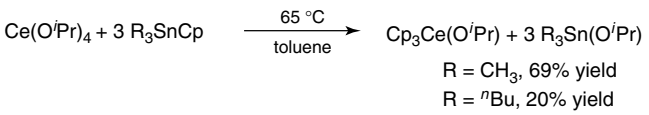
The first well-characterized cyclopentadienyl complexes of tetravalent cerium were the alkoxide derivatives $Cp_3Ce(OR)$ (R = ^{i}Pr, ^{t}Bu) and $Cp_2Ce(O^tBu)_2$. The first compound of this type, $Cp_3Ce(O^iPr)$, was obtained in minute quantities (4% yield) upon treatment of cerium(IV) tetraisopropoxide with magnesocene according to Scheme 21. The new complex $Cp_3Ce(O^iPr)$ could be isolated by sublimation from the reaction mixture in the form of black microcrystals.[21]



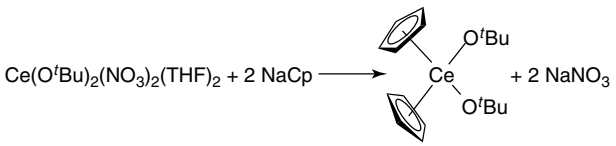
Scheme 21

About 10 years later, a more convenient route has been developed which involves treatment of the same alkoxide precursor with 3 equiv. of Me_3SnCp according to Scheme 22.[22] This method uses an organotin compound which is a weaker reducing agent than the alkali or alkaline-earth metal cyclopentadienides, and is thus less likely to result in reduction to Ce^{3+}. With 69% isolated yield, the new synthetic route represented a major improvement over the previously reported synthesis.[21] The product was shown to be a genuine Ce^{4+} complex by NMR, elemental analysis, and cyclic voltammetry/controlled potential coulometry in $Bu_4N^+BF_4^-$/THF. The latter data indicated that $Cp_3Ce(O^iPr)$ is a relatively strong oxidizing agent ($E_{1/2} = +0.32$ vs silver–silver chloride electrode (SSCE)) and that one-electron reduction is both electrochemically and chemically reversible. Electronic structure calculations at the nonrelativistic X_α-discrete variational method (DVM) level suggested nonnegligible Ce–Cp f orbital covalency and yielded transition state ionization energies in good agreement with He I/He II photoelectron spectra.[22]

An alternative synthetic route utilizes the readily available mixed-ligand alkoxide/nitrate complexes[3] of tetravalent cerium as starting materials. For example, the dark brown compound $Cp_2Ce(O^tBu)_2$ can be prepared in high yield (90%) by treatment of $Ce(O^tBu)_2(NO_3)_2(THF)_2$ with 2 equiv. of NaCp as shown in Scheme 23.[23]



Scheme 22



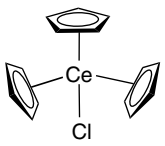
Scheme 23

It was also found that $Ce(O^tBu)(NO_3)_3(THF)_2$ reacts with 3 equiv. of NaCp to form $Cp_3Ce(O^tBu)$ (Scheme 24) admixed with $Cp_2Ce(O^tBu)_2$ from which it can be separated by crystallization and isolated in 50% yield as a black microcrystalline powder. The molecular structure of $Cp_3Ce(O^tBu)$ was unambiguously verified by X-ray diffraction.[23]

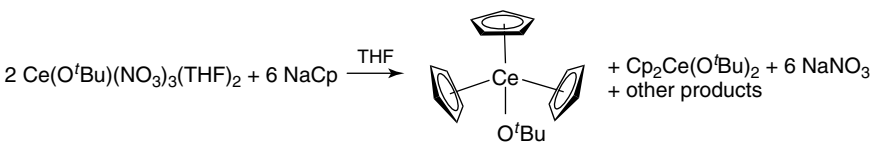
Recently, a further example of the versatility of $PhICl_2$ as an oxidant was demonstrated by the synthesis and structural characterization of tris(cyclopentadienyl) cerium(IV) chloride (Scheme 25), the long sought-after cerium(IV) analog of Cp_3UCl. A material thought to be Cp_3CeCl was first described in 1971[19] but that report was later refuted.[20] Addition of 0.5 equiv. of $PhICl_2$ to a toluene solution of Cp_3Ce produced an immediate color change from yellow to black. Black crystals were isolated, after removing the volatiles, from a concentrated toluene solution at −35 °C in 15% yield. Diamagnetic Cp_3CeCl displays a singlet at δ 4.74 in the ^1H NMR spectrum in C_6D_6. X-ray diffraction analysis revealed these crystals to be Cp_3CeCl. Thus Cp_3CeCl is not only the first new tris(cyclopentadienyl)cerium(IV) complex reported in more than 20 years but also the first chloro-functional species of this type for which a promising derivative chemistry can be envisioned.[12]

7 CARBENE COMPLEXES

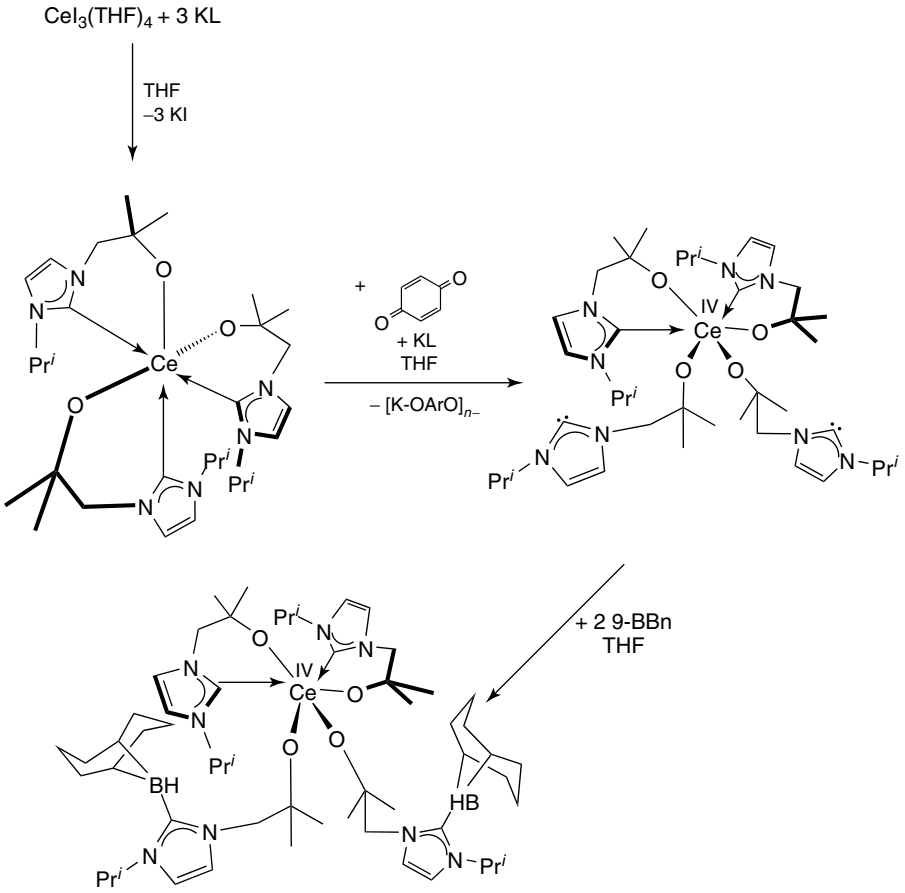
An interesting recent addition to organocerium(IV) chemistry is the successful synthesis and characterization of Ce^{4+} complexes containing a bidentate *N*-heterocyclic carbene alkoxide ligand, $[C\{(N^iPr)CHCHN\}CH_2CMe_2O]^-$. Treatment of $CeI_3(THF)_4$ with 3 equiv. of KL, $K[OCMe_2CH_2(1\text{-}C\{NCHCHN^iPr\})]$, afforded CeL_3 in good yield as a dark yellow microcrystalline powder (Scheme 26). Treatment of CeL_3 with $TeCl_4$, PBr_2Ph_3, or I_2 (reagents previously used for the oxidation of Ce^{3+} amides) did not



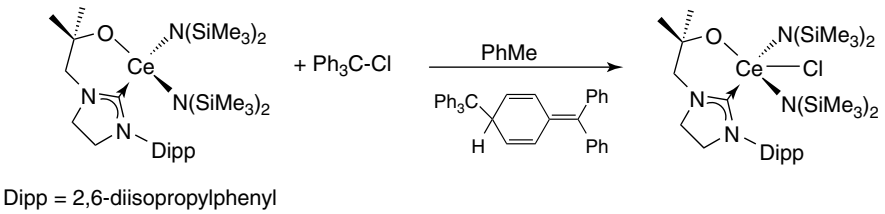
Scheme 25



Scheme 24



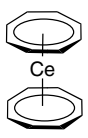
Scheme 26



Scheme 27

yield the desired oxidation products. However, treatment of CeL_3 with benzoquinone afforded tetravalent CeL_4, arising from oxidation and ligand redistribution (Scheme 26). The oxidation could also be affected by XeF_2 and by $[Cp_2Fe][OTf]$, but with lower yields. Subsequent treatment of CeL_4 with 2 equiv. of the borane 9-BBN, 9-borabicyclo[3.3.1]nonane, afforded highly crystalline yellow $L_2Ce(L\text{-}9BBN)_2$ (Scheme 26).[24]

More recently, it was found that trityl chloride is an excellent reagent to achieve the oxidative halogenation of cerium(III) carbene precursors. Scheme 27 illustrates a typical reaction.[13]



Scheme 28

8 CEROCENES

Cerocene, $Ce(C_8H_8)_2$ (Scheme 28), is a particularly interesting metallocene that is formally a lanthanide(IV)

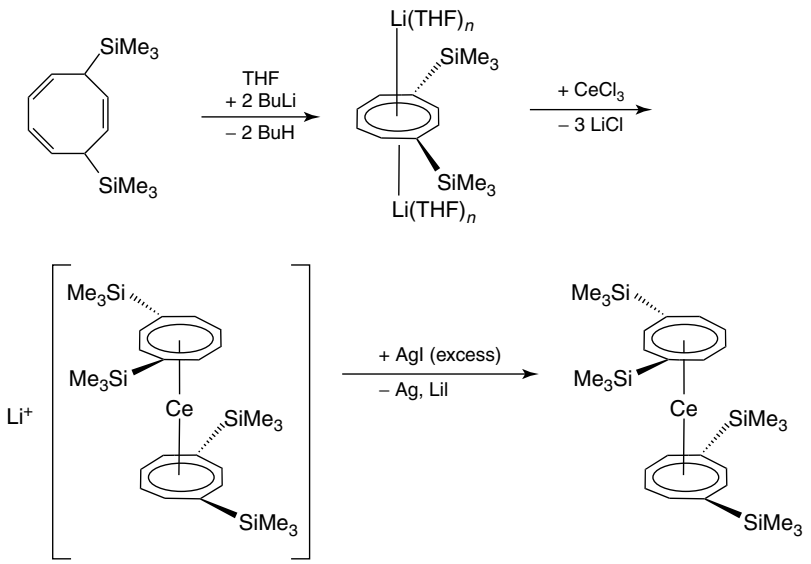
analog of uranocene, $U(C_8H_8)_2$, but combines a strong oxidizing agent, Ce^{4+}, and a strong reducing agent, cyclooctatetraene (COT) dianion, in the same molecule. The first successful synthesis of cerocene resulted surprisingly from the use of a reducing agent, triethylaluminum, in a reaction using cerium(IV) isopropoxide with neutral cyclooctatetraene as a reactant and solvent. Cerocene was isolated as a black-red, pyrophoric solid.[21] A more straightforward synthesis involves oxidation of the anionic cerium(III) sandwich complex $K[Ce(C_8H_8)_2]$ with AgI. The longer known anionic derivative $K[Ce(C_8H_8)_2]$ can be regenerated by reduction of cerocene with potassium metal. Yet another efficiently modified synthesis for unsubstituted cerocene involves oxidation of $K[Ce(C_8H_8)_2]$ with allyl bromide.[25]

In order to cope with the pyrophoric nature of the parent cerocene, synthetic routes to silyl-substituted cerocenes have been developed. These cerocene derivatives can be isolated as deep purple materials, which are readily soluble even in nonpolar organic solvents. Scheme 29 illustrates a typical reaction sequence leading to 1,1′,4,4′-tetrakis(trimethylsilyl)cerocene.[26]

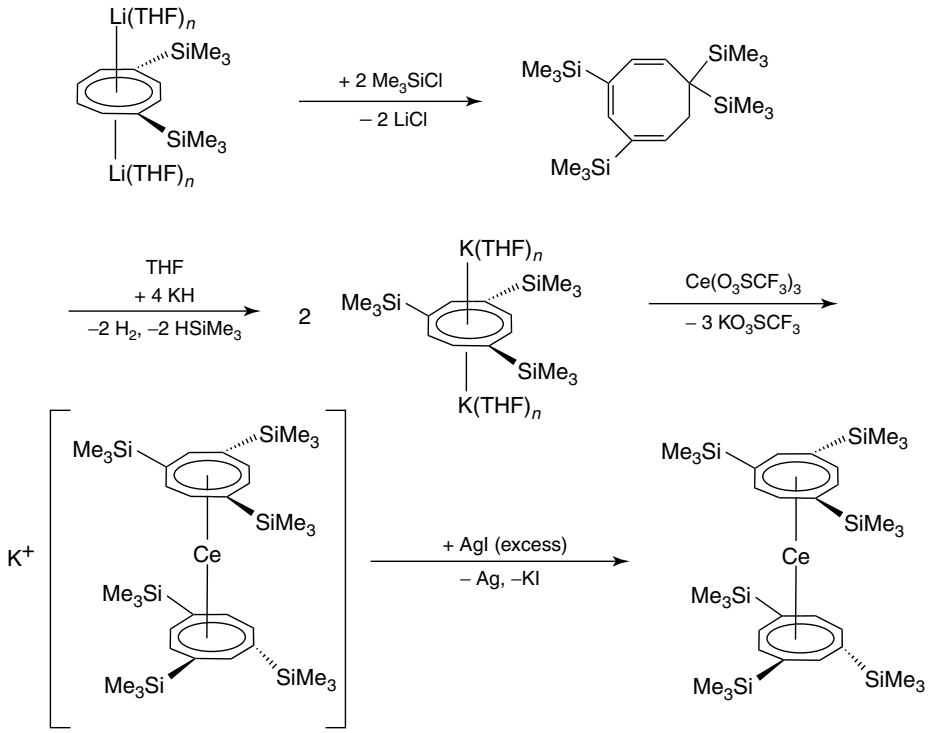
In this case, silver iodide was found to be the reagent of choice for achieving the oxidation of the anionic intermediate. 1,1′,4,4′-Tetrakis(trimethylsilyl)cerocene was isolated as a dark purple oil, which is stable in air for short periods of time. A crystalline polysubstituted cerocene derivative was synthesized as illustrated in Scheme 30 by employing the newly developed 1,3,6-tris(trimethylsilyl)cyclooctatetraenyl ligand. The resulting 1,1′,3,3′,6,6′-hexakis(trimethylsilyl)cerocene forms dark purple, low-melting crystals.[26]

Subsequent work in this field has provided further characterization of cerocene and various ring-substituted analogs. Crystal structures of $Ce(C_8H_7Me)_2$[27] and $Ce[C_8H_5(SiMe_3)_3]_2$[26] showed that cerocenes have a uranocene-type sandwich structure with ring centroid-Ce-ring centroid angles of 176° in both cases. In all cases, the cyclooctatetraenyl ligands are η^8-coordinated to cerium. There is theoretical and spectroscopic evidence (e.g., self-consistent field calculations) that the ground state in cerocene is almost entirely $4f^1$ and that this formally tetravalent cerium sandwich complex is better described as a cerium(III) compound such as $Ce^{3+}[(C_8H_8)_2]^{3-}$.[28,29]

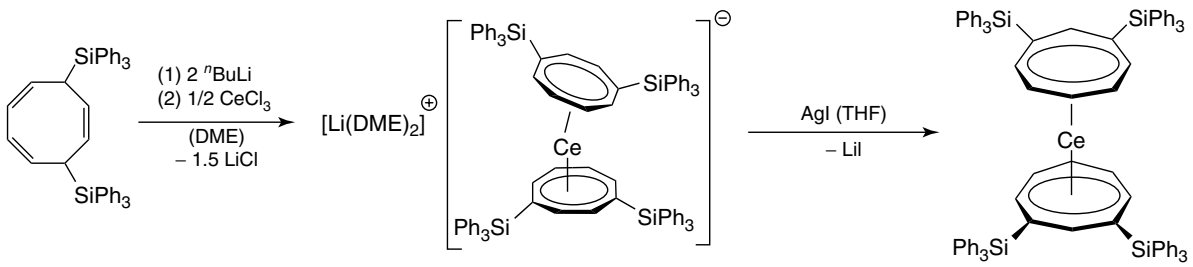
Surprising structural features have recently been discovered for related cerium sandwich complexes containing the superbulky 1,4-bis(triphenylsilyl)cyclooctatetraenide ligand (= COT^{BIG}).[30] First, the anionic cerium(III) sandwich complex $[Li(DME)_2][Ce(COT^{BIG})_2]$ was prepared by reaction of $CeCl_3$ with 2 equiv. of $Li_2(COT^{BIG})$ made *in situ* in DME (Scheme 31). A single-crystal X-ray analysis showed that in contrast to all previously reported $[Ln(COT)_2]^-$ or $[Ln(COT'')_2]^-$ derivatives, the anion in $[Li(DME)_2][Ce(COT^{BIG})_2]$ is significantly bent (tilt angle between the eight-membered rings: 15.1°). Knowing the bent structure of the anionic sandwich complex, it was tempting to see if the bending would increase upon oxidation. AgI oxidation of $[Li(DME)_2][Ce(COT^{BIG})_2]$ proceeded smoothly with formation of the neutral cerocene $Ce(COT^{BIG})_2$ (Scheme 31, dark purple needles, 63%). X-ray diffraction analysis of $Ce(COT^{BIG})_2$ unexpectedly revealed the presence of strictly coparallel rings, but the molecule now contains the 1,3-isomer of the COT^{BIG} ligand. Obviously, steric pressure becomes too severe upon oxidation to the neutral cerocene that $SiPh_3$ group migration is induced for relief, resulting in a sterically more relaxed and highly symmetrical molecular structure of $Ce(COT^{BIG})_2$ as a result of this unprecedented rearrangement.[30]



Scheme 29



Scheme 30



Scheme 31

9 CONCLUSIONS AND FUTURE OUTLOOK

The synthesis and full characterization of organolanthanide(IV) complexes remain a very difficult and often unpredictable task. Thus far, organolanthanide chemistry in the oxidation state +4 remains entirely limited to cerium. This can be traced back to the very highly positive normal potentials of the other tetravalent lanthanide ions Pr^{4+}, Nd^{4+}, Tb^{4+}, and Dy^{4+} (e.g., Pr: +2.86 V), which make them very strong oxidizing agents. Not even well-defined pseudo-organometallics (i.e., alkoxides, amides, and related compounds) of tetravalent lanthanide ions other than Ce^{4+} have ever been isolated. Only alkoxides and amides of tetravalent cerium form fairly well-investigated classes of compounds. In contrast, true organocerium(IV) containing Ce–C bonds remain scarce. The oldest compounds of this type are cerocene and its derivatives, although the electronic structure of these species is far from being fully understood. The chemistry of cerium(IV) complexes containing *N*-heterocyclic carbene ligands is just emerging, and even cyclopentadienyl complexes of the type Cp_3CeX (X = Cl, OR) are limited to a handful of compounds. The recently reported chloro derivative Cp_3CeCl[12] could turn out to be the starting point for a more diverse derivative chemistry. The successful synthesis of ''nonclassical'' organolanthanide(IV) compounds of Pr^{4+}, Nd^{4+}, Tb^{4+}, or Dy^{4+} would certainly constitute a major breakthrough in this area. However, given the current knowledge, the design of suitable ligands for such highly oxidizing species will be very difficult if not impossible.

10 GLOSSARY

acac: Acetylacetonate

9-BBN: 9-Borabicyclo[3.3.1]nonane

CAN: Ceric ammonium nitrate, $(NH_4)_2[Ce(NO_3)_6]$

Cerocene: Bis(η^8-cyclooctatetraenyl)cerium

COT: Cyclooctatetraene or η^8-cyclooctatetraenyl ligand

COT″: 1,4-Bis(trimethylsilyl)cyclooctatetraenyl

COT^{BIG}*:* 1,4-Bis(triphenylsilyl)cyclooctatetraenyl

Cp: Cyclopentadienyl anion

CVD: Chemical vapor deposition

Cy: Cyclohexyl

Dipp: 2,6-Diisopropylphenyl

DMAP: 4-(Dimethylamino)pyridine

DME: 1,2-Dimethoxyethane

$E_{1/2}$*:* Half-wave potential

NN'_3*:* $N(CH_2CH_2NSiMe_2{}^tBu)_3$

NR''_2*:* $NC(Me)_2(CH_2)_3CMe_2$

OTf: Triflate anion, $CF_3OSO_2^-$

py: Pyridine

Uranocene: Bis(η^8-cyclooctatetraenyl)uranium

11 ABBREVIATIONS AND ACRONYMS

CVD = chemical vapor deposition; DVM = discrete variational method; NMR = nuclear magnetic resonance; SSCE = silver–silver chloride electrode.

12 REFERENCES

1. R. D. Shannon, *Acta Cryst.*, 1976, **A32**, 751.
2. R. C. Mehrotra, P. N. Kapoor, and J. M. Batwara, *Coord. Chem. Rev.*, 1980, **31**, 67.
3. W. J. Evans, T. J. Deming, J. M. Olofson, and J. W. Ziller, *Inorg. Chem.*, 1989, **28**, 4027.
4. A. Sen, H. A. Stecher, and A. L. Rheingold, *Inorg. Chem.*, 1992, **31**, 473.
5. S. Suh, J. Guan, L. A. Mînea, J.-S. M. Lehn, and D. M. Hoffman, *Chem. Mater.*, 2004, **16**, 1667.
6. P. S. Gradeff, K. Yünlü, T. J. Deming, J. M. Olofson, R. J. Doedens, and W. J. Evans, *Inorg. Chem.*, 1990, **29**, 420.
7. S. Giessmann, S. Blaurock, V. Lorenz, and F. T. Edelmann, *Inorg. Chem.*, 2007, **46**, 8100.
8. Y. K. Gun'ko, R. Reilly, F. T. Edelmann, and D. Stalke, *Angew. Chem.*, 2001, **113**, 1319, *Angew. Chem. Int. Ed.*, 2001, **40**, 1279.
9. D. C. Bradley, J. S. Ghotra, and F. A. Hart, *J. Chem. Soc., Dalton Trans.*, 1973, 1021.
10. O. Eisenstein, P. B. Hitchcock, A. G. Hulkes, M. F. Lappert, and L. Maron, *Chem. Commun.*, 2001, 1560.
11. P. B. Hitchcock, A. G. Hulkes, and M. F. Lappert, *Inorg. Chem.*, 2004, **43**, 1031.
12. P. Dröse, A. R. Crozier, S. Lashkari, J. Gottfriedsen, S. Blaurock, C. G. Hrib, C. Maichle-Mössmer, C. Schädle, R. Anwander, and F. T. Edelmann, *J. Am. Chem. Soc.*, 2010, **132**, 14046.
13. P. L. Arnold, Z. R. Turner, N. Kaltsoyannis, P. Pelekanaki, R. M. Bellabarba, and R. P. Tooze, *Chem.—Eur. J.*, 2010, **16**, 9623.
14. M. P. Coles, P. B. Hitchcock, A. V. Khvostov, M. F. Lappert, Z. Li, and A. V. Protchenko, *Dalton Trans.*, 2010, **39**, 6780.
15. P. B. Hitchcock, M. F. Lappert, and A. V. Protchenko, *Chem. Commun.*, 2006, 3546.
16. P. B. Hitchcock, A. G. Hulkes, M. F. Lappert, and Z. Li, *Dalton Trans.*, 2004, 129.
17. C. Morton, N. W. Alcock, M. R. Lees, I. J. Munslow, C. J. Sanders, and P. Scott, *J. Am. Chem. Soc.*, 1999, **121**, 11255.
18. F. T. Edelmann, *Chem. Soc. Rev.*, 2009, **38**, 2253.
19. B. L. Kalsotra, R. K. Multani, and B. D. Jain, *Isr. J. Chem.*, 1971, **9**, 569.
20. G. B. Deacon, T. D. Tuong, and D. G. Vince, *Polyhedron*, 1983, **2**, 969.
21. A. Greco, S. Cesca, and G. Bertolini, *J. Organomet. Chem.*, 1976, **113**, 321.
22. A. Gulino, M. Casarin, V. P. Ponticello, J. G. Gaudiello, H. Mauermann, I. Fragalä, and T. J. Marks, *Organometallics*, 1988, **7**, 2360.
23. W. J. Evans, T. J. Deming, and J. W. Zlller, *Organometallics*, 1989, **8**, 1581.
24. I. J. Casely, S. T. Liddle, A. J. Blake, C. Wilson, and P. L. Arnold, *Chem. Commun.*, 2007, 5037.
25. A. Streitwieser, S. A. Kinsley, C. H. Jenson, and J. T. Rigsbee, *Organometallics*, 2004, **23**, 5169.
26. U. Kilimann, R. Herbst-Irmer, D. Stalke, and F. T. Edelmann, *Angew. Chem.*, 1994, **106**, 1685, *Angew. Chem. Int. Ed. Engl.*, 1994, **33**, 1618.

27. T. R. Boussie, D. C. Eisenberg, J. Rigsbee, A. Streitwieser, and A. Zalkin, *Organometallics*, 1991, **10**, 1922.

28. M. Dolg, P. Fulde, H. Stoll, H. Preuss, A. Chang, and R. M. Pitzer, *Chem. Phys.*, 1995, **195**, 71.

29. N. M. Edelstein, P. G. Allen, J. J. Bucher, D. K. Shuh, C. D. Sofield, N. Kaltsoyannis, G. H. Maunder, M. R. Russo, and A. Sella, *J. Am. Chem. Soc.*, 1996, **118**, 13115.

30. V. Lorenz, B. M. Schmiege, C. G. Hrib, J. W. Ziller, A. Edelmann, S. Blaurock, W. J. Evans, and F. T. Edelmann, *J. Am. Chem. Soc.*, 2011, **133**, 1257.

Molecular Magnetic Materials

Bing-Wu Wang and Song Gao

Peking University, Beijing, People's Republic of China

1 Introduction 335
2 Magnetic Ordering Materials 335
3 Magnetic Relaxation Materials 337
4 Conclusions 344
5 Acknowledgments 344
6 Related Articles 344
7 Abbreviations and Acronyms 344
8 References 345

1 INTRODUCTION

Magnetism has a long history going as far back as around 800 bc, when the attractive power of lodestone, a magnetic material, was known both in China and Europe.

In the early years of application, the magnetic materials known were mainly the transition metals, alloys, and oxides. When the ferromagnetism of Gd was discovered in the 1930s, the magnetic properties of other rare earth metals and alloys were explored, benefitting from the development of the purification technique. With the assistance of the neutron scattering experiment and precise measurement of the static and dynamical magnetization, the microscopic and macroscopic magnetic behavior of materials including those of rare earth elements were investigated in detail. A considerable body of scientific work devoted to the magnetism of rare earth element containing systems can be found in the literature; for example, see Refs 1–3. A mature understanding, and the success, of the standard model of rare earth magnetism shifted the interest of some scientists from the magnetism of rare earth metals, alloys, and oxides to their magnetic molecular systems. In this chapter, we focus our attention on this new field of rare earth magnetism and concentrate on the essential principle, providing typical examples of molecular magnetic materials containing rare earths, including magnetic ordering materials and low-dimensional magnetic materials with slow magnetization relaxation behaviors.

2 MAGNETIC ORDERING MATERIALS

For large magnetic anisotropies and angular moments, rare earth ions are good candidates as building blocks to construct magnetic materials with large hysteresis loops. In widely used classical magnetic materials, such as $SmCo_5$ and NdFeB, rare earths play an important role in modulating the bulk magnetic properties. Owing to their intrinsic, large, and anisotropic moments, rare earths are also the excellent building blocks in molecular magnetic materials.

As mentioned above, for the highly contracted 5d orbitals, which are shielded by outer 6s orbitals, the exchange-coupling interactions are generally small in the molecular systems and ordering temperatures are very low compared with those of magnets composed of metals, alloys, and oxides. So the key point in constructing 3D molecular magnetic materials is to enhance the strength of the magnetic coupling interaction. In 1976, Landolt *et al*. prepared a series of Prussian Blue analogs with Ln^{III} ions,[4] which exhibited 3D long-range magnetic ordering with rather large hysteresis loops. Since then, many magnetic compounds composed of rare earth and other paramagnetic species, transition metal ions, or organic radicals have been reported. However, except for the spin-only $4f^7$ Gd^{III} ion, examples of molecular multispin systems involving Ln^{III} ions are scarcely reported, which may be due to the weak interaction between the rare earth ions. So far, only a few lanthanide radical compounds and 4f–3d heterometallic compounds show long-range ordering at low temperatures.

Inspired by the first Prussian-Blue-like magnet, Gao *et al*. synthesized and characterized Prussian-Blue-like

The Rare Earth Elements. Edited by David A. Atwood. © 2012 John Wiley & Sons, Ltd. ISBN 978-1-119-95097-4

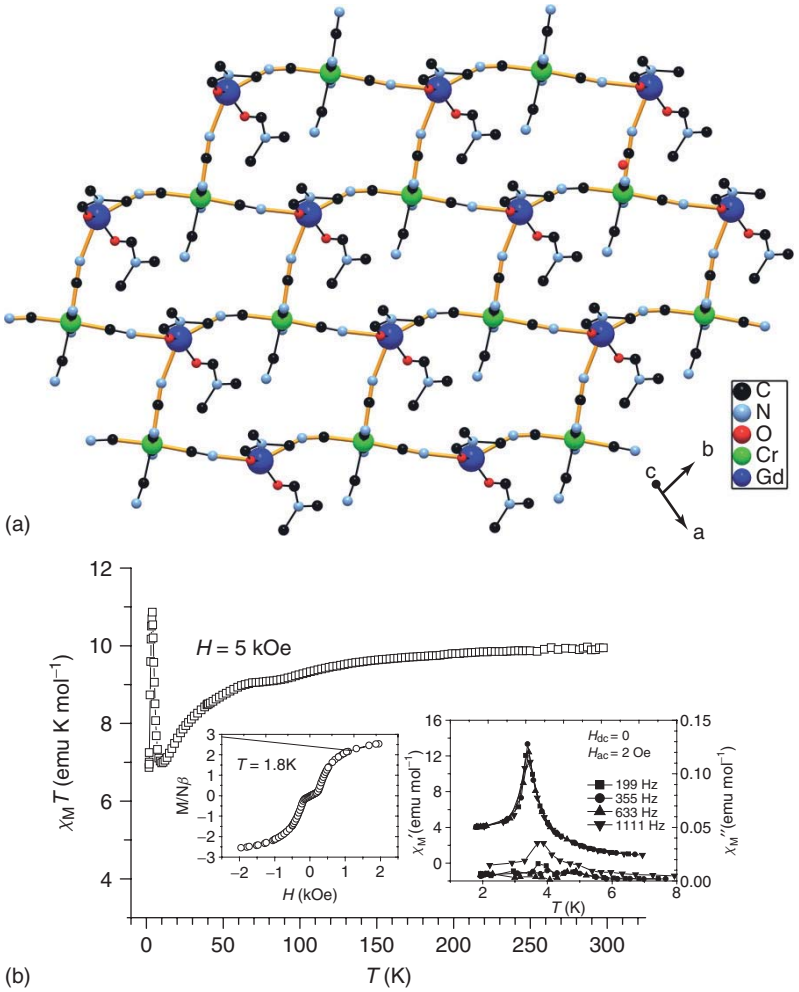


Figure 1 (a) Brick-wall-like structure of $[Gd(DMF)_2(H_2O)_3\ Cr(CN)_6]\cdot H_2O$. (b) Temperature dependence of $\chi_M T$ for $[Gd(DMF)_2(H_2O)_3\ Cr(CN)_6]\cdot H_2O$. Inset: left, isothermal magnetization at 1.8 K; right, real and imaginary AC susceptibilities in zero applied DC field and an AC field of 2 Oe at different frequencies. (Reprinted with permission from Ref. 5. Copyright (2001) American Chemical Society)

compounds. $[Ln(DMF)_2(H_2O)_3Cr(CN)_6]\cdot H_2O$ (M = Gd, Sm) are obtained, which consist of brick-wall-like neutral layers with slightly distorted Cr_3Ln_3 rectangles (Figure 1(a)).[5] In the $[Gd(DMF)_2(H_2O)_3Cr(CN)_6]\cdot H_2O$ compound, each $[Cr(CN)_6]^{3-}$ unit connects with three $[Gd(DMF)_2(H_2O)_3]^{2+}$ units using three cyanide groups in the meridional arrangement. Then each $[Gd(DMF)_2(H_2O)_3]^{2+}$ unit links three $[Cr(CN)_6]^{3-}$ ions with the bridging cyanides. This local molecular disposition extends and generates a flat brick-wall-like structure, which is the first cyano-bridged 3d–4f complex with such a topology. For the $[Sm(DMF)_2(H_2O)_3Cr(CN)_6]\cdot H_2O$ compound, the adjacent Sm^{III} and Cr^{III} ions are antiferromagnetically coupled and behave like a metamagnet (Figure 1(b)). It is the first observation of 2D cyano-bridged 3d–4f complexes. Owing to the antiferromagnetic interaction between the ferrimagnetic layers, these two compounds reach long-range antiferromagnetic ordering at 3.5 and 4.2 K, respectively.

Most magnetic ordering compounds containing rare earths use the cyanide bridge because it can transmit a relatively large exchange-coupling interaction. At the same time, bpdo (4,4′-bipyridine *N*, *N*′-dioxide), bpy (2, 2′-bipyridine), DMA (*N*, *N*-dimethylacetamide), and so on, were used as coligand to generate high-dimensional Prussian Blue derivatives and showed magnetic ordering properties. So far a few 3D, magnetic ordered, lanthanide-based molecular materials have been obtained, and they all exhibit low ordering temperature. However, the existing examples, including the lanthanide-radical systems and lanthanide-transition metal ones, provide us with considerable experimental or theoretical knowledge and experience. The study of 3D, magnetic ordered, lanthanide-based molecular materials is still an open area of research for chemists and physicists.

The use of organic radicals is an effective method of enhancing exchange-coupling interactions between spin carriers. So a successful strategy for preparing molecular

magnets is to directly coordinate organic radicals such as NITR (nitronyl nitrosides), organocyanides $TCNE^{\cdot -}$ (tetracyanoethylene), or $TCNQ^{\cdot -}$ (7,7,8,8-tetracyanoquinodimethane) to rare earth ions. The presence of both metal spin (typically $S > 1/2$) and an organic radical ($S = 1/2$) leads to strong superexchange interactions and results in typical ferro- or ferrimagnetic ordering. Although molecular magnetic materials based on 3d metals and organic radicals are quite common, analogous rare earth compounds are relatively rare (Scheme 1).

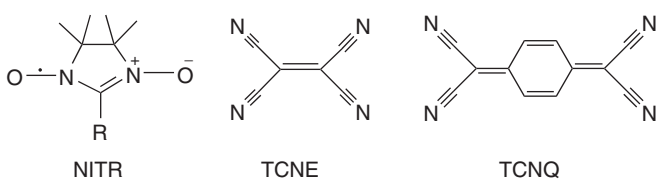
For example, the NITR radical has one unpaired electron that is equally shared by two NO groups. Often this is to link the neighboring metal ions through their two NO groups, forming 1D chains schematized as follows

... M-NITR-M-NITR-M-NITR-M-NITR ...

Gatteschi *et al*. obtained a series of analogous lanthanide–NITR 1D compounds $RE(hfac)_3NITEt$ (RE = Tb, Er, Ho; hfac = hexafluoracetylacetonate; NITEt = 2-ethyl-4,4,5,5-tetramethyl-4,5-dihydro-1*H*-imidazolyl-1-oxy1 3-oxide).[6–8] Their unit cell is monoclinic, and the chains develop parallel to the *b*-axis and are well separated, with the shortest contacts being 10.38 Å between Gd^{III} and 10.95 Å between Dy^{III} ions. The rare earth ions are eight coordinated by oxygen atoms, six from three hfac ions, and two from NITEt radicals.

Among these compounds, $Dy(hfac)_3NITEt$ exhibits an overall antiferromagnetic coupling between Dy^{3+} and NITEt radical, and undergoes magnetic phase transition at ca 4 K, ordering as a weak ferromagnet because of spin canting. For comparison, $Mn(hfac)_2NITR$ is composed of similar chain structure and shows stronger intrachain antiferromagnetic coupling of ca 400 K, reaching long-range magnetic ordering at ca 8 K. The corresponding $Er(hfac)_3NITEt$ shows magnetic phase transitions at temperatures ranging from 1.2 to 3.2 K.

TCNE and TENQ are also good candidate radicals to construct ordering magnetic materials. For example, Miller *et al*. obtained a room temperature molecular/organic-based magnet, $V(TCNE)_x$ ($1.5 < x < 2$) in 1991. They also provided the first examples of $Ln[TCNE]_3$ through the reaction of $LnI_3 \cdot x$MeCN (Ln = Gd, Dy) and TCNE in acetonitrile by thermal annealing, in which 4f elements were coordinated to $[TCNE]^-$.[9] The $[TCNE]^-$ radical weakly couples antiferromagnetically with rare earth ions both in $Gd[TCNE]_3$ and $Dy[TCNE]_3$ compounds, which exhibit a gradual magnetic phase transition to a ferrimagnetic state with critical temperature of 8.5 (Dy) and 3.5 (Gd) K. The temperatures of the magnetic phase transitions are higher than those reported for the 1D NITR chains presumably because of the stronger magnetic interaction of the $Ln(TCNE)_3$ species.



Scheme 1 Geometry structures of NITR, TCNE, and TENQ radicals

A clearer example of the lanthanide-radical ordering system is the Gd^{III}–TCNQ compound $\{[Gd_2(TCNQ)_5(H_2O)_9][Gd(TCNQ)_4 \cdot (H_2O)_3]\} \cdot 4H_2O$, which consists of alternating anionic and cationic layers perpendicular to the *c*-axis with different ratios of Gd^{III} and $TCNQ^-$ radicals (Figure 2).[10] It is an unusual situation that both cationic and anionic networks have the same building blocks but with different ratios. For this compound, susceptibility data fitting to the Curie–Weiss law gives a Curie constant of 27.1 emu K mol^{-1}, consistent with the expected value (27 emu K mol^{-1} for $g = 2$) for three isolated Gd^{III} ions ($S = 7/2$) and nine $TCNQ^-$ radical anions ($S = 1/2$). The small, negative Weiss constant ($\theta = -5.07$ K) indicated that the exchange coupling was antiferromagnetic between the Gd^{III} ion and the TCNQ radical. It is actually magnetically 3D with multiple interactions. In addition to the intralayer interactions, including direct exchange (Gd–TCNQ) and superexchange (between TCNQ groups through the Gd bridges, and vice versa), there are also nonnegligible antiferromagnetic interactions between layers through the short p–p contacts between TCNQ units in adjacent layers. It can be clearly seen from AC magnetic susceptibility measurements (Figure 2(c)) that the material exhibits an out-of-phase signal at $T_c \sim 3.5$ K. This material is a ferrimagnet and behaves as a soft magnet without obvious hysteretic at 1.8 K.

Although chemistry scientists obtained some 4f–3d and 4f-radical molecule-based magnets, the critical temperatures are all far below room temperature for the weak exchange interaction between rare earth ions and other spin carriers. This kind of magnet is used mainly to provide a model system to study the magnetic interactions involving rare earths. More and more researchers have shifted their interest to the fascinating field of magnetic relaxations, in which rare earths play the key role, from single-ion to cluster-type single-molecule magnets (SMMs).

3 MAGNETIC RELAXATION MATERIALS

Magnetic relaxation means that a magnetic equilibrium state relaxes to a new equilibrium state after perturbation of the magnetic field. The time to equilibrium between the two states is called *relaxation time*. Magnetic relaxation time τ, is a parameter describing the magnetic relaxation process, during which the magnetization M_t will reach a new equilibrium value M_0 after a change of the magnetic field from H to $H + \Delta H$. The definition could be expressed as follows:

$$\frac{dM_z}{dt} = \frac{M_0 - M_z}{\tau} \quad (1)$$

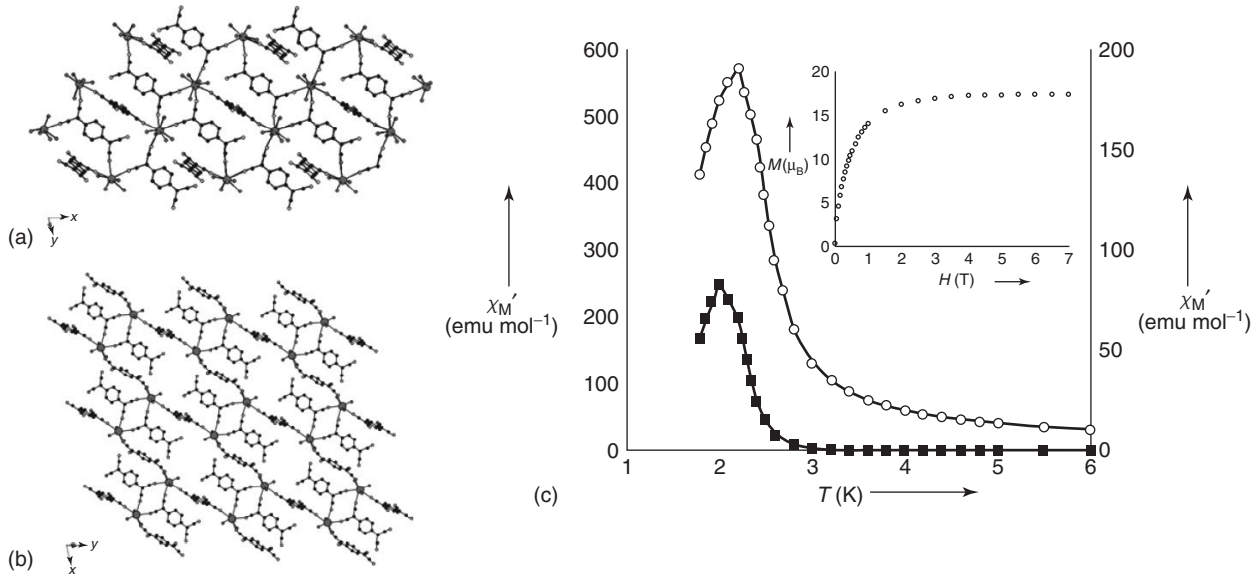


Figure 2 Top view of the tetrameric chains (a) and the 2D anionic network (b) (the terminal TCNQ has been omitted for clarity) in $\{[Gd_2(TCNQ)_5(H_2O)_9]\ [Gd(TCNQ)_4{\cdot}(H_2O)_3]\}{\cdot}4H_2O$ compound. (c) AC susceptibility data for $\{[Gd_2(TCNQ)_5(H_2O)_9][Gd(TCNQ)_4{\cdot}(H_2O)_3]\}{\cdot}4H_2O$, in-phase (empty circle), out-of-phase (solid square). Inset: plot of $M-H$ performed at 1.8 K. (Reprinted from Ref. 10. © Wiley-VCH Verlag GmbH & Co. KGaA, 2003)

Rare earth ion concerned magnetic relaxation includes spin–spin relaxation and spin–lattice relaxation. Spin–spin relaxation time (τ_{SS}) is much smaller than spin–lattice relaxation time (τ_{SL}), and it is temperature independent. As τ_{SS} is generally much smaller than the order of 10^{-10} s, it can only be observed at a very low temperature and high-frequency oscillating field. The better studied magnetic relaxation is the spin–lattice process, which is enabled via spin–orbital coupling involving a phonon process. Generally, there are three types of spin–lattice relaxation processes [11]:

1. Direct process

For a vibrating crystal lattice, the interatomic distances are modulated at the frequency of the lattice vibration to produce an oscillating magnetic field. Suitable vibration with the frequency at the Larmor frequency of the electrons will induce a flip of the electron spin. The corresponding relaxation time can be simplified as

$$\frac{1}{\tau_{SL}} \propto H_0^2 T$$

where H_0 is the magnitude of the external magnetic field.

2. Raman process

It is a two-phonon process involving the simultaneous absorption of one phonon and emission of another phonon, accompanied by a spin flip with energy that equals the energy difference between the corresponding phonons. When the temperature is much smaller than the Debye temperature, in the normal case, the relaxation time can be simplified as

$$\frac{1}{\tau_{SL}} \propto H_0 T^7$$

3. Orbach process

This process is very important in systems with more than one energy level. The spin center is transferred to another energy level via a real intermediate state involving two phonons through a resonant process. The corresponding relaxation time can be simplified as

$$\frac{1}{\tau_{SL}} = K \exp\left(\frac{-\Delta}{k_B T}\right)$$

where K is a constant.

Although the above equations have been oversimplified for the real relaxation process, it can still be concluded that the spin–lattice relaxation time is temperature dependent. The first equation refers to non-Kramers ions; the second refers to Kramers ions with the energy between doublets being small compared with $k_B T$; the third refers to Kramers ions' doublets with the energy gap being large compared with $k_B T$.

The magnetic relaxation phenomena in lanthanide-containing complexes cover a wide range of magnetic materials, among which the SMMs and single-chain magnets (SCMs) are the two most important families of molecular materials.

Different from traditional magnets, SMM is a superparamagnetic molecular compound that does not show

long-range magnetic ordering, and the unpaired spins of molecule cannot spontaneously align parallel to each other in domains. In contrast, the interaction between clusters in SMMs can be negligible. It can be regarded as a kind of magnet for possessing the capability of holding the spin state under blocking temperature (T_B) just as traditional magnets do under Curie (T_C, for ferromagnet) or Neel (T_N, for antiferromagnet) temperature. The relaxation energy barrier (ΔE) could be calculated as $\Delta E = |D|S_T^2$ for integer S_T, and $\Delta E = |D|(S_T^2 - 1/4)$ for half integer S_T. So, generally SMM clusters possess a high-spin ground state (S_T) and a high negative zero-field splitting value (D) owing to high uniaxial magnetic anisotropy. For an SMM with large spin, the low-excited-state energy spectrum can be simulated using a double well model. So SMMs exhibit a stairlike magnetization hysteretic loop under T_B, where the step substructures arise from the quantum-tunneling effect between degenerated spin states under certain magnetic fields. Under T_B, SMMs could relax to another ground spin state under with thermal perturbation, and the corresponding relaxation time (τ) obeys the thermally activated Arrhenius law:

$$\tau(T) = \tau_0 \exp\left(\frac{\Delta E}{k_B T}\right) \tag{2}$$

It can be easily seen that the relaxation time will be longer and the blocking temperature higher with an increasing relaxation energy barrier. In order to take advantage of the extraordinary properties of SMMs, it is very important to increase the ground-state spin and uniaxial magnetic anisotropy of the molecule. For the strong relativistic effect of the rare earths, the spin–orbit coupling is more intense and results in stronger magnetic anisotropy. It is believed that introducing rare earth ions into the molecules will enhance the magnetic relaxation properties of SMMs. At the same time, large ground-state total angular momentum is also preferred in the designation of SMMs. Terbium (Tb^{3+}, f^8, ground-state $^7F_6$), dysprosium (Dy^{3+}, f^9, ground state $^6H_{15/2}$), and holmium (Ho^{3+}, f^{10}, ground state $^5I_8$), which possess a combination of these two points, are often selected in the synthesis because of their large uniaxial anisotropy and large ground state.

The first lanthanide-containing SMM is the [Cu–L–Ln(hfac)$_2$]$_2$ cluster,[12] where H_3L=1-(2-hydroxybenzamido)-2-(2-hydroxy-3-methoxy-benzylideneamino)-ethane, Hhfac = hexafluoroacetylacetone, and Ln = Tb^{3+} or Dy^{3+}. For the [Cu–L–Tb(hfac)$_2$]$_2$ cluster, magnetic measurements show that at 3-Oe oscillating field and frequency range 20–1000 Hz under a zero DC field, the out-of-phase susceptibility shows frequency-dependent peaks (Figure 3), which is indicative of the slow relaxation of the magnetization. By varying the frequency, the χ_M'' curves reach peaks at different temperatures. Through Arrhenius analysis, the energy barrier is 21 K and the relaxation time constant is 2.7×10^{-8} s. However, for the [Cu–L–Dy(hfac)$_2$]$_2$ cluster, the χ_M'' signal shows frequency dependence, but no peak is observed down to 2 K.

The Dy^{III} ion turns to be the core magnetic center in the molecule [Dy(hfac)$_3$]$_2$Cu(dpk)$_2$,[13] where dpk = di-2-pyridyl ketoximate. On taking the alternative current susceptibility measurement from 2 to 17 K at 50–10 000 Hz, both the in-phase and out-of-phase susceptibilities are found to be frequency dependent. The energy barrier fit from the Arrhenius plot is 47 K and τ_0 is 1.1×10^{-7} s. Additionally, χ_M'' against χ_M' as plotted at 8 K from 50 to 10 000 Hz is a semicircle, which indicates that this is a single-relaxation process.

As discussed in the Rare Earth Elements Magnetism, Gadolinium ion possesses an f^7 configuration and the ground state is an $^8S_{7/2}$ singlet. For the zero orbit angular moment and negligible spin–orbit coupling, Gd^{III} is an isotropic ion. However, some examples of

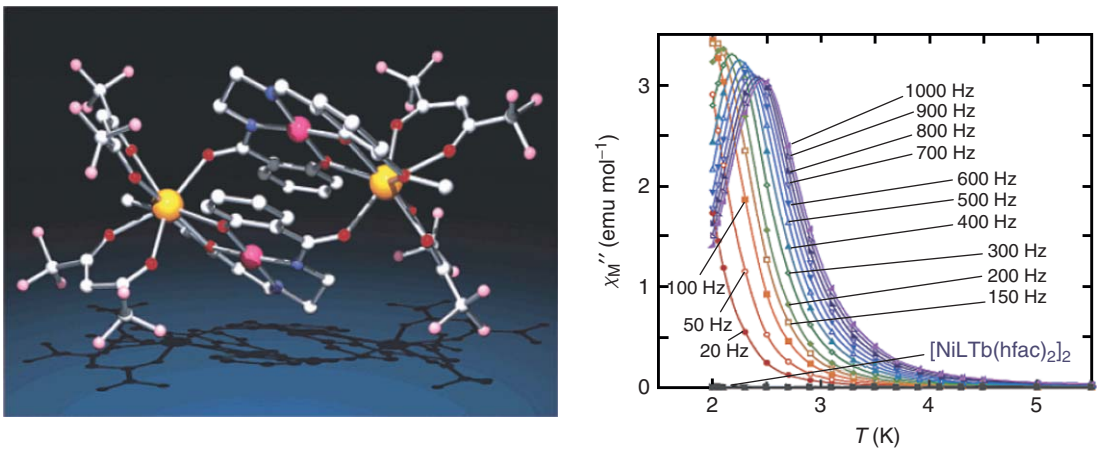


Figure 3 The structure of the [Cu–L–Tb(hfac)$_2$]$_2$ cluster and its relaxation behavior. (Reprinted with permission from Ref. 12. Copyright (2004) American Chemical Society)

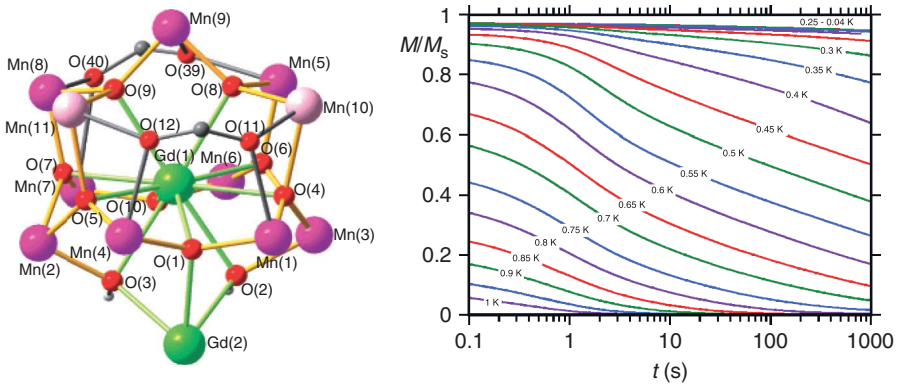


Figure 4 The structure of $Mn_{11}Gd_2$ cluster. (Reprinted with permission from Ref. 14. Copyright (2007) American Chemical Society)

SMMs including Gd^{3+} were found.[14] The geometry structure of the high-nuclearity complex with the formula $[Mn_9^{III}Mn_2^{II}Gd_2^{III}O_8(OH)_2(piv)_{10.6}(fca)_{6.4}(NO_3)_2(H_2O)]\cdot 13CH_3CN\cdot H_2O$, where pivH = *t*-BuCOOH, fcaH = 2-furancarboxylic acid, can be described as bell shaped where the two Gd ions form the bell's clapper (Figure 4).

The DC magnetic susceptibility of the complex measured at 1000 Oe from 1.8 to 300 K suggests that at low temperature, a well-defined high-spin ground state is almost exclusively thermally populated. The Curie Weiss fitting result of $\chi_M T$ versus T above 30 K indicates dominant antiferromagnetic interactions between spin carriers. The AC susceptibility of the complex over 1–1500 Hz from 1.8 to 3 K indicates that the out-of-phase susceptibility displays frequency dependence, but none of the curves reaches a peak at 1.8 K. The DC magnetization decay method determined the effective barrier of 18.4 K and the relaxation time constant of 2×10^{-12} s. As Gd^{III} ion is an isotropic spin ion, the major anisotropy contribution comes from the Mn^{3+} ion, which is the most important anisotropy source of SMMs and SCMs.

The above examples are all of 4f–3d series of SMMs, in which the rare earth ions function either as a magnetic anisotropy source or only an isotropic spin carrier. In fact, a pure lanthanide-composed molecule can also behave as an SMM. In 2006, Powell *et al*. reported that two dysprosium clusters shared similar structure of Dy_3 with the molecular formulae of $[Dy_3(\mu_3\text{-}OH)_2L_3Cl_2(H_2O)_4][Dy_3(\mu_3\text{-}OH)_2L_3Cl(H_2O)_5]Cl_5\cdot 19H_2O$ and $[Dy_3(\mu_3\text{-}OH)_2L_3Cl(H_2O)_5]Cl_3\cdot 4H_2O\cdot 2CH_3OH\cdot 0.7CH_3CN$, where HL = *o* vanillin.[15] Both structures consisted of triangles of Dy^{3+} centers capped by two μ_3-hydroxy bridges (Figure 5). The DC susceptibilities of the two compounds are similar, showing antiferromagnetic coupling between intratrimer spin centers as well as the gadolinium analogs. Dynamical magnetization studies were undertaken for both compounds. The AC susceptibilities of the complexes show strong frequency dependence below 20 K, which is typically observed for SMMs. However, the peaks are quite distorted by a shoulder structure. The relaxation barrier fit from AC data is 61.7 K and the relaxation time constant is 2.2×10^{-8} s (Figure 5).

The most promising example comes from the lanthanide-radical molecule $[K(18\text{-crown-6})]\{[(Me_3Si)_2N]_2(THF)Ln\}_2(\mu\text{-}\eta^2\text{:}\eta^2\text{-}N_2)$ (Ln = Gd, Dy; THF, tetrahydrofuran), in which two lanthanides are equivalent by symmetry and the coordination environment of each lanthanide is pseudotetrahedral with one vertex being occupied by the bridging N_2^{3-} radical.[16] Fitting the DC magnetic susceptibility data gives the exchange-coupling constant $-27\ cm^{-1}$ between the N_2^{3-} radical and the Gd^{III} ion, which is the largest among all the superexchange interactions between rare earth ions and other spin carriers. Variable-frequency AC magnetic susceptibility data show the obviously frequency-dependent peaks of the out-of-phase component in the temperature range 10–20 K, which indicates slow magnetic relaxation. As with other SMMs, the relaxation time exhibits an exponential dependence on temperature. The Arrhenius fit to the AC data gives an effective relaxation barrier of $U_{eff} = 123\ cm^{-1}$. Surprisingly, the isostructural Tb^{III} compound has a relaxation barrier as large as $227\ cm^{-1}$, which is the largest yet reported for exchange-coupled cluster-type SMMs.[17] More interestingly, the molecule can exhibit a large hysteresis loop at 14 K (Figure 6), which is a far higher temperature than that reported earlier for any kind of SMMs.

There are also some other SMMs with the composition 4f–4f, 4f–3d, or 4f-radical. In these cluster-type SMMs, the exchange-coupling interactions and the single-ion anisotropy of rare earths are both important for the slow magnetic relaxation behavior of SMMs. The complex exchange interactions often make it difficult to control the overall uniaxial anisotropy of the individual paramagnetic centers. Besides, the magnetic moments of spin carriers have the tendency to orientate the single-ion anisotropy axes randomly and this results in a small uniaxial anisotropy. Furthermore, the studies on the magnetic anisotropy as well as zero-field splitting properties of a single transition metal or rare earth ion, which is crucial in understanding the nature of the local anisotropy of SMMs, are always confused by

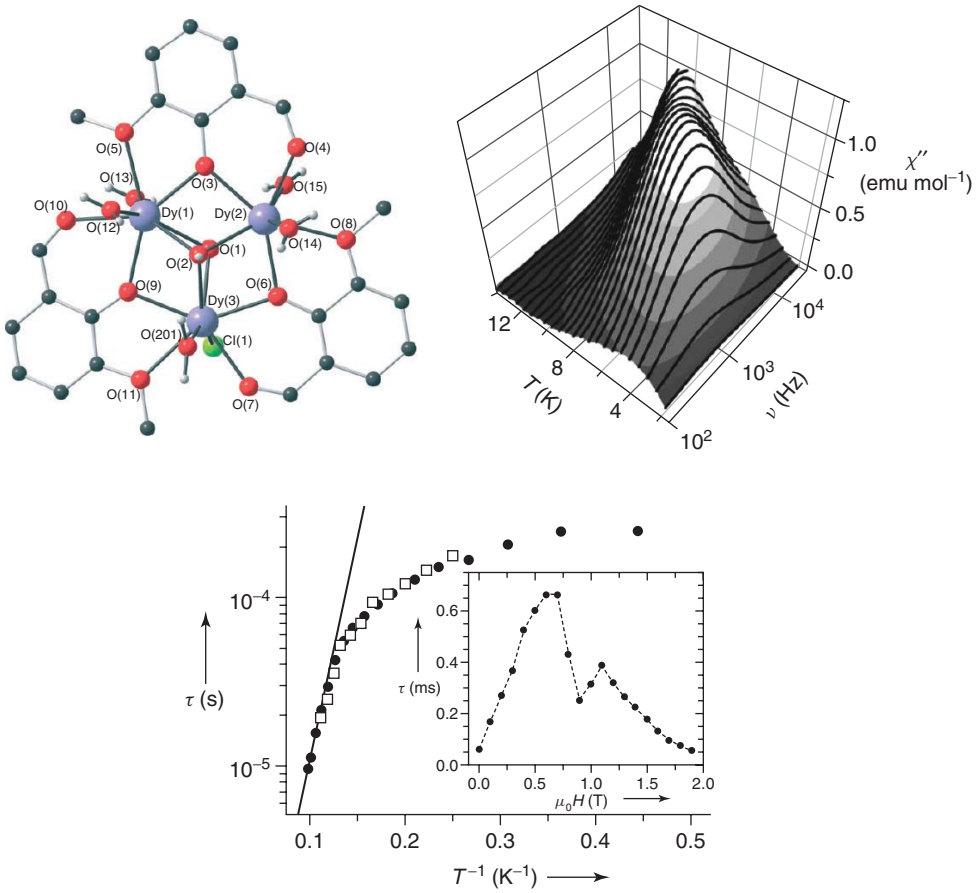


Figure 5 The structures of Dy_3 and its relaxation behavior. (Reproduced from Ref. 15. © Wiley-VCH Verlag GmbH & Co. KGaA, 2006)

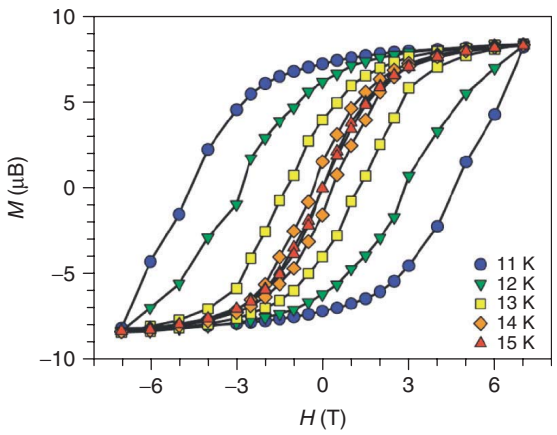


Figure 6 Plot of magnetization vs DC magnetic field for the Tb^{III} compound from 11 to 15 K. (Reprinted with permission from Ref. 17. Copyright (2011) American Chemical Society)

the magnetic coupling between spin centers. An interesting question that will be asked naturally is, ''Is it possible to obtain slow magnetic relaxation using only one rare earth ion?''

In answering this question, Ishikawa *et al*. found that some lanthanide phthalocyanine complexes exhibit a slow relaxation of magnetization at low temperature owing to the single rare earth ion contained in the molecule, which is defined as a single-ion magnet (SIM) now.[18] In 2001, Gao *et al*. discovered another kind of slow magnetic relaxation under a DC field in isolated lanthanide systems, which is quite different from the one in normal spin glass and superparamagnets. These two kinds of slow magnetic relaxation, under zero DC field or nonzero DC field are both attributed to a single lanthanide ion in the systems.

The first SIM bis(phthalocyaninato) terbium or dysprosium compound has a double-decker structure. AC susceptibilities measurement on polycrystalline powder sample of $[Pc_2Tb]^- \cdot TBA^+$ where $TBA^+ = (C_4H_9)_4N^+$ shows that the ratio of χ''_M/χ_M reaches maximum at 15, 32, and 40 K with frequency of 10, 100, and 997 Hz, respectively (the red plots in Figure 7). The measurement for a diluted sample with diamagnetic yttrium ion showed that the χ''_M/χ_M peaks remained (the solid plots in Figure 7). This clearly proves that the slow relaxation of magnetization is the single-molecular property of $[Pc_2Tb]^-$, rather than resulting from intermolecular interactions or magnetic ordering.

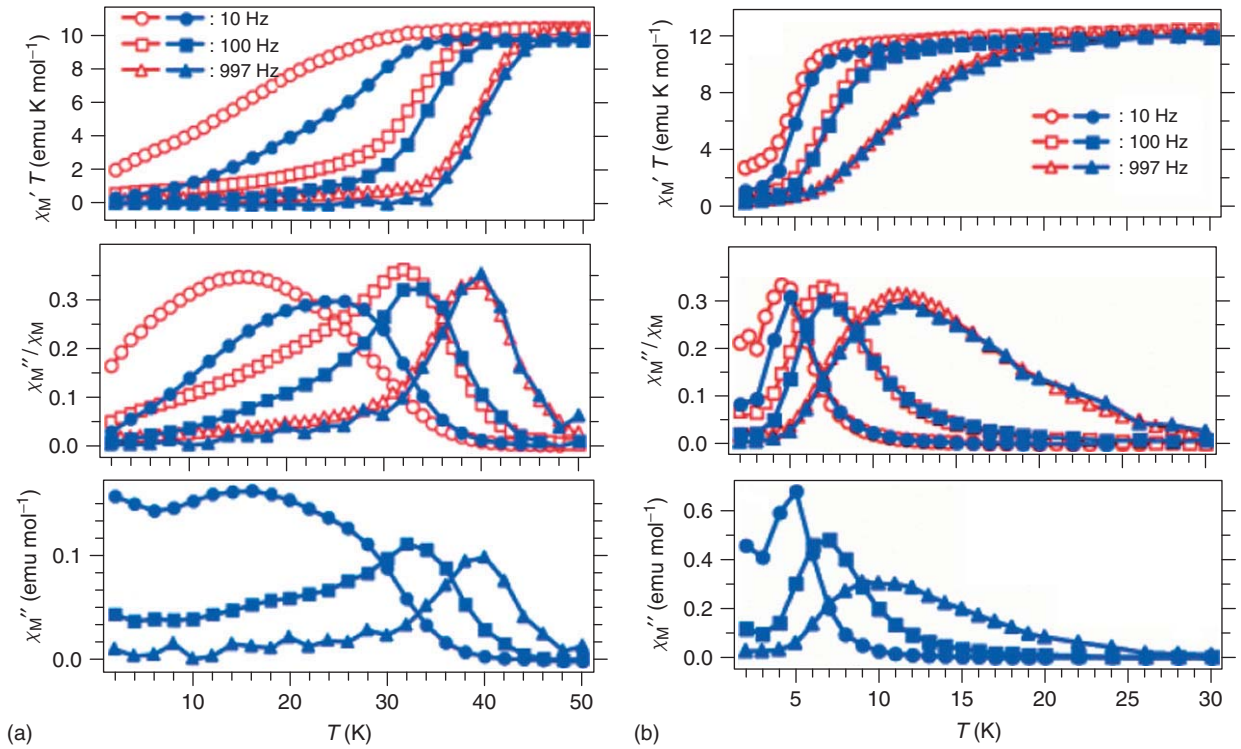


Figure 7 Frequency dependence of $[Pc_2Ln]^- \cdot TBA^+$, where Ln = Tb (a), and Dy (b) (Reprinted with permission from Ref. 18. Copyright (2003) American Chemical Society)

Further investigation on the electronic structure of the molecule reveals that slow magnetization relaxation comes from the ligand-field-induced changes in the ground- and low-excited-state energy spectra, which make Orbach relaxation process possible.[19] In the Tb complex, the lowest substrate is assigned to a degenerated Kramers doublet with $J_z = \pm 6$. In the Dy complex, the lowest substrate is characterized as $J_z = \pm 13/2$, the second largest in the $J = 15/2$ ground state (Figure 8). This means the two complexes have strong uniaxial magnetic anisotropy, which is essential for an SMM. Arrhenius analysis showed that the two-phonon Orbach process was dominant in the temperature range 25–40 K in the Tb complex, and in the 3–12 K range in the Dy complex. The relaxation barrier was estimated to be 260 and 31 cm^{-1} for the Tb and Dy complexes, respectively (Figure 8). These values are close to the energy differences between the lowest and the second lowest sublevels and are consistent with experiment results.

Chemists have also found some other SIMs based on lanthanide ion, for example, Er^{III} polyoxometalates and Dy^{III}-coordinated acetylactonate. These SIMs are all traditional inorganic compounds. In 2011, Gao *et al.* obtained an organometallic compound that shows slow magnetic relaxation and advanced the development of rare earth SIMs.[20] They reported a carbon-ring-coordinated SIM, featuring an Er^{III} ion sandwiched by two aromatic ligands pentamethylcyclopentadienide ($C_5Me_5^-$, Cp*) and cyclooctatetraenide ($C_8H_8^{2-}$, COT). It is composed of only 19 nonhydrogen atoms and is probably the lightest magnet yet reported. The ErCOTCp* molecule displays a butterfly-shaped hysteresis loop at 1.8 K up to even 5 K. AC susceptibility measurement reveals the existence of two thermally activated magnetic relaxation processes with the energy barrier as high as 197 and 323 K, respectively (Figure 9).

Since the composition of cluster type SMMs can be reduced and behaved as sing-ion magnet, is it possible to link the spin moment to one dimension and still show the slow magnetic relaxation properties? Forty years ago, Roy J. Glauber, the 2005 Nobel Prize winner in physics from Harvard University, predicted that slow relaxation can be observed in the 1D ferromagnetic Ising chain at low temperature.[21] This prediction was realized when the first SCM was found.[22] In principle, the 1D Ising chain is in a paramagnetic state at all finite temperature range, and long-range ordering can only be reached at 0 K. However, if the magnetic coupling between spin centers within the chain is large enough, magnetic interaction between chains can be negligible and the magnetic behavior of the chain will be similar to that of SMMs. Usually, the T_B of SCMs could be higher than that of SMMs because of its larger ground spin state value. It should be noticed that to design an SCM, interchain interaction should always be avoided. Although the 3d–4f or 4f–4f magnetic interactions are weaker than that of 3d–3d, lanthanide ions are always considered for use in the design of SCMs because of their large uniaxial magnetic anisotropy.

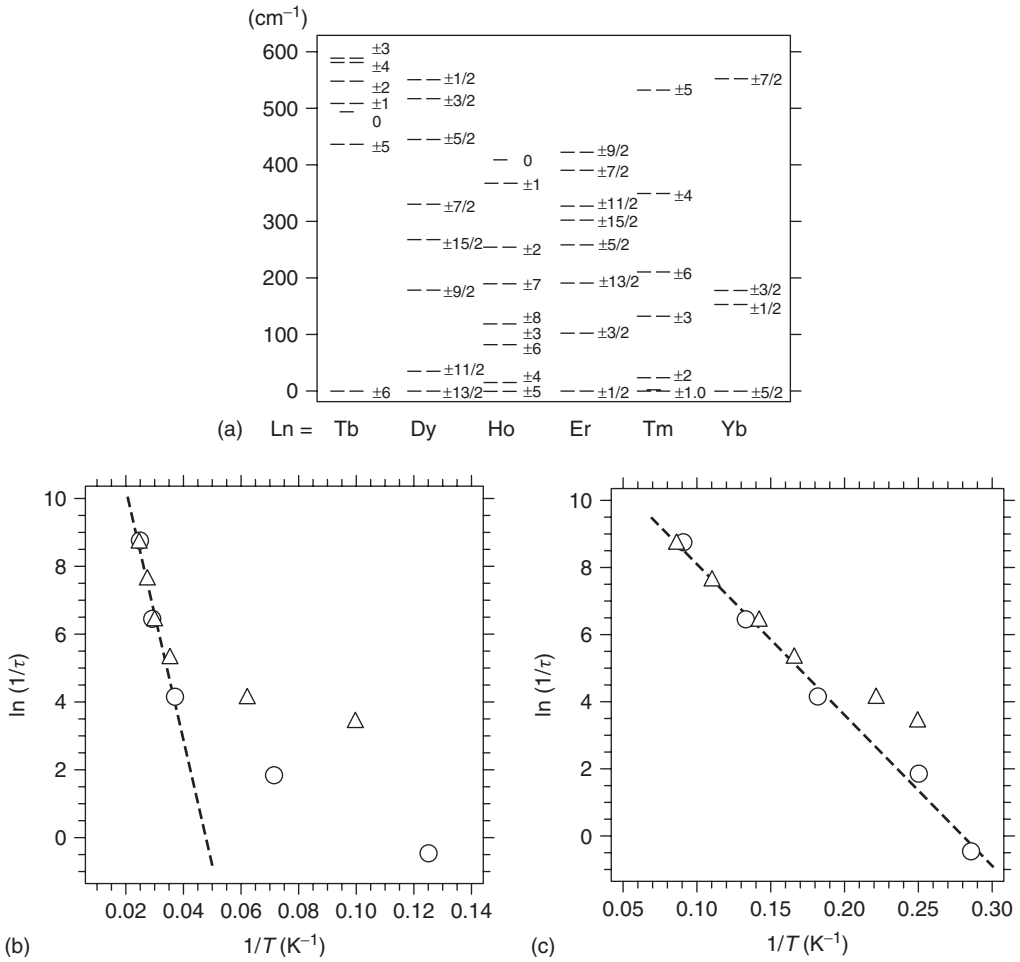


Figure 8 (a) The structure configurations of $[Pc_2Ln]^-\cdot TBA^+$, where Ln = Tb, Dy, Ho, Er, Tm, Yb; and Arrhenius analysis for $[Pc_2Ln]^-\cdot TBA^+$, where Ln = Tb (b), Dy (c) (Reprinted with permission from Ref. 19. Copyright (2004) American Chemical Society)

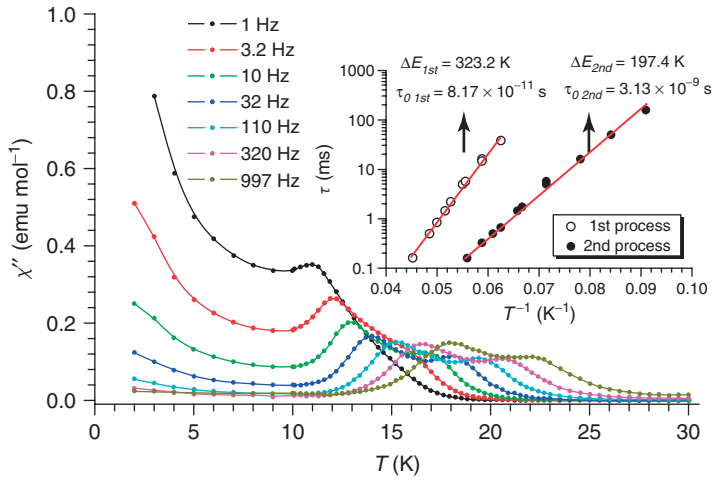


Figure 9 The out-of-phase AC susceptibility at various temperatures and frequencies in the absentce of a DC field at the temperature range 2–30 K. Inset, Arrhenius analysis of the two relaxation processes. (Reprinted with permission from Ref. 20. Copyright (2011), American Chemical Society)

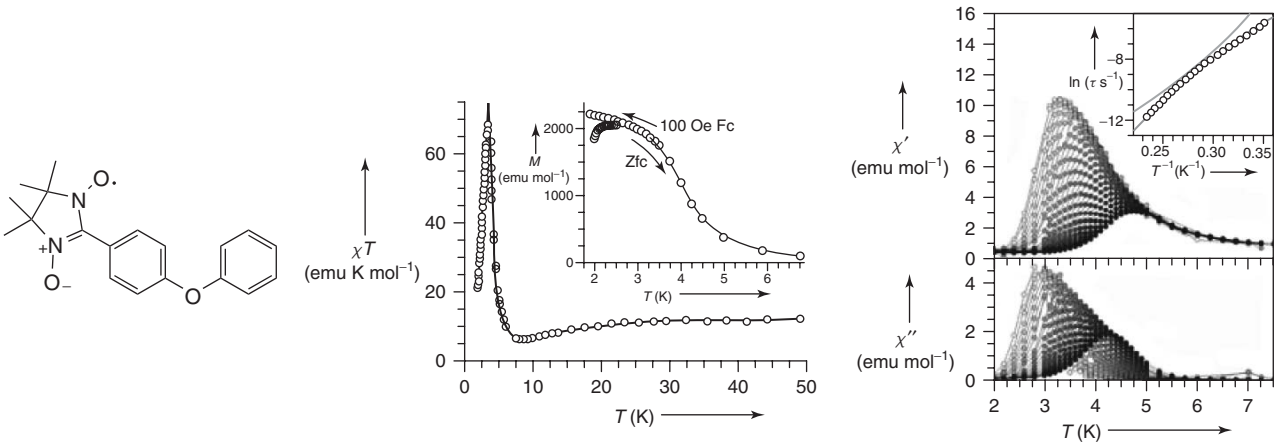


Figure 10 The ligand structures and the DC and AC magnetic susceptibilities of the compound $[Dy(hfac)_3NIT(C_6H_4 \quad p\text{-OPh})]$. (Reproduced from Ref. 24. © Wiley-VCH Verlag GmbH & Co. KGaA, 2005)

The first reported SCM containing rare earth ions is $(LCu)_2Tb(NO_3)$,[23] where H_3L = 2-hydroxy-*N*-2-[(2-hydroxyethyl) amino] ethyl-benzamide. The frequency dependency of the χ''_M is observed below 5 K for the frequency range 1–1000 Hz. Through Arrhenius analysis, the energy barrier is calculated as 28.5 K and relaxation time constant is 3.8×10^{-8} s. It should be noticed that the author failed to obtain the crystal structure of the compound and the formula was determined on the basis of elemental analysis.

$[Dy(hfac)_3NIT(C_6H_4 \quad p\text{-OPh})]$,[24] where $NIT(C_6H_4$ *p*-OPh) is a radical as shown in Figure 13, is a rare earth and radical-based SCM. Actually, $[Dy(hfac)_3NITC_2H_5]$, a similar compound, displays a transition to 3D ordering at 4.8 K although the interchain interaction is relatively weak. By substituting the ethyl into the biphenyl group, the free volume between the chains is alternatively occupied by the biphenyl substituent of two different chains and minimizes any weak magnetic interactions between the radicals. In this way, the average volume per metal center increases from 881 to 1001 Å^3 and, more importantly, the different chains are well separated and the exchange interaction between the chains could be negligible.

The DC magnetic susceptibility measurement for a powder sample shows that $\chi_M T$ reaches a minimum at 8.6 K and a rounded peak of 68.5 emu·K mol^{-1} at 3.6 K, which is a typical 1D behavior, while the cusp that should be found in 3D-ordered systems is not observed (Figure 10). The AC magnetic susceptibility measurement shows that χ''_M reaches peaks under 4.2 K in the range 2.5–20 000 Hz. The Arrhenius plot exhibits a crossover between two different relaxation regimes. The fitted τ_0 values are 5.6×10^{-10} s and 1.9×10^{-12} s and the two relaxation barriers are 42 and 69 K for the low- and high-temperature regimes, respectively. These two activated regimes of SCMs can be due to finite size effects.

4 CONCLUSIONS

The magnetism of rare earth ions and corresponding compounds are introduced briefly in this chapter. For the complicated electronic structures of ground and low excited states, lanthanide ions are good spin carriers to construct versatile molecular magnetic materials. Some important aspects of magnetic ordering material, SMMs, SIMs, and SCMs are all touched upon briefly. For strong magnetic anisotropy and big orbital contribution to the magnetic properties, which are much different from that in the transition metal ions and radicals, studies on molecular magnetic materials containing rare earth ions are far from developed and numerous questions and opportunities still exist.

5 ACKNOWLEDGMENTS

The authors thank the National Natural Science Foundation of China and the National Basic Research Program of China for financial support. The authors also thank Dr. Shang-Da Jiang for the invaluable and fruitful discussions.

6 RELATED ARTICLES

Magnetism.

7 ABBREVIATIONS AND ACRONYMS

SCM = single-chain magnets; SIM = single-ion magnet; SMM = single-molecule magnets.

8 REFERENCES

1. R. J. Elliott, 'Magnetic Properties of Rare Earth Metals', Plenum Press, 1972.
2. K. A. Gschneidner, Jr. and L. Eyring, 'Handbook on the Physics and Chemistry of Rare Earths', North-Holland, Amsterdam, 1979.
3. J. Jensen and A. R. Mackintosh, 'Rare Earth Magnetism: Structures and Excitations', Clarendon Press, Oxford, 1991.
4. F. Hulliger, M. Landolt, and H. Vetsch, *J. Solid State Chem.*, 1976, **8**, 283.
5. H. Kou, S. Gao, and B. Sun, *et al*., *Chem. Mater.*, 2001, **13**, 1431.
6. C. Benelli, A. Caneschi, D. Gatteschi, L. Pardi, and P. Rey, *Inorg. Chem.*, 1989, **28**, 275.
7. C. Benelli, A. Caneschi, D. Gatteschi, L. Pardi, and P. Rey, *Inorg. Chem.* 1989, **28**, 3230.
8. C. Benelli, A. Caneschi, D. Gatteschi, L. Pardi, and P. Rey, *Inorg. Chem.*, 1990, **29**, 4223.
9. J. W. Raebiger and J. S. Miller, *Inorg. Chem.*, 2002, **41**, 3308.
10. H. Zhao, M. J. Bazile, J. R. Galán-Mascarós, and K. R. Dunbar, *Angew. Chem. Int. Ed.*, 2003, **42**, 1015.
11. R. L. Carlin, in 'Magnetochemistry', Springer-Verlag Berlin Heidelberg, Berlin, 1986, p. p. 49.
12. S. Osa, T. Kido, N. Matsumoto, N. Re, A. Pochaba, and J. Mrozinski, *J. Am. Chem. Soc.*, 2004, **126**, 420.
13. F. Mori, T. Nyui, T. Ishida, T. Nogami, K. Y. Choi, and H. Nojiri, *J. Am. Chem. Soc.*, 2006, **128**, 1440.
14. V. M. Mereacre, A. M. Ako, R. Clérac, W. Wernsdorfer, G. Filoti, J. Bartolomé, C. E. Anson, and A. K. Powell, *J. Am. Chem. Soc.*, 2007, **129**, 9248.
15. J. Tang, I. Hewitt, N. T. Madhu, G. Chastanet, W. Wernsdorfer, C. E. Anson, C. Benelli, R. Sessoli, and A. K. Powell, *Angew. Chem. Int. Ed.*, 2006, **45**, 1729.
16. J. D. Rinehart, M. Fang, W. J. Evans, and J. R. Long, *Nat. Chem.*, 2011, **3**, 538.
17. J. D. Rinehart, M. Fang, W. J. Evans, and J. R. Long, *J. Am. Chem. Soc.*, 2011, **133**, 14236.
18. N. Ishikawa, M. Sugita, T. Ishikawa, S. Koshihara, and Y. Kaizu, *J. Am. Chem. Soc.*, 2003, **125**, 8694.
19. N. Ishikawa, M. Sugita, T. Ishikaw, S. Koshihara, and Y. Kaizu, *J. Phys. Chem. B*, 2004, **108**, 11265.
20. S. D. Jiang, B. W. Wang, H. L. Sun, Z. M. Wang, and S. Gao, *J. Am. Chem. Soc.*, 2011, **133**, 4730.
21. R. J. Glauber, *Phys. Rev. Lett.*, 1963, **10**, 84.
22. A. Caneschi, D. Gatteschi, N. Lalioti, C. Sangregorio, R. Sessoli, G. Venturi, A. Vindigni, A. Rettori, M. G. Pini, and M. A. Novak, *Angew. Chem. Int. Ed.*, 2001, **40**, 1760.
23. J. P. Costes, J. M. Clemente-Juan, F. Dahan, and F. Milon, *Inorg. Chem.*, 2004, **43**, 8200.
24. L. Bogani, C. Sangregorio, R. Sessoli, and D. Gatteschi, *Angew. Chem. Int. Ed.*, 2005, **44**, 5817.

Near-Infrared Materials

Lining Sun and Liyi Shi

Shanghai University, Shanghai, People's Republic of China

1	Summary	347
2	Introduction	347
3	Photophysics of NIR-Emitting Lanthanide Ions	348
4	NIR-Luminescent Lanthanide Complexes	350
5	NIR-Luminescent Hybrid Materials Based on Lanthanides	356
6	Conclusions	365
7	Glossary	366
8	Acknowledgments	366
9	Related Articles	366
10	Abbreviations and Acronyms	366
11	References	366

1 SUMMARY

The spectral range of near-infrared (NIR) luminescence starts from 750 to 2500 nm. Yb^{3+}, Nd^{3+}, and Er^{3+} are well known for their NIR luminescence, but other lanthanide ions (Pr^{3+}, Sm^{3+}, Dy^{3+}, Ho^{3+}, and Tm^{3+}) also show transitions in the NIR region besides visible region.[1,2] NIR luminescence attracts interest based on their advantages for biological applications,[3] lasers, NIR organic light-emitting diode (OLED) technology,[4] solar energy conversion,[5,6] and amplifiers for telecommunication.[7,8] This chapter describes the primary themes of current interest in NIR-luminescent lanthanide complexes and materials. We mainly concentrate on NIR-luminescent lanthanide Yb^{3+}, Nd^{3+}, and Er^{3+} ions, and the less well-studied Pr^{3+}, Sm^{3+}, Dy^{3+}, Ho^{3+}, and Tm^{3+} ions are also mentioned when relevant. After a brief introduction, we describe the developments in (i) photophysics of NIR-emitting lanthanide ions; (ii) NIR-luminescent lanthanide complexes on the various sensitizers proposed for encapsulating these ions, such as β-diketone, ligands based on 8-hydroxyquinolinate, d-transition metal complexes, metal–organic frameworks (MOFs), and macrocyclic ligands;and (iii) NIR-luminescent materials based on sol–gel, mesoporous materials, polymer, ionic liquids, and upconverting materials. The chapter ends by conclusion on the possible research trend and critical evaluation of the chromophores for sensitizing NIR-emitting trivalent lanthanide ions.

2 INTRODUCTION

The trivalent lanthanide (Ln) ions have been known for their unique optical properties such as line-like emission spectra and high-luminescence quantum efficiency (see ***Luminescence***).[9] Historically, detailed research has been almost exclusively devoted to visible-luminescent lanthanide ions, particularly europium and terbium.[1] In the last decade, much effort has focused on the sensitization of NIR-luminescent lanthanides (with Ln = Nd, Er, Yb, Ho, Tm, Dy, Sm, and Pr), which are emissive in the NIR region of the spectrum (750–2500 nm).[2,10–14]

As an example, NIR emission is advantageous for biological applications because (i) NIR photons scatter less than visible photons for improved biological imaging resolution,[15] (ii) biological systems have low native autofluorescence in the NIR domain for better signal-to-noise ratio and corresponding detection sensitivity,[16] and (iii) biological tissues are almost transparent to NIR light (NIR photons travel deep, several centimeters, in tissues, organs, or organisms).[3] NIR lanthanide luminescence can also be advantageously used in associated lasers and NIR OLED technology,[4] solar energy conversion,[5,6] and telecommunication where the electronic structure of lanthanide ions such as Er^{3+}, Nd^{3+}, Tm^{3+}, and Ho^{3+} can be used as the active material for optical amplifiers of NIR signals.[7,8]

The Rare Earth Elements. Edited by David A. Atwood. © 2012 John Wiley & Sons, Ltd. ISBN 978-1-119-95097-4

The f–f transitions of lanthanide ions have too small oscillator strengths to yield an efficient excitation path. One of the most useful strategies that has been employed to overcome this drawback is to insert Ln^{3+} ions in a variety of molecular and supramolecular assemblies, the sensitizers, which control and even enhance their photophysical properties through the so-called antenna effect.[17] The sensitizer, whose triplet state matches the accepting level of the lanthanide ion, absorbs the UV–visible light and efficiently transfers the energy to the central lanthanide ion, ultimately resulting in sensitized NIR emission of Ln^{3+} ion. Most investigations have focused on organic ligands such as diketones, quinolines, phenanthrolines, cryptands, and transition metal complexes.

For technological applications, the NIR-luminescent lanthanide complexes have to be incorporated into a stable matrix because of their poor thermal stability and low mechanical strength.[18] So far, the incorporation of luminescent lanthanide complexes in matrices, as a result, the NIR-luminescent lanthanide hybrid materials, is of widespread interest in material science as it allows construction of functional materials with various optical properties.[19] The study of NIR-luminescent lanthanide complexes in hybrid materials is not only of fundamental interest but these materials also have a high potential for different applications (optical amplifiers, optical waveguides, OLEDs, etc.). In general, these hybrid materials have superior mechanical properties and have a better processability than the pure lanthanide complexes. Moreover, embedding a lanthanide complex in a hybrid matrix is also beneficial for its thermal stability and luminescence output.[18,20,21]

The aim of this chapter is to give an overview of the different types of NIR-luminescent lanthanide-based materials and to compare their respective advantages and disadvantages. The literature has been covered until October 2011.

3 PHOTOPHYSICS OF NIR-EMITTING LANTHANIDE IONS

Yb^{3+}, Nd^{3+}, and Er^{3+} are well known for their NIR luminescence, but other lanthanide ions (Pr^{3+}, Sm^{3+}, Dy^{3+}, Ho^{3+}, and Tm^{3+}) also show transitions in the NIR region besides visible region. However, the designation of lanthanide NIR-emitting ions is usually restricted to those ions mainly emitting in the NIR spectral domain. Some relevant electronic levels of NIR-emitting Ln^{3+} ions are shown in Figure 1, where the luminescent levels are indicated by black down triangles when the transition terminates on one of the sublevels of the ground state while other transitions are designated by arrows. A list of the main NIR transitions can be found in Table 1.[20]

As for the ions of prime interest for this chapter, Er^{3+} ion is of interest for use as a planar-waveguide optical amplifier, as it emits approximately at 1.54 μm ($^4I_{13/2} \rightarrow {}^4I_{15/2}$ transition), one of the standard telecommunication wavelengths.[22] The Nd ($^4F_{3/2} \rightarrow {}^4I_{13/2}$) transition at about 1.35 μm falls within the range of another telecommunication window.[23] But this one has not yet been exploited to the same extent as Er. Nd^{3+} ion is an interesting ion and displays fluorescence in three distinct spectral ranges: 0.87–0.92, 1.06–1.09, and 1.32–1.39 μm ($^4F_{3/2} \rightarrow {}^4I_{9/2}$, $^4I_{11/2}$, $^4I_{13/2}$ transitions). Its main fluorescence line at 1.06 μm is the well-known transition used in Nd:YAG (yttrium aluminum garnet) lasers and which can be doubled to yield green emission at 532 nm, tripled to produce blue light, or quadrupled to generate UV emission at 266 nm. In the field of the laser materials, materials with Yb^{3+} ion attract much attention due to the $^2F_{5/2} \rightarrow {}^2F_{7/2}$ transition (in the range of 0.98–1.03 μm) of the Yb^{3+} ion, for its very simple energy levels and relatively broad absorption which will be well suitable for laser diode and pumping in this range, and the smaller Stokes shift between absorption and emission reduces the thermal loading of the material during laser operation.[24] Furthermore, Yb^{3+} ion is less sensitive to nonradiative deactivations in view of the large energy gap between $^2F_{5/2}$ and ground $^2F_{7/2}$ levels, which is capturing much attention with respect to bioapplications.[4,25]

Among the other NIR-emitting ions, Pr^{3+} ion has two main NIR bands at 1.04 μm ($^1D_2 \rightarrow {}^3F_4$) and 1.3 μm ($^1G_4 \rightarrow {}^3H_5$), the latter being used in telecommunications for amplification of the 1.3 μm signals. Sm^{3+} ion features three spin-forbidden NIR-emission lines from the $^4G_{5/2}$ excited state to sublevels of the first excited spectroscopic term, namely ^6F_J with $J = 9/2$, 7/2, and 5/2. The less well-known Dy^{3+} ion exhibits three NIR-emission bands, one around 1.3 μm ($^6H_{9/2}$, $^6F_{11/2} \rightarrow {}^6H_{15/2}$), which has been considered as a third candidate for amplification of the 1.3 μm signals; one ($^6H_{11/2} \rightarrow {}^6H_{15/2}$) at 1.75 μm; and another one at longer wavelength, $^6H_{13/2} \rightarrow {}^6H_{15/2}$ around 2.9 μm. One of the lanthanide ions with the richest spectroscopic properties is Ho^{3+} ion, including upconversion; one emission line is close to the second telecommunication window ($^5F_5 \rightarrow {}^5I_6$, 1.5 μm) while another, at 2.1 μm ($^5I_7 \rightarrow {}^5I_8$), has generated several medical applications in laser surgery for ophthalmic treatments or for enucleating the prostate for instance. The lasers are Ho:YAG systems directly pumped into the $^5I_7$ level, Tm^{3+} ion being used as sensitizer, thanks to its $^3F_4 \rightarrow {}^3H_6$ line at 1.8–1.9 μm, itself pumped by a diode laser. Ho^{3+} emits a second NIR line around 2.2–2.3 μm ($^5I_4 \rightarrow {}^5I_6$). In addition to the transition mentioned above, Tm^{3+} ion displays another NIR line at 1.4–1.5 μm, arising from the $^3H_4 \rightarrow {}^3F_4$ transition.[20]

As discussed in Sections 3 and 4, NIR-emitting lanthanide ions are very sensitive to radiationless deactivation through vibrations, even when embedded into inorganic matrices. Multiphonon relaxation rates have been estimated for the main NIR-emission lines of Nd^{3+}, Dy^{3+}, Tm^{3+}, Pr^{3+}, and Er^{3+} ions in function of the phonon energy,[26] and this set of data should be taken into consideration when new molecules and materials are being designed.[4]

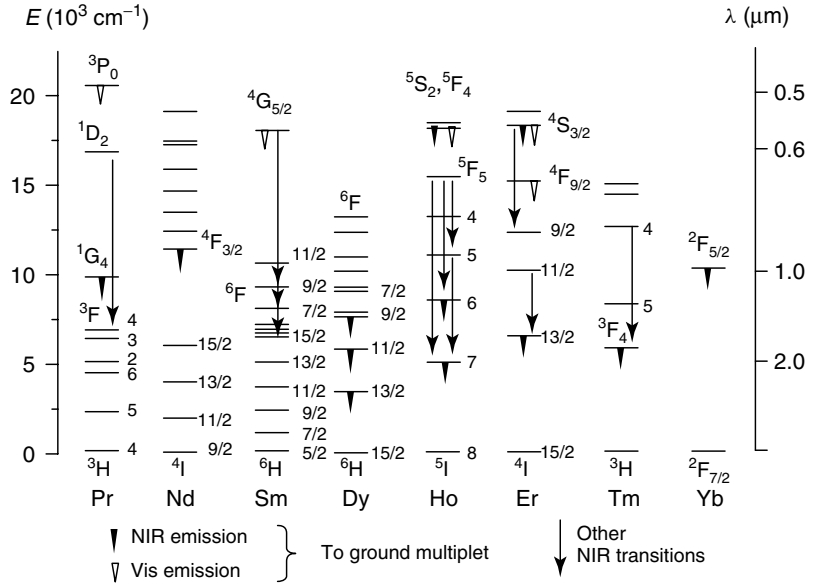


Figure 1 Selected transitions for the most important NIR-emitting lanthanide ions. (Reproduced from Ref. 20. © Elsevier, 2007.)

Table 1 The most important f–f transitions of NIR-luminescent lanthanides, and f–f transitions participating in upconversion (UC) and downconversion (DC) processes

Ln	Ground level	Initial level	Final level	λ (μm)	Comment
Pr	$^3H_4$	$^1D_2$	$^3F_4$	1.01–1.04	NIR
		$^1D_2$	$^1G_4$	1.44	NIR
		$^1G_4$	$^3H_5$	1.30–1.33	NIR, telecom line
Ho	$^5I_8$	$^5F_5$	$^5I_7$	0.965–0.99	NIR, UC
		$^5F_5$	$^5I_6$	1.48–1.51	NIR
		$^5F_5$	$^5I_5$	2.39–2.45	NIR
		$^5I_5$	$^5I_8$	910	UC
		$^5I_5$	$^5I_7$	1.63–1.68	NIR
		$^5I_6$	$^5I_8$	1.16–1.19	NIR
		$^5I_7$	$^5I_8$	1.98–2.104	NIR, laser line
Nd	$^4I_{9/2}$	$^4F_{3/2}$	$^4I_{9/2}$	0.87–0.92	NIR
		$^4F_{3/2}$	$^4I_{11/2}$	1.06–1.09	NIR
		$^4F_{3/2}$	$^4I_{13/2}$	1.32–1.39	NIR
		$^4F_{3/2}$	$^4I_{15/2}$	1.84–1.86	NIR
Sm	$^6H_{5/2}$	$^4G_{5/2}$	$^6F_{1/2}$	0.880	NIR
			$^6F_{7/2}$	1.02–1.04	NIR
			$^6F_{9/2}$	1.16–1.17	NIR
Dy	$^6H_{15/2}$	$^6H_{9/2}$, $^6F_{11/2}$	$^6H_{15/2}$	1.28–1.34	NIR
		$^6H_{11/2}$	$^6H_{15/2}$	1.70–1.80	NIR
		$^6H_{13/2}$	$^6H_{15/2}$	2.89–3.02	NIR
Er	$^4I_{15/2}$	$^4S_{3/2}$	$^4I_{9/2}$	1.705	NIR, laser line
		$^4I_{11/2}$	$^4I_{13/2}$	2.703	NIR, laser line
		$^4I_{13/2}$	$^4I_{15/2}$	1.546	NIR, telecom line
Tm	$^3H_6$	$^3H_4$	$^3H_6$	0.780–0.805	UC
		$^3H_4$	$^3H_5$	2.33	NIR
		$^3H_4$	$^3F_4$	1.4–1.5	NIR
		$^3F_4$	$^3H_6$	1.75–1.90	NIR, DC
Yb	$^2F_{7/2}$	$^2F_{5/2}$	$^2F_{7/2}$	0.96–1.03	NIR, DC, UC

Redrawn after Ref. 20. © Elsevier, 2007.

4 NIR-LUMINESCENT LANTHANIDE COMPLEXES

In order to obtain sufficient NIR-emission intensity arising from the lanthanide ions, the sensitizers—antenna—have to fulfill several requirements. (i) The sensitizers need to remain at sufficiently close distance to the lanthanide ions for a good energy transfer to occur. (ii) The donating levels of the sensitizers should match the accepting energy level of the lanthanide ions. In most of the cases, it is considered that efficient donating levels are triplet states located on sensitizers. (iii) Sensitizers should be synthetically modified to eliminate functional groups with high energy-stretching frequencies that are particularly detrimental to NIR emission, that is, –OH, –NH, and –CH vibrations (Figure 2).[27]

The field of development of sensitizers for NIR-emitting lanthanide ions is currently booming. A large number of examples can be found in the literature, such as β-diketone, ligands based on 8-hydroxyquinolinate, complexes with transition metal ions, MOFs, macrocyclic ligands, and so on.

4.1 NIR-Luminescent Lanthanide β-Diketonates

Lanthanide β-diketonates are complexes of β-diketone ligands (1,3-diketones) with lanthanide ions. These complexes are the most popular and the most intensively investigated luminescent lanthanide coordination compounds (see ***β-Diketonate***). Three main types of lanthanide(III) β-diketonate complexes have to be considered: *tris* complexes, Lewis base adducts of the *tris* complexes (ternary lanthanide β-diketonates), and *tetrakis* complexes. Most Eu^{3+} β-diketonate complexes show an intense visible luminescence, but many β-diketonates are not good ligands to sensitize the luminescence of Tb^{3+} ions. NIR luminescence can be expected for the β-diketonate complexes of Yb^{3+}, Nd^{3+}, Er^{3+} Pr^{3+}, Sm^{3+}, Dy^{3+}, Ho^{3+}, and Tm^{3+} ions.

Sensitization of Yb^{3+} ion luminescence by dibenzoylmethanate (dbm) was demonstrated in 1958,[28] but interest rapidly died out until in the 1990s.[29] Zang and coworkers fabricated the NIR electroluminescence (EL) devices by using $[Tm(dbm)_3bath]$ and $[Tm(dbm)_3phen]$ complexes, from which the EL emissions at 1.4 and 0.8 µm were observed. By comparison with the NIR emissions of four Tm^{3+} complexes with different ligands, it was found that the first β-diketonate ligand played a more important role for the Tm^{3+} ion emissions rather than the second one.[30] Barbillat *et al.* designed a modified Fourier transform Raman bench spectrometer for the detection of NIR luminescence (1.54 µm attributed to $^4I_{13/2} \rightarrow {}^4I_{15/2}$ transition) of $[Er(acac)_3phen]$ and $[Er(tta)_3phen]$ complexes, recorded both in solution and in the solid state.[31]

The ternary lanthanide complexes $[Ln(tfnb)_3L]$ (where Ln = Nd, Er, Yb; tfnb = 4, 4, 4-trifluoro-1-(2-naphthyl)-1,3-butanedionate; L = 1-(4-carbazolylphenyl)-2-pyridinyl benzimidazole) with β-diketonate ligand tfnb were synthesized and showed the characteristic NIR luminescent of the corresponding Ln^{3+} ions, which offer the opportunities to develop new materials suitable for optical amplifiers operating at 1.5 and 1.3 µm.[32] Bünzli and coworkers synthesized two push–pull diketone derivatives, CTPD and CTNP (see Figure 3), and the resulting tris(diketonate) ternary complexes with terpyridine $[Ln(CTPD)_3(tpy)]$ and $[Ln(CNPD)_3(tpy)]$ (Ln = Er, Nd) display sizeable NIR emission with long luminescence lifetimes (in the range 1.17–1.44 µs for Er^{3+} complexes and 0.81–1.01 µs for Nd^{3+} complexes in aerated MeCN solution).[33]

Metal-controlled assembly results in a series of lanthanide clusters with the formula of $Ln_5(dbm)_{10}(OH)_5 \cdot$

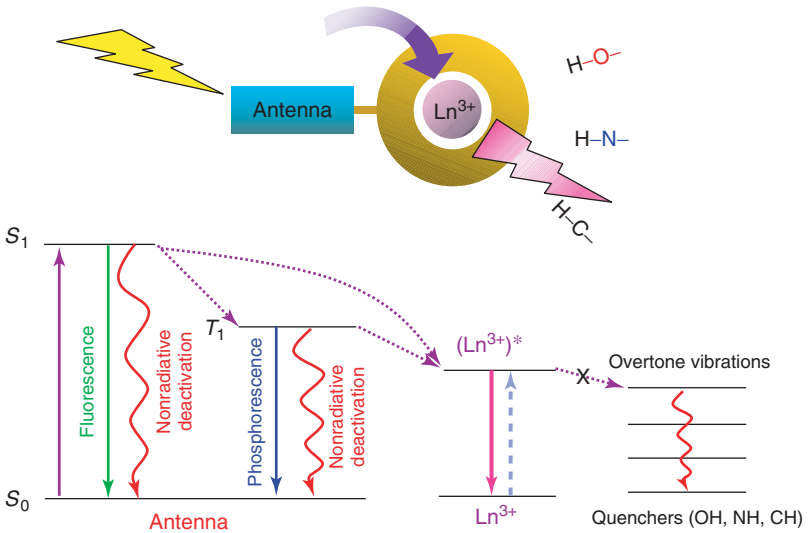


Figure 2 Schematic representation of the antenna effect of the NIR-luminescent lanthanide complexes. (Reproduced from Ref. 27. © Elsevier, 2010.)

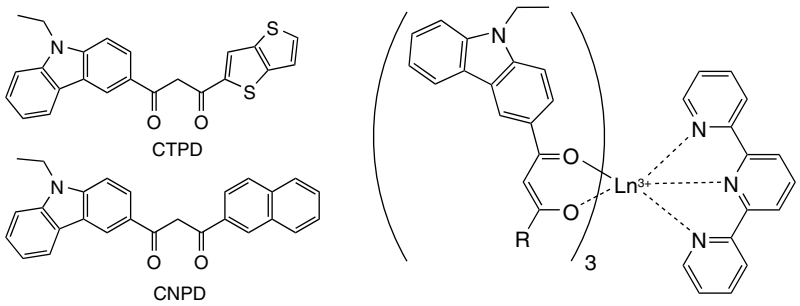


Figure 3 The structures of two diketone derivatives CTPD and CNPD, and complexes $[Ln(CTPD)_3(tpy)]$ and $[Ln(CNPD)_3(tpy)]$ (R = thieno[3,2 − *b*]thiophene or naphthalene moiety).[33] (Reproduced from Ref. 33 with permission of The Royal Society of Chemistry.)

n(solvent) (Ln = Nd, Er, and Yb; solvent = CH_3CN or toluene). The lanthanide β-diketonate clusters show typical NIR luminescence upon excitation at 350 nm, which represents the first examples of pentanuclear lanthanide clusters with sensitized NIR emission. The consistent formation of isostructural clusters through the whole lanthanide series bodes well for the further application of this method with other β-diketone ligands.[34]

According to the literature reported previously, the replacement of C-H bonds in β-diketone ligand with lower energy C-F oscillators is able to lower the vibration energy of the ligand, which decreases the energy loss caused by ligand vibration.[35,36] Owing to the heavy atom effect,[3] which facilitates intersystem crossing, the lanthanide-centered luminescent properties are enhanced.[37] Sun *et al*. synthesized two series of the complexes $[Ln(hfth)_3phen]$ (where Ln = Er, Ho, Yb) and $[Ln(hfth)_3bipy]$ (where Ln = Er, Ho, Yb, Nd) with hfth having the heptafluoropropyl group, members of which have been structurally characterized. After ligand-mediated excitation of the complexes, they all show the characteristic NIR luminescence of the corresponding Ln^{3+} ions. The heptafluorinated substituent in the main sensitizer hfth serves to reduce the degree of vibrational quenching.[14] With these NIR-luminescent lanthanide complexes, the luminescent spectral region from 1300 to 1600 nm, which is of particular interest for telecommunication applications, can be covered completely (see Figure 4). Zhang *et al*. reported six ternary lanthanide complexes $[Ln(tfnd)_3dione]$ and $[Ln(tfnd)_3dafone]$ (Ln = Ho, Pr, Tm) were synthesized based on fluorinated-ligand, Htfnd ligand, and two synergic ligands, respectively. They all show the characteristic NIR luminescence of the corresponding Ln^{3+} ions. This can be attributed to the strong ability of the organic ligands transferring the absorbed energy to the central Ln^{3+} ions, via an antenna effect.[38] The NIR-luminescent lanthanide complexes of Ho^{3+}, Pr^{3+}, and Tm^{3+} ions are less well reported in the open literature so far.[39]

Heterotrinuclear Zn_2Ln (Ln = Nd, Er, Yb) clusters $[(Znq_2)_2](\mu\text{-}CH_3COO)\{Ln(hfac)_2\}$(*q* = 8-hydroxylquinolinate) are formed with β-diketone Hhfac and Znq_2-based

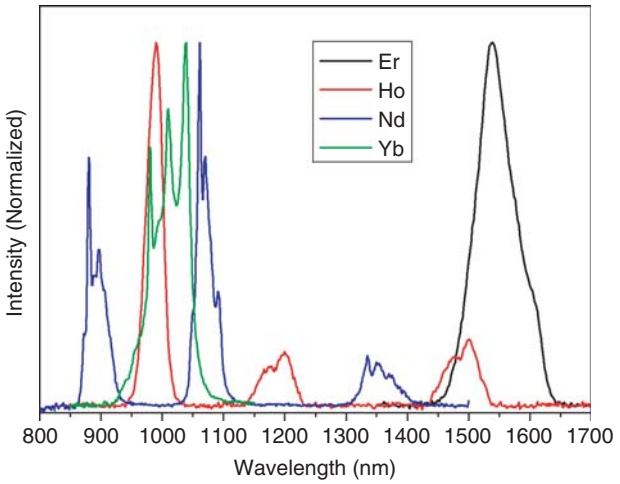
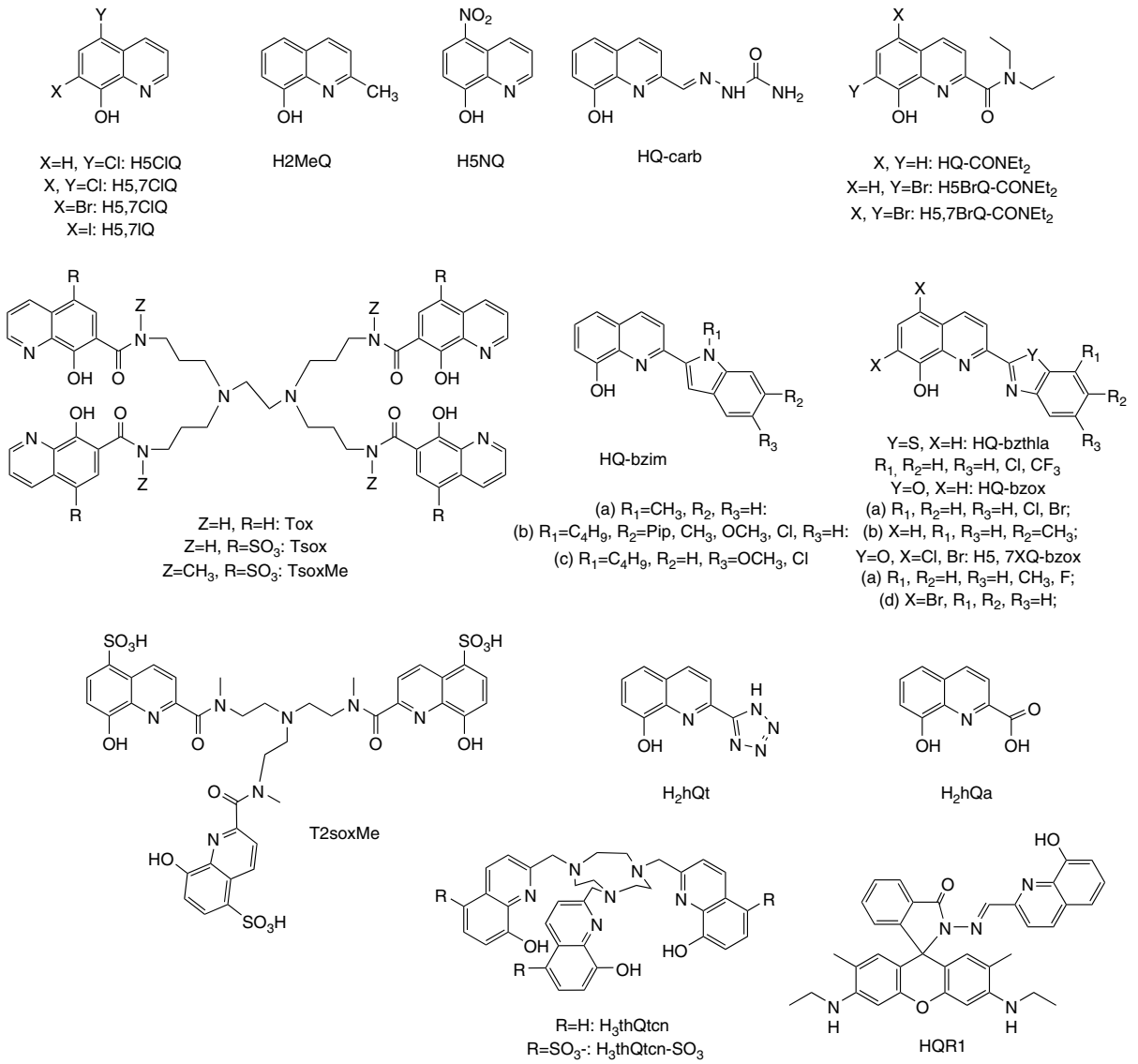


Figure 4 Emission spectra (λ_{ex} = 397 nm) of $[Ln(hfth)_3phen]$ complexes (Ln = Er, Ho, Yb) and $[Nd(hfth)_3bipy]$ (in solid state as powder) at room temperature. (Reproduced from Ref. 14. © Wiley-VCH Verlag GmbH & Co. KGaA, 2006.)

metalloligand. These complexes can be excited with visible light and show the corresponding NIR luminescence. The emissive lifetimes of lanthanide luminescence are in microsecond ranges in both solid state and dichloromethane solution at room temperature, which is much longer than those of $[Ln(hfac)_3(H_2O)_2]$ and $[Lnq_3]$ complexes. This fact can be attributed to the full exclusion of solvent molecules coordination to Ln^{3+} ions, which are the most important lanthanide-luminescent quenchers, by the eight-coordination of diketonate and 8-hydroxyquinoline (HQ) ligands.[40]

4.2 8-Hydroxyquinolinate-Based Lanthanide Complexes

8-HQ ligands are good ''light harvesters'' and possess good photosensitizing properties toward the NIR-emissive lanthanide ions, since, in addition to broad absorption and emission bands in the visible region, they have triplet-state energies (at about 18 000 cm^{-1}) matching well with the



Scheme 1 Some quinolinol derivatives used to prepare luminescent complexes with lanthanide ions[45]

accepting energy levels of the 4f orbitals of Er^{3+}, Nd^{3+}, and Yb^{3+} ions, while are unsuitable for the resting lanthanide ions.[41] Besides the parent HQ, several other HQ derivatives, chloro- and bromosubstituted, bidentate or multidentate, have been employed so far (see Scheme 1). The introduction of substituents on the quinoline ring allows the fine tuning of the single and triplet states leading to a better ligand–metal (Er^{3+}, Nd^{3+}, and Yb^{3+} ions) energy overlap, and therefore to increased emission quantum yields.[42,43] Dihalosubstituted quinolinols, in particular, have been tentatively used to improve the emission efficiency by reducing the number of C–H quenching groups in the complex.[44]

After the discovery of the 1.54 μm Er^{3+} ion luminescence in $[Er(Q)_3]$, in 1999, by Gillin and Curry[46] and subsequently metal-centered luminescence in the corresponding $[Nd(Q)_3]$[47] and $[Yb(Q)_3]$[48] complexes, several derivatives of this chromophore,[49] including podands[45,50] and macrocycles,[51] have been proposed with success for the sensitization of Er^{3+}, Nd^{3+}, and Yb^{3+} ions. Imbert *et al*. synthesized several 8-hydroxyquinolinate-based ligands such as polydentate tripodal ligand (T2soxMe) and polydentate ligands (e.g., Tsox and TsoxMe, see Scheme 1). The lanthanide (Er^{3+}, Nd^{3+}, and Yb^{3+} ions) chelates are resistant toward hydrolysis and show interesting NIR photophysical properties. The emission lifetimes of the Nd^{3+} and Yb^{3} complexes recorded in D_2O and H_2O suggest the absence of water molecules in the first coordination sphere of the lanthanide ions. Moreover, the low energy of the triplet state (16 500–17 500 cm^{-1}) allows efficient energy transfer from the ligands to the lanthanide ions.[50,52,53]

Mazzanti *et al*. reported on the design and synthesis of tripodal 8-quinolinolate ligands based on 1,4,7-triazacyclononane (H_3thQtcn, H_3thQtcn-SO_3, Scheme 1).[45] As a follow-up work, photoluminescence (PL) spectra of NIR-emitting quinolinolate complexes (Er^{3+}, Nd^{3+}, and Yb^{3+} ions), excited in the less-energetic absorption band of the Q ligand (assigned to a $\pi - \pi^*$ transition), are recently reported.[54,55] The fine structure arising from this Stark splitting of the emission bands may be used as a tool to probe the metallic environment, since the spectroscopic shape depends on the symmetry of complexes, and becomes broader as the symmetry lowers. Noteworthy, the spectroscopic breadth may allow one to obtain high-gain bandwidth for optical amplification in laser systems.[3,15,41,56]

On the stoichiometry of lanthanide complexes with HQ and its derivatives, several papers have reported controversial assumptions.[42–57] Van Deun *et al*. reinvestigated commonly used literature synthetic procedures and showed that the reaction products of lanthanide salts with HQ and some halo-derivatives consist of a mixture of species having different stoichiometries rather than a single product. One of the identified species contains three lanthanide ions bridged by the Q ligands (''trimeric'' complexes of general formula $Ln_3Q_8^+$), and is the predominant product when using HQ and 5-chloro-8-quinolinol as ligands. They described that this class of complexes actually possess a rich structural chemistry and that the nature of the products obtained strongly depends on the reaction conditions (solvent, pH) and on the ligand.[58] Bünzli *et al*. recently studied the ligands based on HQ to obtain lanthanide complexes with sensitized NIR luminescence (Nd^{3+} and Yb^{3+} ions). The idea is to extend the coordination site of 8-quinolinol by attachment of a chromophoric substituent (benzimidazole-substituted HQ-bzim, or benzoxazole-substituted HQ-bzthia/HQ-bzox/H5,7Q-bzox, see Scheme 1), bearing an additional donor site, in the 2-position of the Q-ring in order to obtain 3 : 1 complexes. In all of the structures, the Nd^{3+} ion was nine-coordinate, with a tricapped trigonal prism coordination environment.[59,60]

One of the growing challenges in the design of NIR-luminescent lanthanide complex for application in bioanalyses and bioimaging is to extend the excitation wavelength from the UV to the visible range. Indeed, biomolecules are usually damaged by UV light and, in practice, long wavelength sensitization will allow the use of the cheap and widely available semiconductor diode lasers. Van Deun *et al*. prepared the water-soluble and stable 1 : 4 complexes of Nd^{3+} and Yb^{3+} ions with 8-hydroxy-5-nitroquinolinate ligands. These complexes can be sensitized by visible light with wavelengths up to 480 nm and show NIR emission in aqueous solution. The incorporation of a nitro group in the quinoline moiety shifts its absorption bands to longer wavelengths and also increases its molar absorptivity by a factor of 2.5, thereby significantly enhancing its light-harvesting power. The presence of the nitro group also increases the solubility of the resulting complexes, making them water soluble.[61]

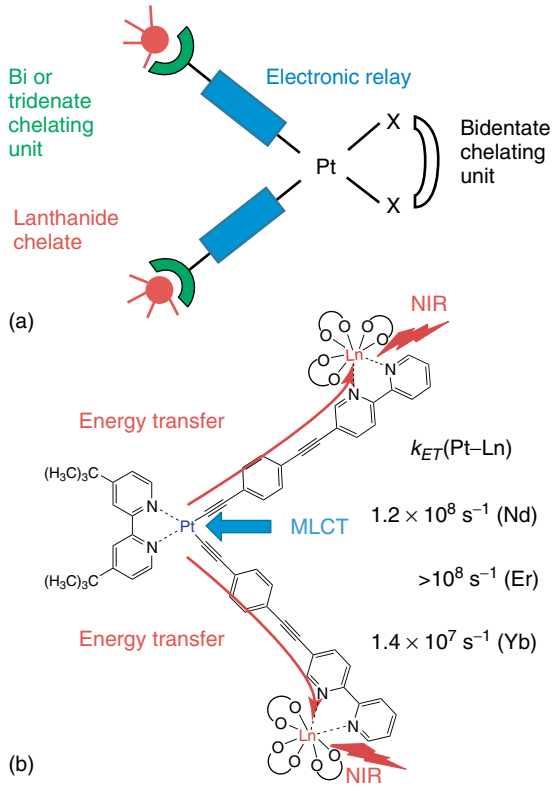
4.3 NIRLuminescence Based on Heteropolymetallic d–f Complexes

As d-block organometallic chromophores frequently exhibit strong absorption in the visible region due to intense metal-to-ligand charge transfer transitions (MLCT), which closely match the receiving luminescence state of lanthanides, a new approach has been recently established to attain sensitized NIR lanthanide emission through effective d $\rightarrow$ f energy transfer from d-block chromophore sensitizers.[62–64] Cr^{3+}, Fe^{2+}, Re^{+}, Ru^{2+}, Os^{2+}, Ir^{3+}, Pd^{2+}, and Pt^{2+} are among the most efficient d-transition metal ions for this purpose. The lanthanide ions can be sensitized using visible absorbing antenna from d-block transition metal complexes and the use of such relatively low-energetic excitation wavelengths is generally less damaging for biological material, as these long excitation wavelengths are often not easily absorbed by biological tissue.[65,66] Edifices containing these d-transition metal ions are presented and discussed in several review articles.[8,15,20,67]

van Veggel *et al*. reported the first example of Nd^{3+} and Yb^{3+} ions NIR luminescence sensitized by the transition metal complexes Ru^{2+} tris(bipyridine) ($[Ru(byp)_3]^{2+}$) and ferrocene. The $[Ru(byp)_3]^{2+}$ complex not only has an intersystem-crossing quantum yield near unity but also it enables excitation of Nd^{3+} and Yb^{3+} ions with visible light of 450 nm. The luminescent nature of the $[Ru(byp)_3]^{2+3}$ MLCT state has allowed a direct study of the sensitization process.[68]

2,2′-bipyridyl (bpy) or 2,2′:6′2″-terpyridyl (tpy) ethynes were utilized for the preparation of a series of $PtLn_2$ heterotrinuclear complexes through both Pt-acetylide σ-coordination and Ln-bpy/tpy chelation by Chen *et al*.[69–73] Sensitized NIR lanthanide luminescence (Er^{3+}, Nd^{3+}, and Yb^{3+} ions) is successfully achieved through effective Pt $\rightarrow$ Ln intercomponent energy transfer from the Pt antenna chromophores. By elaborately designed $PtLn_2$ heterotrinuclear arrays with alterable intramolecular Pt$\cdots$Ln separations through modification of the spacing length between bpy/tpy and acetylide, the rate of Pt $\rightarrow$ Ln energy transfer is tunable. The most studied systems are those containing Pt^{2+} and their design is described in Scheme 2.[72]

Gunnlaugsson *et al*. recently described two examples of water-soluble NIR-emissive f–d dyads made from Nd^{3+}- and Yb^{3+}-based tetraamide-functionalized cyclen complexes bearing a phen unit, which were complexed to a $[Ru^{II}(bpy)_2]$ (bpy = 2, 2′-bipyridine) and a $[Ru(II)(phen)_2]$ core, respectively.[74] And then they demonstrated the controlled synthesis of larger polymetallic conjugates where three of Ln^{3+} cyclen-based complexes have been assembled around a single Ru^{2+} metal center, resulting in the formation of d–f_3 metal ion ($Ru{\cdot}Yb_3$ and $Ru{\cdot}Nd_3$) complexes. They are dual-emitting probes that emit both within the visible and the NIR regions, in water and at physiological pH, upon excitation of their antenna using visible excitation wavelengths. Hence, these systems are therefore well suited for use in biomedical analysis and as



Scheme 2 Design of a $PtLn_2$ edifice for Pt–Ln transfer (a) and practical example of transfer rates in $PtLn_2$ (b)[72]

probes.[75] A new family of novel 3D Ln^{3+}–Cu^{+} coordination polymers $[Ln(pydc)_3Cu_3(bipy)_3 \cdot m(H_2O)]_n$ (pydc = 2,6-pyridinedicarboxylate anion; bipy = 4, 4′-bipyridine) has been synthesized hydrothermally by Bo *et al.*, in which NIR-emission bands from Nd^{3+} and Yb^{3+} ions can be obtained in Nd–Cu and Yb–Cu compounds, respectively. The coexistence of d^{10} with f^n metal ions in coordination polymers provides a new route to construct potential photoactive materials with fascinating structures.[76]

4.4 Metal–Organic Frameworks (MOFs) for NIR-Emitting Lanthanide Complexes

MOFs (see ***Metal–Organic Frameworks***) offer the advantage of being able to encapsulate metal ions at a predetermined distance, therefore avoiding detrimental concentration quenching and, possibly enhancing through-space antenna effect by a better positioning of the chromophoric groups.[4] These rigid architectures provide the ability to control the environment around the lanthanide ions, achieving specific coordination geometries for the ions and also allowing control over the organic components' arrangement in space, enabling interactions between chromophoric groups that possess lower excitation energy ranges.[27]

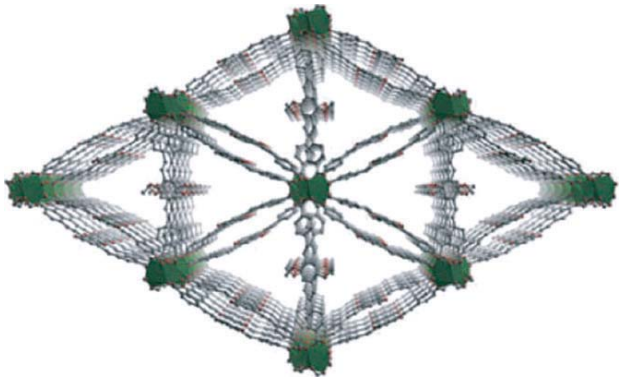


Figure 5 Structural depiction of Yb-PVDC-2 MOF.[78] (Reproduced from Ref. 78 with permission of The Royal Society of Chemistry.)

Zhang *et al.* reported the first highly porous NIR-luminescent MOF, $Yb(BPT)(H_2O)\cdot(DMF)_{1.5}(H_2O)_{1.25}$ (BPT = biphenyl-3,4′,5-tricarboxylate) by the solvothermal reaction, for separation and sensing of small molecules. The highly selective and sensitive sensing function of the MOF indicates the promise of this type of NIR-luminescent materials for the sensing of substrates in biological systems.[77]

Petoud *et al.* synthesized several MOF structures with the characteristic NIR luminescence of Yb^{3+} ion. Two unique MOF structures have been formed with Yb^{3+} and a phenylene moiety, 4,4′-[(2,5-dimethoxy-1,4-phenylene)di-2,1-ethenediyl]-bis-benzoate (PVDC), Yb-PVDC-1, and Yb-PVDC-2 (Figure 5).[78] The MOFs have long luminescence lifetimes (29 and 22 µs for Yb-PVDC-1 and Yb-PVDC-2, respectively), and quantum yields (3.3×10^{-3} and 1.8×10^{-2} for Yb-PVDC-1 and Yb-PVDC-2, respectively) that are among the highest reported values for NIR-emitting lanthanide compounds. The long luminescence lifetimes confirm that the NIR-emitting actions possess good protection of the lanthanide ions against nonradiative deactivations. And then they demonstrated that porous anionic bio-MOF-1 encapsulates and sensitizes NIR-emitting lanthanide ions (Yb^{3+}) in aqueous solution, which is the first example of an MOF that sensitizes NIR-emitting lanthanide ions in water. These results are particularly exciting as water is a highly quenching solvent, and materials which protect lanthanides from water are necessary for enabling the use of NIR-emitting lanthanides in biological environments.[79]

4.5 Other NIR-Emitting Lanthanide Complexes

In light of the rapid development in this field and the literature on ''other ligands'' for the sensitization of NIR luminescence being explosively growing, a selection of the work most representative has been made. Simpler ligands such as the Schiff base salophen, tropolonate, azulene dicarboxylate, or pyridine carboxylate molecules have been the subject of a recent review.[27] Petoud *et al.* successfully

demonstrated that the chromophoric moiety tropolonate can coordinate and sensitize several lanthanide ions emitting in the NIR domain (Ho^{3+}, Er^{3+}, Tm^{3+}, Yb^{3+}, and Nd^{3+}) identified as a formula of $[Ln(Trop)_4]^-$ (Trop = $C_7H_5O_2$; tropolonate).[80,81] The tropolonate chromophoric moiety is efficient in sensitizing five different NIR-emitting lanthanide ions: Ho^{3+}, Er^{3+}, Tm^{3+}, Yb^{3+}, and Nd^{3+} in solution. Quantum yields of the complexes formed with Yb^{3+} (1.9×10^{-2} in DMSO) are comparable to the highest reported quantum yield values for other lanthanide complexes that emit in the NIR domain in organic solvents.[13,27,82] This result is a breakthrough as the chromophore is able to sensitize five different lanthanide cations with a unique electronic structure. They also tested the diethyl 2-hydroxyazulene-1,3-dicarboxylate (HAz) to form $[Ln(Az)_4]^-$ complexes with different NIR-emitting lanthanide ions (Yb^{3+}, Nd^{3+}, Er^{3+}, and Tm^{3+}).[7,27] Because of the wide conjugation in this chromophore, the triplet state of this molecule is located at significantly lower energy ($13\ 600\ cm^{-1}$) in comparison to tropolonate ($17\ 200\ cm^{-1}$). It has been hypothesized to provide a better match of energy with the accepting levels of several NIR-emitting lanthanide ions mentioned above. The quantum yields of these complexes were recorded in solution. It was exciting to observe that the values obtained for the Nd^{3+} and Yb^{3+} complexes (3.7×10^{-3} and 3.2×10^{-2} respectively, both in CH_3CN) are among the highest values reported for NIR-emitting lanthanide complexes in solution. They attribute this good result to a combination of efficient ligand-to-lanthanide energy transfer and good protection of the lanthanide ion against nonradiative deactivations. Acridonebenzimidazole-fused ligands have also been reported to transfer energy on Yb^{3+}, but the corresponding overall quantum yields in acetonitrile are smaller, at most 0.86%.[83]

A neutral bioprobe combining visible-light excitation (488 nm), strong coordinating units, and NIR emission was obtained by grafting fluorescein on the macrocyclic cyclen (1,4,7,10-tetrazacyclododecane) framework; as a result, the luminescence of Nd^{3+} ion can be detected in time-resolved mode in water at pH 8 ($\tau = 2.3\ \mu s$).[84] Most of the work with macrocyclic ligands has concentrated on porphyrinate derivatives. Indeed porphyrins have well-defined absorptions and emission bands, and their low excited states are convenient for populating excited states of NIR-emitting Ln^{3+} ions.[15] Preparation of monoporphyrinate is often difficult and a new method has been proposed, starting from the free base and Ln^{3+} acetate in 1,2,4-trichlorobenzene. The obtained Yb complex is a starting material for the preparation of highly functionalized porphyrinates. For instance, methanol can easily be replaced by a 4-methylphenanthroline chromophore and the corresponding eight-coordinated monoporphyrinate complex has strong NIR-emission efficiency ($Q_{Yb} = 0.86\%$).[85]

Brennan *et al*. prepared the $(DME)_2Ln(OC_6F_5)_3$ (DME = 1,2-dimethoxyethane, Ln = Nd, Er, Tm),[86] $(DME)_2Tm(SC_6F_5)_3$, and tetrametallic $(DME)_4(\mu_2\text{-}SPh)_8Tm_4(SPh)_4$.[87] Emission experiments show that these complexes are highly NIR emissive, especially thiolate complexes of Tm^{3+} because of the low-phonon energy provided by heavy chalcogen-based anions, with 2–11% quantum yields of NIR emission, which is considered to be the highest reported value for a molecular Tm^{3+} emission. They also reported $(py)_{16}Nd_{17}NaSe_{18}(SePh)_{16}$, a spherical cluster with a 1 nm diameter (Figure 6)[88] and the dodecanuclear cluster $[(py)_{18}Nd_{12}O_6\,Se_4(Se_2)_4(SePh)_4(Se_2Ph)_2Hg_2(SePh)_4][(Hg(SePh)_3]_2$ with cluster dimension greater than 1 nm.[89] The NIR-emission studies of the Nd cluster $(py)_{16}Nd_{17}NaSe_{18}(SePh)_{16}$ reveal that this material has a 35% quantum efficiency, with four transitions from the excited state $^4F_{3/2}$ ion to $^4I_{9/2}$, $^4I_{11/2}$, $^4I_{13/2}$, and $^4I_{15/2}$ states clearly evident. It is also a particularly bright NIR-emission source because it combines a high concentration of Nd^{3+} ion encapsulated by a low-phonon environment and relatively few C–H bonds close to Nd^{3+} ion.

Zucchi *et al*. obtained the NIR-luminescent $[Ln(NO_3)_3(bpm)_2]$ complexes (Ln = Dy, Sm, Nd, Yb, Er) by using 2,2′-bipyrimidine (bpm) ligand. Of importance here is the observation of efficiently NIR luminescence of Sm and Dy complexes, which are not well investigated in the open literatures. The three transitions $^4G_{5/2} \rightarrow {}^4F_{5/2}$ (943 nm), $^4G_{5/2} \rightarrow {}^4F_{7/2}$ (1024 nm), and $^4G_{5/2} \rightarrow {}^4F_{9/2}$ (1169 nm) are observed for $[Sm(NO_3)_3(bpm)_2]$, and emission bands with maxima at 933 ($^4F_{9/2} \rightarrow {}^6F_{7/2}$), 1011 ($^4F_{9/2} \rightarrow {}^6F_{5/2}$), and 1172 nm ($^4F_{9/2} \rightarrow {}^6F_{3/2}$) are observed for $[Dy(NO_3)_3(bpm)_2]$.[90] Raymond *et al*. prepared

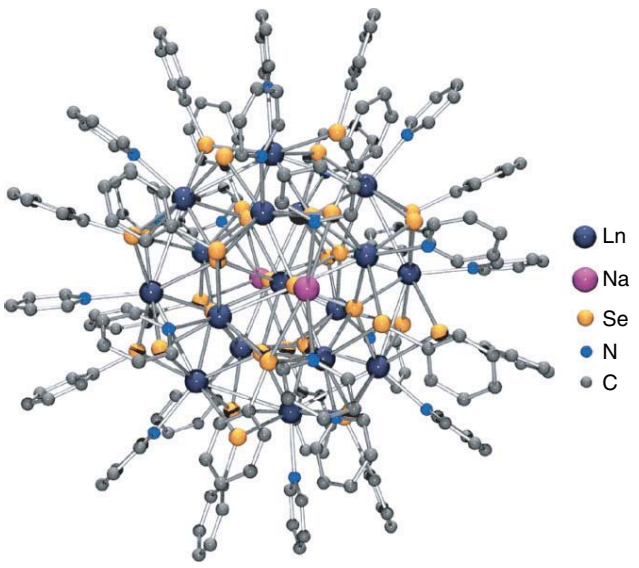


Figure 6 POV-Ray image of the ORTEP diagram of $(py)_{16}Ln_{17}NaSe_{18}(SePh)_{16}$, using spheres of arbitrary size.[88] (Reprinted with permission from Ref. 88. Copyright (2011) American Chemical Society.)

several NIR-luminescent lanthanide complexes $[Ln(5LIO\text{-}Me\text{-}3,2\text{-}hopo)_2]^-$ (Ln = Nd, Yb, Pr and Ho; hopo = 1-hydroxypyridin-2-one) by using the 5LIO-Me-3,2-hopo ligand. All the NIR-emissive properties are performed in aqueous solution, and examples of sensitized emission from Pr^{3+} and Ho^{3+} complexes in the NIR region are quite rare.[91,92] Duan *et al*. reported a new approach to design and synthesize efficient NIR-luminescent Yb^{3+} complex through incorporating a ring-opened rhodamine unit as energy donor with the excitation wavelength in the visible range (<500 nm). The specific rigid tetradentate feature of the sensitizing ligand successfully eliminating the competitive coordination of solvents and other molecules, coupled with the appropriate triplet excited state of rhodamine, facilitates the efficient NIR emission of Yb complex.[93]

The shell of organic ligands has also additional benefits besides acting as an antenna to capture and transfer excitation energy, because the organic ligands can also reduce the clustering of lanthanide ions and because the ligands can protect the lanthanide ion from coordination with water molecules or with other ligands possessing high-energy vibrations. The approach of surrounding the lanthanide ion by a shell of organic ligands has been extended to an extreme by Kawa and Fréchet, who coordinated the lanthanide ions with dendrimeric ligands of different generations,[94] yet the NIR luminescence was not detected. Lindgren and coworkers prepared lanthanide complexes of fluorinated dendrons with carboxylic acid groups.[95] The dendrimers were capped at the periphery with fluorinated phenyl groups. The function of the fluorinated phenyl groups was to enhance the rigidity of the dendrimer complexes, to lower the moisture penetration to the dendrimer core, and to reduce the absorption in the NIR region. The materials (with Ln = Nd and Er) showed the characteristic NIR emission.

Although several sensitizers or antenna have been described for the sensitization of NIR-emitting lanthanide ions,one of the strongest limitations for applications remains the ability to emit a sufficiently large number of photons per unit volume that will allow obtaining good detection sensitivity.[27] Typically, the actual complexes formed with NIR-emitting lanthanide ions have low quantum yields in comparison with visible emitting lanthanide complexes limiting the number of emitted photons per discrete molecule. Therefore, the number of antenna for NIR-emitting lanthanides is still limited and deserved more investigations as only a few lanthanide complexes match the requirements for practical applications.[96]

5 NIR-LUMINESCENT HYBRID MATERIALS BASED ON LANTHANIDES

Lanthanide-based hybrid materials in the visible-light region have been well reported and already established their important value in the display application field.[1] A recent review by Binnemans gives an overview of the literature about ''Lanthanide-based luminescent hybrid materials,'' of the different types of lanthanide-based hybrid materials, which is mainly about the visible-light materials.[18] Yet, the development and exploitation of the NIR-luminescent materials lags a way behind that of the visible-luminescent materials.

5.1 NIR-Luminescent Sol–Gel Hybrid Materials

The *sol–gel* process is a chemical synthesis technique that is used for the preparation of gels, glasses, and ceramic powders and can be used to prepare bulk samples (monoliths) as well as thin films and fibers.[97] Three general methods can be used to incorporate or immobilize luminescent complexes into sol–gel: (i) *impregnation*, (ii)*doping*, (iii)*chemical immobilization.*[98] To impregnate a complex into the sol–gel glass, the silica matrix is immersed for some time in a solution that contains a fairly high concentration of the luminescent complex. To dope the complex in the sol–gel glass, the complex is added to the silica sol prior to gelation. It is also possible to dope the complex in the silica matrix by adding a metal salt and ligand to the silica gel, whereby the complex itself is formed *in situ* in the gel or in the xerogel (often during a heat treatment). Chemical immobilization of the complex is achieved by addition of organosilicon compounds with coordinating groups to the sol–gel precursor solution, so that organically modified silicates are obtained.[18]

Sun *et al*.[100,101] studied the crystal structures of ternary $[Ln(dbm)_3phen]$ complexes (Ln = Er, Nd, Yb), and the Ln^{3+}/DBM/phen codoped NIR-luminescent hybrid gel via *in situ* method (Ln-D-P gel). By Judd–Ofelt theory, the study performed on Er^{3+} ions in the Er-D-P gel shows that the Er-D-P gel is efficient for laser pumping. The radiative properties of Nd^{3+} ion in Nd-D-P gel discussed by using the Judd–Ofelt analysis indicates that the $^4F_{3/2} \rightarrow {}^4I_{11/2}$ transition of Nd^{3+} ion in the Nd-D-P gel can be considered as a possible laser transition. In the follow-up work, the lanthanide complexes $[Ln(tta)_3(phen)]$, $[Ln(tta)_3(bipy)]$, and $[Ln(tta)_3(tppo)_2]$ (where Ln = Ho, Tm) are also introduced in the silica glass via an *in situ* synthesis procedure. NIR emission was observed for both the Ho^{3+} and Tm^{3+} complexes doped gel. However, the luminescence intensities of the complexes in the sol–gel glasses were weaker than those of the pure solid complexes, probably due to the quenching of the excited states by residual OH groups (Figures 7 and 8).[99] They also synthesized a series of Dy-complex-doped xerogels with the same first ligand acac and different neutral ligands (tppo and phen) via the *in situ* sol–gel process. Upon excitation at the maximum absorption wavelength of the ligands, the characteristic NIR luminescence of the Dy^{3+} ion in the xerogels was investigated and compared, and the results revealed that tppo ligand could increase the emission intensity of the Dy complex while phen gave the negative effect (Figure 9).[102]

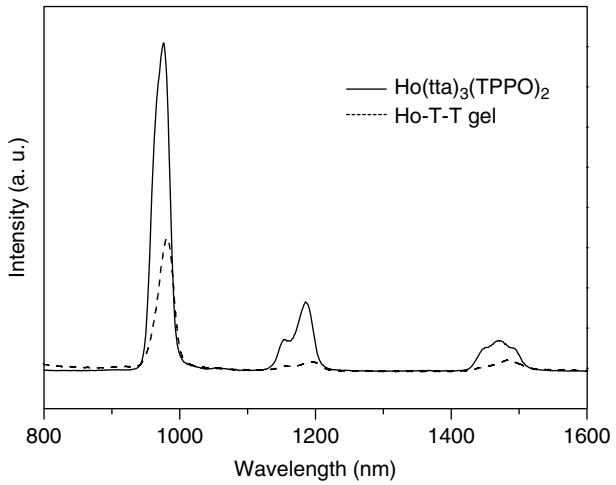


Figure 7 Emission spectra of the $[Ho(tta)_3(tppo)_2]$ complex in solid state ($\lambda_{ex} = 382$ nm) and entrapped in a silica gel (named as Ho-T-T gel) ($\lambda_{ex} = 360$ nm).[99] (Reprinted with permission from Ref. 99. Copyright (2008) American Chemical Society.)

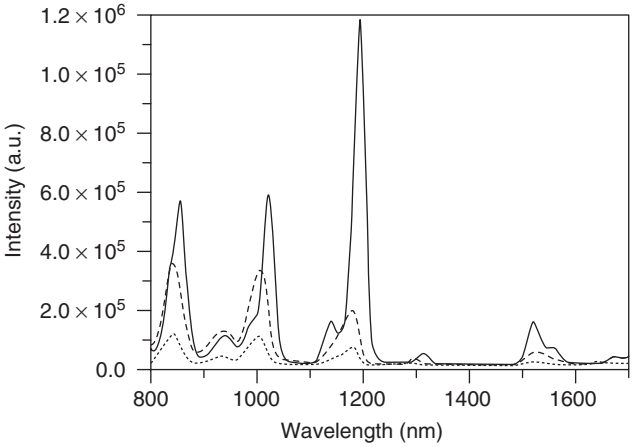


Figure 9 Emission spectra of Dy–A–T (–), Dy–A–P (—), and Dy–A–H_2O (. . .) xerogels (Dy^{3+}-complex-doped xerogels with the same first ligand acac and different second ligands tppo, phen, and H_2O).[102] (Reproduced from Ref. 102 with permission of The Royal Society of Chemistry.)

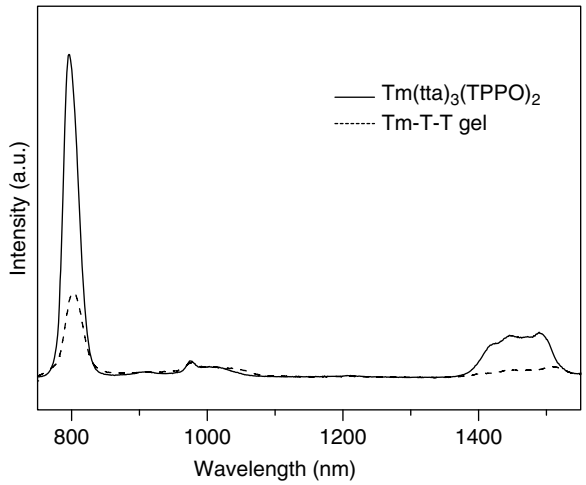


Figure 8 Emission spectra of the $[Tm(tta)_3(tppo)_2]$ complex ($\lambda_{ex} = 379$ nm) and entrapped in a silica gel (named asTm-T-T gel) ($\lambda_{ex} = 367$ nm).[99] (Reprinted with permission from Ref. 99. Copyright (2008) American Chemical Society.)

Some special attention was paid to the Yb^{3+}–Er^{3+}-codoped glasses. Light is absorbed by Yb^{3+} ion, and the excitation energy is transferred to the Er^{3+} ion, which shows NIR luminescence.[103] Ormosils of different composition doped with the ErQ_3 were prepared to study the NIR luminescence of the well-known ErQ_3 complexes in a sol–gel matrix.[104] NIR luminescence of Nd^{3+} could be observed upon excitation of the rhodamine 6G–Nd^{3+} hybrid with an argon ion laser at 488 nm.[105] The $^4F_{3/2} \rightarrow {}^4I_{11/2}$ transition was quite broad with a full width at half maximum (FWHM) of about 40 nm. The luminescence decay time of Nd^{3+} ion could drastically be changed by variation of the concentration of Nd^{3+} ions and by varying the experimental parameters for sol–gel processing and subsequent heat treatment.[105,106] In the absence of the rhodamine 6G dye, no Nd^{3+}-centered luminescence could be detected upon excitation at that wavelength. These experimental observations indicate that the excitation energy can be transferred from rhodamine 6G to the Nd^{3+} ion.

A fruitful approach to avoid clustering of lanthanide ions in a hybrid matrix is to graft the lanthanide complex via a covalent bond to the backbone of the matrix. In general, this is achieved via a hydrolyzable trialkoxysilyl derivative of a polydentate ligand that can coordinate to the lanthanide ion, although linking to the silica matrix can also be achieved via trialkoxysilyl derivatives of strongly binding monodentate ligands such as phosphine oxides.[18] This type of hybrid material can be considered as ''Class II'' hybrid material according to the classification of Sanchez *et al*.[107] The covalent linking of lanthanide complexes to the hybrid matrix also reduces the risk of leaching the complex out of the matrix, and in general, higher doped concentrations can be reached and the luminescent hybrid materials have a better homogeneity.

The derivative of phen, 5-(*N*, *N*-bis-3-(triethoxysilyl) propyl)ureyl-1,10-phenanthroline (abbreviated to phen-Si) (Figure 10), was used to immobilize many lanthanide complexes to a silica matrix by several groups. Binnemans *et al*. incorporated $[Ln(tta)_3phen]$ complexes (Ln = Nd, Sm, Er, Yb) in the silica hybrid matrix via the functionalized phen-Si ligand. This allowed the observation of NIR emission of the corresponding Nd^{3+}, Sm^{3+}, Er^{3+}, and Yb^{3+} in the silica materials.[108] Zhang and Sun prepared similar NIR-emitting

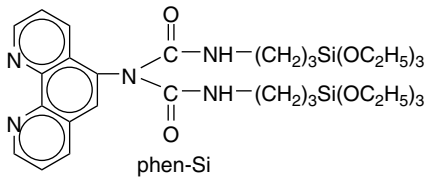


Figure 10 The derivative of 1,10-phenanthroline, phen-Si

hybrid materials (Ln = Nd, Er, Yb) by replacing the tta ligands by dbm ligands. The sol–gel material was prepared by condensation of the phen-Si ligand in the presence of tetraethoxysilane (TEOS). The authors made a detailed study of the spectroscopic properties by using the Judd–Ofelt theory. They determined the Judd–Ofelt parameters for the xerogel-bonded Nd complex material: Ω_t ($t = 2$, 4, and 6) in this work have been fitted to be 94.88×10^{-20}, 3.771×10^{-20}, and 2.818×10^{-20} cm^2, respectively.[109] In a follow-up study, other lanthanide complexes with 4,4,5,5,5-pentafluoro-1-(2-naphthyl)-1,3-butanedione (Hpfnp) were covalently bonded to xerogels by the ligand phen-Si *in situ* via a sol–gel process (Ln = Er, Nd, Yb, Sm), which show the characteristic NIR luminescence after ligand-mediated excitation.[110] Compared with the NIR luminescence of silica hybrid materials containing Er^{3+}, Nd^{3+}, and Yb^{3+}, that of Sm^{3+} is less well studied, although this situation is being remedied.[108] He and coworkers hybridized the new Er^{3+} and Yb^{3+} monoporphyrinate complexes into silica xerogel frameworks through the coordination of phen-Si to the lanthanide ions (Figure 11). The resulting silica films are transparent, homogenous, and exhibit characteristic emissions in the NIR region. The scanning electron microscopy (SEM) and atomic force microscopy (AFM) study reveals that the surface of the film is porous with the silica in particulate or rod shapes.[111]

Binnemans and coworkers also replaced the phen-Si ligand with a two-substituted imidazo[4,5-*f*]-1,10-phenanthroline (Figure 12) and incorporated lanthanide

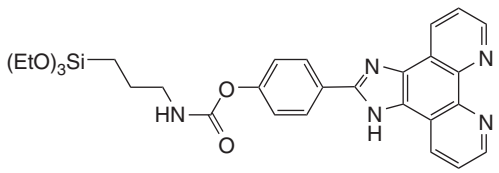


Figure 12 Hydrolyzable derivative of imidazo[4,5-*f*]-1,10-phenanthroline.[112] (Reprinted with permission from Ref. 112. Copyright (2005) American Chemical Society.)

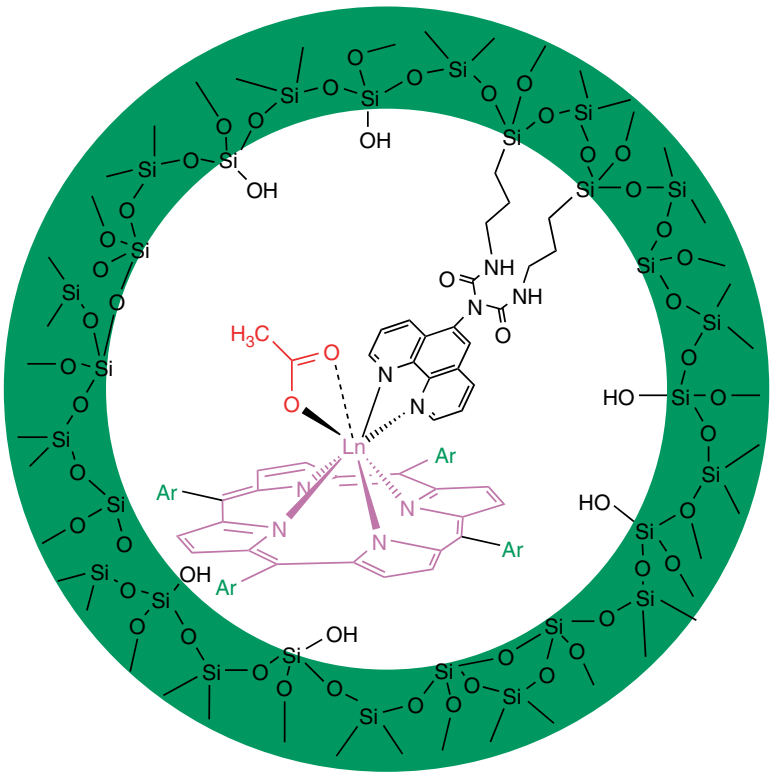


Figure 11 Schematic diagram of the monoporphyrinate lanthanide complex (Ln = Er, Yb) that was encapsulated inside a silica matrix.[111] (Reproduced from Ref. 111 with permission of The Royal Society of Chemistry.)

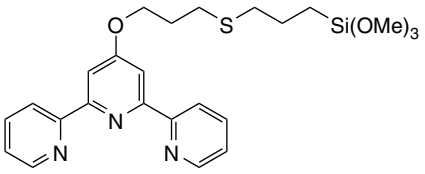


Figure 13 Hydrolyzable derivative of terpyridine.[113] (Reproduced from Ref. 113 with permission of The Royal Society of Chemistry.)

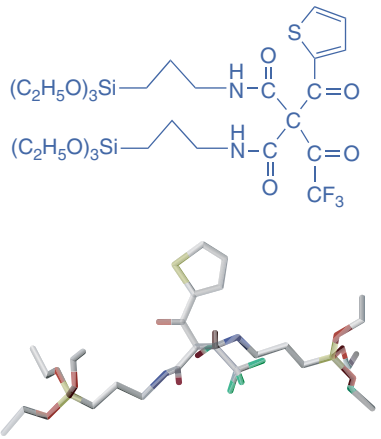


Figure 14 tta-Si.[114] (Reproduced from Ref. 114 with permission of The Royal Society of Chemistry.)

complexes of tta in the hybrid matrix (Ln = Pr, Nd, Sm, Ho, Er, Tm, Yb). For the sol–gel bulk materials covalently linked with lanthanide complexes, all show the characteristic NIR luminescence of Ln^{3+} ions, including the rather low signal for sol–gel materials with Pr^{3+} and Ho^{3+} ions. Yet, no decay time could be measured for the Pr^{3+} and Ho^{3+} samples, because the signals were not intense enough to give reliable results. Thin films were obtained by spin coating on a quartz plate or on a silicon wafer.[112] Tong *et al*. used a modified terpyridine ligand (Figure 13), which was prepared by the thiol-ene photopolymerization between γ-mercaptopropyltrimethoxysilane and 4′-allyloxy-2,2′:6′,2″-terpyridine. The lanthanide ion (Nd^{3+} and Er^{3+}) was coordinated to three dbm ligands and covalently bonded to the silica matrix by using the terpyridine-functionalized ligand, and the NIR luminescence was observed in the hybrid silica materials.[113] Li *et al*. prepared the NIR-luminescent organosilica microcrystals with rectangular plate morphology by a facile method of reacting silylated tta- Si (Figure 14) with Nd^{3+} ion under reflux without any structure-directing agent.[114] Liu and Yan synthesized a series of chemically bonded lanthanide/inorganic/organic hybrid materials (CE-15-Si-Nd, CE-18-Si-Nd) containing the aza-crown ether organic component based on functional molecular precursors (CE-15-Si, CE-18-Si) being synthesized with two or three

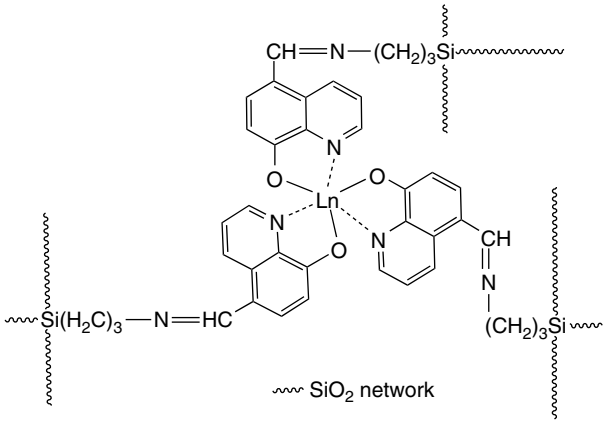


Figure 15 Proposed structure of the LnQSi–gel, Ln = Er, Nd, Yb.[116] (Reprinted with permission from Ref. 116. Copyright (2010) American Chemical Society.)

N-substituted pendant arms containing chelating groups. The resulting amorphous materials exhibit NIR luminescence. For the Nd^{3+} systems, they described that the sensitization mechanism is efficient from the benzene chromophores and no enhancement is observed on addition of phen in the ternary system (CE-15-Si-phen-Nd, CE-18-Si-phen-Nd).[115]

Recently, Sun *et al*. reported the lanthanide quinolinate derivatives $Ln(Q\text{-}Si)_3$ (Ln = Er, Nd, Yb) were covalently bonded to xerogel by using the HQ-functionalized alkoxysilane Q-Si (Figure 15). The xerogels LnQSi–gel appear very homogeneous and no sign of any phase separation as shown by SEM image. Of importance here is that the excitation spectra of the LnQSi–gel extend to the region of visible light (more than 500 nm). Following the visible-light excitation, the LnQSi–gel shows the characteristic NIR luminescence of the corresponding lanthanide ions through the intramolecular energy transfer from the ligands to the lanthanide ions. The good NIR-luminescent properties of the LnQSi–gel hybrid materials upon excitation with the visible light provide an access to multicomposite in optical applications, such as in medical diagnostic probe, lasers, and optical amplifications.[116]

So far most of the studies on covalently bonded NIR-luminescent complexes have been restricted to silica-based materials. However, just as in the case of simple inorganic sol–gel systems, silica (SiO_2) can be replaced by other oxide matrices such as alumina (Al_2O_3), zirconia (ZrO_2), or titania (TiO_2). Li and Zhang grafted lanthanide tta complexes (Ln = Nd, Er) on titania via modification of titanium(IV) isopropoxide by isonicotinic acid, followed by linking of the lanthanide complexes to the matrix via the nitrogen atoms of isonicotinic acid. The obtained hybrid titania Ti-nit-$Ln(tta)_3$ show the characteristic luminescence in the NIR region.[117]

5.2 NIR-Luminescent Mesoporous Silicates

Since the mesoporous silica materials were first introduced in 1992,[118] the development of ordered mesoporous molecular sieves has been of widespread interest in materials science. Ordered mesoporous materials with unique properties (high surface area, ordered pore structure of varying morphologies, and controllable pore size over wide ranges) continue to be widely investigated because of their many potential applications in catalysis, adsorption, and sensing[119,120] It should be noted that the mesoporous materials are synthesized via a sol–gel process by hydrolysis and condensation of a tetraalkoxysilane or an organosilicon compound in the presence of a surfactant. Therefore, these materials can also be considered as sol–gel-derived materials.[18] Recently, one of particular interest is the use of the ordered mesoporous silica material as a support for lanthanide complexes. Mesostructured materials offer the rigidity and photostability, and at the same time have a well-defined hydrophilic/hydrophobic phase separation allowing for more sophisticated tuning of the lanthanide complex microenvironment. However, the lanthanide complexes that are doped or covalently linked to a mesoporous matrix are mainly limited to the Eu^{3+} complex.[121,122] The lanthanide complexes coupled to the mesoporous matrix with NIR-luminescent properties have been less well studied.

Just like in the case of ormosils, it is possible to covalently bind luminescent lanthanide complexes to the host matrix, in this case, the wall of the mesoporous host materials. The grafting of the complexes to the host is a good strategy to prevent leaching of the lanthanide complex out of the mesoporous. Sun *et al*. grafted the ternary lanthanide complexes [Ln(hfth)$_3$phen] (Ln = Er, Nd, Yb, Sm) and [Pr(tfnb)$_3$phen] in the ordered MCM-41 mesoporous materials by the modified phen-Si group (Figure 16). The derivative materials Ln(hfth)$_3$phen–M41 and Pr(tfnb)$_3$phen–M41 all retain their mesoscopically ordered structures.[123] The NIR luminescence obtained in the materials shows that the hfth (or tfnb) and modified phen-Si ligands shield the lanthanide ions well from their surroundings and transfer the energy to the lanthanide ions efficiently. With these lanthanide-complex-functionalized materials, the luminescent spectral region from 1300 to 1600 nm, which is of particular interest for telecommunication applications, can be covered completely. Of importance here is the observation of NIR luminescence efficiently in mesoporous materials covalently linked with Sm and Pr complexes. NIR emission of Tm^{3+} ion was also investigated for [Tm(dbm)$_3$phen] covalently linked to MCM-41.[124]

A comparative study of [Ln(dbm)$_3$phen] (Ln = Nd, Er, Yb) complexes immobilized via the phen-Si ligand on MCM-41 and SBA-15 by Zhang *et al*. showed that SBA-15-supported materials show an overall increase in relative luminescent intensity and lifetime compared to the MCM-41-supported materials, which was investigated by the comparison of the lanthanide ion content and the pore structures of the two kinds of materials.[125] The poorer luminescence performance of the MCM-41-based materials was attributed to the higher number of residual silanol groups on the walls of MCM-41. In general, the materials derived from SBA-15 have a lower lanthanide content than those derived from MCM-41 because the phen ligands in the micropores of SBA-15 are unavailable for complex formation with [Ln(dbm)$_3$(H$_2$O)$_2$] complexes (Figure 17). Recently, they reported the fabrication of magnetic mesoporous silica nanospheres covalently bonded with NIR-luminescent lanthanide complexes [denoted as Ln(DBM)$_3$phen-MMS (Ln = Nd, Yb)] (Figure 18). The nanocomposites with an average size of 80–130 nm have a large surface area, a large pore volume, a well-defined pore size, magnetic separability, and NIR-luminescent properties.[126] This technique could

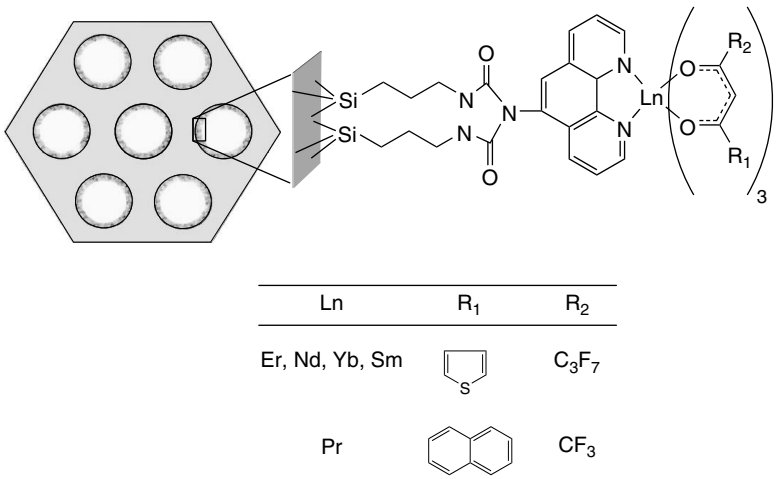


Figure 16 Expected structure of the mesoporous hybrid materials Ln(hfth)$_3$phen–M41 (Ln = Er, Nd, Yb, Sm) and Pr(tfnb)$_3$phen–M41. (Reproduced from Ref. 123. © Elsevier, 2007.)

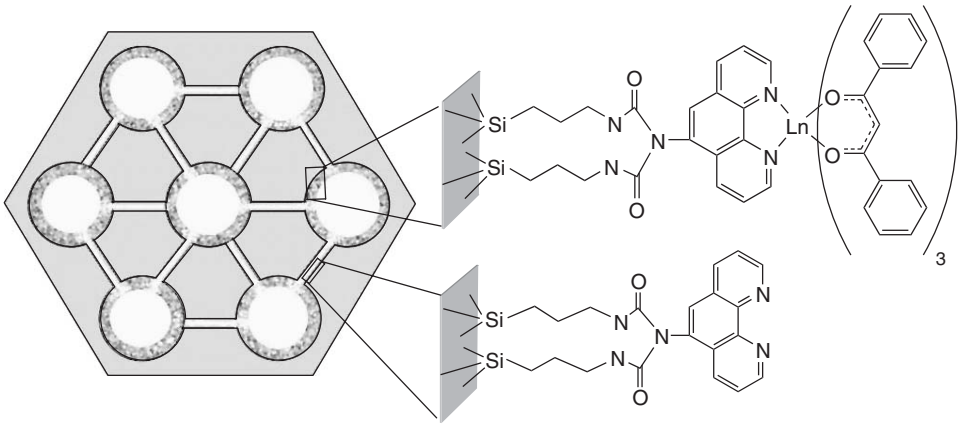


Figure 17 Schematic representation of $Ln(dbm)_3phen–SBA\text{-}15$ structure with micropores, in which the linked phen-Si ligands are not accessible for $Ln(dbm)_3(H_2O)_2$ complexes (Ln = Er, Nd, Yb).[125] (Reprinted with permission from Ref. 125. Copyright (2006) American Chemical Society.)

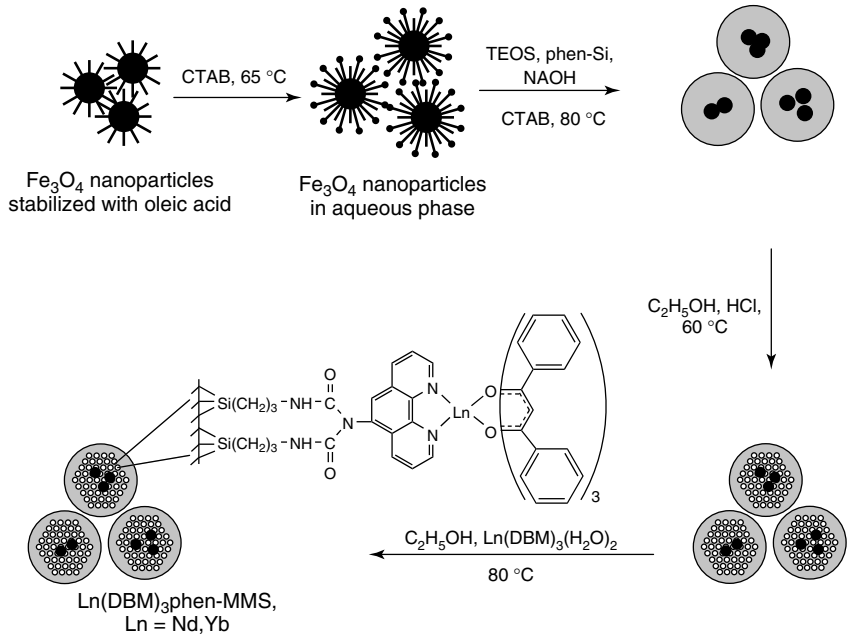


Figure 18 Synthesis of $Ln(DBM)_3phen$-MMS (Ln = Nd, Yb) nanospheres.[126] (Reprinted with permission from Ref. 126. Copyright (2010) American Chemical Society.)

be extended to the other lanthanide complexes, thus opening a door for the development of new multifunctional nanocomposites possessing magnetic, luminescent properties, and mesostructures.

As mentioned in Section 3.2, HQ is a useful ligand to obtain NIR-emitting lanthanide complexes. Sun *et al*. prepared hybrid materials (named as $LnQ_3–SBA\text{-}15$) grafting HQ complexes of Nd^{3+}, Er^{3+}, and Yb^{3+} to SBA-15 by using alkoxysilane-modified 8-hydroxyquinoline (Q-Si) (Figure 19).[127] After the complexation process, the highly ordered mesostructure of the $LnQ_3–SBA\text{-}15$ materials with the shape of curved cylinders can be substantially conserved. Upon excitation at the ligands' absorption bands, all the $LnQ_3–SBA\text{-}15$ materials show the characteristic NIR luminescence of the corresponding lanthanide ions.

5.3 NIR-Luminescent Polymer Materials

One advantage of polymers as host matrix for luminescent lanthanide complexes is their easy processability. Polymer film can be obtained by spin coating or melt casting

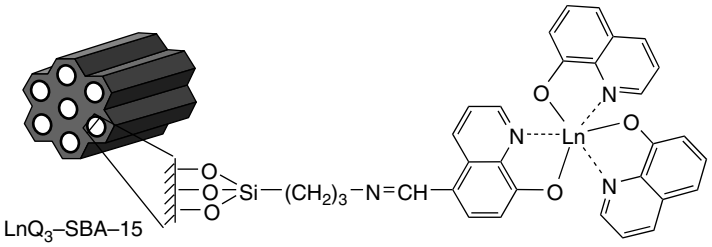


Figure 19 Lanthanide HQ complexes covalently bonded to the SBA-15 mesoporous host LnQ_3–SBA-15 (Ln = Er, Nd, Yb).[127] (Reprinted with permission from Ref. 127. Copyright (2008) American Chemical Society.)

and objects of virtually any desired shape (sheets, rods, fibers, etc.) or size can be made from polymeric materials.[18] Fluorinated or deuterated polymers are of interest as a host matrix for NIR-luminescent lanthanide complexes. To observe NIR luminescence of lanthanide complexes doped into a polymer matrix, it is advantageous to select complexes with deuterated or fluorinated ligands, as well as deuterated or perfluorinated polymer hosts.

Lin *et al*. investigated the solubility of the Nd^{3+} complexes [Nd(tmhd)$_3$], [Nd(hfac)$_3$], and [Nd(tfac)$_3$] in different polymers: polymethylmethacrylate (PMMA), polystyrene, the polyimide Ultem, and the fluorinated polyimide of the Ultradel 9000 series (Figure 20). The best solubility was found for [Nd(hfac)$_3$] in the fluorinated polyimide. Thin films of the Nd-doped polymer could be obtained by spin coating of a solution in γ-butyrolactone. The films showed three emission bands at 880, 1060, and 1330 nm. The luminescence lifetime of the $^4F_{3/2}$ level was about 1 μs.[128]

Pioneering work on NIR-emitting deuterated and perfluorinated lanthanide complexes, such as [Nd(hfac-d)$_3$], were synthesized by Hasegawa *et al*. with reaction of deuterated hexafluoroacetone in methanol-d4.[129] NIR emission was observed for [Nd(hfac-d)$_3$] dissolved in deuterated acetone-d_6. In a follow-up study, the authors reported that this complex showed NIR luminescence in other perdeuterated solvents as well: methanol-d_4, THF-d_8, N,N-dimethylformamide (DMF)d_7, and dimethyl sulfoxide (DMSO)d_6.[36] Enhanced emission properties were observed for [Nd(hfac-d)$_3$] in DMSO-d_6, possibly because that the coordinating ligand replaced water molecules from the first coordination sphere of the Nd^{3+} ion. Deuterated tris(bis-(perfluorooctanoyl)methanato)neodymium(III), Nd(POM-d)$_3$, gave enhanced luminescence in DMSO-d_6 by minimizing the energy migration during diffusional collisions in the liquid matrix.[130] Kuriki *et al*. doped the complexes of deuterated 1,1,1,2,2,6,6,7,7,7-decafluoro-3,5-heptanedione, [R(fhd-d)$_3$] (R = Pr, Nd, Er, Tm), into a perfluorocarbon liquid (3 M PF-5080) and into the perfluorinated polymer cyclic transparent optical polymer (CYTOP). A comparison study of the peak positions in the emission spectrum of [Nd(fhd-d)$_3$] in PMMA-d_8 with that of the same complex in a perfluorocarbon liquid shows that the $^4F_{3/2} \rightarrow {}^4I_{9/2}$ transition in PMMA-d_8 is shifted to shorter wavelengths.[131] NIR emission around 1550 nm was observed for an octupolar Er^{3+} complex in PMMA.[132]

Binnemans and coworkers coupled the luminescent [Ln(tta)$_3$phen] complexes to a Merrifield resin with covalent bond; the NIR luminescence was detected when

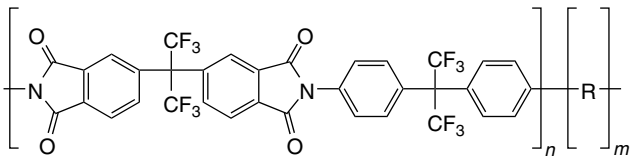


Figure 20 Generic formula of the Ultradel 9000 fluorinated polyimides [128]

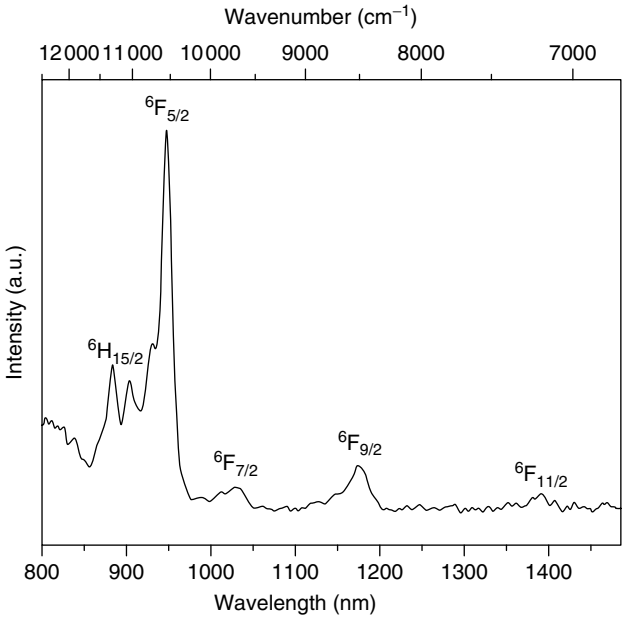


Figure 21 Photoluminescence spectrum of the [Sm(tta)$_3$phen]-functionalized Merrifield resin. Transitions start from the $^4G_{5/2}$ level.[133] (Reprinted with permission from Ref. 133. Copyright (2005) American Chemical Society.)

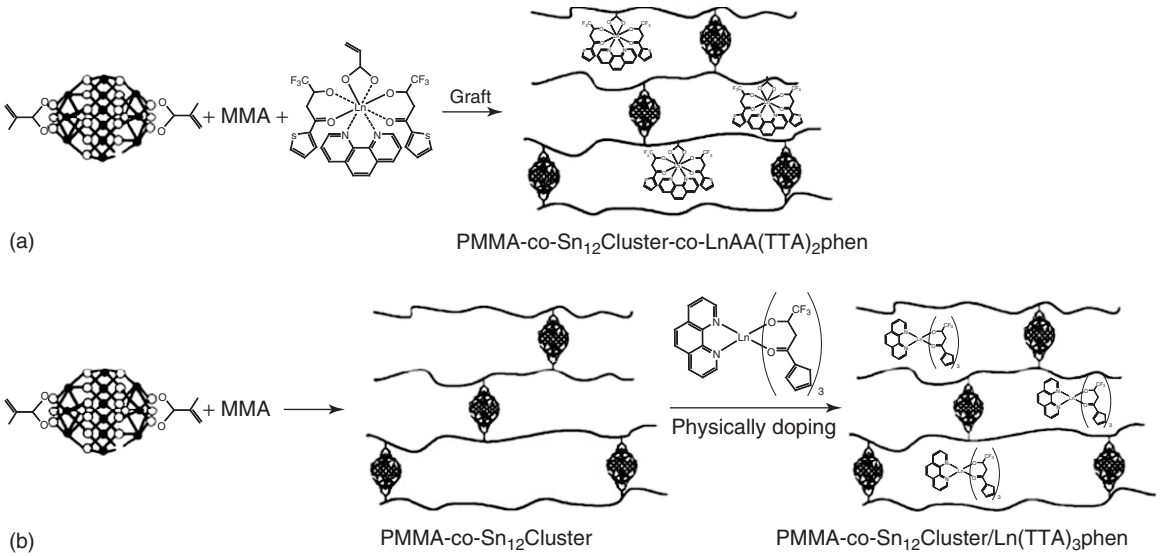


Figure 22 The mechanisms for the formation of (a) PMMA-*co*-Sn_{12}Cluster-*co*-LnAA$(tta)_2$phen and (b) PMMA-*co*-Sn_{12}Cluster/$Ln(tta)_3$phen hybrid materials (Ln = Er, Yb, Nd, and Sm).[135] (Reproduced from Ref. 135 with permission of The Royal Society of Chemistry.)

Ln = Sm, Nd, Er, or Yb. This is one of the few studies in which an NIR-luminescence spectrum of a Sm-containing hybrid material is reported in the earlier time (Figure 21).[133] Er^{3+} porphyrin complexes were incorporated as Er (acetylacetonato)diphenylporphyrin or Er(acetylacetonato) dimesitylporphyrin in the backbone of a conjugated poly(arylene ethynylene) copolymer.[134] The material could be processed by spin-coating method, and emits at 1550 nm. Owing to the greatly increased electronic delocalization throughout the conjugated polymer backbone, the complexes could be excited with a wavelength as long as 750 nm.[18]

Zhang and coworkers introduced two kinds of lanthanide complexes into the PMMA-*co*-Sn_{12}Cluster matrix and obtained the NIR-luminescent copolymerized hybrid materials.[135] The [LnAA$(tta)_2$phen] (AA = acrylic acid; Ln = Er, Sm, Nd, and Yb) complexes with vinyl group were grafted on the PMMA chains of the PMMA-*co*-Sn_{12}Cluster matrix, while the [$Ln(tta)_3$phen] without vinyl group were just physically doped in the matrix (Figure 22). In comparison with the pure NIR lanthanide complexes, the obtained hybrid materials all showed similar NIR PL properties, which indicated that the lanthanide complexes keep their structures inside the polymer matrix. Owing to the good solubility of the copolymerized hybrid materials in organic solvents and capacity to forming films, they also prepared the transparent films of hybrid materials on ITO glasses through spin coating.

5.4 NIR-Luminescent Lanthanide-Containing Ionic Liquids

Ionic liquids are salts with a low melting point (<100 °C) and several of them are liquid at room temperature, with interesting properties such as a negligible vapor pressure, a wide electrochemical window, and tunable physicochemical properties. The cation is generally an organic moiety (e.g., 1-alkyl-3-methylimidazolium, see Figure 23) and the anion modulates are the hydrophilicity of the liquid.[15] *Ionic liquids* have been explored as new solvents for the study of spectroscopic and photophysical properties of lanthanide ions.[18] They are being considered as environmentally friendly solvents for organic synthesis and catalysis.[136] Recent reviews give overviews of the literature about lanthanides and actinides in ionic liquids, including the literature dealing with spectroscopic properties.[137,138] In fact, most of the studies on the luminescence of lanthanides in ionic liquids are carried out on Eu^{3+} ion because of its superior physico-optical properties. Exploratory studies have shown that carefully dried ionic liquids are excellent solvents to study the NIR emission of lanthanide ions in solution.[139,140]

Binnemans *et al*. reported that the Nd^{3+} tosylate, bromide, triflate, and sulfonylimide complexes were dissolved in 1-alkyl-3-methylimidazolium ionic liquids that contain the same anion as the Nd^{3+} complexes. NIR-luminescence spectra of these Nd^{3+} salts were measured by direct excitation of the Nd^{3+} ion. And intense NIR luminescence

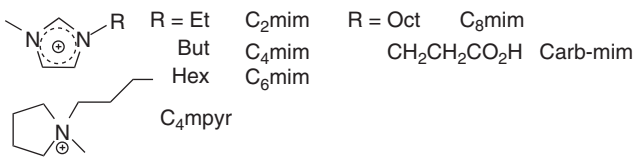


Figure 23 Cations of main *ionic liquids* used in spectroscopic studies.[15] (Reproduced from Ref. 15 with permission of The Royal Society of Chemistry.)

was observed upon ligand excitation for Nd^{3+} ion complexes with 1,10-phenanthroline or β-diketonate ligands. They concluded that ionic liquids are promising solvents for NIR-emitting lanthanide complexes, because ionic liquids are polar noncoordinating solvents that can solubilize lanthanide complexes. In a follow-up paper, anhydrous Nd^{3+} iodide [NdI_3] and Er^{3+} iodide [ErI_3] were dissolved in carefully dried batches of the ionic liquid 1-dodecyl-3-methylimidazolium bis(trifluoromethylsulfonyl)imide, [C_{12}mim][Tf_2N]. Intense NIR emission could be observed for both the Nd^{3+} ion and for the Er^{3+} ion in anhydrous samples, and the luminescence intensity fell back to zero when atmospheric moisture was allowed to enter the solution.[140] Recently, the anionic Sm^{3+} β-diketonate and dipicolinate complexes were dissolved in the imidazolium ionic liquid 1-hexyl-3-methylimidazolium bis(trifluoromethylsulfonyl)imide, [C_6mim][Tf_2N], and the obtained complexes were considered to be [C_6mim][$Sm(tta)_4$], [C_6mim][$Sm(nta)_4$], and [C_6mim][$Sm(hfa)_4$]. The characteristic NIR luminescence of Sm^{3+} ion was observed and the [C_6mim][Tf_2N] was found to be a suitable spectroscopic solvent for the study of NIR luminescence of Sm^{3+} complexes. The luminescence quantum yields of the β-diketonate complexes were found to be high in the ionic liquid in comparison to the data earlier reported for Sm^{3+} complexes in solution.[141]

Bünzli *et al*. studied the NIR luminescence of lanthanide β-diketonate complexes [$Ln(tta)_3$phen] (Ln = Nd, Er, Yb) dissolved in the ionic liquid crystal 1-dodecyl-3-methylimidazolium chloride.[142] An interesting observation is that the quantum efficiency of the [$Yb(tta)_3$phen] complex dissolved in the ionic liquid is higher than that for the complex in the solid state. This indicates that nonradiative relaxation processes are less important in the ionic liquid than in the solid state. For [$Nd(tta)_3$phen], [$Er(tta)_3$phen], and [$Yb(tta)_3$phen], the luminescence decay times are slightly longer in the ionic liquid than in the solid state. Once again, it illustrates the reduction of the nonradiative relaxation processes in the ionic liquid in comparison with these processes in the solid state.

Hybrid materials consisting in an ionic liquid confined inside nanosized pores of a silica matrix, termed *ionogels*, feature the advantages of both the optical transparency of silica and the ionic conductivity of ionic liquids.[143] Ionogels doped with [C_6mim][$Ln(tta)_4$] (Ln = Nd, Sm, Eu, Tb, Ho, Er, Yb) are highly luminescent inorganic–organic hybrids. Depending on the Ln^{3+} ion, emission in the NIR region of the electromagnetic spectrum was observed, including the less well-reported Ho^{3+} ion in [C_6mim][$Ho(tta)_4$]-doped ionogel. It is also ascertained by the lifetimes in the ionogel which are very comparable to those in the ionic liquid, for instance, 1.2 vs 1.3 μs for Nd^{3+}, 86 vs 81 μs for Sm^{3+}, 1.6 vs 1.9 μs for Er^{3+}, and 16 vs 17 μs for Yb^{3+}. Thus the emission region of these gels can easily be tuned by changing the emissive ion and their mechanical properties make them ideal luminophores.[144]

5.5 NIR-Luminescent Upconverting Materials

Among recent developments in lanthanide-aided bioanalysis, rare earth upconversion nanophosphors (UCNPs) attract much attention.[145] Upconversion luminescence is a unique process where low-energy light, usually NIR light, is converted to higher energy light through the sequential absorption of multiple photons or energy transfers.[146] In particular, under continuous-wave excitation at 980 nm, UCNPs exhibit unique upconversion luminescence properties, such as sharp emission lines, long lifetimes, a large anti-Stokes shift of several hundred nanometers, superior photostability, and nonblinking.[147] They bear many advantages, such as low sensitivity to photobleaching, high optical sensitivity due to the presence of many emitting centers per particle, capability for multiplex analyses in view of the possibility of doping different Ln^{3+} ions, as well as cheap diode laser excitation (e.g., at 980 nm).[148]

The most extensively studied upconversion process features Er^{3+} ion as the emitter along with Yb^{3+} ion as activator, in which it has two emission lines in the green (540 nm) and in the red (654 nm), but other pairs such as Tm^{3+}/Ho^{3+} can also be envisaged. In addition, for bioimaging, UCNPs have attractive features: (i) NIR excitation is less harmful to small animals[149]; (ii) upconversion luminescence-based bioimaging offers no autofluorescence from biosamples, because no biosamples show luminescence properties under excitation at 980 nm[150]; (iii) Tm^{3+} provides NIR upconversion emission at around 800 nm, that is, the excitation (980 nm) and emission wavelengths are both in the range of the NIR range (NIR-to-NIR), which is an ideal case for deeper tissue penetration.[151] Using upconversion emission of Tm^{3+} as the output signal, UCNPs can be successfully used as probes for the visualization of biological samples even at high penetration depth.[152]

Prasad *et al*. synthesized aqueous dispersible fluoride ($NaYF_4$) nanocrystals (20–30 nm size) codoped with the rare earth ions, Tm^{3+} and Yb^{3+}, that is, $NaYF_4$:Tm^{3+}, Yb^{3+} UCNPs. The Yb^{3+} ions, excited with 975 nm, transfer energy to Tm^{3+}, which results in the characteristic Tm^{3+} emission bands at 479, 648, and 800 nm (Figure 24). A scan in the range of 700–850 nm showed an intense NIR luminescence peaking at ~800 nm. The visible blue PL peak is a radiative deactivation of the $^1G_4$ to the $^3H_6$ energy levels of Tm^{3+}, whereas the NIR peak at 800 nm corresponds to the $^3H_4 \rightarrow {}^3H_6$ transition; both levels are populated through the $^2F_{5/2}$ level of Yb^{3+}, thus upconverting the energy. *In vitro* cellular uptake was shown by the PL microscopy visualizing the characteristic emission of Tm^{3+} at ~800 nm excited with 975 nm. This NIR-to-NIR upconversion process provides deeper light penetration into biological specimen and results in high-contrast optical imaging due to absence of an autofluorescence background and decreased light scattering. They demonstrated that these UCNPs possess the essential features required for both *in vitro* and *in vivo* bioimaging applications, and shown that

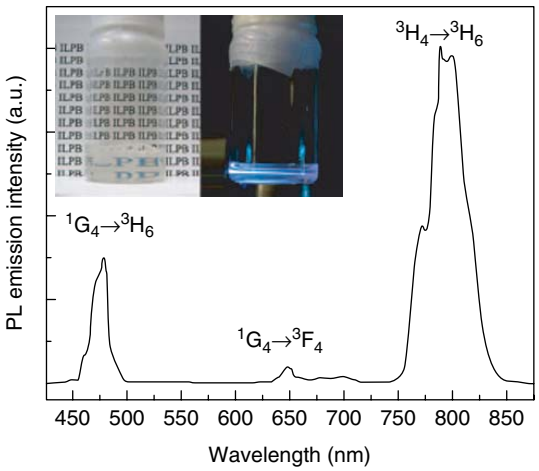


Figure 24 Photoluminescence (PL) spectra of $NaYF_4:Tm^{3+}$, Yb^{3+} UCNPs in aqueous dispersion with excitation wavelength at 975 nm. Inset: sample of the UCNPs aqueous dispersion demonstrating colloidal stability, optical transparency, and efficient visible (blue) PL under excitation with 975 nm.[151] (Reprinted with permission from Ref. 151. Copyright (2008) American Chemical Society.)

this novel approach using NIR-to-NIR UCNPs enables high-contrast cellular and tissue imaging with no overt indication of toxicity.[151]

Recently, Sun *et al.*[153] presented a simple way to self-assembled, multifunctional nanoprobes consisting of a magnetic core and mesoporous silica shell embedded with UCNPs ($NaYF_4:Yb^{3+}$, Tm^{3+}) by the means of an electrostatic interaction and binding scheme. The one-step assembly in which the UCNPs are attached to $Fe_3O_4@SiO_2$, as demonstrated in this chapter, may be expanded to other hydrophobic or hydrophilic nanoparticles. The hybrid nanoprobes are endowed with strong NIR luminescence (around 800 nm) upon 980 nm excitation and superparamagnetism, as well as mesoporous structure, which can be further investigated as a new theranostic nanomedicine, including being monitored deep insight *in vivo* by fluorescence imaging and magnetic resonance imaging (MRI) diagnosis, and simultaneously directed to cancer tumors as a targeted drug delivery vehicle of magnetic motor. Kim *et al.*[154] reported multiplexed imaging complementarily by using different quantum dots (QDs) and $NaYF_4:Tm^{3+}$, Yb^{3+} nanoparticles by alternating the excitation wavelengths and unmixing the emissions. For example, the emission wavelength of the $NaYF_4:Tm^{3+}$, Yb^{3+} nanoparticles overlaps with that of QD800, but the absorption lies on the opposite wavelength side from that of QD800 (QD800 emits at $\lambda = 800$ nm). The ''temporal'' multiplexing is demonstrated by alternating the excitation wavelengths and unmixing the emissions of different probes.

Wolfbeis *et al.*[155] exploited the unique luminescent properties of UCNPs as background-free codes for multiplexed analyses. In particular, the characteristic dual emission

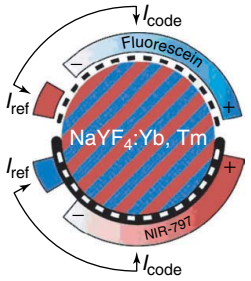


Figure 25 Tuning the dual emission bands of the UCNPs. Fluorescein or the dye NIR-797 screen off the blue or the NIR-emission band of $NaYF_4:Yb^{3+}$, Tm^{3+} UCNPs. In this case, the second emission band, which is not absorbed, serves as an internal reference to yield ratiometric codes. (Reproduced from Ref. 155. © Wiley-VCH Verlag GmbH & Co. KGaA, 2011.)

bands enable a novel spectral encoding strategy that is not available for organic fluorophores or QDs. For UCNPs of type $NaYF_4:Yb^{3+}$, Tm^{3+}, they display blue and NIR emission and were encoded either by fluorescein or dye NIR-797 (Figure 25). The surface of UCNPs is covered with a screen layer containing different amounts of an organic dye such that one of the two emission bands is reabsorbed to various degrees. The second emission band, by contrast, is not absorbed by the dye on the surface and serves as a ratiometric reference to the emission of the first band. Ratiometric optical measurements are largely independent of the light source intensity, the photodetector sensitivity, and the high temperature effects of lanthanide-based upconverting materials. The new spectral encoding strategy enables the identification of analytes in a highly robust and reproducible way.

6 CONCLUSIONS

This chapter shows that research in the field of lanthanide-based NIR-luminescent materials is very active. In general, incorporation of a lanthanide complex into a matrix significantly improves its thermal and (photo)chemical stability. This can partially be explained by the shielding of the lanthanide complex from the atmosphere and especially from atmospheric oxygen and moisture. The encapsulation of the lanthanide complex in the hybrid matrix often leads to a more intense PL because of light absorption by the host matrix and subsequent transfer of the excitation energy to the lanthanide complex and finally to the emitting lanthanide ion.

The number of papers published in a given year indicates that the interest of this filed is still increasing, at the same time, still has an incommensurable, untouched space to expand and yield exciting results, both at the fundamental and applied levels. In the near future, there are several evident

trends that are particularly promising but will require concerted effort for success.

1. Research is gradually shifting to more complex systems. For instance, very few studies on lanthanide complexes doped into pure silica sol–gel glasses are still appearing, whereas present work is more concentrated on lanthanide complexes in organically modified silicates and especially on complexes covalently linked to the host matrix. But the control of the lanthanide quantity inside the host matrices remains a challenge.
2 To enhance the quantum yield of the NIR luminescence. The sensitizers of the lanthanide ions should fulfill the requirements such as (i) remaining at sufficiently close distance to the lanthanide ions for a good energy transfer to occur; (ii) the donating levels of the sensitizers should match the accepting energy level of the lanthanide ions well; (iii) eliminating functional groups with high energy-stretching frequencies that are particularly detrimental to NIR emission, that is,–OH,–NH, and–CH vibrations. In comparison to the sensitization of visible-luminescent lanthanides, the sensitization of NIR-luminescent lanthanides is more challenging, because the excited states of NIR-luminescent lanthanides can often be easily affected by the nonradiative deactivation from the environment. The sensitizers should be well designed to transfer energy to the lanthanides efficiently and to provide adequate protection of lanthanides.
3 To shift the excitation wavelength from UV to the visible range for application in bioanalyses and bioimaging.
4 Life sciences are bound to highly benefit from lanthanide-luminescent bioprobes, especially a field boosted by the advent of upconverting phosphors (NIR-to-NIR). More efficient NIR-emitting probes are also needed to improve the penetration depth of imaging. Bifunctional agents acting both as cell-imaging probes and therapeutic agents should also be the focus of much attention, as well as dual-probe UCNPs for simultaneous MRI and optical imaging.

There are strong needs for NIR-luminescence materials in many fields from information technology to biological applications. This should incite more researchers to join the club!

7 GLOSSARY

Antenna effect: The lanthanide ions are chelated with organic ligands. The ion-centered luminescence originates from the intramolecular energy transfer through the ligand to the emitting level of the lanthanide ion. This is the so-called ''antenna effect''.

Upconversion: is a process where low-energy light, usually near-infrared (NIR), is converted to higher-energy (visible) light via multiple absorptions or energy transfer processes.

8 ACKNOWLEDGMENTS

The authors are grateful to the financial support from the National Natural Science Foundation of China (Grant No. 21001072), the Key Subject of the Municipal Educational Commission of Shanghai (project J50102), the Special Project for Nanotechnology Shanghai (1052 nm03400), the Project sponsored by SRF for ROCS, SEM.

9 RELATED ARTICLES

β-Diketonate; Luminescence; Metal–Organic Frameworks.

10 ABBREVIATIONS AND ACRONYMS

NIR = near-infrared; OLED = organic light-emitting diode; MOFs = Metal–organic frameworks; FWHM = full width at half maximum; UCNPs = upconversion nanophosphors; MRI = magnetic resonance imaging; phen = 1,10-phenanthroline; phen-Si = 5-(*N*, *N*-bis-3-(triethoxysilyl)propyl)ureyl-1,10-phenanthroline; acac=acetylacetone; tta = 2-thenoyltrifluoroacetonate; bath = bathophenanthroline; dbm = dibenzoylmethane; HQ = 8-Hydroxyquinoline; tfnd = 1-(2-naphthyl)-4,4,4-trifluoro-1,3-butanedionate; dione = 1,10-phenanthroline-5,6-dione; dafone = 4,5-diazafluoren-9-one; tpy = 2, 2′:6′2″-terpyridyl; hfth = 4,4,5,5,6,6,6-heptafluoro-1-(2-thienyl)hexane-1,3-dionate; tfnb = 4,4,4-trifluoro-1-(2-naphthyl)-1,3-butanedionate; nta = 2-naphthoyltrifluoroacetonate; hfa = hexafluoroacetylacetonate; tmhd = 2,2,6,6,-tetramethyl-3,5-heptanedionato; hfac = hexafluoroacetylacetonate; tfac = trifluoroacetylacetonate; tppo = triphenyl phosphine oxide; TEOS = tetraethoxysilane

11 REFERENCES

1. K. Binnemans, in 'Handbook on the Physics and Chemistry of Rare Earths', eds. K. A. Gschneidner Jr., J.-C. G. Bünzli, and V. K. Pecharsky, Elsevier, Amsterdam, 2005, Vol. 35, Chap. 225, pp. p. 107.
2. J. C. G. Bünzli, *Acc. Chem. Res.*, 2006, **39**, 53.
3. J. C. G. Bünzli and C. Piguet, *Chem. Soc. Rev.*, 2005, **34**, 1048.
4. J. C. G. Bünzli and S. V. Eliseeva, *J. Rare Earths*, 2010, **28**, 824.
5. Q. Y. Zhang and X. Y. Huang, *Prog. Mater. Sci.*, 2010, **55**, 353.

6. B. M. van der Ende and L. Aarts, *Phys. Chem. Chem. Phys.*, 2009, **11**, 11081.
7. J. Zhang and S. Petoud, *Chem.—Eur. J.*, 2008, **14**, 1264.
8. F. F. Chen, Z. Q. Chen, Z. Q. Bian, and C. H. Huang, *Coord. Chem. Rev.*, 2010, **254**, 991.
9. N. Sabbatini, M. Guardigli, and J. M. Lehn, *Coord. Chem. Rev.*, 1993, **123**, 201.
10. A. Beeby, R. S. Dickins, S. Faulkner, D. Parker, and J. A. G. Williams, *Chem. Commun.*, 1997, 1401.
11. D. Imbert, M. Cantuel, J. C. G. Bünzli, G. Bernardinelli, and C. Piguet, *J. Am. Chem. Soc.*, 2003, **125**, 15698.
12. Y. Hasegawa, T. Ohkubo, K. Sogabe, Y. Kawamura, Y. Wada, N. Nakashima, and S. Yanagida, *Angew. Chem. Int. Ed.*, 2000, **39**, 357.
13. G. A. Hebbink, L. Grave, L. A. Woldering, D. N. Reinhoudt, and F. C. J. M. van Veggel, *J. Phys. Chem.*, 2003, **107**, 2483.
14. L. N. Sun, J. B. Yu, G. L. Zheng, H. J. Zhang, Q. G. Meng, C. Y. Peng, L. S. Fu, F. Y. Liu, and Y. N. Yu, *Eur. J. Inorg. Chem.*, 2006, 3962.
15. S. V. Eliseeva and J. C. G. Bünzli, *Chem. Soc. Rev.*, 2010, **39**, 189.
16. R. Weissleder and V. Ntziachristos, *Nat. Med.*, 2003, **9**, 123.
17. S. I. Weissman, *J. Chem. Phys.*, 1942, **10**, 214.
18. K. Binnemans, *Chem. Rev.*, 2009, **109**, 4283.
19. C. Sanchez, B. Lebeau, F. Chaput, and J. P. Boilot, *Adv. Mater.*, 2003, **15**, 1969.
20. S. Comby and J.-C. G. Bünzli, in 'Handbook on the Physics and Chemistry of Rare Earths', eds K. A. Gschneidner Jr., J. C. G. Bünzli, and V. K. Pecharsky, Elsevier, Amsterdam, 2007, Vol. 37, Chap. 235, pp. p. 217.
21. L. D. Carlos, R. A. S. Ferreira, V. de Zea Bermudez, and S. J. L. Ribeiro, *Adv. Mater.*, 2009, **21**, 509.
22. L. N. Sun, Y. Zhang, J. B. Yu, S. Y. Yu, S. Dang, C. Y. Peng, and H. J. Zhang, *Micropor. Mesopor. Mater.*, 2008, **115**, 535.
23. L. N. Sun, J. B. Yu, H. J. Zhang, Q. G. Meng, E. Ma, C. Y. Peng, and K. Y. Yang, *Micropor. Mesopor. Mater.*, 2007, **98**, 156.
24. G. Boulon, A. Collombet, A. Brenier, T. Cohen-Adad, M. A. Yoshikawa, K. Lebbou, J. H. Lee, and T. Fukuda, *Adv. Funct. Mater.*, 2001, **11**, 263.
25. F. Wang, D. Banerjee, Y. S. Liu, X. Y. Chen, and X. G. Liu, *Analyst*, 2010, **135**, 1839.
26. K. Soga, W. Z. Wang, R. E. Riman, J. B. Brown, and K. R. Mikeska, *J. Appl. Phys.*, 2003, **93**, 2946.
27. H. Uh and S. Petoud, *C. R. Chimie*, 2010, **13**, 668.
28. G. A. Crosby and M. Kasha, *Spectrochim. Acta*, 1958, **10**, 377.
29. M. P. Tsvirko, S. B. Meshkova, V. Y. Venchikov, Z. M. Topilova, and D. V. Bol'shoi, *Opt. Spectrosc. (Engl. Transl.)*, 2001, **90**, 669.
30. F. X. Zang, Z. R. Hong, W. L. Li, M. T. Li, and X. Y. Sun, *Appl. Phys. Lett.*, 2004, **84**, 2679.
31. J. Barbillat, P. Le Barny, L. Divay, E. Lallier, A. Grisard, R. Van Deun, and P. Fias, *Rev. Sci. Instrum.*, 2003, **74**, 4954.
32. J. Wu, H. Y. Li, Q. L. Xu, Y. C. Zhu, Y. M. Tao, H. R. Li, Y. X. Zheng, J. L. Zuo, and X. Z. You, *Inorg. Chim. Acta*, 2010, **363**, 2394.
33. N. S. Baek, Y. H. Kim, Y. K. Eom, J. H. Oh, H. K. Kim, A. Aebischer, F. Gumy, A. S. Chauvin, and J. C. G. Bünzli, *Dalton Trans.*, 2010, **39**, 1532.
34. X. Y. Chen, X. P. Yang, and B. J. Holliday, *Inorg. Chem.*, 2010, **49**, 2583.
35. Y. X. Zheng, J. Lin, Y. J. Liang, Q. Lin, Y. N. Yu, Q. G. Meng, Y. H. Zhou, S. B. Wang, H. Y. Wang, and H. J. Zhang, *J. Mater. Chem.*, 2001, **11**, 2615.
36. Y. Hasegawa, Y. Kimura, K. Murakoshi, Y. Wada, J. H. Kim, N. Nakashima, T. Yamanaka, and S. Yanagida, *J. Phys. Chem.*, 1996, **100**, 10201.
37. J. B. Yu, L. Zhou, H. J. Zhang, Y. X. Zheng, H. R. Li, R. P. Deng, Z. P. Peng, and Z. F. Li, *Inorg. Chem.*, 2005, **44**, 1611.
38. S. Dang, J. Yu, X. Wang, L. N. Sun, R. P. Deng, J. Feng, W. P. Fan, and H. J. Zhang, *J. Lumin.*, 2011, **131**, 1857.
39. S. Dang, J. B. Yu, X. F. Wang, Z. Y. Guo, L. N. Sun, R. P. Deng, J. Feng, W. Q. Fan, and H. J. Zhang, *J. Photochem. Photobiol.*, 2010, **214**, 152.
40. H. B. Xu, Y. T. Zhong, W. X. Zhang, Z. N. Chen, and X. M. Chen, *Dalton Trans.*, 2010, **39**, 5676.
41. F. Artizzu, M. L. Mercuri, A. Serpe, and P. Deplano, *Coord. Chem. Rev.*, 2011, **255**, 2514.
42. R. Van Deun, P. Fias, K. Driesen, K. Binnemans, and C. Görller-Walrand, *Phys. Chem. Chem. Phys.*, 2003, **5**, 2754.
43. M. Iwamuro, T. Adachi, Y. Wada, T. Kitamura, N. Nakashima, and S. Yanagida, *Bull. Chem. Soc. Jpn.*, 2000, **73**, 1359.
44. M. Albrecht, O. Osetska, J. Klankermayer, R. Fröhlich, F. Gumy, and J. C. G. Bünzli, *Chem. Commun.*, 2007, 1834.
45. A. Nonat, D. Imbert, J. Pécaut, M. Giraud, and M. Mazzanti, *Inorg. Chem.*, 2009, **48**, 4207.
46. W. P. Gillin and R. J. Curry, *Appl. Phys. Lett.*, 1999, **74**, 798.
47. O. M. Khreis, R. J. Curry, M. Somerton, and W. P. Gillin, *J. Appl. Phys.*, 2000, **88**, 777.
48. O. M. Khreis, W. P. Gillin, M. Somerton, and R. J. Curry, *Org. Electron.*, 2001, **2**, 45.
49. N. M. Shavaleev, R. Scopelliti, F. Gumy, and J. C. G. Bünzli, *Inorg. Chem.*, 2009, **48**, 7937.
50. S. Comby, D. Imbert, C. D. B. Vandevyver, and J. C. G. Bünzli, *Chem.—Eur. J.*, 2007, **13**, 936.
51. H. He, P. S. May, and D. Galipeau, *Dalton Trans.*, 2009, **24**, 4766.
52. S. Comby, D. Imbert, A. S. Chauvin, and J. C. G. Bünzli, *Inorg. Chem.*, 2006, **45**, 732.
53. D. Imbert, S. Comby, A. S. Chauvin, and J. C. G. Bünzli, *Chem. Commun.*, 2005, 1432.

54. G. Bozoklu, C. Marchal, J. Pécaut, D. Imbert, and M. Mazzanti, *Dalton Trans.*, 2010, **39**, 9112.
55. G. Tallec, D. Imbert, P. H. Fries, and M. Mazzanti, *Dalton Trans.*, 2010, **39**, 9490.
56. F. Artizzu, P. Deplano, L. Marchiö, M. L. Mercuri, L. Pilia, A. Serpe, F. Quochi, R. Orrü, F. Cordella, M. Saba, A. Mura, and G. Bongiovanni, *Adv. Funct. Mater.*, 2007, **17**, 2365.
57. J. Thompson, R. I. R. Blyth, G. Gigli, and R. Cingolani, *Adv. Funct. Mater.*, 2004, **14**, 979.
58. R. Van Deun, P. Fias, P. Nockemann, A. Schepers, T. N. Parac-Vogt, K. Van Hecke, L. Van Meervelt, and K. Binnemans, *Inorg. Chem.*, 2004, **43**, 8461.
59. N. M. Shavaleev, R. Scopelliti, F. Gumy, and J. C. G. Bünzli, *Inorg. Chem.*, 2009, **48**, 2908.
60. N. M. Shavaleev, R. Scopelliti, F. Gumy, and J. C. G. Bünzli, *Inorg. Chem.*, 2008, **47**, 9055.
61. R. Van Deun, P. Fias, P. Nockemann, K. Van Hecke, L. Van Meervelt, and K. Binnemans, *Eur. J. Inorg. Chem.*, 2007, 302.
62. D. Guo, C. Y. Duan, F. Lu, Y. Hasegawa, Q. J. Meng, and S. Yanagida, *Chem. Commun.*, 2004, 1486.
63. J. M. Herrera, S. J. A. Pope, A. J. H. M. Meijer, T. L. Easun, H. Adams, W. Z. Alsindi, X. Z. Sun, M. W. George, S. Faulkner, and M. D. Ward, *J. Am. Chem. Soc.*, 2007, **129**, 11491.
64. T. Lazarides, H. Adams, D. Sykes, S. Faulkner, G. Calogero, and M. D. Ward, *Dalton Trans.*, 2008, 691.
65. T. Lazarides, D. Sykes, S. Faulkner, A. Barbieri, and M. D. Ward, *Chem.—Eur. J.*, 2008, **14**, 9389.
66. F. F. Chen, Z. Q. Bian, Z. W. Liu, D. B. Nie, Z. Q. Chen, and C. H. Huang, *Inorg. Chem.*, 2008, **47**, 2507.
67. M. D. Ward, *Coord. Chem. Rev.*, 2010, **254**, 2634.
68. S. I. Klink, H. Keizer, and F. C. J. M. van Veggel, *Angew. Chem. Int. Ed.*, 2000, **39**, 4319.
69. H. B. Xu, L. Y. Zhang, Z. L. Xie, E. Ma, and Z. N. Chen, *Chem. Commun.*, 2007, 2744.
70. H. B. Xu, L. Y. Zhang, Z. H. Chen, L. X. Shi, and Z. N. Chen, *Dalton Trans.*, 2008, 4664.
71. H. B. Xu, L. Y. Zhang, J. Ni, H. Y. Chao, and Z. N. Chen, *Inorg. Chem.*, 2008, **47**, 10744.
72. H. B. Xu, L. Y. Zhang, X. M. Chen, X. L. Li, and Z. N. Chen, *Cryst. Growth Des.*, 2009, **9**, 569.
73. H. B. Xu, J. Li, L. Y. Zhang, X. Huang, B. Li, and Z. N. Chen, *Cryst. Growth Des.*, 2010, **10**, 4101.
74. A. M. Nonat, S. J. Quinn, and T. Gunnlaugsson, *Inorg. Chem.*, 2009, **48**, 4646.
75. A. M. Nonat, A. Clémence, F. Stephen, and T. Gunnlaugsson, *Inorg. Chem.*, 2010, **49**, 8449.
76. Q. B. Bo, G. X. Sun, and D. L. Geng, *Inorg. Chem.*, 2010, **49**, 561.
77. Z. Guo, H. Xu, S. Su, J. F. Cai, S. Dang, S. C. Xiang, G. D. Qian, H. J. Zhang, M. O'Keeffe, and B. L. Chen, *Chem. Commun.*, 2011, **47**, 5551.
78. K. A. White, D. A. Chengelis, M. Zeller, S. J. Geib, J. Szakos, S. Petoud, and N. L. Rosi, *Chem. Commun.*, 2009, 4506.
79. J. Y. An, C. M. Shade, D. A. Chengelis-Czegan, S. Petoud, and N. L. Rosi, *J. Am. Chem. Soc.*, 2011, **133**, 1220.
80. J. Zhang, P. D. Badger, S. J. Geib, and S. Petoud, *Angew. Chem. Int. Ed.*, 2005, **44**, 2508.
81. J. Zhang, P. D. Badger, S. J. Geib, and S. Petoud, *Inorg. Chem.*, 2007, **46**, 6473.
82. S. J. A. Pope, B. J. Coe, S. Faulkner, E. V. Bichenkova, X. Yu, and K. T. Douglas, *J. Am. Chem. Soc.*, 2004, **126**, 9490.
83. E. Deiters, F. Gumy, and J. C. G. Bünzli, *Eur. J. Inorg. Chem.*, 2010, 2723.
84. K. Aita, T. Temma, Y. Kuge, and H. Saji, *Luminescence*, 2007, **22**, 455.
85. H. He and A. G. Sykes, *Inorg. Chem. Commun.*, 2008, **11**, 1304.
86. K. Norton, G. A. Kumar, J. L. Dilks, T. J. Emge, R. E. Riman, M. G. Brik, and J. G. Brennan, *Inorg. Chem.*, 2009, **48**, 3573.
87. S. Banerjee, G. A. Kumar, T. J. Emge, R. E. Riman, and J. G. Brennan, *Chem. Mater.*, 2008, **20**, 4367.
88. B. F. Moore, G. A. Kumar, M. C. Tan, K. Jesse, R. E. Riman, M. G. Brik, T. J. Emge, and J. G. Brennan, *J. Am. Chem. Soc.*, 2011, **133**, 373.
89. S. Banerjee, G. A. Kumar, R. E. Riman, T. J. Emge, and J. G. Brennan, *J. Am. Chem. Soc.*, 2007, **129**, 5926.
90. G. Zucchi, O. Maury, P. Thuéry, F. Gumy, J. C. G. Bünzli, and M. Ephritikhine, *Chem.—Eur. J.*, 2009, **15**, 9686.
91. E. G. Moore, G. Szigethy, J. Xu, L.-O. Pålsson, A. Beeby, and K. N. Raymond, *Angew. Chem. Int. Ed.*, 2008, **47**, 9500.
92. E. G. Moore, J. Xu, S. C. Dodani, C. J. Jocher, A. D'Aléo, M. Seitz, and K. N. Raymond, *Inorg. Chem.*, 2010, **49**, 4156.
93. W. Huang, D. Wu, D. Guo, X. Zhu, C. He, Q. J. Meng, and C. Y. Duan, *Dalton Trans.*, 2009, 2081.
94. M. Kawa and J. M. J. Fréchet, *Chem. Mater.*, 1998, **10**, 286.
95. C. Pitois, A. Hult, and M. Lindgren, *J. Lumin.*, 2005, **111**, 265.
96. C. P. Montgomery, B. S. Murray, E. J. New, R. Pal, and D. Parker, *Acc. Chem. Res.*, 2009, **42**, 925.
97. L. L. Hench and J. K. West, *Chem. Rev.*, 1990, **90**, 33.
98. D. Avnir, *Acc. Chem. Res.*, 1995, **28**, 328.
99. S. Dang, L. N. Sun, H. J. Zhang, X. M. Guo, Z. F. Li, J. Feng, H. D. Guo, and Z. Y. Guo, *J. Phys. Chem. C*, 2008, **112**, 13240.
100. L. N. Sun, H. J. Zhang, L. S. Fu, F. Y. Liu, Q. G. Meng, C. Y. Peng, and J. B. Yu, *Adv. Func. Mater.*, 2005, **15**, 1041.
101. L. N. Sun, H. J. Zhang, Q. G. Meng, F. Y. Liu, L. S. Fu, C. Y. Peng, J. B. Yu, G. L. Zheng, and S. B. Wang, *J. Phys. Chem.*, 2005, **109**, 6174.
102. J. Feng, L. Zhou, S. Y. Song, Z. F. Li, W. Q. Fan, L. N. Sun, Y. N. Yu, and H. J. Zhang, *Dalton Tran.*, 2009, **33**, 6593.

103. X. Orignac, D. Barbier, X. M. Du, R. M. Almeida, O. McCarthy, and E. Yeatman, *Opt. Mater.*, 1999, **12**, 1.

104. O. H. Park, J. Pinot, and B. S. Bae, *J. Sol.-Gel Sci. Technol.*, 2004, **32**, 273.

105. B. Viana, N. Koslova, P. Aschehough, and C. Sanchez, *J. Mater. Chem.*, 1995, **5**, 719.

106. B. Viana, E. Cordoncillo, C. Philippe, C. Sanchez, F. J. Guaita, and P. Escribano, *Proc. SPIE*, 2000, **3943**, 128.

107. C. Sanchez, F. Ribot, and B. Lebeau, *J. Mater. Chem.*, 1999, **9**, 35.

108. P. Lenaerts, E. Ryckebosch, K. Driesen, R. Van Deun, P. Nockemann, C. Görller-Walrand, and K. Binnemans, *J. Lumin.*, 2005, **114**, 77.

109. L. N. Sun, H. J. Zhang, J. B. Yu, Q. G. Meng, F. Y. Liu, and C. Y. Peng, *J. Photochem. Photobiol., A*, 2008, **193**, 153.

110. J. Feng, J. B. Yu, S. Y. Song, L. N. Sun, W. Q. Fan, X. M. Guo, S. Dang, and H. J. Zhang, *Dalton Trans.*, 2009, **13**, 2406.

111. H. S. He, M. Dubey, A. G. Sykes, and P. S. May, *Dalton Trans.*, 2010, **39**, 6466.

112. P. Lenaerts, A. Storms, J. Mullens, J. D'Haen, C. Görller-Walrand, K. Binnemans, and K. Driesen, *Chem. Mater.*, 2005, **17**, 5194.

113. B. H. Tong, S. J. Wang, Y. Z. Meng, and B. Wang, *Photochem. Photobiol. Sci.*, 2007, **6**, 519.

114. Y. Wang, Y. Wang, P. Cao, Y. N. Li, and H. R. Li, *CrystEngComm*, 2011, **13**, 177.

115. J. L. Liu and B. Yan, *Dalton Trans.*, 2011, **40**, 1961.

116. L. N. Sun, S. Dang, J. Yu, J. Feng, L. Y. Shi, and H. J. Zhang, *J. Phys. Chem. B*, 2010, **114**, 16393.

117. H. R. Li, P. Liu, Y. G. Wang, L. Zhang, J. B. Yu, H. J. Zhang, B. Y. Liu, and U. Schubert, *J. Phys. Chem. C*, 2009, **113**, 3945.

118. C. T. Kresge, M. E. Leonowicz, W. J. Roth, J. C. Vartuli, and J. S. Beck, *Nature*, 1992, **359**, 710.

119. D. E. De Vos, M. Dams, B. F. Sels, and P. A. Jacobs, *Chem. Rev.*, 2002, **102**, 3615.

120. B. J. Scott, G. Wirnsberger, and G. D. Stucky, *Chem. Mater.*, 2001, **13**, 3140.

121. H. R. Li, J. Lin, L. S. Fu, J. F. Guo, Q. G. Meng, F. Y. Liu, and H. J. Zhang, *Micropor. Mesopor. Mater.*, 2002, **55**, 103.

122. C. Y. Peng, H. J. Zhang, J. B. Yu, Q. G. Meng, L. S. Fu, H. R. Li, L. N. Sun, and X. M. Guo, *J. Phys. Chem. B*, 2005, **109**, 15278.

123. L. N. Sun, J. B. Yu, H. J. Zhang, Q. G. Meng, E. Ma, C. Y. Peng, and K. Yang, *Micropor. Mesopor. Mater.*, 2007, **98**, 156.

124. J. Feng, S. Y. Song, Y. Xing, H. J. Zhang, Z. F. Li, L. N. Sun, X. M. Guo, and W. Q. Fan, *J. Solid State Chem.*, 2009, **182**, 435.

125. L. N. Sun, H. J. Zhang, C. Y. Peng, J. B. Yu, Q. G. Meng, L. S. Fu, F. Y. Liu, and X. M. Guo, *J. Phys. Chem. B*, 2006, **110**, 7249.

126. J. Feng, S. Y. Song, R. P. Deng, W. Q. Fan, and H. J. Zhang, *Langmuir*, 2010, **26**, 3596.

127. L. N. Sun, H. J. Zhang, J. B. Yu, S. Y. Yu, C. Y. Peng, S. Dang, X. M. Guo, and J. Feng, *Langmuir*, 2008, **24**, 5500.

128. S. Lin, R. J. Feuerstein, and A. Mickelson, *J. Appl. Phys.*, 1996, **79**, 2868.

129. Y. Hasegawa, K. Murakoshi, Y. Wada, S. Yanagida, J. H. Kim, N. Nakashima, and T. Yamanaka, *Chem. Phys. Lett.*, 1996, **248**, 8.

130. Y. Hasegawa, K. Murakoshi, Y. Wada, J. H. Kim, N. Nakashima, T. Yamanaka, and S. Yanagida, *Chem. Phys. Lett.*, 1996, **260**, 173.

131. K. Kuriki, T. Kobayashi, N. Imai, T. Tamura, A. Tagaya, Y. Koike, and Y. Okamoto, *Proc. SPIE*, 2000, **3939**, 28.

132. A. Q. Le Quang, E. Besson, R. Hierle, A. Mehdi, C. Reye, R. Corriu, and I. Ledoux-Rak, *Opt. Mater.*, 2007, **29**, 941.

133. P. Lenaerts, K. Driesen, R. Van Deun, and K. Binnemans, *Chem. Mater.*, 2005, **17**, 2148.

134. R. Pizzoferrato, T. Ziller, R. Paolesse, F. Mandoj, A. Micozzi, A. Ricci, and C. Lo Sterzo, *Chem. Phys. Lett.*, 2006, **426**, 124.

135. W. Q. Fan, J. Feng, S. Y. Song, Y. Q. Lei, L. Zhou, G. L. Zheng, S. Dang, S. Wang, and H. J. Zhang, *Nanoscale*, 2010, **2**, 2096.

136. V. I. Parvulescu and C. Hardacre, *Chem. Rev.*, 2007, **107**, 2615.

137. A. V. Mudring and S. Tang, *Eur. J. Inorg. Chem.*, 2010, 2569.

138. K. Binnemans, *Chem. Rev.*, 2007, **107**, 2592.

139. K. Driesen, P. Nockemann, and K. Binnemans, *Chem. Phys. Lett.*, 2004, **395**, 306.

140. S. Arenz, A. Babai, K. Binnemans, K. Driesen, R. Giernoth, A. V. Mudring, and P. Nockemann, *Chem. Phys. Lett.*, 2005, **402**, 75.

141. K. Lunstroot, P. Nockemann, K. Van Hecke, L. Van Meervelt, C. Görller-Walrand, K. Binnemans, and K. Driesen, *Inorg. Chem.*, 2009, **48**, 3018.

142. L. N. Puntus, K. J. Schenk and J. C. G. Bünzli, *Eur. J. Inorg. Chem.*, 2005, 4739.

143. K. Lunstroot, K. Driesen, P. Nockemann, C. Görller-Walrand, K. Binnemans, S. Bellayer, J. Le Bideau, and A. Vioux, *Chem. Mater.*, 2006, **18**, 5711.

144. K. Lunstroot, K. Driesen, P. Nockemann, K. Van Hecke, L. Van Meervelt, C. Görller-Walrand, K. Binnemans, S. Bellayer, L. Viau, J. Le Bideau, and A. Vioux, *Dalton Trans.*, 2009, 298.

145. G. F. Wang, Q. Peng, and Y. D. Li, *Acc. Chem. Res.*, 2011, **44**, 322.

146. F. Wang and X. G. Liu, *Chem. Soc. Rev.*, 2009, **38**, 976.

147. C. X. Li and J. Lin, *J. Mater. Chem.*, 2010, **20**, 6831.

148. W. Feng, L. D. Sun, Y. W. Zhang, and C. H. Yan, *Coord. Chem. Rev.*, 2010, **254**, 1038.

149. L. H. Fischer, G. S. Harms, and O. S. Wolfbeis, *Angew. Chem. Int. Ed.*, 2011, **50**, 4546.

150. M. X. Yu, F. Y. Li, Z. G. Chen, H. Hu, C. Zhan, H. Yang, and C. H. Huang, *Anal. Chem.*, 2009, **81**, 930.

151. M. Nyk, R. Kumar, T. Y. Ohulchanskyy, E. J. Bergey, and P. N. Prasad, *Nano Lett.*, 2008, **8**, 3834.

152. D. K. Chatterjee, M. K. Gnanasammandhan, and Y. Zhang, *Small*, 2010, **6**, 2781.

153. Z. Liu, L. N. Sun, F. Y. Li, Q. Liu, L. Y. Shi, D. S. Zhang, S. Yuan, T. Liu, and Y. N. Qiu, *J. Mater. Chem.*, 2011, **21**, 17615.

154. S. Jeong, N. Won, J. Lee, J. Bang, J. H. Yoo, S. G. Kim, J. A. Chang, J. Kim, and S. Kim, *Chem. Commun.*, 2011, **47**, 8022.

155. H. H. Gorris, R. Ali, S. M. Saleh, and O. S. Wolfbeis, *Adv. Mater.*, 2011, **23**, 1652.

Superconducting Materials

Antonio J. Dos santos-García, Miguel Á. Alario-Franco and Regino Sáez-Puche

Universidad Complutense de Madrid, Madrid, Spain (EU)

1	Summary	371
2	Introduction	371
3	Superconductivity and Magnetic Field: Theories	374
4	The High-Temperature Copper Oxide Superconductors	375
5	Superconductivity and Magnetism for the 1212 Cuprates	376
6	Superconducting Applications	378
7	Glossary	380
8	Acknowledgements	381
9	Related Articles	381
10	Abbreviations and Acronyms	381
11	References	381

1 SUMMARY

Superconductivity was discovered 100 years ago by H. K. Onnes at Leiden University in the Netherlands. Different theories to explain this ''exotic'' phenomenon started in the 1920s with the development of quantum mechanics. The highlights of the superconductivity took place later on as the discovery of the Meissner effect in 1933. In 1957, Bardeen, Cooper, and Schrieffer proposed the well-known BCS theory and simultaneously Abrikosov explained the magnetic behavior of the so-called type-II superconductors considering that the magnetic flux penetrates in the form of quantized vortices above the critical field H_{C1}. In 1962, Josephson discovered the so-called Josephson effect now widely used in many applications. In 1986, the discovery of superconductivity in the ceramic oxide $La_{2-x}Ba_xCuO_4$ by Bednorz and Müller was an extraordinary episode in the history of science, and an explosion of research on high-temperature superconducting compounds took place during the following two decades in which the lanthanide-based high-temperature cuprates (HTSC) played an important role. The evolution of the discovery of different superconducting rare earth compounds, their crystal structure, chemical composition, and properties are summarized in this article.

2 INTRODUCTION

The race to reach absolute zero temperature, at the end of the nineteenth century, led to an unexpected discovery, which is called to change our way of life in a comparable magnitude of what internet and computers did in the last and the present century. This is the discovery of superconductivity. In 1911, a group headed by the Dutch physicist Heike Kamerlingh Onnes discovered that the DC resistivity of mercury suddenly drops to zero below 4.2 K.[1,2] Onnes also noticed that a strong enough magnetic field destroys superconductivity. This effect is also called the *Meissner-Ochsenfeld effect*[3,4] after its discovery in 1933. Therefore, a superconducting material has to exhibit zero resistivity, that is, infinite conductivity and also zero magnetic inductance inside the superconductor below a critical temperature, which is named ''superconducting critical temperature'' or T_C and below a certain value of magnetic field, which is the so-called critical magnetic field or H_C, respectively. It is also worth noting that there also exists a critical current density, i.e., J_C, which one can pass through the superconductor without destroying superconductivity.[5,6] These three features common to all superconducting materials allows one to depict an experimental magnetic field-temperature-current superconductor phase diagram as depicted in Figure 1.

The Rare Earth Elements. Edited by David A. Atwood. © 2012 John Wiley & Sons, Ltd. ISBN 978-1-119-95097-4

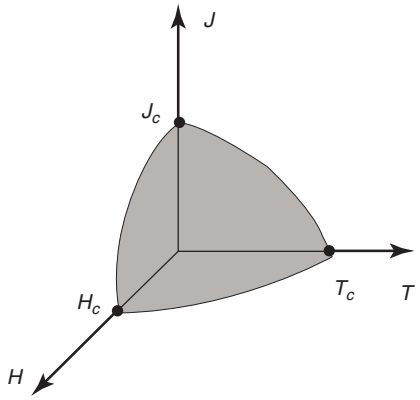


Figure 1 Critical field and critical current density vesus temperature for a type I superconductor

In the subsequent decades, many elements have been found to be superconducting,[7,8] the elements Pb and Nb being the metals with the highest superconducting transition temperatures, 7.2 and 9.3 K, respectively. Otherwise, some elements, for example, rhodium, shows a very low transition temperature such as 325 mK.[9] It was also reported that the metallic elements, which order ferromagnetically as is the case of the classical Fe, Co, Ni, and Gd do not exhibit superconductivity. This seemed to indicate that, ferromagnetism and superconductivity should not be compatible phenomena. Concerning lanthanides, lanthanum and lutetium are the only rare earth elements that, at room pressure, display superconductivity.[6–8,10] Nevertheless, many elements become superconducting under pressure.[6,8,11] In particular, as shown in Figure 2, more than half the elements including Y[12] and the rare earth elements Ce[13,14] and Eu[15] go into a superconducting state after applying pressure.[16] Furthermore, the T_C of some of these elements increases dramatically by applying an external mechanical pressure,[17] for example, La, whose T_C increases from 5.5 K at room pressure up to 12.9 K at 200 bars.[14] Also, certain elements are superconducting when they are displayed in thin film[10] form while others are so when they are irradiated with α-particles, as is the case of Pd.[18] In spite of the efforts made by the scientific community between 1940 and 1970, particularly by Bernd Matthias and Hulm,[19] the slope of T_C as a function of time increased only 3 K per decade (Figure 3). Although Matthias suggested that oxides and halides should be excluded in the search for new superconducting materials, some theoretical predictions made on the nonstoichiometric perovskite $SrTiO_{3-\delta}$ by M. Cohen in 1964[20,21] lead a number of scientists to the search for superconductivity in oxides. Partly as a consequence of this, superconductivity at 13.6 K was observed in both the $Li_{1+x}Ti_{2-x}O_4$ spinel[22] and the $BaPb_{1-x}Bi_xO_3$ perovskite.[23] Somewhat earlier, a series of ternary molybdenum chalcogenide compounds, of general formula $M_xMo_6X_8$, where M represents a large

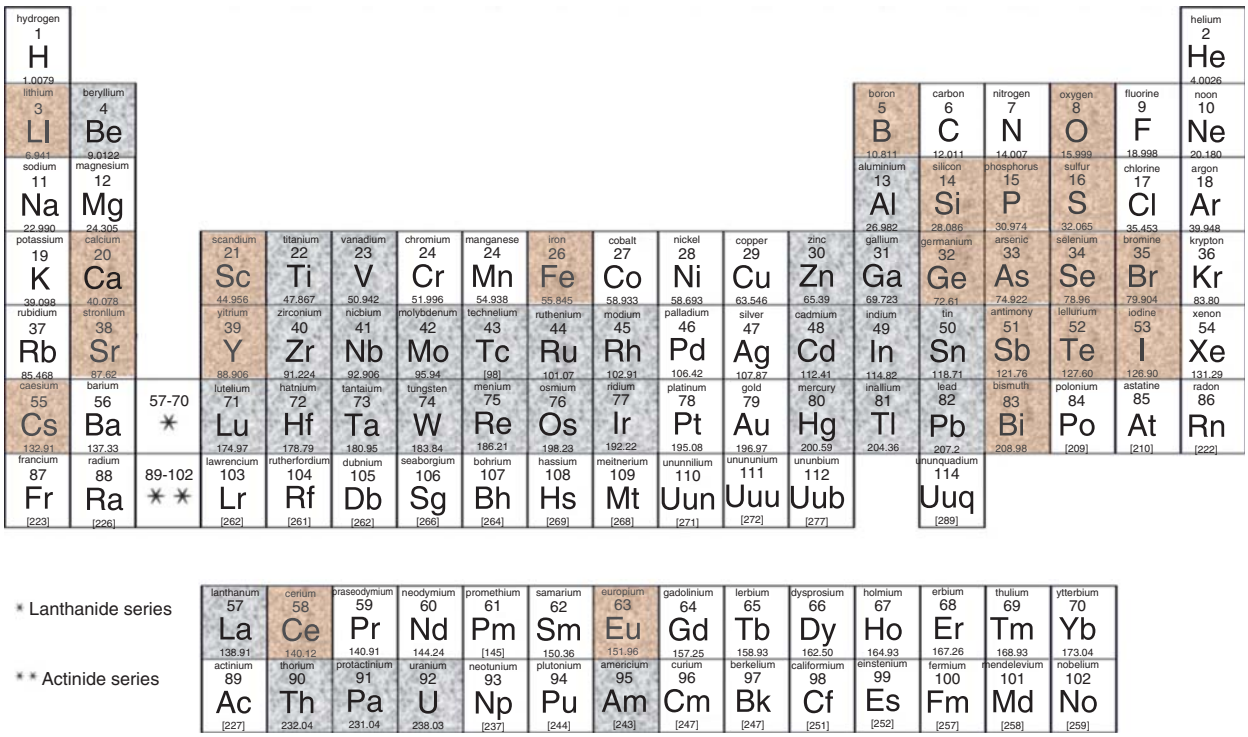


Figure 2 Superconducting tables in the periodic table. Superconductors at ambient conditions are noted in gray colour; brown is used for superconducting elements at high pressure. No superconductivity has been reported for the rest of the elements

number of metallic elements and X is a chalcogen (sulfur, selenium, or tellurium) were discovered by Chevrel and coworkers in 1971[24] and studied by Marezio *et al*.[25] In the particular case that M is a rare earth element, the resulting chalcogenide presents superconductivity and long-range magnetic interactions simultaneously, two phenomena that are indicated to be antagonist.[26–28] It is interesting to note here that there is no direct correlation between the RE spins (that is, the total magnetic moment of the RE) and T_C, although $EuMo_{6.35}Se_8$ appears to be anomalous and it is not superconducting.[29]

Other interesting superconducting compounds are the rare earth ''heavy fermion'' materials,[30] a specific type of intermetallic compounds, containing elements with 4f or 5f electrons. The name ''heavy fermion'' comes from the fact that, below a characteristic temperature, the conduction electrons in these metallic compounds behave as if they had an effective mass up to $\sim(10^2-10^3)$ times the free-electron mass. This sudden increase in mass is obviously reflected in the physical properties of these compounds in comparison to normal metals: unusual temperature dependences of their specific heats and the presence of maxima in the resistivity at low temperatures being among them. We can also recall the presence of superconductivity in $CeCu_2Si_2$, a heavy fermion compound made by Frank Steglich *et al*. in 1979.[31] Following on, in the search for new so-called unconventional superconductors, attempts for partial or total substitutions in the Ce sublattice for other rare earth elements lead to the formation of magnetically ordered states at low temperatures that totally suppress superconductivity. Thirty years later, $CeCu_2Si_2$ and, in general, ''heavy fermion'' compounds are still a topic of ongoing investigation.[32] This is mainly due to the differences existing between unconventional and conventional

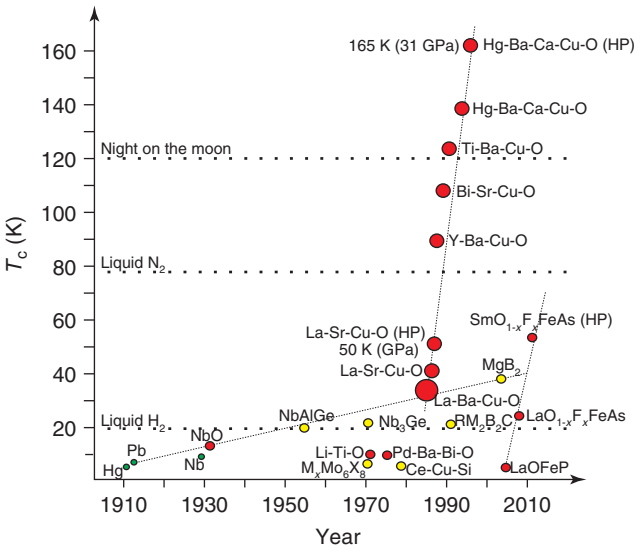


Figure 3 Evolution of the superconducting critical temperature T_C versus date

superconductors, that is, the source of the superconductivity in the former materials is likely to be different from the electron-ion interactions that are at the heart of the latter.[33] Following the evolution of T_C with time, depicted in Figure 3, the perspective of the search for superconductors changed substantially in 1986 with the discovery of superconductivity in the $La_{2-x}M_xCuO_4$ (M <> Ba, Sr, Ca) oxides at temperatures around 30–40 K by Berdnoz and Müller.[34,35] The Sr derivative presents the superconducting state at 36 K,[36,37] and it is remarkable that its T_C can be increased up to 50 K by applying an external mechanical pressure.[38,39] Following this idea, Paul Chu and his collaborators applied ''chemical pressure'' by replacing lanthanum by the smaller yttrium ion.[40] Somewhat unexpected, they observed superconductivity in the new material, of chemical composition $YBa_2Cu_3O_7$, with the astonishing superconducting critical temperature of 90 K. This finding represented a revolution not only in the synthesis of new superconducting materials but also in the field of applications, since both economic and technical barriers of the boiling point of the cheaper liquid nitrogen had been overcome for the first time. New opportunities were opened up to the synthesis of the so-called high-temperature superconductors (HTSCs). Even more, both the cation and anion stoichiometries of these compounds can be tailored keeping their basic structural features; see below.[41] This led to the preparation of many new compounds, both at room pressure or at high pressure. Among them, are the bismuth-[42–45] and thallium-[46,47] based cuprates and, especially, the mercury[48–51] cuprates, which at this time, represent the superconducting materials having the highest T_C value.[52]

In 1994, Robert J. Cava discovered, parallel to his investigations in HTSCs, the presence of reentrant superconductivity in the so-called rare earth borocarbides, of general formula RM_2B_2C (R = rare earth element and M = Ni, Pd, or Pt).[53–55] These constitute a new family of intermetallic superconductors with superconducting transition temperatures rivaling those of the best previously known intermetallics,[56,57] i.e., Nb_3Ga and Nb_3Sn. It is worth mentioning that T_C does not change substantially with changing the rare earth element.[58–60] However, the importance of these compounds stems from the fact that, as already mentioned, it had always been assumed that superconductors cannot be formed from ferromagnetic transition metals such as iron, cobalt, or nickel.

Another example of superconductors containing magnetic transition elements is the recently discovered iron-based layered pnictides.[61] In 2006, the group headed by H. Hosono discovered superconductivity at ~5 K (and ~3 K) in the iron (and nickel)-based layered LaOMP (with M = Fe[61] and Ni[62]) compounds, respectively, and also, as it will be briefly discussed below, that their superconducting transition temperatures can be significantly raised by F-doping.[63] This finding generated high interest in that these compounds could provide an opportunity for understanding the mechanism of high T_C superconductivity in layered structures. From a

structural point of view, LaOFeP is composed of an alternating stack of lanthanum oxide ($La^{3+}O^{2-}$) and iron pnictide ($Fe^{2+}P^{3-}$) layers. Conduction carriers are two-dimensionally confined in the Fe-P layer, while the La-O ones, in analogy with the HTSC cuprates, constitute the ''charge reservoir layer'', which transfers the carriers to the Fe-P conduction layers. In this sense, aliovalent ion doping in the insulating La-O layer, for instance, the replacement of O^{2-} with F^{-}, provide an extra positive charge in the insulating layer and a negative charge in the conduction layer. In fact, superconductivity was also reported by Hosono in the F-doped LaOFeAs compound at the critical temperature of 26 K.[64] Further substitutions by replacing La for another rare element in the $La[O_{1-x}F_x]FeAs$ compound also lead to a superconducting state, and there seems to exist a correlation between the rare earth element size and T_C. The ''chemical pressure'' originated by replacing the lanthanum by a smaller rare earth ion produces, as it has also been observed in the $La_{2-x}Ba_xCuO_4$, a progressive increase in the T_C in the $R[O_{1-x}F_x]FeAs$ compounds (R = La-Sm).[56,57,65–67] Moreover, when the $Sm[O_{1-x}F_x]FeAs$ compound is synthesized under high pressure, the resistivity onset T_C takes the value of 55 K, which is the highest superconducting transition temperature among these family of materials.[68]

3 SUPERCONDUCTIVITY AND MAGNETIC FIELD: THEORIES

Concomitant to the discovery of new superconducting materials, there was also very active research for understanding the origin of the superconducting state, developing a theory that could explain this phenomenon. In 1950, Vitaly Ginzburg and Lev Landau proposed the so-called phenomenological theory of superconductivity[69] based on Landau's general theory of second-order phase transitions. The contribution of Abrikosov and Khalatnokov[70] and Shubnikov *et al*.[71,72] to the study of the behavior of superconductors under the effect of an external magnetic field was also very important; Ginzburg and Abrikosov were awarded the Physics Nobel Price, 50 years later, in 2003. Abrikosov discovered that one can distinguish two types of superconducting materials, namely, type-I and type-II. Type-I materials expel the magnetic flux completely from their interior, while type-II materials do it fully at small fields but partially at high magnetic fields. Then, to characterize type-II superconductors, two magnetic fields, H_{C1} and H_{C2}, must be introduced. H_{C1} represents the critical magnetic field at which flux penetration first begins, that is, below this value the material expels magnetic flux completely. The region below the H_{C1} (T) curve is called the *Meissner state* (Figure 4). On the other hand, H_{C2} is the magnetic field at which flux penetration is complete and the superconducting state is destroyed. The region between H_{C1} and H_{C2} (i.e., below H_{C2} (T) and overhead H_{C1} (T) curves) is known as the *mixed state* or *vortex state*, which is characterized by the existence of magnetic flux filaments, called *vortices*, going through the superconducting matrix. As the field is increased in this region, there is a gradual increase in the flux penetration, and close to the H_{C2} value, a periodic arrangement of these column vortices can be observed forming a flux line lattice parallel to the applied field, also named as *Abrikosov vortex lattice*. Although Abrikosov published the vortex lattice theory in 1958, it was fully accepted by scientific community only 10 years later, after it was demonstrated by experiments and in analogy with a similar situation in He as demonstrated by Leggett. Therefore, the superconducting phase diagram previously shown in Figure 1 can be modified for type-II superconductors as depicted in Figure 4.

Historically, the most important step for developing an accepted microscopic theory for the superconductivity was the model proposed in February 1957 by John Bardeen, Leon Cooper, and Robert Schrieffer, known as the *BCS theory*.[73,74] Although it is outside the scope of this article to develop the formalism of the BCS theory, we will describe the basic principles and major theoretical aspects in a qualitative outline of some of the concepts and their consequences. The BCS theory assumes that pairs of conduction electrons with equal but opposite moments interact with the crystalline lattice. This interaction, which is attractive, consists of an exchange of virtual phonons between two electrons, forming bonded pairs known as *Cooper pairs*,[75] screening the Coulomb fields. In other words, an electron moving through a positively charged lattice of atomic nuclei leaves behind a small wake that ''is seen'' by another electron, and so forming the so-called Cooper pairs. If many of these pairs are formed, at low temperatures their wave functions align, drawing the pairs into a collective state known as *condensed state*. Then, these

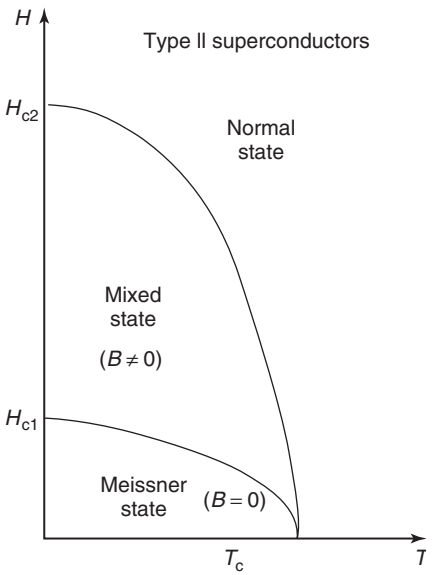


Figure 4 Phase diagram phase II superconductors

pairs of electrons move in a collective manner below a critical temperature and drop into the superconducting state. This theory was successful, and many of their theoretical studies were quickly confirmed by experiments. However, the forces binding the Cooper pairs are weak and are broken either by thermal vibrations or by Coulomb repulsions even at very low temperatures. In fact, this model could not explain the presence of superconductivity above 30 K.

Despite increasingly refined experimental techniques and about several thousand published papers, there does still not exit a complete theoretical explanation for high-temperature superconductivity. The behavior of the HTSC cuprates led scientists to propose different new models to explain the onset of superconductivity in these compounds and, therefore, to complete the already proposed BCS theory or elaborate new ones.

One of the first theories, proposed by Anderson in 1987, is known as the *resonating valence bond theory*.[76] It states that the copper atoms are linked through chemical valence bonds sharing electrons with opposite spins. This antiferromagnetic bonding locks these spin pairs, preventing any flow of current. However, when a small number of holes are doped into the material, the pairs can be mobile and the valence bonds become Cooper pairs that condense into a superconducting state. Another theory concerning ''spin fluctuations'' appears to be more supported by the scientific community.[77,78] It supposes that, without doping, the cuprates are locked into an antiferromagnetic state. In this ordered state, the outer electrons of each copper atom line up so that its spin, for example, down, is opposite to that of its neighbor, the next one down, next up, and so on. In the case of the doped cuprates, the doping atoms break this rigid pattern, giving rise to a pulsating pattern of spins analogous to the lattice distortions of conventional superconductors. This disturbance then draws moving electrons together, forming the Cooper pairs justifying the superconducting state.

4 THE HIGH-TEMPERATURE COPPER OXIDE SUPERCONDUCTORS

The discovery of superconductivity at 35 K in the $La_{1.8}Ba_{0.2}CuO_4$, made by Berdnoz and Müller[34] (1986), set off an explosion of research on the new HTSCs on a worldwide scale until almost the end of the twentieth century. The study of these $La_{2-x}M_xCuO_4$ (M = Sr and Ba) oxides had been done several years before 1986 by Shaplygin and Lazarev[79] and later also studied and characterized by Raveau[80] and Sáez-Puche *et al*.[81] These materials crystallize in the so-called K_2NiF_4 structure type, which can be described as formed by alternate La-O rock-salt-type layers intercalated with $LaCuO_3$ perovskite layers along the c-axis.[41,82] The highest critical temperature of ~40 K of these compounds occurs in $La_{1.8}Sr_{0.2}CuO_4$.[36] The substitution of La by other rare earth elements changes the structural panorama, and Nd_2CuO_4 exhibits a different structural type where the Cu atoms are fourfold coordinated by oxygen atoms, giving rise to square planar [Cu-O_4] groups.[82] Most of the cuprates that adopt this structural type are semiconductors, but, exceptionally, when Nd_2CuO_4 is doped with Th or Ce to give $Nd_{2-x}M_xCuO_4$ (M = Ce,Th)[83,84] they behave as superconductors with T_C around 24 K; since Ce and Th can have a (IV) oxidation state as compared with (III) for Nd they are considered as n-type superconducting cuprates.

Prior to 1986, Nb_3Ge with a $T_C \sim 23$ K had the record for T_C.[85,86] Since the discovery of superconductivity in $La_{2-x}Ba_xCuO_4$, dramatic increases in the superconducting critical temperature have been achieved in different families of layered perovskite cuprate compounds by the use of mechanical or chemical pressure. This last one is considered to be the effect of chemically changing ions size. In January of 1987, superconductivity was reported at 93 K in $YBa_2Cu_3O_7$ by Chu *et al*.,[40] and it was the first superconductor with a T_C value exceeding the boiling point (77 K) of liquid nitrogen at room pressure. Superconductivity was determined for all the members of the family of $REBa_2Cu_3O_7$ oxides with T_C values around 90 K for all the rare earth elements, with exceptions of Ce and Tb, the most stable oxidation state of which is (IV) and does not seem to form the so-called 123-phases.[87] This discovery immediately instigated an unprecedented effort in material synthesis, leading to dramatic increases in transition temperatures in different layered cuprates such as $Bi_2Sr_2Ca_2Cu_3O_{11}$ ($T_C \approx 110$ K),[42–45,88] $Tl_2Ba_2Ca_2Cu_3O_{10}$ (120 K),[46,47,89] and $HgBa_2Ca_2Cu_3O_{10}$.[48–52] The last compound has the maximum value of $T_C = 135$ K at room pressure[49] and seems to increase to 138 K by fluorine treatment (Antipov *et al*.).[90] However, when this layered cuprate oxide is subjected to high mechanical pressure (in excess of 30 GPa), T_C takes the value of 164 K, which is the highest superconducting critical T_C ever reported.[50,91] Although more than 160 different cuprates have been prepared since 1986, there are not any reasons that preclude the possibility to find superconductivity at higher temperatures, including room temperature.

4.1 Structural Aspects of HTSC Cuprates

The crystal structure of $YBa_2Cu_3O_{7-x}$ can be described as derived from the ideal cubic perovskite ABO_3. In this structure, the larger A cation occupies the center of a cuboctahedral hole formed by corner sharing BO_6 octahedra. The B cation is Cu in this 123-superconducting phase, but there are two larger cations, Y and Ba, orderly occupying the A sites. The resulting unit cell is tripled along the c-axis with the sequence Ba-Y-Ba (Figure 5a). Although a triple perovskite $A_3B_3O_9$ should contain nine oxygen atoms, it is found that the 123 unit cell only has seven of them. These two oxygen vacancies are accommodated in an ordered way: one in the yttrium plane, giving, as result, a distorted square pyramid [Cu-O_5]

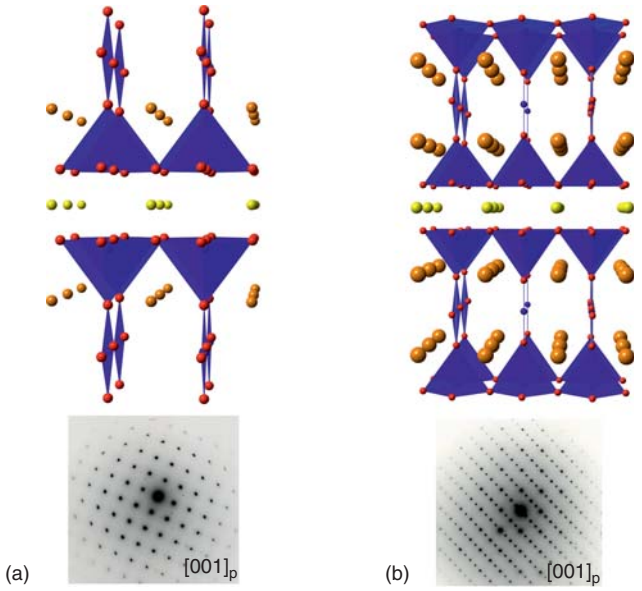


Figure 5 Crystal structure of (a) $YBa_2Cu_3O_7$ and (b) $YBa_2Cu_3O_{6.5}$ cuprates. Corresponding electron diffraction patterns for both oxides are given in the lower part of the figure

and the other in the basal unit cell plane forming square planar [Cu-O_4] units forming chains along the b-axis. Obviously, this also influences Ba coordination, which becomes [Ba-O_{10}]. The square [Cu-O_5] pyramids share the apical oxygen with the square planar CuO_4 units on the basal plane of the orthorhombic structure, *Pmmm* space group.It was found later[41,92–95] that the critical temperature T_C substantially changes with the oxygen content and the newly formed oxygen vacancies are accommodated by the oxygen of the [Cu-O_4] square planar units because of their relative instability in comparison with the other oxygens present in the structure (Figure 5a and b). Moreover, the mentioned lability of the [Cu-O_4] bond allows the ordering process along the Cu-O chains, and it has been proposed to be a $YBa_2Cu_3O_{6.5}$ (i.e., $Y_2Ba_4Cu_6O_{13}$) phase in which the parameters are $a = 2a_p \times b = a_p \times c = 3a_p$, where the b parameter is double that corresponding to the perovskites as a consequence of the oxygen vacancy ordering along the (100) direction,[96] which is indicated in Figure 5(b). This is clearly observed in the electron diffraction pattern, where extra spots are present along the 100 direction, giving as a result a superstructure that justifies the $a = 2a_p$ value for the $YBa_2Cu_3O_{6.5}$ phase. Thus the oxygen stoichiometric control becomes a decisive instrument in establishing the superconducting properties of the 123-phases: from the highest temperature orthorhombic superconducting $YBa_2Cu_3O_{\sim 6.9}$ with $T_C \sim 92$ K through the tetragonal (P4/mmm) antiferromagnetic insulator $YBa_2Cu_3O_{\sim 6.4}$, to nonsuperconducting tetragonal $YBa_2Cu_3O_6$[97] where [Cu-O_2] linear and [CuO_5] pyramid coordinations are present for Cu^+ and Cu^{2+}, respectively. It is worth noting that the replacement of Y by most of the trivalent rare earth cations to give the family $REBa_2Cu_3O_{7-x}$ (RE = rare earth) does not affect very much the superconducting properties.[87]

The superconducting materials $YBa_2Cu_4O_8$ and $Y_2Ba_4Cu_7O_{15}$ with T_C of 80 K and 95 K, respectively, are closely related to orthorhombic $YBa_2Cu_3O_7$. $YBa_2Cu_4O_8$ first observed as an impurity was later prepared as a pure phase in 1988.[98,99] It can formally be described by the insertion into the $YBa_2Cu_3O_7$ of a second chain of [CuO_4] units where the pyramidal copper layers of the 123 phase are interconnected along the c-axis of the structure through double chains of edge sharing square planar groups. On the other hand, $Y_2Ba_4Cu_7O_{15}$ can be described as an ordered intergrowth between $YBa_2Cu_3O_7$ and $YBa_2Cu_4O_8$ along the c-axis of the structure.[100]

Trivalent rare earth cations can also be incorporated into different Bi, Tl, Hg, and Pb layered cuprates, giving rise to various structures that allow the incorporation of more oxygen as consequence of the trivalent oxidation state of these rare earth ions. The influence on the superconducting properties and the crystal chemistry has been reviewed by Raveau *et al.*[101]

5 SUPERCONDUCTIVITY AND MAGNETISM FOR THE 1212 CUPRATES

Since the discovery of the high-T_C ceramic superconductors, for instance, $La_{2-x}Ba_xCuO_4$[34] and $YBa_2Cu_3O_7$,[40] the vast majority of the scientific efforts in the field of solid state physics, chemistry, and materials science related to superconductivity have been focused on the synthesis of new structure-related compounds. In this light, when the square planar Cu sites of the $YBa_2Cu_3O_7$ structure are completely replaced by Nb or Ta atoms, the CuO_4 units are replaced by MO_6 octahedra in the new phases to form the so-called 1212-type structure with the stoichiometry $MRBa_2Cu_2O_8$ (R = Y and rare earth element, M = Nb or Ta).[102] In order to maintain the charge balance, the oxygen occupancy in the basal plane of the unit cell is complete in the form of octahedra as can be clearly seen in Figure 6. These niobates and tantalates have already been synthesized not only with Y but also with other rare earth elements.[102,103] From the experimental point of view, it has been observed that there is a small energy difference between the $MRBa_2Cu_2O_8$ phases and the mixture $Ba_2RMO_6 + CuO$. The Ba_2RMO_6 is a double perovskite with R in the center of a regular octahedron. Therefore, the structural stability of these pervoskites should decrease for large R^{3+} ions, as has also been reported for R-substituted phases based on the $YBa_2Cu_3O_7$ structure. On the other hand, the substitutions in the charge reservoir layer by Nb or Ta does not induce superconductivity, possibly because of insufficient oxidation within the layers of [CuO_5] square pyramids. This suggestion, earlier made by Slater and Greaves[102] and later confirmed by Antipov *et al.*,[51] lead other people to perform

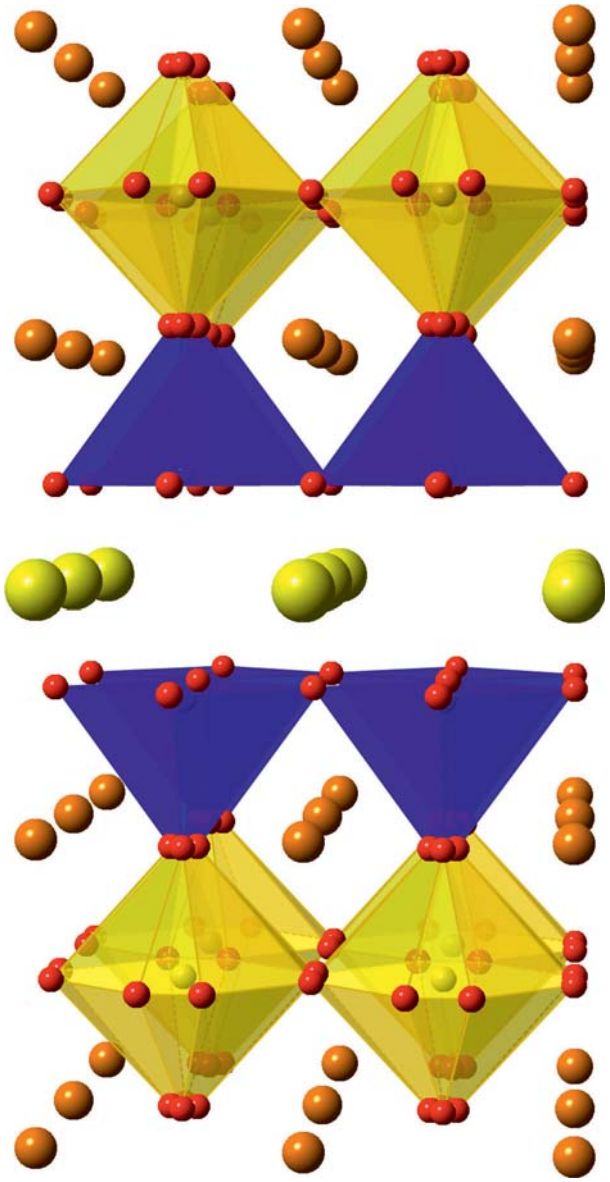


Figure 6 Crystal structure of $MSr_2RCu_2O_3$ cuprates. M and Cu cations are placed in octahedrons and pyramids, respectively. R ions occupy the center of the unit cell and Sr ion are located in the cuboctahedral sites

more substitutions, not only in the charge reservoir layer but also in the R and Ba sublattices. Then, soon after the first successful synthesis of $RuSr_2GdCu_2O_8$ by Bauernfein *et al*. in 1995,[104] the material was found to display not only superconductivity ($T_C = 45$ K) but also coexisting magnetic order with a T_{mag} of 135 K.[105,106] Although this is not the first magnetic superconductor, it is the first HTSC compound where the magnetic ordering temperature is much higher than the superconducting T_C. This fact created the need of understanding the interplay between magnetic and superconducting orders in HTSC-layered cuprates. In fact, the coexistence of these two antagonist states of matter is possible at the microscopic level and stem from the crystal structure of this compound. As it has been previously mentioned, the 1212-type structure formally derives from that of the classical YBCO superconductor by replacing the tetra-coordinated square planar copper [Cu-O_4] in the chains for octahedral [Ru-O_6] to form the so-called charge reservoir layer (Figure 5a and 6). Therefore, superconductivity occurs within infinite CuO_2 planes while magnetism is displayed within the perovskite-like ''charge reservoir layer''.

The effect of doping on the physical properties of $RuSr_2GdCu_2O_8$ has been investigated by several groups. In fact, more than 20 partial substitutions of the Ru,[107–119] Sr,[120–122] Gd,[123–125] and Cu[125,126] atoms have been performed (see Figure 7 for more details); only tin[107] and copper[108] replacing ruthenium seems to have a positive effect, and both show an increase in T_C from 36 to 42 and 70 K, respectively. At the same time, T_N seems to decrease in both cases, something that is attributed to the disorder introduced in the ruthenium sublattice by the dopants. On the other hand, the partial substitution of Gd by Ca had also been reported to increase the T_C, although no detailed data has been presented to corroborate this assumption.[123] On the other hand, a few full substitutions have also been made in the rare earth element position of $RuSr_2GdCu_2O_8$ compound.[127] Yet, for the majority of the rare earth elements (all except Eu, Sm, and Gd), high pressure is required to achieve the substitution.[128] Furthermore, it was found that the Y member, namely, $RuSr_2YCu_2O_8$, exhibits the highest critical temperature of the family ($T_C = 51$ K), although there is no direct correlation between T_C and the rare earth ionic radii. As a continuation of this work, full substitutions on the charge reservoir layer, giving rise to different families of $MSr_2RCu_2O_8$ compounds (M = transition metal cation and R = rare earth element), have also been realized. For instance, M = Cr[129] in the first-row transition series, M = Nb,[102] Mo,[130] and of course Ru in the second one and more recently M = Ta[102] and Ir[131–133] in the third one have been successfully synthesized. In the case of the molybdates, Felner and coworkers reported a paramagnetic behavior for the $MoSr_2RCu_2O_8$ with R = La–Nd; antiferromagnetic behavior for the central lanthanides (R = Sm–Dy), and coexistence of antiferromagnetism and superconductivity for the compounds containing smaller rare earth elements, i.e., R = Y, Ho–Tm. Only the $MoSr_2YbCu_2O_8$ compound displays superconductivity.[130] It is interesting to mentioned here that very recent neutron diffraction data performed in these compounds reveal that the real cation stoichiometry of these compounds is not the nominal $MoSr_2RCu_2O_8$ one, that is, the fully Mo-substituted compound (Marik *et al*., to be published).

Recently, a series of nonsuperconducting phases with the general formula $CrSr_2RECu_2O_8$ was obtained using high pressure and temperature techniques.[129] An antiferromagnetic ordering is present in some of these chromates when R is a

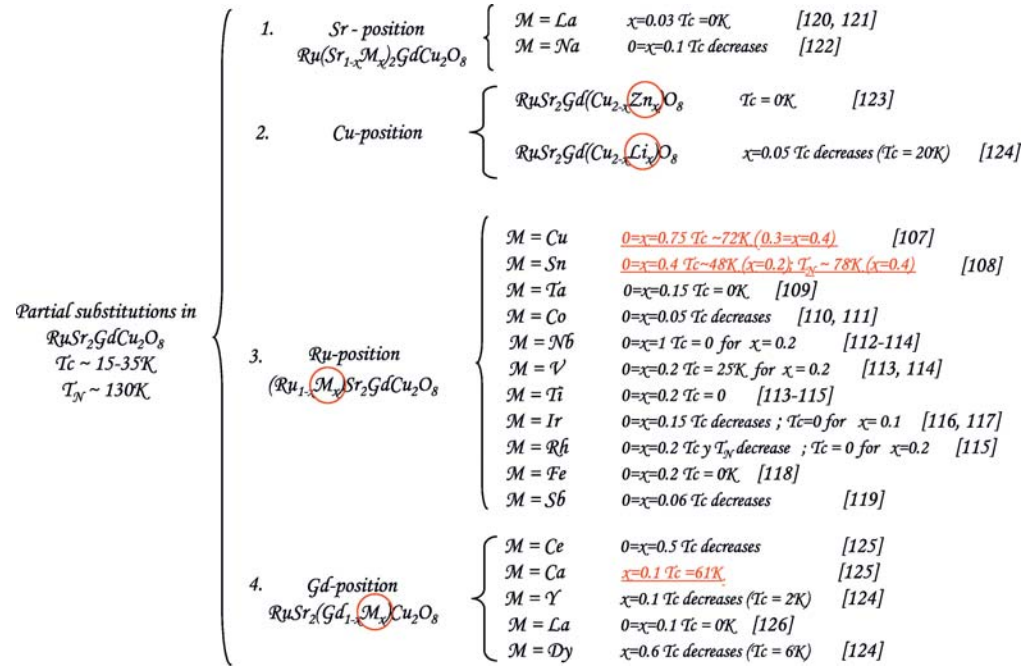


Figure 7 Review of the main partial substitutions performed in the $RuSr_2GdCu_2O_8$ compound

nonmagnetic lanthanide, while the rest of the materials seem to exhibit a paramagnetic behavior.

We have, of late, started a project to fully replace ruthenium by iridium, giving $IrSr_2RCu_2O_8$, using high-pressure and high-temperature synthesis. Although none of the compounds prepared so far present a transition to a superconducting state, this family shows a wide range of magnetic behavior that can be traced back to the rare earth ions anisotropy. For instance, $IrSr_2GdCu_2O_8$ presents ferrimagnetism,[131] while metamagnetic behavior is observed in the $IrSr_2TbCu_2O_8$ compound.[132] A rather interesting case is that of the Eu and Sm iridocuprates[133]; both compounds display a reentrant spin-glass transition, that is, coexistence of spin-glass and ferromagnetism ordering. The ferromagnetism is due to the presence of magnetic clusters in the otherwise paramagnetic regime, and the spin-glass behavior can be understood from the presence of several ions with different magnetic moments. It should be emphasized that frustration in the 1212 lattice can arise from the Cu pyramids[134]; in fact, the random distribution of diamagnetic Cu^{3+} in the O–Cu–O bonds is the main cause of frustration of Cu^{2+} moments in the HTSC.[76,135] It has been pointed out in HTSC cuprate systems, which are magnetically frustrated, that these magnetic clusters exist in pairs. This singlet pairing could occur because of a resonating valence bond interaction, as it has been briefly introduced before,[76] and, having the same role as the Cooper pairs occurring in the BCS theory, be responsible for the superconducting state.[136]

We have also observed a somewhat surprising fact related to the synthesis conditions: these 1212 materials, most of which require high pressure and temperature conditions to be obtained, can only be prepared in a particular and relatively narrow window of those parameters, outside which they cannot be obtained pure or even obtained at all.[137,138] The rare earth element, located at the center of the unit cell of the YBCO setting (Figure 6a and b), seems to control the optimum synthesis conditions. These optimum conditions show a remarkable Gaussian correlation with the rare earth ion size and do not follow the classic lanthanide contraction so often observed in the chemistry of those elements. In other words, higher pressure is needed to make the 1212 materials with the smaller and the bigger rare earth cations than that of the intermediate ones.[137,138]

6 SUPERCONDUCTING APPLICATIONS

Potential applications of superconductors are based on the properties that these materials present: (i) zero resistance below T_C, (ii) Josephson effect, (iii) Meissner effect, and (iv) superconducting magnets.

6.1 Fabrication of Superconducting Wires

The zero resistance of the HTSC made it possible to be employed in the construction of electricity transmission lines. In order to improve the performance, second-generation 2G wires have been developed. These are formed by six layers of different materials, where the YBCO is covered

by an external silver layer, which is the key to improve the mechanical properties of YBCO and also stabilize the wire against local heating. These wires or tapes can carry currents as large as 10^6 Acm^{-2}, and they are 50% more efficient than the conventional cable, giving rise to important energy saving.

The price of these new 2G-HTSC wires decrease rapidly through new technological achievements. In this sense, wire-price performance decreased from \$100 000/kAm in 2004 to around \$600/kAm in 2010. However, because of the still relatively high cost and difficulty to cool these superconducting wires, they have been installed only in few transmission power lines in Europe, United States, and Japan for testing purposes. In 2001, residents of Copenhagen began receiving electricity through three cables of HTSC 30 m long. Sumitomo Electric has already installed an underground HTSC cable in Albany, New York, which was connected to the grid successfully in July 2006, supplying power to 70 000 households.

6.2 Josephson Effect: SQUID

SQUID is the acronym of superconducting quantum interference device and consists of two superconductors separated by a thin insulating layer, which form two parallel Josephson junctions. Josephson predicted that if two superconducting materials were placed next to each other, separated by a thin insulating layer, current can flow without potential drop between the metals. This current originates from the tunneling of Cooper pairs, as can be schematically observed in Figure 8(a). The metal could be Nb, and the junction between the two superconductors is Al_2O_3, also called a *weak junction*.

The SQUID device is the most sensitive set up available for measuring magnetic fields. It may be configured as a magnetometer to detect very small magnetic fields such as the magnetic fields in living organisms. The extremely high sensitivity of this device is associated with measuring changes in the magnetic field associated with one quantum of flux, called *fluxon*. Then the magnetic flux is quantized in fluxon units, as $\phi = \frac{2\pi h}{2e} = 2.0678 \times 10^{-15}$ Tm^2. When a constant moment is maintained, the Cooper pairs flow through the Josephson junctions of the SQUID in the absence of any applied voltage. On the other hand, when a magnetic field is applied, the magnetic flux changes within the ring, giving rise to oscillations in the critical current between a maximum and a minimum value. Instead of the current, in practice, changes in the voltage are measured under the influence of a magnetic field. The SQUID device is an extremely sensitive current-to-voltage converter that could detect variations in magnetic fields as small as 10^{-14} T.

Figure 8(b) shows a magnetometer configuration based on a SQUID sensor. This configuration increases the sensitivity since it does not detect directly the magnetic field from the sample. Instead, the sample moves through a superconducting detection coil, which is connected to the SQUID with superconducting wires, allowing the current from the detection coil to inductively couple to the SQUID sensor. The SQUID produces an output voltage that is proportional to the current flowing in the SQUID input coil. This configuration yields a sensitivity of 10^{-15} T. One femtotesla is 10^{-11} times lower than the earth's magnetic field. Although most SQUIDs are made with superconducting niobium, more recently, high-temperature SQUIDs fabricated with YBCO have been developed, which work by cooling with liquid nitrogen, which is cheaper and easier to handle than liquid helium.

SQUID devices can also be used to measure voltages as small as 10^{-18} V and therefore can be used to fabricate highly sensitive voltmeters. SQUIDs are being used in medical diagnosis to detect small changes in the magnetic field: from a few femtoteslas in the brain to 50 000 fT in the heart. In this sense, magnetoencephalography is a noninvasive technique for detecting very weak magnetic fields originating from the brain. From the variation of the magnetic field within the brain it is possible to get a clear image of it, and anomalies such as tumors, epilepsy, or other diseases may be detected. SQUID devices are continuing to find more and more applications such as the detection of mineral and oil deposits, and they may be used in military applications to detect submarines and

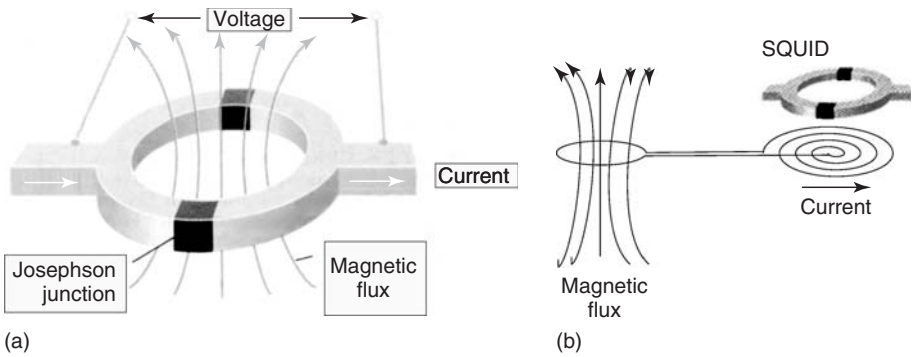


Figure 8 (a) SQUID configuration showing the two Josephson junctions. (b) Magnetometer configuration based in a SQUID sensor

mines by measuring local changes in the earth's magnetic field.

6.3 Magnetic Levitation Trains (MAGLEV)

Magnetic levitation based on the Meissner effect is one potential application that has received a lot of publicity. There have been many efforts to incorporate HTSCs in transport technology, mainly to magnetic levitating trains, MAGLEV. These trains are working since 1970, but they use conventional electromagnets. Nowadays, Japanese are working in the development of a MAGLEV train using superconductors in the train, which are repelled by the magnetic field produced by coils that are located in the track. It moves without friction between the train and the track. In 2003, the Japanese levitation test vehicle attained speeds of 581 km h^{-1}. In 2004, a MAGLEV train arrived at Shanghai station. Although these developments were successful, in all cases low-temperature superconductors (LTSCs) were used, and the use of HTSCs is a future project where refrigeration is only a small percentage of the total high cost that appears to be the most important factor to be able to develop this new mode of transport system.

6.4 Superconducting Magnets

Low-temperature superconducting magnets are replacing conventional electromagnets and are now used in many different applications. Electromagnets are made by passing electric current through copper wires wound around an iron core, giving rise to magnetic fields of several tesla. When a superconductor is used, the HTSC superconducting wires can carry currents as high as 400 000 A cm^{-1}, and the iron or permanent magnet core needed to amplify the strength of the magnetic field is eliminated. As a result, these superconducting magnets are lighter, more powerful (30 T), and consume less power than the conventional counterparts, although they need to be cooled at 4 K or 77 K to become superconducting. It is worth mentioning that the newest NMR spectrometers are fabricated with superconducting magnets now widely used in fundamental research and in the magnetic resonance image (MRI) for medical diagnosis. In 1998, Oxford Magnets Technology built an MRI body scanner with two HTSC coils, and Hitachi fabricated a 23-T superconducting HTSC magnet to be used for NMR spectrometers operating at 1 GHz, producing strong fields that increase the sensitivity and improve the MRI technique, making it possible to obtain high-quality images of the human body in just a few minutes.

6.5 Motors, Generators, and Energy Storage

Electric power is produced by spinning a magnet inside a coil. The use of superconducting materials allows one to make electric motors and generators that are more efficient than the conventional generators wound with copper wire. Recent technology based on HTSC produced a 5000-horse power HTSC ship propulsion motor, which has been designed and built by the US Navy. The advantages of these generators based on HTSC are the smaller size, ~70 Tm, and higher power, 36.5 MW, while the conventional counterpart with a weight of 180 Tm produces lower power, 21 MW. These advantages make them a very interesting market in the future, and it has been estimated that the potential market for superconducting generators is of the order of 20 billion dollars in 2020.

Superconducting magnetic energy storage, SMES, is another interesting application of the HTSC materials since they could store a massive amount of current without energy loss. These SMES dispositive could store high power densities from 100 MW to 1 GW and if necessary could discharge in just a few seconds to stabilize the main power network. Even more, they can store electricity at times of low demand to be delivered later.

6.6 Other Applications

Fusion reactors with magnetic confinement using strong magnetic fields (H = 10 T) are generated with superconducting coils of 12 m diameter. For this purpose, high investment is required since a large amount of superconducting materials such as 8700 Tm need to be used. The project ITER under magnetically confined plasma is now being developed.

Other applications start developing, for example, high-energy colloids that would never have been viable without superconductors. These experiments with high-energy particles require that subatomic particles be accelerated to the speed of the light, and superconducting materials make this possible in two large European installations, such as CERN and LHC located in Switzerland. Other facilities using superconducting magnets are the proton–proton collider at Fermilab, the electron–proton collider in Germany (DESY), and the relativistic heavy-ion collider (RHIC) in Brookheaven National Laboratory. More detailed information of these high-energy colliders can be obtained from their web pages.

The world market for superconducting materials is expected to grow near $38 billion in 2020. Although LTSCs continue to play a dominant role and to be developed, the use of HTSC superconducting materials will increase and new applications will be explored and developed in the future. However, the search for new high-temperature superconducting materials is a challenge, although new findings in this field are not presently as common as they used to be.

7 GLOSSARY

2G: second-generation

BCS: Bardeen, Cooper, and Schrieffer theory

CERN: Organisation européenne pour la recherche nucléaire (European Organization for Nuclear Research)

DC: direct current

DESY: Deutsches Elektronen Synchrotron (German Electron Synchrotron)

HTSC: high temperature superconductors

H_C*:* critical magnetic field

ITER: International Thermonuclear Experimental Reactor

J_C*:* critical current density

LHC: Large Hadron Collider

LTSC: low-temperature superconductor

MAGLEV: magnetic levitating trains

MRI: magnetic resonance image

NMR: nuclear magnetic resonance

RE: rare earth

RHIC: relativistic heavy-ion collider

SMES: superconducting magnetic energy storage

SQUID: superconducting quantum interference device

T_C*:* superconducting critical temperature

YBCO: $YBa_2Cu_3O_7$

8 ACKNOWLEDGEMENTS

The authors thank Prof. Vicent for valuable comments, and A. J. Dos santos-García is also grateful to MICINN and UCM for a ''Juan de la Cierva'' contract (JCI-2010-08229) and also MAT2010-19460 and S-2009/PPQ-1626.

9 RELATED ARTICLES

Lanthanides: Luminescence Applications; Lanthanides: Magnetic Resonance Imaging.

10 ABBREVIATIONS AND ACRONYMS

HTSCs = high-temperature superconductors; LTSCs = low-temperature superconductors; MAGLEV = magnetic levitating trains; MRI = magnetic resonance image; RHIC = relativistic heavy-ion collider; SMES = superconducting magnetic energy storage; SQUID = superconducting quantum interference device.

11 REFERENCES

1. H. K. Onnes, *Commun. Phys. Lab. Univ. Leiden*, 1911, **12**, 120b.
2. H. K. Onnes, *Akad. Van Wet.*, 1911, **14**, 818.
3. W. Meissner and R. Ochsenfeld, *Naturwissenschaften*, 1933, **21**, 787.
4. C. J. Gorter, *Rev. Mod. Phys.*, 1964, **36**, 3.
5. M. Cyrot and D. Pavuna, 'Introduction to Superconductivity and High-T_c Materials', World Scientific, London, 1992.
6. C. Kittel, 'Introduction to Solid State Physics', John Wiley & Sons, New York, 1986.
7. J. Eisenstein, *Rev. Mod. Phys.*, 1954, **26**, 277.
8. C. Buzea and K. Robbie, *Supercond. Sci. Technol.*, 2005, **18**, R1.
9. C. Buchal and J. M. Welter, *Platinum Met. Rev.*, 1983, **27**, 170.
10. C. P. Poole Jr., 'Handbook of Superconductivity', Academic Press, San Diego, CA, 2000.
11. K. Shimizu, H. Ishikawa, D. Takao, T. Yagi, and K. Amaya, *Nature*, 2002, **419**, 597.
12. J. Wittig, *Phys. Rev. Lett.*, 1970, **24**, 812.
13. M. B. Maple, J. Wittig, and K. Kim, *Phys. Rev. Lett.*, 1969, **23**, 1375.
14. H. H. Balster and J. Wittig, *J. Low Temp. Phys.*, 1975, **21**, 377.
15. M. Debessai, J. J. Hamlin, and J. S. Schilling, *Phys. Rev. B*, 2008, **78**, 064519.
16. B. W. Roberts, 'Properties of Selected Superconductive Materials', 1978, Natl. Bur. Stand. (U.S.) Tech., Note 983.
17. V. G. Tissen, E. G. Ponyatovskii, M. V. Nefedova, F. Porsch, and W. B. Holzapfel, *Phys. Rev. B*, 1996, **53**, 8238.
18. S. V. Vonsovsky, Y. A. Jzymov, and E. Z. Kurmaev, 'Superconductivity of Transition Metals: Their Alloys and Compounds', Springer-Verlag, Berlin, 1982.
19. B. T. Matthias and J. K. Hulm, *Phys. Rev.*, 1952, **87**, 799.
20. M. L. Cohen, *Phys. Rev.*, 1964, **134**, A511.
21. J. F. Schooley, W. R. Hosler, and M. L. Cohen, *Phys. Rev. Lett.*, 1964, **12**, 474.

22. D. C. Johnston, H. Prakash, W. H. Zachariasen, and R. Viswanathan, *Mat. Res. Bull.*, 1973, **8**, 777.
23. A. W. Sleight, J. L. Gibson, and P. E. Bierstedt, *Solid State Commun.*, 1975, **17**, 27.
24. R. Chevrel, M. Sergent, and J. Prigent, *J. Solid State Chem.*, 1971, **3**, 515.
25. M. Marezio, P. D. Dernier, J. P. Remeika, E. Corenzwit, and B. T. Matthias, *Mater. Res. Bull.*, 1973, **8**, 657.
26. V. L. Ginzburg, *Zh. Eksp. Teor. Fiz.*, 1956, **31**, 202.
27. V. L. Ginzburg, *Sov. Phys. JETP*, 1957, **4**, 153.
28. M. B. Maple, *Physica B*, 1995, **215**, 110.
29. O. Fisher, A. Treyvaud, R. Chevrel, and M. Sergent, *Solid State Commun.*, 1993, **88**, 867.
30. G. R. Stewart, *Rev. Mod. Phys.*, 1984, **56**, 755.
31. F. Steglich, J. Aarts, C. D. Bredl, W. Lieke, D. Meschede, and W. Franz, *Phys. Rev. Lett.*, 1979, **43**, 1892.
32. H. Q. Yuan, F. M. Grosche, M. Deppe, C. Geibel, G. Sparn, and F. Steglich, *Science*, 2003, **202**, 2104.
33. M. R. Norman, *Science*, 2011, **332**, 196.
34. J. G. Bednorz and K. A. Müller, *Z. Phys. B*, 1986, **64**, 189.
35. K. Oh-Ishi, M. Kikuchi, Y. Syono, N. Kobayashi, T. Sasaoka, T. Matsuhira, Y. Muto, and H. Yamauchi, *Jpn. J. Appl. Phys.*, 1988, **27**, L1449.
36. R. J. Cava, R. B. van Dover, B. Batlogg, and E. A. Rietman, *Phys. Rev. Lett.*, 1987, **58**, 408.
37. C. W. Chu, P. H. Hor, R. L. Meng, L. Gao, Z. J. Huang, and Y. Q. Wang, *Phys. Rev. Lett.*, 1987, **58**, 405.
38. J. E. Schirber, E. L. Venturini, J. F. Kwak, D. S. Ginley, and B. Morosin, *J. Mater. Res.*, 1987, **2**, 421.
39. D. Erskine, E. Hess, P. Y. Yu, and A. M. Stacy, *J. Mater. Res.*, 1987, **2**, 783.
40. M. K. Wu, J. R. Ashburn, C. J. Torng, P. H. Hor, R. L. Meng, L. Gao, Z. J. Huang, Y. Q. Wang, and C. W. Chu, *Phys. Rev. Lett.*, 1987, **58**, 908.
41. R. J. Cava, *Science*, 1990, **247**, 656.
42. C. Michel, M. Hervieu, M. M. Borel, A. Grandin, F. Deslandes, J. Provost, and B. Raveau, *Z. Phys. B*, 1987, **68**, 421.
43. H. Maeda, Y. Tanaka, M. Fukutomi, and T. Asano, *Jpn. J. Appl. Phys.*, 1988, **27**, L209.
44. C. W. Chu, J. Bechtold, L. Gao, P. H. Hor, Z. J. Huang, R. L. Meng, Y. Y. Sun, Y. Q. Wang, and Y. Y. Xue, *Phys. Rev. Lett.*, 1988, **60**, 941.
45. R. M. Hazen, C. T. Prewitt, R. J. Angel, N. L. Ross, L. W. Finger, C. G. Hadidiacos, D. R. Veblen, P. J. Henaey, P. H. Hor, R. L. Meng, L. Gao, J. Bechtold, and C. W. Chu, *Phys. Rev. Lett.*, 1988, **60**, 1174.
46. Z. Z. Sheng and A. M. Hermann, *Nature*, 1988, **332**, 138.
47. Z. Z. Sheng, A. M. Hermann, A. E. I. Ali, C. Almasan, J. Estrada, T. Datta, and R. J. Matson, *Phys. Rev. Lett.*, 1988, **60**, 937.
48. S. N. Putilin, E. V. Antipov, O. Chmaissem, and M. Marezio, *Nature*, 1993, **362**, 226.
49. A. Schilling, M. Cantoni, J. D. Guo, and H. R. Ott, *Nature*, 1993, **363**, 56.
50. C. W. Chu, L. Gao, F. Chen, Z. J. Huang, R. L. Meng, and Y. Y. Xue, *Nature*, 1993, **365**, 323.
51. E. V. Antipov, A. M. Abakumov, and S. N. Putilin, *Supercond. Sci. Technol.*, 2002, **15**, R31.
52. L. Gao, Y. Y. Xue, F. Chen, Q. Xiong, R. L. Meng, D. Ramirez, C. W. Chu, J. H. Eggert, and H. K. Mao, *Phys. Rev. B*, 1994, **50**, 4260.
53. R. J. Cava, H. Takagi, B. Batlogg, H. W. Zandbergen, J. J. Krajewski, W. F. Peck Jr., R. B. van Dover, R. J. Felder, T. Siegrist, K. Mizuhashi, J. O. Lee, H. Eisaki, S. A. Carter, and S. Uchida, *Nature*, 1994, **367**, 146.
54. R. J. Cava, H. Takagi, H. W. Zandbergen, J. J. Krajewski, W. F. Peck Jr., T. Siegrist, B. Baflogg, R. B. van Dover, R. J. Felder, K. Mizuhashi, J. O. Lee, H. Eisaki, and S. Uchida, *Nature*, 1994, **367**, 252.
55. H. Takagi, M. Nohara, and R. J. Cava, *Physica B*, 1997, **237–238**, 292.
56. J. R. Gavaler, M. A. Janocko, and C. Jones, *J. Appl. Phys.*, 1974, **45**, 3009.
57. L. R. Testardi, J. H. Wernick, and W. H. Rogers, *Solid State Commun.*, 1974, **15**, 1.
58. H. Eisaki, H. Takagi, R. J. Cava, B. Batlogg, J. J. Krajewski, W. F. Peck Jr., K. Mizuhashi, J. O. Lee, and S. Uchida, *Phys. Rev. B*, 1994, **50**, 647.
59. H. Takagi, R. J. Cava, H. Eisaki, J. O. Lee, K. Mizuhashi, B. Batlogg, S. Uchida, J. J. Krajewski, and W. F. Peck Jr., *Physica C*, 1994, **228**, 389.
60. S. A. Carter, B. Batlogg, R. J. Cava, J. J. Krajewski, W. F. Peck Jr., and H. Takagi, *Phys. Rev. B*, 1994, **50**, 4216.
61. Y. Kamihara, H. Hiramatsu, M. Hirano, R. Kawamura, H. Yanagi, T. Kamiya, and H. Hosono, *J. Am. Chem. Soc.*, 2006, **128**, 10012.
62. T. Watanabe, H. Yanagi, T. Kamiya, Y. Kamihara, H. Hiramatsu, M. Hirano, and H. Hosono, *Inorg. Chem.*, 2007, **46**, 7719.
63. X. H. Chen, T. Wu, G. Wu, R. H. Liu, H. Chen, and D. F. Fang, *Nature*, 2008, **453**, 761.
64. Y. Kamihara, T. Watanabe, M. Hirano, and H. Hosono, *J. Am. Chem. Soc.*, 2008, **130**, 3296.
65. Z.-A. Ren, J. Yang, W. Lu, W. Yi, X.-L. Shen, Z.-C. Li, G.-C. Che, X.-L. Dong, L.-L. Sun, F. Zhou, and Z.-X. Zhao, *Europhys. Lett.*, 2008, **82**, 57002p1.
66. G. F. Chen, Z. Li, D. Wu, G. Li, W. Z. Hu, J. Dong, P. Zheng, J. L. Luo, and N. L. Wang, *Phys. Rev. Lett.*, 2008, **100**, 247002.
67. Z.-A. Ren, J. Yang, W. Lu, W. Yi, G.-C. Che, X.-L. Dong, L.-L. Sun, and Z.-X. Zhao, *Mater. Res. Innov.*, 2008, **12**, 105.

68. Z.-A. Ren, W. Lu, J. Yang, W. Yi, X.-L. Shen, Z.-C. Li, G.-C. Che, X.-L. Dong, L.-L. Sun, F. Zhou, and Z.-X. Zhao, *Chin. Phys. Lett.*, 2008, **25**, 2215.
69. V. L. Ginzburg and L. D. Landau, *Zh. Eksp. Teor. Fiz.*, 1950, **20**, 1064.
70. A. Abrikosov and I. Khalatnokov, *Usp. Fiz. Nauk*, 1958, **65**, 551.
71. L. W. Schubnikow, W. I. Chotkewitsch, J. D. Schepelew, and J. N. Rjabinin, *Phys. Z. Sowjetunion*, 1936, **10**, 165.
72. L. W. Shubnikov, W. I. Khotkevich, J. D. Shepelev, and J. N. Riabinin, *Zh. Eksper. Teor. Fiz.*, 1937, **7**, 221.
73. J. Bardeen, L. N. Cooper, and J. R. Schrieffer, *Phy. Rev.*, 1957, **106**, 162.
74. J. Bardeen, L. N. Cooper, and J. R. Schrieffer, *Phy. Rev.*, 1957, **108**, 1175.
75. L. N. Cooper, *Phy. Rev.*, 1957, **104**, 1189.
76. P. W. Anderson, *Science*, 1987, **235**, 1196.
77. P. Monthoux, A. V. Balatsky, and D. Pines, *Phys. Rev. Lett.*, 1991, **67**, 3448.
78. A. Mann, *Nature*, 2011, **475**, 280.
79. I. S. Shaplygin and V. B. Lazarev, *Russ. J. Inorg. Chem.*, 1979, **24**, 820.
80. C. Michel and B. Raveau, *Rev. Chim. Miner.*, 1984, **21**, 407.
81. R. Sáez-Puche, M. Norton, and W. S. Glaunsinger, *Mater. Res. Bull.*, 1982, **17**, 1429.
82. H. Shaked, P. M. Keane, J. C. Rodriguez, F. F. Owen, R. L. Hitterman, and J. D. Joergensen, 'Crystal Structures of the High-T_C Superconducting Copper Oxides', Elsevier Science B. V., Amsterdam, 1994.
83. Y. Tokura, H. Takagi, and S. Uchida, *Nature*, 1989, **337**, 345.
84. J. T. Markert and M. B. Maple, *Solid State Commun.*, 1989, **70**, 145.
85. J. R. Gavaler, *Appl. Phys. Lett.*, 1973, **23**, 480.
86. L. R. Testardi, J. H. Wernick, and W. A. Royer, *Solid State Commun.*, 1974, **15**, 1.
87. M. A. Alario-Franco, E. Morán-Miguélez, R. Sáez-Puche, F. García-Alvarado, U. Amador, M. Barahona, F. Fernández, M. T. Pérez-Frías, and J. L. Vicent, *Mater. Res. Bull.*, 1988, **23**, 313.
88. A. K. Cheetham, A. M. Chippindale, and S. J. Hibble, *Nature*, 1988, **333**, 21.
89. D. E. Cox, C. C. Torardi, M. A. Subramanian, J. Gopalakrishnan, and A. W. Sleight, *Phys. Rev. B*, 1988, **38**, 6624.
90. K. A. Lokshin, D. A. Pavlov, S. N. Putilin, E. V. Antipov, D. V. Sheptyakov, and A. M. Balagurov, *Phys. Rev. B*, 2001, **63**, 064511.
91. M. Nuñez-Regueiro, J. L. Tholence, E. V. Antipov, J. J. Capponi, and M. Marezio, *Science*, 1993, **262**, 97.
92. R. J. Cava, B. Batlogg, C. H. Chen, E. A. Rietman, S. M. Zahurak, and D. Werder, *Nature*, 1987, **329**, 423.
93. M. Marezio, *Acta Crystallogr., Sect. A*, 1991, **47**, 640.
94. M. Alario-Franco, J. J. Capponi, C. Chaillout, J. Chenavas, and M. Marezio, *Mater. Res. Soc. Symp. Proc.*, 1988, **99**, 41.
95. C. Chaillout, M. A. Alario-Franco, J. J. Capponi, J. Chenavas, J. L. Hodeau, and M. Marezio, *Phys. Rev. B*, 1987, **36**, 7118.
96. C. Chaillout, M. A. Alario-Franco, J. J. Capponi, J. Chenavas, P. Strobel, and M. Marezio, *Solid State Commun.*, 1988, **65**, 283.
97. P. Bordet, C. Chaillout, J. J. Caponi, J. Chenavas, and M. Marezio, *Nature*, 1987, **327**, 687.
98. P. Bordet, C. Chaillout, J. Chenavas, J. L. Hodeau, M. Marezio, J. Karpinski, and E. Kaldis, *Nature*, 1988, **334**, 596.
99. J. Karpinski, E. Kaldis, E. Jilek, S. Rusiecki, and B. Bucher, *Nature*, 1988, **336**, 660.
100. C. Chaillout, P. Bordet, J. Chenavas, J. L. Hodeau, M. Marezio, J. Karpinski, E. Kaldis, and S. Rusiecki, *Solid State Commun.*, 1989, **70**, 275.
101. B. Raveau, C. Michel, and M. Hervieu, 'Crystal Chemistry of Superconducting Rare Earth Cuprates- Handbook on the Physics and Chemistry of Rare Earths: High Temperature Rare Earths Superconductors - I', eds. K. A. Gschneider, L. Eyring, and M. B. Maple, 2000, Vol. 30, Chap. 188, Elsevier, North Holland.
102. C. Greaves and P. R. Slater, *Physica C*, 1989, **161**, 245.
103. S. Balamurugan, *J. Supercond. Nov. Magn.*, 2010, **23**, 343.
104. L. Bauernfeind, W. Widder, and H. F. Braun, *Physica C*, 1995, **254**, 151.
105. J. L. Tallon, C. Bernhard, and J. W. Loram, *J. Low Temp. Phys.*, 1999, **117**, 823.
106. C. Bernhard, J. L. Tallon, Ch. Niedermayer, Th. Blasius, A. Golnik, E. Brücher, R. K. Kremer, D. R. Noakes, C. E. Stronach, and E. J. Ansaldo, *Phys. Rev. B*, 1999, **59**, 14099.
107. A. C. McLaughlin and J. P. Attfield, *Phys. Rev. B*, 1990, **60**, 14605.
108. P. W. Klamut, B. Dabrowski, S. Kolesnik, M. Maxwell, and J. Mais, *Phys. Rev. B*, 2001, **63**, 224512.
109. Z. Sun, S. Y. Li, Y. M. Xiong, and X. H. Chen, *Physica C*, 2001, **349**, 289.
110. L. T. Yang, J. K. Liang, Q. L. Liu, G. B. Song, F. S. Liu, J. Luo, and G. H. Rao, *Physica C*, 2004, **403**, 177.
111. R. Escamilla, A. Durán, and R. Escudero, *Supercond. Sci. Technol.*, 2005, **18**, 1003.
112. A. C. Mclaughlin, V. Janowitz, J. A. McAllister, and J. P. Attfield, *J. Mater. Chem.*, 2001, **11**, 173.
113. S. Malo, D. Ko, J. T. Rijssenbeek, A. Maignan, D. Pelloquin, V. P. Dravid, and K. R. Poeppelmeier, *Int. J. Inorg. Mater.*, 2000, **2**, 601.
114. J. T. Rijssenbeek, N. Mansourian-Hadavi, S. Malo, D. Ko, C. Washburn, A. Maignan, D. Pelloquin, T. O. Masson, and K. R. Poeppelmeier, *Physica C*, 2000, **341–348**, 481.

115. A. Hassen, J. Hemberger, A. Loidl, and A. Krimmel, *Physica C*, 2003, **400**, 71.

116. S. Andrade, F. C. Fonseca, R. F. Jardim, I. Bossi, M. S. Torikachvili, A. H. Lacerda, and L. Ben-Dor, *Braz. J. Phys.*, 2003, **33**, 686.

117. M. S. Torikachvili, I. Bossi, J. R. O'Brien, F. C. Fonseca, R. Muccillo, and R. F. Jardim, *Physica C*, 2004, **408–410**, 195.

118. R. Escamilla, F. Morales, T. Akachi, and R. Gómez, *Supercond. Sci. Technol.*, 2005, **18**, 798.

119. G. Ilonca, S. Patapis, E. Macocian, F. Beiusan, T. Jurcut, G. Stiufiuc, and R. Stiufiuc, *Int. J. Mod. Phys. B*, 2004, **18**, 2177.

120. P. Mandal, A. Hassen, J. Hemberger, A. Krimmel, and A. Loidl, *Phys. Rev. B*, 2002, **65**, 144506.

121. J. Hemberger, A. Hassen, A. Krimmel, P. Mandal, and A. Loidl, *Physica B*, 2002, **312–313**, 805.

122. A. Hassen and P. Mandal, *Supercond. Sci. Technol.*, 2006, **19**, 902.

123. P. W. Klamut, B. Dabrowski, J. Mais, and M. Maxwell, *Physica C*, 2001, **350**, 24.

124. C. J. Liu, C. S. Sheu, T. W. Wu, L. C. Huang, F. H. Hsu, H. D. Yang, G. V. M. Williams, and C. J. C. Liu, *Phys. Rev. B*, 2005, **71**, 014502.

125. J. E. McCrone, J. L. Tallon, J. R. Cooper, A. C. McLaughlin, J. P. Attfield, and C. Bernhard, *Phys. Rev. B*, 2003, **68**, 064514.

126. J. L. Tallon, J. W. Loram, G. V. M. Williams, and C. Bernhard, *Phys. Rev. B*, 2000, **61**, R6471.

127. R. Ruiz-Bustos, J. M. Gallardo-Amores, R. Sáez-Puche, E. Morán, and M. A. Alario-Franco, *Physica C*, 2002, **382**, 395.

128. R. Ruiz-Bustos, A. J. Dos santos-García, and M. A. Alario-Franco, *Z. Anorg. Allg. Chem.*, 2007, **633**, 1919.

129. R. Ruiz-Bustos, M. H. Aguirre, and M. Á. Alario-Franco, *Inorg. Chem.*, 2005, **44**, 3063.

130. I. Felner and E. Galstyan, *Phys. Rev. B*, 2004, **69**, 024512.

131. A. J. Dos santos-García, M. H. Aguirre, E. Morán, R. Saéz-Puche, and M. Á. Alario-Franco, *J. Solid State Chem.*, 2006, **179**, 1296.

132. A. J. Dos santos-García, J. Van Duijn, R. Saéz-Puche, G. Heymann, H. Hupertz, and M. A. Alario-Franco, *J. Solid State Chem.*, 2008, **181**, 1167.

133. A. J. Dos santos-García, J. Van Duijn, and M. Á. Alario-Franco, *J. Solid State Chem.*, 2008, **181**, 3317.

134. J. K. Srivastava, *Phys. Status Solidi B*, 1998, **210**, 159.

135. M. Inui, S. Doniach, and M. Gabay, *Phys. Rev. B*, 1988, **38**, 6631.

136. J. K. Srivastava and S. M. Rao, 'Models and Methods of High-TC Superconductivity: Some Frontal Aspects', Nova Science Publishers Hauppauge, New York, 2003.

137. M. Á. Alario-Franco, R. Ruiz-Bustos, and A. J. Dos santos-García, *Inorg. Chem.*, 2008, **47**, 6475.

138. A. J. Dos santos-García, R. Ruiz-Bustos, A. M. Arévalo-López, and M. Á. Alario-Franco, *High Press. Res.*, 2008, **28**, 525.

Metal–Organic Frameworks

John Hamilton Walrod II and David A. Atwood

University of Kentucky, Lexington, KY, USA

1 Summary 385
2 Introduction 385
3 Fundamental Chemistry 386
4 Applications 387
5 Conclusions 388
6 Glossary 388
7 Related Articles 388
8 Abbreviations and Acronyms 388
9 References 388

1 SUMMARY

Since the early 1990s, chemistry involving metal–organic frameworks (MOFs) has grown at an exponential rate owing to their ultrahigh surface area ($>6000\,m^2\,g^{-1}$), permanent porosity, and the variability of geometric architectures.[1] MOFs have attracted considerable attention as potential materials in gas storage, separations, catalysis, thin films, imaging, and other electronic applications. Simply changing either the metal or organic building unit provides an endless array of synthetically attainable structures. MOFs containing rare earth (RE) ions or clusters as secondary building units show increased optical properties compared to transition metal-based MOFs, offering an additional advantage of utilization. The optical properties of RE MOFs are not strictly limited to luminescent RE transitions, and can involve transitions from the organic moiety, charge transfers, and guest molecule interactions.[2] Tunable luminescence is observed across the lanthanide series for a host of different MOFs. These porous luminescent materials have allowed increased detection possibilities involving various sensing applications. Examples of luminescent applications include the detections of different cations and anions, gases, and other environmental analytes. Additionally, RE MOFs have potential uses in novel biotechnologies.

2 INTRODUCTION

MOFs, also known as *coordination polymers*, are hybrid inorganic/organic materials comprised of coordinating organic molecules and metal ions. The building units consist of organic moieties or ''linkers'' that extend throughout the polymer network connected by metal ions or ''studs.'' MOFs have shown an array of dimensionality. Thousands of published MOFs exist, which is easily conceivable given the number of different combinations possible for both organic and inorganic building units. The development of MOFs has generated a great deal of attention in materials chemistry due to their useful applications in separations, catalysis, gas storage, and drug delivery. Their usefulness is due to their permanent porosity and extremely high surface areas both of which are easily exploitable in the design of the framework constituents. The organic linkers generally contain singly or multiconnected aromatic rings terminated with coordinating Lewis bases such as amino and carboxylic functional groups. Some of the early work with MOFs incorporated 1,4-benzenedicarboxylate (BDC) and 1,3,5-benzenetricarboxylate (BTC) as organic linkers.

MOF synthesis was originally accomplished by diffusion where the inorganic metals were diffused into solutions containing the organic backbones of the framework.[1,2] However, diffusion was a very slow process that suffered from low yields. Hydrothermal synthesis is a common experimental technique that takes advantage of increased solubility of organic linkers at high temperatures and pressures. This

The Rare Earth Elements. Edited by David A. Atwood. © 2012 John Wiley & Sons, Ltd. ISBN 978-1-119-95097-4

process typically results in MOF formation within hours to days. An increasingly popular synthetic procedure involves solvothermal synthesis where increased solubilities of organic linkers occur. Typically the organic linkers and metal salts are dissolved in an organic solvent and heated at a specific temperature for a specific period of time, typically hours, resulting in MOF precipitation. Dimethylformaldehyde (DMF) has been a very popular choice for solvothermal synthesis. Other methods of MOF synthesis include microwave-assisted radiation, solid-state grinding, liquid-assisted grinding, and sonochemical synthesis.

The large numbers of published MOFs primarily include transition metals. However, incorporation of RE ions, primarily from the lanthanide series, incorporates an added advantage due to their luminescent, magnetic, and electronic properties that arise from the 4f electronic shells.[3] This chapter describes various applications involving RE-containing MOFs besides discussing the fundamental chemistry exploited for their usefulness as potential materials.

3 FUNDAMENTAL CHEMISTRY

3.1 Lanthanide Series

The lanthanide series involves the sequential filling of the 4f electronic shell where the ions exist primarily in the +3 oxidation state. The dominance of the +3 oxidation state across the lanthanide series is a consequence of the fourth ionization energy being greater than the sum of the first three combined ***Variable Valency***. Shielding from the filled $5s^2 5p^6$ subshells allows the 4f orbitals to be well defined. Since the major portion of the 4f wave function is beneath the 5s and 5p orbitals there is little interaction of the 4f orbitals with the chemical environment. Thus, bonding tends to be more electrostatic and nondirectional ***Group Trends***. The coordination numbers for the lanthanide series ranges from 3 to 12 in the solid state. The high coordination numbers are achievable owing to the relaxation of orbital overlap. The Ln^{3+} ions are generally ''hard'' Lewis acids and tend to form coordination complexes with ''hard'' Lewis bases such as OH^-. The radius is known to decrease moving across the series as a result of decreased shielding of the 4f orbitals in accordance with the lanthanide contraction.

3.2 Luminescence

Luminescence in RE MOFs may originate from several different transitions ***Luminescence***. The luminescence may be due to the excited organic ligand, the metal ion, charge transfers, or guest molecule interactions within the framework. Except for La^{3+} and Lu^{3+}, all of the ions in the series show luminescent 4f–4f transitions in the ultraviolet to near-infrared (NIR) ranges. The excited states for the lanthanide series (Ln^{3+}) are shown in Figure 1.[4] Since the 4f shell is within the valence orbitals, ligand effects do not affect these transitions to a large degree and transitions tend to be linelike for each metal. However, molar absorptivities tend to be rather small (€ $< 1\ M^{-1}\ cm^{-1}$) and excitations are inefficient. As an example of luminescent emissions, the Eu^{3+} and Tb^{3+} ions emit red and green light, respectively, while Yb^{3+}, Nd^{3+}, and Er^{3+} emit in the NIR.

The luminescent properties of lanthanide ions in MOFs are enhanced by coordinating organic molecules

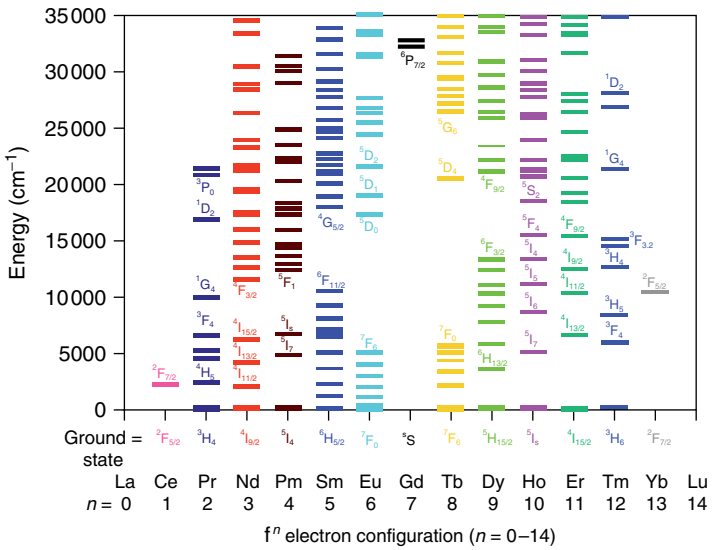


Figure 1 The various electronic states for the lanthanide series Ln^{3+}. (Reprinted (adapted) with permission from Ref. 4. Copyright (2009) American Chemical Society)

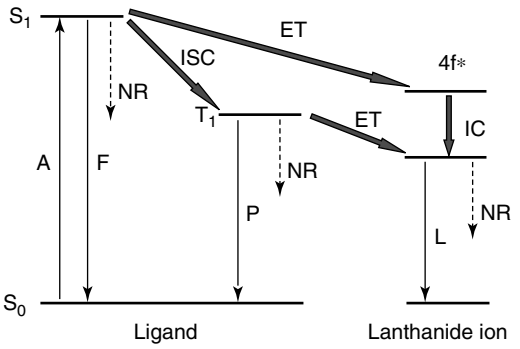


Figure 2 Schematic representation of energy absorption, migration, emission, and processes in MOFs. A, absorption; F, fluorescence; P, phosphorescence; L, lanthanide-centered luminescence; ISC, intersystem crossing; ET, energy transfer; IC, internal conversion; S, singlet; T, triplet. Plain arrows indicate radiative transitions; dotted arrows indicate nonradiative transitions. (Reprinted (adapted) with permission from Ref. 2. Copyright (2011) American Chemical Society)

through a phenomenon referred to as the ''*antenna effect.*''[2,4] When light with the appropriate energy is absorbed by the organic ligand, the energy is transferred to the lanthanide ion, generating luminescence upon relaxation to the ground state. The antenna effect is modeled in the Jablonski diagram shown in Figure 2.[2] The excitation of the organic ligand is followed by intersystem crossing to the triplet state. The excited electron in the triplet state is then transferred to the triplet excited state of the metal followed by emission. An additional pathway for coupled luminescence involves the transfer of an excited singlet from the organic molecule to an excited singlet of the metal followed by emission. The design of highly luminescent RE MOFs incorporates organic ligands with excited states that are very close in energy to the excited states of the lanthanide ion. The luminescence efficiency is significantly reduced if the excited-state energy levels of the ligands do not closely match the excited-state energy levels of the lanthanide ion.

Additional luminescence also occurs via the antenna effect involving guest molecules. The guest-induced luminescence is due to the permanent porosity and large pore windows typically present in MOFs. For this approach to be feasible, the relative size of the exciting organic molecule must be smaller than the pore windows of the MOF. This approach allows for incorporation of optical properties after the MOF has been synthesized.

4 APPLICATIONS

4.1 Sensors

The unique optical properties of RE MOFs are of great utility in sensor applications (***Sensors for Lanthanides and Actinides***).[2,3] Changes in the chemical environment, including coordination, hydrogen bonding, and π interactions, have a direct impact on the luminescent properties of RE MOFs ***Lanthanides: Luminescence Applications***. These changes, whether quenching or enhancing, have been exploited to fine-tune the detection of various chemical species. The porous nature of MOFs allows for reversible interaction of chemical species within the framework structure. Given the different topologies and pore structures for various MOFs, size-selective sensing applications can also be utilized.

The possibilities of coordinatively unsaturated sites in the structure of MOFs allows for unique detection of both Lewis acids and bases. Unsaturation of coordinating ligands allows for possible interactions with cations that may reversibly enter the framework. Cations typically exist in the framework structure of MOFs, and cation exchange may occur readily under appropriate conditions. Such interactions can have dramatic effects on the luminescent properties of MOFs and allows for unique sensing applications involving various cations in solution.

As an example of the sensing applications, a RE anionic MOF $K_5[Tb_5(IDC)_4\text{-}(ox)_4]$ where IDC = imidazole-4,5-dicarboxylate and ox = oxalate, shows selective luminescent activity in the presence of Ca^{2+} ions.[5] The highly negatively charged ligand allows for increased interaction with various cations. The increase in the luminescence is attributed to decreasing vibrational energy loss by oxalate stabilization when coordinated to Ca^{2+} ions. Quenching effects in MOFs have also been reported from other ligand-based vibrational effects.

Alternatively, uncoordinated RE metal sites within the MOF allow for interactions with Lewis bases present in solution. Owing to the ''hard'' Lewis character of the lanthanide series, interesting sensing applications can be utilized that exploits ligands with different ''hard'' and ''soft'' properties. These changes in the coordinating environment have dramatic consequences that affect the antenna effect and luminescent output from various RE MOFs. MOFs often reveal unsaturated metal sites from terminal coordinating organic molecules after vacuum and heat treatment. Coordination of hard electronegative anions such as F^- that are capable of hydrogen bonding can also increase the luminescent properties of RE MOFs. Increased hydrogen bonding lowers the quenching effects commonly associated with vibrations involving –OH and –NH modes.

Additionally, MOFs have been effectively utilized for the sensing of different local environmental conditions including changes in pH and radiation. Temperature-dependent luminescence using RE MOFs has been utilized for sensing applications.[6] As an example, the mixed Eu^{3+}/Tb^{3+} MOF $(Eu_xTb_{1-x})_2(DMBC)_3(H_2O)_4DMF{\cdot}H_2O$, which is synthesized by varying the molar ratios of the RE ions, has been effectively utilized as a luminescent thermometer. The mixed Eu^{3+}/Tb^{3+} MOF offers additional sensing capability due to the dual emission bands from

each distinct ion. Previous luminescent thermometers based solely on single-band emission have often suffered from environmental complications. Thus, incorporation of more than one RE ion into the framework shows an added sensing advantage.

4.2 Bioimaging and Drug Delivery

The use of MOFs for biotechnologies has been thoroughly investigated owing to their ultrahigh surface areas and permanent porosity (***Sensors for Lanthanides and Actinides***).[2] Utilization of these features could result in very high loadings for drug delivery applications due to their mesoporous nature. In addition, the luminescent properties incorporated from RE MOFs allow different imaging possibilities.

Another advantage of RE MOFs in biotechnology is their unique magnetic properties (***Magnetism***). The magnetic properties and ultrahigh surface areas should allow for targeted drug delivery in very high loads. Furthermore, given the ease of functionalization of MOFs, the interaction with biologic molecules seems easily fathomable. MOFs loaded with different luminescent guest molecules capable of crossing cell barriers have been utilized. Here the luminescent properties of the guest molecule are utilized and the MOF functions primarily as a host material.

Several RE MOFs have been used as multimodal imaging materials. The imaging is a combined process that incorporates more than one traditional imaging technology. Very long longitudinal ($R1$) and transverse ($R2$) relaxivities have been observed for different RE MOFs. The high relaxivities and the magnetic properties of RE ions allows for targeted imaging applications.

5 CONCLUSIONS

The future outlook for RE MOFs looks very promising given the broad range and scope of potential applications. Their ultrahigh surface areas and permanent porosity provide unique platforms for utilization. Given the different possible combinations of organic and inorganic building units, the number of RE MOFs is expected to rise. The development of new organic linkers capable of increasing surface area without reducing permanent porosity will continue to be fundamental to the design of new architectures. Additionally, the choice of organic linkers will continue to be evaluated with the antenna effect in mind. The organic linkers must have excited states in close energy proximity to the excited states of the RE ions. The throughput and reach of sensing applications with RE MOFs is predicted to increase. In addition, their incorporation into new and novel biotechnologies is anticipated, given their unique optical properties.

6 GLOSSARY

Lewis acid: An electron pair acceptor such as an electron-deficient metal on the surface of a solid-state material, which would combine with an electron pair donor (a Lewis base) such as water.

Antenna effect: Phenomena that occurs when an organic chromophore is excited close to an RE ion. The excited electron is transferred to excited states corresponding to the RE ion followed by emission of light.

Coordination polymer: An inorganic or organometallic polymer structure containing metal cation centers linked by ligands, extending in an array.

7 RELATED ARTICLES

Lanthanides: Coordination Chemistry.

8 ABBREVIATIONS AND ACRONYMS

BDC = 1,4-benzenedicarboxylate; BTC = 1, 3, 5-*benzenetrica*
DMF = dimethylformaldehyde;
MOF = metal–organic framework; NIR = near-infrared;
RE = rare earth.

9 REFERENCES

1. N. Stock and S. Biswas, *Chem. Rev.*, 2011, **112**(2), 933.
2. Y. Cui, Y. Yue, G. Qian, and B. Chen, *Chem. Rev.*, 2011, **112**(2), 1126.
3. L. E. Kreno, K. Leong, O. K. Farha, M. Allendorf, R. P. Van Duyne, and J. T. Hupp, *Chem. Rev.*, 2011, **112**(2), 1105.
4. E. G. Moore, A. P. S. Samuel, and K. N. Raymond, *Acc. Chem. Res.*, 2009, **42**(4), 542.
5. W.-G. Lu, L. Jiang, X.-L. Feng, and T.-B. Lu, *Inorg. Chem.*, 2009, **48**(15), 6997.
6. Y. Cui, H. Xu, Y. Yue, Z. Guo, J. Yu, Z. Chen, J. Gao, Y. Yang, G. Qian, and B. Chen, *J. Am. Chem. Soc.*, 2012, **134**(9), 3979.

Upconversion Nanoparticles for Bioimaging Applications

Jiefu Jin

The University of Hong Kong, Pokfulam, Hong Kong

and

Wing-Tak Wong

The Hong Kong Polytechnic University, Hunghom, Kowloon, Hong Kong

1	Summary	389
2	Introduction	389
3	Principles and Classifications of Upconversion Processes	390
4	Selection Criteria for Upconversion Materials	391
5	Chemical Syntheses of UCNPs	393
6	Surface Chemical Modifications of UCNPs	395
7	Ln-Doped UCNPs for *in vivo* Imaging	398
8	Conclusion and Outlook	402
9	Glossary	402
10	Acknowledgements	403
11	Related Articles	403
12	Abbreviations and Acronyms	403
13	References	403

1 SUMMARY

Upconversion nanoparticles (UCNPs) have several favorable luminescent characteristics that are largely distinct from other commonly used fluorescence materials. In addition, during the past decade, versatile chemical synthesis and surface modification approaches have been developed by chemists to endow UCNPs with uniform morphology and size distribution, desirable surface chemistry, relatively strong upconversion luminescence, and targeted/therapeutic efficacy. Therefore, UCNP-based nanoprobes have become an alternative and novel generation of bioimaging reporters, especially for *in vivo* disease diagnosis and cancer imaging.

This article provides an understanding of how upconversion takes place, the selection criteria for upconversion materials, and how upconversion differs from two-photon absorption (TPA) and second-harmonic generation (SHG). In addition, the synthesis of UCNPs with controllable size, morphology, and phase and functionalization for biological imaging purposes are described. The article concludes with the prospects of UCNPs for *in vivo* imaging.

2 INTRODUCTION

Solid-state lanthanide luminescent materials have the combined advantages of typical lanthanide luminescence and photophysical stability. In these materials, lanthanide ions are trapped into the rigid crystal host lattice, avoiding adverse quenching by environmental oscillators.[1] Two types of luminescence modes, downconversion and upconversion, are known for lanthanide luminescence. Upconversion relates to a nonlinear optical process where two or more near-infrared (NIR) photons are absorbed sequentially to several real intermediate energy states and luminescence is emitted with a

The Rare Earth Elements. Edited by David A. Atwood. © 2012 John Wiley & Sons, Ltd. ISBN 978-1-119-95097-4

wavelength shorter than the absorbed light. Since 1960s, when Auzel, Ovsyankin, and Feofilov independently discovered and studied this phenomenon for the first time,[2] the upconversion process has aroused huge research interests. Nowadays, upconversion materials are widely used in optical devices such as temperature sensors, infrared quantum counters, and compact solid-state lasers.[3] However, bulk glass or crystalline upconversion materials have remained the major research focus, and no biological applications have been reported during the first 30 years of research on upconversion.[4] Stimulated by the prevalence of nanotechnology since the late 1990s, UCNPs have been manufactured and have attracted enormous attention in biological sciences.

UCNPs have inherited the unique characteristics of upconversion luminescence from their bulk materials,[4] which are emissive under NIR light (approximately at 980 nm) rather than ultraviolet (UV) light (see ***Near-Infrared Materials***). Since most biological molecules and water have their minimal absorption at 980 nm, the use of 980-nm excitation can significantly provide deep tissue penetration. In addition, autofluorescence, Raman scattering, and photodamage to biological species can be effectively avoided.[5] Lanthanide-doped UCNPs have also inherited the characteristics of lanthanide emission, such as narrow emission bands, long emission lifetimes, and large Stokes shift, thereby making the emission easily distinguishable from the excitation source. Compared with conventional fluorophores such as organic dyes[6] and semiconductor quantum dots (QDs),[7] UCNPs possess good chemical stability, high photostability, resistance to photobleaching and tolerable toxicity. In addition, UCNPs are compatible with a low-intensity excitation source ($1-10^3$ W•cm^{-2}), which can be achieved by the cheap continuous-wave diode lasers, without the need of any costly high-intensity pulse laser (10^6-10^9 W•cm^{-2}).[8] Owing to the above-mentioned advantages, UCNPs have been extensively studied in the past few years, building up their unique way to biological applications. This chapter will begin with an introduction to upconversion mechanisms and upconversion materials, followed by the syntheses and chemical surface modifications of UCNPs. The biological applications of UCNPs, focusing on *in vivo* imaging are discussed. And last but not least, the prospects of UCNPs for biological applications are also addressed (see ***Luminescent Bioprobes***; ***Lanthanides in Living Systems***).

3 PRINCIPLES AND CLASSIFICATIONS OF UPCONVERSION PROCESSES

Luminescent materials absorb incident light and subsequently emit the absorbed energy as radiation. A majority of luminescent materials obey Stokes' law, where the emitted radiation has a lower energy (longer wavelength) than the absorbed light. Figure 1(a) demonstrates this most common single-photon luminescence process. In this process, a fluorophore absorbs a photon from incident light, sensitizing it from the ground state to an excited state, state 2. The excited fluorophore goes through some internal relaxations to the lowest vibrational state, state 1. Then, a lower energy emission is released from the fluorophore when returning to the ground state.[9] However, in some special cases, the emitted photon has a higher energy (shorter wavelength) than the absorbed one, and this is called anti-Stokes shift emission. It has been shown that the anti-Stokes process often occurs in three ways: simultaneous two-photon absorption (STPA), SHG, and upconversion.[10] STPA could be referred to as the process in which two long-wavelength photons are absorbed simultaneously to excite TPA molecules to the excited states. SHG could happen with highly hyperpolarizable materials under coherent radiation, in which the emission has half the wavelength and twice the frequency of the incident light. In 1961, SHG was first discovered by Franken *et al*.,[11] who observed second-harmonic light with half the wavelength when ruby laser light was getting through a quartz crystal.

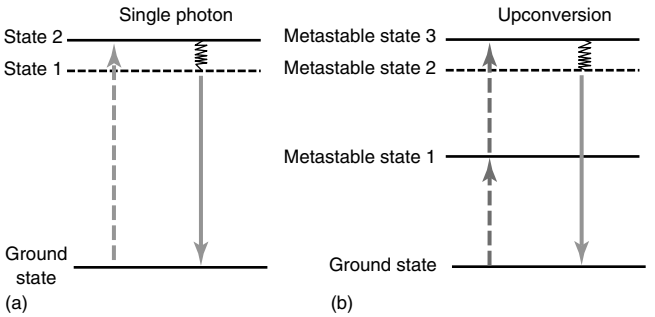


Figure 1 Schematic representations for (a) the typical single-photon fluorescence in which the absorption of one higher energy photon results in the emission of one lower energy photon, (b) a simple upconversion process showing that the emission of higher energy photon comes from the absorption of two lower energy photons and involves metastable states. (Reproduced with permission from Ref. 9. © John Wiley & Sons, Ltd., 2010.)

Similar to STPA and SHG, upconversion is also an anti-Stokes process, but it is more efficient with no requirement of coherent or high-intensity radiation. There are several metastable energy states participating in a typical upconversion process, such as metastable states 1, 2, and 3 in Figure 1(b). Upon absorption of a low-energy photon, the ground state is populated to metastable state 1, which is then promoted to a higher energy state, metastable state 3, by subsequently absorbing another low-energy photon. Following some internal relaxation processes, metastable state 3 relaxes to a slightly lower excited energy state, metastable state 2, and then jumps to the ground state by releasing a photon radiation. This anti-Stokes emission has a shorter wavelength than the absorbed photon.[9] The presence of several real metastable energy states in UCNPs guarantees

this upconversion process with higher efficiency than STPA, in which virtual intermediate energy levels are used for accommodating the absorbed photons.

The upconversion processes are in reality more complicated than that illustrated in Figure 1(b). Several mechanisms are involved,[12] such as excited state absorption (ESA), energy transfer upconversion (ETU), and photon avalanche (PA),[13] and these are illustrated in Figure 2.[3]

3.1 Excited State Absorption (ESA)

ESA was first reported by Bloembergen in 1959.[14] This process involves the sequential absorption of two photons by a single ion (Figure 2a), which is the most common in upconversion materials with a low concentration of dopants. The first step of ESA process is ground-state absorption (GSA), which involves populating ground state G to excited long-lived intermediate excited state E1. A second incident photon is successively absorbed by E1, resulting in the population of a higher excited state E2. Upconversion light with high energy is emitted when E2 transits to G.

3.2 Energy Transfer Upconversion (ETU)

ETU was extensively studied in the mid-1960s. The pioneering and systematic work was accomplished by Auzel and coworkers,[15] who first proposed the addition de photons par transfert d'énergie (ATPE) effect. Similar to ESA, ETU also involves the sequential absorption of two photons, but it differs in having the two photons absorbed by two ions individually, wherein one ion acts as a sensitizer (donor) and the other serves as an activator (acceptor). Since the two ions are in close proximity, there exists a nonradiative energy transfer from the sensitizer to activator, promoting the activator from E1 to a higher excited state E2 (Figure 2b). Then the activator ion returns to G by releasing an upconversion emission.

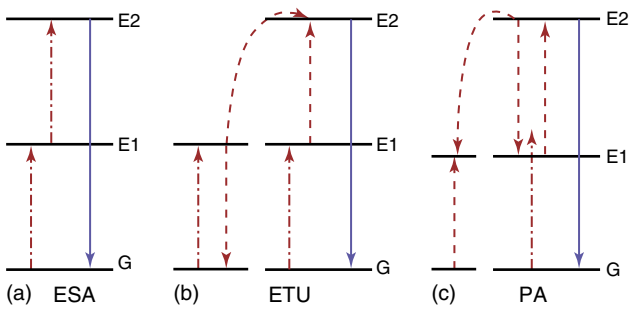


Figure 2 Principal upconversion processes for lanthanide-doped crystals: (a) excited state absorption, (b) energy transfer upconversion, (c) photon avalanche. The dashed/dotted, dashed, and full arrows represent photon excitation, energy transfer, and emission processes, respectively. (Reproduced from Ref. 3. with permission of The Royal Society of Chemistry.)

3.3 Photon Avalanche (PA)

PA was first discovered in Pr^{3+}-based infrared quantum counters by Chivian *et al*.[16] It is the least observed pumping process and exhibits a strong upconversion emission, where a high-energy pumping source is needed. As can be seen in Figure 2(c), first, ESA occurs to one ion by promoting the electron energy level from G to E2. This excited ion then undergoes cross-relaxation energy transfer with a neighboring ground-state ion, resulting in both ions residing in E1. The two E1-state ions absorb light to E2 state and subsequently act as sensitizers to make four ions on E1 state, and this process can be repeated to populate more and more ions on E1 state. In this way, E1 state serves as an energy reservoir to make an avalanche possible.

The three upconversion mechanisms mentioned above have distinct luminescence efficiencies.[3] PA is the most efficient upconversion process, while ESA is the least. However, several limitations of the PA process, such as the demand for a high-energy pumping source, long response duration among excitation and emission (up to a few seconds), and power-dependent emission, have largely hindered its practical applications. Therefore, the conclusion that ETU, with its instant and power-independent upconversion emission, is the optimal choice among the three has been drawn, and ETU-based upconversion materials have attracted increasing research attention in the past few decades.

4 SELECTION CRITERIA FOR UPCONVERSION MATERIALS

A typical upconversion material is composed of two components, an inorganic host matrix and doping lanthanide ions (Figure 3).[9] For achieving efficient ETU, effective energy transfer between the host matrix-embedded ions is essentially required, so the doped ions can also be divided into two types, activator (emitter) and sensitizer (absorber).

4.1 Activators

Efficient upconversion occurs only in materials with multiple metastable excited states. Trivalent lanthanide ions are the best activator candidates because they feature Laporte forbidden f-f transitions, thereby resulting in numerous long-lived (up to 0.1 s) intermediate energy states.[2,17] Even though most lanthanide ions have multiple excited states (except La^{3+}, Ce^{3+}, Yb^{3+} and Lu^{3+}), [12] only three lanthanide ions, Er^{3+}, Tm^{3+}, and Ho^{3+}, are commonly selected as upconversion activators. The reason lies in that these three ions have equally spaced energy levels with a ladderlike configuration (Figure 4), which greatly facilitates their photon absorption and subsequent energy transfer during ETU.[3] In addition, both Er^{3+} and Tm^{3+} have energy levels with large gaps, which

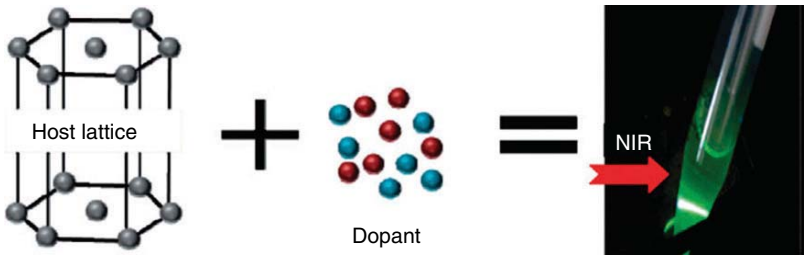


Figure 3 Schematic illustration of the key components of a typical upconversion material. (Reproduced with permission from Ref. 9. © John Wiley & Sons, Ltd., 2010.)

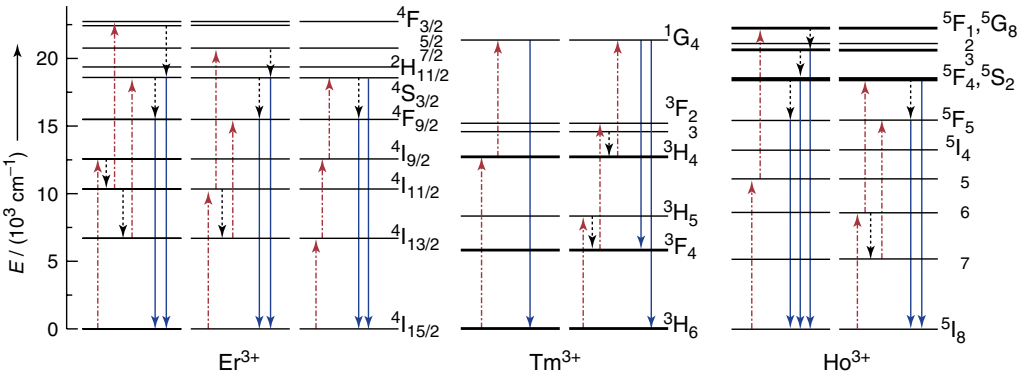


Figure 4 Schematic energy level diagrams showing typical upconversion processes for Er^{3+}, Tm^{3+}, and Ho^{3+}. The dashed-dotted, dotted, and full arrows represent excitation, multiphonon relaxation, and emission processes, respectively. (Reproduced from Ref. 3. with permission of The Royal Society of Chemistry.)

largely decrease the possibilities of nonradiative multiphonon relaxation between the excited energy levels and increase the upconversion efficiency accordingly.[18]

4.2 Sensitizers

It is noted that cross-relaxation will occur to two neighboring lanthanide activators. Therefore, it is of great importance to introduce another lanthanide ion to separate the activators, and thus the sensitizing ions are doped with a higher content than the activators. In addition, sensitizers also act as absorbers of the incident light for transferring to activators. Yb^{3+} is the optimal sensitizer, because it has a simple energy state scheme with only one excited state $^2F_{5/2}$ and it possesses a larger absorption cross-section than other lanthanide ions. Moreover, $^2F_{7/2} \rightarrow {}^2F_{5/2}$ absorption in Yb^{3+} has a good resonance with f-f transitions of the codoped activators (Er^{3+}, Tm^{3+} and Ho^{3+}), where the energy transfer from sensitizer to activator can be enhanced. It is worth noting that the combination and concentration of dopants should be well tuned. In order to maximize upconversion efficiency, the activator should be doped at a low concentration (<2 mol%) to minimize energy loss caused by cross-relaxation, while the content of sensitizer Yb^{3+} should be high at around 20 mol%.[12,19]

4.3 Host Matrix

Host materials are used to accommodate the doped ions. There are several requirements on the selection of host materials in order to optimize the upconversion efficiency. The host matrix, usually inorganic crystals, should have crystal lattices of perfect match with the doped ions to ensure their homogenous distribution. Moreover, the host materials are required to have phonon energies to minimize any undesired energy quenching by the stretching vibrations. Trivalent lanthanide-containing inorganic materials are the ideal host materials because the doped lanthanide ions are compatible with the host matrix owing to the similarities in ionic size and chemical properties in lanthanides. Table 1 shows various combinations of lanthanide-based host matrix doped with lanthanide ions and their corresponding emission properties.[12]

Among the lanthanide-based host materials, heavy halides such as chloride, bromide, and iodide have low phonon energies of lower than 300 cm^{-1}, but these heavy halide-containing materials are hygroscopic (see ***Lanthanide***

Table 1 Different combinations of lanthanide-based host materials with doped ions and their emission properties. (Reproduced from Ref. 12, Copyright (2011), with permission from Elsevier.)

Host matrix	Sensitizer/ activator	Emissions (nm)	Host matrix	Sensitizer/ activator	Emissions (nm)
Oxide			*Tungstate*		
Y_2O_3	Yb/Er	660	$NaY(WO_4)_2$	Yb/Er	526, 553, 660
	Yb/Tm	450, 480		Yb/Tm	476, 647
	Yb/Ho	549, 666	*Gallate*		
Lu_2O_3	Yb/Er	662	$Gd_3Ga_5O_{12}$	Yb/Tm	454, 484, 640–680
	Yb/Tm	477, 490	*Vanadate*		
La_2O_3	Yb/Er	530, 549, 659, 672	YVO_4	Yb/Er	547, 554, 660–670
Gd_2O_3	Yb/Er	520–580, 650–700	*Fluoride*		
Oxysulfide			LaF_3	Yb/Er	521, 545, 659
Y_2O_2S	Yb/Er	520–560, 650–680		Yb/Tm	475, 698, 800
	Yb/Tm	450–500, 650, 690		Yb/Ho	541, 643
Gd_2O_2S	Yb/Er	520–580, 650–700	YF_3	Yb/Er	411, 526, 552, 664
La_2O_2S	Yb/Pr	500, 508, 830		Yb/Tm	347, 363, 454, 477
Oxyhalide			LuF_3	Yb/Tm	481
GdOF	Yb/Er	521, 545, 659	$NaYF_4$	Yb/Er	525, 547, 660
YOF	Yb/Er	525, 545, 656		Yb/Tm	450, 476
Phosphate				Yb/Ho	541
$LaPO_4$	Yb/Er	535–556	$LiYF_4$	Yb/Tm	361, 450, 479, 647
$LuPO_4$	Yb/Tm	476	$NaGdF_4$	Yb/Ho	541, 647, 751
Molybdate			KY_3F_{10}	Yb/Er	522, 545, 656
$La_2(MoO_4)_3$	Yb/Er	519, 541	KGd_2F_7	Yb/Er	525, 552, 666
	Yb/Tm	472, 647	$BaYF_5$	Yb/Tm	475, 650, 800

Halides).[3] Lanthanide oxides or oxysulfide such as Y_2O_3 and Y_2O_2S possess excellent chemical stability, but with relatively high phonon energies (larger than 500 cm^{-1}). Fluorides, owing to their good chemical stability and low phonon energy (around 350 cm^{-1}), are thus widely deployed as upconversion host materials. LaF_3, YF_3, and $NaYF_4$ are some typical examples of fluoride-based upconversion host matrices. It has been widely acknowledged that $NaYF_4$ doped with Yb^{3+}/Er^{3+} and Yb^{3+}/Tm^{3+} are considered the most efficient NIR to green and blue upconversion materials, respectively.[20,21] In addition, crystal structure of the host matrix is an important parameter for determining upconversion efficiency. Taking $NaYF_4$:Yb/Er as an example, bulk hexagonal $NaYF_4$:Yb/Er has about 10 times higher upconversion efficiency than its cubic counterpart.[12] Therefore, hexagonal $NaYF_4$:Yb/Er is preferred for practical use. However, harsh experimental conditions such as a high reaction temperature and prolonged annealing time are inevitable in order to achieve cubic-to-hexagonal (α-β) phase conversion, and such harsh conditions usually lead to the manufacture of large upconversion particles at the micrometer scale or even bigger, a size that is not suitable for biological applications. Therefore, achieving a balance between the size and upconversion luminescence remains a crucial issue. This article reviews the recent development of fluoride-based lanthanide (Ln)-doped UCNPs (mainly on $NaYF_4$ nanoparticles) with respect to their synthesis, surface modifications, and bioimaging applications.

5 CHEMICAL SYNTHESES OF UCNPs

Much attention is paid to the employment of upconversion materials in biological sciences. In particular, UCNPs have attracted enormous research interests because of their comparable size with biomolecules, unique luminescence features, compatibility to biological media, and tunable interactions with biological matters. Synthesis strategies are very critical in producing UCNPs with a desirable phase, size and morphology, and relatively intense upconversion luminescence, while surface modification approaches are essentially important in tailoring surface chemistry to make UCNPs water soluble, biocompatible, and suitable for further modification of bioactive moieties. A variety of synthetic methods have been developed to prepare UCNPs, such as coprecipitation, thermal decomposition, hydrothermal/solvothermal reaction, sol-gel processing, and combustion synthesis.

5.1 Coprecipitation

Coprecipitation is perceived as the most convenient approach to produce UCNPs with an ultrasmall size (sub-10 nm, Figure 5a and b)[22] and narrow size distribution. In a typical synthesis procedure, lanthanide salt solutions are quickly injected into a fluoride solution under vigorous stirring, and $NaLnF_4$ or LnF_3 nanoparticles will be obtained

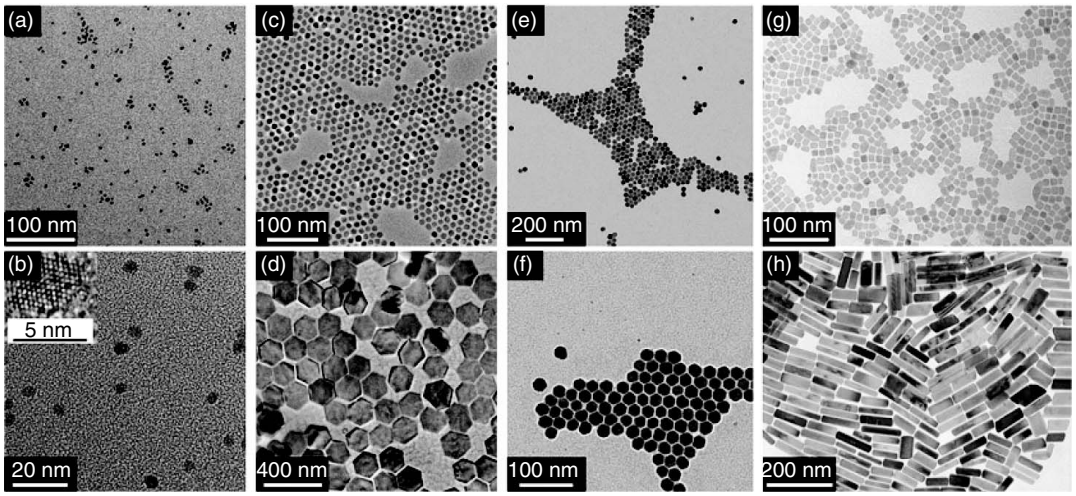


Figure 5 TEM images of upconversion nanocrystals. (a), (b) Ultrasmall LaF_3:Yb/Er nanoparticles prepared by Yi and Chow[22] via coprecipitation method. (c), (d) β-$NaYF_4$:Yb/Er nanoparticles and nanoplates prepared by Yan *et al*.[25] via thermal decomposition method. (e), (f) α-$NaYF_4$:Yb, Er nanoparticles prepared by Capobianco *et al*.[26] via thermal decomposition method. (g), (h) $NaYF_4$:Yb/Er nanoparticles and nanorods prepared by Wang and Li[27] via hydrothermal method. (Reproduced from Ref. 3 with permission of The Royal Society of Chemistry.)

as precipitates.[22,23] For the synthesis of $LnPO_4$ nanoparticles, the procedure is similar except that phosphoric acid instead of fluoride species is used.[24] Several coordinating ligands such as ammonium di-*n*-octadecyldithiophosphate[22] and ethylenediamine tetraacetic acid (EDTA)[23] were employed to coordinate with lanthanide ions, acting as structure regulating agents to control the processes of nanoparticle nucleation and growth and further protecting the nanoparticles against aggregation.

In coprecipitation method, harsh experimental conditions or costly instruments are not required. In view of this advantage, coprecipitation has been utilized for large-scale production of ultrasmall UCNPs. However, for the synthesis of Ln-doped $NaYF_4$ nanoparticles, coprecipitation generally yields cubic (α-) $NaYF_4$ particles, which have low upconversion efficiency. In order to increase the upconversion luminescence, subsequent annealing (calcination) treatment has to be carried out to achieve a cubic-to-hexagonal conversion. This annealing treatment is indeed able to produce high upconversion luminescence hexagonal (β-) phase $NaYF_4$ nanoparticles, but with the consequence of the formation of larger particles. Furthermore, the capping ligands are carbonized and adhered onto the particle surface, making UCNPs poorly water soluble and resistant to surface modifications. On the basis of the above discussion, coprecipitation is still problematic for preparing UCNPs for biological use.

5.2 Thermal Decomposition

Thermal decomposition approach was first employed by Yan *et al*.[28] to produce LaF_3 triangular nanoplates with high monodispersity and crystallinity. In 2006, Yan's group[25] further extended this method into a general approach for preparing high-quality $NaLnF_4$ (Ln = Pr to Lu, Y) nanocrystals (Figure 5c and d). In their studies, lanthanide trifluoroacetates, the fluoride precursors, were thermally decomposed in the presence of oleic acid (or oleyamine) and octadecene (ODE). Oleic acid (or oleyamine) acted as a stabilizing agent to passivate the nanocrystal surface to prevent particle agglomeration, while ODE, with a high boiling point (315 °C), served as a noncoordinating solvent. In the same year, Capobianco *et al*.[17] reported the synthesis of α-$NaYF_4$:Yb, Er/Tm UCNPs by using similar procedures, but the obtained UCNPs had a broad size distribution (10–60 nm). Capobianco's group subsequently refined the synthetic approach by precisely controlling the addition of precursors to separate nucleation and growth stages of UCNPs, and the monodisperse UCNPs were successfully obtained (Figure 5e and f).[26] Without the use of oleic acid, Ju *et al*.[29] reported the single use of trioctylphosphine oxide (TOPO) as both a solvent and coordinating ligand to prepare monodisperse β-$NaYF_4$:Yb, Er/Tm/Ho UCNPs. In this work, TOPO was used for lowering the energy barrier required for α-β phase conversion, and thus β-$NaYF_4$ nanocrystals could be readily obtained with relatively small particle size (~10 nm) and high upconversion efficiency. Chen *et al*.[30] demonstrated the use of lanthanide-oleate complexes instead of lanthanide trifluoroacetates for preparing α- and β-$NaYF_4$:Yb, Er UCNPs. They pointed out that UCNP phases could be conveniently tuned by changing the reaction temperature. The method also led to UCNPs with good monodispersity because the reactants were in different phases, and this liquid-solid two-phase strategy separated the nucleation and growth stages of UCNPs. Moreover, the use of lanthanide-oleate complexes

allowed the preparation of β-$NaYF_4$: Yb, Er UCNPs at a relatively low temperature of 260 °C.

Even though thermal decomposition allows for the synthesis of high-quality Ln-doped β-$NaYF_4$ nanoparticles with high crystallinity, good monodispersity, and small size, this approach also has some drawbacks. First, harsh experimental conditions such as high reaction temperature and water- and oxygen-free solvent system are required. Second, this method would generate some toxic by-products, such as fluorinated and oxy-fluorinated carbon species. Third, the stabilizing agents, such as oleic acid, oleyamine, and TOPO, passivate the nanocrystal surface with outward alkyl chains, resulting in the poor solubility of UCNPs in aqueous solutions. Fourth, it is very difficult to replace the surface-mounted capping ligands, and complex surface modifications are essentially needed to endow them with biocompatibility and functionalities.

5.3 Hydrothermal/Solvothermal Synthesis

The hydro(solvo)thermal method involves a chemical reaction process under high pressure and temperature. In general, a reactant solution is thoroughly mixed and transferred into a Teflon-lined stainless steel autoclave, which is then sealed and further placed in an oven at a temperature above the critical point of the solvent inside. By this way, the solubility of solids can be significantly improved, and the reaction process is greatly accelerated. The hydro(solvo)thermal approach is able to produce highly crystalline UCNPs at a relatively low temperature and without calcination.

Several small-molecule polycarboxylic chelating agents, such as EDTA and citrate acid, were deployed to bind strongly to the reactant lanthanide ions. Thus, the process of nanoparticle growth was accordingly completed by this complexation effect.[31–34] By this means, UCNPs could be obtained with a controllable size and desired morphology via tuning the molar ratio of the capping ligand to lanthanide salts or adjusting the reaction conditions. Besides chelating agents, polyols, with their several favorable physical properties, such as a high boiling point, high viscosity, and good water solubility, functioned as solvents for mediating the synthesis of a variety of nanoscale functional materials.[35] Chen *et al*.[36] put forward the use of three polyols, ethylene glycol (EG), diethylene glycol, and glycerol, as both solvents and capping ligands to prepare water-soluble NaYF4: Yb, Er/Tm UCNPs.

Several coordinating polymers, such as polyvinyl-pyrrolidone (PVP)[37] and polyethylenimine (PEI),[38] were employed by Zhang *et al*. to prepare the cubic phase $NaYF_4$:Yb, Er nanoparticles. In these studies, a high-viscosity solvent, EG, was applied to increase the solubility of reactants. These coordinating polymers would be absorbed on the particle surface to prevent particle aggregation and make UCNPs dispersible in aqueous solutions. Recently, Wang and Liu[8] used the same method to prepare PEI-coated UCNPs and further functionalized them with fluorescein isothiocyanate for preliminary biological detection studies.

In 2005, Li *et al*.[39] developed a general liquid-solid-solution (LSS) strategy for the controlled synthesis of various nanocrystals, including lanthanide-doped UCNPs. In the LSS strategy, oleic acid also acts as a stabilizing agent. Reactants exist in different phases, and reactions occur only at the interfaces. This phase separation and transfer mechanism enables a controllable synthesis of monodisperse nanocrystals. Li *et al*.[27,40,41] further extended this LSS strategy to produce lanthanide fluorides with different morphologies, including nanoparticles, nanorods (Figure 5g and h),[27] and nanoplates. Moreover, they investigated the effects of reactant ratio and other experimental conditions on the formation of lanthanide fluorides nanostructures and provided some hints on the controllable synthesis of Ln-doped UCNPs.

Hydrothermal synthesis of UCNPs has several advantages,[12] such as high crystallinity of UCNPs, easy control of particle size, shape, and phase, and absence of harsh reaction conditions. However, hydrothermal synthesis also suffers from some limitations. In the case of one-pot synthesis of UCNPs with the aid of coordinating polymers, although UCNPs are produced with hydrophilic surface, the surface functionalities are not sufficient or biocompatible to fulfill the requirements of biological applications. In the case of LSS synthesis of UCNPs, the capping ligand of oleic acid makes the obtained UCNPs highly hydrophobic.

5.4 Other Methods

There are still some other uncommon methods to synthesize UCNPs, such as sol-gel,[42–44] combustion,[45,46] and flame synthesis.[47] The conventional sol-gel method is superior in thin-film and glass material synthesis, but not suitable for the preparation of biologically used UCNPs.

Proper synthetic approaches should be selected depending on the scope of applications. For bioimaging, it is recommended to use UCNPs with an adequate upconversion luminescence efficiency, a small size (preferably at sub-10 nm level), a narrow size distribution, and availability/ease of surface modifications. However, in general, small-sized UCNPs have weak upconversion luminescence, and some modification methods would adversely affect or quench the luminescence. Therefore, compromising the luminescence intensity with particle size and functionalization becomes inevitable.

6 SURFACE CHEMICAL MODIFICATIONS OF UCNPs

For biological applications, UCNPs should not only possess high upconversion luminescence efficiency but also have good water solubility and plenty of functional groups for

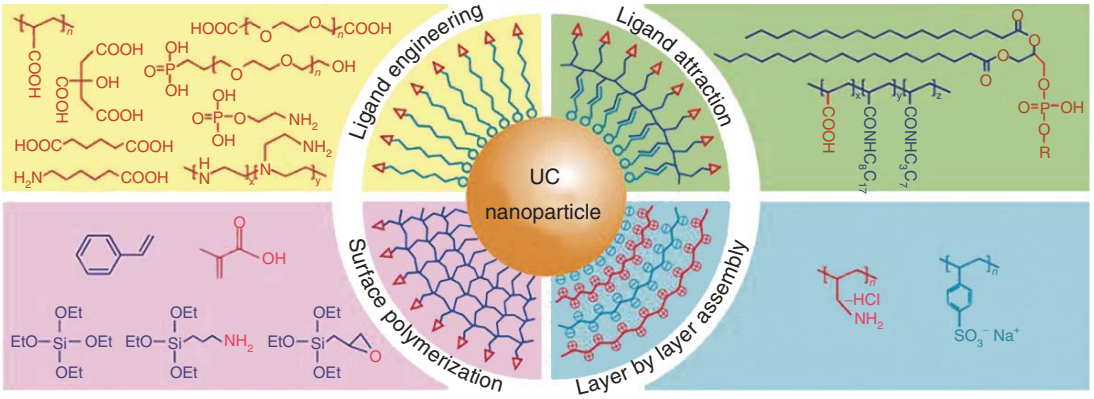


Figure 6 Different strategies of chemical modifications to make UCNPs (in particular hydrophobic UCNPs) biocompatible and with pendant functional moieties. (Reproduced from Ref. 19 with permission of The Royal Society of Chemistry.)

subsequent bioconjugation. For the development of UCNPs as *in vitro* and *in vivo* imaging probes, low cytotoxicity and good water solubility is a prerequisite. However, most of the above-mentioned synthetic approaches involve the use of capping ligands such as oleic acid to control the growth of UCNPs and stabilize the UCNPs against aggregation, which in turn results in UCNPs with poor water solubility and no surface functionalities. Even though several water-soluble small molecules and biocompatible polymers are utilized for one-pot synthesis of UCNPs,[8,38,48] they still suffer from the problems of poor long-term physiological stability and lack of adequate functional groups. Therefore, surface modifications are required for UCNPs prior to the attachment of other biomolecules. Most biomolecules can be attached to the UCNP surface via physical absorption, but covalent linkage is preferred on account of its high chemical stability and ease of controlling labeling degree. From the literature, there are mainly four strategies for UCNP modifications, namely, ligand engineering, ligand attraction, layer-by-layer (LbL) assembly, and surface polymerization (Figure 6).[19]

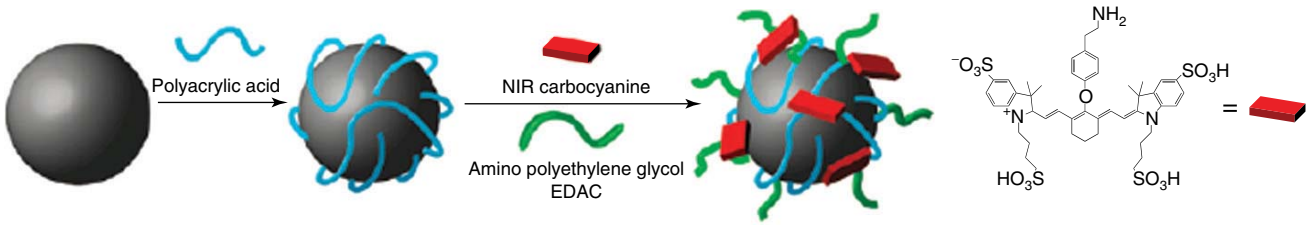
6.1 Ligand Engineering

Ligand engineering involves chemical reactions that occur with the capping ligands on the surface of UCNPs, including ligand exchange by several acid-group-containing small molecules or polymers and direct oxidation of oleic acid.

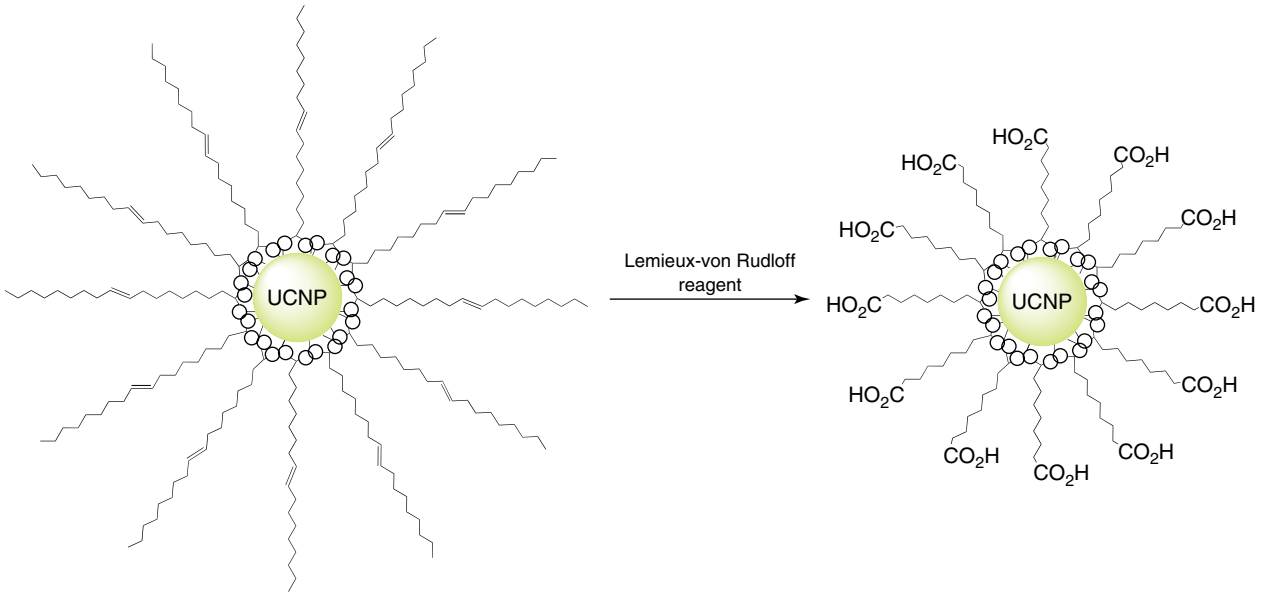
An example of ligand exchange involves the use of poly-(ethylene glycol) (PEG-600) dicarboxy acid. Yi and Chow[49] first prepared oleyamine stabilized β-$NaYF_4$:Yb/Er nanoparticles by thermal decomposition method and subsequently used PEG-600 dicarboxy acid to replace surface oleylamine moieties. The carboxyl group on one end of PEG-600 diacid can be covalently attached to UCNPs and leave the other carboxyl group outward for further bioconjugation. Besides PEG-600 diacid, some other acid-group-bearing molecules, such as PEG-phosphate,[50] 6-aminocaproic acid,[51] hexanedioic acid,[52] citrate acid,[53] and polyacrylic acid (PAA),[54–56] have been developed as surface modifiers in exchange with the original capping ligands. An example of PAA surface modification was demonstrated by Hilderbrand *et al.*,[57] who first coated Y_2O_3 UCNPs with PAA, and then linked amine-modified PEG molecules and NIR dyes with the free carboxyl groups of PAA via conventional amide coupling techniques (Scheme 1).

Ligand oxidation is a special type of ligand engineering first applied by Li *et al.*[58] on UCNP surface modification. This ligand oxidation approach is feasible to UCNPs with oleic acid capping, where the monounsaturated carbon–carbon double bond can be oxidized into two carboxyl groups (Scheme 2) with the aid of a Lemieux–von Rudloff reagent ($KMnO_4$ and $NaIO_4$ in aqueous solutions). The obtained carboxyl-modified UCNPs can be easily dispersed in aqueous solutions, and they can also be further engineered as biological labels by attaching streptavidin to the surface-mounted free carboxyl groups via a routine carbodiimide coupling route.[58]

Taken together, the above-mentioned ligand exchange and direct oxidation strategies seem to be powerful enough to endow UCNPs with desirable functional moieties and biocompatibility. However, there are still some intrinsic problems. For instance, the capping ligands of oleic acid or oleyamine are firmly and covalently bound to UCNPs, and therefore, the simple ligand exchange process under mild conditions cannot guarantee a high ligand replacement efficiency. Moreover, there are some reports concerning the adverse effects of ligand engineering on upconversion fluorescence. Zhang *et al.*[59] pointed out that the processes of ligand exchange with PAA and oleic acid oxidation resulted in a dramatic decrease of upconversion luminescence efficiency, which dropped to $1/8^{th}$ and $1/11^{th}$, respectively, of



Scheme 1 Surface modifications of Y_2O_3 upconversion nanoparticles with PAA, PEG, and NIR dye. (Reproduced from Ref. 57 with permission of The Royal Society of Chemistry.)



Scheme 2 Schematic illustration of a ligand oxidation process. Surface capping oleic acid molecules were oxidized by a Lemieux–von Rudloff reagent. (Reproduced with permission from Ref. 58. Copyright (2008) American Chemical Society.)

the efficiency of the unmodified UCNPs. Therefore, caution should be exercised when using ligand engineering methods for surface modification.

6.2 Ligand Attraction

Ligand attraction is a surface modification method for dealing with hydrophobic UCNPs. It involves the utilization of an amphiphilic polymer whose hydrocarbon chain can intercalate with the capping ligands via van der Waals interactions and leave the hydrophilic chain with functional pendent groups stretching outward. Yi and Chow[60] used a self-synthesized amphiphilic polymer, PAA modified with 25% octylamine and 40% isopropylamine, to functionalize oleyamine-stabilized UCNPs. The octyl and isopropyl groups of the amphiphilic polymer have a hydrophobic attraction with surface-mounted oleyamine groups, and the hydrophilic PAA block extends outside for further derivatization. Another similar example of ligand attraction was demonstrated by Schuck *et al.*[61] It is worth noting that ligand attraction is based on the weak-bond interactions among hydrocarbon chains rather than the covalent interaction, and thus the use of ligand attraction is accompanied by a risk of leaching of absorbed molecules when using UCNPs for a long period in physiological medium.

6.3 Layer-by-Layer (LbL) Assembly

The LbL assembly involves the alternate electrostatic deposition of oppositely charged polyions on particle surface and has the capability to coat nanoparticles with a controllable thickness of polyions. This method was first applied in UCNP modification by Li *et al.*[62,63] In their studies, UCNPs were negatively charged in basic solutions at first and then sequentially coated with positively charged poly(allylamine hydrochloride) (PAH) and poly(sodium 4-styrenesulfonate) (PSS) through electrostatic attraction. The outmost layer is PAH with plenty of amino groups. The LbL assembly

strategy is advantageous over the aforementioned modification methods in its simplicity, reproducibility, and ease of precise control of coated layer thickness. However, this method is only applicable to hydrophilic UCNPs and not oleic-acid-stabilized hydrophobic UCNPs, since the original UCNPs are required to form a stable colloidal dispersion in aqueous solution before modification.

6.4 Surface Polymerization

Surface polymerization can be defined as a process of growing an inorganic shell on the nanoparticle core. Styrene,[64] silica, and titanate can all be polymerized on the surface of UCNPs, but surface silanization, which involves the formation of an amorphous silica shell by hydrolysis and condensation of siloxane monomers, is the most common strategy. The prevalence of surface silanization can be explained by several of its favorable qualities. The silica coating layer is biocompatible and stable in physiologic medium. The toxicity of UCNPs can be reduced by silica coating owing to the prevention from free lanthanide ion leaching. Silica coating is also able to enhance the upconversion efficiency of UCNPs through protecting the UCNP core from energy quenching by environmental factors.[60] Moreover, silanization is a well-established technique, and many functional groups can be conveniently anchored on silica shells. In addition, surface silanization is applicable to both hydrophilic and hydrophobic UCNPs via the Stober method and reverse-microemulsion method, respectively. Surface silanization of upconversion particles was first reported by Niedbala *et al*.,[65,66] but the reported silica-coated upconversion particles have large particle size, and thus their biological applications are largely limited. Until 2007, Shan and Ju[67] first corroborated the use of reverse-microemulsion method to prepare a layer of silica coating on hydrophobic UCNPs. For hydrophilic UCNPs, Stober method was used by Zhang *et al*.[37] to introduce a controllable thin silica layer on PVP-stabilized $NaYF_4$:Yb/Er nanoparticles. Even though the surface silanization method possesses several aforementioned advantages, this method increases the particle size because of the technical difficulty in thin-layer silica coating. Moreover, surface silanization may bring about the encapsulation of several UCNPs together within one single silica coating, thus resulting in detrimental particle aggregation. Therefore, this method requires well-adjusted conditions in order to achieve even thin-layer silica coating.

7 Ln-DOPED UCNPs FOR *IN VIVO* IMAGING

UCNPs are capable of converting low-energy (long-wavelength) photons to high-energy (short-wavelength) light; this luminescence feature distinguishes UCNPs from other

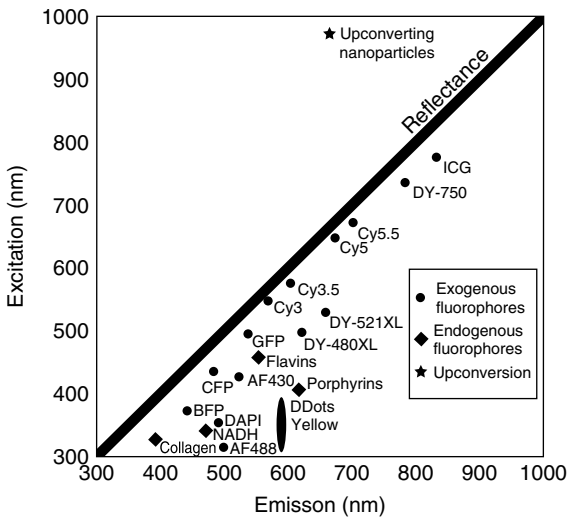


Figure 7 Excitation and emission wavelengths of luminescence sources are plotted on a graph. Fluorophores are below the reflectance line because they absorb a higher energy photon and emit a lower energy photon. Upconversion nanoparticles are fundamentally different; a high-energy photon is emitted following absorption of two low-energy photons. (Reproduced with permission from Ref. 68. © The Optical Society, 2008.)

frequently used fluorochoromes and makes them a promising novel bioimaging agent. Mahmood *et al*.[68] compared the commonly used fluorochromes with UCNPs in terms of excitation and emission wavelengths, and this comparison is shown in Figure 7. This work explicitly suggested that conventional endogenous (diamond points) and exogenous fluorophores (circle points) are very close to each other and crowded in the lower left portion of the graph, indicating that the use of these exogenous fluorophores may be interfered with the autofluorescence of biological tissues. However, UCNPs, with a unique luminescence pattern, stand out from all the conventional fluorophores and lie in the upper right portion of the graph. In addition, long-wavelength excitation is associated with deep tissue penetration and low photodamage to biological species. Therefore, some groups are endeavoring to apply UCNPs for *in vivo* imaging applications.

7.1 NIR-to-Visible Upconversion *in vivo* Imaging

The first use of NIR-to-visible UCNPs for *in vivo* imaging was demonstrated by Lim *et al*.[69] in 2006. In their studies, live *Caenorhabditis elegans* were injected with upconversion particles of 150 nm and imaged under a custom-made microscope. They found that strong upconversion luminescence could be observed in the intestines of the worms during a long-term imaging period (Figure 8). Moreover, no toxic effects of UCNPs were detected within the monitoring duration of 24 h.

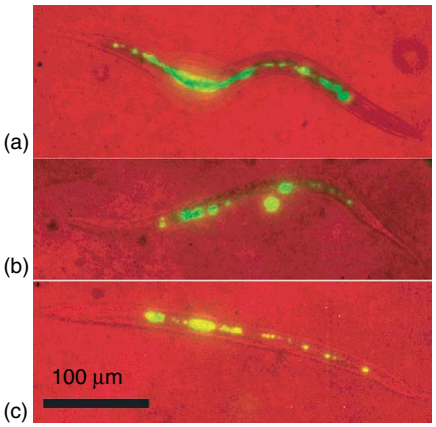


Figure 8 False-color two-photon images of *C. elegans* at 980 nm excitation, with red representing the bright field and green the phosphor emission. The worms were deprived of food over a period of 24 h, and showed little or no changes at (a) 0 h, (b) 4 h, and (c) 24 h. (Reproduced with permission from Ref. 69. Copyright (2006) American Chemical Society.)

For small-animal imaging studies, Zhang *et al*.[70] were the first to inject UCNPs subcutaneously into rats for a preliminary *in vivo* spot study (Figure 9). Conventional inorganic QDs were also subcutaneously injected for comparison. They proved that 980 nm excitation, special for UCNPs, provided a higher penetration depth and a higher signal-to-noise ratio than UV excitation. Strong upconversion luminescence could be seen clearly in the muscle tissue injected with UCNPs, while no QD signals were getting through the rat skin. However, emphasis needs to be laid on the point that these subcutaneously injected UCNPs would be trapped underneath the skin and could not participate in blood circulation, and thus it is just a preliminary study. Administration of these UCNPs intravenously would be more meaningful and scientifically valuable.

A technical difficulty with respect to the use of UCNPs for *in vivo* imaging is to design and construct a small-animal upconversion imager (SAUCI) because there are no commercially available imaging instruments for capturing upconversion luminescence in living subjects. An elaborately designed SAUCI system was achieved by Mahmood *et al*. in the Center for Molecular Imaging Research, Massachusetts General Hospital (Figure 10).[68] They used this SAUCI to investigate the dynamic localization of intravenously injected UCNPs *in vivo* and *ex vivo*, and their results proved that

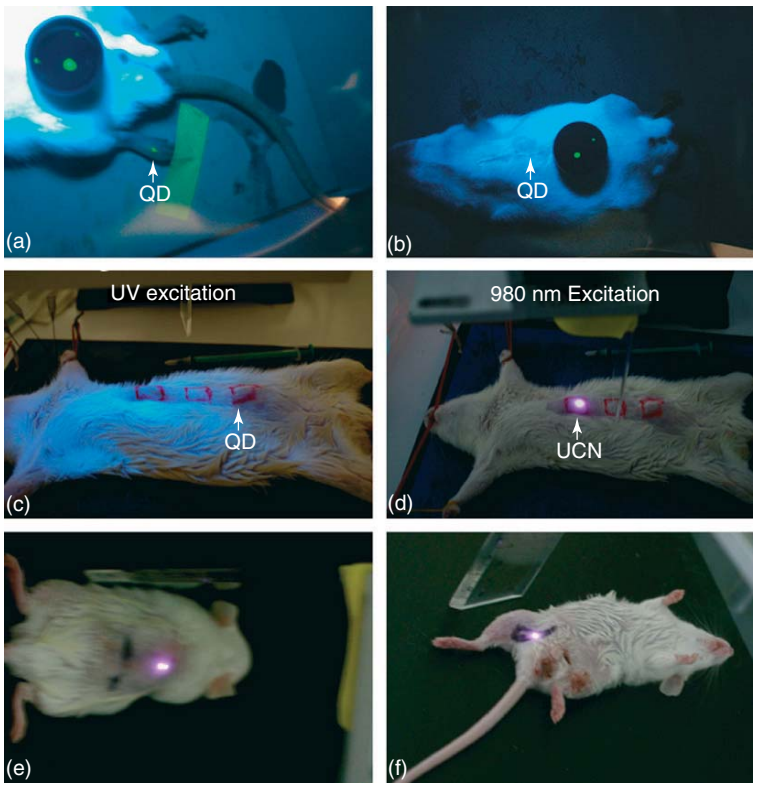


Figure 9 *In Vivo* imaging of rat: quantum dots (QDs) injected into the translucent skin of foot (a) show fluorescence, but not the thicker skin of the back (b) or abdomen (c); PEI/$NaYF_4$:Yb, Er nanoparticles injected below abdominal skin (d), thigh muscles (e), or below skin of back (f) show luminescence. QDs on a black disk in (a, b) are used as the control. (Reproduced from Ref. 70, Copyright (2011), with permission from Elsevier.)

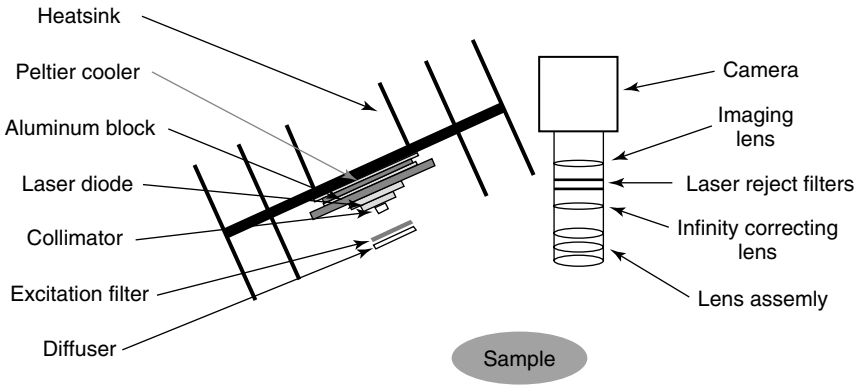


Figure 10 An overview of small-animal upconversion imager (SAUCI) system. Illumination is provided by a 2 W laser diode. The diode is cooled through an aluminum block by a Peltier device attached to a heat sink. The laser light is collimated, filtered, and diffused. Images are captured by the camera following focusing by the lens assembly and filtering by laser reject filters. (Reproduced with permission from Ref. 68. © The Optical Society, 2008.)

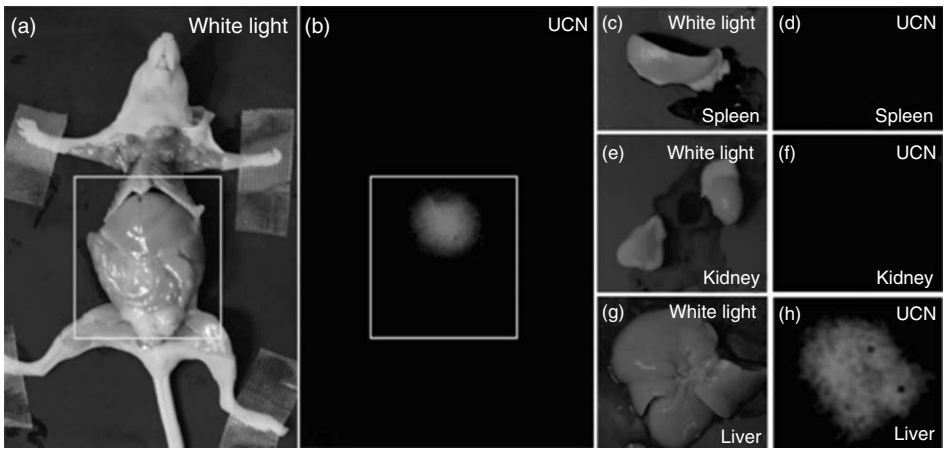


Figure 11 *In Vivo* upconversion imaging. (a) White-light picture of prepared mouse showing the upconversion imaging area. (b) Upconversion image of a mouse showing liver uptake of particles. (c, e, g) White-light images of spleen, kidney, and liver respectively. (d, f, h) Upconversion images corresponding to the white-light images in C, E, and G. (Reproduced with permission from Ref. 68. © The Optical Society, 2008.)

UCNPs had preferential accumulation in the liver compared with other organs, such as kidney and spleen (Figure 11).[68]

Recently, Hilderbrand *et al*.[57] employed the same SAUCI system to track UCNPs in the blood vessels. They used red-upconverting (660 nm) Y_2O_3:Yb, Er nanoparticles, which were purchased from Nanocerox Inc., as the inorganic emitting core, and further subjected them to PAA loading, PEG conjugation, and cyanine dye conjugation. This multicolor nanoconjugate was intravenously administrated into the mouse through tail vein injection. Then the mouse ear lobe was imaged under the aforementioned SAUCI system. It was discerned that both the upconversion and NIR fluorescence signals, with high signal-to-background ratio, were observed in the blood stream of the mouse ear (Figure 12). In addition, the perfect colocalization of these two signals indicated that the nanoconjugate remained intact in the mouse ear blood vessels.

7.2 NIR-to-NIR Upconversion *in Vivo* Imaging

It is perceived that $NaYF_4$ host matrix codoped with Tm^{3+} and Yb^{3+} can absorb at 980 nm and emit at 800 nm, both of which are in the NIR region. This NIR-to-NIR upconversion luminescence facilitates high-contrast fluorescence imaging with much enhanced tissue penetration. Recently, Prasad *et al*.[71] demonstrated the use of $NaYF_4$: Yb^{3+}/Tm^{3+} NPs (20 $\sim$ 30 nm) for *in vitro* and *in vivo* imaging (Figure 13). They also showed that nil autofluorescence was associated with NIR-to-NIR upconversion imaging compared to high background noises in conventional downconverting fluorophores.

Li *et al*.[72] from Fudan University developed a laboratory-used upconversion luminescence *in vivo* imager system (Figure 14). They used this imager to test the ability

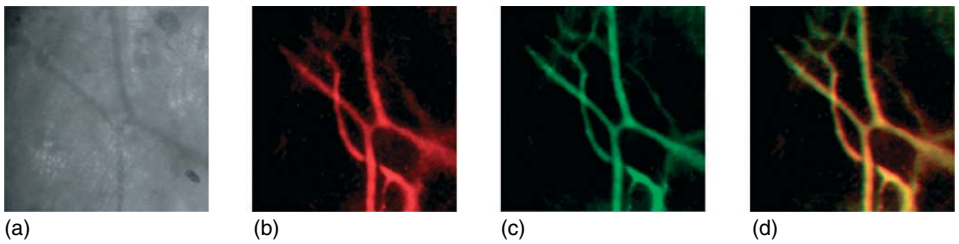


Figure 12 Optical imaging of blood vessels in the mouse ear following tail vein injection of the nanoparticles (10 mg); (a) blood vessels imaged with a blue light filter, (b) upconversion image with excitation at 980 nm and a laser power density of 550 mW cm^{-2}, (c) fluorescence image of the carbocyanine dye with excitation at 737 nm, and (d) merged image of the upconversion and fluorescence signals. Both the upconversion and carbocyanine fluorescence images were taken with an exposure time of 10 s. (Reproduced from Ref. 57 with permission of The Royal Society of Chemistry.)

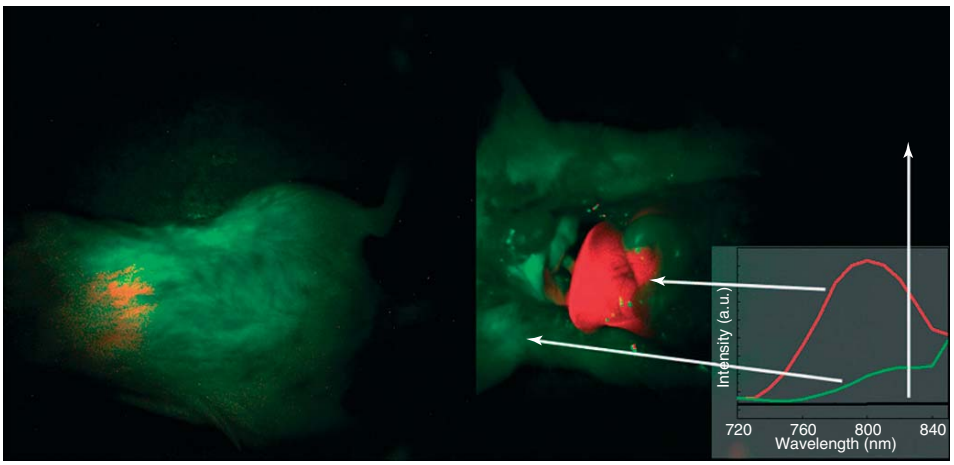


Figure 13 Whole-body images of mouse injected intravenously with UCNPs; intact mouse (left), and the same mouse after dissection (right). The red color indicates emission from UCNPs; green and black show background as indicated by the arrows. The inset presents the photoluminescence spectra corresponding to the spectrally unmixed components of the multispectral image obtained with the Maestro system. (Reproduced with permission from Ref. 71. Copyright (2008) American Chemical Society.)

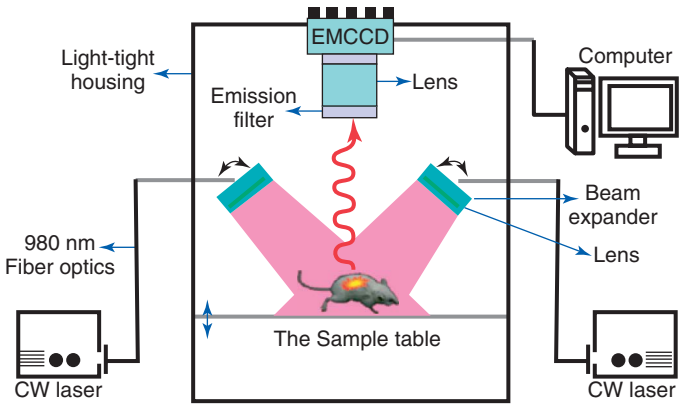


Figure 14 Diagram depicting the experimental setup for the upconversion luminescence *in vivo* imaging system designed by Li's group. Two external 0–5 W adjustable CW 980 nm lasers were used as the excitation sources, and an Andor DU897 EMCCD was used as the signal collector. (Reproduced with permission from Ref. 72. Copyright (2009) American Chemical Society.)

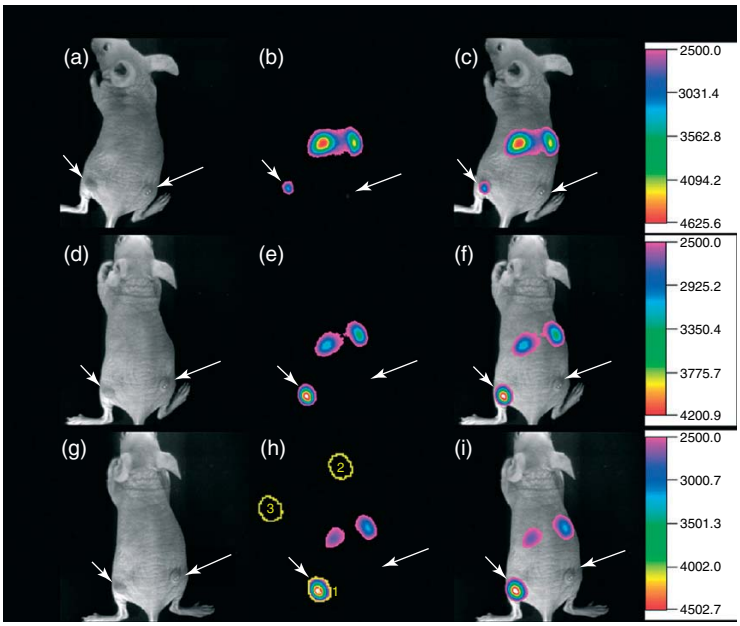


Figure 15 Time-dependent *in vivo* upconversion luminescence imaging of subcutaneous U87MG tumor (left hind leg, indicated by short arrows) and MCF-7 tumor (right hind leg, indicated by long arrows) borne by athymic nude mice after intravenous injection of UCNP-RGD over a period of 24 h. (Reproduced with permission from Ref. 72. Copyright (2009) American Chemical Society.)

of tridoped UCNPs ($Yb^{3+}/Er^{3+}/Tm^{3+}$) for targeted NIR-to-NIR upconversion imaging of tumor. Before intravenous injection of UCNPs, surface modification and bioconjugation were performed on UCNPs by attaching PEG-NH_2 and cyclic pepetide, c(RGDFK), which is for targeting human glioblastoma (U87MG) xenograft tumor. Subcutaneous human breast carcinoma (MCF-7) tumor modal was established for comparison. From the results of whole-body mouse imaging, it could be seen that this upconversion nanoprobe demonstrated excellent specificity toward U87MG tumor (Figure 15). This pioneering work points to the potentials of NIR-to-NIR upconversion nanoprobes for cancer detection.

8 CONCLUSION AND OUTLOOK

Even though the capabilities of UCNPs for *in vivo* imaging have been demonstrated, this research field is still at an early stage of development, and the use of UCNPs for *in vivo* imaging faces many problems. The first issue is the particle size of UCNPs. Small-sized nanoparticles are favored for *in vivo* imaging applications to prevent nonspecific accumulation of nanoparticles in the reticuloendothelial system. However, the upconversion fluorescence efficiency would be greatly reduced with the decrease of particle size. Therefore, it is highly indispensable to search for novel synthetic strategies to integrate a small size with high upconversion efficiency in UCNPs. Another concern comes from the aspect of toxicity. Even though relatively low toxicity was found in UCNPs compared with QDs, these lanthanide-containing inorganic nanoparticles are not degradable as are several clinically used polymers. Study on their potential side effects and long-term toxicity is extremely necessary. In addition, even though NIR fluorescence imaging allows for tissue penetration deeper than UV and visible light, the penetration depth is still not sufficient for whole-body imaging. In spite of these difficulties, the future of UCNPs for *in vivo* imaging is still bright.

9 GLOSSARY

Activator: In energy transfer upconversion (ETU) process, an activator receives energy from the nearby excited ions and releases an emission light with a specific wavelength.

Autofluorescence: Autofluorescence is the fluorescent signals derived from various endogenous biological entities, such as NADPH, flavins, collagen, and some proteins containing amino acids tryptophan, tyrosine, and phenylalanine.

Fluorophore: A fluorophore is an emissive molecule that absorbs a specific incident light and gives an emission light. Typical fluorophores are small organic dyes, fluorescent proteins, and quantum dots, used to fluorescently label tissues, cells for fluorescence imaging, and spectroscopy.

in vivo: *In vivo* is a Latin word for ''within the living'', which refers to the experiments conducted in living subjects, typically animal studies and clinical trails.

Nanoparticle: Nanoparticles are ultrafine particles with a size between 1 and 100 nm.

Phonon: A phonon is generated by a periodic, elastic arrangement of atoms or molecules in condensed matter.

Photobleaching: Photobleaching is the photochemical destruction of a fluorophore, which is common to organic dyes and in time-lapse microscopy. It means that high-energy excitation light renders a fluorophore not to fluoresce or with a lower quantum yield.

Sensitizer: In energy transfer upconversion (ETU) process, a sensitizer is generally a lanthanide ion (i.e., Yb^{3+}), which absorbs incident light strongly and transfers the absorbed energy to nearby emitter ions. A sensitizer serves as an energy reservoir for sensitizing activators.

Upconversion: Upconversion is an anti-Stokes-type emission. It is a nonlinear optical process in which two or more low-energy photons are absorbed sequentially, leading to a shorter wavelength emission than the excitation light.

10 ACKNOWLEDGEMENTS

This work was funded by grants from The Hong Kong Research Grants Council (PolyU 503510P), The University of Hong Kong and Shenzhen Bio-industry Development Fund-Basic Research Program (JC201005280607A). Dr. J. Jin acknowledges the receipt of postgraduate studentship from The University of Hong Kong.

11 RELATED ARTICLES

Near-Infrared Materials; Luminescent Bioprobes; Lanthanides in Living Systems; Lanthanide Halides.

12 ABBREVIATIONS AND ACRONYMS

ATPE = addition de photons par transfert d'énergie; EDTA = ethylenediamine tetraacetic acid; EG = ethylene glycol; ESA = excited state absorption; ETU = energy transfer upconversion; GSA = ground-state absorption; HRTEM = high-resolution transmission electron microscopy; LbL = layer-by-layer; Ln = lanthanide; LSS = liquid-solid-solution; NIR = near-infrared; NPs = nanoparticles; OA = oleic acid; ODE = octadecene; PA = photon avalanche; PAA = polyacrylic acid; PAH = poly(allylamine hydrochloride); PEI = polyethylenimine; PSS = poly(sodium 4-styrenesulfonate); PVP = polyvinylpyrrolidone; QDs = quantum dot; SAUCI = small-animal upconversion imager; SHG = second-harmonic generation; STPA = simultaneous two-photon absorption; TOPO = trioctylphosphine oxide; TPA = two-photon absorption; UCNPs = Upconversion nanoparticle; UV = ultraviolet.

13 REFERENCES

1. J. Shen, L. D. Sun, and C. H. Yan, *Dalton Trans.*, 2008, **42**, 5687.
2. F. Auzel, *Chem. Rev.*, 2004, **104**, 139.
3. F. Wang and X. Liu, *Chem. Soc. Rev*, 2009, **38**, 976.
4. H. S. Mader, P. Kele, S. M. Saleh, and O. S. Wolfbeis, *Curr. Opin. Chem. Biol.*, 2010, **14**, 582.
5. S. A. Hilderbrand and R. Weissleder, *Curr. Opin. Chem. Biol.*, 2010, **14**, 71.
6. J. Weber, *Phys. Lett. A*, 1973, **45**, 35.
7. R. Hardman, *Environ. Health Perspect.*, 2006, **114**, 165.
8. F. Wang and X. Liu, *J. Am. Chem. Soc.*, 2008, **130**, 5642.
9. L. C. Ong, M. K. Gnanasammandhan, S. Nagarajan, and Y. Zhang, *Luminescence*, 2010, **25**, 290.
10. D. K. Chatterjee, M. K. Gnanasammandhan, and Y. Zhang, *Small*, 2010, **6**, 2781.
11. P. Franken, A. Hill, C. Peters, and G. Weinreich, *Phys. Rev. Lett.*, 1961, **7**, 118.
12. M. Wang, G. Abbineni, A. Clevenger, C. Mao, and S. Xu, *Nanomed. Nanotechnol.*, 2011, **7**, 710.
13. M. F. Joubert, *Opt. Mater.*, 1999, **11**, 181.
14. N. Bloembergen, *Phys. Rev. Lett.*, 1959, **2**, 84.
15. F. E. Auzel, *Proc. IEEE*, 1973, **61**, 758.
16. J. S. Chivian, W. Case, and D. Eden, *Appl. Phys. Lett.*, 1979, **35**, 124.
17. J. C. Boyer, F. Vetrone, L. A. Cuccia, and J. A. Capobianco, *J. Am. Chem. Soc.*, 2006, **128**, 7444.
18. J. Van Dijk and M. Schuurmans, *J. Chem. Phys.*, 1983, **78**, 5317.
19. F. Wang, D. Banerjee, Y. Liu, X. Chen, and X. Liu, *Analyst*, 2010, **135**, 1839.
20. R. H. Page, K. I. Schaffers, P. A. Waide, J. B. Tassano, S. A. Payne, W. F. Krupke, and W. K. Bischel, *J. Opt. Soc. Am. B*, 1998, **15**, 996.
21. K. W. Kramer, D. Biner, G. Frei, H. U. Güdel, M. P. Hehlen, and S. R. Luethi, *Chem. Mater.*, 2004, **16**, 1244.

22. G. S. Yi and G. M. Chow, *J. Mater. Chem.*, 2005, **15**, 4460.
23. G. Yi, H. Lu, S. Zhao, Y. Ge, W. Yang, D. Chen, and L. H. Guo, *Nano Lett.*, 2004, **4**, 2191.
24. S. Heer, O. Lehmann, M. Haase, and H. U. Güdel, *Angew. Chem. Int. Ed.*, 2003, **42**, 3179.
25. H. X. Mai, Y. W. Zhang, R. Si, Z. G. Yan, L. D. Sun, L. P. You, and C. H. Yan, *J. Am. Chem. Soc.*, 2006, **128**, 6426.
26. J.-C. Boyer, L. A. Cuccia, and J. A. Capobianco, *Nano Lett.*, 2007, **7**, 847.
27. L. Wang and Y. Li, *Chem. Mater.*, 2007, **19**, 727.
28. Y. W. Zhang, X. Sun, R. Si, L. P. You, and C. H. Yan, *J. Am. Chem. Soc.*, 2005, **127**, 3260.
29. J. Shan, X. Qin, N. Yao, and Y. Ju, *Nanotechnology*, 2007, **18**, 445607.
30. Y. Wei, F. Lu, X. Zhang, and D. Chen, *Chem. Mater.*, 2006, **18**, 5733.
31. Z. Wang, F. Tao, L. Yao, W. Cai, and X. Li, *J. Cryst. Growth*, 2006, **290**, 296.
32. C. Li, Z. Quan, J. Yang, P. Yang, and J. Lin, *Inorg. Chem.*, 2007, **46**, 6329.
33. Y. Sun, Y. Chen, L. Tian, Y. Yu, X. Kong, J. Zhao, and H. Zhang, *Nanotechnology*, 2007, **18**, 275609.
34. J. Zhuang, L. Liang, H. H. Y. Sung, X. Yang, M. Wu, I. D. Williams, S. Feng, and Q. Su, *Inorg. Chem.*, 2007, **46**, 5404.
35. C. Feldmann, *Adv. Funct. Mater.*, 2003, **13**, 101.
36. Y. Wei, F. Lu, X. Zhang, and D. Chen, *J. Alloys Compd.*, 2008, **455**, 376.
37. Z. Q. Li and Y. Zhang, *Angew. Chem. Int. Ed.*, 2006, **45**, 7732.
38. F. Wang, D. K. Chatterjee, Z. Q. Li, Y. Zhang, X. P. Fan, and M. Q. Wang, *Nanotechnology*, 2006, **17**, 5786.
39. X. Wang, J. Zhuang, Q. Peng, and Y. Li, *Nature*, 2005, **7055**, 121.
40. X. Liang, X. Wang, J. Zhuang, Q. Peng, and Y. Li, *Adv. Funct. Mater.*, 2007, **17**, 2757.
41. L. Wang and Y. Li, *Nano Lett.*, 2006, **6**, 1645.
42. A. Patra, C. S. Friend, R. Kapoor, and P. N. Prasad, *J. Phys. Chem. B*, 2002, **106**, 1909.
43. A. Patra, C. S. Friend, R. Kapoor, and P. N. Prasad, *Chem. Mater.*, 2003, **15**, 3650.
44. V. Venkatramu, D. Falcomer, A. Speghini, M. Bettinelli, and C. Jayasankar, *J. Lumin.*, 2008, **128**, 811.
45. A. M. Pires, O. A. Serra, and M. R. Davolos, *J. Lumin.*, 2005, **113**, 174.
46. S. F. Lim, R. Riehn, C. Tung, W. S. Ryu, R. Zhuo, J. Dalland, and R. H. Austin, *Nanotechnology*, 2009, **20**, 405701.
47. X. Qin, T. Yokomori, and Y. Ju, *Appl. Phys. Lett.*, 2007, **90**, 073104.
48. J. Q. Gu, J. Shen, L. D. Sun, and C. H. Yan, *J. Phys. Chem. C*, 2008, **112**, 6589.
49. G. S. Yi and G. M. Chow, *Adv. Funct. Mater.*, 2006, **16**, 2324.
50. J. C. Boyer, M. P. Manseau, J. I. Murray, and F. C. J. M. van Veggel, *Langmuir*, 2009, **26**, 1157.
51. Z.-L. Wang, J. Hao, H. L. W. Chan, G.-L. Law, W.-T. Wong, K.-L. Wong, M. B. Murphy, T. Su, Z. H. Zhang, and S. Q. Zeng, *Nanoscale*, 2011, **3**, 2175.
52. Q. Zhang, K. Song, J. Zhao, X. Kong, Y. Sun, X. Liu, Y. Zhang, Q. Zeng, and H. Zhang, *J. Colloid Interface Sci.*, 2009, **336**, 171.
53. T. Cao, T. Yang, Y. Gao, Y. Yang, H. Hu, and F. Li, *Inorg. Chem. Commun.*, 2010, **13**, 392.
54. C. Liu, H. Wang, X. Li, and D. Chen, *J. Mater. Chem.*, 2009, **19**, 3546.
55. L. Xiong, T. Yang, Y. Yang, C. Xu, and F. Li, *Biomaterials*, 2010, **31**, 7078.
56. J. Jin, Y.-J. Gu, C. W.-Y. Man, J. Cheng, Z. Xu, Y. Zhang, H. Wang, V. H.-Y. Lee, S. H. Cheng, and W.-T. Wong, *ACS Nano*, 2011, **5**, 7838.
57. S. A. Hilderbrand, F. Shao, C. Salthouse, U. Mahmood, and R. Weissleder, *Chem. Commun.*, 2009, **28**, 4188.
58. Z. Chen, H. Chen, H. Hu, M. Yu, F. Li, Q. Zhang, Z. Zhou, T. Yi, and C. Huang, *J. Am. Chem. Soc.*, 2008, **130**, 3023.
59. Z. Li, Y. Zhang, B. Shuter, and N. Muhammad Idris, *Langmuir*, 2009, **25**, 12015.
60. G. S. Yi and G. M. Chow, *Chem. Mater.*, 2007, **19**, 341.
61. S. Wu, G. Han, D. J. Milliron, S. Aloni, V. Altoe, D. V. Talapin, B. E. Cohen, and P. J. Schuck, *Proc. Natl. Acad. Sci. U.S.A.*, 2009, **106**, 10917.
62. L. Wang and Y. Li, *Chem. Commun.*, 2006, **24**, 2557.
63. L. Wang, R. Yan, Z. Huo, J. Zeng, J. Bao, X. Wang, Q. Peng, and Y. Li, *Angew. Chem. Int. Ed.*, 2005, **44**, 6054.
64. H. S. Qian, Z. Q. Li, and Y. Zhang, *Nanotechnology*, 2008, **19**, 255601.
65. R. S. Niedbala, H. Feindt, K. Kardos, T. Vail, J. Burton, B. Bielska, S. Li, D. Milunic, P. Bourdelle, and R. Vallejo, *Anal. Biochem.*, 2001, **293**, 22.
66. H. Zijlmans, J. Bonnet, J. Burton, K. Kardos, T. Vail, R. Niedbala, and H. Tanke, *Anal. Biochem.*, 1999, **267**, 30.
67. J. Shan and Y. Ju, *Appl. Phys. Lett.*, 2007, **91**, 123103.
68. C. Salthouse, S. Hildebrand, R. Weissleder, and U. Mahmood, *Opt. Express*, 2008, **16**, 21731.
69. S. F. Lim, R. Riehn, W. S. Ryu, N. Khanarian, C. Tung, D. Tank, and R. H. Austin, *Nano Lett.*, 2006, **6**, 169.
70. D. K. Chatteriee, A. J. Rufalhah, and Y. Zhang, *Biomaterials*, 2008, **29**, 937.
71. M. Nyk, R. Kumar, T. Y. Ohulchanskyy, E. J. Bergey, and P. N. Prasad, *Nano Lett.*, 2008, **8**, 3834.
72. L. Xiong, Z. Chen, Q. Tian, T. Cao, C. Xu, and F. Li, *Anal. Chem.*, 2009, **81**, 8687.

Oxide and Sulfide Nanomaterials

Takuya Tsuzuki

Deakin University, Geelong, VIC, Australia

1 Summary 405
2 Introduction 405
3 Synthesis of Nanoparticles 406
4 Properties Unique to Nanoparticles 409
5 Industrial Applications 410
6 Conclusions 413
7 Related Articles 413
8 Abbreviations and Acronyms 413
9 References 413

1 SUMMARY

This article reviews the synthesis, characterization, and applications of rare earth oxide and sulphide nanomaterials. Special focus is placed on nanoparticulate materials and the description on nanoscale films and bulk nanoporous materials are intentionally excluded. In the first section, the synthesis methods of nanoparticles in general are reviewed, and examples of the production of rare earth oxides and sulphides are presented. The second section deals with the applications of rare earth oxides and sulphides, and they are discussed in relation to the unique properties of nanoscale particles.

2 INTRODUCTION

Nanoparticulate materials are defined as small particles with a characteristic scale of less than 100 nm. Particles with many shapes, including sphere, hollow-shell, rods, belt, needle, wire, tube, disk, and plate, can be regarded nanoparticulate materials as long as one of the dimensions, for example, the thickness of the plates, is less than 100 nm. Nanoparticles exhibit new or enhanced size-dependent properties compared with the bulk counterparts or larger particles of the same material.[1] The unique properties are influenced by the size and shape of the nanoparticles. As such, the control of size and shape enables the design of nanomaterials with desired properties. Owing to these unique properties of nanoparticles and recent development in their synthesis methods, the current and potential applications of nanoparticles are rapidly growing, encompassing an extremely broad range of markets and industries including biomedical and cancer treatment, renewable energy, environmental protection, pharmaceuticals, personal care, surface coatings, plastics, textiles, food, building materials, electronics, and automotives. Nanoparticles are indeed regarded as a new class of materials and have been a forerunner of nanotechnology commercialization.[2]

Colloidal chemistry has been dealing with the synthesis and characterization of nanoparticles for decades. For example, Michael Faraday worked on gold colloid in the 1850s.[1] Nonetheless, nanotechnology is often regarded as a relatively young field of science. In particular, research on lanthanide oxide and sulphide nanoparticles started only in the 1980s, around the period when nanoparticle technology for semiconductors rapidly advanced.[3] After nearly 20 years of intensive research on the methods to synthesize rare earth compound nanoparticles, a large-scale production of CeO_2 and some other rare earth oxide nanoparticles has met commercial success in the mid-2000s. The combination of the unique properties of lanthanide oxides and nanoscale objects has already found many commercial applications in electronics and automotive industries.

The Rare Earth Elements. Edited by David A. Atwood. © 2012 John Wiley & Sons, Ltd. ISBN 978-1-119-95097-4

3 SYNTHESIS OF NANOPARTICLES

3.1 Common Synthesis Techniques

In the last two decades, significant research efforts have been made to develop the methods to synthesize a variety of nanoparticulate materials. There are more than 20 laboratory-scale techniques frequently appearing in scholarly journals. In general, these methods can be divided into 2 approaches. One is the so-called top-down approach where nanoparticles are produced from bulk materials through size reduction, often by grinding or etching. The other is the bottom-up approach where nanoparticles are built up from atoms and molecules. The assembling of nanoparticles using the bottom-up approach can be done in matrices including solid, liquid, and gas phases. These methods are summarized in Figure 1. In the following sections, the details of each method are discussed, and some examples of rare earth oxides/sulphide nanoparticles produced using those methods are given.

3.2 Top-Down Approach

Mechanical milling has been widely utilized for producing nanostructured and ultrafine materials. Generally, the grinding of coarse materials is conducted in a ball mill by imparting mechanical energy to the raw material to reduce the particle size.[4] Traditional comminution through higher energy input, longer milling times, and the addition of milling aids can reduce the particle size down to nanoscale. The equipment is commercially available, and the number of process parameters is relatively small, so that the process is easily scalable. In recent years, much improvement was made on the milling instruments and the quality of grinding media in the <0.1-mm-diameter range, which has led to significant progress in the use of this technique for the production of a wide range of metal oxide nanoparticles. The disadvantage of this method is that, in some cases, the required milling can be as long as 100 hours and hence substantial contamination from milling balls and mill itself may be introduced into the nanoparticles. Longer milling time also introduces a substantial amount of strain in the crystal lattice and hence defect-sensitive properties such as photoluminescence are often degraded in the nanoparticles. Even if milling time is considerably long, particle size distribution can become broad, and particle morphology would have poor uniformity.

Recently, the author's group has demonstrated that those obstacles can be overcome by careful choice of raw materials and the use of a second ''diluent'' phase to produce rare earth oxide nanoparticles.[5] Since rare earth oxides are generally hard ceramics, milling of large particles of rare earth oxides into nanoscale requires a long milling time. However, milling of soft precursors such as carbonates and hydroxides allows shorter milling time to form smaller particles. Of particular significance is the use of the second ''diluent'' phase during milling. Water-soluble salts such as NaCl can be effectively milled together with the precursor compounds, enabling the separation of precursor nanoparticles during milling. The carbonate and hydroxide nanoparticles can be thermally decomposed into oxide nanoparticles. Water-soluble diluent phase also enables the separation of oxide nanoparticles during the thermal decomposition of precursor nanoparticle, resulting in the production of oxide nanoparticles with uniform morphology, a narrow size distribution and a low degree of agglomeration. Figure 2 shows the transmission electron microscopy (TEM) image of CeO_2 nanoparticles obtained via a salt-assisted top-down approach.[5]

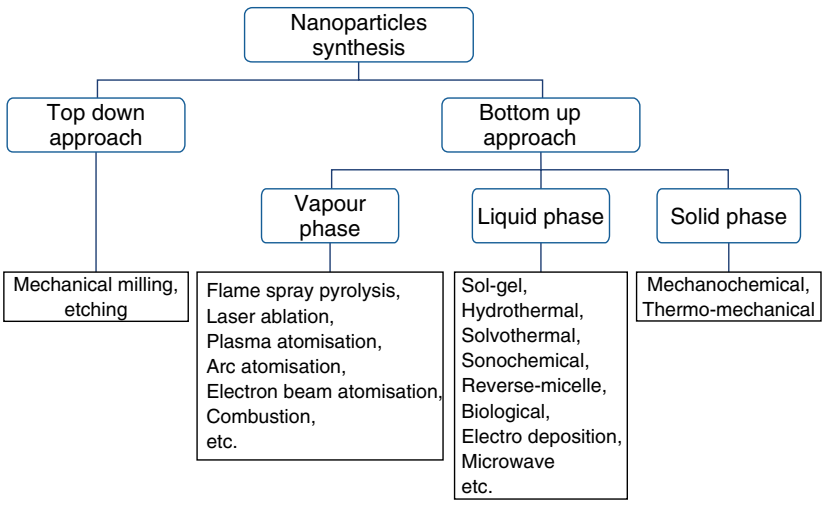


Figure 1 Techniques used for the laboratory scale synthesis of inorganic nanoparticles

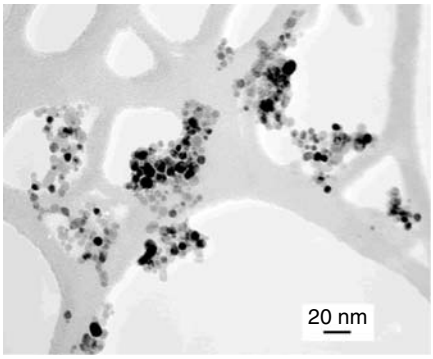


Figure 2 TEM image of the CeO_2 nanoparticles obtained via a salt-assisted top-down approach, by milling of $Ce(OH)_4$ with NaCl powder for 10 h and subsequent heat treatment at 500 °C

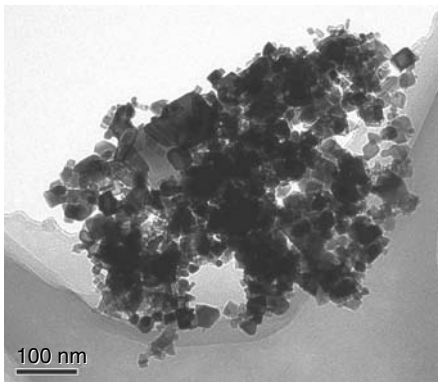


Figure 3 TEM images of an example of vapor/gas phase synthesized CeO_2 nanoparticles

3.3 Vapor-phase Synthesis

Gas phase condensation techniques assemble nanoparticles by the rapid solidification of a liquid or vapor in a gaseous medium.[6] Even when the synthesis is done under vacuum, seed gas molecules are often introduced in the reaction chamber. A variety of techniques to vaporize the precursors are developed, including laser ablation, explosion, electric arc discharge, plasma, electric resistance, and electron beam. Since the melting temperatures of metal oxides are normally extremely high, corresponding metals are often used as the precursors that are vaporized under an oxidative atmosphere to form metal oxide nanoparticles. Particle size, agglomeration and size distribution can be controlled by adjusting the vaporization rate, gas pressure and composition, and the flow of the newly formed particles in the gas phase. The uniformity in stoichiometry, oxidation states, and dopant concentration, as well as particle size among the nanoparticles, is often difficult to control by this technique.

Flame spray pyrolysis involves the ultrafine droplets of the solution of precursor materials (often salt) to be sprayed into a high-temperature chamber.[6] On evaporation of the solvent, the dissolved precursors are converted into nanoparticles after reaction with oxygen. Each droplet contains the stoichiometric amount of precursors required in the final nanopowder product. This ensures the uniform composition in each nanoparticle and is a distinctive advantage over the chemical vapor reaction technique mentioned above. Highly uniform nanoparticles are produced in a commercial quantity using this method. The size distribution is controlled by the droplet size, concentration of the precursor salt in the solvent, and the velocity of the droplets in the furnace.

Nanoblast technique is a relatively new method that utilizes the combustion or explosion of an organic host liquid to cause rapid oxidation under high temperature and high pressure conditions in a short period.[7] This technique enables the formation of multicomponent nanoparticles with uniform stoichiometry and morphology because of the extremely rapid reaction the precursor materials experience. The evolution of gas during the combustion of host liquid assists to separate nanoparticles from each other during the particle growth stage, resulting in a low degree of agglomeration in the final nanopowder product.

The vapor phase techniques involve fewer sources of contaminants and higher temperatures than other methods. As such, it normally results in nanoparticles with high purity, high crystallinity, and geometrical shapes. However, because of the lack of a solid medium between the particles during the particle growth stage, the nanoparticles made using this technique normally suffer from a high degree of agglomeration. The involvement of high temperature also causes sintering between particles. Figure 3 shows a typical appearance of CeO_2 nanoparticles made using vapor phase synthesis methods.

3.4 Liquid-Phase Synthesis

In the liquid-phase methods, nanoparticles are precipitated out from a solution that consists of a mixture of reagents. The advantages are the ability to control particles sizes, shapes, and stoichiometry in a precise manner, as well as flexibility in reaction paths. Decreasing particle size relies on systems to limit the growth of particles after nucleation. For that purpose, polymeric surfactants, small molecules of capping agents, or emulsifiers are frequently used as size-limiting additives in the solution. In a laboratory-scale production, an uniform reaction environment can be created in the solution to produce nanoparticles with uniform size and morphology. However, the use of growth-limiting agents may remain on the particle surface unless special processes are applied to remove the agents. The principles and characteristics of common liquid-phase techniques are listed in Table 1. Figure 4(a) shows an example of hydrothermally synthesized CeO_2 nanoparticles.[8]

The properties of nanoparticles depend not only on the size and crystallinity but also on the shape of the particles. Hydrothermal synthesis is extensively used to obtain

Table 1 Operation principles and unique attributes of liquid-phase methods commonly used for the synthesis of rare earth oxide and sulfide nanoparticles

Methods	Features
Hydrothermal	*Process:* Precipitation from an aqueous solution of precursor salts under a high pressure and temperature condition in an autoclave *Particle size control*: By reaction temperature and duration, precursor concentration, pH, surfactant additives, and precursor materials *General attributes*: High crystallinity; often geometrical shapes; mostly oxides
Solvothermal	*Process:* Precipitation from a nonaqueous solution of precursor salts under high temperature. Application of high pressure is optional *Particle size control*: By reaction temperature and duration, precursor concentration, pH, surfactant additive, precursor materials, and solvent *General attributes*: High crystallinity; spherical shapes as well as unique morphologies; not only oxides but also sulfides and other chalcogenide compounds
Sol-gel	*Process:* Hydrolysis of precursor salts in an aqueous or nonaqueous environment to form a colloidal suspension of precipitates often in the form of hydroxide, oxalate, and carbonate *Particle size control*: By reaction temperature and duration, precursor concentration, pH, surfactant additive, precursor materials, and solvent *General attributes*: Spherical shapes; further heat treatment is necessary for the nonoxide precipitates and often leads to severe agglomeration
Microemulsion	*Process*: Hydrolysis of precursor salt in ultrafine emulsion droplets (micelles) in an aqueous or nonaqueous environment (oil in water or water in oil) *Particle size control*: By micelle size, precursor concentration, pH, precursor materials, and temperature *General attributes*: Mostly equiaxed shapes but unique morphology is possible by templating methods
Sonochemical	*Process*: Utilization of microcavities generated by ultrasonic cavitation. Chemical reactions occur in localized hot spots with short-lived high temperature and pressure *Particle size control*: By ultrasonic power and frequency, solvents, precursor concentration, pH, precursor materials, temperature, surfactants *General attributes*: Mostly equiaxed shapes, some rod shape reported; high degree of dispersion due to sonication

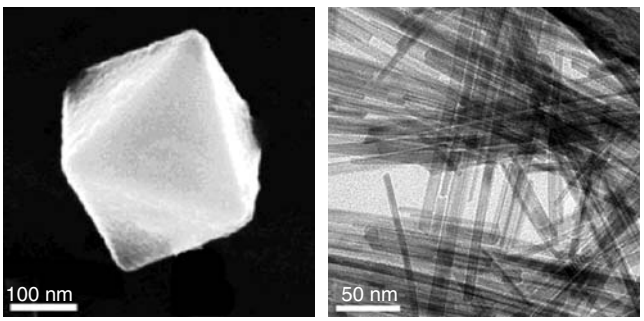


Figure 4 TEM images of an example of hydrothermally synthesized CeO_2 nanoparticles via hydrothermal treatment of a mixed aqueous solution of $Ce(NO_3)_3 \cdot 6H_2O$ and $Na_3PO_4 \cdot 6H_2O$ at 170 °C for (a) 12 h and (b) 144 h. (Reprinted with permission from Ref. 8. Copyright (2009) American Chemical Society.)

nanoparticles with unique shapes (Figure 4b). By careful control of synthesis parameters, hydrothermal technique can also produce rare earth hydroxide nanoparticles with a variety of shapes, including rod, needle, tube, disk, and belt/ribbon.[9] Those hydroxide nanoparticles can be further processed to obtain oxide nanoparticles while retaining the same morphology.

3.5 Solid-Phase Synthesis

Solid-phase synthesis of nanoparticles is mainly represented by mechanochemical methods.[10] The method utilizes a ball mill as a chemical reactor where the precipitation of nanoparticles is induced in a solid matrix. In order to form nanoscale particles, a nanoscopically uniform reaction environment needs to be created. In a solid-state reaction, this is achieved by ball milling of precursor powders to form a nanoscale composite structure of the starting materials. In the nanoscopically uniform environment, the reactant atoms are required to diffuse only a nanoscale distance to cause chemical reactions. Hence, the reactions that normally occur at elevated temperatures can be induced near room temperature by mechanical energy input during ball milling. The reactants are often milled in the presence of an inert diluent phase to control the agglomeration of resulting nanoparticles, because the volume ratio between nanoparticle and inert salt matrix phases should be sufficiently low to ensure that the precipitated nanoparticles are separated from each other by the solid

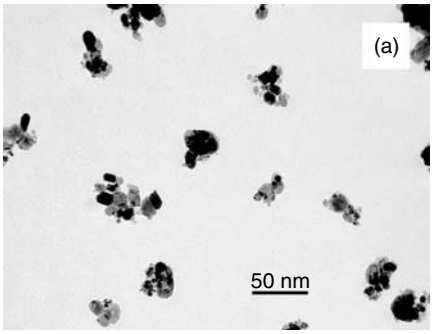


Figure 5 TEM image of CeO_2 nanoparticles synthesized via a mechanochemical reaction followed by heat treatment in air. (Reproduced by permission of Australian Ceramic Society. Ref. 11.)

matrix. This enables the synthesis of nanoparticles with a low degree of agglomeration. The nanoparticles can be further heat treated to improve their crystallinity without causing temperature-induced agglomeration when they are embedded in the inert solid matrix. Then the nanoparticles are collected simply by selective removal of the matrix phase, although the use of inert diluent may induce contamination. Similar to the top-down approach described earlier, the number of process parameters in mechanochemical processing is relatively small and the process is easily scalable. So far, the synthesis of CeO_2, Y_2O_3, and Gd_2O_3 were demonstrated using this technique. Figure 5 shows a typical appearance of CeO_2 nanoparticles prepared via a mechanochemical reaction of $CeCl_3 + 3NaOH = Ce(OH)_3 + 3NaCl$ followed by calcination in air.[11]

3.6 Sulfide and Oxysulfide Nanoparticles

Lanthanum oxysulfide nanoparticles such as Y_2O_2S can be produced using many of the techniques in Figure 1, including sol-gel thermolysis and spray pyrolysis. Among them, hydrothermal synthesis gives advantages over other methods in terms of shorter reaction time, lower reaction temperature, and the possibility of morphology control, while achieving high crystallinity.[9] The comprehensive list of the synthesis methods of lanthanum oxysulfide ultrafine particles can be found in Ref. 12.

The synthesis of lanthanide sulfide nanoparticles is more challenging than oxides or oxysulfides. Rare earth sulfide is conventionally produced by the sulfidization of rare earth elements or Sesquioxides, by heat treatment under H_2S, S, or CS_2 gas or by mechanical alloying of rare earth metals with sulfur. The heat treatment method requires a high temperature ($>800\,^{\circ}C$) and a long processing time (>10 h), and hence the resulting particles are normally in micron scale. Mechanical alloying techniques also result in the formation of nanograined but large particle forms. In addition, the chemical instability of rare earth sulfide toward oxidation adds to the difficulty in the production of ultrafine particles. To date, only four reports have appeared on the successful synthesis of nonagglomerated rare earth sulfide nanoparticles in the laboratory scale using mechanochemical, solvothermal, sonochemical, and thermal decomposition methods. Figure 6 shows the typical TEM image of Ce_2S_3 nanoparticles produced by mechanochemical processing.[13]

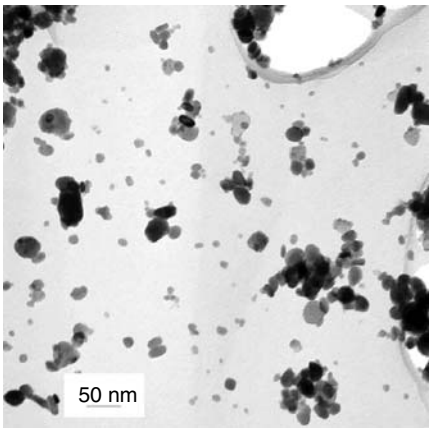


Figure 6 TEM image of Ce_2S_3 nanoparticles produced by mechanochemical processing of $2CeCl_3 + 3CaS = Ce_2S_3 + 3CaCl_2$. (Reproduced by permission of Trans Tech Publications. Ref. 13.)

4 PROPERTIES UNIQUE TO NANOPARTICLES

4.1 Surface Area

The unique property of nanoparticles that is most widely utilized in the applications of rare earth oxides and sulphides is their high specific surface area. Specific surface area is defined as the surface area per unit weight. As the particle size is reduced, more atoms are exposed on the particle surface and hence the specific surface area increases drastically (Table 2). For example, when the particle diameter is reduced to 1 nm, only 1 g of CeO_2 nanoparticles can have a surface area of $\sim 800\ m^2$, three times larger than the official tennis court. On the other hand, if the particles have a diameter of 100 μm, then 1 g of the powder has only $0.008\ m^2$ of surface

Table 2 Ratio between the atoms inside and on the surface of spherical CeO_2 particles

Particle diameter (nm)	Total atom count	Surface atoms (%)	Specific surface area ($m^2\ g^{-1}$)
1000	~30 000 000 000	~0.2	0.8
100	~30 000 000	~2	~8
10	~30 000	~20	~80
1	~30	~90	~800

area, so that 100 kg of powder is required to provide the same surface area as 1 g of CeO_2 with a diameter of 1 nm. This high surface area is useful to enhance surface-related functionality including catalytic activities and gas sensing abilities, as well as increasing solubility and reactivity of the particles.

Crystallographically speaking, particle surfaces consist of physical defects that can act as luminescence-quenching sites. Owing to the high specific surface area, nanoparticles tend to have much lower luminescence intensity than micron-sized particles. However, surface modification of nanoparticles can be used to enhance or tailor the luminescence properties of nanoparticles.[14]

4.2 Optical Transmission of Nanoparticle Suspension System

Another widely used property of nanoparticles is the high optical transmission of particle suspension systems. When the diameter of particles becomes smaller than the optical wavelength, the scattering of light by the particles becomes negligible. This effect is described by the Rayleigh approximation of Mie scattering theory as expressed in Equation (1):

$$I_{\text{scat}} = I_0 \frac{8\pi^4 a^6}{r^2 \lambda^4} \left(\frac{m^2 - 1}{m^2 + 2} \right)^2 (1 + \cos^2 \theta) \tag{1}$$

where I_o is the intensity of incident light, I_{scat} is the intensity of scattered light by a particles, a is the particle diameter, λ is the wavelength of incident light, r is the radial distance, θ is the scattering angle, and m is the relative refractive index defined as

$$m = \frac{n_{\text{particle}}}{n_{\text{media}}} \tag{2}$$

where n_{particle} and n_{media} are the refractive indexes of the particle and its surrounding medium, respectively. This approximation is valid when the particle diameter and the optical wavelength fulfil the following conditions:

$$\frac{2\pi a}{\lambda} \ll 1 \tag{3}$$

As can be seen in Equation (1), the light scattering efficiency of a particle decreases proportional to the sixth powder of particle diameter. Normally nanoparticles smaller than 100 nm meet this condition for the scattering of visible light (λ: 400–750 nm). Hence, when rare earth nanoparticles of this size range are well dispersed in a medium with no optical absorption, the particle suspension system will appear highly transparent. This effect is useful in the applications such as phosphorescent panels, UV screening coatings and diesel fuel additives where transparency has high commercial values.

4.3 Quantum Confinement Effects

When the nanoparticles become smaller than the exciton-Bohr diameter, semiconductor nanoparticles show quantum size effects due to the spatially confined electron–hole pairs that are created by photo or thermal excitation.[1] The quantum size effects appear most frequently as a bandgap broadening. Hence optical properties such as radiative and nonradiative electronic transitions are significantly influenced by quantum confinement effects in nanoparticles. Although most of the rare earth oxides are insulators, quantum size effects are of particular importance to the bandgap engineering of semiconductors such as CeO_2 and some rare earth sulphides.

Rare earth oxides and oxysulfides are commonly used as host materials for luminescent applications through the doping of rare earth ions such as Eu^{3+}. The localized electronic states of those doped rare earth ions are influenced by the nanoscale dimension of particles through electron–phonon interactions. Because of the phonon confinement effect in a nanoscale particle, the phonon density of states is modified to have discrete states, resulting in the lack of low-frequency phonon modes. Since low-frequency phonons largely contribute to the nonradiative relaxation between the closely spaced crystal-field levels, the phonon-confinement effect gives rise to significant changes in the luminescence dynamics of doped rare earth ions.[15]

4.4 Physical Size

Another widely utilized unique property of nanoparticles is their small physical size.[1] The size of nanoparticles is comparable with virus, DNA, and other organic components in biological cells. Nanoparticles less than 100 nm in diameter can go through the smallest blood vessels to carry drugs or imaging agents to designated diseased areas in the body. Hence the small physical size is appreciated in many biomedical applications.[16] Nanoparticles also share the same critical scale range with modern electronic devices and hence can be used as a building block of novel electronic devices such as quantum lasers and single electron transistors.

5 INDUSTRIAL APPLICATIONS

As mentioned earlier, the combination of the unique properties of lanthanide compounds and nanoscale objects has already found a wide range of commercial applications in many industries. New potential applications in medical diagnosis are also actively being pursued. In this section, brief descriptions of some common applications are given.

5.1 Luminescent Materials

Rare earth oxides and oxysulfides are excellent host materials of rare earth ions to produce phosphors with high luminescence intensity. Nanophosphors are useful for the miniaturization of electronic devices and improved resolution of displays. Nanophosphors are also useful in biomedical applications such as biomarkers and diagnostic imaging agents, because nanoparticles are smaller than cellular dimensions and similar in size to common biomolecules. Some of the applications of luminescent nanoparticles are listed in Table 3.

5.2 Catalysts

Owing to the large specific surface area, rare earth compound nanoparticles have many applications as advanced catalysts. In particular, large quantities of CeO_2 nanoparticles are commercially used in the automotive industry as exhaust fume three-way catalysts and diesel fuel additives.

The most prominent pollutants in the exhaust fume of combustion engines are carbon monoxide, nitrogen oxides, and hydrocarbons. Three-way catalysts, which convert these three pollutants into relatively safe gases simultaneously, are hence important materials for the reduction of air pollution. CeO_2, in particular ZrO_2-doped CeO_2, is one of the technologically most important metal oxides owing to its ability to reversibly store and release oxygen and high oxygen storage capacity, which is critical to increasing the efficiency of three-way catalysis. Its improved thermal stability at elevated temperatures adds further advantages over other ceramic catalysts for the application. Further, ceria–zirconia and ceria-based solid solutions are receiving considerable interest because of their numerous applications as active components or supports in many chemical reactions such as low temperature water–gas shift reaction, deNO_x, removal of particulate matter from diesel engine, synthesis of dimethyl carbonate from methanol and CO_2, removal of volatile organic compounds (VOCs), direct conversion of methane to synthesis gas, dehydration of alcohols, preferential oxidation of CO, steam reforming of ethanol, and oxidative dehydrogenation of ethyl benzene.[17]

The number of diesel-powdered vehicles is increasing rapidly because of the depletion of petroleum reserves and the interest in the use of biodiesel fuels. Current challenges of diesel fuel technology lies in the improvement of fuel efficiency and the reduction of harmful gas molecules and particulate carbon matter emitted upon combustion. CeO_2 is known for its high redox catalytic effects and is commercially sold as diesel fuel additives for the purpose. It was demonstrated that addition of as low as 25 ppm of ~10-nm size CeO_2 nanoparticles to diesel increased the fuel efficiency via reduced light-off temperature (by 250 °C) while reducing the emission of particulated carbon (by 50%) as well as CO and NO_x gas emission.[18] Commercial diesel fuel additives are sold as a transparent liquid wherein nanoparticles are dispersed in a solvent. The transparency is commercially important, as customers tend to have a negative view about adding muddy substances in their fuel tank. The low light scattering power of ~10-nm size nanoparticles is thus important to achieve the successful marketing of the product.

5.3 Chemical Mechanical Planarization

Integrated circuits are the most important component in computers as central processing and high-density memory units. They consist of multilayer structures made by repeated deposition of thin layers. Lithography is applied to each layer to form micro- and nanoscale three-dimensional circuits.

Table 3 Applications of nanophosphors

Application	Description
Plasma/electroluminescent display	Higher resolution, lower power requirement, low voltage operation
Thermometry	Noncontact temperature sensing based on the change in the excitation and emission spectra, decay lifetime and intensity of luminescence with temperature. Unlike infrared temperature sensors, the measurements are not influenced by the infrared absorption by glass, water, gas, biological cells, and other materials
Biomarker, molecular tagging	Advantages over conventional fluorescent chromophores in terms of long luminescent lifetime, excellent photofastness, large Stokes shift, sharp emission spectra, and greater chemical stability
Near-infrared medical imaging	Targeted infrared imaging agent for medical diagnosis such as cancer and atherosclerosis. Often administered by vascular ingestion for *in vivo* applications. Advantages over conventional fluorescent chromophores in terms of long luminescent lifetime, excellent photofastness, large Stokes shift, sharp emission spectra, and greater chemical stability. Ability to target and deliver drugs at the same time
Solar cell	Up-conversion and down-conversion to utilize the solar spectrum outside of the normal photoresponsive spectrum range of solar cells

Normally the surface of the deposited layers requires planarization to make the surface completely parallel to the substrate before the deposition of the next layer. This is critical because any curved or warped layer will compromise device integrity. For the planarization of the layers, polishing compounds in a form of a powder slurry have been used. The abrasive powders remove unnecessary parts of the layers by the synergistic effect of both physical and chemical forces and hence the process is called *chemical–mechanical planarization* (CMP).

The device performance of integrated circuits, such as calculation speed and memory density, can be improved by reducing the dimension of the structural unit. Since the invention of the integrated circuit in 1958, the structural unit has been shrinking every year and the number of transistors on an integrated circuit has been increasing exponentially. In 2011, the characteristic length scale of the components reached approximately 22 nm. Here, the size of the powder in the CMP slurry becomes important. The size of the particles needs to be nanoscale so as to not cause deep scratches on the deposited layers. The enhanced reactivity due to increased surface area also assists the efficient CMP effect. Most common CMP slurries have been made with Al_2O_3 and SiO_2 nanoparticles. However, recent integrated circuits use copper instead of aluminum as a conductor, and insulating layer material is also changing from oxides to nitrides. Hence greater material selectivity in polishing removal rate is required. It was found that CeO_2 has much greater selectivity than SiO_2 or Al_2O_3, although the fundamental mechanism of the selectivity is not fully understood.[19] The demand for CeO_2 nanoparticle CMP slurry has been increasing rapidly since mid-2000s. Its commercial production is now in the scale of hundreds of tonnes per year and has become an important part of the billion-dollar CMP-slurry industry.

5.4 Solid-Oxide Fuel Cell Electrodes

Solid-oxide fuel cells (SOFCs) are one of the most efficient and environmentally friendly energy conversion technologies to generate electricity from fuels such as hydrogen and methanol. Currently, yttria-stabilized zirconia is commonly used as an anode material. Doped CeO_2 has higher oxygen ion conductivity than stabilized zirconia and thus potentially enables reduction of the operation temperature of SOFC from ~1000 °C to ~700 °C. This helps avoid many problems associated with insulation and interconnections of SOFC. However, conventional large particles of CeO_2 require high sintering temperatures (~1500 °C) to form full density anode, which hinders the application of CeO_2 in SOFC. This problem can be overcome by using nanoparticles that normally have significantly lower sintering temperatures than large particles.[20] Incorporation of CeO_2 nanoparticles in anode materials also increases the cell efficiency by catalytically assisting the decomposition of methanol and also by creating a nanoscale network of conduction pathways.[21] Current challenges lie in the method to incorporate nanoparticles in the anode as well as the improvement of sintering density.

5.5 UV Screening Agents

Significant health and environmental problems result from UV-induced degradation of human skin and other organic materials such as plastics, paints, textiles, and dyes. The development of suitable UV-shielding agents is therefore of great importance to the society. Compared to organic UV absorbing molecules, inorganic UV screening agents have superior light fastness. As such, many sunblock products have been manufactured using wide bandgap semiconductor particles such as TiO_2 and ZnO. However, TiO_2 and ZnO have strong photocatalytic activity that results in the production of free radicals upon exposure to UV light. The photoinduced free radicals can damage the organic materials that these particles are supposed to protect from UV rays. Hence new types of inorganic UV screening agents with no photocatalytic activity are being sought. CeO_2 is a semiconductor with a bandgap energy similar to TiO_2 and ZnO and hence absorbs UV rays (mostly in UVB range of 290–320 nm) (Figure 7). Yet, CeO_2 has significantly weaker photocatalytic activity than TiO_2 and ZnO. As such, CeO_2 is considered as a candidate for new safe UV screening agents. Nanodimension of particles provides high transparency to the final nanoparticle suspension products, which is commercially important. However, high oxidation catalytic activity of CeO_2 hinders its practical applications as UV screening agents.[11]

5.6 Gas Sensors

Semiconductor metal oxide nanoparticles such as CeO_2 can be utilized to manufacture highly sensitive gas sensors. Gas sensing mechanism is based on the reactions of gas molecules with particle surfaces that alter the electron

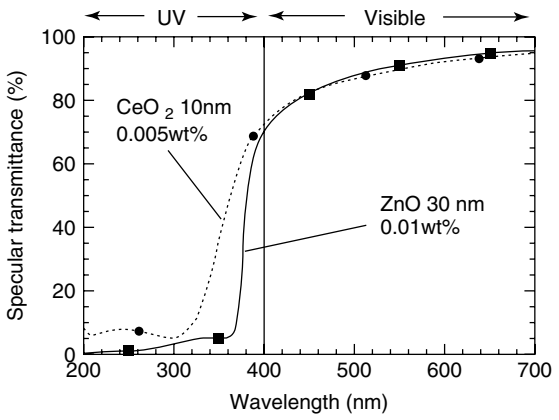


Figure 7 UV–vis spectra of 30-nm ZnO and 10-nm CeO_2 nanoparticles dispersed in water. (Reproduced by permission of Australian Ceramic Society. Ref. 11.)

charge states near the particle surface. When a thin layer of nanoparticles is exposed to a certain gas, the overall conductivity of the layer is modified because of the change in electron charge states near the particle surface. Hence the gas can be detected as the change in the film conductivity. The sensing layers made with nanoparticles possess high gas sensitivity because of the high specific surface area. CeO_2 nanoparticle gas sensors are demonstrated for the detection of methanol and oxygen.[22]

5.7 Magnetic Resonance Imaging Contrast Agents

Magnetic resonance imaging (MRI) is a noninvasive, safe, and painless diagnostic technique that uses magnetic field and radiowaves to produce a detailed image of the body's organs and structures. The signal of MRI is dependent on the longitudinal (T_1) and transverse (T_2) proton relaxation times of mainly water. Differences in proton relaxation times result in differences in contrast in MR images. MRI contrast agents are often administered to the diseased part to enhance the imaging capability. MRI contrast agents can decrease the T_1 and T_2 relaxation times to improve the contrast between normal and diseased tissues.

Gd^{3+} can induce T_1 relaxation of water proton more than any other element. Although commercial Gd-chelates are commonly used, they have a possibility of anaphylactic reactions as a side effect. On the other hand, nanoparticle MRI contrast agents offer better targeted imaging capability as well as the possibility of drug delivery functionality. In addition, Gd_2O_3 nanoparticles of <5 nm in diameter showed higher T_1 relaxivity than Gd^{3+} chelates, which enables higher MRI contrast than the chelates.[23] Unlike Fe_2O_3 nanoparticle T_2 contrast agents, Gd_2O_3 nanoparticles are not commercially available, but are considered as the next-generation MRI contrast agent.

5.8 Pigments

Red inorganic pigments are in high demand because of their excellent photostability compared to red organic dyes. Ce_2S_3-based particles have been hailed as a next generation of safe red pigments to replace highly toxic cadmium sulfoselenide pigments.[24] Ce_2S_3 pigment is normally doped with Ca or Na to stabilize the crystal structure and to enhance chemical stability. The control of hues from yellow to dark red can be achieved by changing the amount of doped Ca or Na. Micron-sized particles of Ce_2S_3-based pigments have achieved commercial success in the late 1990s. When the particle size is reduced, the pigment normally gives sharper color. Recent advancement of high-resolution inkjet printing technology also requires nanoscale pigment of <100 nm in diameter. Hence the demand for Ce_2S_3-based nanoparticle pigments is expected to increase. However, commercial scale production of Ce_2S_3-based nanoparticles has not been successful so far.

6 CONCLUSIONS

The combination of the unique properties of lanthanide oxides and nanoscale objects has found many current and future applications in a wide range of industries. Extensive progress in the development of synthesis methods in the past enabled the practical applications of some lanthanum oxide nanoparticles. However, the range of nanoparticle compositions that those methods can prepare is still limited. Further investigation on the techniques to produce rare earth oxides and sulfides in a scalable manner is necessary to realize important industrial applications. The development of new synthesis methods is also required to expand the capability to tailor the properties of those nanoparticles.

7 RELATED ARTICLES

Lanthanide Oxide/Hydroxide Complexes; Molecular Magnetic Materials.

8 ABBREVIATIONS AND ACRONYMS

CMP = chemical–mechanical planarization; MRI = Magnetic resonance imaging; SOFCs = Solid-oxide fuel cells; TEM = transmission electron microscopy; VOCs = volatile organic compounds.

9 REFERENCES

1. M. Hosokawa, K. Nogi, M. Naito, and T. Yokoyama, 'Nanoparticle Technology Handbook', Elsevier, Radarweg, 2007.
2. T. Tsuzuki, *Int. J. Nanotechnol.*, 2009, **6**, 567.
3. M. Imanaka and M. Masui, in 'Binary Rare Earth Oxides', eds. G. Adachi, M. Imanaka, and Z. C. Kang, Springer, Dordrecht, 2004, Chap. 6, p. 135.
4. C. De Castro and B. S. Mitchell, in 'Synthesis, Functionalization and Surface Treatment of Nanoparticles', eds. M. I. Baraton, American Scientific Publishers, Valencia, 2003, p. 1.
5. P. G. McCormick and T. Tsuzuki, Process for the production of ultrafine powders, PCT/AU99/00368, WO9959754 (May, 1999).
6. C. G. Granqvist, L. B. Kish, and W. H. Marlow, 'Gas Phase Nanoparticle Synthesis', Springer, Dordrecht, 2004.
7. O. Vasylkiv, Y. Sakka, and V. V. Skorokhod, *J. Am. Ceram. Soc.*, 2006, **89**, 1822.
8. L. Yan, R. Yu, J. Chen, and X. Xing, *Cryst. Growth Des.*, 2009, **8**, 1474.

9. X. Wang and Y. Li, *Chem.—Eur. J.*, 2003, **9**, 5627.
10. P. G. McCormick, T. Tsuzuki, J. S. Robinson, and J. Ding, *Adv. Mater.*, 2001, **13**, 1008.
11. T. Tsuzuki, J. S. Robinson, and P. G. McCormick, *J. Aust. Ceram. Soc.*, 2002, **38**, 15.
12. R. Chandramohan, J. Thirumalai, and T. A. Vijayan, 'Nanocrystals', Intech Open Access Publisher, Rijeka, Croatia, 2010, p. 45.
13. T. Tsuzuki and P. G. McCormick, *Mater. Sci. Forum*, 1999, **315–317**, 586.
14. C. H. Yan, Z. G. Yan, Y. P. Du, J. Shen, C. Zhang, and W. Feng, in 'Handbook on the Physics and Chemistry of Rare Earths', eds. K. A. Gschneidner Jr., J. C. Bünzli, and V. K. Pecharsky, Elsevier, North-Holland, 2011, Vol. 41, Chap. 251, p. 275.
15. G. K. Liu, X. Y. Chen, H. Z. Zhuang, S. Li, and R. S. Niedbala, *J. Solid State Chem.*, 2003, **171**, 123.
16. S. Bellucci, 'Nanoparticles and Nanodevices in Biological Applications', Springer, New York, 2009.
17. A. Trovarelli, 'Catalysis by Ceria and Related Materials', Catalytic Science Series, World Scientific Publishing Company, London, 2002, Vol. 2.
18. V. A. M. Selvan, R. B. Anand, and M. Udayakumar, *ARPN J. Eng. Appl. Sci.*, 2009, **4**, 1.
19. D. Merricks, B. Santora, B. Her, and C., Zedwick, In *Proceedings International Science and Technology Center*, Shanghai, 2008, p. 531.
20. C. Kleinlogel and L. J. Gauckler, in 'Solid Oxide Fuel Cells', eds. S. C. Singhal and M. Dokiya, Electrochemical Society, Pennington, NJ, 1999, p. 225.
21. T. Z. Sholklapper, C. P. Jacobson, S. J. Visco, and L. C. De Jonghe1, *Fuel Cell*, 2008, **8**, 303.
22. C. Wang, L. Yin, L. Zhang, D. Xiang, and R. Gao, *Sensors*, 2010, **10**, 2088.
23. J. Y. Park, M. J. Baek, E. S. Choi, S. Woo, J. H. Kim, T. J. Kim, J. C. Jung, K. S. Chae, Y. Chang, and G. H. Lee, *ACS Nano*, 2009, **3**, 3663.
24. P. Maestro and D. Huguenin, *J. Alloys Compd.*, 1995, **225**, 520.

Rare Earth Metal Cluster Complexes

Gerd Meyer

Universität zu Köln, Köln, Germany

1	Summary	415
2	Introduction	415
3	Synthesis	418
4	Lanthanide Halides with Empty Clusters	418
5	Halides with Cluster Complexes Centered by Endohedral Atoms	419
6	Conclusions	432
7	Glossary	433
8	Related Articles	433
9	Abbreviations and Acronyms	433
10	References	434

1 SUMMARY

The valence electron (VE) situation of the group 3 elements scandium, yttrium, lanthanum, and the following 14 ''4f elements'' cerium through lutetium is such that three electrons may be considered as the valence shell (s^2d^1), with the 4f electrons to be considered as core electrons. The latter often determine important properties (magnetism, absorption and emission of light) but their contribution to chemical bonding is negligible. With the paucity of three VEs, these elements may form (in the majority of cases octahedral) clusters, although almost always incorporating an endohedral atom (or atom group) that contributes to the overall electron count. For a general cluster complex $\{ZR_x\}X_z$, contributions to chemical bonding are mostly heteroatomic, of the Z–R and R–X type, with little homoatomic Z–Z and R–R contributions. Thus, these cluster complexes may be understood as anti-Werner-type complexes with the polarity of the atoms being textsf−(Z), +(R), −(X). In rare cases, the cluster complexes are isolated, or, more frequently, connected via common ligands. In the majority of cases, the clusters share common edges (or faces) to oligomers, chains, layers, or even networks.

2 INTRODUCTION

Clusters consist of two or more atoms of the same element bound together by considerable bonding interactions.[1] Clusters may be naked and neutral like $\{Au_{20}\}$ or charged as $\{Bi_9\}^{5+}$ and $\{Pb_5\}^{2-}$, respectively. Cluster complexes are clusters surrounded by ligands. Prominent examples are $[\{Mo_6\}Cl_{14}]^{2-}$ or $\{Rh_6\}(CO)_{16}$. These examples represent two types of transition metal cluster complexes. The first type consists of the rather electron-rich metal atom clusters surrounded by electronegative ligands without any ability for π back bonding. In the second type, the ligands are involved in distinct π back bonding, with the 18 valence-electron rule being typically obeyed.

In early transition metal clusters, 24- or 16-electron rules play an important role. In the salt $K_2[\{Mo_6\}Cl_{14}]$, there are 24 electrons available for intracluster bonding. In a valence bond (VB) interpretation, they build 12 equal two-center–two-electron (2 c–2e) bonds, locally associated with the edges of the octahedral $\{Mo_6\}$ cluster. In a molecular orbital (MO) theory description, 12 bonding MOs are occupied, with the LUMO already antibonding. In $K_4[\{Nb_6\}Cl_{18}]$, 16 cluster-based electrons occupy eight three-center–two-

The Rare Earth Elements. Edited by David A. Atwood. © 2012 John Wiley & Sons, Ltd. ISBN 978-1-119-95097-4

electron (3c–2e) bonds, according to the VB theory. Elements such as Zr (4 VE), with fewer VE than Mo (6 VE) or Nb (5 VE), may also form cluster complexes and obey, more or less, the 16-electron rule through incorporation of an endohedral atom in the center of the cluster as in $K_2Zr[\{CZr_6\}Cl_{18}]$, a single carbon atom in this case. Note that there are only nine cluster-based electrons—mostly for carbon–lutetium bonding interactions—in $Cs_2Lu[\{CLu_6\}Cl_{18}]$, although it has the same structure as the just mentioned zirconium compound.

The binary chloride $\{Nb_6\}Cl_{14}$ has the same number of cluster-based electrons, 16, as the ternary salt $K_4[\{Nb_6\}Cl_{18}]$, but fewer ligands to surround the cluster. Thus, the cluster complexes have to share ligands. In $\{Nb_6\}Cl_{14}$, this is accomplished in a rather complicated way, depicted as $\{Nb_6\}Cl_{10/1}{}^{i}Cl_{4/2}{}^{a-a}Cl_{2/2}{}^{i-a}Cl_{2/2}{}^{a-i}$, see Figure 1. The nomenclature used here is that of Niggli, Schäfer, and Schnering as well as that proposed recently by the author of this chapter; clusters with or without endohedral atoms are included in waved braces.[2–5] $\{CZr_6\}Cl_{14}$ has essentially the same structure, with a carbon atom in the center of the zirconium octahedron. The $\{CZr_6\}$ cluster is short of two electrons to obey the 16-electron rule. However, a view of the MO diagram calculated by extended Hueckel molecular orbital (EHMO) theory shows that the a_{2u} orbital, although bonding in character, is rather high in energy, see Figure 2. Quite obviously the cluster complex compound is stabilized by the formation of an extended salt through lattice energy contributions.

The rare earth elements (Sc, Y, and the lanthanides La–Lu) have only three VEs available for bonding in clusters, $ns^2(n-1)d^1(n-2)f^n$; f electrons, if present, do not engage in bonding. Therefore, clusters without an endohedral atom (''interstitial'') are extremely rare, although Gd_2Cl_3 with empty $\{Gd_6\}$ clusters was the first known example containing a

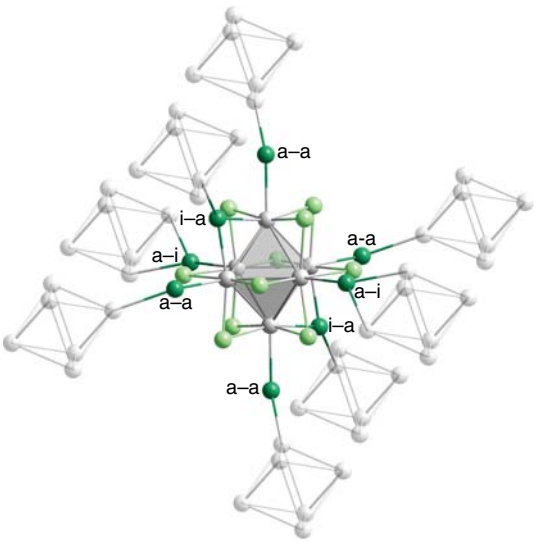


Figure 1 One cluster complex $\{Nb_6\}Cl_{12}{}^{i}Cl_6{}^{a}$ connected via a–a and i–a/a–i bridges to eight surrounding clusters (a stands for outer, German: äußere, i for inner(e) ligands

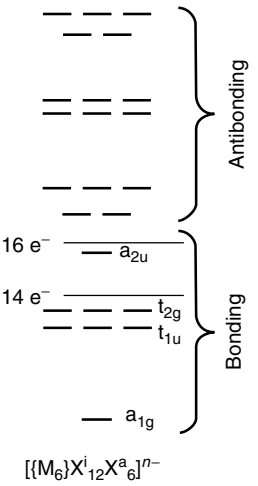


Figure 2 Schematic MO diagram for $[\{ZM_6\}X^{i}{}_{12}X^{a}{}_6]^{n-}$ cluster complexes

rare earth metal cluster, see Chapter 4 and Refs 19–22 therein. Isolated rare earth cluster complexes with interstitials such as $Cs_2Lu[\{CLu_6\}Cl_{18}]$ are also rare; more frequent are cluster complexes connected via common ligands, for example, $\{CSc_6\}I_{12}Sc$ (with a 13-electron cluster) or $\{IrPr_6\}Cl_{10}$ (with a 17-electron cluster). Most frequent are, however, compounds in which the clusters are connected via common edges (or faces). Examples are $\{(C_2)_2Dy_{10}\}Br_{18}$ (common edge of two $\{(C_2)Dy_6\}$ clusters in a dimer) or $\{OsSc_4\}Cl_4$ (two common opposite faces of square antiprisms, resulting in a chain).

Cluster complexes are not known for all rare earth elements. Bonding in the cluster $\{ZR_x\}$ is predominantly achieved by heteroatomic Z-R interactions with usually little homoatomic R-R contributions. Therefore, p states for main-group elements and d states for transition metal atoms as endohedral atoms Z have to match d states of the rare earth elements in energy and symmetry. In a localized view, the number of electrons has to be sufficient to occupy enough bonding orbitals. As almost all cluster complexes are structurally of the $[\{ZR_6\}X^{i}{}_{12}X^{a}{}_6]$ type, 16–18 electrons with an endohedral transition metal atom and 14 with a main-group atom are good rules of thumb. Figure 3 shows an EHMO calculation for $[\{IrY_6\}I_{18}]^{8-}$, a 17-electron cluster cut out of the extended solid $\{IrY_6\}I_{10}$; the SOMO still has bonding character and is separated from the LUMO by almost 4 eV.

Crystal orbital Hamiltonian population (COHP) diagrams derived from band structure calculations for the extended solid $\{IrY_6\}I_{10}$ show that Ir–Y and Y–I bonding interactions are most prominent, with considerable Ir–Y bonding and some Y–I antibonding interactions just below the Fermi level. Y-Y bonding plays only a negligible role, see Figure 4.

In a thermodynamic view, only those rare earth elements may form clusters for which the reduction to an alkaline-earth-like divalent state with no occupation of a

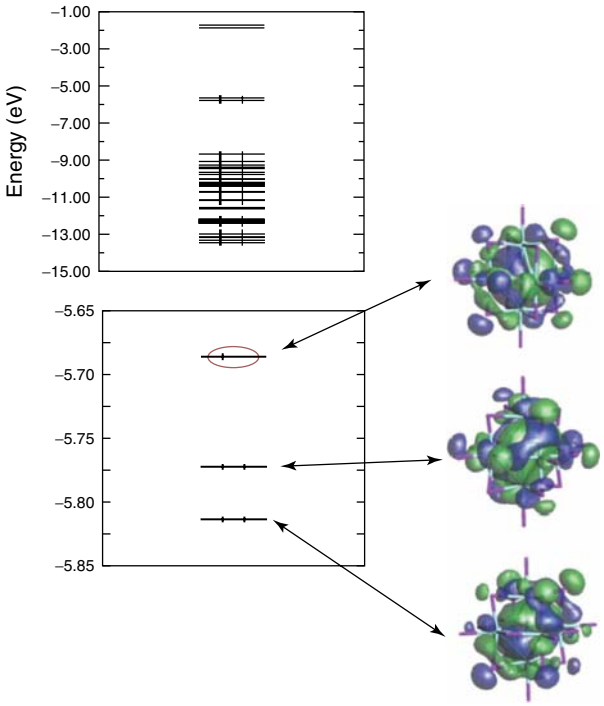


Figure 3 EHMO calculation for $[\{IrY_6\}I_{18}]^{8-}$, a 17-electron cluster cut out of the extended solid $\{IrY_6\}I_{10}$. The lower part shows two HOMOs and the SOMO

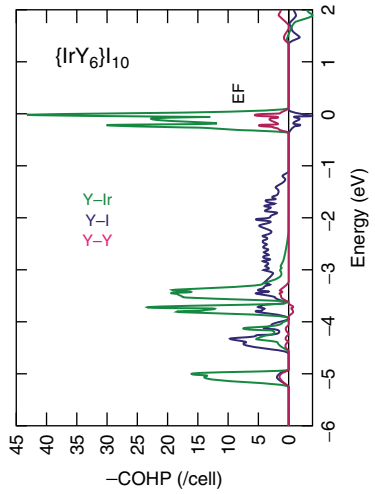


Figure 4 A crystal orbital Hamiltonian population (COHP) diagram for $\{IrY_6\}I_{10}$, derived from LMTO-ASA band structure calculations

5d state is not feasible. Important terms in an appropriate thermodynamic cycle are the lattice energies and atomic data as enthalpies of sublimation and of ionization. Most of these values parallel the lanthanide contraction and are aperiodic. However, the third ionization potentials show a periodic behavior throughout the lanthanide series, see Figure 5. For further information, see Refs 6–11.

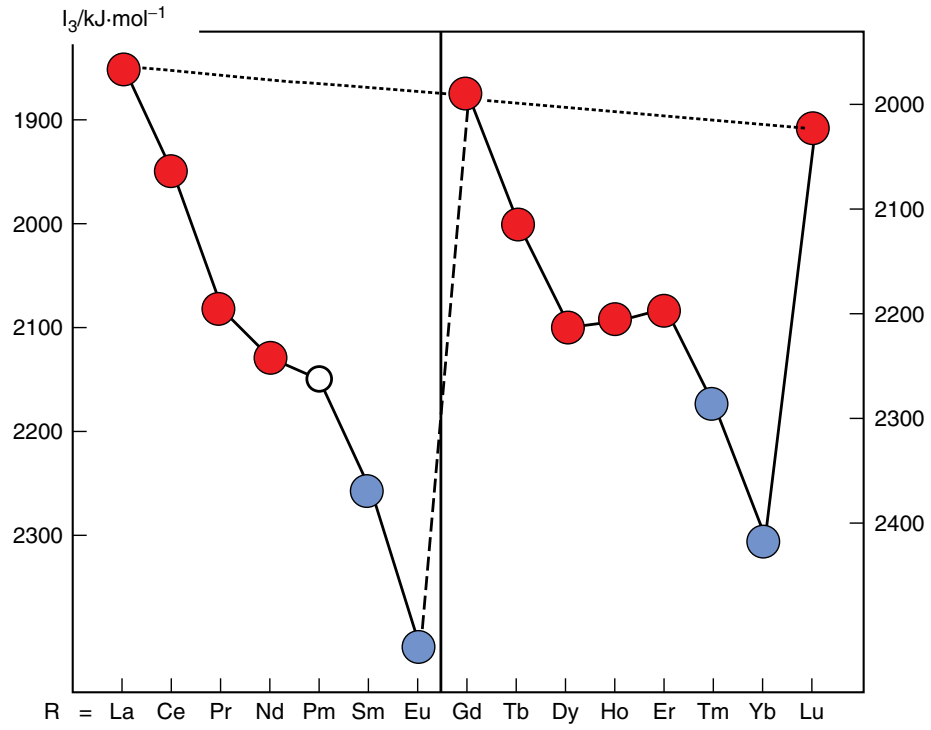


Figure 5 Third ionization potential I_3 versus atomic number for the lanthanide series. Elements marked in red form clusters, elements marked in blue form stable divalent compounds with $4f^n 5d^0$ electronic configurations

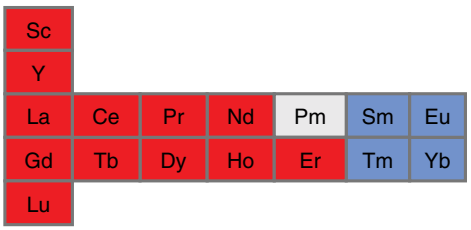


Figure 6 A periodic table of the rare earth elements with cluster-forming elements marked in red

The pattern as seen in Figure 5 may be transferred to a periodic table of the rare earth elements, see Figure 6. Only elements underlaid in red form clusters. The lower I_3 is, the easier it is to produce cluster complexes. Elements underlaid in blue form stable divalent compounds, for example $EuCl_2$; the divalent state with the electronic configuration $4f^n5d^0$ (with $n = 7, 14, 6, 13$ for R = Eu, Yb, Sm, Tm) has the highest stability and, thus, is the easiest to achieve when the third ionization potential is the highest. The divalent chemistry of these elements is alkaline-earth and saltlike; this is described in ***The Divalent State in Solid Rare Earth Metal Halides***.

3 SYNTHESIS

The synthesis of compounds of the lanthanides containing cluster complexes follows in general the same routes as described in ***The Divalent State in Solid Rare Earth Metal Halides***, the conproportionation route and the metallothermic reduction route, for example

$$4\ ScCl_3 + 8\ Sc + 3\ Os \rightarrow 3\ \{OsSc_4\}Cl_4,\ \text{or}$$
$$6\ Rb + 5\ PrCl_3 + 2\ C \rightarrow Rb[\{(C_2)Pr_5\}Cl_{10}] + 5\ RbCl \quad (1)$$

The reactions are carried out at high temperatures (up to 1000 °C) in sealed refractory metal containers (niobium, tantalum) over a prolonged period of time. Details may be found in the literature.[12–14] An advantage of the metallothermic reduction route is the simultaneous production of alkali-metal halides that may serve as a flux for crystal growth; and the disadvantage is that pure single-phase products are obtained only in rare cases. One severe drawback of both methods is that the phase diagrams are not known; therefore research in this area is largely based on intuition and serendipity.

4 LANTHANIDE HALIDES WITH EMPTY CLUSTERS

Sc_7Cl_{10}, LaI, and a number of sesquichlorides and bromides, R_2X_3, seem to be the only true binary reduced rare earth metal halides.[15,16] All the others that had once been claimed as monohalides, such as GdCl,[17] contain some endohedral atom (or atom group) in the center of a cluster, usually a metal octahedron.

Sesquihalides R_2X_3 (X = Cl, Br) have been observed for a number of R metals, namely, Sc, Y, Gd, Tb, and also La, Tm, Lu (which are doubtful), see Table 1. Although the crystal structures of Sc_2X_3 (X = Cl, Br) were never determined because the the crystals grow in extremely thin needles, there is no doubt about their existence, judging from phase diagram determinations. Sc_2Br_3, for example, the only compound in the $ScBr_3$/Sc system, melts incongruently at 880° C. The phase diagram of the $ScCl_3$/Sc system is similar.[18]

Gd_2Cl_3 was the first sesquichloride to be discovered and it is probably the best characterized.[19–22] It melts incongruently at 632 °C. Crystals grow in needles. This is reflected by the crystal structure. It is built from chains of edge-connected $\{Gd_6\}$ clusters surrounded by chloride ions (Figure 7). The parent cluster complex is of the $\{Gd_6\}Cl^i{}_8$ type. Owing to the trans-edge connection of the clusters, the number of chloride ions is reduced through redundancies from eight to six, according to the formulation $\{Gd_{4/2}Gd_{2/1}\}Cl_6$. The Gd-Gd distances are shortest for the connecting edge (335 pm), the others are considerably larger than 370 pm, suggesting weaker metal–metal bonding. Gd_2Cl_3 is a semiconductor and of only marginal stability with respect to the conproportionation reaction, $GdCl_3 + Gd = Gd_2Cl_3$, with $\Delta H^\circ = -30 \pm 15$ kJ mol^{-1}.[22]

Except for Sc_2Cl_3 (= $ScCl_{1.5}$) a slightly further reduced scandium chloride, $ScCl_{1.43}$ (= Sc_7Cl_{10}) was secured that may, as with Gd_2Cl_3, be derived from the parent $\{R_6\}X_8$ cluster complex. Parallel chains of edge-connected $\{Sc_6\}$ octahedra are further connected to double chains as shown in Figure 8; an additional scandium atom resides in octahedral chloride interstices, in accord with the formulation $\{Sc_6\}Cl_{10}Sc$.[23] Again, the edge-shared Sc–Sc distances are the shortest, only 315 pm due to the smaller scandium atoms.

Other reduced scandium halides such as ''Sc_7Cl_{12}'' and ''ScCl'' are not free of interstitial atoms (H, C, N) although ''ScCl'', which crystallizes just like ZrCl, has a double layer structure which would be the end member of further condensation of edge-connected octahedral chains.

Table 1 Binary reduced rare earth metal halides

	Chloride	Bromide	Iodide
Scandium	Sc_2Cl_3, **Sc_7Cl_{10}**	Sc_2Br_3	—
Yttrium	**Y_2Cl_3**	Y_2Br_3	—
Lanthanum	La_2Cl_3	—	**LaI**
Gadolinium	**Gd_2Cl_3**	**Gd_2Br_3**	—
Terbium	**Tb_2Cl_3**	**Tb_2Br_3**	—
Thulium	Tm_2Cl_3	—	—
Lutetium	Lu_2Cl_3	—	—

Bold letters: Structure determined from single crystal data.

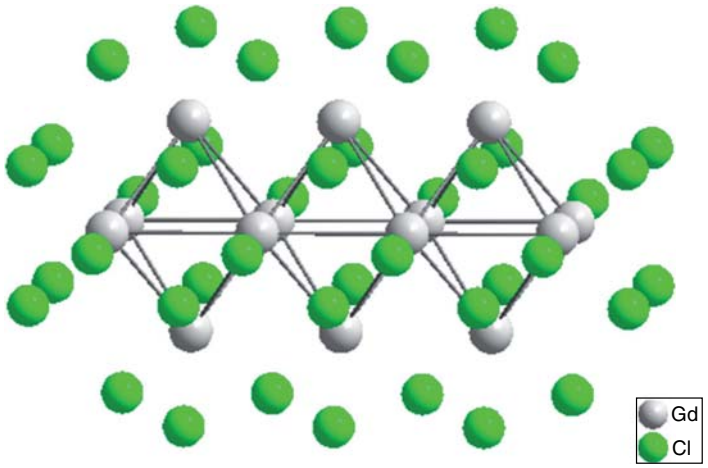


Figure 7 Chains of edge-connected $\{Gd_6\}$ octahedra surrounded by chlorido ligands in the crystal structure of Gd_2Cl_3

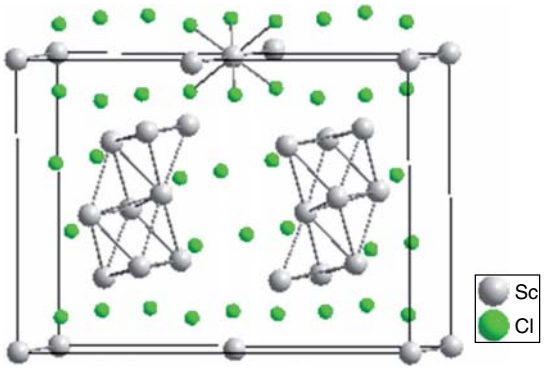


Figure 8 Double chains in the crystal structure of Sc_7Cl_{10} (a) and their connection through an additional scandium atom with the chains running down [010] (b)

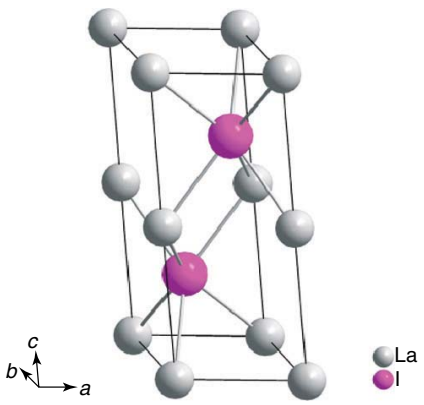


Figure 9 Crystal structure of NiAs-type lanthanum monoiodide, LaI

Lanthanum shows a unique feature with the only true monohalide of the rare earth elements, LaI.[24] It was first obtained by a conproportionation reaction and quite recently stabilized with aluminum as $(La_{1-x}Al_x)I$ with $x < 0.15$. Through metallothermic reduction of LaI_3 and LaI_2, it is now available as pure phase.[25] LaI crystallizes with the NiAs type of structure (Figure 9), although with an unusual c/a ratio of 2.47. There are two electrons available for La–La bonding. The bonding interactions are stronger parallel (001), reflected by d(La–La) = 393 pm, than in the [001] direction, d(La–La) = 485 pm. LaI shows metallic behavior.

5 HALIDES WITH CLUSTER COMPLEXES CENTERED BY ENDOHEDRAL ATOMS

The vast majority of metal-rich rare earth-metal halides form clusters $\{R_x\}$ that incorporate an atom Z, or a small atom group, in the center of the cluster, hence heteroatomic clusters $\{ZR_x\}$ need to be considered. These clusters are surrounded by ligands, usually halido ligands X^- of the triad chloride, bromide, and iodide. Figure 10 depicts such an isolated cluster complex $[\{ZR_6\}X^i{}_{12}X^a{}_6]^{n-}$.

In these cluster complexes, the endohedral atom Z is considered as the central atom (be it a nonmetal or a metal atom), which is surrounded by metal atoms R with a coordination number of—in the majority of cases—six (CN_6), as shown in Figure 10. This $\{ZR_6\}$ unit is a complex *anti* to Werner's classical complexes in that the charges, or better, polarities, of the central and the coordinating atoms are opposite to those in Werner complexes. We shall call it a cluster although it would not qualify as such according to a definition by Cotton, in that ''a metal atom cluster may be defined as a group of two or more metal atoms in which there are substantial and direct bonds between the metal atoms.''[1] In the present $\{ZR_6\}$ clusters, bonding interactions are mainly heteroatomic Z–R, with minor R–R contributions. This is symbolized by the thickness of the ''bonding sticks''

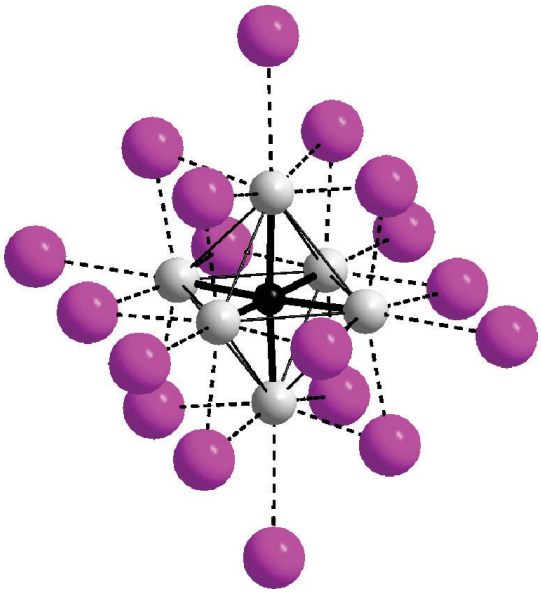


Figure 10 Isolated cluster complex with endohedral atom, $[\{ZR_6\}X^{i}{}_{12}X^{a}{}_{6}]^{n-}$

in Figure 10. Further polar bonding results from R···X interactions. In the following, $[\{ZR_6\}X^{i}{}_{12}X^{a}{}_{6}]^{n-}$ type cluster complexes are regarded as *anti*-Werner complexes,[4] for the following reasons.

In a typical Werner complex, such as in solid $[PtCl_6]K_2$, to use the original formulation (today we usually write $K_2[PtCl_6]$),[26] the central atom as the zeroth coordination sphere is surrounded by six chlorido ligands as the first coordination sphere followed by eight potassium cations in the second coordination sphere, see Figure 11. In a purely ionic description this would read $[(Pt^{4+})(Cl^{-})_6](K^{+})_2$, or simplified $[+-]+$.

In $Cs_2Lu_7Cl_{18}C$, as has been written previously, a single carbon atom (central atom, zeroth coordination sphere) is surrounded by an octahedral cluster of six lutetium atoms, which is written as $\{CLu_6\}$ to distinguish a Werner complex from an *anti*-Werner complex. This ''cluster'' is surrounded (in the second coordination sphere to the central carbon atom) by 12 chlorido ligands capping the edges of the cluster and 6 terminal chlorido ligands (capping the corners), and in third coordination sphere by 12 cesium cations. A seventh lutetium cation fills octahedral holes that are provided by the chlorido ligands in the crystal structure, see Figure 11. Thus, $Cs_2Lu_7Cl_{18}C$ should better be written as $[\{CLu_6\}Cl_{12}{}^{i}Cl_6{}^{a}]Cs_2Lu$, as this formulation carries structural information. Note that $[\{CLu_6\}Cl_{12}{}^{i}Cl_6{}^{a}]Cs_2Lu$ is also a Werner complex as the whole cluster $\{CLu_6\}$ could be considered a ''super central atom'' with coordination number 18. The anion $[\{CLu_6\}Cl_{18}]^{5-}$ needs to be called a ''cluster complex.'' In a purely ionic description, this compound would have to be formulated as $[\{(C^{4-})\ (Lu^{3+})_6\}(Cl^{-})_{18}](Cs^{+})_2(Lu^{3+})$. There would be one excess electron; of course, this is an oversimplified picture but it shows that the charges in the succession of coordination spheres move in a direction, $[\{-+\}-]+$, opposite to Werner's classical complexes.

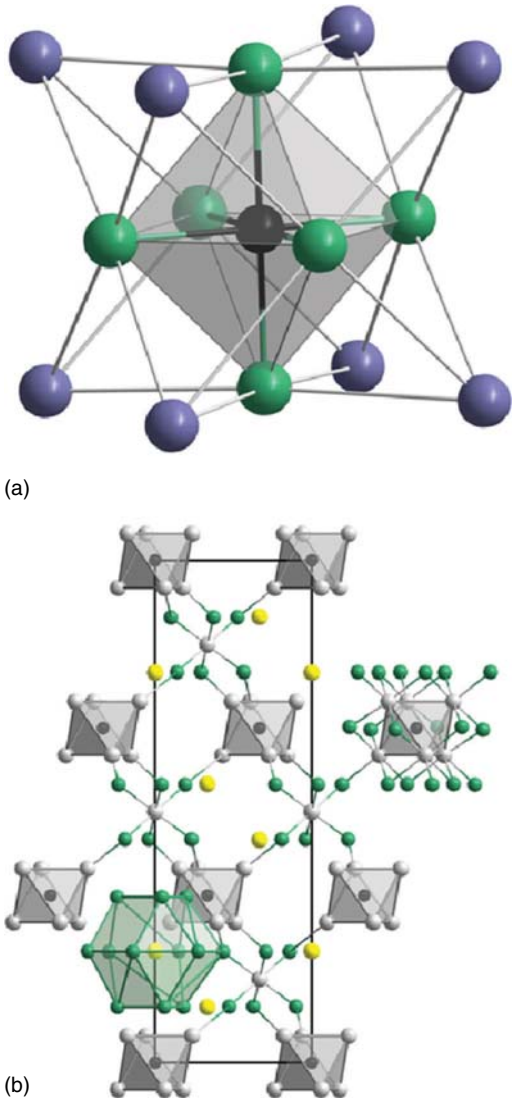


Figure 11 (a) Werner complex, $[PtCl_6]K_{8/4}$, with a central metal atom (Pt^{4+}) surrounded by six ligands (Cl^{-}) in the first and eight (K^{+}) in the second coordination sphere, hence with polarities $[+-]+$. (b) An analogous picture for the cluster complex salt $[\{CLu_6\}Cl_{12}{}^{i}Cl_6{}^{a}]Cs_2Lu$ with polarities of $[\{-+\}-]+$, an *anti*-Werner cluster complex

Cluster complexes that obey Cotton's strict definition such as $[\{Nb_6\}Cl_{18}]K_4$ and $[\{Mo_6\}Cl_{14}]Cs_2$ have 16 and 24 electrons, respectively, for bonding interactions within the octahedral niobium and molybdenum clusters. In a VB picture, these electrons are consumed for eight two-electron-three-center (2e–3c) or 12 2e–2c bonds, situated in the eight triangular faces and the 12 edges of the respective octahedra.

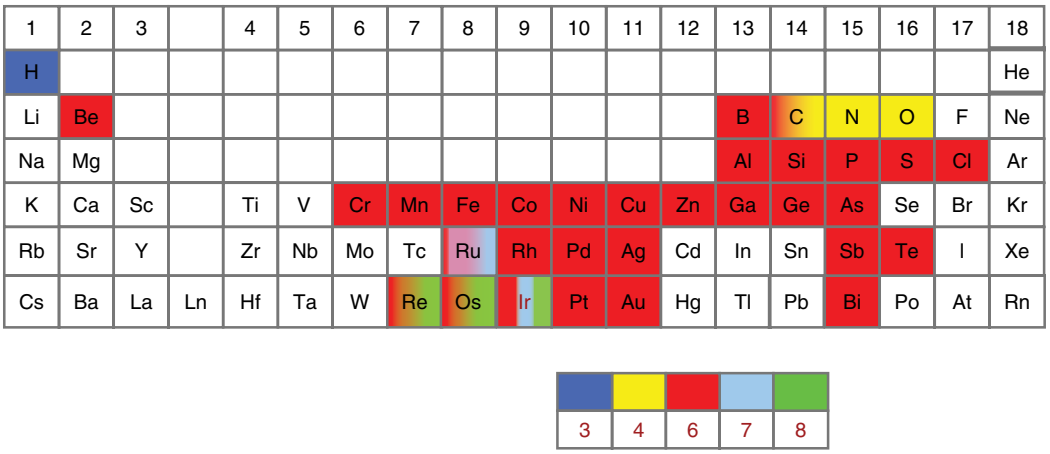


Figure 12 Endohedral atoms Z (colored for their different coordination numbers) as found in cluster complexes $[\{ZR_6\}X^i_{12}X^a_6]^{n-}$

Group 3 elements have only three VEs to contribute to intracluster bonding because the 4f electrons of the lanthanoid elements are rather corelike and can thus not be involved in bonding. Compounds such as $[\{\square Lu_6\}Cl_{18}]Cs_2$, $[\{\square Lu_6\}Cl_{18}]Cs_4$, or $[\{\square Lu_6\}Cl_{18}]Cs_2Lu$ would only have 2, 4, and 5 electrons for Lu–Lu bonding, which is much less than 16! The endohedral carbon atom is needed to contribute its four VEs. Still, with nine electrons, $[\{CLu_6\}Cl_{18}]Cs_2Lu$ is very electron poor and remains a mystery. As the carbon atom is more electronegative than the lutetium atoms, these nine electrons cannot be used for Lu–Lu bonding.

Therefore, bonding in the clusters that are discussed in this chapter is predominantly Z–R bonding. The paucity of electrons is also the reason that isolated cluster complexes are rare. The connection of clusters (mostly) via common edges to oligomers or extended structures (chains, layers) saves electrons and thereby contributes to the stability of these compounds.

An endohedral atom sequestered in a cluster needs space. Therefore, only hydrogen can be incorporated in triangles, but hydrogen atoms are also found in tetrahedra or octahedra (sometimes two H atoms in one octahedron, or seven capping statistically the eight faces). Oxygen, nitrogen, and carbon as electronegative atoms qualify for tetrahedral interstices; nitrogen and carbon are also found in octahedral clusters. Most of the other endohedral atoms see Figure 12 occupy octahedral interstices. Only a few clusters have higher nuclearities; large atoms such as ruthenium, osmium, and iridium are needed for coordination numbers of 7 and 8, only in extended structures.

5.1 Tetrahedral Clusters, {ZR$_4$}

Oxide-halides of the alkaline-earth-like divalent lanthanides, $\{OR_4\}X_6$ (R = Eu, Yb, Sm) are discussed in ***The Divalent State in Solid Rare Earth Metal Halides***. Although, these have the topology of cluster complexes with isolated $\{OR_4\}$ clusters, the R^{2+} ions have $4f^n5d^0$ configurations and the compounds are therefore best considered as ionic, $\{(O^{2-})(R^{2+})_4\}(X^-)_6$. There is, however, a lanthanum bromide, $\{ZLa_4\}Br_7$ (the nature of Z, be it O or N, is not really clear), with a structure similar to that of $\{OR_4\}X_6$, but the connection between the cluster complexes via common bromide ions is different in $\{ZLa_4\}Br_7$; Figure 13 shows one isolated $\{ZLa_4\}$ cluster and the surrounding ligands.[27]

Except for this monomeric cluster complex, there are tetrahedral clusters with Z = O, N that have edge-connected $\{ZR_4\}$ tetrahedra, either as dimers or chains. The dimers are not so frequent but have first been observed for $Gd_3NCl_6 = \{NGd_{2/2}Gd_{2/1}\}Cl_6$.[28] The dimers may be connected in different ways to chains. Most frequently observed is the connection via two trans-edges as in $Gd_2NCl_3 = \{NGd_{4/2}\}Cl_3$, see Figure 14. The composition $\{NR_2\}Cl_3$ is known for R = La, Cr, Pr, Nd, Gd, Y and comes with two structure types where the larger lanthanides form a more symmetric structure (R = La, Ce, Pr) than the smaller ones (R = Nd, Gd, Y).[29,30] The dimers may also be connected via four common vertices to a double chain as observed for another modification of Gd_2NCl_3 (named β). There are a number of other compositions that include trans-edge connected tetrahedral chains, for example, $[\{ZPr_{4/2}\}_2Cl_9]Na_2$[31–33] or $[\{ZLa_{4/2}\}_2I_8]Ba$ with Z = O, N.[27]

Although carbon atoms in tetrahedral clusters are rare, they have been found in the isolated cluster in $\{CCe_4\}Cl_8$[34] as well as in tetrahedral dimers (two tetrahedra sharing a common edge) in $\{C_2La_6\}Br_9$ and $\{C_2Pr_6\}Cl_{10}$.[35,36] They have also been found in the supertetrahedral molecular cluster complex $\{Sc_4C_{10}Sc_{20}\}I_{30}$; in this spectacular compound, an inner empty $\{Sc_4\}$ tetrahedron is surrounded by 10 carbon atoms such that a T2–$\{Sc_4C_{10}\}$ supertetrahedron appears, which is incorporated in a T3–Sc_{20} supertetrahedron; the $\{Sc_4C_{10}Sc_{20}\}$ cluster is enveloped in a truncated and hollow T4–I_{30} supertetrahedron, see Figure 15.[37] If viewed in an ionic model, $(Sc^{3+})_{24}(C^{4-})_{10}(I^-)_{30}$, there are two excess electrons that are believed, in a local bonding model, to reside

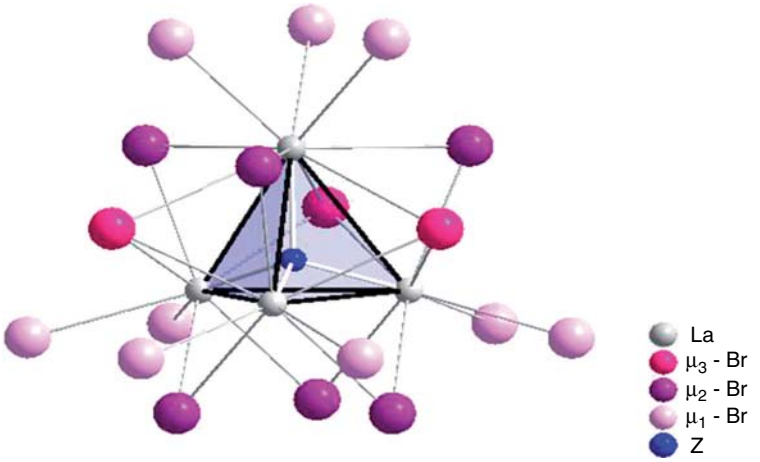


Figure 13 Isolated $\{ZLa_4\}$ clusters and their surrounding ligands in the crystal structure of $\{ZLa_4\}Br_7$

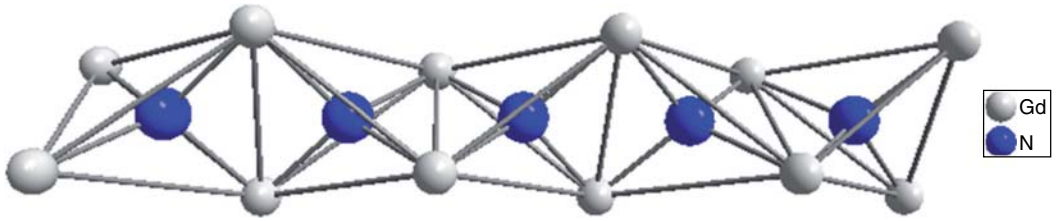


Figure 14 Edge-connected $\{ZR_4\}$ clusters in the crystal structure of, e.g., α-$\{NGd_{4/2}\}Cl_3$

in a 4c–2e orbital of the same shape as the inner $\{Sc_4\}$ cluster. This is then an analogous situation as in the naked $\{Au_{20}\}$ cluster, a T3 supertetrahedron with 20 electrons, consisting of 10 tetrahedra and thus with 10 4c–2e ''bonds.''[38,39]

5.2 Trigonal Bipyramidal Clusters, $\{ZR_5\}$

Two tetrahedra sharing a common face form a trigonal bipyramid, $\{R_5\}$. This appears to be an exceptional case, because it is only seen with a dicarbon unit centering the two tetrahedra and arranged along the threefold axis. This motif was first observed for $[\{C_2Pr_5\}Cl_{10}]Rb$, see Figure 16.[40] The cluster complex anion represents a three-dimensional network, $[\{C_2Pr_5\}Cl^{i-a}{}_{9/2}Cl^{a-i}{}_{9/2}Cl^{a-a-a}{}_{3/3}Cl^{a}{}_{3/3}]^-$, in which the Rb^+ cations are incorporated. There is a small class of compounds with the compositions $[\{C_2R_5\}X_{10}]A$ and $[\{C_2R_5\}X_9]$ with, in principle, A = K, Rb; R = La, Ce, Pr, Nd, X = Cl, Br, I.[40–45]

In all these compounds, the C–C distance is in the range of a single bond such that a C_2^{6-} ''anion'' can be assumed or, in other words, this ethanide unit contributes six electrons to intracluster bonding, which is mostly C–Pr interactions. All of these halides, $[\{C_2R_5\}X_{10}]A$ and $[\{C_2R_5\}X_9]$, have the same number of electrons, 12, for intracluster bonding. In an oversimplified picture, these 12 electrons could be attributed to six 3c–2e ''bonds,'' associated with the six triangular faces of the trigonal bipyramid.

5.3 Monomeric Octahedral Clusters, $\{ZR_6\}$

By far, the largest group of reduced rare earth metal halide cluster complexes contains octahedral $\{ZR_6\}$ clusters. They may be distorted directing to a trigonal prism or two tetrahedra sharing a common edge. We will, however, not trouble ourselves with these peculiarities, as important as they might be for the ''fine structure'' of chemical bonding in these metal-rich compounds.

Isolated octahedral clusters are scarce. There appears to be only one example, $Cs_2Lu[\{CLu_6\}Cl_{18}]$, in which not only the $\{CLu_6\}$ cluster is isolated but also the $[\{CLu_6\}Cl_{18}]^{5-}$ cluster complex unconnected.[46] The most prolific families with isolated clusters are the so-called 7–12 and 6–10 type compounds, halides of the compositions $\{ZR_6\}X_{12}R$ and $\{ZR_6\}X_{10}$. These are mostly iodides; for the 6–10 type, bromides are equally frequent, perhaps a packing problem.[47]

The crystal structure of the $\{ZR_6\}X_{12}R$ type consists of $\{ZR_6\}$ ''octahedra'' of 3 or usually –3 symmetry. These are surrounded by 18 X^- ligands that connect the cluster complexes to a three-dimensional structure according to $\{ZR_6\}X^{i}_{6/1}X^{i-a}{}_{6/2}X^{a-i}{}_{6/2}$ with additional R^{3+}

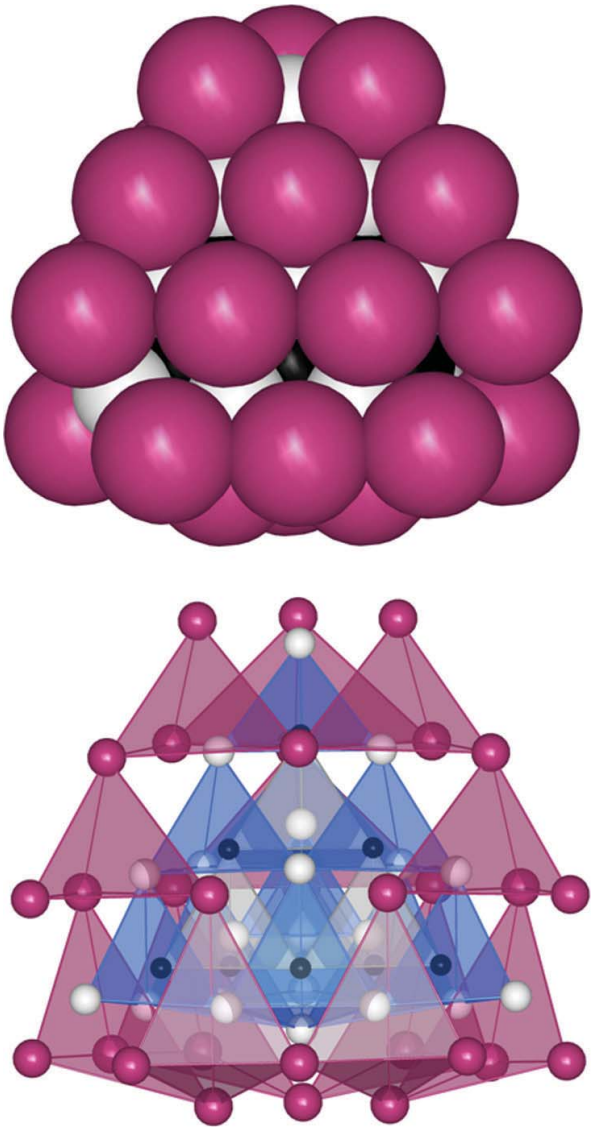


Figure 15 The $\{Sc_4C_{10}Sc_{20}\}I_{30}$ cluster complex molecule shown both as a space filling and a polyhedral model

in octahedral holes. Figure 17 shows, for the example of $\{IrEr_6\}I_{12}Er$, the sequence of one $\{IrEr_6\}I^i{}_{12}I^a{}_6$ cluster complex and two connected $[ErI_6]$ octahedra. The connection of the cluster complexes with each other is depicted in Figure 18. In $\{IrEr_6\}I_{10}$, for example, the connectivity between the cluster complexes is more pronounced, according to $\{IrEr_6\}I^i{}_{2/1}I^{i-i}{}_{4/2}I^{i-a}{}_{6/2}I^{a-i}{}_{6/2}$, see Figure 19. Endohedral atoms that have been observed for both types are mostly group 8–10 metal atoms, also B, C, and N for the 7–12 type.[47–50] C_2 is also an option as $\{C_2Dy_6\}I_{12}Dy$ shows.[51] Rare earth elements that form these two types of compounds are, in principle, all that are marked red in Figure 6. Electron counts, i.e., the number of electrons that are available for intracluster Z–R bonding, are between 11 and 14 for main-group Z and from 15 to 21 for transition-metal Z atoms.

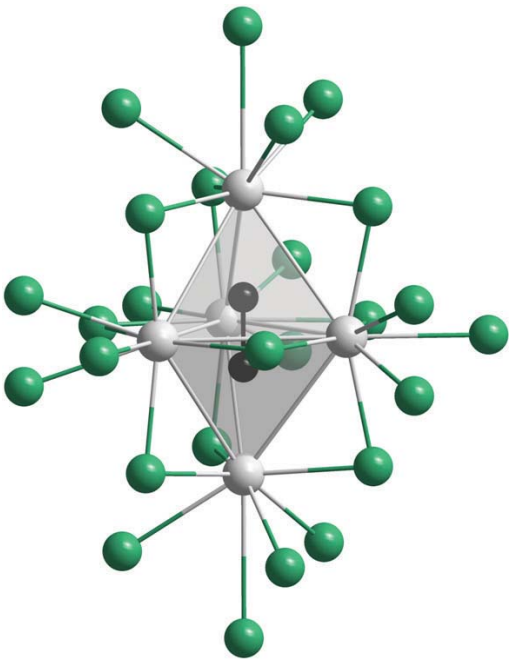


Figure 16 The cluster complex $\{C_2Pr_5\}Cl_{24}$ as it appears in the crystal structure of $[\{C_2Pr_5\}Cl_{10}]Rb$

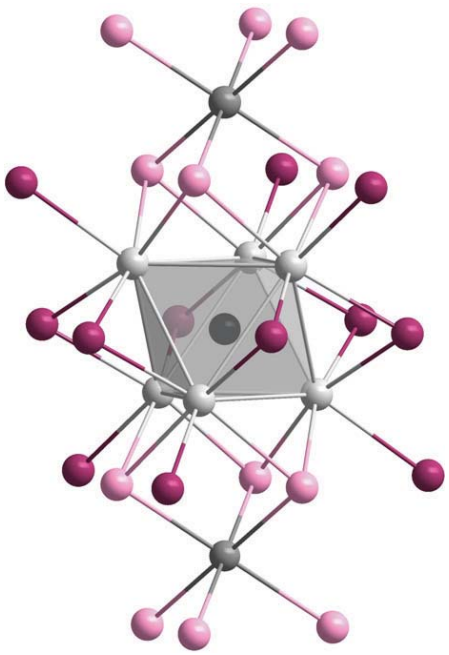


Figure 17 Cluster complex $\{IrEr_6\}I^i{}_{12}I^a{}_6$ connected with $[ErI_6]$ octahedra in $\{IrEr_6\}I_{12}Er$

Isolated clusters are also found in compounds such as $\{C_2Sc_6\}I_{11}$ or $\{RuY_6\}I_{10}$ with different connections of the 6–12 clusters to chains.[49,52] During the exploration of the

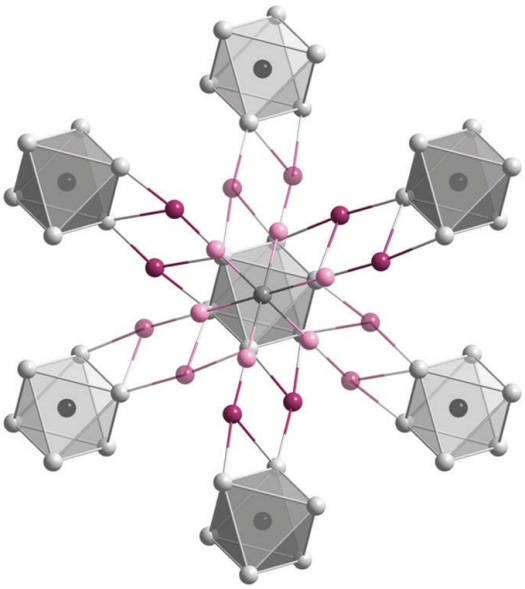


Figure 18 Interconnection of the cluster complexes $\{IrEr_6\}I^i{}_{12}I^a{}_6$ in $\{IrEr_6\}I_{12}Er$

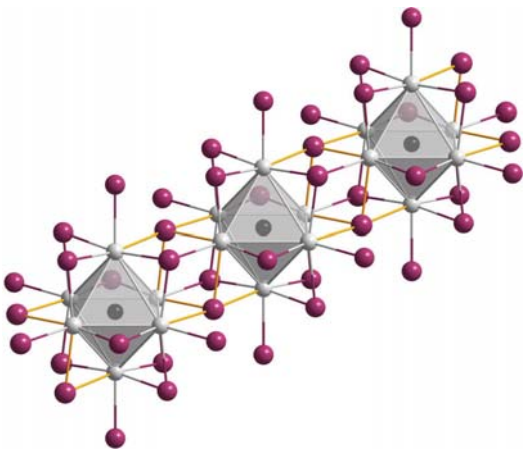


Figure 19 Interconnection of the cluster complexes $\{IrEr_6\}I^i{}_{12}I^a{}_6$ in $\{IrEr_6\}I_{10}$

metallothermic reduction of rare earth metal trihalides with alkali metals, a small number of compounds with isolated clusters have been obtained, all with single carbon or dicarbon units sequestered in an octahedron of metal atoms R = Sc, Pr, Er, Lu, for example, $[\{CEr_6\}I_{12}]Cs$ or $[\{C_2Pr_6\}I_{13}]Cs_4$. Electron counts are low, between 9 in $[\{CLu_6\}Cl_{18}]Cs_2Lu$ and 15 in $[\{C_2Pr_6\}I_{13}]Cs_4$.[53]

5.4 Oligomeric Clusters

Two octahedra sharing a common edge have first been found for $Gd_5Cl_9C_2 = \{(C_2)_2Gd_{10}\}Cl_{18}$.[54] In its structure

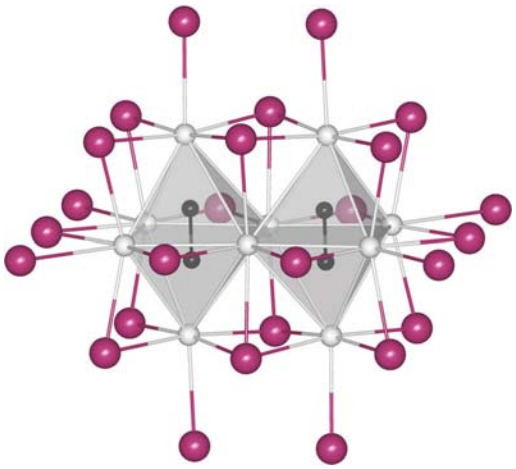


Figure 20 The $\{(C_2)_2R_{10}\}X_{26}$ dimer as it appears for example in $Cs[\{(C_2)_2Er_{10}\}I_{18}]$

and the structures of a number of ternary and quaternary halides with R = Gd, Tb, Er, Y, C_2 dumbbells as the endohedral unit are observed, see Figure 20 (boron and transition metal atoms were also observed as Z). In all of these, the parent unit $\{(C_2)_2R_{10}\}X_{26}$ is connected via halide bridges to three-dimensional structures, such that a halide stoichiometry between X_{16} and X_{21} is achieved.[53] An example for the highest halide content, and thus with the least connections of the dimers via halide bridges is $Cs_3[\{(C_2)_2Tb_{10}\}Cl_{21}] = Cs_3[\{(C_2)_2Tb_{10}\}Cl^i{}_{18/1}Cl^{i-i}{}_{2/2}Cl^{i-a}{}_{2/2}Cl^{a-a}{}_{2/2}]$.[55]

Two types of trimers were recently found. Open, trans–trans edge-connected trimers in $\{(C_2)_3R_{14}\}I_{20}$ with R = La, Ce, Pr,[56,57] see Figure 21. There is evidence from high-resolution transmission microscopic pictures that higher all-trans-edge connected oligomers exist before the infinite chains appear. Closed trimers have been observed for the first time for $\{Ir_3Gd_{11}\}Br_{15}$; the $\{Ir_3Gd_{11}\}$ part of the structure is isostructural with $\{O_3Cs_{11}\}$, see Figure 21.[58]

Two types of tetramers have been observed in crystal structures, but neither of them are all trans-edge connected. Rather the connection is trans–cis–trans in the tetrameric units $\{Z_4R_{16}\}X_{36}$ (Figure 22) that appear in $\{B_4Tb_{16}\}Br_{23}$[59] and $\{Ru_4Gd_{16}\}Br_{23}$[60]. In both compounds B and Ru atoms, respectively, center R_6 octahedra; the endohedral atoms build a rhombus. B–B distances within that rhombus are around 410 pm, whereas Ru–Ru are much shorter, with only 340 pm for the short diagonal and 370 pm for the edges. This hints at much stronger Ru–Ru than B–B bonding.

In an alternative, closed tetramer that was first observed for $\{Ru_4Y_{16}\}I_{20}$,[61] the endohedral atoms form a tetrahedron. The parent unit has the composition $\{Z_4R_{16}\}X_{36}$. There is a remarkable structural diversity with compositions as shown in Table 2.[61–67] Especially remarkable is the composition ZR_5X_7, for example $\{Ru_4Ho_{16}\}I_{20}\{\square Ho_4\}I_8$ (Figure 23), as it not only contains the iodide-bridged tetramer $\{Ru_4Ho_{16}\}I_{36}$ but also an empty tetrahedral cluster $\{\square Ho_4\}I_8$

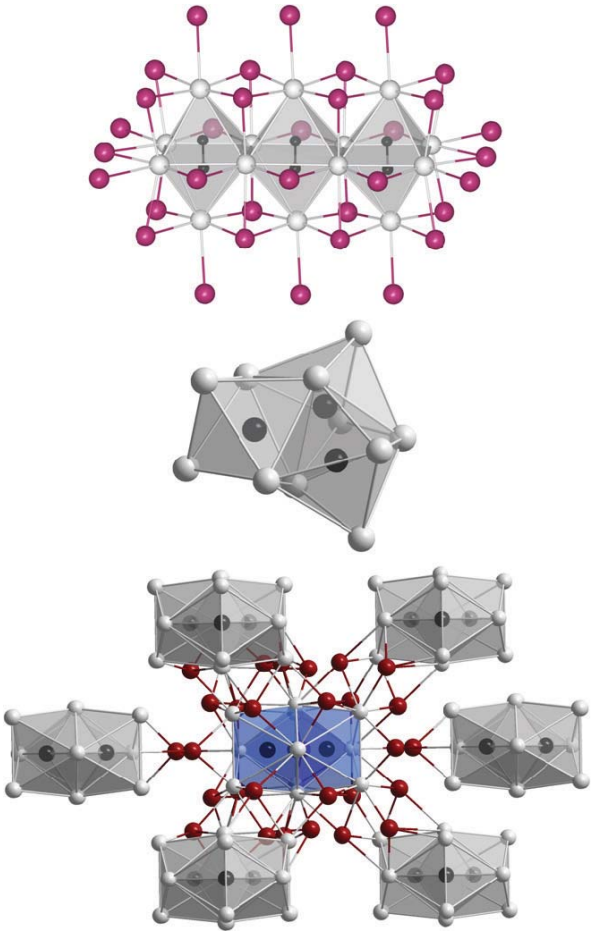


Figure 21 Open and closed trimers as they appear in, for example, $\{(C_2)_3Pr_{14}\}I_{20}$ and $\{Ir_3Gd_{11}\}Br_{15}$

which is isostructural with that first found in PrI_2–V.[68] When scaled to one endohedral atom Z, all these clusters have 15 ± 1 cluster-based electrons.

Hetero-endohedral cluster tetramers have been observed in $\{(C_2)_2(O)_2Dy_{14}\}I_{24}$. The terameric units $\{(C_2)_2(O)_2Dy_{14}\}I_{32}$ (Figure 24) are connected via i–a and a–i bridges to chains.[69]

Finally, spectacular pentameric units have been observed for $\{Ru_5La_{14}\}Cl_{20}$[70] and $\{Ru_5La_{14}\}_2Br_{39}$ (Figure 25).[71]

5.5 Single and Double Chains of Clusters

An infinite extension of the dimers, trans-trimers, and the trans–cis tetramers leads to chains, either linear or zigzag. In all cases, (less or more distorted) octahedral clusters $\{ZR_6\}$ are connected via common edges to chains in accord with the general formula $\{Z_xR_{4x+2}\}$; with $x \to \infty$, the formula type $\{ZR_4\}X_6$ results. There is a slowly growing number of examples, and they can be divided in three groups: I represents

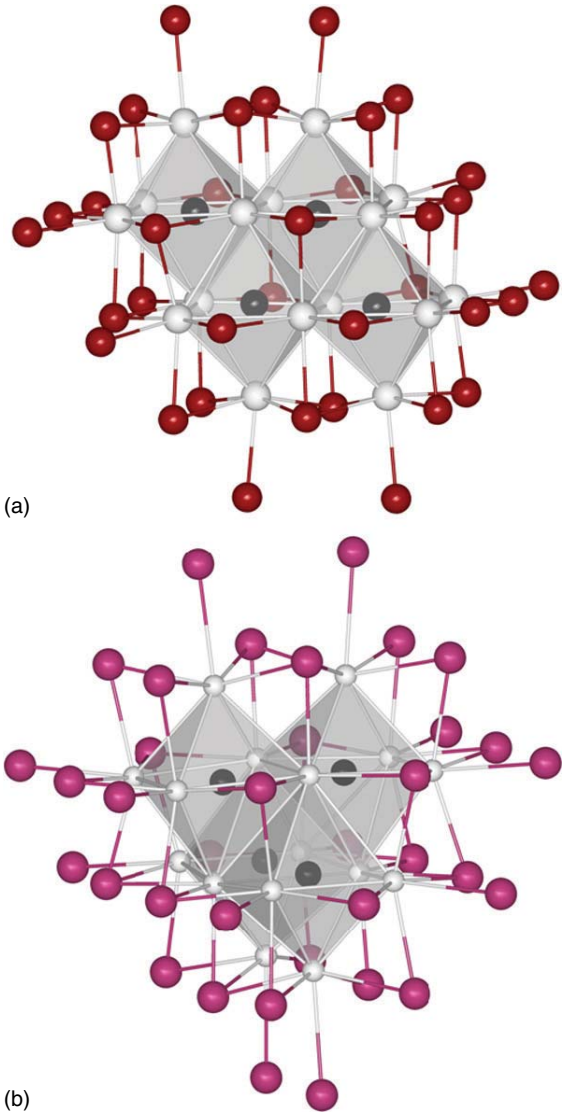


Figure 22 Two tetramers, $\{Z_4R_{16}\}X_{36}$ (a) and $\{Z_4R_{16}\}X_{36}$ (b), as they appear in, for example, $\{Ru_4Gd_{16}\}Br_{23}$ and $\{Ru_4Y_{16}\}I_{20}$, in which the endohedral Ru_4 tetramers build a rhombus and a tetrahedron, respectively

Table 2 Cluster complex tetramers $\{Z_4R_{16}\}X_{36}$ as incorporated in four different compositions

	Examples	$n(e^-)$
ZR_4X_5	$\{Fe_4Sc_{16}\}X_{20}$ (X = Cl, Br)	15
	$\{Ru_4Y_{16}\}X_{20}$ (X = Br, I)	15
	$\{Os_4Sc_{16}\}Br_{20}$	15
ZR_4X_6	$\{Ir_4Y_{16}\}Br_{24}$ (X = Cl, Br)	15
ZR_5X_7	$\{Z_4Sc_{16}\}Br_{20}\{\square Sc_4\}Br_8$ (Z = Mn, Fe, Ru, Os)	15/16
	$\{Mn_4Gd_{16}\}I_{20}\{\square Gd_4\}I_8$	15
	$\{Ru_4Ho_{16}\}I_{20}\{\square Ho_4\}I_8$	16
ZR_5X_9	$\{Z_4Sc_{16}\}Cl_{24}(ScCl_3)_4$ (Z = Ru, Os, Ir)	14/15
	$\{Z_4Y_{16}\}Br_{24}(YBr_3)_4$ (Z = Ru, Ir)	14/15
	$\{Z_4Tb_{16}\}Br_{24}(TbBr_3)_4$ (Z = Rh, Ir)	15

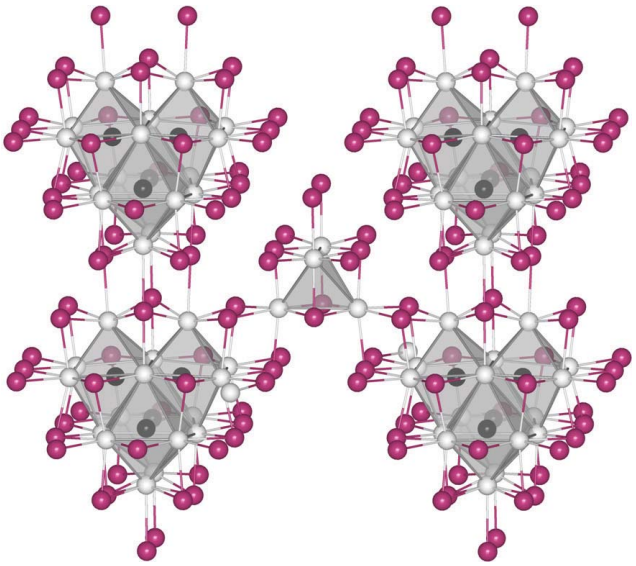


Figure 23 Part of the crystal structure of $RuHo_5I_7 = \{Ru_4Ho_{16}\}I_{20}\{\square Ho_4\}I_8$, exhibiting the empty $\{Ho_4\}$ cluster in the center

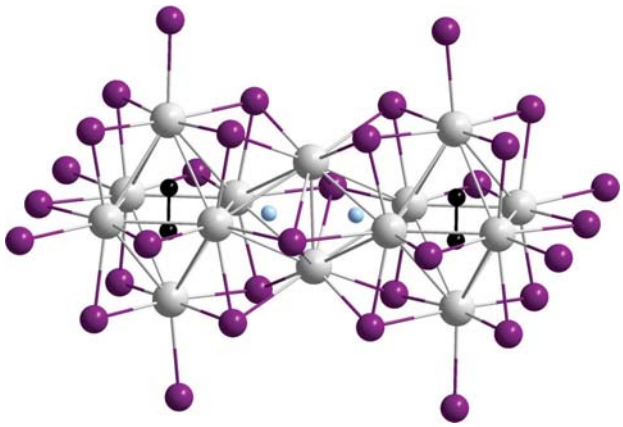


Figure 24 The tetrameric hetero-endohedral unit $\{(C_2)_2(O)_2Dy_{14}\}I_{32}$, as observed in $\{(C_2)_2(O)_2Dy_{14}\}I_{24}$ and $\{(C_2)_2(O)_2Dy_{12}\}I_{18}$

a rather highly symmetric chain, Figure 26, and was observed for $\{ZSc_4\}Cl_6$ (Z = B, N) and $\{SiR_4\}Br_6$ (Z = Gd, Tb).[50,72,73] The inclusion of C_2 dumbbells oriented along one of the fourfold axes of the R_6 octahedra leads to elongations in this direction, for which two varieties have been observed, IIa, $\{(C_2)R_4\}I_6$ (Dy, Er)[66,74] and IIb, $\{(C_2)Sc_4\}I_6$,[52] (Figure 26). Small clusters, $\{Sc_6\}$, and large ligands, I^-, cause the most severe distortions of the previously linear chain. In group III, edge-connected dimers are connected via further edges to a zigzag chain (Figure 26).[67,75–77]

In the chains of group IIa, octahedra are, alternatively, elongated and compressed. The compressed octahedra can also be viewed as two tetrahedra sharing a common edge, with the edge passing through the middle of the C–C bond.

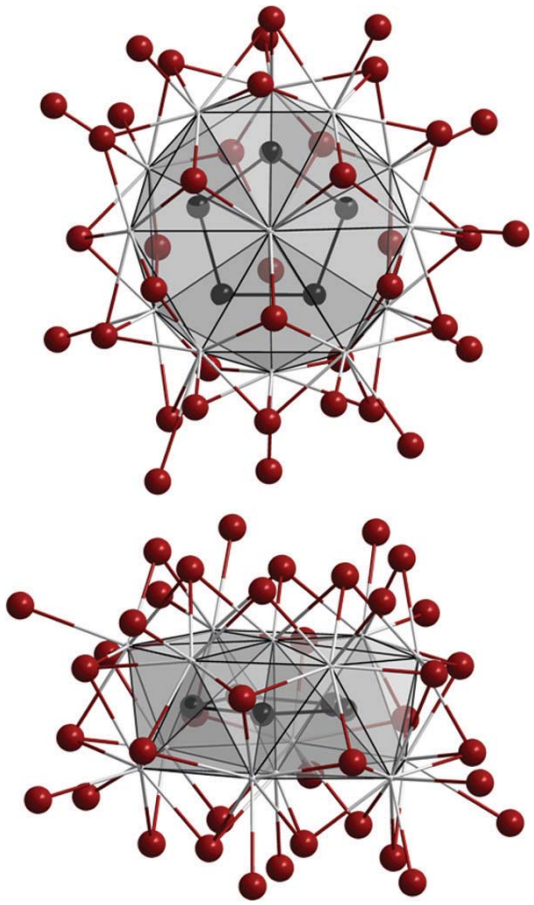


Figure 25 The pentameric cluster complex unit $\{Ru_5La_{14}\}Br_{39}$ (top and side views) in the crystal structure of $\{Ru_5La_{14}\}_2Br_{39}$

One octahedron added and two carbon atoms substituted by oxygen atoms, lead to a tetrameric unit, for example $\{(C_2)_2(O)_2Dy_{14}\}I_{32}$, see Figure 24. These tetramers may be connected via common edges to an infinite chain, as observed in $\{(C_2)_2(O)_2Dy_{12}\}I_{18}$ (Figure 27) such that (elongated) octahedra (O) and tetrahedra (T) are all edge-connected with a sequence of $\cdots$OOTT$\cdots$.[69]

Chains as observed for group I, $\{ZSc_4\}Cl_6$ (Z = B, N) and $\{SiR_4\}Br_6$ (Z = Gd, Tb), are also observed in compounds with other stoichiometries, $\{ZR_4\}X_5$ and $\{ZR_4\}X_8R$, respectively. In the beginning, both formula types were addressed as binaries, for example Er_4I_5 and Sc_5Cl_8.[78–85] In $\{ZR_4\}X_5$ type compounds, for example, $\{CY_4\}I_5$ or $\{SiGd_4\}I_5$, the chains are further connected via halide ligands to layers, see Figure 28. In $\{ZR_4\}X_8R$, the chains are connected via additional metal halide octahedra, as for example in $\{CSc_4\}Cl_8Sc$, see Figure 28.

Single chains similar to those as observed in group III $\{ZR_4\}X_6$ halides are also found for the $\{(C_2)R_4\}X_{5.67} = \{(C_2)R_4\}_3I_{17} = R_{12}(C_2)_3I_{17}$ family, R = La, Cr, Pr, Nd, Gd, Dy, with trans–cis–cis connections throughout the corrugated chains, see Figure 29.[86–88]

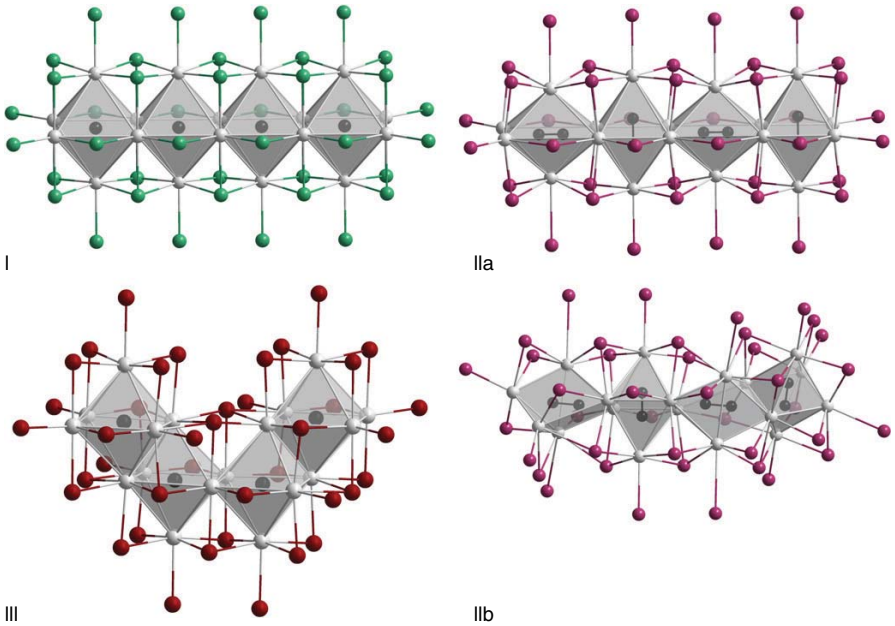


Figure 26 The variety of chains of edge-connected $\{ZR_6\}$ octahedra in $\{ZR_4\}X_6$ type compounds

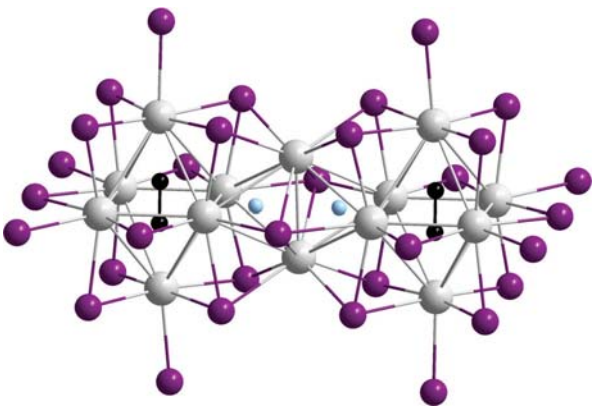


Figure 27 Part of the infinite chain of edge-connected octahedra and tetrahedra ($\cdots$OTTO$\cdots$) as observed in $\{(C_2)_2(O)_2Dy_{12}\}I_{18}$

The $\{ZR_3\}X_3$ stoichiometry is found for the usual suspects, R = La, Ce, Pr, Gd, Tb, Y, Er, and with a great variety of endohedral atoms, Z = B, C, C_2, Si, P, Ga, As, Sb, Pb, Co, Ru, Rh, Os, Ir, Pt, Au; iodides and bromides are more frequent than chlorides, so far. $\{CGd_3\}Cl_3$ was perhaps the first to be observed.[89] Its structure is also known from the insulator $\{PCa_3\}I_3$ and may be understood as an ordered and defective derivative of the rocksalt type of structure. The structure is still cubic, although noncentrosymmetric in space group $I4_132$ and can be understood as built of interpenetrating edge-connected helical chains, see Figure 30. An orthorhombic variant ($C222_1$) has been observed with C_2 units for $\{(C_2)R_3\}Br_3$ (R = La, Ce).[90]

The chains as they were observed first for monoclinic $\{RuPr_3\}I_3$[91,92] can either be understood as if $\{ZR_4\}X_6$ type single chains were connected to a double chain, or, likewise as zigzag chains of edge-connected octahedra, see Figure 31. The Z–R distances are rather uniform in $\{RuPr_3\}I_3$ but the relative sizes of the Z and R atoms seem to have some effect on their spread. Distortions of the edge-connected $\{ZR_6\}$ octahedra direct at monocapped trigonal prisms, see Figure 31. Peculiar R/Z/X size ratios appear to be responsible for the degree of distortion and the actual space group symmetry. Distortions appear to be larger for bromides and especially chlorides. $\{RuPr_3\}Cl_3$ is an example for a pronounced distortion that, however, leads to a higher space group symmetry (Pnma).[93] When moving from $\{RuPr_3\}I_3$ (almost undistorted edge-connected octahedra) on to $\{RuPr_3\}Cl_3$ (face-sharing distorted monocapped trigonal prisms), these distortions also have their effect on the electronic structure; for example, Ru–Ru bonding is negligible in $\{RuPr_3\}I_3$, whereas it is rather pronounced in $\{RuPr_3\}Cl_3$, although there are also considerable antibonding interactions closer to the Fermi level, see Figure 32.[94]

As just mentioned for $\{ZR_3\}X_3$ type compounds, the edge-connected zigzag chains $\{ZR_{6/2}\}$ may also be understood as double chains of edge-connected single chains, $\{ZR_4\} = \{ZR_{2/1}R_{4/2}\} \rightarrow \{ZR_{1/1}R_{2/2}R_{3/3}\}$. Such double chains were first observed for the binary Sc_7Cl_{10}, see Chapter 4. With good approximation, the same structure is adopted by $\{ZSc_3\}_2Cl_{10}Sc$ with Z = C, N, see Figure 33.[95,96] There is a 7% volume decrease from $\{Sc_3\}_2Cl_{10}Sc$ to $\{CSc_3\}_2Cl_{10}Sc$ attesting for the contraction of the scandium clusters due to C/N–Sc bonding.

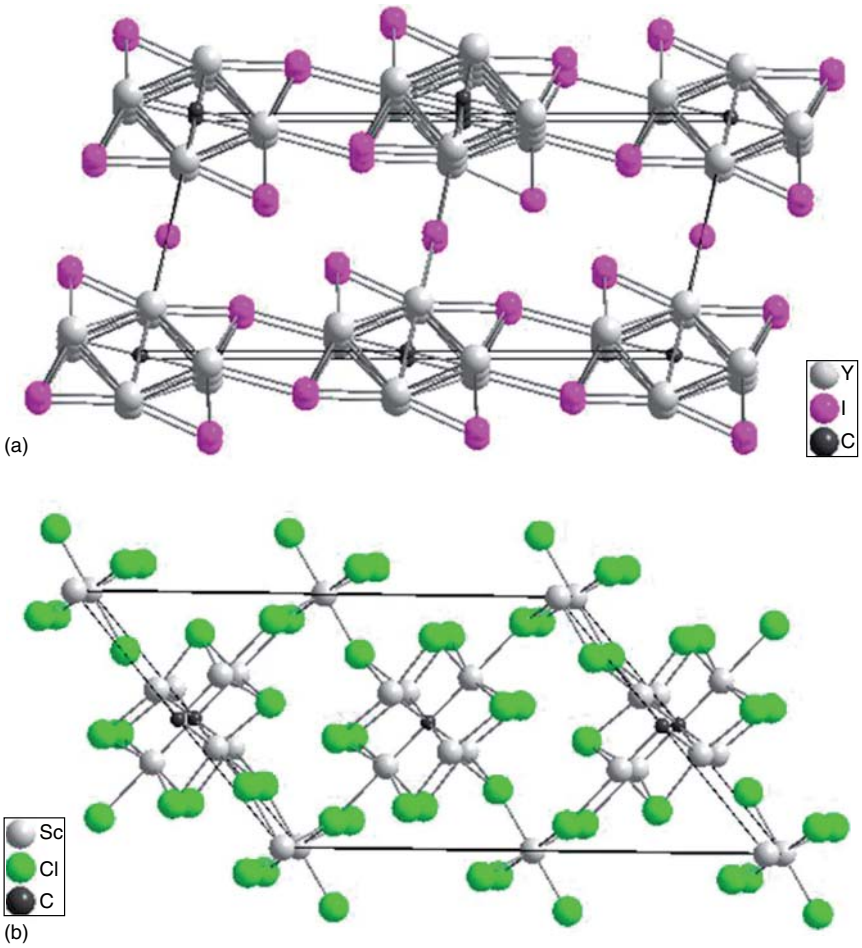


Figure 28 Chains as in type I $\{ZR_4\}X_6$ compounds connected further via halide, $\{ZR_4\}X_5$ type (a), and via additional metal halide octahedra as in the $\{ZR_4\}X_8R$ type (b)

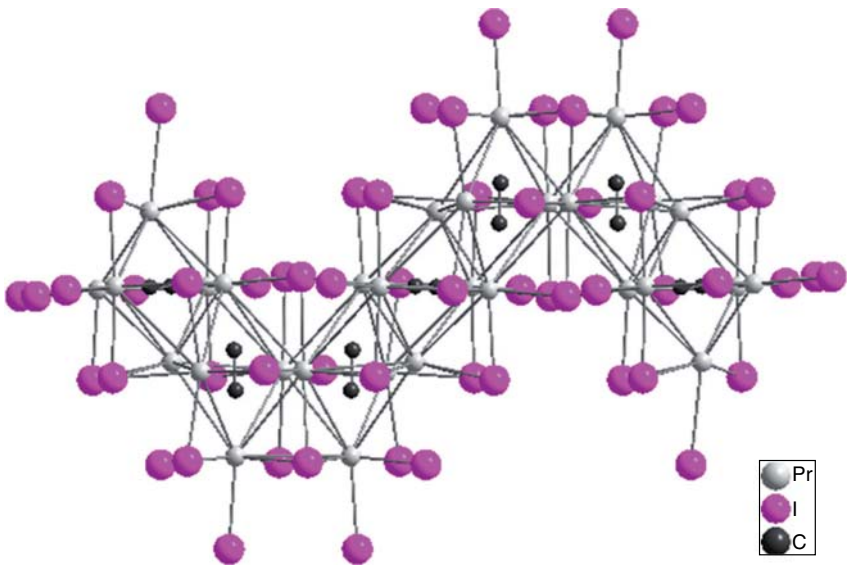


Figure 29 Corrugated chains of trans and cis edge-connected $\{(C_2)R_6\}$ clusters as observed in the crystal structures of the $\{(C_2)R_4\}_3I_{17} = R_{12}(C_2)_3I_{17}$ family, with R = La, Cr, Pr, Nd, Gd, Dy

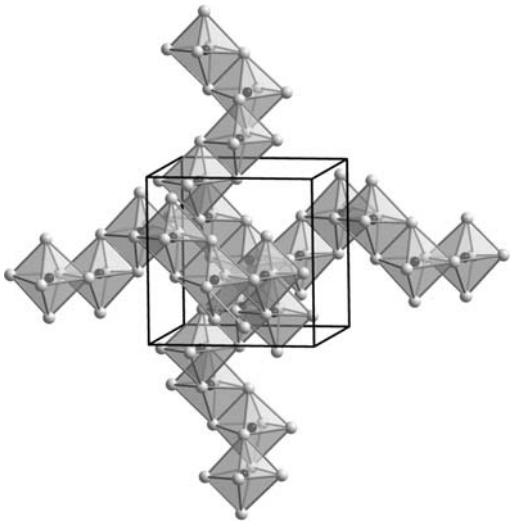


Figure 30 Helical, interpenetrating chains of edge-connected octahedra $\{ZR_{6/2}\}$ as observed, for example, in cubic body-centered $\{CGd_3\}Cl_3$

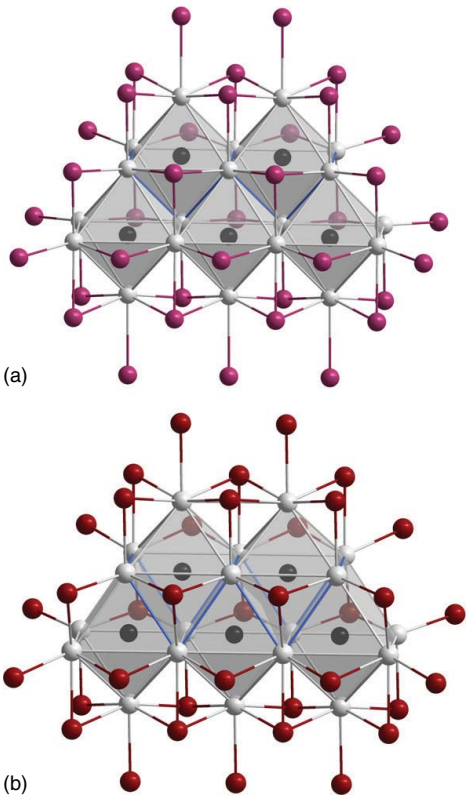


Figure 31 Zigzag chains of $\{ZR_6\}$ octahedra as they occur for example in $\{RuPr_3\}I_3$ (a) and their distortion to chains of face-sharing monocapped trigonal prisms as observed in $\{RuTb_3\}Br_3$ (b)

$\{ZR_{1/1}R_{2/2}R_{3/3}\}$ double chains are also known from bromides and iodides, which were formerly thought

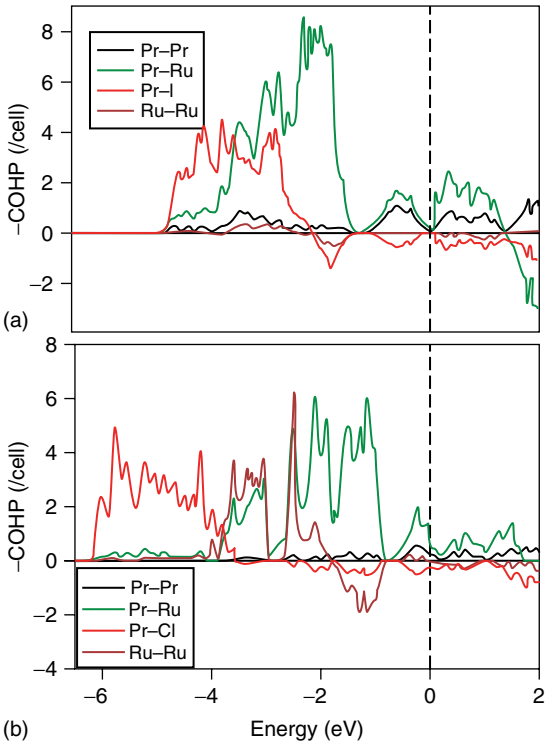


Figure 32 Crystal overlap Hamiltonian population (COHP) calculations for $\{RuPr_3\}I_3$ (a) and $\{RuPr_3\}Cl_3$ (b) showing the differences in bonding interactions

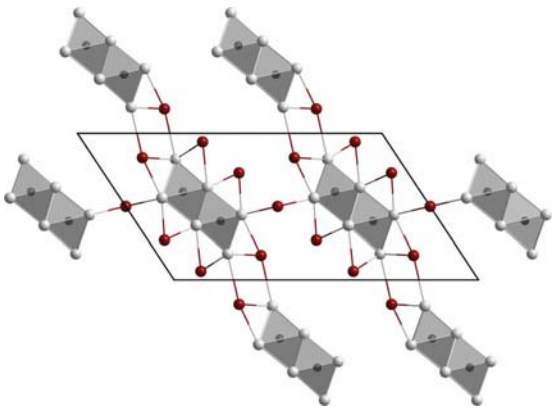


Figure 33 A view down the double chains $\{NSc_{1/1}Sc_{2/2}Sc_{3/3}\}$ (black) and their connection via $[ScCl_6]$ octahedra in the crystal structure of $\{NSc_3\}_2Cl_{10}Sc$

to be binaries, for example, Er_6I_7. The number of examples has increased in the meantime, and they appear to be all ternary compounds, $\{ZR_3\}_2I_7$, with Z always a C_2 dumbbell: $\{CR_3\}_2Br_7$ (R = Gd, Tb) and $\{CR_3\}_2I_7$ (R = Y, Gd, Er).[79,97–99] The double chains are surrounded by halido ligands and connected according to $\{CEr_{1/1}Er_{2/2}Er_{3/3}\}_2I^i{}_{4/1}I^{i-i}{}_{2/2}I^{a-i/i-a}{}_{4/2}$ to a three-dimensional structure, see Figure 34.

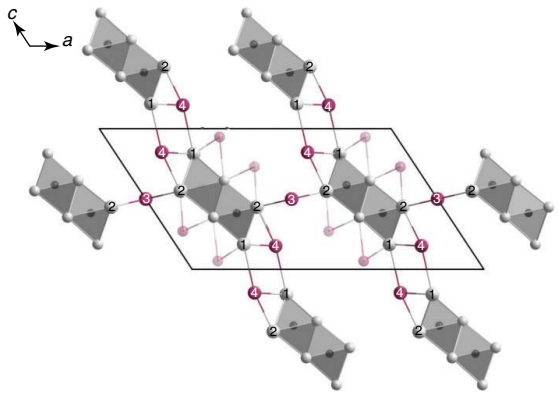


Figure 34 A view down the double chains $\{ZR_{1/1}R_{2/2}R_{3/3}\}$ and their connection via halide bridges in the crystal structures of $\{CR_3\}_2Br_7$ (R = Gd, Tb) and $\{CR_3\}_2I_7$ (R = Y, Gd, Er)

Further condensation to triple or quadruple chains has not been observed crystallographically, which is, by the way, the same with silicates. The next step of condensation is to build layers.

5.6 Layers

Layers were first found in ''GdCl'' that turned out to be a hydride of undetermined hydrogen content, $\{H_xGd_{6/6}\}Cl$.[17] Other than the hydride halides of the alkaline-earth-like rare earth metals, RHX (R = Eu, Yb, Sm; X = Cl, Br, I), which crystallize with the PbFCl type of structure, hydride halides $\{H_xR_{6/6}\}X$ with R = Sc, Y, La, Ce, Pr, Gd, Tb, Er, Lu[100] crystallize with one of two structure types, ZrCl or ZrBr.[101,102] They both contain four-layer slabs XRRX with hydrogen incorporated in the octahedral interstices between the RR metal double layers. The layers are two-dimensional, infinitely condensed chains of $\{ZR_6\}$ octahedra. Both structures need to be described in space group $R-3m$ with the four-layer slabs stacked in the ABC or the ACB fashion, hence reverse and observe in the [001] direction, see Figure 35. All compounds are ''nonstoichiometric,'' they have a homogeneity range, with $x = 1.0$ (for $\{H_xR\}X$) being the upper limit. They are all two-dimensional metals. Higher hydrogen contents lead to insulators with RH_2X being the upper limit, transparent ionic compounds, $(R^{3+})(H^-)_2(X^-)$. The $\{H_xR_{6/6}\}X$ type hydride halides may also be intercalated between the halide double layers with alkali metals, preferably Li and less Na.[103]

Equal four-layer slabs are also observed for carbide halides $\{CR_2\}X_2$ and $\{(C_2)R_2\}X_2$ with single carbon atoms and dicarbon units, respectively, residing in all of the octahedral interstices between the metal double layers. There are also three-layer slab structures of the composition $\{CR_2\}X$ in which one halide layer is missing such that the sequence is of the RRX type. In principle, they may be obtained with the same rare earth elements as the hydride halides.

The parent ZrBr type of structure appears to be preferred for $\{CR_2\}X_2$ type compounds (denoted 3R). The alternative is the so-called 1T structure type, whose identity period along [001] of the trigonal unit cell ($P-3m1$)

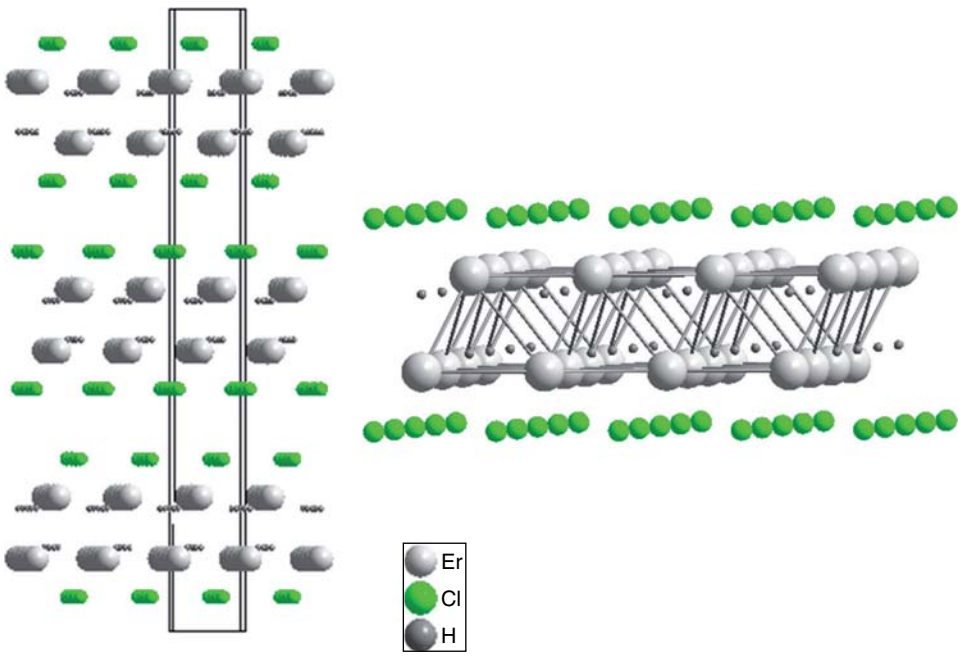


Figure 35 Schematic representation of the ZrCl and ZrBr types of structures in which the $\{H_xR_{6/6}\}X$-type rare earth hydride halides crystallize

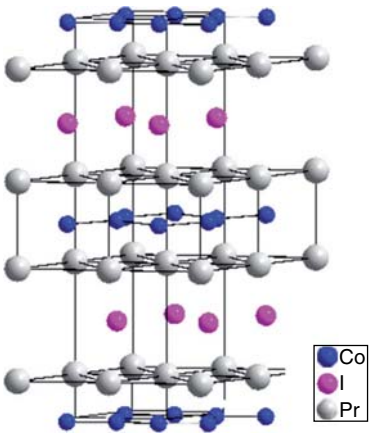


Figure 36 Crystal structure of $\{Co_2Pr_2\}I$ exhibiting the $\{CoPr_6\}$ clusters connected via common rectangular faces to layers sheathed by single iodide layers

corresponds to only one slab. For $\{CLu_2\}Cl_2$, both structures have been observed.[104,105] The only layered structure with nitrogen atoms in octahedral metal interstices seems to be $\{NSc_2\}Cl_2$. It crystallizes with the 1T structure type.[50]

Except for the nonmetal atoms H, C, and N, transition metal atoms have also been found as endohedral atoms in layered structures, for example Z = Fe, Co, Ni, Ru, Os. In principle, all rare earth elements with possible $5d^1$ configurations can adopt $\{Z_2R_2\}X$ compositions with X predominantly I, but Br is also possible. The ... XRZ$_2$RX... layers are stacked such that trigonal prisms $\{R_6\}$ occur, which are all filled by Z atoms, see Figure 36 for the example of $\{Co_2Pr_2\}I$.[106] Ample investigations have been carried out for R = La, Pr, and Gd.[107–109] An alternative to this structure is that of $\{CGd_2\}Cl$, where $\{CGd_6\}$ octahedra share common edges. It may be understood as a stuffed *anti*-$CdCl_2$ derivative according to $\{CGd_2\}Cl = \{CdCl_2\}\square$.[110]

Layers do not have to be flat. They may be corrugated, waved, or steplike, as has been observed for a small number of mixed-interstitial iodides, $\{(C_3O)Y_7\}I_6$ and $\{(C_4O)R_9\}I_8$ (R = Y, Ho, Er, Lu), see Figure 37, and also for $\{C_3Gd_6\}Cl_5$.[111–113]

5.7 High-Coordinate Endohedral Atoms, $\{ZR_x\}$ with $x = 7, 8$

The vast majority of reduced rare earth metal halides incorporate nonmetal or metal atoms (or atom groups) in octahedral interstices, as we have seen, see also Figure 12. It requires large atoms to expand the coordination environment beyond a coordination number of six. For $\{RuPr_3\}Cl_3$, we have assigned CN = 7 to the ruthenium atom that resides off-center in a monocapped trigonal prism; this has been discussed in connection with $\{ZR_3\}X_3$ phases, see above. Atoms of the sixth-period elements are even larger, especially their 5d orbitals—which are needed to establish bonding interactions between Z and R—are more expanded. So far, rhenium, osmium, and iridium are the only metals found as endohedral atoms with CN = 8. The associated polyhedra can either be square antiprisms or cubes.

Compounds of the $\{ZR_4\}X_4$ type have been observed for $\{OsR_4\}Br_4$ with R = Y, Er as well as for $\{OsSc_4\}Cl_4$ and the higher symmetric $\{ReGd_4\}Br_4$.[114,115] In all compounds, square antiprisms of R atoms, encapsulating a Re/Os atom, share common faces to chains $\{ZR_{8/2}\}$, which are surrounded by and connected through halide anions, see Figure 38. These compounds have 15/16 cluster-based electrons, scaled per one Z.

A small number of variants of these face-sharing chain compounds have recently emerged, $\{Ir_3Sc_{12}\}Br_{16}$[114,115] in which square antiprisms and cubes in a 2 : 1 ratio share common square faces and $\{Os_5Lu_{20}\}I_{24}$[116] with a 4 : 1 ratio, see Figure 39. The number of electrons per Z is 16 for $\{OsSc_4\}Cl_4$,

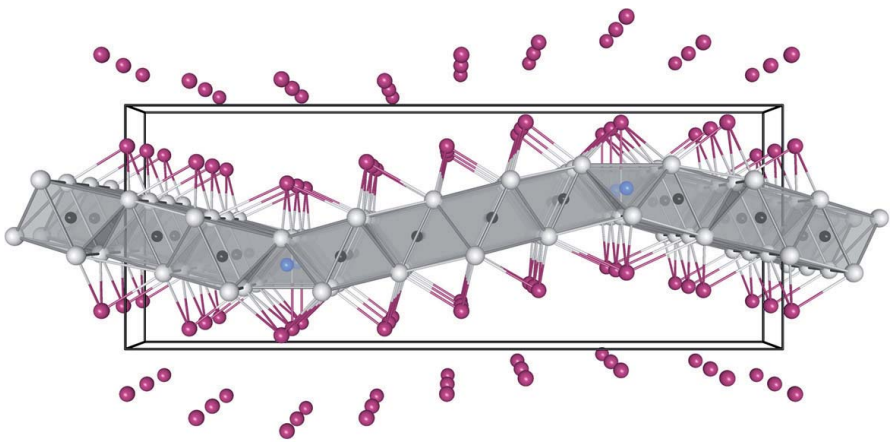


Figure 37 Corrugated layers as observed in $\{(C_4O)Y_9\}I_8$ with carbon atoms occupying octahedral interstices and oxygen atoms tetrahedral voids

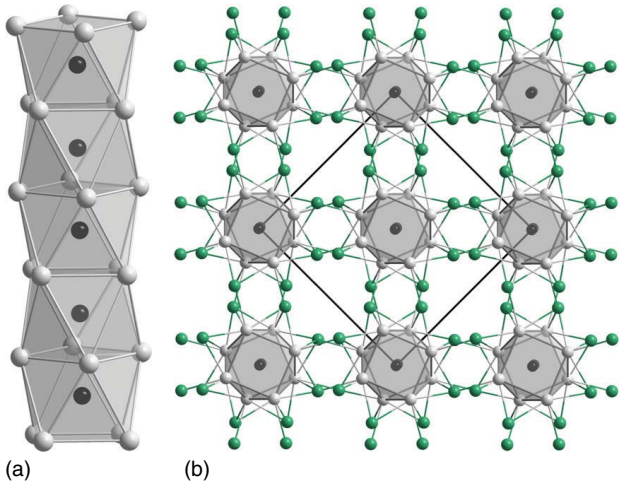


Figure 38 $\{OsSc_{8/2}\}$ chains of face-sharing square antiprisms (a) and their surrounding and connection in the crystal structure of $\{OsSc_4\}Cl_4$ and in the isostructural bromides $\{OsR_4\}Br_4$ (R = Y, Er) (b)

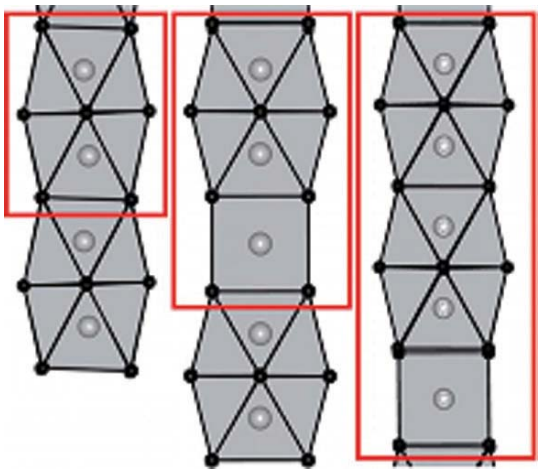


Figure 39 A comparison of the chains $\{Z_nR_{4n}\}$ with $n = 1, 3, 5$ as observed (from left to right) in $\{OsSc_4\}Cl_4$, $\{Ir_3Sc_{12}\}Br_{16}$, and $\{Os_5Lu_{20}\}I_{24}$. The repeat units are indicated by red rectangles

15.67 for $\{Ir_3Sc_{12}\}Br_{16}$, and 15.2 for $\{Os_5Lu_{20}\}I_{24}$. This electron count has roughly been seen for many compounds with oligomeric or extended structures of cluster complexes with endohedral transition metal atoms. In this connection, it must be noted that $\{Ru_3Sc_{12}\}Te_8Sc_{2-x}$ [117] has, if x were 0, the same number of cluster-based electrons as $\{Ir_3Sc_{12}\}Br_{16}$ and, furthermore the cluster chain structure $\{Z_3Sc_{12}\}$ (Z = Ru, Ir) is the same. This is an important hint at a chemistry in which bromide and telluride ligands could also be partially substituted.

Again, chemical bonding must be considered as predominantly intracluster Z–R bonding and polar R–X bonding. Figure 40 shows crystal orbital overlap populations

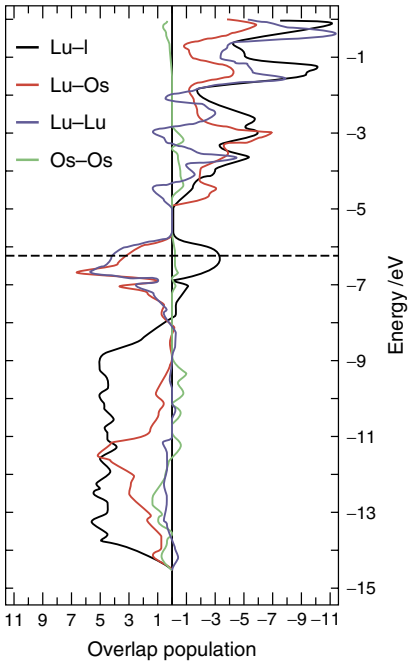


Figure 40 Crystal orbital overlap populations for Lu–I, Lu–Os, Lu–Lu, and Os–Os in $\{Os_5Lu_{20}\}I_{24}$

(COOP) for $\{Os_5Lu_{20}\}I_{24}$. It is the usual pattern: Os–Lu and Lu–I bonding interactions are low in energy, with some Lu–I antibonding close to the Fermi level. It is remarkable that there is considerable Lu–Lu bonding right at the Fermi level, which is not seen with other rare earth elements. This means that there is, although the electronic configuration should be $4f^{14}$, a remarkable contribution of 5d states, and, thus, lutetium could already be considered a transition metal.

6 CONCLUSIONS

Rare earth elements R with high reduction potentials $E°$ (R^{3+}/R^{2+}) originating from low third ionization potentials I_3, i.e., R = La, Ce, Pr, (Nd), Gd, Tb, Dy, Ho, Er, Lu, Y, Sc, are capable of forming clusters $\{R_x\}$. Almost all of the observed clusters contain an endohedral atom Z. The majority of these clusters are octahedral, $\{ZRx_6\}$, but the coordination number of the endohedral atom can also be four, or seven and eight. The clusters are surrounded by halido ligands X; the cluster complexes then have the general composition $\{ZR_x\}X_z$. Isolated cluster complexes are rare. They are usually connected via common ligands and, more importantly, share common cluster atoms building oligomers, chains, and layers. Bonding in cluster complexes is predominantly Z-R and polar R-X bonding with usually only little homoatomic R-R or Z-Z bonding.

7 GLOSSARY

anti-Werner complex: a central metal (or nonmetal) atom with high electron affinity surrounded by unlike metal atoms forming a cluster and further by electronegative ligands

Band structure: *k*-space-dependent energy-level diagram for an extended solid, similar to the molecular orbital diagram at the gamma point

Configuration crossover: transition from one electronic configuration to another

Conproportionation: compounds with higher and lower oxidation states of one element react to a compound with an oxidation state in between

Coordination number (CN): the number of atoms surrounding a central (metal) atom in a coordination complex

Cluster: according to Cotton ''a group of two or more metal atoms in which there are substantial and direct bonds between the metal atoms,'' put in braces {. . .} in this chapter

Cluster complex: a cluster surrounded by ligands, $\{R_x\}X_z$

Crystal orbital Hamiltonian population (COHP): like COOP, different weighting scheme

Crystal orbital orbital population (COOP): from the density of states of band structure calculations, showing the degree of bonding and antibonding interactions between atom types in a solid

Density of states (DOS): number of states per interval of energy at each energy level that are available to be occupied by electrons in a solid

Electronic configuration: energy levels in the shell of an atom that are occupied with electrons; symbolized by quantum numbers

Endohedral atom: atom Z in the center of a cluster, $\{ZR_x\}X_z$

Extended structures: crystal structures with polyhedra connected to a one-, two-, or three-dimensional arrangement

Fermi level: highest occupied energy level in a solid

Interstitial: an atom occupying an interstice; synonymous with endohedral atom

Isolated cluster: a cluster that does not share cluster atoms with other clusters

Lanthanides: the elements La, Ce–Lu

Metallothermic reduction: reduction of a metal oxide or halide with a highly reductive metal

Naked cluster: a cluster of metal atoms that has no ligand sphere

Oligomeric cluster: a cluster that is built from clusters sharing common cluster atoms

Rare earth elements (metals): the elements Sc, Y, La, and the lanthanoids Ce through Lu

Rare earths: oxides of the rare earth elements, in most cases of the composition R_2O_3

Reduced rare earth halides: halides with the rare earth element in an oxidation state less than +3

Supertetrahedron: a tetrahedron built of tetrahedra; the edge length of a supertetrahedron T3, for example, is three times the edge length of the constituting tetrahedron

Valence: according to Pauling (1949) ''the number of other atoms with which an atom of a certain element can combine''

Valence electron(s): electron(s) constituting the valence shell beyond the core (usually a noble gas configuration)

Werner complex: a central metal atom surrounded by ligands

8 RELATED ARTICLES

The Electronic Structure of the Lanthanides; Lanthanides: Coordination Chemistry; The Divalent State in Solid Rare Earth Metal Halides; Lanthanide Halides.

9 ABBREVIATIONS AND ACRONYMS

[. . .]	Square brackets indicate a Werner-type complex
{. . .}	Braces indicate a cluster
A	Alkali metal atom
°C	Degrees Celsius; temperature scale after Celsius
CN	Coordination number
COHP	Crystal orbital Hamiltonian population
COOP	Crystal orbital overlap population
D	Distance (between the nuclei of two atoms)
DOS	Density of states
E°	Standard electrode potential (in V)
EHMO	Extended Hückel molecular orbital (theory)

$\Delta H°$	Enthalpy difference under standard conditions (in kJ mol^{-1})
$\Delta H°(\mathbf{3})$	Third ionization potential (in kJ mol^{-1})
HOMO	Highest occupied molecular orbital
I_3	Third ionization potential (in eV or kJ mol^{-1})
K	Kelvin; absolute temperature scale
LMTO-ASA	The linear muffin tin orbital method implemented in the atomic sphere approximation
LUMO	Lowest unoccupied molecular orbital
MO	Molecular orbital
pm	Picometer, 10^{-12} m
R	Rare earth and lanthanide element (Sc, Y, La, Ce–Lu)
SOMO	Singly occupied molecular orbital
X	Halogen atom, X^- halide ion
[Xe]	Electronic configuration of a xenon atom
V	Volt; unit of voltage
VB	Valence bond (theory)
VE	Valence electron(s)

10 REFERENCES

1. F. A. Cotton and G. Wilkinson, 'Advanced Inorganic Chemistry', Wiley-Interscience, New York, Chichester, Brisbane, Toronto, Singapore, 5th edition, 1988, Chap. 23, p. 1053.
2. P. Niggli, *Z. Anorg. Allg. Chem.*, 1916, **94**, 207.
3. H. Schäfer and H. G. Schnering, *Angew. Chem.*, 1964, **76**, 833.
4. G. Meyer, *Z. Anorg. Allg. Chem.*, 2008, **634**, 2729.
5. P. Niggli, 'Grundlagen der Stereochemie', Birkhäuser, Basel, 1946.
6. D. A. Johnson, *J. Chem. Soc. A*, 1969, 1525, 1529, 2578.
7. L. R. Morss, in 'Standard Potentials in Aqueous Solution', eds. A. J. Bard, R. Parsons, and J. Jordan, Marcel Dekker, New York, 1985, p. 587.
8. G. Meyer, *Chem. Rev.*, 1988, **88**, 93.
9. D. A. Johnson, 'Some Thermodynamic Aspects of Inorganic Chemistry', 2nd edition, Cambridge University Press, Cambridge, 1982.
10. D. A. Johnson, in 'Inorganic Chemistry in Focus', eds. G. Meyer, D. Naumann, and L. Wesemann, Wiley-VCH, Weinheim, 2006, Vol. 3, p. 1.
11. L. R. Morss, *Chem. Rev.*, 1976, **76**, 827.
12. J. D. Corbett, in 'Synthesis of Lanthanide and Actinide Compounds', eds. G. Meyer and L. R. Morss, Kluwer Academic Publishers, Dordrecht, NL, 1991, p. 159.
13. G. Meyer and T. Schleid, in 'Synthesis of Lanthanide and Actinide Compounds', eds. G. Meyer and L. R. Morss, Kluwer Academic Publishers, Dordrecht, NL, 1991, p. 175.
14. G. Meyer, *Z. Anorg. Allg. Chem.*, 2007, **633**, 2537.
15. A. Simon, *Angew. Chem. Int. Ed.*, 1981, **20**, 1.
16. A. Simon, H. J. Mattausch, G. J. Miller, W. Bauhofer, and R. K. Kremer, in 'Handbook on the Physics and Chemistry of Rare Earths', eds. K. A. Gschneidner, Jr. and L. Eyring, North Holland, Amsterdam, 1991, Vol. 15, p. 191.
17. A. Simon, H. Mattausch, and N. Holzer, *Angew. Chem. Int. Ed.*, 1977, **15**, 624.
18. B. C. McCollum, M. J. Camp, and J. D. Corbett, *Inorg. Chem.*, 1973, **12**, 778.
19. J. E. Mee and J. D. Corbett, *Inorg. Chem.*, 1965, **4**, 88.
20. D. A. Lokken and J. D. Corbett, *Inorg. Chem.*, 1973, **12**, 556.
21. A. Simon, N. Holzer, and H. Mattausch, *Z. Anorg. Allg. Chem.*, 1979, **456**, 207.
22. L. R. Morss, H. Mattausch, R. K. Kremer, A. Simon, and J. D. Corbett, *Inorg. Chim. Acta*, 1987, **140**, 107.
23. K. R. Poeppelmeier and J. D. Corbett, *Inorg. Chem.*, 1977, **16**, 1107.
24. J. D. Martin and J. D. Corbett, *Angew. Chem. Int. Ed.*, 1995, **34**, 233.
25. M. Ryazanov, L. Kienle, A. Simon, and H. Mattausch, *Inorg. Chem.*, 2006, **45**, 2068.
26. A. Werner, *Z. Anorg. Chem.*, 1915, **92**, 376.
27. N. Gerlitzki, S. Hammerich, I. Pantenburg, and G. Meyer, *Z. Anorg. Allg. Chem.*, 2006, **632**, 2024.
28. A. Simon and T. Koehler, *J. Less-Common Met.*, 1986, **116**, 279.
29. U. Schwanitz-Schüller and A. Simon, *Z. Naturforsch.*, 1985, **40b**, 705.
30. S. Uhrlandt and G. Meyer, *J. Alloys Compd.*, 1995, **225**, 171.
31. H. Mattfeld and G. Meyer, *Z. Anorg. Allg. Chem.*, 1994, **620**, 85.
32. M. Lulei and J. D. Corbett, *Inorg.Chem.*, 1995, **34**, 2671.
33. U. Beck and A. Simon, *Z. Anorg. Allg. Chem.*, 1997, **623**, 1011.
34. M. C. Schaloske, L. Kienle, C. Hoch, H. Mattausch, R. K. Kremer, and A. Simon, *Z. Anorg. Allg. Chem.*, 2009, **635**, 1023.
35. H. Mattausch, C. Hoch, and A. Simon, *Z. Naturforsch.*, 2007, **62b**, 143.
36. M. C. Schaloske, H. Mattausch, L. Kienle, and A. Simon, *Z. Anorg. Allg. Chem.*, 2008, **634**, 1493.
37. L. Jongen, A.-V. Mudring, and G. Meyer, *Angew. Chem. Int. Ed.*, 2006, **45**, 1886.
38. J. Li, H.-J. Zhai, and L.-S. Wang, *Science*, 2003, **299**, 864.
39. R. B. King, Z. Chen, and P. R. Schleyer, *Inorg. Chem.*, 2004, **43**, 4564.
40. G. Meyer and S. Uhrlandt, *Angew. Chem. Int. Ed.*, 1993, **32**, 1318.
41. S. Uhrlandt and G. Meyer, *Z. Anorg. Allg. Chem.*, 1994, **620**, 1872.

42. S. Uhrlandt, T. Heuer, and G. Meyer, *Z. Anorg. Allg. Chem.*, 1995, **621**, 1299.
43. S. Uhrlandt and G. Meyer, *Z. Anorg. Allg. Chem.*, 1995, **621**, 1466.
44. T. Heuer, F. Steffen, and G. Meyer, *Eur. J. Solid State Inorg. Chem.*, 1996, **33**, 265.
45. H. Mattausch, C. Hoch, and A. Simon, *Z. Anorg. Allg. Chem.*, 2008, **634**, 641.
46. H. Artelt, T. Schleid, and G. Meyer, *Z. Anorg. Allg. Chem.*, 1992, **618**, 18.
47. C. Rustige, M. Brühmann, S. Steinberg, E. Meyer, K. Daub, S. Zimmermann, M. Wolberg, A.-V. Mudring, and G. Meyer, *Z. Anorg. Allg. Chem.*, 2012, **638**.
48. J. D. Corbett, R. L. Daake, K. R. Poeppelmeier, and D. H. Guthrie, *J. Am. Chem. Soc.*, 1978, **100**, 652.
49. T. Hughbanks and J. D. Corbett, *Inorg. Chem.*, 1989, **28**, 631.
50. S.-J. Hwu and J. D. Corbett, *J. Solid State Chem.*, 1986, **64**, 331.
51. K. Daub and G. Meyer, *Acta Crystallogr.*, 2008, **E64**, i4.
52. D. S. Dudis and J. D. Corbett, *Inorg. Chem.*, 1987, **26**, 1933.
53. G. Meyer and M. S. Wickleder, in 'Handbook on the Physics and Chemistry of Rare Earths', eds. K. A. Gschneidner, Jr. and L. Eyring, Elsevier, 2000,, Vol. 28, p. 53.
54. A. Simon, E. Warkentin, and R. Masse, *Angew. Chem. Int. Ed.*, 1981, **20**, 1013.
55. H. M. Artelt and G. Meyer, *Z. Anorg. Allg. Chem.*, 1994, **620**, 1527.
56. H. Mattausch, A. Simon, L. Kienle, C. Hoch, C. Zheng, and R. K. Kremer, *Z. Anorg. Allg. Chem.*, 2006, **632**, 1661.
57. R. Wiglusz and G. Meyer, *Z. Kristallogr., New Cryst. Struct.*, 2007, **222**, 9.
58. M. Brühmann and G. Meyer, *Eur. J. Inorg. Chem.*, 2010, 2609.
59. H. Mattausch, G. V. Vajenine, O. Oeckler, R. K. Kremer, and A. Simon, *Z. Anorg. Allg. Chem.*, 2001, **627**, 2542.
60. M. Brühmann, Cluster-Komplexe der Seltenerdmetalle Gadolinium und Lutetium mit endohedralen Übergangsmetall-Atomen, Dr. rer. nat. Dissertation, Universität zu Köln, 2011.
61. M. W. Payne, M. Ebihara, and J. D. Corbett, *Angew. Chem. Int. Ed. Engl.*, 1991, **30**, 856.
62. M. Ebihara, J. D. Martin, and J. D. Corbett, *Inorg. Chem.*, 1994, **33**, 2079.
63. S. J. Steinwand and J. D. Corbett, *Inorg. Chem.*, 1996, **35**, 7056.
64. S. J. Steinwand, J. D. Corbett, and J. D. Martin, *Inorg. Chem.*, 1997, **36**, 6413.
65. S. Zimmermann, Hochkoordinierte endohedrale Übergangs-metallatome in Scandiumclustern, Dr. rer. nat. Dissertation, Universität zu Köln, 2008.
66. K. Daub, New Interstitially Stabilized Cluster Complexes of Dysprosium, Holmium and Erbium, Dr. rer. nat. Dissertation, Universität zu Köln, 2009.
67. C. Rustige, Interstitiell stabilisierte Clusterkomplexe der Seltenerdmetalle Terbium und Erbium, Dr. rer. nat. Dissertation, Universität zu Köln, 2011.
68. E. Warkentin and H. Bärnighausen, *Z. Anorg. Allg. Chem.*, 1979, **459**, 187.
69. K. Daub and G. Meyer, *Z. Anorg. Allg. Chem.*, 2010, **636**, 1716.
70. C. Zheng, J. Köhler, H. Mattausch, C. Hoch, and A. Simon, *J. Am. Chem. Soc.*, 2012, **134**, 5026.
71. S. Steinberg, Dr. rer. nat. Dissertation, Universität zu Köln, 2013.
72. H. Mattausch and A. Simon, *Z. Kristallogr., New Cryst. Struct.*, 2005, **220**, 313.
73. H. Mattausch, O. Oeckler, and A. Simon, *Z. Kristallogr., New Cryst. Struct.*, 2003, **218**, 282.
74. H. Mattausch, C. Hoch, and A. Simon, *Z. Naturforsch.*, 2007, **62b**, 148.
75. H. Mattausch and A. Simon, *Z. Kristallogr., New Cryst. Struct.*, 1997, **212**, 99.
76. H. Mattausch, O. Oeckler, and A. Simon, *Z. Kristallogr., New Cryst. Struct.*, 2000, **215**, 199.
77. M. Lukachuk, H. Mattausch, and A. Simon, *Z. Kristallogr., New Cryst. Struct.*, 2006, **221**, 3.
78. K. R. Poeppelmeier and J. D. Corbett, *J. Am. Chem. Soc.*, 1978, **100**, 5039.
79. S. M. Kauzlarich, T. Hughbanks, J. D. Corbett, P. Klavins, and R. N. Shelton, *Inorg. Chem.*, 1988, **27**, 1791.
80. A. Nagaki, A. Simon, and H. Borrmann, *J. Less-Common Met.*, 1989, **156**, 193.
81. H. Mattausch, M. C. Schaloske, C. Hoch, Ch. Zheng, and A. Simon, *Z. Anorg. Allg. Chem.*, 2008, **634**, 491.
82. H. Mattausch, M. C. Schaloske, C. Hoch, and A. Simon, *Z. Anorg. Allg. Chem.*, 2008, **634**, 498.
83. H. Mattausch, O. Oeckler, and A. Simon, *Z. Anorg. Allg. Chem.*, 2008, **634**, 503.
84. H. Mattausch, A. Simon, and R. Eger, *Rev. Chim. Miner.*, 1980, **17**, 516.
85. S.-J. Hwu, D. S. Dudis, and J. D. Corbett, *Inorg. Chem.*, 1987, **26**, 469.
86. A. Simon and E. Warkentin, *Z. Anorg. Allg. Chem.*, 1983, **497**, 79.
87. S. Uhrlandt and G. Meyer, *Z. Kristallogr., New Cryst. Struct.*, 1995, **210**, 361.
88. M. Ryazanov, H. Mattausch, and A. Simon, *J. Solid State Chem.*, 2007, **180**, 1372.
89. E. Warkentin and A. Simon, *Rev. Chim. Miner.*, 1983, **20**, 488.
90. C. Zheng, O. Oeckler, H. Mattausch, and A. Simon, *Z. Anorg. Allg. Chem.*, 2001, **627**, 2151.
91. M. W. Payne, P. K. Dorhout, S.-J. Kim, T. R. Hughbanks, and J. D. Corbett, *Inorg. Chem.*, 1992, **31**, 1389.
92. R. Llusar and J. D. Corbett, *Inorg. Chem.*, 1994, **33**, 849.

93. N. Herzmann, A.-V. Mudring, and G. Meyer, *Inorg. Chem.*, 2008, **47**, 7954.
94. S. Gupta, G. Meyer, and J. D. Corbett, *Inorg. Chem.*, 2010, **49**, 9949.
95. S.-J. Hwu, J. D. Corbett, and K. R. Poeppelmeier, *J. Solid State Chem.*, 1985, **57**, 43.
96. S. Zimmermann, Hochkoordinierte endohedrale Übergangs-metallatome in Scandiumclustern, Dr. rer. nat. Dissertation, Universität zu Köln, 2008.
97 K. Berroth, Dr. rer. nat. Dissertation, Universität Stuttgart, 1980.
98. K. Berroth, H. Mattausch, and A. Simon, *Z. Naturforsch.*, 1980, **35b**, 626.
99. A. Simon, *J. Solid State Chem.*, 1985, **57**, 2.
100. H. Mattausch, W. Schramm, W. Eger, A. Simon, *Z. Anorg. Allg. Chem.*, 1985, **530**, 43.
101. D. G. Adolphson and J. D. Corbett, *Inorg. Chem.*, 1976, **15**, 1820.
102. R. L. Daake and J. D. Corbett, *Inorg. Chem.*, 1977, **16**, 2029.
103. G. Meyer, S.-J. Hwu, S. Wijeyesekera, and J. D. Corbett, *Inorg. Chem.*, 1986, **25**, 4811.
104. U. Schwanitz-Schüller and A. Simon, *Z. Naturforsch.*, 1985, **40b**, 710.
105. T. Schleid and G. Meyer, *Z. Anorg. Allg. Chem.*, 1987, **552**, 90.
106. A. Palasyuk, I. Pantenburg, and G. Meyer, *Z. Anorg. Allg. Chem.*, 2006, **632**, 1969.
107. M. Ruck and A. Simon, *Z. Anorg. Allg. Chem.*, 1993, **619**, 327.
108. Y. Park, J. D. Martin, and J. D. Corbett, *J. Solid State Chem.*, 1997, **129**, 277.
109. C. Lefevre, C. Hoch, R. K. Kremer, and A. Simon, *Solid State Sci.*, 2008, **10**, 1625.
110. H. Mattausch, C. Schwarz, and A. Simon, *Z. Kristallogr.*, 1987, **178**, 156.
111. A. Simon, C. Schwarz, and W. Bauhofer, *J. Less-Common Met.*, 1988, **137**, 343.
112. H. Mattausch, H. Borrmann, and A. Simon, *Z. Naturforsch.*, 1993, **48b**, 1828.
113. H. Mattfeld, K. Krämer, and G. Meyer, *Z. Anorg. Allg. Chem.*, 1993, **619**, 1384.
114. P. K. Dorhout and J. D. Corbett, *J. Am. Chem. Soc.*, 1992, **114**, 1697.
115. S. Zimmermann, M. Brühmann, F. Casper, O. Heyer, T. Lorenz, C. Felser, A.-V. Mudring, and G. Meyer, *Eur. J. Inorg. Chem.*, 2010, 2613.
116. M. Brühmann, A.-V. Mudring, M. Valldor, and G. Meyer, *Eur. J. Inorg. Chem.*, 2012, 4083.
117. L. Chen and J. D. Corbett, *J. Am. Chem. Soc.*, 2003, **125**, 1170.

Organic Synthesis

Yuichiro Mori and Shũ Kobayashi

The University of Tokyo, Tokyo, Japan

1	Summary	437
2	Introduction	437
3	Catalysis in Organic Solvents	438
4	Catalysis in Aqueous Media	448
5	Conclusions	455
6	Glossary	456
7	Related Articles	456
8	Abbreviations and Acronyms	456
9	References	456

1 SUMMARY

Rare earth elements are important as catalysts for various organic transformations based on their unique physical and chemical properties. The fine-tuning of ligands and selection of center metals results in various applications of rare earth metals as catalysts for a number of catalytic reactions. Furthermore, rare earth metal-based Lewis acids are compatible with water. This property is largely different from traditional Lewis acids such as $AlCl_3$, $TiCl_4$, and BF_3, which need strictly anhydrous conditions. Various organic reactions including catalytic asymmetric reactions can be performed using rare earth metal-based Lewis acids not only in organic solvents but also in water. This will lead to environmentally friendly reaction systems in future.

2 INTRODUCTION

The importance of rare earth metal salts as catalysts is growing rapidly based on their unique chemical and physical properties. Rare earth metal cations have high coordination numbers and function as hard acids. They usually adopt the 3+ oxidation state, which is stable and not easily changed to other oxidation states under normal conditions. Their reactivity can be controlled by two methods: one is fine-tuning of the structure of ligands utilizing the high coordination numbers of rare earth metals, and the other is changing the center metals since appropriate ion size and structures can be selected from a series of lanthanides based on the lanthanide contraction. The fine-tuning of ligands and selection of center metals result in various applications of rare earth metals as catalysts in a number of catalytic reactions. A range of well-designed rare earth catalysts with hard Lewis base-containing chiral ligands have been developed.

Lewis acid-catalyzed reactions are of great interest due to their increased reactivity and selectivity under mild reaction conditions. A wide variety of reactions using Lewis acids have been developed, and they have been applied to the synthesis of natural and unnatural compounds. Traditionally, Lewis acids such as $AlCl_3$, BF_3, $TiCl_4$, and $SnCl_4$, have been employed in these reactions; however, more than stoichiometric amounts of the Lewis acids are needed in many cases. Moreover, these Lewis acids are moisture sensitive and are easily decomposed or deactivated in the presence of even a small amount of water. Furthermore, these Lewis acids cannot be recovered and reused after the reactions are completed. In 1991, the first water-compatible Lewis acids, lanthanide triflates [$Ln(OTf)_3$], was reported.[1]

The most characteristic feature of $Ln(OTf)_3$ is that they are stable and work as Lewis acids in water. After the first report, not only $Ln(OTf)_3$ (Ln = La, Ce, Pr, Nd, Sm, Eu, Gd, Tb, Dy, Ho, Er, Tm, Yb, Lu) but also scandium (Sc) and yttrium (Y) triflates were shown to be water-compatible Lewis acids, and these rare earth metal triflates [$RE(OTf)_3$] have been regarded as new types of Lewis acids. Many useful reactions are catalyzed by rare earth metal triflates in aqueous media.

The Rare Earth Elements. Edited by David A. Atwood. © 2012 John Wiley & Sons, Ltd. ISBN 978-1-119-95097-4

Only catalytic amounts of the triflates are enough to complete the reactions in most cases. Furthermore, rare earth metal triflates can be recovered easily after reactions and reused without loss of activity. The triflates are still active in the coexistence of many Lewis bases containing nitrogen, oxygen, phosphorus, and sulfur atoms. While large amounts of conventional Lewis acids are required and treatment of the residues of the Lewis acids after reactions may induce some serious environmental problems, rare earth metal triflate-catalyzed reactions are clean and the triflates are regarded as environmentally benign catalysts. The catalytic efficiency of rare earth metal triflates vary from one reaction to another. Generally, $Sc(OTf)_3$ has higher Lewis acidity and shows a higher catalytic activity than $Ln(OTf)_3$ and $Y(OTf)_3$. The relative Lewis acidity of rare earth metal triflates were evaluated based on their competitive ligand dissociation from complexes, $M(OTf)_3(L)_4$ (L = hexamethylphosphoramide, triethylphosphine oxide, or trimethyl phosphate) using tandem mass spectrometry.[2] The results are in accordance to the extraordinary catalytic activity of scandium and ytterbium in the Lewis acid-catalyzed reactions. The high Lewis acidity of scandium and ytterbium may be attributed to their small ionic radii. Rare earth metal triflates are readily prepared by heating the corresponding metal oxides or chlorides in an aqueous trifluoromethanesulfonic acid (TfOH) solution.[3,4] They are also prepared by the reaction of aqueous solutions of the corresponding metal halides with silver triflate. Typically, eight or nine molecules of water are contained in the triflates after removal of water at room temperature. Anhydrous triflates are obtained after drying at elevated temperature under high vacuum. According to these special characteristics, rare earth metals have been utilized as fine-tuned catalysts not only in organic solvents but also in aqueous solvents.

In this chapter, recent development of rare earth metal-catalyzed organic transformations, mainly highly controlled catalytic asymmetric reactions, in organic solvents and in aqueous media are highlighted. For more or other examples using rare earth metal catalysts, see reviews and references cited therein.[5–9]

3 CATALYSIS IN ORGANIC SOLVENTS

The first example of the use of rare earth metal complexes for asymmetric catalysis in organic solvents was reported in 1983 in chiral europium-catalyzed hetero Diels–Alder reactions.[10] As for scandium catalysts, the first chiral catalyst was reported in 1994.[11] Diels–Alder reactions using a chiral catalyst prepared from $Sc(OTf)_3$, (*R*)-BINOL, and an amine afforded the desired products in up to 97% ee. Following these results, many chiral rare earth metal catalysts have been developed.

3.1 Catalytic Asymmetric Reactions

3.1.1 Addition to Carbonyl Compounds and Related Reactions

Chiral scandium–bis(oxazolinyl)pyridine (Sc-pybox) complexes catalyze various catalytic asymmetric addition reactions with carbonyl compounds. The first report of this complex was addition and annulation reactions of allenylsilanes with ethyl glyoxylate using the scandium complex.[12] The application of these complexes[13,14] was expanded to various catalytic asymmetric transformations such as aldol reactions,[15] allylation,[16] and ene reactions.[17]

Sc-pybox complex-catalyzed enantioselective aldol reactions affords chiral malate derivatives and aryl-substituted α-hydroxy-β-ketoesters in high yields with high diastereo- and enantioselectivities. In this process, cationic $[Sc\text{-pybox}](Cl)_2^+$ was found to be effective whereas $[Sc\text{-pybox}](OTf)_3$ gave unsatisfactory results. The use of 2 equiv. of chlorotrimethylsilane was essential to facilitate the catalyst turnover when aryl ketone-derived silyl enol ethers were employed (Scheme 1).

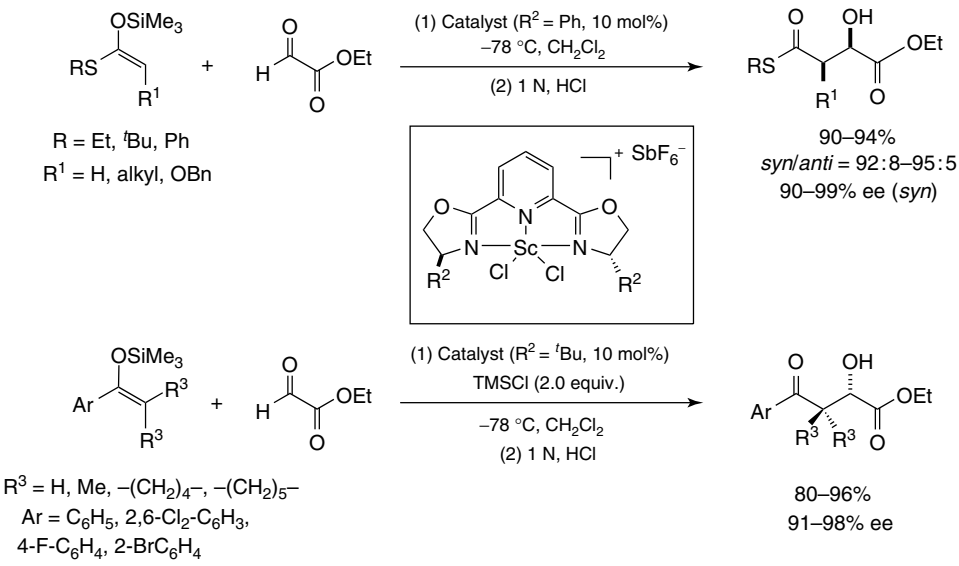
A chiral Sc-pybox catalyst from $Sc(OTf)_3$ catalyzes a highly enantioselective Michael-type indole Friedel–Crafts reactions with a variety of β-substituted α,β-unsaturated acyl phosphonates and β-substituted α,β-unsaturated 2-acyl imidazoles (Scheme 2).[18] The acyl phosphonate products were efficiently transformed into the corresponding esters and amides, whereas the acyl imidazole products were converted to more diverse functionalities such as esters, amides, carboxylic acids, ketones, and aldehydes. A mild and efficient cleavage protocol for the diversification of the 2-acyl imidazole products utilizing methylating conditions was also developed.

Chiral samarium and gadolinium–pybox complexes catalyze highly enantioselective Diels-Alder reactions (Scheme 3).[19] The reaction scope has been extended to include three quinones and five dienes, all of which exclusively provide the expected *endo* products in excellent yields and enantioselectivities.

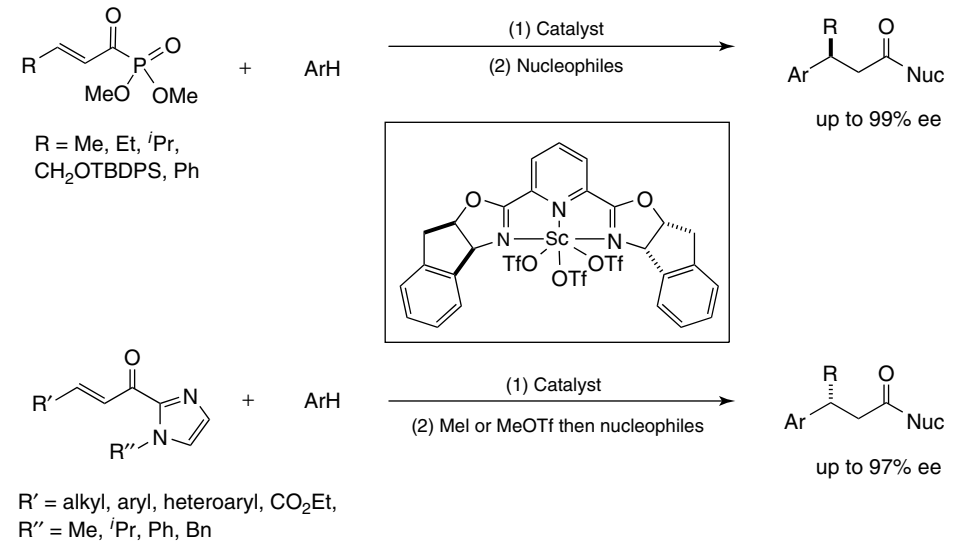
A chiral Sc-pybox catalyst catalyzes Lewis acid-catalyzed enantioselective alkenylation of air- and moisture-stable trimethylvinylsilanes under mild conditions.[20] Most products are highly crystalline solids, which are ideally suited for industrial process chemistry (Scheme 4).

Two distinct chiral metal complexes operate cooperatively to catalyze a highly enantioselective conjugate addition of cyanide to unsaturated imides (Scheme 5).[21] Under optimized conditions, the dual-catalyst system afforded distinctly superior results relative to the (salen)AlCl complex.

A concept of multifunctional chiral catalysis, where the catalysts exhibit both Lewis acidity and Brønsted basicity was developed. The multifunctional catalysts were first reported in a catalytic asymmetric nitroaldol reaction using rare earth metal complexes.[22] Interestingly, heterobimetallic



Scheme 1 Chiral scandium-catalyzed aldol reactions

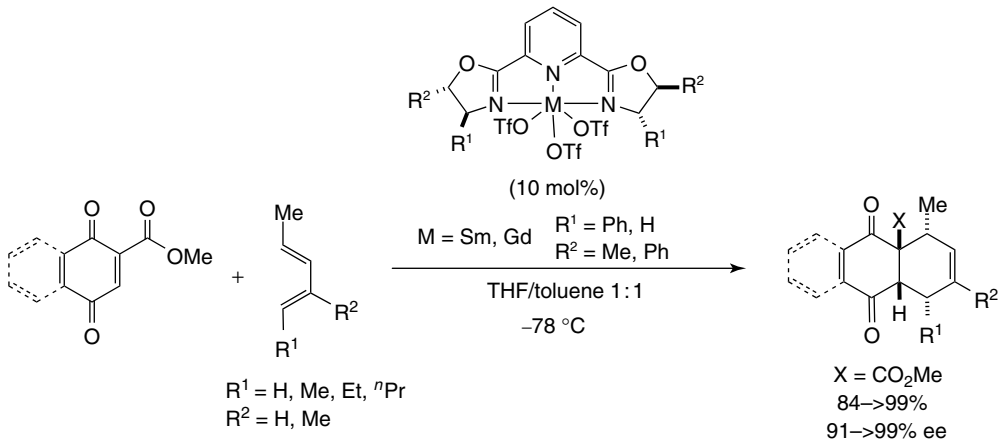


Scheme 2 Enantioselective Friedel–Crafts alkylations and further transformations

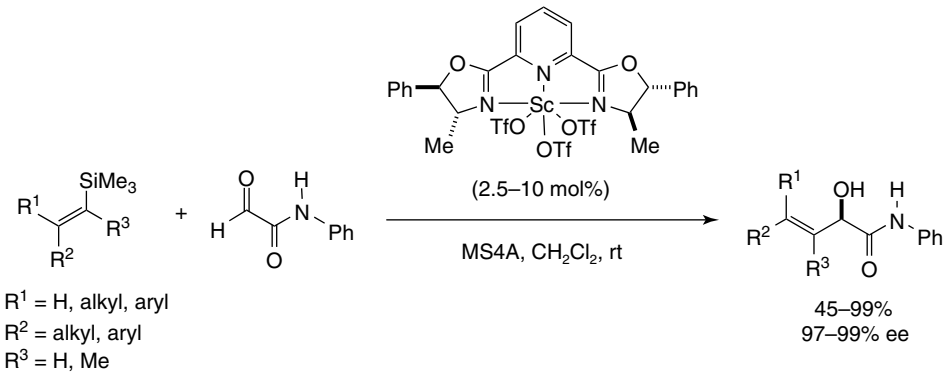
complexes that contain a rare earth metal, three alkali metals, and three BINOLs offer a versatile framework for asymmetric catalysts. The structure of the rare earth–alkali-metal–BINOL (REMB; RE, rare earth metal; M, alkali metal; B, BINOL) complex is shown in Figure 1. The synergistic effects of the two functions in REMB complexes enabled various transformations (Figure 2) that were difficult to achieve using conventional monometallic catalysts with only Lewis acidity. A variety of enantioselective transformations have been realized by selecting combinations of metals based on the type of the reaction. REMB complexes have also been applied to the synthesis of several biologically active compounds.

A heterobimetallic Ga/cationic Yb/Schiff base complex as a Lewis acid/Lewis acid bifunctional catalyst catalyzes asymmetric α-addition of α-isocyanoacetamides to aryl, heteroaryl, alkenyl, and alkyl aldehydes (Scheme 6).[23] The Schiff base derived from *o*-vanillin was suitable to utilize cationic rare earth metal triflates with good Lewis acidity in bimetallic Schiff base catalysis.

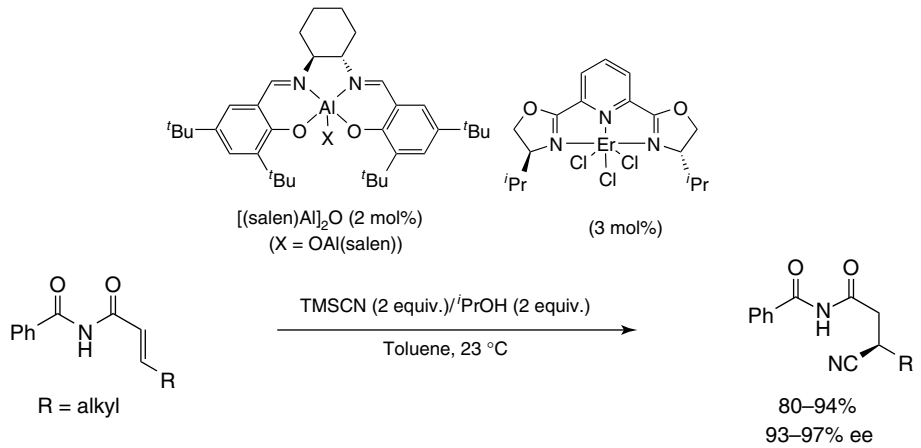
Nd/Na heterobimetallic complex promoted an *anti*-selective catalytic asymmetric nitroaldol reaction.[24] The



Scheme 3 Enantioselective, rare earth-catalyzed quinone Diels–Alder reactions

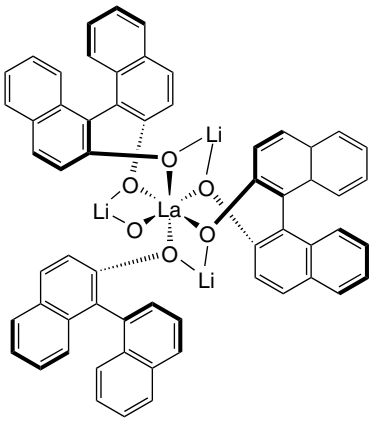


Scheme 4 Enantioselective alkenylation using trimethylvinylsilanes

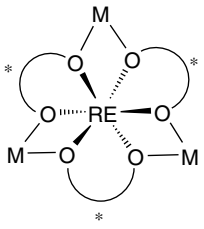


Scheme 5 Conjugate addition of TMSCN to α,β-unsaturated imides promoted by the dual-catalyst system

reaction was used for the enantioselective synthesis of zanamivir, a potent neuraminidase inhibitor for treatment and prophylaxis of influenza (Scheme 7).[25] An *anti*-selective catalytic asymmetric nitroaldol reaction utilizing hetero-bimetallic Pd/La/Schiff base complex with 4-bromophenol as an additive was also developed.[26]



$LaLi_3$tris(binaphthoxide) (LLB)



(*S*)-REMB

Figure 1 Structures of heterobimetallic RE-M_3-tris(binaphthoxide) (REMB) catalysts[8]

It was demonstrated that a chiral *N*,*N*′-dioxide–scandium triflate complex acted as a catalyst for enantioselective Michael addition of β-ketoesters to methyl vinyl ketone.[27] The utility of chiral lanthanide/*N*,*N*′-dioxide catalysts was expanded and various catalytic asymmetric reactions were reported.[28]

A chiral La$(OTf)_3$/*N*,*N*′-dioxide complex catalyzes enantioselective conjugate addition of nitroalkanes to nitroalkenes (Scheme 8).[29] This process provides various 1,3-dinitro compounds bearing two stereocenters in high diastereo- and enantioselectivities under mild conditions.

Chiral rare earth metal/*N*,*N*′-dioxide complexes catalyze highly enantioselective Michael addition reactions of 4-substituted pyrazolones to 4-oxo-4-arylbutenoates, which give a range of 4-substituted-5-pyrazolone derivatives (Scheme 9).[30] Both enantiomers of the product were obtained in good to excellent enantioselectivities and diastereoselectivities using the same ligand by changing metals. In gram-scale reactions, high yields and enantioselectivities were also obtained.

A catalytic enantioselective Friedel–Crafts alkylation of indole with β,γ-unsaturated α-ketoesters was developed. By changing metals (samarium and silver), the

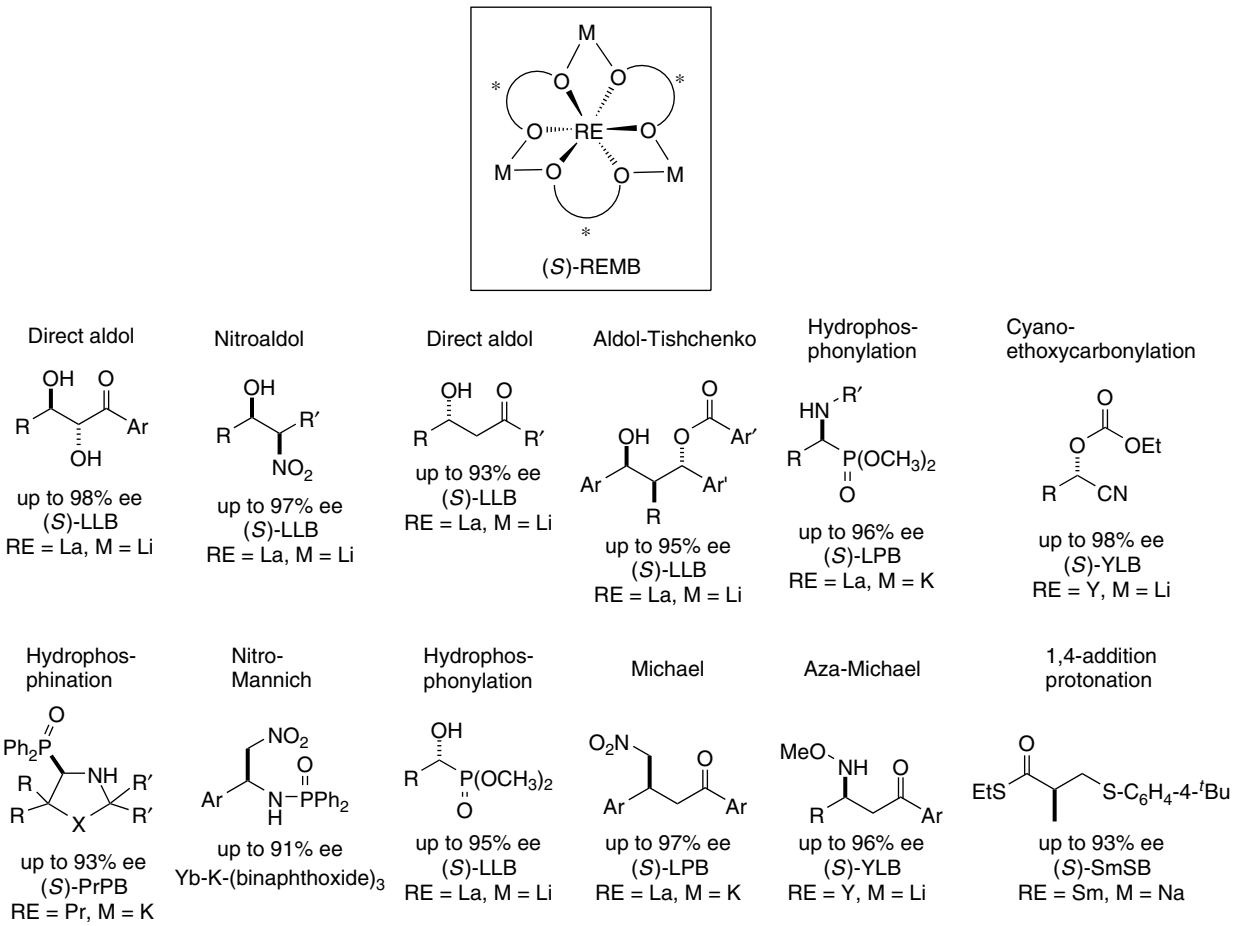
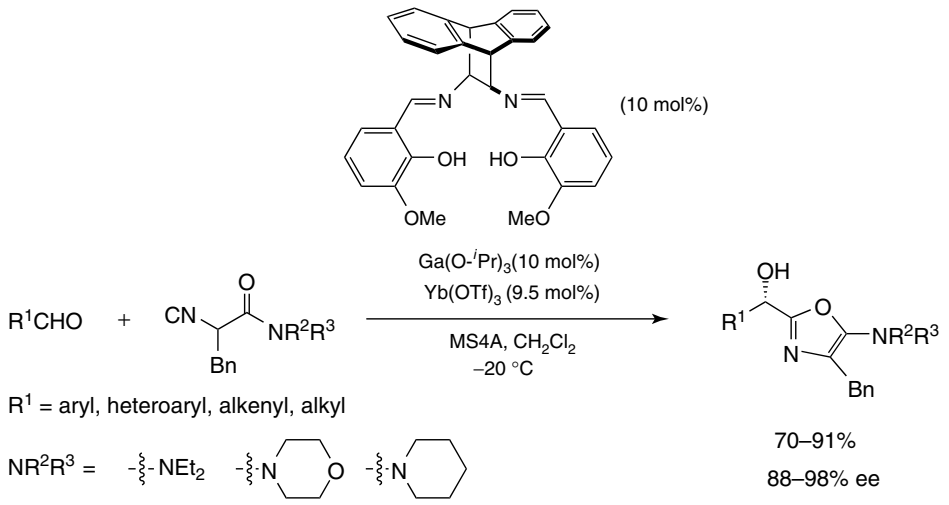
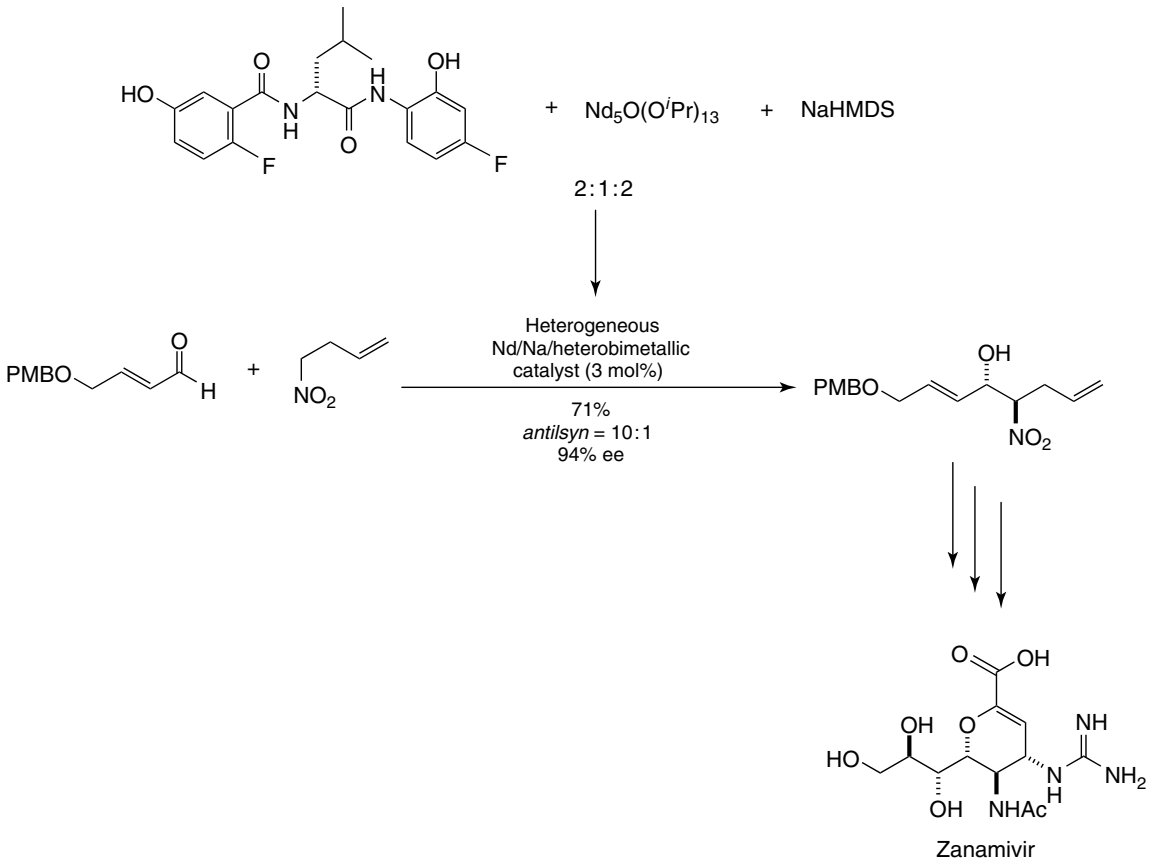


Figure 2 Selected examples of catalytic asymmetric reactions promoted by REMB complexes[8]



Scheme 6 Catalytic asymmetric α-addition of isocyanides to aldehydes using Ga/Yb/Schiff base complex

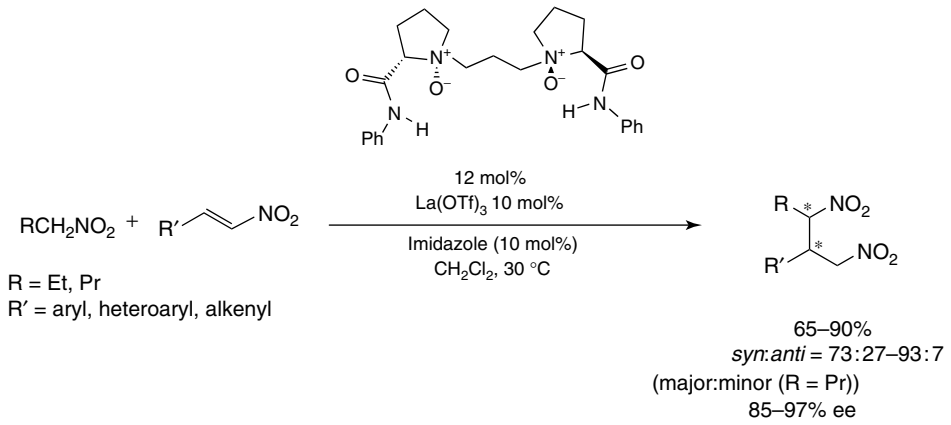


Scheme 7 Catalytic asymmetric nitroaldol reaction promoted by a heterogeneous Nd/Na heterobimetallic complex toward zanamivir

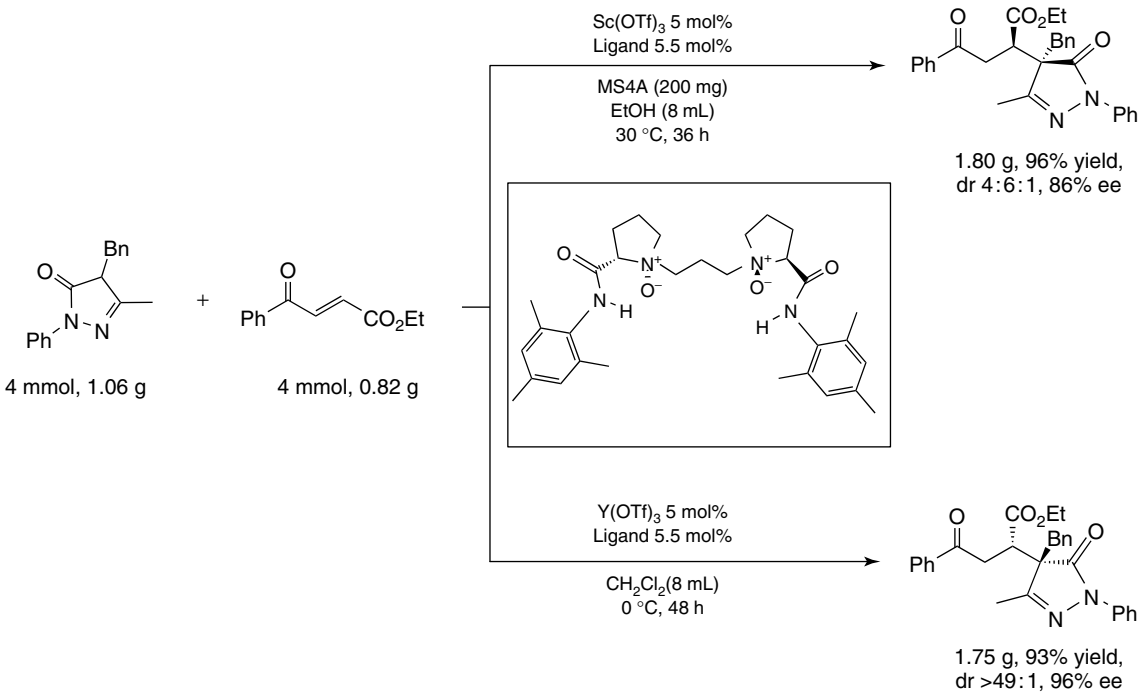
reversal of enantioselectivity in the Friedel–Crafts alkylation of different indoles with a variety of β,γ-unsaturated α-ketoesters has been achieved using ligands derived from the same chiral starting material.[31]

3.1.2 Addition to Imines

A heterobimetallic transition metal/rare earth metal system with a dinucleating Schiff base is also a promising



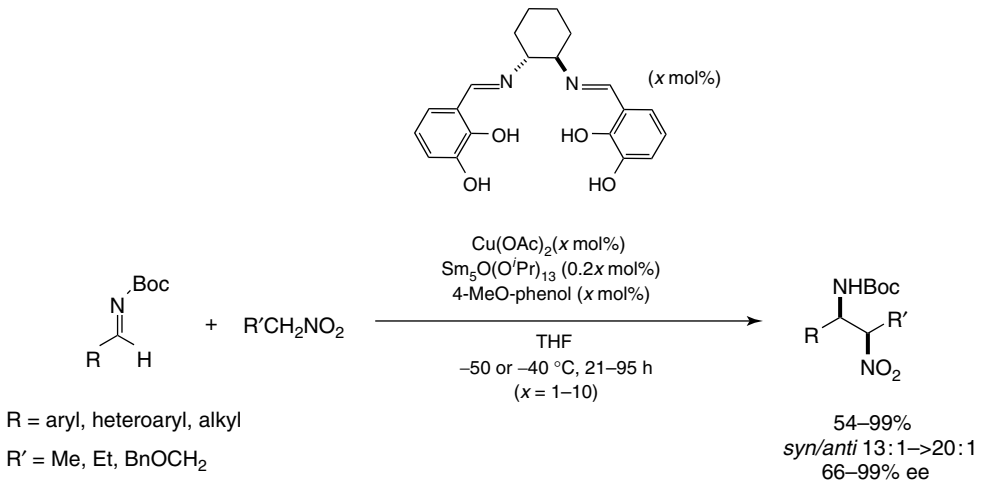
Scheme 8 Catalytic asymmetric Michael addition reactions of nitroethane to nitroalkenes promoted by a lanthanum catalyst



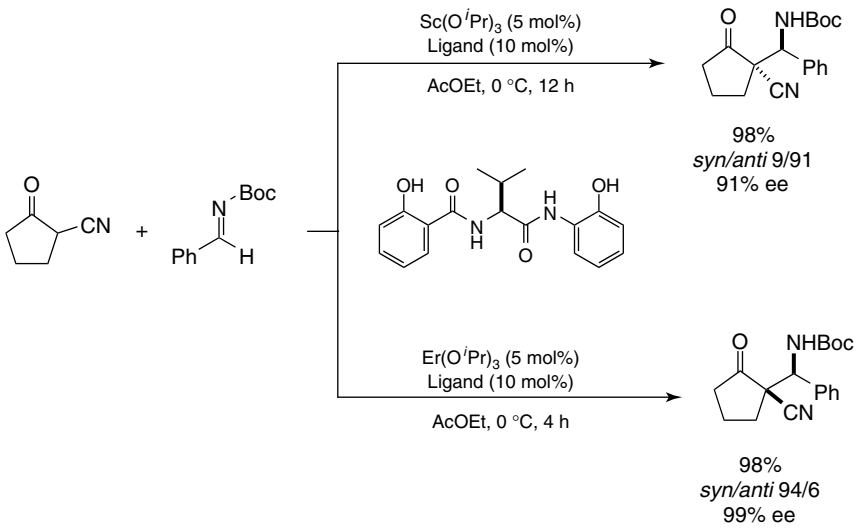
Scheme 9 The gram-scale synthesis that demonstrates the switch in enantioselectivity

catalyst.[32] A mixture of $Cu(OAc)_2/Sm(O\text{-}^iPr)_3$/Schiff base complex with an achiral phenol additive was partially successful for achieving a *syn*-selective catalytic asymmetric nitro-Mannich reaction. Since the substrate generality of the first-generation system remained a little problematic, the catalyst preparation method had to be reinvestigated. The second-generation catalyst derived from $Sm_5O(O^iPr)_{13}$ showed broader substrate generality as well as higher reactivity and stereoselectivity compared to $Sm(O\text{-}^iPr)_3$ (Scheme 10).

A single chiral ligand provides enantioselective catalysts with different chiroptical properties upon complexation with $Sc(O^iPr)_3$ or $Er(O^iPr)_3$. Either an *anti*- or *syn*-selective catalytic asymmetric Mannich-type reaction of α-cyanoketones with *N*-Boc imines was developed (Scheme 11).[33] The structural dynamics and functional diversity of this catalytic system resulted in timely functional switching over the course of the reaction. The related chiral rare earth metal catalysts were applied to a catalytic asymmetric amination of nonprotected succinimide derivative,[34] a catalytic asymmetric conjugate addition of α-cyanoketone pronucleophiles to vinyl ketones,[35] and an asymmetric Conia-ene reaction of malonamates with β-ketoesters.[36]



Scheme 10 A catalytic asymmetric *syn*-selective nitro-Mannich reaction promoted by heterobimetallic Cu/Sm/dinucleating Schiff base complexes



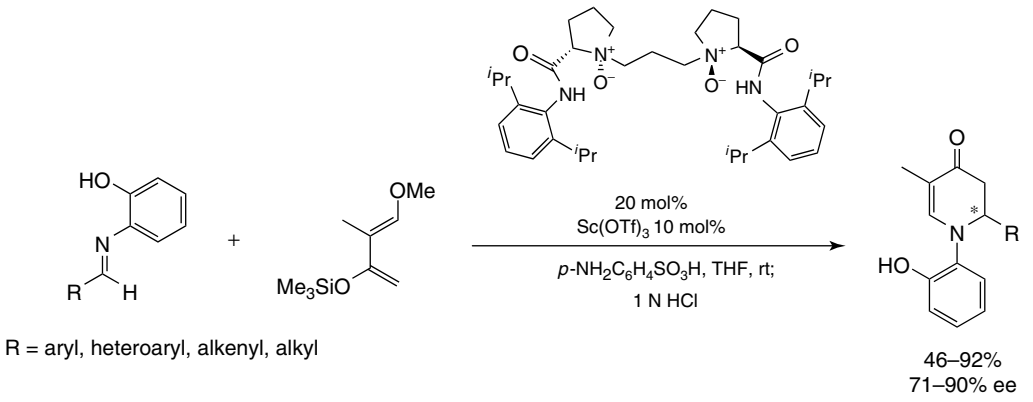
Scheme 11 *Anti*- and *syn*-selective catalytic asymmetric Mannich-type reaction of α-cyanocyclopentanone with *N*-Boc imine

Direct catalytic asymmetric Mannich-type reactions of various aromatic and heteroaromatic hydroxyketones are catalyzed by a Y{N(SiMe$_3$)$_2$}$_3$/TMS-linked-BINOL complex,[37] whereas a heterobimetallic lanthanum aryloxide/lithium aryloxide/pybox complex catalyzes direct catalytic asymmetric Mannich-type reactions of α-keto anilides as synthetic equivalents of homoenolates.[38] A La(OTf)$_3$/Me-PyBox/amine base/Brønsted acid combination was found to be effective for direct catalytic asymmetric Mannich-type reactions of γ-butenolides.[39]

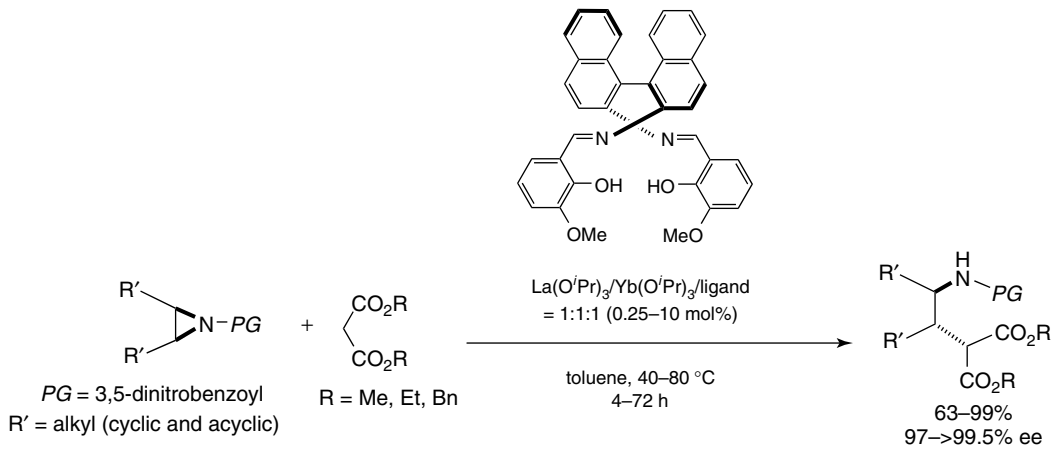
Chiral Gd catalysts are effective for Strecker α,α-disubstituted amino acid synthesis.[40] Two types of complexes are constructed via assembly of the same chiral modules derived from D-glucose, but their assembly modes differ. The enantioselectivity in the Strecker reaction was switched depending on which assembly mode was used.

In the catalytic asymmetric aza-Morita–Baylis–Hillman reaction using unactivated methyl acrylate, the combined use of a La(O-^{i}Pr)$_3$/(*S*,*S*)-TMS-linked-BINOL complex with a catalytic amount of 1,4-diazabicyclo[2.2.2]octane (DABCO) promoted the aza-Morita–Baylis–Hillman reaction of a broad range of *N*-diphenylphosphinoyl imines.[41]

Chiral scandium(III)-*N*, *N*′′-dioxide complexes catalyze enantioselective aza-Diels–Alder reaction of aldimines with Danishefsky-type diene (Scheme 12).[42] The complexes catalyzes the reaction between 1,3-butadiene and aldimines,



Scheme 12 Enantioselective aza-Diels–Alder reaction of aldimines



Scheme 13 Catalytic enantioselective ring-opening of *meso*-aziridines with malonates

affording the corresponding 2,5-disubstituted dihydropyridinones in moderate-to-high yields with good enantioselectivities at room temperature.

3.1.3 Other Catalytic Asymmetric Reactions

A heterodinuclear rare earth metal Schiff base catalyzes enantioselective desymmetrization of cyclic and acyclic *meso*-aziridines with malonates (Scheme 13).[43] The combined use of two rare earth metal sources with different properties, Brønsted basic rare earth metal alkoxide and Lewis acidic rare earth metal triflate, was important to promote the desired ring-opening reactions. The La(O-^{i}Pr)$_3$/Yb(OTf)$_3$/Schiff base complex gave chiral cyclic and acyclic γ-amino esters in high yields and high enantiomeric excesses.

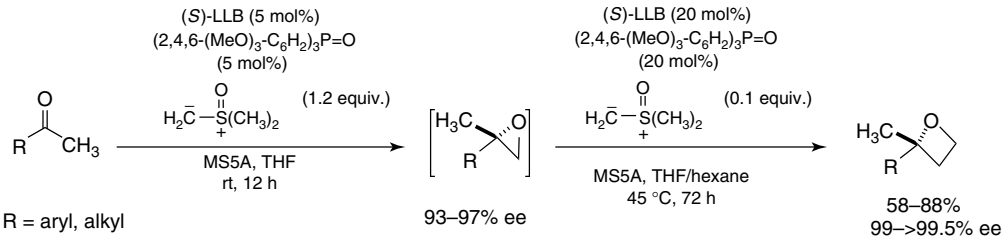
Gd complex generated from Gd(O^{i}Pr)$_3$ and a chiral ligand is a highly active and enantioselective catalyst in a catalytic asymmetric ring-opening reaction of *meso*-aziridines with TMSCN, a useful reaction for the synthesis of optically active β-amino acids.[44] A catalytic asymmetric epoxidation reaction of α,β-unsaturated esters via conjugate addition of an oxidant using a yttrium-chiral biphenyldiol complex was also reported by the authors.[45]

In a one-pot synthetic method for chiral 2,2-disubstituted oxetanes, a sequential addition reaction of a sulfur ylide to ketones and intermediate epoxides was promoted by the heterobimetallic catalyst LaLi$_3$tris(binaphthoxide) (LLB). [46] Chiral amplification was observed in the second reaction and was the key to affording the desired oxetanes with excellent enantioselectivity (Scheme 14).

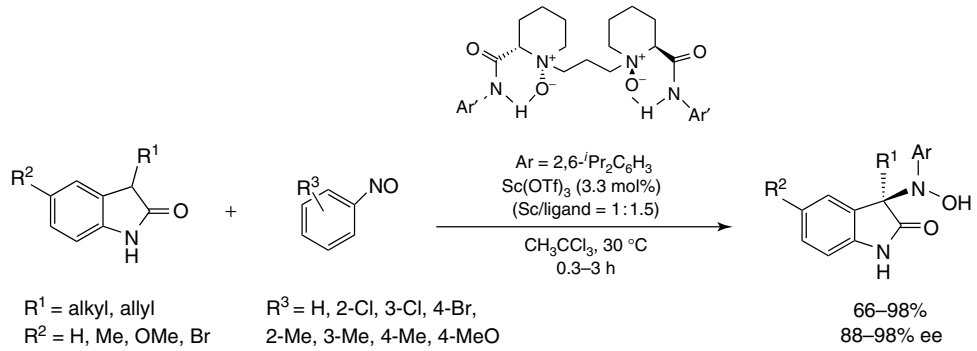
A chiral Sc(OTf)$_3$/N,N'-dioxide complex catalyzes hydroxyamination of N-unprotected 3-substituted-2-oxindoles with high enantioselectivity (Scheme 15).[47]

3.2 Addition to Olefins

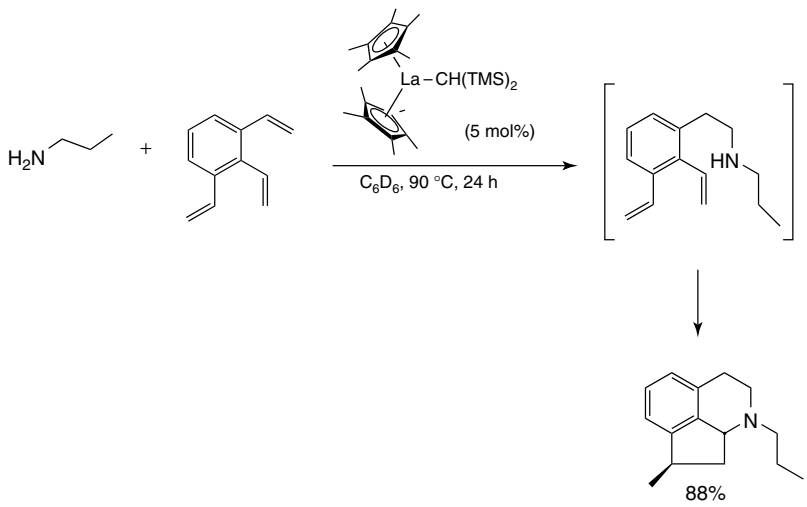
The first chiral rare earth metal-based hydroamination catalysts were reported in 1992 using chiral lanthanocene.[48] Organolanthanide complexes catalyze regioselective intermolecular hydroamination of alkenes, alkynes,



Scheme 14 Catalytic asymmetric synthesis of 2,2-disubstituted oxetanes from ketones by using a one-pot sequential addition of sulfur ylide



Scheme 15 Catalytic asymmetric hydroxyamination reactions of oxindoles with nitrosoarenes

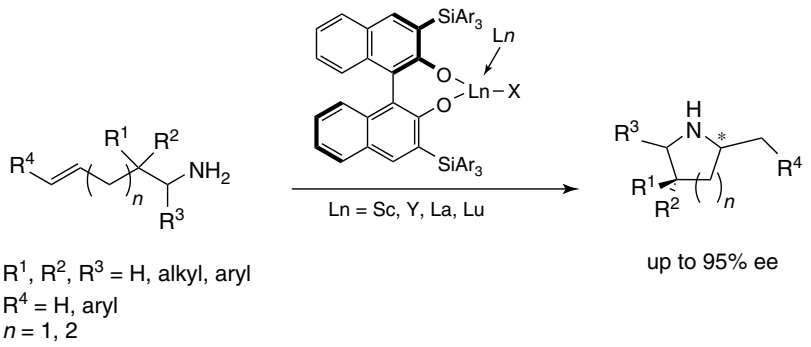


Scheme 16 Organolanthanide-catalyzed intermolecular hydroamination of trivinylarene

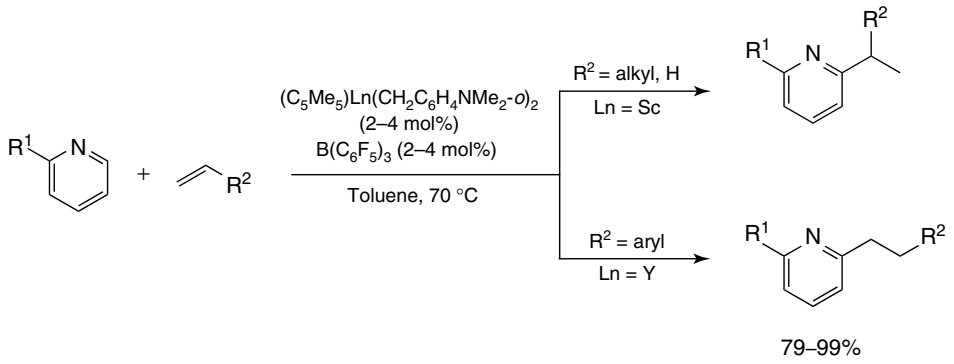
vinylarenes, di- and trivinylarenes, and methylenecyclopropanes (Scheme 16).[49] The catalysts are also effective for hydroalkoxylation[50] and hydrophosphination.[51]

Rare earth metal complexes with sterically demanding tris(aryl)silyl-substituted binaphtholate ligands efficiently catalyze asymmetric hydroamination/cyclization of aminoalkenes and the kinetic resolution of α-substituted aminopentenes.[52] The catalytic activities are comparable to those of lanthanocene catalyst systems, and high enantioselectivities up to 95% ee were achieved in the cyclization of achiral aminopentenes (Scheme 17).

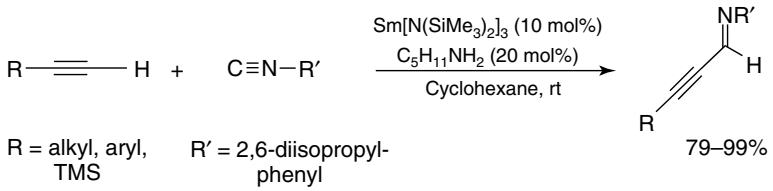
Half-sandwich rare earth dialkyl complexes such as $(C_5Me_5)Ln(CH_2C_6H_4NMe_2\text{-}o)_2$ (Ln = Sc, Y) in combination with an activator such as $B(C_6F_5)_3$ can serve as an excellent catalyst for *ortho*-selective C–H addition of pyridines to a variety of olefins (Scheme 18). A series of alkylated



Scheme 17 Catalytic asymmetric hydroamination/cyclization of aminoalkenes



Scheme 18 Catalytic C–H addition of pyridine derivatives to olefins



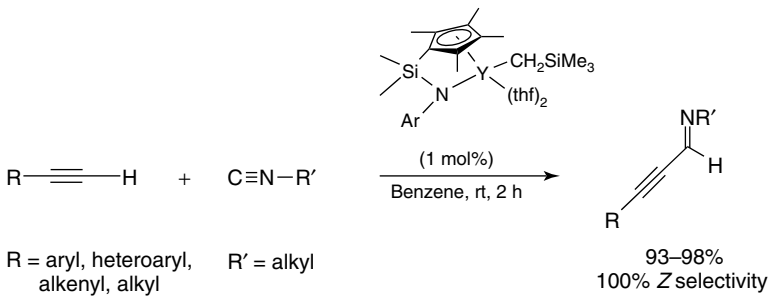
Scheme 19 Rare earth silylamide-catalyzed monocoupling reactions of isocyanides with terminal alkynes

pyridine derivatives were obtained in an atom-economical way (Scheme 18).[53] These catalysts are complementary to late transition metal catalysts in terms of selectivity, functional group tolerance, and substrate scope.

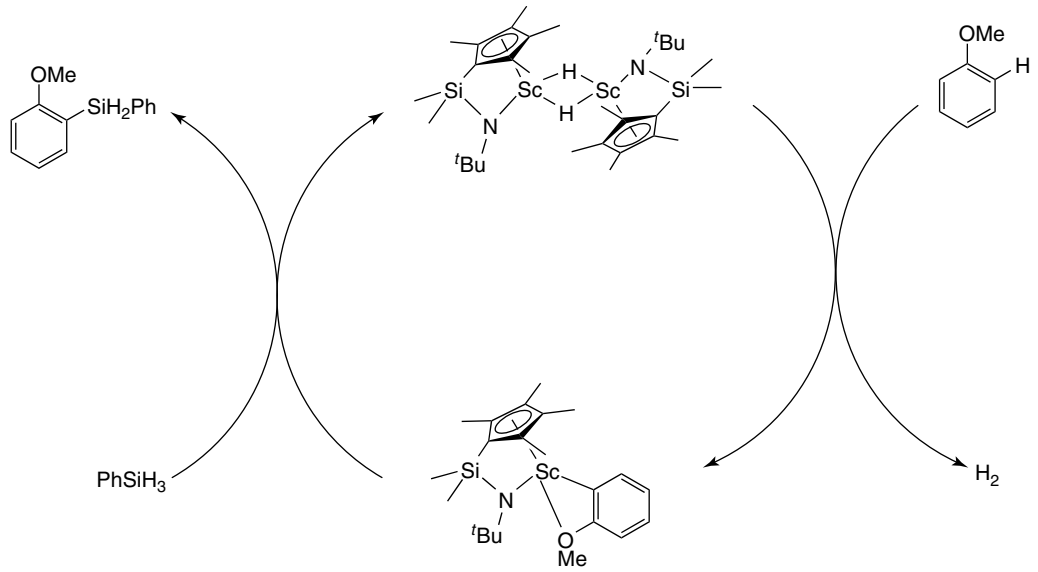
3.3 Coupling Reactions

Catalytic monoinsertion of isocyanides into terminal alkynes proceed utilizing rare earth silylamides in the presence of aliphatic primary amine additives under mild conditions.[54] Variously functionalized terminal alkynes could be converted to the corresponding 1-aza-1,3-enynes in excellent yields owing to good compatibility of the silylamide catalyst (Scheme 19). Mechanistic investigation revealed that the amine additives played an important role as proton sources to prevent oligomerization of isocyanides and as suitable ligands to activate the rare earth catalysts. Rare earth silylamide catalyzes selective dimerization of terminal alkynes and subsequent hydrophosphination in one pot.[55]

Half-sandwich rare earth metal alkyl complexes can act as catalyst precursors for the cross-coupling of various terminal alkynes with isocyanides selectively affording the (*Z*)-1-aza-1,3-enyne products (Scheme 20).[56] The unprecedented *Z* selectivity could arise from the formation of an alkynide-bridged binuclear catalyst species, in which the cross-coupling reaction took place at the two metal centers in an intermolecular fashion.



Scheme 20 Catalytic monoinsertion of isocyanides into terminal alkynes



Scheme 21 Scandium-catalyzed silylation of aromatic C–H bonds

3.4 Other Reactions

ortho-Selective C–H silylation of various alkoxy-substituted benzene derivatives using half-sandwich scandium alkyl complexes without any hydrogen acceptor affords high conversion (Scheme 21).[57] Aromatic C–X bonds (X = Cl, Br, I, SMe, NMe_2) can survive under the reaction conditions. The successful isolation and structural characterization of the anisyl and the hydride complexes have offered important insight into the mechanistic aspects of the catalytic process.

4 CATALYSIS IN AQUEOUS MEDIA

4.1 Background

The importance of organic reactions in water is now generally recognized. It is desirable to perform the reactions in water instead of organic solvents from the viewpoint of green chemistry. Most chemical reactions of organic substrates conducted in the laboratory as well as in industry still need organic solvents as reaction media, although water is safe, benign, environmentally friendly, and cheap compared with organic solvents. On the other hand, Lewis acid-catalyzed carbon–carbon bond-forming reactions have been of great interest in organic synthesis because of their unique reactivity and selectivity, and for the mild conditions used. Lanthanide triflates were expected to be one of the strongest Lewis acids because of the electron-withdrawing triflate group. On the other hand, their hydrolysis was postulated to be slow, on the basis of their hydration energies and hydrolysis constants. Scandium triflate ($Sc(OTf)_3$) and yttrium triflate ($Y(OTf)_3$) are excellent water-tolerant Lewis acids, and new synthetic reactions using these rare earth triflates as catalysts have been developed. In this chapter, recent synthetic technologies using rare earth Lewis acid catalysts in aqueous media are highlighted.

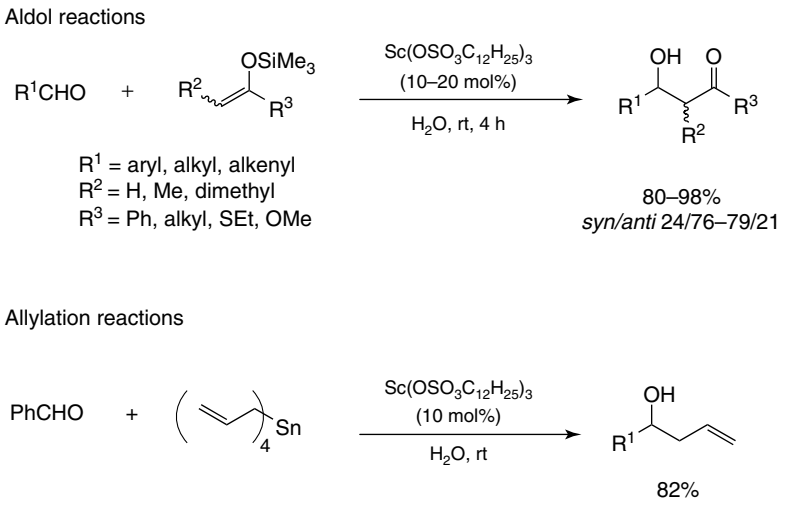
Table 1 Hydrolysis constant and exchange rate constants for substitution of inner-sphere water ligand

Element	Hydrolysis constant	Exchange rate constant	Element	Hydrolysis constant	Exchange rate constant
Li^{I}	13.64	$\mathbf{4.7 \times 10^7}$	Cd^{II}	**10.08**	$\mathbf{>1 \times 10^8}$
Na^{I}	14.18	$\mathbf{1.9 \times 10^8}$	In^{III}	4.00	4.0×10^4
Mg^{II}	11.44	5.3×10^5	Hf^{IV}	0.25	—
Al^{III}	1.14	1.6×10^0	Pt^{II}	**4.8**	—
K^{I}	14.46	$\mathbf{1.5 \times 10^8}$	Hg^{II}	3.40	$\mathbf{2 \times 10^9}$
Ca^{II}	12.85	$\mathbf{5 \times 10^7}$	Tl^{III}	0.62	7×10^5
Sc^{III}	**4.3**	$\mathbf{4.8 \times 10^7}$	Pb^{II}	**7.71**	$\mathbf{7.5 \times 10^9}$
Ti^{IV}	<23	—	Bi^{III}	1.09	—
V^{III}	2.26	1×10^3	La^{III}	**8.5**	$\mathbf{2.1 \times 10^8}$
Cr^{III}	4.0	5.8×10^{-7}	Ce^{III}	**8.3**	$\mathbf{2.7 \times 10^8}$
Mn^{II}	10.59	$\mathbf{3.1 \times 10^7}$	Pr^{III}	**8.1**	$\mathbf{3.1 \times 10^8}$
Fe^{II}	**9.5**	$\mathbf{3.2 \times 10^6}$	Nd^{III}	**8.0**	$\mathbf{3.9 \times 10^8}$
Co^{II}	**9.65**	2×10^5	Sm^{III}	**7.9**	$\mathbf{5.9 \times 10^8}$
Ni^{II}	**9.86**	2.7×10^4	Eu^{III}	**7.8**	$\mathbf{6.5 \times 10^8}$
Cu^{II}	**7.53**	$\mathbf{2 \times 10^8}$	Gd^{III}	**8.0**	$\mathbf{6.3 \times 10^7}$
Zn^{II}	**8.96**	$\mathbf{5 \times 10^8}$	Tb^{III}	**7.9**	$\mathbf{7.8 \times 10^7}$
Ga^{III}	2.6	7.6×10^2	Dy^{III}	**8.0**	$\mathbf{6.3 \times 10^7}$
Y^{III}	**7.7**	$\mathbf{1.3 \times 10^7}$	Ho^{III}	**8.0**	$\mathbf{6.1 \times 10^7}$
Zr^{IV}	0.22	—	Er^{III}	**7.9**	$\mathbf{1.4 \times 10^8}$
Rh^{III}	3.4	3×10^8	Tm^{III}	7.7	$\mathbf{6.4 \times 10^6}$
Pd^{II}	2.3	—	Yb^{III}	7.7	$\mathbf{8 \times 10^7}$
Ag^{I}	12	$\mathbf{>5 \times 10^6}$	Lu^{III}	**7.6**	$\mathbf{6 \times 10^7}$

The stability and catalytic activity of lanthanide triflates in water were ascribed to their large ionic radii and an equilibrium between the Lewis acids and water. In addition, as common characteristics, a certain range of hydrolysis constants (the value is between 4.3 and 10.08), and a high order of exchange rate constants (the value is more than 3.2×10^6 M^{-1} s^{-1}) for substitution of inner-sphere water ligands (water exchange rate constant (WERC)) have been found among these water-stable Lewis acids (Table 1, see the reference for the details of calculation). It was found that Lewis acids based on rare earths (Sc^{III}, Y^{III}, Ln^{III}) were both stable and active in water.[58]

Although today's environmental consciousness imposes the use of water as a solvent on both industrial and academic chemists, organic solvents are still used instead of water for mainly two reasons. First, most organic substances are insoluble in water, and as a result, water does not function as a reaction medium. Second, many reactive substrates, reagents, and catalysts are decomposed or deactivated by water. The first drawback in the use of water (the solubility problem) can be overcome by using surfactants, which solubilize organic materials or form colloidal dispersions with them in water. A Lewis acid–surfactant-combined catalyst (LASC) has been developed and applied to Lewis acid-catalyzed organic reactions in water. LASCs are composed of water-stable Lewis acidic cations such as scandium and anionic surfactants such as dodecyl sulfate and dodecanesulfonate and are easily prepared. These catalysts can be successfully used for various typical carbon–carbon bond-forming reactions such as aldol, allylation, and Mannich-type reactions in water (Scheme 22). Furthermore, the results of aldol reactions in various solvents show that water is the best solvent for the LASC-catalyzed reactions. A preliminary kinetic study of the aldol reaction showed that the initial rate in water was 1.3×10^2 times higher than that in dichloromethane (DCM).[59] The LASCs form stable colloidal dispersions rapidly in the presence of reaction substrates in water, even when the substrates are solid (Figure 3).

Optical microscopic observations of the colloidal particles revealed their spherical shape (Figure 4). When an LASC ($Sc(O_3SC_{12}H_{25})_3$) was mixed with benzaldehyde in a ratio of 1 : 10, both the spherical colloidal particles and the crystals of the LASC were observed (a). As the amount of benzaldehyde increased (b and c), the amount of the crystals of the LASC decreased, and finally, all of the LASC formed the spherical colloidal particles with the aldehyde in LASC:benzaldehyde ratio of 1 : 100 (c). The shape and the size of the colloidal particles were also confirmed by transmission electron microscopy (TEM) (Figure 5) and atomic force microscopy (AFM) (Figure 6). The TEM pictures also reveal that scandium ions, which act as a stain in the pictures, are mainly located on the surface of the colloidal particles and inside the particles. By AFM analysis, the diameter of the particle (the distance between the circle and the square at the bottom of the particle) is 1.93 μm. The height of the particle (the height of the position shown by the triangle at the top of the particle) is 0.226 μm.



Scheme 22 LASC-catalyzed carbon–carbon bond-forming reactions in water

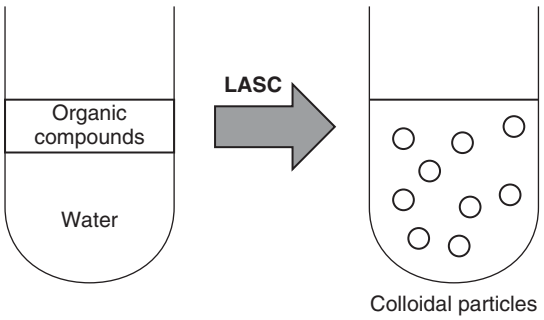


Figure 3 Efficient reaction environments (colloidal particles) created by a LASC with organic substrates in water

The characterization of the colloidal particles was also carried out by means of dynamic light scattering. It was suggested that most of the substrates and catalyst molecules were concentrated in the spherical particles, which acted as a hydrophobic reaction environment and enabled the rapid organic reactions in water.

4.2 Catalytic Asymmetric Reactions Using Rare Earth Catalysts in Aqueous Media

4.2.1 Asymmetric Aldol Reaction

$Pr(OTf)_3$-chiral bis-pyridino-18-crown-6 complex catalyzes asymmetric aldol reactions in aqueous media (Scheme 23).[60] Slight changes in the ionic diameters

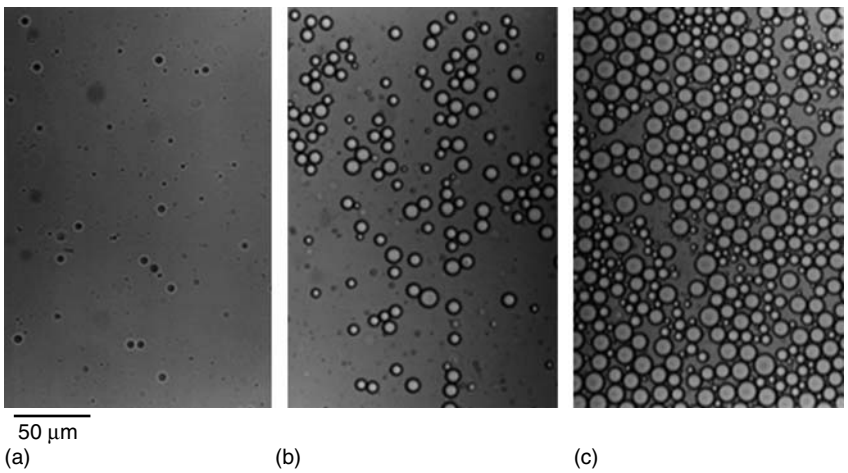


Figure 4 Photographs by optical microscopy. Colloidal particles formed from a LASC ($Sc(O_3SC_{12}H_{25})_3$) and benzaldehyde. (a) LASC/benzaldehyde = 1/10; (b) 1/20; (c) 1/100. The concentration of the LASC was 16.7 mM

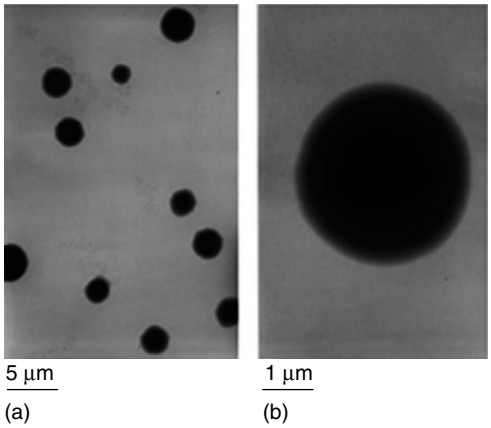


Figure 5 TEM images of the colloidal particles ($Sc(O_3SC_{12}H_{25})_3$ and benzaldehyde). (a) × 2600 and (b) × 10000

of the metal cations greatly affected the diastereo and enantioselectivities of the products. The substituents at the 4-position of the pyridine rings of the crown ether did not significantly affect the selectivities in the asymmetric aldol reaction, although they affected the binding ability of the crown ether with rare earth cations and the catalytic activity of $Pr(OTf)_3$-crown ether complexes. From the X-ray structures of $RE(NO_3)_3$-crown ether complexes, it was found that they had similar structures regardless of the cations and the crown ethers. Various aromatic and α,β-unsaturated aldehydes and silyl enol ethers derived from ketones and a thioester can be employed in the catalytic system, to provide the aldol adducts in good-to-high yields and stereoselectivities. In the case using the silyl enol ether derived from a thioester, 2,6-di-*tert*-butylpyridine significantly improved the yields of the aldol adducts.

A chiral lanthanide complex catalyzes asymmetric Mukaiyama aldol reactions in aqueous media (Scheme 24).[61] The changes in the water-coordination number is key to the mechanism of the catalytic reaction. The precatalysts yielded β-hydroxy carbonyl compounds from aliphatic and aryl substrates with high diastereomeric ratios and enantiomeric excesses of up to 49 : 1 and 97%, respectively.

Formaldehyde is one of the most important C1 electrophiles in organic synthesis. Although hydroxymethylation of enolates with formaldehyde provides an efficient method to

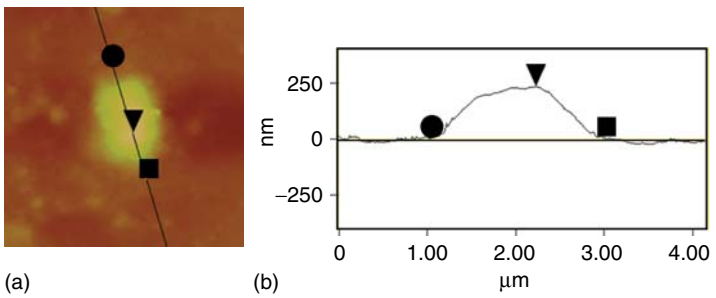
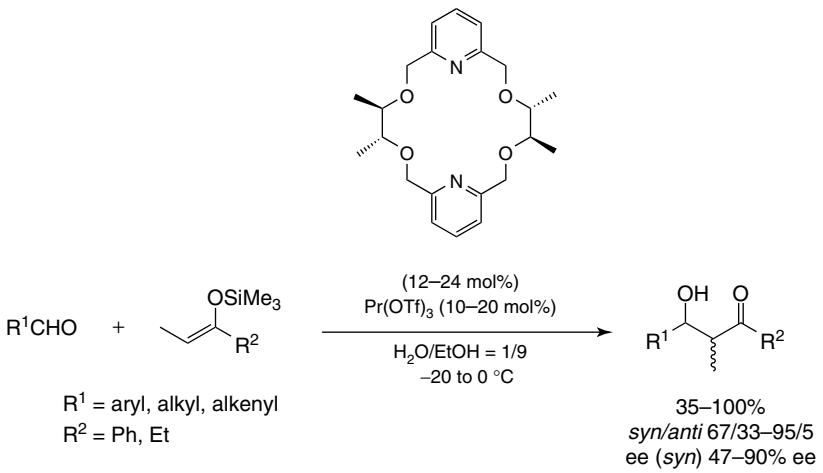
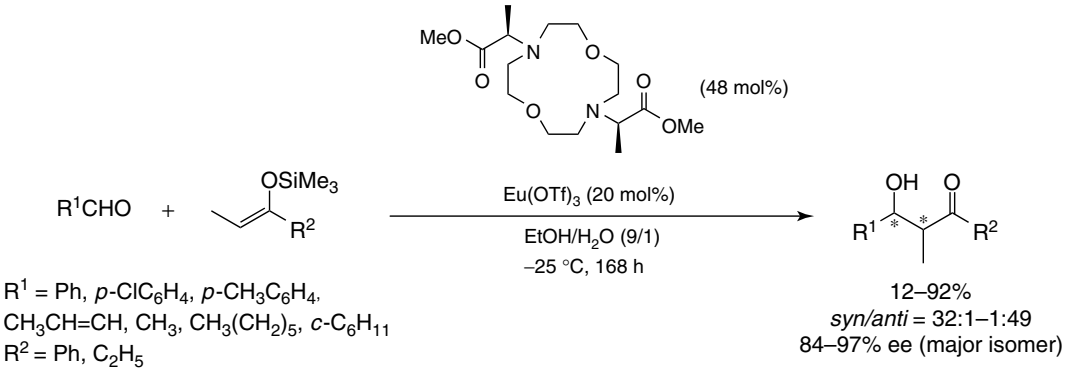


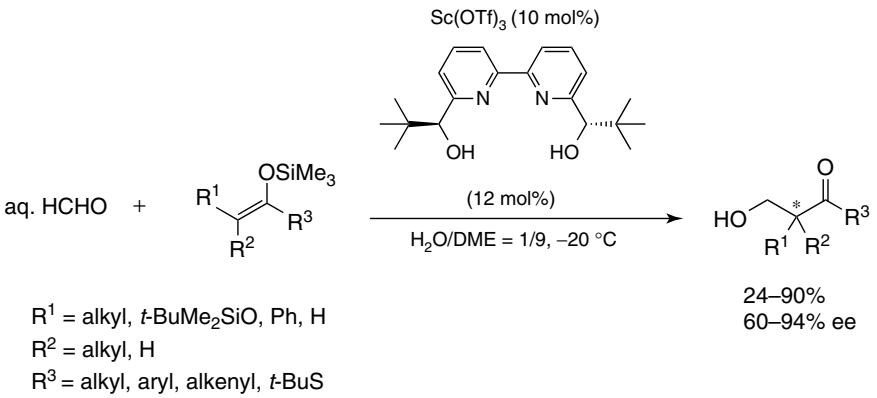
Figure 6 AFM analysis of colloidal particles formed from a mixture of LASC ($Sc(O_3SC_{12}H_{25})_3$) and benzaldehyde. (a) image of a colloidal particle; (b) vertical sectional view taken on the line of (a)



Scheme 23 Asymmetric aldol reactions using $Pr(OTf)_3$ and chiral bis-pyridino-18-crown-6



Scheme 24 Asymmetric Mukaiyama aldol reactions using a chiral europium catalyst



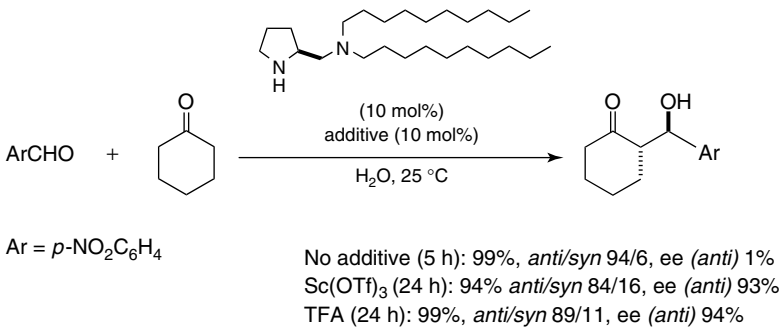
Scheme 25 Catalytic asymmetric hydroxymethylation of silicon enolates using a chiral scandium catalyst

introduce a C1 functional group at the α-position of carbonyl groups, there have been few successful examples of catalytic asymmetric hydroxymethylation that satisfy synthetic utility in terms of both yield and selectivity for a wide range of substrates. As for the source of formaldehyde, use of a commercial aqueous solution of formaldehyde is the most convenient, because tedious and harmful procedures to generate formaldehyde monomer from formaldehyde oligomers such as paraformaldehyde and trioxane can be avoided. A chiral catalyst prepared from scandium triflate and Bolm's chiral bipyridine ligand affords successful catalytic asymmetric hydroxymethylation of silicon enolates (Scheme 25).[62]

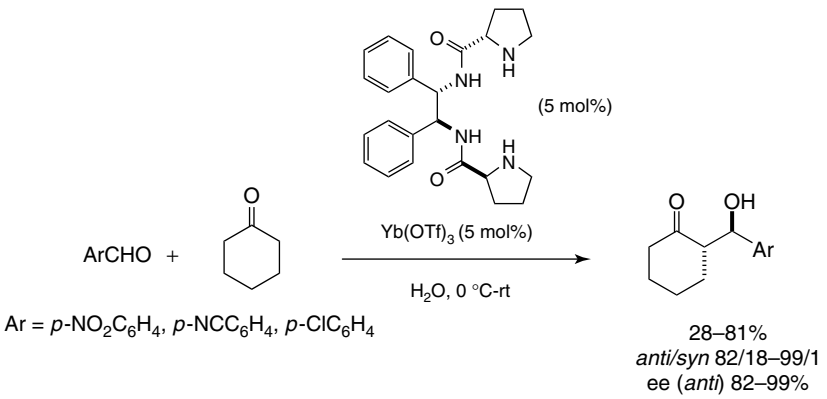
Scandium-catalyzed hydroxymethylation reaction with aqueous formaldehyde in water proceeds without any organic cosolvents. In the presence of $Sc(OSO_3C_{12}H_{25})_3$, a representative LASC, both achiral and asymmetric hydroxymethylations proceed smoothly with high selectivities. Lewis acid–base interactions between the scandium catalyst and formaldehyde were suggested to be crucial on the basis of several experiments. This is the first example of a catalytic hydroxymethylation of silicon enolates with aqueous formaldehyde in water that does not require any organic solvents.[63] Instead of silyl enol ethers, ketones could also be applied to the scandium-catalyzed enantioselective hydroxymethylation using aqueous formaldehyde in water by addition of a catalytic amount of pyridine.[64]

Direct asymmetric cross-aldol reactions of ketones with aromatic aldehydes proceed in the presence of an L-proline-derived tertiary diamine and additives using water as a solvent (Scheme 26).[65] L-Proline-derived diamines give racemic product in the absence of an acid cocatalyst. While trifluoroacetic acid (TFA) is the most effective additive for the aldol addition of cyclohexanone to 4-nitrobenzaldehyde in the presence of L-proline-derived diamine, addition of scandium triflate is also effective for the reaction with similar enantioselectivity.

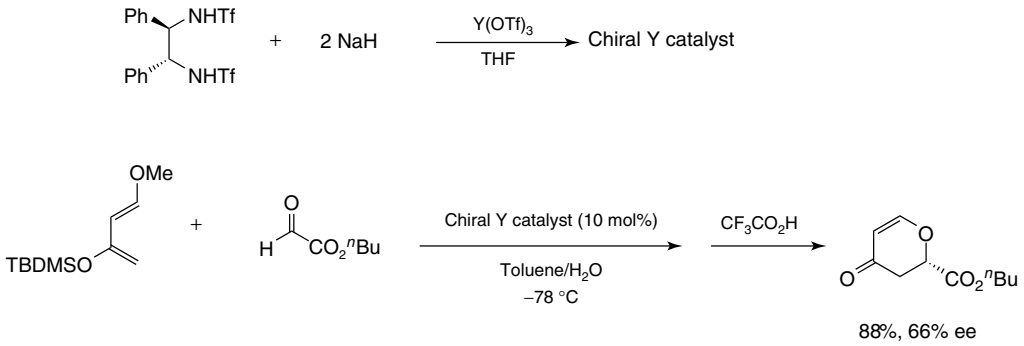
A combination of ytterbium (or zinc) triflate and chiral C_2-symmetric prolinamide ligand leads to high enantioselectivities in direct aldol reactions under aqueous conditions (Scheme 27).[66] The presence of 5 mol% of the catalyst affords an asymmetric intermolecular aldol reaction between unmodified ketones and aldehydes to give antiproducts with excellent enantioselectivities up to 99% ee.



Scheme 26 Chiral diamine/TFA-catalyzed aldol reactions of ketones and aldehydes in water



Scheme 27 Direct catalytic asymmetric aldol reactions using chiral Yb catalyst in water



Scheme 28 Catalytic asymmetric hetero Diels–Alder reactions in aqueous system

4.3.2 Asymmetric Hetero Diels–Alder Reaction

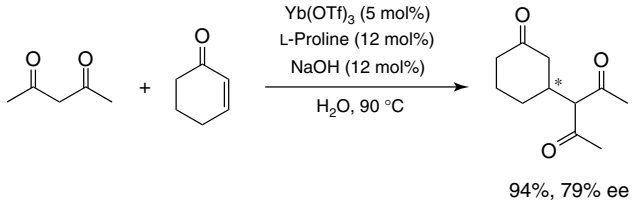
In the asymmetric hetero Diels–Alder reactions of Danishefsky's diene by chiral lanthanide bis(trifluoromethanesulfonyl)amide (bis-triflamide) complexes, particularly yttrium bis-triflamide, a significant effect of water as an additive was observed in increasing not only the enantioselectivity but also the chemical yields (Scheme 28).[67]

4.3.3 Asymmetric Michael Reaction

$Yb(OTf)_3$ with native α-amino acids as chiral ligands catalyzes asymmetric Michael addition reactions in water.[68] Although the reaction conditions require only 5 mol% of the Lewis acid, it provides enantiomeric excesses of up to 79% and is applicable to a wider range of donors and acceptors than previously demonstrated (Scheme 29). This catalyst might have potential for large-scale applications as it displays not

only large ligand accelerations but also good solubility and stability in water. It can be recycled multiple times without significant loss of activity.

Asymmetric Michael reactions of thiols with enones are catalyzed by a $Sc(OTf)_3$-chiral bipyridine complex in water without using any organic solvents.[69,70] The reactions afford the desired sulfides in high yields with high enantioselectivities (Scheme 30).



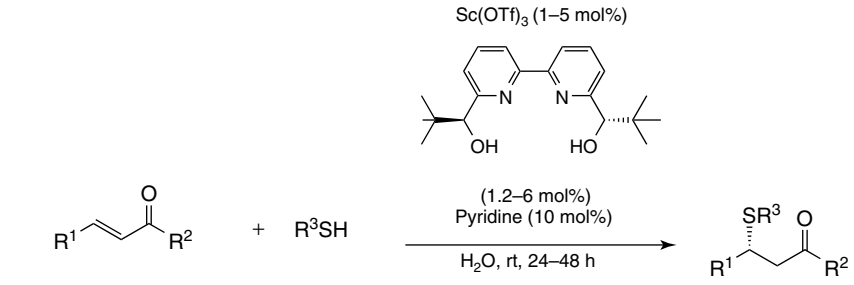
Scheme 29 Aqueous Michael additions catalyzed by Yb-$(OTf)_3$/L-proline

4.3.4 *Asymmetric Ring-Opening Reaction*

Catalytic enantioselective addition of amines to *meso*-epoxides can be realized by employing a scandium–bipyridine complex in 100% water (Scheme 31). Chiral β-amino alcohols were prepared in mostly high yields with excellent enantioselectivities (Scheme 31). It is noted that the use of water as a solvent gave a higher yield and enantioselectivity than the use of dichloromethane as a solvent.[71,72]

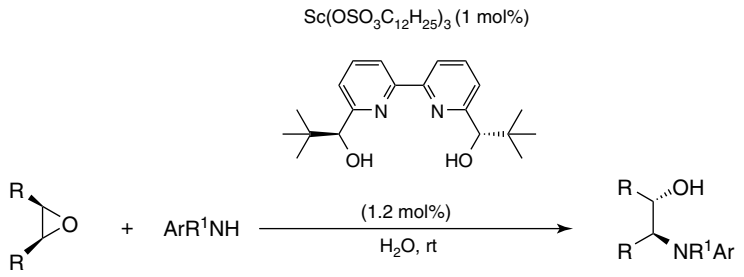
Utilizing the same catalyst complex, aromatic *N*-heterocycles, an alcohol, and thiols also act as nucleophiles to afford the corresponding products in moderate to good yields (34–85%) with high to excellent enantioselectivities (74–96% ee) in water.[73]

Reversal of enantioselectivity in Cu-chiral bipyridine-catalyzed asymmetric ring-opening reactions of *meso*-epoxides with indole and aniline derivatives is observed compared to Sc-chiral bipyridine-catalyzed reactions, where the same chiral ligand is used (Scheme 32).[74] It was revealed from X-ray crystal structural analysis that a square pyramidal structure for the Cu^{II} complex and a pentagonal bipyramidal



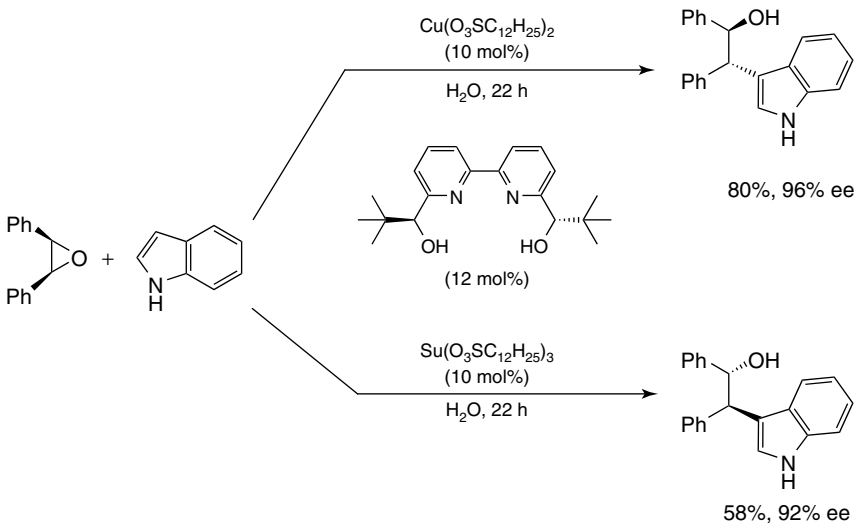
R^1 = Me, C_5H_{11}, Ph, *p*-ClC_6H_4, 2-thienyl
R^2 = Me, Et, Ph
R^3 = Bn, Et, ^{i}Pr, *c*C_5H_9, *p*-^{t}Bu$C_6H_4CH_2$

Scheme 30 Chiral Sc-catalyzed catalytic asymmetric Michael reactions of thiols with enones[69]

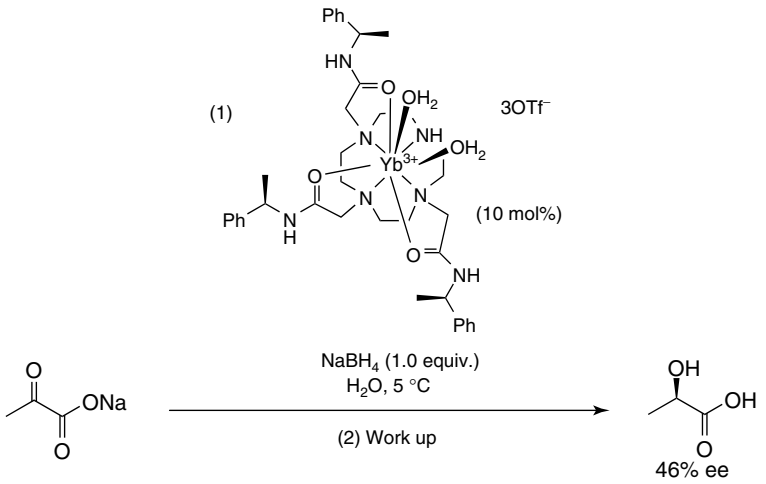


R = aryl, alkyl
R^1 = Me, H
Ar = Ph, *o*-$MeOC_6H_4$, α-naphthyl, 1-(4-bromonaphthyl)

Scheme 31 Asymmetric ring opening of *meso*-epoxides using chiral scandium catalyst



Scheme 32 Reversal of enantioselectivity in Cu- and Sc-catalyzed ring-opening reactions of *meso*-epoxides



Scheme 33 Asymmetric reduction by a chiral lanthanide complex in water

structure for the Sc^{III} complex were formed, which could explain the reversal of the enantioselectivity. Some reactions were also tested in dichloromethane (DCM), and it was revealed that the reactions proceeded faster in water than in DCM. Several nonlinear effect experiments suggested a unique structure for these chiral catalysts.[75]

4.3.5 Asymmetric Reduction

Stable, well-defined chiral ytterbium complexes catalyze the asymmetric reduction of α-keto acids in aqueous solution (Scheme 33).[76] Although the enantiomeric excesses are modest (40–50%), this is the first example of asymmetric reduction by a chiral lanthanide complex in water.

5 CONCLUSIONS

Rare earth metal-based Lewis acids, mostly rare earth metal triflates, are novel catalyst series from which we can select the most effective metal that has appropriate size and structure. Owing to their high coordination number and hard acid character, fine-tuning of ligands is also possible. Various multifunctional bimetallic catalysts have been developed thanks to these characteristics. Furthermore, rare earth metal-based Lewis acids are compatible with water. This property is largely different from that of traditional Lewis acids such as $AlCl_3$, $TiCl_4$, and BF_3, which need strictly anhydrous conditions. Various organic reactions including catalytic asymmetric reactions can be performed using rare earth metal-based Lewis acids in aqueous systems.

In addition, catalytic amounts of rare earth metal triflates have been successfully used, while stoichiometric amounts of conventional Lewis acids have been employed in many cases. From the viewpoint of sustainable green chemistry, it is remarkable that rare earth metal triflates can be recovered and reused without loss of activity. These properties will lead to really environmental-friendly chemical processes using rare earth metals as catalysts.

6 GLOSSARY

Chiral: Of or relating to the structural characteristic of a molecule that makes it impossible to superimpose it on its mirror image

Enantioselective: Relating to or being one enantiomer (one of a pair of chemical compounds whose molecular structure have a mirror-image relationship each other) of a chiral product is produced preferentially

Lewis acid: Electron pair acceptor

Schiff base: A class of derivatives of the condensation of aldehydes or ketones with primary amines

7 RELATED ARTICLES

Heterogeneous Catalysis; Homogeneous Catalysis; Lanthanides: Coordination Chemistry; Organometallic Chemistry Fundamental Properties.

8 ABBREVIATIONS AND ACRONYMS

AFM = atomic force microscopy; DABCO = 1,4-diazabicyclo[2.2.2]octane; DCM = dichloromethane; LASC = Lewis acid–surfactant-combined; LLB = LaLi3tris-(binaphthoxide); REMB = rare-earth–alkali-metal–BINOL; TEM = transmission electron microscopy; TFA = trifluoroacetic acid; TfOH = trifluoromethanesulfonic acid; WERC = water exchange rate constant.

9 REFERENCES

1. S. Kobayashi, *Chem. Lett.*, 1991, **20**, 2187.
2. H. Tsuruta, K. Yamaguchi, and T. Imamoto, *Chem. Commun.*, 1999, 1703.
3. K. F. Thom, U.S. Patent 3615169, 1971.
4. K. F. Thom, *Chem. Abstr.* 1972, **76**, 5436a.
5. C. Ogawa, Y. Gu, M. Boudou, and S. Kobayashi, in 'Acid Catalysis in Modern Organic Synthesis', eds. H. Yamamoto and K. Ishihara, Wiley-VCH, Weinheim, 2008, p. 589.
6. M. Shibasaki, S. Matsunaga, and N. Kumagai, in 'Acid Catalysis in Modern Organic Synthesis', eds. H. Yamamoto and K. Ishihara, Wiley-VCH, Weinheim, 2008, p. 635.
7. S. Kobayashi, M. Sugiura, H. Kitagawa, and W. W.-L. Lam, *Chem. Rev.*, 2002, **102**, 2227.
8. M. Shibasaki, M. Kanai, S. Matsunaga, and N. Kumagai, *Acc. Chem. Res.*, 2009, **42**, 1117.
9. M. Nishiura and Z. Hou, *Nat. Chem.*, 2010, **2**, 257.
10. M. Bednarski, C. Maring, and S. Danishefsky, *Tetrahedron Lett.*, 1983, **24**, 3451.
11. S. Kobayashi, M. Araki, and I. Hachiya, *J. Org. Chem.*, 1994, **59**, 3758.
12. D. A. Evans, Z. K. Sweeney, T. Rovis, and J. S. Tedrow, *J. Am. Chem. Soc.*, 2001, **123**, 12095.
13. S. Fukuzawa, H. Matsuzawa, and K. Metoki, *Synlett*, 2001, **5**, 709.
14. G. Desimoni, G. Faita, S. Filippone, M. Mella, M. G. Zampori, and M. Zema, *Tetrahedron*, 2001, **57**, 10203.
15. D. A. Evans, C. E. Masse, and J. Wu, *Org. Lett.*, 2002, **4**, 3375.
16. D. A. Evans, Y. Aye, and J. Wu, *Org. Lett.*, 2006, **8**, 2071.
17. D. A. Evans and J. Wu, *J. Am. Chem. Soc.*, 2005, **127**, 8006.
18. D. A. Evans, K. R. Fandrick, H.-J. Song, K. A. Scheidt, and R. Xu, *J. Am. Chem. Soc.*, 2007, **129**, 10029.
19. D. A. Evans and J. Wu, *J. Am. Chem. Soc.*, 2003, **125**, 10162.
20. D. A. Evans and Y. Aye, *J. Am. Chem. Soc.*, 2006, **128**, 11034.
21. G. M. Sammis, H. Danjo, and E. N. Jacobsen, *J. Am. Chem. Soc.*, 2004, **126**, 9928.
22. H. Sasai, T. Suzuki, S. Arai, T. Arai, and M. Shibasaki, *J. Am. Chem. Soc.*, 1992, **114**, 4418.
23. H. Mihara, Y. Xu, N. E. Shepherd, S. Matsunaga, and M. Shibasaki, *J. Am. Chem. Soc.*, 2009, **131**, 8384.
24. T. Nitabaru, A. Nojiri, M. Kobayashi, N. Kumagai, and M. Shibasaki, *J. Am. Chem. Soc.*, 2009, **131**, 13860.
25. T. Nitabaru, N. Kumagai, and M. Shibasaki, *Angew. Chem. Int. Ed.*, 2012, **51**, 1644.
26. S. Handa, K. Nagawa, Y. Sohtome, S. Matsunaga, and M. Shibasaki, *Angew. Chem. Int. Ed.*, 2008, **47**, 3230.
27. M. Nakajima, Y. Yamaguchi, and S. Hashimoto, *Chem. Commun.*, 2001, 1596.
28. X. Liu, L. Lin, and X. Feng, *Acc. Chem. Res.*, 2011, **44**, 574.
29. X. Yang, X. Zhou, L. Lin, L. Chang, X. Liu, and X. Feng, *Angew. Chem. Int. Ed.*, 2008, **47**, 7079.
30. Z. Wang, Z. Yang, D. Chen, X. Liu, L. Lin, and X. Feng, *Angew. Chem. Int. Ed.*, 2011, **50**, 4928.

31. Y. Liu, D. Shang, X. Zhou, Y. Zhu, L. Lin, X. Liu, and X. Feng, *Org. Lett.*, 2010, **12**, 180.
32. S. Handa, V. Gnanadesikan, S. Matsunaga, and M. Shibasaki, *J. Am. Chem. Soc.*, 2010, **132**, 4925.
33. A. Nojiri, N. Kumagai, and M. Shibasaki, *J. Am. Chem. Soc.*, 2009, **131**, 3779.
34. T. Mashiko, N. Kumagai, and M. Shibasaki, *J. Am Chem. Soc.*, 2009, **131**, 14990.
35. Y. Kawato, N. Takahashi, N. Kumagai, and M. Shibasaki, *Org. Lett.*, 2010, **12**, 1484.
36. A. Matsuzawa, T. Mashiko, N. Kumagai, and M. Shibasaki, *Angew. Chem. Int. Ed.*, 2011, **50**, 7616.
37. M. Sugita, A. Yamaguchi, N. Yamagiwa, S. Handa, S. Matsunaga, and M. Shibasaki, *Org. Lett.*, 2005, **7**, 5339.
38. G. Lu, H. Morimoto, S. Matsunaga, and M. Shibasaki, *Angew. Chem. Int. Ed.*, 2008, **47**, 6847.
39. A. Yamaguchi, S. Matsunaga, and M. Shibasaki, *Org. Lett.*, 2008, **10**, 2319.
40. N. Kato, T. Mita, M. Kanai, B. Therrien, M. Kawano, K. Yamaguchi, H. Danjo, Y. Sei, A. Sato, S. Furusho, and M. Shibasaki, *J. Am. Chem. Soc.*, 2006, **128**, 6768.
41. T. Yukawa, B. Seelig, Y. Xu, H. Morimoto, S. Matsunaga, A. Berkessel, and M. Shibasaki, *J. Am. Chem. Soc.*, 2010, **132**, 11988.
42. D. Shang, J. Xin, Y. Liu, X. Zhou, X. Liu, and X. Feng, *J. Org. Chem.*, 2008, **73**, 630.
43. Y. Xu, L. Lin, M. Kanai, S. Matsunaga, and M. Shibasaki, *J. Am. Chem. Soc.*, 2011, **133**, 5791.
44. I. Fujimori, T. Mita, K. Maki, M. Shiro, A. Sato, S. Furusho, M. Kanai, and M. Shibasaki, *J. Am. Chem. Soc.*, 2006, **128**, 16438.
45. H. Kakei, R. Tsuji, T. Ohshima, and M. Shibasaki, *J. Am. Chem. Soc.*, 2005, **127**, 8962.
46. T. Sone, G. Lu, S. Matsunaga, and M. Shibasaki, *Angew. Chem. Int. Ed.*, 2009, **48**, 1677.
47. K. Shen, X. Liu, G. Wang, L. Lin, and X. Feng, *Angew. Chem. Int. Ed.*, 2011, **50**, 4684.
48. M. R. Gagne', L. Brard, V. P. Conticello, M. A. Giardello, T. J. Marks, and C. L. Stern, *Organometallics*, 1992, **11**, 2003.
49. J.-S. Ryu, G. Y. Li, and T. J. Marks, *J. Am. Chem. Soc.*, 2003, **125**, 12584.
50. X. Yu, S. Seo, and T. J. Marks, *J. Am. Chem. Soc.*, 2007, **129**, 7244.
51. M. R. Douglass, C. L. Stern, and T. J. Marks, *J. Am. Chem. Soc.*, 2001, **123**, 10221.
52. D. V. Gribkov, K. C. Hultzsch, and F. Hampel, *J. Am. Chem. Soc.*, 2006, **128**, 3748.
53. B.-T. Guan and Z. Hou, *J. Am. Chem. Soc.*, 2011, **133**, 18086.
54. K. Komeyama, D. Sasayama, T. Kawabata, K. Takehira, and K. Takaki, *J. Org. Chem.*, 2005, **70**, 10679.
55. K. Komeyama, T. Kawabata, K. Takehira, and K. Takaki, *J. Org. Chem.*, 2005, **70**, 7260.
56. W.-X. Zhang, M. Nishiura, and Z. Hou, *Angew. Chem. Int. Ed.*, 2008, **47**, 9700.
57. J. Oyamada, M. Nishiura, and Z. Hou, *Angew. Chem. Int. Ed.*, 2011, **50**, 10720.
58. S. Kobayashi, S. Nagayama, and T. Busujima, *J. Am. Chem. Soc.*, 1998, **120**, 8287.
59. K. Manabe, Y. Mori, T. Wakabayashi, S. Nagayama, and S. Kobayashi, *J. Am. Chem. Soc.*, 2000, **122**, 7202.
60. T. Hamada, K. Manabe, S. Ishikawa, S. Nagayama, M. Shiro, and S. Kobayashi, *J. Am. Chem. Soc.*, 2003, **125**, 2989.
61. Y. Mei, P. Dissanayake, and M. J. Allen, *J. Am. Chem. Soc.*, 2010, **132**, 12871.
62. S. Ishikawa, T. Hamada, K. Manabe, and S. Kobayashi, *J. Am. Chem. Soc.*, 2004, **126**, 12236.
63. M. Kokubo, C. Ogawa, and S. Kobayashi, *Angew. Chem. Int. Ed.*, 2008, **47**, 6909.
64. S. Kobayashi, M. Kokubo, K. Kawasumi, and T. Nagano, *Chem. Asian J.*, 2010, **5**, 490.
65. N. Mase, Y. Nakai, N. Ohara, H. Yoda, K. Takabe, F. Tanaka, and C. F. Barbas, III *J. Am. Chem. Soc.*, 2006, **128**, 734.
66. J. Paradowska, M. Stodulski, and J. Mlynarski, *Adv. Synth. Catal.*, 2007, **349**, 1041.
67. K. Mikami, O. Kotera, Y. Motoyama, and H. Sakaguchi, *Synlett*, 1995, 975.
68. K. Aplander, R. Ding, M. Krasavin, U. M. Lindström, and J. Wennerberg, *Eur. J. Org. Chem.*, 2009, 810.
69. M. Ueno, T. Kitanosono, M. Sakai, and S. Kobayashi, *Org. Biomol. Chem.*, 2011, **9**, 3619.
70. S. Bonollo, D. Lanari, F. Pizzo, and L. Vaccaro, *Org. Lett.*, 2011, **13**, 2150.
71. S. Azoulay, K. Manabe, and S. Kobayashi, *Org. Lett.*, 2005, **7**, 4593.
72. C. Ogawa, N. Wang, M. Boudou, S. Azoulay, K. Manabe, and S. Kobayashi, *Heterocycles*, 2007, **72**, 589.
73. M. Boudou, C. Ogawa, and S. Kobayashi, *Adv. Synth. Catal.*, 2006, **348**, 2585.
74. M. Kokubo, T. Naito, and S. Kobayashi, *Chem. Lett.*, 2009, **38**, 904.
75. M. Kokubo, T. Naito, and S. Kobayashi, *Tetrahedron*, 2010, **66**, 1111.
76. R. S. Dickins, S. Gaillard, S. P. Hughes, and A. Badari, *Chirality*, 2005, **17**, 357.

Homogeneous Catalysis

Yingming Yao and Kun Nie

Soochow University, Suzhou, People's Republic of China

1 Summary 459
2 Introduction 459
3 Application in Organic Transformation 460
4 Polymerization 467
5 Conclusions 473
6 Glossary 473
7 Related Articles 473
8 Abbreviations and Acronyms 473
9 References 473

1 SUMMARY

Organolanthanide (see ***Organometallic Chemistry Fundamental Properties***) complexes are those compounds containing Ln-X σ-bonds such as alkyls, (see ***Alkyl***) amides, hydrides, alkoxides, (see ***Lanthanide Alkoxides***) and aryloxides. These complexes are generally much more reactive to both air and water in comparison with those of the d-block metals, giving the lanthanide hydroxides. The potential applications of organolanthanide complexes in homogeneous catalysis are the main driving force for the development of organolanthanide chemistry. In early years, the studies in this area focused on the use of lanthanide compounds in organic chemistry (see ***Organic Synthesis***). The use of cerium(IV) compounds, especially $(NH_4)_2[Ce(NO_3)_6]$ (CAN), as oxidants was widespread. Samarium(II) compounds, such as SmI_2, are routinely used as one-electron reducing reagents in organic synthesis. The trifluoromethanesulfonate (triflate) salts of lanthanide metals are widely used as water-soluble Lewis acid catalysts because of their hard Lewis acid character. In recent years, considerable study is being made of the ability of organolanthanide complexes to catalyze the reactions of organic substrates, involving organic synthesis and polymerization. The reactivity of organolanthanide complexes depends on not only the metal itself but also the coordination environment around the metal center because of the unique electron structure of lanthanide metals. Therefore, a variety of ligand systems including cyclopentadienyl and non-cyclopentadienyl groups were developed to stabilize numerous organolanthanide complexes, and it was found that many of them show exciting catalytic activity in homogeneous catalysis. For example, lanthanide amides are active catalysts for a variety of olefin and alkyne transformations, including hydroamination/cyclization, hydroalkoxylation/cyclization, hydrophosphination/cyclization, hydroboration, hydrosilylation, and hydrogenation. Organolanthanide complexes are also found to be catalysts for the amidation of aldehydes with amines, Tishchenko reaction, addition of amines to nitriles, alkyne dimerization, and guanylation of terminal alkynes, amines, and phosphines with carbodiimides. On the other hand, they can also catalyze the polymerization of nonpolar and polar monomers. Cationic half-sandwich lanthanide alkyl complexes show high catalytic activity and stereoselectivity for butadiene and isoprene polymerization. Many organolanthanide complexes are highly efficient initiators for the ring-opening polymerization (ROP) of cyclic esters to give the aliphatic polycarbonates with high molecular weights and, in some cases, with high stereoselectivity. In this article, the recent developments of the application of organolanthanide complexes in homogeneous catalysis are summarized.

2 INTRODUCTION

The development of new, efficient selective catalysts for organic synthesis and polymerization has been a challenging research subject for both academic and industrial scientists. Transition-metal-based catalysts have been explored extensively, and many catalysts have been developed and applied

The Rare Earth Elements. Edited by David A. Atwood. © 2012 John Wiley & Sons, Ltd. ISBN 978-1-119-95097-4

in industry. In contrast, organolanthanide catalysts are under development. In the past decades, enormous growth in the chemistry of organolanthanide has been witnessed, particularly because of their potential applications as homogenous catalysts in organic transformation and polymerization.

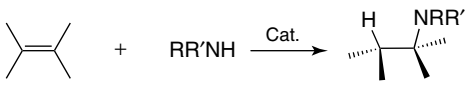
Lanthanides, nontoxic and relatively abundant in nature, have unique features for the development of new catalytic transformations. Valence electrons of lanthanide metals are located in 4f orbitals, which are well shielded by filled 5s and 5p orbitals and hence experience only negligible interactions with ligand orbitals. Lanthanide elements usually adopt the +3 oxidation state as the most stable oxidation state, which is not easily changed to other oxidation states under normal conditions. Thus, anionic ligands are required to electrostatically balance the positive charge of the lanthanide ions, which tend to form ionic complexes. The large coordination numbers of these metal ions, normally from 6 to 12, makes it difficult to saturate the coordination sphere around the ions. Their reactivity can be tuned not only by modifying the ancillary ligands but also by changing the ion size of the central metals in a series of complexes with similar structures. Owing to the high electrophilicity and kinetic lability, organolanthanide centers exhibit two distinctive reactivity patterns: σ-bond metathesis and olefin insertion. These features make organolanthanide complexes unique candidates for the formation of novel single-site catalysts for chemical transformations. Thus, this chapter focuses on the main progress of organolanthanide complexes in homogenous catalysis in recent years.

3 APPLICATION IN ORGANIC TRANSFORMATION

Organolanthanide complexes are known to be highly active catalysts for a variety of organic transformations, which can be either intramolecular or intermolecular in character. Successful intramolecular transformations include hydroelementation processes, which is the addition of a H–E (E = N, O, P, Si, S, H) bond across unsaturated C–C bonds, such as hydroamination, hydroalkoxylation, and hydrophosphination. Intermolecular transformations include a series of asymmetric syntheses, the amidation of aldehydes with amines, Tishchenko reaction, addition of amines to nitriles, alkyne dimerization, and guanylation of terminal alkynes, amines, and phosphines with carbodiimides.

3.1 Hydroamination

Hydroamination, the addition of an N–H bond to unsaturated C–C bonds, is an efficient, atom-economical method to construct nitrogen-containing molecules that are important for fine chemicals, pharmaceuticals, or useful chiral building blocks (Scheme 1).



Scheme 1 Hydroamination

Organolanthanides such as metallocene or half-metallocene and nonmetallocene lanthanide amides, alkylides, and hydrides are highly efficient catalysts for the intramolecular hydroamination/cyclization of a wide range of substrates such as aminoalkenes (Scheme 2), aminoalkynes, aminoallenes, and aminodienes.[1]

The aminoallene hydroamination/cyclization reactions are highly diastereoselective and can provide concise routes to synthesize some natural products (Scheme 3). Using chiral organolanthanide complexes as catalysts, enantioselective hydroamination/cyclization reactions are achieved, which provide a convenient route for the synthesis of chiral amines from simple, readily available prochiral substrates in a single step.

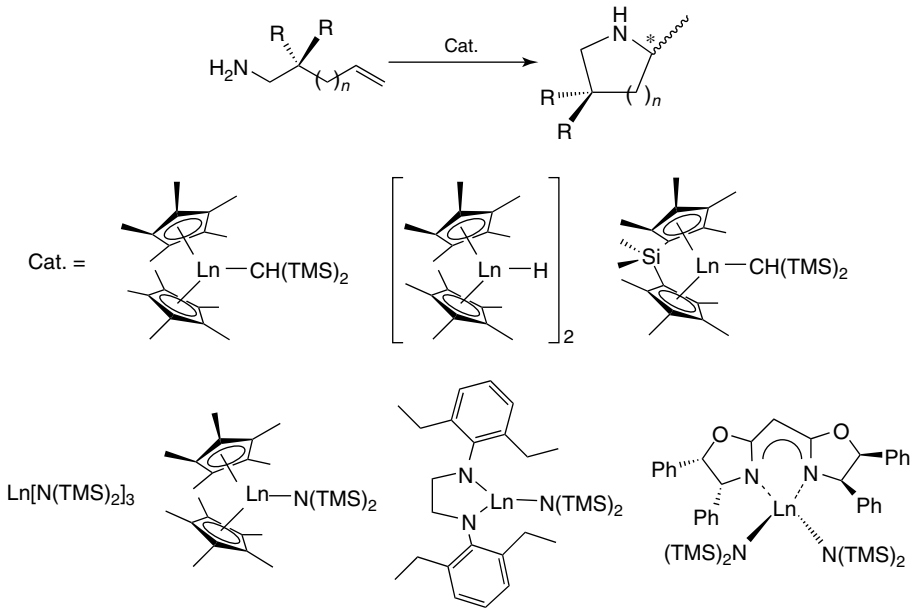
The ionic radii of lanthanide metals have a profound effect on the hydroamination/cyclization reaction. Organolanthanide complexes having the largest ionic radii exhibit the greatest turnover frequencies as well as enantioselectivities. In addition, the ligand plays an important role in catalytic activity and enantioselectivity. Sterically less encumbered ligand designs have been developed to improve reaction rate, and metallocene and nonmetallocene chiral lanthanide complexes have been synthesized for interesting enantioselective hydroamination processes.

The real active intermediates are organolanthanide amides, which are formed by the rapid protonolysis reactions of precatalysts with amine substrates, then turnover-limiting C–C multiple bond insert into the Ln-N bond, followed by rapid protonolysis by other amine substrates. The proposed catalytic cycle of hydroamination/cyclization of aminoalkenes is presented in Scheme 4.

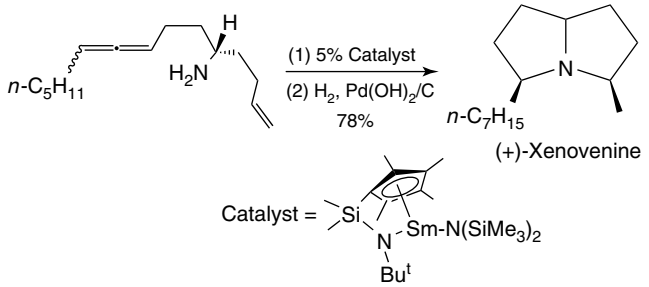
3.2 Hydroalkoxylation

Oxygen-containing heterocycles are abundant in nature and are important in fine chemicals. The addition of alcohols across unsaturated C–C bonds represents an atom-economical and direct route for the synthesis of these cyclic ethers. Hydroalkoxylation transformations mediated by a wide range of transition-metal and alkali-metal catalysts yield a variety of vinyl ethers. Organolanthanide complexes offer an alternative agent for the efficient and highly selective synthesis of both aliphatic and vinyl ethers with selectivities often complementary to those of transition-metal catalysts.

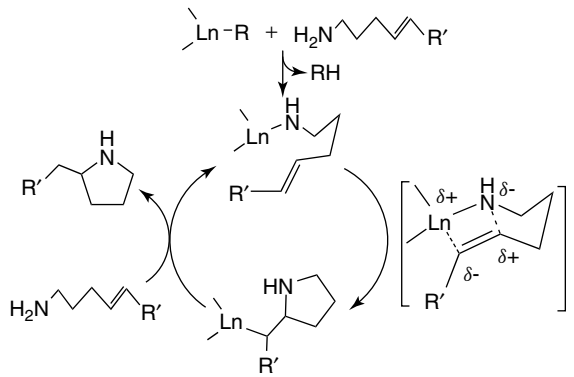
$Ln[N(SiMe_3)_2]_3$ (Ln = La, Sm, Y, Lu) can serve as effective precatalysts for the rapid, exoselective, and highly regioselective intramolecular hydroalkoxylation/cyclization of primary and secondary alkynyl alcohols to yield the



Scheme 2 Several efficient catalysts for hydroamination/cyclization of aminoalkenes



Scheme 3 The synthesis of (+)-xenovenine



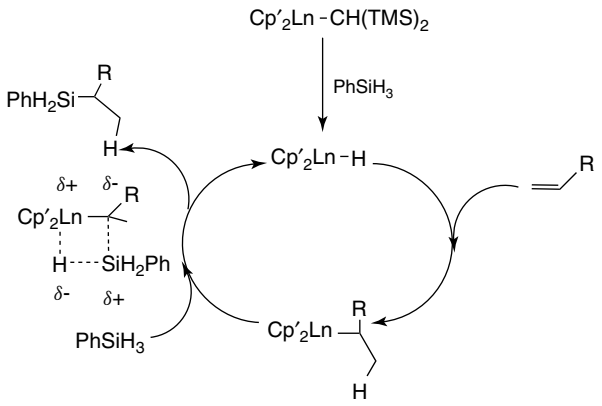
Scheme 4 The proposed catalytic cycle of hydroamination/cyclization of aminoalkene

corresponding exocyclic enol ethers.[2] The proposed mechanism is similar to hydroamination/cyclization. $Ln[N(SiMe_3)_2]_3$ is first activated via rapid, alcohol-mediated protonolysis of the amide ligands, which is followed by turnover-limiting insertion of the alkyne into the Ln–OR bond. The vinyl ether formed is then rapidly protonolyzed from the lanthanide metal center to regenerate the catalyst and yield the cyclic product. Organolanthanide-mediated alkyne hydroalkoxylation is the first known example of the insertion of unsaturated C–C bond into a Ln–O bond. Steric bulkiness around the metal center has apparent effect on the catalytic activity. 1,1,3,3-Tetramethylguanidine solvated organolanthanide aryloxides were used to catalyze alkyne hydroalkoxylation, which exhibit selectivity identical to that of the homoleptic lanthanide amides, but the activity is much lower because of increased steric encumbrance around the metal center.

Other catalytic hydroelementations, E–H (E = P, B, Si, H) addition to C–C multiple bonds, are efficiently mediated by organolanthanide complexes, and many are highly diastereoselective. Hydrophosphination/cyclization appears to follow the catalytic pathway similar to hydroamination/cyclization, whereas hydroboration, hydrosilylation, and hydrogenation proceed via different catalytic cycles, in which a lanthanide-hydride is the intermediate that is generated from protonolysis of the precatalyst. The proposed catalytic cycle of hydrosilylation of alkene using $Cp'LnCH(TMS)_2$ is presented in Scheme 5.

3.3 Asymmetric Synthesis

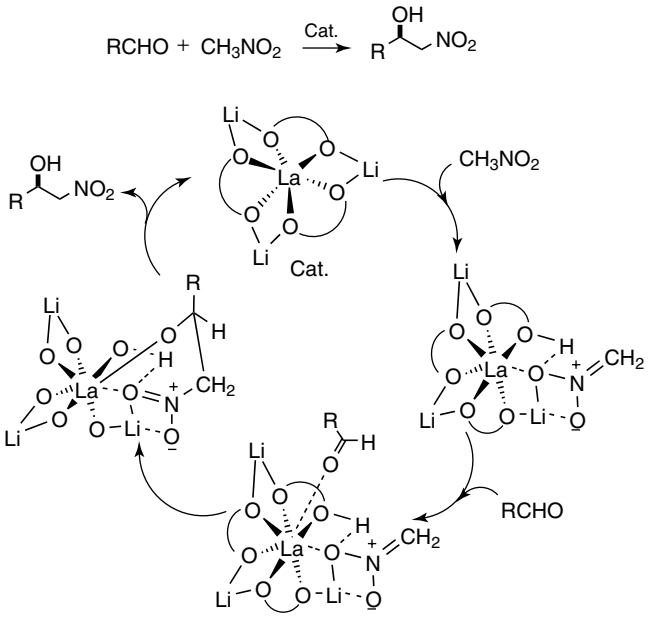
Asymmetric synthesis has received more and more attention over the past few decades, because of the wide application in pharmaceutical industry. A wide variety of enantioselective transformations are now achieved only in



Scheme 5 The proposed catalytic cycle of hydrosilylation of alkene

the presence of catalytic amounts of chiral compounds, and some of these enantioselective synthesis reactions have been applied to industrial production. The most successful organolanthanide-based catalysts for asymmetric synthesis are the heterobimetallic lanthanide/alkali metal complexes stabilized by binapthoxide group[3] (Scheme 6), much of these works associated with Masakatsu Shibasaki. The design of this kind of catalyst is based on the concept of multifunctional catalysis, in which the catalysts exhibit both Lewis acidity and Brønsted basicity. Furthermore, the development of heterobimetallic lanthanide/alkali metal complexes offers a versatile framework for asymmetric catalysts, because the catalytic activity and enantioselectivity of these catalysts can be tuned dramatically according to the choice of alkali metal (Li, Na, K) and the proper lanthanide metal.

This kind of heterobimetallic complexes are excellent catalysts for a wide range of reactions, including epoxidation of enones, hydrophosphonylation of imines and aldehydes, and a range of asymmetric C–C bond formation reactions, involving Michael addition reaction, Diels-Alder reaction, aldol and nitroaldol reaction, etc. The alkali metal has a profound effect on the catalytic property of these compounds.

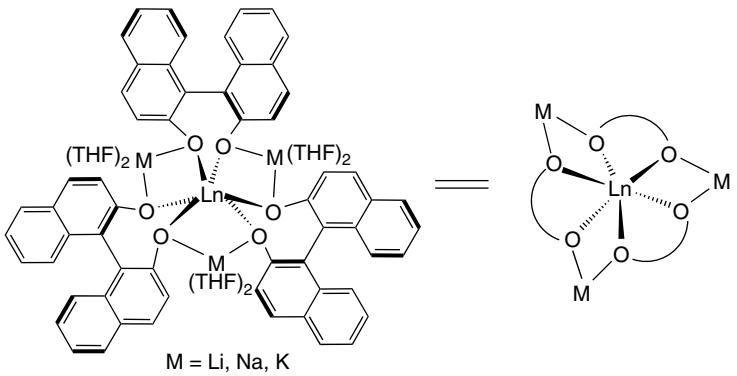


Scheme 7 Proposed mechanism for the catalytic asymmetric nitroaldol reaction

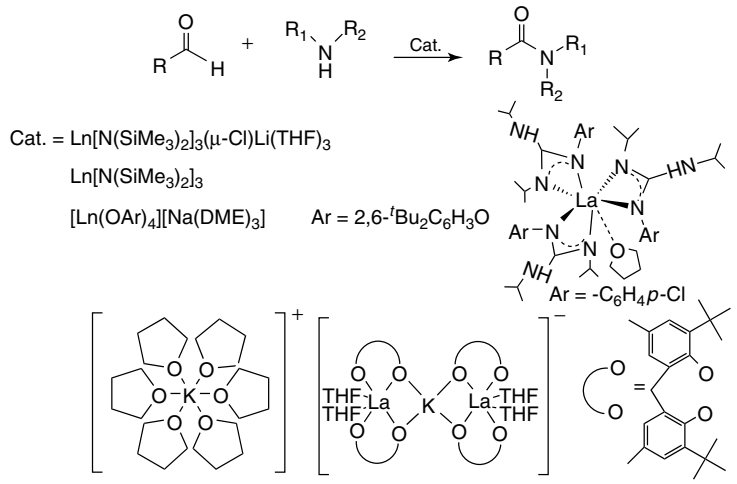
For example, using LnM_3(binapthoxide)$_3$ (M = Li, Na) as catalysts, the yields for the nitroaldol reaction are very similar, but the ee value is 94% for Li compound, and only 2% for Na compound. The proposed mechanism for the catalytic asymmetric nitroaldol reaction is shown in Scheme 7.

3.4 Amidation of Aldehydes with Amines

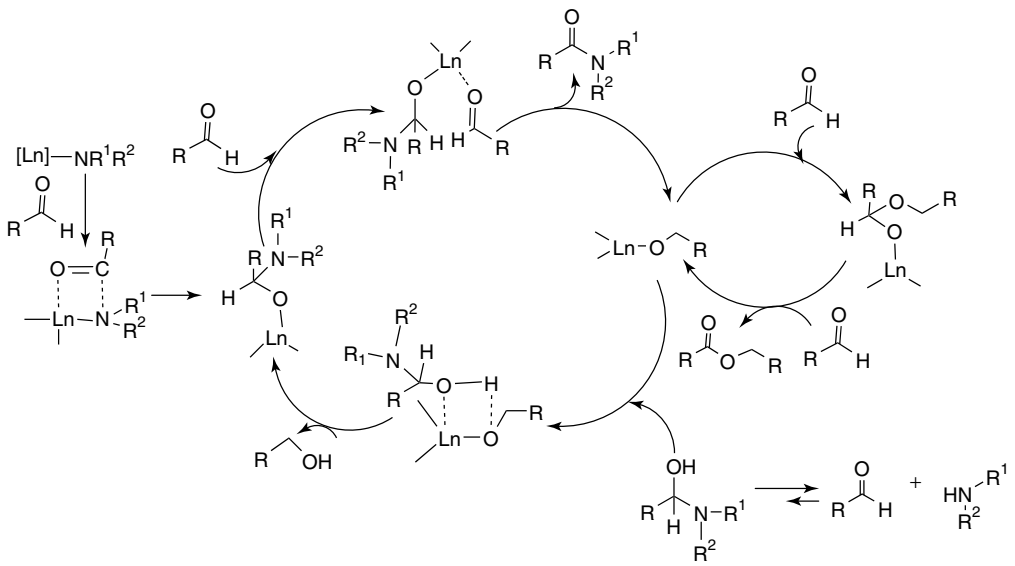
The amide group is an essential motif in biological systems as well as in important molecules in the areas of polymers, natural products, and pharmaceuticals. Direct amidation of aldehydes with amines is the most desired approach to amides because of economics and the availability of starting materials. Various efficient catalysts have been



Scheme 6 Lanthanide/alkali metal complexes stabilized by binapthoxide group



Scheme 8 Several efficient catalysts for amidation of aldehydes with amines



Scheme 9 Proposed catalytic cycle for lanthanide amido-mediated amidation of aldehydes and amines

explored for this process, and some of these systems need to use peroxide, heating, or equivalent alkali metal amides. In recent years, the amidation reactions of aldehydes with amines mediated/catalyzed by organolanthanide complexes (Scheme 8) have received considerable attention because of their high efficiency and mild reaction conditions.

Lanthanide amides $Ln[N(SiMe_3)_2]_3(\mu\text{-}Cl)Li(THF)_3$ or $Ln[N(SiMe_3)_2]_3$ have been reported to be efficient catalysts for amidation of aldehydes with amines under mild conditions without the use of peroxide and base.[4] But this kind of catalyst is not suitable for the amidation of aldehydes with secondary cyclic amines. Heterobimetallic lanthanide/alkali metal complexes stabilized by phenolate ligand are new classes of bimetallic catalysts for amidation of aldehydes with amines.[5] These catalysts show high activity and a wide range of substrates to produce amides in good to excellent yields under mild conditions. A cooperative effect between lanthanide and alkali metals is proposed for high activity. Trisguanidinate lanthanide complexes are also efficient catalysts for this reaction with a wide range of amines including secondary cyclic amines.[6] The isolation of a bisguanidinate lanthanum amido complex demonstrates that the reaction of a trisguanidinate lanthanum complex with an amine is the first step in the present process.

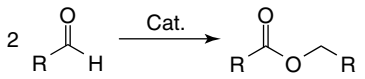
The proposed mechanism for organolanthanide amido-mediated amidation of aldehydes with amines is shown in Scheme 9. The addition of Ln−N bond to a carbonyl group gave the intermediate, an organolanthanide alkoxide, which

transferred a hydride to the second aldehyde molecule to give another organolanthanide alkoxide and amide. The new organolanthanide alkoxide reacted then with amino alcohol to produce the catalytic species.

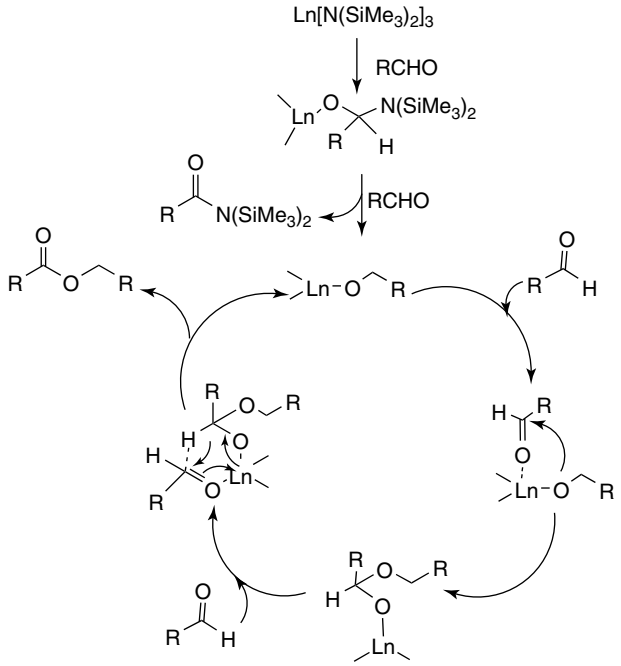
3.5 Tishchenko Reaction

The Tishchenko reaction, which converts an aldehyde into carboxylic ester is an atom economic reaction, and has been known for about a century (Scheme 10).

Traditionally, aluminum alkoxides have been used as homogeneous catalysts for the Tishchenko reaction. Other catalysts such as boric acid and a few transition-metal complexes have also been used. However, these catalysts are either reactive only under extreme reaction conditions or very slow. Recently, great effort has been focused on the development of organolanthanide complexes as catalysts because of their high Lewis acidity, easily tunable coordination sphere around the metal, and environmentally friendly property. Series of organolanthanide complexes, such as alkyls, amides, and amidinates,[7] were found to be highly efficient catalysts for the Tishchenko reaction. The proposed catalytic mechanism is provided in Scheme 11, and the precatalyst reacts with aldehyde to give lanthanide alkoxide as the catalytic active species.



Scheme 10 Tishchenko reaction

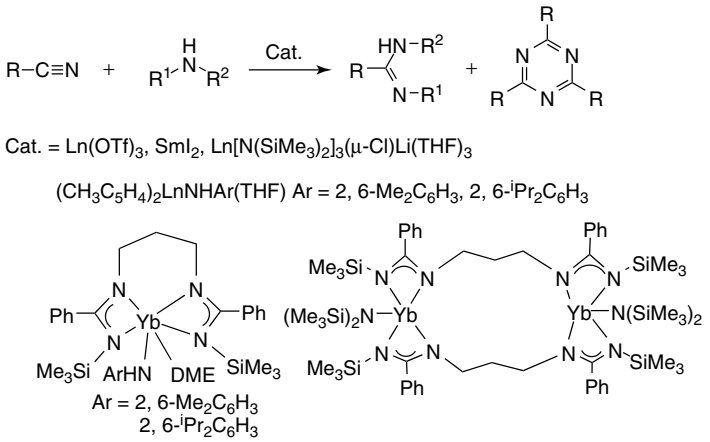


Scheme 11 Suggested mechanism for the $Ln[N(SiMe_3)_2]_3$-catalyzed Tishchenko reaction

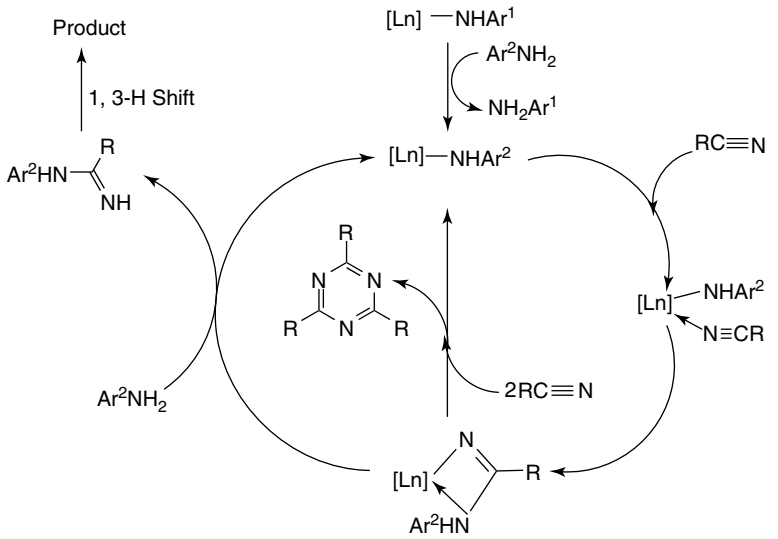
3.6 Addition of Amines to Nitriles

Amidines are of interest as the structural units with wide utility in drug design and as synthons for the synthesis of heterocyclic compounds. Addition of amines to nitriles is a highly atom-economic approach for the formation of amidines (Scheme 12). The one-step synthesis of amidines from nitriles and amines can be realized only if the nitriles are activated by electronwithdrawing groups or under more forcing conditions in the presence of Lewis acids or with aluminum amides for unactivated nitriles.

Trivalent lanthanide triflates and SmI_2 have been employed successfully as catalysts in the condensation of nitriles with primary amines and diamines into N,N'-disubstituted and cyclic amidines, but monosubstituted



Scheme 12 Several efficient catalysts for reaction of nitriles with amines



Scheme 13 Proposed mechanism for the reaction of nitriles with amines

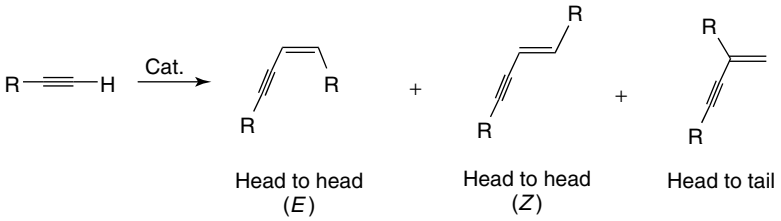
amidines cannot be synthesized. No efficient catalyst for the synthesis of monosubstituted amidine was known until 2008, when it was found that some ytterbium and yttrium amide complexes can serve as efficient catalysts for the addition of amines to nitriles to give monosubstituted *N*-arylamidines.[8]

The reaction mechanism was proposed as shown in Scheme 13. Reaction of an aniline with the lanthanide amide gave the new amido species through an acid–base reaction. A nitrile was then coordinated to the metal center, and then an intramolecular insertion of amide to cyano group of nitrile gave the corresponding intermediate. The intermediate underwent protonolysis by amine to release the product and regenerate the lanthanide amide as the active species. If the reaction of the intermediate with additional nitrile is more favorable than that with amine, triazine was produced as the main product.

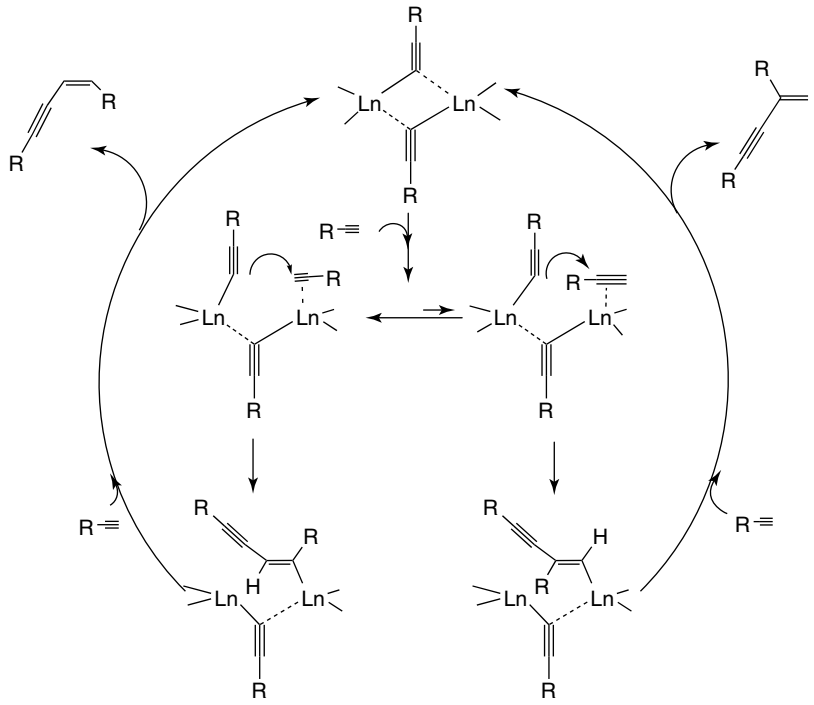
3.7 Alkyne Dimerization

Dimerization of terminal alkynes is an atom-economical and practical method to prepare conjugated enynes, which are the most versatile building blocks in organic synthesis found in bioactive molecules, drug intermediates, and organic electronic materials. Various transition-metal and f-element catalysts are known to catalyze this reaction; however, in most cases, a mixture of regio- and stereoisomers is obtained as shown in Scheme 14.

''Geometry constrained'' cyclopentadienyl-amide lanthanide alkyl complexes are the first organolanthanide catalysts for highly regio- and stereoselective head-to-head (*Z*)-dimerization of terminal alkynes, which yield solely the (*Z*)-enynes for aromatic alkynes.[9] In addition, this catalyst system is recoverable and reusable. Cationic lanthanide alkyls are also reported to catalyze the linear head-to-head dimerization of a range of (hetero)aromatic alkynes to (*Z*)-enynes with 100% selectivity and high rates. Yttrium and lanthanum benzyl and alkynyl complexes with the *N*-(2-pyrrolidin-1-ylethyl)-1,4-diazepan-6-amido (L) ligand and the cationic monobenzyl species $[(L)Ln(CH_2Ph)]^+$ are efficient catalysts for the *Z*-selective linear head-to-head dimerization of phenylacetylenes.[10] Both the metal ionic radius and the nature of the catalyst species have an influence on the catalytic performance. The cationic yttrium and the neutral lanthanum systems are the most effective catalysts in the series. The related scandium species show poor activity and selectivity. In contrast, neutral lanthanocene alkyl complexes catalyze the dimerization of terminal alkynes to provide predominately



Scheme 14 Dimerization of terminal alkyne



Scheme 15 The dimerization of terminal alkyne

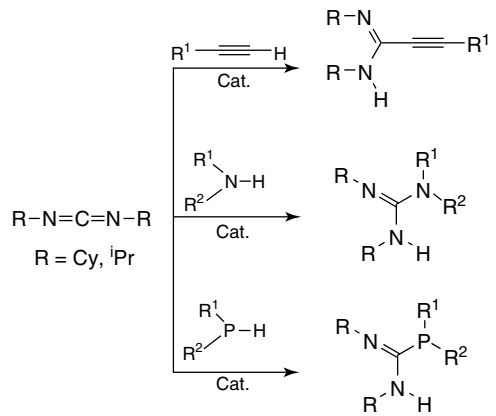
the linear enynes dimer with a trans configuration around the enyne double bond.

The real catalyst for this dimerization may be a dinuclear organolanthanide alkynide species, which is structurally characterized in cyclopentadienyl-amide lanthanide alkyl system. The proposed mechanism is shown in Scheme 15.

3.8 Addition of Carbodiimide to Alkyne, Amine, and Phosphine

Catalytic addition of carbodiimides to terminal alkyne C–H, amine N–H, and phosphine P–H bonds gives a new family of propiolamidines, guanidines, and phophaguanidines (Scheme 16), which are widely used as ancillary ligands for stabilization of various metal complexes.

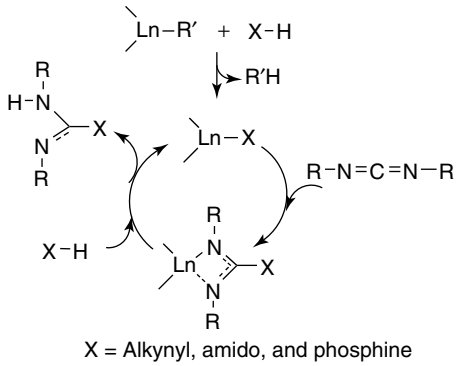
Half-sandwich organolanthanide alkyl complexes are found to be highly efficient catalysts for the cross-coupling reactions of carbodiimides with alkynes, amines, and phosphines with a wide range of substrates.[11] Although the half-sandwich lanthanide alkyl complexes can also catalyze the dimerization of alkynes, no homodimerization product is observed in the reaction of alkynes with carbodiimides. Lanthanocene silylamido complexes $[(CH_2)_2(\eta^5\text{-}C_9H_6)_2]LnN(SiMe_3)_2$ (Ln = Y, Sm), Cp-free lanthanide amido complexes $[\{(Me_3Si)_2N\}_3Ln(\mu\text{-}Cl)Li(THF)_3]$ (Ln = La, Sm, Eu, Y, and Yb), $\{(Me_3Si)_2N\}_3Ln$ (Ln = Y, and Yb),[12] and divalent lanthanide amido complexes $Ln[N(TMS)_2]_2(THF)_3$ (Ln = Sm, Eu, Yb)[13] were also



Scheme 16 Addition of carbodiimide to alkyne, amine, and phosphine

reported to be efficient catalysts for the addition of terminal alkynes to carbodiimides in an analogous way. Recently, heterobimetallic dianionic guanidinate lanthanide and lithium complexes $[Li(THF)(DME)]_3Ln[\mu\text{-}\eta^2\text{:}\eta^1(^i PrN)_2C(NC_6H_4\text{-}p\text{-}Cl)]_3$ were found to be excellent precatalyst for the addition of various monoamines to carbodiimides, leading to the formation of a series of monoguanidine derivatives with a wider range of substituents on the nitrogen atoms under mild condition.[14]

The proposed mechanism for the addition of terminal alkynes, amines, and phosphines to carbodiimides is shown



Scheme 17 The proposed mechanism for the addition of alkyne, amine, and phosphine to carbodiimide

in Scheme 17. The organolanthanide alkynyl, amide, and phosphide formed *in situ* is the active intermediate, and the key step is the hydrolysis of a lanthanide amidinate, guanidinate, and phosphaguanidinate species.

4 POLYMERIZATION

4.1 Polymerization of Olefins

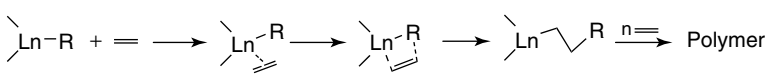
Many neutral trivalent organolanthanide alkyl and hydride complexes can serve as single-component homogeneous catalysts for the polymerization of ethylene. They can also be used as models fo mechanistic studies of Ziegler-Natta polymerization of ethylene.[15] The polymerization undergoes a coordination–insertion mechanism (Scheme 18). Generally, a lanthanide hydride complex is much more active than the corresponding alkyl complex. However, most of these organolanthanide catalysts show low to moderate activity, except the dimeric bi(pentamethylcyclopentadienyl) lanthanide hydrides, which show very high activity for the polymerization to yield high-molecular-weight polyethylene. The catalytic activity depends on the radius of lanthanide metal and the structure of the ancillary ligand. The polymerization activity increases with the ionic radius. The *ansa*-lanthanocene complexes and ''geometry-constrained'' half-sandwich lanthanide complexes show higher catalytic activity than the corresponding unlinked bi(cyclopentadienyl) lanthanide compounds because the former complexes provide a more open ligand sphere for the metal center.

Divalent samarium complexes can also catalyze ethylene polymerization, initially through one-electron transfer from the Sm(II) species to an ethylene molecule to form a Sm(III)–carbon bond, which is the active intermediate to induce ethylene polymerization.[16] The less reducing divalent organometallic ytterbium and europium complexes are generally inert.

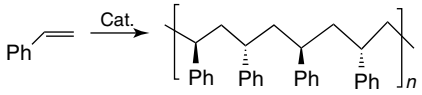
Cationic alkyl complexes of group four metals are the actually active species in homogeneous olefin polymerization and related catalytic transformations, which has promoted the investigation in cationic organolanthanide chemistry in recent years. Indeed, a large number of mono- and dicationic lanthanide alkyl complexes, which were generated by the reactions of the organolanthanide alkyl precursors with borate, are found to be more efficient catalysts for homo- and copolymerization of ethylene than the neutral ones. In certain cases, the dicationic lanthanide derivatives show higher activity and selectivity than their monocationic relatives. Ionic radii of both lanthanide metals and the ancillary ligands have significant influence on the catalytic behavior, and polymerization activity often increases with ionic radius. Solvents also affect the polymerization activity. Generally, the strongly coordinative solvents are disadvantageous for the polymerization.

Cationic organolanthanide alkyl complexes can also efficiently catalyze the polymerization of 1-hexene. The average number molecular weight of the polymers obtained depends apparently on the polymerization temperature. The lower the polymerization temperature is, the higher the molecular weights of the polymers are, which can be attributed to a rapid chain-transfer reaction at room temperature. The dicationic organolanthanide alkyl complexes also showed higher activity than the monocationic analog. In most cases, the cationic scandium complexes showed the highest activity for 1-hexene polymerization, reflecting the metal dependence of the catalyst activity.

The styrene polymerization catalyzed by an organolanthanide complex is much more difficult than ethylene polymerization because of steric hindrance. Some lanthanocene methyl complexes, half-sandwich lanthanide alkyls, anionic guanidinate lanthanide methyl complexes, and anionic divalent mixed-ligand samarium complexes can initiate styrene polymerization in moderate to high activity at high temperature, affording atactic polystyrenes. Recently, it has been reported that the bridged cyclopentadienyl-fluorenyl (Cp-CMe_2-Flu) allyl complexes and cationic half-sandwich lanthanide alkyl complexes catalyze the highly syndiospecific polymerization of styrene (Scheme 19), whereas the single-component bridged bi(indenyl) allyl lanthanide complexes



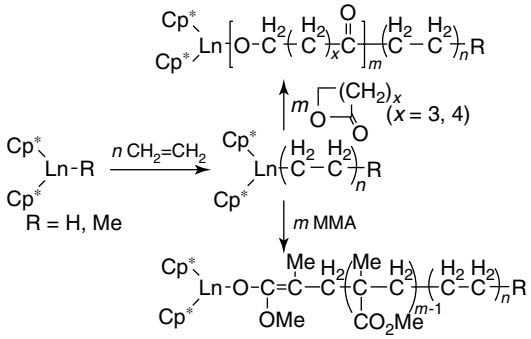
Scheme 18 The polymerization mechanism of ethylene catalyzed by organolanthanide alkyl



Scheme 19 Syndiospecific polymerization of styrene

catalyze the highly isospecific polymerization of styrene.[17] The cationic half-sandwich scandium alkyl complex showed the highest activity and stereoselectivity to give syndiospecific polystyrenes (rrrr >99%) with high molecular weights and very narrow molecular weight distributions, suggesting an excellent ''living polymerization'' character.

Organolanthanide complexes can catalyze not only the homopolymerization of olefins, but also the copolymerization of ethylene with some nonpolar and polar monomers.[18] A series of neutral, anionic, and cationic organolanthanide complexes catalyze the copolymerization of ethylene with styrene, α-olefin, methylenecyclopropane, norbornene, and dicyclopentadiene. For the copolymerization of ethylene with 1-hexene, the activity of a cationic monocyclopentadienyl scandium alkyl complex increased significantly with the increase of 1-hexene feed, which represented a rare example of a homogeneous polymerization catalyst with significant positive ''comonomer effect'' in the copolymerization of ethylene with an α-olefin. Furthermore, cationic half-sandwich lanthanide alkyl complexes can catalyze the selective copolymerization of styrene with ethylene to give a polymer with syndiotactic styrene–styrene sequences connected by repeated ethylene units, and homopolymers were not observed in this system. The content of styrene in the copolymers can be controlled simply by changing the initial styrene feed under 1 atm of ethylene. Half-sandwich scandium aminobenzyl complex is highly active for the alternating copolymerization of ethylene with norbornene or dicyclopentadiene, which can serve as high performance materials. Bi(pentamethylcyclopentadienyl) lanthanide hydride and methyl complexes, as well as divalent samarocene catalyze the copolymerization of ethylene α-olefins with methyl methacrylate (MMA) or acrylates or cyclic esters by sequential monomer addition[18] as shown in Scheme 20. The reverse monomer addition, i.e., a polar monomer followed by a nonpolar monomer, does not give the copolymers.

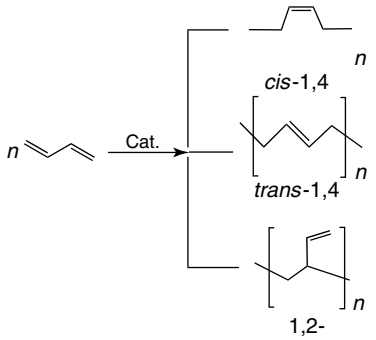


Scheme 20 The copolymerization of ethylene with MMA or lactone

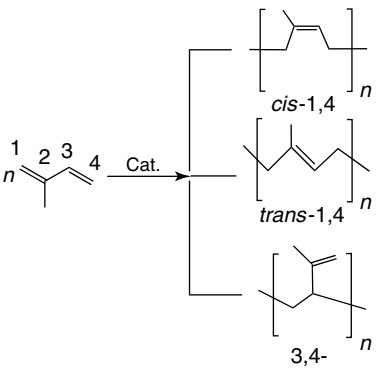
4.2 Stereoselective Polymerization of Dienes

cis-1,4-Regulated polyisoprene (PIP) and polybutadiene (PBD) are among the most important elastomers used for tires and other elastic materials. As the demand for high-performance synthetic rubbers has increased, the development of high-quality elastomers by polymerization of isoprene and butadiene has grown in importance. Generally, single-component neutral organolanthanide complexes are inactive for the polymerization of conjugated dienes. However, in the presence of a cocatalyst, such as aluminum alkyls, modified methylaluminoxane (MMAO), and organic borate, these organolanthanide complexes can serve as excellent catalysts for regio- and/or stereoselective polymerization of conjugated dienes as presented in Schemes 21 and 22. The real active species in these catalytic systems should be a cationic alkyl species.

The polymerization of butadiene can take place in different ways to yield PBD with different microstructures, including *trans*-1,4; *cis*-1,4; and 1,2-polymers. In the



Scheme 21 Stereoselective polymerization of butadiene



Scheme 22 Stereoselective polymerization of isoprene

presence of an activator, organolanthanide complexes stabilized by cyclopentadienyl, aluminate, carboxylate, bis(phosphinophenyl)amido, and aryldiimine NCN-pincer ligands and cationic lanthanide methyl complexes can catalyze controllable, or even living, polymerization of butadiene with a *cis*-1,4 selectivity within 97–99%. The selectivity depends apparently on the polymerization temperature. A *cis*-1,4 selectivity as high as 99.9% can be reached at low polymerization temperatures. The ancillary ligands have significant effect on tuning the polymerization selectivity. The lanthanide dialkyl complexes stabilized by a thiophene-NPN ligand in combination with alkyl aluminum or organic borate, as well as some orgnolanthanide complexes in combination with dialkylmagnesium can catalyze the highly trans-selective polymerization of butadiene.

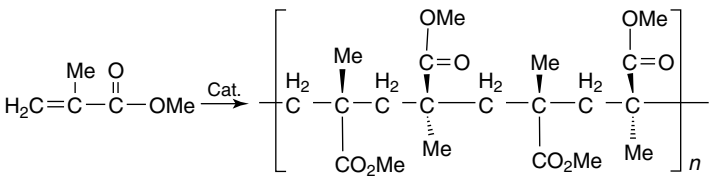
The polymerization of isoprene in different ways can also yield PIP with different microstructures, including *trans*-1,4; *cis*-1,4; and 3,4-polymers (Scheme 22), which have different chemical, physical, and mechanical properties. 1,2-PIP is usually not accessible through coordination polymerization approaches because the coordination of isoprene to a metal center in a 1,2-fashion is sterically less favored than that at the 3,4 double bond. *cis*-1,4-PIP is a major component of natural rubber. Many cationic organolanthanide complexes are efficient catalysts for the polymerization of isoprene, some of which showed high regio- and stereoselectivity. The ligands, lanthanide metals, and cocatalysts have significant effects on the catalyst activity and selectivity. Most of these catalyst systems give high *cis*-1,4 selective PIP, whereas $Ln(allyl)_2Cl(MgCl_2)_2/AlR_3$, $(C_5Me_5)Ln(BH_4)_2(THF)/Mg(n\text{-}Bu)_2$, and $(C_5Me_5)Ln(AlMe_4)_2/[Ph_3C][B(C_6F_5)_4]/Al(i\text{-}Bu)_3$ catalyze trans-selective polymerization of isoprene.[19] Recently, highly 3,4-selective polymerization of isoprene to produce isospecific PIP was also achieved by half-sandwich lanthanide alkyls or amidinate lanthanide alkyls combined with organic borates. The most attractive feature of the latter system is that the regio- and stereoselectivity for isoprene polymerization can be switched conveniently. Addition of $AlMe_3$ to the amidinate lanthanide alkyl/borate system changes the regio- and stereoselectivity of the polymerization dramatically from 3,4-isospecific to 1,4-cis selective.[20]

The half-sandwich scandium dialkyl complex combined with $[Ph_3C][B(C_6F_5)_4]$ can also catalyze the syndiospecific copolymerization of styrene with isoprene. Because of the excellent living character of this catalytic system, the sequential copolymerization of styrene, isoprene, and styrene produced the corresponding ABA triblock polymer with two perfect syndiotactic polystyrene blocks connected by a PIP block. Cationic half-sandwich lanthanide alkyl complexes are also efficient catalysts for the copolymerization of isoprene with ethylene, and the selectivity depends significantly on the ancillary ligands to yield the random or alternating copolymers with different microstructures and compositions. The cis-1,4 living copolymerization of isoprene with butadiene can be achieved by using the cationic bis(phosphinophenyl)amido yttrium alkyl complex as the catalyst.

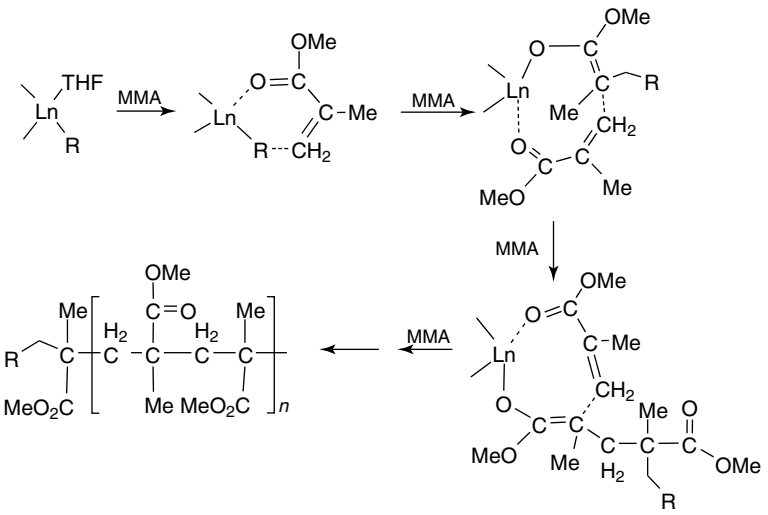
4.3 Polymerization of Methyl Methacrylate (MMA)

Bi(pentamethylcyclopentadienyl) lanthanide hydride and methyl complexes $[(C_5Me_5)_2LnR]_2$ (R = H, Me) are first reported to be excellent initiators for the highly syndiospecific polymerization of MMA to give PMMAs with high molecular weights and extremely narrow molecular distributions (Scheme 23). The syndiotacticity of the polymer depends apparently on the polymerization temperature and increases with the decrease in temperature. The stereoselectivity in MMA polymerization initiated by organolanthanide complexes is susceptible to the coordination environment around the lanthanide metal. Most lanthanocene hydride, alkyl, and amide complexes initiate MMA polymerization to produce syndiotactic or syndiorich PMMAs. However, the bulky chiral lanthanocene alkyl complexes bearing the (+)-neomenthyl chiral auxiliary and samarium alkyl complexes stabilized by the pyrrolylaldiminato ligand initiate the highly isospecific MMA polymerization. The lanthanide allyl complexes initiate MMA polymerization to give atactic polymers.[21]

The coordination anionic mechanism is proposed for this polymerization (Scheme 24). At first, the R group attacks the CH_2 group of MMA to generate a transient Ln-O-C(OMe)=$C(CH_3)CH_2R$ species, and then the incoming MMA molecule participates in a 1,4-addition to afford the eight-membered-ring enolate intermediate. In the propagation step, another MMA molecule attacks the growing end, and the coordinated ester group is liberated. The polymerization proceeds by repeating these reactions. The eight-membered-ring intermediate has been isolated and structurally characterized in the case of $[(C_5Me_5)_2SmH]_2$ as the initiator.



Scheme 23 Syndiospecific polymerization of MMA



Scheme 24 The proposed anionic polymerization mechanism of MMA

Divalent organolanthanide complexes can also initiate MMA polymerization. Divalent lanthanide complex, as a single-electron transfer reagent, can readily react with the monomer to generate a radical anion species, which subsequently couples into a bimetallic trivalent lanthanide enolate intermediate, which is the active center. Therefore, divalent organolanthanide complexes serve as bisinitiators for MMA polymerization.

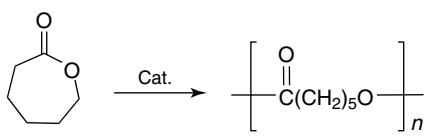
$[(C_5Me_5)_2LnMe]_2$ can also initiate the living polymerization of a series of acrylates. Because of the living characteristic, these organolanthanide complexes can be used to synthesize ABA triblock copolymerization of acrylates with MMA to provide thermoplastic elastomers. Furthermore, bi(methylcyclopentadienyl) lanthanide amides can initiate effectively the coordination polymerization of (dimethylamino)ethyl methacrylate to give polymers with high molecular weights and narrow molecular distributions.[22]

4.4 Polymerization of Cyclic Esters

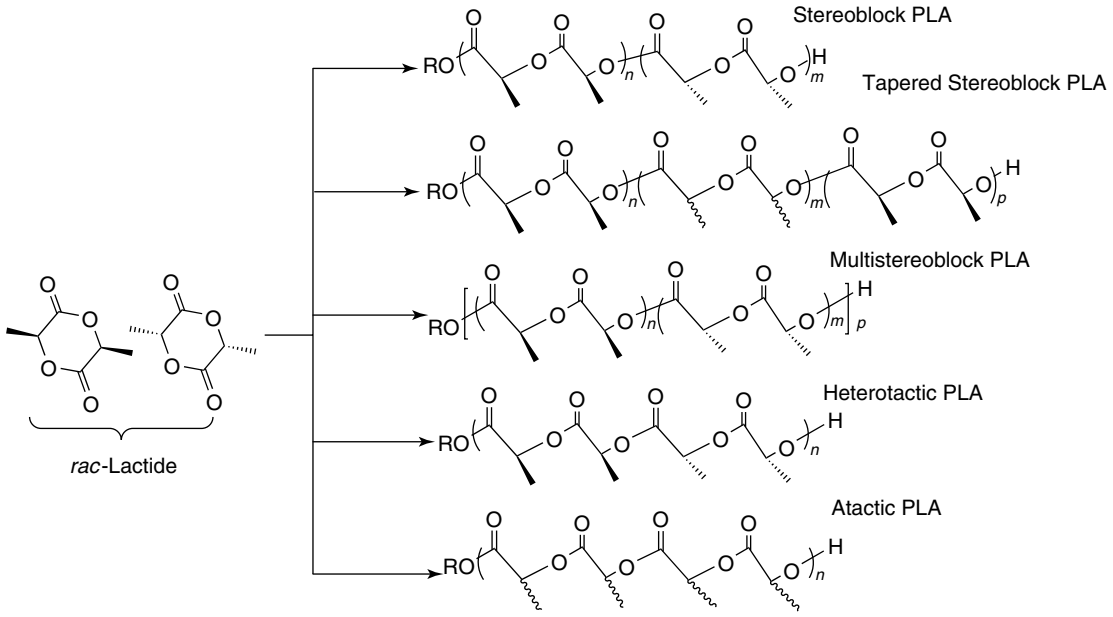
Aliphatic polycarbonates are of great interest for use in medical applications, such as sutures, dental devices, orthopedic fixation devices, and tissue engineering, owing to their high biocompatibility, facile biodegradation, low toxicity, and superior mechanical properties. Of the variety of biodegradable polymers known, linear aliphatic polyesters, polycarbonates, and their copolymers are particularly attractive and most used. Aliphatic polycarbonates can be prepared mainly by three routes: (i) condensation polymerization of diols and carbonates, (ii) copolymerization of epoxides with carbon dioxide, and (iii) ROP of suitable cyclic carbonates. Among them, the straightforward ROP method is currently receiving much attention because of the mild polymerization conditions, handy control of the structure of the polymer, purity of the polymer, and use of low toxic and easily removable catalyst. Many kinds of organolanthanide complexes have been found to be effective initiators for ROP of cyclic esters, such as lactones (ε-caprolactone, δ-valerolactone and β-butyrolactone), lactide, and functionally related compounds to give polyesters with high molecular weights. Bulkier ligands shield the active center more efficiently from the growing polymer chain, thereby decreasing transesterification reactions, which are the main side reactions causing molecular weight distribution broadening. Therefore, multidentate ligands containing heteroatoms are intended to encapsulate lanthanide metal ions and thus control the geometry of organolanthanide complexes to form discrete single-site complexes.

$Y(OCH_2CH_2NMe_2)_3$ was the first compound to polymerize lactide in a rapid and controlled fashion. Subsequently, a large number of organolanthanide complexes, including alkyl, hydride, amide, alkoxide, and aryloxide with multidentate ligands such as Schiff base, Salen, β-diiminate, guanidinate, amidinate, phenolate, and bridged bis(phenolate) were found to be efficient initiators for the ROP of lactones (Scheme 25) to afford linear polyesters with high molecular weights and narrow molecular weight distributions.[23]

Lactide possesses two stereocenters and therefore three distinct diastereomers: DD-, LL- and DL-(*meso*-lactide). The enantiopure isomers are commercially available as single enantiomers or a racemic mixture (*rac*-lactide). In the absence of epimerization, ROP of either enantiopure monomer results



Scheme 25 Polymerization of ε-caprolactone



Scheme 26 Polymerization of *rac*-lactide

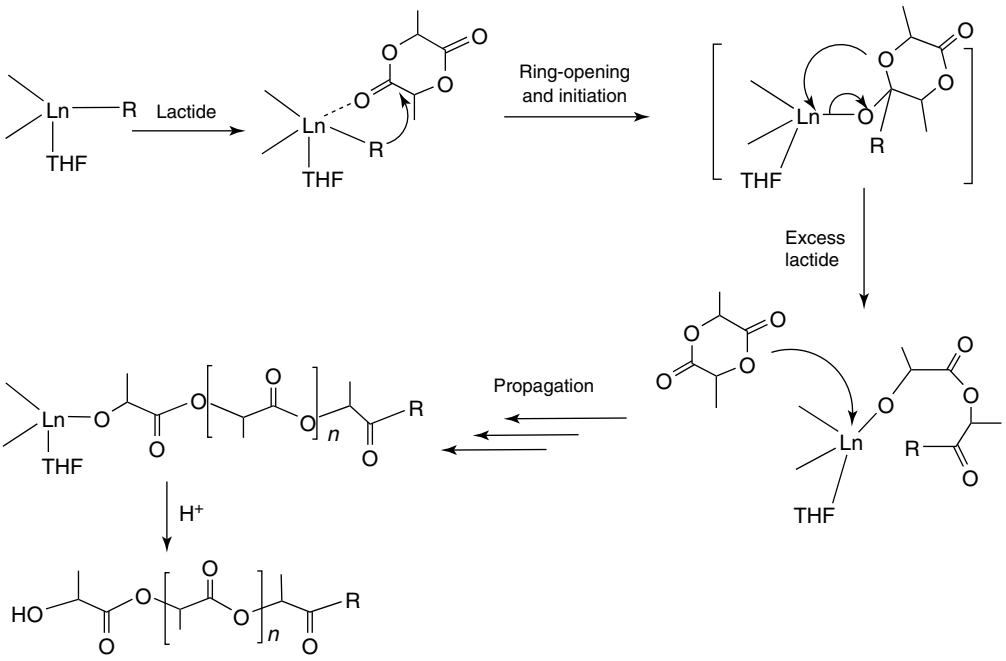
in an isotactic polymer in which all of the stereocentres are aligned along the same side of the polymer chain. Obviously, the stereocontrolled ROP of *rac*- and *meso*-lactide can result in a wider range of polymer microstructures (Scheme 26). In the area of enantioselective ROP of lactide, promising results have been obtained using organolanthanide complexes as initiators. A range of organolanthanide complexes bearing amino bridged bis(phenolate) ligands have been used to synthesize highly heterotactic polylactide (PLA) from *rac*-lactide, and in some cases the highest P_r value is 0.99.[24] However, few organolanthanide compounds can catalyze the stereoselective polymerization of *rac*-lactide to obtain isotactic-rich PLA.[25]

The structure of the ancillary ligand has significant effects on the catalytic behavior of organolanthanide complexes for the polymerization of lactide. The steric bulky ancillary ligands are favorable for the synthesis of controlled polymerization initiators. The environment created by the combination of the ligand system and the growing polymer chain end can result in significant differences in the rates of insertion of the different enantiomers of lactide, thus directing stereocontrol.

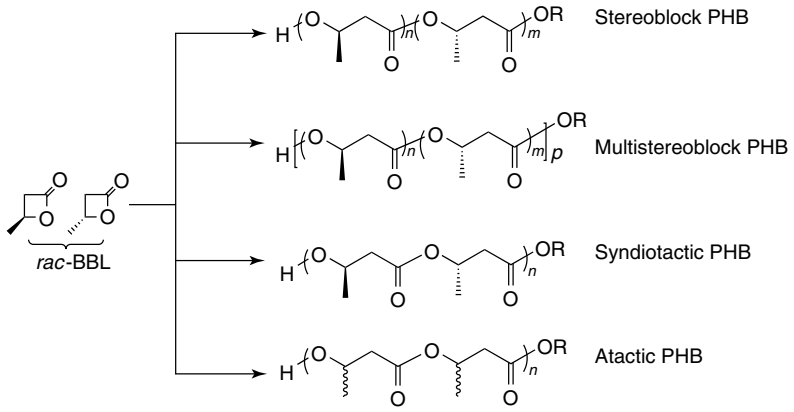
The polymerization undergoes coordination–insertion mechanism. The initiation step involves nucleophilic attack of the active group, such as hydride, alkyl, amide, or alkoxide group, on the carbonyl carbon atom of a lactide or lactone to form a new lanthanide alkoxide species via acyl-oxygen cleavage. The continued monomer coordination and insertion into the active metal-alkoxo bond formed completes the propagation step as shown in Scheme 27. The reactions with stereoselectivity proceed by means of a ''chain-end control mechanism'', which is the chirality of the propagating chain end that determines the chirality of the next monomer to be inserted, and this is generally associated with hindered but achiral catalyst.

Among the new biodegradable polymers, polyhydroxyalkanoates (PHAs) are of particular interest because they combine the film-barrier properties of polyesters with the mechanical performance properties of petroleum-based polyethylene and polypropylene. One of the most convenient and promising synthetic routes to PHAs is the ROP of β-butyrolactone (BBL) initiated by organometallic complexes, where the relief of ring strain is the driving force for polymerization. Highly isotactic (R)- or (S)-PHB can be obtained when optically pure (*R*)- or (*S*)-BBL is involved, while use of a racemic (*rac*) mixture of BBL gives rise to atactic PHB and PHB enriched in isotactic or syndiotactic diads (Scheme 28). As previously demonstrated for the ROP of *rac*-lactide, yttrium complexes supported by dianionic aminoalkoxy bridged bis(phenolate) ligands proved to be efficient initiators in the ROP of *rac*-BBL to give highly syndiotactic PHB. The most notable feature of these initiators is to exhibit high polymerization activity and productivity, combined, in some cases, with high stereoselectivity.[26] The most selective catalysts for the syndiospecific ROP of *rac*-BBL can give polymers containing 94% syndiotactic PHB. The mechanism of the ROP of *rac*-BBL using organolanthanide complexes as the initiators has been investigated by NMR and shown to occur via a coordination–insertion pathway, and a statistical Bernoullian analysis has evidenced that syndioselectivity originates from a chain-end control mechanism.

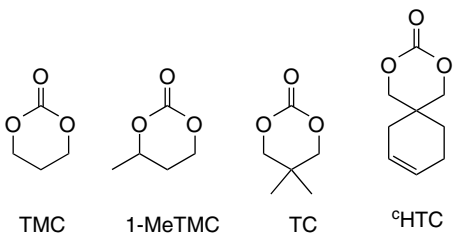
Organolanthanide catalysts, such as the divalent samarium complex, trivalent organolanthanide alkyls, lanthanide aryloxides, alkoxides, guanidinates, and thiolates,



Scheme 27 The polymerization mechanism of lactide initiated by lanthanide alkyl



Scheme 28 Polymerization of *rac*-β-butyrolactone



Scheme 29 The structures of various cyclic carbonates

have been reported to be active for the ROP of various cyclic carbonates, including trimethylene carbonate (TMC), 1-methyl trimethylene carbonate (1-MeTMC), 2,2-dimethyl trimethylene carbonate (DTC), and 2,2-(2-pentene-1,5-diyl)trimethylene carbonate (^{c}HTC) (Scheme 29). The first single-component organolanthanide aryloxides as initiators for DTC polymerization are lanthanide tris(2,6-di-*tert*-butyl-4-methylphenolate) ($Ln(OAr)_3$, Ln = La, Nd, Dy, Y). Ionic radii have profound effect on the catalytic activity. The activities of various lanthanide aryloxides are decreasing with the decrease in ionic radii. The polymerization of DTC occurs according to a coordination anionic mechanism, and the ring is opened via acyl-oxygen cleavage leading to an Ln–O active center.[27]

5 CONCLUSIONS

In the past decades, the exploration of successful ligand systems including cyclopentadienyl and noncyclopentadienyl groups allows for the development of various organolanthanide catalysts for homogeneous catalysis, involving organolanthanide alkyls and their cationic partners, hydrides, amides, alkoxides, aryloxides, and divalent lanthanide complexes, etc. These organolanthanide catalysts, as competitors of other already applied d-block transition metals, behave excellently and have wide applications both in organic synthesis and multiform polymerization field, such as ethylene polymerization, stereospecific polymerization of dienes, and stereoselective polymerization of racemic cyclic esters.

However, there is still a lot to do. The development of highly active ''activatorless'' olefin polymerization catalysts and chiral versions of these families of complexes and the stereoblock polymerization of racemic cyclic esters are still the challenges. So, the application of organolanthanide complexes in homogeneous catalysis will continue to be an attractive field for organometallic chemists and there are many opportunities for the future.

6 GLOSSARY

atom-economical: all raw materials used in the reaction are converted to the final product as much as possible

chain-end control mechanism: the chirality of the propagating chain end determines the chirality of the next monomer to be inserted that is associated with hindered

homogeneous catalysis: catalyst and reactants work in one phase

hydroelementation: addition of a H–E (E = N, O, P, Si, S, H) bond to unsaturated C–C bonds

heterobimetallic complex: the compound containing two different metals

organolanthanide complex: the compound containing Ln–X (X = C, N, H, O, S) σ-bond, which readily hydrolyzes when it is exposed to moist air

Tishchenko reaction: reaction converting an aldehyde into carboxylic ester

7 RELATED ARTICLES

Alkyl; Lanthanide Alkoxides; Lanthanide Complexes with Multidentate Ligands; Lanthanides: Luminescence Applications.

8 ABBREVIATIONS AND ACRONYMS

BBL = β-butyrolactone; DTC = 2,2-dimethyl trimethylene carbonate; ^{c}HTC = 2,2-(2-pentene-1,5-diyl)trimethylene carbonate; 1-MeTMC = 1-methyl trimethylene carbonate; MMA = methyl methacrylate; MMAO = modified methylaluminoxane; PBD = polybutadiene; PIP = polyisoprene; PHAs = polyhydroxyalkanoate; PLA = polylactide; ROP = ring-opening polymerization; TMC = trimethylene carbonate.

9 REFERENCES

1. S. Y. Hong and T. J. Marks, *Acc. Chem. Res.*, 2004, **37**, 673.
2. S. Y. Hong, X. H. Yu, and T. J. Marks, *J. Am. Chem. Soc.*, 2009, **131**, 263.
3. M. Shibasaki and N. Yoshikawa, *Chem. Rev.*, 2002, **102**, 2187.
4. S. Y. Hong and T. J. Marks, *Org. Lett.*, 2008, **10**, 317.
5. B. Xu, L. L. Huang, Y. Y. Yao, and Q. Shen, *Organometallics*, 2011, **30**, 3588.
6. C. W. Qian, F. Xu, and Q. Shen, *Organometallics*, 2009, **28**, 3856.
7. A. Zuyls, P. W. Roesky, and P. C. Junk, *Eur. J. Org. Chem.*, 2008,, 693.
8. J. F. Wang, F. Xu, and Q. Shen, *Org. Lett.*, 2008, **10**, 445.
9. M. Nishiura, Z. M. Hou, and T. Miyamoto, *J. Am. Chem. Soc.*, 2003, **125**, 1184.
10. S. Z. Ge, A. Meetsma, and B. Hessen, *Organometallics*, 2009, **28**, 719.
11. W. X. Zhang and Z. M. Hou, *Org. Biomol. Chem.*, 2008, **6**, 1720.
12. Q. Li, S. Wang, S. Zhou, and Y. Liu, *J. Org. Chem.*, 2007, **72**, 6763.
13. X. Zhu, F. Xu, and Q. Shen, *J. Org. Chem.*, 2008, **73**, 8966.
14. X. Zhang, F. Xu, and Q. Shen, *Tetrahedron*, 2011, **67**, 8790.
15. Z. M. Hou and Y. Wakatsuki, *Coord. Chem. Rev.*, 2002, **231**, 1.
16. E. Ihara, M. Nodono, and K. Katsura, *Organometallics*, 1998, **17**, 3945.
17. A. S. Rodrigues, E. Kirillov, and T. Roisnel, *Angew. Chem. Int. Ed.*, 2007, **46**, 7240.
18. H. Yasuda, *J. Organomet. Chem.*, 2002, **647**, 128.
19. M. Zimmermann, K. W. Tornroos, and R. Anwander, *Angew. Chem. Int. Ed.*, 2008, **47**, 775.
20. M. Nishiura and Z. M. Hou, *Nat. Chem.*, 2010, **2**, 257.
21. C. K. Simpson, R. E. White, and C. N. Carlson, *Organometallics*, 2005, **24**, 3685.
22. Q. Shen, Y. R. Wang, and K. D. Zhang, *J. Polym. Sci., Part A: Polym. Chem.*, 2002, **40**, 612.

23. O. Dechy-Cabaret, B. Martin-Vaca, and D. Bourissou, *Chem. Rev.*, 2004, **104**, 6147.

24. C. M. Thomas, *Chem. Soc. Rev.*, 2010, **39**, 165.

25. M. J. Stanford and A. P. Dove, *Chem. Soc. Rev.*, 2010, **39**, 486.

26. A. Amgoune, C. M. Thomas, and J. F. Carpentier, *Angew. Chem.*, 2006, **118**, 2848.

27. J. Ling, Z. Q. Shen, and Q. H. Huang, *Macromolecules*, 2001, **34**, 7613.

Heterogeneous Catalysis

John Hamilton Walrod II and David A. Atwood

University of Kentucky, Lexington, KY, USA

1	Summary	475
2	Introduction	475
3	Fundamental Chemistry	475
4	Basic Catalysis	476
5	Applications	478
6	Conclusions	478
7	Glossary	478
8	Related Articles	478
9	Abbreviations and Acronyms	478
10	References	479

1 SUMMARY

The use of rare earths in heterogeneous catalysis has traditionally been limited to doping zeolites for catalytic cracking in the petroleum industry and the use of ceria in three-way-catalyst in the automobile industry. Catalytic utility typically depends on the basicity of the rare earth oxide. Their basicity is known to decrease across the lanthanide period because of the decreasing cation size (***Group Trends***). The range and scope of catalytic transformations possible for the rare earth oxides are based on their basicity. Rare earth oxides are of great utility because of their activity and since they can be thermally activated and are thermally stable. Examples of the potential uses of rare earth oxides as heterogeneous catalysts include the oxidative coupling of methane (OCM) to C2 products (ethylene/ethane) and the transesterification of triglycerides to glycerol and fatty acid methyl esters (FAME).

2 INTRODUCTION

The catalytic properties of the lanthanide elements have been extensively explored and used throughout academia and industry for some time. However, the majority of the catalytic systems are homogeneous with relation to reactants and products (***Homogeneous Catalysis***). Additional refining of crude products and separations are generally required for these systems. Heterogeneous catalytic systems offer the ease of separation of catalyst from the resulting products. Historically, the use of rare earth elements for heterogeneous catalytic applications has been heavily centered on petroleum refining with rare earth doped zeolites and the use of cerium in catalytic converters in the automobile industry. Catalytic cracking is enhanced by doping small amounts of rare earths inside the zeolite framework, which serves as a Lewis acid catalyst. Cerium-based three-way catalysts have been effectively used in the simultaneous reduction of emissions of hydrocarbons (HC), carbon monoxide (CO), and nitrogen oxides (NOx) from gasoline engines.[1] Both of these two-phase systems have been studied for several decades and reviewed.[2,3] This article describes the use of rare earth oxides and the fundamental properties that are exploited for catalytic purposes for both supported and nonsupported systems.

3 FUNDAMENTAL CHEMISTRY

Rare earth elements are very reactive with ambient oxygen, and the oxides are the most stable form of the element. The lanthanide elements generally acquire a +3 valence state and acquire sesquioxide combinations with oxygen to form M_2O_3 with some variances. For several of the lanthanide elements, the +2 and +4 oxidation states are stable. Cerium

The Rare Earth Elements. Edited by David A. Atwood. © 2012 John Wiley & Sons, Ltd. ISBN 978-1-119-95097-4

is the best known example and readily forms the +4 oxidation state oxides; CeO_2. This oxidation state can be explained by the stability gained by oxidation of the additional 4f electron resulting in a completely empty shell. However, the fourth oxidation resulting from removal of an electron from the 4f orbital of most of the lanthanide elements is generally greater than the sum of the first three.

An interesting property of rare earth oxides is their high degree of ionic mobility. The anionic oxygen atoms are known to migrate through the lattice and may influence the amount of oxygen content for a given oxide. The rare earth lanthanide elements are readily hydrated and carbonated by ambient levels of oxygen and carbon dioxide, respectively. The latter is limited to surface coverage, while hydration may occur much deeper into the oxide. Water desorption and dehydration is easily seen for most oxides during calcination below 800 °C. The rate of oxidation is generally faster for the heavier lanthanide elements, which can be explained by the gain in lattice energy resulting from the smaller cation size (***Group Trends***). The lanthanide oxides may contain different phases and are heavily influenced by changes in temperature and pressure.[4]

The melting points for the Ln_2O_3 series generally increases across the period as can be seen in Figure 1. The melting points can effectively be compared to the relative gain in lattice energy resulting from the lanthanide contraction across the period. Here the small size of the oxygen anion and decreasing size of the +3 lanthanide element are cooperating effects toward the increasing energy. The observed nonlinearity of the melting point curve is most evident for Gd_2O_3, which can be explained on the basis of the half-full 4f electron configuration (***Variable Valency***) (Table 1).[4]

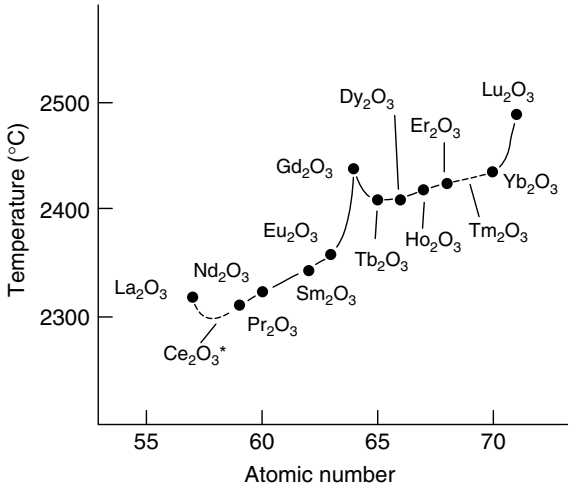


Figure 1 The relation between the solidification point and the atomic number of lanthanoid sesquioxides. (Reprinted with permission from Ref. 4. Copyright (1998) American Chemical Society.)

Table 1 Freezing and boiling points of the lanthanoid sesquioxides[a]

Lanthanoid oxide	Freezing point (°C)	Boiling point (°C)
La_2O_3	2256 2304 ± 5	3620
Ce_2O_3[b]	2210 ± 10	3760
Pr_2O_3	2183	3760
Nd_2O_3	2233	3760
Pm_2O_3	2320	—
Sm_2O_3	2269	3780
Eu_2O_3	2291	3790
Gd_2O_3	2339	3900
Tb_2O_3	2303	—
Dy_2O_3	2228	3900
Ho_2O_3	2330	3900
Er_2O_3	2344	3920
Tm_2O_3	2341	3945
Yb_2O_3	2355	4070
Lu_2O_3	2427	3980

[a] Data from Haire, R. G.; Eyring, L. Handbook on the Physics and Chemistry of Rare Earths; North-Holland: Amsterdam, 1994; Vol. 18, p 413
[b] This is a nonstoichiometric oxide, for example, $CeO_{1.53-1.50}$, but designated Ce_2O_3.

4 BASIC CATALYSIS

Heterogeneous basic catalysis has been fundamental in the development of two-phase systems. The acidic and basic nature of any oxide material lies at the interface between the bulk material and its exposed surface where oxygen atoms may be protonated or deprotonated and exposed metal sites have the potential to function as Lewis acid (Figure 2).[3,5]

Generally, metal atoms with higher charge and smaller size will be more acidic in nature, while metals with lower charge and larger size will be more basic. The acidic nature of a cation is governed by three parameters: the charge z, size, and electronegativity. The most important determinant for lanthanide acidity is the charge of the metal cation. Highly charged cations are better at stabilizing the deprotonated oxyanions through σ- and π-bonding interactions. Cations

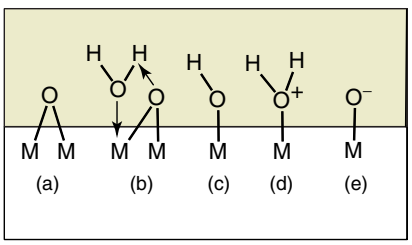


Figure 2 The interaction of water with a metal oxide surface showing coordination to the Lewis acidic site (a) coordination to separate metal sites, (b) neighboring hydrogen bond formation, (c) neutral charged protonated oxygen, (d) positively charged protonated oxygen, and (e) negatively charged deprotonated oxygen

of lower charge and larger size are not as polarizing toward oxyanions. This effectively increases the basicity of oxyanions by having a stronger ability to bond with protons at the surface. Thus, the basicity of Ln_2O_3 decreases as the elements increase in atomic number as the cations become smaller and more polarizing. As the bond strength between oxyanions and protons on the surface is increased so too is the basicity with these types of metals. The protonation/deprotonation of surface oxygen atoms is strongly dependent on the pH. The acidity of an oxide can be modeled by the equilibria shown in equations (1) and (2).

$$MOH_2^+ \rightleftharpoons MOH + H^+ \quad K_1 = \frac{[MOH][H^+]}{[MOH_2]} \tag{1}$$

$$MOH \rightleftharpoons MO^- + H^+ \quad K_2 = \frac{[MOH][H^+]}{[MOH_2]} \tag{2}$$

The charge can be negative, positive, or neutral, depending on the nature of the oxide. The structure of the surface groups is variable. They may be mono-, di-, or tricoordinated, depending on the structure of the solid and orientation of the crystal surface. Neighboring groups are also subject to electrostatic interactions. The charge is the result of the acid–base equilibrium shown in equations (1) and (2). The polarization of the cation is related to its charge and size. If the cation is small and highly charged, the electron transfer from oxygen to the cation becomes important and the basicity of surface oxygens is small. The crystal structure and surface morphology are important aspects to consider regarding acid–base behavior of solid materials.

For the series of rare earth oxides, the acidity increases across the period from La to Lu. The increase in acidity is attributed to the contraction of the radius and not to major gains in charge, rather only charge density. Therefore, the lighter rare earth oxides function as the main catalytic sources for basic catalysis. In order for the lighter lanthanide oxides to function as basic catalysts, they must be activated or calcined at high temperatures generally greater than 800 °C. The heated desorption removes the carbonated and hydroxylated species from the surface exposing the basic sites. It can be seen from a typical desorption to elevated temperatures that more than one type of basic site exists for a given oxide as shown in the thermogravimetric analysis (TGA) graphs in Figure 3.[6] The most basic oxide site would correlate to the one that needs the highest temperature for desorption.[7]

Current applications of lighter rare earth oxides have paid particular attention to several different aspects regarding the basicity. Some of these aspects include the role of atmospheric gases used during the calcination process or activation, the thermal activation process, and the optimization of basic sites for oxides on supported and nonsupported materials.

The effectiveness of any heterogeneous catalyst relies on the reusability and isolation methods. The lighter rare earth oxides are efficient catalysts for heterogeneous applications. Their usefulness relies on their ability to activate either the C–H or the O–H bond during catalytic cycles. The oxides are very stable with regards to decomposition at elevated temperatures, which is a very good characteristic for any catalyst. The general reactivity of the oxides increases from La to Eu but falls dramatically as the size of the cation decreases. Discrepancies arise for Ce and Pr, which form CeO_2 and Pr_6O_{11} and have reduced effectiveness as basic catalysts for some reaction schemes.

Rare earth oxides have been used for catalytic applications in the bulk form and supported on various different host materials. The inclusion of small amounts of Ln_2O_3 into oxidic supports following calcination results in mixed oxide materials. The basic properties of the mixed oxide material are dependent on the type of mixed oxides formed. The support should be crafted in order to minimize the amount of Ln_2O_3 needed while maximizing the basic sites in the supported material. Examples of different support

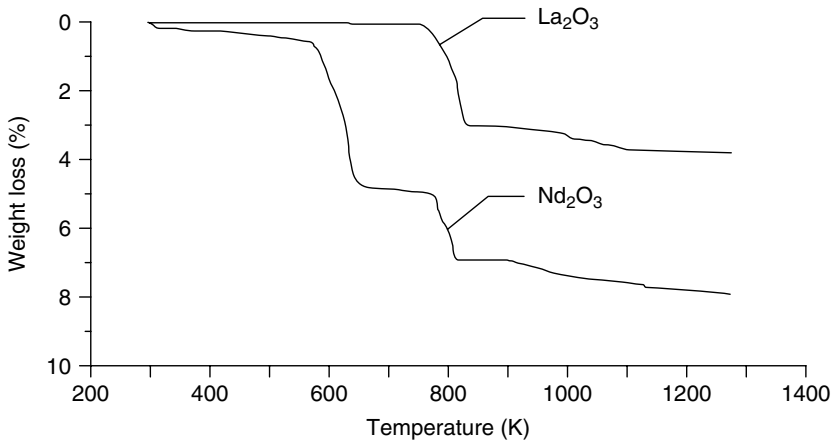


Figure 3 Thermogravimetric curves of La_2O_3 and Nd_2O_3. (Reproduced from Ref. 6, Copyright (2003), with permission from Elsevier.)

media include alumina, MgO, ZrO_2, activated carbon, and aluminates.[7]

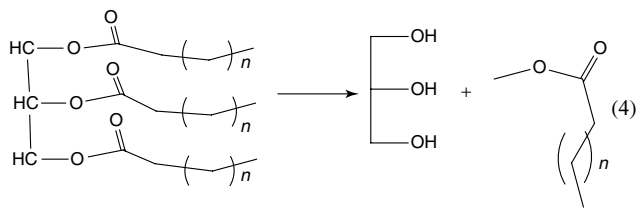
5 APPLICATIONS

The C–H activation of natural gas during OCM is a good example of the potential use of Ln_2O_3. The reaction proceeds by equation (3).

$$CH_4 + O_2 \xrightarrow{Ln_2O_3} \underbrace{\left[C_2H_6 + C_2H_4\right]}_{\text{C2 products}} + CO_2 \qquad (3)$$

In this catalytic cycle the conversion to products is strongly dependent on the basicity of the rare earth oxide.[6] Higher conversions are achieved with lighter rare earth oxides for this catalytic cycle. The highest yields are those of La_2O_3, corresponding to 46% conversion. Another desirable quality is the relatively high degree of selectivity of these catalysts for the OCM cycle. The C2 products are highly selective and tend to favor the formation of ethylene. The OCM represents a unique catalytic opportunity for basic catalysis because of increased demand for C2 products that do not originate from petroleum.

The usefulness of rare earth oxides as basic mediums has also been demonstrated in the transesterification of triglycerides into FAMEs by equation (4).



(4)

One of the main problems associated with this reaction when conducted with traditional homogeneous catalysts has been the extra purification steps needed to separate the catalyst from the products to acquire relatively pure glycerol.[7] In addition, the use of lower quality animal fat sources of triglycerides are not compatible with homogeneous catalysts because of concentrations of free fatty acids (FFAs). The FFAs and traditional homogeneous bases result in complications in the catalytic workup and lower yields because of emulsifications. In contrast, conversion yields of 98% can be achieved even with high levels of FFAs by using Ln_2O_3 on a variety of host supports. The products of this reaction cycle are used in the production of biodiesel fuel. This reaction represents a novel catalytic aspect toward developing future heterogeneous catalysis. All products formed during the cycle are easily separated and can be used for different applications. Furthermore, the reaction represents a catalytic pathway for obtaining fuels that are not derived from petroleum.

6 CONCLUSIONS

It can be seen from these examples that the rare earth oxides have tremendous application in the field of basic catalyzed heterogeneous catalysis. It should be noted that the long-term potential use of rare earth oxides as catalyst may be dampened by the growing needs of materials and availability issues in the future (***Geology, Geochemistry, and Natural Abundances of the Rare Earth Elements***). Long-term growth as heterogeneous catalysts is unlikely, but their contribution to the field of catalysis is very important nonetheless.

7 GLOSSARY

Heterogeneous Catalyst: A catalyst that is not in the same phase as the reactants in a reaction or transformation. Typically, this is a solid-state material that is either catalytically active or contains a catalytically active component.

Lewis Acid: An electron-pair acceptor such as an electron-deficient metal on the surface of a solid-state material (which would combine with an electron-pair donor (a Lewis base) such as water.

Sesquioxide: A formula with two atoms of a metal and three atoms (or equivalents) of oxygen such as La_2O_3. ''Sesqui'' is Latin for ''more by a half''.

8 RELATED ARTICLES

Homogeneous Catalysis.

9 ABBREVIATIONS AND ACRONYMS

CO = carbon monoxide; FAME = fatty acid methyl esters; FFA = free fatty acid; HC = hydrocarbons; NOx = nitrogen oxides; OCM = oxidative coupling of methane; TGA = thermogravimetric analysis.

10 REFERENCES

1. Q. Wang, B. Zhao, G. Li, and R. Zhou, *Environ. Sci. Technol.*, 2010, **44**(10), 3870.
2. P. Granger and V. I. Parvulescu, *Chem. Rev.*, 2011, **111**(5), 3155.
3. A. Corma and H. García, *Chem. Rev.*, 2003, **103**(11), 4307.
4. G.-Y. Adachi and N. Imanaka, *Chem. Rev.*, 1998, **98**(4), 1479.
5. H. Hattori, *Chem. Rev.*, 1995, **95**(3), 537.
6. S. Kuś, M. Otremba, and M. Taniewski, *Fuel*, 2003, **82**(11), 1331.
7. B. M. E. Russbueldt and W. F. Hoelderich, *J. Catal.*, 2010, **271**(2), 290.

Supramolecular Chemistry: from Sensors and Imaging Agents to Functional Mononuclear and Polynuclear Self-Assembly Lanthanide Complexes

Jonathan A. Kitchen and Thorfinnur Gunnlaugsson

School of Chemistry, Trinity College, University of Dublin, Dublin 2, Ireland

1	Summary	481
2	Introduction	481
3	Sensing and Imaging and the Formation of Self-Assembled Mononuclear Ln^{III} Containing Architectures	482
4	Self-Assembly of Polynuclear Ln^{III} Containing Architectures	484
5	Conclusion	493
6	Glossary	493
7	Acknowledgment	493
8	Related Articles	493
9	Abbreviations and Acronyms	493
10	References	494

1 SUMMARY

Recent advances in the field of supramolecular lanthanide chemistry are presented with emphasis on their role in the formation of functional self-assembly structures. Such systems are important for future applications in sensing and functional nano-materials, and therefore a small portion of the work from some of the leaders in this field are presented to give an overview of the state of the art to date. We have limited our overview to examples from the literature that have emerged in the last few years. We begin with a short overview of the use of lanthanide complexes and self-assembly structures for use in sensing of biologically important cations and anions and their application in luminescence imaging of bone structures. We then discuss the formation of simple self-assemblies that are formed from the use of pyridyl-based ligands, usually giving rise to the formation of discrete luminescent lanthanide complexes, some of which give rise to chiral emission. The formation of polynuclear lanthanide complexes is then described. Their luminescent and magnetic properties and the use of such ligands in the formation of higher order self-assemblies such as boxes and helicates are discussed. The idea of using mixed f- and d-metal ions in such systems is then presented. We pay particular attention to examples where the self-assembly structures have been analyzed by X-ray crystal structure analysis and by using changes in the luminescent properties to observe their formation *in situ*.

2 INTRODUCTION

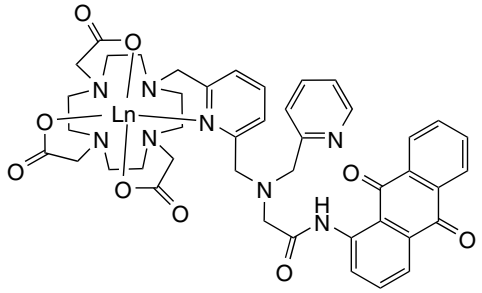
Owing to the unique physical and coordination properties of the lanthanides, they have become important players in the field of supramolecular chemistry. In the past few years, a large number of reviews have been published that deal with the use of the lanthanides in the formation of simple coordination complexes, sensors, magnetic resonance imaging (MRI) contrast agents, luminescent markers, and imaging agents ***Lanthanides: Luminescence Applications***; ***Lanthanide Shift Reagents***; ***Lanthanides: Magnetic Resonance Imaging***; ***Luminescent Bioprobes***; ***Sensors for Lanthanides and Actinides***.[1–7] Moreover, their use in directing

The Rare Earth Elements. Edited by David A. Atwood. © 2012 John Wiley & Sons, Ltd. ISBN 978-1-119-95097-4

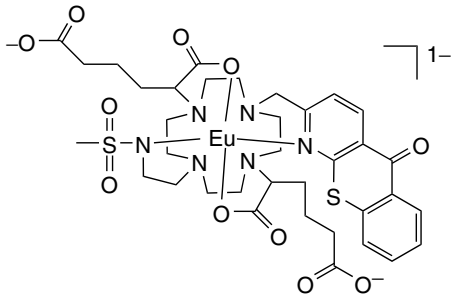
the formation, or synthesis, of complex architectures such as Metal Organic Framework (MOFs), polymers, and helicates has also been dealt with in several recent reviews.[8–10] This clearly reflects their unique place in supramolecular chemistry—a place that has become well recognized by the fact that their use in such systems usually adds a function to the resulting supramolecular architecture or network. It is clear that in such a short contribution as herein, it is impossible to comprehensively review the large body of work that has emerged in recent times. Consequently, we have focused on the development of self-assembly complexes, both mononuclear and polynuclear (some also made from mixed *f*- and *d*-metal ions), as this is an emerging field of research where the high coordination requirements of the lanthanides are employed to form complex and beautiful structures, which inherently alter the photophysical and magnetic properties of the lanthanides in a specific manner. This chapter is thus divided into two sections where the two aforementioned mononuclear and polynuclear complexes will be dealt with. Our effort is focused on highlighting only very recent examples from the literature, emphasizing, in the process, on how the various physical properties have added value to these supramolecular systems. For further reading, we direct the interested reader to the reviews listed above, which again only give a flavor of the rich activity within the field of supramolecular chemistry of the lanthanides.

3 SENSING AND IMAGING AND THE FORMATION OF SELF-ASSEMBLED MONONUCLEAR Ln^{III} CONTAINING ARCHITECTURES

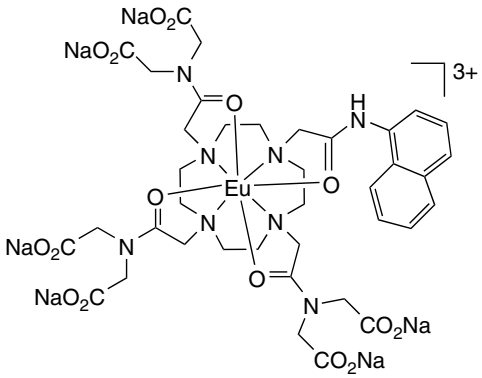
Lanthanide ions possess characteristic 4f shell configurations and exhibit similar properties across the periodic table ***The Electronic Structure of the Lanthanides***; ***Group Trends***. Their most stable oxidation state is 3+, particularly in water, and the ions possess high charge densities and demonstrate high electrostatic interactions due to their strong Lewis acidity and polarity. They display varied coordination numbers (usually from 6 to 12), where the most common coordination numbers are 8 or 9 for ions such as Eu^{III} and Tb^{III} ***Lanthanides: Coordination Chemistry***. Owing to their Lewis acidity, the lanthanide ions show a preference for ligands that are easily polarized and act as Lewis bases; therefore, functional groups such as amines, carboxylic acids ***Carboxylate***, and amides bind strongly to the lanthanide ions. Because of these characteristics, the use of a single ligand to complex a single lanthanide ion is challenging; however, structures such as tetra-substituted cyclen ligands can achieve the required high denticity and hence have been extensively employed, for example, in the development of sensors and imaging agents ***Lanthanide Complexes with Multidentate Ligands***. Examples of such structures (**1**–**3**) have been developed by Pope,[11] Parker,[12] and our own research group,[13] respectively. Compound (**1**) was developed as a near infrared emitting sensor for transition metal ions ***Near-Infrared Materials***. In this structure, the sensitizing antenna, anthraquinone, enabled excitation of this system within the visible region, but the Yb^{III} emission ($Ln = Yb^{III}$) observed was centered at ~1000 nm, being modulated upon binding of d-metal ions such as Cd^{II}, Hg^{II}, Zn^{II}, and Cu^{II}. The excited state lifetimes were also greatly affected, where in the case of Hg^{II} the lifetimes increased from 6.31 to 10.60 μs upon binding of Hg^{II} to (**1**). The same ligand was also formed using Nd^{III} and Eu^{III}, and these complexes were also tested for sensing of the same d-metal ions, the former giving rise to quenching of the Nd^{III} emission upon binding to Hg^{II}. For all these complexes, the recognition event was found to be fully reversible as the addition of EDTA reversed the changes seen in the lanthanide emission for these complexes. Compound (**2**) is a novel pH probe developed by Parker, where protonation and deprotonation events at the azathioxanthone antenna modulate the luminescence arising from the Eu^{III} center. However, this ligand also contains a pH-dependant alkylsulfonamide moiety, and the authors demonstrated that the coordination number of the Eu^{III} center could be changed from 8 in basic media to 7 in acidic media because of protonation of the sulfonamide moiety, again by observing the changes in the relevant intensities of the Eu^{III} emission bands, which were found to be fully reversible. The authors also investigated the application of this and related structures in mouse embryonic fibroblast (NIH 3T3) cells using confocal and epifluorescence fluorescence imaging. These investigations demonstrated rapid cellular uptake and localization of the Eu^{III} complex of (**2**) within protein-rich regions of the nucleolus with the localszation being restricted to the ribosomal and the perinuclear regions of the cells. The authors demonstrated that such complexes could be employed as ratiometric intracellular pH probes in living cells. In keeping with the subject of imaging, compound (**3**) was developed in our laboratory for the imaging of damaged bone structures. Using confocal fluorescence microscopy, we were able to demonstrate that the iminodiacetate components of three of the four arms in (**3**) could bind to exposed Ca^{II} sites within the damaged bone area (generated by scratching of a bovine bone surface that had been pretreated by polishing), and as such locking the imaging agent in place in the damaged region either within the surface or within the bone matrix. Unlike the two previous examples, the emission arising from the Eu^{III} center was found to be largely independent of the binding of various group I and II metals as well as d-metal ions to the iminodiacetate ligands. However, the emission was highly pH dependent, being both *switched off* in acid and basic media, but *switched on* within the physiological pH range. Consequently, this allowed for the imaging of exposed Ca^{II} sides within the damaged bone structure by (**3**) at physiological pH.



(1)

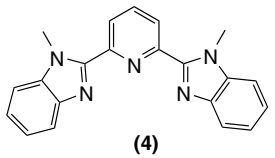


(2)

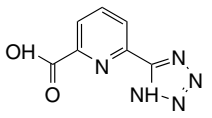


(3)

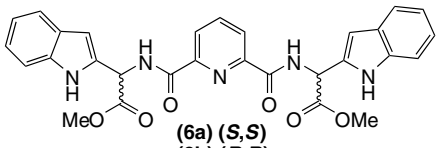
The above three examples are focused on the use of a robust coordination environment based on the cyclen framework. This gives rise to both kinetically and thermodynamically stable complexes which are, as demonstrated by the above discussion, essential for sensing and imaging applications. Nevertheless, by careful design, highly stable complexes can also be formed from acyclic ligands, which at the same time enable the use of more than one ligand to fulfill the high coordination of the lanthanides. Consequently, this also opens up the avenue of developing self-assembly complexes with precise geometry and function, where at the same time the unique physical properties of the lanthanides can be incorporated into the final self-assembly.



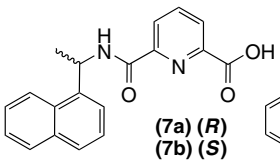
(4)



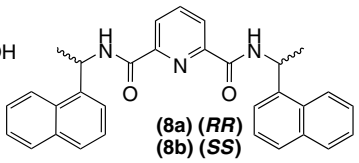
(5)



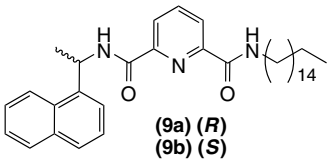
(6a) (*S,S*)
(6b) (*R,R*)



(7a) (*R*)
(7b) (*S*)



(8a) (*RR*)
(8b) (*SS*)



(9a) (*R*)
(9b) (*S*)

The formation of self-assemblies using lanthanide-directed synthesis has been elegantly explored by many researchers in recent times; a research endeavor has been pioneered in part by researchers such as Bünzli, Piguet, Raymond, Pecoraro, and others. Much of their work within this area has been dealt with in the reviews mentioned earlier.[1–10] However, recent examples from these leaders include structures such as (**4**), developed by Piguet, for studying the thermodynamic and steric effects that can influence the formation of-metal driven self-assembly formations where (**4**) was shown to be able to form triple-helical complexes with lanthanide ions, in what the authors describe as being ''anticooperative both in the solid state and in solution.''[14] The simple structural units employed in (**4**) have been previously used by several researchers, for instance, in the formation of triple-stranded-dimetallic helicates.[9] An example of the formation of a self-assembly of a helicate from a simple pyridyl carboxyl ligand is that of Mazzanti and coworkers who developed (**5**).[15] The ligand was found to form complexes with various lanthanide ions in a 1 : 3 (metal to ligand) stoichiometry, where the helical appearance was shown by solid-state crystallography. The resulting complexes were also shown to be luminescent in methanolic solution in the case of Eu^{III} and Tb^{III}. The idea of using simple pyridyl-based ligands for forming structurally complex architectures has also been investigated by our research group, resulting in the formation of both ligands (**6**)[16] and (**7**) (as both *RR* and *SS* isomers)[17]. The former of these is based on a symmetrical pyridyl diamide structure, incorporating two tryptophan moieties, which are well known to be able to populate the excited state of Tb^{III}. Building on previous work from our laboratory where the use of ligands such as (**8**) (as both *RR* and *SS* isomers)[18] gave rise

to highly ordered and symmetrical structures in 1 : 3 (metal to ligand) stoichiometry, it was predicted that (**6**) would also form such self-assembly complexes in 1 : 3 stoichiometry. However, analysis of its formation in solution using both UV–Vis absorption and metal-centered luminescence measurements, where the changes in the spectroscopic properties of (**6**) were monitored upon addition of various lanthanide ions, including Tb^{III}, only showed the formation of a 1 : 2 stoichiometry and not the expected 1 : 3 stoichiometry. It was concluded that steric hindrance was a governing factor in the formation of the 1 : 2 self-assembly. Because of this, ligand (**7**) was formed, which represents an asymmetric analog of (**8**), and the formation of a self-assembly between (**7**) (as both *R* and *S*) and several lanthanide ions was investigated in organic solution by observing the changes in the UV–Vis absorption, the fluorescence emission of the ligand, as well as, in the case of Tb^{III} and Eu^{III}, the metal-centered emission, which became *switched on* upon formation of the self-assembly in solution. As had been carried out previously in the case of (**6**) and (**8**), these spectral changes were analyzed by fitting the global changes using nonlinear regression analysis, from which the various stoichiometries and binding constants could be determined. Unlike that seen for (**6**), ligand (**7**) gave rise to the formation of a 1 : 3 (metal to ligand) self-assembly, which was thought to be formed as a single stereoisomer and not as a mixture of diastereoisomers. While the analysis of the resulting 1 : 3 self-assembly was unsuccessful using solid-state X-ray crystallography, molecular modeling supported this finding. However, unlike that seen for (**8**), the 1 : 3 self-assembly formation between (**7**) and Eu^{III} gave rise to a more ''open'' structure, which was also reflected in the lower stability constant obtained for (**7**) in the presence of Eu^{III} vs that of (**8**) in the presence of Eu^{III}. However, as had been seen for (**8**) in the presence of various lanthanides, excitation of the antennae gave rise to metal-centered circular polarized luminescence (CPL), reflecting the fact that just as in the case of (**8**), the chirality of the ligand had been transferred to the lanthanide ion, which now sat within a coordination environment that itself was chiral. Hence, these results demonstrated that such self-assemblies can be formed using asymmetric ligands in both high yield and as a single isomer. In addition, the resulting self-assemblies gave rise to circularly polarized luminescence. Consequently, compounds (**7a**) and (**7b**) were structurally modified to give ligands (**9a**) and (**9b**),[19] with the incorporation of a long hydrophobic hexadecyl chain onto the carbocyclic acid terminus of (**7**). Just as had been seen for (**6**) previously, ligands (**9a**) and (**9b**) both gave rise to the formation of 1 : 3 (metal to ligand) self-assemblies with a variety of lanthanide ions. In the case of Eu^{III}, the complexes were found to be highly luminescent, and gave rise to circularly polarized luminescence upon excitation of the naphthalene antennae. Moreover, the resulting complexes formed single monolayers on quartz slides using Langmuir–Blodgett (LB) techniques that were also shown to be luminescent and indeed also displayed metal-centered CPL, i.e., the immobilization of the complexes on solid supports did not alter their photophysical properties.

In the first part of this chapter, we have tried to demonstrate that the lanthanide ions can give rise to the formation of a variety of mononuclear supramolecular systems that can be employed for sensing and imaging, and in the formation of novel self-assembly structures that can be further exploited for use in materials-based systems. The next part of this chapter demonstrates that such supramolecular structures can be expanded to polynuclear lanthanide complexes and self-assemblies.

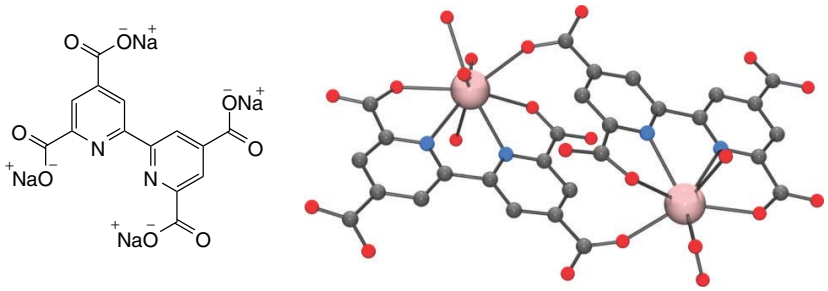
4 SELF-ASSEMBLY OF POLYNUCLEAR Ln^{III} CONTAINING ARCHITECTURES

There is currently a drive toward the design and preparation of multinuclear systems. Their interest stems from the same origins as the mononuclear variants; however, the interesting photophysical and magnetic properties of the Ln^{III} series can be enhanced and/or altered when in close proximity with other 4f metal centers.

To this end, there has been significant interest in the past 2–3 years in the design of ligand species that allow for the self-assembly of multiple Ln^{III} centers. While we have a strong research program developing chiral dimetallic triple-stranded helicates[20–22] and other dinuclear systems[23] using Ln^{III} metal centers, there are also other research groups investigating similar systems. This section focuses particularly on the rational design of multinuclear assemblies through careful ligand design and utilizing self-assembly processes.

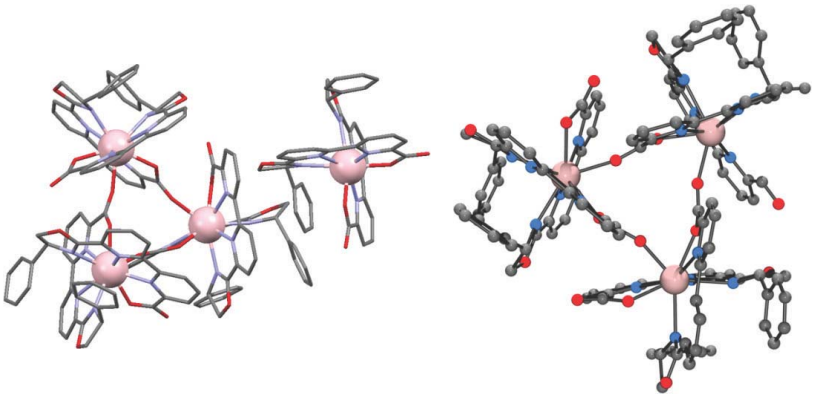
The first part of this section focuses on the development of *homometallic* multinuclear assemblies, and although there are a significant number of these systems in the literature we have only focused on a small number of the most recent examples.

We begin our discussion with a dinuclear system prepared by Gunnlaugsson, Kruger, and coworkers where a simple tetrasodium-4,4′,6,6′-tetracarboxy-2,2′-bipyridine ligand (**10**) (Figure 1) was complexed with $Ln(NO_3)$ (Ln = Eu, Nd, Gd, and Tb) in water to yield complexes of the general formula $\{Na_2[Ln_2(\mathbf{10})_2]\}$.[24] Single crystals of the resulting complexes formed and the structures revealed the dinuclear nature (Figure 1) of the complex and showed the bridging ability of the carboxylate oxygen atoms. These complexes displayed strong Ln^{III} centered luminescence in the visible (Tb and Eu) and NIR (Nd) regions of the spectrum despite the high hydration state (four water molecules per Ln^{III}). This water-based luminescence is important as any potential imaging agent would need appreciable water solubility and luminescence. A full, solution-based characterization was carried out in buffered water, and the formation of the



(10) $Na_2[Eu_2(\mathbf{10})_2]$

Figure 1 Tetrasodium ligand (**10**) and resulting crystal structure of the Eu^{III} complex $Na_2[Eu_2(\mathbf{10})_2]$. Sodium and hydrogen atoms are omitted for clarity

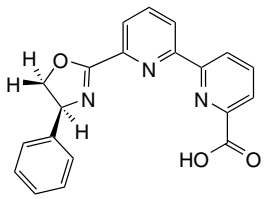


(a) $[\Delta\Delta\Delta\text{-}\{Eu\text{-}(\mathbf{11})_2\}_3]\cdot[\Lambda\text{-}Eu\cdot(\mathbf{11})_2]^{4+}$ (b) $[\Delta\Delta\Delta\text{-}\{Eu\text{-}(\mathbf{11})_2\}_3]^{3+}$

Figure 2 (a) View of the crystal structure of $[\Delta\Delta\Delta\text{-}\{Eu\text{-}(\mathbf{11})_2\}_3]\cdot[\Lambda\text{-}Eu\cdot(\mathbf{11})_2](CF_3SO_3)_4$. (b) View of the triangle component $[\Delta\Delta\Delta\text{-}\{Eu\text{-}(\mathbf{11})_2\}_3]$ only

complexes monitored in solution via spectrophotometric titrations.

Mazzanti and coworkers developed a self-assembled chiral Eu^{III} triangle from the chiral carboxylate containing bipyoxazoline ligand (**11**) as shown in Figure 2.[25]



(11)

In this system, the chirality of the ligand (*S*) is transferred to the metal centers to give the enantiopure $\Delta\Delta\Delta$ isomer. Interestingly, the transfer of chirality is concentration dependent as at low concentrations the diasteriomeric mononuclear complexes (Δ)-$[Eu\cdot(\mathbf{11})_2]^+$ and (Λ)-$[Eu\cdot(\mathbf{11})_2]^+$ form with a slight preference for the Λ isomer (Λ/Δ ratio $\approx$ 1.8), whereas at high concentrations the $\Delta\Delta\Delta$-Eu triangle forms via the assembly of three of (Δ)-$[Eu\cdot(\mathbf{11})_2]^+$ where the free carboxylate group acts as a bridging moiety. Proton NMR spectroscopic studies were used to elucidate the concentration dependence of the triangle formation, initially showing that the reaction of $Eu(CF_3SO_3)_3$ and 2 equiv. of (**11**) gave rise to a mixture of (Δ)-$[Eu\cdot(\mathbf{11})_2]^+$ and (Λ)-$[Eu\cdot(\mathbf{11})_2]^+$ at 7 mM. At concentrations in excess of 14 mM, the NMR spectra display an extra set of signals corresponding to $[\Delta\Delta\Delta\text{-}\{Eu\text{-}(\mathbf{11})_2\}_3]^{3+}$ (Figure 2). Single crystals were also grown and confirm the chiral assignment of the trinuclear species as Δ; however, the Eu-triangle cocrystallized with the mononuclear species (Λ)-$[Eu\cdot(\mathbf{11})_2]^+$ to give $[\Delta\Delta\Delta\text{-}\{Eu\text{-}(\mathbf{11})_2\}_3]\cdot[\Lambda\text{-}Eu\cdot(\mathbf{11})_2](CF_3SO_3)_4$ (Figure 2).

The diastereoselectivity of the self-assembly process was investigated through detailed NMR studies, which revealed that the self-assembly process for the trinuclear species only occurs for (Δ)-$[Eu\cdot(\mathbf{11})_2]^+$ and not (Λ)-$[Eu\cdot(\mathbf{11})_2]^+$, hence only the $\Delta\Delta\Delta$ species is observed and not the other possible chiral systems of $\Delta\Delta\Lambda$, $\Delta\Lambda\Lambda$, or

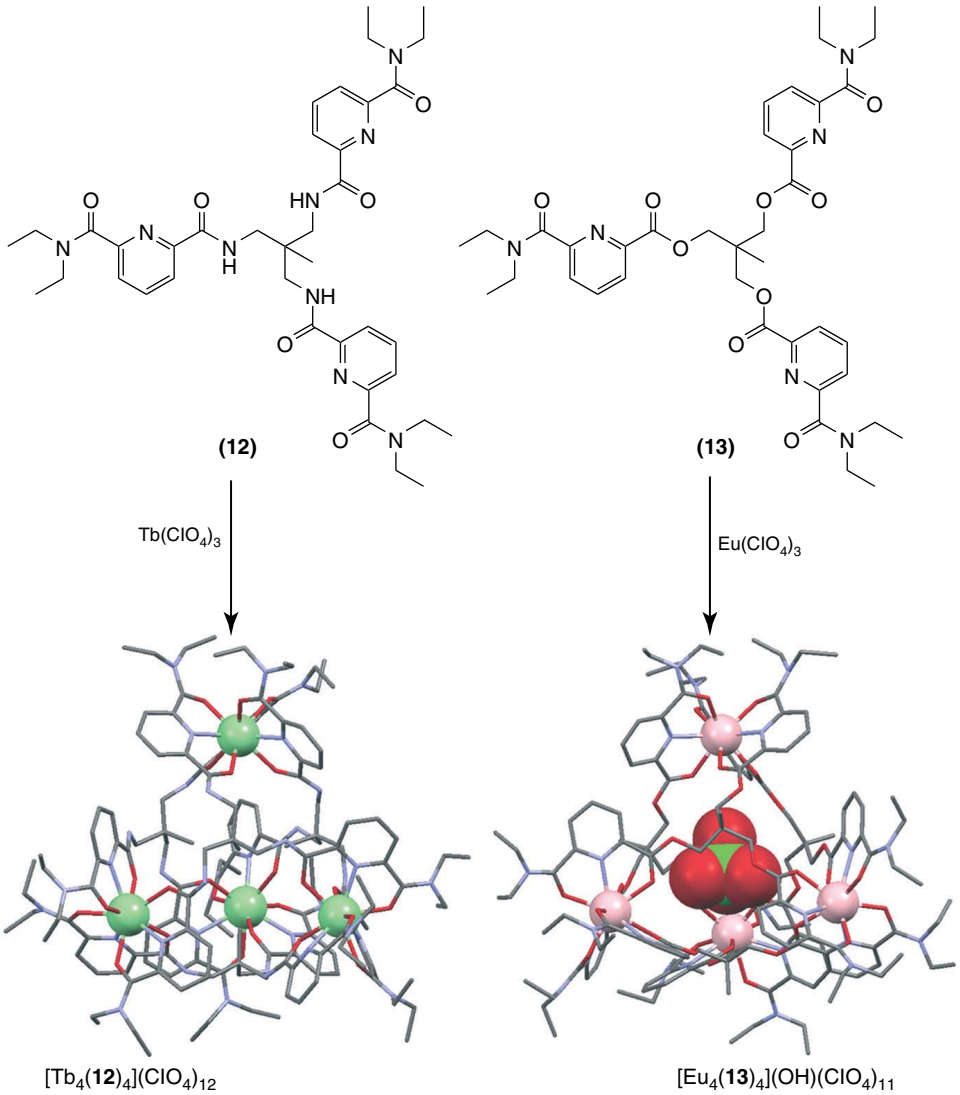


Figure 3 Synthetic scheme to form tetrahedral cages from ligands (**12**) and (**13**)

ΛΛΛ. This system represented a rare example of selective homochiral recognition processes.

Of particular note is the work of Hamacek and coworkers who have elegantly put lanthanide-directed self-assembly to use in the preparation of a variety of multinuclear systems including dinuclear helicates,[26–28] tetranuclear supramolecular cages,[29–31] and pentanuclear Ln^{III} helicates.[32] In each case, the supramolecular architectures utilize ligands based on terdentate pyridine-2,6-dicarbonyl binding sites, a common motif found in such multinuclear assemblies. However, the use of different spacers to connect the binding sites results in markedly different self-assemblies on complexation with various Ln^{III} metals. For example, they utilized tripodal-based ligands (**12**)[29] and (**13**)[31] to effect the synthesis of tetrahedral Ln cages with central cavities (Ln = La, Lu, Nd, and Eu) (Figure 3). The rationale behind this was to potentially use the central cavities for host–guest chemistry with sensing applications. The cages were prepared by the reaction of 1 equiv. of ligand with 1 equiv. of $Ln(ClO_4)_3$. Single crystals of $[Tb_4(\mathbf{12})_4](ClO_4)_{12}$ and $[Eu_4(\mathbf{13})_4](OH)(ClO_4)_{11}$ were obtained and revealed the tetrahedral nature of the complexes; however, the subtle difference in ligand structure (ester versus amide links) results in dramatically different tetrahedral complexes. The Tb complex of the amide ligand (**12**) has a smaller central cavity than the Eu complex of the ester ligand (**13**) because the *exo*-CH_3 is orientated into the cavity, whereas in $[Eu_4(\mathbf{13})_4](OH)(ClO_4)_{11}$ the *exo*-CH_3 is oriented away from the cavity. This results in a central cavity in $[Eu_4(\mathbf{13})_4](OH)(ClO_4)_{11}$, which is occupied by a perchlorate counter anion.

The thermodynamic stability of these systems is different for each of the ligands, as the tetranuclear complexes formed from (**12**) are not stable when excess metal is added

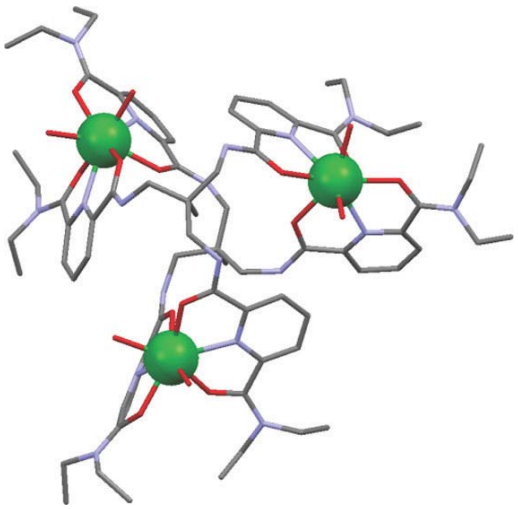


Figure 4 View of the crystal structure of the trinuclear complex isolated when ligand (**12**) was reacted with excess $La(ClO_4)_3$. Hydrogen atoms, solvent molecules, and counter anions are omitted for clarity

and form a complex mixture that most likely contains the trinuclear species $[Ln_3(\mathbf{12})_2]^{9+}$ as the crystal structure of $[La_3(\mathbf{12})_2](ClO_4)_9$ was obtained when crystallizing from a solution containing excess metal (Figure 4).

The cages formed with the ester-based ligand (**13**) were thermodynamically stable in metal excess except for $[La_4(\mathbf{13})_4]^{12+}$, which reverted to the trinuclear species $[La_3(\mathbf{13})_2]^{9+}$. The stability of the latter cages meant that they were ideally suited for anion exchange studies of the encapsulated ClO_4^-. Detailed NMR studies showed that anion exchange occurs where the ClO_4^- is slowly exchanged with a range of anions (BF_4^-, Im^-, I^-, Br^-, Cl^-, SO_4^{2-}, PO_4^{3-}, F^-); however, the cavity size is too small for the large spherical anion PF_6^-. The ability of these supramolecular systems to undergo host–guest chemistry means that they may be further developed into sensing systems by utilizing Ln^{III} centered luminescence or even catalytic systems.

Hamacek and coworkers have also undertaken a rational design approach to higher order Ln^{III} architectures by combining the aforementioned tetrahedral cages with their previously reported dinuclear helicate ligands to give rise to large pentanuclear assemblies (Figure 5).[32] The design strategy involved combining the symmetrical helicate (**14**) and symmetrical tripodal (**12**) ligand systems to give the unsymmetrical multimodal ligand (**15**) (Figure 5). When 3 equiv. (**15**) and 1 equiv. (**12**) are reacted with 5 equiv. $Ln(ClO_4)_3$ (Ln = Eu^{III} or Nd^{III}), the result is complexes of the general formula $[Ln_5(\mathbf{12})(\mathbf{15})_3](ClO_4)_{15}$ where the three ligands of (**15**) arrange the five metal centers into a tower-like configuration and (**12**) caps the bottom of the assembly (Figure 5). NMR and electrospray mass spectrometry (ESMS) were used to identify successful formation of the pentanuclear system as well as for semiempirical molecular modeling. This pentanuclear system is a good example of how the rational design of ligands allows for the predicted structure to be readily isolated, an important feature for the development of more complex heterometallic polynuclear systems.

An additional level of complexity can be added to multinuclear systems by moving from homonuclear to heteronuclear systems. Two such approaches that can be used to generate these mixed metal systems are the self-assembly of two preformed complexes through ternary complex formation via a free site on one or both of the complexes and careful ligand design to allow two distinct binding sites where each metal center is selectively bound to a particular set of coordinating atoms. Both approaches will be briefly discussed with appropriate examples for the formation of both heterometallic 4f and heterometallic mixed 3d–4f systems.

Faulkner and coworkers have used a ternary complex formation approach to bring about mixed Eu^{III}–Tb^{III} complexes.[33] This work is based on kinetically stable cyclen DO3A type frameworks and initially focused on the self-assembly of mononuclear Tb^{III} and Eu^{III} complexes where the charge neutral Eu^{III} complex contained a free carboxylic acid on the periphery of the complex (Figure 6), free to bind to the cationic Tb^{III} through electrostatic interactions.

The benzoate group was chosen for this study as excitation into this chromophore should only effectively sensitize Tb^{III} when the bimetallic complex forms, thus allowing monitoring of the formation of the desired heterometallic system. Unfortunately, when [Eu(**16**)] was titrated with $[Tb(\mathbf{17})]^{3+}$ in water the result was a complicated system owing to the fact that both complexes are heptadentate and there was no discrimination between forming Eu·Tb and Eu·Eu systems; in addition, the ability of the carboxylate to bind via either mono- or bidentate modes further complicated the system, thus giving rise to a minimum of five species present during the titration and a less than simple binding model. While the heterometallic complex formed with the aforementioned complex systems, the research moved onto the development of more stable systems utilizing a di-nuclear charge neutral Eu(III) complex, $[Eu_2(\mathbf{18})]$, where two DO3A Eu(III) complexes are linked via an aniline derived linker, to bind the phthalic acid derivatives shown in Figure 7.

In this elegant system, the phthalic acids bind not only through electrostatic interactions but also through π-interactions between the relatively electron-deficient ring of the phthalate and the electron-rich aniline moiety. After carrying out initial studies using simple phthalate derivatives (phthalic acid, isophthalic acid, and terephthalic acid) and showing stable binding to $[Eu_2(\mathbf{18})]$, particularly with isophthalic acid, Faulkner and coworkers derivatized a Tb^{III} DO3A complex with an isophthalate appended to allow the formation of the desired heterometallic self-assembly. The

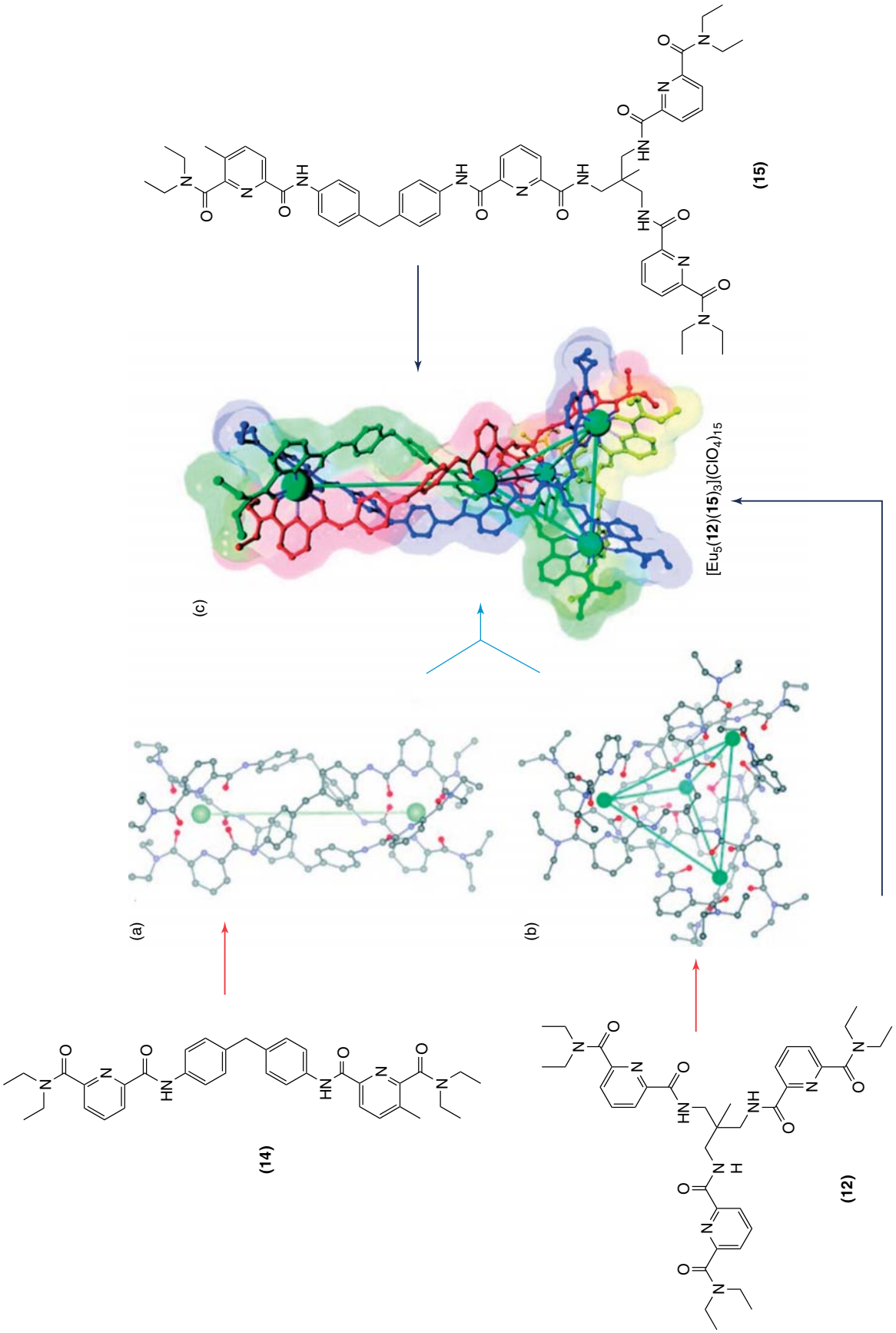


Figure 5 Depiction of the rational design of the tower-like pentanuclear assembly of $[Eu_5(\mathbf{12})(\mathbf{15})_3](ClO_4)_{15}$ showing how the symmetrical ligands (**12**) and (**14**) (a) and (b) can be combined to give the unsymmetrical ligand (**15**) (c). The helicate and cage compounds are crystal structures, whereas the pentanuclear tower is a calculated model. (Adapted with permission from Ref. 32. Copyright (2011) American Chemical Society.)

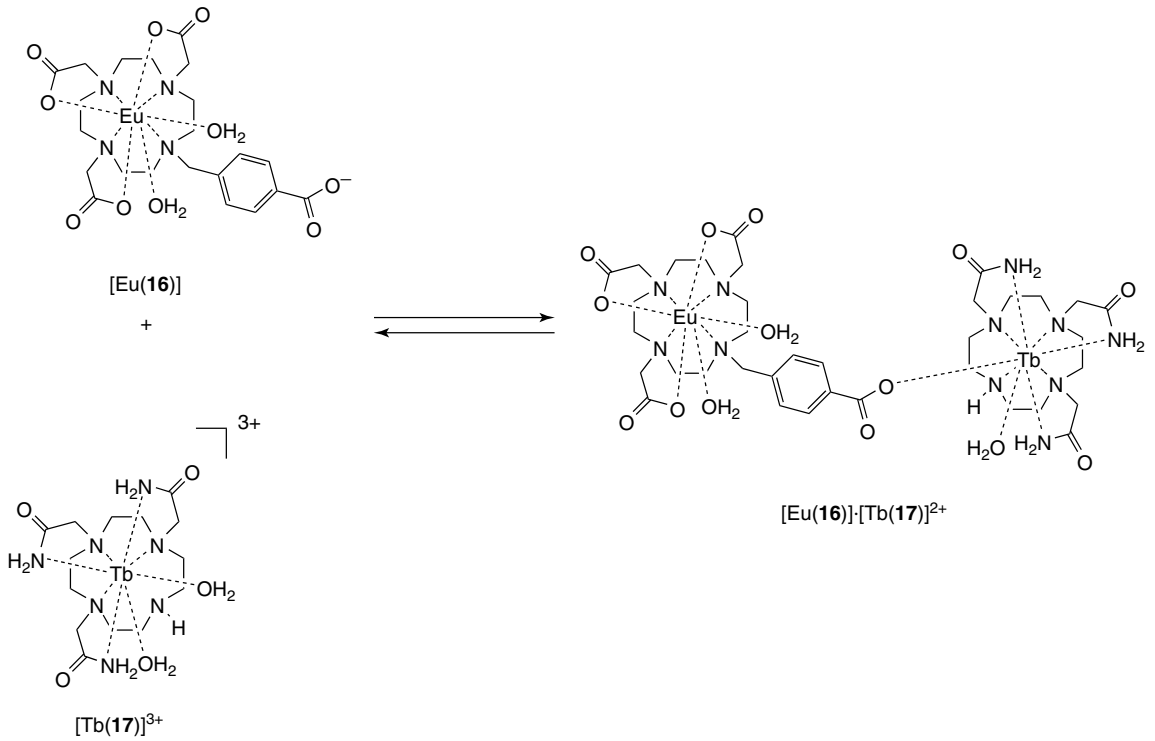


Figure 6 Schematic of the formation of the heteronuclear Tb·Eu dimer [Eu(**16**)]·[Tb(**17**)]$^{2+}$

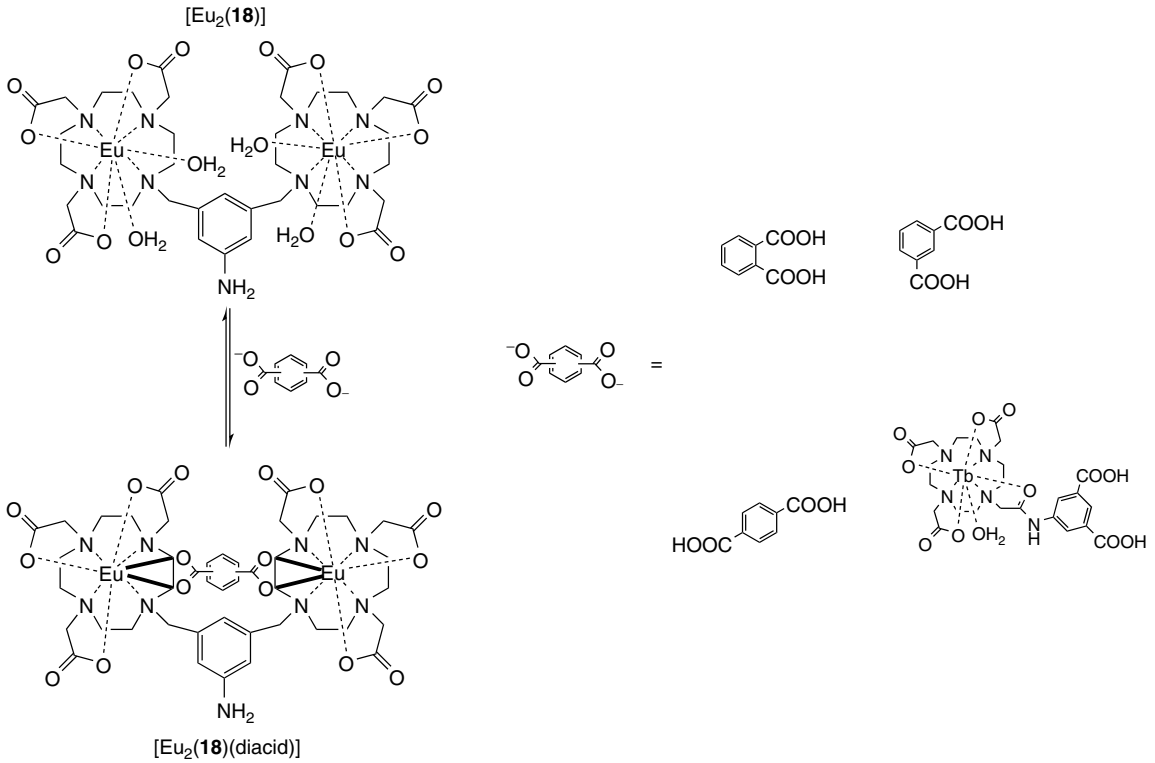


Figure 7 Formation of self-assemblies between the dinuclear Eu complex [Eu_2(**18**)] and various diacids including the formation of the trinuclear Eu·Tb species [Eu_2(**18**)]·[Tb(**19**)]

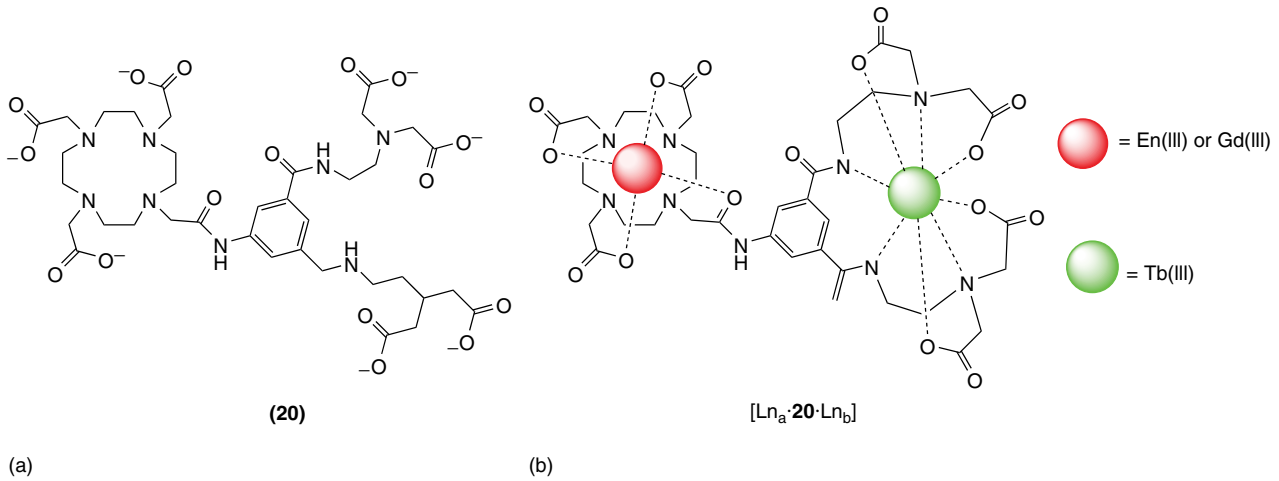


Figure 8 (a) Ditopic ligand (**20**) used by Angelovski and coworkers to prepare heterodinuclear Ln^{III} complexes (b)

Tb^{III} complex in this system, [Tb·(**19**)], is octadentate, thus removing the problem of self-association as observed in the previous systems. Titrations monitoring the Tb^{III} centered emission in aqueous buffer solutions (Phosphate Buffered Saline (PBS) and 4-(2-hydroxyethyl)-1-piperazineethanesulfonic acid (HEPES) both at pH 7.4, where the isophthalate is fully deprotonated), indicate successful formation of [Eu_2(**18**)]·[Tb(**19**)] with comparable binding constants for each of the buffer systems of $K = 225\,600$ M^{-1} (PBS) and 226 500 M^{-1} (HEPES). These results highlight the ternary complex formation approach to generating heterometallic 4f systems through careful matching of interactions between kinetically stable complexes.

Other examples of heterometallic 4f systems have emerged in the literature in recent years, including systems where one ligand contains two slightly different binding sites for Ln^{III} centers. The work of Angelovski and coworkers highlights this approach where they fused cyclic and acyclic, carboxylate-rich groups for Ln^{III} complexation to give (**20**) (Figure 8).[34] In this system, stable complexes of Eu^{III} or Gd^{III} are formed where the cyclic component hosts the lanthanide ion leaving the acyclic component free for further complexation to other Ln^{III} centers. In this particular work, Angelovski and coworkers formed a dual emissive [Eu·**20**·Tb] complex through titration of [Eu·**20**] with Tb^{III} and a dual modal complex of [Gd·**20**·Tb], which exhibited Tb^{III} centered luminescence and characteristic Gd^{III} relaxivity.

In recent years, there has been significant interest in the development of mixed d−f heterometallic systems, for both photophysically and magnetically interesting systems. From a photophysical point of view, the development of mixed d−f systems is attractive for biological imaging purposes as it allows the possibility of combining the relatively long wavelength absorption of the metal to ligand charge transfer (MLCT) in d-block metals with time-delayed luminescence from the Ln^{III}. In particular, there is significant interest in combining NIR emitting lanthanide ions [Nd^{III} and Yb^{III}] with transition metals as the visible wavelength range for the MLCT absorption band of some d-block metals is ideal for sensitizing the NIR emitting Ln^{III} ions. In addition, systems of this type may give rise to dual emission, i.e., mixed metal complexes emitting in the visible and the NIR ranges. A recent example of such a system is from Nonat *et al.* where *d*−*f* dyads[35] and tetrads[36] were prepared via the assembly of 1,10-phenanthroline appended Nd^{III} or Yb^{III} cyclen complexes $[Ln(\mathbf{21})]^{3+}$ with Ru^{II}. Initial studies investigated dinuclear systems where one Ln^{III} containing moiety was complexed with $Ru^{II}(bpy)_2$ (bpy = 2, 2′-bipyridine);[35] however, in later studies larger more complex systems were synthesized where three Ln^{III} moieties were complexed with $RuCl_3·H_2O$ giving rise to tetranuclear complexes $\{[Ln(\mathbf{21})]_3·Ru\}^{11+}$ that were emitting both visible light and NIR in H2O (Figure 9).[36]

In order to fully characterize these large tetranuclear systems, Nonat *et al.* prepared the diamagnetic $\{[Lu(\mathbf{21})]_3·Ru\}^{11+}$ and used ^{1}H-NMR spectroscopy and NMR diffusion experiments to fully characterize the large, highly symmetric complex. Along a similar vein, Parac-Vogt and coworkers prepared a trinuclear mixed Ru^{II}_2–Ln^{III} system (Ln = Eu or Gd) where the ligand (**22**) contained two 1,10-phenanthroline groups for Ru^{II} complexation and a central octadentate acyclic amino-carboxylate group for Ln^{III} complexation (Figure 10).[37] The synthesis of the trinuclear system began with formation of the Ln^{III} complex followed by reaction of this with $Ru^{II}(bpy)_2$ to give the desired trinuclear system $[Ru_2(bpy)_4·\mathbf{22}·Ln]^{4+}$. The $[Ru_2(bpy)_4·\mathbf{22}·Eu]^{4+}$ complex was red luminescent, displaying both Eu^{III} and Ru^{II} centered emission, whereas the $[Ru_2(bpy)_4·\mathbf{22}·Gd]^{4+}$ displayed both relaxometric and luminescent properties, and is thus is considered a potential bimodal imaging agent for *in vivo* studies.

These two studies show how careful ligand design can be used to prepare mixed d−f complexes through preferential

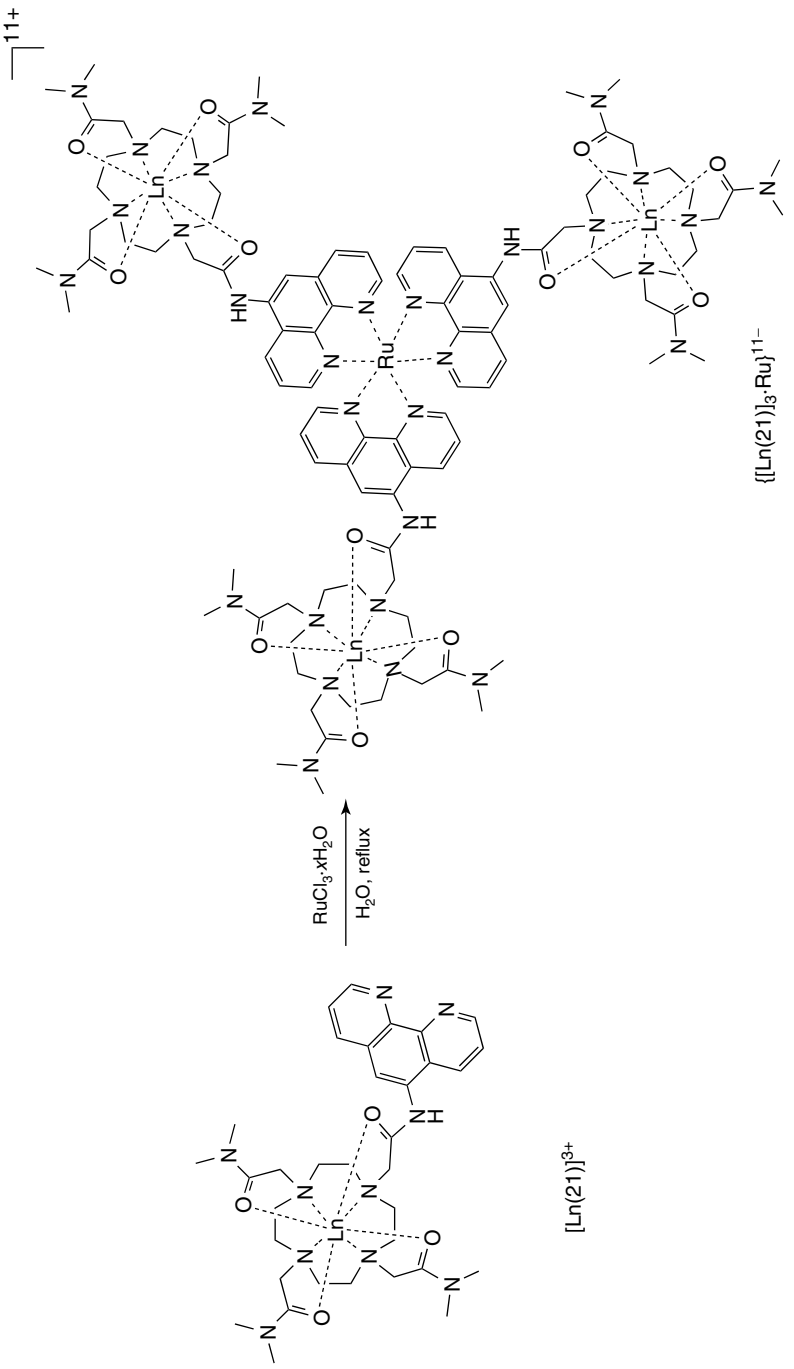


Figure 9 Schematic representation of the formation of mixed d−*f* tetrads from reaction of $[Ln(\mathbf{21})]^{3+}$ with ruthenium

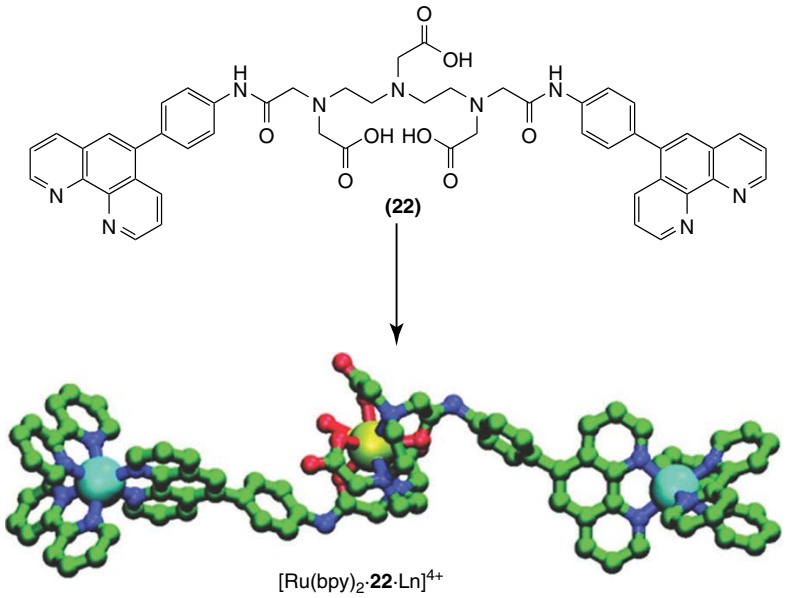


Figure 10 Formation of mixed Ru_2·Ln complexes using ligand (**22**). (Adapted with permission from Ref. 38. Copyright (2011) American Chemical Society.)

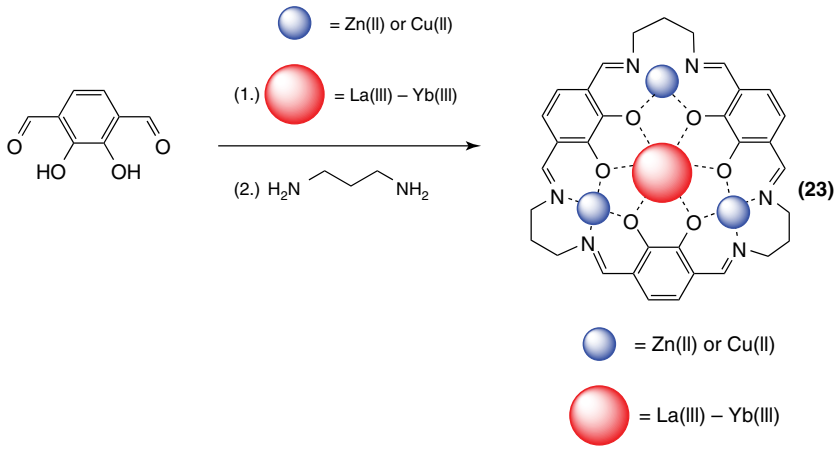


Figure 11 One-pot synthesis of macrocyclic $[M_3Ln(\mathbf{23})(NO_3)_3 \cdot x\text{solvent}]$ complexes where the metal ions template the formation of the large [3 × 3] macrocycle (**23**)

binding of one metal in a particular binding site over another.

Very recently Brooker and coworkers have elegantly used careful ligand design and self-assembly processes to prepare a large series of marcrocyclic tetranuclear d–f systems through the formation of [3 × 3] metal templated macrocyclic complexes.[38–40] The primary research goals for these systems were the generation of single molecule magnets (SMM's), i.e., molecules that can act as magnets at the molecular level through slow relaxation of magnetization at low temperatures. In addition, the use of large organic macrocyclic components also allowed for tuning of the systems as well as enhanced solubility. The macrocycle chosen, (**23**), was inspired by the work of Nabeshima and coworkers[41,42] and MacLachlan and coworkers[43,44] and was based around the 1,4-diformyl-2,3-dihydroxybenzene head unit where the reaction of three dialdehyde components with three diamines would result in the formation of a cavity capable of binding three d-block transition metal ions and one 4f lanthanide (Figure 11).

Brooker and coworkers have prepared 15 mixed d–f complexes utilizing Zn^{II} and Cu^{II} as the d-block components and La–Yb as the 4f components. The self-assembly process is exemplified by the one-pot synthetic procedure where 1,4-diformyl-2,3-dihydroxybenzene is stirred with both the

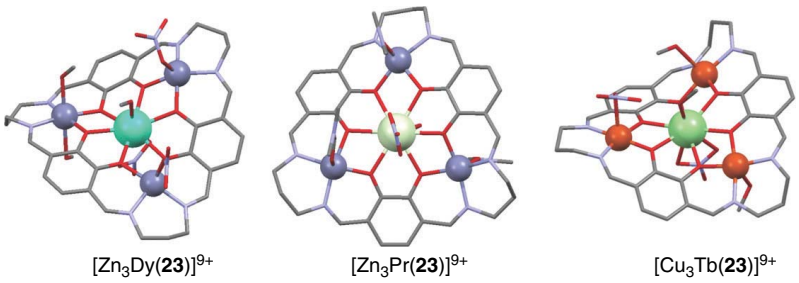


Figure 12 View of the crystal structures of marcocyclic $[M_3Ln(\mathbf{23})(NO_3)_3 \cdot x\text{solvent}]$ complexes. Solvent molecules, hydrogen atoms, and unbound anions are omitted for clarity

d-block and 4f metal salts before 1,3-diamino propane was added and the resulting $[M_3Ln(\mathbf{23})(NO_3)_3 \cdot x\text{solvent}]$ complexes isolated through diffusion methods (Figure 12). Of the 15 complexes prepared, 14 featured Zn^{II} as the 3d metal ion with the general formula, $[Zn_3Ln(\mathbf{23})(NO_3)_3 \cdot x\text{solvent}]$, and three of these displayed SMM behavior (where Ln = Dy, Er, and Yb). In addition, the Nd, Er, and Yb complexes also displayed solid-state luminescence. The research of Brooker and coworkers highlights how the combination of macrocyclic chemistry and lanthanides results in nice examples of functional (SMMs) 3d–4f mixed heteronuclear complexes.

This section has dealt with polynuclear Ln^{III}-based systems and has shown that when incorporated with other 4f ions or d-block metal ions the lanthanides can give rise to highly interesting systems with multiple functionalities. This rich area of chemistry is ever growing and over the next few years we expect to see many more examples of polynuclear lanthanide-based supramolecular systems with novel applications throughout all branches of chemistry. One recent example of such new application is that of Bünzli and Piguet, who have developed a trinuclear d–f–d complex for use in NIR to visible light up conversion, demonstrating the scope of the use of the lanthanides in new technologies.[45]

5 CONCLUSION

This chapter has dealt with some of the many examples of lanthanide-based supramolecular systems. We have attempted to give a short overview of the field with much of our discussion focusing on the most recent examples. Owing to limited space, we can only give a snapshot of this very active area of research and consequently, apologize to the many thousands of researchers that we were unable to include. The area of lanthanide-based supramolecular chemistry is fast growing and, as seen from the examples chosen for this chapter, can give rise to functional systems with potential applications in sensing and imaging (both luminescent and MRI imaging), luminescent light-emitting materials and magnetically interesting material (SMMs). This particular area is now central to supramolecular chemistry, and we look forward to witnessing the growth in this field in the years to come.

6 GLOSSARY

Supramolecular: Compounds that are created through the interaction of multiple molecular units with bonding that can range from electrostatic to coordinate covalent.

7 ACKNOWLEDGMENT

We would like to thank the many PhD students and postdoctoral fellows from the Gunnlaugsson group, who, through their work, have contributed greatly to the writing of this chapter. In particular, we would like to thank Dr Brian McMahon, Dr Jennifer Molloy, Dr Christophe Lincheneau, and Ms Dawn Barry. Dr Kitchen would like to thank IRCSET for the award of an EMPOWER postdoctoral fellowship. Professor Gunnlaugsson would like to thank IRCSET (Postdoc and PhD studentships), SFI (RFP 2006, 2008, 2009, and PI2010 awards) and Enterprise Ireland and HEA PRTLI for financial support.

8 RELATED ARTICLES

Carboxylate; Lanthanide Complexes with Multidentate Ligands; Lanthanides: Luminescence Applications; Lanthanides in Living Systems; Luminescence; Luminescent Bioprobes; Metal–Organic Frameworks; Molecular Magnetic Materials; Near-Infrared Materials.

9 ABBREVIATIONS AND ACRONYMS

CPL = circular polarized luminescence; LB = Langmuir–Blodgett; SMMs = single molecule magnets.

10 REFERENCES

1. C. Huang, ed., 'Rare Earth Coordination Chemistry Fundamentals and Applications', John Wiley & Sons (Asia), Singapore, 2010.
2. J. P. Leonard, C. B. Nolan, F. Stomeo, and T. Gunnlaugsson, *Top. Curr. Chem.*, 2007, **281**, 1.
3. L. M. De Leon-Rodriguez, A. J. M. Lubag, C. R. Malloy, G. V. Martinez, R. J. Gillies, and A. D. Sherry, *Acc. Chem. Res.*, 2009, **42**, 948.
4. S. Aime, D. D. Castelli, S. G. Crich, E. Gianolio, and E. Terreno, *Acc. Chem. Res.*, 2009, **42**, 822.
5. A. Datta and K. N. Raymond, *Acc. Chem. Res.*, 2009, **42**, 938.
6. K. Binnemans, *Chem. Rev.*, 2009, **109**, 4283.
7. J. L. Major and T. J. Meade, *Acc. Chem. Res.*, 2009, **42**, 893.
8. C. Lincheneau, F. Stomeo, S. Comby, and T. Gunnlaugsson, *Aust. J. Chem.*, 2011, **64**, 1315.
9. S. V. Eliseeva and J.-C. G. Bünzli, *Chem. Soc. Rev.*, 2010, **39**, 189.
10. J.-C. G. Bünzli and C. Piguet, *Chem. Soc. Rev.*, 2005, **34**, 1048.
11. M. Andrews, J. E. Jones, L. P. Harding, and S. J. A. Pope, *Chem. Commun.*, 2011, **47**, 206.
12. R. Pal and D. Parker, *Org. Biomol. Chem.*, 2008, **6**, 1020.
13. B. McMahon, P. Mauer, C. P. McCoy, T. C. Lee, and T. Gunnlaugsson, *J. Am. Chem. Soc.*, 2009, **131**, 17542.
14. A. Escande, L. Guénée, K.-L. Buchwalder, and C. Piguet, *Inorg. Chem.*, 2009, **48**, 1132.
15. E. S. Andreiadis, D. Imbert, J. P'ecaut, R. Demadrille, and M. Mazzanti, *Dalton Trans.*, 2012, **41**, 1268.
16. C. Lincheneau, J. P. Leonard, T. McCabe, and T. Gunnlaugsson, *Chem. Commun.*, 2011, **46**, 7119.
17. C. Lincheneau, C. Destribats, D. E. Barry, J. A. Kitchen, R. D. Peacock, and T. Gunnlaugsson, *Dalton Trans.*, 2011, **40**, 12056.
18. J. P. Leonard, P. Jensen, T. McCabe, J. E. O'Brien, R. D. Peacock, P. E. Kruger, and T. Gunnlaugsson, *J. Am. Chem. Soc.*, 2007, **129**, 10986.
19. J. A. Kitchen, D. E. Barry, L. Mercs, M. Albrecht, R. D. Peacock, and T. Gunnlaugsson, *Angew. Chem. Int. Ed.*, 2012, **51**, 704.
20. F. Stomeo, C. Lincheneau, J. P. Leonard, J. E. O'Brien, R. D. Peacock, C. P. McCoy, and T. Gunnlaugsson, *J. Am. Chem. Soc.*, 2009, **131**, 9636.
21. S. Comby, F. Stomeo, C. P. McCoy, and T. Gunnlaugsson, *Helv. Chim. Acta*, 2009, **92**, 2461.
22. C. Lincheneau, R. D. Peacock, and T. Gunnlaugsson, *Chem. Asian J.*, 2010, **5**, 500.
23. J. K. Molloy, O. Kotova, R. D. Peacock, and T. Gunnlaugsson, *Org. Biomol. Chem.*, 2012, **10**, 314.
24. C. Butler, S. Goetz, C. M. Fitchett, P. E. Kruger, and T. Gunnlaugsson, *Inorg. Chem.*, 2011, **50**, 2723.
25. G. Bozoklu, C. Marchal, C. Gateau, J. Pécaut, D. Imbert, and M. Mazzanti, *Chem. Eur. J.*, 2010, **16**, 6159.
26. N. Dalla-Favera, J. Hamacek, M. Borkovec, D. Jeannerat, G. Ercolani, and C. Piguet, *Chem. Eur. J.*, 2008, **14**, 2994.
27. J. Hamacek, *J. Alloys Compd.*, 2008, **451**, 347.
28. K. Zeckert, J. Hamacek, J.-M. Senegas, N. Dalla-Favera, S. Floquet, G. Bernardinelli, and C. Piguet, *Angew. Chem.*, 2005, **44**, 7954.
29. J. Hamacek, G. Bernardinelli, and Y. Filinchuk, *Eur. J. Inorg. Chem.*, 2008, **22**, 3419.
30. J. Hamacek, C. Besnard, T. Penhouet, and P.-Y. Morgantini, *Chem. Eur. J.*, 2011, **17**, 6753.
31. B. E. Aroussi, L. Guénée, P. Pal, and J. Hamacek, *Inorg. Chem.*, 2011, **50**, 8588.
32. B. E. Aroussi, S. Zebret, C. Besnard, P. Perrottet, and J. Hamacek, *J. Am. Chem. Soc.*, 2011, **133**, 10764.
33. J. A. Tilney, T. J. Sørensen, B. P. Burton-Pye, and S. Faulkner, *Dalton Trans.*, 2011, **40**, 12063.
34. I. Mamedov, T. N. Parac-Vogt, N. K. Logothetis, and G. Angelovski, *Dalton Trans.*, 2010, **39**, 5721.
35. A. M. Nonat, S. J. Quinn, and T. Gunnlaugsson, *Inorg. Chem.*, 2009, **48**, 1646.
36. A. M. Nonat, C. Allain, S. Faulkner, and T. Gunnlaugsson, *Inorg. Chem.*, 2010, **49**, 8449.
37. G. Dehaen, P. Verwilst, S. V. Eliseeva, S. Laurent, L. Vander Elst, R. N. Muller, W. M. De Borggraeve, K. Binnemans, and T. N. Parac-Vogt, *Inorg. Chem.*, 2011, **50**, 10005.
38. H. L. C. Feltham, Y. Lan, F. Klöwer, L. Ungur, L. F. Chibotaru, A. K. Powell, and S. Brooker, *Chem. Eur. J.*, 2011, **17**, 4362.
39. H. L. C. Feltham, F. Klöwer, S. A. Cameron, D. S. Larsen, Y. Lan, M. Tropiano, S. Faulkner, A. K. Powell, and S. Brooker, *Dalton Trans.*, 2011, **40**, 11425.
40. H. L. C. Feltham, R. Clérac, A. K. Powell, and S. Brooker, *Inorg. Chem.*, 2011, **50**, 4232.
41. S. Akine and T. Nabeshima, *Dalton Trans.*, 2009, 10395.
42. S. Akine, S. Sunaga, T. Taniguchi, H. Miyazaki, and T. Nabeshima, *Inorg. Chem.*, 2007, **46**, 2959.
43. P. D. Frischmann and M. J. MacLachlan, *Comments Inorg. Chem.*, 2008, **29**, 26.
44. P. D. Frischmann, J. Jiang, J. K. H. Hui, J. J. Grzybowski, and M. J. MacLachlan, *Org. Lett.*, 2008, **10**, 1255.
45. L. Aboshyan-Sorgho, C. Besnard, P. Pattison, K. R. Kittilstved, A. Aebischer, J. C. G. Bünzli, A. Hauser, and C. Piguet, *Angew. Chem. Int. Ed.*, 2011, **50**, 4108.

Endohedral Fullerenes

Daniel L. Burriss and David A. Atwood

University of Kentucky, Lexington, KY, USA

1 Summary 495
2 Introduction 495
3 Synthesis and Characterization 496
4 Structure and Bonding 496
5 Applications 498
6 Conclusions 499
7 Glossary 499
8 Related Articles 499
9 Abbreviations and Acronyms 499
10 References 499

1 SUMMARY

One allotrope of carbon is the fullerene, which when comprised of 60 carbon atoms (C_{60}) is often referred to as a *buckyball*. A fullerene is a hollow sphere of carbon atoms with a diameter of 400–1000 pm ranging in catenation from C_{60}–C_{240}. The discovery of fullerenes was immediately followed by the discovery of endohedral fullerenes. An endohedral fullerene has one or more atoms encapsulated within the hollow interior of the fullerene. The encapsulated atoms can be metals, nonmetals, or clusters of atoms. In the metal- and cluster-containing endohedral fullerenes, the encapsulated atoms are covalently bound to the interior of the carbon cage. However, covalent bonding does not occur when noble gases are encapsulated in a fullerene cage.

Many elements have been encapsulated in fullerenes, including most of the Group 1 and Group 2 elements. All noble gases with the exception of Rn have been encapsulated. Endohedral fullerenes are also known for all the rare earth elements (except Pm) where the bonding is largely ionic, similar to that found for the Groups 1 and 2 elements. Only a few transition metals and nonmetals such as Ti, Zr, Hf, N, C, and P have been encapsulated, which can be attributed, in part, to synthetic difficulties.

Some proposed applications of endohedral fullerenes include MRI contrast agents, radiopharmaceuticals, photovoltaics, and quantum computing. While some of the proposed applications have been recently achieved, a problem that has to be overcome for most applications is the insolubility of endohedral fullerenes. For some applications, the endohedral fullerene can be exohedrally modified with a molecule on the exterior of the carbon cage, which assists in increasing solubility and for medical applications provides the means of controlling where the fullerene will bind.

2 INTRODUCTION

Within a week after fullerenes were first discovered in 1985, it was predicted that the nanometer-sized hollow interior of the fullerene could encapsulate an additional atom. The isolation of the first endohedral metallofullerenes was achieved in 1991, with the synthesis and extraction of La@C_{82}. The @ symbol denotes that the La atom is encapsulated in the C_{82} fullerene cage. In contrast to the IUPAC nomenclature, which names the compound [82] fullerene-*incar*-lanthanum written *i*LaC_{82}, the @ nomenclature became popular and is now common in the literature.[1]

The only characterization data for La@C_{82} was Fourier transform ion cyclotron resonance (FT-ICR) mass spectrometry data, which did not provide unambiguous evidence that the La atom was actually encapsulated in the fullerene.[2] The unambiguous characterization of an endohedral fullerenes was achieved in 1995, using synchrotron X-ray diffraction maximum entropy method (XRD–MEM)-Rietveld method to provide physical details about the structure of Y@C_{82}. Interestingly, the Y atom is not located in the center

The Rare Earth Elements. Edited by David A. Atwood. © 2012 John Wiley & Sons, Ltd. ISBN 978-1-119-95097-4

Table 1 Examples of lanthanide-containing endohedral fullerenes

Metal only				Clusters		
M@Cn	M_2@Cn	M_3@Cn	M_4@Cn	M_3N@Cn	MC_2@Cn	MCH@Cn
La@C_{82}	La_2@C_{72}	Sc_3@C_{82}	Sc_4@C_{82}	Sc_3N@C_{70}	Sc_2C_2@C_{84}	Sc_3CH@C_{80}
La@C_{60}	La_2@C_{82}			Tb_3N@C_{84}	Sc_2C_2@C_{82}	
La@C_{90}	Sc_2@C_{74}			Tm_3N@C_{84}	Y_2C_2@C_{82}	
La@C_{70}	Sc_2@C_{82}			Gd_3N@C_{84}	Sc_3C_2@C_{80}	
Ln@C_{82}	Sc_2@C_{84}			Gd_3N@C_{82}	Gd_2C_2@C_{92}	
	Gd_2@C_{80}					

Ln = Y, Sc, Ce, Pr, Nd, Sm, Eu, Gd, Tb, Dy, Ho, Er, Yb, Lu, Yb

of the cage as might be assumed, but is covalently bonded to the interior carbon cage.[2] The presence of interior covalent bonds between the encapsulated rare earth element and the fullerene is a common feature of this class of compounds.

While many other metallic and nonmetallic elements have been encapsulated in fullerenes, rare earth element endohedral metallofullerenes were the first endohedral fullerenes synthesized. All the rare earth elements, with the exception of Pm, have been encapsulated inside fullerenes.[3] Indeed, the rare earth-containing endohedral fullerenes dominate the literature on this subject, most likely because the compounds are relatively easy to synthesize, in contrast to potential transition-metal-containing endohedral fullerenes.

The range of lanthanide-containing fullerenes includes those containing only metal atoms, $Ln_x@C_n$ (where $x = 1–4$) and the compound fullerenes $Ln_xE@C_n$ (where $x = 1–3$ and E = N, C_2, CH, etc.). Some representative examples are given in Table 1.

3 SYNTHESIS AND CHARACTERIZATION

The only effective methods for producing endohedral metallofullerenes are laser ablation and DC arc discharge, techniques that are similar to the production of fullerenes. The DC arc method has become more popular because the laser ablation method has low yields and is costly.

Laser ablation was the first method used to synthesize endohedral fullerenes. To synthesize La@C_{82}, a graphite rod doped with La_2O_3 was vaporized with a Nd:YAG laser under argon at a temperature of 800 °C.[2] Laser ablation is now mainly used to study the formation of endohedral fullerenes rather than used for actually synthesizing them.

The DC arc technique is carried out in a water-cooled chamber with a graphite cathode and a graphite anode that has been doped with the desired metal and a catalyst in the presence of a gas, usually helium. One reason for the lack of transition-metal endohedral fullerenes can be attributed to the difficulty of current DC arc-discharge methods to cause encapsulation of transition metals in fullerenes, for which the reason remains unclear. For this reason, transition metals are often used as catalysts in endohedral fullerene production by the DC arc method.

The major products formed by DC arc discharge are empty fullerenes, with the endohedral fullerenes composing only about 1% of the raw soot. For this reason, better extraction methods are always being sought. Sublimation is a fairly efficient method for extraction and is a solventless technique. Nevertheless, the most popular method for extraction of endohedral fullerenes is solvent extraction. Some popular solvents for extraction are xylene, carbon disulfide, and toluene. The efficiency of this method is not great because about half of the endohedral fullerenes remain in the extracted residue, which needs further processing with other solvents. Extraction of trimetallic nitride endohedral fullerenes has a higher efficiency because of increased solubility in common solvents.

For the production of cluster fullerenes, the trimetallic nitride template method is used, which is a modification of the DC arc technique. This technique introduces a reactive gas rather than helium in the production process. The yields of trimetallic-nitride-containing endohedral fullerenes can be increased from 2% to a maximum of 98% using NH_3 rather than nitrogen as the reactive gas.[4] The high yields make the extraction process more efficient.

The first characterization method used for endohedral fullerenes was mass spectrometry, which revealed the relative amounts of endohedral fullerenes to empty fullerenes in the carbon soot. Another popular characterization technique is ^{13}C-NMR, which can determine the symmetry of the compound and provide evidence of structural isomers.

While mass spectrometry and ^{13}C-NMR sometimes cannot determine that the rare earth is actually encapsulated in the fullerene, X-ray diffraction is an unambiguous technique that was used to prove the endohedral nature of the rare earth species.

4 STRUCTURE AND BONDING

4.1 Fullerenes with One Metal

The electronic configuration of La@C_{82} has been characterized by electron spin resonance (ESR) hyperfine

splitting as $La^{3+}[@C_{82}]^{3-}$. Encapsulation with electron transfer to the fullerene cage, resulting in the general formula, $Ln^{3+}[@C]^{3-}$, is a general feature of the compounds where a single metal is encapsulated. This charge transfer is one of the most important factors in the stability of endohedral fullerenes.

La and Y are both trivalent elements, but there was uncertainty whether Sc in $Sc@C_{82}$ was in the divalent or trivalent state. Synchrotron X-ray data was used to determine that the electron count for the Sc atom is 18.8, which confirmed that Sc is a divalent species donating both s electrons to the fullerene cage.[5]

In $La@C_{82}$, the nearest and next-to-nearest C–La bond distances are 247 ± 2 pm and 294 ± 7 pm, respectively.[6] In C_{82} single-metal endohedral fullerenes, the metal tends to be located under a hexagonal ring along the C_2 axis. The fact that the metal coordinates to the hexagonal ring, rather than the [6, 6] junction, can be rationalized by the fact that rare earth metals tend to adopt high coordination numbers.[7]

An interesting case arises in the situation of C_{80}, which only contains [6, 6] junctions along the C_2 axis. Yb in $Yb@C_{80}$ would prefer to be in position A or B (Figure 1) if it preferred to stay along the rotational axis, but its position found by XRD is C. In studies of $La@C_{80}(C_6H_3Cl_2)$, the La atom is found in almost the same position despite the cage distortion due to the bonding of $C_6H_3Cl_2$. This evidence supports the fact that the position of the rare earth element in a medium-sized fullerene is influenced by the high coordination number preference of rare earth elements.[7]

There is a range of nearest lanthanide–carbon distances within the endohedral fullerene. For example, there is a 37 pm difference in the lanthanide–carbon distance between $Sc@C_{82}$ and $Y@C_{82}$. Examples of lanthanide–carbon distances are given in Table 2.

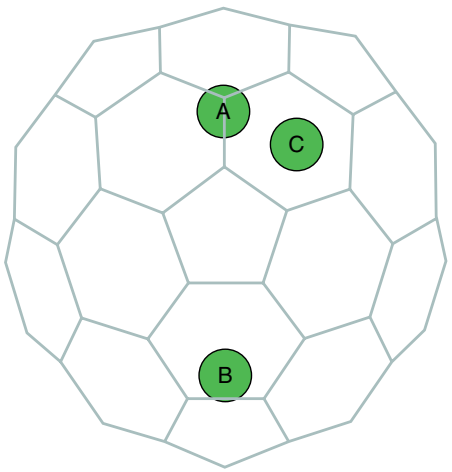


Figure 1 Possible positions of Yb in $Yb@C_{80}$ (A and B) and actual position by XRD (C). (Reprinted with permission from Ref. 7. Copyright (2011) American Chemical Society.)

Table 2 Ln–C distances

Endohedral fullerene	Nearest Ln–C distance (pm)
$Sc@C_{82}$	253
$Sc_2@C_{84}$	240
$Y@C_{82}$	290
$La@C_{82}$	255

Within the C_{82} endohedral fullerenes, the lanthanide–carbon distances do not follow the expected trend based on the ionic radii of the trivalent elements. On the basis of ionic radii, the distance should increase in the order La, Y, Sc, if all were trivalent. Instead, the distance increases in the order Sc, La, Y. This further supports the fact that Sc is a divalent cation in $Sc@C_{82}$.

On the basis of the electron density maps in C_{82} monometallofullerenes, it was found that La is in a ''floating motion'', while Sc and Y are at fixed positions at room temperature. The floating motion of La can be attributed to it being heavier than Sc and Y, thus being less strongly bound to the carbon cage.[5]

4.2 Fullerenes with Two Metals

There are some interesting properties associated with the dimetallofullerenes, such as $La_2@C_{80}$. From ^{13}C-NMR and ^{139}La-NMR data, the two La atoms in $La_2@C_{80}$ move in a circular motion inside the fullerene cage. The circulation of these two cations creates a new magnetic field inside the fullerene. $Sc_2@C_{84}$ is also interesting because three structural isomers have been isolated.[5]

4.3 Fullerenes with Ln_3N

The first trimetallic nitride endohedral synthesized was $Sc_3N@C_{80}$. The cationic clusters are three metals bound to a central nitrogen atom with an overall charge of +6. For example, the Dy_3N cluster in $Dy_3N@C_{82}$ has a trigonal planar geometry, with Dy–Dy distances of 345–356 pm and Dy–N distances of 200–207 pm (Figure 2). The clusters in $ErSc_2N@C_{80}$, $CeSc_2N@C_{80}$, $Lu_3N@C_{80}$, and $Tb_3N@C_{84}$ also remain planar. The cluster is different in $Gd_3N@C_{80}$, where the geometry is pyramidal with the nitrogen atom displaced 50 pm out of the plane of the Gd atoms. This difference in geometry is attributed to the slightly larger ionic radius of Gd^{3+} (94 pm), compared to Dy^{3+} (91 pm). Furthermore, the Gd_3N cluster is the largest cluster encapsulated in a fullerene to date. Thus, a dominating force of the geometry of the clusters is cluster size.[8]

Incarcerating rare earth trimetallic nitride clusters inside of fullerene cages has the ability to create stable compounds from what would otherwise be unstable molecules. The trimetallic nitride clusters and the C_{80} fullerene are not stable as individual species, but when the trimetallic nitride

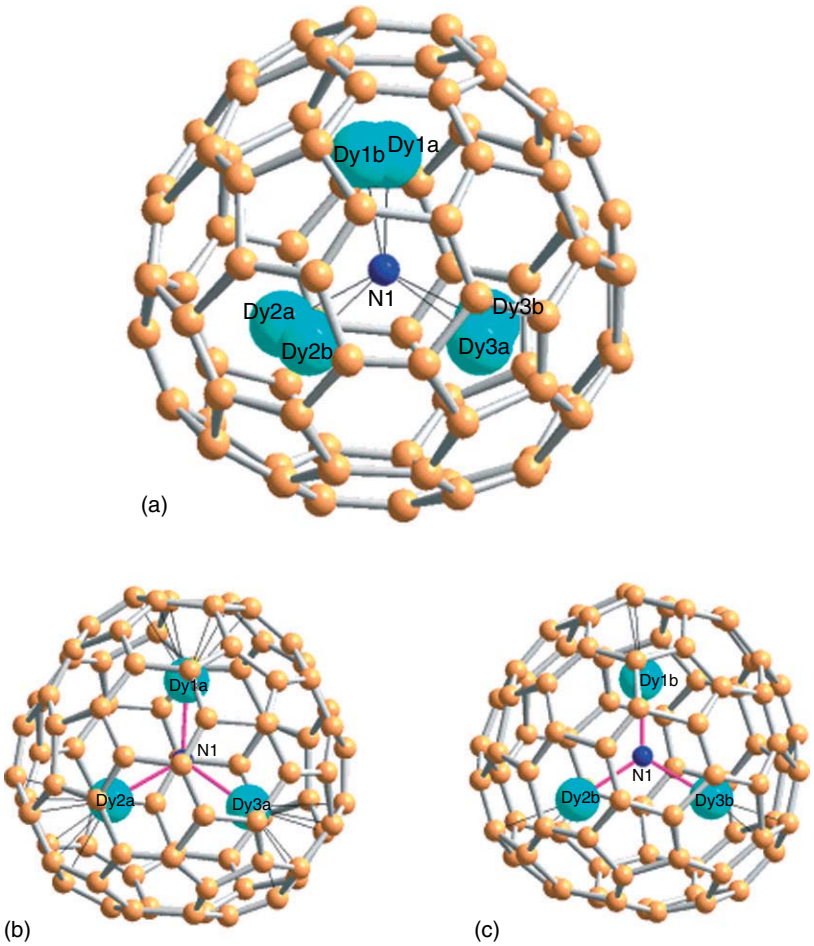


Figure 2 The trigonal geometry of $Dy_3N@C_{80}$, with the Dy atoms in two different bonding environments (a). These are shown separately where the Dy atoms make six contacts (b) and two contacts (c) with the fullerene. (Reprinted with permission from Ref. 8. Copyright (2006) American Chemical Society.)

cluster is encapsulated inside the C_{80} cage a stable compound is produced.[9]

Another stabilizing feature is the ability to stabilize nonisolated pentagon rule fullerenes when a metal or cluster is encapsulated. All empty fullerenes to date obey the isolated pentagon rule, in that there are no [5, 5] junctions that cause strain that destabilizes the molecule, because all pentagons are connected to hexagons. Nonisolated pentagon rule endohedral fullerenes such as $Sc_2@C_{66}$ and $Sc_3N@C_{68}$ are known to exist.[1]

5 APPLICATIONS

An endohedral fullerene, $Lu_3N@C_{80,}$ has been used as an acceptor material in organic photovoltaic applications. For processing into devices the endohedral fullerene must be exohedrally modified to overcome the insolubility of unmodified endohedral fullerenes in common solvents. The modified $Lu_3N@C_{80}$ has the advantage of increasing the open circuit voltage and power conversion efficiencies relative to reference devices using the most common acceptor [6,6]-phenyl-C_{61}-butyric methyl ester. The endohedral fullerene lowest unoccupied molecular orbital (LUMO) is much higher than the LUMO of empty fullerenes and is able to capture more energy for each photon.[9]

Trimetallic nitride endohedral fullerenes have been sought for use in MRI contrast agent (see ***Lanthanides: Magnetic Resonance Imaging***) and optoelectronic devices because of the wide variety of trimetallic nitride clusters that can be encapsulated in the fullerene, which can be used to tune properties of the material.[9]

A possible application of endohedral fullerenes is radiopharmaceuticals, where the toxic metal, which is used as a radiotracer, is protected by the fullerene cage. A Ho-based endohedral fullerene was used as a radiotracer. It traveled to all organs except those with limited blood flow.[10]

6 CONCLUSIONS

Although advances in applications of rare earth endohedral metallofullerenes are being made, there is a lack of toxicology data for endohedral fullerenes. This might not slow advances in device applications, but the toxicology will have to be evaluated before any practical advances in biological applications can be made.

In crystal structures of $Y@C_{82}$, the endohedral fullerenes are aligned in a head-to-tail fashion, which indicates a strong dipole–dipole and charge transfer interaction. This directionality could lead to novel solid-state materials based on endohedral metallofullerenes.

Progress is still being made in increasing production efficiencies of endohedral fullerenes. High yields allow for better characterization because higher purity can be obtained than when endohedral fullerenes are produced in low yields. There is a need for more characterization data to elucidate the structures of some of the endohedral fullerenes produced in low yields.

7 GLOSSARY

Allotrope: different structural forms of an element due to different bonding patterns, i.e., graphite and graphene.

Fullerene: hollow spherical allotrope of carbon containing only carbon atoms.

Metallofullerene: molecule composed of a metal encapsulated in a carbon cage.

8 RELATED ARTICLES

Group Trends; Lanthanides: Magnetic Resonance Imaging.

9 ABBREVIATIONS AND ACRONYMS

ESR = Electron Spin Resonance; FT-ICR = Fourier Transform Ion Cyclotron Resonance; LUMO = lowest unoccupied molecular orbital; MRI = Magnetic Resonance Imaging; XRD = X-ray Diffraction; MEM = Maximum Entropy Method.

10 REFERENCES

1. For a detailed review of lanthanide-containing fullerenes see: C.-H. Huang, 'Rare Earth Coordination Chemistry: Fundamentals and Applications', Wiley-Blackwell, Oxford, 2010.
2. Y. Chai, T. Guo, C. Jin, R. E. Haufler, L. P. F. Chibante, J. Fure, L. Wang, J. M. Alford, and R. E. Smalley, *J. Phys. Chem.*, 1991, **95**, 7564.
3. S. Yang and L. Dunsch, in 'Nanomaterials: Inorganic and Biological Perspectives', eds. C. M. Lukehart and R. A. Scott, John Wiley & Sons, New York, 2008, p. 189.
4. S. Yang and L. Dunsch, *J. Phys. Chem. B*, 2005, **109**, 12320.
5. H. Shinohara, in 'Fullerenes: Chemistry, Physics, and Technology', eds. K. M. Kadish and R. S. Ruoff, John Wiley & Sons, New York, 2000, p. 357.
6. H. Shinohara, *Rep. Prog. Phys.*, 2000, **63**, 843.
7. X., Y. Lian, C. M. Beavers, N. Mizorogi, Z. Slanina, S. Nagase, and T. Akasaka, *J. Am. Chem. Soc.*, 2011, **133**, 10772.
8. S. Yang, S. I. Troyanov, A. A. Popov, M. Krause, and L. Dunsch, *J. Am. Chem. Soc.*, 2006, **128**, 16733.
9. C. M. C. Russel, B. Ross, D. M. Guldi, S. G. Sankaranarayanan, M. O. Reese, N. Kopidakis, J. Peet, B. Walker, G. C. Bazan, E. V. Keuren, B. C. Holloway, and M. Drees, *Nat. Mater.*, 2009, **8**, 208.
10. D. W. Cagle, S. J. Kennel, S. Mirzadeh, J. M. Alford, and L. J. Wilson, *Proc. Natl. Acad. Sci. U.S.A.*, 1999, **96**, 5182.

Lanthanide Shift Reagents

Carlos F.G.C. Geraldes

University of Coimbra, Coimbra, Portugal

1	Summary	501
2	Introduction	501
3	Basic Theory of Lanthanide-Induced NMR Shifts	502
4	Structural Information from LIS Data	506
5	Shift Reagents for MRS of Alkali Metal Ions in Biological Systems	515
6	Conclusions	517
7	Glossary	517
8	Acknowledgements	518
9	Related Articles	518
10	Abbreviations and Acronyms	518
11	References	518

1 SUMMARY

In this chapter, we describe the main applications of paramagnetic Ln^{3+} ions as NMR shift reagent (SR) probes in a wide range of research fields. The binding of a paramagnetic Ln^{3+} causes increased shift and relaxation effects on the resonances of ligand NMR-active nuclei. The basic theory of the induced paramagnetic shifts caused by the influence of the magnetic moment of the metal-based electron spins is described, including bulk susceptibility, contact, and dipolar shifts. The main applications of the paramagnetic NMR shift effects as structural reporters of small flexible ligands, strong paramagnetic complexes useful for MRI and MRS applications, as well as their supramolecular species, are illustrated with important examples. The methods to obtain or refine the structure and dynamics of proteins and protein complexes using Ln^{3+}-based paramagnetic restraints such as pseudocontact shift (PCS), residual dipolar coupling (RDC), cross-correlation (CCR), and relaxation effects, are discussed, including the use of metal substitution, covalently attached tags, and protein surface probes. Finally, some applications of powerful NMR SRs for *in vivo* MRS of alkali ions are presented.

2 INTRODUCTION

The first report by Hinckley,[1] more than 40 years ago, of the use of lanthanide complexes to simplify unresolved proton resonances in low-field NMR spectra of organic molecules in nonaqueous solvents, marked the start of the application of the so-called lanthanide-induced shift (LIS) method to the resolution of a variety of NMR problems.[2–5] The early results led to the extensive use of lanthanide(III) ions and complexes as NMR shift and relaxation reagents in nonaqueous and aqueous solvents, in applications ranging from qualitative spectral simplification, proof of molecular stereochemistry, and quantitative analysis of the solution structure and dynamics of Ln^{3+} complexes relevant to the design of contrast agents for MRI, as well as of small biological molecules and proteins, and as SRs for *in vivo* NMR spectroscopy of perfused cells, organs, and intact animals.[2–11]

Each of these applications is based on three fundamental properties of the Ln^{3+} cations: their Lewis acid characteristics, their unpaired f electrons, and their preference to form complexes with coordination numbers of between 8 and 10. Lanthanum and the lanthanides form a unique series in the periodical system, as the trivalent ions of the first and the last members (La^{3+} and Lu^{3+}, respectively) are diamagnetic, whereas all others are paramagnetic, with one to seven unpaired 4f electrons. As they are shielded by the 5s

The Rare Earth Elements. Edited by David A. Atwood. © 2012 John Wiley & Sons, Ltd. ISBN 978-1-119-95097-4

and 5p electrons, they are not readily available for covalent interactions with ligands. Interactions are largely electrostatic and, as a consequence of such Lewis acid behavior, the geometry of Ln^{3+} complexes is usually determined by steric rather than by electronic factors. Another consequence of this shielding is a large similarity in chemical behavior among the 15 Ln^{3+} ions. Any difference in chemical behavior may be ascribed to the decrease in ionic radius from La^{3+} to Lu^{3+} (1.36–1.17 Å).[12] Usually, the various Ln^{3+} complexes of a particular ligand are nearly isostructural. Each of the Ln^{3+} ions, however, has its own characteristic effects on the NMR parameters of nuclei in its proximity. The perturbations of NMR parameters of nuclei of the same ligand by various Ln^{3+} ions can be exploited for the elucidation of the molecular structures in solution of the complexes under study.

When a Lewis base interacts with a Ln^{3+} ion, any NMR-active nucleus within that base is influenced by the presence of the unpaired f electrons, leading to its paramagnetic relaxation and broadening of its resonance, and in most cases to a shift to a different NMR frequency. Gd^{3+} has seven unpaired electrons distributed isotropically throughout its 4f shell and, therefore, cannot produce an NMR dipolar shift in solution. The other Ln^{3+} ions, with an anisotropic spatial distribution of unpaired f electrons, originate a dipolar LIS in solution, called PCS, which is the kind of LIS useful in obtaining structural information. If, however, the Lewis acid–base interaction with any paramagnetic Ln^{3+} is partially covalent, a small amount of unpaired electron spin density can reach the molecular framework of the base and result in a second type of LIS, the contact (or scalar) shift. Thus Gd^{3+} can produce only a contact shift.

The high efficiency of Gd^{3+} in nuclear relaxation led to the successful introduction of Gd^{3+}-based contrast agents for MRI. The increasing demand for more effective and specific contrast agents led to much research toward gaining insight into the parameters that govern the relaxivity of these agents.[11] Because all these parameters are related to the solution structure and/or dynamics of the complexes involved, extensive knowledge of such properties of small Ln^{3+} complexes in solution has accumulated.[11]

The traditional qualitative uses of Ln^{3+} complexes to simplify complex NMR spectra in organic solvents, reviewed extensively,[3,4] have been replaced by the use of high magnetic fields and two- and three-dimensional NMR methods. Applications of chiral SRs have also been extensively reviewed.[5] This chapter describes LIS methodologies for those who wish to apply them to their particular systems, and their recent quantitative applications as NMR structural probes in aqueous solution of small Ln^{3+} complexes including some of their supramolecular constructs, as well as of small biological molecules and proteins, and as SRs for *in vivo* NMR spectroscopy.

3 BASIC THEORY OF LANTHANIDE-INDUCED NMR SHIFTS

The LIS for a ligand nucleus on coordination to a Ln^{3+} cation (Δ) can be expressed as the sum of four terms: the bulk magnetic susceptibility (BMS) shift (Δ_χ), the diamagnetic shift (Δ_d), the contact shift (Δ_c), and the PCS (Δ_p) (equation (1)). The BMS shift has only to be taken into account when the NMR spectrometer is not frequency-locked and no internal reference is present in the same compartment of the sample. It is dependent on the shape of the sample and its position in the magnetic field, the absolute temperature, and the effective magnetic moment of the paramagnetic Ln^{3+} ion and its concentration, but is independent of the structure of the compound.[13] Each of the other shift contributions, particularly Δ_c and Δ_p, contain useful information regarding the structure of the concerning Ln^{3+} complex.[2,13–15]

$$\Delta = \Delta_\chi + \Delta_d + \Delta_c + \Delta_p \tag{1}$$

3.1 Diamagnetic Shifts

The diamagnetic or complexation shift is usually small and is often neglected. It originates from effects such as conformational changes, inductive effects, and direct field effects. In saturated ligands, the diamagnetic shifts are usually insignificant, with exception of the nuclei directly coordinated to the Ln^{3+} cation.[15]

3.2 Contact Shifts

Contact shifts arise from through-bond transmission of unpaired electron spin density from the lanthanide 4f-orbital to the nucleus under study. It is given by equation (2), where $< S_z >$ is the reduced value of the average spin polarization, μ_B the Bohr magneton, k the Boltzmann constant, γ_I the gyromagnetic ratio of the nucleus in question, A/h the hyperfine coupling constant (in radians per second), and Δ_c expressed in parts per million. Values of $< S_z >$ have been calculated at 300 K and later refined for all reasonable temperatures.[15]

$$\Delta_c = < S_z > F = < S_z > \frac{\mu_B}{3kT\gamma_I}\frac{A}{\hbar}10^6 \tag{2}$$

The magnitude of Δ_c generally decreases rapidly upon increase of the number of bonds between the Ln^{3+} and the nucleus under study, from the largest values generally observed for the directly Ln^{3+}-bonded donor sites, allowing easy identification of the donor sites in a ligand.[7] The tabulated $< S_z >$ values show a linear relationship with, for example, the ^{17}O LIS values for water in both the Ln^{3+}–aquo complexes[16,17] and the first coordination sphere of $Ln(EDTA)^-$.[15] This confirms that the LIS for a donor site is predominantly of contact origin and that the isotropic

hyperfine coupling constant does not vary significantly along the lanthanide series.[15]

For coordinated O-atoms the magnitude of F is always in a narrow range ($F = -70 \pm 11$ ppm, at 73 °C, corresponding to $A/h = -3.9 \times 10^6$ rad·s^{-1}), irrespective of the ligand in question and of the other ligands coordinated to the Ln^{3+} ion.[15] If the experimental paramagnetic shifts are extrapolated to a molar ratio Ln^{3+}/ligand $\rho = 1$, the separation of contact shift and PCS (see below) affords nF, where n is the number of coordinated ligands. Division of nF by -70 gives n. This has been applied to a variety of oxygen-containing functional groups, such as carboxyl, carbonyl, hydroxyl, ether, and phosphate, in order to obtain the stoichiometry of an LnL_n complex. This technique has also been exploited for the determination of the number of Ln^{3+}-bound water molecules in a variety of Ln^{3+} complexes, such as those useful as MRI contrast agents.[15,18,19]

It should be noted that the large LIS of the donor site nucleus is accompanied by extensive line broadening. As a result, the signal for the bound state is often not observable if exchange between the bound and free states is slow on the NMR timescale. Under these circumstances, information may be obtained from the decrease in intensity of the signal of the donor sites in the free ligand on titration with a paramagnetic Ln^{3+} ion.

The magnitude of A/h and thus of Δ_c is related to the unpaired spin density on the nucleus under study, which may be transmitted via the bonds in the ligand by direct spin delocalization and/or by spin polarization. The latter mechanism gives rise to alternating signs of the corresponding contact shifts. A critical evaluation of the literature data on contact shifts of various Ln^{3+} complexes[6,15] suggests that spin delocalization dominates in straight carbon chains, whereas spin polarization dominates in cyclic compounds. Contact shifts for nuclei not directly coordinated to the Ln^{3+} ion are commonly separated off and ignored or are treated only in a qualitative manner.

3.3 Pseudocontact Shifts

The PCS or dipolar shift results from the local magnetic field induced in the nucleus under study by the magnetic moment of the Ln^{3+} ion. In the frame of the magnetic susceptibility tensor of the paramagnetic Ln^{3+} ion, the PCS can be expressed as in equations (3)–(5).[2,13,15,20]

$$\Delta_p = \frac{1}{12\pi r^3}\left[\Delta\chi_{ax}(3\cos^2\theta - 1) + \frac{3}{2}\Delta\chi_{rh}(\sin^2\theta\cos 2\varphi)\right] \quad (3)$$

$$\Delta\chi_{ax} = \chi_{zz} - \frac{\chi_{xx} + \chi_{yy}}{2} \quad (4)$$

$$\Delta\chi_{rh} = \chi_{xx} - \chi_{yy} \quad (5)$$

Here, r, θ, and φ are the spherical coordinates of the observed nucleus with respect to the principal magnetic axes

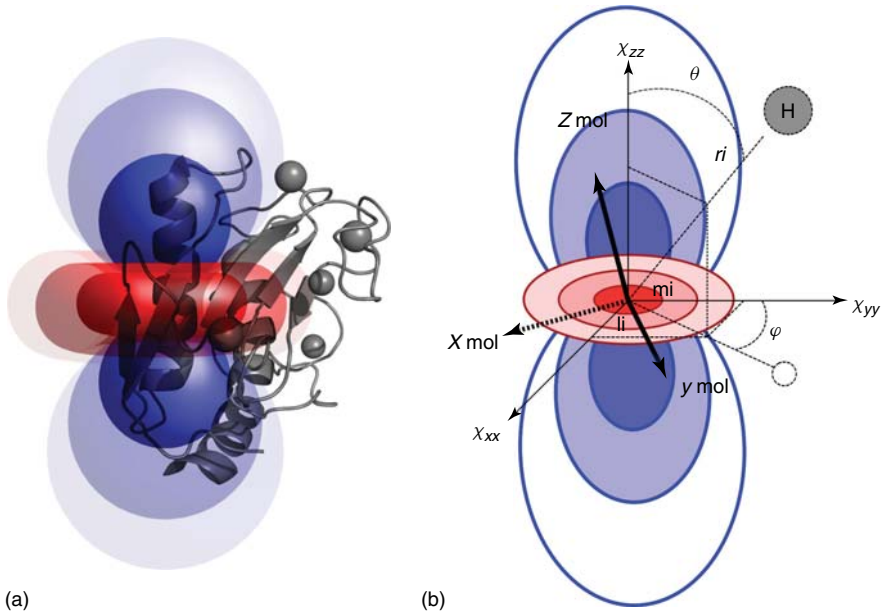


Figure 1 (a) Isosurfaces depicting the pseudocontact shifts (PCSs) induced by Yb^{3+} plotted on a ribbon representation of the calculated structure of the catalytic domain of the MMP-1 protein (pdb file 1SU3).[21] Blue and red surfaces identify the spatial locations of positive and negative PCSs, respectively, by ±3, ±1.5, and ±0.5 ppm. The PCS isosurfaces are a representation of the $\Delta\chi$ tensor. (b) Schematic representation of the PCS isosurfaces together with the χ tensor, illustrating the electron–nucleus distance r (the nuclear spin being exemplified by a ^{1}H) and the angles θ and φ (equation (1)) in the Cartesian axes that diagonalize the χ tensor. The molecular axes are also represented. (Images made using the free programs LibreOffice 3.4.4, www.libreoffice.org and PyMol, www.pymol.org)

and the Ln^{3+} ion at the origin (Figure 1), whereas $\Delta\chi_{ax}$ and $\Delta\chi_{rh}$ are the axial and the rhombic anisotropy parameters of the magnetic susceptibility tensor, respectively. The second term of equation (3) vanishes for the special case of axial symmetry ($\chi_{xx} = \chi_{yy}$). Equation (3) can, alternatively, be expressed in the laboratory frame using the five components of the magnetic susceptibility tensor.[22]

Bleaney has calculated PCSs with the assumption that the ligand field splittings for the lowest J state in the Ln^{3+} complexes are small compared to kT.[23] If the principal magnetic axes system is used, equation (3) can be written as equation (6) or (7),

$$\Delta_p = \frac{C_j \mu_B^2}{60k^2T^2}\left[\frac{A_2^0\langle r^2\rangle(3\cos^2\theta - 1)}{r^3} + \frac{A_2^2\langle r^2\rangle \sin^2\theta\cos 2\varphi}{r^3}\right] \quad (6)$$

$$\Delta_p = D_1\frac{3\cos^2\theta - 1}{r^3} + D_2\frac{\sin^2\theta\cos 2\varphi}{r^3} \quad (7)$$

where C_j is Bleaney's constant, characteristic of the Ln^{3+} ion, and $A_2^0 < r^2 >$ and $A_2^2 < r^2 >$ are ligand field coefficients of the second degree. A usual assumption is that the ligand field coefficients do not vary along the lanthanides for a series of isostructural complexes.

Alternative approaches have been presented using a more general field theory with all the J multiplets of the ground state serving as a basis.[7,15] This leads to deviations of the T^{-2} dependence of Δ_p (except for Eu^{3+} and Sm^{3+}). However, McGarvey has shown that equation (6) is adequate for estimating shifts to an accuracy of 10–20%.[7,15]

The constants D_1 and D_2 and the corresponding ligand field coefficients have been determined for several complexes, both on the basis of magnetic anisotropy measurements on single crystals and also independently of them, assuming that the solid-state structure persists in solution.[7,15] They have also been calculated from luminescence spectra, e.g., using the separation of the two emission bands observed in the $\Delta J = 1$ transition in a series of macrocyclic Eu^{3+} complexes.[24] The effects observed reflect the polarizability of the axial donor ligand in the complexes. The ligand field coefficient also determines the sign and the magnitude of the major CD band in a series of related enantiopure Yb^{3+} complexes.

For systems with an n-fold axis of symmetry ($n \geq 3$), the second term in equation (7) is zero. Frequently in structural analyses, only the first term of equation (7) is needed to calculate the LIS properly, even if the complex has no axial symmetry. Any n-fold rotational axis ($n \geq 3$) in the system may serve as an effective axial magnetic axis for the concerning part of the system, provided that for a particular nucleus, r and θ are equal for each of the rotamers and that the populations of the rotamers are equal.[7,15] Then, equation (7) reduces to

$$\Delta_p = C\frac{3\cos^2\theta - 1}{r^3} \quad (8)$$

$$C = \frac{1}{2}D_1(3\cos^2\alpha - 1) + \frac{1}{2}D_2\sin^2\alpha\cos 2\beta \quad (9)$$

In this situation of effective axial symmetry, the new proportionality constant C is related to D_1 and D_2 via equation (9), where α and β are the Euler angles that define the position of the effective axis with respect to the (old) principal magnetic susceptibility axis. It should be noted that equations (8) and (9) are valid as well when the rotation takes place via dissociation–association as long as the fast exchange conditions with respect to the NMR timescale are met, leading to a random variation of the axis of the susceptibility tensor of the complex.

3.4 Evaluation of Bound Shifts

The exchange of nuclei of the organic ligand between the bound and free state is commonly slow on the NMR timescale for highly polydentate complexes, thus the evaluation of the bound LIS values is straightforward for those cases. The observation of signals, particularly for complexes with Ln = Dy➔Tm is sometimes hampered by extreme line broadening, mainly because of exchange broadening and the effect of the Curie relaxation mechanism.[15] Measuring at low magnetic field strengths and at high temperatures may alleviate the latter problem. The assignment of the NMR signals may be difficult, particularly because they are usually shifted substantially from their diamagnetic positions and because of the possibility of multiple isomers. Longitudinal relaxation rates and 2D techniques, particularly correlation spectroscopy (COSY) and 2D exchange spectroscopy (EXSY),[14] are useful to obtain the assignments. Furthermore, plotting of the chemical shifts for various Ln^{3+} ions according to equations (12) and (13) may be helpful to establish the correlation of the signals among complexes for the various Ln^{3+} ions (see below). A computer program has been developed to analyze LIS data, including an assignment routine that permutes the LIS values over a number of selected nuclei until the best fit between calculated and observed LIS values is achieved.[25]

3.5 Separation of Shift Contributions

Diamagnetic shifts are usually small and can be determined directly from the corresponding diamagnetic complexes (La^{3+}, Lu^{3+}, or Y^{3+}) or by interpolation from the shifts induced by La^{3+} and Lu^{3+}. Subtraction of the diamagnetic contributions gives the paramagnetic shift Δ''. If the principal magnetic axis system is used as the coordinate system, a combination of equations (2) and (6) gives equations (10) and (11),

$$\Delta' = \Delta_c + \Delta_p = < S_z > F + C_j D \quad (10)$$

$$D = A_2^0 < r^2 > G_1 + A_2^2 < r^2 > G_2 \quad (11)$$

Table 1 Values of $< S_z >$, relative values of C_j at room temperature, longitudinal relaxation times (T_{1e}) in Ln^{3+} aquo complexes at 312 K and 2.1 T, and theoretical effective magnetic moments (μ_{eff}) of Ln^{3+} ions[7]

Ln	$< S_z >$	C_j	T_{1e} (10^{-13} s)	μ_{eff} (Bohr magneton)
Ce	−0.974	−6.3	0.9	2.56
Pr	−2.956	−11.0	0.57	3.62
Nd	−4.452	−4.2	1.15	3.68
Sm	0.224	−0.7	0.45	1.55–1.65
Eu	7.569	4.0	0.09	3.40–3.51
Gd	31.500	0	10^4–10^5	7.94
Tb	31.853	−86	2.03	9.7
Dy	28.565	−100	2.99	10.6
Ho	22.642	−39	1.94	10.6
Er	15.382	33	2.38	9.6
Tm	8.210	53	3.69	7.6
Yb	2.589	22	1.37	4.5

where G_1 and G_2 represent the first and second geometric terms in equation (7). It should be noted that $< S_z >$ and C_j are terms that are characteristic of the Ln^{3+} ion but independent of the ligand, whereas F and D are characteristic of the nucleus under study, but independent of the Ln^{3+} ion.

Very often, the various Ln^{3+} complexes of a particular ligand are isostructural and the crystal field coefficients are invariant along the Ln^{3+} series. Then, F and D can be determined by linear regression if the Δ' values of a ligand nucleus are known for two or more Ln^{3+} cations.[8,15,26] To test the assumption that the complex structures and the crystal field coefficients do not vary along the Ln^{3+} series, it is convenient to rewrite equation (11) in two linear forms:[8,15]

$$\frac{\Delta'}{< S_z >} = F + \frac{C_j}{< S_z >} D \tag{12}$$

$$\frac{\Delta'}{C_j} = \frac{< S_z >}{C_j} F + D \tag{13}$$

When these assumptions hold, the F and D values for the various ligand nuclei are independent of the Ln^{3+} cation and, consequently, plots according to equations (12) and (13) are straight lines. Since the ionic radii of the Ln^{3+} ions decrease steadily across the series, slight changes in the orientation of the ligands around the Ln^{3+} often occur, which is reflected in small changes of D only. The absolute values of C_j for the first part of the series (Ce → Eu) are much smaller (0.7–11, Table 1) than those of the second part (Tb → Yb) (22–100). Small changes of D are thus magnified by using equation (12), and breaks are frequently observed in plots according to this equation.[14] However, the F values are not affected by these slight structural changes, and plots according to equation (13) show no breaks in these cases. Nonlinearity of both the plots of the LIS values according to equations (12) and (13) indicates that either a significant structural change occurs across the Ln^{3+} series (i.e., a change of coordination mode of a ligand) or that the crystal field coefficients vary across the series, or an increased contribution to the nonaxial term to the measured LIS values occurs in a given part of the series. Typical examples of the different behaviors are shown in Figure 2.[15,27,28]

Discrimination between these two situations is possible for complexes with (effective) axially symmetric magnetic susceptibilities ($G_2 = 0$). Then it is possible to factor out the remaining crystal field coefficient. Several procedures to achieve this have been outlined in the literature.[8] For example, equation (14) can be derived,[30] where $\Delta_{i,j}$ and $\Delta_{k,j}$ denote the paramagnetic-induced shifts (after subtraction of the diamagnetic contributions) of two given ligand nuclei, i and k, by Ln^{3+} ion, j, where $R_{ik} = G_i/G_k$.

$$\frac{\Delta_{i,j}}{< S_z >_j} = (F_i - R_{ik}F_k) + \frac{R_{ik}\Delta_{k,j}}{< S_z >_j} \tag{14}$$

Accordingly, plots of $\Delta_{i,j}/< S_z >_j$ versus $\Delta_{k,j}/< S_z >_j$ should give straight lines for isostructural complexes. The slopes give the relative G values (R_{ik}), and the intercepts give the values of $(F_i - R_{ik}F_k)$. Structural variations along the lanthanide series can be easily detected by deviations from linearity of the slopes, whereas variations of the crystal field parameters that are not associated with structural changes have no effect. A similar approach can be applied to eliminate also $< S_z >$ from equations of this type, in cases where data for at least three nuclei in Ln^{3+} complexes of the same ligand are available.[31] The applicability of the various model-free methods in the structural analysis has been tested for a large series of sterically rigid ligands.[8]

Kemple *et al*. have included contact shifts as variable parameters in a fitting procedure of LIS values with the laboratory frame version of equation (3).[22] Forsberg *et al*. have further expanded this procedure and demonstrated its usefulness by a study on the solution structure of a 1,4,7,10-tetraazacyclododecane-N, N', N'', N'''-tetraacetic acid (DOTA) derivative.[25]

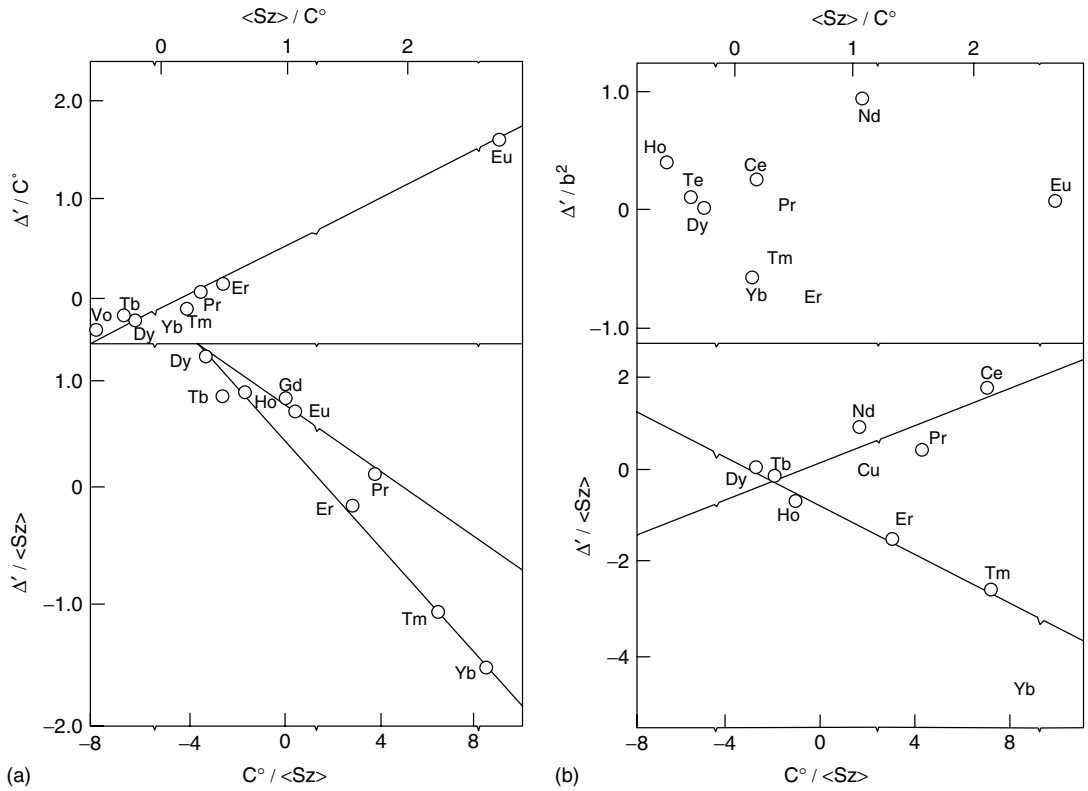


Figure 2 Plots of LIS data according to equations (13) and (14) for (a) the carboxylate carbons of L-proline[27] and (b) oxydiacetate[28], illustrating the typical effect of gradual structural changes and of a major structural change across the lanthanide series, respectively[15] (Reproduced from Ref. 15. © Elsevier, 1996.)

4 STRUCTURAL INFORMATION FROM LIS DATA

A large number of molecules has been studied, where the angular and distance information present in the LIS data after separation of the contact contribution, is combined with Gd^{3+}-induced relaxation (LIR) data. In fact, nuclear (e.g., ^{1}H, ^{13}C, ^{31}P) relaxation measurements on the substrates in the presence of Gd^{3+} provides additional information about the geometry of the complex since the paramagnetic relaxation rate at each nucleus, which is dominated by the dipolar contribution, is inversely proportional to the sixth power of the distance (r) between the metal ion and the nucleus. Thus, the relaxation ratios of nuclei i and j may be described by[6,7,15]

$$\frac{(T_{1p}^{-1})_i}{(T_{1p}^{-1})_j} = \frac{(r^6)_j}{(r^6)_i} \tag{15}$$

The combined geometrical information allows, in principle, the determination of the solution structure of any molecule that has a well-defined lanthanide-ion-binding site. Some of these studies in aqueous solution have been discussed briefly, referring to the literature for a more complete overview.[6–10]

4.1 Structure of Small Flexible Ligands

There is an enormous amount of early work on the use of LIS and LIR data from Ln^{3+} aqueous ions and complexes as structural probes of small flexible biological molecules, such as monosaccharides, nucleotides, aminoacids and peptides, phospholipid aggregates, vitamin B_{12}, Ca^{2+} ionophores, and so on.[15,32,33] These obtained structures are valid as long as the averaging effect of the ligand conformational equilibrium on the measured paramagnetic effects is taken into account by the simultaneous use of independent conformational information from other NMR parameters, such as vicinal coupling constants and nuclear Overhauser effects (NOEs).[32] The extensively used aqueous Ln^{3+} ions are limited to pH < 6.5, since the hydroxides precipitate at higher pH values. An optimal aqueous SR should be stable up to high pH values, and the LIS of the substrate ligands should be large and have (effective) axial symmetry.

Some examples with nucleotides, the most widely studied molecules in aqueous solution, are discussed here. 5′-AMP[34] and other 5′-, 3′- and cyclic mononucleotides[32,35] form 1 : 1 complexes with the Ln^{3+} ions at low pH, causing easily observable LIS values in fast chemical exchange on the NMR timescale due to bidentate binding to the phosphate

group. The measured ^{1}H shifts follow Bleaney's theoretical values, and the shift ratios are independent of the Ln^{3+} used, in agreement with the axial symmetry model. A computer search procedure located a closely related family of structures[34] that agrees with the LIS and LIR ratios. However, further experiments have shown that the geometries obtained from such measurements only do not necessarily agree with independent measurements of vicinal coupling constants and NOEs.[35] More elaborate computational procedures that adjust the molecular conformational equilibrium to agree with all these independent measurements have been developed.[32,35,36]

Several Ln^{3+} complexes of linear and macrocyclic (***Lanthanide Complexes with Multidentate Ligands***) aminocarboxylate ligands (Scheme 1) have been used as aqueous shift probes at high pH, such as the neutral Ln(NTA) and Ln(NOTA) complexes, and the negatively charged $[Ln(EDTA)]^-$ and $[Ln(DOTA)]^-$ complexes.[14,37,38] Of these complexes, all except Ln(NTA) are very stable in a wide pH range. The NOTA and DOTA complexes are axially symmetric, with a C_3 and C_4 symmetry axis, respectively. In most cases, the adducts of $[Ln(EDTA)]^-$ show effective axial symmetry, although the complexes themselves do not.[15] Cationic, anionic, and neutral substrates interact with these complexes, getting inserted in the first coordination sphere of the $[Ln(EDTA)]^-$ and Ln(NOTA) complexes, by replacing, at least partially, their inner-sphere water molecules, which change from three to two along the lanthanide series. They bind in the second coordination sphere of $[Ln(DOTA)]^-$, with a constant hydration number of one, with the advantage that the induced shifts are purely dipolar.[15]

The aqueous SR method, however, does suffer some limitations under certain experimental conditions, particularly when Ln^{3+} complexes rather than aqueous cations are used as probes. Besides exchange broadening or slow exchange, the shift ratios are not always constant along the lanthanide series, and as discussed above, the LIS data often show breaks near the center of the series when plotted according to equations (12) and/or (13). When breaks are present only in equation (12), this simply reflects small changes in Ln^{3+}–ligand bond distances resulting from the lanthanide ion contraction along the series magnified by large changes of the absolute values of C_j. When both plots are nonlinear, the formed adducts are not isostructural along the series (which may be tested experimentally by the variation of induced relaxation ratios according to equation (15)), the crystal field coefficients vary across the series, or nonaxial symmetry is present. Besides the examples shown in Figure 2, many others can be found in literature reviews.[6–8]

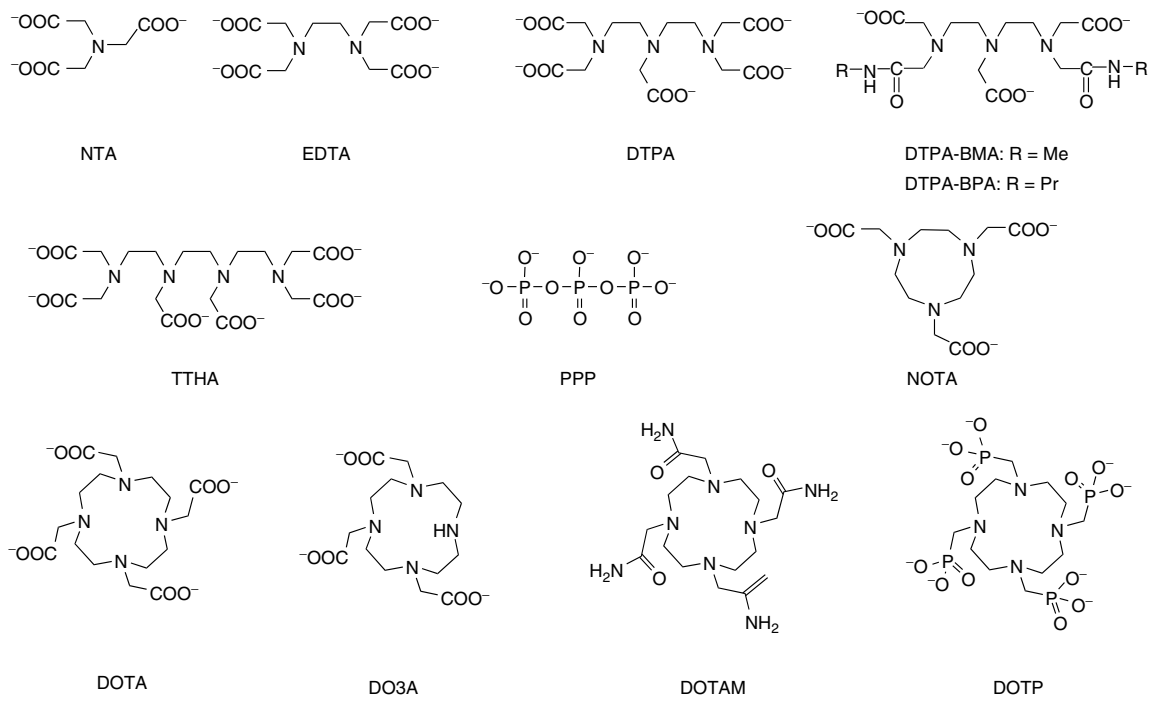
4.2 Structure of Ln(III) Complexes Useful as MRI and MRS Agents

The LIS solution structural method has been applied extensively to study the solution structures of fairly rigid linear and macrocyclic chelates useful as MRI contrast agents or as MRS SRs. A thorough description of this area can be found in literature reviews.[7,15] Only some typical examples of complexes of ligands whose structures are shown in Scheme 1 are discussed here. The information obtained from LIS and LIR data ranges from solution structures to isomer characterization and studies of their dynamic interconversion processes.

The structure and internal conformational equilibria of the Ln^{3+} complexes of DTPA and DTPA-PA_2 have been studied in detail. The dipolar Nd^{3+}-induced relaxation rate enhancements of ^{13}C ligand nuclei gave the metal–C distances in the complexes, showing that the metal is in both cases coordinated by the ligand in an octadentate fashion, to the three backbone nitrogens and five oxygens of the COO^- groups in DTPA, while in the DTPA-PA_2 complex, two bound oxygens come from the amide carbonyl oxygens. One water is also present in the first coordination sphere, as shown by ^{17}O NMR LIS measurements.[39,40] Evaluation of G values with the methods outlined above gave results consistent with those calculated from X-ray crystal structures.[15] Since the three N atoms of the diethylenetriamine backbone are bound to the Ln^{3+} ion, their inversion is inhibited. In the DTPA complexes, the central N atom is chiral because of the helicity of the central carboxylate relative to the backbone, leading to the presence of two isomers, in accordance with their NMR spectra, which show, at low temperature, two sets of resonances in slow exchange.[41] In the bis(amide) derivatives, the three N atoms are chiral, which results in eight possible forms of the complex (four diastereoisomeric pairs of enantiomers), all of which have been observed by ^{13}C NMR (Figure 3).[39] The dynamics of the interchange of the various isomers in these complexes have been studied by line-shape analysis[40] and by 2D EXSY.[41] The racemization process for the central backbone N atom is faster than that for the terminal ones, and does not require decoordination of the concerning N and its neighboring acetate groups, but rather a nondissociative interconversion (''wagging'') of the backbone ethylene groups between two gauche conformations.[40]

The $[Ln(DOTA)]^-$ complexes have been investigated in solution using analysis of LIS and LIR NMR data.[38,43–47] The ^{17}O water LIS values have shown that the hydration number is one along the lanthanide series. Two sets of resonances are observed in the ^{1}H and ^{13}C NMR spectra of the complexes at room temperature,[43] showing the presence of two isomeric species in slow exchange on the NMR timescale.[42,44–47] Figure 4 illustrates the proton spectra of some paramagnetic complexes, one isomer having larger induced shifts than the other.

The interpretation of the observed proton and ^{13}C PCS led to the conclusion that the two structural isomers are enantiomeric pairs of diastereoisomers differing in the octadentate ligand conformation, namely, capped square antiprismatic (SA or M) and twisted capped square antiprismatic (TSA or m) geometries, respectively (Figure 5).[15,42–47] The Ln^{3+} coordination polyhedral of SA and TSA have two opposite parallel faces occupied by the ligand ring nitrogen



Scheme 1 Chemical structure and abbreviated names of the ligands discussed in this chapter

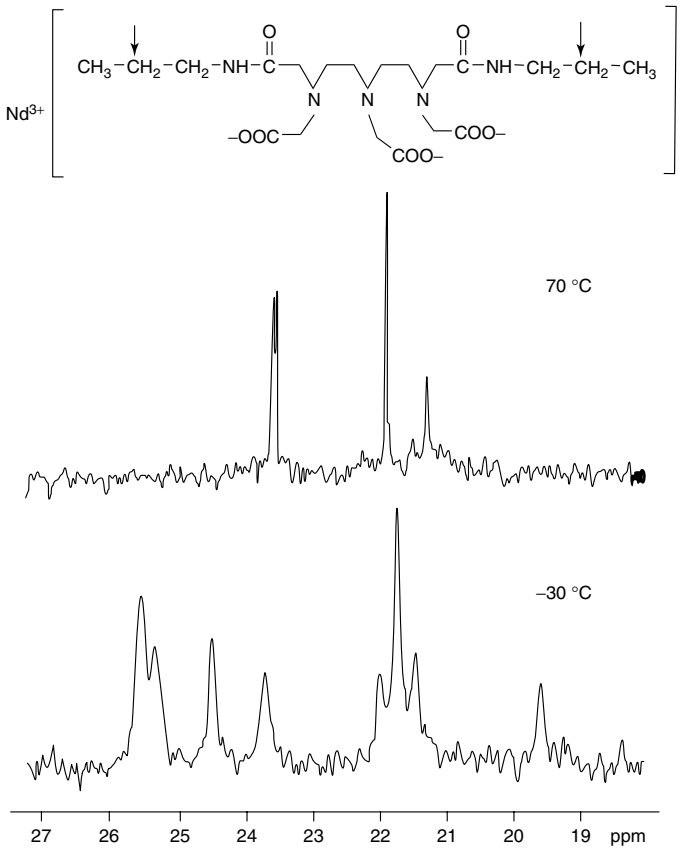


Figure 3 Influence of the temperature on the ^{13}C NMR resonances of the β-methylene carbons ($-N-CH_2-CH_2-CH_3$) of [Nd(DTPA-PA_2)] (100.6 MHz) in CD_3OD-D_2O (1 : 1, v/v); top 70 °C, bottom −30 °C[39] (Reproduced from Ref. 15. © Elsevier, 1996.)

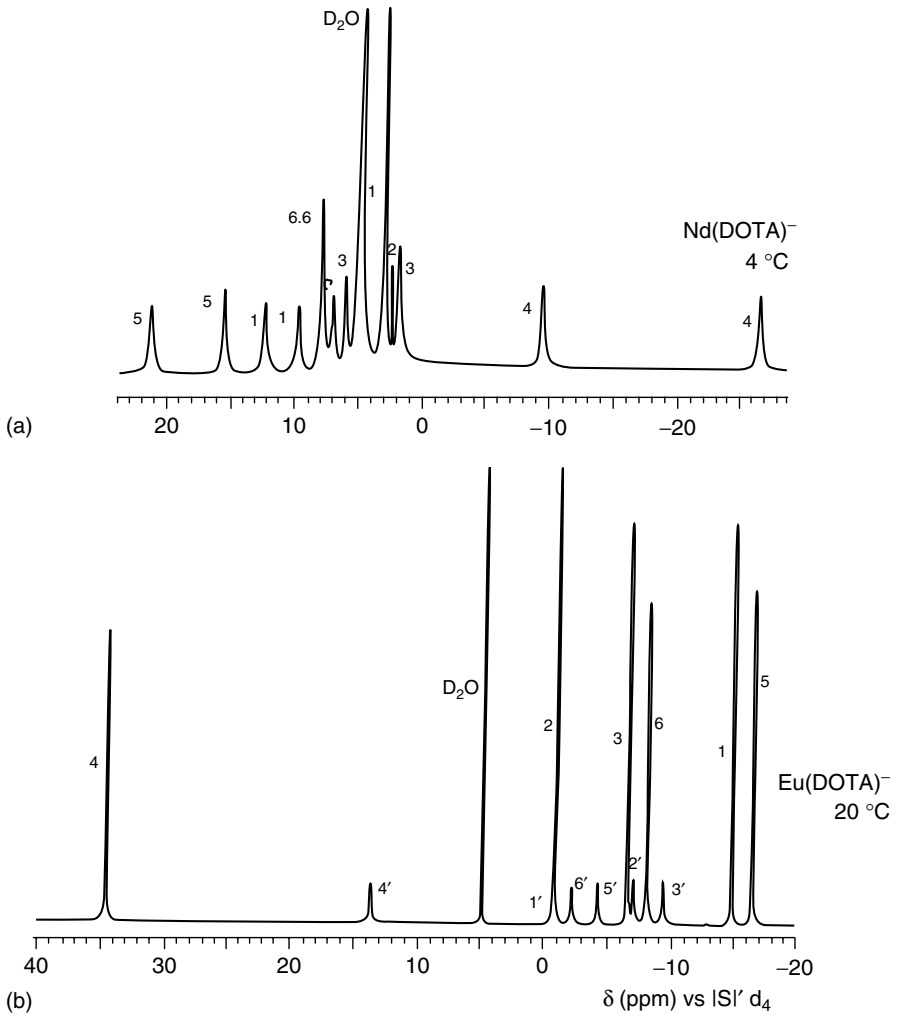


Figure 4 Proton NMR spectra of 10 mM $[Ln(DOTA)]^-$ complexes in D_2O, pH 7.0. (a) $[Nd(DOTA)]^-$ at 4 °C; (b) $[Eu(DOTA)]^-$ at 20 °C. The unprimed and primed numbers refer to the isomer with larger (M) and smaller (m) magnetic anisotropies, respectively[42] (Adapted from Ref. 42. © Elsevier, 1995.)

(N_4 plane) and acetate arm oxygen (O_4 plane) donors and the oxygen of a water molecule at the capping position. All ethylene groups of the 12-membered macrocyclic ring of the two isomers adopt an identical gauche conformation, either δ or λ,... leading to one of two possible square [3333] conformations of the ring, which interconvert through concerted exchange between the two gauche conformations of each of the ethylene bridges. The SA and TSA geometries result from the inverted layout of the acetate arms in both isomers, leading to the Δ and Λ helicities, which can be described by a twist angle between the N_4 and O_4 planes (θ) of ca. 40° for SA and of ca. −30° for TSA. The two stereochemical elements outlined above combine into two stereoisomeric pairs of enantiomers, $\Lambda(\delta\delta\delta\delta)/\Delta(\lambda\lambda\lambda\lambda)$, with opposite helicity of the ring and the arms, leading to the SA coordination, and $\Delta(\delta\delta\delta\delta)/\Lambda(\lambda\lambda\lambda\lambda)$, with the same ring and acetate helicity, giving the TSA structure. The ^1H and ^{13}C PCS-based SA and TSA structures are in agreement with the X-ray crystal structures observed for the complete series of $[Ln(DOTA)]^-$ complexes.[42,44,45] Since these structures have a C_4 symmetry axis, the axial symmetry model for the observed PCS could be applied (first term of equation (7)).

The dynamic interconversion processes of the two isomers have been studied by variable temperature 1D lineshape analysis and 2D exchange (EXSY) methods.[43,45–47] The temperature dependence of the ^1H and ^{13}C NMR spectra of both the dia- and paramagnetic Ln^{3+} complexes shows that the macrocyclic ring is very rigid. The dynamics of the complexes is summarized in Figure 5. The species can interconvert in solution by either ring inversion ($(\delta\delta\delta\delta) \rightleftharpoons (\lambda\lambda\lambda\lambda)$) or acetate arm rotation ($\dot{\Delta} \Leftrightarrow (\Lambda)$. Either process alone results in exchange between the SA and TSA geometries, or both processes combined, either in succession or concerted, result in an exchange between enantiomeric pairs.

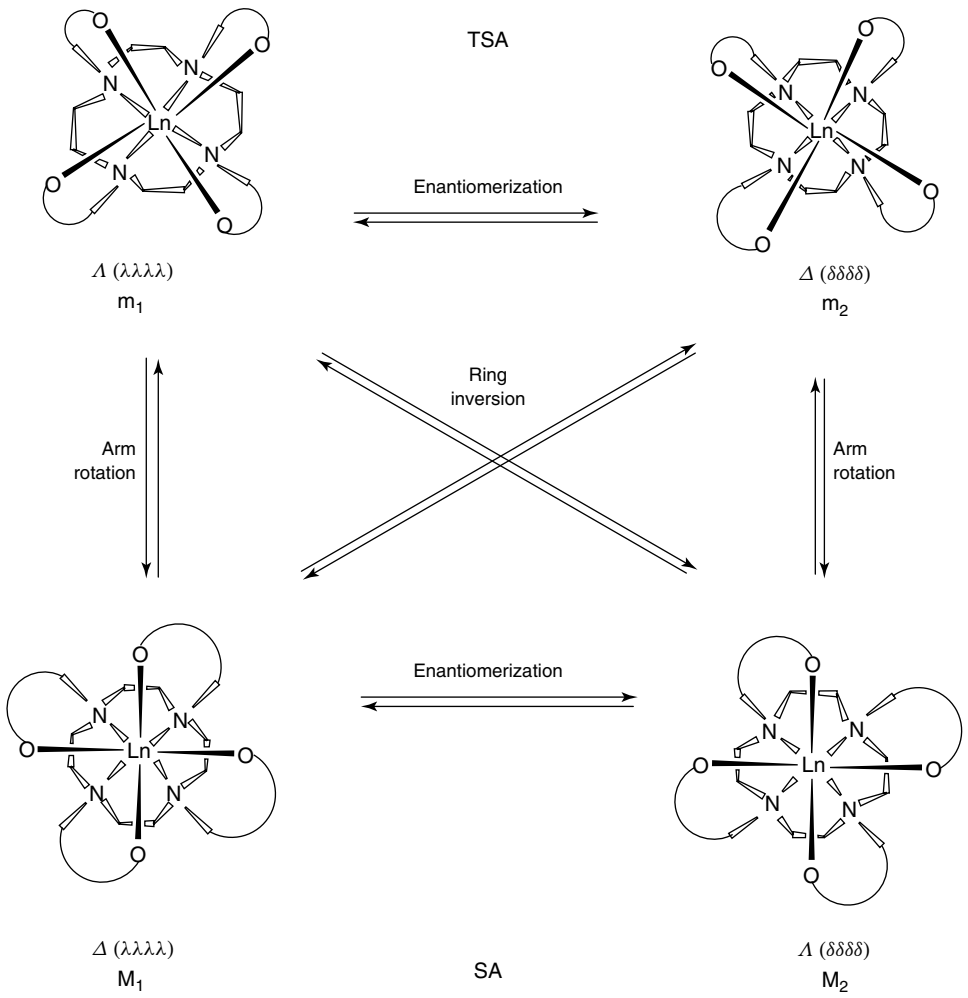


Figure 5 Schematic representation of the structure and dynamics of the diastereoisomers of the $[Ln(DOTA)]^-$ complexes. The symbols Λ and Δ refer to the helicity of the acetate arms, whereas $\lambda\lambda\lambda\lambda$ and $\delta\delta\delta\delta$ refer to the cycle. M_1 and M_2, as well as m_1 and m_2, are NMR indistinguishable enantiomeric pairs, respectively, for the M and m forms detected by NMR[47]

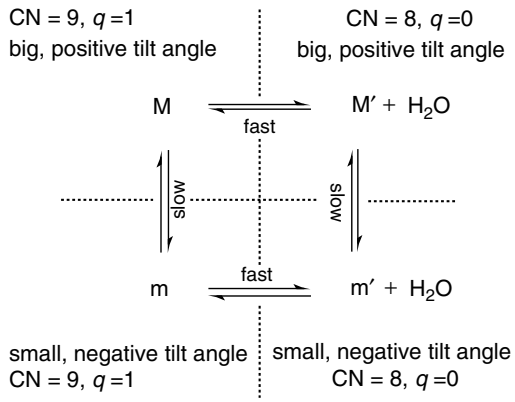


Figure 6 Conformational and coordination equilibria for the $[Ln(DOTA)(H_2O)_x]^-$ complexes in aqueous solution. Enantiomeric pairs are not represented [47] (Reproduced with permission from Ref. 47. Copyright (1997) American Chemical Society.)

The relative concentrations of the two species depend on the size of the Ln^{3+} ion, temperature, pressure, and concentration of added inorganic salts. While the TSA geometry is the ''major'' isomer for the complexes of the larger cations, La^{3+}–Nd^{3+}, the SA geometry becomes the most stable for the smaller cations Sm^{3+}–Er^{3+}. In all these cases, the isomerization process is purely conformational, as shown by the near-zero reaction volumes obtained by high-pressure NMR.[47] However, for the complexes of the smallest cations (Tm^{3+}–Lu^{3+}), the large positive isomerization volumes obtained show that the ''minor'' isomer results from a fast water dissociation process superimposed on the conformational rearrangement leading to an eight-coordinate TSA′ (or m′) geometry (Figure 6). The SA form can also lose one water molecule, but only in the case of the very small cation Sc^{3+} could the m′⇔ M′ equilibrium be detected.[47] The values of the reaction enthalpies and entropies were found to be concordant with this scheme.

The isomer possibilities in DOTA derivatives can increase dramatically. For example, introducing a chiral center by substitution at C_α of the acetate arms of DOTA can gives rise to six ligand isomers defined by the absolute configuration at the carbon: *RRRR* (*SSSS*), *RSSS* (*SRRR*), and the achiral diastereoisomers*RSRS* and*RRSS*. In the corresponding Ln^{3+} complexes, there are four possible stereoisomeric complexes for each ligand configuration, as the presence of at least one substituent at the chiral center makes the two pairs of enantiomers of LnDOTA no longer equivalent, and the four stereoisomers become diastereomers on chelation. However, the number of isomers actually occurring in solution is much lower. For example, it was found in many cases that a single acetate $C_{\alpha.}$ substituent on $[Ln(DOTA)]^-$ can sterically lock the conformation of the pendant arms, whereas their orientation is determined by the configuration at the C_α: an *R* configuration generates the Λ orientation, while an *S* configuration leads to a Δ orientation.[7,48–50] This determines the least sterically hindered helical form of the complex, which has the substituent equatorially positioned, pointing away from the coordination cage.

The solution TSA/SA composition of Ln^{3+} complexes can be simply studied by ^1H NMR, where the signature of these two isomers is easily seen since the macrocyclic H_4 proton has very different PCS values in the two isomers. For example, a comparison of the H_4 resonance areas in the SA (20–36 ppm) and TSA (5–12 ppm) isomers of Eu^{3+} complexes of DOTA derivatives[48–50] and substituted tetraamides[51] provides a direct readout of the isomer ratio present in solution. Such NMR studies with Eu^{3+} complexes bearing various kinds of substituents showed that increasing the steric bulk and hydrophobicity of the substituents increases the TSA isomer population. On the contrary, introduction of negative charges or increasing the polarity of the substituents increases the SA isomer population and slows down water exchange, a very important property to be used to optimize paramagnetic chemical exchange saturation transfer (PARACEST) contrast agents.[51]

The solution structure of the Ln^{3+} complexes of the tetraazamacrocyclic phosphonate ligand $DOTP^{8-}$, $Ln(DOTP)^{5-}$ (Scheme 1), as obtained by analysis of the ^1H, ^{13}C, and ^{31}P LIS and LIR values using the axial symmetry model and molecular mechaniscs (MM) calculations.[52] The solution structure of all the Ln^{3+} chelates of this series is of the eight-coordinate TSA′ (m′) type (with no inner-sphere water, as shown by ^{17}O Dy^{3+}-induced shifts), which was confirmed by the X-ray crystal structure of $Na_5Tm(DOTP)$.[53] The thermodynamics of $DOTP^{8-}$ complexation by the Ln^{3+} ions and of protonation of the complexes was studied in detail by potentiometry and ^{31}P NMR, showing that the chelates can monoprotonate the four phosphonate groups, with four pK_a values in the 7.9–4.4 range, forming protonated species of lower negative charge up to $Ln(DOTPH_4)^-$.[54]

The LIS data of some Ln^{3+} complexes with rhombic symmetry has also been analyzed quantitatively, yielding solution structures in agreement with X-ray crystal structures.[55,56]

4.3 Structure of Supramolecular Architectures Including Lanthanide Complexes

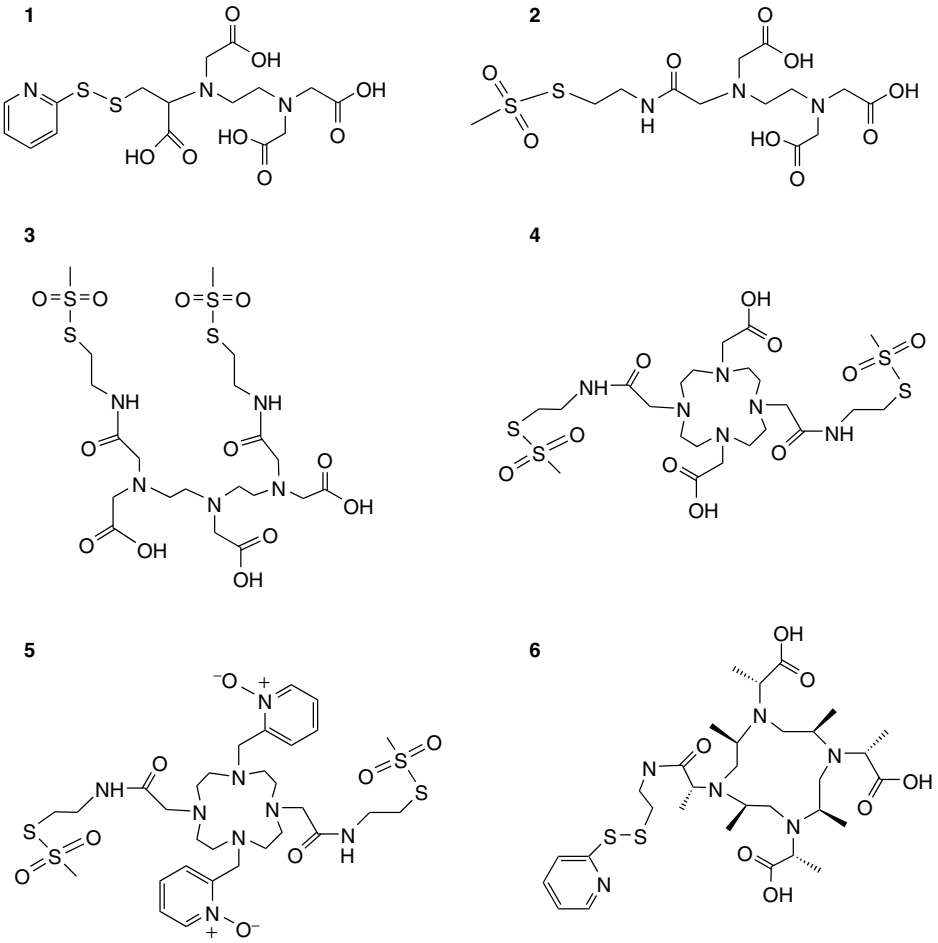
The paramagnetic NMR LIR and LIS of nuclei of small organic molecules induced by paramagnetic complexes such as $[Ln(DOTP)]^{5-}$ and $[Ln(DOTA)]^-$ can been used to obtain the structures of supramolecular complexes (***Supramolecular Chemistry: from Sensors and Imaging Agents to Functional Mononuclear and Polynuclear Self-Assembly Lanthanide Complexes***) resulting from their noncovalent interactions when those interactions are specific, thus not leading to extensive averaging between different structures. The strongest and most specific interactions have been found between the highly negatively charged $Ln(DOTP)^{5-}$ chelates and protonated linear and macrocyclic amines. For example, two $[Ln(DOTP)]^{5-}$ complexes are able to sandwich the diprotonated tetraazamacrocyclic amine cyclen, forming a 2 : 1 adduct.

The $[Ln(DOTP)]^{5-}$ complexes exist in solution as only one enantiomeric pair, $\Delta(\delta\delta\delta\delta)$ and $\Lambda(\lambda\lambda\lambda\lambda)$, corresponding to the TSA (m′) isomer. In this racemic mixture, the two enantiomers furnish indistinguishable NMR signals at room temperature using conventional NMR techniques. Chiral NMR resolution, using the formation of diastereomeric adducts between the two enantiomers of $Ln(DOTP)^{5-}$ and a chiral substrate, has provided indirect, and yet conclusive, evidence for the existence of these two enantiomers.[57,58] The ion-pair interactions between $Ln(DOTP)^{5-}$ complexes and the chiral organic base, *N*-methyl-D-(-)-glucamine (Meg), were investigated through the use of ^1H, ^{13}C, and ^{31}P NMR spectroscopy.[58] Addition of Meg to a solution of $[Eu(DOTP)]^{5-}$ lifted the signal degeneracy of the NMR spectra, resulting in doubling of the corresponding signals. Similar spectral resolution in the ^1H NMR spectrum of $[Eu(DOTP)]^{5-}$ was achieved by the addition of the chiral transition metal complex, $(+)\text{-}Co(en)_3^{3+}$.[57]

It was also found that $[Tm(DOTP)]^{5-}$ is capable of weak but specific hydrophobic interactions with γ-cyclodextrin (γ-CD), forming a 1 : 1 inclusion complex of well-defined structure, which was again obtained from analysis of ^1H LIS and LIR data (Figure 7).[59] In this supramolecular structure, the hydrophobic surface of $Tm(DOTP)^{5-}$ fits at the entrance of the hydrophobic basket on the top rim of γ-CD, with the negatively charged, strongly hydrated phosphonate groups in contact with the solvent. It was also shown that the interaction of the less negative $[Ln(DOTA)]^-$ complex with γ-CD is not as specific, involving also hydrogen bonding to the lower rim.[60]

4.4 Structure and Dynamics of Biomacromolecules

The use of Ln^{3+} ions as NMR extrinsic structural probes of biomacromolecules such as proteins and nucleic



Scheme 2 Structures of some paramagnetic Ln^{3+}-chelating tags for protein NMR: (**1, 2**) EDTA-based tags; 3,6-biscarboxymethyl-3,6-diaza-2-methyldithio-(2-pyridyl)octane-1,8-dicarboxylic acid (**1**); [*S*-methanethiosulfonylcysteaminyl]ethylenediaminetetraacetic acid (**2**);(**3**–**5**) Caged lanthanide NMR probes (CLaNPs): diethylenetriaminepentaacetic acid-*N*, *N*′′-bis(2-(acetylamino)ethylmethanesulfono thioate) (CLaNP-1, **3**); 1,4,7,10-tetraazacyclododecane-*N*, *N*′, *N*′′, *N*′′′-tetraacetic acid-1,7-bis(2-(acetyl amino)ethylmethanesulfonothioate) (CLaNP-3, **4**); 1,4,7,10-tetraazacyclododecane-1,7-[di-(*N*-oxido-pyridine-2-yl)methyl]-4,10-bis(2-(acetylamino)ethylmethanesulfonothioate) (CLaNP-5, **5**); methyldithio-(2-pyridyl)-(*R*)-2-[(2*S*, 5*S*, 8*S*, 11*S*)-4,7,10-tris-((*R*)-1-carboxyethyl)-2,5,8,11-tetramethyl-1,4,7,10-tetraaza cyclododecan-1-yl] propionic acid (DOTAM8, **6**) (adapted from Ref. 72). Structures drawn with free software BKChem, http://bkchem.zirael.org/)

acids has proved to be a versatile research tool, either through their specific binding to systems without metal ions or by isomorphic substitution of those naturally present in metalloproteins. The similarity of the ionic radii of the Ln^{3+} ions to Ca^{2+} (0.99 Å) led to many studies using Ln^{3+} as isomorphic replacements for Ca^{2+}, although only in few cases perfect isomorphic and functional replacement has actually been shown to occur.[9,10]

In spite of all these limitations, Ln^{3+} affords extensive applications as NMR probes of the structure of proteins.[10] The Ln^{3+} chelator now being the macromolecule itself, two new distinct features appear: the vast majority of the LIS values are pseudocontact (which simplifies the analysis of the PCS) and Curie relaxation becomes the dominant T_2 effect at high field because of the slow tumbling of the protein.[10] Many pioneering but meaningful experiments were performed before the introduction of high magnetic fields, and multidimensional techniques in NMR spectroscopy allowed the development and extensive use of quantitative structural methods for proteins based mainly in interproton distance constraints derived from NOE effects.[61] Thus, they relied on comparison of the experimental proton LIS and LIR data with those calculated on the basis of the protein crystal structure assuming axial symmetry for the LIS. This was the case for the first protein quantitative NMR structural study based on the LIS/LIR method performed by the Oxford Enzyme Group on lysozyme.[62,63] Although the agreement for many resonances was found to be excellent, indicating general accord between the crystal structure of lysozyme and the solution structure as determined by the LIS/LIR method, the assumption of axial symmetry of the LIS values was later found not to be

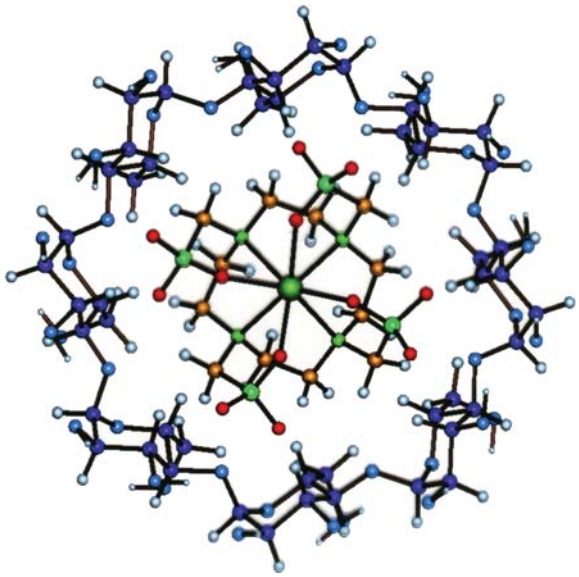


Figure 7 Top view of the structure of the $[Tm(DOTP)]^{5-}$ -γ-CD inclusion complex calculated from the analysis of Ln^{3+}-induced paramagnetic effects[59]

generally correct.[64] Therefore, the possibility of obtaining a more detailed structure of the protein from the paramagnetic data independently of the crystal structure was not warranted. Such an approach was employed by replacing Mg^{2+} by Ln^{3+} to use PCS and LIR data to map the active site geometry of phosphoglycerate kinase (PGK) using Ln-ATP as probes.[65] Isomorphic substitution by Yb^{3+} was also used to study the Ca^{2+}-binding protein parvalbumin.[66–68] ^1H NMR studies of the apoprotein in the presence of increasing amounts of Yb^{3+} showed sequential loading of the two Ca^{2+} EF and CD sites by Yb^{3+}, as shown by large PCS of proton resonances in a slow-exchange regime with the diamagnetic positions. The proton PCS and LIR induced by Yb^{3+} binding on several of the shifted signals were assigned on the basis of the known X-ray structure of the protein, after locating the orientation and the magnitude of the Yb^{3+} susceptibility tensor χ using the X-ray coordinates for five nuclei that had been assigned with certainty. With these parameters, LIS values for all other nuclei in the protein could be predicted.

The simultaneous availability of a reliable magnetic anisotropy tensor, and of an extensive assignment of both the diamagnetic and paramagnetic derivative of a metalloprotein, such as that achievable with 2D NMR techniques,[61] opened the way to the use of PCS as structural constraints in protein structure determination.[10] Besides the PCS, other effects related to the Ln^{3+} magnetic susceptibility and its anisotropy can be used as protein structural constraints. The CCR contribution to paramagnetic relaxation of a ^{15}N nucleus in a peptide bond $^1H-^{15}N$ pair, for example, arises from the rotational average of the cross-term between the ^{15}N Curie relaxation and its dipole–dipole (dd) relaxation with the attached ^1H, which can be positive or negative depending on the relative orientation of the $Ln-^{15}N$ and $^{15}N-^1H$ interaction vectors. CCR manifests itself as an additional broadening of one of the two J-split components of the ^{15}N doublet, and a corresponding sharpening of the other component by the same amount.[10] Another effect of the magnetic susceptibility anisotropy of the Ln^{3+} in the protein is its self-orientation in an external magnetic field B_0, which minimizes the magnetic interaction energy by orienting the axis of its largest susceptibility component along B_0.[10,69] Consequently, all internuclear dd interactions, such as in the $^{15}N-^1H$ pair, will no longer be averaged to zero as it happens in a nonoriented sample but reappear to a small extent depending on the Boltzmann distribution of all molecules over all the possible orientations. The recovered dipolar interactions cause additional small splittings on top of the scalar J splittings, e.g., on the ^{15}N doublet, and are called RDC. The value of the RDC increases with the susceptibility anisotropy of the Ln^{3+} bound to the protein (maximum for Tb^{3+} and Dy^{3+} if χ has axial symmetry)[10] and depends on the orientation of the internuclear (e.g., $^{15}N-^1H$) vector relative to the principal axes of the χ tensor.

The use of four types of paramagnetic constraints (PCS, RDC, CCR, and paramagnetic relaxation (R_{1p})) to refine the structure of a protein obtained using NOE constraints was tested systematically for Ln^{3+}-substituted calbindin D_{9k}.[70,71] Figure 8 illustrates the large improvement in the quality of the structure of the diamagnetic protein (global backbone RMSD of 0.69 Å) to the paramagnetic structure (global backbone RMSD of 0.25 Å), in particular in the resolution of two metal-binding loops and the linker region between the two EF-hands, as the first two regions lacked NOE information lost by the proximity of the paramagnetic Ln^{3+}. This type of approach has been explored for other protein systems.[10]

When an intrinsic diamagnetic metal substitution is not possible, a Ln^{3+}-binding motif, such as an EF hand or a

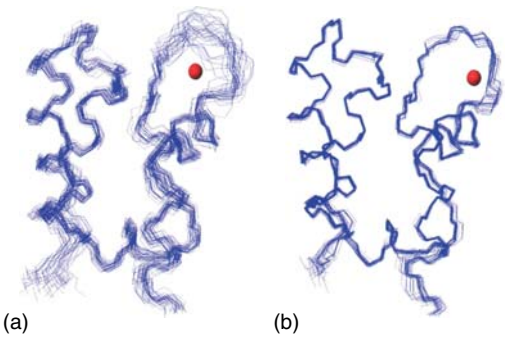


Figure 8 Family of 30 conformers of calbindin D_{9k} backbone obtained without (diamagnetic structure, root mean square deviation (RMSD) = 0.69 Å, (a)) and with (paramagnetic structure, RMSD = 0.25 Å, (b)) paramagnetism-based constraints[70] (Adapted from Ref. 70. © With kind permission from Springer Science + Business Media)

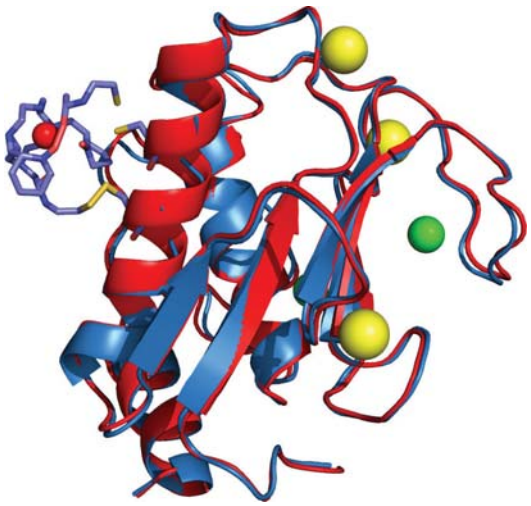


Figure 9 Comparison of the X-ray structure of Yb^{3+}-CLaNP-5-tagged catalytic domain of MMP-1 (blue) with the structure of the same tagged protein domain (red) obtained from refining the X-ray structure of the untagged protein domain (pdb code 3SHI) using the experimental PCS and RDC data obtained for the Ln^{3+}-CLaNP-5-tagged catalytic domain (Ln = Yb, Tm, and Tb)[21]

zinc finger, can be engineered by N- or C-terminal fusion into a given protein leading to weak self-orientation in B_0 of the Ln^{3+}-bound chimeric protein,[10,72–74] generating sizable RDCs but only small PCSs because of averaging of the $\Delta\chi$ tensor. Alternatively, paramagnetic probes or tags can be constructed for covalent attachment to the protein.[10,72–74] A number of paramagnetic Ln^{3+} chelating tags have been designed in the last years to be rigidly attached to proteins, leading to its effective orientation in B_0 and yielding substantial PCS and RDC values (Scheme 2). CLaNP-5 represents one of the last advances, showing no mobility due to binding at two close cysteinyl residues introduced by site-directed mutagenesis at a strategically chosen site on the protein surface.[72] It also has no multiple conformations, thus providing a single magnetic susceptibility tensor. The PCS and RDCs induced by this tag have been successfully used for protein structure refinement, protein dynamics, protein–ligand interactions, as well as structures and dynamics of protein complexes, such as the conformational heterogeneity of the complex formed by adrenodoxin reductase and its electron receiving partner adrenodoxin and by cytochrome *c* and adrenodoxin.[72] The same tag has also been used to demonstrate a method for validation and refinement of the structure of proteins in solution once a model, such as a crystallographic structure, is available, using the CLaNP-5-tagged catalytic domain of matrix metalloproteinase MMP-1 as example (Figure 9).[21]

Lanthanide chelates have also been used as shift and relaxation probes of protein surfaces by interacting noncovalently with surface residues organized in positive, negative, or hydrophobic patches. Analysis of the location of their binding sites is possible through observation of LIS and LIR NMR effects on specific proton resonances, which function as reporter groups.[10,75] The most efficient method involves observing those effects on the protein backbone using $^{1}H-^{15}N$ HSQC spectra of ^{15}N-labeled proteins. Neutral or low negatively charged complexes with one inner-sphere water, such as [Ln(DTPA-BMA)(H_2O)], [Ln(DTPA)(H_2O)]$^-$, or [Ln(DOTA)(H_2O)]$^-$, show no or very limited site specificity. However, the [Ln(DOTP)]$^{5-}$ chelates, with high negative charge, bind selectively at positively charged patches of ^{13}C-enriched methylated lysyl residues at the surface of the bacteriophage ss-DNA-binding gene 5 protein (G5P), which are those involved in the binding to ss-DNA, as shown by

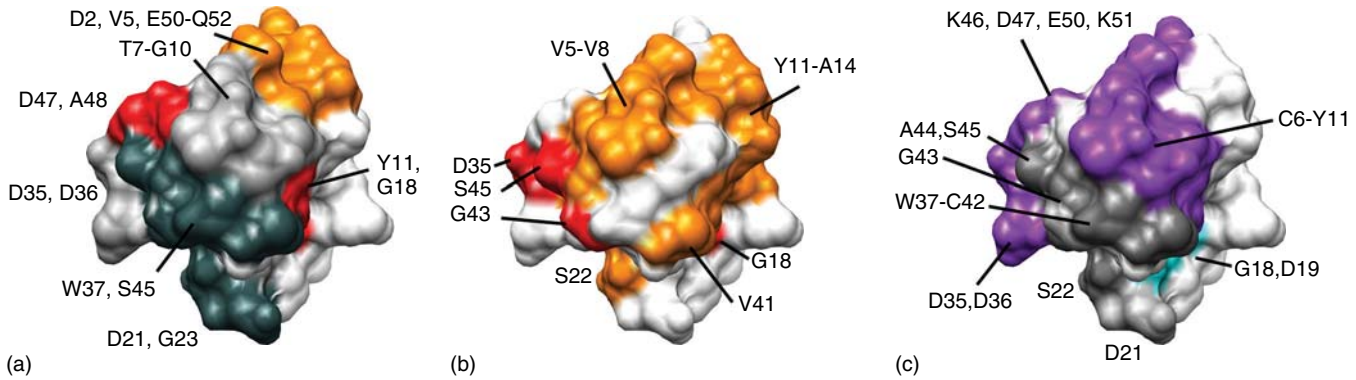


Figure 10 Mapping of the rubredoxin surface according to the volume ratio of the peaks of rubredoxin $^{15}N-^{1}H$ HSQC amide resonances, comparing the free rubredoxin with rubredoxin in the presence of (a) 2 mol equiv. of $[Gd(DOTAM)]^{3+}$: residues whose amide resonances have a decrease in volume ratio between 25% and 60% (orange), 60% and 90% (red), 90% and 100% (light gray), and 100% (dark gray); (b) 2 mol equiv. of cytochrome c_3: residues whose amide resonances have a decrease in volume ratio between 20% and 40% (orange) and 40% and 60% (red); and (c) 2 mol equiv. of $[Gd(DOTAM)]^{3+}$ and 2 mol equiv. of cytochrome c_3: residues whose amide resonances have a significant recovery in their volume ratio (violet), small recovery (light blue), 4% recovery (light gray), and no recovery (dark gray)[78] (Reproduced with permission from Ref. 78. Copyright (2011) American Chemical Society.)

competition experiments.[76] Also, the relaxation effects of $[Gd(DO3A)(H_2O)_2)]$, with two hydration water molecules, on the spectra of ^{15}N-labeled calbindin D_{9k} showed that the probe interacts specifically with carboxylate-rich negative surface regions of the protein.[77]

These probes can also be used to obtain specific information on protein–protein complex formation by binding to one partner and observing the effect of competition by the other.[10] A recent example is the use of $[Gd(DOTP)]^{5-}$ and $[Gd(DOTAM)]^{3+}$ to probe the interaction of *Desulfovibrio gigas* rubredoxin and *D. gigas* cytochrome c_3. While $[Gd(DOTP)]^{5-}$ binds to cytochrome c_3 near heme IV, causing pronounced LIRs, $[Gd(DOTAM)]^{3+}$ caused LIRs on a well-defined patch near the metal center of rubredoxin, which was partially reversed for some resonances when cytochrome c_3 was added (Figure 10).[78] This enabled a better definition of the binding site of the protein pair.

5 SHIFT REAGENTS FOR MRS OF ALKALI METAL IONS IN BIOLOGICAL SYSTEMS

Water-soluble SRs for discriminating intra- and extracellular cations were introduced in the earlier 1980s.[79,80] This is accomplished by designing a paramagnetic anionic SR chelate, which remains extracellular and binds to the ion of interest, thereby inducing an isotropic shift in those nuclei. The nuclei of interest in intracellular compartment(s) remain unshifted (except for BMS effects), as the exchange of cations between compartments is not fast enough to average their chemical shifts. This results in two resolved NMR signals, which may be monitored to examine ionic concentrations in each compartment. Most studies of this type have been concerned with alkali metal ion NMR (^{23}Na, ^{39}K, as well as ^{7}Li and ^{133}Cs) measurements, involving reports of transmembrane ion transport and compartmentation.[6,15,79,80] The SRs used are anionic lanthanide chelates that bind the alkali ions by forming ion pairs with coordinated or pendant negatively charged groups in the chelate at physiological pH. A large through space dipolar shift is produced if those ion-pairing sites are located in favorable geometric positions relative to the axis of the chelate susceptibility tensor.

Very poor SRs are those binding several cations exchanging among different locations, averaging out the dipolar shift geometrical function G, such as $[Dy(DTPA)]^{2-}$ (Figure 11)[40] or $[Dy(DOTA)]^{-}$.[38] The most efficient reagents, on the basis of the ability to shift the metal ion resonance per unit concentration, are $[Dy(PPP)_2]^{7-}$[79] and $[Tm(DOTP)]^{5-}$,[81] whose structures in solution (Figure 11) have been determined using multinuclear NMR shift and relaxation data.[52,83] The large ^{23}Na-induced LIS result from preferential metal ion binding near the main symmetry axis of the chelate (e.g., six Na^+ ions bind to $[Dy(PPP)_2]^{7-}$ and four to $[Tm(DOTP)]^{5-}$.

^{23}Na NMR studies with the $[Tm(DOTP)]^{5-}$ complex revealed two possible binding sites for the Na^+ countercations.[54,82] One strong ($\log K_1 = 2.58$) preferential Na^+ binding site A, observed at low $Na^+/[Tm(DOTP)]^{5-}$ ratios and under basic conditions, gave rise to an extremely large ^{23}Na LIS, indicating a binding position near the fourfold symmetry axis, where the dipolar term G is maximum. MM calculations generated a model where the Na^+ ion interacts with one inner Ln-bound O atom and an axial O atom of an adjacent phosphonate group (average $\theta = 26°$, $r = 3.7$ Å), leading to a very large fully bound $^{23}Na^+$ shift of 423 ppm. At high $Na^+/[Tm(DOTP)]^{5-}$ ratios or under acidic conditions, there is evidence for at least three weaker ($\log K_i \sim 1.5$) sites of a second type B, which impart significantly smaller bound shifts. The MM model associated the Na^+ ions with two unbound axial oxygens of adjacent phosphonate groups with less favorable geometric parameters (average $\theta = 34°$, $r = 4.5$ Å) and smaller fully bound shifts (162 ppm). The sign of the LIS for ^{23}Na in both cases is the same as with $[Ln(DOTA)]^{-}$ complexes, indicating that the two binding locations are located within the positive shift cone.

Figure 12 illustrates the excellent resolution of intra- and extracellular $^{23}Na^+$ resonances of human erythrocytes achieved with 3.5 mM $[Dy(PPP)_2]^{7-}$ or $[Dy(DOTP)]^{5-}$.[81] $[Tm(DOTP)]^{5-}$ is a better ^{23}Na SR than $[Dy(DOTP)]^{5-}$ because of the favorable sign of the BMS shift in the former case. The very large ^{23}Na shifts induced by $[Tm(DOTP)]^{5-}$ led to its successful application as SR for separation of NMR signal degeneracy normally observed for intra- and extracellular compartments since it is impermeable to cell membranes.

The use of SRs in tissues, organs, or live animals involves much more stringent conditions than in isolated cell systems. For example, $[Dy(PPP)_2]^{7-}$ is known to dissociate in the presence of tissue Ca^{2+} and degrades to Dy^{3+} and inorganic phosphate in tissues that contain active pyrophosphatases.[84] The use of $[Dy(TTHA)]^{3-}$ has been advocated[80] because of its high stability constant, biological stability, and lower sensitivity of the induced $^{23}Na^+$ shift to the presence of Ca^{2+} and pH between 5.5 and 12 than $[Dy(PPP)_2]^{7-}$. Unfortunately, its ability as an SR per unit concentration is about a factor of five less than that of $[Dy(PPP)_2]^{7-}$ and $[Tm(DOTP)]^{5-}$. This means that a much higher concentration (typically 10 mM) of $[Dy(TTHA)]^{3-}$ must be used to resolve the $^{23}Na^+$ resonances in different compartments, which cause much larger bulk susceptibility shift interferences. The observed shift is much smaller (and of opposite sign) in this complex, mainly because of its lower negative charge and the unfavorable spatial locations of the Na^+ binding sites (the free carboxylate group is outside the dipolar cone), relative to the main symmetry axis of the complex.

The presence of Ca^{2+} and Mg^{2+} in tissues may negatively affect the observed metal-induced shift. It was observed that the $[Tm(DOTP)]^{5-}$ ^{23}Na-induced shift is much less sensitive to the presence of those ions

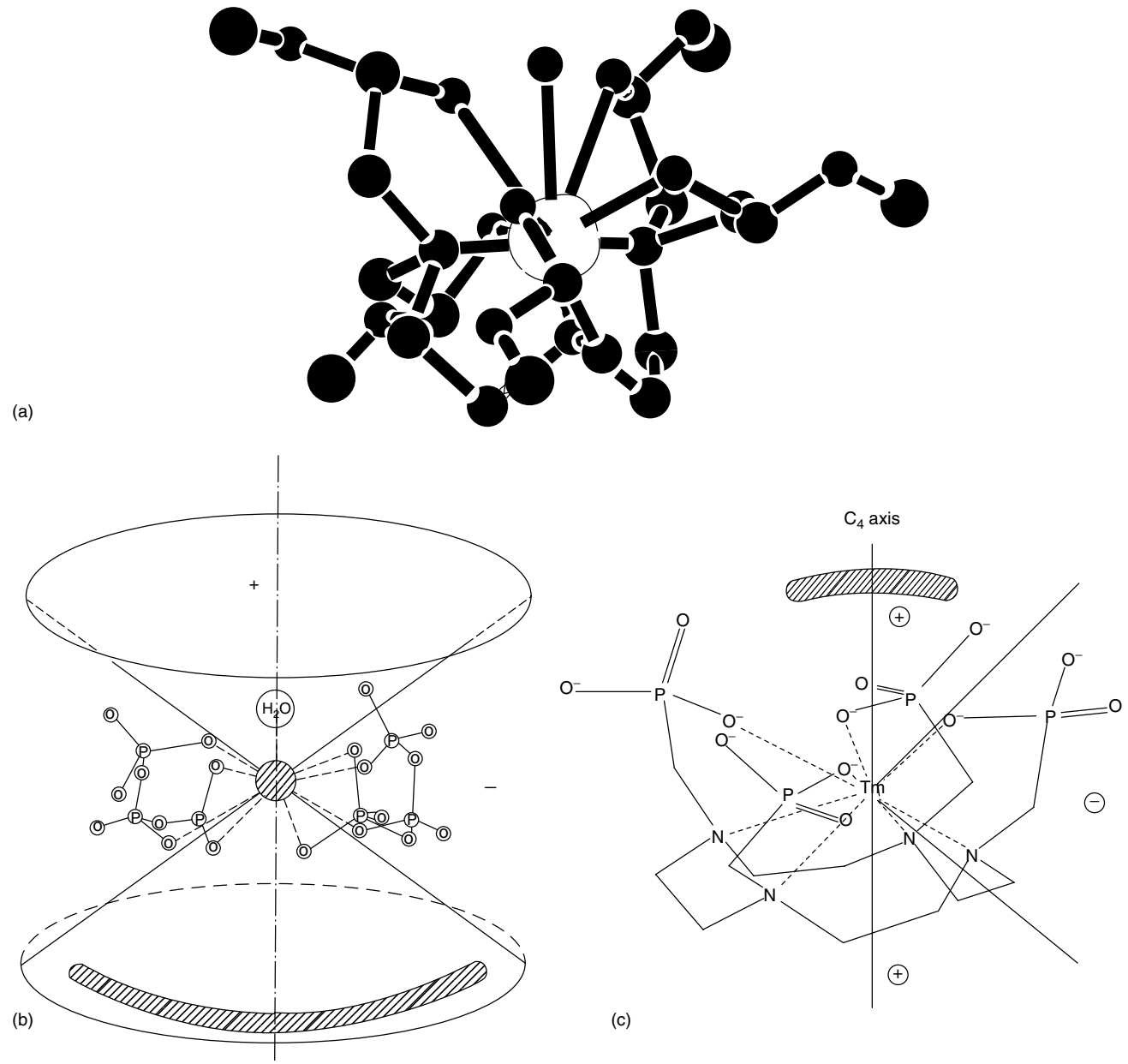


Figure 11 Structure of shift reagents for *in vivo* MRS of alkali metal ions and location of the binding sites for the counterions, obtained from LIS and LIR data: (a) $[Dy(DTPA)]^-$: 2 Li^+ ions exchanging between five sites,[40,41] (b) $[Dy(PPP)_2]^{7-}$ and average location of the six Na^+ sites,[81] (c) $[Tm(DOTP)]^{5-}$ and the average location of the four Na^+ sites[52,82]

than $[Dy(PPP)_2]^{7-}$.[54,82] This is because in $[Tm(DOTP)]^{5-}$, although site A also binds Ca^{2+} and Mg^{2+} with high affinity, leading to a marked decrease in the $^{23}Na^+$ shift as it is displaced from that site, the weaker sites B are only blocked by divalent ions when they fully occupy site A.

In summary, $[Tm(DOTP)]^{5-}$ is thermodynamically and kinetically very stable, is not degraded by phosphatases, produces isotropic $^{23}Na^+$ shifts comparable to those of $[Dy(PPP)_2]^{7-}$ and much lower bulk susceptibility shifts. The $^{23}Na^+$ shifts are also less sensitive to Ca^{2+} ions than for $[Dy(PPP)_2]^{7-}$. These properties make it an extremely effective SR for ^{23}Na NMR studies in perfused organs (e.g., hearts) or in *in vivo* spectroscopic studies in rat brain, liver, or kidney (Figure 13).[85,86]

Finally, cationic Ln^{3+} chelates can be devised, which act as SRs for *in vivo* NMR of anionic metabolites present in the blood or in cells, such as inorganic phosphate, carbonate, chloride, or lactate.

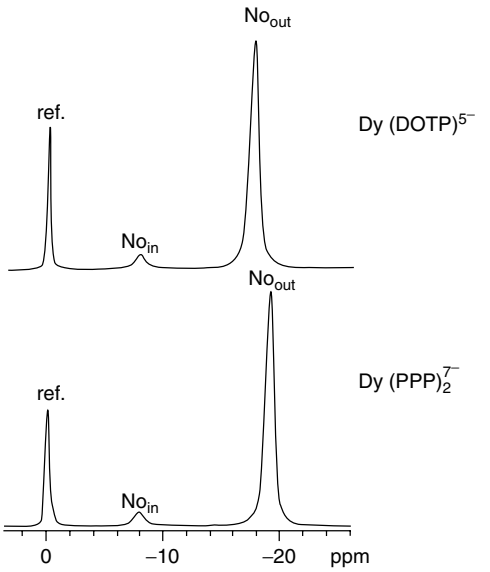


Figure 12 ^{23}Na NMR spectra of human erythrocytes in solution containing 3.6 mM $[Dy(PPP)_2]^{7-}$ or $[Dy(DOTP)]^{5-}$ and 150 mM NaCl. The reference signal comes from a capillary containing 100 mM NaCl and 50 mM $DyCl_3$[81] (Reproduced from Ref. 81. © Elsevier, 1988.)

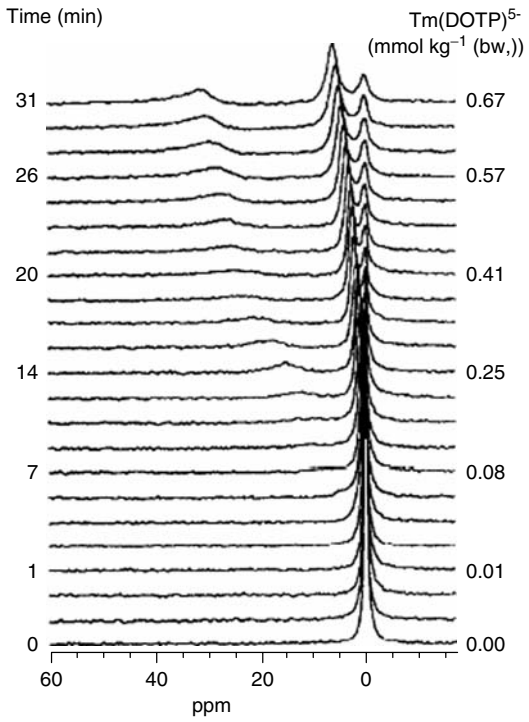


Figure 13 ^{23}Na NMR spectrum of an *in vivo* rat kidney during infusion of $[Tm(DOTP)]^{5-}$, illustrating the high chemical shift dispersion of the intra- and extracellular ^{23}Na resonances. The broad signal at 35 ppm in the top spectrum is from filtrate Na^+[85] (Reproduced with permission from Ref. 85. © John Wiley and Sons, Ltd.)

6 CONCLUSIONS

The examples presented in this chapter illustrate the main uses of the paramagnetic shift (and relaxation) effects of Ln^{3+} on the NMR parameters in Chemistry, Biosciences, and Medicine. The last years witnessed a tremendous resurgence of the interest for these Ln^{3+}-induced effects. Their highly informative power allows to compare the crystal and solution structures of MRI contrast agents and proteins, to refine protein structures and dynamic features in solution obtained by classical NOE-based NMR methodologies, and even to study protein−protein and protein−ligand interactions. Some of this solution information is not directly available in the solid state. In the future, new methodologies should be developed to tackle difficult problems. In the field of Structural Biology, these include challenges such as (i) the use of paramagnetic restraints for the study of protein conformational heterogeneity, in particular in multidomain proteins and in protein complexes; (ii) the use of ^{13}C direct detection in liquid- and solid-state NMR, which provides structural restraints close to the paramagnetic metal center; (iii) exploiting paramagnetic restraints in solid-state NMR for protein structure calculation; and (iv) the synergistic use of solution and MAS solid-state NMR for the study of large systems.[87] The applications of *in vivo* MRS SRs for common metabolites could also be pursued in order to study metabolic compartmentation.

7 GLOSSARY

Correlation spectroscopy (COSY): two-dimensional NMR technique where cross-peaks result from magnetization transfer through scalar couplings between nuclei

Cross correlation (CCR): contribution to the paramagnetic relaxation of a nucleus arising from the rotational average of the cross-term between the Curie relaxation of that nucleus and its dipole-dipole relaxation with another nucleus (eg. in a ^{15}N−^{1}H pair)

Exchange spectroscopy (EXSY): two-dimensional NMR technique where cross-peaks result from magnetization transfer through chemical exchange between nuclei

Relaxivity: relaxation rate enhancement per mM concentration of paramagnetic species

Residual dipolar coupling (RDC): partial average of a dipolar interaction between two nuclei in a molecule with anisotropic rotational diffusion resulting from its partial orientation in a magnetic field

8 ACKNOWLEDGEMENTS

The author acknowledges financial support for his research work by Fundação para a Ciência e Tecnologia (FCT), Portugal. He also thanks the insight, collaboration, and discussion of many researchers using lanthanide-based NMR probes, with whom he interacted throughout the years, in particular to R.J.P. Williams (Oxford University), A. Dean Sherry (University of Texas at Dallas), Joop Peters (T.U. Delft), André Merbach (EPFL, Lausanne), Erno Brücher (University of Debrecen), Duarte Mota Freitas (Loyola University of Chicago), Ravichandran Ramasamy (Columbia University), Robert Muller (University of Mons), Claudio Luchinat (CERM, University of Florence), Éva Tóth (CBM, CNRS Orleans), Lothar Helm (EPFL, Lausanne) Claude Piguet (University of Geneva), David Parker (University of Durham), Ivan Lukeš (Charles University of Prague), Petr Herrman (Charles University of Prague), and Carlos Platas-Iglesias (University of La Coruña). Finally he thanks Dr. Joop Peters (T.U. Delft) and João Teixeira (University of Coimbra) for help in the preparation of some of the figures of this chapter.

9 RELATED ARTICLES

Lanthanide Complexes with Multidentate Ligands; Supramolecular Chemistry: from Sensors and Imaging Agents to Functional Mononuclear and Polynuclear Self-Assembly Lanthanide Complexes.

10 ABBREVIATIONS AND ACRONYMS

5′-AMP = adenosine5′-mononucleotide; BMS = bulk magnetic susceptibility; CCR = cross-correlation; CLaNP-5 = caged lanthanide NMR probe 5 = 1, 4, 7, 10-tetraazacyclododecane-1,7-[di-(*N*-oxido-pyridine-2-yl) methyl]-4,10-bis(2-(acetylamino)ethylmethanesulfonothioate); COSY = correlation spectroscopy; γ-CD = γ-cyclodextrin; DO3A = 1, 4, 7, 10-tetraazacyclododecane-*N*, *N*′, *N*″-triacetic acid; DOTA = 1, 4, 7, 10-tetraazacyclododecane-*N*, *N*′, *N*″, *N*‴-tetraacetic acid; DOTAM = 1, 4, 7, 10-tetraazacyclodo decane-*N*, *N*′, *N*″, *N*‴-tetraamide; DOTP = 1, 4, 7, 10-tetra azacyclododecane-*N*, *N*′, *N*″, *N*′-tetramethylenephosphonic acid; DTPA = diethylenetriaminetetraacetic acid; DTPA-BMA = DTPA bis(methylamide); DTPA-PA_2 = DTPA bis(propylamide); EDTA = ethylenediaminetetraacetic acid; G5P = gene 5 protein; LIR = lanthanide-induced relaxation; LIS = lanthanide-induced shift; MRS = magnetic resonance spectroscopy; MRI = magnetic resonance imaging; NMR = nuclear magnetic resonance; NTA = nitrilotriacetic acid; NOE = nuclear Overhauser effect; NOTA = 1, 4, 7-triazacyclononane-*N*, *N*′, *N*″-triacetic acid; PARACEST = paramagnetic chemical exchange saturation transfer; PCS = pseudocontact shift; PGK = phosphoglycerate kinase; RDC = residual dipolar coupling; RMSD = root mean square deviation; TPP = tripolyphosphate; TTHA = triethylenetetraaminehexaacetic acid.

11 REFERENCES

1. C. C. Hinckley, *J. Am. Chem. Soc.*, 1969, **91**, 5160.
2. G. N. La Mar, W. DeW. Horrocks, and R. Holm, eds, 'NMR of Paramagnetic Molecules', Academic Press, New York, 1973.
3. T. C. Morrill, ed., 'Lanthanide Shift Reagents in Stereochemical Analysis', VCH Publ., New York, 1986.
4. T. J. Wenzel, 'NMR Shift Reagents', CRC Press, Boca Raton, 1987.
5. D. Parker, *Chem. Rev.*, 1991, **91**, 1441.
6. A. D. Sherry and C. F. G. C. Geraldes, in 'Lanthanide Probes in Life, Chemical and Earth Sciences', eds. J. C. G. Bünzli and G. R. Choppin, Elsevier, Amsterdam, 1989, p. 93.
7. J. A. Peters, E. Zitha-Bovens, D. Corsi, and C. F. G. C. Geraldes, in 'The Chemistry of Contrast Agents in Medical Magnetic Resonance Imaging', eds. A. E. Merbach and É. Tóth, John Wiley & Sons, Chichester, 2001, p. 315.
8. C. Piguet and C. F. G. C. Geraldes, in 'Handbook of Physics and Chemistry of the Rare Earths', eds. K. A. Gschneider, Jr., J.-C. Bünzli, and V. K. Pecharsky, Elsevier Science Publishers B.V., Amsterdam, 2003, Vol. 33, Chap. 215, p. 353.
9. C. F. G. C. Geraldes, *Methods Enzymol.*, 1993, **227**, 43.
10. C. F. G. C. Geraldes and C. Luchinat, in 'Metal Ions in Biological Systems', eds. H. Sigel and A. Sigel, Marcel Dekker, Inc. and FontisMedia S.A., New York, 2003, Vol. 40, Chap. 14, p. 513.
11. P. Caravan, J. J. Ellison, T. J. McMurry, and R. B. Lauffer, *Chem. Rev.*, 1999, **99**, 2293.
12. R. D. Shannon, *Acta Crystallogr. Sect. A*, 1976, **32**, 751.
13. I. Bertini, C. Luchinat, and G. Parigi, *Prog. Nucl. Magn. Reson. Spectrosc.*, 2002, **40**, 249.
14. I. Bertini and C. Luchinat, *Coord. Chem. Rev.*, 1996, **150**, 1.
15. J. A. Peters, J. Huskens, and D. J. Raber, *Prog. Nucl. Magn. Reson. Spectrosc.*, 1996, **28**, 283.
16. W. B. Lewis, J. A. Jackson, J. F. Lemons, and H. Taube, *J. Chem. Phys.*, 1962, **36**, 694.
17. J. Reuben and D. Fiat, *Chem. Commun.*, 1967, 729.
18. M. C. Alpoim, A. M. Urbano, C. F. G. C. Geraldes, and J. A. Peters, *J. Chem. Soc., Dalton Trans.*, 1992, 463.
19. K. Djanashvili and J. A. Peters, *Contrast Media Mol. Imaging*, 2007, **2**, 67.

20. R. J. Kurland and B. R. McGarvey, *J. Magn. Reson.*, 1970, **2**, 286.
21. I. Bertini, V. Calderone, L. Cerofolini, M. Fragai, C. F. G. C. Geraldes, P. Hermann, C. Luchinat, G. Parigi, and J. M. C. Teixeira, *FEBS Lett.*, 2012, **586**, 557.
22. M. D. Kemple, B. D. Ray, K. B. Lipkowitz, F. G. Prendergast, and B. D. N. Rao, *J. Am. Chem. Soc.*, 1988, **110**, 8275.
23. B. Bleaney, *J. Magn. Reson.*, 1972, **8**, 91.
24. R. S. Dickins, S. Aime, A. S. Batsanov, A. Beeby, M. Botta, J. I. Bruce, J. A. K. Howard, C. S. Love, D. Parker, R. D. Peacock, and H. Puschmann, *J. Am. Chem. Soc.*, 2002, **124**, 12697.
25. J. H. Forsberg, R. M. Delaney, Q. Zhao, G. Harakas, and R. Chandran, *Inorg. Chem.*, 1995, **34**, 3705.
26. C. N. Reilley, B. W. Good, and R. D. Allendoerfer, *Anal. Chem.*, 1976, **48**, 1446.
27. M. Singh, J. J. Reynolds, and A. D. Sherry, *J. Am.Chem. Soc.*, 1983, **105**, 4172.
28. J. A. Peters, *J. Chem. Soc., Dalton Trans.*, 1988, 961.
29. S. C. K. Chu, Y. Xu, J. A. Balschi, and C. S. Springer, *Magn. Reson. Med.*, 1990, **13**, 239.
30. C. Platas, F. Avecilla, A. de Blas, C. F. G. C. Geraldes, T. Rodríguez-Blas, H. Adams, and J. Mahía, *Inorg. Chem.*, 1999, **38**, 3190.
31. C. F. G. C. Geraldes, S. Zang, C. Platas, T. Rodríguez-Blas, A. de Blas, and A. D. Sherry, *J. Alloys. Compd.*, 2001, **323–324**, 824.
32. F. Inagaki and T. Miyazawa, *Prog. Nucl. Magn. Reson. Spectrosc.*, 1981, **14**, 67.
33. H. B. Silber and S. J. Paquette, in 'Metal Ions in Biological Systems', eds. H. Sigel and A. Sigel, Marcel Dekker, Inc. and FontisMedia S.A., New York, 2003, Vol. 40, Chap. 3, p. 69.
34. C. D. Barry, A. C. T. North, J. A. Glasel, R. J. P. Williams, and A. V. Xavier, *Nature*, 1971, **232**, 236.
35. C. M. Dobson, C. F. G. C. Geraldes, G. Rattcliffe, and R. J. P. Williams, *Eur. J. Biochem.*, 1978, **88**, 259.
36. B. Birdsall, N. J. Birdsall, J. Feeney, and J. Thornton, *J. Am. Chem. Soc.*, 1975, **97**, 2845.
37. C. M. Dobson, R. J. P. Williams, and A. V. Xavier, *J. Chem.Soc., Dalton Trans.*, 1974, 1762.
38. C. C. Bryden, C. N. Reilley, and J. F. Desreux, *Anal. Chem.*, 1981, **53**, 1418.
39. C. F. G. C. Geraldes, A. M. Urbano, M. A. Hoefnagel, and J. A. Peters, *Inorg. Chem.*, 1993, **32**, 2426.
40. J. A. Peters, *Inorg. Chem.*, 1988, **27**, 4686.
41. B. G. Jenkins and R. B. Lauffer, *Inorg. Chem.*, 1988, **27**, 4730.
42. M. P. M. Marques, C. F. G. C. Geraldes, A. D. Sherry, A. E. Merbach, H. Powell, D. Pubanz, S. Aime, and M. Botta, *J. Alloys Compd.*, 1995, **225**, 303.
43. J. F. Desreux, *Inorg. Chem.*, 1980, **19**, 1319.
44. M.-R. Spirlet, J. Rebizant, J. F. Desreux, M. F. Loncin, *Inorg. Chem.*, 1984, **23**, 359.
45. S. Aime, M. Botta, and G. Ermondi, *Inorg. Chem.*, 1992, **31**, 4291.
46. V. Jacques and J. F. Desreux, *Inorg. Chem.*, 1994, **33**, 4048.
47. S. Aime, M. Botta, M. Fasano, M. P. M. Marques, C. F. G. C. Geraldes, D. Pubanz, and A. E. Merbach, *Inorg. Chem.*, 1997, **36**, 2059.
48. M. Woods, S. Aime, M. Botta, J. A. K. Howard, A. M. Kenwright, J. M. Moloney, M. Navet, D. Parker, M. Port, and O. Rousseau, *J. Am. Chem. Soc.*, 2000, **122**, 9781.
49. J. P. André, E. Brücher, R. Király, R. A. Carvalho, H. Mäcke, and C. F. G. C. Geraldes, *Helv. Chim. Acta*, 2005, **88**, 633.
50. S. Aime, M. Botta, G. Ermondi, E. Terreno, P. L. Anneli, F. Fedeli, F. Uggeri, *Inorg. Chem.*, 1996, **35**, 2726.
51. T. Mani, G. Tircsó, P. Zhao, A. D. Sherry, and M. Woods, *Inorg. Chem.*, 2009, **48**, 10338.
52. C. F. G. C. Geraldes, A. D. Sherry, and G. E. Kiefer, *J. Magn. Reson.*, 1992, **97**, 290.
53. F. Avecilla, J. A. Peters, and C. F. G. C. Geraldes, *Eur. J. Inorg. Chem.*, 2003, 4179.
54. A. D. Sherry, J. Ren, J. Huskens, E. Brücher, É. Tóth, C. F. G. C. Geraldes, M. M. C. A. Castro, and W. P. Cacheris, *Inorg. Chem.*, 1996, **35**, 4604.
55. L. Valencia, J. Martinez, A. Macías, R. Bastida, R. A. Carvalho, and C. F. G. C. Geraldes, *Inorg. Chem.*, 2002, **41**, 5300.
56. M. P. C. Campello, S. Lacerda, I. C. Santos, G. A. Pereira, C. F. G. C. Geraldes, J. Kotek, P. Hermann, J. Vaník, P. Lubal, V. Kubíek, É. Tóth, I. Santos, *Chem. Eur. J.*, 2010, **28**, 8446.
57. J. Ren, C. S. Springer, and A. D. Sherry, *Inorg. Chem.*, 1997, **36**, 3493.
58. S. Aime, M. Botta, S. G. Crich, E. Terreno, P. L. Anelli, and F. Uggeri, *Chem. Eur. J.*, 1999, **5**, 1261.
59. A. D. Sherry, R. Zarzycki, and C. F. G. C. Geraldes, *Magn. Reson. Chem.*, 1994, **32**, 361.
60. E. Zitha-Bovens, H. van Bekkum, J. A. Peters, and C. F. G. C. Geraldes, *Eur. J. Inorg. Chem.*, 1999, 287.
61. M. P. Williamson, T. F. Havel, and K. Wüthrich, *J. Mol. Biol.*, 1985, **185**, 295.
62. I. D. Campbell, C. M. Dobson, R. J. P. Williams, and A. X. Xavier, *Ann. N.Y. Acad. Sci.*, 1973, **222**, 163.
63. I. D. Campbell, C. M. Dobson, and R. J. P. Williams, *J. Magn. Reson.*, 1973, **11**, 172.
64. D. G. Agresti, R. E. Lenkinski, and J. D. Glickson, *Biochem. Biophys. Res. Commun.*, 1977, **76**, 711.
65. P. Tanswell, E. Westhead, and R. J. P. Willimas, *Eur. J. Biochem.*, 1976, **63**, 249.
66. L. Lee and B. D. Sykes, *Biochemistry*, 1980, **19**, 3208.
67. L. Lee and B. D. Sykes, *Biochemistry*, 1981, **20**, 1156.
68. L. Lee and B. D. Sykes, *Biochemistry*, 1983, **22**, 4366.
69. I. Bertini, C. Luchinat, and M. Piccioli, *Meth. Enzymol.*, 2001, **339**, 314.

70. I. Bertini, A. Donaire, B. Jiménez, C. Luchinat, G. Parigi, M. Piccioli, and L. Poggi, *J. Biomol. NMR*, 2001, **21**, 85.

71. I. Bertini, M. B. L. Janik, G. Liu, C. Luchinat, and A. Rosato, *J. Magn. Reson.*, 2001, **148**, 23.

72. P. H. J. Keizers, M. Ubbink, *Prog. Nucl. Magn. Reson. Spectrosc.*, 2011, **58**, 88.

73. G. Pintacuda, M. John, X. C. Su, and G. Otting, *Acc. Chem. Res.*, 2007, **40**, 206.

74. J. Koehler and J. Meiler, *Prog. Nucl. Magn. Reson. Spectrosc.*, 2011, **59**, 360.

75. C. O. Arean, G. R. Moore, G. Williams, and R. J. P. Williams, *Eur. J. Biochem.*, 1988, **173**, 607.

76. C. R. Dick, C. F. G. C. Geraldes, A. D. Sherry, C. W. Gray, and D. M. Gray, *Biochemistry*, 1989, **28**, 7896.

77. S. Aime, N. D'Amelio, M. Fragai, Y.-M. Lee, C. Luchinat, E. Terreno, and G. Valensin, *J. Biol. Inorg. Chem.*, 2002, **7**, 617.

78. R. M. Almeida, C. F. G. C. Geraldes, S. R. Pauleta, and J. J. G. Moura, *Inorg. Chem.* 2011, **50**, 10600.

79. R. K. Gupta and P. Gupta, *J. Magn. Reson.*, 1982, **47**, 344.

80. M. M. Pike and C. S. Springer, *J. Magn. Reson.*, 1982 **46**,, 348.

81. A. D. Sherry, C. R. Malloy, F. M. H. Jeffrey, W. P. Cacheris, and C. F. G. C. Geraldes, *J. Magn. Reson.*, 1988, **76**, 528.

82. J. Ren and A. D. Sherry, *Inorg. Chim. Acta*, 1996, **246**, 331.

83. R. Ramasamy, D. M. Freitas, C. F. G. C. Geraldes, and J. A. Peters, *Inorg. Chem.*, 1991, **30**, 3188.

84. N. A. Matwiyoff, C. Gasparovic, R. Wenk, J. D. Wicks, and A. Rath, *Magn. Reson. Med.*, 1986, **3**, 164.

85. V. Seshan, M. J. Germann, P. Preisig, C. R. Malloy, A. D. Sherry, and N. Bansal, *Magn. Reson. Med.*, 1995, **34**, 25.

86. D. C. Buster, M. M. C. A. Castro, C. F. G. C. Geraldes, C. R. Malloy, A. D. Sherry, and T. Siemers, *Magn. Reson. Med.*, 1990, **15**, 25.

87. I. Bertini, C. Luchinat, and G. Parigi, *Coord. Chem. Rev.*, 2011, **255**, 649.

Lanthanides: Magnetic Resonance Imaging

Sophie Laurent, Luce Vander Elst, Sebastien Boutry and Robert N. Muller

University of Mons, Mons, Belgium

1	Summary	521
2	Introduction	521
3	Contrast Mechanism in MRI	522
4	MRI Contrast Agents	524
5	Relaxation Mechanisms	527
6	Examples of MRI Applications	530
7	Conclusions	533
8	Glossary	533
9	Acknowledgements	534
10	Related Articles	534
11	Abbreviations and Acronyms	534
12	References	534

1 SUMMARY

Magnetic resonance imaging (MRI) represents an important development in diagnostics. MRI is based on the NMR signal generated by hydrogen nuclei present in water and its changes that are dependent on the environment. The use of a contrast agent (CA) in MRI is aimed at improving the diagnostic accuracy of clinical studies by providing images that contain physiological information along with exquisitely high anatomical detail. Paramagnetic ions, such as gadolinium(III) complexes (see ***Lanthanides: Luminescence Applications***), reduce the longitudinal relaxation time and increase the T_1 signal intensity, giving a positive contrast. The first CAs developed were nonspecific agents or extracellular fluid space agents. Research is now focused on the development of new classes of CAs with improved properties, such as smart CAs, target-selective CAs, and macromolecular CAs. Target-selective CAs are gadolinium complexes that are delivered in a selective way to cells or tissues of interest thanks to bioactive molecules such as peptides and antibodies; in this approach, specific receptors or membrane proteins overexpressed by cells are the molecular targets where the gadolinium complexes derivatized with peptides or antibodies are intended to accumulate. Our team has developed some CAs based on Gd-DTPA complexes for molecular imaging, for example, to target apoptosis in atherosclerotic plaques (Gd-DTPA-R826), inflammation (Gd-DTPA-B(SleX)A), or $\alpha_v\beta_3$ integrin expression (Gd-DTPA-mRGD).

2 INTRODUCTION

MRI has gained considerable importance among diagnostic modalities. MRI is a noninvasive method based on the nuclear magnetic resonance (NMR) phenomenon, which relies on the specific magnetic properties of some nuclei in atoms (spin) and their capability of absorption and emission of radiofrequency waves in a strong magnetic field. The first MR image was published in 1973, and the first MRI scan of a human body was done in 1977. Paul Lauterbur and Peter Mansfield were awarded a Noble Prize in 2003 for their major contributions to the invention of MRI. MRI has many advantages over other diagnostic techniques such as X-ray and computed tomographic (CT) scanning, both of which involve the use of ionizing radiation. MRI, on the other hand, uses a harmless magnetic field and electromagnetic radiation and is therefore referred to as a noninvasive technique.

The principle of this technique is based on the repeated application of magnetic field gradients in three directions of space, as well as of radiofrequency waves (excitation pulses). Magnetic field gradients are applied in

The Rare Earth Elements. Edited by David A. Atwood. © 2012 John Wiley & Sons, Ltd. ISBN 978-1-119-95097-4

addition to the main magnetic field B_0. Gradients perform the following three main tasks in encoding the spatial information: (i) slice selection, (ii) frequency encoding, and (iii) phase encoding. The image results from the spatial identification of analyzed nuclei and consists of picture elements (pixels), where the gray levels represent the intensity of the signal corresponding to the volume element (voxel). The frequency of the excitation pulse depends on the observed nuclei and on the B_0 field strength. Because of its abundance in each living organism, proton (the ^{1}H nucleus) is the most studied nucleus in MRI (excitation pulse: 42.58 MHz T^{-1}). Since the signal depends on the proton concentration relaxation times T_1 (the longitudinal or spin lattice relaxation time) and T_2 (the transverse or spin–spin relaxation time), the intensity modulations of the image can be observed, mainly by adjusting the cadence at which excitation pulses are generated (repetition time, TR) and the time interval before collecting the resulting NMR signal (echo time, TE)

In order to reach an accurate medical diagnosis, CAs are used to facilitate the distinction between normal and diseased tissues. Their role is to change the nuclear relaxation time. These substances, generally Gd-complexes, (see ***Organometallic Chemistry Fundamental Properties***, ***Lanthanides: Coordination Chemistry***, ***Lanthanide Complexes with Multidentate Ligands***) must be nontoxic, biocompatible, and efficient at low doses. The choice of instrumental parameters, such as the sequence used, can also play a role on the contrast. The intensities of the MRI images are dependent on the proton relaxation of water molecules. This relaxation process depends on the environment of water molecules and varies between tissues. The contrast can be modulated essentially by two factors governing proton relaxation: the T_1 effect or longitudinal relaxation, which increases the signal strength,[1,2] and the T_2 effect or transverse relaxation, which reduces the signal intensity.[3] The images are T_1- or T_2-weighted depending on the predominant relaxation.[4]

3 CONTRAST MECHANISM IN MRI

3.1 T_1-Weighted Contrast

The repetition time TR (time interval between two successive excitation pulses) is a key parameter responsible for T_1 contrast during a pulse sequence. For T_1 contrast, a pulse sequence with short TR is selected together with a short TE (to minimize T_2-related contrast effects). Tissues with relatively short T_1 relax quickly and thus exhibit a large signal intensity after the application of excitation pulses with short TR. On the other hand, tissues with a long T_1 undergo only little relaxation between two excitation pulses and thus yield a low (saturated) signal intensity. In the mouse head T_1-weighted MR image illustrated in Figure 1, fat (blue arrow) has a shorter T_1 because it has a relatively slow tumbling rate and thus will appear with stronger signal intensity, while tissues (e.g., brain tissue (white arrow)) that have a relatively longer T_1 (due to a relatively fast tumbling rate) will appear with lower signal intensity. As aqueous fluids have long relaxation times, cerebrospinal fluid (CSF) will not be distinguishable from brain tissue also because of a signal saturation phenomenon.[5]

3.2 T_2-Weighted Contrast

The effect of T_2 on the image contrast is closely related to the echo time TE (the time interval between excitation pulse and signal collection). To create T_2 contrast in MR images, a long TE is used in pulse sequences, together with a long TR (to minimize T_1-related contrast effects). The tissues with relatively shorter T_2 will undergo most of their relaxation process before signal collection occurs and will thus yield low signal intensity, while tissues with relatively longer T_2 will exhibit high signal intensity. In the mouse head T_2-weighted MR image shown in Figure 2, compared to the brain (white arrow), muscles (red arrow) appear with lower signal intensity, as their T_2 is shorter than that of brain. Furthermore, CSF (yellow arrow) appears with high signal intensity in such long TE MRI sequences. As its relaxation is very slow, its signal can be collected relatively long after the excitation pulse. One can notice that fat also has a long T_2 and appears as a hypersignal (blue arrow).[5]

3.3 Proton Density Images

In proton density images, acquisition parameters are selected in the range $TE \ll T_2$ and $TR \gg T_1$ so that they do not significantly affect the image contrast and thus it primarily depends on proton density. Because of the short TE, no or little T_2 contrast will be created between brain, CSF, and muscle because neither these tissues nor fluid will have the time to significantly relax before signal collection. Differences in terms of T_2 signals between soft tissues and ''aqueous'' regions will thus not have the time to take place. Because of the long TR, the influence of T_1 contrast will also be very limited on the image. Indeed, apart from differences in relaxation times in different tissues, the difference in the number of protons per unit volume in different tissues will also create contrast in the MRI images. In the mouse head MR image shown in Figure 3, as proton density weighting dominates, the CSF–tissue contrast and the contrast between tissues are attenuated regarding T_2-weighting because of a short TE. Tissues globally exhibit a higher gray level than in T_1-weighting thanks to less signal saturation phenomenon. Fat is relatively bright since it has a higher proportion of MRI-visible protons than muscle. However, its proton density is the same as that for muscle.[6]

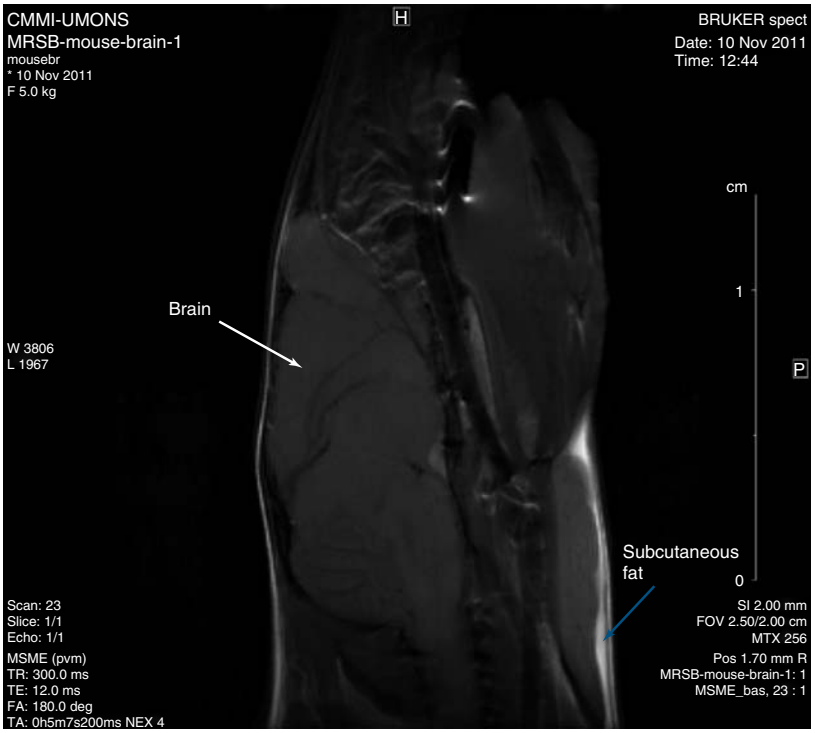


Figure 1 T_1-weighted MR image (spin-echo pulse sequence at $B_0 = 9.4$ T, TR = 300 ms, TE = 12 ms) of a mouse head showing contrast between fat (blue arrow) and tissue (brain: white arrow)



Figure 2 T_2-weighted MR image (spin-echo pulse sequence at $B_0 = 9.4$ T, TR = 2000 ms, TE = 48 ms) of a mouse head showing contrast between tissues (red arrow: muscle, white arrow: brain) and cerebrospinal fluid (yellow arrow); subcutaneous fat is pointed by a blue arrow

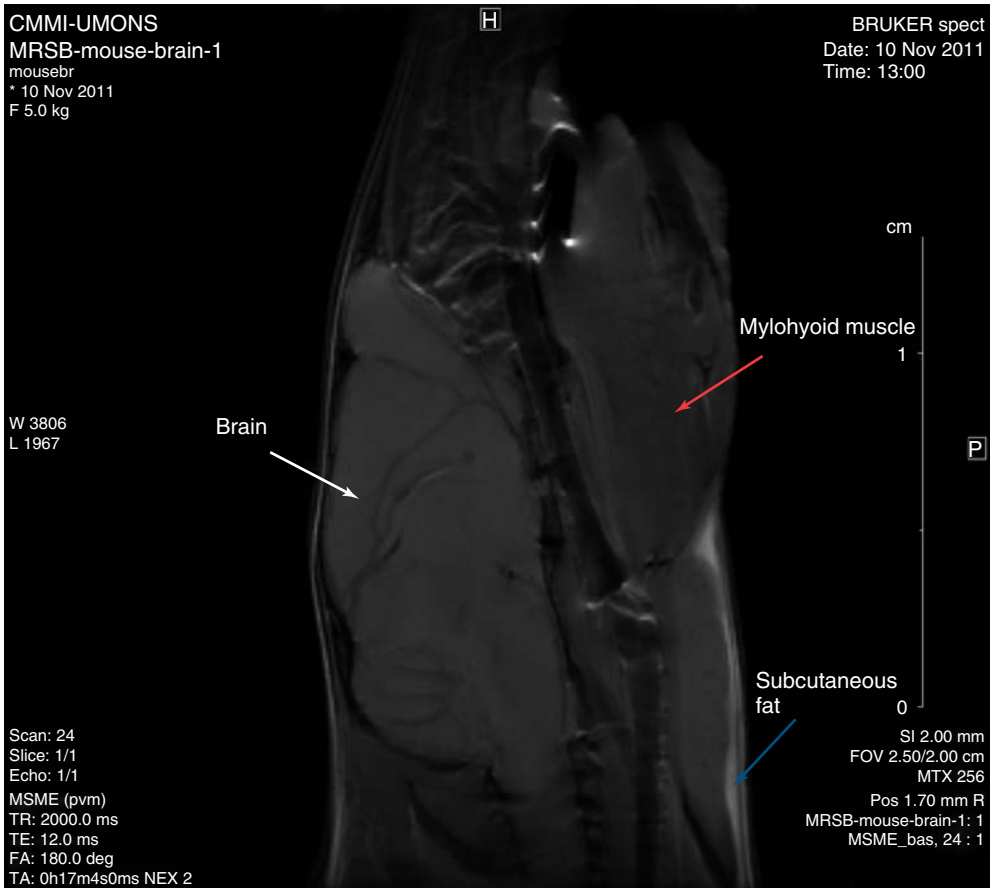


Figure 3 Proton density-weighted MR image (spin-echo pulse sequence at $B_0 = 9.4$ T, TR = 2000 ms, TE = 12 ms) of a mouse head showing MRI-visible protons in tissues (red arrow: muscle, white arrow: brain); subcutaneous fat is pointed by a blue arrow

3.4 Chemical Shift Imaging

In conventional MRI, various hydrogen atoms in the body are not differentiated depending on their chemical environment, which, however, induces a very small shift (in the hecto- or kilohertz order) of the frequency (in the megahertz order) that is absorbed and subsequently emitted by protons in MR. For instance, water protons actually undergo a frequency shift that is different from that of protons bound to aliphatic carbon chains (such as methylene protons in lipids or tissues). This phenomenon, called *chemical shift*, (see ***Lanthanide Shift Reagents***) is the basis of MR spectroscopy, which was discovered more than two decades before MRI and allows for fine determination of the chemical or molecular composition of samples made of NMR active nuclei (not only ^{1}H but also ^{13}C, ^{31}P, ^{17}O). MR spectroscopic imaging allows for a multivoxel mapping of spectra thanks to the use of phase-encoding gradients. This technique thus adds a spatial dimension to the spectral identification of NMR active molecules and is called *chemical shift imaging* (CSI).[7] Mainly based on ^{1}H (but not exclusively), CSI can be complementary to MRI in diagnostic studies but should not be subsequent to Gd-enhanced MRI, as spectra are perturbed by the CA.[8]

4 MRI CONTRAST AGENTS

On an MR image, the natural contrast in soft tissues depends on endogenous differences in water (proton) content, relaxation times, and diffusion characteristics of the visualized tissues. It can be improved by optimizing the parameters of the image acquisition sequences. However, when inherent contrast cannot be changed in this way, CAs are used with the aim of increasing the sensitivity of the method and helping to answer diagnostic questions. These CAs shorten the relaxation times of hydrogen nuclei situated in their neighborhood, so that the contrast between the nuclei influenced by the CA and those not influenced is increased. CAs are also useful to obtain better tissue characterization, to reduce image artifacts, and even to get functional information on the observed living system (blood perfusion, vascular permeability).

The essential property of CAs is their ''relaxivity'', which is defined as the increase in the relaxation rate of water protons achieved by 1 mmol l^{-1} of magnetic center. These substances act as true catalysts on relaxation; they decrease the relaxation times and can reduce therefore the time for

image acquisition: more signal can be accumulated, which increases the quality and the image contrast.

Negative CAs shorten T_2 and T_2* (additional influence of magnetic field inhomogeneities on T_2) much more than the T_1 of the nuclei situated in their neighborhood, generating a signal darkening on MR images. They are produced by a monocrystalline (USPIO) or polycrystalline (SPIO) iron oxide core with a diameter of 5–90 nm generally embedded within a polymer coating.[3]

Positive CAs are based on metal ions containing unpaired electrons, such as Gd^{3+} or Mn^{2+}.[1,2] The effect of these ions, called *paramagnetic ions*, is a similar shortening of T_1 and T_2 of their adjacent hydrogen nuclei. Since T_1 is longer than T_2 in tissues, paramagnetic ions have a more marked effect on T_1 than on T_2. Thus, positive CAs brighten the regions taking them up on a T_1-weighted MR image (currently recommended normal dose: 0.1 mmol kg^{-1}).

Gd^{3+} is an ideal paramagnetic relaxation agent because it has a large magnetic moment (7.98 BM at $T = 298$ K, seven unpaired electrons in the 4f orbital, $S = 7/2$) and nanosecond electronic spin relaxation time. (see ***Magnetism*** Although dysprosium (Dy^{3+}, 10.6 BM) and holmium (Ho^{3+}, 10.9 BM) have larger magnetic moments than Gd^{3+}, the asymmetry of their electronic states leads to very rapid electron spin relaxation. Gd^{3+} has one electron in each of its f orbitals and is therefore electronically very stable. The 4f orbitals are directly responsible for the magnetic and absorbance properties of the lanthanides.

Gadolinium ions are highly toxic in their hydrated form $[Gd(H_2O)_8]^{3+}$. *In vivo*, Gd^{3+} ions compete with calcium ions and block the reticuloendothelial system. To avoid this toxicity, gadolinium is complexed with an organic thermodynamically stable matrix. (see ***Lanthanide Complexes with Multidentate Ligands***, ***Organometallic Chemistry Fundamental Properties***, ***Lanthanides: Coordination Chemistry***) In addition, ligands that allow coordination sites for one (or more) water molecule(s) are preferred since they increase relaxivity. The first commercial gadolinium complexes were Magnevist® (Gd-DTPA, from Bayer Schering Pharma AG) and Dotarem® (Gd-DOTA, from Guerbet). These compounds have counterions that increase the osmolality of the solution injected. Two other ''neutral'' complexes have been developed, Omniscan® (Gd-DTPA-BMA, from GE HealthCare) and Prohance® (Gd-HP-DO3A, from Bracco). These four paramagnetic complexes are distributed in the extracellular space and do not show specificity (Figure 4).

4.1 Recent Advances and Developments in MRI Contrast Agents

An example of a tissue-specific CA is the Gd^{3+} complex of ethoxy-benzyl (EOB)-DTPA. This lipophilic complex, known as Primovist® (formerly Eovist®, from Bayer Schering Pharma AG), enters the hepatocytes through the membrane-bound organic anion transporter and allows for the detection of hepatic lesions characterized by a decrease (metastases, hepatocellular carcinoma) or an increase (focal nodular hyperplasia) in the hepatocytes' signal. This liver-specific CA is then eliminated via the biliary pathway and by the kidneys.[9]

Blood pool agents form another group of tissue-specific paramagnetic CAs. They are useful for MRI of the blood vessels, known as *magnetic resonance angiography* (MRA), to diagnose vascular disease. Two types of blood pool agents can be found: serum-albumin-binding Gd chelates and high-molecular-weight compounds with long blood circulating times. MS-325 (Vasovist®, Bayer Schering Pharma AG) belongs to the first category. Binding to serum albumin leads to high relaxivity and longer residence times in the blood for this small-molecular CA. P-792 (Vistarem®, Guerbet) is a polymeric compound based on a low-molecular-weight CA, and Gadomer-17 (Bayer Schering Pharma AG) is made of a polymer (a 24-mer polyamine) called *dendrimer* with the 24 free amino groups linked to a macrocyclic DOTA

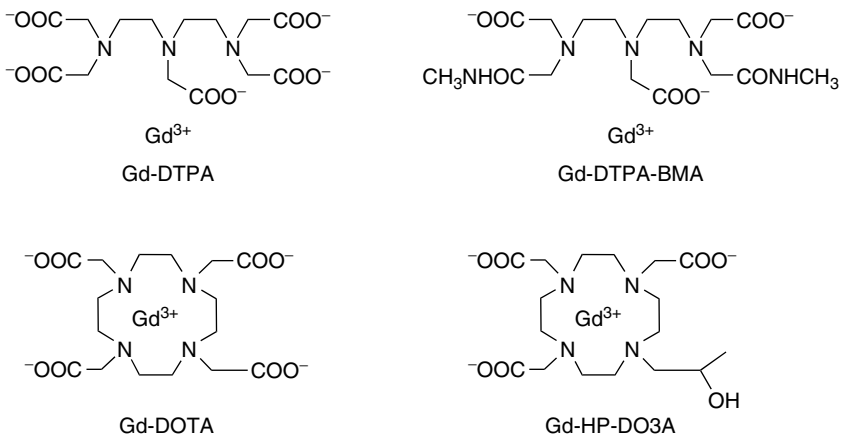


Figure 4 Structures of some paramagnetic contrast agents

gadolinium chelate, allowing for the complexation of 24 Gd atoms. Both are found in the second category. These macromolecular blood pool CAs have increased relaxivity and low extravasation but are small enough to be quickly and completely eliminated by glomerular filtration.[10] Finally, some types of paramagnetic chelates are able to accumulate in nonviable tissues. Two categories of necrosis-avid contrast agents (NACAs), the porphyrin (e.g., gadophrin-2 (bis-gadolinium mesoporphyrins from Bayer Schering Pharma AG)) and the nonporphyrin species (e.g., ECIV-7 and ECIII-60), have been developed. These NACAs can be useful for the detection of necrosis in the context of pathologies such as myocardial infarction.[11] Low-molecular-weight Gd chelates contain only one Gd^{3+} ion. Thus, as high relaxivity is needed for molecular MRI, several types of molecular carriers, able to bring high Gd concentrations to the target site, have been built. Among them, proteins such as albumin, avidin, and poly-L-lysine or dendrimers have been conjugated to metal chelates in order to carry a large number of Gd atoms[12–14]. Liposomes loaded with a molar concentration of Gd also have provided high T_1 relaxivity[15,16]. There are several reports in the literature of Gd-complexes (i.e., Gd chelates) covalently attached to macromolecules or macromolecular species, such as dendrimers, micelles, liposomes, nanoemulsions, and carbon nanotubes (Figure 5),[1,2] in order to enhance the efficiency of MRI CAs.

To improve their selective delivery, molecular carriers must be conjugated to ligands specific for a given target (e.g., peptides, antibodies, or antibody fragments). In the case of avidin-Gd-DTPA complexes, avidin allows for the binding of the CA to the target after it has been prelabeled with a biotinylated antibody. This Gd carrier has been used to image tumor cells expressing the HER-2/*neu* receptor-1 in an animal model of breast

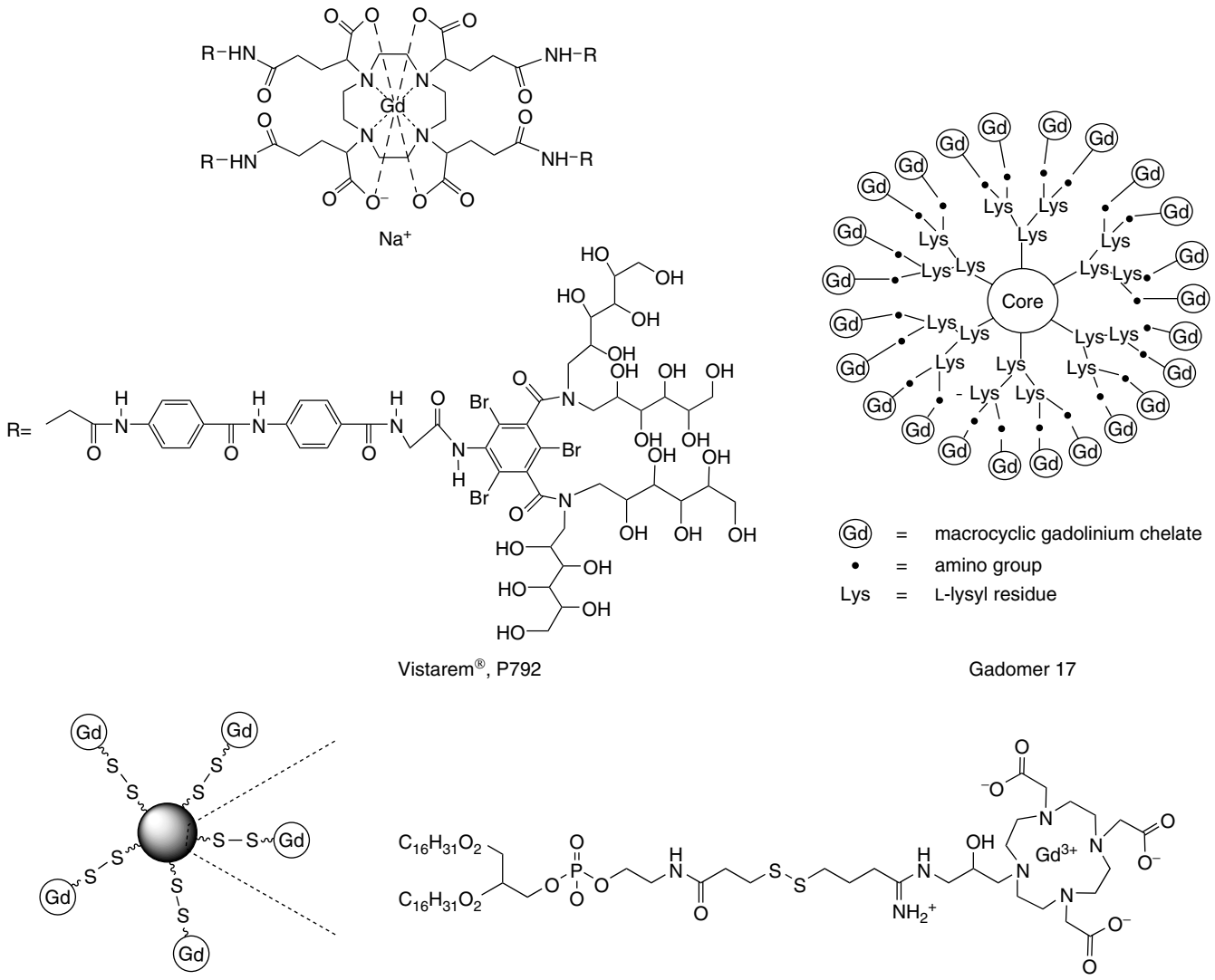


Figure 5 Structures of some Gd-loaded species (e.g., dendrimers, micelles, and liposomes)[1,2]

cancer.[12] The avidin–biotin system has also been used to link biotinylated Gd perfluorocarbon nanoparticles to a biotinylated antibody specific for an endothelial integrin characteristic of angiogenic vessels, $\alpha_v\beta_3$, in order to image neovessels in an animal model of angiogenesis.[17] Paramagnetic liposomes conjugated to a specific antibody have allowed to image endothelial cells expressing an inflammatory surface molecule (ICAM-1) in an animal model of brain inflammation (experimental autoimmune encephalomyelitis (EAE)).[18] Another inflammatory marker expressed by endothelial cells, E-selectin, has been imaged *in vitro* using a poly-l-lysine-based Gd carrier linked to a specific antibody fragment.[19] Antihuman carcinoembryonic antigen (CEA) fragments have been coupled to poly-l-lysine-Gd-DOTA and poly-l-lysine-Gd-DTPA for *in vivo* MRI of tumors in mice grafted with human colorectal carcinoma.[20–21] Also, Gd chelates have been conjugated directly to an antibody or to a synthetic mimetic of the natural ligand of E-selectin (the sialyl-LewisX molecule) in order to target inflamed endothelial cells *in vivo*.[22–24]

Recent developments in CAs concern the targeting of disease or, more precisely, of its manifestations; for example, by detecting tumors at an early stage. This strategy is based on the recognition of specific receptors. Their vectors, like peptides, antibodies, folate, and so on, are grafted onto the Gd chelate or carrier. Smart CAs modulate their efficiency according to the biological environment (presence of enzymes, pH, O_2, etc.). For example, these smart CAs are useful for disease conditions that acidify the medium (in tumors the pH is ~6.8, whereas in the healthy extracellular medium it is ~7.4).

In the context of molecular imaging, the specificity of MRI can be increased by directing CAs to specific molecular entities. High concentrations of the CA at the target site will be needed because of the intrinsically low sensitivity of MRI. So, targeted CAs should recognize their target with high affinity and specificity and have high relaxivity.

5 RELAXATION MECHANISMS

5.1 Nuclear Relaxation

Nuclear relaxation is the return to thermodynamic equilibrium of a spin system excited by an appropriate frequency of an electromagnetic field. The interaction of magnetic moments of excited spins with the environment creates microscopic local magnetic fields that fluctuate. These magnetic fluctuations are related to molecular motions. The longitudinal R_1 and transverse R_2 relaxation rates are modulated by the phenomenon of molecular distribution and expressed by the following relation:

$$\frac{1}{T_i} = R_i = K E_c^2 f(\tau_c) \tag{1}$$

where $i = 1, 2$
K is a constant
E_c is the amplitude of the interaction responsible for relaxation
$f(\tau_c)$ is a function of a correlation time.

5.2 Paramagnetic Relaxation

The presence of paramagnetic ions allows increasing the relaxation rate of water protons. There are several mechanisms affecting the relaxation of surrounding protons by paramagnetic metal complexes; the most dominant is the dipole–dipole interaction between the paramagnetic center and the surrounding water molecules. The dipolar mechanism is highly dependent on the rate of tumbling of coupled species. The general theory of solvent nuclear relaxation was developed by the groups of Bloembergen, Solomon, and others. According to this theory, the metal complexes affect both the spin lattice relaxation rate ($1/T_1$) and the spin–spin relaxation rate ($1/T_2$). The observed relaxation rate of surrounding water protons ($1/T_1$(obs) in the presence of a paramagnetic substance is generally given by the following mathematical equation:

$$R_{i(\text{obs})} = \frac{1}{T_{i(\text{obs})}} = \frac{1}{T_{i(\text{d})}} + \frac{1}{T_{i(\text{p})}} = \frac{1}{T_{i(\text{d})}} + r_i C \quad \text{with } i = 1 \text{ or } 2 \tag{2}$$

In equation (2), $1/Ti$(d) is the relaxation rate in the absence of any paramagnetic substance, while $1/Ti$(p) is the relaxation rate enhancement by the paramagnetic substance, related to C, the concentration of the magnetic center, (mmol l^{-1}) and r_i, the relaxivity (s^{-1} mmol l^{-1}). The relaxivities r_1 and r_2 are complex functions of several parameters of the molecular structure and dynamics of the CAs.

The paramagnetic center influences the proton water relaxation rate that interacts directly with it and its neighbors. The effectiveness of contrast is related to molecular motion and also to the intrinsic properties of the nucleus (magnetic susceptibility, gyromagnetic ratio, spin density). Paramagnetic relaxation R_1^p is characterized by two main contributions: the inner-sphere (IS) and the outer-sphere contributions (Figure 6). Sometimes a third contribution called *second-sphere mechanism* is observed. This contribution concerns the water molecules that are not directly coordinated to the paramagnetic center but organized in a second coordination sphere (Figure 6).

Three types of water molecules can thus be associated with the one paramagnetic center (i.e., Gd^{3+}): (a) IS water molecules, which are directly coordinated with the paramagnetic center; (b) second-sphere water molecules,

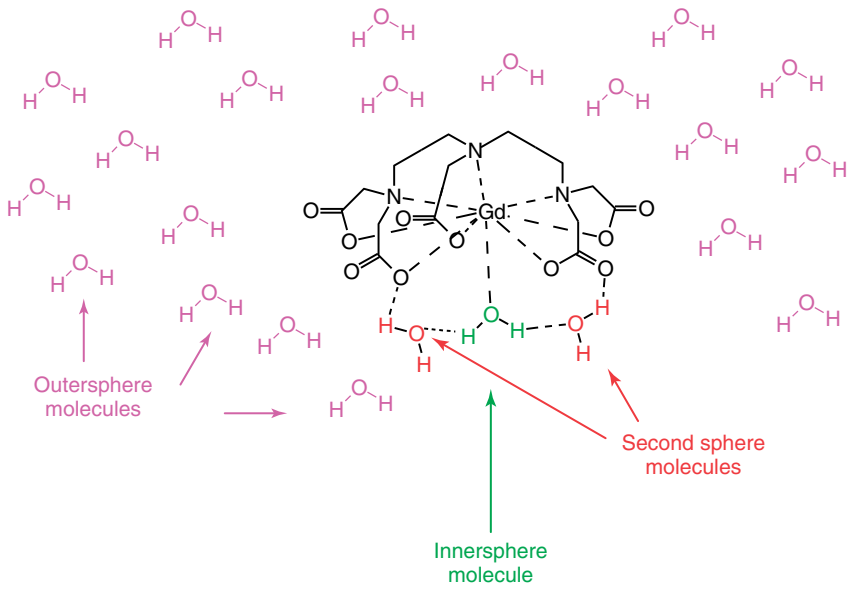


Figure 6 Inner-sphere, second-sphere, and outer-sphere contributions

which are indirectly coordinated with the paramagnetic center; these water molecules are bound to the ligand via weak interaction forces; and (c) outer-sphere water molecules, which come into close proximity of the paramagnetic chelate as a result of translational motion of the complex and water molecules. These exchangeable water molecules are responsible for transferring the effect of the magnetic moment from the Gd^{3+} center to the surrounding water protons. Thus, the observed relaxivity in the presence of a paramagnetic center is the sum of IS relaxivity and outer-sphere relaxivity (and sometimes second-sphere relaxivity). However, only the IS relaxivity can be significantly modified, and thus, for the new generation of CAs, it plays a crucial role in the overall relaxivity.

The principle of IS relaxation is a chemical exchange in which one or more water molecules of the first coordination sphere of the paramagnetic center are replaced by others. This mechanism allows the propagation of the paramagnetic effect. The IS model is described by the Solomon-Bloembergen-Morgan theory.

The IS contribution is given by the following equations:

$$R_1^{\text{is}} = f q \frac{1}{T_{1\text{M}} + \tau_{\text{M}}} \tag{3}$$

$$R_2^{\text{is}} = f q \frac{1}{\tau_{\text{M}}} \frac{{T_{2\text{M}}}^{-2} + {\tau_{\text{M}}}^{-1}{T_{2\text{M}}}^{-1} + {\Delta\omega_{\text{M}}}^2}{({\tau_{\text{M}}}^{-1} + {T_{2\text{M}}}^{-1})^2 + {\Delta\omega_{\text{M}}}^2} \tag{4}$$

where f is the relative concentration of the paramagnetic complex and of the water molecules, q is the number of water molecules in the first coordination sphere, τ_{M} is the water residence time of the water, and $\Delta\omega_{\text{M}}$ is the chemical shift difference between bulk and coordinated water.

For Gd-complexes, $T_{1\text{M}}$ and $T_{2\text{M}}$ are given by equations (5) and (6):

$$\frac{1}{T_{1\text{M}}} = \frac{2}{15}\left(\frac{\mu_0}{4\pi}\right)^2 \gamma_{\text{H}}^2 \gamma_{\text{S}}^2 \hbar^2 S(S+1) \frac{1}{r^6}\left[\frac{7\tau_{\text{c2}}}{1+(\omega_{\text{S}}\tau_{\text{c2}})^2} + \frac{3\tau_{\text{c1}}}{1+(\omega_{\text{H}}\tau_{\text{c1}})^2}\right] \tag{5}$$

$$\frac{1}{T_{2\text{M}}} = \frac{1}{15}\left(\frac{\mu_0}{4\pi}\right)^2 \gamma_{\text{H}}^2 \gamma_{\text{S}}^2 S(S+1) \frac{1}{r^6}\left[4\tau_{\text{c1}} + \frac{13\tau_{\text{c2}}}{1+(\omega_{\text{S}}\tau_{\text{c2}})^2} + \frac{3\tau_{\text{c1}}}{1+(\omega_{\text{H}}\tau_{\text{c1}})^2}\right] \tag{6}$$

With

$$\frac{1}{\tau_{\text{ci}}} = \frac{1}{\tau_{\text{R}}} + \frac{1}{\tau_{\text{M}}} + \frac{1}{\tau_{\text{si}}} \tag{7}$$

$$\frac{1}{\tau_{\text{S1}}} = \frac{1}{5\tau_{\text{SO}}}\left[\frac{1}{1+\omega_{\text{S}}{}^2\tau_{\text{V}}{}^2} + \frac{4}{1+4\,\omega_{\text{S}}{}^2\tau_{\text{V}}{}^2}\right] \tag{8}$$

$$\frac{1}{\tau_{\text{S2}}} = \frac{1}{10\tau_{\text{SO}}}\left[3 + \frac{5}{1+\omega_{\text{S}}{}^2\tau_{\text{V}}{}^2} + \frac{2}{1+4\,\omega_{\text{S}}{}^2\tau_{\text{V}}{}^2}\right] \tag{9}$$

where
μ_0 = the permeability of the vacuum
γ_{H} = the gyromagnetic ratio of the proton
γ_{S} = the gyromagnetic ratio of the electron (S)
S = the total spin quantum number ($S(Gd^{3+}) = 7/2$)
$\omega_{\text{S,H}}$ = the angular frequencies of the electron and of the proton, respectively
r = the distance between the coordinated water protons and the unpaired electron spins
$\tau_{\text{c1,2}}$ = the correlation times modulating the interaction
τ_{R} = the rotational correlation time of the hydrated complex

$\tau_{s1,2}$ = the longitudinal and transverse relaxation times of the electrons
τ_{SO} = the value of $\tau_{s1,2}$ at zero field
τ_v = the correlation time characteristic of the electronic relaxation times.

Thus, the main parameters governing the efficiency of Gd-complexes as MRI CAs are q, τ_M, and τ_R.

The second contribution to paramagnetic relaxation is the outer-sphere relaxation. It is explained by dipolar interactions at longer distances between the spins of the paramagnetic center and the nuclear spin. This intermolecular mechanism is modulated by the translational correlation time τ_D, which takes into account the relative diffusion constant (D) of the Gd center and of the solvent molecule and their distance of closest approach (d). The outer-sphere contribution has been described by Freed and is given by equations (10) and (11):

$$R_1^{os} = \frac{6400\pi}{81}\left(\frac{\mu_0}{4\pi}\right)^2 \gamma_H^2\gamma_S^2\hbar^2 S(S+1)NA\frac{[C]}{dD} [7j(\omega_S\tau_D) + 3j(\omega_H\tau_D)] \quad (10)$$

$$R_2^{os} = \frac{6400\pi}{81}\left(\frac{\mu_0}{4\pi}\right)^2 \gamma_H^2\gamma_S^2\hbar^2 S(S+1)NA\frac{[C]}{dD} [6.5j(\omega_S\tau_D) + 1.5j(\omega_I\tau_D) + 2j(0)] \quad (11)$$

where NA is the Avogadro number and [C] is the molar concentration.

And with

$$\tau_D = \frac{d^2}{D} \quad (12)$$

$$j(\omega\tau_D) = \mathrm{Re}\left[\frac{1 + \frac{1}{4}(i\omega\tau_D + \tau_D/\tau_{S1})^{1/2}}{1 + (i\omega\tau_D + \tau_D/\tau_{S1})^{1/2} + \frac{4}{9}(i\omega\tau_D + \tau_D/\tau_{S1}) + \frac{1}{9}(i\omega\tau_D + \tau_D/\tau_{S1})^{3/2}}\right] \quad (13)$$

5.3 Physicochemical Characterization of Paramagnetic Complexes

The complexity of the equations describing the relaxation rate is due to the numerous parameters describing the different contributions: τ_M, q, τ_R, τ_V, τ_{S0}, r, D, and d. The estimation of those parameters by a single technique is very difficult and ambiguous. Thus, the determination of certain parameters by independent methods is important. All these parameters determine the evolution of the paramagnetic relaxation as a function of the magnetic field (nuclear magnetic relaxation dispersion (NMRD) profiles). These profiles are characteristic of CAs (Figure 7).

To increase the efficiency of paramagnetic Gd-complexes as MRI CAs, the following parameters among those cited above can be optimized: the hydration number q of the metal ion, the residence time of the coordinated water τ_M, the rotational correlation time τ_R, and the metal–proton distance r.

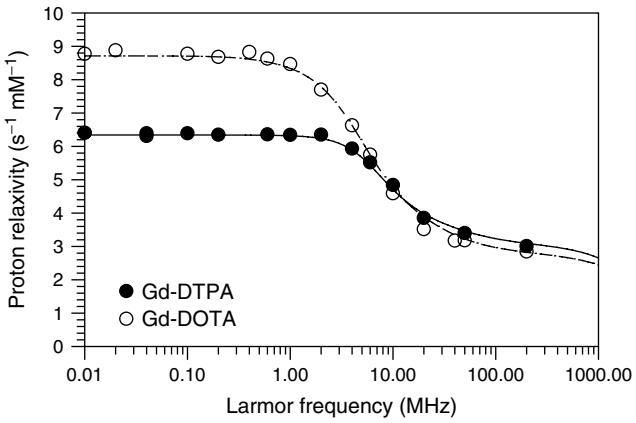


Figure 7 NMRD profiles of Gd-complexes (Gd-DTPA and Gd-DOTA at 310 K)

The rotational correlation time τ_R: several methods have been proposed to lengthen τ_R; for example, noncovalent interactions with endogenous macromolecules such as HSA, DNA, specific receptors of the cellular membrane, paramagnetic polymers, liposomes, or micelles. This parameter can be determined by various methods such as ^{2}H NMR of diamagnetic lanthanum complexes or ^{17}O NMR of Gd-complexes.

The hydration number q: this parameter influences strongly the IS contribution (equations (3) and (4)). If this number increases from 1 to 2, the relaxivity increases by about 30%, but most of the Gd-complexes have a q number equal to one. This number can be measured by fluorescence study of europium or terbium complexes or by ^{17}O NMR measuring the lanthanide induced shift (LIS).

The metal–proton distance r: a small decrease in r allows a quite large increase in relaxivity because of the $1/r^6$ dependence of T_{1M}. However, this distance is nearly constant in all stable Gd-complexes ($r = 0.31 \pm 0.01$ nm) already described. A reduction in r can partly explain the higher relaxivity of Gd-EOB-DTPA (5.5 mM^{-1}s^{-1} at 310 K and 20 MHz) compared to that of Gd-DTPA (3.9 mM^{-1}s^{-1} at 310 K and 20 MHz).

The residence time of the coordinated water τ_M: the mechanism of IS relaxation is based on an exchange between bulk water molecules surrounding the complex and the water molecule(s) coordinated to the lanthanide. Consequently, the exchange rate ($k_{ex} = 1/\tau_M$) is an essential parameter for transmitting the ''relaxing'' effect to the solvent. Its measurement is based on the works of Swift and Connick for diluted paramagnetic solutions and consists of an analysis of the ^{17}O transverse relaxation rate as a function of temperature.

6 EXAMPLES OF MRI APPLICATIONS

6.1 Targeting of Apoptosis

Apoptosis is an attractive target for the diagnosis of vulnerable atherosclerotic plaques prone to a thrombotic event. Burtea *et al*. showed that it is possible to screen apoptosis peptide binders by phage display with the final purpose of detecting apoptotic cells in atherosclerotic plaques by MRI.[25] A phosphatidylserine-specific peptide was used to design an MRI CA, which was evaluated as a potential *in vivo* reporter of apoptotic cells. This selected peptide and its scrambled homolog were conjugated to Gd-DTPA. After their evaluation using apoptotic cells and a mouse model of liver apoptosis, the phosphatidylserine-targeted complex (Figure 8) was used

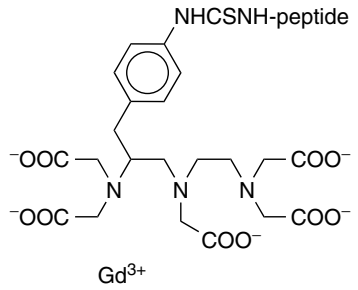


Figure 8 Structure of the Gd-complex for targeting apoptosis (the peptide has the LIKKPF sequence)

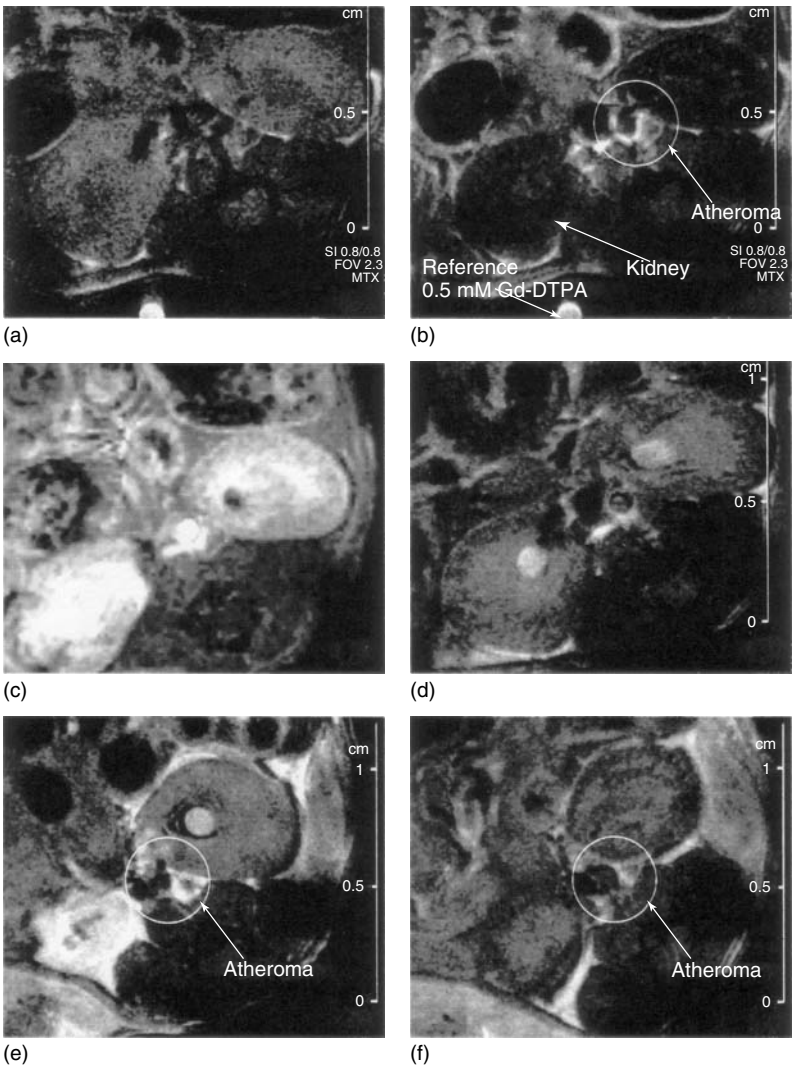


Figure 9 MRI RARE images at 4.7 T are shown in precontrast (a) and 30 min post Gd-DTPA-g-R826 (b). They are compared to a time-of-flight (TOF) image (c) and to an image obtained post Gd-DTPA (d). The comparison between Gd-DTPA-g-R826 (e) and Gd-DTPA-g-R826.Sc (f) is shown 60 min postcontrast. Images compared in (a)–(d) and those in (e) and (f) are located at the same level of abdominal aorta (Reprinted with permission from Ref. 25. Copyright (2009) American Chemical Society.)

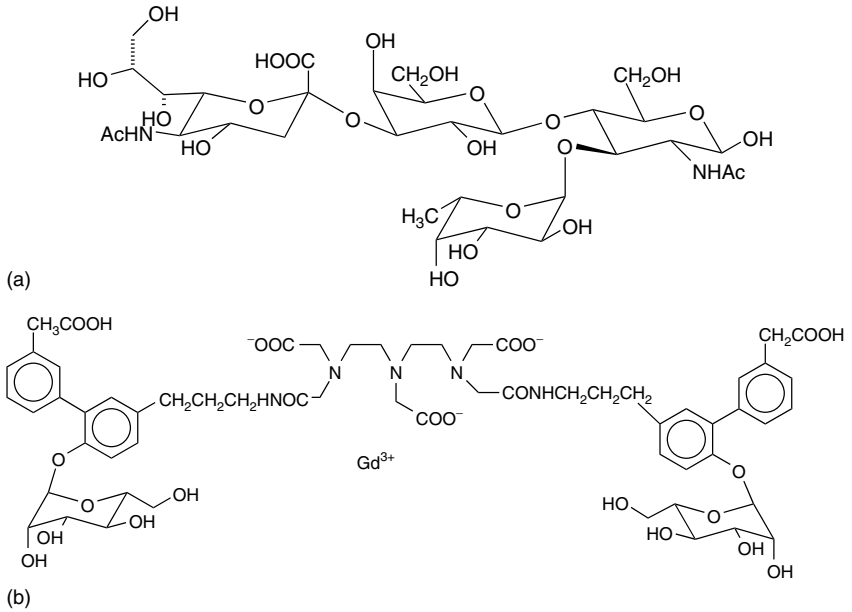


Figure 10 Molecular structure of sialyl-Lewis X (a) and the E-selectin-targeted CA, Gd-DTPA-B(sLex)A (b)

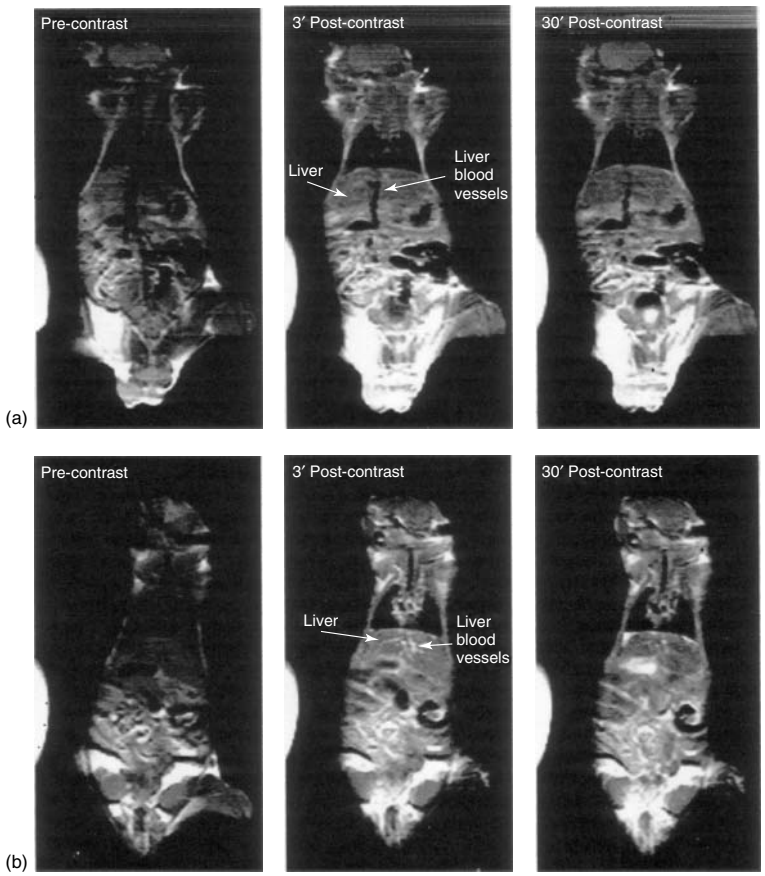


Figure 11 MR coronal images of a healthy mouse (a) and a mouse with hepatitis (b) before and several time intervals after i.v. administration of Gd-DTPA-B(sLeX)A. The images were obtained with a Siemens® Magnetom Impact System at 1.0 T. Note: The urinary bladder of the healthy mouse (a) is apparent and filled with CA 30 min after injection, which attests to the excretion of the compound. (Reprinted with permission from Ref. 24. © Wiley-Liss, Inc., 2005.)

to image atherosclerotic lesions on ApoE/transgenic mice. Apoptotic cells were detected in liver and aorta specimens by immunostaining of phosphatidylserine and of active caspase-3. The *in vivo* MRI studies provide proof of concept that apoptosis-related pathologies could be diagnosed by MRI with a low-molecular-weight paramagnetic agent (Figure 9). This Gd-complex could have real potential in the diagnosis and therapy monitoring of atherosclerotic disease and of other apoptosis-associated pathologies, such as cancer, ischemia, chronic inflammation, autoimmune disorders, transplant rejection, neurodegenerative disorders, and diabetes mellitus.

6.2 Targeting Inflammation

E-selectin, absent from normal liver tissue, is strongly expressed on sinusoidal lining cells in inflammatory liver diseases. It has been targeted by a specific marker for MRI diagnosis. The CA mimics the sialyl-Lewis X molecule, which is the main ligand of E-selectin, and has been proposed for the morphological diagnosis of inflammatory lesions and as a functional marker of immune response. Gd-DTPA-B(sLeX)A carries two groups of 3-(2α-d-mannopyranosyl-oxyphenyl) phenyl acetic acid (Figure 10).[24] This complex was evaluated in mice and rats with respect to its pharmacokinetics, biodistribution, and potential to image inflammation by MRI. A fulminant hepatitis model was used, in which the pathological conditions were induced by the coadministration of d-galactosamine and lipopolysaccharide. The neutrophil (white blood cell) adhesion to the sinusoid wall is an early event in this process of liver inflammation, which is related to E-selectin expression during the first few hours.

A significant and prolonged contrast enhancement between blood vessels and liver parenchyma was obtained in pathological conditions, which attests to the specificity of the agent for E-selectin. The MRI studies demonstrate that the new compound significantly enhanced the liver blood vessels of the animals with hepatitis over a period of 60 min. The prolonged vascular residence suggests that Gd-DTPA-B(sLeX)A interacts with the specific receptors expressed during inflammation. The biodistribution of the compound indicates its retention in inflamed liver by both specific mechanisms and nonspecific accumulation due to the necrotic lesions.

These results confirm the potential of Gd-DTPA-B(sLeX) A, as was demonstrated in the context of brain injury and inflammation.[22,23] Gd-DTPA-B(sLeX)A shows promise as an *in vivo* tool for the noninvasive analysis of E-selectin expression in inflammatory disorders.

6.3 Targeting $\alpha_v\beta_3$ Integrin

The integrin $\alpha_v\beta_3$ is highly expressed in atherosclerotic plaques by medial and intimal smooth muscle cells and by endothelial cells of angiogenic microvessels. Burtea *et al.*[26] have assessed noninvasive MRI of plaque-associated $\alpha_v\beta_3$ integrin expression on transgenic ApoE2/2 mice with a low-molecular-weight peptidomimetic of Arg-Gly-Asp (mimRGD) grafted to Gd-DTPA (Gd-DTPA-mimRGD, Figure 12). The specific interaction of Gd-DTPA-mimRGD with $\alpha_v\beta_3$ integrin was furthermore confirmed on Jurkat T lymphocytes (Figure 13).

The blood pharmacokinetics of Gd-DTPA-mimRGD was assessed in rats and mice. The presence of angiogenic blood vessels and the expression of $\alpha_v\beta_3$ integrin were confirmed in aorta specimens by immunohistochemistry. Gd-DTPA-mimRGD produced a strong enhancement of the external structures of the aortic wall and of the more profound layers (possibly tunica media and intima). The aortic lumen seemed to be restrained and distorted. Preinjection of Eu-DTPA-mimRGD diminished Gd-DTPA-mimRGD binding to atherosclerotic plaque and confirmed specific molecular targeting.

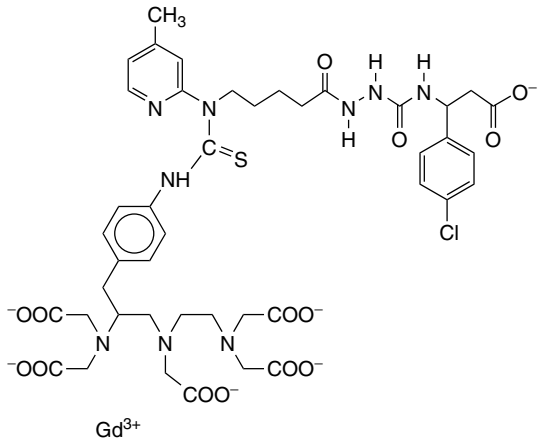


Figure 12 Structure of Gd-DTPA-mimRGD

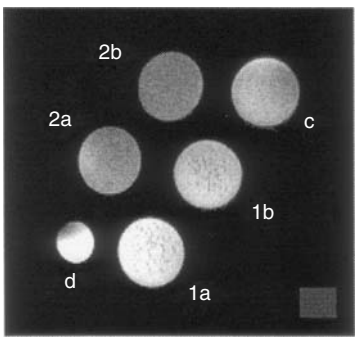


Figure 13 *In vitro* validation of the specific interaction with integrins expressed by Jurkat T lymphocytes of Gd-DTPA-mimRGD. MR images of Jurkat cells stimulated with phorbol 12-myristate 13-acetate (PMA; to stimulate integrin expression) (1a and 2a) or not (1b and 2b) and incubated with 0.4 mM of Gd-DTPA-mimRGD (1a and 1b) or with Gd-DTPA (2a and 2b). The test samples are compared with reference samples: cells in gelatin (c) and 0.025 mM Gd-DTPA in gelatin (d). (Reprinted with permission Ref. 26. © Oxford University Press, 2008.)

This Gd-complex is potentially useful for the diagnosis of vulnerable atherosclerotic plaques and of other pathologies characterized by $\alpha_v\beta_3$ integrin expression, such as cancer and inflammation.

7 CONCLUSIONS

Medical imaging plays a central role in modern medicine. Molecular imaging is a growing discipline that aims at the *in vivo* visualization and characterization of cellular and molecular biological processes reflecting the evolution of a disease. Gd-based CAs for MRI are an important tool in this field. The understanding of their contrast enhancement and body distribution mechanisms is a key step in the scope of molecular imaging.

8 GLOSSARY

MRI: magnetic resonance imaging: non-invasive 2D or 3D pixel by pixel cartography of atoms (mainly hydrogens, called protons (^{1}H)), featuring abundance and/or magnetic (relaxometric) properties of atoms as gray levels.

NMR: nuclear magnetic resonance: absorption and subsequent emission of energy (radiofrequency range) at a certain (resonance) frequency by several atoms (^{1}H, 19F, 13C, 31P, 17O) placed in an external magnetic field. The resonance frequency must be adjusted, depending on the observed atom and on the external magnetic field strength. The emitted wave (relaxation) constitutes the NMR signal that is collected and transformed in spectrum or image.

Excitation pulse: energy (radio wave of adequate frequency) that is provided from outside to atoms placed in a magnetic field, which allows for the subsequent emission of the NMR signal. Magnetization is flipped away from its original orientation, with a certain angle value that is determined by the strength of the excitation pulse.

Relaxation: phenomenon of energy emission that starts when the excitation pulse is stopped. It is allowed by the coming back of magnetization from a (unstable) high energy state to its original orientation. This happens at a certain speed (depending on the atoms' local magnetic properties) which is characterized by two time parameters: T1 (concerns the coming back of magnetization to its original (B0-induced) position), and T2 (concerns the decrease of magnetization perpendicularly to the B0 orientation, thus from its unstable (excitation pulse-induced) position)

Magnetic field gradient: modifications of the external magnetic field that are added as magnetic fields of strength increasing in the three directions of space, for locally individualizing the NMR signal, since it directly depends on the magnetic field strength. These gradients allows for the formation of an MR images.

External magnetic field: called B0, induces an optimization of magnetic properties of atoms; their magnetic moment gets oriented towards the direction of this external magnetic field, which creates a global magnetization (eg. in a sample or organism) that can be used for nuclear magnetic resonance experiments.

TR: repetition time: time interval between two successive excitation pulses in the acquisition sequence of MR images. This parameter is adjusted: shortened when protons with rapid relaxation properties have to be positively contrasted (T1-weighted MRI), and extended when such protons have to be negatively contrasted (T2-weighted MRI), or to avoid T1-based contrast in general.

TE: echo time: time interval between excitation pulse and NMR signal (echo) collection in the acquisition sequence of MR images. This parameter is adjusted: shortened when protons with rapid relaxation properties have to be positively contrasted (T1-weighted MRI) or to avoid T2-based contrast in general, and extended to allow a positive contrast of protons with slow relaxation properties on MR images.

Echo: NMR signal collected after a maximization process (echo generation) in magnetic resonance acquisitions

Contrast agent: compound based on magnetically active ions, which can help to improve the difference between healthy and pathological tissues by increasing the magnetic properties (relaxation rates) of tissues' protons.

Relaxivity: efficiency of the contrast agent to increase the proton relaxation rate achieved by 1 mmol l^{-1} ofmagnetic ion

NMRD profiles: nuclear magnetic relaxation dispersion profiles showed the evolution of the paramagnetic relaxation versus the magnetic field.

Cerebrospinal fluid: liquid formed from the blood that fills cavities (ventricles) and surrounds the brain. It is also found in the spinal cord.

Apoptosis: multi-step, multi-pathway cell-death program that is inherent in every cell of the body

E-selectin: is a cell surface adhesion molecule expressed only on endothelial cells activated by cytokines (eg. in inflammatory situations)

mylohyoid muscle : neck muscle, forming the floor of the oral cavity

9 ACKNOWLEDGEMENTS

This work was financially supported by the ARC (research contract 00/05-258, 05/10-335 and AUWB-2010—10/15-UMONS-5), FNRS, and ENCITE. Programs of Research of the French Community of Belgium, and it was performed in the framework of COST D38 (Metal-Based Systems for Molecular Imaging Applications) and the European Network of Excellence EMIL (European Molecular Imaging Laboratories) program LSCH-2004-503569. The authors thank the Center for Microscopy and Molecular Imaging (CMMI, supported by the European Regional Development Fund and the Walloon Region) for their support, and Patricia DeFrancisco for her help in preparing the manuscript.

10 RELATED ARTICLES

Lanthanides: Coordination Chemistry; Luminescent Bioprobes; Organometallic Chemistry Fundamental Properties.

11 ABBREVIATIONS AND ACRONYMS

DTPA = diethylenetriaminepentaacetic acid; DOTA = 1,4,7,10-tetraazacyclododecane-1,4,7,10-tetraacetic acid; MRI = magnetic resonance imaging; NMR = nuclear magnetic resonance; T_1 = longitudinal or spin lattice relaxation time; T_2 = transverse or spin-spin relaxation time; r_1 = longitudinal relaxivity; r_2 = transverse relaxivity.

12 REFERENCES

1. C. F. G. C. Geraldes and S. Laurent, *Contrast Med. Mol. Imaging*, 2009, **4**(1), 1.
2. S. Aime, D. D. Castelli, S. G. Crich, E. Gianolio, and E. Terreno, *Acc. Chem. Res.*, 2009, **42**(7), 822.
3. S. Laurent, D. Forge, M. Port, A. Roch, C. Robic, L. Vander Elst, and R. N. Muller, *Chem. Rev.*, 2008, **108**(6), 2064.
4. P. A. Rinck, R. A. Jones, J. Kvaerness, T. E. Southon, P. De Francisco, R. N. Muller, and S. B. Petersen, 'Magnetic Resonance in Medicine, The Basic Textbook of the European Magnetic Resonance Forum', 3rd Edition, Blackwell Scientific Publications, 1993.
5. G. J. Stanisz, E. E. Odrobina, J. Pun, M. Escaravage, S. J. Graham, M. J. Bronskill, and R. M. Henkelman, *Magn. Reson. Med.*, 2005, **54**, 507.
6. M. A. Foster, J. M. S. Hutchison, J. R. Mallard, and M. Fuller, *Magn. Reson. Imaging*, 1984, **2**, 187.
7. S. J. Nelson, *Mol. Cancer Ther.*, 2003, **2**, 497.
8. P. E. Sijens, M. J. van den Bent, P. J. Nowak, P. van Dijk, and M. Oudkerk, *Magn. Reson. Med.*, 1997, **37**, 222.
9. P. Reimer and R. Vosshenrich, *Biologics*, 2010, **4**, 199.
10. H. J. Weinmann, W. Ebert, B. Misselwitz, and H. Schmitt-Willich, *Eur. J. Radiol.*, 2003, **46**, 33.
11. Y. Ni, G. Bormans, F. Chen, A. Verbruggen, and G. Marchal, *Invest. Radiol.*, 2005, **40**, 526.
12. D. Artemov, N. Mori, R. Ravi, and Z. M. Bhujwalla, *Cancer Res.*, 2003, **63**, 2723.
13. Z. M. Bhujwalla, D. Artemov, K. Natarajan, M. Solaiyappan, P. Kollars, and P. E. Kristjansen, *Clin. Cancer Res.*, 2003, **9**, 355.
14. E. C. Wiener, M. W. Brechbiel, H. Brothers, R. L. Magin, O. A. Gansow, D. A. Tomalia, and P. C. Lauterbur, *Magn. Reson. Med.*, 1994, **31**, 1.
15. D. A. Sipkins, K. Gijbels, F. D. Tropper, M. Bednarski, K. Li, and L. Steinman, *J. Neuroimmunol.*, 2000, **104**, 1.
16. D. A. Sipkins, D. A. Cheresh, M. R. Kazemi, L. M. Nevin, M. D. Bednarski, and K. C. Li, *Nat. Med.*, 1998, **4**, 623.
17. S. A. Anderson, R. K. Rader, W. F. Westlin, C. Null, D. Jackson, G. M. Lanza, S. A. Wickline, and J. J. Kotyk, *Magn. Reson. Med.*, 2000, **44**, 433.
18. D. A. Sipkins, K. Gijbels, F. D. Tropper, M. Bednarski, K. C. P. Li, and L. Steinman, *J. Neuroimmun.*, 2000, **104**(1), 1.
19. H. W. Kang, R. Weissleder, and A. Bogdanov, *Amino Acids*, 2002, **23**, 301.
20. C. Curtet, F. Maton, T. Havet, M. Slinkin, A. Mishra, J. F. Chatal, and R. N. Muller, *Invest. Radiol.*, 1998, **33**, 752.
21. D. Artemov, Z. M. Bhujwalla, and J. W. Bulte, *Curr. Pharm. Biotechnol.*, 2004, **5**, 485.
22. N. R. Sibson, A. M. Blamire, M. Bernardes-Silva, S. Laurent, S. Boutry, R. N. Muller, P. Styles, and D. C. Anthony, *Magn. Reson. Med.*, 2004, **51**, 248.
23. P. A. Barber, T. Foniok, D. Kirk, A. M. Buchan, S. Laurent, S. Boutry, R. N. Muller, L. Hoyte, B. Tomanek, and U. I. Tuor, *Ann. Neurol.*, 2004, **56**, 116.
24. S. Boutry, C. Burtea, S. Laurent, G. Toubeau, L. Vander Elst, and R. N. Muller, *Magn. Reson. Med.*, 2005, **53**, 800.
25. C. Burtea, S. Laurent, E. Lancelot, S. Ballet, O. Murariu, O. Rousseaux, M. Port, L. Vander Elst, C. Corot, and R. N. Muller, *Mol. Pharm.*, 2009, **6**(6), 1903.
26. C. Burtea, S. Laurent, O. Murariu, D. Rattat, G. Toubeau, A. Verbruggen, D. Vansthertem, L. Vander Elst, and R. N. Muller, *Cardiovasc. Res.*, 2008, **78**, 148.

Luminescent Bioprobes

Anne-Sophie Chauvin

École Polytechnique Fédérale de Lausanne, Vaud, Switzerland

1 Summary 535
2 Introduction 535
3 Performing the Study of a Lanthanide Complex 537
4 The Choice of the Ligand 539
5 Formation of the Complexes 539
6 Helicates Acting as Bioprobes 549
7 Conclusion 557
8 Glossary 557
9 Acknowledgments 557
10 Related Articles 558
11 Abbreviations and Acronyms 558
12 References 558

1 SUMMARY

After a complete survey of the previous chapters dealing with fundamentals aspects, the reader has now a good knowledge about luminescence, with the fundamental concepts in photophysics discussed in article ***Luminescence***. This article presented an overview of the different kinds of spectra obtained with the various lanthanide ions emitting in UV–visible as well as in the near-infrared (NIR) region, and of the different criteria to characterize the luminescence of a lanthanide complex (such as lifetime, quantum yield, and q numbers). A previous article also described the ligands that are commonly used to fine-tune the luminescent properties, depending on the applications to be achieved with these complexes (***Lanthanides: Luminescence Applications***). However, until now, neither the criteria to conduct a good study nor the requirements of the complex to become an efficient luminescent complex have been discussed. Furthermore, what is needed to make an efficient probe or a bioprobe? In this article, the case of a family of ditopic ligands yielding homononuclear 2 : 3 Ln:L helicate structures in the presence of lanthanide ions is presented. The properties needed to claim that they are good luminescent probes and how they can also interact with biological material is discussed. For each section, some practical guide lines and general information are given regarding how to perform the study, together with the results obtained with the helicate complexes.

2 INTRODUCTION

Molecular medicine is certainly one of the most important aspects of chemistry to be developed in the coming years. It includes (i) molecular imaging in order to visualize, localize, and study molecular processes *in vivo* for diagnostics and therapy, (ii) *in vitro* diagnostic developments to ensure an accurate and early detection of diseases, and (iii) healthcare prevention that implies a better understanding of diseases including the study of the chemical mechanisms involved, such as perturbations in the local environment of a given organelle (such as concentration modifications). In addition, delivering a drug in a restricted area—exclusively to the target organelle—would reduce the toxic side effects. This emphasizes the necessity to develop probes able to specifically interact with biological material and to extend the techniques for cell labeling in order to report the localization, movement, nature, and functions of cells *in vivo*. However, organelle-specific targeting still remains a major challenge nowadays. The possibility to access the different compartments, to report local changes, and, ideally, to modify it (i.e., drug delivery) is

The Rare Earth Elements. Edited by David A. Atwood. © 2012 John Wiley & Sons, Ltd. ISBN 978-1-119-95097-4

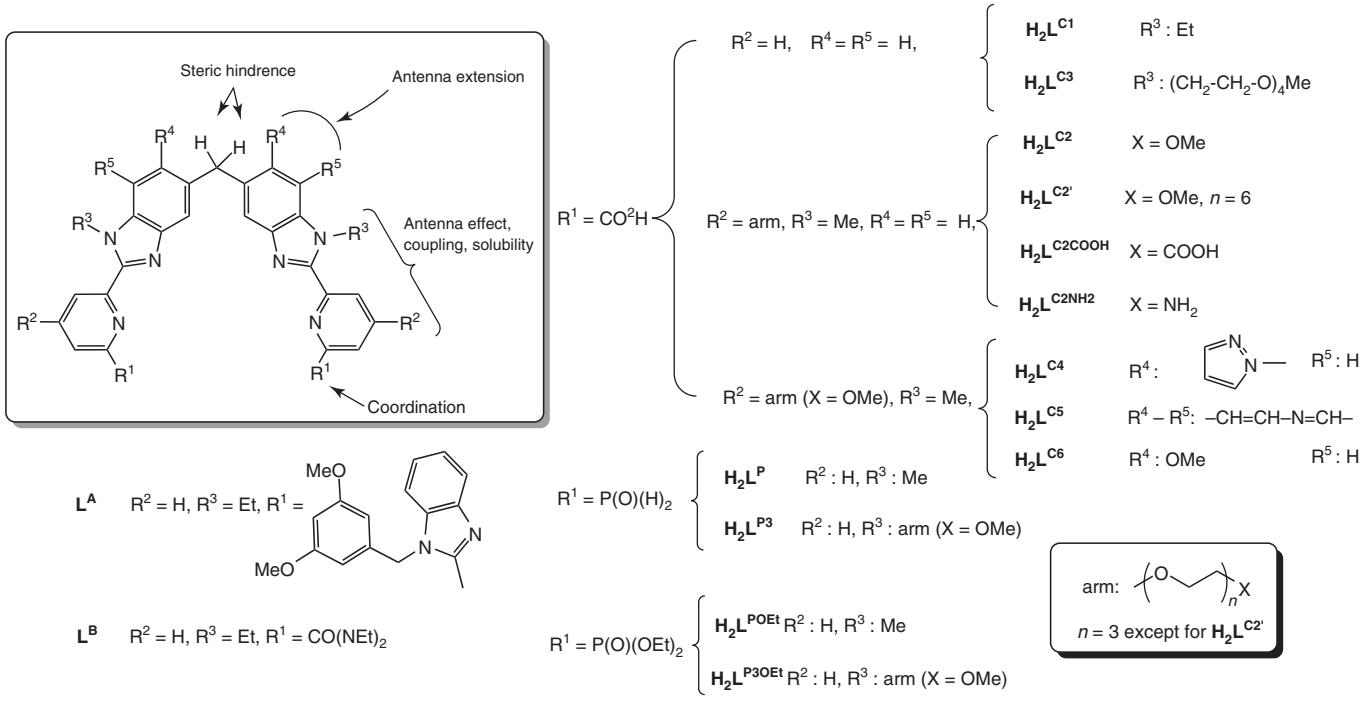


Figure 1 Ditopic ligands able to form 2 : 3 Ln:L helicates

still to be achieved and imply developing responsive probes. Optical probes are important in this field because of their noninvasive properties, high sensitivity, and easy detection with spatial resolution.[1] Among them, luminescent lanthanide-based probes are of utmost importance because of their particular luminescent properties. Furthermore, compared to organic dyes, they possess a longer lifetime, which is an advantage for their detection, and they do not suffer from photobleaching. Designing such a bioimaging lanthanide probe or sensor requires the synthesis of water-soluble lanthanide complexes that are highly stable, are resistant toward dissociation at low concentration (subnanomolar range), and exhibit exploitable luminescent properties with the ability to respond to a given signal, e.g., ability of the bioprobe to target a receptor or of the sensor to detect the presence of the analyte. The probes can be directly used in solution or, in order to improve their properties, can be encapsulated in different matrices (e.g., nanoparticles). In addition, the properties of the probe can be improved in terms of luminescence, thus giving access not only to UV or visible emitting reporters but also to NIR range emitting ones. This is of particular interest since the biological material is transparent in this spectral range; however, NIR emitting probes are hard to obtain in solution because of a lot of drawbacks (in particular, nonradiative deactivations due to O–H or C–H oscillators).

The most famous helical structure ever reported is certainly the DNA double strand, for which the DNA double helix structure has been elucidated in 1953 by James Watson and Francis Crick, and has been a source of inspiration for decades. In particular, in coordination chemistry, artificial supermolecules forming helical structures have been extensively investigated. The stability of the edifices is provided by the presence of hydrogen bonds or by π-stacking interactions as well as by rigidification on coordination to cations. Owing to the presence of these cations, it is possible to associate specific properties such as magnetic or spectroscopic properties to the helicate structure. Lanthanide ions are then very useful, because of their ability to provide luminescence. The case study reported here is a helical structure obtained in the presence of lanthanide ions and a hexadentate ligand, the structure of which is depicted in Figure 1. The ligand is ditopic, meaning that it possesses two distinct binding sites. Association of three of these ligands and two identical lanthanide ions yields a single molecular homonuclear triple-stranded structure.

The history of these helicates started in 1990s, with the first publication in 1992. Piguet *et al*. described the first model of helicates $[Ln_2(\mathbf{L}^A)_3]^{6+}$, with a tricapped homonuclear dinuclear structure.[2,3] The complex was studied in acetonitrile and gave an interesting stability of the edifice. Other candidates were obtained later, such as $\mathbf{L}^B$, which was soluble in acetonitrile and contained carboxamide coordinating units (in position R^1), or $H_2\mathbf{L}^C$, which was the first, yet sparingly, water-soluble candidate. Further studies were conducted by the group of Piguet, which led to the development of sophisticated supramolecular edifices, containing d and/or f elements, the thermodynamic properties of which were carefully established.[4]

In parallel, Bunzli and coworkers developed unsymmetrical ligands in order to rationalize the effect of coordination, the ultimate goal being to obtain heteronuclear probes combining two different luminescent lanthanide ions in a single complex. All of these studies were conducted in organic solvents, in particular acetonitrile. Then we turned our attention to water-soluble complexes. Our interest originally came from the protective wrapping of the ligand stranding around the metal ions. It induced a solvent-protected coordination sphere for both lanthanide ions, giving access to intense luminescent emission. This was of particular interest for the design of water-soluble probes, being one of the criteria to be fulfilled, because solvent molecules (and particularly water) are detrimental to the luminescence of the Ln ions. Among the other criteria allowing a good probe, one can cite

- water solubility of the edifice
- thermodynamic stability and kinetic inertness
- good luminescent properties, including lifetime, and quantum yield
- possibility to excite in a range at least >300 nm
- possibility to interact with cells demanding to establish both the nontoxicity and the possibility to permeate cells.

Developing a water-soluble complex implies adding solubilizing groups on the ligand backbone. One can envisage decorating the ligand by inserting cationic groups (e.g., ammonium substituents), anionic groups (e.g., phosphonates or sulfonates), or hydrophilic groups. With regard to this later point, polyethylene glycol (PEG) $HO-(CH_2-CH_2-O)_n-H$ ($M > 2000 g{\cdot}mol^{-1}$) is of huge interest and has been reported for its water-solubilizing effect, together with its bioinnocuity. To a lesser extent, polyoxyethylene substituent, with shorter length ($n = 4$ vs $n = 44$ for PEG2000) is also of interest for providing water solubility. For instance, the particularly well-known texaphyrin lutetium or gadolinium complex (Figure 2) developed by Sessler *et al.* consisted in a porphyrin containing these solubilizing moieties and conducted to the development of very active anticancer agents.[5] The alternative to make the helicates water soluble was to insert polyoxyethylene units, either in R^2 or R^3 positions according to Figure 1. Future work would consist in modifying the extremity of the arm to create a covalent link between the probe and any biological material, as reported below. Upcoming possibilities of ligand design involved shifting the excitation wavelength by introducing modifications in position R^4/R^5 (Figure 1). Alternatively, exploring the coordination mode by inserting a phosphonic acid group rather than a carboxylic one in R^1 position was also envisaged. One has also to take care not to prevent the formation of the helical structure in case of too important steric hindrance in proximity of the methylene bridge. A complete and comparative study of these ligands and the photophysical properties of the resulting complexes are out of interest for the present discussion, and only some aspects are discussed and illustrated. The reader should refer to the publications listed at the end of the article for a full access to the data.

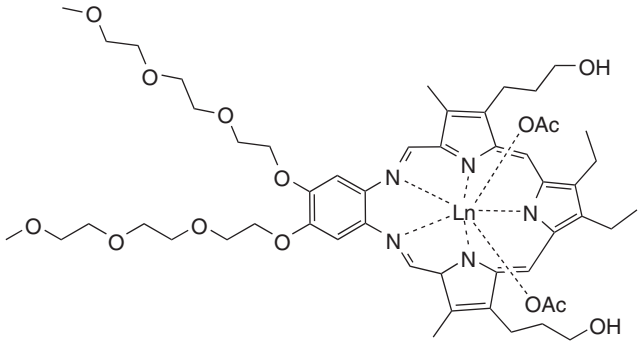


Figure 2 Ln = Gd: gadolinium texaphyrin is an effective radiation sensitizer active toward tumor cells. Ln = Lu: the lutetium complex has potentiality for photodynamic therapy, active for breast cancer or brain tumor cells. The presence of polyoxyethylenglycol chains decorating the ligand backbone make the complexes water soluble

3 PERFORMING THE STUDY OF A LANTHANIDE COMPLEX

Performing a complete study of a lanthanide complex is not trivial and takes time. Figure 3 is a summary of the principal steps for performing such a study. The first step consists in designing the ligand. Inspiration comes from the literature, in particular for the feasibility, but innovative aspects are of course welcome and necessary. Depending on the domain of applications, the properties expected for the probe will influence the design of the ligand. Some examples have been given in ***Lanthanides: Luminescence Applications*** regarding the possibilities of tuning the physicochemical properties of the lanthanide complex by modifying the ligand backbone. Computational chemistry can also be helpful at this step, as great improvements of the calculation models have been implemented.

The next step will then consist in obtaining the ligand, and that is the first difficulty when going back to the laboratory. The ligand must be obtained, isolated, and fully characterized by different analytical methods. The third step will deal with the synthesis of the lanthanide complexes. They also have to be fully characterized and to be stable ones (which can be proved by several techniques, as illustrated below).

Once the physicochemical study is performed and the results are satisfying, it will be time to start the investigation of the photophysical properties. This study will be done with complexes containing several lanthanide ions in order to get different data. The nonemitting ones (Ln = La, Lu, Gd, etc.) will give ligand-centered information such as the position of the singlet state (at room temperature) and the triplet state (at low temperature) by recording the emission

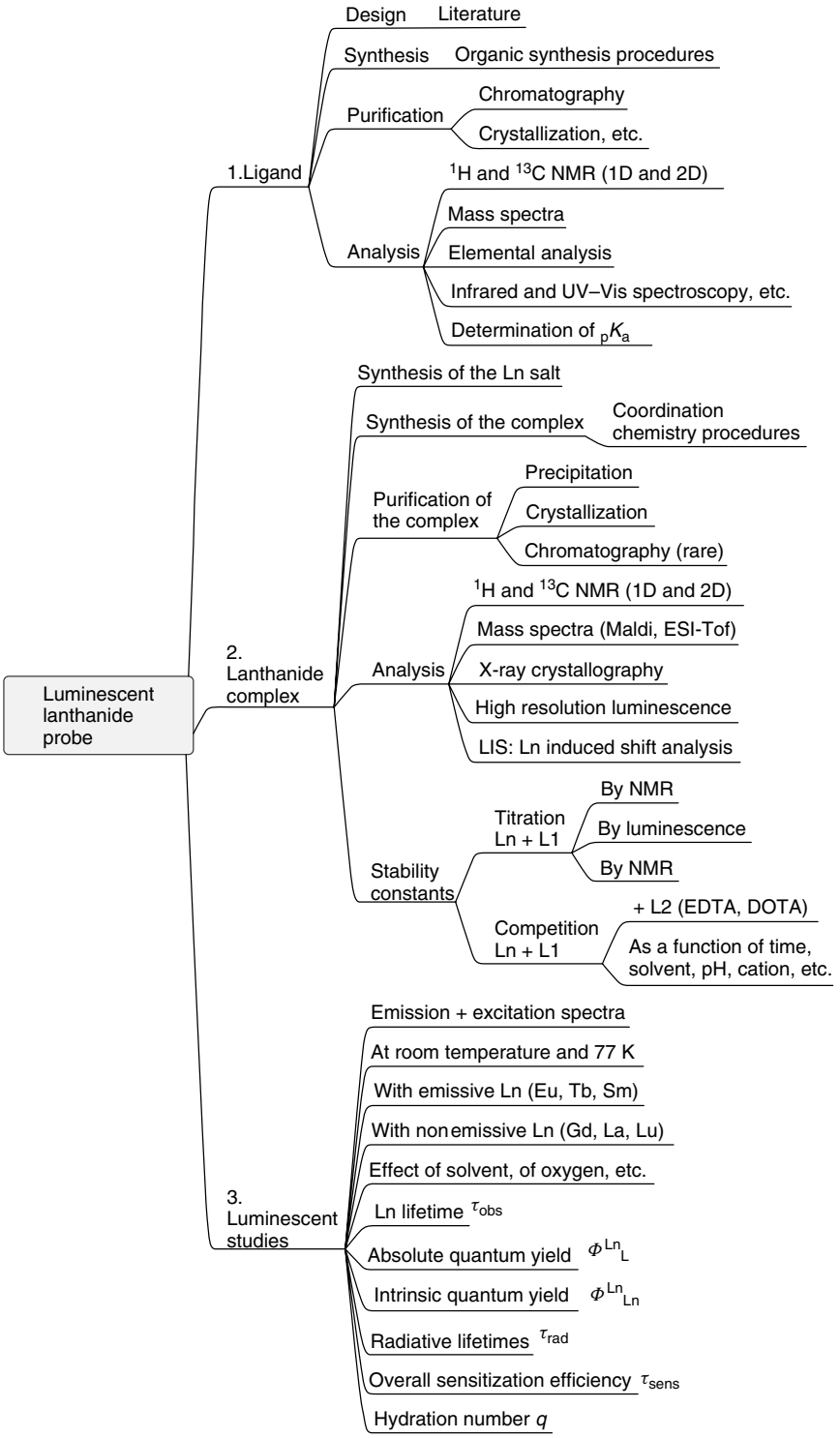


Figure 3 Summary of the main steps to perform the study of a lanthanide complex. This list is nonexhaustive, and the items listed here are illustrated throughout the article

spectra with and without delay. In parallel, the emissive lanthanide ions will give information regarding the metal-centered properties of the complex (Ln = Eu, Tb, Sm, etc.). The influence of several external factors, such as the solvent effect and the influence of the oxygen (known to have a quenching effect on the luminescence of the excited state of the lanthanide ions) will be studied among other factors.

A comparison of the photophysical data of the complexes (Ln^{III} lifetimes τ_{obs}, absolute Φ_L^{Ln} and intrinsic Φ_{Ln}^{Ln} quantum yields, radiative lifetimes τ_{rad}, and overall sensitization efficiency η_{sens}) with the literature will help estimating the importance of these complexes to act as probes for several applications. Only the most interesting probes will be tested for applications; among those, one can cite electroluminescent compounds, LEDs, or any device using the energy conversion properties. The water-soluble complexes can also be used as sensors or for bioapplications. We will now go through each of these steps for establishing the interest of the helicates before applying them for various bioapplications.

4 THE CHOICE OF THE LIGAND

4.1 Synthesis

The difficulty of synthesizing the ligand should never be ignored, and it often takes longer time than expected. When designing the ligand, one has to take into account the number of steps, the price of the starting materials, their possible toxicity, and the time-consuming separation and purification steps. In any case, the goal is to access quite easily a ''reasonable amount'' of the desired ligand, whatever the strategy. The term ''reasonable amount'' has still to be quantified, which is always difficult. However, depending on the molecular weight and on the number of experiments planned, one batch of approximately 50–100 mg of the ligand is generally sufficient to complete the study. If the ligand is found to be of great interest, it will be time to rationalize the synthesis strategy and optimize the different steps without forgetting that any scale-up process would certainly proceed by a totally different strategy.

Accessing the first ligands $H_2\mathbf{L}^{\mathbf{C2}}$ and $H_2\mathbf{L}^{\mathbf{C3}}$ took time, and two different strategies were developed. In the first case, the starting material was chelidamic acid, and the strategy implied the introduction of the polyoxyethylene arm in para position through a Mitsunobu reaction in an early step of the creation of the ligand backbone.[6] In the second strategy, the ligand backbone was first created using drastic conditions (polyphosphoric acid at 210 °C) and then the water-solubilizing arm was inserted in the R^3 position.[7] These strategies were then easily applied to new generation of ligands and gave access to the different candidates depicted in Figure 1. All the ligands are obtained in a reasonable yield and are water soluble (except $\mathbf{L}_A$ and $\mathbf{L}_B$).

4.2 Acidity Constants

The carboxylic-containing ligands are referred to as $H_2\mathbf{L}^{\mathbf{Ci}}$ labels and those containing phosphonic acid moieties as $H_2\mathbf{L}^{\mathbf{Pi}}$ ones, where C and P indicate the nature of the coordinating unit. The notation also implies two protons that are indicative of the presence of protonated carboxylic or phosphonic acid moieties. It indicates that the ligands were isolated in an acidic form. However, several protonation sites are present in solution, which can be protonated or not depending on the pH. Moreover, the coordination of the ligand to a lanthanide ion is *favored* when the coordination site is deprotonated (carboxylate form $RCOO^-$ rather than RCOOH) but is not precluded in its protonated form (***Carboxylate*** and ***Lanthanide Complexes with Amino Acids***). It is therefore important to get information about the acidity constant of the carboxylic acid moieties and of the amine functions. Such a study can be performed by a so-called UV–visible titration by monitoring the evolution of the UV–visible spectra as a function of the pH. By fitting the data with appropriate software, it is possible to determine the acidity constants (pK_a values). Alternatively, a potentiometric titration can give access to the same results, even though the experimental requirements and limitations of each method are different.

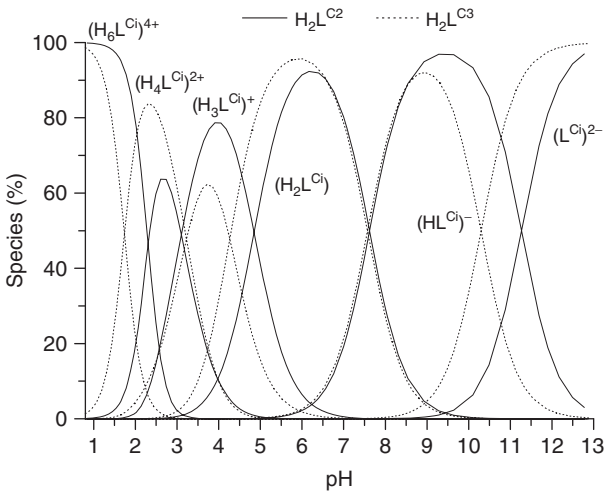


Figure 4 Distribution diagram as a function of pH for H_2L^{C2} and H_2L^{C3} ligands. (Taken from thesis report of S. Comby.[8])

From these pK_a values, the distribution diagram of the different species as a function of pH is a convenient way to visualize the predominant species in solution at a given pH value. In Figure 4, both distributions of $H_2\mathbf{L}^{\mathbf{C2}}$ and $H_2\mathbf{L}^{\mathbf{C3}}$ are represented as a function of pH. When working in buffered water solution, for instance, at physiological pH (pH 7.4), two main species are present, $(H_2\mathbf{L}^{\mathbf{C}})$ and $(H\mathbf{L}^{\mathbf{C}})$. The position of insertion of the polyoxyethylene arm (R^2 or R^3 position in the ligand backbone) is then noninnocent even if of moderated effect.

5 FORMATION OF THE COMPLEXES

5.1 Synthesis

The complex is generally synthesized in a solvent in which both the ligand and the lanthanide ions are soluble, and often the reaction is performed at room temperature in the

presence of stoichiometric amounts of lanthanide vs ligand (Ln:L ratio). There are always exceptions, for instance, some complexes with porphyrin derivatives will form with difficulty so that the reaction will be completed in high boiling solvents (such as 1,3,5-trichlorobenzene). Ideally, the reaction can occur in a solvent in which the complex is insoluble, for ease of purification, but in most cases it will be prepared in the same solvent in which the study will be performed.

When complexing the ligand with the lanthanide ion, many processes occur, including desolvation/solvation processes and successive formation of intermediate species (***Lanthanides: Coordination Chemistry***). In most cases, the complex is formed within seconds, with some exceptions such as 1,4,7,10-tetraazacyclododecane-1,4,7,10-tetraacetic acid (DOTA) complexes. In the latter, the reaction is very slow and the equilibrium will take several days to establish. As a consequence, at room temperature, the solution will be stirred for more than 5 days, whereas on gentle warming of the solution, the delay can be reduced to half (this is the ''golden rule'' in kinetics: on increasing the reaction from room temperature to 10 °C more, the rate should be increased by approximately a factor of two).

The reaction process and the formation of different intermediate species can be studied by steady-state techniques. In the case of the helicate family, a complete study has been performed in acetonitrile with $\mathbf{L^B}$, leading to the establishment of the different species successively formed, which is not reported here.[9]

The complexation reaction is performed with a lanthanide salt (perchlorate, nitrate, triflate, etc.) and sometimes directly from the lanthanide oxide Ln_2O_3 (for an example of such a synthesis the reader can refer to the synthesis of dipicolinic acid (H_2dpa) containing europium complex $Cs_3[Ln(dpa)_3]$, which is used as a reference for quantum yield determination).[10,11] The salt, for example, $Ln(ClO_4)_3 \cdot nH_2O$ is obtained by refluxing the corresponding lanthanide oxide (whose purity is generally very high >99.99% to ensure a correct photophysical investigation) in a minimum volume of a given acid (in stoichiometric amount), for instance, perchloric acid, up to the complete dissolution of the lanthanide oxide (this can take several days); a small amount of oxide is then added to ensure the completion of the reaction and that all the perchloric acid is consumed. The excess of lanthanide oxide is removed by filtration, and the lanthanide perchlorate salt is obtained from the solution by repeated precipitations or crystallizations to achieve high purity.[12] The solid always contains water molecules, part of which can be removed on drying in high vacuum. However, in the case of perchlorate salts, the amount of solid to be dried at one time should be less than 500 mg for safety reasons—since perchlorate derivatives are potentially explosive.

When the solvent for the complexation reaction is not water, the most dehydrated salts should be used to prevent interaction with water in the first coordination sphere, which can have a dramatic influence on the luminescent properties (quenching processes, ***Luminescence*** and ***Lanthanides: Luminescence Applications***). This can also be crucial for synthesizing complexes that are unstable in the presence of water molecules. In fact, working in absolute anhydrous conditions has been one of the key parameters to access complexes of lanthanides and has allowed the separation and purification of different lanthanide ions in the 1950s. On the other hand, when dealing with water-soluble complexes, no care has to be taken when using the lanthanide hydrated salt. Nevertheless, adding stoichiometric amounts of a lanthanide salt will require knowing the exact ratio of water molecules entrapped in the solid salt. This can easily be performed by determining the exact concentration of the lanthanide ion in a solution of the salt (with known concentration) by a well-known titration procedure in the presence of xylene orange and urotropine.[13]

Regarding the choice of the lanthanide salt, the nature of the counteranion (triflate, nitrate, perchorate, etc.) is not innocent, depending on the solvent in which the complex will be studied. Indeed, the solvation process is total in water, and the aqua anion will not interact, whereas, in an organic solvent, there are possibilities of coordination of the counteranion. As an example, triflate is more coordinating than a nitrate ion, and the choice of the counterions—with relatively weak or strong coordination abilities—may allow predicting the final structure of the lanthanide complexes.

Depending on the amount of ligand in hand, the complex can be synthesized and isolated, for instance, by precipitation or by crystallization; there are, however, few examples of purification by chromatography (by ionic exchange processes or by mass exclusion). Access to the isolated complex allows full characterization, e.g., by elemental analysis or, to a lesser extent, by high-resolution mass spectroscopy HR-MS (if the complex can be analyzed by such a method).

Alternatively, the complex can be synthesized in situ by using both ligand and lanthanide solutions with known concentrations (titration with xylenol orange). When working with water, both the ligand and the lanthanide solution have to be fresh, and at a known pH (not too basic to avoid the presence of hydroxide species). A buffer solution can be used, but in that case, no interaction has to occur between the complex and the buffering anion if it has a coordination ability. For instance, interaction with phosphate anions can be detrimental in the presence of complexes of low stability and because these anions are in a large excess (when working, for instance, in a buffer solution 0.1 M compared to a solution of the complex in the millimolar range). To prove that the complex is formed (the lanthanide ion has been totally consumed), the xylenol procedure can be used for a back titration (indirect titration, the presence of residual lanthanide ion would be evidenced); this can be performed only if the complex formed is very stable (to prevent transmetallation processes leading to destruction of the complex studied); this procedure is often used with DOTA or diethylenetriaminepentaacetic acid (DTPA) complexes).

5.2 Formation of 2 : 3 Complexes in Aqueous Solution

In the case of water-soluble helicate complexes, the formation of the 2 : 3 complex is expected to occur in water similarly to what has been reported previously in acetonitrile with $\mathbf{L^A}$ or $\mathbf{L^B}$ ligands, except if steric hindrance of the polyoxyethylene chains prevents it. The ligands and the complexes formed were all water soluble. As shown next, the structure was not disrupted by the presence of the arms. Unless stated, the studies mentioned in this article have been performed in water or buffer solution (Tris–HCl buffer at pH = 7.4). Several techniques help establish the presence of one major species in solution, such as NMR, mass spectra, or luminescence detection.

5.2.1 Mass Spectra

The formation of the helicates in water can be detected by electrospray mass spectrometry. For example, solutions have been prepared starting from the perchlorate salt of several lanthanide ions (Ln = La, Eu, Gd, Tb) and the free $H_2\mathbf{L^{POEt}}$ ligand (7×10^{-4} M in water in the presence of 10% acetonitrile to induce ionization). For each solution, the +2 charged species is detected. It is important to compare the shapes of these peaks and particularly their isotopic distributions with the calculated spectra. As observed from Figure 5, the spectra match the predicted ones.[14]

5.2.2 NMR Spectra

NMR spectra can be recorded in the presence of the ligand and a nonparamagnetic Ln ion, which gives an NMR spectrum shifted compared to that of the free ligand. ^{1}H-NMR is generally preferred for these studies and more rarely ^{13}C-NMR. The most shielded protons are the ones for which the environment is modified on coordination to the metal ion; generally, they are close to the coordination site. For instance, the pyridine protons belonging to the ligand are the most shifted on formation of the helicate compared to the free ligand.

Lutetium, lanthanum, and, to some extent, yttrium are often chosen in these NMR experiments, as they are nonparamagnetic ions. The presence of one main species is attested by the presence of one series of peaks, and the more symmetrical the coordination sphere the less peaks present (ligands are then equivalents at the NMR time scale). A titration can also be conducted with increasing amounts of the Ln^{III}, giving information on the formation of intermediate species. Alternatively, ^{1}H-NMR spectra of europium species (paramagnetic ion) have been reported in the literature, giving access to spectra with extended chemical shift scale and broader peaks but for which information can still be obtained for the coordination sphere of the lanthanide ion.

Figure 6 illustrates the difference in ^{13}C-NMR between free ligand $H_2\mathbf{L^{C2COOH}}$ and coordinated one (in deuterated solution). Few peaks are observed for the 2 : 3 Ln:L species, pointing to a symmetrical distribution of the ligands around the two cations; therefore, the three ligands are equivalent to the NMR time scale.

^{1}H-NMR titrations of $H_2\mathbf{L^{C2}}$ ligand with Lu^{III} perchlorate is also reported in Figure 7. While the free ligand spectrum is broadened and reflects a slow conformational exchange on the NMR time scale between at least two conformations, addition of the Lu^{III} salt results in the appearance of sharp signals concomitant with a complete disappearance of the ligand resonances at $R = 0.66$ equiv. This points to a single species being present in solution, which is the 2 : 3 Ln:L species. Again, the presence of one series of peaks indicates that the three ligands are equivalent at the NMR time scale, and thus indicates a symmetrical arrangement of the ligands wrapped around the two lutetium ions.

5.2.3 Luminescence Intensity

Another way to determine the presence of one main species in solution consists in monitoring the intensity of the

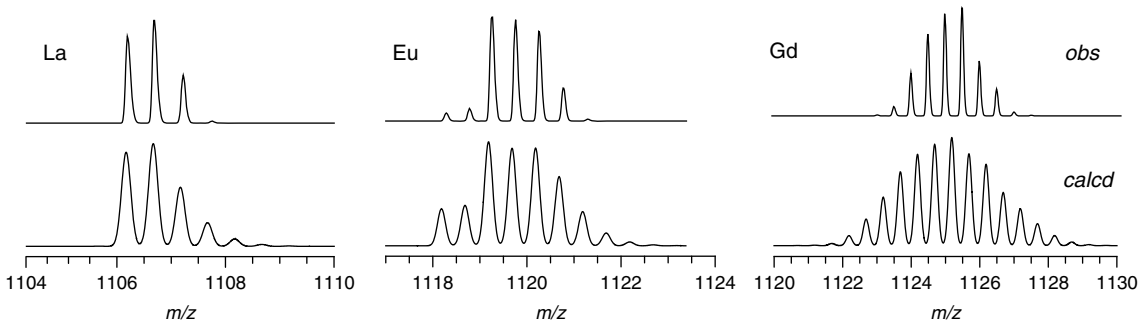


Figure 5 Parts of the observed electrospray mass spectra of solutions containing 2 : 3 stoichiometric amounts of Ln^{III} and H_2L^{POEt}, $[H_2L^{POEt}] = 7 \times 10^{-4}$ M in water/acetonitrile 90/10; calculated spectra are given for comparison. (Reprinted with permission from Ref. 14. Copyright (2009) American Chemical Society)

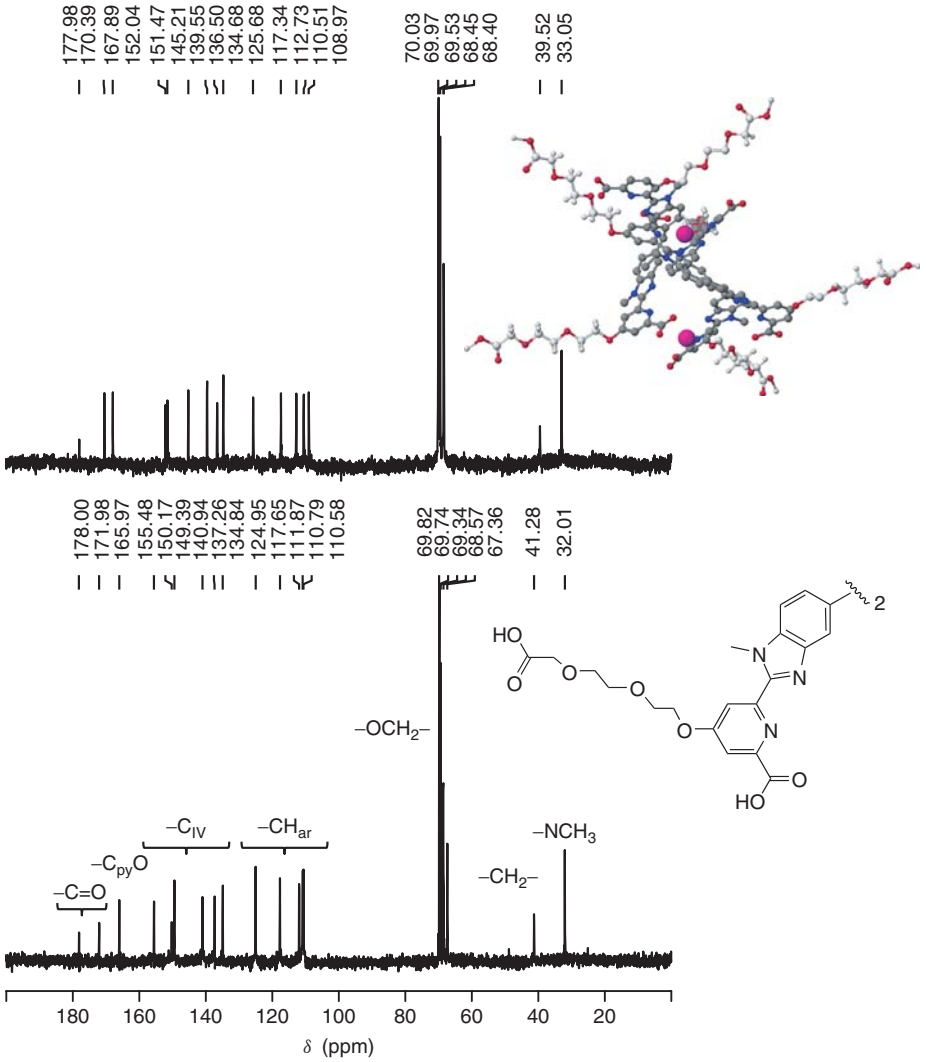


Figure 6 ^{13}C-NMR spectra of the free H_2L^{C2COOH} ligand (above) and of its 2:3 Lu:L complex (top). $[H_2L^{C2COOH}] = 8 \times 10^{-4}$ M. The chemical shifts in presence of the lutetium anions evidence the formation of the complex.[15]

luminescence as a function of the concentration of a lanthanide ion, for instance, Eu^{III}. As can be observed from Figure 8, the maximum intensity is reached in the presence of 0.66 equiv. of Eu^{III}, pointing to the presence of the 2 : 3 Ln:L species in solution.

5.2.4 X-ray Spectroscopy

Ideally, the complex should crystallize and its structure be elucidated by X-ray spectroscopy. It gives strong evidence of the coordination mode of the lanthanide ion in solid state, and this structure can be correlated to that existing in solution. One should never forget that the X-ray pattern gives access to the structure of the complex in the solid state and does not take into account the stability of the complex in solution. Therefore, it does not report potential decomposition of the complex, decomplexation due to solvent effect or hydrolysis, fluxional effect of the ligand, etc. Also, it may happen that a minor species does crystallize, which is not representative of the main species present in solution. This is why a comparison must always be performed between structures in the solid state vs those in solution before comparing their photophysical properties.

5.2.5 High-Resolution Luminescence Studies

No crystallographic structure was obtained with Ln-complexes containing $H_2\mathbf{L}^{Ci}$ or $H_2\mathbf{L}^{Pi}$, which can be explained by the presence of the six pendants polyoxyethylene arms, but yet can expect the helicate structure to be comparable to that of the 2 : 3 complex reported with $\mathbf{L}^{B}$ in acetonitrile. Some evidences of a similar structure were obtained on NMR studies of the complex and

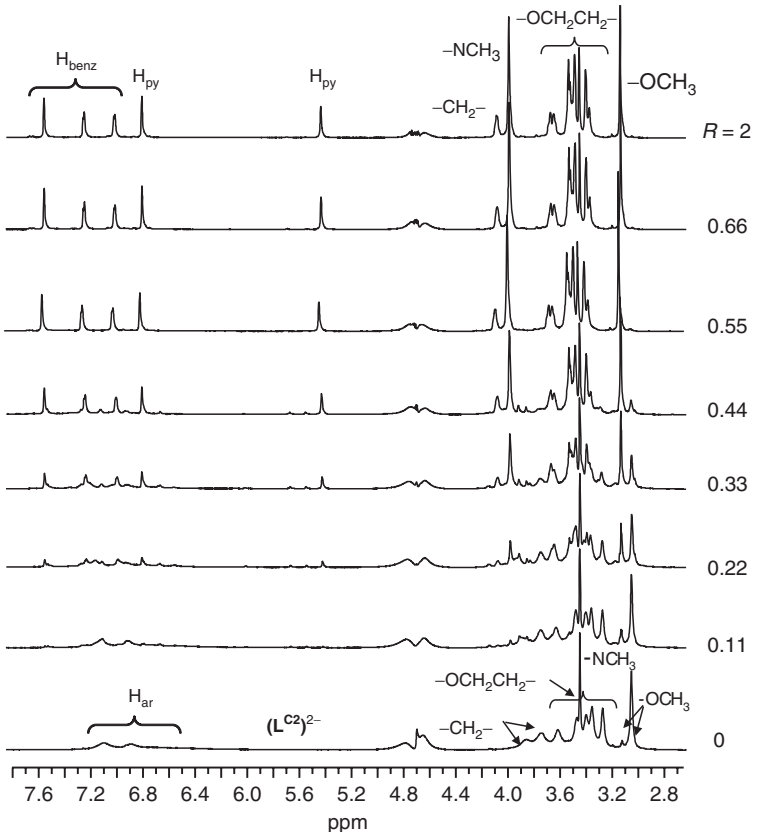


Figure 7 ^{1}H-NMR titration of H_2L^{C2} 10^{-3} M by $Lu(ClO_4)_3$ in Tris-d_{11}-DCl (0.1 M, pD = 7.8); R = $[Lu^{III}]_t/[H_2L_{C2}]_t$. (Taken from thesis report of S. Comby.[8])

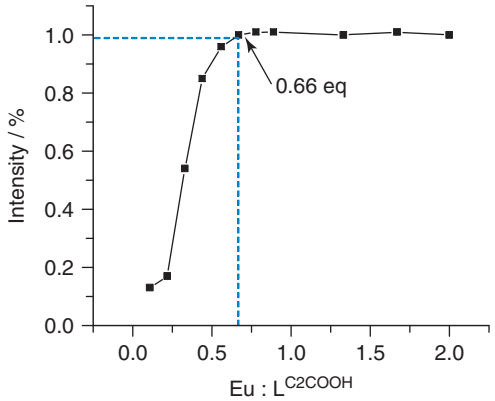


Figure 8 Luminescence intensity of H_2L^{C2COOH} in the presence of increasing amounts of $Eu(ClO_4)_3$, in Tris–HCl 0.1 M pH 7.4 [L] = 3×10^{-5} M, λ_{ex} = 320 nm.[15]

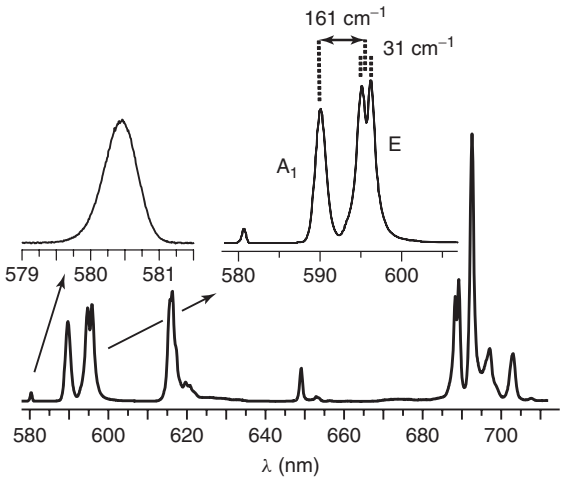


Figure 9 High-resolution luminescence spectrum of a stoichiometric 2 : 3 solution (Eu: H_2L^{C2}) in water/glycerol (9/1, v/v) at 10 K under ligand excitation (355 nm); $[H_2L^{C2}]t = 3 \times 10^{-4}$ M. (Reproduced from Ref. 17. © New York Academy of Sciences, 2008)

can be reinforced by high-resolution luminescence studies (***Lanthanides: Luminescence Applications***). High-resolution luminescence spectra are recorded at low temperatures (10 K on frozen solutions in water/glycerol solutions (9 : 1, v/v) (Figure 9). These spectra are analyzed in terms of group-theory considerations. In this case, it points to a pseudo-D_3

symmetrical environment around the lanthanide ions.[7] For more information regarding the splitting of a spectrum as a function of the symmetry around the lanthanide ions, the reader can access the review of Bunzli and Eliseeva.[16] In addition, a unique and symmetrical $^5D_0 \rightarrow ^7F_0$ transition is observed, indicating the presence of a single luminescent species in solution.

5.2.6 *Lanthanide-induced Shift (LIS) Analysis*

The last method presented here is LIS analysis.

We take advantage of the shifted signals of the spectra of complexes containing paramagnetic lanthanide ions with respect to the spectra of similar complexes with the nonparamagnetic ones (e.g., La, Lu). This is the concept of lanthanide-induced paramagnetic shift (LIS). Each H_i proton in contact with a paramagnetic lanthanide ion Ln_j will generate a LIS. It can be determined by subtracting the chemical shift in the presence of the isostructural diamagnetic lanthanide ion taken as a reference. Both contact (through chemical bonds) and pseudocontact (dipolar; through space) contributions are considered. The LIS of a proton, H_i, in a compound with one paramagnetic lanthanide ion Ln_j can be obtained by subtracting the chemical shift of a suitable isostructural diamagnetic reference from the measured chemical shift and is the sum of the contact c (through chemical bonds) and pseudocontact pc (dipolar; through space) contributions

$$\Delta_{i,j} = \delta_{i,j} - \delta_{i,\mathrm{dia}} = \Delta_c + \Delta_{pc} \quad (1)$$

Considering a threefold axis, equation (1) can be expressed as the following:

$$i, j = Fi \; <S_Z> \; j + C_J \; B_0^2 \; Gi \quad (2)$$

where the first term is the contact and the second term the pseudocontact term, respectively.

Both terms are characteristic of a given paramagnetic Ln ion, where:

$< S_Z >_j$ is the spin expectation value

C_j is the second-order magnetic axial anisotropy value for the free ion

$B_0{}^2$ is the ligand field parameter of the H_i nucleus

F_i is the hyperfine coupling constant of the H_i nucleus

G_i is its geometric factor given by $(3\cos^2\theta i - 1)/ri^3$ with r_i being the Ln–Hi distance and θ_i the angle between the Ln–Hi vector and the molecular axis (in the precise case, it is the Ln–Ln axis).

$< S_Z >_j$ and C_j values have been calculated according to the values reported in Table 1:

A conformational study of the complex is obtained by this method. It has been successfully applied to different helicates, such as heterobimetallic ones or more elaborated structures, in organic solvents.[18,19]

Table 1 Values of $< S_z >$ and C_j

	$< S_z >$	C_j
Ce	−0.974	−6.3
Pr	−2.956	−11
Nd	−4.452	−4.2
Sm	0.224	−0.7
Eu	7.5	4
Tb	31.853	−86
Dy	28.565	−100
Ho	22.642	−39
Er	15.382	33
Tm	8.21	53
Yb	2.589	22

5.3 Stability Constants

According to the data presented above, the presence of one main 2 : 3 Ln : L species has been established in water, corresponding to the 2 : 3 complex, but there is no information regarding the stability of this edifice in solution. For that reason, the stability constants have to be determined.

5.3.1 *UV–Vis Titration*

The stability constants can be determined by UV–visible spectrometry on addition of increasing amounts of Ln ions. The spectra present isosbestic points; their presence is generally believed to reflect the presence of equilibria between the different species present in solution. However, the definition of the isosbestic point according to IUPAC specifies that the presence of an isosbestic point does not prove that the reaction is quantitative.[20] The data can be fitted by an appropriate mathematical treatment, taking into account the general equation

$$m\mathrm{Ln}^{3+} + n\mathrm{L}^{2} \rightleftharpoons \Delta[\mathrm{Ln}_m(\mathrm{L})_n]^{(3m-2n)}$$

$$\beta_{nm} = \left[\{Ln_m(\mathrm{L})_n\}^{(3m-2n)}\right] / \left[Ln^{3+}\right]^m \cdot \left[\mathrm{L}^{2-}\right]^n$$

and giving access to the conditional stability constants (see Table 2). For instance, with $H_2\mathbf{L}^{C2}$ ligand, we get values amounting to $\log\beta_{13} = 18.1$, $\log\beta_{21} = 11.8$, and $\log\beta_{23} = 25.5$ for Eu^{III} and similar values for La and Lu ions (at pH = 7.4). Knowledge of these values allows constructing the distribution diagrams such as that illustrated in Figure 10. The main information from this diagram is that the 2 : 3 complex is the major species in solution for $0.47 < R < 1.65$.

In addition, it is possible to access the percentage of different species present in solution at a given concentration (this is calculated, taking into account the $\log\beta$ values). Figure 11 features the percentage of 2 : 3 species as a factor of the concentration. At $R = 0.66$ and a total $H_2\mathbf{L}^{C2}$ ligand concentration of 10^{-4} M, the main species is the helicate (95%), while the free ligand (1%) and the other two Eu^{III}

Table 2 Conditional stability constants for some helicates at pH 7.4 (Tris–HCl 0.1 M) and at 298 K

	$\log \beta_{13}$	$\log \beta_{23}$	$\log \beta_{21}$	References
$[Eu_2(\mathbf{L^{C2}})_3]$	18.1(2)	25.5(4)	11.8(5)	6
$[Eu_2(\mathbf{L^{C3}})_3]$	16.8(1)	23.4(1)	11.4(1)	7
$[Eu_2(\mathbf{L^{P3}})_3]$	18.3[(a)]	24.3(1)	11.2(1)	14
$[Eu_2(\mathbf{L^{P3OEt}})_3]$	n.d.	21.4(4)	n.d.	14
$[Eu_2(\mathbf{L^{POEt}})_3]$	17.9[(b)]	24.6(1)	11.6(2)	14
$[Tb_2(\mathbf{L^{POEt}})_3]$	18.3(2)	24.4(2)	11.6(1)	14

Standard deviation (2σ) are given within parentheses.
[(a)] Value fixed, otherwise convergence was not reached.

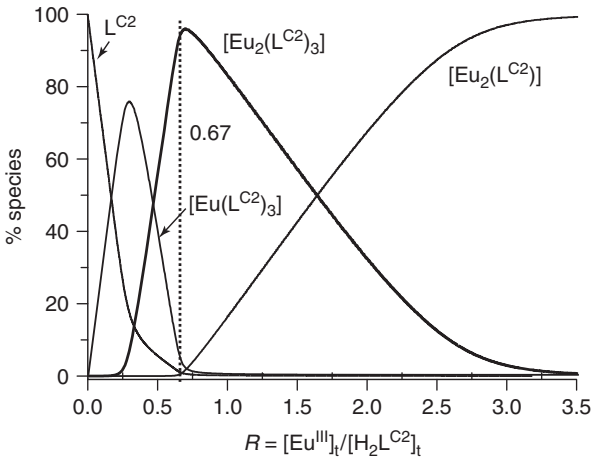


Figure 10 Distribution diagram for Eu^{III}, for $[H_2L^{C2}]_t = 10^{-4}$ M. (Reproduced from Ref. 7. © Wiley-VCH Verlag GmbH & Co. KGaA, 2008)

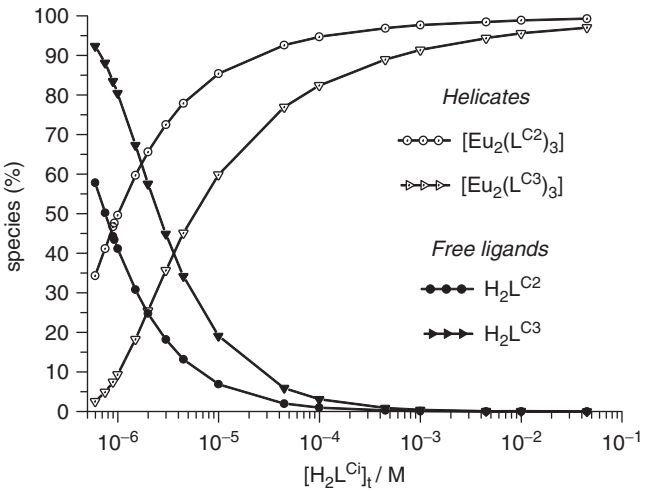


Figure 11 Percentage of $[Eu_2(L^{Ci})_3]$ helicates and uncomplexed ligands present in solution for different total ligand concentration; concentrations are displayed on a logarithmic scale to allow better visualization of the evolutions. (Taken from thesis report of S. Comby.[8])

complexes (4%) account for about 5% of the total species at equilibrium. On dilution of the solution by a factor of 10, $H_2\mathbf{L}^{C2}$ will still remain the main species in solution (95%), but the dissociation will increase. The phenomena prevails upto concentrations as low as 9×10^{-7} M. Working at high dilution is then possible with limited dissociation of the complex, which is of importance for biological applications (see below). Alternatively, the stability of the complexes with the $H_2\mathbf{L}^{C3}$ ligand is lower, and the concentration for which the 2 : 3 species remain predominant is approximately five times more.

Remark: It has been reported that the complex stability constants can alternatively be determined by using the variation of the luminescence as a function of the Ln:L ratio and by fitting the corresponding data with an appropriate mathematical model.

5.3.2 Conditional Stability Constants and pM Values

The difficulty is in fact to compare these $\log \beta_{23}$ values with other stability constants: $\log \beta_{13}$ for 1 : 3 complexes (such as betadiketonate complexes, dpa and derivatives, bipyridine, etc.) or $\log \beta_{11}$ for 1 : 1 complexes (DOTA, cyclam, etc.). This is the reason why Kenneth Raymond introduced the notion of conditional stability constant, which is determined at a fixed pH (pH = 7.4). The limitation of this method is that one predominant species must be present at this pH, which is not always the case, making the comparison sometimes impossible. He also introduced the notion of pM value, defined as -log[free metal ion], allowing a direct comparison of the affinity of a given ligand for an M ion at a precise pH, and taking into account the protonation competition. The conditions for establishing these pM values are well defined, in order to be able to compare the pM values. More information can be found in the literature.[21]

5.3.3 Competitive Luminescence Experiments

To ensure that the stability of the complex is comparable to already reported polyaminocarboxylates complexes, it is possible to perform a competitive luminescence

titration. The pieces of choice to conduct such a competition are commercially available ethylenediamine tetraacetate (EDTA) and diethylenetriamine pentaacetate (DTPA), with $\log \beta_{11}(\mathrm{Eu}) = 17.3$ and 22.4, respectively. They are devoid of an antenna group. The luminescence of $[\mathrm{Eu(EDTA)(H_2O)}_n]^-$ and $[\mathrm{Eu(DTPA)(H_2O)}_n]^{2-}$ complexes is then very weak, originating from direct f–f transitions. They display two main bands at 317 and 394 nm, which may be excited under long-wave UV excitation and which are assigned to the $^5\mathrm{H}_6 \leftarrow {}^7\mathrm{F}_0$ and $^5\mathrm{L}_6 \leftarrow {}^7\mathrm{F}_0$ transitions of the $\mathrm{Eu^{III}}$ ion, respectively. The lifetimes of the EDTA and DTPA complexes amount to 0.29 and 0.63–2.49 ms, respectively (the latter value corresponds to a different q value). The luminescence of these two compounds is noncomparable to any antenna-containing complex and can also be easily differentiated by the shape of the emission spectra (splitting of each band and to the integrated emission ratios $^7\mathrm{F_J}/^7\mathrm{F_1}$).

Several ways can be envisaged to reveal the competition with another ligand such as monitoring a change in the emission intensity, or in the lifetime of the $\mathrm{Eu}(^5\mathrm{D}_0)$ excited state as well as in the peaks ratio of the emission profile.

There are also several ways to deal with the luminescence intensity; among them one can imagine monitoring the luminescence intensity of the 2 : 3 complex as a function of increasing amount of EDTA or DTPA ligand. A decrease in the total intensity would result in decomplexation of the helicate to form the 1 : 1 DTPA or EDTA:Ln complex. On the contrary, in a solution of few luminescent EDTA or DTPA 1 : 1 Ln : L complexes, if an increasing amount of the ditopic $\mathbf{L^{C/Pi}}$ ligand is added, and results in the appearance of the luminescence intensity, it means that the emissive 2 : 3 Ln: $\mathbf{L^{C/Pi}}$ complex forms, pointing to the helicate being more stable than the 1 : 1 Ln : L complex with L = EDTA or DTPA.

From a practical point of view, the intensities are always corrected for the absorbance (E/A) of the solution at the excitation wavelength (323 nm in this case, referring to the maximum absorption of the $\mathrm{H_2}\mathbf{L}^{C2}$ ligand). For better accuracy, the $\mathrm{Eu^{III}}$ lifetime or the luminescence intensity is determined by monitoring the $^5\mathrm{D}_0 \rightarrow {}^7\mathrm{F}_2$ (615 nm) and $^7\mathrm{F}_4$ (691 nm) transitions ($\mathrm{I_{615}/I_{691}}$ ratio). In addition, it is possible to detect any change in the coordination sphere of the $\mathrm{Eu^{III}}$ ions by monitoring the variation in the integrated emission intensity ratios $\mathrm{I}(^5\mathrm{D}_0 \rightarrow {}^7\mathrm{F_J})/\mathrm{I}(^5\mathrm{D}_0 \rightarrow {}^7\mathrm{F}_1) = {}^7\mathrm{F_J}/{}^7\mathrm{F}_1$ [J = 0–4]; in that case, the purely magnetic dipole $^5\mathrm{D}_0 \rightarrow {}^7\mathrm{F}_1$ transition is taken as an internal reference.

As an illustration, the ratio of the intensity at 615 and 691 nm (I_{615}/I_{691}) has been determined as a function of time for a solution of $[\mathrm{Eu(EDTA)(H_2O)_3}]^-$ in the presence of 1 equiv. of $\mathrm{H_2}\mathbf{L}^{C2}$ (Figure 12). The rapid increase in the luminescence intensity is representative of the formation of the $[\mathrm{Eu_2}(\mathbf{L}^{C2})_3]$ complex in solution, with characteristic $^5\mathrm{D}_0 \rightarrow {}^7\mathrm{F_J}$ splitting. It points to the better stability of the helicate compared to the EDTA complex. The experiment has been continued over a period of 35 days, demonstrating the stability of the complex over time and that the equilibrium is really shifted in favor of the formation of the helicate.

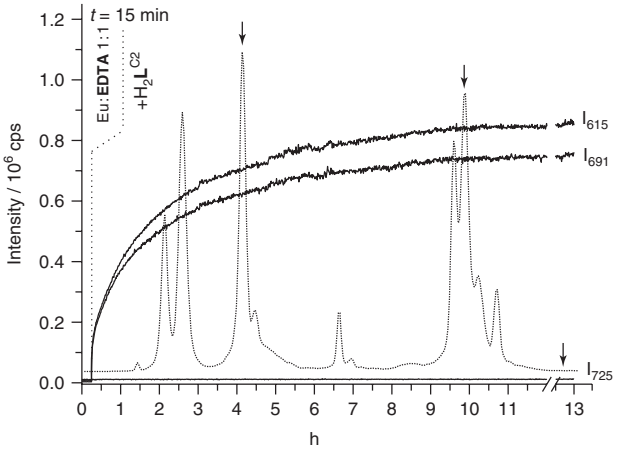


Figure 12 Rise in luminescence intensity (bottom) with time on adding 4.5×10^{-5} M $\mathrm{H_2}\mathrm{L}^{C2}$ to a solution of $[\mathrm{Eu(EDTA)(H_2O)_3}]^-$ 3.0×10^{-5} M in Tris–HCl 0.1 M; $T = 298$ K. (Taken from thesis report of S. Comby.[8])

5.3.4 *Kinetic Inertness of the Complex over Time*

The competition titrations presented in the previous paragraph are interesting to establish the stability of a given complex compared to another. They are also useful tools to ensure the kinetic inertness of the complex over time. Any decrease of intensity would indicate a modification of the coordination sphere. On release of any ligand, the lanthanide ion would be exposed to water molecules in its vicinity, thus causing a decay of its luminescence intensity. Nevertheless, in such long experiments, one has to ensure that the lamp is stable over time, that no evaporation of the solution or precipitation takes place over time, etc.

5.4 Mimicking the Conditions Encountered in the Cell

The same kind of experiments can be applied to test various conditions in the medium (e.g., pH effect, competition with anions, cations, etc.). It is of great importance to guarantee the integrity of the lanthanide complex in the composite environment of the biological medium. Any decomposition/exchange reaction of the Ln ions would result in a loss of the luminescence intensity and a possible toxic exposure of the cells to the free Ln ions. This means that the stability of the complex has to be checked under conditions as close as possible to those encountered within cells.

5.4.1 *pH Effect*

Contrary to commonly stated ideas, pH is not equal to 7.4 in all cell compartments, and harsh conditions can be

found in some specific organelles, such as pH = 2. At this pH and after 1 day, it was checked that more than 85% of the $[Eu_2(\mathbf{L}^{C2})_3]$ helicate remained undissociated, (whereas most of the lanthanide complexes would be dissociated under such conditions).

5.4.2 *Influence of Endogenous Anions such as Ascorbate or Citrate*

Citrate and ascorbate (the strongest antioxidant in the body, ubiquitous within cells) are present in high concentrations (for instance, [ascorbate] = 0.2 mM) and possess a high complexing ability ($\log \beta_{11} \approx 8$). Furthermore, ascorbate can efficiently quench the europium excited state (via an electron or charge transfer process). Similar to what has been reported for the polyaminocarboxylate ligands, citrate has no antenna, so that Eu:citrate solution exhibits weak luminescent intensity. Addition of 100 equiv. of ascorbate or citrate anions to a solution of $[Eu_2(\mathbf{L}^{C2})_3]$ complex results in neither any loss of its luminescence nor any change of the $^7F_J/^7F_1$ ratios, even after 1 month. The complex is then stable—over time—over huge concentration of these anions.

5.4.3 *Transmetallation Process (Zn^{2+}, Ca^{2+})*

The possibility of cation exchange—transmetallation—is always problematic and can be favored by the high concentrations of some cations present within cells. For instance, Zn^{2+} and Ca^{2+} are present in low concentrations in the cytoplasm (10^{-11} M) but reach 10^{-3} M in some vesicles. Several experiments were conducted with $[Eu_2(\mathbf{L}^{C2})_3]$ in the presence of Zn^{2+} (100 equiv.), resulting in a decrease in the Eu^{III} luminescence and correlating with an increase in the ligand fluorescence. This is due to a transmetallation process. However, in presence of 10 equiv. of zinc cation (which is still larger than concentrations typically encountered in biological media) and after 24 h, 90% of the $[Eu_2(\mathbf{L}^{C2})_3]$ still remains undissociated in solution. The stability of the helicate is then still acceptable for bioapplications.

With these experiments, it was possible to ascertain good stability of the helicate not only in solution (water or buffered solution or culture media) but also in the stringent conditions that can be found in biological media. Having established the thermodynamic stability of the complexes as well as their kinetic inertness, it is time to study their luminescent properties in detail.

5.5 Luminescent Properties of 2 : 3 Complexes in Water

The concepts for understanding the luminescence of these 2 : 3 complexes have been fully explained in ***Luminescence*** and illustrated in ***Lanthanides: Luminescence Applications***. They are not discussed here again, but focus is on the information gained for this family of complexes, regarding the spectra of Figure 13 for $[Ln_2(\mathbf{L}^{C2})_3]$ complexes.

- The excitation and absorption spectra match with each other, pointing to the efficient antenna effect provided by the ligand on excitation of the complex.

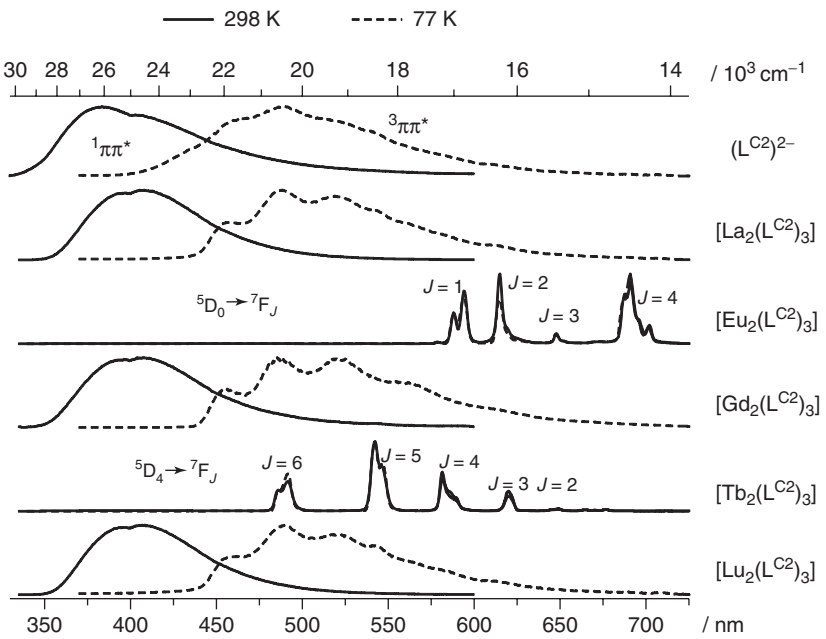


Figure 13 Luminescence of ligand H_2L^{C2} and its Ln^{III} 2:3 complexes, recorded at 298 K (—) without delay and at low temperature (—-) with a 0.05-ms delay; $[H_2L^{C2}]_t = 4.5 \times 10^{-5}$ M (Taken from thesis report of S. Comby.[8])

- The excitation maximum is located above 320 nm. Ideally it should be located above 350 nm to be in the near-visible range; however, even so, it is already possible to use plastic or glass cuvettes instead of quartz ones. The interest is to be able to work later with biological material, and most of the cell assays are performed in sterile plastic material.
- By comparing the emission spectra of free ligand or $[Ln_2(\mathbf{L}^{C2})_3]$ complexes with nonluminescent Ln ions (Ln = La, Lu, Gd) with emissive ones (Ln = Eu, Tb, Sm), no residual signal is observed originating from the singlet $^1\pi\pi^*$ or triplet state $^3\pi\pi^*$ for the spectra of Tb or Eu; only the characteristic sharp lines typical of the $^5D_I \rightarrow {}^7F_J$ transitions (Eu: $I = 0$; Tb $I = 4$) are observed. This is indicative of an efficient intersystem crossing ISC process (see ***Luminescence***) and an efficient energy transfer to the Ln ions (with no back transfer from the excited state of the lanthanide ions to the triplet state of the ligand).

The high-resolution spectra of the $[Ln_2(\mathbf{L}^{C2})_3]$ spectrum has been performed at 77 K and gave information regarding the geometry of the coordination sphere (Figure 9); the data have been presented above.

The luminescence data are to be fully characterized. It means measuring the quantum yields and evaluating the efficiency of the sensitization vs the intrinsic quantum yield and the lifetime. A careful measure of the data must be performed, in particular for the determination of the quantum yields. Two kinds of measurements can be done:

- In the first strategy, the quantum yield is determined comparatively to a sample for which the quantum yield is well known. Organic molecules and in particular are fluorescent dyes being often used as references, with high quantum yields (for instance, rhodamine 101 has a quantum yield $\Phi = 98 \pm 2\%$ in an ethanol solution[22] and quinine sulfate in sulfuric acid 1 M has a quantum yield of 54.6%)[23]. However their broad band emission does not compare well with the narrow spike lines arising from the emission of the Eu or Tb ions. It is then better to use a complex as a reference. The most classic ones are $Ln(terpy)_3](ClO_4)_3$ (Ln = Eu, Tb) 10^{-3} M in anhydrous acetonitrile, with quantum yields amounting to 1.3% for Eu^{III} and 4.7% for Tb^{III} or $[Ru(bpy)_3]Cl_2$ (bpy = bipyridine) with $\Phi = 2.8\%$ in air-saturated water.[24–26] The difficulty to handle the terpyridine complexes is that the complexes are moisture sensitive so that the preparation of the sample is quite difficult. More recently, we introduced $Cs_3[Ln(dpa)_3]$ (Ln = Eu, $\Phi = 24 \pm 2.5\%$, Tb, $\Phi = 22 \pm 2.5\%$) as water soluble references, which are stable complexes easy to handle.[11]
- The second method consists in using an integration sphere to directly measure the quantum yield by an ''absolute'' method.[27] This can also be applied to solid-state samples.

The measurement of the absolute quantum yield Φ_L^{Ln} has to be completed by the determination of the lifetimes τ_{obs} and the radiative lifetimes τ_{rad}, giving access to the intrinsic Φ_{Ln}^{Ln} quantum yields, and overall sensitization efficiency η_{sens}. These values are sometimes neglected; however, they allow a better understanding of the electronic structure of the ligand and therefore of the influence of the ligand for sensitizing the lanthanide ion. They can allow a better prediction of the properties of the complexes. For a better definition of each of these values, the reader is referred to ***Luminescence***, and for a discussion of the influence of these parameters within the helicate families, to the article of Bünzli *et al*.[28]

The data of the helicates $[Ln_2(\mathbf{L}^{C/Pi})_3]$ are presented in Table 3. The quantum yields for $[Eu_2(\mathbf{L}^{Ci})_3]$ complexes are around 20%, (within exceptions of $i = 4$, 6) and for $[Eu_2(\mathbf{L}^{POEt})_3]$ ($\Phi_L^{Eu} = 25$), which is highly sufficient for application in biological material. On the other hand, the two Tb complexes with higher quantum yields are $[Tb_2(\mathbf{L}^{Ci})_3]$

Table 3 Comparative photophysical data for the Ln^{III}-centered luminescence of the $[Ln_2(L^{C/Pi})_3]$ helicates with Eu^{III} and Tb^{III}, at room temperature, pH 7.4 (Tris buffer 0.1 M solution), $[L]_t = 10^{-4}$ M: Ln^{III} lifetimes tobs, absolute $\Phi^{Ln}{}_L$ and intrinsic $\Phi^{Ln}{}_{Ln}$ quantum yields, radiative lifetimes τ_{rad} and overall sensitization efficiency ν_{sens}

Ligand	Φ_L^{Eu} (%)	$\tau_{obs}(^5D_0)$ (ms)	$\tau_{rad}(^5D_0)$ (ms)[a]	Φ_{Eu}^{Eu} (%)[b]	η_{sens} (%)[c]	Φ_L^{Tb} (%)	$\tau_{obs}(^5D_4)$ (ms)	References
H_2L^{C1}	24 ± 2[c]	2.4 ± 0.1	6.8 ± 0.3	37	67 ± 10	1.2 ± 0.2[c]	0.050 ± 005	6
H_2L^{C2}	21 ± 2	2.4 ± 0.1	6.9 ± 0.3	36	58 ± 8	11 ± 2	0.65 ± 0.02	6
$H_2L^{C2'}$	19 ± 2	2.4 ± 0.1	6.6 ± 0.3	37	52 ± 7	10.9 ± 0.3	0.66 ± 0.02	29
H_2L^{C3}	11 ± 2	2.2 ± 0.1	6.2 ± 0.3	36	30 ± 5	0.34 ± 0.06	0.39 ± 0.04	7
H_2L^{C4}	2.52 ± 0.02	15 ± 2	6.4 ± 0.2	40	38	2.5 ± 0.3	0.12 ± 0.01	30
H_2L^{C5}	9 ± 1	2.3 ± 0.2	6.7 ± 0.3	37	35 ± 4	0.31 ± 0.05	0.040 ± 0.003	30
H_2L^{C6}	0.54 ± 0.06	0.35 ± 0.05	6.8 ± 0.4	8	4	n.d	$(10.5 \pm 0.08).10^{-3}$	30
H_2L^{P3}	6 ± 2	1.9 ± 0.1	4.2 ± 0.3	37	45 ± 6	n.d.	0.2 ± 0.07	14
H_2L^{P3OEt}	2.5 ± 0.3	3.23 ± 0.1	n.d.	n.d.	n.d.	0.46 ± 0.01	1.6 ± 0.6	14
H_2L^{P}	4.6 ± 0.7	2.54 ± 0.2	n.d.	n.d.	n.d.	0.22 ± 0.05	2.7 ± 0.4	14
H_2L^{POEt}	25 ± 1	3.2 ± 0.2	4.8 ± 0.3	37	67 ± 5	0.13 ± 0.01	2.5 ± 0.4	14

[a] Estimated error ±5%.
[b] Estimated error ±10%.
[c] Estimated error ±15%.

Table 4 Equations used for the determination of hydration numbers of the helicate complexes using phenomenological equations. Δk_{obs} represents the difference $k_{H_2O} - k_{D_2O}$ and q^N the number of amide N–H oscillators present in the first coordination sphere

Ln ions	Equation	Unit	References
Eu^{II}	$q = 1.2 \cdot (\Delta k_{obs} - 0.25 - 0.075 \cdot q^N)$	ms^{-1}	31, 32
	$q = 1.11 \cdot (\Delta k_{obs} - 0.31 - 0.075 \cdot q^N)$		
Tb^{III}	$q = 5.0 \cdot (\Delta k_{obs} - 0.06)$	ms^{-1}	32
Sm^{II}	$q = 0.026 \cdot k_{obs}(H_2O) - 1.6$	ms^{-1}	33, 34
	$q = 0.0225 \cdot (\Delta k_{obs} - 31.5)$		
Dy^{III}	$q = 0.024 \cdot k_{obs}(H_2O) - 1.3$	ms^{-1}	33
Nd^{III}	$q = 130 \cdot (\Delta k_{obs}) - 0.40$	ns^{-1}	35
Yb^{III}	$q = 1.0 \cdot (\Delta k_{obs} - 0.20)$	μs^{-1}	31

with $i = 2, 3$ ($\Phi_L^{Tb} \sim 10\%$); this reflects that the triplet state of the ligands are not as well located as for Eu^{3+}, which limits the energy transfer from the ligand to the excited state of Tb^{3+}. With smaller quantum yield ($\Phi_{LC2}^{Sm} = 0.38\% \pm 0.06$, $\tau_{obs} = 30.4 \pm 0.4$ ms), the Sm complex is not as interesting as Tb and Eu complexes in a first approach; however, these three complexes are characterized by very different lifetimes. This is an advantage because one can not only imagine performing a multilabel assay but also work on differences in lifetime for assessing different targets (see below).

The ligand $H_2\mathbf{L}^{C2}$ sensitizes the luminescence of several lanthanide ions at room temperature emitting either in the visible or NIR ranges. For more details, see the emission spectra in ***Lanthanides: Luminescence Applications***.

To finish, a last parameter of crucial importance is the determination of the solvent molecules present in the first sphere of coordination. In particular, the presence of water molecules with O–H has a quenching effect on the excited states of the lanthanide ions (this is why some experiments are performed in deuterated solvents such as D_2O, especially for NIR emitting probes, which limit the quenching effect, but they also limit the domains of applications). For more information, the reader is referred to ***Luminescence*** introducing the notion of hydration numbers q. These values are calculated from well-known phenomenological following equation $q = A \cdot [\tau_{obs}^{-1}(H_2O) - \tau_{obs}^{-1}(D_2O) - k_{XH}]$ with $k_{XH} = \alpha + \beta \cdot n_{OH} + \gamma \cdot n_{NH} + \delta \cdot n_{O=CNH}$ where $\tau_{obs}(H_2O)$ is the lifetime in water, $\tau_{obs}(D_2O)$ the lifetime in deuterated water. As $k = \tau_{obs}^{-1}$, the equation can be expressed as a function of $\Delta k_{obs} = k_{H_2O} - k_{D_2O}$. The equations also take into account the influence of the different oscillators in the first coordination sphere with the contribution of an OH oscillator (β), of a NH oscillator (γ), and of an amide O = CNH oscillator (δ value). An additional correction factor α takes into account the contribution of the water molecules in the outer coordination sphere. This formula has been widely used for different families of lanthanide-containing complexes, and refined as a function of the nature of the lanthanide cation or of the ligand. The results are reported in Table 4, and applied to the case of the helicates ions. Note that the units are totally different when working with visible emitting probes compared to NIR emitting probes.

The preparation of the sample is of crucial importance when working with deuterated water, as D_2O is very hygroscopic. A high quality of the solvent has to be chosen, with very low traces of water. Starting from a solid sample, which may contain hydrated water, the sample will have to be submitted to high vacuum to eliminate these water traces (without destroying the complex); starting from a water solution of the complex, the normal way is to perform several cycles of evaporation of the solvent, the solid being redissolved in D_2O, by working with Schlenk techniques, and the final solution will be transferred into quartz cells in a glove box. Care will be taken to prevent exposure of the quartz cells to the air humidity when performing the photophysical experiments by efficient closure system. Freshly prepared solutions will be preferred to ensure no contamination of the sample.

With the whole series of helicates, and whatever the lanthanide ions (Eu or Tb), it was found that q values were close to zero, pointing to the absence of water molecules in the first coordination sphere, in line with the good wrapping of the ligands around the lanthanide ions, which protect them from external interactions.

6 HELICATES ACTING AS BIOPROBES

As a conclusion of the data presented until now, the photophysical properties of the helicates are quite good, with intense luminescence recorded for several lanthanide ions, with relatively high quantum yields and long lifetimes, and this allows expecting that these probes might interact with some biological material without losing their luminescent properties. Therefore, their abilities as reporters of biological events can now be envisaged; the next chapter will treat several applications developed with these bioprobes, including an analytical application (determination of DNA concentration), bioimaging, and targeting abilities. Figure 14 is a summary

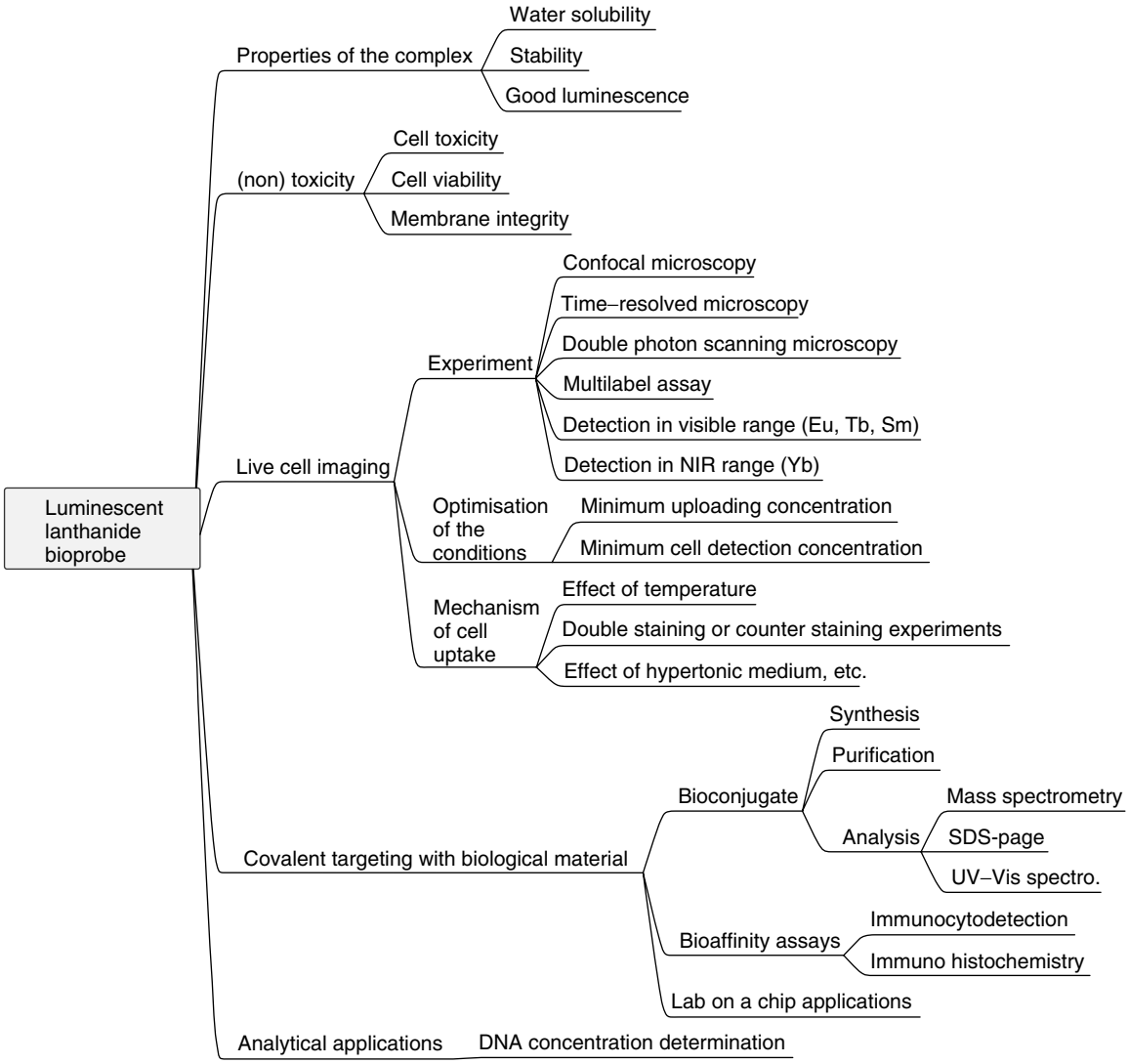


Figure 14 Examples of bioapplications developed with the helicates

of the applications and the kind of studies that have to be performed.

6.1 Interaction with DNA

The interaction of a luminescent probe with an analyte is expected to induce several effects, among them being modifications of the luminescent intensity, lifetime, etc. Positive as well as negative effects can be recorded. In other words, one can monitor a quenching or, on the contrary, the appearance of the luminescence of the probe.

For instance, ethidium bromide (ED) and acridine orange (AO) are well known to interact with DNA strands. We also noticed that AO dynamically quenches the luminescence of the $[Eu_2(\mathbf{L}^{C2})_3]$ complex. Taking advantage of that property led to the development of a new assay to determine DNA concentration: a solution containing both AO and $[Eu_2(\mathbf{L}^{C2})_3]$ (quenched by the presence of OA) will, on intercalation of AO into the DNA strand, show an increase in the $[Eu_2(\mathbf{L}^{C2})_3]$ luminescence that will be proportional to the amount of DNA present in the solution (Figure 15). This method was successfully applied to determine DNA concentrations down to $0.5\,ng \cdot \mu L^{-1}$ by monitoring the luminescence intensity as well as the lifetime as a function of [DNA]. The advantage is that the method is not specific to the nature of the DNA sample (mono vs double strand DNA vs circular DNA) and can be applied to samples from various origins: plasmids vs oligonucleotides vs genomic vs polymerase chain reaction (PCR) products. The method has an excellent accuracy, with standard deviation less than 4%. Moreover, it is independent of the pH (in the range 3–10) and does not suffer from the presence of contaminants such as salts, metals, or detergents usually found in biological samples (so that this procedure

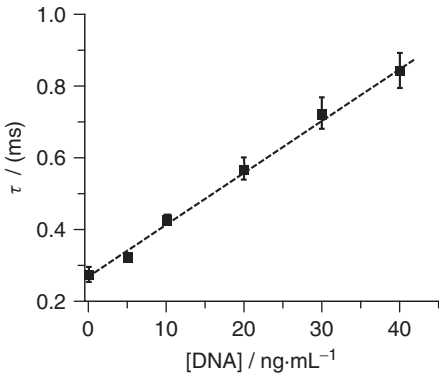


Figure 15 Linear increase in the Eu($^5D_0$) excited state lifetime as a function of the DNA concentration (0.1 mM $[Eu_2(L^{C2})_3]$ + 10 mg mL^{-1} AO in 0.1 M Tris–HCl buffer (pH 7.4). (Taken from Ref. **36**. Reproduced by permission of The Royal Society of Chemistry)

does not require tedious purifications of the sample before analysis). However, compared to already developed methods, the sensitivity of detection should be ideally increased to the picomolar range per microliter.

6.2 Live-Cell Imaging

6.2.1 Toxicity of the Complexes

The first step before interacting with cells consists in determining the nontoxicity of the complex. The WST-1 proliferation assay is widely used for this purpose: WST-1 dye (slightly red) is converted into a dark red formazan compound on enzymatic modification; this will occur only if cells are alive.[37] The assay is performed after incubation with increasing amounts of the complex to be tested. Cell viability will be tested by the same way, over a period of incubation of more than 24 h. Such an essay has been performed with $[Ln_2(\mathbf{L}^{C/Pi})_3]$ complexes and without any effect up to concentrations of 500 μM. There is no toxicity of the complexes toward cells, which can be expressed as following: the half maximal inhibitory concentration IC_{50} is more than 500 μM. This can be compared to some cyclen-based bioprobes for which IC_{50} values are around 200 μM.

The integrity of cell membrane has also to be considered. In that case, another colored assay is performed in the presence of lactate dehydrogenase (LDH).[38] The reaction will occur only if the enzyme is released in the media, implying a leaking of the cell components, thus indicating a degradation of the membrane structure. No effect was detected in the presence of the various Ln helicates complexes. The nontoxicity of the complexes is then proved.

After incubation of cells in the presence of the complexes, the presence of the complex in the cells can be detected by microscopy. Confocal microscopy is often used in laboratories, giving access to high sensitivity. Another possibility is to use time-resolved microscopy yielding improved signal to noise ratio and increased sensitivity compared to conventional microscopy.

6.2.2 Time-Resolved Imaging

In that technique, we take advantage of the long lifetime of the luminescence of the lanthanide ion: the fluorescence and scattering of the excitation light source is long gone when the lanthanide emission has just begun. This is a huge advantage because the autofluorescence of the biological material adds a considerable amount of noise to the measurement. By exciting with a pulsed light source, such as a flash lamp, and capturing the emission after a certain delay, we can get rid of all the background fluorescence and scattered light and ''take a picture'' of the lanthanide luminescence only. By repeating this measurement a certain time per second, the contrast will be greatly improved. Imaging with a time-resolved microscope thus allows visualizing some labeled parts or events in cellulo with a better signal to noise ratio and higher sensitivity than conventional fluorescence methods. For a complete review regarding time-resolved microscopy, the reader is referred to the article by H.J. Tanke.[39]

6.2.3 Minimum Uploading Concentration and Cell Detection Concentration

The lower the complex concentration for incubating cells, the better the interest for bioapplications. The detection limit will depend on the microscope, of course, and also on the properties of the complex within cells. For these reasons, the stability of the complex is of crucial importance, and there are always risks of quenching the excited state of the emissive lanthanide ions in the specific cell environment. Studies conducted in the presence of some cell components gave positive arguments, in favor of the stability of the complex in this environment; see above. In addition, by comparing the emission spectra of the Eu complex in solution vs in cellulo (as presented in Figure 16), the integrity of the helicate structure has been confirmed. No modification of the shape of the spectra or of the relative $^5D_0 \rightarrow {}^7F_J$ integrated values is evidenced. As a consequence, there is no alteration of the coordination sphere within cell, and the same helical structure is conserved.

The minimum concentration of the complex for the incubation process has been determined, as well as the detection limit of the complex within cells. With $[Eu_2(\mathbf{L}^{C2})_3]$ the first value was found to be 5 μM, while the later value was found to be less than 10^{-9}M, with uploading concentrations around 0.1 μM.

6.2.4 Localization of the Probe within Cell

A careful study must be conducted to determine the exact localization of the probe within a cell. The helicates

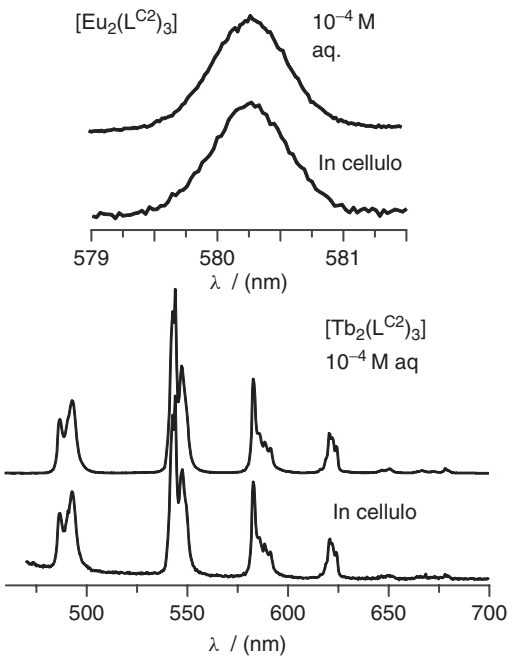


Figure 16 Comparison of emission spectra of $[Ln_2(L^{C2})_3]$ in water (10^{-4} M, pH 7.4, $\lambda_{ex} = 330$ nm) and in cellulo (HeLa cells, initial concentration 250 µM, incubation time: 15 h, 37 °C). (a) Ln = Eu; (b) Ln = Tb, $^5D_0 \rightarrow {}^7F_0$ transition; (initial concentration 500 µM, incubation time: 24 h, 37 °C). (Reproduced from Ref. 7. © Wiley-VCH Verlag GmbH & Co. KGaA, 2008)

complexes were found to be present in the cytoplasm and not in the nucleus. To get more information, numerous experiments are dealing with colocalization experiments in the presence of specific stains. For instance, LyzoTracker blue DN22 is a specific stain for secondary lysozomes and endosomes and ER-Tracker Blue-White DPX for endoplasmic reticulum (for more details, Invitrogen web site is very informative regarding staining experiments). Several colocalization experiments were performed, and it was clearly demonstrated that $[Eu_2(\mathbf{L}^{C2})_3]$ mainly stains vesicles localized within the endoplasmic reticulum.

6.2.5 *Cellular Uptake of $[Eu_2(L^{C2})_3]$ in Living Cells*

The way the complex enters cells is also very informative. Several investigations can be commonly conducted:

- Temperature effect: the mechanism can be active or passive. In a passive transport mechanism, no energy is required when a substance enters or leaves a cell. On the contrary, active transport mechanisms involve the cell to use cellular energy. The most common process is the conversion of ATP into ADP, releasing inorganic phosphor; proceeding through cascade reactions, protein pumps will be eventually activated to let molecules entering cells. An easy way to discriminate between the two pathways is to lower the temperature: at 4 °C the passive process will end, while no effect will be noticed if the process is active. In the presence of the helicates and with decreasing temperature, cellular uptake was not affected, thus revealing an active transport mechanism.
- An endocytotic uptake of the probe can be inhibited when the cells are placed in a hypertonic medium (e.g., 0.45 M sucrose), thus blocking receptor clustering, which is necessary for the formation of the endosomes. In the presence of the helicates in this medium, such an inhibition process was observed, with a decrease in cell uptake up to 85%. The internalization mechanism is then proved to occur through a receptor-mediated endocytosis pathway.

More details regarding the internalization process studies can be found in the literature.[40]

6.2.6 *Versatility of the complexes*

The $[Eu_2(\mathbf{L}^{C2})_3]$ complex has been systematically used for live-cell imaging experiments, but other ligands from Figure 1 have also been successfully applied to cellular uptake experiments. It was found that all the complexes permeate cells and are localized in the same region within cells, whatever the charge of the complex (neutral in most cases, positively charged with $[Eu_2(\mathbf{L}^{NH2})_3]$, or negatively charged with $[Eu_2(\mathbf{L}^{C2COO-})_3]$) (the extremity of the arms are fitted with carboxylate moieties at this pH). Even negatively charged species $[Eu_2(\mathbf{L}^{C2COO-})_3]$ could permeate cells, whereas the cell membrane is negatively charged, which should produce a repulsion with this latter complex. This entry can be explained by the nonspecific endocytosis mechanism leading to an internalization process of the complex, and by possible neutralization processes of the carboxylate functions that are present at the extremity of the arms by the numerous cations presents in the media. However, with the same loading concentrations, a dramatic decrease in the luminescence intensity was observed with $[Eu_2(\mathbf{L}^{C2COO-})_3]$ complex, indicating that the permeability was not as high as in previous cases (and/or that quenching of the excited state of the lanthanide would occur in this specific case, which is less probable).

Some minor changes in the ligand backbone of a complex can induce huge modifications. For instance, adding a methylene group in a cyclam complex provided important modifications regarding its biological activity.[41] For the helicate family, it was important to ensure that modifications of the chain would not transform its behavior.

$[Eu_2(\mathbf{L}^{C2'})_3]$ with a longer chain was developed and proved to interact similarly with cells as $[Eu_2(\mathbf{L}^{C2})_3]$, with very small changes in its physicochemical properties.[29] The presence of longer arms could be an advantage when linking the probe to a substrate, limiting steric hindrance and possible quenching effect due to the proximity of the substrate.

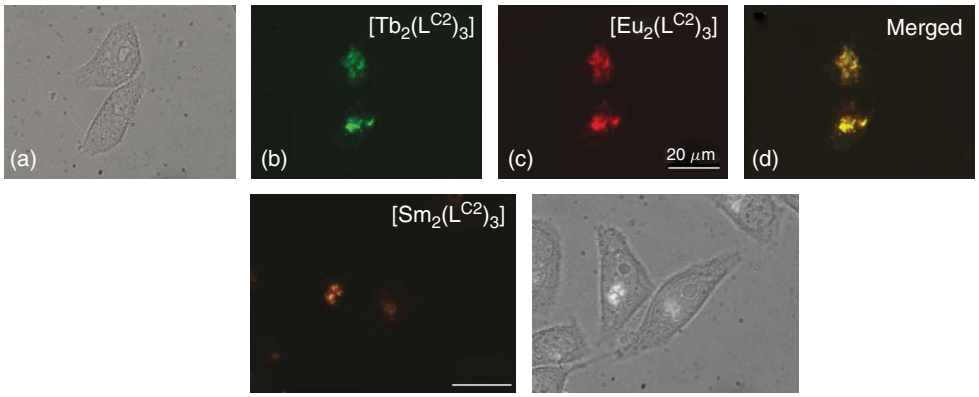


Figure 17 Time-resolved luminescence images of living HeLa cells loaded with different Ln^{III} complexes. (a). Cells were incubated in the presence of 100 μM $[Eu_2(L^{C2})_3]$ and $[Tb_2(L^{C2})_3]$ in RPMI-1640 for 6 h at 37 °C: (A) bright field; (B) Tb^{III} luminescence (excitation: 340 nm (Band pass, BP 70 nm) filter; emission: 545 (BP 35 nm) filter; delay time: 100 μs; 60 s exposure time); (C) Eu^{III} luminescence (excitation: 340 nm (BP 70 nm) filter; emission: 585 nm LP filter; delay time: 100 μs; 60 s exposure time); (D) merged images. (b). HeLa cells were incubated in the presence of 500 μM $[Sm_2(L^{C2})_3]$ in RPMI-1640 for 24 h at 37 °C; Sm^{III} luminescence (excitation: 340 nm (BP 70 nm) filter; emission: 420 nm LP filter, delay time: 50 μs; 60 s exposure time). (Taken from Ref. **40**. Reproduced by permission of The Royal Society of Chemistry.)

$[Eu_2(\mathbf{L}^{C5})_3]$ was specifically designed to shift the wavelength (from 330 up to 365 nm), which results in a loss of quantum yield (9%), but proved to be good enough in time-resolved spectroscopy and a better bioprobe than $[Eu_2(\mathbf{L}^{C2})_3]$ for confocal microscopy.[30] $[Eu_2(\mathbf{L}^{Cx})_3]$ with $x = 4$, 6 where two other probes developed for the same purpose, but their physicochemical and/or photophysical properties were not good enough to consider them for any application.

6.2.7 *Multilabel Assay*

In parallel, other lanthanide ions have also been used in these experiments, in particular, the $[Ln_2(\mathbf{L}^{C2})_3]$ complexes with $Ln = Eu^{III}$, Tb^{III}, and, to a lesser extent Sm^{III} (with overall quantum yields in water at pH 7.4 of 21%, 11%, 0.38%, and lifetimes amounting to 2.43 ms, 0.65 ms, and 30.4 μs, respectively).[7] It is possible to perform time-resolved microscopy with these different probes. They have specific spectral signatures, and the discrimination can be done as a function of the luminescence intensity as well as a function of the lifetime decay of the excited states. A proof of concept has been performed with HeLa cells and is presented in Figure 17. The present probes are localized within the same cell compartment. However, once being addressed to different compartments or different targets (such as receptor at the surface of cell membrane) a specific detection can be envisaged. This concept will be illustrated below.

6.2.8 *Detection in the NIR Range*

The $[Yb_2(\mathbf{L}^{C2})_3]$ complex was found to emit in the NIR region, exhibiting an overall quantum yield in water at pH 7.4 of 0.15% and lifetime of 4.40 ± 0.06 μs. Even if modest compared to complexes of lanthanide emitting in the visible range, these values are in an acceptable range for an NIR emitter so that Yb helicates can be considered for NIR detection (for more details regarding NIR emitting probes, see ***Lanthanides: Luminescence Applications***). It was even possible to detect the presence in cellulo of the Yb^{III} emission after incubating HeLa cells 24 h at 37 °C with a 250-μM solution of $[Yb_2(\mathbf{L}^{C2})_3]$ complex (Figure 18). The lifetime of the probe in cellulo was of 4.3 ± 0.1 μs totally in line with the value found in aqueous solution.

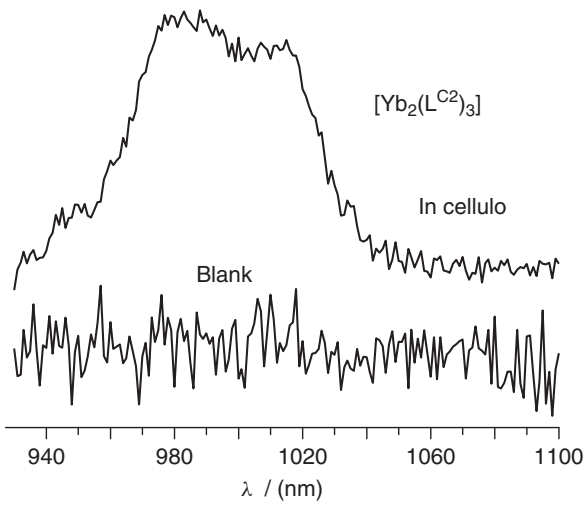


Figure 18 Emission spectrum of $[Yb_2(L^{C2})_3]$ (24 h incubation at 250 μM, $\lambda_{ex} = 330$ nm/Bp = 14 nm and $\lambda_{em} = 930-1100$ nm/Bp = 14 nm, integration time 1 s). (Reproduced from Ref. 7. © Wiley-VCH Verlag GmbH & Co. KGaA, 2008)

6.2.9 Interest and Limitations of the Use of the Helicates for Imaging

As already stated, helicates are water soluble and demonstrated a good ability to permeate cells, with no toxicity. The complex does not dissociate after internalization of the probe, with no alteration of its structure (coordination sphere), yet with a decrease of the quantum yield and the lifetime (within experimental errors). This bioprobe stains cells for a long time, without any alteration during cell division, and can be detected with low limit detection. Cell uptake is performed in presence of low concentration of helicate, and is neither dependent on the ligand structure nor on the nature of the lanthanide ions. Several cell lines were tested, in suspension or adherent cells, and no difference in cell permeation was detected. The versatile character of the bioprobe can be advantageous in some cases, with few limitations of its use, and further developments could design a heterobimetallic helicate, with two distinct lanthanide ions encapsulated, emitting in two different ranges (two colors in the UV–vis range, or one color and one ion emitting in NIR range, for instance). Another possibility consists in developing a helicate containing a lanthanide together with a d element; the latter might exhibit a magnetic signal or can be submitted to heating processes. However, the cell permeation process (endocytosis) is not specific to the cell, and thus these bioprobes cannot target specifically a cell line mixed with another one. This is the disadvantage of these bioprobes. Unless another entry pathway can be developed, the problem will not be overcome, and the huge molar weight of the probes (around 2500 $g \cdot mol^{-1}$) is not favorable to other processes. To specifically target a given cell, it is rather advised to develop a recognition process at the surface of the cell; this is what was then undertaken.

6.3 Ability of the Probe to Covalently Link a Given Target

6.3.1 Formation of the Bioconjugate

The most classic way to covalently link a given biological target consists in creating a peptide/amide bond (–CONH–) between two entities containing an amine and a carboxylate function. Depending on the amine or carboxylic pendants functions being present at the surface of the target, which are classically residues of the amino acid belonging to a protein or a peptide, the bioprobe will possess a carboxylate or an amine function, respectively, able to interact with the biological target. These carboxylate or amine functions should be activated prior to the coupling reaction. This reaction has to be optimized, taking into account several factors: (i) the nature of the constituents of the buffer solution, which should not react with the activated species leading to undesirable side reactions; (ii) the choice of the pH value that would favor the activation of the carboxylic function belonging to the bioprobe, without altering it by hydrolysis or any secondary reaction; at the same time, it should be basic enough to favor the presence of the amine acting as nucleophiles rather than inactive ammonium residues: for instance, a coupling with aliphatic amines such as lysine residues ($pK_a \approx 9.2$) occurs above pH 8.0; (iii) presence of these nucleophilic species at the surface rather than being internal, to favor the probability of the coupling reaction; this depends on the conformations of the protein, influenced among others factors by the pH of the solution; (v) the time of the reaction; (vi) the temperature; (vii) the nature and the number of equivalents of the activating species, etc. All these parameters have to be monitored to obtain the expected coupling reactions.

With respect to these coupling reactions, one should consider that a higher degree of linking is not always optimal: even if the size of the protein is most of the time much larger than the one of the bioprobes to be coupled, the presence of too many bioprobes at the surface may alter the conformation of the protein, resulting in a loss of its activity. It can also prevent interaction with other species, such as the substrate of the enzyme, thus also altering its activity. In addition, self-quenching effects can occur if numerous bioprobes are in a close contact.

Many activation processes for coupling biomaterial or proteins are a source of inspiration. For more details, see the book of Hermanson dealing with bioconjugate techniques.[42] One of the most classical reactions is performed with water-soluble carbodiimide crosslinker such as 1-ethyl-3-[3-dimethylaminopropyl]carbodiimide hydrochloride (EDC) as an activation agent, sometimes followed by a second activation process in the presence of *N*-hydroxsuccinimide (NHS) or sulfo-NHS, prior to coupling with an amine. These NHS additives generally increase the yields and lower the amount of side reactions. When working with EDC crosslinking agents, the reaction does not require the presence of organic solvents, which would anyway be detrimental for the protein conformation; in addition, the excess of activating agents can be easily removed by acidic aqueous treatments.

Sometimes, it can be advantageous to monitor the activation reaction by a color change, including quantitative measurements performed by UV–visible spectrophotometry. Such an approach has been applied to Eu-containing helicates $[Eu_2(\mathbf{L}^{\mathbf{C2(COO-)}})_3]$, whose pendant arms end in a carboxylic function (with a total of six carboxylates exposed at the surface of the bioprobe; the purpose was not to link these six arms, which would have led to crosslinking reactions that are detrimental, but to statistically link one of them to the surface of the target biomaterial). The carboxylic acid functions were activated by EDC and then by 1-hydroxy-2-nitrobenzene-4-sulfonic acid, (HNSA, whose synthesis is reported in the literature), ensuring a colorimetric change on completion of the coupling reaction. The targeted avidin protein was purified by chromatography and then submitted to osmosis to eliminate any residual Eu-probe not covalently linked.[43]

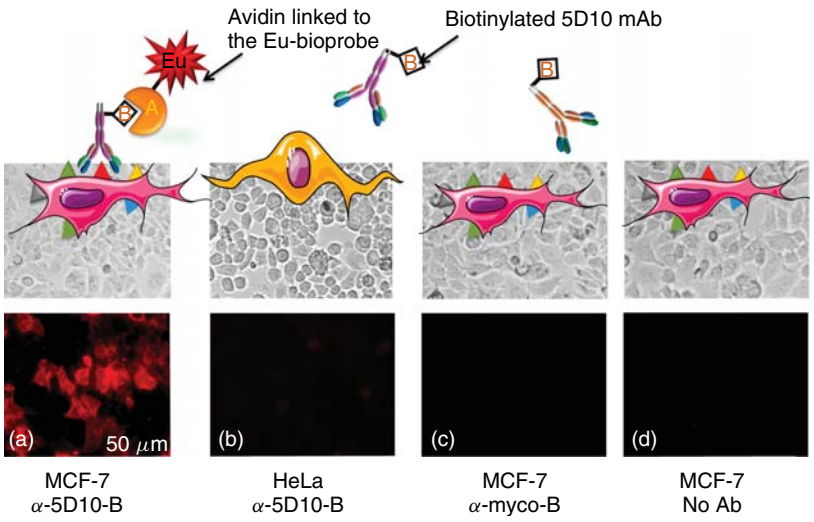


Figure 19 Microscopic images of the immunoluminescence assay: the avidin linked to the Eu-helicate (bioprobe) in the presence of biotinylated 5D10 mAb specifically interacts with MCF 7 cells expressing at their surface the 5D10 tumor factor. B = biotin, A = avidin. Negative controls: (D) no Ab, MCF-7 cells; (C) mycoplasma and MCF-7 cells; (B) biotinylated 5D10 and HeLa cells. Positive control: (A) biotinylated 5D10-biotin and MCF-7. (a) Bright field images. (b) TR images: excitation, BP filter 340 nm (35 nm); emission, LP filter LP (420 nm); delay time, 100 µs; exposure time, 60 s

6.3.2 *Linking Luminescent Europium Helicate to Avidin: toward Immunocytodetection*

The carboxylate-containing helicate was first coupled to avidin. Avidin marked with this bioprobe will then interact with a biotinylated agent. The strategy is to use bioaffinity assays that imply the recognition of an antigen by its monoclonal antibody (mAb). In this case, we take advantage of the extremely strong biotin–avidin coupling ($K \approx 10^{15}$ M), one of the highest reported in biological media.

By several methods (MS experiments, sodium dodecyl sulfate polyacrylamide gel electrophoresis (SDS-PAGE), UV–visible spectrometry) it was proved that the yield of this reaction between avidin and the Eu-helicate is around 32%. This coupling ratio prevents the aggregation of the bioprobes at the surface of the avidin and does not affect its activity, as demonstrated by bioaffinity assays. The presence of the europium helicate allows working in time-resolved microscopy, with an easy detection of the luminescent material coupled to the protein. However, the quantum yield is decreased from 15% for the free complex to 9.3% for the coupled one, thus reflecting quenching effect due to the vicinity of the protein. Anyway, this value is still good enough to provide a sufficient sensitivity of the detection.

It is possible to perform an enzyme-linked immunosorbent assay (ELISA) using a streptavidin-coated 96-well plate: the primary antibody, biotinylated-rabbit-anti-streptavidin, specifically recognizes the avidin linked to the helicate as the bioprobe. The detection limit is better than that with commercially available organic dyes such as antistreptavidin-FICT (FiB3).

It is also possible to develop an immunocytochemistry assay in order to detect the tumor marker 5D10. This is a receptor that is over expressed in the breast cancer cells MCF-7. Biotinylated 5D10 mAb as primary antibody and the previously described bioprobe were used for the experiment. The specificity of the experiment was monitored by performing in parallel three negative controls; by using a different cell line, such as HeLa cells, that dos not express the tumor marker 5D10 (B in Figure 19); and by using the same cell line, MCF-7, but with either a nonspecific biotinylated antibody expressed at his surface (antimycoplasma α-myco-B) or no antibody expressed (C and D in Figure 19, respectively). The specificity of the detection was ascertained by time-resolved spectroscopy, as can be seen from image A in Figure 19.

6.3.3 *Encapsulating the Probe in Nanoparticles*

The next application presented here concerns the use of nanoparticles. By doping SiO_2/NH_2 nanoparticles with $[Eu(\mathbf{L}^{\mathbf{C2}})_3]$, spherical nanoparticles with sizes less than 90 nm are obtained, which contain around 500 helicates per nanoparticle. They are highly luminescent, exhibit a quantum yield of 28%, and have a lifetime that is increased to 3.4 ms. The nanoparticles are conjugated to an IgG monoclonal antibody for target-specific bioassays. They can be subjected to the same immunocytochemistry assays as described in Figure 19, in order to detect the tumor marker 5D10. The signal to noise ratio is even better than that obtained with the $[Eu(\mathbf{L}^{\mathbf{C2COOH}})_3]$ complex. The use of these nanoparticles is then an interesting alternative to generate nanobioprobes.

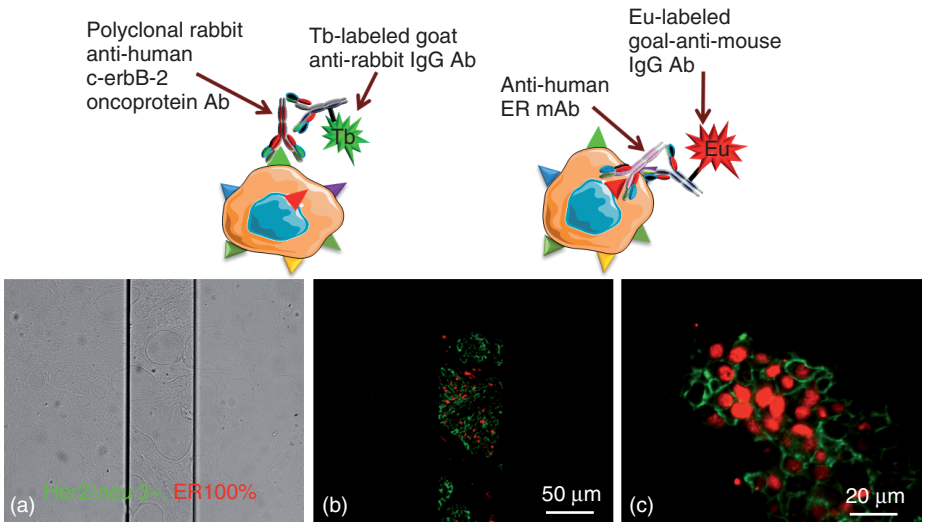


Figure 20 On-chip immunohistochemical detection of Her2/*neu* and ER in a breast cancer tissue sample. (A) Bright field image; (B) merged luminescent image, Her2/*neu* detected by green-emitting Tb-bioprobe and ER stained with red-emitting Eu-bioprobe; (C) magnified image. Note the nuclear expression of ER and the strictly membranous decoration of cells with Her2/*neu*. (Adapted from from Ref. **44**, by permission of The Royal Society of Chemistry.)

6.3.4 *Immunoassays Using Lab-on-a-Chip Technology*

A lab-on-a-chip is a small device that allows working on a small surface, by using microfluidics. It increases the speed of analysis and decreases the amount of reactants to be used. Fibronectin-coated microchannels 100 µm wide are carved in polydimethylsiloxane (PDMS), a biocompatible and optically transparent material. It is possible to culture cells in these microchannels, leading to immunocytochemistry experiments, or directly insert sections of tissues to perform immunohistochemistry experiments. The experiments described above have been successfully applied to this technology and will not be described again. As an illustration, an immunohistochemical assay has been discussed.

6.3.5 *Linking the Luminescent Lanthanide Helicate to Immunoglobulin: toward Immunohistochemical Assay*

In everyday clinical practice, for instance, choosing an anticancer therapy in the case of breast cancer will depend on the tumor sensitivity to different therapies (hormone therapy or immunotherapy with trastuzumab). In particular, two receptors, estrogen receptors (ERs) and Her2/*neu* (human epidermal growth factor receptor) are overexpressed in breast cancer cells and located on the nuclear membrane or the cell membrane, respectively. The aim is to detect simultaneously both receptors. In the immunohistochemical assay, the luminescent lanthanide helicate is bioconjugated to an immunoglobulin, either a goat anti-mouse IgG polyclonal Ab or a goat anti-rabbit IgG Ab. These labeled detection antibodies react with the targeting primary antibody mouse anti-human ER mAb and the rabbit anti-human Her2/*neu* polyclonal Ab, respectively. Taking advantage of red-emitting Eu-bioprobe and green-emitting Tb-bioprobe, the goat anti-rabbit IgG was chosen to be labeled with Tb helicate and the goat anti-mouse-IgG was chosen to be labeled with europium helicate. Analysis of human breast cancer tissue was done using a lab-on-a-chip immunohistochemical technology. After incubation with the corresponding primary antibody, multiplex tumor biomarker detection was observed; the Eu probe accumulated in the nuclear membranes and the Tb-bioprobe on the cancerous cell surface (Figure 20). These results were in complete agreement with those obtained in the clinical laboratory using a classic immunohistochemical setting, but with the difference that detection was performed simultaneously, in only 10 min versus 2 h and using five times less reagent than in the case of the classic protocol.

6.3.6 *Overcoming the Excitation Wavelength Limitation by Multiphoton Excitation*

Multiphoton or two-photon laser scanning microscopy is an alternative to confocal and time-resolved microscopy for bioimaging applications. The principle has been discussed in ***Lanthanides: Luminescence Applications*** and concerns a two-photon excitation from the simultaneous absorption of two photons in a single quantized event. A bioprobe that normally absorbs ultraviolet light ($\lambda_{ex} = 350$ nm) can also be excited by two photons of NIR light, at 700 nm (the wavelength is twice that required for one-photon excitation). These two photons must interact simultaneously, which means in a very small lapse time. The instrumentation requires pulse lasers to provide sufficient power, as the photon density must

be approximately 10^6 times higher than that of a one-photon absorption used in conventional microscopy. The advantage of using this nonlinear technique is that the excitation wavelength is shifted to the NIR range and that biomolecules are transparent in that range. The bioprobes reported have been successfully submitted to these multiphoton experiments, in particular $[Eu_2(\mathbf{L}^{C2})_3]$ and $[Eu_2(\mathbf{L}^{C5})_3]$, after incubation with HeLa cells. More details can be found in the article by Eliseeva *et al*.[45]

7 CONCLUSION

This article has described how a luminescent complex can be successfully developed and used as a bioprobe. The properties of these bioprobes have been reported. Several examples of bioapplications were reviewed: (i) how the bioprobe interacts with DNA (in presence of AO) for accessing the DNA concentration, (ii) how it is possible to perform cell imaging (time-resolved or confocal microscopy) with UV–visible emitting probes (Ln = Eu, Sm,Tb) including multilabel assays as well as with NIR emitting probes (Ln = Yb), (iii) how the probes can be included in silica nanoparticles, (iv) how to perform immunocytochemical assays or immumohistochemical assays, (v) how these assays can be adapted to lab-on-a-chip technology to shorten detection time and reduce the amount of reactants and biomaterial used for the analysis, and finally (vi) how two-photon laser scanning microscopy can be applied to these bioprobes to shift the excitation wavelength to the NIR range when performing bioimaging. The examples have been essentially but not exclusively focusing on $[Eu_2(\mathbf{L}^{C2})_3]$ and $[Eu_2(\mathbf{L}^{C2COOH})_3]$, and different candidates fitted with carboxylate or phosphonic units, for which modifications have been done on the ligand backbone in view of modifying and fine-tuning their photophysical properties, have been cited. Having illustrated these bioapplications, the reader should be ready to discover many other applications in the literature, and other examples of bioprobes arising, for instance, from cyclen derivatives (some of them are presented in ***Lanthanides: Luminescence Applications***). The use of bioprobes for exploring and reporting biological events is of crucial importance and lots of efforts have been devoted yet to develop efficient bioprobes. However, taking into account the extraordinary complexity of the events occurring in cells and the necessity to better understand them for improving the so-called molecular medicine in terms of healthcare prevention and *in vitro* diagnostic and molecular imaging, enormous efforts have still to be undertaken to develop new bioprobes for sensing, ligand–receptor targeting, and drug delivery. Luminescence will certainly remain an important tool in the coming years, and luminescent lanthanide-containing complexes should certainly be a source of inspiration for the next generation of researchers.

8 GLOSSARY

Ditopic ligand: a receptor possessing two distinct binding sites.

Acidity constant: K_a, refers to the strength of an acid in solution.

Stability constant: refers here to the strength of the interaction between a ligand and a lanthanide cation. It represents the equilibrium constant for the formation of the complex in the aqueous solution.

Mass spectrometry (MS): is an analytical method to determine the masses of charged particles.

Nuclear magnetic resonance spectroscopy (NMR): is an analytical method to determine the structure if organic compounds.

X-ray spectroscopy: is a technique using X-ray excitation to elucidate the structure of a molecule.

active transport: refers of the moving of material in a cell (cellular uptake) using metabolic energy

passive transport: refers of the moving of material in a cell (cellular uptake) which is not involve chemical energy.

cellular uptake: entry of molecular substances through the cell membrane.

Bioconjugate: molecule covalently attached to a biological material.

immunocytochemistry: refers to cytochemistry, by using a selected labelled antibody which specifically detectsa cellular biological element.

9 ACKNOWLEDGMENTS

The author thanks Prof. Jean-Claude Bünzli and Dr Caroline Vandevyver for the excellent and fruitful collaboration during several years to construct step by step these fascinating applications of helicates. The data presented here result from the huge work performed by the collaborators of the laboratory: PhD student Steve Comby, Dr Song Bo, Dr Svetlana Eliseeva, Dr Vanesa Fernandez-Moreira, Dr Emmanuel Deiters, M. Frederic Gumy, and M. Frederic Thomas. Without the contribution of the whole team, nothing would have been possible. Thanks to Julien Andres for judicious comments and help.

10 RELATED ARTICLES

Lanthanides: Luminescence Applications; Luminescence.

11 ABBREVIATIONS AND ACRONYMS

BP = band pass; NHS = *N*-hydroxsuccinimide; DOTA = 1,4,7,10-tetraazacyclododecane-1,4,7,10-tetraacetic acid; EDC = 1-ethyl-3-[3-dimethylaminopropyl]carbodiimide hydrochloride; HNSA = 1-hydroxy-2-nitrobenzene-4-sulfonic acid; AO = acridine orange; bpy = bipyridine; DTPA = diethylenetria- minepentaacetic acid; ELISA = enzyme-linked immunosorbent assay; ER = estrogen receptor; ED = ethidium bromide; HR-MS = high-resolution mass spectroscopy; LDH = lactate dehydrogenase; PDMS = polydimethylsiloxane; PCR = polymerase chain reaction; SDS-PAGE = sodium dodecyl sulfate polyacrylamide gel electrophoresis.

12 REFERENCES

1. E. J. New, D. Parker, D. G. Smith, and J. W. Walton, *Curr. Opin. Chem. Biol.*, 2010, **14**, 238.
2. G. Bernardinelli, C. Piguet, and A. F. Williams, *Angew. Chem. Int. Ed.*, 1992, **31**, 1622.
3. C. Piguet, J.-C. G. Bünzli, G. Bernardinelli, G. Hopfgartner, and A. F. Williams, *J. Am. Chem. Soc.*, 1993, **115**, 8197.
4. C. Piguet and J.-C. G. Bünzli, in 'Handbook on the Physics and Chemistry of Rare Earths', eds. K. A. Gschneidner Jr., J.-C. G. Bünzli, and V. K. Pecharsky, Elsevier Science, B.V., Amsterdam, 2010 Vol. 40, Chap. 247.
5. J. L. Sessler and R. A. Miller, *Biochemistry*, 2000, **59**, 733.
6. A.-S. Chauvin, S. Comby, B. Song, C. D. B. Vandevyver, and J.-C. G. Bünzli, *Chem.—Eur. J.*, 2007, **13**, 9515.
7. A.-S. Chauvin, S. Comby, B. Song, C. D. B. Vandevyver, and J.-C. G. Bünzli, *Chem.—Eur. J.*, 2008, **14**, 1726.
8. S. Comby, 'Luminescent Lanthanides Bioprobes Emitting in the Visible and/Or Near-infrared Ranges', Ph. D. thesis, Ecole Polytechnique Fédérale, Lausanne (EPFL), 2008.
9. M. Elhabiri, J. Hamacek, J.-C. G. Bünzli, and A.-M. Albrecht-Gary, *Eur. J. Inorg. Chem.*, 2004, 51.
10. P. A. Brayshaw, J.-C. G. Bünzli, P. Froidevaux, J. M. Harrowfield, Y. Kim, and A. N. Sobolev, *Inorg.Chem.*, 1995, **34**, 2068.
11. A.-S. Chauvin, F. Gumy, D. Imbert, and J.-C. G. Bünzli, *Spectrosc. Lett.*, 2004, **37**, 517. Erratum 2007, **40**, 193.
12. J. F. Desreux, in 'Lanthanide Probes in Life, Chemical and Earth Sciences. Theory and Practice', eds. J.-C. G. Bünzli and G. R. Choppin, Elsevier Science Publ. B.V., Amsterdam, 1989, p. 43.
13. G. Schwarzenbach, 'Complexometric Titrations', Chapman & Hall, London, 1957.
14. A.-S. Chauvin, S. Comby, M. Baud, C. De Piano, C. Duhot, and J.-C. G. Bünzli, *Inorg. Chem.*, 2009, **48**, 10687.
15. A.-S. Chauvin, F. Thomas, B. Song, C.D.B. Vandevyver and J.-C. G. Bünzli, Synthesis and Cell Localization of Self-assembled Dinuclear Lanthanide Bioprobes, submitted to Philosophical Transactions A.
16. J.-C. G. Bünzli and S. V. Eliseeva, in 'Springer Series on Fluorescence. Lanthanide Luminescence: Photophysical, Analytical and Biological Aspects', eds. P. Hänninen and H. Härmä, Springer Verlag, Berlin, 2011, p. p. 1.
17. J.-C. G. Bünzli, A.-S. Chauvin, C. D. B. Vandevyver, B. Song, and S. Comby, *Ann. N.Y. Acad. Sci.*, 2008, **1130**, 97.
18. T. B. Jensen, 'Heterobimetallic Lanthanide Helicates: Deciphering Substituent Effects by Crystallography and NMR Analyses', Ph. D. thesis, Ecole Polytechnique Fédérale, Lausanne (EPFL), 2006.
19. T. B. Jensen, R. Scopelliti, and J.-C. G. Bünzli, *Chem.—Eur. J.*, 2007, **13**, 8404.
20. IUPAC, 'Compendium of Chemical Terminology', 2nd edition (the ''Gold Book''), Compiled by A. D. McNaught and A. Wilkinson, Blackwell Scientific Publications, Oxford, 1997, XML on-line corrected version: http://goldbook.iupac.org (2006) created by M. Nic, J. Jirat, and B. Kosata; updates compiled by A. Jenkins. ISBN 0-9678550-9-8. doi:10.1351/goldbook.
21. W. R. Harris, K. N. Raymond, and F. L. Weitl, *J. Am. Chem. Soc.*, 1981, **103**, 2667.
22. D. F. Eaton, *Pure Appl. Chem.*, 1988, **60**, 1107.
23. W. H. Melhuish, *J. Phys. Chem.*, 1961, **65**, 229.
24. S. Petoud, J.-C. G. Bünzli, K. J. Schenk, and C. Piguet, *Inorg. Chem.*, 1997, **36**, 1345.
25. L. J. Charbonniére, C. Balsiger, K. J. Schenk and J.-C. G. Bünzli, *J. Chem. Soc., Dalton Trans.*, 1998, 505.
26. K. Nakamaru, *Bull. Chem. Soc. Jpn.*, 1982, **55**, 2697.
27. F. Gumy, System and method for the optical analysis of luminescent materials, WO 2009/050536 A1 (Patent application PCT/IB2007/054187). 15-10-2007.
28. J.-C. G. Bünzli, A.-S. Chauvin, H. K. Kim, E. Deiters, and S. V. Eliseeva, *Coord. Chem. Rev.*, 2010, **254**, 2623.
29. E. Deiters, B. Song, A.-S. Chauvin, C. D. B. Vandevyver, and J.-C. G. Bünzli, *New J. Chem.*, 2008, **32**, 1140.
30. E. Deiters, B. Song, A.-S. Chauvin, C. Vandevyver, and J.-C. G. Bünzli, *Chem.—Eur. J.*, 2009, **15**, 885.
31. A. Beeby, I. M. Clarkson, R. S. Dickins, S. Faulkner, D. Parker, L. Royle, A. S. de Sousa, J. A. G. Williams, and M. Woods, *J. Chem. Soc., Perkin Trans. 2*, 1999, 493.
32. R. M. Supkowski and W. D. Horrocks Jr., *Inorg. Chim. Acta*, 2002, **340**, 44.

33. H. Hakala, P. Liitti, J. Peuralahti, J. Karvinen, V. M. Mukkala, and J. Hovinen, *J. Lumin.*, 2005, **113**, 17.

34. T. Kimura and Y. Kato, *J. Alloys Compd.*, 1995, **225**, 284.

35. S. Faulkner, A. Beeby, M.-C. Carrié, A. Dadabhoy, A. M. Kenwright, and P. G. Sammes, *Inorg. Chem. Commun.*, 2001, **4**, 187.

36. B. Song, C. D. B. Vandevyver, E. Deiters, A.-S. Chauvin, I. A. Hemmilä, and J.-C. G. Bünzli, *Analyst*, 2008, **133**, 1749.

37. M. Ishiyama, K. Sasamoto, M. Shiga, Y. Ohkura, K. Ueno, K. Nishiyama, and I. Taniguchi, *Analyst*, 1995, **120**, 113.

38. T. Decker and M. L. Lohmannmatthes, *J. Immunol. Methods*, 1988, **115**, 61.

39. H. J. Tanke, Imaging of lanthanide luminescence by time-resolved microscopy, Springer Series on Fluorescence 7 (Lanthanide Luminescence), 2011 p. 313.

40. B. Song, C. D. B. Vandevyver, A.-S. Chauvin, and J.-C. G. Bünzli, *Org. Biomol. Chem.*, 2008, **6**, 4125.

41. K. J. Heroux, K. S. Woodin, D. J. Tranchemontagne, E. Southwick, E. H. Wong, G. R. Weisman, S. A. Tomellini, T. J. Wadas, C. J. Anderson, S. Kassel, J. A. Golen, and A. L. Rheingold, *Dalton Trans.*, 2007, 2150.

42. G. T. Hermanson, 'Bioconjugate Techniques', Academic Press, Elsevier, Amsterdam, 2008.

43. L. Aldwin and D. E. Nitecki, *Anal. Biochem.*, 1987, **164**, 494.

44. V. Fernandez-Moreira, B. Song, V. Sivagnanam, A.-S. Chauvin, C. D. B. Vandevyver, M. A. M. Gijs, I. A. Hemmilä, H.-A. Lehr, and J.-C. G. Bünzli, *Analyst*, 2010, **135**, 42.

45. S. V. Eliseeva, G. Auböck, F. van Mourik, A. Cannizo, B. Song, E. Deiters, A.-S. Chauvin, M. Chergui, and J.-C. G. Bünzli, *J. Phys. Chem. B*, 2010, **114**, 2932.

Sensors for Lanthanides and Actinides

Gabriela I. Vargas-Zúñiga and Jonathan L. Sessler

University of Texas at Austin, Austin, TX, USA

1	Summary	561
2	Introduction	562
3	Ion-Selective Electrodes	562
4	Colorimetric Chemosensors	567
5	Conclusion	570
6	Glossary	571
7	Acknowledgments	571
8	Related Articles	571
9	Abbreviations and Acronyms	571
10	References	571

1 SUMMARY

The development of sensors for the detection of metal ions is an ongoing challenge that is attracting the attention of researchers across a range of disciplines. Such sensor systems are of interest because of the ubiquity of metal ions in the lithosphere, the toxic impact of many cations and their associated physiological and environmental impact, the role they play in biological systems, their potential for use as drugs, and their importance to industry. In the particular case of chemical agents that trigger an easy-to-monitor response (e.g., optical, fluorescent, or electrochemical), so-called chemosensors, both sensitivity and selectivity are critical elements of a successful design. This is particularly true in the case of chemosensors (herein sensors for short) developed for f-block elements, since specific cation recognition is critical to identifying species that might be present in the environment as the result of, e.g., a radioactive spill or a terrorist attack involving a so-called dirty bomb (i.e., a radiological device). This need has spawned efforts to develop a variety of convenient and direct methods for assaying lanthanide and actinide cations. Currently, a variety of techniques are being developed. These include analytical methods, such as inductively coupled plasma mass spectrometry (ICP-MS), inductively coupled plasma atomic emission spectroscopy (ICP-AES), isotope dilution mass spectrometry, capillary electrophoresis, X-ray fluorescence (XRF), and resonance light scattering (RLS). However, these methods are costly, often involve multiple sample manipulations, can be less than ideal in terms of selectivity, or display poor precision and accuracy.[1–6] This makes alternative, chemosensor-based approaches of particular appeal. Unlike pure instrument-based techniques, chemosensor strategies are expected to benefit both from their inherent simplicity and the potential to tune the selectivity through synthesis.

Systems capable of effecting the detection of lanthanide and actinide ions using electrochemical methods have generally consisted of a receptor or ionophore immobilized within a membrane to form an ion-selective electrode (ISE). This electrode is then perturbed when a cation guest is bound. On the other hand, optical sensors or optodes are based on a molecule that is either free standing or attached to a polymer matrix. In both cases, the expectation is that an optical response will be produced when the system is exposed to a particular analyte.[7] Needless to say, for either approach it is beneficial to have a receptor that is well tuned for the lanthanides and actinides. In practice, this has translated to the use of macrocycles rich in O, N, S, or P donor atoms as will be clear from the summary of recent work provided in this article. This article focuses on ISE- and optode-based approaches to lanthanide and actinide cation sensing.

The Rare Earth Elements. Edited by David A. Atwood. © 2012 John Wiley & Sons, Ltd. ISBN 978-1-119-95097-4

2 INTRODUCTION

Lanthanides constitute a group of elements that occupy one-sixth of all naturally occurring elements on Earth. With the exception of promethium (Pm), the lanthanides are nonradioactive elements that are often found mixed with the early actinides thorium and uranium, in minerals such as monoazite and bastnasite, as well as silicate rocks.[8] Lanthanides are also proposed as nuclear fission products in nuclear reactors.[8] Currently, lanthanides ions are involved in several industrial applications, including the production of television displays and devices for lighting.[9] They are also used to prepare compact discs,[9] in metallurgy,[9–11] in the glass and ceramics industry,[12] as components of nuclear control rods,[9] and as catalysts in the petroleum refining industry.[13] Certain lanthanides have found utility in medicine and biology, including MRI contrast agents,[14,15] hypophosphatemic agents for kidney dialysis, luminescent probes in cell studies, and palliatives for bone pain.[16] The similarity between the trivalent lanthanide cations and Ca^{2+} in terms of ionic radius (1.14 Å) and affinity for oxygen-donor groups has led to the study of lanthanide as possible T-channel antagonists and as biochemical probes for the study calcium transport in mitochondria and other organelles.[16]

The actinide elements are those with atomic number from 89 (actinium, Ac) to 103 (lawrencium, Lr) and whose valence electronics involve the 5f subshell. Among theseelements, only actinium, thorium, protactinium, and uranium occur naturally, with thorium being the most abundant of the three. These elements possess unique chemical and physical properties, which include in many cases a propensity to undergo spontaneous and induced nuclear fission, very large ionic radii, and an ability to exist in a large number of oxidation states.[8,17] Both uranium and thorium have been known for almost two centuries. However, they continue to attract attention as the result of their recognized importance in the production of ceramics, incandescent mantles, catalysts, nuclear energy, and weapons production.[17]

The broad diversity of applications involving both lanthanide and actinide cations underscores the need for accurate and precise determination methods, as well as those that would permit the continuous monitoring of both lanthanide ions and trace-level radionuclides in the environment. Described below are two key techniques, ISEs and optical analyses, which have been applied to the detection of lanthanides, as well as the recognition and determination of thorium and uranium. For the purpose of organization, the presentation is given in terms of the type of technique, but is also subdivided according to the targeted analyte and the type of recognition unit employed.

3 ION-SELECTIVE ELECTRODES

ISEs have been used increasingly since the 1930s in the detection of lanthanides. They offer several advantages over other analytical methods. These include inexpensive manufacturing cost, fast and reliable preparation procedures, simple instrumentation, low detection limits (DLs), and reasonable selectivity.[18] The electrochemical detection of lanthanide and actinide ions by ISEs generally involves the preparation of a polymeric matrix (consisting of poly(vinyl chloride) (PVC), silicone rubber, or a polysiloxane) mixed with a neutral electroactive molecule or an ionophore that is selective toward one or more of the targeted metal ions. An ionic additive is often added to the matrix. This additive can act as an anion excluder and can catalyze the exchange kinetics at the membrane interface and is especially useful when the solutions contain lipophilic anions that can diminish the ohmic resistance. Typically, a plasticizer is added as solvent mediator to control the dielectric constant of the membrane phase. This membrane separates the standard internal solution of the lanthanide ion from the solution, which contains the primary metal ion to be analyzed, as well as in most applications one or more interfering metal ions. There are thus two solutions of relevance, namely, the standard solution within the ISE and an external solution that is subject to analysis or analyte solution (Figure 1). When the lanthanide ion concentrations in the standard solution and the analyte solution differ, selective diffusion of the lanthanide ions occurs across the membrane. This leads to a change in the potential across the membrane, which can be related to the concentration of Ln^{III} according to the Nernst equation (1):

$$\Delta E = \frac{(RT/nF)\ln[\mathrm{Ln}]_{\mathrm{analyte}}}{[\mathrm{Ln}]_{\mathrm{standard}}} \quad (1)$$

where $[Ln]$ is the concentration of lanthanide ions, ΔE is the change in potential, R is the universal gas constant, T is the absolute temperature, F is the Faraday constant, and n is the charge of the cation.[7]

Although a wide number of ISEs has been used in the determination of a range of metal ions (i.e., alkali, alkaline earth, transition, and some heavy metal ions),[19,20] the development of highly selective ISEs for lanthanide and actinide ions remains a challenge. This is because lanthanide ions have very similar chemical properties with respect to one another. For instance, the most stable oxidation state for all the lanthanide ions is +3, and nearly without exception these ions form compounds with anions, such as hydroxide (OH^-), nitrate (NO_3^-), sulfate (SO_4^{2-}), carbonate (CO_3^{2-}), phosphate (PO_4^{3-}), and halides (F^-, Cl^-, Br^-, and I^-), which makes the detection of only a single ionic species even more difficult.[8,21] In fact, ISEs have been published for almost every single 4f-block element. However, many of these electrodes are characterized by narrow working pH ranges,[22,23] long response times,[24–26] high DLs,[24–28] or significant interference

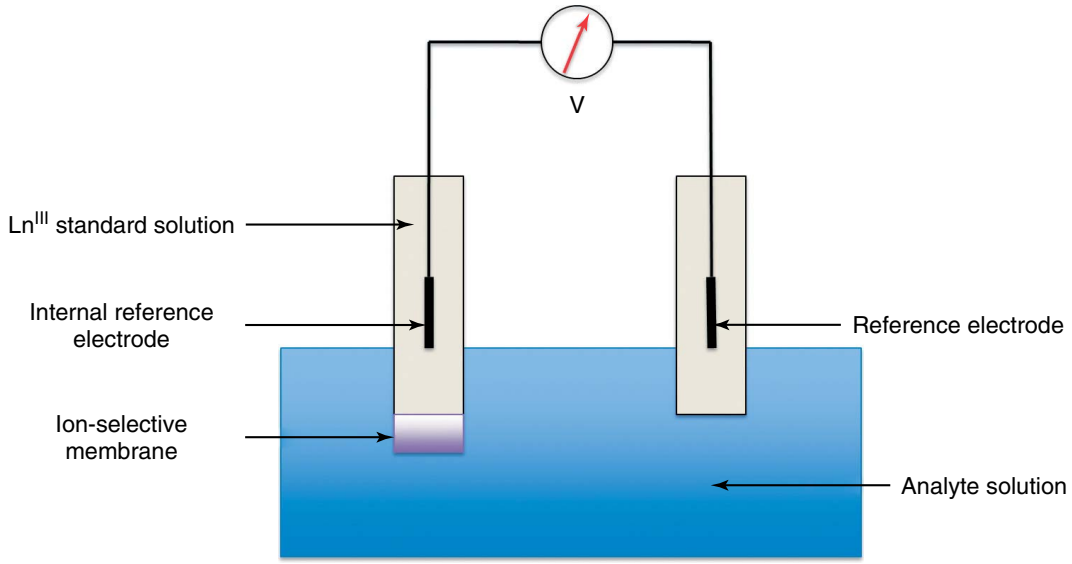


Figure 1 Schematic representation of an electrochemical cell containing a chemical-based membrane sensor element. (Adapted from Ref. 7. © John Wiley & Sons, Inc., 2011.)

from other ions, including other lanthanide ions and transition metal ions, such as Cu^{II}, Ni^{II}, and Zn^{II}.[22–27]

In the case of actinide ions, reports of ISEs are still scarce. Most of the systems described in the literature have focused on the recognition of U^{VI}, which in solution occurs as uranyl ion (UO_2^{2+}), and have been based on organophosphorus compounds,[29–33] thiourea,[34] Schiff base,[35,36] and calix[6]arene derivatives.[37] However, almost without exception, the reported sensors are subject to interference by other cations, including various alkali, alkaline earth, transition metal, and lanthanide ions, and anions, such as nitrate (NO_3^-), perchlorate (ClO_4^-), phosphate (PO_4^{3-}), and the halides (F^-, Cl^-, Br^-, and I^-). Also, these sensors, specifically sensors based on organophosphorus recognition elements, operate over a very narrow concentration range ($10^{-4}-10^{-1}$ M). Moreover, many of the reported electrodes are plagued by non-Nernstian behavior.

Complicating the development of ISEs for higher actinide ions is their inherent radioactivity. They also have chemistry that often differs from that of the uranyl cation. Actinides from americium to lawrencium display solution-phase chemical features that resemble those of the trivalent lanthanides. Conversely, in certain oxidation states, the early actinides (thorium through neptunium) often mimic transition metals. Also, as mentioned above, many of the actinides can exist in a large number of oxidation states. For instance, in the case of plutonium, four oxidation states can exist simultaneously in aqueous solution.[17] Finally, as true for the lanthanides, complex salts with hydroxide, halogens, perchlorates, sulfates, carbonates, and phosphates are well known for most of the actinides.

3.1 ISEs Based on Schiff Base Ionophores

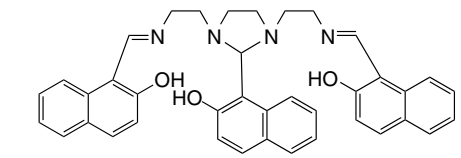
The design of ionophores that are able to extract selectively a metal ion into a membrane phase should have the following characteristics: they should be easy to prepare, display adequate ligand topology, and include binding sites with the shape, conformational flexibility, cavity size, and charge needed to accommodate the targeted cation; they should also display adequate stability under a variety of oxidative and reductive conditions.[19,38] The need for facile synthesis has made Schiff bases attractive for the fabrication of lanthanide-selective ISE-based sensors. Because Schiff base ligands can often be synthesized in high yields via the simple condensation of an aldehyde and an amine, a variety of bulky, electron withdrawing or donating groups can be incorporated into the receptor framework. This can allow the electronic and steric properties to be tuned. Finally, this class of ligands can easily accommodate N, O, or S donor atoms, which permits stabilization of complexes containing both hard or soft lanthanide or actinide cations and can allow operation over a wide pH range (i.e., from 3.0 to 10.0). Applied appropriately, these design features can lead to the production of ISEs that discriminate for lanthanide or actinide cations over various undesirable metal ions.[19,39]

There are a number of reports of potentiometric membranes based on Schiff bases that have been applied to the problem of lanthanide and actinide metal ion sensing.[19] The ionophores that underlie the success of these systems may be divided into two classes, specifically symmetric and asymmetric. To date, most symmetric Schiff bases used for ISE production have consisted of tetra- or hexadentate ligands

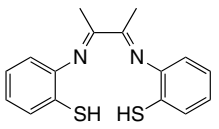
Table 1 ISEs based on symmetric and asymmetric Schiff bases

Cation	Ionophore	Slope (mV decade^{-1})	Linear range (M)	Most important interfering ions (log $K_{sel} > -2$)	Detection limit (M)	References
La^{III}	(**1**)	19.5	$10^{-9}-4.0 \times 10^{-4}$	—	4.5×10^{-10}	40
	(**2**)	19.7	$10^{-5}-10^{-1}$	Ce^{3+}, Gd^{3+}	—	42
	(**3**)	19.6	$10^{-7}-10^{-1}$	Sm^{3+}, Ce^{3+}	2.0×10^{-8}	43
	(**4**)	19.4	$10^{-6}-10^{-2}$	Yb^{3+}	4.0×10^{-7}	44
	(**5**)	20.3	$10^{-7}-10^{-1}$	Pr^{3+}	8.0×10^{-8}	45
	(**6**)	19.2	$10^{-6}-10^{-1}$	Sm^{3+}, Nd^{3+}	7.0×10^{-7}	46
Ce^{III}	(**7**)	20	$10^{-7}-10^{-2}$	La^{3+}	8.91×10^{-8}	47
Pr^{III}	(**8**)	21.1	$10^{-2}-10^{-6}$	Sm^{3+}, Er^{3+}	8.0×10^{-7}	48
	(**9**)	19.6	$10^{-5}-10^{-2}$	La^{3+}, Sm^{3+}	2.0×10^{-6}	49
Eu^{III}	(**10**)	19.8	$10^{-5}-10^{-2}$	La^{3+}, Gd^{3+}, Sm^{3+}	5.0×10^{-6}	50
Gd^{III}	(**11**)	19.8	$10^{-5}-10^{-1}$	Tb^{3+}, Dy^{3+}, Eu^{3+}	3.0×10^{-6}	51
	(**12**)	19.4	$10^{-6}-10^{-1}$	La^{3+}, Mg^{2+}, Hg^{2+}	7.0×10^{-7}	52
Tb^{III}	(**13**)	19.8	$10^{-5}-10^{-1}$	La^{3+}, Yb^{3+}, Dy^{3+}	7.0×10^{-6}	53
Dy^{III}	(**14**)	20.6	$10^{-5}-10^{-1}$	Ce^{3+}, La^{3+}	6.0×10^{-6}	41
	(**15**)	17.5	$3.0 \times 10^{-10}-10^{-3}$	—	2.0×10^{-10}	13
Tm^{III}	(**16**)	19.5	$10^{-5}-10^{-2}$	Er^{3+}	8.0×10^{-6}	54
Yb^{III}	(**17**)	19.2	$10^{-7}-10^{-2}$	Nd^{3+}, Pb^{2+}, Gd^{3+}	4.0×10^{-8}	55
Lu^{III}	(**18**)	20.5	$10^{-6}-10^{-2}$	Nd^{3+}, Dy^{3+}, Gd^{3+}	8.0×10^{-7}	56
U^{VI}	(**19**)	28.5	$10^{-7}-10^{-1}$	Mg^{2+}, Cu^{2+}	7.0×10^{-8}	35
	(**20**)	29.3	$5.0 \times 10^{-2}-5.0 \times 10^{-6}$	—	2.0×10^{-7}	36

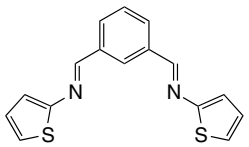
and include both salen and salophen derivatives. Asymmetric Schiff base ligands have been based on these latter cores, as well as various hydrazone derivatives. Many receptors, including (**1**)–(**13**), have been used to make ISEs. Although symmetric and asymmetric Schiff bases have been widely used for the detection of lanthanide ions, there appear to be strengths and weaknesses associated with the basic choice of ligands, at least where direct comparisons may be safely made (Table 1). These strengths and weaknesses are exemplified by ionophores (**14**) and (**15**), which have been applied for the ISE-based monitoring of the Dy^{III} ion.[40] The symmetric ionophore (**14**) revealed good sensitivity for Dy^{III} over the whole working concentration range (1.0×10^{-5} to 1.0×10^{-1} M), whereas the system displayed a limited response level for the La^{III} and Ce^{III} ions. On the other hand, in the case of a microsensor based on (**15**), the electron-rich Schiff base provides an asymmetric binding site that displays good selectivity and sensitivity for Dy^{III} ions over other lanthanide ions, as well as the alkali and alkaline earth metal ions and most transition metals over a wide working range (ion concentration: $3.0 \times 10^{-10}-1.0 \times 10^{-3}$ M). Interestingly, the symmetric system (**14**) was found to provide a higher DL (DL = 6.0×10^{-6} M) than the asymmetric ionophore (**15**) (DL = 0.20×10^{-9} M), at least over the 3.0–8.5 pH range.[13,41]



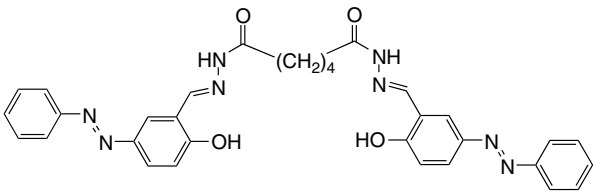
(1)



(2)



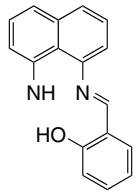
(3)



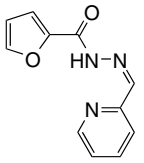
(4)

3.2 ISEs Based on Cyclic Ionophores

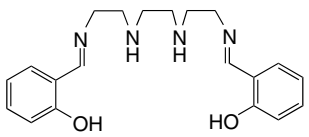
A number of cyclic ionophores for ISEs are known. Their design optimization has generally been based on consideration of many input parameters, including a need to create a cavity that matches the targeted ion, the stability of



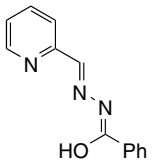
(5)



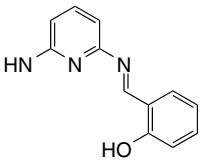
(6)



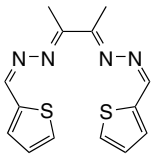
(7)



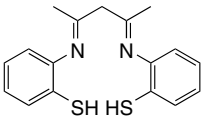
(8)



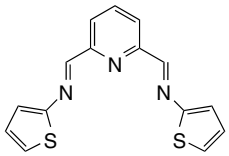
(9)



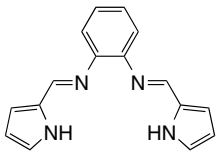
(10)



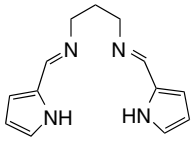
(11)



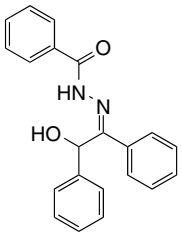
(12)



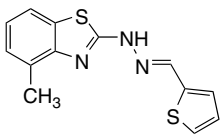
(13)



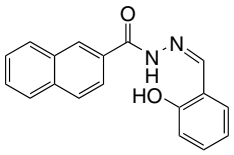
(14)



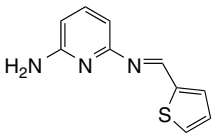
(15)



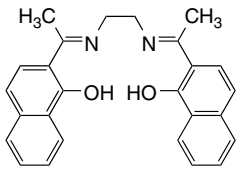
(16)



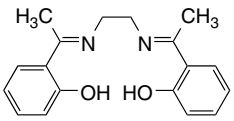
(17)



(18)



(19)



(20)

the resulting metal complex and the selectivity with which it is formed, and the ability to produce an organic soluble species that allows extraction of the metal ion into the membrane phase.

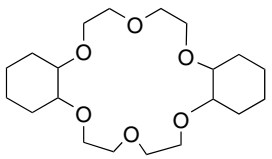
Among the most venerable of the systems employed to date are the crown ethers. These ionophores are attractive in the construction of ISEs because of their recognized ability to selectively coordinate cations as a function of ring size. The encapsulation of lanthanide ions by 18-crown-6 has been achieved by the modification of the cavity size in the crown ether ring that matches the size of the lanthanide ion. In 2004, Mittal *et al*. reported an ISE based on dicyclohexano-18-crown-6 (**21**), with the latter receptor being employed as a putative neutral carrier for La^{III} ions. This sensor displayed high sensitivity and selectivity for La^{III} ions over mono-, di-, and trivalent anions and gave a good response over a wide pH range (i.e., from pH 4.0 to 9.0). A DL of 5.0×10^{-7} M was achieved, and only a slight interference from the Tb^{III}, Dy^{III}, and Ce^{III} cations was observed.[57]

The replacement of the oxygen atoms present in classic Pederson-type crown ethers by S atoms results in the formation of thia-crown ligands. These latter ligands are characterized by a tendency to form complexes with softer ions, including those of the transition, lanthanide, and actinide series. This stands in contrast to what is true for oxygen-based crown ethers, for which a preference for hard cations, such as alkali metal ions, is well established.[19] One of the earliest examples of ISEs based on a thia-crown ether was reported

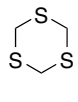
by Shamsipur and coworkers and involved the use of the sulfur-containing ligand 1,3,5-trithiane (**22**).[58] This particular ionophore was used as a neutral carrier in the construction of ion-selective membrane electrodes effective for the Ce^{III} and La^{III} ions. In an initial 2000 report, this thia-crown ether was used to construct a Ce^{III}-selective membrane sensor that was found to be largely free of interference from heavy metals, such as Pb^{II}, Tl^{II}, Ag(I), or Cu^{II}. However, the function of the ISE in question was found to be perturbed in the presence of the La^{III}, Cd^{II}, and Zn^{II} cations. Nevertheless, it displayed a high DL for the Ce^{III} cation (3.0×10^{-5} M) and an acceptable response time of about 15 s.[58]

In 2002, ionophore (**22**) was used in the construction of a membrane-coated graphite electrode (MCGE) that proved effective for the La^{III} ion. Under conditions of use, it was observed that this new ISE based on (**22)** displayed a low DL (2.0×10^{-8} M), a fast response time (<10 s), and a higher selectivity for the La^{III} ions over the Ce^{III} and transition metal ions (i.e., Cd^{II}, Zn^{II}, and Cu^{II}); presumably, this is due to the decreased solvation energy of La^{III} with respect to Ce^{III} ion (by about 50 kJ mol^{-1}).[27,59]

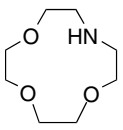
Another ISE based on a cyclic ionophore for heavier lanthanides was predicated on a diazatetrathia-18-crown-6 derivative containing the 4,5-dithio-1,3-dithiole-2-thione unit (**23**). These ISEs allowed for the recognition of the Ho^{III} ions selectively over many heavy metals, transition metals, alkali metal, and lanthanide ions. In particular, little interference from the La^{III} ion was observed (selectivity coefficient, log $K_{sel} > -2$) and a DL for Ho^{III} of 6.3×10^{-7} M was achieved.[60]



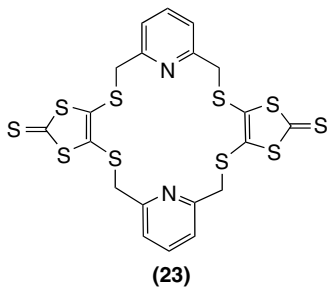
(21)



(22)



(24)

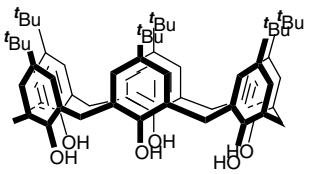


(23)

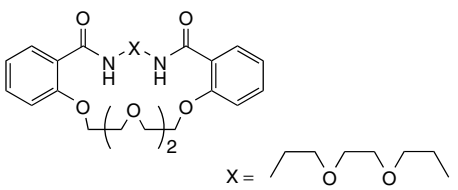
The incorporation of N atoms in the crown ether framework, leading to so-called aza crown ethers, permits fixation of the crown on an electrode surface. This is a general strategy that has been used inter alia for the determination of lanthanide ions. In 2003, Gupta and Jain used the monoaza-12-crown-4 (**24**), as an ionophore for the construction of La^{III}-selective electrodes. Here, the design rationale was predicted on the fact that nitrogen-containing crowns form stronger complexes with higher valent metal ions than they do with alkali metals. Unfortunately, an ISE based on (**24**) failed to permit the effective recognition of La^{III} ions when sodium and chromium ions were present in concentrations $\geq 10^{-4}$ M.[61]

Cyclic ionophores have also been used to generate ISEs targeting the actinides, most typically the uranyl^{II} cation, UO_2^{2+}. Among the recognition units most widely utilized in the construction of such ISEs, calixarenes, long recognized as highly selective molecules for the detection of cations and anions,[62] have played a central role. In 1997, Gupta *et al*. reported an ISE based on 4-*tert*-butylcalix[6]arene (**25**) for the determination of the uranyl ion. This electrode displayed moderate selectivity for the uranyl ion over mono-, di-, and trivalent ions in a concentration range from 3.9×10^{-5} to 1.0×10^{-1} M; it also displayed a Nernstian response (29.1 mV per decade). The presence of sodium ions caused interference when the concentration of uranyl was $\leq 5.0 \times 10^{-5}$ M. However, the interference of sodium ions could be overcome if the concentration range of uranyl ions is reduced ($1.1 \times 10^{-4} - 1.0 \times 10^{-1}$ M); over this latter concentration regime, good selectivity could be achieved in the presence of 5.0×10^{-4} M Na^+. [63]

The determination of U^{VI} ions (as uranyl) using a macrocylic N-subsstituted amide (**26**) as the ionophore was reported by Shamsipur *et al*. in 2002. The ISE in question was based on (**26**). It displayed a Nernstian response (29.2 mV per decade) with a DL of 3.5×10^{-7} M and was found to operate over a wide concentration range (from 5.0×10^{-7} to 1.5×10^{-3} M). Gratifyingly, this system displayed good selectivity for uranyl ions and was subject to almost negligible interference from other cations (e.g., alkali, alkaline earth, transition, and heavy metal ions).[64]



(25)

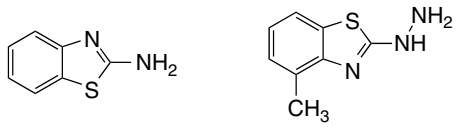


(26)

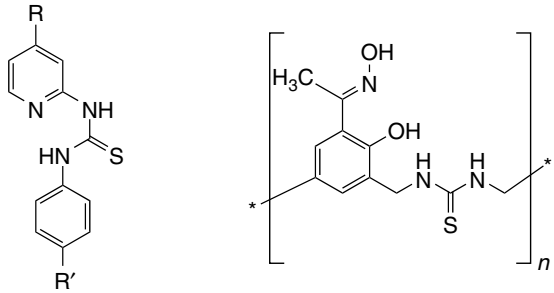
3.3 ISEs Based on Other Recognition Elements

Although ionophores based on Schiff bases and crown ethers are the recognition units most used for the construction of ISEs, other groups, including benzothiazoles and thioureas, have been explored in the design of ISEs for the recognition of lanthanides and actinides. Among the systems used for this purpose are 2-aminobenzothiazole (**27**),[65] 4-methyl-1,2-hydrazinobenzothiazole (**28**),[66] *N*-(2-pyridyl)-*N′*-(2-methoxyphenyl)-thiourea,[23] *N*-(2-pyridyl)-*N′*-(4-methoxyphenyl)-thiourea (**29**),[67] *N*-(2-pyridyl)-*N′*-4-nitrophenyl)thiourea (**30**),[68] and 2-hydroxyacetophenone-oxime-thiourea-trioxane (**31**).[34] In 2004, a membrane electrode based on (**27**) was reported; it was found to act as a highly selective sensor for the Ce^{III} cation that was subject to only modest interference from the Fe^{III} and Cu^{II} ions (log $K_{sel} = -2.33$ and -2.39 for these two cations, respectively).[65] A Nernstian response over a wide working concentration range (19.6 mV decade^{-1}, from 2.0×10^{-6} to 2.0×10^{-2} M) was found, although a relatively poor DL of 1.8×10^{-6} M was likewise seen. The synthetic addition of hydrazine to benzothiazole resulted in ionophore (**28**), a receptor unit that was utilized in the construction of a La^{III}-selective ISE. This sensor system displayed no appreciable interference from any of the alkali, alkaline earth, transition metal, or other lanthanide ions tested over a wide concentration range (from 1.0×10^{-7} to 1.0×10^{-1} M) and displayed a DL for La^{III} of 2.5×10^{-8} M.[65]

Non-crown nitrogen-sulfur-containing ligands have also been explored recently for the purpose of producing ISEs for the lanthanide ions. Among most of the systems used to support these efforts are ionophores based on thiourea. These recognition elements are attractive since they have a low inherent affinity for the alkali and alkaline earth metal ions in aqueous solution. This inherent benefit is apparent in the case of ISE systems based on ionophores (**29a**) and (**29b**). Here, it proved possible to detect the La^{III} and Yb^{III} ions at the parts per billion (ppb) concentration level (limits of detection of approximately 2.0×10^{-8} M and 50×10^{-7} M for ionophores (**29a**) and (**29b**), respectively). Further, the ISE based on (**29a**) displayed essentially no interference from other common metal cations and good selectivity for La^{III} over other trivalent lanthanide cations. On the other hand, an ISE sensor system based on ionophore (**29b**) displayed good selectivity for the Yb^{III} ion in the presence of several other potentially competing metal ions. However, the latter sensor was found to respond to larger lanthanide ions, such as Nd^{III}, Gd^{III}, and Dy^{III}, with the result that the selectivity for Yb^{III} ion was reduced when these interferants were present in solution, (log $K_{sel} = -2.4$, -2.5, and -2.1 for Nd^{III}, Gd^{III}, and Dy^{III}, respectively). The higher affinity for Yb^{III} over the rest of Ln^{III} ions was rationalized in terms of the size and shape of the semi-cavity present in the ionophore, as well as the relative flexibility of the pyridine-thiourea moiety and the better match with the Yb^{III} ion that these structural features permitted (i.e., Nd^{III}, Gd^{III}, and Dy^{III}, ionic radius = 0.995, 0.938, 0.894 Å, respectively vs Yb^{III} radius = 0.858 Å).[69] Finally, an ISE based on receptor (**30**) was prepared by Ganjali and coworkers and reported as a potential sensor for the Gd^{III} cation. This sensor displayed a Nernstian response with a corresponding Nernstian slope of 19.95 mV per decade in a wide concentration range of 3.0×10^{-7}–1.0×10^{-1} M.[68] Moreover, it was found to have a high selectivity for Gd^{III} with a DL of 3.0×10^{-7} M over the La^{III}, Ce^{III}, Sm^{III}, and Eu^{III} ions.



(27) **(28)**



R = H, R′ = OMe, **(29a)**
R = CH_3, R′ = OMe, **(29b)**
R = H, R′ = NO_2, **(30)**

(31)

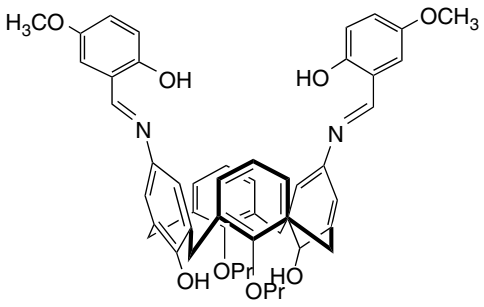
The determination of U^{VI} (as the uranyl (UO_2^{2+}) ion) was reported by Gupta and coworkers. These researchers used an organic resin built up from 2-hydroxyacetophenoneoxime-thiourea-trioxane repeat units (**31**) The resulting ISE was able to detect U^{VI} ions in partially nonaqueous media (methanol–water 20% (v/v) over a relatively wide concentration range (i.e., 8.0×10^{-6}–1.0×10^{-1} M). However, this electrode suffered from a poor DL (1.0×10^{-4} M), a long response time (~30 s), and a narrow pH range (2.5–3.5). Moreover, its performance was seriously affected when the concentration of Na^+ was $\geq 10^{-4}$ M.[34]

4 COLORIMETRIC CHEMOSENSORS

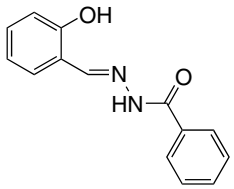
An optical sensor or optode is a system that gives rise to a visible or spectroscopic response when exposed to the targeted analyte. For the purpose of lanthanide and actinide detection, such systems have generally been based on a ligand immobilized within an organic or inorganic matrix that forms a complex with one or more metal cations and that generates an optical response signal proportional to the

amount of the cation in question. Typically, PVC or cellulose derivatives have been employed as the supporting matrices because of their transparency. The use of these supports offers several further advantages, such as freedom from electrical noise, possibility of remote sensing, and low cost of manufacturing.

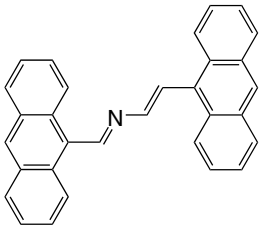
However, colorimetric sensors have at least one disadvantage with respect to other analytical methods (electrochemical, potentiometric, etc.), namely, they are generally characterized by low sensitivity. However, lower limits of detection can be obtained using fluorescent- or luminescent-based approaches. Therefore, in an effort to improve the sensitivity of an optode, fluorophores are often coupled to the substrate binding subunit. Using this strategy, it is often possible to obtain sensors that produce both colorimetric and luminescent responses that allow analyte detection via instrumental analysis, as well as in certain cases via the naked eye.[7] Currently, the number of colorimetric sensors for lanthanide ions is still limited. Reviewed below, is recent progress in this area.



(32)



(33)



(34)

4.1 Optodes for Lanthanides

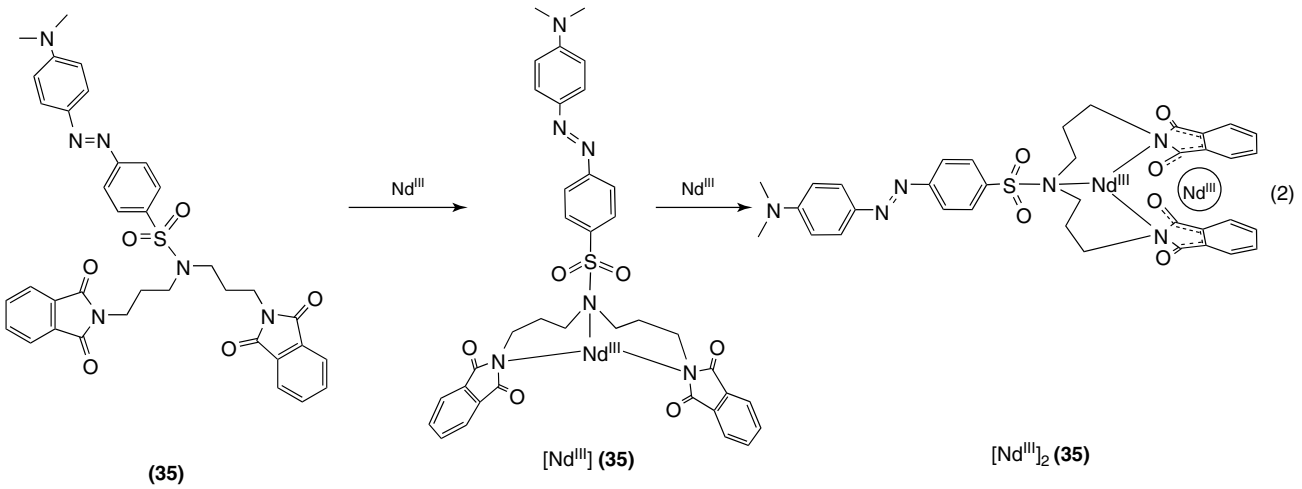
One of the earliest examples of an optode able to recognize selectively the Dy^{III} and Er^{III} ions was reported by Gao and coworkers. In this case, the colorimetric chemosensor (**32**), based on Schiff base-calixarene framework, was used. This system gave rise to distinctive color changes when exposed to the dysprosium or erbium ions (from colorless to pink and from colorless to pale yellow for these two cations, respectively). Complexation studies revealed that on coordination of Dy^{III} or Er^{III}, the intensity of absorption band at 450 nm decreased, while a new absorption bands appeared at 550 nm. This change in the absorption spectra was attributed to an increase in the extent of π-conjugation in the presence of these metal ions and a degree of donor–acceptor charge transfer in the complexes. Also, a large chelation-induced increase in the fluorescence intensity was observed (as well as a red shift in λ_{em} from 550 to 598 nm) when the optode (**32**) was exposed to the Dy^{III} or Er^{III} ions in water. The selective recognition of these lanthanide ions by (**32**) was rationalized in terms of an appropriate receptor–analyte complementarity (e.g., a good size fit and the stabilization of a π-cation interaction).[68]

In 2009, Ganjali *et al*. reported an optical sensor for the Dy^{III} ion that is based on *N′*-[(2-hydroxyphenyl)-methylene]benzohydrazide, **29**. This receptor was immobilized on a triacetylcellulose membrane to create an optical sensor that displayed both high selectivity and sensitivity toward the dysprosium ion. While a DL of 35 μM was achieved, this system was plagued by a narrow effective pH range (3.0–5.0) and a long response time (50 s).[10]

In 2010, Zapata *et al*. reported a selective Yb^{III}-optode, which was based on the aza-substituted anthracene ionophore (**34**).[70] In this system, the aza-butadiene bridge acts as a cation-binding site as well as a quencher of the inherent fluorescence emission intensity, whereas the anthracene moiety acts as a built-in flurophore. The molecule as a whole is yellow in color in the absence of an added cation. On the other hand, treatment of optode (**34**) with one equivalent of Yb^{III} (as the trifluoromethanesulfonate salt) in acetonitrile produced a dark orange solution. UV–vis analysis revealed the presence of a new band at 503 nm as the result of this exposure. The addition of other metal ions, including other trivalent lanthanide ions, resulted in no visible change in the absorption spectrum φ. The fluorescence spectral properties revealed a dramatic increase in the quantum yield of (**34**) when ytterbium is coordinated to the ligand (from $\varphi = 6.2 \times 10^{-4}$ to 2.1×10^{-2}). Presumably, this increase reflected a ''turning off'' of internal electron transfer from the aza-butadiene and hence the quenching of the anthracene fluorescence that would normally occur in the absence of a coordinated cation. In accord with the design expectations underlying optode (**34**), essentially no change in the emission features was seen on exposure to other lanthanide ions (i.e., Sm^{III}, Eu^{III}, Gd^{III}, Tb^{III}, and Lu^{III}), producing an almost negligible increase in the emission signals.[70]

In 2010, Das *et al*. reported the colorimetric sensor (**35**). This sensor exhibits colorimetric recognition of Nd^{III} ions at the parts per million (ppm) level in acetonitrile solution, and does so with solutions of other lanthanide ions, such as La^{III}, Pr^{III}, Yb^{III}, Eu^{III}, Er^{III}, Sm^{III}, Tb^{III}, Ce^{III}, and Dy^{III}. On the exposure of Nd^{III} (as the nitrate salt) in acetonitrile, a redshift of 68 nm (from 440 to 508 nm) is observed. Unlike other complexants that coordinate

lanthanide ions with a 1 : 1 stoichiometry, spectroscopic analysis revealed that (**35**) forms a 2 : 1 complex (i.e., $[Nd^{III}]^2 \cdot$(**35**)). This unexpected complexation stoichiometry led to the suggestion that the complexation of a second Nd^{III} cation would induce a quenching in the luminescence intensity due to an intramolecular charge transfer between the dimethyl azobenzene (donor) and the coordinated phthalimide fragment (acceptor) present in (**35**) (Equation (2)).[71]



overall trend were seen in the case of the La^{III}, As^{III} and Sb^{III} ions, where the selectivity ratio of [M]/[Th] was approximated three.[74]

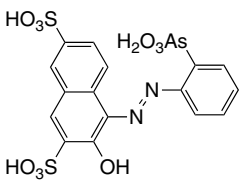
Owing to its sensitive response to the uranyl ion (UO_2^{2+}) in aqueous media, several uranium-sensitive optical sensors based on Arsenazo III (**37**) have also been developed for the spectrophotometric determination of this cation at trace

4.2 Optodes for Actinides

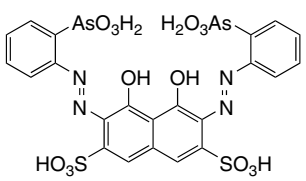
Perhaps not surprisingly, given their availability and relatively high safety profiles, thorium and uranium have received the greatest attention as target for optical sensor development. Much of this work has involved the use of chromogenic compounds containing azo groups for thorium detection. Traditionally, indicators based on azo compounds containing arsonic groups have been used for the chemical sensing of the thorium and uranium ions. Among the best known of this chromophore class are Thorin (**36**) and Arsenazo III (**37**), which are employed in the Thoron I and Arsenazo III sensing methods, respectively. These dyes display high sensitivity toward Th^{IV} in aqueous solution under acidic conditions. However, for selective use, it is necessary to subject the analyte to a preliminary extraction using an extractant such as tri-*n*-butyl phosphate, TBP, or tri-*n*-octyl phosphine oxide, TOPO. This is required since in the case of both (**36**) and (**37**) significant interference from Fe^{III}, Ce^{IV}, Ti^{IV}, Zr^{IV}, Hf^{IV}, Nb^{IV}, U^{IV}, and La^{III} is observed. Also, in the presence of fluoride, oxalate, phosphate, or sulfate, serious interference is observed.[72,73]

In 2010, Rastegarzeh and Saeedi reported a sensing membrane based on the methyltrioctylammonium salt of (**36**) (Thorin) embedded in a polymeric triacetylcellulose matrix. This system displayed good selectivity for Th^{IV} salts (in acidic medium, pH = 2.5) in the presence of most interfering ions and was generally characterized by a short response time (<20s), with a DL of 1.85×10^{-6} M. Exceptions to this levels (<20 ppb in water). Useful as are these systems, most of the optical sensors in question are plagued by long response times (35–25 min), as well as by interference from other metal cations, such as the Ca^{II} and Th^{IV} ions.[75,76]

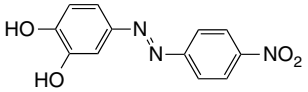
In 2006, Safavi and Sadeghi reported an optode based on 4-(*p*-nitrophenylazo)-pyrocathecol (NAP) (**38**), which was prepared for use as a sensor by embedding into a PVC membrane. The resulting optode was found to undergo a reversible change in color from yellow to red-brown in 12 min, with a DL of 6.0×10^{-6} M when exposed to $Th(NO_3)_4 \cdot 6H_2O$ in a buffered solution at pH 3.5. Interference from other ions, particularly Fe^{III}, and Ga^{III}, was found when salicylic acid was added and a pH = 3 was used.[77]



(36)



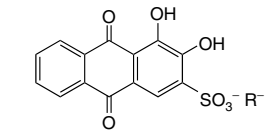
(37)



(38)

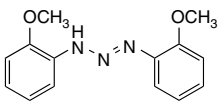
In 2005, Safavi and Bagheri proposed an optical, triacetylcelullose-based sensor that relied on alizarin red S (**39**) as the sensing element. The resulting system was found to respond well to the U^{VI} (as UO_2^{2+} ion) in an acetate buffer solution at pH 5 undergoing a reversible change in color from yellow to violet. A response time of 6 min and a DL of 5×10^{-6} M were reported. Unfortunately, the determination of uranyl ions was found to be adversely affected when lanthanide ions are present in solution, even if masking agents (i.e., diethylenetriaminepentaacetic acid (DTPA), ethylenediaminetetraacetic acid (EDTA), or sulfosalicylic acid) were used. As a consequence, it proved necessary to carry out a solvent-based extraction or subject the sample to purification via ion exchange prior to analysis if accurate determinations were to be made.[78]

In another report, Mahani *et al*. detailed an optode based on triazene-1,3-di(2-methoxyphenyl) (**40**) that was supported on a PVC membrane. The system in question was found capable of detecting Th^{VI} and U^{VI} ions in aqueous samples. The linear concentration range for the determination of Th^{VI} and U^{VI} by this sensor was $2.26–48.44 \times 10^{-6}$ and $2.85–58.47 \times 10^{-6}$ M, with DLs of 1.95×10^{-6} and 2.44×10^{-6} M, respectively, under acidic conditions (pH = 3.0). However, the sensor (**40**) could not be regenerated and was used as a one-time probe for the determination of Th^{IV} and U^{VI}.[79]



R = Na, tetraoctylammonium

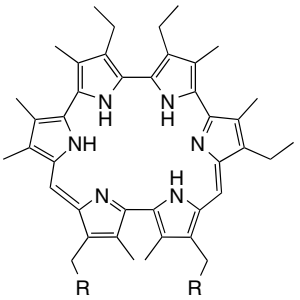
(39)



(40)

Recently, expanded porphyrins have been recognized as ligands able to form complexes with cations that are too large to form stable 1 : 1 complexes with porphyrins. Some of these systems have been exploited as sensors for the colorimetric detection of high-valent actinides (i.e., the U^{VI}, Np^{V}, and Pu^{V} ions).[80] In 2004, Sessler and coworkers reported the expanded porphyrin, isomethyrin (**41**), which undergoes colorimetric changes on the exposure of U^{VI}, Np^{V}, and Pu^{V} ions. This change of color was attributed to a change in the macrocycle π-electron periphery from nonaromatic to aromatic after the coordination of the actinide ions in mixed $MeOH–CH_2Cl_2$ solutions. Specifically, the exposure of (**41**) in MeOH to aqueous Np^{V} and Pu^{V} solutions resulted in an instantaneous color change from yellow to pink, which was easily detectable by the naked eye. The same color change was seen on the addition of U^{VI} solution, but was only fully achieved after 24 h. This difference in the kinetics of the response was explained in terms of the ligand (**41**) being noninnocent and undergoing oxidation during the course of metal complexation. This process was thought to be accelerated in the case of the Np^{V} and Pu^{V} cations, which could access several oxidation states. However, because of the highly radioactive nature of Np^{V} and Pu^{V} ions, detailed analyses of this proposed phenomenon were not carried out. Moreover, quantitative colorimetric studies were only conducted using depleted uranium acetate in $MeOH–CH_2Cl_2$ 95 : 5 (v/v) solutions. Under these conditions, (**41**) displayed a DL for the uranyl cation of 5.8 ppm as determined by naked-eye analyses and 28 ppb as recorded using a standard laboratory UV/vis spectrometer. Gratifyingly, isomethyrin (**41**) displayed negligible interference of other metals (e.g. Gd^{III}, Zn^{II}, Ce^{III}, and La^{III} ions).[80–82] Further studies involved immobilizing a modified form of isomethyrin (**42**) to a TentaGel resin, which allowed for the construction of a matrix-supported system for the determination of the U^{VI} cation. While analyses revealed that complexation takes place and a colorimetric response is produced, the dynamics of response (>1day typically) make this system impractical as a viable method for the determination of uranyl cation concentrations.[83]

In 2008, Hayes *et al*. attached a different modified isomethyrin (**42**) to a plastic fiber optic and used the resulting system for the detection of U^{VI} cation in aqueous solution. The resulting device displayed no interference from other metal ions with the exception of Gd^{III} (which gave rise to a color change similar to that produced by the uranyl cation, but a different response function) and allowed for very low DLs (<100 ppb) in controlled aqueous environments.[84]



R = H, **(41)**
R = $–CH_2CH_2CO_2H$, **(42)**

5 CONCLUSION

In conclusion, the art of chemical-based lanthanide and actinide sensing is both well developed and still in its infancy. Considerable progress has been made in the area of ISE-based determinations, although a need for improved selectivity and sensitivity remains, as does a need to expand the technique to include a greater diversity of actinide cations. In the case of optical sensors for lanthanides and actinides, most of the work to date has focused on the use of a few classic indicator systems. Here, the lack of selectivity has hampered the development of ready-to-use devices that do not require pretreatment of samples. There is thus room for

the development of additional colorimetric core systems that provide an easy-to-discern change in their electronic features or fluorescence emission profiles when exposed to either the lanthanides or actinides. Here, it is proposed that expanded porphyrin systems, such as those developed in the author's laboratory, could have a role to play.

6 GLOSSARY

Electrochemical monitoring: systematic review of the interaction or interconvertion of electric and chemical phenomena over a period of time

Ion-selective electrode: a potentiometric electrode with a semipermeable membrane that produces a potential in the presence of a specific ion but not in the presence of other ions of a similar concentration

Optode: an optical sensor device that optically measures a specific substance

7 ACKNOWLEDGMENTS

This work was supported by the Office of Basic Energy Sciences, U.S. Department of Energy (DOE) (grant DE-FG02-01ER15186 to J.L.S.).

8 RELATED ARTICLES

Geology, Geochemistry, and Natural Abundances of the Rare Earth Elements; Lanthanide Complexes with Multidentate Ligands; Lanthanides: Luminescence Applications; Lanthanide Shift Reagents.

9 ABBREVIATIONS AND ACRONYMS

DTPA = diethylenetriaminepentaacetic acid; DL = detection limit; EDTA = ethylenediaminetetraacetic acid; ICP-MS = inductively coupled plasma mass spectrometry; ISE = ion-selective electrode; MCGE = membrane-coated graphite electrode; NAP = 4-(*p*-nitrophenylazo)-pyrocathecol; PVC = poly(vinyl chloride; RLS = resonance light scattering; TBP = tri-*n*-butyl phosphate; TOPO = tri-*n*-octyl phosphine oxide; XRF = X-ray fluorescence

10 REFERENCES

1. A. L. Morss, N. M. Edelstein, and J. Fuger, 'The Chemistry of the Actinide and Transactinide Elements', 3rd edition, Springer, Dudrecht, The Netherlands, 2006, Vol. 5, p. 3273.
2. A. Hrdlick, J. Havel, C. Moreno, and M. Valiente, *Anal. Sci.*, 1991, **7**, 925.
3. R. S. Houk, V. A. Fassel, G. D. Reach, and H. J. Svec, *Anal. Chem.*, 1980, **52**, 2283.
4. A. Mazzucotelli, E. DePaz, E. Magi, and B. Frache, *Anal. Sci.*, 1992, **8**, 189.
5. S. F. Marsh, *Anal. Chem.*, 1967, **39**, 641.
6. D. H. Cornell, *Pure Appl. Chem.*, 1993, **65**, 2453.
7. B. Wang and E. V. Anslyn, 'Chemosensors: Principles, Strategies, and Applications', John Wiley & Sons, Hoboken, NJ, 2011, p. 275.
8. M. Halka and B. Nordstrom, 'Lanthanides and Actinides', Facts On File, New York, p. 1.
9. O. R. Kirk and F. D. Othmer, 'Encyclopedia of Chemical Technology', Wiley, New York, 1982, Vol. 19, p. 851.
10. M. R. Ganjali, R. Zare-Dorabei, and P. Norouzi, *Sens. Actuators, B*, 2009, **143**, 233.
11. C. L. Wilson and D. W. Wilson, 'Comprehensive Analytical Chemistry', Elsevier, Amsterdam, 1962, Vol. 1C, p. 477.
12. M. R. Ganjali, S. Rasoolipour, M. Rezapour, P. Norouzi, M. Amirnasr, and S. Meghdadi, *Sens. Actuators, B*, 2006, **119**, 89.
13. F. Faridbod, M. R. Ganjali, B. Larijani, P. Norouzi, S. Riahi, and F. S. Mirnaghi, *Sensors*, 2007, **7**, 3119.
14. A. E. Mebach and E. Tóth, 'The Chemistry of Contrast Agents in Medical Magnetic Resonance Imaging', Wiley, New York, 2001, p. 437.
15. P. Caravan, *Chem. Soc. Rev.*, 2006, **35**, 512.
16. S. P. Fricker, *Chem Soc. Rev.*, 2006, **35**, 524.
17. R. L. Morss, N. M. Edelstein, and J. Fuger, 'The Chemistry of the Actinide and Transactinide Elements', 3rd edition, Springer, Dordrecht, The Netherlands, 2006, Vol. 1, p. 1.
18. S. Amarchand, S. K. Menon, and Y. K. Agrawal, *Electroanalysis*, 2000, **12**, 522.
19. F. Faridbod, M. R. Ganjali, R. Dinarvand, P. Norouzi, and S. Riahi, *Sensors*, 2008, **8**, 1645.
20. M. K. Mahani, F. Divsar, M. Chaloosi, M. G. Maragheh, A. R. Khanchi, and M. K. Rofouei, *Sens. Actuators, B*, 2008, **133**, 632.
21. K. A. Gschneidner Jr., 'Rare Earths: The Fraternal Fifteen', U. S. Atomic Energy Commission, Tennessee, 1966, p. 1.
22. J. B. Harrell, A. D. Jones, and G. R. Choppin, *Anal. Chem.*, 1969, **41**, 1459.
23. M. R. Ganjali, P. Norouzi, T. Alizadeh, A. Tadjarodi, and Y. Hanifehpour, *Electroanalysis*, 2006, **18**, 1091.
24. H. Zamani, M. R. Ganjali, and M. Adib, *Sens. Actuators, B*, 2007, **120**, 545.

25. M. R. Ganjali, R. Kiani-Anbouhi, M. Shampisur, T. Poursaberi, M. Salavati-Niasari, Z. Talebpour, and M. Emami, *Electroanalysis*, 2004, **16**, 1002.
26. M. Shamsipur, M. Yousefi, and M. R. Ganjali, *Anal. Chem.*, 2000, **72**, 2391.
27. M. Shamsipur, M. Yousefi, M. Hosseini, and M. R. Ganjali, *Anal. Chem.*, 2002, **74**, 5538.
28. M. R. Ganjali, M. Tahami, M. Shampisur, T. Poursaberi, S. Haghgoo, and M. Hosseini, *Electroanalysis*, 2003, **15**, 1038.
29. A. Florido, I. Casas, J. Garcia-Raurich, R. Arad-Yellin, and A. Warshawsky, *Anal. Chem.*, 2000, **72**, 1604.
30. D. L. Manning, J. R. Stokely, and D. W. Magouyrk, *Anal. Chem.*, 1974, **46**, 116.
31. G. J. Moddy, J. M. Slater, and J. D. R. Thomas, *Analyst*, 1988, **113**, 699.
32. C. S. Luo, F. C. Chang, and Y. C. Yeh, *Anal. Chem.*, 1982, **54**, 2333.
33. O. M. Petrukhin, E. N. Avdeeva, A. F. Zhukov, B. Polosuchina, S. A. Krylova, S. L. Rogatinskaya, G. V. Bodrin, N. P. Nesterova, Y. M. Polikarpov, and M. I. Kabachnik, *Analyst*, 1991, **116**, 715.
34. A. K. Jain, V. K. Gupta, J. Khurama, and L. P. Singh, *Electroanalysis*, 1997, **9**, 857.
35. M. Shampisur, M. Saeidi, A. Yari, A. Yageneh-Faal, M. H. Mashhadizadeh, G. Azimi, H. Naemi, and H. Sharghi, *Bull. Korean Chem. Soc.*, 2004, **25**, 629.
36. A. Shokrollahi, M. Chaedi, M. Montazerozohori, N. Khanjari, and M. Najibzadeh, *J. Chin. Chem. Soc.*, 2009, **56**, 812.
37. V. K. Gupta, R. Mangh, U. Khurama, and P. Kumar, *Electroanalysis*, 1999, **11**, 573.
38. D. A. Atwood, *Coord. Chem. Rev.*, 1997, **165**, 267.
39. R. Drozdzak, B. Allaert, N. Ledoux, I. Dragutan, V. Dragutan, and F. Verpoort, *Coord. Chem. Rev.*, 2005, **249**, 3055.
40. M. R. Ganjali, H. Ganjali, B. Larijani, and P. Norouzi, *Int. J. Electrochem. Sci.*, 2009, **4**, 914.
41. M. R. Ganjali and M. R. Baezzat, *Electroanalysis*, 2004, **16**, 1771.
42. M. R. Ganjali, M. Qomi, A. Daftari, P. Norouzi, M. Salavati-Niasari, and M. Rabbani, *Sens. Actuators, B*, 2004, **98**, 92.
43. M. R. Ganjali, R. Kiani-Anbouhi, M. Salavati-Niasari, Z. Talebpour, and M. Emami, *Electroanalysis*, 2004, **16**, 1002.
44. M. Shampisur, S. Ershad, N. Samadi, A. R. Esmaeilbeig, R. Kia, and A. Abdolmaleki, *Electroanalysis*, 2005, **17**, 1828.
45. M. R. Ganjali, P. Norouzi, T. Alizadeh, and M. Adib, *Anal. Chim. Acta*, 2006, **576**, 275.
46. H. A. Zamani, M. R. Ganjali, P. Norouzi, M. Adib, and M. Aceedy, *Anal. Sci.*, 2006, **22**, 943.
47. V. K. Gupta, A. K. Singh, and B. Gupta, *Anal. Chim. Acta*, 2006, **575**, 198.
48. M. R. Ganjali, F. S. Mirnaghi, P. Norouzi, and M. Adib, *Sens. Actuators, B*, 2006, **115**, 374.
49. M. R. Ganjali, A. Ahmadalinezhad, P. Norouzi, and M. Adib, *J. Appl. Electrochem.*, 2006, **36**, 931.
50. M. R. Ganjali, P. Norouzi, A. Daftari, F. Faridbod, and M. Salavati-Niasari, *Sens. Actuators, B*, 2007, **120**, 673.
51. M. R. Ganjali, M. Emami, M. Rezapour, M. Shamsipur, B. Maddah, M. Salavati-Niasari, M. Hosseini, and Z. Talebpoui, *Anal. Chim. Acta*, 2003, **495**, 51.
52. M. R. Ganjali, M. Rexapour, P. Norouzi, and M. Salavati-Niasari, *Electroanalysis*, 2005, **17**, 2032.
53. M. R. Ganjali, A. Ghesmi, M. Hosseini, M. R. Pourjavid, M. Rezapour, M. Shamsipur, and M. Salavati-Niasari, *Sens. Actuators, B*, 2005, **105**, 334.
54. M. R. Ganjali, S. Rasoolipour, M. Rezapour, P. Norouzi, and M. Adib, *Electrochem. Commun.*, 2005, **7**, 989.
55. E. R. Ganjali, P. Norouzi, A. Tamaddon, and M. Adib, *Sens. Actuators, B*, 2006, **114**, 855.
56. M. R. Ganjali, A. Tamaddon, P. Norouzi, and M. Adib, *Sens. Actuators, B*, 2006, **120**, 194.
57. S. K. Mittal, A. Kumar, and H. K. Sharma, *Talanta*, 2004, **62**, 801.
58. M. Shampisur, M. Yousefi, and M. R. Ganjali, *Anal. Chem.*, 2000, **72**, 2391.
59. W. E. Morf, 'The Principles of Ion-Selective Electrodes and Membrane Transport', Elsevier, New York, 1981.
60. M. R. Ganjali, R. Nemati, F. Faridbod, P. Norouzi, and F. Daruiche, *Electrochem. Sci.*, 2008, **3**, 1288.
61. V. K. Gupta and S. C. Jain, *Anal. Chim. Acta*, 2003, **485**, 199.
62. G. D. Gutsche, 'Calixarenes', The Royal Society of Chemistry, London, 1992, p. 209.
63. V. K. Gupta, R. Mangla, U. Khurana, and P. Kumar, *Electroanalysis*, 1999, **11**, 573.
64. M. Shamsipur, A. Soleymanpour, M. Akhond, H. Sharghi, and A. R. Massah, *Talanta*, 2002, **58**, 237.
65. M. Akhond, M. B. Najafi, and J. A. Tashkouriam, *Sens. Actuators, B*, 2004, **99**, 410.
66. M. R. Ganjali, P. Norouzi, L. Shamsolahrari, and A. Ahmadi, *Sens. Actuators, B*, 2006, **114**, 713.
67. M. R. Ganjali, P. Norouzi, T. Alizadeh, A. Tajarodi, and Y. Hanifehpour, *Sens. Actuators, B*, 2007, **120**, 487.
68. Z. Liang, Z. Liu, and Y. Gao, *Tetrahedron Lett.*, 2007, **48**, 3587.
69. F. A. Cotton and G. Willkinson, 'Advanced Inorganic Chemistry', 4th edition, New York, Willey-Interscience, p. 982.
70. F. Zapata, A. Caballero, A. Espinosa, A. Tárraga, and P. Molina, *Eur. J. Inorg. Chem.*, 2010, **2010**, 697.
71. P. Das, A. Ghosh, and A. Das, *Inorg. Chem.*, 2010, **49**, 6909.
72. R. Koroda, M. Kurosaki, Y. Hayashibe, and S. Ishimaru, *Talanta*, 1990, **37**, 619.
73. H. T. Tukuma, E. A. N. Fernandes, M. R. L. Nascimento, and A. L. Quinelato, *J. Radioanal. Nucl. Chem.*, 2001, **248**, 549.
74. S. Rastegarzadeh, N. Porreza, and I. Saeedi, *J. Hazard. Mater.*, 2010, **173**, 110.

75. K. L. Cheng, K. Ueno, and T. Imamura, 'CRC Handbook of Organic Analytical Reagents', CRC Press, Boca Raton, FL, 1992, p. 195.

76. H. Rohwer, N. Rheeder, and E. Hasten, *Anal. Chim. Acta*, 1997, **341**, 263.

77. A. Safavi and M. Sadeghi, *Anal. Chim. Acta*, 2006, **567**, 184.

78. A. Savafi and M. Bagheri, *Anal. Chim. Acta*, 2005, **530**, 55.

79. M. K. Mahani, F. Divsor, M. Chaloosi, M. Ghanadi Maragheh, A. R. Khanchi, and M. K. Rofouei, *Sens. Actuators, B*, 2008, **133**, 632.

80. B. M. Rambo and J. L. Sessler, *Chem.—Eur. J.*, 2011, **17**, 4996.

81. J. L. Sessler, D. Siedel, A. E. Vivian, V. Lynch, B. L. Scott, and D. W. Keough, *Angew. Chem.*, 2001, **113**, 611.

82. J. L. Sessler, P. J. Melfi, D. Siedel, A. E. V. Gorden, D. K. Ford, P. D. Palmer, and C. D. Tait, *Tetrahedron*, 2004, **60**, 11089.

83. J. L. Sessler, P. J. Melfi, E. Tomat, and V. M. Lynch, *Dalton Trans.*, 2007, **36**, 629.

84. N. W. Hayes, C. J. Tremlett, P. J. Melfi, J. L. Sessler, and A. M. Shaw, *Analyst*, 2008, **133**, 616.

Index

+2 oxidation states
  halides, 161
  liquids, 49–50
  solids, 48–49
  variable valency, 44, 47–50
+3 oxidation states
  ground and excited state configurations, 29–31
  variable valency, 43–44, 47–50
+4 oxidation states
  liquids, 46–47
  solids, 44–46
  tetravalent lanthanum compounds, 313–320
  variable valency, 44–47
2:3 lanthanide complexes
  aqueous solution, 541–544
  cell condition mimicry, 546–547
  formation, 541–544
  luminescent bioprobes, 535–558
  luminescent properties, 547–549
  stability constants, 544–546
  water, 547–549
2D *see* two-dimensional
3d–4f systems
  coordination lanthanide polymers, 290–291, 292, 293
  magnetism, 157
  polynuclear lanthanide complexes, 287–290, 291–296
3d metals
  angular momentum, 108
  comparisons, 105–109
  coordination numbers, 106
  crystal fields, 107–108
  electronic properties, 107–108
  electronic spectra, 107–108
  f–f spectra, 107–108
  lanthanide comparisons, 105–109
  magnetic properties, 108
  orbital angular momentum, 108
  organometallic compounds, 106–107
  oxidation states, 105–106
  reactivity, 105
  reduction potentials, 105, 106
  spin–orbit coupling, 108
4f–4f systems, magnetism, 157–158
4f coordination lanthanide polymers, 290–291, 292, 293
4f polynuclear lanthanide complexes, 287–290, 291–296
1212 cuprate superconducting materials, 376–378

Abrikosov vortex lattice, 374
absorption, 56, 118–119, 128–130
abundance normalization, 3–4
acetates, 315
acid–base synthesis, 96
π-acid derivatives, 85–86, 100
acidity
  constants, 539, 557
  lanthanide oxides, 476–477, 478
acids
  see also Lewis acids
  solvento complexes, 57
AC susceptibility, 342–344
actinide ions
  cation sensing, 561–571
  colorimetric chemisensors, 567–568, 569–571
  electrochemical sensors, 561, 562–567, 570–571
  ion-selective electrodes, 561, 562–567, 570–571
  optical sensors/optodes, 561, 567–568, 569–571
  sensors, 561–571
activators, upconversion, 391–392, 402
active transport, lanthanide complexes, 552, 557
additive synthesis, 140, 439, 442–447
adduct formation, 96–97
AFM *see* atomic force microscopy
aggregation, 83, 90, 207–208
alcohols
  exchange, alkoxides, 198
  halides, 178–179
  lanthanide halides, 178–179
aldehyde amidation, 462–464
aldol catalysis, 450–453
aliphatic polycarbonates, 470–472
aliphatic polyesters, 470
alkali metal catalysts, 439
alkali metal ions
  biosystems, 515–517
  lanthanide shift reagents, 515–517
  MRS shift reagents, 515–517
alkenylations, 438, 440
alkoxides, 197–203
  alcohol exchange, 198
  aminolysis, 198
  aryloxide compounds, 201–202
  cerium, 321, 322–324, 328–329
  characterization, 199–202
  crystallography, 199–202
  halide metathesis, 198
  metal alcoholysis, 198
  organometallics, 321, 322–324, 328–329
  siloxides, 202, 208–209
  synthesis, 197–198
  tetravalent chemistry, 321, 322–324, 328–329
alkoxylation, 460–461
alkylations, 438, 439

alkyls, 299–302
  aryls, 303–305
  benzyls, 300
  coordination numbers, 74–75
  hydrocarbyl ligands, 299, 301
  isolation, 299, 301
  lanthanide alkoxide characterization, 199, 200–201
  methyls, 299–301
  neopentyl compounds, 300–301
  organometallic chemistry, 83–96, 98
  scandium, 299–301
  synthesis, 299–301
  (trimethylsilyl)methyl compounds, 300–301
  yttrium, 299–301
alkynes
  carbodiimine, 466–467
  dimerization, 465–466
  homogeneous catalysis, 465–467
  organolanthanide complexes, 465–467
  organometallic chemistry, 85–86
allotropes, 495–499
α-additions, 439, 442
α-amino acids, 238–239
aluminum diboride tiling compounds, 269–270, 276
ambient condition synthesis, 226
amidation, 462–464
amides
  cerium, 321, 325–327
  coordination numbers, 75
  homogeneous catalysis, 459
  organometallics, 321, 325–327
  tetravalent chemistry, 321, 325–327
amidinates, 321, 327–328
amidines, 464–465
amination, 460
amines
  addition to nitriles, 464–465
  aldehyde amidation, 462–464
  carbodiimine, 466–467
  homogeneous catalysis, 462–465, 466–467
  organolanthanide complexes, 462–465, 466–467
amino acids, 237–247
  clusters, 237, 239, 243–247
  coordination chemistry, 237, 238–247
  coordination numbers, 238
  crystal structure, 237, 239–247
  hydrolysis, 237, 239–247
  lanthanide complexes, 237–247
  lanthanide ions, 238
  low pH synthesis, 237, 239–241
  pH, 237, 239–241
  structure, 237, 239–247
  synthesis, 239–247
aminocarboxylic acids, 49–50
aminolysis, 198
ammonium nitrate, 316–317, 319
ammonium sulfate, 317
anaerobic conditions, 90
angiography, 525–526
angular momentum
  3d metals, 108
  lanthanides
    3d metals, 108
    luminescence, 132–133
    magnetism, 153–158
  oxidation states, group trends, 43
  quantum number, 29–31
anhydrides, 177–178
anhydrous conditions, 90
ansa-cyclopentadienyl complexes, 310
antenna effect
  luminescence, 350, 366, 386–387, 388
  metal-organic frameworks, 386–387, 388
  NIR-luminescent complexes, 350, 366
antenna ligands
  biological and medical applications, 66, 67, 69
  β-diketonate/β-diketones, 250
anthraquinone, 482, 483
antiferromagnetism
  borides, 264, 265–266, 267, 269–270
  borocarbides, 273
  carbides, 271–272
anti-Werner-type cluster complexes, 415, 419, 420, 433
AO *see* atomic orbitals
apoptosis targeting, 530–532, 533
aqueous media
  2:3 lanthanide complexes, 541–544
  catalysis, 448–455
  enantioselective synthesis, 453, 454–455, 456
  lanthanide complexes, 185, 541–544
  lanthanide ions, 55, 56–59
  organic synthesis, 448–455
  scandium, 56–58
  solvento complexes, 55, 56–59
  yttrium, 56–57, 58–59
archean eon, 11, 12–15, 17
arenes, 84, 86–87, 96
Arrhenius law, 339
arsenazo, 569
arylchalogenolates, 216
aryl-functionalized imidodiphosphinate ligands, 250, 253
aryloxide compounds, 201–202
aryls, 303–305
  alkyls, 303–305
  monoaryls, 304
  organometallic chemistry, 84, 93, 96–98
  phenyls, 303–305
  triaryls, 303–304
ascorbates, 547
asymmetric synthesis
  catalytic organic synthesis, 438–445, 446, 447, 450–455, 461–462
  homogeneous catalysis, 461–462
asymmetric units, 257, 258, 281, 282
ate complexes, 207–209, 212
atom distances, 208–209
atom-economical homogeneous catalysis, 460, 473
atomic force microscopy (AFM), 449, 451

atomic numbers
  geology/geochemistry, 3, 4
  group trends, 43–44
  solidification points, 476
atomic orbitals (AO)
  degeneracy, 114–115, 132
  lanthanide ion luminescence, 112–115, 132
atomic weight, 3, 4
authigenic phases, 4, 12, 17
autofluorescence, 390, 398, 400, 402
auxochromes, 144–147, 151
avidin, 555
avidin-gadolinium complexes, 526–527
aza-Morita–Baylis–Hillman reactions, 444
azathioxanthone, 482, 483

band structure
  cluster complexes, 416, 417, 433
  halides, 161, 165, 166–167, 172
Bardeen-Cooper-Schrieffer (BCS) theory, 374–375
basicity, heterogeneous catalysis, 475
Bayan Obo deposit, 7–8
BCS *see* Bardeen-Cooper-Schrieffer theory
1,4-benzene dicarboxylate (1,4-BDC) linker, 292–295
benzoate groups, 487–488
benzothiazoles, 567
benzyls, alkyls, 300
β–hydrogen stability, 90–92
bimetallic complexes, 135
binary compounds
  borides, 264–269
  carbides, 271–272
  halides, 161–168
  nitrides, 274–275
binding sites, 135
binuclear complexes, 326
bioconjugates, 554–555, 557
bioimaging
  chemical surface modifications, 395–398
  luminescence, 389–403
  metal-organic frameworks, 388
  nanoparticles, 389–403
  phosphor nanoparticles, 389–403
  surface chemical modifications, 395–398
  synthesis, 389, 393–395
  upconversion nanoparticles, 389–403
biological activity, 65–67
biological analysis, 65–67
biological applications, NIR luminescence, 347
biomacromolecule dynamics/ structure, lanthanide-induced shifts, 511–515
biomedicine
  cellular activity, 175
  lanthanide oxide/hydroxide complexes, 192
  luminescent bioprobes, 535–536
  magnetic resonance imaging, halides, 175
bioprobes, luminescence, 355, 535–558
biosystems
  alkali metal ions, 515–517
  lanthanide-induced shifts, 511–517
  macromolecules, 511–517
  metal ion distribution, 515–517
  MRS shift reagents, 515–517
biotechnology, metal-organic frameworks, 385, 388
bipyoxazoline ligands, 485–486
4,4′-bipyridyl linker, 292–295
*bis*arene derivatives, 86–87
bis-cyclopentadienyl complexes, 309
bis(β-diketones), 249, 251, 254
bis(phthalocyaninato), 341, 342
bis(trimethylsilyl) amides, 325
blood pool contrast agents, 525–526
BMS *see* bulk magnetic susceptibility
boiling points, 476
bonding
  aryls, 304
  borides, 264–271
  borocarbides, 272–274
  chalogenolates, 215–221
  cluster complexes, 415, 416, 419–432
  cyclopentadienyl, 307–310
  β-diketonate/β-diketones, 249, 250
  endohedral fullerenes, 496–498
  lanthanide chalogenolates, 215–221
  organometallic chemistry, 83, 84–87, 88, 97–98, 100
  siloxides, 205–206, 208–211
bone disorders, 68–69, 482, 483
borides, 263–271
  aluminum diboride tiling compounds, 269–270
  applications, 263
  binary compounds, 264–269
  bonding, 264–271
  borocarbides, 263, 272–274
  borocarbonitrides, 263, 275–276
  boronitrides, 263, 275
  calcium copper structures, 270
  crystal structure, 263, 264–271, 276
  layered compounds, 269–270, 276
  magnetism, 263, 264–271, 276
  physical properties, 263, 264–271, 276
  structure, 263, 264–271
  superconductivity, 263, 264, 266, 276
  ternary compounds, 269–271
  thermoelectrics, 263, 267–269, 276
  tiling compounds, 269–270, 276
  transition metals, 269–271
borocarbides, 263, 272–274
  bonding, 272–274
  crystal structure, 272–274
  magnetism, 273–274
  physical properties, 273–274
  superconductivity, 274, 373
  transition metals, 274
borocarbonitrides, 263, 275–276
  crystal structure, 275–276
  layered compounds, 275–276
  thermoelectrics, 275–276
boronitrides, 263, 275
  crystal structure, 274, 275

boronitrides (*continued*)
magnetism, 274
superconductivity, 274
transition metals, 274
borosilicates, 269
bottom-up synthesis, 406, 407–409
bound lanthanide-induced shifts, 504
bridging modes, 227, 229–233
Brillouin functions, 154
bromide, divalency, 164
bromine precursors, 175
(*N*, *N*′-bis(5-bromo-3-methoxysalicylidene) phenylene-1,2-diamine), 282–286
Brønsted basicity, 438–439
buckyballs, 495
bulk continental crust, 13
bulk lanthanide oxides, 477–478
bulk magnetic susceptibility (BMS) shift, 502
bulk nanoporous materials, 405
butadiene, 468–469

cadmium, 166
cage-like structures, 293, 296
calcium
cuprate superconducting materials, 377
luminescent bioprobes, 547
calcium copper, borides, 270
calixarenes, 143
calorimetry, 88
cancers, 68, 69
carbenes, 84, 87, 97–98, 321, 329–330
carbides, 263–264, 271–274
applications, 263
binary compounds, 271–272
borocarbides, 263, 272–274
borocarbonitrides, 263, 275–276
carbonitrides, 263, 275–276
crystal structure, 263, 271–274, 276
encapsulated fullerines, 272
fullerenes, 272
halides, divalent state, 162
layered compounds, 271–274, 276
magnetism, 263, 271–274, 276
physical properties, 271–274, 276
superconductivity, 263, 271, 272, 274, 276
ternary compounds, 272–274
thermoelectrics, 263, 276
transition metals, 272
carbodiimine, 466–467
carbon–13 nuclear magnetic resonance, 507, 508, 541, 542
carbonaceous chondrites, 8–9, 17
carbonates
polymerization, 470–472
siloxides, 207–209, 212
carbonatites, 7, 8, 17
carbon–hydrogen bond activation, aryls, 304
carbonitrides, 263, 275–276
carbonyls, organometallic chemistry, 83, 85, 99, 100
carboxylates, 225–235
ambient condition synthesis, 226
bridging modes, 227, 229–233
coordination modes, 225, 227, 233
coordination numbers, 225, 227, 235
dinuclear compounds, 229–230, 235
gel synthesis, 226
hydrothermal synthesis, 226, 234
mononuclear compounds, 225, 229–233, 235
nuclearity, 225, 227–235
polynuclear compounds, 225, 227, 229–235
solvothermal synthesis, 226, 234
structure, 225, 227–235
synthesis, 225–227, 233–234
tetranuclear carboxylates, 230–231
thermal synthesis, 226, 234
carboxylic acid, 225, 226–234, 235
carboxylic-containing ligands, 539
CASPT2 calculations, 156
CASSCF method, lanthanide ion magnetism, 156
catalysis/catalysts
see also synthesis
aqueous media, 448–455
asymmetric reactions, 438–445, 446, 447, 450–455
carboxylates, 225, 233–234
catalytic converters, 23
cyclopentadienyl, 307
halides, organic synthesis, 175
heterogeneous catalysis, 475–479
homogeneous catalysis, 459–473
lanthanide oxide/hydroxide complexes, 191–192
Lewis acids, 437–439, 445, 448–449, 452–454, 455–456
metal complexes, 438–441, 442–445, 446–448
nanomaterials, 411
organic synthesis, 437–456
water, 448–455
oxide nanomaterials, 411
siloxides, 205, 209
solvents, 438–448
water, 448–455
cathodic reduction, halides, 162, 172
cation chemistry, 175–181
cation exchange, 547
cation sensing, 561–571
CCR *see* cross-correlation
CCT *see* correlated color temperatures
cell condition mimicry, 546–547
cell detection concentration, 551
cell imaging, 551–554
cell permeability, 552, 557
cellular activity, 175
cellular uptake, 552, 557
centroids, cyclopentadienyl, 307–308, 310
ceramic oxide superconducting materials, 371
cerebrospinal fluid, 522–524, 533
ceria (cerium dioxide), 314–315
ceric ammonium nitrate, 313, 316–317, 323
cerium
+4 oxidation state, 46–47
alkoxides, 321, 322–324, 328–329

amides, 321, 325–327
amidinates, 321, 327–328
applications, 313, 314–315
carbenes, 321, 329–330
cerocenes, 321, 330–332
chemistry, 313–320, 321–333
color characteristics, 136
coordination compounds, 313, 315–320
cyclopentadienyl complexes, 321, 328–329
β-diketonates, 313, 317–319
future outlooks, 332
geology/geochemistry, 1, 2, 4–5
halide valency, 165–166, 168–169
halogeno complexes, 316
heterogeneous catalysis, 475–476
inorganic compounds, 313–320
medical diagnostics, 69
organometallics, 321–333
oxidation states, 313–314
oxo acids, 316–317
redox behavior, 4–5
salts, 315
sandwich complexes with tetrapyrrole-type ligands, 319–320
superconducting materials, 372
synthesis, 321–332
tetrapyrrole-type ligands, 319–320
tetravalent chemistry, 313–320, 321–333
cerium–carbon bonds, 321–322
cerium dioxide, 314–315
cerium nitrates, 313, 316–317, 322, 323
cerocene sandwich complexes, 321, 330–332
chain-end control mechanism, 471, 473
chains, cluster complexes, 425–430
chalcogenido anions, 215, 217–219
chalcogenolates, 215–221
bonding, 215–221
cluster chemistry, 215, 217–219
divalent bonds, 215–217, 218
homoleptic bonds, 215–217
molecular synthesis, 215, 219–220
near infrared emission, 220–221
organometallics, 215–217
physical properties, 220–221
selenolates, 215–219
solid-state materials, 215, 219–220
synthesis, 215–219
tellurolates, 215–219
thiolates, 215–219
trivalent bonds, 215–217
characterization
alkoxides, 199–202
endohedral fullerenes, 495–496
lanthanide alkoxides, 199–202
nanomaterials, 405, 409–410
oxide nanomaterials, 405, 409–410
sulfide nanomaterials, 405, 409–410
charge transfer (CT)
endohedral fullerenes, 499
lanthanide ion luminescence, 111, 125–126, 132
chelating ligands, 93–95
chemical behavior, cyclopentadienyl, 307
chemical bonding, 415, 416, 419–432
chemical mechanical planarization, 411–412
chemical properties, compounds, 46–48
chemical reactivity, metallic lanthanides, 45
chemical sensors, 387–388
chemical shift imaging (CSI), 524
chemical structures, lanthanide-induced shifts, 506–507, 508
chemical surface modifications, 395–398
chemical synthesis, upconversion nanoparticles, 389, 393–395
chemical vapor deposition (CVD), 323
chemistry
cerium, 313–320, 321–333
heterogeneous catalysis, 475–476
inorganic compounds, 313–320
lanthanide chalogenolates, 215, 217–219
metal-organic frameworks, 385, 386–387
organometallics, 83–101, 321–333
siloxides, 205–212
tetravalent inorganic compounds, 313–320
tetravalent organometallics, 321–333
chiral catalysis, 438–439, 443–447, 450–455, 456
chiral systems, self-assembly lanthanide supramolecular chemistry, 484–486
chlorine divalency, 161, 162–163, 168
chlorine precursors, 175
chondrite-normalization, 3–7, 10, 12–16
chondritic meteorites, 3–4, 5
chromaticity, 141
chromophores
lanthanide ion luminescence, 118–119, 123, 126–129, 132
ligand sensitization, 144–147
luminescence
lanthanide ions, 118–119, 123, 126–129, 132
sensitization, 144–147, 347–348, 350–351
CIELAB color space, 141–142
citrate, 547
classification
cosmochemistry, 2–3
geochemistry, 2–3
upconversion, 390–391
clean energy, resource sustainability, 21–24
cleavage, 96–97, 209
clusters
amino acids, 237, 239, 243–247
bonding, 415, 416, 419–432
chains, 425–430
chalcogenolates, 215, 217–219
chemistry, lanthanide chalogenolates, 215, 217–219
cluster–polymer hybrids, 192
complexes
amino acids, 237, 239, 243–247
fundamentals, 415–434
lanthanides
amino acids, 237, 239, 243–247
oxide/hydroxides, 183–193
crystal orbital Hamiltonian population diagrams, 416, 417, 429, 432, 433
crystal structure, 419–425

clusters (*continued*)
double chains, 425–430
electronic configuration, 417–418, 432, 433
electronic structure, 415–416
endohedral atoms, 419–432, 433
halides, 161, 172, 419–432, 433
high-coordinate endohedral atoms, 431–432
hydroxide complexes, 183–193
isolated clusters, 419–424, 432, 433
lanthanide amino acid complexes, 237, 239, 243–247
lanthanide complexes, oxide/hydroxides, 183–193
layers, 426, 430–431
linear chains, 425–430
monomeric octohedral geometry, 422–424
octohedral geometry, 422–426
oligomeric clusters, 424–425, 433
oxide/hydroxide complexes, 183–193
selenolates, 217–219
single chains, 425–430
structure, 415–416, 419–425
supertetrahedrons, 421–422, 433
synthesis, 416–418, 433
tellurolates, 217–219
tetrahedral geometry, 421–422, 426, 433
thiolates, 217–219
trigonal bipyramidal geometry, 422, 423
valence electrons, 415, 416, 421, 433
zigzag chains, 425–430
CN *see* coordination numbers
COHP *see* crystal orbital Hamiltonian population diagrams
collider experiments, 380
colloidal chemistry, 405
color characteristics
emission spectra, 136–142
europium, 136–138
gadolinium, 139
lanthanide ions, 136–142
terbium, 136, 137, 138–139
colorimetry
actinide ions, 567–568, 569–571
chemisensors, 567–568, 569–571
color spaces, 140–142, 151
lanthanide ions, 135–142, 567–569, 570–571
luminescence applications, 135–142
color-matching functions, 141
color quality scales (CQS), 141–142
color-rendering indices (CRI), 141–142
color reproduction, 135–142
color spaces, 140–142, 151
comparisons, 3d metals and lanthanides, 105–109
competitive experiments, 545
complexation, 3, 540
complexes
see also hydroxide...; lanthanide...; oxide...
coordination numbers, 106
cyclooctatetraenyl complexes, 321, 330–332
cyclopentadienyl complexes, 321, 328–329
diethylentetramine-pentaacetate, 68–69, 521, 525–527
DOTA complexes, 67–68, 149, 525–526
formation constants, 48–50, 53
group trends, formation constants, 48–50, 53
half-sandwich alkyl complexes, 446–448
halogen complexes, 76, 313, 316
heterobimetallic complexes, 462, 473
homogeneous catalysis, 459–473
ionic radii, group trends, 46–48
lanthanide ions
luminescence applications, 148–150
solvento complexes, 55–61, 74, 78, 79, 80
luminescence
bioprobes, 535–558
lanthanide ions, 148–150
organolanthanides, homogeneous catalysis, 459–473
organometallic redox chemistry, 83, 100
sandwich complexes, 319–320, 321, 330–332
solvento complexes, 55–61, 74, 78, 79, 80
tris-cyclopentadienyl complexes, 308–309
water-soluble complexes, 537
composition phase diagrams, dihalides, 164
compounds, ionic radii, 46–48
comproportionation, 162–163, 168, 172, 178, 181, 418, 433
condensation, nanomaterials, 407
condensed state superconducting materials, 374–375
conditional stability constants, 545
configuration crossover, 161, 165, 172, 433
confocal microscopy, 550, 551, 553, 556, 557
conformation, lanthanide-induced shifts, 507, 508–510
conjugation
ligand sensitization, 144–147, 151
luminescence applications, 144–147
MRI contrast agents, 526–527
organic solvents, 438, 440, 441
Schiff-base ligands, 282–289, 296
consumption considerations, resource sustainability, 23
contact shifts, 502–504, 505–506
continental crust, 12–15
contraction, coordinate numbers, 77
contrast agents
advances and developments, 525–527
amino acids, 237, 245, 247
angiography, 525–526
developments, 525–527
endohedral fullerenes, 498
gadolinium, 521, 522, 523, 524–527, 529–530, 533
lanthanide amino acid complexes, 237, 245, 247
lanthanide complexes, oxides/hydroxides, 191, 192, 193
magnetic resonance angiography, 525–526
MRI
gadolinium, 521, 522, 523, 524–527, 529–530, 533
halides, 175
nanomaterials, 413
nanomaterials, 413
contrast mechanisms, MRI, 522–524
COOP *see* crystal orbital orbital population
Cooper pairs, 374–375
coordination
hydroxide ligands, 183–193
lanthanide-induced shifts, 507, 508–510
lanthanide ions, 237
oxide ligands, 183–193

coordination chemistry
see also coordination numbers
alcohols, 178
amino acids, 237, 238–247
donor atoms, 74
halides, 178
helical structures, 536–537
hydroxide complexes, 183–193
lanthanide complexes, 73–80
amino acids, 237, 238–247
hydroxides, 183–193
monodentate O-donor ligands, 78–80
O-donor ligands, 78–80
oxides, 183–193
lanthanide ions, 55–61, 65–70, 73–80
ligands, 73–80
monodentate O-donor ligands, 78–80
O-donor ligands, 78–80
oxide complexes, 183–193
scandium, 73, 78–79
solvento complexes, 55–61
X-ray diffraction, 77–78
yttrium, 73, 79–80
coordination complexes, ionic radii, 47–48
coordination compounds
cerium, 313, 315–320
tetravalent lanthanide compounds, 313, 315–320
coordination modes
carboxylates, 225, 227, 233
polycarboxylates, 233
siloxides, 205–206, 207, 211
coordination numbers (CN), 74–75
3d metals, lanthanides, 106
amides, 75
amino acids, 238
carboxylates, 225, 227, 235
cluster complexes, 419, 431–432, 433
complexes, 106
contraction, 77
coordination chemistry, 73, 74–76
β-diketonate/β-diketones, 253–257
examples, 74–76
geology/geochemistry, 3
geometry, 74–77
halides, 165–166, 170, 172
ionic radii, group trends, 46–48, 53
lanthanides
3d metals, 106
amino acids, 238
contraction, 77
organometallics, 75
solvento complexes, lanthanide ions, 55
coordination polymers, 281–297, 385–388
see also metal–organic frameworks
coordination sites
lanthanide ions, 135, 148–150
luminescence, lanthanide ions, 135, 148–150
organometallic chemistry, 92–93
coordination spheres
electronic structure, 117
ionic radii, 47, 53
saturation, 92–93
solvento complexes, 55–56
copper, self-assembly lanthanide supramolecular chemistry, 492–493
copper oxide superconducting materials, 371, 373, 375–380
coprecitation, 393–394
correlated color temperatures (CCT), 141
correlation spectroscopy (COSY), 517
corrosion inhibitors, 225
Coryell–Masuda plots, 4, 5
cosmochemistry, 1, 2–3
COSY *see* correlation spectroscopy
Coulomb interactions, 31, 33
Coulomb's law, 133
coupling, 153–158, 447–448
covalent bonding
immunocytodetection, 555
lanthanide complexes, 554–557
lanthanide-induced shifts, 501
luminescent bioprobes, 554–557
organometallic chemistry, 83, 84–87
oxidation states, 43–44
CQS *see* color quality scales
cracking
heterogeneous catalysis, 475
resource sustainability, 23
CRI *see* color-rendering indices
critical current density, 371–372
critical magnetic fields, 371–372
cross-aldol reactions, 452
cross-correlation (CCR), 501, 513, 517
crown ethers, 565–566
crystal fields
3d metals, 107–108
electronic structure, 30–33
lanthanides
3d metals, 107–108
magnetism, 154
crystal fractionation, 2, 4, 7, 9–11, 14, 16, 17
crystal growth, 226
crystallization, 540
crystallography, 199–202, 375–376
crystal orbital Hamiltonian population (COHP) diagrams, 167, 172, 416, 417, 429, 432, 433
crystal orbital orbital population (COOP), 432, 433
crystal structure
amino acids, 237, 239–247
borides, 263, 264–271, 276
borocarbides, 272–274
borocarbonitrides, 275–276
boronitrides, 274, 275
carbides, 263, 271–274, 276
carbonitrides, 275
cluster complexes, 419–425
β-diketonate/β-diketones, 249, 253–260
halide valency, 165–166, 169–171, 172
high-temperature cuprates, 375–376
lanthanide amino acids complexes, 237, 239–247
lanthanide oxide/hydroxide complexes, 186–187, 189–190

crystal structure (*continued*)
nitrides, 263, 275–276
polynuclear lanthanide complexes, 281–282, 283–285, 286, 287–290
self-assembly lanthanide supramolecular chemistry, 484–485, 486–487
siloxides, 205–206
CSI *see* chemical shift imaging
CT *see* charge transfer
cuprate superconducting materials, 371, 373, 375–380
Curie's law, 154
current status, luminescence, 112
cyanides, 336–337
cyclen frameworks, 145, 149, 482–483, 487–491
cyclic esters, 470–472
cyclic ionophores, 564–566
cyclooctatetraenyl complexes, 321, 330–332
cyclopentadienides, 308
cyclopentadienyl
bonding, 307–310
centroids, 307–308, 310
complexes, 321, 328–329
electrostatics, 307–308
hypervalency, 310
organometallic chemistry, 84, 85, 88–90, 92–94, 97
pendent, 308–310
reactivity, 307, 308–310
structure, 307, 308–310
substitution, 307–310
synthesis, 307, 308
trivalent chemistry, 307–310

data analysis, 506–515
DC arc discharge, 496
DC susceptibility, 340, 341, 342–344
deactivations, lanthanide ion luminescence, 122, 123, 128–130
decomposition, upconversion nanoparticles, 394–395
degeneracy
atomic orbitals, 114–115, 132
electronic structure, 29–32, 33
lifting, 31–32
dendrimers, 249, 251, 255, 260, 525–526
density of states (DOS), 167, 172, 433
design, ligands, 481–493
detection
actinide ions, 561, 562–568, 569–571
lanthanide ions, 561, 562–569, 570–571
luminescent bioprobes, 551
Dexter energy transfer mechanism, 124–125
d–f polynuclear β-diketonates, 258–260
diagnostics
see also magnetic resonance...
nanomaterials, 410, 413
diamagnetic shifts, 502, 504–505
diastereoisomers, 507, 508–510
dibenzyl phenoxide ligands, 202
diborides, 264
dicarbides, 271
Diels-Alder reactions, 438, 440, 444–445, 453
dienes, 468–469
diethylentetramine-pentaacetate (DTPA), 68–69, 521, 525–527
1,4-diformyl-2,3-dihydroxybenzene, 492–493
dihalides, 161–168
2,6-di(iso-propyl) phenoxides, aryloxide compounds, 201
β-diketonate/β-diketones, 249–260
coordinate numbers, 253–257
crystal structure, 249, 253–260
dendrimers, 249, 251, 255, 260
eight-coordinate lanthanide complexes, 254–257
luminescence, 350–351, 364
molecular structure, 250–251, 253–255, 258, 259
mononuclear lanthanide complexes, 249, 253–257
nine-coordinate lanthanide complexes, 257
NIR materials, 350–351, 364
ORTEP molecular structure diagrams, 254, 256–257, 259, 260
polynuclear lanthanide complexes, 249, 257–260
sensitization, luminescence applications, 135, 143, 144–145
seven-coordinate lanthanide complexes, 254, 256
six-coordinate lanthanide complexes, 253–254, 256
structure, 249–260
ten-coordinate lanthanide complexes, 257, 258
tetravalent lanthanide compounds, 313, 317–319
types, 249, 250–253, 254, 255, 260
dimerization, 465–466
dimers, 179, 180
dimetallofullerines, 497–498
1,2-dimethoxyethane, 355
dimethoxyethylene, 308–310
2,6-dimethylphenoxide, 201
dinuclear carboxylates, 229–230, 235
dinuclear lanthanide oxide/hydroxide complexes, 186
dioxides, 314–315
diphenyl phenoxide ligands, 202
dipicolinic-acid-based ligands, 145–146
dipolar shifts, 501, 502, 503–504
direct magnetic relaxation, 338
direct metathesis, 198
disiloxanediolate complexes, 323–324
display devices, 135
disposition, resource sustainability, 24
di-*tert*-butyl derivatives, 201–202
ditopic ligands, 490, 535–558
divalent states
chalogenolates, 215–217, 218
halides, 161–173, 175–176, 178
oxides, 171–172
siloxides, 205–206
solid halides, 161–173, 175–176, 178
synthesis, halides, 162–163, 168–169
DNA, luminescent bioprobes, 536, 550–551
dodecaborides, 266
dodecahedral geometries, 76
donor atoms, 74
donor cleavage, 96–97
donor-functionalized chelating ligands, 93–95
donor ligands, 78–80, 93–95
DOS *see* density of states
DOTA complexes, 67–68, 149, 525–526

double chains, 425–430
double-decker lanthanide complexes, 282, 286–289
double-decker ligands, 319
double–double effect, 5–6
downconversion, 136
drug delivery, 388
DTPA *see* diethylentetramine-pentaacetate
dynamics
  biomacromolecules, 511–515
  lanthanide ion luminescence, 128–129, 132
dysprosium
  color characteristics, 136, 137, 139
  halide valency, 166–167, 169, 170–171
  molecular magnetic materials, 339, 340, 341–342
  NIR luminescence, 347–349, 356–359
  optodes, 568
  photophysics, 348–349
  sol-gels, 356–359

Early–Middle Proterozoic carbonate rocks, 7–8
Earth's crust, 1–8, 10–18
echo, 522–524, 533
echo times, 522–524, 533
EDTA *see* ethylenediaminetetra-acetate
EHMO *see* extended Hueckel molecular orbital theory
eight-coordinate lanthanide complexes, 254, 256–257
electric dipole transitions, 122
electroceramics, 197, 203
electrochemical sensors, 561, 562–567, 570–571
electronegativity, 3, 4
electron–electron interactions, 30–32
electronic absorption, 118–119
electronic angular momentum, 43
electronic configurations
  borides, 264
  carbides, 264
  cluster complexes, 417–418, 432, 433
  endohedral fullerenes, 496–498
  geology/geochemistry, 3, 4
  halides, 161, 165, 166–167, 172
  lanthanide ion magnetism, 154–155
  magnetism, 154–155
  nitrides, 264
electronic level classification, 115
electronic properties
  3d metals, lanthanides, 107–108
  siloxides, 205
electronic spectra, 3d metals, lanthanides, 107–108
electronic states, metal-organic frameworks, 386
electronic structure
  cluster complexes, 415–416
  coordination sphere effects, 117
  Coulomb interactions, 31, 33
  crystal fields, 30–33
  cyclopentadienyl, 307
  degeneracy, 29–32, 33
  electron–electron interactions, 30–32
  energy levels, 29–31
  excited state configurations, 29–32
  f-lanthanide ions, 112–117
  ground state configurations, 29–32
  halide valency, solids, 161, 165, 166–167, 172
  Hamiltonians, 31–32
  Hunds rules, 115–117
  lanthanide ions, luminescence, 111, 112–117, 130–131
  lanthanides, 27–33
  luminescence, 111, 112–117, 130–131
  oxidation states, 29–31
  quantum numbers, 29–32
  relativistic effects, 27–28, 33
  spin–orbit coupling, 29–32, 33
  Stark effect, 31, 32, 33
  term symbols, 29
  Zeeman effect, 31, 33
electrostatics, 133, 307–308
elimination, organometallic chemistry, 95
emission spectra
  chalogenolates, 220–221
  color characteristics, 136–142
  lanthanide ions, 111, 136–142
  polynuclear lanthanide complexes, 285–286, 289, 290, 291–292, 293, 294
emitters, lanthanide ion luminescence, 111, 127, 130
empty clusters, lanthanide halides, 418–419
enantioselective synthesis, 438–445, 453, 454–455, 456
encapsulation
  endohedral fullerenes, 495–498
  fullerines, 272
  nanoparticles, 555–556
encoding, MRI, 522
endangered elements, resource sustainability, 22–23
endogenous anions, 547
endohedral atoms, 162, 172, 419–432, 433
endohedral fullerenes, 495–499
  applications, 495, 498
  bonding, 496–498
  characterization, 495–496
  electronic configurations, 496–498
  encapsulation, 495–498
  isolation, 495, 496
  nitrides, 497–498
  structure, 496–498
  synthesis, 495, 496
energy barriers, 338
energy conversion, 136, 142, 347
energy levels, 29–31, 154–155
energy shifts, 133
energy storage, superconducting materials, 380
energy transfer
  lanthanide ion luminescence, 111, 124–125
  upconversion, 391
enthalpy
  +2 oxidation state, 48–49
  +4 oxidation state, 45, 46
  of formation, 45, 48–49, 51–53
  group trends, 43, 45–46, 50, 51–53
  halides, 166
  of hydration, 43, 50
  organometallic chemistry, 88

enthalpy (*continued*)
oxidation states, 43
of vaporization, 43, 45, 46, 51
entropy of hydration, 50–51
erbium
aryls, 303–304
color characteristics, 136, 137, 140
β-diketone ligands, 348–351
8-hydroxyquinolinate-based lanthanide complexes, 352–353
ionic liquids, 364
lanthanide ion luminescence, 66–67
molecular magnetic materials, 342
NIR luminescence, 347–353, 356–361, 364
photophysics, 348–349
self-assembly supramolecular chemistry, 493
silicates, 360–361
siloxides, 205
sol-gels, 356–359
upconversion, 364
ESA *see* excited state absorption
E-selectin, MRI, 532, 533
esters, 470–472
etching, 406–407
ethane, 475, 478
ethoxy-benzyl contrast agents, 525
ethylene, 467, 475, 478
ethylenediaminetetra-acetate (EDTA), 57
europium
alkoxides, 200
avidin, 555
catalysis, 438
cellular uptake, 552
chalcogenolates, 217, 218
color characteristics, 136–138
electronic structure, 116
geology/geochemistry, 1, 4–5
halide valency, 161, 162, 163–168, 169
optodes, 568
quantum yields, 147
redox behavior, 4–5
Schiff-base ligands, 283–284, 292–294
self-assembly supramolecular chemistry, 482, 484–485, 486–491
superconducting materials, 372
triplet state energy correlation, 147
europium–terbium, 487–490
exchange-coupling interactions, 153–158
exchange rate constants, 449
exchange spectroscopy (EXSY), 509, 517
excitation
lanthanide ion luminescence, 111–132
polynuclear lanthanide complexes, Schiff-base ligands, 285–286, 289, 290, 291–292, 293, 294
pulse, 521–522, 533
wavelength limitations, 556–557
excited state absorption (ESA), upconversion, 142, 391
excited state configurations, 29–32
EXSY *see* exchange spectroscopy
extended Hueckel molecular orbital (EHMO) theory, 416, 417
extended structures, 162, 172, 421, 432, 433
external magnetic fields, 533

FAME *see* fatty acid methyl esters
fate, resource sustainability, 24
f atomic orbitals, 113–114
fatty acid methyl esters (FAME), 475, 478
f electrons, 28–29, 32
Fermi levels, 167–168, 172, 416, 427, 432, 433
ferromagnetism
borides,264, 265–266, 267, 269–270
borocarbides, 273
carbides, 271–272
gadolinium, 335
nitrides, 274
f–f polynuclear β-diketonates, 257–258, 259
field emitters, 266
filling orbitals, 27, 28, 114
films, nanomaterials, 405
first order effects, coordination numbers, 74, 76
flame spray pyrolysis, 407
f-lanthanide ions, 112–117
flexibility, lanthanide ion luminescence applications, 148–150
flexible ligands, 506–507
Schiff-base ligands, 282, 286–291, 296
fluorescein, 355
fluorescence, 111, 112, 123–124, 132
fluorinated chalcogenolates, 217
fluorinated β-diketones, 250, 251
fluorine, 164, 175, 313–314
fluoroimmunoassay, 66–67
fluorophores
lanthanide ion luminescence, 123, 127, 130, 132
upconversion nanoparticles, 390, 398, 400, 402–403
fluxons, 379
formaldehyde, 451–452
formation
see also synthesis
2:3 lanthanide complexes, 541–544
bioconjugates, 554–555, 557
constants, 48–50, 53
lanthanide complexes, 539–549
self-assembly lanthanide supramolecular chemistry, 481–493
Förster energy transfer mechanism, 125
Fourier transform infrared spectroscopy (FTIR), 176
fractionation, 2, 4, 7, 9–11, 14, 16, 17
Frank–Condon principle, 120, 123
freezing points, 476
frequency encoding, 522
Friedel–Crafts alkylations, 438, 439, 441–442
FTIR *see* Fourier transform infrared spectroscopy
fullerenes, 272, 495–499
fundamental chemistry
heterogeneous catalysis, 475–476
metal-organic frameworks, 385, 386–387
organometallics, 83–101
fusion reactors, 380

future outlooks
  cerium, 332
  organometallics, 332
  tetravalent chemistry, 332
  upconversion nanoparticles, 402
f–f spectra, 107–108

gadolinium
  break, 43–44
  catalysis, 438
  color characteristics, 139
  contrast agents, 521, 522, 523, 524–527, 529–530, 533
  cuprate superconducting materials, 377
  halides, 418, 419, 430
  magnetism, 155–158
  medical diagnostics, 67–69
  molecular magnetic materials, 339–340
  MRI, 67–69, 521–527, 529–530, 533
  radial charge density, 27, 28
  self-assembly supramolecular chemistry, 484–485, 490–491
  siloxides, 205
  texaphyrin, 537
  valence orbitals, 27, 28
gadolinium–copper systems, 156–157
gadolinium-diethylentetramine-pentaacetate, 68–69, 521, 525–527
gamuts, colorimetry, 142
gas phase synthesis, 406, 407
gas sensors, 412–413
gels, crystal growth, 226
gel synthesis, 226
generators, superconducting materials, 380
geology/geochemistry, 1–18
  abundance normalization, 3–4
  archean eon, 11, 12–15, 17
  authigenic phases, 4, 12, 17
  carbonaceous chondrites, 8–9, 17
  carbonatites, 7, 8, 17
  chondrite-normalization, 3–7, 10, 12–16
  classification, 2–3
  continental crust, 12–15
  cosmochemistry, 1, 2–3
  double–double effect, 5–6
  Earth's crust, 1–8, 10–18
  hydrosphere, 15–16
  mantle, 8, 9–10, 11, 17
  meteorites, 3–4, 5, 8–9
  minerals/mineralogy, 1–9
  oceanic crust, 11–12
  ocean water, 15–16
  ores, 7–8
  planets, 1, 2–3, 8–10
  redox behavior, 3, 4–5
  rocks, 1–8, 12–16
  solar system, 1, 2–3, 8–10
  terrestrial reservoirs, 10–16
  tetrad effect, 5–6
  trace elements, 1–18
geometry
  coordination numbers, 74–77
  lanthanide-induced shift reagents, 507, 508–511
Glauber, Roy J., 342
glycerols, 475, 478
gradients, MRI, 522, 533
granulites, 14, 17
graphite intercalated borocarbides, 273–274, 276
graphite intercalated carbides, 272, 276
grinding, nanomaterials, 406–407
ground states
  degeneracy lifting, 31–32
  electronic structure, 29–32
  lanthanide ion magnetism, 154–155
  oxidation states, 29–31
  subshell electronic structure, 115–117
group trends, 43–53
  complexes, 48–50, 53
  enthalpy, 43, 45, 46, 50, 51–52, 53
  enthalpy of formation, 51–52, 53
  enthalpy of hydration, 43, 50
  enthalpy of vaporization, 43, 45, 46, 51
  entropy of hydration, 50–51
  formation constants, 48–50, 53
  inclined W plots, 44, 49, 50
  ionic radii, 46–48
  lanthanide contraction, 44
  metallic lanthanides, 44–46
  metallic radii, 44–45
  oxidation states, 43–44, 50–52
  thermodynamic stability, 48–52
  W plots, 44, 49, 50
  Z-plots, 43–44, 49, 50, 52
guanidinate, 327–328
guanylation, 459, 460, 466–467

half-sandwich alkyl complexes, 446–448
half-wave potentials, 47, 49, 50
halide metathesis, 198
halides, 175–181
  alcohols, 178–179
  anhydrides, structure, 177–178
  catalysis/catalysts, 175
  cluster complexes
    divalent state, 161
    empty clusters, 418–419
    endohedral atoms, 419–432, 433
  comproportionation, divalent state, 162, 168
  dimers, structure, 179, 180
  divalent states, 161–173, 175–176, 178
  empty clusters, 418–419
  endohedral atoms, 419–432, 433
  enthalpy of formation, group trends, 51–52
  hydrates, 176–177
  inorganic tetravalent chemistry, 175–176
  ionic radii, 47
  ligands, 177–181
  luminescent materials, 175
  metallothermic reduction, 162–163, 168

halides (*continued*)
methanol, 178–179
monomers, 179, 180
nuclear magnetic resonance, 175, 176
oxidation states, 161, 162, 166, 172
oxides, 171–172
phosphorescent materials, 175
polymers, 179, 180–181
reduction methods, 162–163, 168–169
salts, 179, 180
scintillators, 175, 178, 181
solids, 161–173, 175–176, 178
solvates, 178–181
structure, 176–181
synthesis, 162–163, 168–169
tetravalent chemistry, 175–176, 313–314, 316
valency, 161–173
halogen complexes, 76, 313, 316
Hamiltonians, 31–32, 155
hard Lewis acidity, 183
HDVV *see* Heisenberg-Dirac-Van Vleck spin Hamiltonian
heat of formation, 45–46, 48–49
heavy fermions, 373
Heisenberg-Dirac-Van Vleck (HDVV) spin Hamiltonian, 155
helicates
ditopic ligands, 535–558
ligand sensitization, luminescence applications, 138, 139–140, 151
luminescent bioprobes, 535–558
self-assembly lanthanide supramolecular chemistry, 482, 483–484, 486–488
heterobimetallic complexes, 462, 473
N-heterocyclic carbene ligands, 321, 329–330
hetero Diels-Alder reactions, 453
heterogeneous catalysis, 475–479
applications, 477–478
chemistry, 475–476
effectiveness, 477–478
ethylene/ethane, 475, 478
fundamental chemistry, 475–476
lanthanide oxides, 475–478
Lewis acids, 476, 478
methane oxidative coupling, 475, 478
oxides, 475–478
siloxides, 205
triglyceride transesterification, 475, 478
heteroleptic structures
cylopentadienyl, 308–309
siloxides, 205, 207, 211, 212
heterometallic multinuclear assemblies, 487–493
heteropolymetallic lanthanide complexes, 353–354
hexaborides, 265–266
hexanuclear lanthanide complexes, 189–190
hexene, 467
high-coordinate endohedral atoms, 431–432
high-energy colloids, 380
high nuclearity polynuclear lanthanide complexes, 291–296
high-resolution luminescence, 542–543
high-strength permanent magnets, 153
high-temperature cuprates (HTSC)
applications, 378–380
crystal structure, 375–376
structure, 375–376
superconducting materials, 371, 373, 375–380
historical overviews
luminescence, 111–112
organometallic chemistry, 83–84
holmium
aryls, 303–304
color characteristics, 136, 137, 139
molecular magnetic materials, 339
NIR luminescence, 347–349, 356–359, 364
photophysics, 348–349
sol-gels, 356–359
upconversion, 364
homogeneous catalysis, 459–473
alkoxylation, 460–461
alkynes, 465–467
amidation, 462–464
amidines, 464–465
amination, 460
amines, 462–465, 466–467
asymmetric synthesis, 461–462
cyclic esters, 470–472
dimerization, 465–466
esters, 470–472
guanylation, 459, 460, 466–467
hydroalkoxylation, 460–461
hydroamination, 460
intermolecular organic transformation, 460, 461–467
intramolecular organic transformation, 460–461
methyl methacrylate, 469–470
nitriles, 464–465
olefins, 467–468
organic transformation, 460–467
organolanthanide complexes, 459–473
phosphines, 466–467
polymerization, 459, 467–472
siloxides, 205, 209
stereoselective polymerization, 468–469
Tishchenko reaction, 464, 473
homoleptic structures
alkoxides, 197–203, 322–326
chalcogenates, 215–217
complexes with multidentate ligands, 287–290
cyclopentadienyl, 308
β-diketonate complexes, 317–319
homogeneous catalysis, 461
organometallic chemistry, 91, 96–98
siloxides, 205, 207–208, 211, 212
solvento complexes of lanthanide ions, 59
homometallic multinuclear assemblies, 484–487
homonuclear helicate structures, 535–558
host matrices, 392–393
HTSC *see* high-temperature cuprates
Hunds rules, 113, 115–117, 124
hybrid lanthanide NIR luminescence, 347, 356–365
hydrated nitrates, ionic radii, group trends, 47–48
hydrates, 176–177

hydration, 185
hydration energies, 29
hydration enthalpy, 43, 50
hydroalkoxylation, 460–461
hydroamination, 445–446, 447, 460
hydrocarbyl ligands, 299, 301
hydroelementation, 460–461
hydrogen-nuclear magnetic resonance
  polynuclear lanthanide complexes, 294, 295
  structural information, 507, 509
  titrations, 541, 543
hydrogenoid orbitals, 112–113
hydrogen relaxation, 522, 527–529, 533
hydrolysis
  amino acids,237, 239–247
  constants, 449
  lanthanide oxide/hydroxide complexes, 185–187, 189, 193
  phosphate esters, 67
hydrolytic cleavage, 209
hydrosilylation, 205, 206
hydrosphere, geology/geochemistry, 15–16
hydrothermal synthesis
  carboxylates, 226, 234
  metal-organic frameworks, 385–386
  nanomaterials, 407–408
  upconversion nanoparticles, bioimaging, 395
hydrothermal waters, 16
hydroxide complexes, 183–193
  applications, 190–192
  clusters, 183–193
  coordination chemistry, 183–193
  nuclearities, 185–190
  properties, 190–192
  rational synthesis, 184–185
  structure, 185–190
hydroxides
  coordination, 183–193
  tetravalent lanthanide compounds, 315
hydroxymethylation, 451–452
8-hydroxyquinolinate-based lanthanide complexes, 351–353
hypersensitive transformations, 131, 137
hypervalency, cyclopentadienyl, 310
hypophosphatemia, lanthanide ions, 69
hysteresis loops, 335–337

imaging
  see also bioimaging; MRI
  lanthanide oxide/hydroxide complexes, 192
  luminescent bioprobes, 551–554
  medical diagnostics, 67–69
  metal-organic frameworks, 388
  self-assembled mononuclear lanthanide supramolecular chemistry, 481–484, 493
imines, 442–445
iminodiacetate, 482, 483
immunoassays, 66–67, 556
immunocytochemistry, 555, 557
immunoglobulin, 556
immunohistochemical assays, 556
inclined W plots, 44, 49, 50
incongruent melting, 172
industrial applications, nanomaterials, 405, 410–413
inflammation targeting, MRI, 532
information storage, 192
inner series periodicity, 43–44
innerspheres, 176–177, 181
inner transition elements *see* lanthanides
inorganic compounds
  chemistry, 313–320
  tetravalent chemistry, 313–320
    coordination compounds, 313, 315–320
    β-diketonates, 313, 317–319
    dioxides, 314–315
    halides, 313–314, 316
    halogeno complexes, 313, 316
    inorganic chemistry, 313–320
    ligand complexes, 317–320
    multi-ligand complexes, 317–320
    oxo acids, 313, 316–317
    porphyrinates, 313, 316, 320
    salts, 315
    sandwich complexes with tetrapyrrole-type ligands, 319–320
    tetrapyrrole-type ligands, 319–320
inorganic tetravalent chemistry, 175–176
in situ synthesis, 540
integrin $\alpha_v\beta_3$ targeting, 532–533
intercalated carbides, 272
interelectronic repulsion, 154, 155
interligand repulsions, 76
intermolecular organic transformation, 460, 461–467
interstitial atoms, 416, 418, 431, 433
intersystem crossing, 113, 124
intramolecular organic transformation, 460–461
inversion population, 142–143
in vivo imaging, 389, 398–402, 403
in vivo magnetic resonance spectroscopy, 501
iodide
  divalency,161, 164, 167–168
  precursors, 175
  tetravalency, 168–169
  valency, 161, 164, 167–169
ionic bonding, 83, 84, 85–86
ionic lanthanides, valence configuration, 29
ionic liquid luminescence, 347, 363–364
ionic radii, 46–48
  atomic number, 2–3, 4
  complexes, 46–48
  compounds, 46–48
  coordination numbers, 46–48, 53
  coordination spheres, group trends, 47, 53
  oxidation states, 43
ionization energy, 43, 45–46, 53
ionization potentials, 416, 417
ionogels, 363–364
ionophores, 563–567
ion-selective electrodes (ISE), 561, 562–567, 570–571
iridium, 378
iron-based layered pnictides, 373–374

isolated clusters, 419–424, 432, 433
isolated pentagon rule, 498
isolation
  alkyls, 299, 301
  endohedral fullerenes, 495, 496
isoprene, 205, 206, 468–469

Jablonski diagrams, 122–123, 124, 386
Josephson effect, 378, 379–380

keto-enol tautomerisms, 249, 250
kinetic inertness, 546
kinetics
  lanthanide ion luminescence, 128–129, 132
  organometallic chemistry, 83, 88, 100
Klemm graphs, 164
Kondo lattice systems, 266

lab-on-chips, 556
lactides, 470–472
Lambert–Beer law, 128
Landé factor, 153–154
Landé's interval rule, 32
lanthanide 3d metal comparisons, 105–109
  angular momentum, 108
  coordination numbers, 106
  crystal fields, 107–108
  electronic properties, 107–108
  electronic spectra, 107–108
  electronic structure, 27–33
  filling order, 27
  f–f spectra, 107–108
  magnetic properties, 108
  orbital angular momentum, 108
  organometallic compounds, 106–107
  oxidation states, 43–50, 105–106
  reactivity, 105
  reduction potentials, 105, 106
  spin–orbit coupling, 108
  valence configuration, 27–29
lanthanide alkoxides, 197–203
  alkyl compounds, characterization, 199, 200–201
  characterization, 199–202
  crystallography, 199–202
  phenol derivatives, characterization, 199–202
  synthesis, 197–198
lanthanide alkyls, 299–302
lanthanide chalogenolates, 215–221
  bonding, 215–221
  chemistry, 215, 217–219
  cluster chemistry, 215, 217–219
  molecular synthesis, 219–220
  physical properties, 220–221
  solid-state materials, molecular synthesis, 219–220
  thermolysis, 219–220
lanthanide complexes
  see also complexes, polynuclear...
  α-amino acids, 238–239
  amino acids, 237–247
  aqueous media, 185, 541–544
  1,4-benzene dicarboxylate linker, 292–295
  4,4′-bipyridyl linker, 292–295
  cell condition mimicry, 546–547
  clusters, 237, 239, 243–247
  competitive experiments, 545
  conditional stability constants, 545
  conjugated Schiff-base ligands, 282–289, 296
  coordination chemistry, 73–80
    amino acids, 237, 238–247
    monodentate O-donor ligands, 78–80
    O-donor ligands, 78–80
  covalent bonding, 554–557
  crystal structure, amino acids, 237, 239–247
  flexible Schiff-base ligands, 282, 286–291, 296
  formation, 539–549
  hexanuclear complexes, 189–190
  hydrolysis, 237, 239–247
  hydroxides, 183–193
    applications, 190–192
    clusters, 183–193
    coordination chemistry, 183–193
    nuclearities, 185–190
    properties, 190–192
    rational synthesis, 184–185
    structure, 185–190
  kinetic inertness, 546
  lanthanide-induced shifts, 507–511, 544
  low pH synthesis, 237, 239–241
  luminescence
    bioprobes, 535, 537–549
    NIR materials, 347, 348, 350–356
    sensing, 148
    water, 547–549
  metal–organic frameworks, 354, 386
  monodentate O-donor ligands, 78–80
  mononuclear complexes, 249, 253–257, 481–484, 493
  multidentate ligands, 281–297
  NIR material luminescence, 347, 348, 350–356
  O-donor ligands, 78–80
  oxides, 183–193
    applications, 190–192
    clusters, 183–193
    coordination chemistry, 183–193
    nuclearities, 185–190
    properties, 190–192
    rational synthesis, 184–185
    structure, 185–190
  pentanuclear tetradecker complexes, 283–285
  pH, 237, 239–241, 546–547
  photophysics, 535, 537–539
  pM values, 545
  proteinogenic amino acids, 238–239, 247
  quantum yields, 535, 537–541, 548–550, 553–555
  Schiff-base ligands, 281–297
  sensing, 148

stability constants, 544–546, 557
structure, 237, 239–247, 281–296, 507–511
synthesis, 239–247, 539–549
titrations, 541, 543, 544–545, 546
toxicity, 551
transmetallation, 547
trinuclear lanthanide, 186
triple-decker complexes, 282–286
types, β-diketonate/β-diketones, 249, 250–253, 254, 255, 260
ultraviolet-visible titration, 544–545
versatility, 552–553
water, 547–549
lanthanide contraction, 44, 77
lanthanide coordination polymers, 281–297
lanthanide halides, 175–181
alcohols, 178–179
anhydrides, 177–178
cluster complexes, 418–432, 433
dimers, structure, 179, 180
divalent states, 161–173
empty clusters, 418–419
endohedral atoms, 419–432, 433
hydrates, 176–177
ligands, 177–181
monomers, 179, 180
polymers, 179, 180–181
salts, structure, 179, 180
scintillators, 175, 178, 181
solvates, 178–181
structure, 176–181
lanthanide hybrid NIR luminescence, 347, 356–365
lanthanide-induced shifts (LIS), 501–518
alkali metal ions, 515–517
applications, 501–502
biomacromolecules, 511–515
biosystems, 511–517
bound shifts, 504
contact shifts, 502–504, 505–506
diamagnetic shifts, 502, 504–505
dipolar shifts, 501, 502, 503–504
lanthanide complexes, 507–511, 544
ligands, structure, 506–507, 508
macromolecules, biosystems, 511–517
metal ion distribution, 515–517
MRI, 507–511
MRS, 507–511, 515–517
nucleic acids, 511–515
proteins, structure, 511–515
pseudocontact shift, 501, 502, 503–504
reagents, 501–518
relaxation, 501–507, 512–517
separation shift contributions, 504–506
shift reagents, 515–517
small flexible ligands, structure, 506–507
structure, 506–515
supramolecular architectures, structure, 511
theory, 502–506
lanthanide ions
amino acids, 237–247
angular momentum, 153–158
aqueous media, 55, 56–59
atomic orbitals, 112–115, 132
biological activity, 65–67
biological analysis, luminescence, 65–67
bone disorders, 68–69
cancers, 68, 69
cation sensing, 561–571
charge transfer, 111, 125–126, 132
chromophores, 118–119, 123, 126–127, 128–129, 132
color characteristics, 136–142
colorimetry, 135–142, 567–569, 570–571
color reproduction, 135–142
complex architectures, 148–150
coordination chemistry, 73–80
biological and medical applications, 65–70
solvento complexes, 55–61
coordination numbers, 238
coordination sites, 135, 148–150
coupling, 153–158
detection, 561, 562–569, 570–571
electrochemical sensors, 561, 562–567, 570–571
electronic configuration, 154–155
electronic structure, 111, 112–117, 130–131
emission spectra, 136–142
energy conversion, 136, 142
exchange-coupling interactions, 153–158
excitation, 111–132
flexibility, 148–150
fluorescence, 111, 112, 123–124, 132
hypersensitive transformations, 131
ion-selective electrodes, 561, 562–567, 570–571
lasers, 135, 136, 142–143
lifetimes, 128–130
ligand field effect, 131
ligands
luminescence, 117–123, 125–126
solvento complexes, 56–57, 59–61
light–matter interactions, 117–123
luminescence, 111–133
applications, 135–151, 535–558
atomic orbitals, 112–115, 132
biological analysis, 65–67
bioprobes, 535–558
charge transfer, 111, 125–126, 132
chromophores, 118–119, 123, 126–129, 132
colorimetry, 135–142
coordination sites, 135, 148–150
electronic structure, 111, 112–117, 130–131
excitation, 111–132
hypersensitive transformations, 131
lasers, 135, 136, 142–143
lifetimes, 128–130
ligands, 117–123, 125–126
light–matter interactions, 117–123
medical diagnostics, 67–69
medical therapy, 67–68
NIR emission, 135, 136, 139–140, 150–151, 347–349
organic ligands, 117–123
photophysics, 111–133, 347, 348–349
quantum yield, 127–128, 129, 130

lanthanide ions (*continued*)
sensitization, 111, 124–128, 129–130
sensitizing ligands, 135, 136, 143–150
solvatochromism, 126–127, 132
solvent effects, 130
upconversion, 135, 136, 142
visible emission, 139–140
magnetism, 153–158
matter–light interactions, luminescence, 117–123
medical diagnostics, 65–66, 67–69
medical therapy, 67–68
MRI, 65–66, 67–69
NIR emission, luminescence, 135–136, 139–140, 150–151, 347–349
NMR shift reagents, 501–518
nonaqueous media, 59–60
optical sensors/optodes, 561, 567–569, 570–571
orbitals, 153–158
organic ligands, 117–123
organic radicals, magnetism, 155–158
paramagnetism, 157–158, 501–518
phosphorescence, 111, 112, 123–124, 132
photophysics, 111–133, 347, 348–349
probes, 131, 535–558
purification, 112
quantum yield, 127–128, 129, 130
radicals, 153–158
salts, solvento complexes, 57–59
sensitization, 111, 124–128, 129–130
sensitizing ligands, 135, 136, 143–150
sensors, 561–571
separation, 112
shift reagents, 501–518
solubility, 148
solvatochromism, 126–127, 132
solvent effects, 130
solvento complexes, 55–61
spin, 153–158
spin–orbit coupling, 153–155
stability, 148
structure, 55–61
toxicity, 65–66, 69
transition metal ions, 153–158
upconversion, 135, 136, 142
visible emission, 139–140
lanthanide oxides, 475–478
lanthanum
aminocarboxylic acids, 49–50
enthalpy of formation, group trends, 51–52
halide valency, 165–166, 168–169
medical diagnostics, 69
superconducting materials, 372
LASC *see* Lewis acid–surfactant-combined catalyst
lasers
lanthanide ion luminescence, 135, 136, 142–143
laser ablation, 496
laser scanning microscopy, 556–557
NIR luminescence, 347, 348–349
lattice energy, 45–46
layer-by-layer (LbL) assembly, 397–398
layers
borides, 269–270, 276
borocarbonitrides, 275–276
carbides, 271–274, 276
cluster complexes, 426, 430–431
LbL *see* layer-by-layer assembly
LED *see* light-emitting diodes
leucogranites, 6, 17
Lewis acids
heterogeneous catalysis, 476, 478
lanthanide oxide/hydroxide complexes, 183
metal-organic frameworks, 386, 387, 388
organic synthesis, 437–439, 445, 448–449, 452–456
Lewis acid–surfactant-combined catalyst (LASC), 449–450
lifetimes, lanthanide ion luminescence, 128–130
ligands
acidity constants, 539, 557
conjugation, 526–527
coordination chemistry, 73–80
design
luminescent bioprobes, 537
self-assembly lanthanide supramolecular chemistry, 481–493
helicate structures, luminescent bioprobes, 535–558
lanthanide halides, 177–181
lanthanide-induced shifts, 506–507, 508
lanthanide ions
luminescence, 117–123, 125–126
solvento complexes, 56–57, 59–61
ligand field effect, 131, 154, 155
luminescence
bioprobes, 535–558
lanthanide ions, 117–123, 125–126
NIR materials, 350–356
selection, 539
synthesis, 539–549
multiple bond linkages, 83, 86–87, 100
NIR material luminescence, 350–356
organometallic chemistry, 83, 86–87, 93–95, 100
photophysics, 117
properties, siloxides, 206
self-assembly lanthanide supramolecular chemistry, 481–493
sensitization, 125–126, 135, 136, 143–150
siloxides, 206–210
solvento complexes, 56–57, 59–61
structure, 506–507, 508
supramolecular chemistry, 481–493
synthesis, 539–549
tetrahedral cages, 486–487
tetravalent lanthanide compounds, 317–320
upconversion nanoparticles, 396–397
vacant coordination site protection, 93
light, definitions, 117–118
light amplification by stimulated emission radiation *see* lasers
light-emitting diodes (LED), 135
lighting, luminescence applications, 135
light–matter interactions
absorption, 118–119
electronic absorption, 118–119
Jablonski diagrams, 122–123

lanthanide ions, 117–123
luminescence, 117–123
selection rules, 121–122, 132
transitions, 120, 121–122
vibrational modes, 118, 119–121
linear chains, 425–430
linkers, polynuclear lanthanide complexes, 291–296
liquid phase synthesis, nanomaterials, 406, 407–408
liquids, variable valency, 46–47, 49–50
LIS *see* lanthanide-induced shifts
lithium salts, 83, 89–90
lithophiles, 24
lithosphere, 11, 17
living-cells
cellular uptake, 552, 557
luminescent bioprobe imaging, 551–554
localization considerations, 551–552
longitudinal relaxation, MRI, 522–523, 527–529
low pH synthesis, 237, 239–241
low-temperature magnets, magnets, 378, 380
luminescence
antenna effect, 350, 366, 386–387, 388
applications
bioprobes, 535–558
lanthanide ions, 135–151
metal-organic frameworks, 385
atomic orbitals, 112–115, 132
autofluorescence, 390, 398, 400, 402
biological analysis, 65–67
bioprobes, 535–558
2:3 lanthanide complexes, 535–558
acidity constants, 539, 557
bioconjugates, formation, 554–555, 557
cell conditions, 546–547
cell detection concentration, 551
cell imaging, 551–554
cellular uptake, 552, 557
competitive experiments, 545
conditional stability constants, 545
confocal microscopy, 550, 551, 553, 556, 557
covalent bonding, 554–557
detection concentration, 551
ditopic ligands, 535–558
DNA interactions, 550–551
encapsulated nanoparticles, 555–556
europium cellular uptake, 552
excitation wavelength limitations, 556–557
helicate structures, 535–558
imaging, 551–554
immunoassays, 556
immunocytodetection, 555
immunoglobulin, 556
immunohistochemical assays, 556
kinetic inertness, 546
lab-on-chips, immunoassays, 556
lanthanide complexes, 535, 537–539
competitive experiments, 545
covalent bonding, 554–557
formation, 539–549
pH, 546–547
laser scanning microscopy, 556–557
ligands, 535–558
living cells, 551–554
localization considerations, 551–552
multilabel assays, 553
multiphoton excitation, 556–557
nanoparticle encapsulation, 555–556
near infrared, 553
photophysics, 535, 537–539
pM values, 545
quantum yields, 535, 537–541, 548–550, 553–555
stability constants, 544–546, 557
synthesis, 539–549
ligands, 539
time-resolved imaging, 551
titrations, 541, 543, 544–545, 546
toxicity, 551
two-photon laser scanning microscopy, 556–557
ultraviolet-visible titration, 544–545
uploading concentration, 551
uptake, 552
versatility, 552–553
charge transfer, 111, 125–126, 132
chromophores, 118–119, 123, 126–129, 132, 144–147
colorimetry, 135–142
color reproduction, 135–142
complex architectures, 148–150
coordination sites, 135, 148–150
current status, lanthanide ions, 112
β-diketonate ligands, 135, 143, 144–145, 350–351, 364
dipicolinic-acid-based ligands, 145–146
electronic structure, 111, 112–117, 130–131
energy conversion, 136, 142
excitation, 111–132
f-lanthanide ions, 112–117
flexibility, 148–150
fluorescence, 111, 112, 123–124, 132
heteropolymetallic lanthanide complexes, 353–354
historical overviews, 111–112
hybrid lanthanides, NIR materials, 347, 356–365
8-hydroxyquinolinate-based lanthanide complexes, 351–353
hypersensitive transformations, 131
intensity, 541–542, 543
ionic liquids, 347, 363–364
lanthanide complexes, 148, 347, 348, 350–356
lanthanide hybrids, 347, 356–365
lanthanide ions, 111–133
applications, 135–151
atomic orbitals, 112–115, 132
biological analysis, 65–67
charge transfer, 111, 125–126, 132
chromophores, 118–119, 123, 126–129, 132
coordination sites, 135, 148–150
electronic structure, 111, 112–117, 130–131
excitation, 111–132
hypersensitive transformations, 131
lasers, 135, 136, 142–143
lifetimes, 128–130
ligands, 117–123, 125–126
light–matter interactions, 117–123

luminescence (*continued*)
medical diagnostics, 67–69
medical therapy, 67–68
NIR emission, 135–136, 139–140, 150–151, 347–349
organic ligands, 117–123
photophysics, 111–133, 347, 348–349
quantum yield, 127–128, 129, 130
sensitization, 111, 124–128, 129–130
sensitizing ligands, 135, 136, 143–150
solvatochromism, 126–127, 132
solvent effects, 130
upconversion, 135, 136, 142
visible emission, 139–140
lasers, 135, 136, 142–143
lifetimes, lanthanide ions, 128–130
ligand field effect, 131
ligands, 117–123, 125–126, 350–356
light–matter interactions, 117–123
materials
halides, 175
metal-organic frameworks, 385
nanomaterials, 405, 411
NIR materials, 347–366
phosphorescence, 175
matter–light interactions, 117–123
medical diagnostics, 67–69
medical therapy, 67–68
mesoporous silicates, 359, 360–361
mesoporous sol-gels, 347, 359
metal–organic frameworks, 354, 385, 386–387
nanomaterials, 405, 411
NIR materials, 347–366
β-diketone ligands, 350–351, 364
heteropolymetallic lanthanide complexes, 353–354
hybrid lanthanides, 347, 356–365
8-hydroxyquinolinate-based lanthanide complexes, 351–353
ionic liquids, 347, 363–364
lanthanide complexes, 347, 348, 350–356
lanthanide hybrids, 347, 356–365
lanthanide ions, 135–136, 139–140, 150–151, 347–349
ligands, 350–356
mesoporous silicates, 359, 360–361
mesoporous sol-gels, 347, 359
polymers, 347, 361–363
Schiff-base ligands, 354–355
silicates, 359, 360–361
sol-gels, 347, 356–359
upconversion, 347, 364–365, 366
organic ligands, 117–123
phosphorescence, 111–112, 123–124, 132, 144, 175
photoluminescence, 364–365
photophysics, 111–133, 347, 348–349
polyaminopolycarboxylic acids, 143, 146–147
polymers, 347, 361–363
polynuclear lanthanide complexes, 281–282, 285–286, 289–291, 294–296
probes, 66–67, 131, 535–558
properties, 547–549
quantum yield, 127–128, 129, 130
Schiff-base ligands, 354–355
self-assembly lanthanide supramolecular chemistry, 481–485, 487, 490–493
sensing, 148
sensitization, 111, 124–128, 129–130
sensitizing ligands, 135, 136, 143–150
silicates, 359, 360–361
sol-gels, 347, 356–359
solubility, 148
solvatochromism, 126–127, 132
solvent effects, 130
stability, 148
supramolecular chemistry, 481–485, 487, 490–493
upconversion
bioimaging, 389–403
lanthanide ions, 135, 136, 142
NIR materials, 347, 364–365, 366
visible emission, 139–140
water, 547–549
lutetium, 303–304, 372, 490–492

macrocyclic complexes, 504, 507–511
macromolecules, 511–517
macroscopic behavior, molecular magnetic materials, 335
MAGLEV *see* magnetic levitation
magnetic dipole moments, 133
magnetic dipole transitions, 122, 130, 137
magnetic field gradients, 522, 533
magnetic fields
lanthanide ion luminescence, 133
SQUIDS, 379
superconducting materials, 371–372, 374–375, 376–378, 379
theory, 371–372, 374–375
magnetic levitation (MAGLEV) trains, 380
magnetic materials
lanthanide oxide/hydroxide complexes, 192
molecular materials, 156–158
magnetic ordering, 335–337
magnetic properties
3d metals, lanthanides, 108
lanthanides, 3d metals, 108
magnetic relaxation, 335, 337–344
direct processes, 338
Orbach process, 338
Raman processes, 338
magnetic resonance angiography (MRA), 525–526
magnetic resonance imaging (MRI), 521–534
apoptosis targeting, 530–532, 533
applications, 530–533
cerebrospinal fluid, 522–524, 533
chemical shift imaging, 524
contrast agents, 521, 523, 524–527, 529–530, 533
amino acid lanthanide complexes, 237, 245, 247
endohedral fullerenes, 498
gadolinium, 521, 522, 523, 524–527, 529–530, 533
halides, 175
nanomaterials, 413
contrast mechanisms, 522–524

E-selectin, 532, 533
excitation pulse, 521–522, 533
gadolinium, 67–69, 521–527, 529–530, 533
gradients, 522, 533
halides, 175
hydrogen relaxation, 522, 527–529, 533
inflammation targeting, 532
integrin $\alpha_v\beta_3$ targeting, 532–533
lanthanide-induced shifts, 507–511
lanthanide ions, 65–66, 67–69
lanthanide oxide/hydroxide complexes, 192
longitudinal relaxation, 522–523, 527–529
magnetic field gradients, 522, 533
medical diagnostics, 65–69, 521–534
medical therapy, 67–68
molecular imaging, 521, 527, 533
nanomaterials, contrast agents, 413
nanoparticles, 68
nuclear magnetic resonance, 521–534
nuclear relaxation, 527
paramagnetic contrast agents, 525–527, 529–530
paramagnetic relaxation, 525–529
principles, 521–522
proton density images, 522, 524
pulse sequences, 522–524
radioisotopes, 65, 68–69
relaxation, 67–68, 522–529, 533
specificity, 527
spin-echo pulse sequences, 522–524
spin lattice relaxation, 522–523, 527–529
spin–spin relaxation, 522–523, 527–529
structure, 507–511
transverse relaxation, 522–523, 527–529
magnetic resonance spectroscopy (MRS), 507–511, 515–517
magnetic susceptibility, 154
magnetism, 153–158
applications, 153
borides, 263, 264–271, 276
borocarbides, 273–274
boronitrides, 274
carbides, 263, 271–274, 276
coupling, 153–158
electronic configuration, 154–155
exchange-coupling interactions, 153–158
gadolinium, 155–158
lanthanide ions, 153–158
molecular materials, 156–158, 335–345
nitrides, 263, 274–276
orbital angular momentum, 153–158
orbitals, 153–158
organic radicals, 155–158
spin, 153–158
spin–orbit coupling, 153–155
superconducting materials, 371–372, 374–375, 376–378
magnetocaloric effect (MCE), 192
magnetometer configurations, SQUIDs, 379
magnets
carboxylates, 225
self-assembly lanthanide supramolecular chemistry, 492–493
superconducting materials, 378, 380
transition metal borides, 269
Mannich-type reaction, 443–444
mantle, 8, 9–10, 11, 17
marcrocyclic tetranuclear systems, 492–493
marine waters, 15–16
markets, resource sustainability, 23
Mars, 9, 10
mass balance methods, 14
mass spectrometry, 557
materials precursors, lanthanide oxide/hydroxide complexes, 183–193
matrix assembly, nanomaterials, 406, 407–409
matter–light interactions, 117–123
maximum entropy, 496–497
mechanical planarization, 411–412
medical diagnostics
gadolinium, 67–69
imaging, 67–69
lanthanide ions, 65–66, 67–69
luminescence
bioprobes, 535–536
lanthanide ions, 67–69
MRI, 65–69, 521–534
nanomaterials, 410, 413
radioisotopes, 65, 68–69
medical therapy, 65–68
Meissner effect, 378, 380
Meissner-Ochsenfeld effect, 371
melting points, 268, 476
Merrifield resins, 362–363
meso-aziridine ring-opening, 445
mesoporous NIR luminescence materials, 347
mesoporous silicates, 359, 360–361
mesoporous sol-gels, 347, 359
metal alcoholysis, 198
metal–carbon multiple bond linkages, 86–87
metal-catalyzed transformation, 438–456
metal-centered photophysics, definitions, 117
metal complexes, catalysis, 438–441, 442–445, 446–448
metal ion distribution, 515–517
metallic diiodides, 161
metallic lanthanides
chemical reactivity, 45
enthalpy of vaporization, 45, 46
group trends, 44–46
ionization energy, 45–46
valence configuration, 27–29
variable valency, 43–50
metallic radii, 44–45
metal–ligand interactions, 307
metallofullerenes, 495–499
metallorganics, 175, 181
metallothermic reduction, 162–163, 168, 172, 418, 433
metal–organic frameworks (MOF), 385–388
see also coordination polymers
applications, 385, 387–388
bioimaging, 388
biotechnology, 385, 388
carboxylates, 225, 226, 233–234
chemical sensors, 387–388

metal–organic frameworks (MOF) (*continued*)
chemistry, 385, 386–387
drug delivery, 388
electronic states, 386
fundamental chemistry, 385, 386–387
imaging, 388
lanthanide complexes, 354
lanthanide series, 386
Lewis acids, 386, 387, 388
luminescence, 354, 385, 386–387
NIR luminescence, 354
sensors, 387–388
synthesis, 385–386
metal substitution, 501
metal vapor synthesis, 96
metathesis, 96, 97–98, 100
meteorites, 3–4, 5, 8–9
methane oxidative coupling, 475, 478
methanol, 178–179
methyl methacrylate (MMA), 469–470
methyls, 299–301
Michael-type indole Friedel–Crafts alkylations, 438, 439
Micheal addition, 441, 443, 453–454
microemulsion synthesis, 408
microscopic behavior, molecular magnetic materials, 335
Middle Proterozoic Mountain Pass, 8
mid-oceanic ridge basalts (MORB), 11, 12
milling nanomaterials, 406–407
minerals/mineralogy, 1–9
mining ores, 66
mixed ligands, 321, 329–330
mixed valence halides, 161–172
MOF *see* metal–organic frameworks
molality, 53
molecular imaging, 521, 527, 533
molecular magnetic materials, 156–158, 335–345
lanthanide oxide/hydroxide complexes, 192
magnetic ordering, 335–337
magnetic relaxation, 335, 337–344
quantum tunneling, 339
relaxation, 335, 337–344
slow relaxation, 335, 337–344
spin–lattice relaxation, 338–344
spin–spin relaxation, 338–344
molecular medicine, 535–536
molecular structure
β-diketonate/β-diketones, 250–251, 253–255, 258, 259
polynuclear lanthanide complexes, 284–296
molecular synthesis, chalcogenolates, 215, 219–220
molecular vibration, 118, 119–121
molybdenum, 372–373, 377
monoaryls, 304
monocarboxylic acid, 225, 229–230, 235
monodentate O-donor ligands, 78–80
mono(β-diketones), 249, 250–251, 252, 253
monomeric octohedral geometry, 422–424
monomers, lanthanide halides, structure, 179, 180
mononuclear compounds
carboxylates, 225, 229–233, 235
coordinate numbers, 253–257
β-diketonate/β-diketones, 249, 253–257
self-assembly lanthanide supramolecular chemistry, 481–484, 493
MORB *see* mid-oceanic ridge basalts
Morita–Baylis–Hillman reactions, 444
motors, superconducting materials, 380
mouse embryonic fibroblast cells, 482
MRA *see* magnetic resonance angiography
MRI *see* magnetic resonance imaging
MRS *see* magnetic resonance spectroscopy
Mukaiyama aldol reactions, 451, 452
multi-bidentate ligands, 321, 329–330
multi-decker ligands, 319–320
multi-decker polynuclear lanthanide complexes, 282–289, 296
multidentate ligands
biological and medical applications, 66, 68, 69
conjugated Schiff-base ligands, 282–289, 296
coordination polymers, 281–297
flexible Schiff-base ligands, 282, 286–291, 296
lanthanide complexes, 281–297
lanthanide coordination polymers, 281–297
polynuclear lanthanide complexes, 281–297
Schiff-base ligands, 281–297
multifunctional catalysts, 438–439, 455
multilabel assays, 553
multi-ligand complexes, 317–320
multimetal endohedral fullerenes, 497–498
multiphoton excitation, 556–557
multiple bond linkages, 83, 86–87, 100
multiplets, 153–154
mylohyoid muscle, 533

NACA *see* necrosis-avid contrast agents
naked clusters, 415, 422, 433
nanoblast synthesis, 407
nanomaterials
applications, 405, 410–413
bottom-up synthesis, 406, 407–409
catalysts, 411
characterization, 405, 409–410
chemical mechanical planarization, 411–412
contrast agents, MRI, 413
diagnostics, 410, 413
gas phase synthesis, 406, 407
gas sensors, 412–413
industrial applications, 405, 410–413
liquid phase synthesis, 406, 407–408
luminescence, 405, 411
matrix assembly, 406, 407–409
mechanical planarization, 411–412
medical diagnosis, 410, 413
MRI contrast agents, 413
optical properties, 410
optical transmission, 410
oxides, 405–413
phosphors, 364–365, 411
physical properties, 409–410
pigments, 413
planarization, 411–412

quantum confinement, 410
size effects, 410
sol-gels, 395, 408
solid-oxide fuel cells, 412
solid phase synthesis, 406, 408–409
sulfides, 405–413
surface area, 409–410
suspension optical transmission, 410
synthesis, 405, 406–409
top-down synthesis, 406–407
UV screening agents, 412
vapor phase synthesis, 406, 407
nanoparticles, 389–403
bioimaging, 389–403
encapsulation, 555–556
luminescent bioprobes, 555–556
MRI, 68
phosphors, 389–403
nanotubes, 68
natural waters, 2, 15–16
Nd:YAG (neodymium-doped yttrium aluminum garnet) lasers, 136, 143
near-infrared (NIR) emission
chalogenolates, 220–221
in vivo imaging, 398–402
lanthanide ion luminescence, 135–136, 139–140, 150–151
luminescence
bioprobes, 553
β-diketone ligands, 350–351, 364
heteropolymetallic lanthanide complexes, 353–354
hybrid lanthanides, 347, 356–365
8-hydroxyquinolinate-based lanthanide complexes, 351–353
ionic liquids, 347, 363–364
lanthanide complexes, 347, 348, 350–356
lanthanide hybrids, 347, 356–365
lanthanide ions, 135–136, 139–140, 150–151, 347–349
ligands, 350–356
mesoporous silicates, 359, 360–361
mesoporous sol-gels, 347, 359
polymers, 347, 361–363
polynuclear lanthanide complexes, 285–286, 289, 290, 291
Schiff-base ligands, 354–355
silicates, 359, 360–361
sol-gels, 347, 356–359
upconversion, 347, 364–365, 366
materials, 347–366
β-diketonate/β-diketones, 250, 350–351, 365
heteropolymetallic lanthanide complexes, 353–354
hybrid lanthanides, 347, 356–365
8-hydroxyquinolinate-based lanthanide complexes, 351–353
in vivo imaging, 398–402
ionic liquids, 347, 363–364
lanthanide complexes, 347, 348, 350–356
lanthanide hybrids, 347, 356–365
lanthanide ion luminescence, 347–349
ligands, 350–356
luminescence, 347–366
mesoporous silicates, 359, 360–361
mesoporous sol-gels, 347, 359
metal–organic frameworks, luminescence, 354
photoluminescence, 364–365
photophysics, 347, 348–349
polymers, 347, 361–363
Schiff-base ligands, 354–355
silicates, 359, 360–361
sol-gels, 347, 356–359
upconversion, 347, 364–365, 366, 398–402
self-assembly lanthanide supramolecular chemistry, 482, 484–485
to-visible upconversion, 398–400
necrosis-avid contrast agents (NACA), 526
neodymium
color characteristics, 136, 140
halide valency, 165–166, 169–170
NIR luminescence, 347–348
β-diketone ligands, 350–351
heteropolymetallic lanthanide complexes, 353–354
8-hydroxyquinolinate-based lanthanide complexes, 352–353
ionic liquids, 363–364
photophysics, 348–349
polymers, 361–363
silicates, 360–361
sol-gels, 356–359
optodes, 568–569
Schiff-base ligands, 283–284, 286–289, 292, 294–296
self-assembly supramolecular chemistry, 482, 484–485, 487, 493
neodymium-doped yttrium aluminum garnet (Nd:YAG) lasers, 136, 143
neodymium–iron–boron magnets, 153
neo-pentoxide ligands, 200
neopentyl compounds, 300–301
neutral derivatives, 85–86
neutral π-acid derivatives, 85–86, 100
nine-coordinate lanthanide complexes, 257
niobium cuprate superconducting materials, 376–378
niobium halides, 419
NIR *see* near-infrared emission
nitrates
ionic radii, 47–48
organometallics, 322
tetravalent lanthanide compounds, 315, 316–317
nitrides, 263–264, 274–276
applications, 263, 274–275
binary compounds, 274–275
borocarbonitrides, 263, 275–276
boronitrides, 263, 275
carbonitrides, 263, 275–276
crystal structure, 263, 275–276
endohedral fullerenes, 497–498
magnetism, 263, 274–276
physical properties, 263, 274–276
superconductivity, 263, 275, 276
ternary compounds, 275
thermoelectrics, 263, 276

nitriles
  amine addition, 464–465
  coordination numbers, 75
  homogeneous catalysis, 464–465
  organolanthanide complexes, 464–465
nitroaldol reactions, 439–440, 442
nitrogen-sulfur-containing ligands, 567
nitronyl nitrosides, 337
4-(*p*-nitrophenylazo)-pyrocathecol, optodes, 569
NMR *see* nuclear magnetic resonance
nonaqueous media, 59–60
nonfluorinated β-diketones, 250, 252
nonlinear optics *see* upconversion
nonradiative deactivations, 122, 130
nonvanishing crystal field parameters, electronic structure, 32
nuclearity
  amino acids, 237, 244, 246–247
  carboxylates, 225, 227–235
  lanthanide complexes, 237, 244, 246–247
  lanthanide oxide/hydroxide complexes, 185–190, 193
nuclear magnetic resonance (NMR)
  halides, 175, 176
  lanthanide complex formation, 541
  lanthanide-induced shifts, 501–518
  lanthanide ion solvento complexes, 59
  MRI, 521–534
  shift reagents, 175, 501–518
nuclear material detection, scintillators, 175
nuclear relaxation, 527
nucleases, 186, 193, 247
nucleation, halides, 166, 172
nucleic acids, 511–515

occlusion, 83, 89–90
oceanic crust, 11–12
oceanic island basalts (OIB), 11, 12
oceans/water, 15–16
octanuclear complexes, 188, 190
octohedral complexes, 422–426
Oddo–Harkins effect, 3–4, 5
O-donor ligands, 78–80
OIB *see* oceanic island basalts
olation, 183, 185, 193, 238, 243–244, 247
OLED *see* organic light-emitting diodes
olefins
  addition, 445–447
  homogeneous catalysis, 467–468
  hydrosilylation, 205, 206
  organometallic chemistry, 85–86
  polymerization, 467–468
oligomeric cluster complexes, 424–425, 433
one-electron redox, 98–100
Onnes, Heike Kamerlingh, 371
optical microscopy, 449, 450
optical properties
  metal-organic frameworks, 385
  nanomaterials, 410
optical sensors/optodes, 561, 567–571
optical transmission, 410
Orbach process, 338
orbital angular momentum, 108, 132–133, 153–158
orbital penetration, 44, 53
orbitals
  filling order, 27, 28, 114
  lanthanide ions, magnetism, 153–158
  magnetism, lanthanide ions, 153–158
  variable valency, 43–44
orbital shielding, 44
ore geology, 7–8
ore toxicity, 66
organic ligands, 117–123
organic light-emitting diodes (OLED), 225, 347, 348
organic linkers, 385–386
organic photovoltaic applications, 498
organic radicals, 155–158, 336–337
organic synthesis, 437–456
  aqueous media, 448–455
  asymmetric reactions, 438–445, 446, 447, 450–455
  catalysis, 437–456
    aqueous media, 448–455
    asymmetric reactions, 438–445, 446, 447, 450–455
    halides, 175
    water, 448–455
  enantioselective reactions, 438–445, 453, 454–455, 456
  halides, 175
  homogeneous catalysis, 460–467
  Lewis acids, 437–439, 445, 448–449, 452–456
  metal-catalyzed transformation, 438–456
  multifunctional catalysts, 438–439, 455
  organolanthanide complexes, 460–467
  solvents, catalysis, 438–448
  water, 448–455
organocyanides, 337
organolanthanide complexes
  alkoxylation, 460–461
  alkynes, 465–467
  amidines, 464–465
  amination, 460
  amines, 462–465, 466–467
  asymmetric synthesis, 461–462
  cyclic ester polymerization, 470–472
  dienes stereoselective polymerization, 468–469
  dimerization, 465–466
  homogeneous catalysis, 459–473
  hydroalkoxylation, 460–461
  hydroamination, 460
  intermolecular organic transformation, 460, 461–467
  intramolecular organic transformation, 460–461
  methyl methacrylate polymerization, 469–470
  nitriles, 464–465
  olefins polymerization, 467–468
  organic transformation, 460–467
  phosphines, 466–467
  polymerization, 459, 467–472
  synthesis, 460–473
  Tishchenko reaction, 464, 473
organometallics
  3d metals, lanthanides, 106–107
  acid–base synthesis, 96

π-acid derivatives, 85–86, 100
adduct formation, 96–97
aggregation, 83, 90
alkoxides, 321, 322–324, 328–329
alkyls, 83–96, 98
alkyne derivatives, 85–86
amides, 321, 325–327
amidinates, 321, 327–328
anaerobic conditions, 90
anhydrous conditions, 90
arenes, 84, 86–87, 96
aryls, 84, 93, 96–98
β-hydrogen, 90–92
*bis*arene derivatives, 86–87
bonding, 83, 84–87, 88, 97–98, 100
carbenes, 84, 87, 97–98, 321, 329–330
carbonyls, 83, 85, 99, 100
cerium, 321–333
cerocene sandwich complexes, 321, 330–332
chalogenolates, 215–217
chelating ligands, 93–95
chemistry, 83–101, 321–333
cleavage, 96–97
coordination numbers, 75
coordination sites, 92–93
coordination sphere saturation, 92–93
covalent bonding, 83, 84–87
cyclooctatetraenyl complexes, 321, 330–332
cyclopentadienyl, 84, 85, 88–90, 92–94, 97, 321, 328–329
donor cleavage, 96–97
donor-functionalized chelating ligands, 93–95
elimination, 95
future outlooks, 332
historical overviews, 83–84
ionic bonding, 85–86
kinetics, 83, 88, 100
lanthanide-3d metal comparisons, 106–107
lanthanide halides, 175, 181
ligands, 83, 86–87, 93–95, 100
metal–carbon multiple bond linkages, 86–87
metal vapor synthesis, 96
metathesis, 96, 97–98, 100
multiple bond linkages, 83, 86–87, 100
neutral derivatives, 85–86
neutral π-acid derivatives, 85–86, 100
occlusion, 83, 89–90
olefin derivatives, 85–86
one-electron redox, 98–100
oxidation, 96, 98–100
oxidation states, tetravalent chemistry, 321–333
physicochemical properties, 83, 88
π-acid derivatives, 85–86, 100
π-bonding, 84, 85–87, 100
reactivity, 83, 88, 98–100
redox, 98–100
salt elimination, 95
salt occlusion, 83, 89–90
saturation, 92–93
selenolates, 215–217
σ-bonding, 84, 85, 97–98, 100
solvation, 83, 89
stability, 83, 90–95
sterically demanding ligands, 93
synthesis, 83, 95–100, 215–217, 321–332
tellurolates, 215–217
tetravalency, 321–333
tetravalent chemistry, 321–333
thermodynamics, 83, 88
thiolates, 215–217
transmetallation, 96
vacant coordination sites, 93
zero-valent bonding, 86
ORTEP molecular structure diagrams
amino acids, 245–246
chalcogenolates, 219
β-diketones, 254, 256–257, 259, 260
lanthanide complexes, 245–246
oscillator strength, 120
outerspheres, 176–177, 181
oxidation
methane coupling, 475, 478
organometallic chemistry, 96, 98–100
solvento complexes, 56
oxidation states
3d metals, 105–106
alkoxides, 197–199
electronic structure, 29–31
enthalpy, 43
enthalpy of formation, 51–52
entropy of hydration, 50–51
excited state configurations, 29–31
ground state configurations, 29–31
group trends, 43–44, 50–52
halides, 161, 162, 166, 172
hydration enthalpy, group trends, 43, 50
lanthanides, 43–50
3d metals, 105–106
liquids, 46–47, 49–50
organometallics, 321–333
siloxides, 205–212
solids, 44, 47–49
tetravalent chemistry, 313–320, 321–333
variable valency, 43–50
oxide condensation, 3, 4
oxides
applications, 190–192, 405, 410–413
clusters, 183–193
complexes, 183–193
coordination chemistry, 183–193
divalent states, halides, 171–172
enthalpy of formation, group trends, 51–52
halides, divalent states, 171–172
heterogeneous catalysis, 475–478
ligand coordination, 183–193
nanomaterials, 405–413
applications, 405, 410–413
catalysts, 411
characterization, 405, 409–410
gas sensors, 412–413
MRI contrast agents, 413

oxides (*continued*)
solid-oxide fuel cells, 412
synthesis, 405, 406–409
UV screening agents, 412
nuclearities, 185–190
properties, 190–192
rational synthesis, 184–185
structure, 185–190
oxo acids, 313, 316–317
oxophilicity, 183, 211

paleoplacers, 7–8, 17
paramagnetic contrast agents, 525–527, 529–530
paramagnetic relaxation, 525–529
paramagnetic shift reagents, 501–518
paramagnetism
lanthanide ions, 157–158, 501–518
organic radicals, 157
partial melting, 4–5, 9, 11–14, 17
partial pressures, 293–294
partition coefficients, 293–294
passive transport, 552, 557
Pauli exclusion principle, 113, 124
Pauling electronegativity, 3, 4
PCS *see* pseudocontact shift
pegmatites, 5–6, 17
Peierls distortion, 169, 172
pendent groups, cyclopentadienyl, 308–310
2,4-pentanedione, 250, 251
pentanuclear complexes, 188–189, 283–285
pentanuclear helicates, 486–487
perovskite superconducting materials, 372
petroleum refining, 475
pH
amino acids, 237, 239–241
lanthanide complexes, 237, 239–241, 546–547
luminescent bioprobes, 546–547
phase diagrams, 164–165, 371–372, 374
phase encoding, MRI, 522
phenanthroline groups, 490–493
phenol derivatives, 199–202
3-phenyl-4-acyl-5-isoxazolones, 250, 253
phenyliodine(III) dichloride, 325
1-phenyl-3-methyl-4-acyl-5-pyrazolones, 250, 253
phenyls, 303–305
phonons, 126–127, 391–393, 403
phosphate esters, 67
phosphines, 466–467
phosphorescence, 111–112, 123–124, 132, 144
phosphors, 364–365, 389–403, 411
photobleaching, 390, 403
photoluminescence, 364–365
photon avalanche, 391
photon density, 128
photons, 111–133
photophysics
lanthanide complexes, 535, 537–539
lanthanide ion luminescence, 111–133, 136, 347, 348–349
luminescence
bioprobes, 535, 537–539
lanthanide ions, 111–133, 136, 347, 348–349
NIR luminescence, 347, 348–349
polynuclear lanthanide complexes, 282–286, 289–291, 294
photospheres, 8–9, 18
photovoltaics, endohedral fullerenes, 498
phthalic acids, 487–488
phthalocyanine, 341, 342
physical properties
borides, 263, 264–271, 276
borocarbides, 273–274
carbides, 263, 271–274, 276
carbonitrides, 275
chalogenolates, 220–221
lanthanide chalogenolates, 220–221
nanomaterials, 409–410
nitrides, 263, 274–276
physicochemistry
luminescent bioprobes, 537
MRI, 529–530
organometallic chemistry, 83, 88
picture elements (pixels), MRI, 522
pigments, 413
π-acid derivatives, 85–86, 100
π-bonding, 43–44, 84, 85–87, 100
π-conjugate molecules, 282
pixels *see* picture elements
placers, geology/geochemistry, 7–8, 17
planar borocarbides, 273–274
planarization, nanomaterials, 411–412
planets/planetary compositions, 1, 2–3, 8–10
pM values, stability constants, 545
pnictides, 373–374
polarization, 155–156
polyaminopolycarboxylic acids, 143, 146–147
polycarbonates, 470–472
polymerization
cyclic esters, 470–472
esters, 470–472
homogeneous catalysis, 459, 467–472
isoprene, 205, 206
lactides, 470–472
methyl methacrylate, 469–470
olefins, 467–468
organolanthanide complexes, 459, 467–472
upconversion nanoparticles, 398
polymers
hybrid lanthanide oxide/hydroxide complexes, 192
lanthanide halides, 179, 180–181
NIR luminescence materials, 347, 361–363
polymeric chains, 291–292
polynuclear carboxylates, 225, 227, 229–235
polynuclear chalcogenido anions, 215, 217–219
polynuclear lanthanide complexes
amino acids, 237, 239, 241, 244, 247
conjugated Schiff-base ligands, 282–289, 296
crystal structure, 281–282, 283–285, 286, 287–290
β-diketonate/β-diketones, 249, 257–260
flexible Schiff-base ligands, 282, 286–291, 296
lanthanide amino acids, 237, 239, 241, 244, 247

lanthanide oxide/hydroxide complexes, 183–193
linkers, 291–296
luminescence, 281–282, 285–286, 289–291, 294–296
molecular structure, 284–296
multidentate ligands, 281–297
Schiff-base ligands, 281–297
self-assembly lanthanide supramolecular chemistry, 481–482, 484–493
small linkers, 291–296
structure, Schiff-base ligands, 281–296
supramolecular chemistry, 481–482, 484–493
(poly)pyridines, 143, 148–149
porous luminescent materials, 385
porphyrinates, 313, 316, 320
porphyrins, 570
potassium, 169–170
potential energy, 133
power generators, superconducting materials, 380
praseodymium
alkoxides, 200
color characteristics, 136, 137, 139
halide valency, 164–167, 169–170
NIR luminescence, 347–349, 360–361
tetravalent chemistry, 313–314
precipitation, 540
precursors
lanthanide oxide/hydroxide complexes, 183–193
siloxides, 205
primitive mantle, 8, 9–10, 11, 17
Primovist® (formerly Eovist®), 525
principal reaction types, 83
principles
MRI, 521–522
upconversion, 390–391
probes
bioprobes, 535–558
lanthanide ion luminescence, 66–67, 131, 535–558
product/production considerations, 23–24
1,3-propanedione, 250, 252
properties
lanthanide oxide/hydroxide complexes, 190–192
ligands, 206
organometallic chemistry, 83–101
siloxides, 205, 206
proteinogenic amino acids, 238–239, 247
protein-protein interactions, 515, 517
proteins
lanthanide-induced shifts, 511–515
surface probes, 501
Proterozoic Eon, 17
proton density images, 522, 524
Prussian-Blue-like compounds, 335–336
pseudocontact shift (PCS), 501, 502, 503–504
pseudo-organometallics, 321–328
pulse sequences, 522–524
purification, 112
pyridines, 143, 148–149
pyridinethiolate ligands, 217
pyridyl-based ligands, 481–482, 483–484
pyrolysis, 407
quantization, lanthanide ion luminescence, 112–115, 118–120, 126, 132
quantum confinement, 410
quantum numbers, 29–32, 113–114, 115, 124
quantum tunneling, 339
quantum yields
lanthanide complexes, 535, 537–541, 548–550, 553–555
lanthanide ion luminescence, 127–128, 129, 130
luminescent bioprobes, 535, 537–541, 548–550, 553–555
triplet state energy correlation, 135, 144, 147–148
quenching, 122, 123–125, 128–130, 132
quinolinol derivatives, 351–353

R_2C and R_3C binary carbides, 271–272
$R_{15}C_{19}$ binary carbides, 272
radial charge density, 27, 28
radial integrals, electronic structure, 31
radiationless deactivations, 122
radicals, 153–158, 340
radioisotopes, 65, 68–69
radiopharmaceuticals, 498
Raman processes, 338
Raman spectroscopy, 58
rate laws, 128–129, 132
rational synthesis, 184–185
RB_{25} binary borides, 266
RB_{66} binary borides, 268–269
RC_2 binary carbides, 271
RC_3 binary carbides, 271
RDC *see* residual dipolar coupling
reactivity
cyclopentadienyl, 307, 308–310
lanthanide-3d metals comparisons, 105
organometallic chemistry, 83, 88, 98–100
siloxides, 205
reagents, lanthanide-induced shifts, 501–518
recycling resources, 23–24
reduced use concepts, resource sustainability, 23–24
reduction/redox
aqueous media, 455
cerium dioxide, 314–315
cluster complexes, 418, 433
geology/geochemistry, 3, 4–5
halides, 162–163, 168–169
organometallic chemistry, 98–100
potentials, 46–47, 49–50, 105, 106
regolith deposits, 7–8, 18
relativistic effects, 27–28, 33
relaxation
lanthanide-induced shifts, 501–507, 512–517
lanthanide ion luminescence, 122, 128–129
light–matter interactions, 122
molecular magnetic materials, 335, 337–344
MRI, 67–68, 522–529, 533
REMB complexes, 439, 441
repetition times, MRI, 522–524, 533
residual dipolar coupling (RDC), 501, 513–514, 517
resonance stability, 217
resonating valence bond theory, 375

resource sustainability, 21–25
application considerations, 23
clean energy, 21–24
consumption considerations, 23
disposition, 24
endangered elements, 22–23
fate, 24
markets, 23
product considerations, 23
production considerations, 23–24
recycling, 23–24
reduced use concepts, 23–24
strategic elements, 21–24
Rietveld method, 496–497
ring-opening, 445, 454–455
river waters, 16
rocks, geology/geochemistry, 1–8, 12–16
rubidium, 169, 353–354
ruthenium, 377–378, 490–493

salen-style Schiff-base ligands, 281–296
salt elimination, 95
salt occlusion, 83, 89–90
salts
halides, 164
ionic radii, 47
lanthanide complexes, 540
lanthanide halides, 179, 180
lanthanide ions, 57–59
solvento complexes, 57–59
tetravalent lanthanide compounds, 315
samarium
catalysis, 438
color characteristics, 136, 137, 139
halide valency, 161, 162–168, 169–170
NIR luminescence, 347–348
photophysics, 348–349
silicates, 360–361
sandwich complexes, 319–320, 321, 330–332
saturation, organometallic chemistry, 92–93
scandium
3d metals comparisons, 105
alkyls, 299–301
aqueous solvento complexes, 56–58
aryls, 303, 304
borides, 266
catalysis, 438, 439, 444–445, 448, 452
coordination chemistry, 73, 78–79
halides, 418–419
halide valency, 161, 164–165, 167–168, 169
siloxides, 210
solvento complexes, 56–58
Schiff-bases
coordination lanthanide polymers, 286–291, 296
coordination numbers, 75
ion-selective electrodes, 563–564
lanthanide complexes, 281–297
lanthanide coordination polymers, 286–291, 296
linkers, 291–296
NIR material luminescence, 354–355
organic solvents, 439–445, 456
polynuclear lanthanide complexes, 281–297
small linkers, 291–296
solvents, 439–445, 456
tetravalent chemistry, 313, 319
scintillators, 175, 178, 181
second-harmonic generation (SHG), 389, 390–391
sediment, 5, 7, 10–16, 17
selection criteria
bioimaging, 389, 391–393, 402, 403
lanthanide ion luminescence, 121–122, 132
light–matter interactions, 121–122, 132
luminescent bioprobes, 539
upconversion, 389, 391–393, 402, 403
selenolates, 215–221
bonding, 215–221
cluster chemistry, 215, 217–219
molecular synthesis, 219–220
organometallics, 215–217
physical properties, 220–221
thermolysis, 219–220
self-assembly lanthanides
chiral systems, 484–486
cyclen frameworks, 482–483, 487–491
formation, 481–493
helicates, 482, 483–484, 486–488
imaging, 481–484, 493
ligands, 481–493
luminescence, 481–485, 487, 490–493
mononuclear complexes, 481–484, 493
polynuclear complexes, 481–482, 484–493
sensing, 481–484, 493
supramolecular chemistry, 481–482, 484–493
synthesis, 481–493
seminal phase diagrams, 164–165
sensing/sensors
actinide ions, 561–571
ion-selective electrodes, actinide ions, 561, 562–567
lanthanide ions, 561–571
lanthanide luminescence, 148
metal-organic frameworks, 387–388
self-assembled mononuclear lanthanides, 481–484, 493
sensitization
chromophores,144–147, 347–348, 350–351
β-diketonate ligands, 135, 143, 144–145
dipicolinic-acid-based ligands, 145–146
lanthanide ion luminescence, 111, 124–128, 129–130
ligands, 125–126, 135, 136, 143–150
luminescence, 111, 124–128, 129–130
polyaminopolycarboxylic acids, 143, 146–147
upconversion, 392, 403
sensors *see* sensing/sensors
separation
lanthanide-induced shifts, 504–506
lanthanide ion luminescence, 112
sesquicarbides, 271
sesquichlorides, 418–419
sesquioxides, 475–476, 478
seven-coordinate lanthanide complexes, 254, 256

shale meteorites, 3–4, 5
Shannon–Prewitt radii, 46–47
Shastry–Sutherland lattice, borides, 265
SHG *see* second-harmonic generation
shift reagents
  halides, 175
  lanthanide-induced shifts, 501–518
  lanthanide ions, 501–518
  MRS, 515–517
  NMR, 175, 501–518
  paramagnetic lanthanide ions, 501–518
sialons, 275
σ–bonding, 84, 85, 97–98, 100
silanolates *see* siloxides
silicates
  NIR material luminescence, 359, 360–361
  precursor materials, 205
silicon
  binary borides, 266–268
  enolates, 451–452
  nitrides, 275
  ternary borides, 269
siloxanes, 324
siloxides, 205–212
  aggregation, 207–208
  alkoxides, 202, 208–209
  atom distances, 208–209
  bonding, 205–206, 208–211
  divalency, 205–206
  heteroleptic structures, 205, 207, 211, 212
  homoleptic structures, 205, 207–208, 211, 212
  hydrolytic cleavage, 209
  ligands, 206–210
  oxidation states, 205–212
  oxophilic metals, 211
  properties, 206
  spectator ligands, 209–210
  structure, 205, 207–208
  synthesis, 205–207, 210
  tetravalent chemistry, 205–206, 211, 321, 323
  trivalency, 205–211
silsesquioxane, 207
silylated chalcogenolates, 216–217
silylation, 448
silyloxides *see* siloxides
simple harmonic oscillation, 119–120
simultaneous two-photon absorption, 390–391
single-chain clusters, 425–430
single-chain magnets, 338, 342
single crystal X-ray characterization, 179–181
single crystal X-ray crystallography, 57
single-cyclopentadienyl complexes, 309–310
single ion magnets, 341–342
single metal endohedral fullerenes, 496–497
single molecule magnets (SMM), 338–344, 492–493
six-coordinate lanthanide complexes, 253–254, 256
size effects, nanomaterials, 410
Slater's radial integrals, 31
slice selection, MRI, 522
slow relaxation, 335, 337–344
small flexible ligands, 506–507
small linkers, 291–296
SMM *see* single molecule magnets
sodium, reduction methods, 168
SOFC *see* solid-oxide fuel cells
solar energy conversion, 347
solar photosphere, 8–9, 18
solar system, 1, 2–3, 8–10
sol-gels
  nanomaterials, 395, 408
  NIR material luminescence, 347, 356–359
  upconversion, 395
solidification points, 476
solid-oxide fuel cells (SOFC), 412
solid phase synthesis, nanomaterials, 406, 408–409
solids
  +2 oxidation state, 48–49
  +4 oxidation state, 44–46
  binary halides, 161–168
  chalcogenolates, 215, 219–220
  divalent halides, 161–173, 175–176, 178
  halide valency, 161–173
    crystal structure, 165–166, 169–171, 172
    divalent states, 161–173, 175–176, 178
    electronic structure, 161, 165, 166–167, 172
    structure, 161, 165–167, 169–171, 172
  mixed valence halides, 161–172
  molecular lanthanide chalcogenolates, 215
  molecular synthesis, 215, 219–220
  oxidation states, 44, 47–49
  ternary halides, 161, 162–163, 168–171, 172
solubility
  chalcogenolates, 216–217
  endohedral fullerenes, 495
  lanthanide ions, 148
solution states, variable valency, 46–47, 49–50
solvates, 178–181
solvation, 83, 89
solvatochromism, 126–127, 132
solvento complexes
  aqueous media, 55, 56–59
  coordination chemistry, 55–61
  lanthanide ions, 55–61, 74, 78, 79, 80
  ligands, 56–57, 59–61
  nonaqueous media, 59–60
  salts, 57–59
  scandium, 56–58
  structure, 55–61
  yttrium, 56–57, 58–59
solvents
  catalysis, 438–448
  enantioselective organic synthesis, 438–445
  lanthanide ion luminescence, 130
  organic synthesis, 438–448
  Schiff bases, 439–445, 456
solvothermal synthesis
  carboxylates, 226, 234
  metal-organic frameworks, 386
  nanomaterials, 408
  upconversion nanoparticles, 395

sonochemical synthesis, 408
space filling, 293, 294
specificity, 527
spectator ligands, 209–210
spectroscopy, lanthanide ion luminescence, 115, 116–117, 132
spherical contributions, paramagnetic relaxation, 527–529
spin, lanthanide ion magnetism, 153–158
spin angular momentum, 133
spin-echo pulse sequences, 522–524
spinels, 372
spin Hamiltonians, 155
spin–lattice relaxation, 338–344, 522–523, 527–529
spin–orbit coupling, 29–33, 108, 114–117, 153–155
spin–orbit interaction, 133
spin polarization, 155–156
spin–spin relaxation, 338–344, 522–523, 527–529
square antiprismatic geometries, 76
SQUID *see* superconducting quantum interference devices
stability
  constants, 544–546, 557
  lanthanide ion luminescence, 148
  luminescent bioprobes, 544–546, 557
  organometallic chemistry, 83, 90–95
stacked π-conjugate molecules, 282
Stark effect, 31, 32, 33
stereoselective polymerization, 468–469
sterically demanding ligands, 93
steric considerations, cyclopentadienyl, 307
steric properties, siloxides, 205
stoichiometry, 8-hydroxyquinolinate-based lanthanide complexes, 353
Stokes shift, 112, 126, 130, 132
strategic elements, resource sustainability, 21–24
strontium, 165, 377–378
structure
  amino acids, 237, 239–247
  anhydrides, 177–178
  biomacromolecules, 511–515
  borides, 263, 264–271
  carboxylates, 225, 227–235
  cluster complexes, 415–416, 419–425
  cyclopentadienyl, 307, 308–310
  data analysis, 506–515
  β-diketonate/β-diketones, 249–260, 350–351
  endohedral fullerenes, 496–498
  halides, 176–181
    anhydrides, 177–178
    hydrates, 176–177
    valency, 161, 165–167, 169–171, 172
  high-temperature cuprates, 375–376
  hydrates, 176–177
  lanthanide complexes, 237, 239–247, 281–296, 507–511
  lanthanide halides, 176–181
  lanthanide hydroxides, 185–190
  lanthanide-induced shifts, 506–515
  lanthanide ions, 55–61, 237
  lanthanide oxides, 185–190
  ligands, 506–507, 508
  metal-organic frameworks, 385
  MRI, 507–511
  MRS, 507–511
  nucleic acids, 511–515
  polycarboxylates, 231–235
  polynuclear lanthanide complexes, 281–296
  proteins, 511–515
  siloxides, 205–206, 207–208
  small flexible ligands, 506–507
  solvento complexes, 55–61
  supramolecular architectures, 511
styrene, 467–468
subshell electronic structure, 113, 115–117
substitution, 307–310
sulfates, 315, 317
sulfide nanomaterials, 405–413
  applications, 405, 410–413
  characterization, 405, 409–410
  pigments, 413
  synthesis, 405, 409
superconducting materials, 371–381
  1212 cuprate structures, 376–378
  applications, 378–380
  borides, 263, 264, 266, 276
  borocarbides, 274
  boronitrides, 274
  carbides, 263, 271, 272, 274, 276
  copper oxides, 371, 373, 375–380
  crystallography, 375–376
  cuprates, 371, 373, 375–380
  energy storage, 380
  generators, 380
  high-temperature cuprates, 371, 373, 375–380
  magnetic fields, 371–372, 374–375, 376–378, 379
  magnetic levitation trains, 380
  magnetism, 371–372, 374–375, 376–378
  magnets, 378, 380
  Meissner effect, 378, 380
  motors, 380
  nitrides, 263, 275, 276
  power generators, 380
  resonating valence bond theory, 375
  wires, 378–379
superconducting quantum interference devices (SQUID), 379–380
supermolecules, luminescent bioprobes, 536
supertetrahedrons, 421–422, 433
supramolecular chemistry, 481–494
  chiral systems, 484–486
  cyclen frameworks, 482–483, 487–491
  formation, self-assembly lanthanides, 481–493
  helicates, 482, 483–484, 486–488
  heterometallic multinuclear assemblies, 487–493
  homometallic multinuclear assemblies, 484–487
  imaging, 481–484, 493
  lanthanide-induced shifts, 511
  ligands, self-assembly lanthanides, 481–493
  luminescence, 481–485, 487, 490–493
  mononuclear complexes, 481–484, 493
  polynuclear complexes, 481–482, 484–493
  self-assembly lanthanides, 481–493
  sensing, 481–484, 493

structure, lanthanide-induced shifts, 511
synthesis, self-assembly lanthanides, 481–493
surface area, 409–410
surface chemical modifications, 395–398
susceptibility, 154, 340–344
suspensions, optical transmission, 410
sustainability *see* resource sustainability
synthesis
see also catalysis/catalysts; formation; organic synthesis
alkoxides, 197–198
alkyls, 299–301
amino acids, 239–247
bioimaging upconversion nanoparticles, 389, 393–395
carboxylates, 225–227, 233–234
cerium, 321–332
cerium dioxide, 314–315
chalcogenido anions, 217–219
chalogenolates, 215–219
cluster complexes, 416–418, 433
cyclopentadienyl, 307, 308
divalent halides, 162–163, 168–169
endohedral fullerenes, 495, 496
halides, 162–163, 168–169
heterogeneous catalysis, 475–479
homogeneous catalysis, 459–473
lanthanide alkoxides, 197–198
lanthanide complexes, 239–247, 281–291, 539–549
ligands, 539–549
luminescent bioprobes, 539–549
metal-organic frameworks, 385–386
nanomaterials, 405, 406–409
organolanthanide complexes, 460–473
organometallics
chalogenolates, 215–217
chemistry, 83, 95–100
tetravalent chemistry, 321–332
oxide nanomaterials, 405, 406–409
polycarboxylates, 233–234
polynuclear lanthanide compounds, 217–219
self-assembly lanthanide supramolecular chemistry, 481–493
siloxides, 205–207, 210
sulfide nanomaterials, 405, 409
supramolecular chemistry, 481–493
tetravalent chemistry, 321–332
upconversion nanoparticles, 389, 393–395

tantalum, 376–378
tautomerisms, 249, 250
tellurolates, 215–221
bonding, 215–221
cluster chemistry, 217–219
molecular synthesis, 219–220
organometallics, 215–217
physical properties, 220–221
thermolysis, 219–220
TEM *see* transmission electron microscopy
temperature phase diagrams, 164
ten-coordinate lanthanide complexes, 257, 258
terbium
color characteristics, 136, 137, 138–139
conjugated Schiff-base ligands, 282–283, 285
electronic structure, 116–117
lanthanide ion luminescence, 67
molecular magnetic materials, 339, 341–342
quantum yields, 147
self-assembly supramolecular chemistry, 483–485, 486–491
tetravalent chemistry, 313–314
triplet state energy correlation, 147
terdentate pyridine-2,6-dicarbonyl binding sites, 486–487
term symbols, electronic structure, 29
ternary borides, 269–271
ternary carbides, 272–274
ternary halides, 161–163, 168–172
ternary nitrides, 275
terrestrial reservoirs, 10–16
tetraborides, 264–265
tetracarbides, 271
tetracyanoethylene, 337
tetrad effect, 5–6, 43–44
tetrahedral cages, 486–487
tetrahedral geometry, 421–422, 426, 433
tetramethylpiperidide derivatives, 325
tetranuclear carboxylates, 230–231
tetranuclear complexes, 186–188
tetrapyrrole-type ligands, 319–320
tetrasodium-4,4′,6,6′-tetracarboxy-2,2′-bipyridine ligand, 484–485
tetravalent chemistry
alkoxides, 321, 322–324, 328–329
amides, 321, 325–327
amidinates, 321, 327–328
carbenes, 321, 329–330
cerium, 313–320, 321–333
cerocenes, 321, 330–332
coordination compounds, 313, 315–320
cyclooctatetraenyl complexes, 321, 330–332
cyclopentadienyl complexes, 321, 328–329
β-diketonates, 313, 317–319
dioxides, 314–315
future outlooks, 332
halides, 175–176, 313–314, 316
halogeno complexes, 313, 316
inorganic compounds, 313–320
ligand complexes, 317–320
multi-ligand complexes, 317–320
organometallics, 321–333
oxidation states, 313–320, 321–333
oxo acids, 313, 316–317
porphyrinates, 313, 316, 320
pseudo-organometallics, 321–328
salts, 315
sandwich complexes with tetrapyrrole-type ligands, 319–320
Schiff-bases, 313, 319
siloxides, 205–206, 211, 321, 323
synthesis, 321–332
tetrapyrrole-type ligands, 319–320
TGA *see* thermogravimetric analysis

theory
  lanthanide-induced shifts, 502–506
  superconducting material magnetism, 371–372, 374–375
theranostics, 68
thermal decomposition, 394–395
thermal synthesis, 226, 234, 386
thermochemical cycles, 45, 48
thermochemical properties, 43
thermodynamics
  cluster complexes, 416–417
  group trends, 48–52
  organometallic chemistry, 83, 88
  self-assembly lanthanide supramolecular chemistry, 486–487
thermoelectrics
  borides, 263, 267–269, 276
  borocarbonitrides, 275–276
  carbides, 263, 276
  nitrides, 263, 276
thermogravimetric analysis (TGA), 477
thermolysis, 219–220
thiolates, 215–221
  bonding, 215–221
  cluster chemistry, 217–219
  molecular synthesis, 219–220
  organometallics, 215–217
  physical properties, 220–221
  thermolysis, 219–220
thioureas, 567
thorin, 569
thulium
  aryls, 303–304
  color characteristics, 136, 137, 139
  halide valency, 163, 167–168, 169, 170–171
  NIR luminescence, 347–348
  photophysics, 348
  sol-gels, 356–359
  upconversion, 364
tiling compounds, 269–270, 276
time-resolved imaging, 551
Tishchenko reaction, 464, 473
titrations, 541, 543, 544–545, 546
top-down nanomaterial synthesis, 406–407
toxicity, 65–66, 69, 551
TPA *see* two-photon absorption
trace elements, 1–18
trains, superconducting materials, 378, 380
transesterification, 475, 478
transition metals
  borides, 269–271
  borocarbides, 274
  boronitrides, 274
  carbides, 272
  coordination numbers, 75–76
  exchange-coupling interactions, 153–158
transitions
  europium, 137–138
  lanthanide ion luminescence, 120, 121–122, 129
  terbium, 138–139
  vibronic levels, 120
transmetallation, 96, 547
transmission electron microscopy (TEM), 449, 451
transverse relaxation, 522–523, 527–529
treatments, ores, toxicity, 66
triaryls, 303–304
bis(trimethylsilyl)methyl compounds, 301
tricapped trigonal prismatic geometry, 76
triflate catalysis, 438, 448–449, 452–453
triglyceride transesterification, 475, 478
trigonal bipyramidal geometry, 75, 422, 423
trimetallic nitride, 497–498
trinuclear lanthanide complexes, 186
triple-decker lanthanide complexes, 282–286
triplet state energy correlation, 135, 144, 147–148
tris-cyclopentadienyl complexes, 308–309
tris(*tert*-butyl) methoxide derivatives, 200–201
(trimethylsilyl)methyl compounds, 300–301
trivalent chemistry
  chalogenolates, 215–217
  cyclopentadienyl, 307–310
  siloxides, 205–211
tropolonate, 355
two-dimensional (2D) planar borocarbides, 273–274
two-photon absorption (TPA), 389, 390–391
two-photon laser scanning microscopy, 556–557

ultraviolet (UV) emission
  lanthanide ion luminescence, 139
  screening agents, 412
  titrations, 544–545
unsymmetrical ligands, 537
upconversion
  activators, 391–392, 402
  bioimaging, 389–403
  carboxylates, 225
  classifications, 390–391
  energy transfer, 391
  excited state absorption, 391
  host matrices, 392–393
  lanthanide ion luminescence, 135, 136, 142
  luminescence
    bioimaging, 389–403
    lanthanide ions, 135, 136, 142
    NIR materials, 347, 364–365, 366
  nanoparticles
    bioimaging, 389–403
    chemical surface modifications, 395–398
    coprecitation, 393–394
    decomposition, 394–395
    future outlooks, 402

hydrothermal synthesis, 395
in vivo imaging, 389, 398–402, 403
layer-by-layer assembly, 397–398
ligand attraction, 397
ligand engineering, 396–397
luminescent bioimaging, 389–403
NIR materials, 398–402
phosphors, bioimaging, 389–403
polymerization, 398
solvothermal synthesis, 395
surface chemical modifications, 395–398
synthesis, 389, 393–395
thermal decomposition, 394–395
visible light, 398–400
NIR luminescence, 347, 364–365, 366
photon avalanche, 391
principles, 390–391
second-harmonic generation, 389, 390–391
selection criteria, 389, 391–393, 402, 403
sensitization, 392, 403
two-photon absorption, 389, 390–391
uploading concentration, 551
uptake, living cells, 552
UV *see* ultraviolet

vacant coordination sites, 93
valency
see also variable valency
bonds, 415–416
configuration, 27–29
halides, 161–173
orbitals, 27, 28
radial charge density, 27, 28
valence electrons, 155–156, 172, 415–416, 421, 433
vapor phase synthesis, 406, 407
variable valency, 43–50
half-wave potentials, 47, 50
metallic lanthanides, 43–50
orbital shapes, 43–44
oxidation states, 43–50
reduction/redox potentials, 46–47, 49–50
Vasovist®, 525
versatility, luminescent bioprobes, 552–553
vibrational modes, 118, 119–121, 122–123
vibronic excitation, 120
visible emission, 139–140
visible light *in vivo* imaging, 398–400
volatility, geology/geochemistry, 3
voltage measurements, 379–380
volume elements (voxels), 522
vortices, 374

waste disposal, 66
water
geology/geochemistry, 2
heterogeneous catalysis, 476
luminescent properties, 547–549
organic synthesis, 448–455
water-soluble complexes, 537
wavelength extension, 353
Werner cluster complexes, 419–420, 433
wires superconducting materials, 378, 379–380
Wöhler's metallothermic reduction, 162–163
W plots, 44, 49, 50

XAFS *see* X-ray absorption fine structure
xenoliths, 10, 14, 18
X-ray absorption fine structure (XAFS), 58
X-ray characterization, 179–181
X-ray crystallography, 57
X-ray crystal structure analysis, 481–482
X-ray diffraction (XRD)
coordination chemistry, 77–78
endohedral fullerenes, 496–497
halides, 176
solvento complexes, 58–59
X-ray spectroscopy, 542, 557
XRD *see* X-ray diffraction

ytterbium
catalysis, 452–453
chalogenolates, 216, 219–220
color characteristics, 136, 140
conjugated Schiff-base ligands, 282, 285
halide valency, 161, 162, 163–168, 169
NIR luminescence, 347–348
β-diketone ligands, 350–351
heteropolymetallic lanthanide complexes, 353–354
8-hydroxyquinolinate-based lanthanide complexes, 352–353
ionic liquids, 364
photophysics, 348–349
silicates, 360–361
sol-gels, 356–359
upconversion, 364–365
optodes, 568
self-assembly supramolecular chemistry, 482, 492–493
yttrium
3d metal comparisons, 107
alkyls, 299–301
aqueous solutions, 56–57, 58–59
catalysis, 448
coordination chemistry, 73, 79–80
geochemistry, 2–3
medical diagnostics, 68
siloxides, 210
solvento complexes, 56–57, 58–59
superconducting materials, 372, 373, 375–378
yttrium-barium-copper-oxide superconducting materials, 373, 375–377, 378–379

Zeeman effect, 31, 33
zeolites, 475
zero magnetic inductance, 371
zero oxidation states, 44
zero resistivity, 371
zero-valent bonding, 86
zigzag chains, 425–430
zinc
  luminescent bioprobes, 547
  self-assembly lanthanide supramolecular chemistry, 492–493
  triflates, 452–453
zinc–neodymium complexes, 286–289, 292, 294–296
zirconium halides, 430–431
Z-plots, 43–44, 49, 50, 52
zwitterions, 239, 244, 246, 247

Abbreviations and Acronyms used in this Volume

γ-CD	γ-Cyclodextrin
^{i}Bu	Secondary Butyl
^{t}Bu	Tertiary Butyl
^{c}HTC	2,2-(2-Pentene-1,5-diyl)Trimethylene Carbonate
(DOS	Density of States
1,4-BDC	1,4-Benzene Dicarboxylate
1-MeTMC	1-Methyl Trimethylene Carbonate
abptz	4-Amino-bis(2,6-(2-Pyridyl))-1,3,5-Triazine
AFM	Atomic Force Microscopy
AO	Acridine Orange
AO	Atomic Orbital
ATPE	Addition De Photons Par Transfert D'énergie
BBL	β-Butyrolactone
BDC	1,4-Benzenedicarboxylate
bipy	2,2′-Bipyridyl
BMS	Bulk Magnetic Susceptibility
bpy	Bipyridine
BTC	1,3,5-Benzenetricarboxylate
Bu	Butyl
CAI	Calcium–Aluminum Refractory Inclusions
CAN	Ceric Ammonium Nitrate
CA	Contrast Agent
CCR	Cross-Correlation
CCT	Correlated Color Temperature
CEA	Carcinoembryonic Antigen
CFL	Compact Fluorescent Lamps
CIE	Commission Internationale De L'éclairage
CMP	Chemical–Mechanical Planarization
CN	Coordination Number
COHP	Crystal Orbital Hamiltonian Population
COOP	Crystal Orbital Overlap Populations
COSY	Correlation Spectroscopy
cote	Cyclooctatetraene
CO	Carbon Monoxide
Cp*	Permethylcyclopentadienyl
CPL	Circular Polarized Luminescence
Cp	Cyclopentadienyl
CQS	Color Quality Scale
CRI	Color-Rendering Index
CRT	Cathode Ray Tube
CSF	Cerebrospinal Fluid
CSI	Chemical Shift Imaging
CT	Charge Transfer
CT	Computed Tomographic
CVD	Chemical Vapor Deposition
DABCO	1,4-Diazabicyclo[2.2.2]octane
DCM	Dichloromethane
dd	Dipole–Dipole
DFT	Density Functional Theory
dipic	2,6-Pyridinedicarboxylate
DLs	Detection Limits
DME	Dimethoxyethylene, $MeOCH_2CH_2OMe$
DMF	Dimethylformaldehyde
DMF	Dimethylformamide
DMM	Depleted Mantle Source of Morb
dmpu	N,N′-dimethylpropyleneurea
DMP	2,6-dimethylphenoxide
DMSO	dimethylsulfoxide
DOTA	1,4,7,10-tetraazacyclododecane-N, N', N'', N'''-Tetraacetic Acid
DOTA	1,4,7,10-tetraazacyclododecane-1,4,7,10-tetraacetic Acid
DTC	2,2-dimethyl Trimethylene Carbonate
DTPA	Diethylenetriaminepentaacetate
DTPA	Diethylenetriaminepentaacetic Acid
DVM	Discrete Variational Method
EAE	Experimental Autoimmune Encephalomyelitis
EDC	1-Ethyl-3-[3-dimethylaminopropyl]carbodiimide Hydrochloride
EDTA	Ethylenediaminetetraacetic Acid
ED	Electric Dipole
EG	Ethylene Glycol
EHMO	Extended Hueckel Molecular Orbital
ELISA	Enzyme-Linked Immunosorbent Assay
EL	Electroluminescence
EL	Electroluminescent
EOB	Ethoxy-Benzyl
ERs	Estrogen Receptors
ESA	Excited State Absorption
ESR	Electron Spin Resonance
ETU	Energy Transfer Upconversion
EXSY	Exchange Spectroscopy
FAME	Fatty Acid Methyl Esters
FFAs	Free Fatty Acids
FRET	Förster Resonant Energy Transfer
FT-ICR	Fourier Transform Ion Cyclotron Resonance
FTIR	Fourier Transform Infrared Spectroscopy
FWHM	Full Width at Half Maximum
G5P	Gene 5 Protein
GICs	Graphite Intercalation Compounds
GSA	Ground-State Absorption
HC	Hydrocarbons
HDVV	Heisenberg–Dirac–Van Vleck
HED	Howardite–Eucrite–Diogenite
HEV	Hybrid Electric Vehicles
hmpa	Hexamethylphosphoramide
HNSA	1-Hydroxy-2-Nitrobenzene-4-Sulfonic Acid
HOMO	Highest Occupied Molecular Orbital
HR-MS	High-Resolution Mass Spectroscopy
HREE	Heavy Rare Earth Elements
HSAB	Hard Soft Acid Base
HTSCs	High-Temperature Superconductors
ICP-AES	Inductively Coupled Plasma Atomic Emission Spectroscopy
ICP-MS	Inductively Coupled Plasma Mass Spectrometry
ILCT	Intraligand Charge Transfer
IL	Intraligand
IR	Infrared
ISE	Ion-Selective Electrode
IS	Inner-Sphere
LASC	Lewis Acid–Surfactant-Combined
LAXS	Large-Angle X-Ray Scattering
LbL	Layer-by-Layer
LB	Langmuir–Blodgett
LCAO	Linear Combination of Atomic Orbitals
LCDs	Liquid Crystal Displays
LDH	Lactate Dehydrogenase
LEDs	Light-Emitting Devices
LIS	Lanthanide Induced Shift
LLB	LaLi3tris(binaphthoxide)
LLCT	Ligand to Ligand Charge Transfer
LMCT	Ligand to Metal Charge Transfer
Ln	Generic Rare Earth Element
LREE	Light Rare Earth Elements
LSS	Liquid-Solid-Solution

LTSCs	Low-Temperature Superconductors
LUMO	Lowest Unoccupied Molecular Orbital
MAGLEV	Magnetic Levitating Trains
MCE	Magnetocaloric Effect
MCGE	Membrane-Coated Graphite Electrode
MD	Magnetic Dipole
mes	Mesityl
Me	Methyl
MLCT	Metal-to-Ligand Charge Transfer Transitions
MMAO	Modified Methylaluminoxane
MMA	Methyl Methacrylate
MOCVD	Metal Organic Chemical Vapor Deposition
MOFs	Metals–Organic Frameworks
MOH	Metal–Oh
MORB	Mid-Oceanic Ridge Basalts
MO	Molecular Orbital
MRA	Magnetic Resonance Angiography
MRI	Magnetic Resonance Imaging
NACAs	Necrosis-Avid Contrast Agents
naph	1,8-Naphthyridine
NAP	4-(*p*-Nitrophenylazo)-Pyrocathecol
NHS	*N*-Hydroxsuccinimide
NIR	Near Infrared
NIST	National Institute of Standards and Technology
NLO	Nonlinear Optics
NMRD	Nuclear Magnetic Relaxation Dispersion
NMR	Nuclear Magnetic Resonance
NOEs	Nuclear Overhauser Effects
NOx	Nitrogen Oxides
OCM	Oxidative Coupling of Methane
ODE	Octadecene
OIB	Oceanic Island Basalts
OLED	Organic Light-Emitting Diode
PAA	Polyacrylic Acid
PAH	Poly(Allylamine Hydrochloride)
PARACEST	Paramagnetic Chemical Exchange Saturation Transfer
PA	Photon Avalanche
PBD	Polybutadiene
PCR	Polymerase Chain Reaction
PCS	Pseudocontact Shift
PDMS	Polydimethylsiloxane
PEI	Polyethylenimine
PET	Positron Emission Tomography
PGK	Phosphoglycerate Kinase
PHAs	Polyhydroxyalkanoates
phen	1,10-Phenanthroline
Ph	Phenyl
PIP	Polyisoprene
PLA	Polylactide
PL	Photoluminescence
PMA	Phorbol 12-Myristate 13-Acetate
PMO	Perturbative Molecular Orbital
PSS	Poly(Sodium 4-Styrenesulfonate)
PVC	Poly(Vinyl Chloride)
PVP	Polyvinylpyrrolidone
QCM	Quartz Crystal Microbalance
QDs	Quantum Dots
RDC	Residual Dipolar Coupling
REEs	Rare Earth Elements
REMB	Rare Earth–Alkali-Metal–Binol
REOs	Rare Earth Oxides
RE	Rare Earth
RHIC	Relativistic Heavy-Ion Collider
RLS	Resonance Light Scattering
RMSD	Root Mean Square Deviation
ROP	Ring-Opening Polymerization
SA	Square Antiprismatic
SAUCI	Small-Animal Upconversion Imager
SCMs	Single-Chain Magnets
SDS-PAGE	Sodium Dodecyl Sulfate Polyacrylamide Gel Electrophoresis
SHG	Second-Harmonic Generation
SIM	Single-Ion Magnet
SMES	Superconducting Magnetic Energy Storage
SMM's	Single Molecule Magnets
SOFCs	Solid Oxide Fuel Cells
SQUID	Superconducting Quantum Interference Device
SR	Shift Reagent
SSCE	Silver–Silver Chloride Electrode
STPA	Simultaneous Two-Photon Absorption
TBM	Tris(*tert*-Butyl)Methoxide
TBP	Tri-*n*-Butyl Phosphate
TEM	Transmission Electron Microscopy
TERPY	2,2′:6′,2″-Terpyridyl
TEs	Thermoelectrics
TE	Echo Time
TFA	Trifluoroacetic Acid
TfOH	Trifluoromethanesulfonic Acid
TGA	Thermogravimetric Analysis
THF	Tetrahydrofuran
TMC	Trimethylene Carbonate
TOF	Time-of-Flight
TOPO	Tri-*n*-Octyl Phosphine Oxide
TOPO	Trioctylphosphine Oxide
TPA	Two-Photon Absorption
TPTZ	2,4,6-tri(2-Pyridyl)-1,3,5-triazine
TR	Repetition Time
TSA	Twisted Capped Square Antiprismatic
TTP	Tricapped Trigonal Prismatic
UCNPs	Upconversion Nanoparticles
UCNPs	Upconversion Nanophosphors
UV	Ultraviolet
VB	Valence Bond
VE	Valence Electron
VOCs	Volatile Organic Compounds
WERC	Water Exchange Rate Constant
XAFS	X-Ray Absorption Fine Structure
XANES	X-Ray Absorption near-Edge Structure
XRD–MEM	X-Ray Diffraction Maximum Entropy Method
XRF	X-Ray Fluorescence

Periodic Table of the Elements

Group →	1	2	3	4	5	6	7	8	9	10	11	12	13	14	15	16	17	18
Period → 1	1 H 1.0079																	2 He 4.0026
2	3 Li 6.941	4 Be 9.0122											5 B 10.811	6 C 12.0107	7 N 14.0067	8 O 15.9994	9 F 18.9984	10 Ne 20.179
3	11 Na 22.9898	12 Mg 24.305											13 Al 26.9815	14 Si 28.0855	15 P 30.9738	16 S 32.066	17 Cl 35.453	18 Ar 39.948
4	19 K 39.0983	20 Ca 40.078	21 Sc 44.9559	22 Ti 47.867	23 V 50.9415	24 Cr 51.996	25 Mn 54.9380	26 Fe 55.845	27 Co 58.933	28 Ni 58.693	29 Cu 63.546	30 Zn 65.409	31 Ga 69.723	32 Ge 72.64	33 As 74.9216	34 Se 78.96	35 Br 79.904	36 Kr 83.798
5	37 Rb 85.4678	38 Sr 87.62	39 Y 88.9059	40 Zr 91.224	41 Nb 92.9064	42 Mo 95.94	43 Tc 98.9062	44 Ru 101.07	45 Rh 102.9055	46 Pd 106.42	47 Ag 107.8682	48 Cd 112.41	49 In 114.818	50 Sn 118.710	51 Sb 121.760	52 Te 127.60	53 I 126.9045	54 Xe 131.29
6	55 Cs 132.9054	56 Ba 137.327	57 * La 138.9055	72 Hf 178.49	73 Ta 180.9479	74 W 183.84	75 Re 186.207	76 Os 190.2	77 Ir 192.22	78 Pt 195.08	79 Au 196.9665	80 Hg 200.59	81 Tl 204.3833	82 Pb 207.2	83 Bi 208.9804	84 Po (209)	85 At (210)	86 Rn (222)
7	87 Fr (223)	88 Ra (226.0254)	89 ** Ac (227.0277)	104 Rf (261.1088)	105 Db (262.1141)	106 Sg (266.1219)	107 Bh (264.12)	108 Hs (277)	109 Mt (268.1388)	110 Ds (271)	111 Rg (272)							

Atomic number → 3 (Li)

Atomic weight → 6.941 (Li)

Zintl border → between B and Al

* LANTHANIDES	58 Ce 140.12	59 Pr 140.9077	60 Nd 144.24	61 Pm (147)	62 Sm 150.36	63 Eu 151.96	64 Gd 157.25	65 Tb 158.9254	66 Dy 162.50	67 Ho 164.9304	68 Er 167.26	69 Tm 168.9342	70 Yb 173.04	71 Lu 174.967
** ACTINIDES	90 Th 232.0381	91 Pa 231.0359	92 U 238.0289	93 Np 237.0482	94 Pu (244)	95 Am (243)	96 Cm (247)	97 Bk (247)	98 Cf (251)	99 Es (252)	100 Fm (257)	101 Md (260)	102 No (259)	103 Lr (262)

Based on information from IUPAC, the International Union of Pure and Applied Chemistry (version dated 1st November 2004).
For updates to this table, see http://www.iupac.org/reports/periodic_table.